

# UNCLASSIFIED

AD NUMBER
AD811356
NEW LIMITATION CHANGE
TO Approved for public release, distribution unlimited
FROM Distribution authorized to U.S. Gov't. agencies and their contractors; Administrative/Operational Use; Dec 1966. Other requests shall be referred to Air Force Avionics Laboratory, Attn: AVPT, Wright-Patterson AFB, OH 45433.
AUTHORITY
AFWAL ltr, 25 Mar 1988

THIS PAGE IS UNCLASSIFIED

AFAL-TR-66-391  
VOLUME II

811356

**TECHNIQUES FOR  
AIRBORNE RADOME DESIGN  
VOLUME TWO**

**EDITOR-IN-CHIEF**

**JESSE D. WALTON, JR.  
GEORGIA INSTITUTE OF TECHNOLOGY  
ATLANTA, GEORGIA**

**TECHNICAL REPORT AFAL-TR-66-391, VOLUME II**

**DECEMBER 1966**



This document is subject to special export controls and each transmittal to foreign governments or foreign nationals may be made only with prior approval of AFAL (AVPT), Wright-Patterson AFB, Ohio 45433.

**AIR FORCE AVIONICS LABORATORY  
RESEARCH AND TECHNOLOGY DIVISION  
AIR FORCE SYSTEMS COMMAND  
WRIGHT-PATTERSON AIR FORCE BASE, OHIO**

**Best Available Copy**

## NOTICES

When Government drawings, specifications, or other data are used for any purpose other than in connection with a definitely related Government procurement operation, the United States Government thereby incurs no responsibility nor any obligation whatsoever; and the fact that the Government may have formulated, furnished, or in any way supplied the said drawings, specifications, or other data, is not to be regarded by implication or otherwise as in any manner licensing the holder or any other person or corporation, or conveying any rights or permission to manufacture, use, or sell any patented invention that may in any way be related thereto.

Copies of this report should not be returned to the Research and Technology Division unless return is required by security considerations, contractual obligations, or notice on a specific document.

PAGES \_\_\_\_\_  
ARE  
MISSING  
IN  
ORIGINAL  
DOCUMENT



PAGES NOT FILMED ARE BLANK

**TECHNIQUES FOR  
AIRBORNE RADOME DESIGN  
VOLUME TWO**

*EDITOR-IN-CHIEF*

*JESSE D. WALTON, JR.  
GEORGIA INSTITUTE OF TECHNOLOGY  
ATLANTA, GEORGIA*

This document is subject to special export controls and each transmittal to foreign governments or foreign nationals may be made only with prior approval of AFAL (AVPT), Wright-Patterson AFB, Ohio 45433.

## FOREWORD

The preparation of this report was initiated by the Information and Training Services division of F. W. Dodge, McGraw-Hill, Inc., 330 West 42nd Street, New York, New York 10036, on Air Force Contract Number AF-33(657)-11176, Project Number 4161, Task Number 416102. The work was completed by the Publications Services Division of Lino-Tech, Inc., 718 Broadway, New York, New York 10017, on Air Force Contract Number AF-33(615)-5020. The work was administered under the direction of the Antenna Radome Group, Electromagnetic Environment Branch, Electronic Warfare Division, Air Force Avionics Laboratory (AFSC), Systems Engineering Group (RTD), Wright-Patterson Air Force Base, Ohio. The Project Engineers were Mr. Gene Tarrants and Mr. Richard A. Ireland.

Included among those who cooperated in the preparation of the report are:

Jesse D. Walton, Jr. ....	Editor-in-Chief
Georgia Institute of Technology Atlanta, Georgia	
Harry Mileaf ....	Project Manager (Task completion)
Publications Services Division Lino-Tech, Incorporated	
Warren W. Yates ....	Associate Editor
Publications Services Division Lino-Tech, Incorporated	
Peter J. Zurita ....	Associate Editor
Publications Services Division Lino-Tech, Incorporated	
Lydia M. Zelaya ....	Editorial Assistant
Publications Services Division Lino-Tech, Incorporated	
Walter S. Baker ....	Project Manager (Task initiation)
Information and Training Services F. W. Dodge McGraw-Hill, Incorporated	

## AUTHORS

Donald Lee Loyet .....	Chapter 1
Hughes Aircraft Company	
Dr. J. H. Richmond .....	Chapter 2
Ohio State University	
Jerry Guarini .....	Chapter 3
CDB Enterprises, Inc.	
George Tatnall .....	Chapter 3
U.S. Naval Air Development Center Johnsville, Pennsylvania	
Jesse D. Walton, Jr. ....	Chapter 3
Georgia Institute of Technology	
Dr. G. M. Butler .....	Chapter 4
	Part I
Interpace Los Angeles, California	
S. A. Miller .....	Chapter 4
	Part II
Technical Plastics	
Eino J. Luoma .....	Chapter 5
	Part I
Emerson and Cuming, Inc.	
J. L. Pentecost .....	Chapter 5
	Part II
Melpar, Inc.	
Dr. E. F. Buckley .....	Chapter 5
	Part III
Emerson and Cuming, Inc.	
R. W. Sutton .....	Chapter 6
The Boeing Company	

Mr. Loyet, the author of Chapter 1, expresses his appreciation to Mr. R. C. McCormack, Senior Technical Editor for the Infrared Systems and Guidance Heads Laboratory of Hughes Aircraft Company, who reviewed this chapter and offered valuable suggestions. The author also gratefully acknowledges the assistance of Mr. S. Stevens, who encouraged this undertaking and proofread the rough draft.

Mr. Pentecost, the author of Chapter 5, Part II, gratefully acknowledges the permission to use portions of the Asilomar High-Temperature Symposium of September 1963.

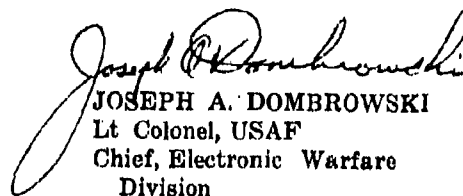
Mr. Sutton, the author of Chapter 6, thanks Mr. T. L. Norin and Mr. R. L. Noltimier for their contributions to the sections on Materials Design and Structural Design, respectively, and Miss Glenda Nichols for her assistance in typing the manuscript.

### ABSTRACT

This is the second report on radome design. It was written to provide information on the technological gains made since the first volume was released. Both volumes are intended to provide scientists and engineers working on radomes with a concise reference containing most of the information they will need. Topics covered in this volume are: physical design; electrical design; environmental simulation and testing; materials and construction; evaluation and correction; and hypersonic applications. Comprehensive bibliographies are included.

(This abstract is subject to special export controls and each transmittal to foreign governments or foreign nationals may be made only with prior approval of AFAL (AVPT), Wright-Patterson AFB, Ohio.)

The publication of this report does not constitute approval by the Air Force of the findings or conclusions contained herein. It is published only for the exchange and stimulation of ideas.

  
JOSEPH A. DOMBROWSKI  
Lt Colonel, USAF  
Chief, Electronic Warfare  
Division

## TABLE OF CONTENTS (cont)

<i>Paragraph</i>	<i>Page</i>
1-2.6. Transmission Loss . . . . .	33
1-2.7. Reflection Loss . . . . .	33
1-2.8. Pattern Distortion . . . . .	39
1-2.9. Variations in Phase . . . . .	39
1-2.10. Bandwidth . . . . .	42
1-2.11. Boresight Error and Derivatives . . . . .	43
1-2.12. Wall Thickness Tolerances . . . . .	44
1-2.13. Aerodynamic Heating and Thermal Stress . . . . .	44
1-2.14. Structural . . . . .	47
1-2.15. Size Limitations . . . . .	48
1-2.16. Attachment . . . . .	48
1-2.17. Handling . . . . .	48
1-3. Methods of Attaching Ceramic Radomes . . . . .	49
1-3.1. Introduction . . . . .	49
1-3.2. Types of Attachments . . . . .	51
1-3.3. Types of Loading . . . . .	51
1-3.3.1. Aerodynamic Forces . . . . .	51
1-3.3.2. Inertial Forces . . . . .	51
1-3.3.3. Pressure . . . . .	51
1-3.3.4. Vibrational Forces . . . . .	52
1-3.4. Types of Stress . . . . .	52
1-3.5. Attachment Joints . . . . .	53
1-3.6. Chemical Attachments . . . . .	54
1-3.7. Mechanical Attachments . . . . .	55
1-3.8. Design Examples . . . . .	55
1-4. Test Methods for Determining the Physical Properties of Radomes . . . . .	60
1-4.1. Introduction . . . . .	60
1-4.2. General Properties . . . . .	61
1-4.3. Environmental Tests . . . . .	61
1-4.4. Thermal Properties . . . . .	62
1-4.5. Electrical Properties . . . . .	63
1-4.6. Mechanical Properties . . . . .	64
1-5. Factors Affecting the Strength of Radomes . . . . .	70
1-5.1. Shape . . . . .	70
1-5.2. Thermal Environment . . . . .	70
1-5.3. Mechanical . . . . .	71
REFERENCES . . . . .	71

## CHAPTER 2

### RADOME DESIGN—ELECTRICAL

SYMBOLS . . . . .	78
2-1. Electrical Design Techniques . . . . .	79
2-1.1. General Design Considerations . . . . .	79

## TABLE OF CONTENTS (cont)

<i>Paragraph</i>	<i>Page</i>
2-1.2. Thin-Wall Radome Design .....	79
2-1.3. Half-Wave Radome Design .....	81
2-1.4. Radome Design by Insertion Phase Delay .....	88
2-1.5. Radome Sandwich Design .....	89
2-1.6. Dual-Frequency Airborne Radome Design .....	90
2-2. Application of Digital Computers to Radome Design .....	90
2-2.1. Introduction .....	90
2-2.2. Digital Optimization of Radome Walls .....	92
2-2.3. Complete Radome Design by Computer .....	95
2-3. Techniques for Electrical Evaluation of Electromagnetic Window and Radome Shapes .....	97
2-3.1. Introduction .....	97
2-3.2. Typical Shapes .....	97
2-3.3. Shape Definition .....	98
2-3.4. Computer Use .....	99
2-3.5. Electromagnetic Window Shapes .....	99
2-3.6. Conclusions .....	100
2-4. Boresight-Error Prediction Techniques .....	100
2-4.1. Introduction .....	100
2-4.2. Optical Methods Technique .....	101
2-4.3. Ray-Tracing Technique .....	101
2-4.4. Scattering Technique .....	102
2-4.5. Integral-Equation Technique .....	103
2-5. Metal-Loaded Radome Design .....	104
2-5.1. Metal Grating for Suppression of Cross-Polarization .....	104
2-5.2. Loading With Wire Grids or Perforated Metal Sheets .....	106
2-5.3. Resonant-Wall Designs .....	110
2-5.4. Slotted Metal Radomes .....	111
2-5.5. Dipole Feed-Through Radomes .....	113
2-6. Broadband Radome Design .....	116
2-6.1. Bandwidth of Solid-Wall Radomes .....	117
2-6.2. Broadband Three-Layer Sandwiches .....	120
2-6.3. Broadband Multilayer Sandwiches .....	121
2-6.4. Surface Treatment for Reduced Reflection .....	125
2-6.5. Broadband Metal-Loaded Radomes .....	125
2-6.6. Inhomogeneous Radomes .....	128
2-7. Tunable Radome Design .....	131
2-7.1. Summary .....	134
2-8. Millimeter-Wavelength Radome Design .....	135
2-9. Flush-Mounted Radiating Systems Design .....	137
2-9.1. Introduction .....	137
2-9.2. Slotted Waveguide Arrays .....	138
2-9.3. Other Flush-Mounted Radiating Systems .....	142
2-9.4. Geodesic Lenses .....	147
2-10. Space Frames for Radome Structural Support .....	149
2-10.1. Introduction .....	149

## TABLE OF CONTENTS (cont)

<i>Paragraph</i>	<i>Page</i>
2-10.2. Axial Supporting Member for Nose-Cone Radome	149
2-10.3. Quadripod Space Frames	150
2-10.4. Electrical Effects of Metal Ribs in Large Chin Radomes (Reference 97)	151
2-10.5. Diffraction by Obstacles in the Near Zone of an Antenna	154
2-10.6. Plane-Wave Scattering by Metal Ribs of Arbitrary Cross-Section Shape	158
2-10.7. Diffraction by Metal and Dielectric Rings	159
BIBLIOGRAPHY	167
A. Alleviation of Boresight-Error Problem by Control System Modification	167
B. Combination Radome-Irdome Design Techniques	167
APPENDIX	169
2-A1. Radome Design Curves	169
2-A1.1. The Interface Reflection Coefficients	169
2-A2. Solid-Wall Radome Curves	172
2-A3. Radome Sandwich Curves	173
2-A4. Frequency Bands and Wavelength	174
APPENDIX REFERENCES	175

## CHAPTER 3

### ENVIRONMENTAL SIMULATION AND TEST DATA

SYMBOLS	200
3-1. The Rain Environment	201
3-1.1. Rain Intensity and Frequency	201
3-1.2. Classification of Rain	202
3-2. The Mechanism of Rain Erosion	203
3-2.1. Conditions For Rain Damage in Materials	203
3-2.2. Materials That Resist Rain Damage	203
3-2.3. Experimental Considerations of Rain Erosion	203
3-3. Test Methods for Simulating Rain Erosion	206
3-3.1. The Centrifuge	206
3-3.2. The Rain Gun	207
3-3.3. Mithras Erosion Simulator	208
3-3.4. The Ballistic Range	209
3-3.5. The Rocket Sled	210
3-4. Sled Tests	210
3-4.1. NADC Tests	211
3-4.2. U. S. Naval Ordnance Test Station Runs	227
3-4.3. Sandia Tests	227
3-4.4. Summary of Sled Tests	227



## TABLE OF CONTENTS (cont)

<i>Paragraph</i>	<i>Page</i>
3-5. Thermal Shock Testing .....	229
3-5.1. Introduction .....	229
3-5.2. Convective Heat Transfer .....	231
3-5.2.1. The Hot Flue .....	231
3-5.2.2. The Supersonic Wind Tunnel .....	232
3-5.2.3. The Hot-Gas Wind Tunnel .....	232
3-5.2.4. Jet Engine Exhaust .....	232
3-5.2.5. Oxypropane Burners .....	232
3-5.2.6. Oxyacetylene Burners .....	232
3-5.2.7. Oxyhydrogen Burners .....	233
3-5.2.8. Rocket Motor Exhausts .....	235
3-5.2.9. Plasma Jets .....	235
3-5.3. Conductive Heat Transfer .....	236
3-5.3.1. The Hot Salt Bath .....	236
3-5.3.2. The Molten Metal Bath .....	236
3-5.4. Radiative Heat Transfer .....	236
3-5.5. Evaluating Thermal Shock Test Data .....	238
3-5.6. Choice of Thermal Shock Test Facilities .....	240
3-5.7. Results of Selected Thermal Shock Tests .....	240
3-5.7.1. Screening Tests .....	240
3-5.7.2. Aerodynamic Heat Simulation .....	242
3-5.7.3. Obtaining Thermal Data on Production Radomes .....	245
3-5.7.4. Quality Control on Proof Testing .....	247
3-6. Radiation Effects on Radome Materials .....	248
3-6.1. Introduction .....	248
3-6.2. Plastics .....	249
3-6.3. Ceramics .....	250
3-7. Vibration Testing .....	251
REFERENCES .....	253
APPENDIX 3A EFFECTIVE EMITTANCE CALCULATION .....	255
APPENDIX REFERENCES .....	255

## CHAPTER 4

### RADOME MATERIALS AND CONSTRUCTION

SYMBOLS .....	258
PART I. CERAMIC RADOMES .....	259
4-1. Introduction .....	259
4-2. Properties of Ceramic Radome Materials .....	260
4-2.1. General Comparison of Candidate Materials .....	260
4-2.1.1. Alumina .....	260
4-2.1.2. Glass-Ceramics .....	260

## TABLE OF CONTENTS (cont)

<i>Paragraph</i>	<i>Page</i>
4-2.1.3. Sintered Fused Silica	260
4-2.1.4. Beryllia	261
4-2.1.5. Other Ceramics	262
4-2.1.6. Summary	262
4-2.2. Evaluating Physical Property Data	262
4-3. Properties of Alumina Radome Materials	263
4-3.1. Porous Alumina and Sandwich Alumina Materials	268
4-3.2. Properties of Mosaic Alumina Construction	269
4-3.3. Composite Plastic-Alumina Radomes	269
4-4. Properties of Glass-Ceramic Radome Materials	271
4-5. Properties of Fused Silica	273
4-5.1. Vitreous Silica	273
4-5.2. Sintered Fused Silica	275
4-6. Properties of Beryllia Radome Materials	280
4-7. Properties of Inorganic-Bonded Glass Fiber Laminates	281
4-8. Processes For Fabricating Ceramic Radomes	284
4-8.1. Production of Alumina Radome Blanks	284
4-8.1.1. Raw Materials and Their Processing and Blending	285
4-8.1.2. Forming and Shaping the Radome Blank	286
4-8.1.2.1. Forming by Isostatic Pressing	286
4-8.1.2.2. Forming by Slip-Casting	286
4-8.1.3. Shaping, Sintering, Grinding, and Inspecting	287
4-8.1.4. Limitations of Alumina Radomes	288
4-8.1.5. Comparison of Alumina Radome Fabrication Project	288
4-8.1.6. Fabrication of Multilayer Alumina Sandwich Radomes	289
4-9. Fabrication of Glass-Ceramic Radomes	289
4-9.1. Radome Finishing	290
4-9.2. Production Capability	290
4-10. Fabrication of Sintered Fused Silica Radomes	290
4-10.1. Slip-Casting	291
4-10.2. Sintering	291
4-10.3. Finishing the Sintered Radome	291
4-10.4. Surface Treatments for Sintered Silica Radomes	291
4-11. Production of Beryllia Radomes	292
REFERENCES	293
 <b>PART II. REINFORCED PLASTIC RADOMES</b>	 295
4-12. Radome Material Design	295
4-13. The Anisotropic Nature of Fiber-Reinforced Plastic Radomes	295
4-14. Matrix Materials	296
4-15. Types of Glass Fibers Used in Radome Production	296
4-15.1. Drawing Continuous Filaments	299
4-15.2. Glass Fiber Composition and Properties	299

## TABLE OF CONTENTS (cont)

<i>Paragraph</i>	<i>Page</i>
4-16. Fabrication .....	302
4-16.1. Introduction .....	302
4-16.2. Filament Control .....	302
4-16.2.1. The Electromagnetic Tensioner .....	303
4-16.2.2. The Magnetic Tensioner .....	303
4-16.2.3. The Friction Tensioner .....	303
4-16.3. The Resin Bath .....	304
4-16.3.1. The Wet-Dip Method .....	304
4-16.3.2. The Pre-impregnation Method .....	305
4-16.3.3. The Hybrid Impregnation Method .....	305
4-16.4. Filament Winding .....	306
4-16.4.1. Helical Winding .....	306
4-16.4.2. The Circ-Longo Drop-Stitch Method .....	306
4-16.4.3. The Circ-Gore Method .....	308
4-16.4.4. The Circ-Longo Grind and Circ-Longo Sock Method .....	309
4-16.5. Methods of Cure .....	309
4-16.6. Dimensional Control .....	310
4-16.6.1. Physical Grinding Control: Ultrasonics ..	310
4-16.6.2. Electrical Grinding Control .....	310
4-16.6.3. Physical Thickness Measurement: The Feeler Gauge Method .....	311
4-16.7. Additional Methods of Composite Radome Fabrication	312
4-17. Finishing Methods .....	313
4-18. Part Removal Methods .....	313
REFERENCES .....	314
APPENDIX 4A. PROPERTIES OF SELECTED RESINS .....	315
APPENDIX 4B. DIELECTRIC PROPERTIES OF SELECTED RESINS, GLASSES, AND LAMINATES .....	321

## CHAPTER 5

### RADOME EVALUATION AND CORRECTION TECHNIQUES

SYMBOLS .....	332
PART I. MICROWAVE DIELECTRIC INSTRUMENTATION .....	335
5-1. Introduction .....	335
5-2. Dielectric Instrumentation Terminology .....	335
5-2.1. The Dielectrometer .....	335
5-2.2. The Interferometer .....	337
5-2.3. The Reflectometer .....	337
5-3. Interferometer, Reflectometer, and Ultrasonic Techniques for Quality Control of Radomes .....	337

## TABLE OF CONTENTS (cont)

<i>Paragraph</i>	<i>Page</i>
5-4. Applications of Interferometers, Reflectometers, and Physical Thickness Gages in Quality Control of Radomes	346
5-4.1. Sheffield Radome Thickness Gage	346
5-4.1.1. Typical Applications	346
5-4.1.1.1. Wall Thickness Gage During Final Inspection	346
5-4.1.1.2. Inside Diameter and In-Process Gage	346
5-4.2. Branson Vidigage—An Ultrasonic Physical Thickness Gage	348
5-4.2.1. Principle of Operation	348
5-4.2.2. Typical Applications	348
5-4.2.2.1. Methods Available	350
5-4.2.2.2. The Reflection Test	350
5-4.2.2.3. The Through-Transmission Test	350
5-4.2.2.4. Summary of Tests	350
5-4.3. North American Aviation—Microwave Thickness Gage	351
5-4.3.1. Typical Application	351
5-4.3.1.1. Instrument Sensitivity	351
5-4.3.1.2. Summary of Tests	352
5-4.4. Microwave Instruments Co.—Microwave Thickness Gages for Nonmetals	352
5-4.5. Microwave Instruments Co.—Dielectrometer Model 622A	352
5-4.6. A Microwave Reflectometer That Reads Dielectric Constant Directly	353
5-4.7. Emerson and Cuming, Inc.—The Ecco Interferometer	357
5-5. Techniques for Electrical Testing of Radomes and Panels at Elevated Temperatures	358
5-5.1. The Boeing Co.—X-Band High-Temperature Transmission Gage	358
5-5.1.1. X-Band High-Temperature Transmission Gage	358
5-5.1.2. Emerson and Cuming, Inc.—High-Temperature Reflectometer	359
 <b>PART II. MATERIAL TESTING AT VERY HIGH TEMPERATURES (2000°F TO 4000°F)</b>	 361
5-6. Introduction	361
5-6.1. Need for High-Temperature Data	361
5-6.2. Types of Materials Useful in the 2000 to 4000°F Range	361
5-6.2.1. Oxide Ceramics	361
5-6.2.2. Refractory Glass	362
5-6.2.3. Recrystallized Glass (Pyroceram)	362
5-6.2.4. Nonoxide Ceramics (BN, Si <sub>3</sub> N <sub>4</sub> )	362

## TABLE OF CONTENTS (cont)

<i>Paragraph</i>	<i>Page</i>
5-6.3. General Dielectric Behavior of Materials at High Temperatures	362
5-6.4. Problems Associated with High-Temperature Dielectric Measurements	364
5-7. Dielectric Measurement Techniques	364
5-7.1. General	364
5-7.1.1. The 1- to 5-Gc Region	364
5-7.1.2. The 5- to 15-Gc Region	364
5-7.1.3. The Region Above 15 Gc	364
5-7.1.4. Construction Materials for Specialized Equipment	364
5-7.2. Laboratory Equipment	365
5-7.2.1. Coaxial Techniques	365
5-7.2.2. Waveguide Techniques	367
5-7.2.3. Resonant Cavities for Use Above 5 Gc	370
5-7.2.4. Low-Frequency Cavity Designs (1 to 5 Gc)	373
5-7.2.5. Free-Space Techniques	374
5-8. Dielectric Data Processing	377
5-8.1. Manual Methods	377
5-8.2. Automated Computations	378
5-9. Thermal Measurements	379
5-9.1. Thermal Conductivity Measurements	380
5-9.2. Thermal Diffusivity Measurements	382
5-9.3. Specific Heat Measurements	384
5-9.3.1. Adiabatic Calorimetry	384
5-9.3.2. "Dropping" Calorimetry	385
5-10. Mechanical Property Measurements	385
5-10.1. Tensile Strength Measurements	385
5-10.2. Compressive Strength Measurements	389
5-10.3. Flexural Strength Measurements	389
5-10.4. Elastic Moduli	389
5-10.5. Thermal Expansion Measurements	390
<b>PART III. DESIGN, EVALUATION AND PERFORMANCE OF MODERN MICROWAVE ANECHOIC CHAMBERS</b>	<b>391</b>
5-11. Introduction	391
5-12. Design of Microwave Anechoic Chambers	391
5-12.1. Characteristics of Absorbing Materials	392
5-12.2. Shaping of the Anechoic Chamber	393
5-13. Evaluation of Microwave Anechoic Chambers as Antenna Pattern and Boresight Ranges	397
5-13.1. The Pattern Comparison Evaluation Method	398
5-13.1.1. Data Accumulation	399
5-13.1.1.1. Test Equipment	399
5-13.1.1.2. Pattern Recording	399
5-13.1.2. Data Reduction	400
5-13.1.3. Computation of Chamber Reflectivity	400
5-13.2. The Free-Space VSWR Evaluation Method	405

## TABLE OF CONTENTS (cont)

<i>Paragraph</i>	<i>Page</i>
5-13.3. The Field-Probe Evaluation Method	405
5-13.4. Comparison of Evaluation Methods and Their Applicability to Boresight Ranges	406
5-14. Performance of Microwave Anechoic Chambers As Antenna Pattern and Boresight Ranges	406
REFERENCES	407

## CHAPTER 6

### HYPERSONIC RADOME APPLICATIONS

SYMBOLS	414
6-1. Introduction	415
6-1.1. Determination of the Thermal Environment	416
6-1.2. The Structural Design	416
6-1.3. The Electrical Design	416
6-2. The Thermal Environment	417
6-2.1. Introduction	417
6-2.2. Aerodynamic Heating at Hypersonic Velocities	417
6-2.2.1. Ballistic Reentry	418
6-2.2.2. Glide Reentry	418
6-2.2.3. Orbital Decay Reentry	418
6-2.2.4. High-Acceleration Boost	418
6-2.3. Heating Rate and Surface Temperature Calculations	419
6-2.3.1. Heating Rates and Surface Temperatures of Glide Reentry Vehicles	419
6-2.3.1.1. Stagnation Point Heating, Laminar Flow	420
6-2.3.1.2. Stagnation Point Temperature	421
6-2.3.1.3. Turbulent Heating near the Sonic Point	421
6-2.3.1.4. Flat-Plate Heating, Laminar Flow	423
6-2.3.1.5. Flat-Plate Heating, Turbulent Flow	424
6-2.3.2. Heating Rates and Surface Temperatures of Ballistic Reentry Vehicles	424
6-2.3.2.1. Turbulent Heating Near the Sonic Point	424
6-2.3.2.2. Surface Temperatures of Ballistic Reentry Vehicles	425
6-2.3.3. Heating Rates and Surface Temperatures of Orbital Decay Reentry Vehicles	426
6-2.3.4. High-Acceleration Boost Vehicles	426

## TABLE OF CONTENTS (cont)

<i>Paragraph</i>	<i>Page</i>
6-3. The Structural Design of Radomes for Hypersonic Vehicles . . .	426
6-3.1. General Structural Design Considerations . . . . .	426
6-3.2. Calculation of Stresses in an Electromagnetic Window . . .	427
6-3.3. The Ablative Window . . . . .	429
6-3.4. The Thermal Shock Problem . . . . .	429
6-3.5. New Techniques . . . . .	430
6-4. Electrical Design of Radomes for Hypersonic Vehicles . . . . .	430
6-4.1. General Considerations . . . . .	430
6-4.2. Electrical Design of a Flat Window . . . . .	431
6-4.3. Electrical Design of Nose-Mounted Ogival Shaped Radomes . . . . .	433
6-4.4. Effect of Plasma on R-F Propagation . . . . .	433
6-4.4.1. Prediction of R-F Performance in a Plasma Environment . . . . .	434
6-4.4.2. Inhomogeneous Plasmas . . . . .	435
6-4.4.3. Plasma-Induced Antenna Pattern Distortion . . . . .	436
6-4.4.4. Allevation of Plasma Effects on R-F Propagation . . . . .	438
6-4.4.4.1. Operating Frequency Above Plasma Resonance . . . . .	438
6-4.4.4.2. Sharply Pointed Reentry Bodies . . . . .	438
6-4.4.4.3. Injection of Fluids Into the Boundary Layer . . . . .	438
6-4.4.4.4. Aerodynamic Spikes . . . . .	439
6-4.4.4.5. Steady Magnetic Field . . . . .	439
6-5. Materials For Use in Hypersonic Vehicle Electromagnetic Windows . . . . .	439
6-5.1. Introduction . . . . .	439
6-5.2. Ceramics . . . . .	440
6-5.2.1. Alumina . . . . .	440
6-5.2.2. Beryllia . . . . .	441
6-5.2.3. Pyroceram . . . . .	441
6-5.2.4. Slip-Cast Fused Silica . . . . .	441
6-5.2.5. Other Ceramics . . . . .	441
6-5.3. Organic Resin-Fiberglass Laminates . . . . .	441
6-5.4. Inorganic Laminates . . . . .	443
6-5.5. Ablative Materials . . . . .	446
6-6. Examples of Electromagnetic Windows . . . . .	448
6-6.1. General Considerations . . . . .	448
6-6.2. Examples of Glide Reentry Electromagnetic Vehicles . . .	450
6-6.2.1. Asset . . . . .	450
6-6.2.2. Dyna-Soar . . . . .	450
6-6.3. Ballistic Reentry Vehicles . . . . .	451
6-7. Future Radome Requirements . . . . .	452
6-7.1. Current State-of-the-Art . . . . .	452
6-7.1.1. Supersonic Aircraft . . . . .	452
6-7.1.2. Ground-to-Air and Air-to-Air Supersonic Missiles . . . . .	452

## TABLE OF CONTENTS (cont)

<i>Paragraph</i>	<i>Page</i>
6-7.1.3. Electromagnetic Windows for Hypersonic Vehicles .....	453
6-7.2. Future Electromagnetic Window Requirements .....	454
6-7.2.1. Aircraft .....	454
6-7.2.2. Offensive Missiles .....	456
6-7.2.3. Defensive Missiles .....	456
6-7.2.3.1. Missiles: Electronic Counter-measures .....	456
6-7.2.4. Aerospace Plane .....	456
6-7.2.5. Mars Exploration Vehicles .....	456
REFERENCES .....	456
INDEX .....	459



## LIST OF ILLUSTRATIONS

<i>Figure</i>		<i>Page</i>
<b>CHAPTER I</b>		
1-1.	Types of Solid-Wall Radomes .....	4
1-2.	Types of Laminated Radomes .....	5
1-3.	Ellipsoidal Radome .....	7
1-4.	Logarithmic Spiral Radome .....	7
1-5.	Ogival Radome .....	8
1-6.	Various Radome Shapes .....	10
1-7.	Radomes with Power Shapes .....	10
1-8.	Parabolic Radomes .....	10
1-9.	Ogival Radomes with Various Types of Nose Blunting .....	11
1-10.	Drag Coefficient vs Fineness Ratio for Several Mach Numbers .....	11
1-11.	Drag Coefficient vs Mach Number for Various Nose- Blunting Radii .....	12
1-12.	Maximum Surface Temperatures vs Radome Axial Stations .....	14
1-13.	Stagnation Point Temperature Gradients .....	15
1-14.	Maximum Thermal Stress vs Radome Axial Station .....	16
1-15.	Maximum Stress at Stagnation Point .....	17
1-16.	Stagnation Point Temperature Histories for Radomes Having Various Tip Radii .....	17
1-17.	Tensile Thermal Stress at Stagnation Point for Various Radome Tip Radii vs Flight Time .....	17
1-18.	Stagnation Point Temperature Histories for Radomes with Various Tip Radii and Teflon Protective Covers .....	18
1-19.	Cross Section of Radome Tip Protected by Ablative Cover .....	19
1-20.	Stagnation Point Electrical Effects for Radomes with 0.5-in. Tip Radius .....	20
1-21.	Electrical Index vs Fineness Ratio .....	21
1-22.	Relative Thermal Shock Resistance of Candidate Reentry Radome Materials as a Function of Thermal Shock Environment .....	28
1-23.	Maximum Surface Temperatures of Radome vs Tip Radii for Several Ceramic Materials .....	29
1-24.	Tensile Thermal Stress on Inner Surface of Radome vs Tip Radii for Several Ceramic Materials .....	30
1-25.	Radome Used for Electrical Tests .....	32
1-26.	Power Transmission Coefficient for Pyroceram (Parallel Polarization) .....	34
1-27.	Power Transmission Coefficient for Pyroceram (Perpen- dicular Polarization) .....	35
1-28.	Power Transmission Coefficient for Alumina (Parallel Polarization) .....	36
1-29.	Power Transmission Coefficient for Alumina (Perpen- dicular Polarization) .....	37
1-30.	Thickness/Free-Space Wavelength vs Dielectric Constant for Various Angles of Incidence and $ R_{\perp} ^2$ Equal to 90 Percent .....	39

## LIST OF ILLUSTRATIONS (cont)

<i>Figure</i>		<i>Page</i>
1-31.	E-Plane Transmission vs Offset Angle for Various Wall Thicknesses .....	39
1-32.	H-Plane Transmission Loss vs Offset Angle for Various Wall Thicknesses .....	40
1-33.	H-Plane Transmission Loss vs Offset Angle at Various Frequencies for Radome with Half-Wavelength Wall Thickness .....	40
1-34.	H-Plane Transmission Loss vs Offset Angle at Various Frequencies for Thin-Wall Radome .....	41
1-35.	Effect of Radome Wall Thickness on E-Plane Antenna Pattern .....	42
1-36.	Effect of Radome Wall Thickness on H-Plane Antenna Pattern .....	43
1-37.	Temperature Gradients at Stagnation Point for Pyroceram and Alumina Radomes with 1.0-in. Tip Radius and Various Wall Thicknesses .....	46
1-38.	Peak Inner Surface Tensile Thermal Stress for Radomes with Wall Thicknesses of One-Half and One-Twelfth Wavelength .....	47
1-39.	Peak Inner Surface Tensile Thermal Stress vs Radome Tip Radius for Two Cases .....	48
1-40.	Peak Inner Surface Tensile Stress vs Launch Mach Number .....	49
1-41.	Thickness of Teflon Ablative Cover at Tip vs Launch Mach Number for Pyroceram and Alumina Radomes .....	50
1-42.	Free-Body Diagram of Radome in Flight .....	52
1-43.	Types of Joint Loading .....	52
1-44.	Types of Joints .....	58
1-45.	Chemical Attachments .....	56
1-46.	Mechanical Attachments .....	58
1-47.	Combined Chemical-Mechanical Attachments .....	59
1-48.	Methods of Attaching Radome Mounting Ring to Missile or Aircraft Structure .....	60
1-49.	Methods of Attaching "A" Sandwich Radomes .....	61
1-50.	Stresses in Cylindrical Ring with Uniform Internal Pressure .....	66
1-51.	Comparison of Stresses on Thick- and Thin-Shell Radomes .....	67
1-52.	Variation of Stress Through Wall Thickness .....	68
1-53.	Measurement of Tensile Strength by Use of Ceramic Rings .....	69

## CHAPTER 2

2-1.	Electrical Properties of 99.5% Alumina Ceramic Material .....	80
2-2.	Broadband Study of Average Transmission Data of Very Thin Wall at C-Band .....	80
2-3.	Wall Thickness Tolerance of Average Transmission Data of Very Thin Wall at C-Band .....	80
2-4.	Wall Thickness Tolerance Study of Phase Data of Very Thin Wall at C-Band .....	81
2-5.	Broadband Study of Phase Data of Very Thin Wall at C-Band .....	81

## LIST OF ILLUSTRATIONS (cont)

<i>Figure</i>	<i>Page</i>
2-6. Broadband Study of Average Transmission Data of Thin Wall at X-Band .....	82
2-7. Wall Thickness Study of Average Transmission Data of Thin Wall at X-Band .....	82
2-8. Broadband Study of Phase Data of Thin Wall at X-Band ..	82
2-9. Wall Thickness Tolerance Study of Phase Data of Thin Wall at X-Band .....	82
2-10. F-106A/B Radome, Experimental and Predicted Characteristic Errors .....	83
2-11. $d/\lambda$ vs Incident Angle for Constant Transmission $ T ^2$ and Constant IPD°, Perpendicular Polarization .....	84
2-12. $d/\lambda$ vs Incident Angle for Constant Transmission $ T ^2$ and Constant IPD°, Parallel Polarization .....	85
2-13. End View of Radome and Cutting Planes .....	85
2-14. F-106A/B Radome, 45° Cut at $F_L$ , $F_o$ , $F_H$ — Crosstalk Error vs Look Angle, Before Correction .....	86
2-15. F-106A/B Radome, 45° Cut at $F_L$ , $F_o$ , $F_H$ — Crosstalk Error vs Look Angle, After Correction .....	87
2-16. Orientation of Horns Behind Radome .....	89
2-17. Transmission Characteristics of Final Design .....	90
2-18. Original Concept of Radome Size and Shape .....	91
2-19. Flat Panel Theoretical Data .....	91
2-20. IPD vs Angle of Incidence for "A" Sandwich Flat Panel at 6 gc .....	92
2-21. IPD vs Angle of Incidence for "A" Sandwich Flat Panel at 16 gc .....	92
2-22. Figure of Merit Contour Map for "A" Sandwich and the Path Taken in Arriving at Optimum Design .....	94
2-23. Computer Design Procedure .....	95
2-24. Subdivision of Computer Design Program .....	96
2-25. Analytic Determination of a Conic by 3 Points and 2 Slopes ..	97
2-26. Typical Radome Shapes .....	98
2-27. Typical Radial Plane Definition .....	99
2-28. Computer Program .....	99
2-29. Typical Electromagnetic Window Definition .....	100
2-30. Horn Antenna and Wedge Radome Used to Illustrate Integral-Equation Solution .....	104
2-31. Cross-Section View of Horn Antenna and Wedge Radome ..	104
2-32. Calculated Values of Incident and Total Electric Field Intensity Set Up in Wedge Radome by Horn Antenna at 9400 mc .....	105
2-33. Measured and Calculated Far-Field Patterns of Horn Antenna with Wedge Radome Using Integral-Equation Solution (H-Plane Patterns) .....	105
2-34. Combination Radome-Grating for Paraboloidal Antenna ..	105
2-35. Construction Details of Gratings .....	105
2-36. Electrical Characteristics of Thin Dielectric Sheet with Perforated Metal Sheet at Midplane .....	106

## LIST OF ILLUSTRATIONS (cont)

<i>Figure</i>	<i>Page</i>
2-37. Power Transmission of "A" Sandwich Radomes	108
2-38. Insertion Phase Delay of "A" Sandwich Radomes	108
2-39. Radomes Showing Metal Foil Coverage	109
2-40. Several Resonant-Wall Radome Configurations	110
2-41. Nose Radome of Resonant-Wall Type Covered with Dielectric	110
2-42. Slotted Metal Sheet	111
2-43. Calculated Transmission Coefficient as a Function of $k_a$	111
2-44. Transmission Loss as a Function of Frequency (Normal Incidence)	112
2-45. Measured Transmission Loss as a Function of Frequency (Oblique Incidence)	112
2-46. Experimental Setup for Radiation Pattern Measurements	113
2-47. Silver Slotted Radome for Boeing 707	113
2-48. Antenna Patterns of Metal Radome Taken at Several Frequencies	114
2-49. Antenna Patterns of Metal Radome at 4.875 gc Taken at Different Scan Angles, $\phi$	115
2-50. Plane Version of Dipole Feed-Through Radome with Pyramidal Horn	116
2-51. Coordinate System for Dipole Array	116
2-52. Driving-Point Resistance vs Scan Angle for Large Arrays	117
2-53. Efficiency vs Scan Angle for Impedance-Matched Arrays	117
2-54. Transmission Coefficient vs Frequency for Lossless Solid-Wall Radome, Showing Pass Bands, Stop Bands, and Bandwidth	118
2-55. Thickness Times Bandwidth for Lossless Thin-Wall Radomes with Perpendicular Polarization	118
2-56. Thickness Times Bandwidth for Lossless Thin-Wall Radomes with Parallel Polarization	119
2-57. Contours of Minimum Power Transmission Coefficient over Broad Frequency Band for Solid-Wall Radomes with Perpendicular Polarization	119
2-58. Contours of Minimum Power Transmission Coefficient over Broad Frequency Band for Solid-Wall Radomes with Parallel Polarization	120
2-59. Power Transmission Coefficient vs Frequency for Thin-Wall Radomes	121
2-60. Power Transmission Coefficient vs Frequency for Lossless "A" Sandwich with Normal Incidence	122
2-61. Power Transmission Coefficient vs Frequency for Lossless "A" Sandwich with Oblique Incidence and Perpendicular Polarization	122
2-62. Power Transmission Coefficient vs Frequency for Lossless "A" Sandwich with Oblique Incidence and Parallel Polarization	123
2-63. Initial Transmission Volume for Case 1	124
2-64. Final Transmission Volume for Case 1	124

## LIST OF ILLUSTRATIONS (cont)

<i>Figure</i>		<i>Page</i>
2-65.	Time History for Case 2 .....	125
2-66.	Transmission Curves for Case 3 .....	126
2-67.	Transmission Curves for Case 4 .....	126
2-68.	Time History for Case 4 .....	127
2-69.	Transmission Curves for Case 6 .....	127
2-70.	Transmission Curves for Case 5 .....	128
2-71.	Transmission Curves for Solid-Wall Radome with 60° Angle of Incidence and Perpendicular Polarization .....	128
2-72.	Transmission Curves for Single "A" Sandwich Radome with 60° Angle of Incidence and Perpendicular Polarization .....	128
2-73.	Impedance-Matched Thick-Skin Single Sandwich .....	129
2-74.	Transmission Curves for Impedance-Matched Thick-Skin Sandwich Radome with 60° Angle of Incidence and Perpen- dicular Polarization .....	129
2-75.	Transmission Curves for Impedance-Matched Thick-Skin Sandwich Radome with Wires Parallel to Electric Vector, Perpendicular Polarization .....	129
2-76.	Transmission Coefficient vs Angle of Incidence for Homo- geneous and Inhomogeneous Radomes .....	130
2-77.	Magnitude of Reflection from Plane Lossless Dielectric Walls for Normal Incidence of Plane Wave as a Function of Thickness .....	132
2-78.	Magnitude of Reflection from Symmetrically Inhomoge- neous Dielectric Wall .....	133
2-79.	Conditions for Maximum Transmission Efficiency for Loss- less Solid-Wall Radome with Parallel and Perpendicular Polarization .....	133
2-80.	Conditions for Maximum Transmission Efficiency for Loss- less, Symmetrical Three-Layer Sandwich with $\epsilon_r = 4$ and $d_0 = 0.05\lambda_0$ .....	135
2-81.	Broadband Study of Average Transmission Data of Ceramic Half-Wave Wall at K-Band .....	136
2-82.	Broadband Study of Phase Data of Ceramic Half-Wave Wall at K-Band .....	137
2-83.	TE and TM Slotted Waveguides Used as Radiating Elements in Arrays .....	138
2-84.	TE and TM Slot Arrays in Monopulse System .....	138
2-85.	TE and TM Slot Arrays in Monopulse System .....	139
2-86.	Sum and Difference Patterns of Monopulse Antenna Using Plane of TE Slots with 1/3 Overlap .....	140
2-87.	Sum and Difference Patterns of Monopulse Antenna Using Plane Array of TM Slots with 1/2 Overlap .....	141
2-88.	Sum and Difference Patterns of Monopulse Antenna Using Plane Array of 16 TM Slots .....	142
2-89.	Sum and Difference Patterns of Monopulse Antenna Using Plane Array of 16 TE Slots .....	143
2-90.	Scanning System of Linear Arrays on Cone .....	144
2-91.	Rear View of 8-Array Cone Showing Feed Configuration ..	144

## LIST OF ILLUSTRATIONS (cont)

Figure		Page
2-92.	$\theta$ -Patterns in Plane of Scan for 8-Linear Array Cone .....	145
2-93.	Pattern in Plane Perpendicular to Plane of Scan for 8-Linear Array Cone Scanned $10^\circ$ .....	146
2-94.	Helical Waveguide Frequency Scan Cone .....	146
2-95.	Multiple-Disk Cone with Helical Waveguide Scanner .....	146
2-96.	Rectangular Array Feeding Hyperbolic Plates .....	146
2-97.	End View of Conical Transmission Line Antenna .....	147
2-98.	Cross-Section View of Transmission Line Antenna .....	147
2-99.	Definition of Lens Patterns .....	147
2-100.	Patterns of Beam Elevation Positioning Lens Antenna .....	148
2-101.	Geodesic Lens Mounted in Nose Cone .....	149
2-102.	Antenna-Radome System Using Long Focal Length Dish and Central Structural Cylinder .....	149
2-103.	Cross-Section View of Dish Antenna, Nose-Cone Radome, and Central Structural Cylinder .....	150
2-104.	Far-Field Pattern of Dish with Two-Horn Feed and $0^\circ$ Scan Angle .....	150
2-105.	Far-Field Pattern of Dish with Two-Horn Feed and $10^\circ$ Scan Angle .....	151
2-106.	Far-Field Pattern of Dish with Two-Horn Feed and $15^\circ$ Scan Angle .....	152
2-107.	Quadripod Space Frame .....	153
2-108.	Quadripod and Long Focal Length Fixed-Feed Antenna .....	153
2-109.	H-Plane Patterns of Long Focal Length Antenna in Space Frame .....	153
2-110.	E-Plane Patterns of Long Focal Length Antenna .....	154
2-111.	Shaped-Beam Antenna .....	155
2-112.	Cylinder Perpendicular to Generating Element of Reflector .....	155
2-113.	Cross Section of Antenna in Transverse Plane Showing Location of Cylinders and Dimensions of Cylinder Spacing .....	155
2-114.	Comparison of Principal Longitudinal Plane Pattern with and without Cylinder .....	155
2-115.	Measured Principal Transverse Plane Pattern of Antenna with and without Cylinders, Position 1 .....	156
2-116.	Measured Principal Transverse Plane Pattern of Antenna with and without Cylinders, Position 2 .....	156
2-117.	Measured Principal Transverse Plane Pattern of Antenna with and without Cylinders, Position 3 .....	157
2-118.	Measured Principal Transverse Plane Pattern of Antenna with and without Cylinders, Position 4 .....	157
2-119.	Scattering Patterns of Perfectly Conducting Cylinders of Circular, Square, and I-Beam Cross-Section Shapes .....	158
2-120.	Dielectric Wall, Fenestrated by I-Beam Members .....	159
2-121.	Insertion Phase Delay; Perpendicular Polarization at $45^\circ$ Incidence; I-Beam Perpendicular to E-Field .....	159
2-122.	Patterns of Magnetic Line Source on Axis of Metal Toroid .....	160
2-123.	Patterns of Magnetic Dipole at Center of Dielectric Toroid .....	161

## LIST OF ILLUSTRATIONS (cont)

<i>Figure</i>	<i>Page</i>
<b>APPENDIX</b>	
2-A1. Interface Reflection Coefficient for Lossless Dielectric with Perpendicular Polarization .....	168
2-A2. Interface Reflection Coefficient for Lossless Dielectric with Parallel Polarization .....	169
2-A3. Magnitude of Interface Reflection Coefficient vs Angle of Incidence for Lossless and Lossy Dielectric Materials .....	170
2-A4. Phase Angle of Interface Reflection Coefficient vs Angle of Incidence for Lossless and Lossy Dielectric Materials .....	171
2-A5. Brewster Angle vs Relative Dielectric Constant .....	172
2-A6. Angle of Refraction vs Angle of Incidence (Snell's Law) for Lossless Dielectric Media .....	173
2-A7. Conditions for Perfect Transmission Through Lossless Half-Wave Radomes .....	174
2-A8. Contours of Constant Power Transmission for Lossless Solid Walls with Perpendicular Polarization .....	175
2-A9. Contours of Constant Power Transmission for Lossless Solid Walls with Parallel Polarization .....	177
2-A10. Contours of 80 Percent Power Transmission Efficiency for Lossless Solid Walls with Perpendicular Polarization .....	178
2-A11. Power Transmission and Insertion Phase Delay vs Thickness for Lossless Solid Walls with $\epsilon_r = 2$ and Perpendicular Polarization .....	179
2-A12. Power Transmission and Insertion Phase Delay vs Thickness for Lossless Solid Walls with $\epsilon_r = 2$ and Parallel Polarization .....	180
2-A13. Power Transmission and Insertion Phase Delay vs Thickness for Lossless Solid Walls with $\epsilon_r = 4$ and Perpendicular Polarization .....	181
2-A14. Power Transmission and Insertion Phase Delay vs Thickness for Lossless Solid Walls with $\epsilon_r = 4$ and Parallel Polarization .....	182
2-A15. Power Transmission and Insertion Phase Delay vs Thickness for Lossless Solid Walls with $\epsilon_r = 6$ and Perpendicular Polarization .....	183
2-A16. Power Transmission and Insertion Phase Delay vs Thickness for Lossless Solid Walls with $\epsilon_r = 6$ and Parallel Polarization .....	184
2-A17. Power Transmission vs Thickness for Lossless Solid Walls with $\epsilon_r = 9$ and Perpendicular Polarization .....	185
2-A18. Power Transmission vs Thickness for Lossless Solid Walls with $\epsilon_r = 9$ and Parallel Polarization .....	185
2-A19. Insertion Phase Delay vs Thickness for Lossless Solid Walls with $\epsilon_r = 9$ and Perpendicular Polarization .....	186
2-A20. Insertion Phase Delay vs Thickness for Lossless Solid Walls with $\epsilon_r = 9$ and Parallel Polarization .....	186

## LIST OF ILLUSTRATIONS (cont)

<i>Figure</i>	<i>Page</i>
2-A21. Nomograph Giving Weight of Tangent Ogive Nose in Terms of Base Diameter, L/D Ratio, Wall Thickness, Material Specific Weight, and Very Low Material Volume .....	187
2-A22. Nomograph Giving Weight of Tangent Ogive Nose in Terms of Base Diameter, L/D Ratio, Wall Thickness, Material Specific Weight and Low Material Volume .....	188
2-A23. Nomograph Giving Weight of Tangent Ogive Nose in Terms of Base Diameter, L/D Ratio, Wall Thickness, Material Specific Weight, and Moderate Material Volume .....	189
2-A24. Nomograph Giving Weight of Tangent Ogive Nose in Terms of Base Diameter, L/D Ratio, Wall Thickness, Material Specific Weight, and High Material Volume .....	190
2-A25. Contours of Constant Power Transmission Efficiency for "A" Sandwich with 95 Percent Power Transmission Coefficient .....	191
2-A26. Contours of Constant Power Transmission Efficiency for "A" Sandwich with 90 Percent Power Transmission Coefficient .....	192
2-A27. Contours of Constant Power Transmission Efficiency for "A" Sandwich with 85 Percent Power Transmission Coefficient .....	193
2-A28. Contours of Constant Power Transmission Efficiency for "A" Sandwich with 80 Percent Power Transmission Coefficient .....	194
2-A29. Conditions for Maximum Transmission Efficiency for Pyrocera Air-Core Sandwiches with Perpendicular Polarization and Various Angles of Incidence .....	195
2-A30. Conditions for Maximum Transmission Efficiency for Alumina Air-Core Sandwiches with Perpendicular Polarization and Various Angles of Incidence .....	196
2-A31. Conditions for Maximum Transmission Efficiency for "A" Sandwiches with Perpendicular Polarization and Various Angles of Incidence .....	197
2-A32. Free-Space Wavelength vs Frequency .....	198

## CHAPTER 3

3-1. Instantaneous Rain Rate Expectancy for New Orleans (Ref. 2) .....	203
3-2. Rain Rate vs Altitude for Normal Rain and Mature Thunderstorm (Ref. 2) .....	204
3-3. Particle Size Distribution of Natural Rainfall (Ref. 3) .....	205
3-4. Test Specimen for "Whirling Arm" Rain Erosion Simulator .....	206
3-5. Diagrammatic Arrangement of Supersonic Liquid Drop Impact Apparatus .....	207
3-6. Projectile About to Strike 2-mm Diameter Water Drop at 1200 ft/sec .....	208



## LIST OF ILLUSTRATIONS (cont)

<i>Figure</i>	<i>Page</i>
3-7. Projectile About to Strike 2-mm Diameter Water Drop at 3000 ft/sec .....	208
3-8. Projectile with Molded Polyethene Body for Carrying Solid Specimen .....	208
3-9. Projectile with Molded Polyethene Body for Carrying Sheet Specimen .....	208
3-10. View of Model, without Sleeve, in Extreme Downstream Position and Water Nozzle in Extreme Upstream Position ..	209
3-11. Test Photos of Water Slug with Sleeved Model .....	209
3-12. Uptrack View of NADC SNORT Track .....	212
3-13. SNORT Sled Showing Methods of Attaching Test Specimens. Coors Porcelain 99% Alumina Radome on Right (Head-On View) and Corning Glass Ware Pyroceram Radome on Left .....	213
3-14. Coors Porcelain 99% Alumina (AD-99) Radome with $t = 0.050$ in. on Right (Head-On View) Survived the Environment. Corning Pyroceram with $t = 0.050$ in. and Nylon Tip on Left Survived the Environment. (Maximum Run Velocity = 1960 ft/sec) .....	214
3-15. Brunswick Corp. Filament-Wound Radome with Vibrin 135 and $t = 0.100$ in. (Left). Zenith Plastics Compression Molded Diallyl 128 with $t = 0.100$ in. (Right) .....	215
3-16. Brunswick Radome (Left) Is Heavily Eroded Over First Inch of Tip Area, with Secondary Erosion Over Next Two Inches. Zenith Radome (Right) Has Minor Erosion on Tip, with Negligible Pitting as Far Back as $5\frac{1}{2}$ in. (Maximum Run Velocity = 1985 ft/sec) .....	216
3-17. USNADC Fiberglass Laminate Radome with $t = 0.250$ in. (Left). USNADC Fiberglass Laminate Radome with $t = 2.250$ in. and Spike ( $1/r = 3.4$ ) (Right) .....	216
3-18. USNADC Radome without Spike Is Heavily Eroded Across Face of Dome. USNADC Radome with Spike Is Heavily Eroded Across Face of Dome Except for Small 2-in. Diameter Area at Base of Spike .....	217
3-19. Douglas Aircraft Ribbon-Wound Radome with DC-7141 Silicone and $t = 0.100$ in. (Left). Brunswick Corp. Filament-Wound Radome with Vibrin 135 and $t = 0.050$ in. (Right) .....	217
3-20. Douglas Radome (Left) Is Lightly Eroded Over First 0.5 in. Brunswick Radome (Right) Is Heavily Eroded in Tip Area .....	218
3-21. Douglas Aircraft Ribbon-Wound Radome with DC-7141 Silicone and 1.5 in. Stainless Steel Tip (Left). Zenith Plastics Compression Molded Diallyl 128 with $t = 0.100$ in. (Right) .....	218

## LIST OF ILLUSTRATIONS (cont)

<i>Figure</i>	<i>Page</i>
3-22. Douglas Radome (Left) Is Very Lightly Eroded Aft of Tip, and Tip Is Loosened. Zenith Radome (Right) Has Minor Erosion on Tip, with Negligible Pitting as Far Back as 5½ in. ....	219
3-23. Brunswick Corp. Chopped Fibers with DC-2106 Silicone Resin Binder Radome, with $t = 0.375$ in., and Sprayed Ceramic Cap 0.015 in. Thick Deposited Over First 3 in. of Dome (Left). Corning Multifomed Fused Silica (CGW #7941) Radome with $t = 0.375$ in. (Right) ....	219
3-24. Brunswick Radome (Left); Synchro-Ballistic Photos Showed Ceramic Cap Completely Eroded During First Half of Rain Field and Plastic Body Heavily Eroded During Second Half of Rain Field. Corning Radome (Right); Synchro-Ballistic Photos Showed Dome Broke Before Rain Field Entrance Due to Poor Attachment Bonding. (Maximum Sled Velocity = 2775 ft/sec) ....	219
3-25. Coors 99% Alumina (AD-99) Radome with $t = 0.050$ in. (Left). Corning Pyroceram Radome with $t = 0.050$ (Right) ....	220
3-26. Coors Radome (Left) Survived Environment but Showed Evidence of Hairline Fracture Pattern. Corning Radome (Right) Failed During First Half of Rain Field (Maximum Sled Velocity = 2839 ft/sec) ....	220
3-27. Corning Radome (Bottom) Lost During First Rain Field ..	220
3-28. RDI Woven Fiberglass Sock Radome with Epoxy Resin and $t = 0.050$ in. (Left). Raytheon 97% Alumina Radome with $t = 0.050$ in. (Right) ....	221
3-29. RDI Radome (Left) Survived Environment + Received 1-in. Diameter Hole in Nose. Raytheon Radome (Right); Synchro-Ballistic Photos Showed Dome Broke Before Midpoint in Rain Field (Maximum Sled Velocity = 2908 ft/sec) ....	221
3-30. Corning Pyroceram (960X) Radome with $t = 0.090$ in. (Left). Coors 99% Alumina (AD-99) Radome with $t = 0.090$ in. (Right) ....	221
3-31. Corning Radome (Left). Synchro-Ballistic Photos Showed Dome Broke Before Rain Field. Coors Radome on Right Survived Rain Field but Broke After Middle of Rain Field (Maximum Sled Velocity = 2852 ft/sec) ....	221
3-32. Coors Radome (Bottom) Survived Rain Impact Well Beyond Peak Velocity but Broke in Second Half of Rain Field .....	222
3-33. Convair Slip-Cast Fused Silica Radome with $t = 0.350$ in. and Unglazed Round Tip on Left. Same Radome with Glazed Tip (Right) ....	222
3-34. Both Radomes Survived Environment but Showed Heavy Tip Erosion (Maximum Sled Velocity = 2950 ft/sec) ....	222
3-35. Convair Fused Silica Radome with Unglazed Tip After Test Shows Heavy Tip Erosion .....	223

## LIST OF ILLUSTRATIONS (cont)

<i>Figure</i>	<i>Page</i>
3-35. Convair Slip-Cast Fused Silica Radome with $t = 0.350$ in. and Unglazed Pointed Tip (Left). Same Radome with Glazed Tip (Right) .....	223
3-37. Convair Radome (Left) Broke Between 1975 and 3175 Feet of Run. Convair Radome (Right) Survived Environment but Showed Heavy Tip Erosion (Maximum Sled Velocity $= 2930$ ft/sec) .....	223
3-38. Coors 99% Alumina (AD-99) Radome with $t = 0.100$ in. (Left Rear). Douglas Ribbon-Wound Radome with Silicone Resin and $t = 0.100$ in. (Right Front). Special $1\frac{1}{2}$ -in. Long Stainless Steel Tip Is Bonded to Front of Douglas Radome. ....	224
3-39. Coors Radome (Left) Survived Environment with No Signs of Erosion. Douglas Radome (Right) Showed Heavy Erosion for 5 in. Behind Steel Tip (Maximum Sled Velocity $= 2852$ ft/sec) .....	224
3-40. Synchro-Ballistic Photos Showed Rocket Motor Breaking Loose from Vehicle .....	224
3-41. Convair Slip-Cast Fused Silica Radome with $t = 0.350$ in. (Left) Is Rerun of Radome Shown in Figure 3-33 (Left) with Metal Tip Added. Convair Slip-Cast Fused Silica Radome with $t = 0.350$ in. and Pointed Shape Glazed Tip (Right) .....	225
3-42. Convair Radome (Left) Survived Environment but Showed Minor Erosion Aft of Tip. Convair Radome (Right) Survived Environment but Showed Slight Erosion on Tip ....	225
3-43. Corning Multiformed Fused Silica Radome with $t = 0.350$ in. (Left). Attachment Area of this Radome Is Strengthened with Fiberglass Warp. Convair Slip-Cast Fused Silica Radome with $t = 0.350$ in. (Right) Is Rerun of Radome Shown in Figure 3-41 (Right) .....	225
3-44. Corning Radome (Left) Broke During First Half of Rain Field. Convair Radome (Right) Showed Additional Erosion in Tip Area .....	225
3-45. USNADC Fiberglass Hemisphere Radome with $t = 0.250$ in. (Left). Same Radome with Metallic Spike ( $1/r = 3.4$ ) (Right) .....	226
3-46. Both Radomes Survived Environment but Showed Heavy Erosion for Small Annular Ring at Base of Spike .....	226
3-47. Silicone-Impregnated Radome in Shrike Configuration (Left). Same Radome with Thicker Skin and Different Radius of Curvature (Right) .....	226
3-48. Shrike Configuration Radome (Left) Survived Environment but Showed Heavy Tip Erosion. Radome on Right Failed in Second Half of Rain Field .....	227
3-49. Synchro-Ballistic Photos of AEC-Sandia Epoxy Fiberglass Radome During Run No. 10 .....	229

## LIST OF ILLUSTRATIONS (cont)

<i>Figure</i>	<i>Page</i>
3-50. Standard Epoxy Fiberglass Radome After One Exposure to Rain Facility at 1100 ft/sec, Sandia Run No. 4 .....	229
3-51. Standard Epoxy Fiberglass Radome After One Exposure to Rain Facility at 1600 ft/sec, Sandia Run No. 5 .....	229
3-52. Supersonic Radome Rain Erosion Graph of Erosion Time vs Velocity .....	231
3-53. 600-Burner Oxyhydrogen Thermal Test Facility .....	233
3-54. Water-Cooled Oxyhydrogen Burners in Thermal Test Facility .....	234
3-55. Oxyhydrogen Thermal Test Facility in Operation .....	235
3-56. General Dynamics/Pomona Infrared High-Temperature Test Facility .....	237
3-57. High-Temperature Boresight Test Setup at General Dynamics/Pomona .....	238
3-58. High-Temperature Structural Test Setup at General Dynamics/Pomona .....	239
3-59. Temperature-Time History of Fused Silica Exposed to 300 Btu/sq ft-sec Heat Flux Environment .....	240
3-60. Setup for Evaluating Ceramic Materials in Exhaust of Oxyhydrogen Rocket Motor .....	242
3-61. Heat Flux of Exhaust of Oxyhydrogen Rocket Motor .....	243
3-62. Temperature Measurements of 1/4-in. Thick Slip-Cast Fused Silica Plate Located 14 in. from Exit Plane of Oxyhydrogen Rocket Motor .....	244
3-63. Temperature Measurements of 1/4-in. Thick Pyroceram Plate Located 14 in. from Exit Plane of Oxyhydrogen Rocket Motor .....	244
3-64. Temperature Measurements on 1/4-in. Thick Alumina Plate Located 14 in. from Exit Plane of Oxyhydrogen Rocket Motor .....	245
3-65. Oxyacetylene Test Facility .....	246
3-66. Outer Skin-Inner Skin Temperature vs Flight Time for Alumina Radome .....	246
3-67. Fused Silica Nose Cone Showing Mounting Brackets Cemented in Place with Adhesive Resin .....	247
3-68. Nose Cone Engulfed in Flame from Oxyacetylene Test Nozzle .....	248
3-69. Slip-Cast Fused Silica Nose Cone After Test .....	249
3-70. Calculated Inner Surface and Outer Surface Temperatures for Alumina (AD-99) Radome Exposed to Hot Flue Gas Test .....	250
3-71. Hemispherical and Toroidal Radomes Used to Obtain Thermal Shock Data .....	250
3-72. Graph of Temperature of Inside Surface of Radome Nose After Instant Immersion of Radome into Superheated, Molten Babbitt .....	251
3-73. Inner to Outer Wall Temperature Distribution vs Time .....	252

## LIST OF ILLUSTRATIONS (cont)

<i>Figure</i>		<i>Page</i>
<b>CHAPTER 4</b>		
4-1.	Effect of Porosity on Room-Temperature Bend Strength of Aluminas (Ref. 5) .....	263
4-2.	Strength-Temperature-Grain Size Surface for Dense Hot-Pressed Alumina (Ref. 6) .....	264
4-3.	Bend Strengths of Radome Aluminas .....	265
4-4.	Modulus of Elasticity of Radome Aluminas .....	266
4-5.	Linear Thermal Expansion of Radome Aluminas .....	266
4-6.	Specific Heat of Aluminas (Ref. 5) .....	266
4-7.	Dielectric Constant of Aluminas as a Function of Temperature .....	267
4-8.	Loss Tangent of Aluminas as a Function of Temperature .....	267
4-9.	Thermal Conductivities of Radome Aluminas .....	267
4-10.	Normal Total Emittance of Aluminas .....	268
4-11.	Interface Between Dense Alumina Skin and Porous Alumina Core: Magnification 100X .....	269
4-12.	Enlarged View of Cross-section of 95% Alumina "A" Sandwich Skins 0.023-in. Thick; Core 0.207-in. Thick (Density 1.3 gm/cm <sup>3</sup> ); Magnification 10X .....	269
4-13.	Approximate Dielectric Constants of 95% Alumina Sandwich Skin and Core Materials: Core Density 1.29 gm/cm <sup>3</sup> at 10 gc .....	270
4-14.	Approximate Loss Tangents of 95% Alumina Sandwich Skin and Core Materials: Core Density 1.29 gm/cm <sup>3</sup> at 10 gc .....	270
4-15.	Modulus of Elasticity of 95% Alumina "A" Sandwich Material (Ref. 8) .....	271
4-16.	Modulus of Rupture of Pyroceram .....	272
4-17.	Modulus of Elasticity of Pyroceram by Sonic Method .....	272
4-18.	Poisson's Ratio of Pyroceram .....	273
4-19.	Linear Thermal Expansion of Pyroceram .....	273
4-20.	Thermal Conductivity of Pyroceram .....	273
4-21.	Specific Heat of Pyroceram .....	274
4-22.	Normal Total Emittance of Pyroceram (Ref. 13) .....	274
4-23.	Dielectric Constant of Pyroceram .....	274
4-24.	Loss Tangent of Pyroceram .....	274
4-25.	Strength Data on Slip-Cast Sintered Fused Silica .....	277
4-26.	Poisson's Ratio of Slip-Cast Sintered Fused Silica (Ref. 23) .....	277
4-27.	Thermal Conductivity of Slip-Cast Sintered Fused Silica .....	277
4-28.	True Specific Heat of Slip-Cast Sintered Fused Silica (Ref. 23) .....	278
4-29.	Thermal Expansion of Slip-Cast Sintered Fused Silica (Ref. 23) .....	278
4-30.	Dielectric Constant of Slip-Cast Sintered Fused Silica .....	278
4-31.	Loss Tangent of Slip-Cast Sintered Fused Silica .....	278
4-32.	Comparison of Effective Emittance vs Corrected Surface Temperature of Slip-Cast Fused Silica with and without Chromium Oxide .....	279

## LIST OF ILLUSTRATIONS (cont)

<i>Figure</i>	<i>Page</i>
4-33. Approximate Modulus of Rupture of Radome Beryllia, 99 % Pure, 95 % Dense (Ref. 25) .....	260
4-34. Modulus of Elasticity of Beryllia .....	281
4-35. Linear Thermal Expansion of Beryllia (Ref. 5) .....	281
4-36. Thermal Conductivity of Beryllia as a Function of Tempera- ture .....	282
4-37. Specific Heat of Beryllia as a Function of Temperature (Ref. 5) .....	282
4-38. Normal Total Emittance of Beryllia (Ref. 12) .....	283
4-39. Dielectric Constant of Radome Beryllias .....	283
4-40. Loss Tangent of Beryllia as a Function of Temperature ....	283
4-41. Radome Finish of Glass-Reinforced Aluminum Phosphate .....	285
4-42. Sketch Showing Anisotropic Nature of Reinforced Plastic Radomes .....	296
4-43. Vibrin 135 and Glass Composite—Dielectric Constant and Loss Tangent, Electrical Properties vs Temperature .....	298
4-44. E-Glass and Vibrin 135—Dielectric Constant vs Resin Content .....	300
4-45. Hollow Glass and Vibrin 135—Dielectric Constant vs Resin Content .....	301
4-46. S-994 Glass and Vibrin 135—Dielectric Constant vs Resin Content .....	302
4-47. Schematic Diagram of Radome Filament Fabrication .....	303
4-48. Diagram of Resin Bath Setup for Wet-Dip Method .....	304
4-49. Schematic Diagram of Pre-Impregnation Operation .....	305
4-50. Schematic Diagram of Hybrid Impregnation Operation ....	305
4-51. Helical Pattern on Radome Mandrel .....	306
4-52. Circo and Longo Fiber Pattern on Radome Mandrel .....	307
4-53. Diagram for Calculating Circo and Longo Fibers for Desired Wall Thicknesses .....	307
4-54. Diagram of Circo Fibers on High Curvature Portion of Mandrel .....	307
4-55. Diagram of Plate of Tip Method for Controlling Slippage of Circo Fibers on High Curvature Portion of Mandrel .....	307
4-56. Diagram Showing Effect of Bandwidth of Fiber on Overlap Pattern .....	308
4-57. Diagram of Longitudinal Fiber Pattern .....	308
4-58. Sketch of Gore Pattern on Fiberglass Tape .....	309
4-59. Drawing of Setup Used to Remove Filament-Wound Radome from Mandrel .....	313

### APPENDIX 4A

4-A1. Vibrin 135 and S994 Glass—Dielectric Constant vs Tem- perature and Resin Content .....	317
4-A2. Measured and Calculated Values at Vacuum Laminate Room Temperature and 9875 mc for VC-8359 Epoxy—Dielectric Constant vs Resin .....	317

## LIST OF ILLUSTRATIONS (cont)

<i>Figure</i>	<i>Page</i>
<b>APPENDIX 4B</b>	
4-B1. Vibrin 135 Resin—Dielectric Constant and Loss Tangent vs Frequency .....	322
4-B2. Epon 828-CL Resin—Dielectric Constant vs Temperature for Various Frequencies .....	322
4-B3. Epon 828-CL Resin—Loss Tangent vs Temperature for Various Frequencies .....	323
4-B4. Teflon—Dielectric Constant and Loss Tangent vs Temperature .....	323
4-B5. E-Glass—Dielectric Constant vs Temperature for Various Frequencies .....	324
4-B6. E-Glass—Loss Tangent vs Temperature for Various Frequencies .....	324
4-B7. S-994 Glass—Dielectric Constant vs Temperature for Various Frequencies .....	325
4-B8. S-994 Glass—Loss Tangent vs Temperature for Various Frequencies .....	325
4-B9. D-556 Glass—Dielectric Constant vs Temperature for Various Frequencies .....	326
4-B10. D-556 Glass—Loss Tangent vs Temperature for Various Frequencies .....	326
4-B11. L-498 Glass—Dielectric Constant vs Temperature for Various Frequencies .....	326
4-B12. L-498 Glass—Loss Tangent vs Temperature for Various Frequencies .....	327
4-B13. Vibrin Laminates of E-Glass and H-Glass—Dielectric Constant vs Resin Content for Various Void Percentages .....	327
4-B14. Vibrin Laminates of D-556 Glass and S-994 Glass—Dielectric Constant vs Resin Content for Various Void Percentages .....	328
4-B15. Vibrin 135 (Polyester) Laminate—Dielectric Constant vs Temperature .....	328
4-B16. Epon 828-BF <sub>3</sub> 400 Resin Casting and Laminate—Dielectric Constant and Loss Tangent vs Frequency .....	329
4-B17. Polybenzimidazole Laminate (PBI)—Dielectric Constant and Loss Tangent vs Temperature .....	329
<b>CHAPTER 5</b>	
5-1. Geometry of Typical Interferometer Horn Showing Sample .....	344
5-2. Graph for Focusing Correction .....	345
5-3. Sheffield Radome Thickness Gage; Used as Wall Thickness Gage During Final Inspection .....	347
5-4. Sheffield Radome Thickness Gage; Used as In-Process Gage to Check Inside Diameter .....	347

## LIST OF ILLUSTRATIONS (cont)

<i>Figure</i>	<i>Page</i>
5-5. Ultrasonic Equipment Setup at Douglas Aircraft Company	345
5-6. Vidigage Being Used to Measure Radome Wall Thickness	349
5-7. Oscilloscope Presentation for Wall Thickness Measurement Using North American Aviation Microwave Thickness Gage	351
5-8. Comparison Null Shift Measurements of Radomes Using Microwave Thickness Gage	352
5-9. Fiberglass Laminate Test Sample	352
5-10. Power Reflection Coefficient for Plane Sheet at Normal Incidence	354
5-11. Microwave Instrumentation for Dielectric Constant Measurement	354
5-12. Reflection Coefficient Curves for Four Different Materials	355
5-13. Increased Sensitivity Measurement for Pyroceram	355
5-14. Modified Ends of Waveguide	356
5-15. Horn with Spring Fingers	356
5-16. Quarter-Wave Peaks of Power Transmission Coefficient	357
5-17. Adapter Used for Loss Tangent Measurements	357
5-18. High-Temperature Transmission Gage	359
5-19. Inside High-Temperature Transmission Gage	360
5-20. Instrument to Measure Power Reflection Coefficient at Normal Incidence	360
5-21. Dielectric Dispersion and Absorption	362
5-22. Dielectric Constant vs Temperature for Selected Dielectric Materials	363
5-23. Loss Tangent vs Temperature for Selected Dielectric Materials	363
5-24. Coaxial Dielectric Measuring Line Modified for High-Temperature Measurements by Adding Length of Platinum Alloy Tubing	365
5-25. Block Diagram of Equipment Used with Coaxial Line Dielectric Measurements	366
5-26. Commercial Dielectrometer for Use to 500°C at 1, 3, and 8.5 gc. Coaxial Sample Holder Used at Two Lower Frequencies Is Used without Center Conductor at Higher Frequencies	366
5-27. Sample Holder for 1-in. Disks to 2550°F with Pt Foil, or >1400°C with Pt-Rh Foil (Longitudinal Cross Section)	367
5-28. High-Temperature (1650°C) Shorted Waveguide Dielectrometer for Operation near 10 gc	368
5-29. Notation Used in Shorted Waveguide Calculations	369
5-30. Sample Fit Corrections	369
5-31. General Features of Resonant Cavity Showing Methods of Input Coupling; (A) Bleaney Coupler, (B) Adcock Tee	370
5-32. High-Temperature (1500°C) Resonant Cavity Dielectrometer for Operation near 10 gc	371
5-33. Typical TE Cavity Configuration. Small Cylindrical Sample Is Inserted into Center of Cavity	373
5-34. Equipment for Resonant Cavity Measurements	373



## LIST OF ILLUSTRATIONS (cont)

<i>Figure</i>		<i>Page</i>
5-35.	Schematic Diagram of 10 gc Analogue of Michelson Interferometer .....	375
5-36.	Computation Sheet for Shorted Waveguide Technique .....	376
5-37.	Graphical Solution of Waveguide Equation for Calculating Dielectric Constant .....	377
5-38.	Graphical Solution of $F_u$ for Use in Calculating Loss Tangent .....	378
5-39.	Graphical Correction for Sample Fit .....	379
5-40.	Details of a Typical Radial Heat-Flow Thermal Conductivity Technique .....	380
5-41.	Essential Features of a Cut-Bar or Longitudinal Heat-Flow Technique for Thermal Conductivity Measurements .....	381
5-42.	Essential Features of a Guarded-Hot-Plate Method for Measuring Thermal Conductivity .....	382
5-43.	Schematic Diagram of Flash Technique for Thermal Diffusivity Measurement .....	383
5-44.	Sample and Instrumentation for Longitudinal Thermal Diffusivity Technique .....	384
5-45.	Ice Calorimeter .....	386
5-46.	Copper Block Calorimeter Design Features .....	387
5-47.	Grip and Loading System for Use to 3000°F with Brittle Materials .....	387
5-48.	Schematic Diagram of Self-Aligning Air Bearing for Axial Loading of Tensile Specimen .....	388
5-49.	Schematic Diagram of Dynamic Modulus Measurement Showing Excitation Techniques .....	390
5-50.	Sapphire Rod Dilatometer .....	392
5-51.	Aperture-Type Anechoic Chamber. View Toward Transmitter in Eccosorb Anechoic Chamber No. 225 at Warner-Robins Air Force Base, Georgia .....	394
5-52.	Evolution of Aperture and Funnel Anechoic Chambers .....	395
5-53.	Vertical Transverse Section Through Typical Longitudinal Baffle Chamber Configuration .....	396
5-54.	Longitudinal-Baffle Eccosorb Anechoic Chamber No. 250 at Canadian Westinghouse Co., Ltd., Hamilton, Ontario .....	397
5-55.	Longitudinal-Baffle Eccosorb Anechoic Chamber No. 423 at Motorola, Scottsdale, Arizona .....	398
5-56.	Comparing Pattern by Pattern Comparison Evaluation Method .....	401
5-57.	Deviation Plot and Computation of Results by Pattern Comparison Evaluation Method .....	402
5-58.	Perturbation of Antenna Pattern by Reflected Energy .....	404

## CHAPTER 6

6-1.	Heating Rate vs Reentry Time for Ballistic, Glide, and Orbital Decay Vehicles .....	419
6-2.	Nose Laminar Heating Rate at Stagnation Point .....	420

## LIST OF ILLUSTRATIONS (cont)

<i>Figure</i>		<i>Page</i>
6-3.	Glide Reentry Flight Spectrum .....	421
6-4.	$T_w$ as a Function of $\dot{q}$ .....	422
6-5.	Nose Turbulent Heating Rate at Sonic Point .....	423
6-6.	Generalized Ballistic Reentry Heating Rate for Laminar and Turbulent Flow .....	425
6-7.	Electrical Design of a Flat Window .....	431
6-8.	Normalized Attenuation Constant as a Function of Nor- malized Collision Frequency and Wave Frequency .....	435
6-9.	Normalized Phase Constant as a Function of Normalized Collision Frequency and Wave Frequency .....	435
6-10.	Effect of Helium Plasma at X-Band on Far-Field Radiation Pattern of Horn Antenna .....	436
6-11.	Patterns of Slot Antenna Covered with Simulated Isotropic Plasma .....	437
6-12.	Dielectric Constant of Magnesia at X-Band .....	442
6-13.	Dielectric Constant of Magnesium Aluminate Spinel at 9375 mc .....	442
6-14.	Loss Tangent of Magnesium Aluminate Spinel at 9375 mc ..	443
6-15.	Dielectric Constant of Boron Nitride at 9375 mc .....	443
6-16.	Loss Tangent of Boron Nitride at 9375 mc .....	443
6-17.	Dielectric Constant of Barium Aluminum Silicate at 9375 mc .....	443
6-18.	Loss Tangent of Barium Aluminum Silicate at 9375 mc ...	443
6-19.	Dielectric Constant of Typical Polyamide Resin-Fiberglass Laminate at 9375 mc .....	444
6-20.	Loss Tangent of Typical Polyamide Resin-Fiberglass Lami- nate at 9375 mc .....	444
6-21.	Dielectric Constant of Brunswick Corp. Aluminum Phos- phate-5994 Glass Laminate at 9375 mc .....	445
6-22.	Loss Tangent of Brunswick Corp. Aluminum Phosphate- 5994 Glass Laminate at 9375 mc .....	445
6-23.	Flexural Strength of Glass Reinforced Aluminum Phosphate ..	446
6-24.	Flexural Modulus for Glass Reinforced Aluminum Phos- phate .....	446
6-25.	Electrical Performance Data on Armstrong 2755 Cork ....	449
6-26.	Electrical Performance Data on Tyloron Phenolic-Nylon ..	449
6-27.	Electrical Performance Data on Teflon TFE .....	450
6-28.	Electrical Performance Data on Duroid 5650 .....	451
6-29.	Electrical Performance Data on Thermolag 500 .....	452
6-30.	Electrical Performance Data on Avcoat II .....	453
6-31.	Loss Tangent Properties of Ablation Materials .....	454
6-32.	Dielectric Constants of Ablation Materials .....	455

## LIST OF TABLES

<i>Table</i>	<i>Page</i>
1-1. Physical Properties Involved in Radome Design . . . . .	25
1-2. Thicknesses (In.) of One-Half-Wavelength and Thin-Wall Radomes for Normal Incidence . . . . .	31
1-3. E- and H-Plane Antenna Pattern Parameters for Several Radome Wall Thicknesses . . . . .	41
2-1. Design Parameters for Radome with One Embedded Per- forated Metal Sheet . . . . .	106
2-2. Design Parameters for "A" Sandwich Radomes . . . . .	107
2-3. Parameter Values for Case 1 . . . . .	125
2-4. Parameter Values for Case 2 . . . . .	125
2-5. Transmission Coefficient of Lossless Inhomogeneous Layer with Perpendicular Polarization . . . . .	131
2-A1. Reference Table of Band Code Letters vs Frequency . . . . .	176
3-1. Maximum Rainfall Accumulation and Average Rainfall Rate for Western U.S.A. . . . .	202
3-2. Comparison of Three Sled-Test Facilities . . . . .	211
3-3. Summary of Radome Rain Erosion Experiments at Nav Ordnance Test Station . . . . .	228
3-4. Summary of Radome Rain Erosion Experiments by Sandia Corp. . . . .	230
3-5. Test Conditions and Results for Fused-Silica Specimens Exposed to an Arc Plasma Jet Effluent . . . . .	241
3-6. Test Conditions and Results for Fused-Silica Specimens Exposed to an Arc Plasma Jet Effluent . . . . .	241
3-7. Operational Data for Oxyhydrogen Rocket Motor . . . . .	243
3-8. Ramjet Test Conditions for Alumina Radome Flight Simu- lation . . . . .	243
3-9. Thermal Shock Conditions for Alumina Radomes . . . . .	247
3-10. Characteristics of Vibrin and Selectron Polyesters After Exposure to Radiation . . . . .	251
4-1. Comparison of Properties of the Four Principal Ceramic Monolithic Radome Materials . . . . .	261
4-2. Properties of Monolithic Radome Aluminas . . . . .	265
4-3. Properties of 95% Alumina "A" Sandwich Materials . . . . .	270
4-4. Typical Properties of Adhesives and Joints Between 97.6% Alumina Tiles . . . . .	271
4-5. Physical Properties of Vitreous Silica . . . . .	275
4-6. Physical Properties of Slip-Cast Sintered Fused Silica . . . . .	276
4-7. Interim Properties of Glass Reinforced Aluminum Phos- phate Material . . . . .	284
4-8. Average Interlaminar Shear Values of Selected Resin Sys- tems . . . . .	297
4-9. Properties of Vibrin 135 . . . . .	298

## LIST OF TABLES (cont)

<i>Table</i>		<i>Page</i>
4-10.	Composite Properties of E-Glass and Vibrin 135 .....	298
5-1.	Radome Dielectric Check List .....	336
5-2.	Sample Computer Printout of Interferometer Tables .....	339
5-3.	Computer Printout of Dielectric Slab Tables .....	341
6-1.	Physical and Thermal Properties of Ceramics .....	440
6-2.	Ablation Materials Tested .....	448

## **CHAPTER 1**

### **PHYSICAL DESIGN TECHNIQUES**

*by* DONALD LEE LOYET  
*Hughes Aircraft Company*  
*Culver City, California*

# SYMBOLS

A	Effective diameter of antenna	g	Distance from radome major axis to coordinate center of ogive
B	Boresight error derivative (slope)	h	Heat transfer coefficient
C	A constant	k	Thermal conductivity
CG	Center of gravity	l	Total length of radome
D	Outer diameter of radome at the base	m	A constant
E	Young's modulus of elasticity	n	Any positive integer
F	Total force on radome	p	Internal pressure
F <sub>D</sub>	Drag force colinear with radome major axis	r	Cartesian coordinate; radius at an axial station
F <sub>N</sub>	Drag force normal to radome major axis	s	Distance from vertex to gimbal center for log spiral radome
F <sub>I</sub>	Force due to inertia	t <sub>1</sub> , t <sub>2</sub> , t <sub>3</sub>	Flight times
F <sub>P</sub>	Force due to pressure differential	x	Cartesian coordinate; distance measured from radome tip
F <sub>O</sub>	Force due to effect of O-ring or gasket seal	θ	Half-power beamwidth of antenna pattern
F <sub>V</sub>	Force due to vibration	α	Linear coefficient of thermal expansion
G	Modulus of rigidity	α <sub>t</sub>	Thermal diffusivity = k/ρc <sub>p</sub>
IPD	Insertion phase difference	β	Vertex angle
K	A constant	δ	Loss tangents
M <sub>1</sub> , M <sub>2</sub> , M <sub>3</sub>	Mach numbers	γ	Angular error in loading the radome
MOR	Modulus of rupture	ε	Relative dielectric constant
N	A constant	θ	Angle of incidence
R	Radius of curvature of ogive	λ <sub>0</sub>	Wavelength in free space
R <sub>⊥</sub>	Reflection coefficient (perpendicular)	μ	Poisson's ratio
R <sub>∥</sub>	Reflection coefficient (parallel)	π	A constant = 3.1416
T	Temperature	ρ	Density of radome material
T <sub>⊥</sub>	Transmission coefficient (perpendicular)	σ	Normal stress; tension is positive
T <sub>∥</sub>	Transmission coefficient (parallel)	σ <sub>r</sub>	Normal stress in radial direction
a	Semimajor axis of ellipse	σ <sub>θ</sub>	Normal stress in circumferential direction
b	Seminor axis of ellipse	σ <sub>φ</sub>	Normal stress in meridional direction
c <sub>p</sub>	Specific heat capacity at constant pressure	φ	$\cos^{-1} \left( 1 - 2 \frac{x}{l} \right)$
d	Thickness of radome wall		
l	Distance from radome tip to coordinate center of ogive		

## CHAPTER 1

### PHYSICAL DESIGN TECHNIQUES

During the past decade, aircraft and guided missiles have undergone a number of major advances. The most significant advance is the transition from transonic to hypersonic velocities. The effect of these velocities on the electrical and structural characteristics of the radome must, therefore, be considered in any design. In this chapter, the various radome types and configurations are reviewed. The design criteria for hypersonic radomes are provided and the various aerodynamic, thermal, structural, electrical, and environmental trade-offs are discussed. One type of radome construction, the thin wall, is examined in detail. Methods of attaching the radome to the missile structure are described. Methods used to evaluate radome performance are presented, and the chapter concludes with a review of the factors that affect radome strength.

#### 1-1 DESIGN CRITERIA FOR RADOMES USED ON SUPERSONIC AND HYPERSONIC VEHICLES

##### 1-1.1 DEFINITION OF RADOME TYPES

A radome is a dielectric cover that protects an internal structure from its environment without impairing the performance of the vehicle on which it is mounted. Radomes for hypersonic vehicles are of two types: (1) those that form the leading structure of a missile or an aircraft, and (2) those that are mounted flush with the fuselage. Radomes of the first type protect radar system components, such as directional guidance, mapping, or weather antennas. Radomes of the second type protect fixed or flush-mounted antennas. The radome must not only protect the system, but it must also

have a minimal effect on antenna characteristics. In particular, its effects on boresight error angle, the rate of change of this angle with antenna beam position, and on the antenna gain and pattern must be kept to a minimum. Such effects result from complex electromagnetic interactions affecting the radome, antenna, and other components of the vehicle near the radiating system. Since the radome is nearest to the system and is usually in the near field of the antenna, it causes the primary distortions. Since electrical performance of the radome is essentially determined by its wall construction and aerodynamic shape, these parameters can be used to define the radome.

##### 1-1.2 TYPES OF WALL CONSTRUCTION

A great deal of time and effort has been spent in attempting to minimize the effects of wall construction and thickness on antenna performance. Since the various radiating systems have different purposes and, therefore, different requirements, many types of construction have been investigated. A review of the literature on radome design shows that the various types of construction can be grouped in a logical sequence as follows, based upon electromagnetic boundary conditions and wall composition:

###### Solid Walls

###### Thin

###### Multiple one-half wavelength

###### Laminated Walls

###### "A" sandwich

###### "B" sandwich

###### "C" sandwich

###### Double wall

###### Half sandwich

###### Multiple layer

Detailed descriptions of these constructions and analyses of their respective merits are contained in References 1 through 3. A summary of the various radome constructions follows.

### 1-1.2.1 Solid Wall

Solid-wall radomes are divided according to thickness as either thin wall or multiple one-half wavelength, and are constructed either as a monolithic or composite structure. A monolithic wall is made from a single material and is usually formed by a casting process. A composite wall is made of several materials. It is formed by casting a filled plastic or ceramic material, a filament, or roving winding; and by laying up sheets of these materials with suitable binders.

### 1-1.2.2 Thin Wall

Thin-wall radomes are so called because the wall thickness is small in comparison with the wavelength of the incident radiation. A wall thickness of  $1/20$  of the wavelength in the material is usually adequate. Physically, this thickness is on the order of hundredths of an inch at X-band and increases to tenths of an inch at S-band. The advantages of thin-wall radomes are lightness, negligible effect of wall-thickness tolerance on electrical performance, high transmission efficiency, and negligible sensitivity to changes in polarization and angle of incidence; it is also relatively broadband. In the past, thin-wall radomes made of plastic materials have been limited to low-velocity, clear-weather applications. The recently developed ability to fabricate thin ceramic walls, which, as shown in Chapter 3, have greater resistance to rainfall at relatively high velocities, should encourage renewed interest in this type of construction. They are especially useful for low-frequency applications such as those for C- and S-band radomes.

### 1-1.2.3 Multiple One-Half Wavelength

Thick solid-wall radomes are classified by the number of multiples of one-half wavelengths of electrical thickness they contain. For a specific radome fabricated from a material having a

dielectric constant of  $\epsilon$ , an effective angle of incidence of  $\theta$ , and that operates at a wavelength of  $\lambda_0$ , the mechanical thickness is approximately

$$d = \frac{n\lambda_0}{2(\epsilon - \sin^2\theta)^{1/2}} \quad (1-1)$$

where  $n$  is an integer equal to or greater than zero. Note that the thin-wall radome is an approximation of the zeroth order.

In classifying thick solid-wall radomes, it is conventional to define thickness in terms of  $n$ , which determines the number of one-half wavelengths of electrical thickness. Thus, for  $n$  equal to 1, 2, or 3, the wall is called one-half wavelength, full wavelength, or three-half wavelength, respectively. Figure 1-1 illustrates the thin-wall radome and the first three orders of one-half wavelengths. The simplest structure, one-half wavelength, has been employed for most high-speed radomes. It has the advantages of being light, structurally adequate at high frequencies, and simple in electrical design; it has the least adverse effect on system performance and has good resistance to rainfall at high missile velocities. The wide use of this type of structure has provided a wealth of information on physical design, electrical correction, and environmental reliability. The use

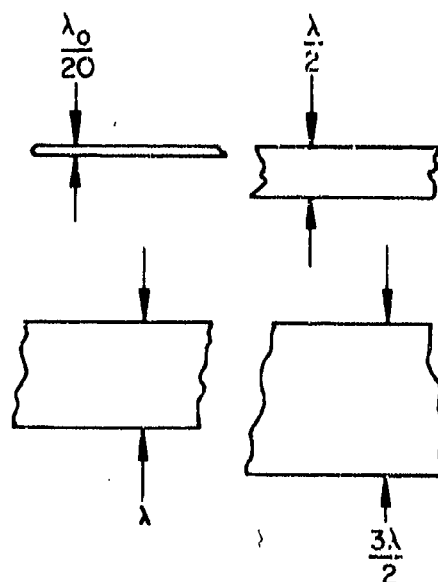


Figure 1-1. Types of Solid-Wall Radomes



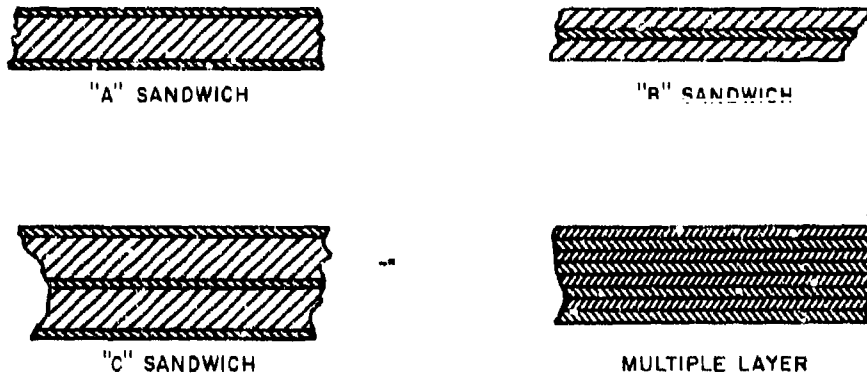


Figure 1-2. Types of Laminated Radomes

of higher-order thicknesses causes greater electrical degradation, but also affords greater structural reliability at frequencies above X-band.

#### 1-1.2.4 Laminated Wall

Laminated radomes differ electrically from solid-wall radomes in that they have a greater number of boundary conditions and several different types of materials make up their structure. The two distinct types of construction favored, cored and multilayer, are illustrated in Fig. 1-2. The cored construction of the "A" and "C" sandwiches consists of an effective low-dielectric-constant core contained by two high-dielectric-constant skins, while the "B" sandwich consists of a high-dielectric-constant core with in two low-dielectric-constant skins. Since the dielectric constant of most materials increases with density, a low value of dielectric constant implies low density, and vice versa. The low-dielectric-constant core is obtained by using a foamed material, i.e., one of low density.

The low-dielectric-constant core can be simulated by using a high-dielectric-constant material in a fluted or honeycomb configuration. These latter constructions, however, are not electrically isotropic, whereas the foamed materials are. Other disadvantages are that a mosaic is needed to produce a doubly curved surface (only slight curvature can be obtained in any section), thus limiting their use to large radomes. Fluted and honeycomb constructions

have an advantage of allowing the passage of air for ducted heating of the skins. Foamed cores are easy to fabricate and can be used with both large and small radomes.

#### 1-1.2.5 "A" Sandwich

The "A" sandwich construction consists of outer and inner skins of a material having a higher dielectric constant than that of the core. The optimum skin spacing, measured through the core material, is approximately one-quarter wavelength. Thus, this construction is analogous to that of a one-quarter-wavelength transformer. In this construction, the strength-to-weight ratio and bandwidth are greater than in a solid-wall radome. Also, the hard surface is more impervious to possible damage caused by handling and the environment. The sandwich is, however, more sensitive to variations in polarization and angle of incidence.

#### 1-1.2.6 "B" Sandwich

The "B" sandwich construction, which consists of skins having a low dielectric constant and a thin solid core having a high dielectric constant, is similar to the one-quarter-wavelength coating used in optical systems. As the thickness of the core approaches zero, this type of radome approaches the one-half wavelength construction. Although the "B" sandwich can be designed to provide equal transmission for perpendicular and parallel polarizations, it does

not afford maximum transmission. Although it is superior electrically to the "A" sandwich, the "B" sandwich is not suitable for use in extreme environments or in applications requiring a strong durable surface.

#### 1-1.2.7 "C" Sandwich

The "C" sandwich construction consists of five layers, i.e., three dense skins and two cores. Thus, it is basically two "A" sandwich radomes with no spacing between them. This type of construction has the best strength-to-weight ratio and is ideally suited to very-high frequency applications in which greater rigidity is required. Its transmission efficiency and bandwidth are somewhat greater than those of the "A" sandwich.

It should be noted that although Fig. 1-2 illustrates identical skin thicknesses for the sandwich constructions, the sandwich design is not limited to this symmetrical construction. If different dielectric constants are used for the two skins, an asymmetrical construction can be employed for greater structural resistance in the outer skin, or to provide a means of compensating for the change in electrical thickness of the outer skin caused by aerodynamic heating. Although the sandwich design has been limited to plastic materials, future designs should consider the use of the ceramics, especially for "A" sandwiches. As indicated in References 4 through 6, recent studies have shown the feasibility of employing a ceramic foam between ceramic skins, eliminating the bond line reflection found in plastic sandwiches.

#### 1-1.2.8 Double Wall

The double-wall radome consists of two solid skins separated by an air core. For this reason it has also been called an *air-core radome*. As shown in Reference 7, the optimum skin spacing is somewhat less than one-quarter wavelength. If the skins are thin, rather than one-half wavelength, the design can then be considered as a degenerate "A" sandwich, i.e., the dielectric constant of the core is unity. Although a radome of this design is light and has a passage for air to heat the skins, maintenance of the spacing is difficult, especially in the presence of high vibration.

#### 1-1.2.9 Half Sandwich

A construction similar to the thin solid-wall radome is the one-half "A" sandwich, which consists of a thin wall with a portion of the core added for greater rigidity. If the ceramic foam construction described in References 4 and 5 is used, such a structure combines the advantage of additional rigidity with the performance of a thin solid wall. This design is especially attractive for use at low frequencies.

#### 1-1.2.10 Multiple Layer

The multilayer wall, consisting of thin layers of materials having different dielectric constants, is best for ECM radomes. Reference 8 includes a series of reports that illustrate the design, and Reference 9 illustrates the complexity of designing a radome having a large number of sheets, each with an optimum thickness and dielectric constant. Because of this complexity, the use of multilayer radomes has been limited to applications requiring extreme structural rigidity or broadband capability. Although, at present, this design consists of plastic laminates, recent advances in materials technology, reported in Reference 10, indicate that the use of ceramics is feasible. It is expected that such a radome will be characterized by high structural reliability, good electrical performance over wider bandwidths, better resistance to thermal shock and rainfall, and that it will be less expensive to fabricate.

### 1-1.3 TYPES OF AERODYNAMIC CONFIGURATIONS

The contour of flush-mounted radomes follows that of the body of the vehicle and is usually a right circular cylinder or cone. If the surface area of the radome is small compared with the missile diameter, a planar cover can be used. However, such radomes are not considered to be separate structures as are nose radomes, which act as a transition between the body and the airstream. An aerodynamicist takes considerable care to minimize the effect of aerodynamic drag caused by a nose radome, but he usually does not consider flush-mounted radomes specifically. Since a radome designer approaches the radome from the standpoint of

electromagnetic theory, he usually desires a hemispherical shape, which is not acceptable to the aerodynamicist. Let us, therefore, review the various radome contours considered during the early phases of missile design. This discussion will serve as an introduction to the design of such contours. Reference 11 should be consulted if more detailed information is desired.

### 1-1.3.1 Ellipsoid

An ellipsoidal shape is obtained by revolving an ellipse or elliptic segment about one of its major axes. If the ellipse is rotated about its major (minor) axis, an oblate (prolate) ellipsoid is obtained. As shown by Eq. 1-2, the exact shape depends on the magnitude of  $a$  and  $b$ , which are the lengths of the major and minor axes, respectively. As  $a$  approaches  $b$ , the contour becomes more bulbous and finally becomes a hemisphere. The equation for an ellipse is

$$r = b \left[ 1 - \left( \frac{x-a}{a} \right)^2 \right] \quad (1-2)$$

The symbol convention is shown in Fig. 1-3.

With the ellipsoid at its limiting value, i.e., the hemisphere, electrical characteristics are affected the least, but only at the expense of aerodynamic performance. Hemispheric shapes are usually employed at low velocities, where the drag is not an important factor, or at high reentry velocities, where the additional drag increases deceleration or where a larger nose radius is required to minimize aerodynamic heating and the resultant thermal stresses.

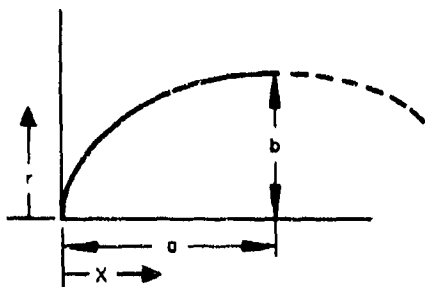


Figure 1-3. Ellipsoidal Radome

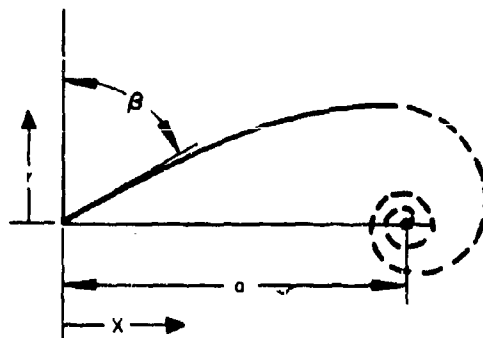


Figure 1-4. Logarithmic Spiral Radome

### 1-1.3.2 Logarithmic or Equiangular Spiral

The logarithmic or equiangular spiral is generated by revolving a segment of a spiral about its major axis. This contour, which may require an aft fairing since it recedes before reaching the gimbal center, is primarily of importance to the radome designer, since, if the antenna is mounted at the center of the spiral, the central ray will strike the radome at a constant angle of incidence, which is the same as the vertex angle,  $\beta$ . This contour degenerates into a hemisphere when  $\beta$  equals zero. The general equation for the logarithmic spiral is

$$r^2 + (x - s)^2 = s^2 \exp \left[ -2 \tan \beta \tan^{-1} \left( \frac{r}{x - s} \right) \right] \quad (1-3)$$

The general surface and symbol conventions are shown in Fig. 1-4.

A hemisphere is the optimum electrical contour, since, if the antenna is located at the origin, the central ray strikes the radome at normal incidence at all look angles. This is an advantage, since transmission coefficients are equal for both parallel and perpendicular polarizations, but it is also a disadvantage since any signal reflected from the inner surface is reflected back to the antenna. Like the ellipsoid, this shape is used to minimize heating at high velocities. For this reason, the hemisphere has been extensively used as a means of blunting the nose of radomes.

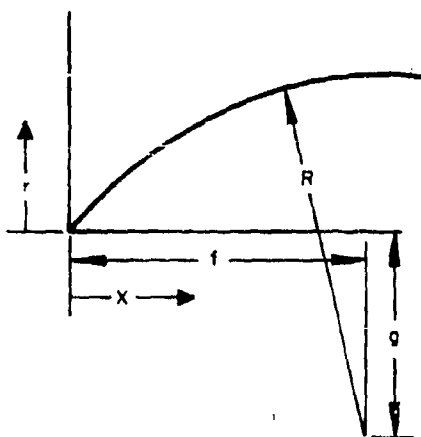


Figure 1-5. Ogival Radome

#### 1-1.3.3 Ogive

The term *ogive* has been extended to include not only the normal architectural construction, but also all convex solids bounded in part by an arc of a circle having a radius  $R$  whose center lies on the side of the axis of revolution that is opposite to the arc. If the bounding arc cuts the axis, the ogive is said to be *pointed*. If the figure is truncated, the ogive is called *blunted*. An ogive that includes its base is known as a *tangent ogive*, while one that does not is called a *secant ogive*. As is true of the previously described shapes, the ogive has been used extensively in radome design because it is easily fabricated and is relatively acceptable aerodynamically at high speeds. As shown by reviewing the following general equation and Fig. 1-5, an ogive also degenerates to a hemisphere:

$$r = [R^2 - (x - f)^2]^{1/2} - g \quad (1-4)$$

#### 1-1.3.4 Power

The power series of contours was designed to provide minimum drag under specific aerodynamic conditions. The three-quarter power shape is an approximation to the true Newtonian shape. Since the equation for the three-quarter power shape is simpler than the complex equation defining the Newtonian shape and

the differences between the shapes are small (the power shape is less bulbous), the approximate shape is usually used. The general power shapes are generated by rotating the figure defined by Eq. 1-5 about its major axis:

$$r = \frac{D}{2} \left( \frac{x}{l} \right)^m \quad (1-5)$$

where  $D$  = base diameter  
 $l$  = total radome length  
 $m$  = constant

If exponent  $m$  is equal to unity, the equation is that for a cone; if  $m$  is equal to  $1/2$ , the equation is that of a parabola. The familiar three-quarter nose shape that approximates the Newtonian shape is obtained by letting  $m$  equal  $3/4$ .

#### 1-1.3.5 Parabolic

Like the power series, the parabolic series of shapes was derived to minimize aerodynamic drag for a particular set of conditions. These shapes are obtained by revolving the shape defined by Eq. 1-6 about its major axis:

$$r = \frac{D}{2} \left( \frac{2 \frac{x}{l} - C \frac{x}{l}}{2 - C} \right)^2 \quad (1-6)$$

The symbols have the same definitions as for the power series, where  $m$  is replaced by  $C$ . Again, a right circular cone is obtained when  $C$  is equal to zero. If  $C$  is equal to unity, the shape becomes a parabolic segment.

#### 1-1.3.6 Haack-Von Karman

The Haack-Von Karman contours have become well known to many radome designers through the fame of the originators and the complexity entailed in generating these shapes. Note that the Haack body is also known as the Sears and Sears-Haack body since the shapes were independently derived by these two aerodynamicists. As shown in Reference 14, a general equation can be derived that is based on the requirement of minimum drag as expressed in Eq. 1-7. Here, aerodynamic drag can be varied in accordance with the radome length, area, and volume desired.

$$r = \frac{1}{\sqrt[3]{\pi}} (\phi - \frac{1}{2} \sin 2\phi + K \sin^3 \phi)^{1/2} \quad (1-7)$$

where  $\phi = \cos^{-1} \left( 1 - 2 \frac{x}{l} \right)$

If K is equal to zero, Eq. 1-7 becomes that for the Von Karman nose, which has the least drag for a given length and base diameter. If K is equal to 1/3, this equation reduces to that for the Sears-Haack nose, which has been optimized for minimum drag on the basis of length and nose volume.

#### 1-1.4 FACTORS AFFECTING RADOME DESIGN

Although it is assumed that the various factors affecting radome design that are considered in the following paragraphs apply primarily to nose-mounted radomes, they are equally applicable to radomes mounted elsewhere on the missile. A nose-mounted radome was selected for discussion because all the design criteria associated with an object subjected to the environment surrounding a leading aerodynamic body must be considered. The radome designer must, of course, consider all the basic factors affecting missile performance, which include the weight, volume, length, size, and position of the antenna, as well as the interface between the radome and the missile body. In addition, with airborne missiles there are environmental variables associated with pylon and bay mounting. The factors directly affecting radome design can be grouped into the following general categories: aerodynamic, thermal, electrical, structural, environmental, wall construction, and physical. Since each of these is directly affected by the properties of the material of which the radome is made, the effect of this material must also be considered.

The following discussion summarizes the many factors influencing radome design. It does not, however, present detailed design data. Such information is generally available in design reports such as Reference 1. Although a detailed list of references is provided at the end of this chapter, the reader should also consult the bibliography compiled by the Lincoln Laboratory Library. These two reports, References 12 and 13, contain the unclassified and classified documents, respectively, published between January 1962 and October 1962.

##### 1-1.4.1 Aerodynamic

A radome designer rarely evaluates the aerodynamic performance of a radome. He must be aware, however, of the various interacting effects that prompt an aerodynamicist to propose shapes that cannot be readily modified to obtain optimum electrical performance. Aerodynamically, a radome is defined by its shape and fineness ratio. The fineness ratio is the ratio of  $l$ , the distance from radome tip to the maximum missile transverse section, to  $D$ , the diameter of the maximum transverse section. These two parameters determine the aerodynamic drag of the radome. For every fineness ratio, there is a shape that results in the least aerodynamic drag for any given Mach number.

The various radome shapes previously discussed represent those usually employed in radome design. These are illustrated in Figs. 1-6 through 1-9 and are based on a fineness ratio of 2.5:1. The use of the hemisphere, Haack, ellipsoid, and paraboloid is usually restricted to the transonic region where these shapes cause the least drag. Between Mach 1 and 2, the Von Karman, the one-half and three-quarter power series, the one-half and three-quarter power paraboloid, and the logarithmic spiral cause the least drag. At velocities greater than Mach 2, the Von Karman, ogive, three-quarter power series, paraboloid, and cone are the most suitable shapes.

The effect of nose shape on the drag coefficient was expressed by Jorgensen, who said, "Although for the similarity-parameter range investigated, the wave-drag of a Newtonian shape (which is approximated by the three-quarter power curve) is at most 10 percent less than that of a Von Karman shape, it is 20 to 25 percent less than that of a tangent ogive, and 15 to 20 percent less than that of a cone." (See Reference 18.)

References 14 through 20 present data on aerodynamic drag useful for specific design information. Since the ogive and cone together with the Von Karman and three-quarter power shape are the best radome configurations for the velocities of interest today, we will consider their relative merits. Although a Von Karman nose causes little aerodynamic drag, it is not easy to fabricate and requires template grinding. The three-quarter power shape also presents the same problem. The ogive and cone are

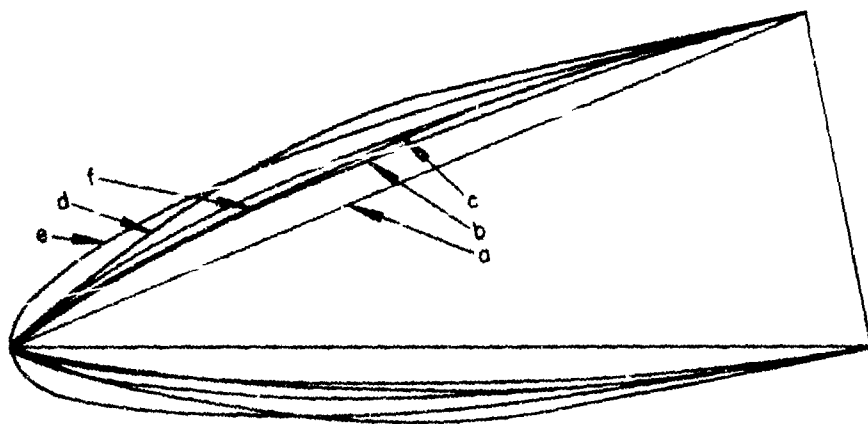


Figure 1-6. Various Radome Shapes

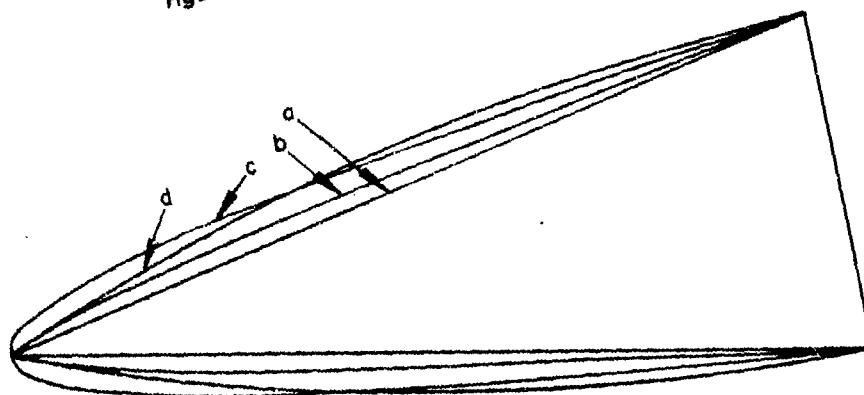


Figure 1-7. Radomes with Swept Shapes

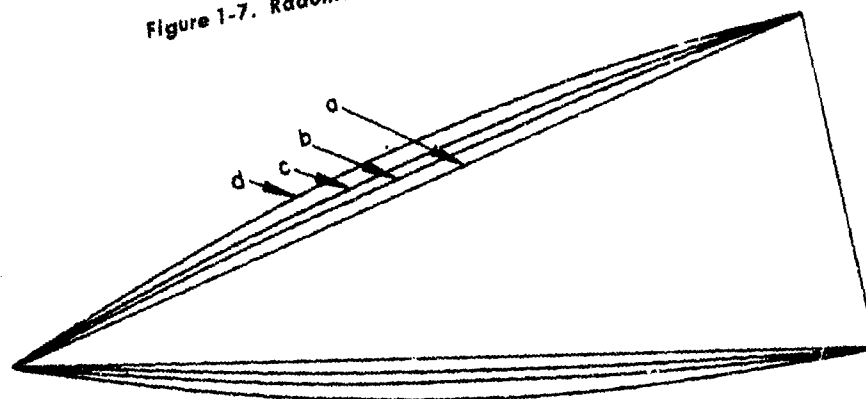


Figure 1-8. Parabolic Radomes

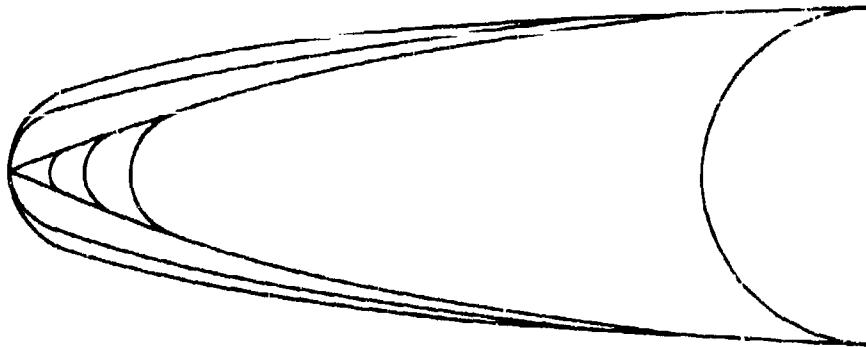


Figure 1-9. Ogival Radomes with Various Types of Nose Blunting

not difficult to fabricate since templates for them can be readily made, and if special grinding equipment is used, templates are not even required. The ogive has the advantages of slightly greater volume for a given fineness ratio, low drag, inherently greater structural reliability because of its bulbous shape, and ease of electrical design because considerable electrical design data are available for this shape.

The effect of the shape of the nose on aerodynamic drag is of secondary importance when compared with that of the fineness ratio. If the drag induced by the nose were the only consideration of importance in selecting a radome for the missile, a high fineness ratio would be chosen. Figure 1-10 shows how drag decreases as the fineness ratio and missile velocity are varied. On the basis of these curves, the maximum fineness ratio would seem to be the best. If, however, the effects of a reduction in transverse area on antenna size are considered, a compromise design must be adopted. It should also be noted that for a given missile length, diameter, weight, and the amount of propellant needed, drag can be increased or decreased by lengthening the nose as the amount of propellant is decreased or increased. In this way, an additional variable is introduced that reduces the fineness ratio to a value less than that which considerations of drag would imply.

The thermal environment and stress encountered at high velocities dictate the use of a blunt nose for greater structural reliability. This shape must also be considered by the aerodynamicist, since it affects total missile drag. Nose blunting

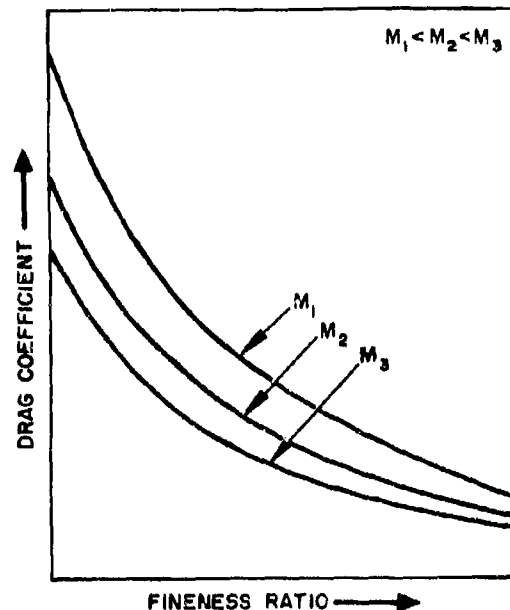


Figure 1-10. Drag Coefficient vs Fineness Ratio for Several Mach Numbers

is achieved by replacing the pointed tip of the radome with an elliptical or ogival section that is tangent to the major contour. Two methods can be used to blunt a radome: (1) blunt the tip and maintain the fineness ratio and base diameter constant, as illustrated in Figure 1-9; (2) blunt the tip and maintain the base diameter constant and reduce the fineness ratio.

The effect of blunting the radome tip is discussed in References 17, 19, and 20. It is shown that for any Mach number, a decrease in fineness ratio increases drag, but as the blunting radius is increased, this radius becomes the more important criterion since all shapes tend to approach a hemisphere as the radius of the tip increases. It should be noted, however, that for small blunting radii, drag actually becomes less than it is when an unblunted shape is employed. This fact can be explained by considering a conical body. At high velocities, the surface pressure is high. If the tip is blunted, this pressure becomes much greater at the tip. However, as the aerodynamic flow expands, the pressure decreases aft of the tip and the total pressure on the body, and hence the drag, becomes less. If the base diameter and ogive radius are maintained constant, the effective fineness ratio decreases as the tip radius increases. The decrease in  $l/D$  gradually cancels this blunting effect and, as would be expected, drag increases. This point is illustrated in Fig. 1-11. A general rule-of-thumb is that if the ratio of the blunting radius to the ogive radius is less than 0.15 to 0.2, drag increases by only a negligible amount.

Blunting the tip radius and maintaining the fineness ratio and base diameter constant pro-

vide an additional advantage. Increasing the tip radius while maintaining the length constant increases the effective fineness ratio of the nose because if the ogive is continued until it intersects the major axis, a higher fineness ratio is obtained (see Fig. 1-11). This effective fineness ratio results in less drag than that encountered with the original fineness ratio. If the increase in drag due to tip radius is compared with the decrease in drag caused by the effective fineness ratio, it is found that a blunted radome can cause less drag than a pointed radome having the same fineness ratio. However, this is true only of small blunting radii, since the limiting shape is a hemispherical nose with a cylindrical skirt that produces high drag.

Although the overall drag of a missile depends on velocity and altitude, other aerodynamic factors, such as acceleration, flight time, and trajectory, must be carefully considered because of their effect on radome temperature and structural reliability.

#### 1-1.4.2 Thermal

A radome is subjected to a thermal environment not only during the short period during which it is in tactical operation, but also while it is on an aircraft or in storage. Since radomes for air-to-air missiles are exposed to all three of these, each is considered in detail. Storage temperatures depend on geographic location and storage conditions. The usual temperature extremes of  $-80^{\circ}\text{F}$  to  $+160^{\circ}\text{F}$  encountered in storage are not significant. Air-to-air missiles on high-speed aircraft encounter one of two types of environment. Bay-mounted missiles are subjected to high temperatures when the bay doors are open at high velocities and to very low temperatures when the doors are closed, especially at high altitudes. These conditions are very similar to those encountered in storage. Pylon-mounted missiles, however, are subjected to the environment of the aircraft and react directly to the free-stream conditions. Thus, these radomes undergo aerodynamic heating similar to that of the aircraft radome or of a free missile following the path of the aircraft. Once a missile has been launched, it undergoes a sudden acceleration and then begins to decelerate because of aerodynamic drag and maneuvers. An air-to-air missile, therefore, experiences an instantaneous increase in tem-

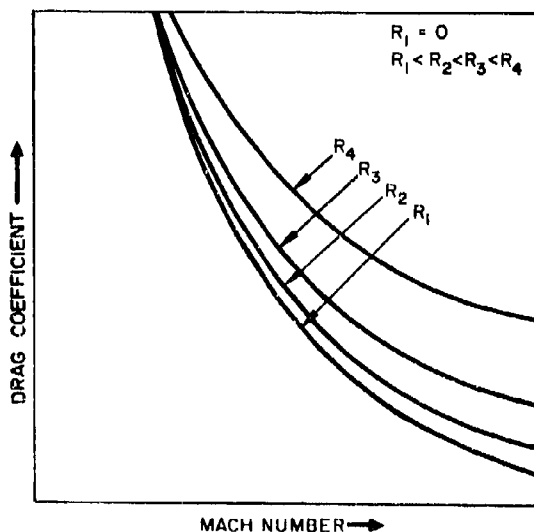


Figure 1-11. Drag Coefficient vs Mach Number for Various Nose-Blunting Radii



perature rather than the gradual increase that is characteristic of ground-launched missiles. The temperature of a bay-mounted missile increases more than that of a pylon-mounted missile, since the bay-mounted missile goes directly from the low temperature to the free-stream environment.

Several areas of a radome can be thermally critical. They are the forward or stagnation region, the transition region, and the region where the radome is attached to the missile. The first area is characterized by laminar flow and high local rates of heat transfer to the wall. The second region is the most forward point on the radome at which turbulent flow occurs and turbulent heating rates occur. The third region should be examined because there may be great differences in the temperature of the radome and the missile structure.

Radome heat transfer rates always depend on the Mach number history of a missile. This history depends in turn on the weight, configuration, and specific mission of the missile. For air-to-air missiles, the thermally critical flight condition is also governed by capabilities of the launching aircraft. The critical launch condition is usually the lowest altitude at which the aircraft can fly at maximum speed. The critical attack mode is less dependent on the launching aircraft; in general, a snap-down attack is more severe thermally than a co-altitude or snap-up attack.

The methods used to calculate the temperature distribution through a radome wall and along its axis are beyond the scope of this chapter. References 21 through 25 should provide a basic understanding of the heat transfer analyses. In general, the effects of angle of attack, i.e., circumferential and axial thermal gradients, are neglected. On a straight and level (co-altitude attack) mission, these effects tend to be averaged by missile roll and oscillatory pitching motions caused by aerodynamic system noise. In a hard-turn maneuver, missile roll again tends to average these effects; in addition, missile velocity decreases more rapidly because of the increase in drag at all angles of attack and thus decreases the driving temperature. This practice of assuming zero angle of attack is conservative for the stagnation point where temperatures are highest.

Analyses of the temperatures of the outer surface of a radome reveal that the temperature

is highest at the stagnation point or at the sonic point, if tip blunting is used, and that it decreases aft of this point. The axial and circumferential thermal gradients are usually several orders of magnitude less than the thermal gradient induced in the wall. The radial temperature gradient is, therefore, the most important factor in radome design since it can vary from hundreds to thousands of degrees Fahrenheit per inch, depending on the conditions of flight. The temperature gradient produced by this aerodynamic heating of a radome is higher near the outer surface than it is at the inner surface. The gradients through the wall produce thermal stresses in the wall because of differential expansion from point to point. Since the temperature of the outer surface of a radome increases rapidly during boost, large compressive stresses are imposed on this surface, while lower tensile stresses occur on the inner surface. As the missile decelerates, the temperature of the outer surface decreases and the above conditions are reversed. Various methods of evaluating the effect of the thermal gradient are discussed in the literature of radome design. References 25 through 32, together with their references, provide a reasonably complete summary of recent work in this field. The methods employed range from detailed analyses to simple cylindrical and planar approximations. The consensus is that a spherical approximation is valid at points near the tip of a blunted radome if the meridional thermal gradient is not sharp and if the modulus of elasticity is not a strong function of temperature. At points aft of the tip of a blunted radome, where the inner radius is large compared with the wall thickness, a cylindrical or conical analysis gives good approximate stress values. References 21 and 26 present the approximate methods and Reference 25 presents the more detailed methods. It has been found that the simple assumption of physical properties that do not vary with temperature is not valid at high velocities. (Reference 25.)

Since the tangent ogive is usually chosen as the optimum radome shape, let us consider such a radome and the effects that missile launch and burn-out velocity, acceleration, fineness ratio, and tip blunting have on temperature and thermal stress. The following conclusions are equally valid for radomes of any shape; only the magnitude of the change is different. A review

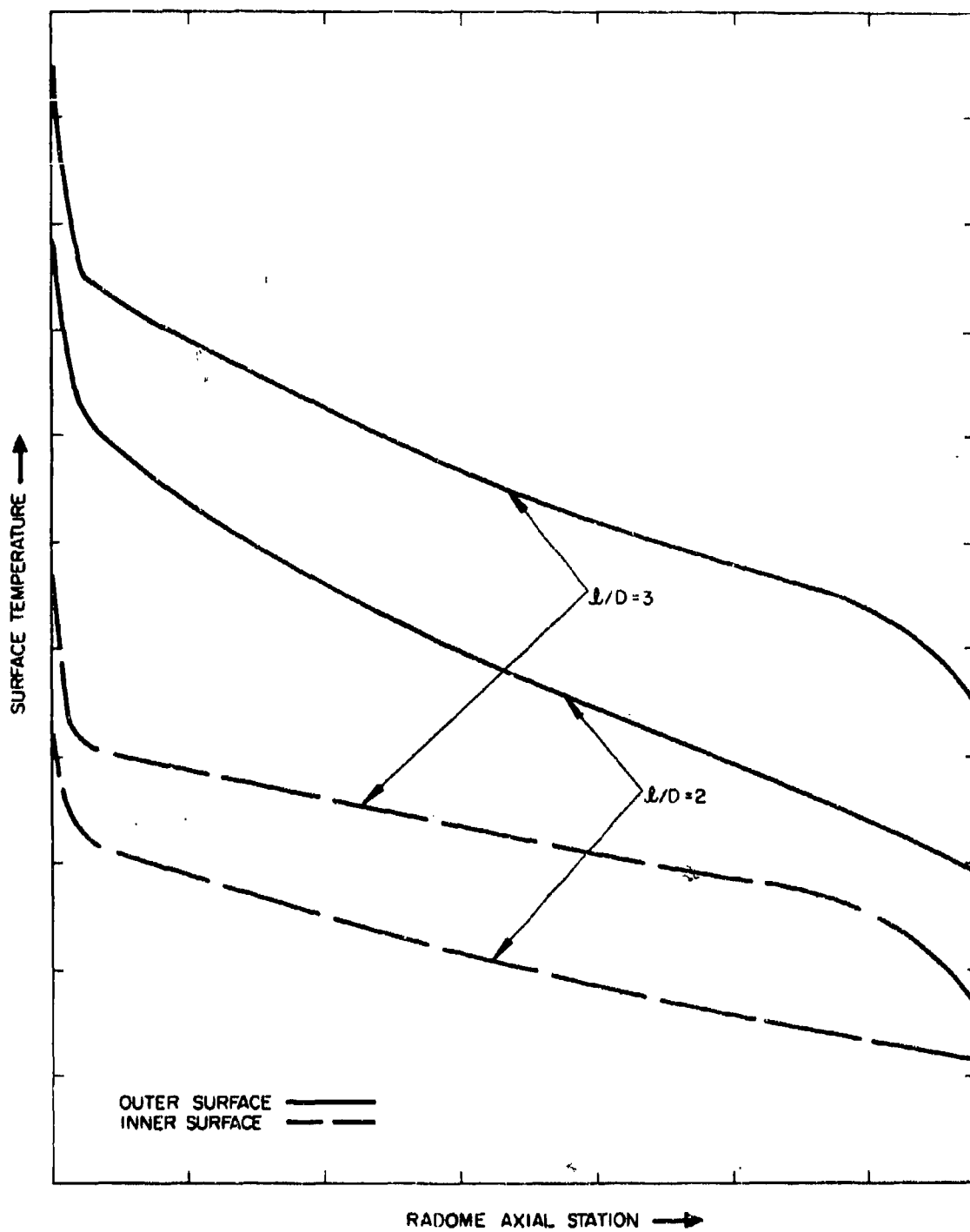


Figure 1-12. Maximum Surface Temperatures vs Radome Axial Stations

of the stress equations shows that: (1) the radial stress vanishes at the outer and inner surfaces, (2) circumferential and meridional stresses are equal in magnitude but vary with position through the wall thickness, and (3) circumferential and meridional stresses are maximum at the surface. Since the maximum radial stress is significantly less than the maximum meridional stress, this discussion will be concerned only with the meridional stress. If two ogival radomes having a tip blunting radius of 1.5 in. and fineness ratios of 3:1 and 2:1, respectively, are fabricated of the same material and are subjected to the same velocity and altitude profiles, they experience considerably different thermal environments as shown in Fig. 1-12. In general, it is found that the temperature of these radomes decreases with increasing distance from the tip; however, for high fineness ratios, the temperatures are greatly in excess of those encountered with low fineness ratios. Figure 1-13 shows the thermal gradients at the stagnation point for a radome with a high fineness ratio. Figure 1-14 was obtained by using these data to compute thermal stress. It shows the differences between the various stress components. Similar data for the other missile stations provide the information given in Fig. 1-15. The decrease in temperature and thermal stress at the lower fineness ratios is self-evident. If a radome is flown on a snap-down and co-altitude trajectory, the temperature and peak tensile stress are approximately 10 to 15 percent greater for the snap-down trajectory.

Acceleration has little effect on maximum temperatures if the missiles attain the same peak velocity. However, thermal stress increases with increasing acceleration. Temperature, thermal gradient, and thermal stress increase for a radome subjected to the same acceleration but to different initial velocities. An increase of one in Mach number can cause a 50- to 100-percent increase in stress, depending on the radome material.

The peak temperature of the outer surface is relatively independent of wall thickness. Thermal gradients and thermal stresses, however, become less with major increases or decreases in thickness. Since in the former case, the heat is distributed through a greater mass, the temperatures are lower. Since in the latter

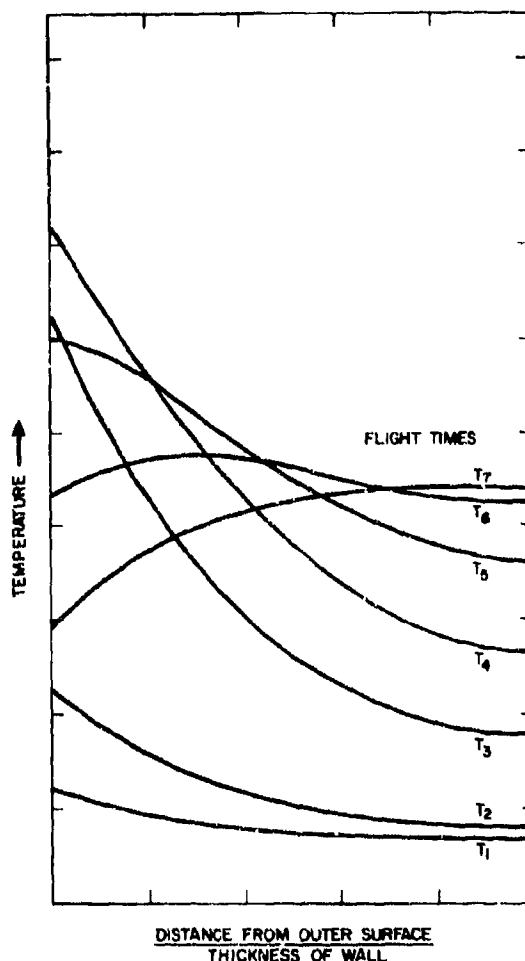


Figure 1-13. Stagnation Point Temperature Gradients

case there is less mass, the thermal gradients are less but the average temperature throughout flight is higher. A decrease in initial temperature increases the thermal gradient and thermal stress; however, the peak temperature does not become appreciably less. The relationship of radome material to temperature is illustrated in a following section. Here, it is sufficient to say that the properties of radome material as a function of temperature must be included in all analyses dealing with hypersonic velocities. The temperature profile of hypersonic radomes is discussed in TDR-AFAL-64-342, "Temperature Profile for Hyper Environ-

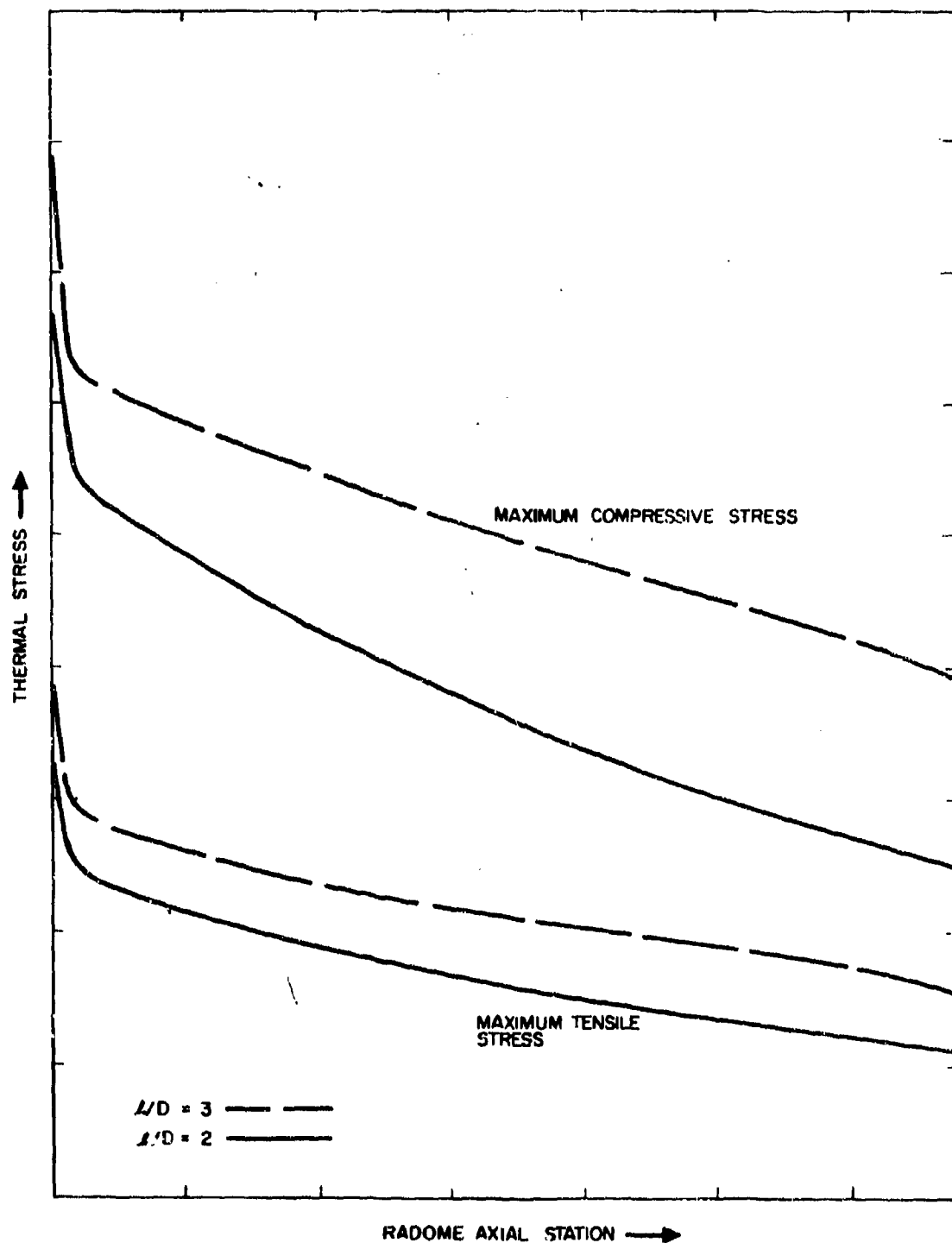


Figure 1-14. Maximum Thermal Stress vs Radome Axial Station

mental Radomes," Final Report under AF 33-(615)-1277.

As shown in Fig. 1-12, the temperature is highest at the tip of the radome. It affects the radome both electrically by increasing the bore-sight error and structurally by producing high thermal stresses. Thermal stresses are related to thermal expansion, thermal conductivity, strength, and elastic modulus of the dielectric material. A discussion of the effect of these and other properties of the material on the thermal shock resistance of the radome is covered in Paragraph 1-1.5.5.

The reduction of the temperature and thermal gradient to the extent that they do not impair radome performance has led to an in-

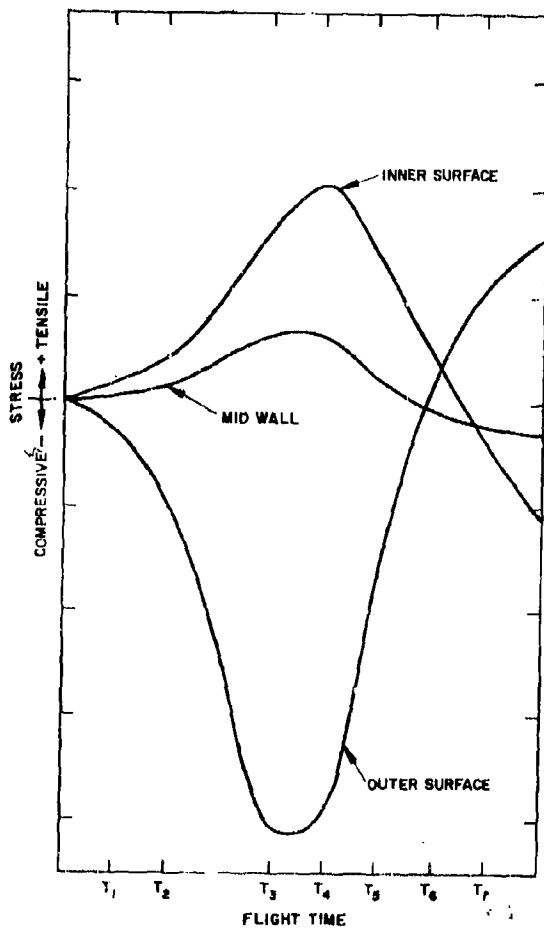


Figure 1-15. Maximum Stress at Stagnation Point

vestigation of the effect of the tip radius. If tips having various radii are used to blunt the radome, the temperature decreases as the radius increases, as shown in Fig. 1-16. The effect of a decrease in temperature on the tensile thermal stress on the inner surface of the radome is shown in Fig. 1-17. It can be seen that a large reduction in stress occurs as the radius increases from 0.5 to 1 in., but that with further increases in the radius, there is less reduction in stress. Note that as the tip radius increases, the time of peak thermal stress is deferred. This

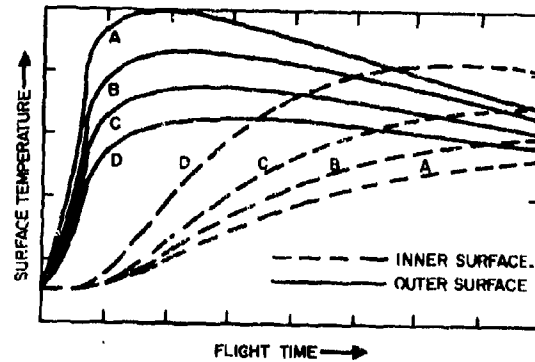


Figure 1-16. Stagnation Point Temperature Histories for Radomes Having Various Tip Radii

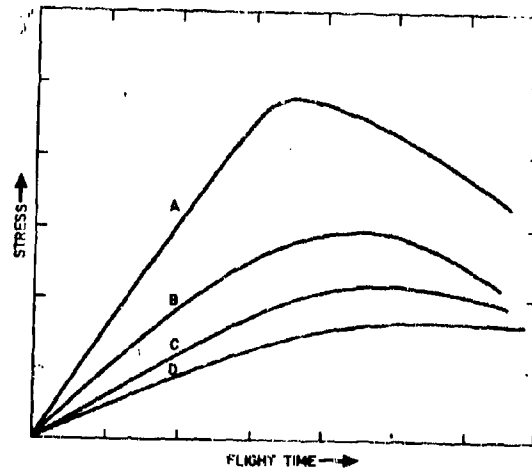


Figure 1-17. Tensile Thermal Stress at Stagnation Point for Various Radome Tip Radii vs Flight Time

fact can be utilized to prevent catastrophic failure in specific systems. An example is a ground-to-air missile, which has a life expectancy of seconds. Here, before intercept, the stress can be reduced to a value below that at which failure can occur.

In many systems, the relief afforded by nose blunting is not sufficient to prevent radome failure. In these cases, additional steps must be taken. One method, discussed in References 33 through 35, is to use an aerodynamic spike at the tip. This spike has been found to be effective at low angles of attack. It causes a decrease not only in radome temperature but also in drag. Reference 36 presents data indicating that the spike does not adversely affect the electrical performance of the radome beyond that expected for a radome with a fineness ratio that is the same as the ratio of the distance from the tip of the spike to radome base to the diameter of this base. Jets of gas or fluids directed forward from the tip reduce the radome temperature. Although systems proposed in References 33 and 37 attain their objectives, they impair the electrical characteristics of the radome and increase the complexity and weight of the missile because facilities for the storage and transfer of gas are required. However, these systems should be considered, especially for large-diameter missiles. Other methods of cooling, such as transpiration and convection, are summarized in Reference 25. Cooling by transpiration is desirable if weight and internal pressure are important considerations. Transpiration and convective cooling require internal pressurization and either porous or slotted walls. For this reason, these methods are not applicable to evacuated systems. The use of a heat sink and ablative cover is considered in References 23, and 38 through 40, each of which contains a list of references dealing with this subject. An ablative cover has the advantages of being self-regulatory and not requiring the pump and storage equipment needed with transpiration or mass injection systems. Ablatives, such as Teflon, polyethylene, and fused silica or quartz, not only absorb heat in the ablative process, but also act as insulators because of their low thermal conductivity. They also offer the advantages of low electrical loss, the absence of a char residue or a conductive liquid layer, and smooth ablation that leaves an aero-

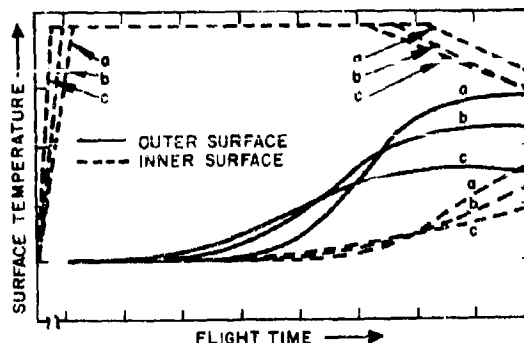


Figure 1-18. Stagnation Point Temperature Histories for Radomes with Various Tip Radii and Teflon Protective Covers.

dynamically clean surface. They can be readily molded and then bonded to the radome to protect the tip area. These materials remove heat by heating the solid to its ablation temperature, melting or subliming the surface, injecting the gaseous product into the boundary layer, and chemically reacting with the boundary layer. Because of its high ablation temperature, the use of silica (or quartz) is limited to reentry conditions. Teflon, having an ablation temperature of approximately 1000°F, is ideal for use at hypersonic velocities. Reference 21 cites one example of the use of Teflon to reduce the high temperature and thermal stress in the tip area. Figure 1-18 presents temperature histories for the same conditions as those on which Fig. 1-16 is based. Teflon 0.390, 0.275, and 0.190 in. thick was used for the 0.5-, 1.0-, and 2.0-in. radii, respectively. The advantage of an ablation insulation system is obvious. Since the heat flux decreases aft of the tip, the thickness of the Teflon can also decrease, as shown in Fig. 1-19. Ablators that become charred provide additional thermal protection, but have the disadvantage of leaving a conductive and molten layer. Materials such as phenolics, epoxides, phenylsilanes and furans, if they are all reinforced with nylon, silica, glass, and other fibers, are examples of charring ablators. The phenolic-nylon system discussed in Reference 23 has the desirable properties of a charring ablator, i.e., gaseous products, a molten layer, a porous char layer, and an insulating layer are formed.

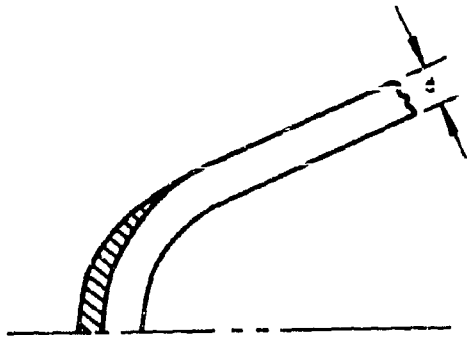


Figure 1-19. Cross Section of Radome Tip Protected by Ablative Cover

#### 1-1.4.3 Electrical

The primary electrical requirement a radome must satisfy is to cause minimum distortion of the electrical characteristics of the antenna; therefore, boresight errors and derivatives as well as absorption and transmission losses must be kept small. Compensating techniques are available to the radome designer (Reference 1) to minimize these undesirable effects at ambient temperatures. Since facilities for the direct measurement of boresight errors during a simulation of the expected thermal environment are not available, such errors can be determined only by theoretical analysis. The electrical characteristics of a radome of a given shape and fineness ratio are directly related to the electrical wall thickness, which at all frequencies depends on dielectric constant, coefficient of thermal expansion, and loss tangent. Hence, the variation in these properties with temperature becomes important as velocity and, therefore, radome temperature increase.

Since the temperatures of various portions of the radome are a function not only of position but also of altitude, trajectory, shape, fineness ratio, and time, the radome should have either of the following properties: (1) compensation for the variation in dielectric constant by an appropriate variation in thermal expansion and vice versa, or (2) a uniform dielectric constant and uniform thermal expansion. The compensation techniques documented in Reference 41 have been investigated at the Hughes

Aircraft Company. The incorporation of dielectric fillers in selected plastic materials has resulted in materials that have essentially constant electrical thickness up to approximately 500°F. Silicone materials are favored because their dielectric constant changes less than in most plastics. However, their electrical thickness varies as much as 2.9 percent over the temperature range from 70°F to 500°F. Since this change is primarily due to the effect of thermal expansion, filler materials having a negative coefficient of thermal expansion were studied. These materials, titanium dioxide and the titanates of calcium, barium, and strontium, were used to load silicone plastics. The primary conclusions reached were: (1) the use of strontium titanate in the proper quantity can result in negligible changes in electrical thickness, and (2) this effect is predominant over the temperature range from 70°F to 500°F and diminishes at higher temperatures. Recent surveys and studies of the properties of ceramic materials show that no material having these characteristics is available at present. Thus, materials having these characteristics are not available for use at hypersonic velocities because the peak temperatures encountered exceed the capability of plastics.

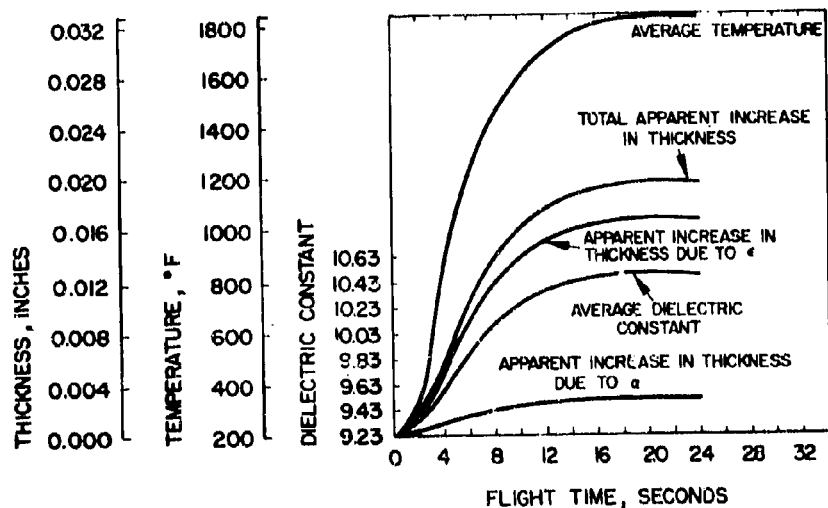
The requirements for invariant dielectric constant and thermal expansion are not met with plastic or ceramic materials. Thus, the material with the smallest change in dielectric constant and thermal expansion must be chosen. The properties of two materials that best approximate this condition, Pyroceram and fused silica, are discussed in References 42 and 43, respectively. The effect of a variation in the above properties must, therefore, be evaluated. Reference 21 presents methods of approximating the effect of the thermal environment by considering the change in wall thickness attributable to thermal expansion and dielectric constant. Two materials commonly considered for use with hypersonic missiles are evaluated. Figure 1-20 presents the results of such an analysis for a one-half-wavelength solid-wall radome. It is apparent from these data that the increase in wall thickness is great enough to increase boresight errors and decrease transmission coefficients.

If tip blunting and an ablative cover are employed, the increase in electrical wall thickness can be appreciably reduced. For the case in

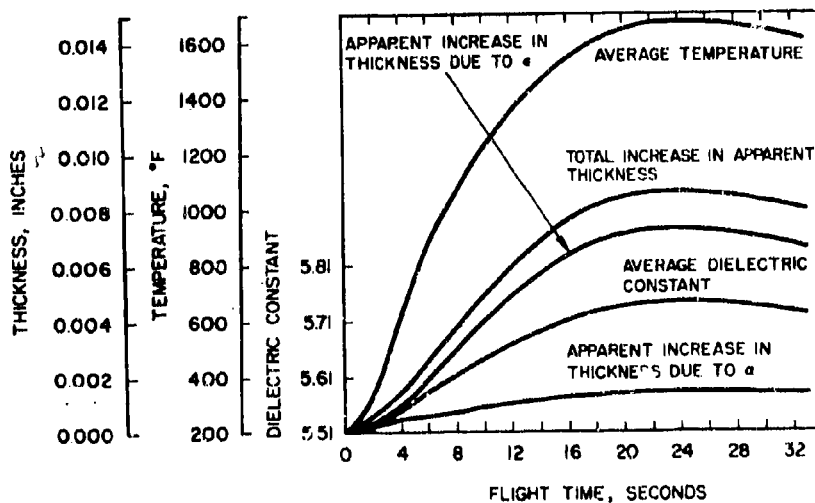
question, this thickness can be less than 0.002 in. with a minimum ablative thickness and tip radius.

Reflection, transmission, and absorption coefficients and variations in internal phase difference are based on the mean radome wall temperature, the wall thickness, the angle of incidence, and the physical properties of the

radome material. For most materials capable of withstanding hypersonic flight, a no-loss analysis is valid because of the low loss of such materials. Pattern distortions can be evaluated by using the appropriate change in wall thickness associated with the temperature of the radome wall. The use of the average temperature in the region of the wall cut by the antenna main beam



(a) ALUMINA



(b) PYROCERAM

Figure 1-20. Stagnation Point Electrical Effects for Radomes with 0.5-in. Tip Radius



to determine the effective wall thickness and thus pattern distortion based on room-temperature measurements at that thickness is also valid.

As indicated previously, the aerodynamic considerations usually dictate that a radome have a high fineness ratio and a small included vertex angle. Since boresight error derivatives are most sensitive to these variables, these derivatives are useful in evaluating the expected electrical performance of a radome. If it is remembered that for a specific illumination the half-power beamwidth  $\Theta$  of an antenna is given by

$$N = \Theta \frac{A}{\lambda_0} \quad (1-8)$$

where  $A$  = operative diameter of antenna  
 $\lambda_0$  = free-space wavelength  
 $N$  = a constant

it is not surprising to find that a similar parameter has evolved for the boresight error derivative. (See Reference 44.) It has been found experimentally that for a fixed fineness ratio the variation in boresight error derivative is

$$N = B \frac{A}{\lambda_0} \quad (1-9)$$

where the variables are as defined before. A review of the copious literature available shows that although the inplant component of error derivative is usually larger than the crosstalk component, the sum of these components remains fairly constant. Figure 1-21 was derived empirically from data on radomes developed at the Hughes Aircraft Company, and others discussed in the literature. The information it contains is, in general, conservative. For a fineness ratio greater than 2, the effects of the elongated shape predominate; for a fineness ratio less than 2, the near-field effects predominate. Thus, the boresight derivative approaches the expected minimum value for the hemisphere. As the fineness ratio increases, this derivative increases. A general rule-of-thumb indicates that for a blunted shape, this derivative is slightly less than that for an unblunted radome. The effect of shape is also shown in Fig. 1-21. The ogive provides the lowest value of  $B$ , which increases for the three-quarter power shape and the cone. These increases are expected since these shapes are not the best

electrically. The position of the antenna within the radome can modify the results shown in Fig. 1-21, which are based on the assumption that the antenna has a minimum wall clearance. If the antenna is close to the radome tip, the value of  $B$  becomes less, since the angles of incidence are slightly less. Note that the proper choice of frequency and of antenna diameter can minimize the effect of radome shape on  $B$ . As shown in Figs. 1-6 through 1-9, the choice of an ogival shape permits the use of a larger antenna, and boresight derivatives can be reduced.

The effect of corrective techniques is illustrated in Fig. 1-21 for the ogival shape. Similar reductions are possible for other shapes. Experience has shown that although such reductions in the value of  $B$  are attainable, the cost of developing a radome and producing it in quantity may outweigh the choice of the most desirable shape or fineness ratio when total system costs are considered; i.e., the additional cost of a better propulsion system to provide the same velocity even though a radome with high drag is used could be less than the cost of correcting a radome. The effect of temperature on boresight error derivative can be approximated by calculating the effective increase in electrical thickness discussed previously and then converting this change to a corresponding decrease in frequency at room temperature. This decrease can, in turn, be converted to an increase in boresight error derivative by using the data contained in Fig. 1-21. This information will

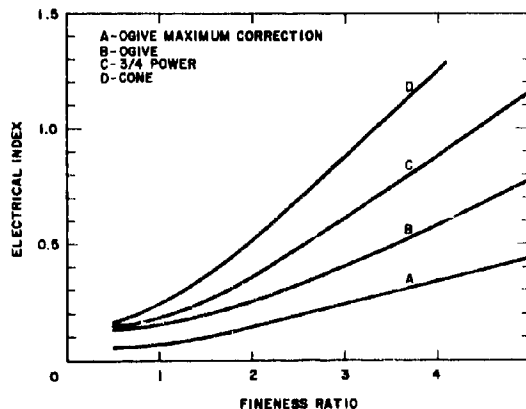


Figure 1-21. Electrical Index vs Fineness Ratio

provide another means of choosing a suitable radome material.

Transmission and reflection coefficients vary in the same manner as boresight error derivative. The approximate magnitude of these variations can be calculated by using the methods presented in Reference 21.

If an ablative cover is used to reduce thermal stress and/or temperature at the tip of the radome, its effect on electrical performance must be considered. The radome is analyzed by considering it as a two-layer laminated structure in which the thickness of the outer ablative layer varies with flight time and trajectory. Since the thickness of this layer decreases with time, the effect of this cover on radome performance decreases. If the cover is just thick enough to reduce stress and temperature during the acceleration phase of flight, it will disappear before the end of flight. Thus, such a cover decreases boresight error and error derivative during the final critical phase of the flight.

The effect of various ablative materials on electrical performance has undergone extensive experimentation. References 45 and 46 present the results of recent experiments dealing with electrical transmission through ablative materials. The materials studied were cork, phenolic-nylon, Duroid, Thermolag, Avcoat, silicones and polyimide plastic loaded with asbestos and glass fibers, and both TFE and FEP Teflon loaded with glass and silica fibers. The conclusions were similar and confirmed the results given in Reference 21, which studied the problem analytically. The superior material was found to be Teflon in either of its forms. However, it must be loaded to achieve dimensional stability at high temperatures. Thus, the reinforced Teflon materials are better suited to designs that do not employ ceramic materials with small ablative covers, but employ instead ablative materials to form the complete radome. In this case, an analysis of electrical performance is simplified since the substrate is not present. Although the transmission of these radomes is greater, boresight errors in the tip area are less because of the elimination of the mismatch at the ablator-substrate interface. However, the overall performance is worse because of the greater loss and variation in dielectric constant in the aft structure. A ceramic radome with an ablative tip is superior for those applications in

which the forward area of the radome must be protected. If the environment is severe, the use of ceramic ablators, such as optical or fused silica, should be considered.

#### 1-1.4.4 Structural

The effects of pressure and inertial loading must also be considered in choosing a radome contour. A bulbous shape has greater strength, while large fineness ratios increase the stress since the bending moments that occur at any radome station is greater. The radome is subjected to compressive forces caused by aerodynamic loads during level flight. However, as the missile maneuvers, bending moments occur that cause tensile stress. This stress reaches a maximum where the radome is attached to the missile. This area is perhaps the only one where nonthermal loading is of primary importance. Even in the attachment area, depending on the method of attachment, mechanical loading can be of secondary importance when compared with the loads imposed by the thermal environment. Structural reliability in this area is chiefly determined by the design of the attachment, not by the shape or fineness ratio of the radome.

#### 1-1.4.5 Environmental

Environmental factors encountered during storage, handling, and captive flight usually pose no problem in designing a radome capable of withstanding hypersonic flight. The most important environmental consideration is rainfall encountered during flight at high velocities. The rate and probability of rainfall and the distribution of the sizes of the raindrops depend on such factors as geographic location and altitude (see Paragraph 3-1). Data on these factors are given in Reference 47. Since each radome will encounter different conditions, depending on its mission, each design must be evaluated separately. The primary factor determining the resistance of a radome to rainfall is the angle at which the raindrops strike its surface. As presented in Reference 48 for tests of wedge-shaped specimens of Perspex, there was a wedge angle below which no erosion took place. Investigation revealed that with plastic materials, it is the normal component of velocity that is sig-

nificant in initiating erosion, but that the tangential component is the important parameter if the rate of erosion is considered. Investigations of the erosion of ceramic materials, reported in Reference 49, showed that the damage is proportional to the normal component of velocity and that the effect of the tangential component on dense ceramic bodies is negligible. Various analyses have demonstrated that a selection of the proper radome shape can reduce the probability of failure due to rain erosion. These optimum shapes include the cone and ogive and other pointed ones having a high fineness ratio. The data summarized in References 50 and 51 confirm that ceramic materials usually show no evidence of progressive damage from erosion, but that there does occur a progressive propagation of microcracks that depends on the total time the material has been subjected to rainfall. Ceramic radomes fail by a catastrophic release of energy that depends on the angle at which the rainfall strikes them, the intensity of the rainfall, and the duration of test.

Recent tests have shown that pointed ceramic radomes do not fail in environments in which blunted radomes fail. Thus, radomes designed for high-velocity flight through rainfall should have a high fineness ratio and low included angles. The use of an ablative cover affords some protection for blunted bodies. This expedient is limited, however, since large quantities of ablative material cannot be used because of the increase in the weight and length of the radome. Chapter 3 contains data on the resistance of ceramic materials to rain erosion; this recently gathered information should be reviewed before any radome design is undertaken.

#### 1-1.4.6 Wall Construction

The performance of a high-velocity missile depends not only on its weight, but also on its center of gravity and its transverse and polar moments of inertia. These parameters, therefore, must be considered in radome design, but for most aerodynamic shapes, their calculation is a complex task. The tables and equations in Reference 52 permit rapid calculation of the weight, volume, center of gravity, and moments of inertia for cones, ogives, and other solids of revolution that are either pointed or blunted.

Using this reference will greatly reduce the time required to obtain the data needed in comparing various designs. The more bulbous shapes are heavier and those with high fineness ratios have larger moments of inertia. Weight can be reduced by: (1) placing the antenna far within the missile nose and making the aft nonelectrical portions from thin metallic materials, and (2) using a wall that has high specific strength.

The lightest wall is the thin wall. If it is acceptable electrically, a one-half sandwich radome, although somewhat heavier, has the advantage of greater strength. The thick solid-wall radome is by far the heaviest. Development of the ceramic materials required for an "A" sandwich radome, discussed in References 4 and 5, provides the radome designer with a light and strong wall. Such a wall also has low thermal diffusivity and thus serves as an insulator to maintain the internal components at almost their initial temperature. The thick and thin solid walls, on the other hand, do not provide insulation unless special material requirements are imposed. It is not unusual for inner-surface temperatures to rise to more than 1000°F. This increase in temperature, in turn, causes the temperature of the antenna to increase several hundred degrees Fahrenheit and thus adversely affects the antenna pattern.

Another consideration of importance in radome design that has been described previously is the effect that increasing the size of the antenna has on reducing boresight error derivatives. Since the thickness of the radome wall falls within the aerodynamic contour, this thickness limits the size of the antenna. The small increase in diameter permitted by thin walls offers no advantage since the resulting increase in gain is usually offset by the greater transmission loss of the radome. For thick solid walls and sandwich constructions having low losses, an increase of several tenths of a decibel can often be realized.

The requirements for an internal vacuum or for pressurization limit the choice of materials and fabrication techniques to those that provide a dense wall that gases cannot permeate. The sandwich and multilayer walls require core materials having a low dielectric constant; such walls are usually permeable by gas. The type of wall chosen affects thermal stress since thin walls can be designed on which stress has a negligible effect. The solid wall used in previous

illustrations of design criteria is the one most susceptible to failure because of thermal stress. The "A" sandwich, which has a porous low-conductivity core, is more resistant to thermal stress since the temperatures of the skins are uniform and the temperature gradient occurs within the core, which may not support crack propagation and which is not a prime structural member. The "B" sandwich can also be designed to resist failure due to thermal stress.

As discussed previously, the thin-wall sandwich and the multilayer walls are broadband. For example, a multilayer wall can be designed to have a bandwidth of 40 to 1. This is a considerably greater bandwidth than the 2-percent bandwidth usually cited for thick solid walls.

In choosing the type of wall to be used for a given design, it must be considered that solid-wall radomes are usually isotropic (certain oriented crystalline materials are exceptions), whereas sandwich and multilayer radomes are never isotropic. At best, physical properties vary in directions perpendicular and parallel to the radome wall. The fluted and honeycomb cores can exhibit a threefold anisotropy since the orientation of flutes can be such that variations occur in each of the three orthogonal axes. If this anisotropy is great, the mechanical and/or electrical design becomes complicated.

Factors such as field handling and reliability must also be considered. The destruction of a radome before use can be prevented by employing suitable protective devices. Field interchangeability is not a normal requirement for small radomes as it is for large ones. Thus, the designs must ensure essentially constant properties from radome to radome. All radomes must be highly reliable and, hence, must be capable of withstanding stresses in excess of those encountered in normal service. The complexity of radomes requires that a detailed quality control program be enforced. Dimensional tolerances other than those for wall thickness can be easily met. Since the tolerance for thickness of sandwich walls is usually at least twice that required for solid walls, sandwich walls are much easier to fabricate. Broadband multilayer radomes, however, involve extremely close tolerances and are expensive to manufacture, even in large quantities. Since tolerances decrease as the dielectric constant decreases, a low dielectric constant is desirable for solid-wall radomes.

Manufacturability and reproducibility must also be considered since they limit the choice of radome type. A design that is feasible analytically may not be so practical or may be impossible to fabricate in production quantities. The choice of a radome design must also be based on a review of the fabrication methods available since it is they that largely govern cost. A slip-cast ceramic radome may be ten times less expensive than a completely ground ceramic radome.

The method used to attach the radome to the missile depends on the type of radome wall and material and also affects the final cost. Solid walls can be readily attached. However, the small experience available with the ceramic sandwiches limits a designer to essentially original designs that must undergo detailed analyses and complete testing before their merits can be determined.

#### 1-1.5 PHYSICAL PROPERTIES OF RADOME MATERIALS\*

A review of the relationships between radome shape, fineness ratio, and wall thickness and the restrictions imposed by aerodynamic, structural, electrical, thermal, environmental, and physical requirements indicates that special materials are required. Since there is not one material that has all of the desirable characteristics for all radome designs, it is important to review the various properties of materials that affect radome performance. It will then be possible to select a compromise material. The properties of a material can be grouped in five categories: general, environmental, thermal, electrical, and mechanical. The standard question asked by material suppliers and/or fabricators is: "Which properties are important in radome design?" The fairly complete list presented in Table 1-1 includes many properties that need not be analyzed but that should be considered in choosing a material. Those properties that are essential are marked with a double asterisk. However, accurate and detailed analyses are possible only if the physical properties are known as a function of temperature over the complete range of temperatures expected.

\* See Paragraphs 1-4, 5-9 and 5-10.

TABLE 1-1. PHYSICAL PROPERTIES INVOLVED IN RADOME DESIGN\*

1. GENERAL	4. ELECTRICAL
Color	Reflection coefficient
Surface finish	Absorption coefficient
Surface texture	Transmission coefficient
Composition	Loss tangent**
Homogeneity	Dielectric constant**
Isotropy	Dielectric strength
	Loss factor
	Volume resistivity
2. ENVIRONMENTAL	
Resistance to moisture and rain	
Water absorption	
Gas permeability	
Outgassing	5. MECHANICAL
Resistance to chemical solubility, salt spray, and fungus	Hardness
Radiation effects	Impact strength
Storage life	Density
	Young's modulus of elasticity**
3. THERMAL	Modulus of rigidity
Maximum use temperature	Poisson's ratio**
Softening point	Bulk modulus**
Melting point	Shear strength and modulus**
Ablation data**	Compressive strength and modulus
Resistance to thermal shock	Tensile strength and modulus**
Thermal conductivity**	Flexural strength and modulus**
Thermal diffusivity**	Dimensional return
Specific heat**	Porosity
Coefficient of linear expansion**	Fatigue effects
Total normal emissivity**	Dimensional stability

\* Review Paragraph 1-4, and see Chapters 4 and 5.

\*\* Properties essential in choosing a radome material.

#### 1-1.5.1 General

The general properties include such optical properties as color, translucence, opaqueness, and transparency that are normally not considered in radome design. Surface texture and finish do, however, affect aerodynamic performance since a rough surface increases drag. A 125-microinch finish is adequate for all but the most stringent aerodynamic requirements.

A surface increase or decrease of 0.005 in. does not measurably increase aerodynamic drag. The material must be both structurally and electrically homogeneous since unpredictable variations in these properties from point to point reduce structural reliability and increase the complexity of the electrical correction needed. Although structural isotropy may be a desirable characteristic, electrical isotropy is usually not because radiated energy is then affected dif-

ferently for each orientation of the radome. The hysteresis effects that are commonly associated with the dielectric constant of plastic materials are not desirable.

### 1-1.5.2 Environmental

Many factors affect the environmental suitability of the material. Since water absorption, which varies with temperature and pressure, increases the effective dielectric constant, it gives rise to an uncontrollable electrical characteristic. A material that is permeable by gases or that outgasses when heated is not suitable for use in an evacuated or pressurized radome. Resistance to solution by chemicals other than petroleum products or others associated with missile storage and use is not required. Many materials, however, are affected by these solutions. Salt spray does not usually impair the properties of ceramic materials, which seldom support fungus growth. As previously discussed, resistance to rainfall is important for all but clear-weather missiles. Changes in properties caused by radiation of any frequency are not desirable. Resistance to nuclear and atomic radiation must be considered in designing a radome for operation in or near such environments. The effect of the passage of time on the physical properties of a material is most important; a material whose characteristics vary from day to day cannot be used.

### 1-1.5.3 Thermal

A radome is subjected to very high velocities over relatively short periods of time; therefore, its melting point or preferably its maximum use temperature as a function of heating rate must be known. A calculation of surface temperatures and of thermal gradients requires a knowledge of the total normal emittance and of two of the following three properties: thermal conductivity,  $k$ ; diffusivity,  $\alpha_t$ ; and specific heat capacity,  $c_p$ . The relation between these properties and density,  $\rho$ , is given by

$$\alpha_t \leq \frac{k}{\rho c_p} \quad (1-10)$$

If spectral emittance data are the only data available, they can be readily converted to total normal emittance by the methods presented in

Reference 53. Specific heat capacity,  $c_p$ , is defined as the ratio of heat flowing into a substance per unit mass to the increase in the temperature of this substance. The higher the value of  $c_p$  is, the less the temperature of the radome wall increases. Thermal conductivity is a measure of the ability of a substance to conduct heat; therefore, a high value is desirable if thermal stress is to be kept to a minimum. Thermal diffusivity, a measure of the rate of heat transfer, should be as high as possible to reduce thermal gradients and, hence, thermal stress. Transfer of heat by radiation is a two-way transfer of energy, i.e., radiation both to and from the radome, depending on whether the radome or its environment is hotter. Radiant heat transfer, a function of the fourth power of absolute temperature, is most efficient for bodies at high temperatures, such as a hypersonic radome. Emittance is a measure of the efficiency of the radiator compared with that of a black body at the same temperature; therefore, high values of emittance are desirable to reduce temperature buildup. White materials are good reflectors at visual wavelengths and, therefore, have low emittance, but they are not necessarily good reflectors at the infrared wavelengths that are important in heat transfer. Pyroceram and alumina are materials having low emittance in the visible region but high emittance in the infrared region. If the material ablates at high temperatures, such information as ablation rate and temperature must be known to accurately predict the temperatures within the radome wall. Resistance to thermal shock and coefficient of linear thermal expansion (thermal expansivity) should be high and low in magnitude, respectively. The effect of these properties is discussed in a later portion of this chapter.

### 1-1.5.4 Electrical

The most important electrical properties in radome design are dielectric constant and loss tangent. Since reflection, absorption, and transmission coefficients can be calculated from these parameters, measured data are not required during the early stages of design. Loss tangent, which is a measure of the loss of energy due to heating, should be low, as it is for most ceramic materials. The dielectric constant should in-

crease only slightly with temperature in order to offset the effect of the thermal environment and it should be as low as possible. High dielectric constants imply low mechanical tolerances and narrow band operation. An ideal material would undergo a negligible change in dielectric constant and loss tangent over a 5-percent bandwidth since this small change in these values increases broadband capability.

### 1-1.5.5 Mechanical

Mechanical characteristics are extremely important because, to a large extent, they determine the acceptability of a material; i.e., inferior electrical and thermal performance may be tolerable if the radome can remain intact during flight. The data presented in Chapter 3 and in the literature indicate that resistance to rain erosion and catastrophic failure because of rainfall can be roughly correlated with hardness and impact strength, respectively. Thus, a hard noneroding surface is electrically desirable and one with high impact strength is structurally desirable. Low density is assumed to be analogous to low weight. Note, however, that density alone does not control the weight of a radome since the dielectric constant determines the wall thickness. The value of the ratio of density to the square root of the dielectric constant should be the lowest possible.

Tensile, compressive, and flexural strength should be high. Nonductile ceramics always fail under tension. For this reason, the ceramics industry has gradually tended to eliminate tests of tensile strength because of the problems of alignment encountered in such tests. The Modulus of Rupture (MOR), which is found by a test similar to a flexural test, is measured instead. The effect of surface quality on strength must be considered since, to a certain extent, all ceramics are notch sensitive and subject to failure if their surface is marred by grinding imperfections or scratches. Because ceramics are brittle, they are susceptible to microcracks due to improper assembly or field handling and these cracks induce failure under loading.

The ability of a radome to withstand thermal shock is associated with a mechanical index, one form of which is

$$\frac{(1-\mu)}{\alpha E} \frac{k}{\rho c_p} \frac{\text{MOR}}{d} > 1 \quad (1-11)$$

where  $\mu$  = Poisson's ratio  
 $\alpha$  = linear coefficient of thermal expansion  
 $E$  = Young's modulus of elasticity  
 $k$  = thermal conductivity  
 $\rho$  = density  
 $c_p$  = specific heat capacity at constant pressure  
 $\text{MOR}$  = Modulus of Rupture  
 $d$  = wall thickness

For a given radome shape and environment, this index provides a means of determining which materials should be considered. However, experience has shown that the use of this index is not foolproof and that a detailed analysis often reverses the sequence of materials listed in the order of preference based on this mechanical index. This reversal is primarily due to: (1) the effect of variations in the physical properties of materials with temperature, and (2) the magnitude of the heat transfer coefficient. Findings reported in References 54 through 57 generally concur with the above statements. The use of either two or three indexes, depending on the magnitude of the heat transfer coefficient, has been proposed.

If the heat transfer coefficient,  $h$ , is low, Eq. 1-11 takes the form

$$\frac{\text{MOR}(1-\mu)k}{\alpha E} > 1$$

If the heat transfer coefficient is high, it takes the form

$$\frac{\text{MOR}(1-\mu)}{\alpha E} > 1$$

Several sources, for example, Reference 56, suggest using an expression of the form given by Eq. 1-11 if the heat transfer coefficient lies in some intermediate region. In all cases, the effect of wall thickness,  $d$ , was neglected, most probably because only in radome design does wall thickness necessarily vary from material to material. To illustrate the effect of the heat transfer coefficient, let us consider the findings in Reference 54. The thermal shock resistance of beryllia and alumina was studied by using media having low (air) and high (water) heat transfer coefficients. It was observed that beryllia is superior to alumina at low heat transfer rates, but that alumina is superior at high rates. This reversal is caused by the inef-

fectiveness of the high conductivity of beryllia at high heat transfer rates and to the higher values of Young's modulus, expansion coefficient, and MOR of alumina under these conditions. To further illustrate this dependence of the index on the heat transfer coefficient, let us consider the results reported in Reference 57. A graph showing the thermal shock index was constructed by finding the maximum temperature at which a material could be quenched to room temperature for various heat transfer coefficients. Figure 1-22 shows this

graph in which maximum temperature is plotted vs.  $ah$  for representative ceramic materials. Although these data are based on the assumption that the physical properties remain constant, they do confirm the results reported in Reference 54, i.e., for low values of  $h$ , beryllia is superior to alumina, whereas for high values of  $h$ , the converse is true. It should be noted that the author has obtained similar data in investigating actual missile radomes. Analyses in which fused silica, Pyrocera, alumina, and beryllia ceramics were studied, resulted in tab-

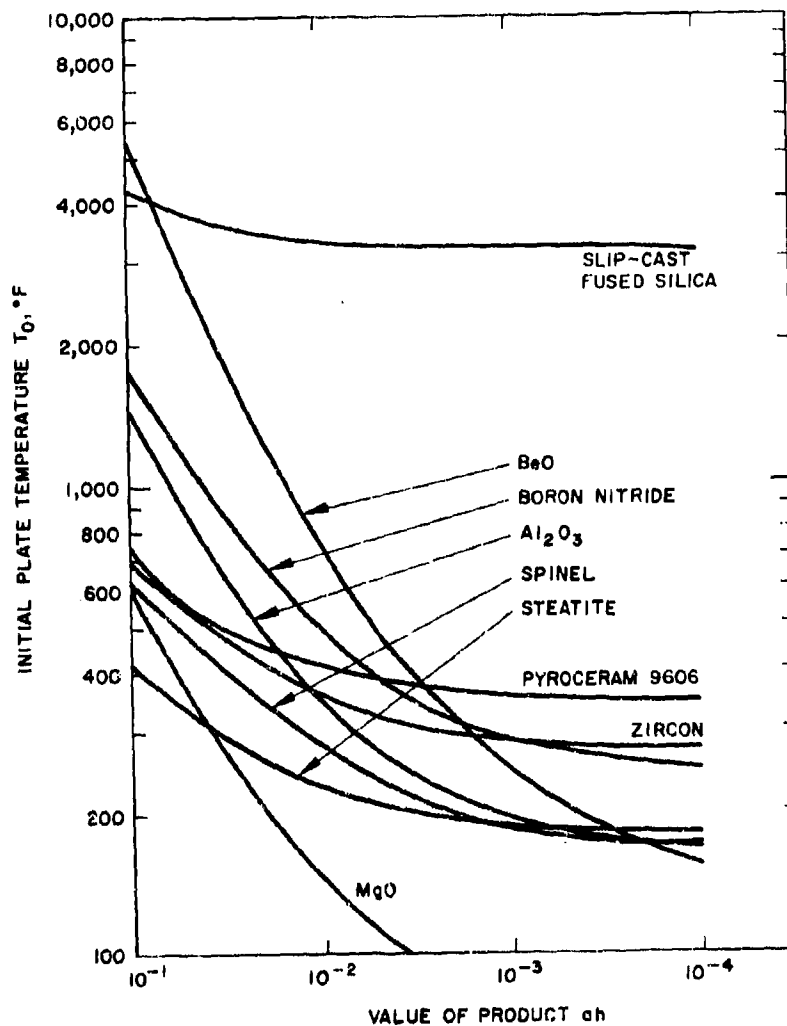


Figure 1-22. Relative Thermal Shock Resistance of Candidate Reentry Radome Materials as a Function of Thermal Shock Environment



ulations identical to those predicted by Fig. 1-22. Although this figure assumes a down-shock, similar curves can be constructed for an up-shock test. The use of conservative values of MOR, i.e., values several standard deviations below the mean strength, enhances the validity of the analysis.

The index should serve only as a guide in investigations of materials and not as a final criterion, since it shows the general behavior of the physical properties. Increases in wall thickness, thermal expansivity, and Young's modulus increase thermal stress, whereas an increase in thermal diffusivity and a decrease in Poisson's ratio reduce thermal stress.

Dimensional stability and return are similar to electrical hysteresis and affect the radome structurally. The effects of fatigue on ceramic

materials are relatively unknown quantities, but they should be considered for radomes that are subjected to many pylon-mounted captive flights, where a gradual decrease in strength could cause the radome to fail after the missile was launched.

The characteristics of several ceramic materials are illustrated in Figs. 1-23 and 1-24, in which these materials are compared on the basis of maximum inner- and outer-surface temperatures and tensile thermal stress at the inner surface for a specific radome design. The high thermal diffusivity of beryllia results in identical peak inner- and outer-surface temperatures. Materials having the least thermal diffusivity exhibit a greater difference in surface temperatures. The high thermal stress in the alumina wall is primarily caused by its high thermal expansivity.

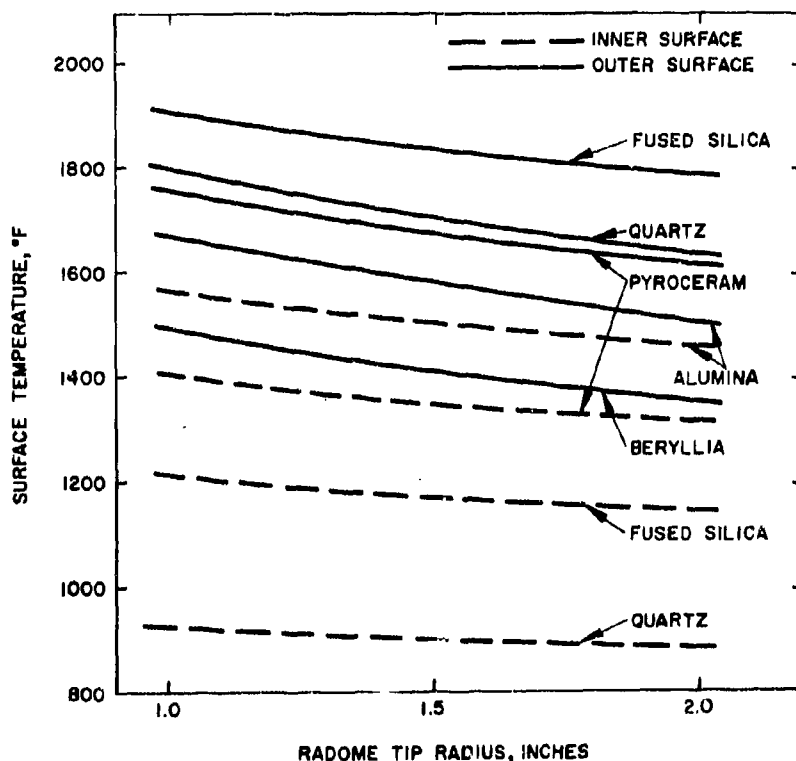


Figure 1-23. Maximum Surface Temperatures of Radome vs Tip Radii for Several Ceramic Materials

## 1-2 THIN-WALL RADOMES

### 1-2.1 INTRODUCTION

In the preceding paragraphs, the various factors that affect the design of a high-velocity radome were discussed. They affect each type of radome wall differently. For example, rainfall may not impair the structural reliability of a one-half-wavelength wall, but it limits the use of thin-wall radomes to applications involving low velocities. The primary advantage of thin-wall radomes is that for any aerodynamic shape, they are lightweight. Since weight is a significant consideration in missile design, it is important to consider the relative merits of this type of construction. In this section, the various factors affecting thin-wall radomes and the merits and disadvantages of such radomes are discussed. A specific radome shape is used to

illustrate the difference between a half-wavelength and thin-wall radomes.

### 1-2.2 DEFINITION

The term *thin wall* has a twofold meaning. Mechanically, it means that the thickness of the wall is small when compared with the thickness normally used in structural applications. Electrically, this term is defined as a solid wall that approximates the zeroth order. Generally, a thickness of  $1/20$  of a wavelength in the material is considered thin enough for obtaining most of the electrical properties desired in a thin wall. If Eq. 1-1 is modified for the case in which the angle of incidence is equal to 90 degrees, it becomes:

$$d = \frac{\lambda_0}{2} \frac{1}{\sqrt{\epsilon}} \quad (1-12)$$

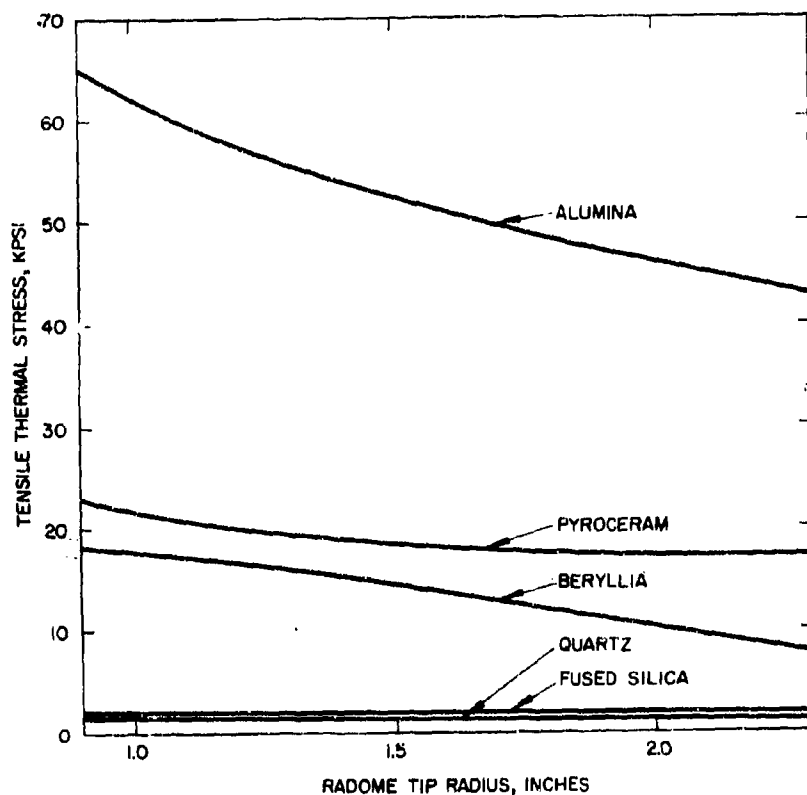


Figure 1-24. Tensile Thermal Stress on Inner Surface of Radome vs Tip Radii for Several Ceramic Materials

TABLE 1-2. THICKNESSES (IN.) OF ONE-HALF-WAVELENGTH AND THIN-WALL RADOMES FOR NORMAL INCIDENCE

Frequency, (gc)	Wavelength, (in.)	Thickness (2)	Dielectric Constant					
			2	4	6	8	10	12
2.2	5.3046	$\lambda/2$	1.8967	1.3411	1.0905	0.9483	0.8482	0.7743
		thin	0.3793	0.2682	0.2181	0.1897	0.1396	0.1549
4.5	2.6227	$\lambda/2$	0.9273	0.6557	0.5353	0.4636	0.4147	0.3785
		thin	0.1855	0.1311	0.1071	0.0927	0.0829	0.0757
9.0	1.3113	$\lambda/2$	0.4636	0.3278	0.2677	0.2318	0.2073	0.1893
		thin	0.0927	0.0655	0.0535	0.0464	0.0415	0.0379
18.0	0.6557	$\lambda/2$	0.2318	0.1639	0.1338	0.1159	0.1037	0.0946
		thin	0.0464	0.0328	0.0268	0.0232	0.0207	0.0189
36.0	0.3278	$\lambda/2$	0.1159	0.0820	0.0669	0.0579	0.0518	0.0473
		thin	0.0232	0.0164	0.0134	0.0116	0.0104	0.0095

By solving this equation for various frequencies and dielectric constants, the data in Table 1-2 can be obtained. The values in this table are representative of the approximate wall thicknesses of radomes operating from S- to K<sub>u</sub>-bands\* and of materials such as Teflon, fused silica, Pyroceram, and alumina. It is apparent that mechanical thickness decreases as frequency and dielectric constant increase. For a dielectric constant of 2 at S-band, thin and one-half-wavelength radomes are both mechanically thick.

A material with a dielectric constant of 2 is structurally adequate in the one-half-wavelength thickness at K<sub>u</sub>-band. The K<sub>u</sub>-band thin wall is, however, so thin that it is not structurally suitable. A review of the data shows that at low frequencies a wall that is thin electrically is thick mechanically and that at high frequencies the one-half-wavelength wall is also thin mechanically. At very high frequencies, the thin wall is too thin to be used as a structural member. Thus, a radome can be thin both electrically and mechanically (as it is at X-band); it can be thick electrically and thin mechanically (K-band); or it can be thin electrically and thick mechanically (S-band). Unless otherwise noted, we will consider that the radome is a thin elec-

trical wall; for the high frequencies of interest today, this implies a thin mechanical wall.

### 1-2.3 AERODYNAMIC CONFIGURATION

The shape of the radome is determined by the requirements associated with aerodynamic drag, electrical characteristics, resistance to rainfall, and thermally induced stresses. Fundamentally, these characteristics depend on the radome fineness ratio. A high fineness ratio reduces aerodynamic drag and thermal stress, but it increases loss and boresight error derivatives. The radome also has greater resistance to rainfall when its fineness ratio is high. As was shown in Paragraph 1-1.2.1, the effects of these factors on overall missile performance are so complex that it is impossible to derive a simple formula for choosing the optimum shape. Extensive studies of the design of airborne missiles consistently indicate that a fineness ratio of from 2:1 to 3:1 represents the best compromise.

For any given fineness ratio, there is a radome shape for which aerodynamic drag is reduced to a minimum. This shape is usually defined by the power curves discussed previously. The radome is usually blunted to reduce aerodynamic drag and heating of the tip. A

\* For band code letters, see Appendix A, Chapter 2.

power shape can be effectively approximated by several ogival sections as was done for the radome shown in Fig. 1-25. This radome, which has a fineness ratio of 2.0:1, a base diameter of 12 in., and a tip blunting radius of 1.5 in., will be used in comparing the characteristics of one-half-wavelength and thin-wall radomes.

#### 1-2.4 MATERIALS

As the requirements for missiles capable of higher velocities and operation in all types of weather increase, the number of suitable radome materials available becomes more and



Figure 1-25. Radome Used for Electrical Tests

more restricted. High-speed rain-erosion tests that were sponsored by the Naval Air Development Center and that are reported in Chapter 3 demonstrate that thin sections of ceramic materials can withstand such erosion. References 6, 51, and 58 through 61 contain most of the data obtained in tests of thin-wall ceramic radomes made of Pyroceram and alumina. These data show that such radomes with wall thicknesses greater than 0.082 in. and 0.060 in., respectively, can withstand the impact of rain falling at the rate of 2 in./hr with a mean drop-let size of 2 mm during flight at velocities ranging from 2800 to 2900 ft/sec. If the flight velocity is reduced to 2000 ft/sec, a thickness of 0.050 in. is adequate. Thus, solid walls having a thickness greater than these values can, as a rule, withstand rainfall. As reported in Reference 51, plastic materials erode at high rates if the velocity to which they are subjected is supersonic. At the high temperatures encountered during supersonic flight, such materials tend to char or their dielectric constant becomes so high that they are no longer usable.

Thus, ceramic materials or ceramic-protected plastic materials are the best for thin-wall radomes. The choice between one-half-wavelength and thin-wall radomes depends primarily on their relative merits in terms of such factors as electrical transmission, resistance to thermal stress, and weight. Weight becomes significant at X-band frequencies and lower, since a thin-wall radome weighs 80 to 85 percent less than one with one-half-wavelength walls.

#### 1-2.5 ELECTRICAL

When placed in front of an antenna, an ideal radome causes negligible changes in the antenna pattern and only minimum losses in the energy transmitted. However, an ideal radome cannot be realized in practice because the phase and amplitude of the antenna energy are a function of the radome material, shape, and electrical thickness. The designer of a thin-wall radome must consider such electrical factors as transmission and reflection losses, changes in phase, boresight error derivatives, antenna distortions, and broadband perform-

ance. Each of these points is discussed in the following paragraphs.

Transmissibility, i.e., the ability of a material to transmit energy, is one of the critical requirements in radome design. This is especially true of active systems in which a decrease in antenna gain must be considered during both the transmit and receive periods. A reduction in signal strength is manifested primarily as a reduction in tracking range. The greater missile weight and electrical power that are needed to overcome this disadvantage impose a heavy penalty on the overall system design. The loss in antenna gain is due primarily to three factors: phase distortions that increase antenna beamwidth, reflection losses, and transmission losses. The first two factors are discussed apart from transmission losses since they affect other design parameters. A fourth cause of reduction in antenna gain, attenuation through the radome, can be neglected since the loss is usually small, even for thin sections of plastic materials.

In Reference 7, it is shown that for  $\tan \delta \ll 1$ , the attenuation coefficient is approximately equal to  $0.5 \tan \delta$ . Thus, for materials for which the value of  $\tan \delta$  is less than 0.001, the attenuation coefficient is less than 0.05 percent.

### 1-2.6 TRANSMISSION LOSS

The transmission loss of plane sheets has been studied extensively. References 62 and 63 present transmission data for materials with dielectric constants ranging from 1.2 to 10 for both the lossy and lossless cases. While it is primarily of use to the designer of thick-wall radomes, this information does provide a means of evaluating thin-wall radomes.

Additional information on two ceramic materials that in thin sections are resistant to rainfall at relatively high velocities is presented in Figs. 1-26 through 1-29. A review of these figures shows that transmission losses increase as the dielectric constant increases. An increase in the angle of incidence causes a decrease in loss for parallel polarization, but an increase for perpendicular polarization. This loss is greatest,

however, for perpendicular polarization. Reference 1 shows that for very thin sections, transmission loss increases as frequency increases, but that as the thin section approaches a one-half-wavelength wall, the opposite is true. Reference 64 reports the study of transmission loss for C-, X-, and K-bands and the findings are similar to those of Reference 1. Reference 64 shows that at X- and C-bands, adequate performance can be obtained up to angles of incidence of 50 to 60 degrees for thin walls, but that in the K-band, a thin-wall radome is not structurally adequate and that a one-half-wavelength wall is needed. It also shows that loss increases as the radome temperature increases. If the losses due to attenuation are neglected, the limiting transmission coefficient for a thin-wall radome can be expressed as:

$$|T_{\parallel}|^2 \approx 1 - \left[ \frac{\pi(1 - \epsilon)}{\epsilon \cos \theta} \frac{d}{\lambda_0} (\epsilon \cos^2 \theta - \sin^2 \theta) \right]^2 \quad (1-13)$$

$$|T_{\perp}|^2 \approx 1 - \left[ \frac{\pi(1 - \epsilon)}{\cos \theta} \frac{d}{\lambda_0} \right]^2 \quad (1-14)$$

Figure 1-30 presents data obtained by solving Equation 1-14 for  $d/\lambda_0$  when  $|T_{\perp}|^2$  is equal to 90 percent. These data permit the selection of a proper wall thickness if the maximum angle of incidence is known.

Reference 65 contains measured values of transmission losses for the radome shown in Fig. 1-25 for both thin and one-half-wavelength thicknesses. Figures 1-31 and 1-32 present measurements at X-band for the E- and H-planes. These figures show that loss increases as the deviation from one-half-wavelength thickness increases. Figures 1-33 and 1-34 show the measured variation in transmission loss as the frequency varies about the design value. These measurements reveal that transmission loss becomes greater as the radome deviates from the ideal half-wavelength thickness. As expected, the greatest loss occurs through the pointed section of the radome. Note that a thin-wall radome is equivalent to one that is one-half wavelength thick increased by the dimension of the thin-wall radome.

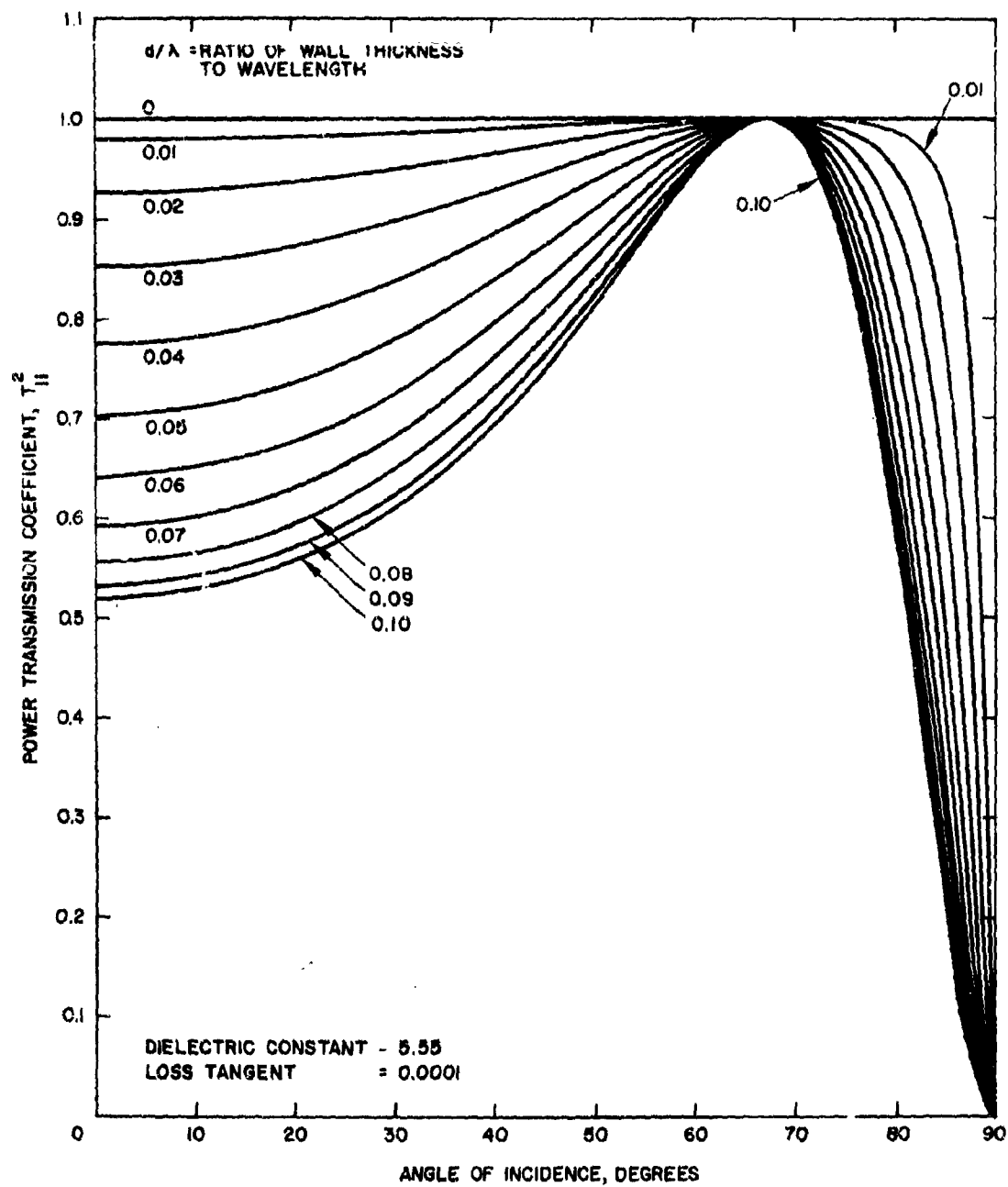


Figure 1-26. Power Transmission Coefficient for Pyroceram  
 (Parallel Polarization)

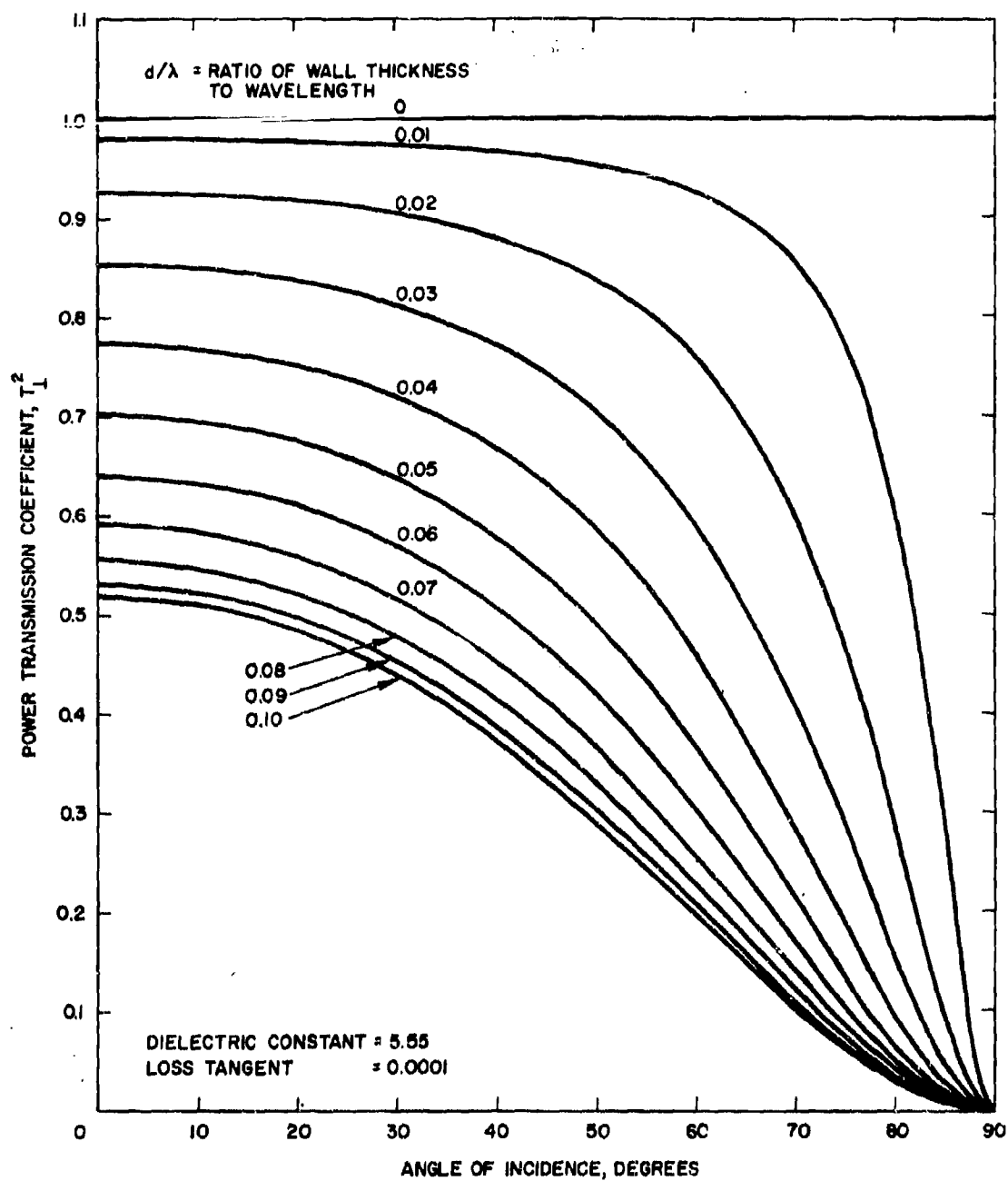


Figure 1-27. Power Transmission Coefficient for Pyroceram  
(Perpendicular Polarization)

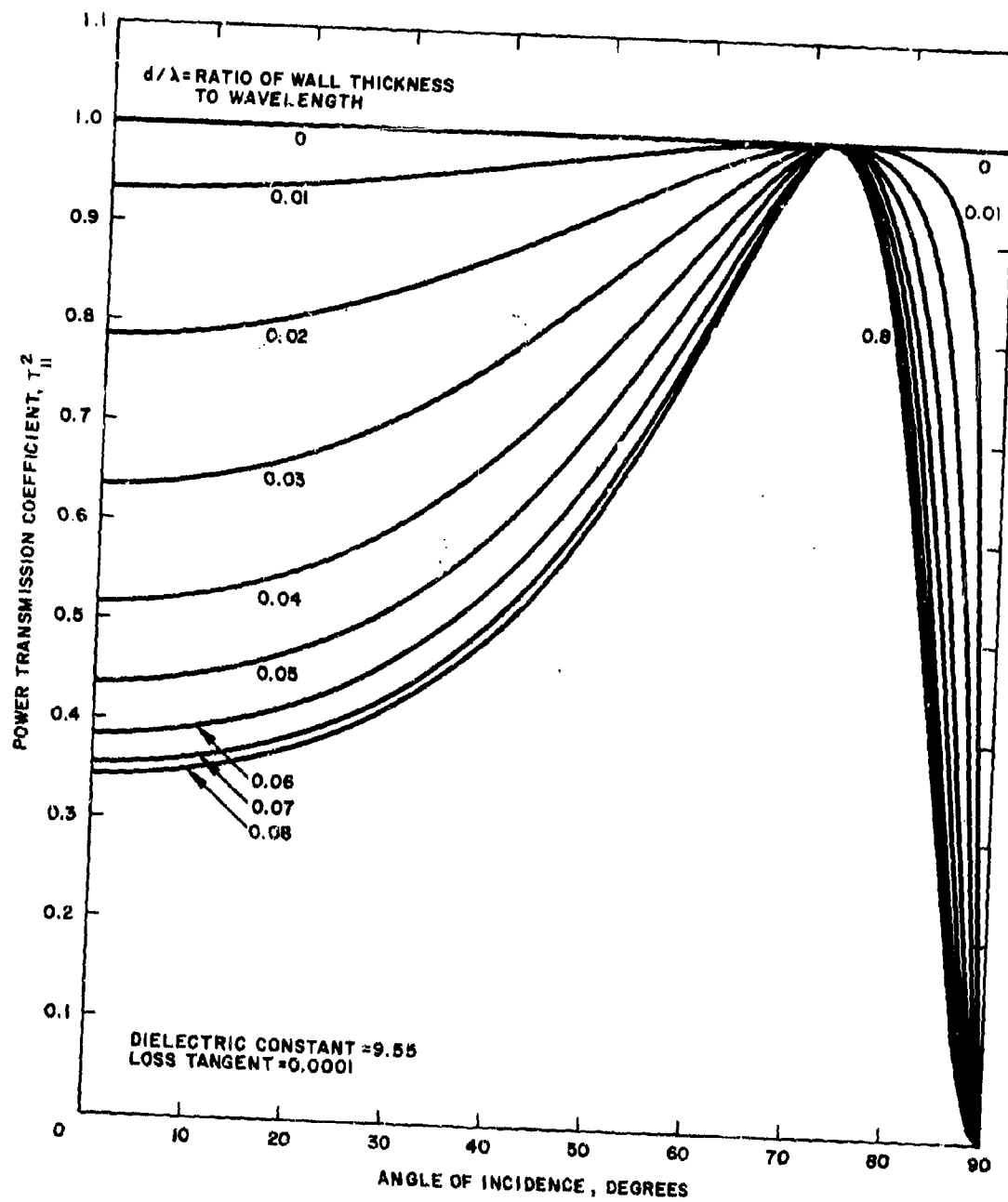


Figure 1-28. Power Transmission Coefficient for Alumina  
(Parallel Polarization)



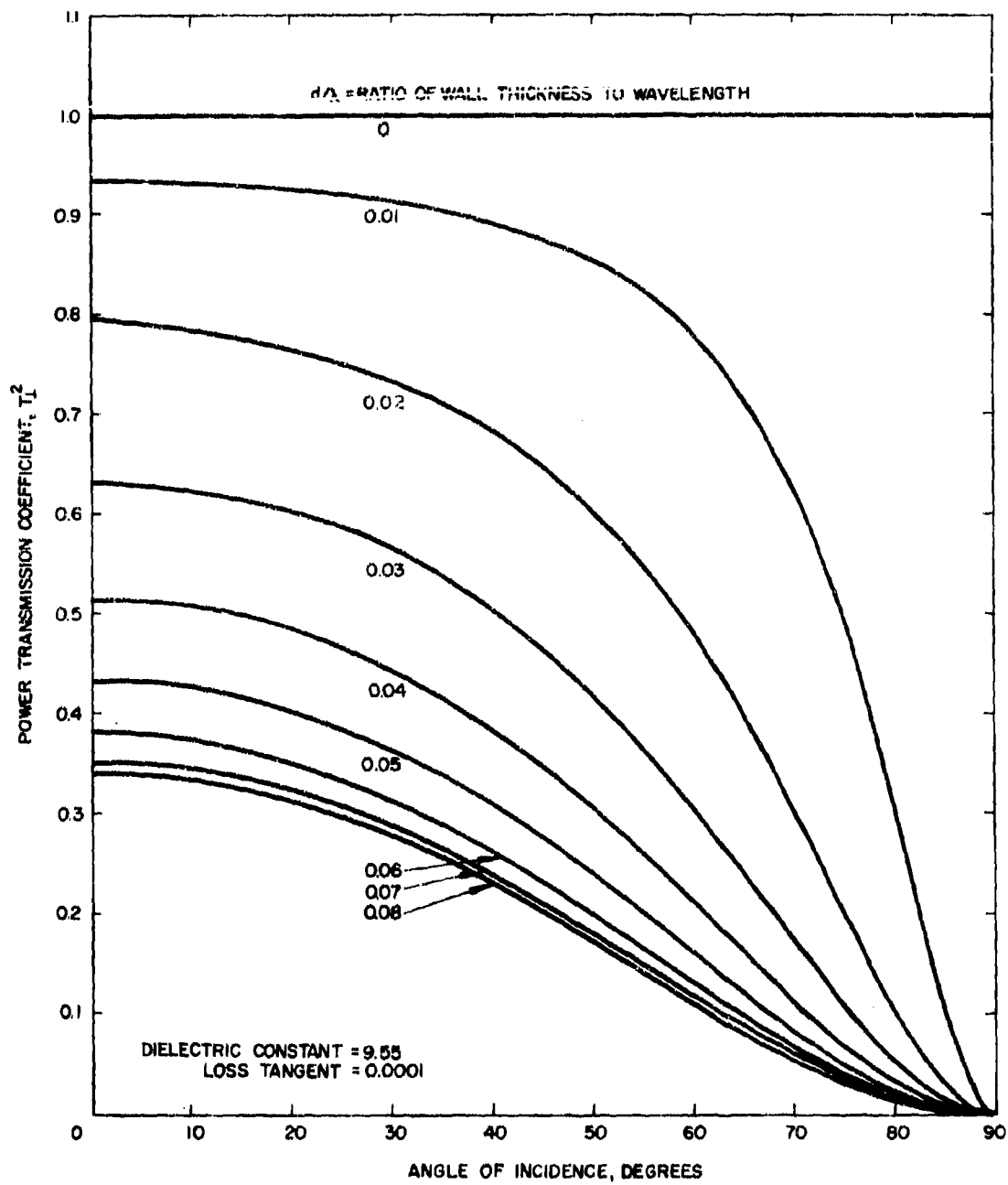


Figure 1-29. Power Transmission Coefficient for Alumina  
 (Perpendicular Polarization)

### 1-2.7 REFLECTION LOSS

Since a thin-wall radome does not have zero thickness, its reflection coefficient can approach zero but never be equal to it. Thus, for an active system in which reflection of energy from the inner surface of the radome is not desired, since it can cause antenna mismatch and a change in the frequency, the wall must be designed to minimize internal reflections. It has been previously shown that the limiting thickness is determined by the perpendicular polarization. Since the lossless conditions are assumed in Eqs. 1-13 and 1-14 and the law of conservation of energy for these conditions is

$$|T|^2 + |R|^2 = 1$$

the reflection coefficient is approximated by

$$|R_{\perp}|^2 \approx \left[ \frac{\pi(1-\epsilon)}{\epsilon \cos \theta} \frac{d}{\lambda_0} (\epsilon \cos^2 \theta - \sin^2 \theta) \right]^2 \quad (1-15)$$

$$|R_{\perp}|^2 \approx \left[ \frac{\pi(1-\epsilon)}{\cos \theta} \frac{d}{\lambda_0} \right]^2 \quad (1-16)$$

It is apparent that the amplitude and power reflection coefficients are proportional to the thickness and to the thickness squared, respectively. Thus, for a low-reflection radome, either the dielectric constant must be small or the radome wall must be thin.

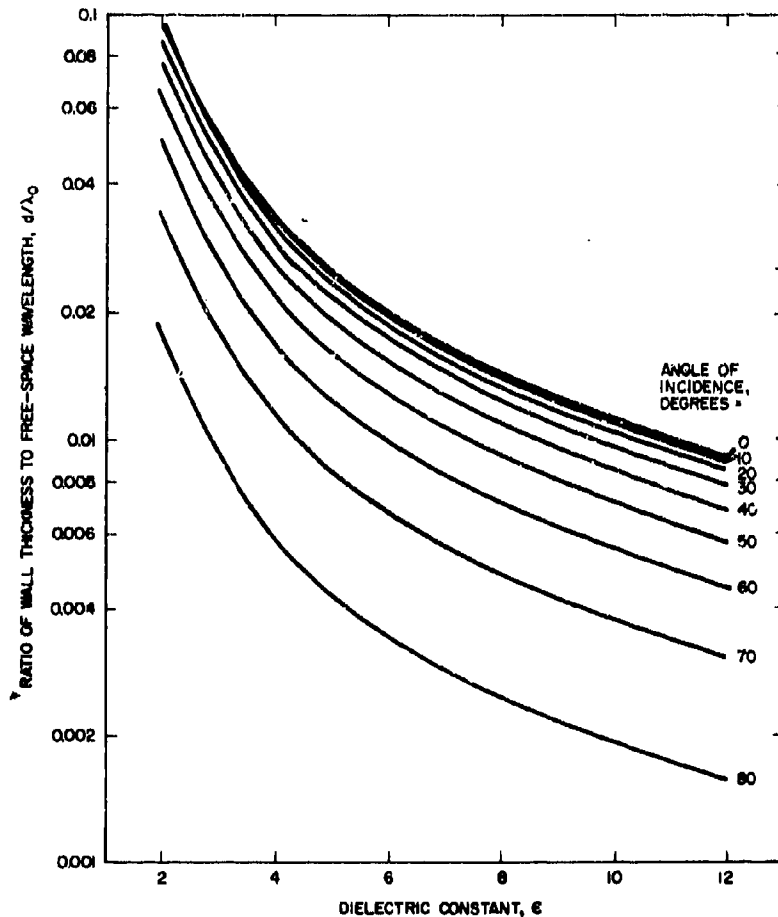


Figure 1-30. Thickness/Free-Space Wavelength vs Dielectric Constant for Various Angles of Incidence and  $|R_{\perp}|^2$  Equal to 90 Percent

### 1-2.8 PATTERN DISTORTION

Even if it has a half-wavelength thickness, a radome with a high fineness ratio distorts the near-field antenna pattern because of differential phase distortion through various sections of the radome. This distortion manifests itself as a change in the far-field antenna pattern. Figures 1-35 and 1-36 are patterns obtained with radomes having the contour shown in Fig. 1-25 and having various wall thicknesses. All patterns were obtained at zero look angle and at X-band. Table 1-3 presents the data reduced from these figures. It can be seen that the beam-width and sidelobe level increase as the wall deviates from zero or one-half-wavelength thickness.

### 1-2.9 VARIATIONS IN PHASE

For boresight radomes, the variations in phase must be kept to a minimum. Such varia-

tions have been found to be negligible up to angles of incidence of 50 degrees. Beyond this point, phase changes rapidly and a thin-wall radome is no longer desirable. Reference 66 shows that for a thin-wall radome, the phase difference between the perpendicular and parallel polarizations can be approximated by

$$\frac{\pi d (\epsilon - 1)^2}{\lambda_0 \epsilon \cos \theta} \sin^2 \theta \quad (1-17)$$

The insertion phase difference for the individual polarizations can be shown to be

$$\text{IPD}_\perp = \frac{\pi d (\epsilon - 1)}{\lambda_0 \cos \theta} \quad (1-18)$$

$$\text{IPD}_\parallel = \frac{\pi d}{\epsilon \lambda_0 \cos \theta} [\epsilon \cos^2 \theta + \sin^2 \theta] (\epsilon - 1) \quad (1-19)$$

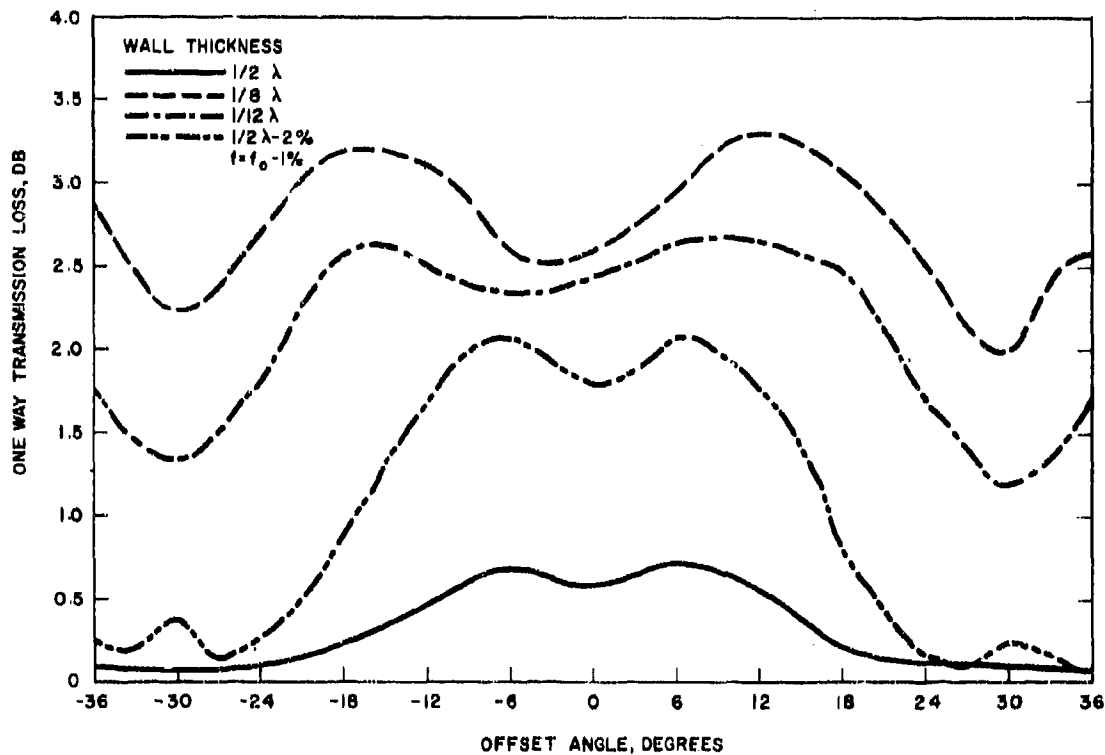


Figure 1-31. E-Plane Transmission Loss vs Offset Angle for Various Wall Thicknesses

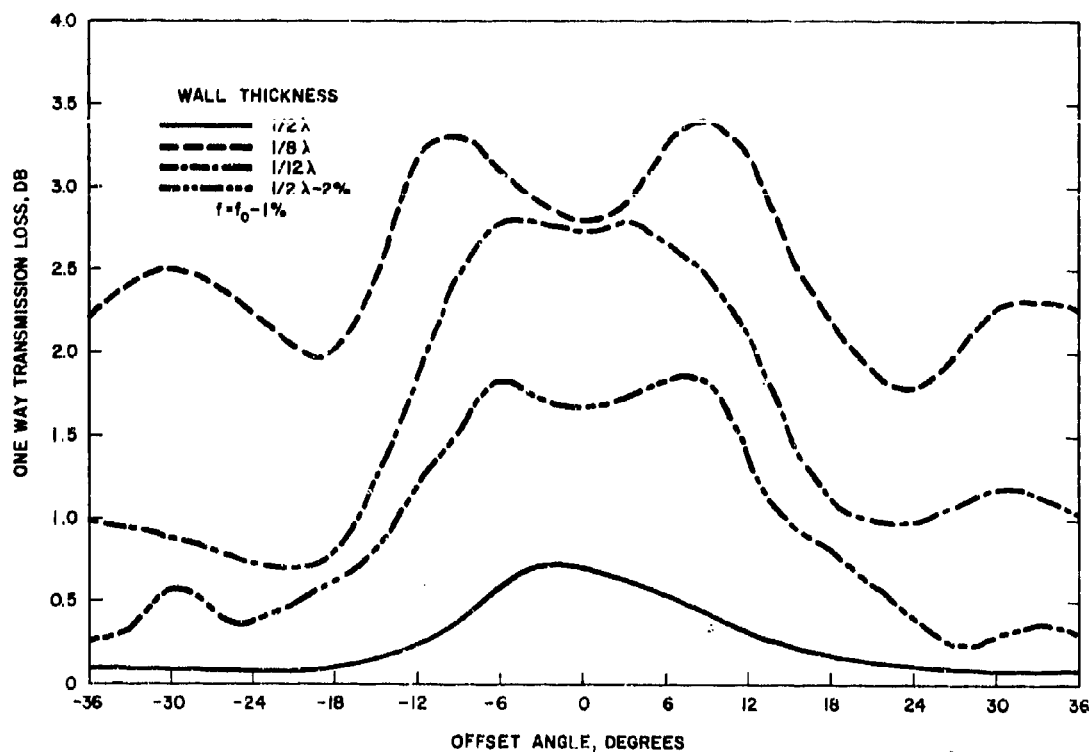


Figure 1-32. H-Plane Transmission Loss vs Offset Angle for Various Wall Thicknesses

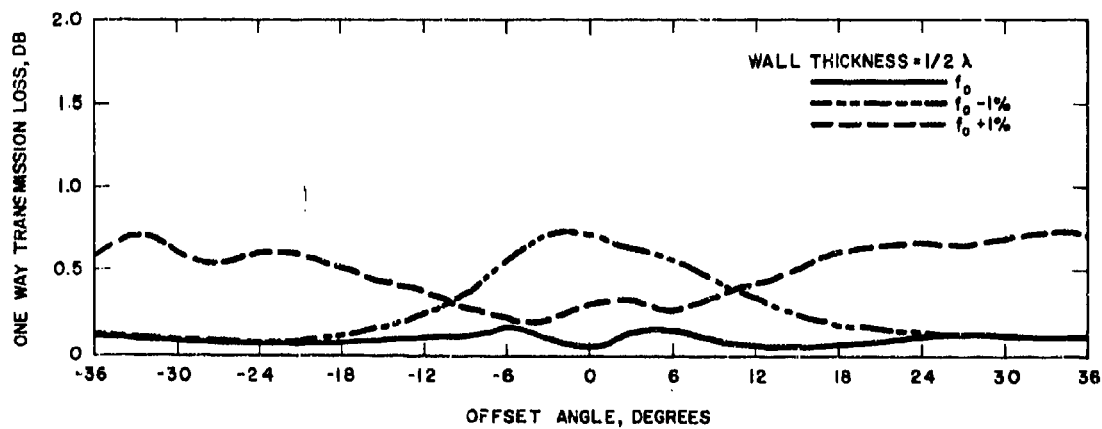


Figure 1-33. H-Plane Transmission Loss vs Offset Angle at Various Frequencies for Radome with Half-Wavelength Wall Thickness

TABLE 1-3. E- AND H-PLANE ANTENNA PATTERN PARAMETERS FOR SEVERAL RADOME WALL THICKNESSES

Antenna Pattern Parameters	Radome Wall Thickness (2)					
	1/2		1/8		1/12	
Plane of pattern	E	H	E	H	E	H
Reduction in gain, db	0.7	0.8	3.0	3.3	2.3	2.2
Half-power beamwidth, degrees	8.0	8.3	7.0	10.0	7.0	9.5
First sidelobe level,* db	18.0	14.8	7.6	15.1	9.8	14.8

\* In db below main beam; only the highest sidelobe is indicated.

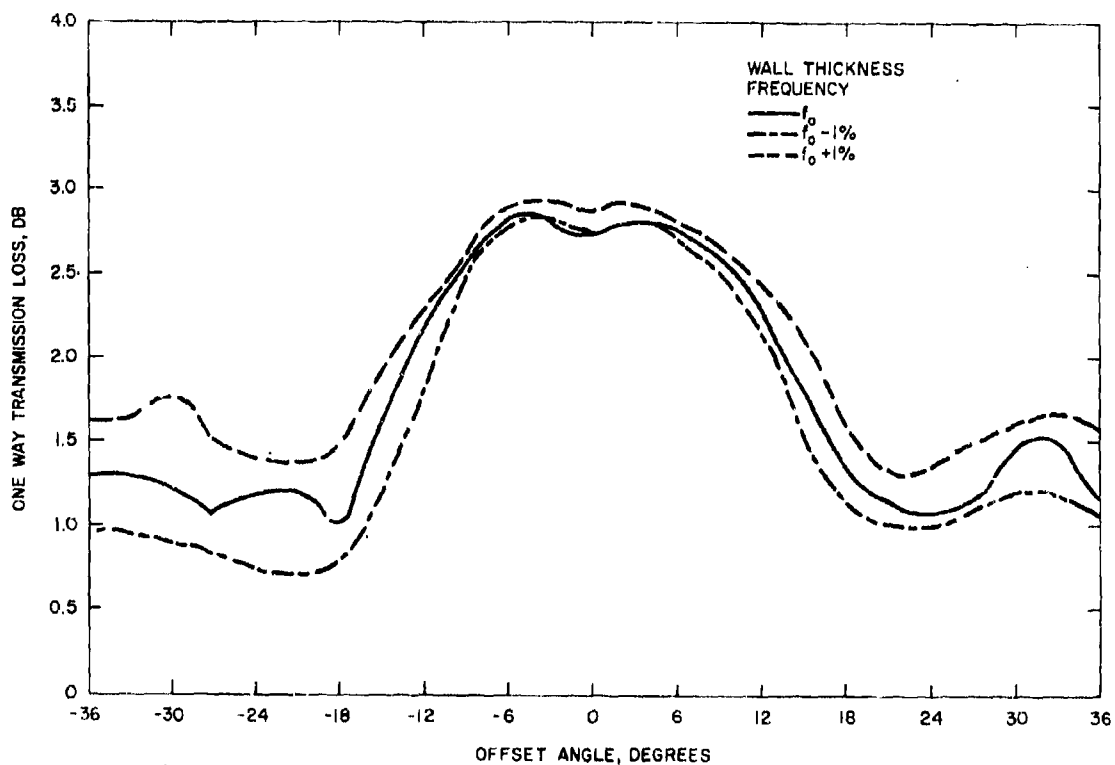


Figure 1-34. H-Plane Transmission Loss vs Offset Angle at Various Frequencies for Thin-Wall Radome

### 1-2.10 BANDWIDTH

It is interesting to note that using a thin wall is a means of obtaining a radome that can operate at several frequencies. For example, a radome designed for a one-half-wavelength thickness at  $K_u$ -band is thin at X-band and very thin at C- or S-bands. Thus, an electrically thin wall permits the use of the same radome at any frequency below that at which it is electrically thin, since performance improves as frequency decreases. This situation is somewhat analogous to that for one-half-wavelength radomes,

where a radome is designed as a one-half-wavelength radome at X-band. This same wall is full wave at  $K_u$ -band and two wavelengths thick at  $K_u$ -band. Note, however, that in this case, performance tends to become less satisfactory as the frequency increases. These two design methods can be used for the two- and three-band performance that will be required of future radomes. Reference 64 shows the effect of a change in frequency on transmission and phase. For a wall 0.030-in. thick and operation at C-band, the electrical performance does not vary appreciably over a  $\pm 10$ -percent frequency band.

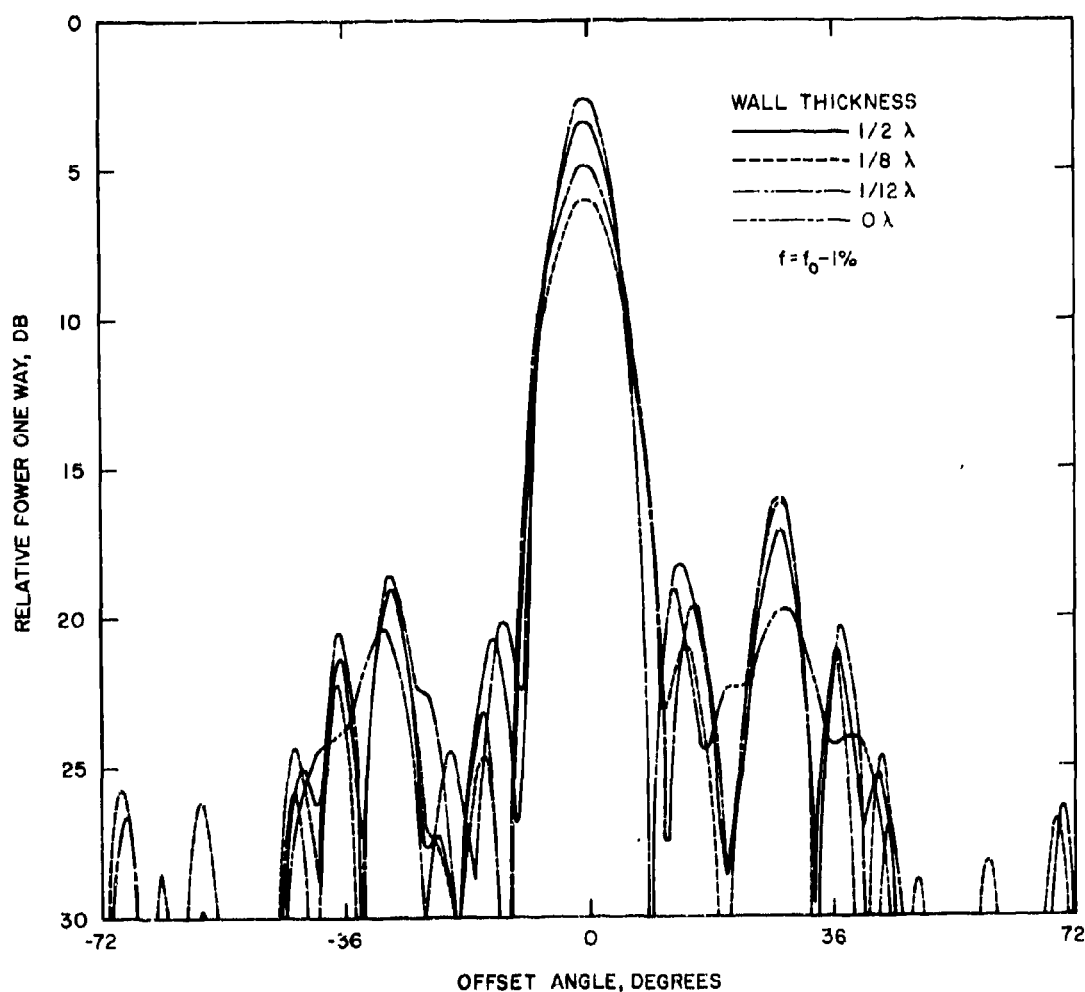


Figure 1-35. Effect of Radome Wall Thickness on E-Plane Antenna Pattern

Similar results were found for a wall 0.025-in. thick at X-band. At K<sub>a</sub>-band, the thin wall is not acceptable structurally unless the dielectric constant is very small. Table 1-2 indicates that a thin wall would not be acceptable at frequencies greater than 18 gc. For frequencies above this general range, a one-half-wavelength wall must be used and, as reported in Reference 64, the bandwidth is limited to between 2 to 2.5 percent. Similar data can be obtained by cross plotting Fig. 1-30 or by using Tables 5-2 through 5-19 in Reference 1, which show this same trend. Satisfactory performance can be

obtained with thin walls at frequencies below X-band and at angles of incidence of less than 50 degrees. At higher frequencies, each design must be evaluated separately to determine if a thin or a one-half-wavelength wall is more desirable.

#### 1-2.11 BORESIGHT ERROR AND DERIVATIVES

Besides transmitting electromagnetic energy with a minimum loss due to reflection, absorption, and pattern distortion, the radome should have minimum effect on the direction in which

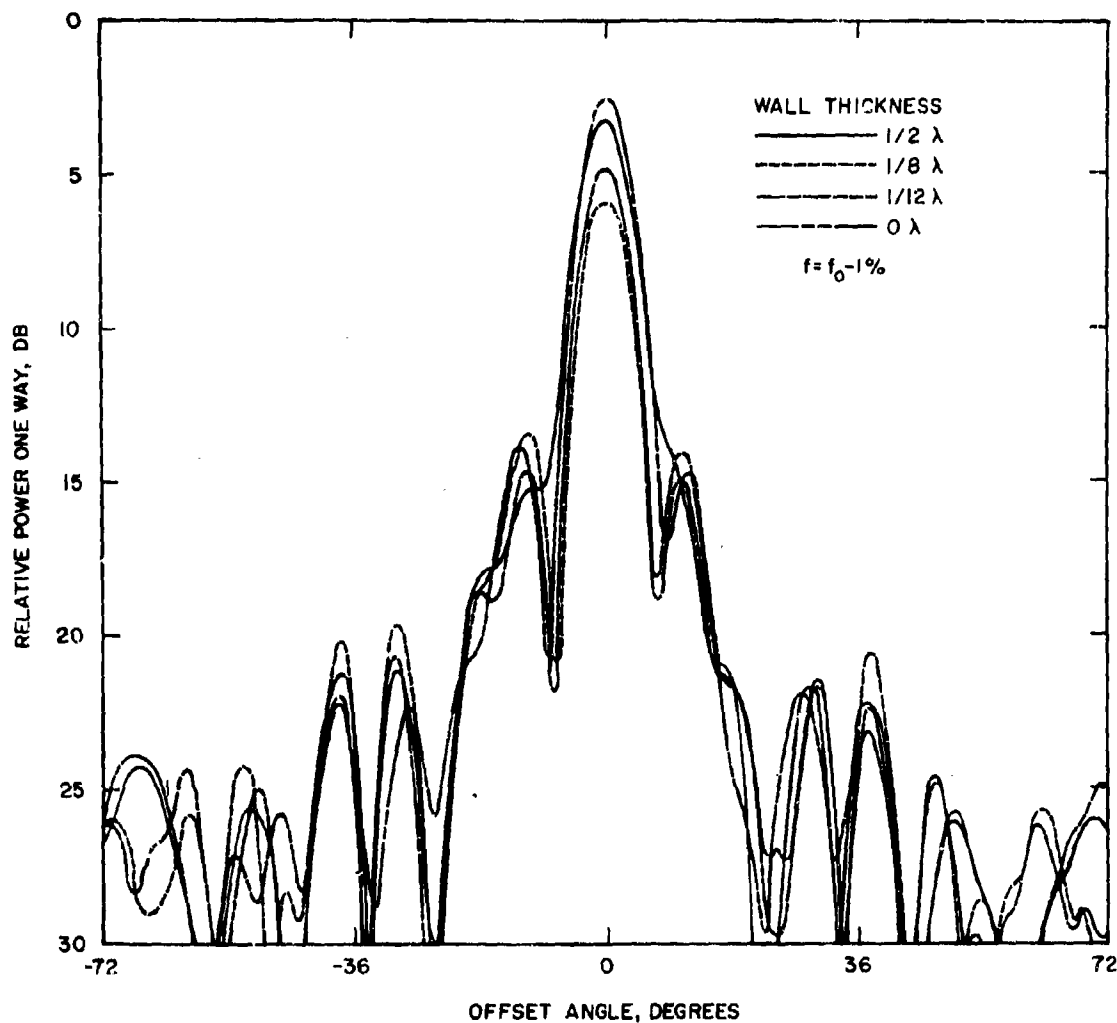


Figure 1-36. Effect of Radome Wall Thickness on H-Plane Antenna Pattern

the energy is propagated. Boresight error results from complex electromagnetic interactions of the radome, antenna, and missile fuselage. Other contributing causes include variation in the angle of refraction and in the transmission coefficients of the antenna signal because of depolarization of the energy by the radome. Boresight error and its derivatives increase as the radome fineness ratio increases and as the radome wall deviates from the optimum one-half-wavelength thickness. The electrical radome thickness must, therefore, be accurately controlled to keep these errors to a minimum. In fact, these derivatives impose a closer tolerance requirement than does the overall transmission loss. Tests of hemispherical and of half-wavelength and thin-wall radomes show that boresight error slopes are greater for thin-wall radomes (0.01 vs. 0.04 deg/deg). Tests conducted at the Hughes Aircraft Company, in which an ogival radome with a fineness ratio of 2.0 was used, show that at X-band frequencies, these errors increase with thickness. For a ratio of antenna diameter to free-space wavelength of 7.35, the maximum boresight error derivative for a radome with a constant wall thickness was found to be 0.032 deg/deg, a value that compares favorably with that of 0.034 deg/deg predicted on the basis of Fig. 1-21. For these same parameters,  $l/d = 2.0$  and  $d/\lambda_0 = 7.35$ , it has been found that the error derivatives are 0.055, 0.12, and 0.13 deg/deg for wall thicknesses of 0.010, 0.050, and 0.070 in., respectively.

#### 1-2.12 WALL THICKNESS TOLERANCES

The effect of wall thickness tolerance is discussed in References 7 and 64. It has been shown that a tolerance of  $\pm 0.003$  in., a value that can be maintained during fabrication, is acceptable for thin-wall radomes. Because, however, each radome is subject to a different range of angles of incidence and varying requirements for boresight error derivatives and transmission loss, no general rule can be given for wall thickness tolerance.

#### 1-2.13 AERODYNAMIC HEATING AND THERMAL STRESS

The temperatures and thermal stress experienced by a radome depend on the material of

which it is made. Since both Pyroceram and alumina have shown resistance to rainfall at high velocities, these materials will be used to illustrate the differences between thin-wall and one-half-wavelength-wall ceramic radomes. The radome shape shown in Fig. 1-25 will be used; however, the tip radius and wall thickness will be different.

The thermal studies discussed in Paragraph 1-1.2.2 indicate that the peak temperature occurs at the stagnation point and that it then gradually decreases along the axis of the radome until the region of turbulent flow is reached, where it again rises but only to a value less than that at the stagnation point. Temperatures beyond this region decrease toward the aft end of the radome. These studies also reveal that at any point on the radome axis, the variation in temperature around the circumference is negligible when compared with the variation at different axial positions. These temperatures produce thermal gradients radially through the radome wall that vary as the peak temperature varies. Studies have shown that the maximum thermal gradient occurs through the radome wall and that it presents the major structural limitation. The axial and circumferential gradients are negligible in comparison with the radial gradient.

Heat transfer rates at any point on the radome depend on the Mach number history of the missile, which in turn, depends on missile weight, configuration, impulse, trajectory, and, for air-launched missiles, on the capabilities of the launching aircraft. The following Mach number histories have been assumed to be representative of hypersonic velocities:

- Case 1. Snap-up trajectory, 43,000- to 65,000-ft altitude, Mach 2.0 launch to a peak of Mach 5.1 after 40 sec, deceleration to Mach 4.5 after 60 sec.
- Case 2. Snap-down trajectory, 70,000- to 60,000-ft altitude, Mach 4.0 launch to a peak of Mach 6.9 after 6 sec, deceleration to Mach 4.4 after 60 sec.

In the thermal analysis based on the methods given in Reference 21, an initial temperature was assumed that depends on the particular trajectory employed. It is to be noted, however,



that only the actual temperatures depend on this value and that thermal gradients are relatively independent of the initial temperature since the recovery temperature is high.

Although Pyroceram and alumina both exhibit similar surface temperature profiles, they are significantly different from the standpoint of thermal gradients. Figure 1-37 compares Pyroceram and alumina radomes having one-half-wavelength and one-twelfth-wavelength thickness, respectively, at X-band. Peak temperatures depend on wall thickness, but are similar for the two materials of the same thickness. The thermal gradients are greatest for the one-half-wavelength Pyroceram radome since its thermal diffusivity is significantly less than that of alumina. In the thin-wall radome, the thermal gradients are similar because the thin wall tends to override the effect of thermal diffusivity. Note that temperatures approximately 300°F higher occur with the thin wall because of its lesser thermal capacity. Thus, in a thin-wall radome, the thermal gradients are less but the operating temperature of the radome simultaneously increases.

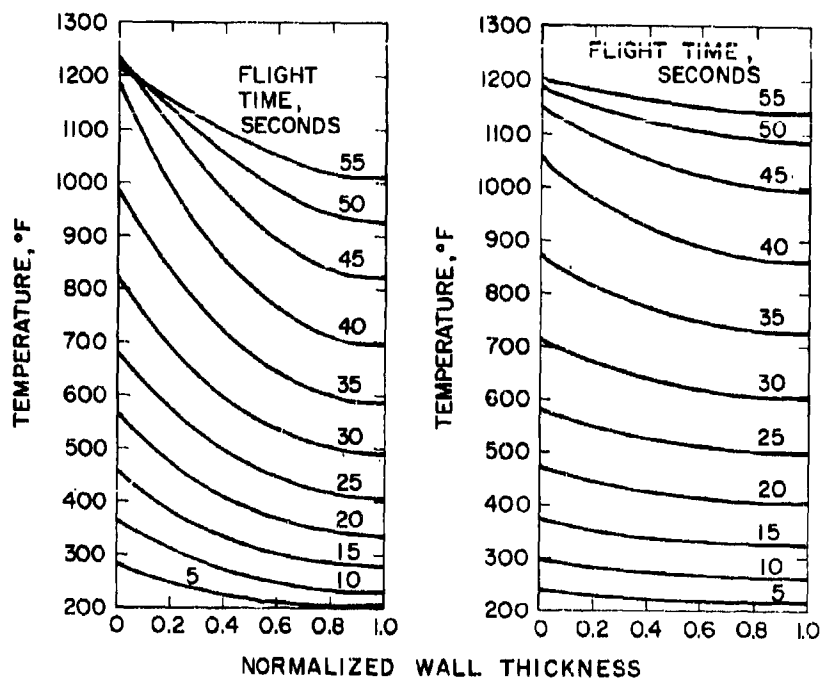
Thermal stress varies as a function of position along the radome axis. Maximum stress occurs at the tip or stagnation point and decreases aft of this point. If the missile is accelerating, its outer surface heats up rapidly and a thermal gradient is produced through the radome wall that causes a tensile stress on the inner surface and a compressive stress on the outer surface that is less than the tensile stress. If the missile is decelerating, the outer surface becomes cooler and undergoes tensile stress while the inner surface undergoes compression. Since the rate of acceleration is usually at least an order of magnitude greater than that of deceleration, peak stress occurs during acceleration. Therefore, maximum tensile stress occurs on the inner surface. As was shown in Paragraph 1-1.2.2, the tip area defines the structural limits of the radome since tensile thermal stress at any other point, including the attachment area, is not as severe.

Inner-surface tensile thermal stress as a function of flight time for the thin-wall (one-twelfth-wavelength) and one-half-wavelength Pyroceram and alumina radomes is shown in Fig. 1-38. These radomes were assumed to have the Mach number history previously described as *Case 2*, modified to a launch Mach number

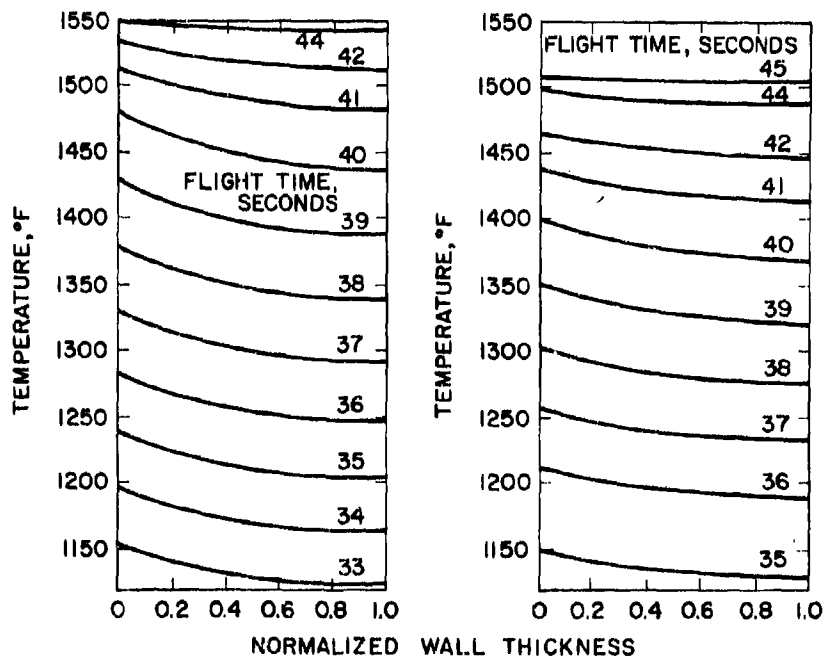
of 3.0. In both cases, the radomes made of alumina were subjected to more severe stresses. These data also show the relationship of the stresses to the acceptable design values for the two materials (10,000 and 14,000 psi for Pyroceram and alumina, respectively). The maximum stresses for both of the one-half-wavelength radomes are approximately three times greater than the design limit, whereas those for the thin-wall radomes are less than this limit.

As shown in Fig. 1-39, tensile thermal stress at the stagnation point (the inner surface of Pyroceram, and alumina radomes) decreases as the radius increases. It can be seen that for any trajectory, the stress on thin-wall radomes is appreciably less than that on one-half-wavelength radomes. Figure 1-39A is based on the Mach number history described as *Case 1*, whereas Fig. 1-39B is based on the Mach number history for *Case 2*. The acceleration rates for *Case 1* and *Case 2* are Mach 0.08 per sec and Mach 1.0 per sec, respectively. Therefore, a tenfold increase in acceleration causes approximately a thirtyfold increase in tensile thermal stress. Figure 1-40 presents data for the standard radome with the Mach number history for *Case 2* and various initial launch velocities. The stress on both the one-half-wavelength and the thin-wall radomes increases as the launch velocity increases, although that on the thin-wall radome is much less.

The use of an ablative cover reduces thermal stresses to acceptable design values. It also protects a blunted thin nose if rainfall should be encountered. Since the maximum velocities for most types of missiles are encountered at high altitudes, where such a cover is required to reduce thermal stress, the use of a slightly thicker cover will provide material for use as an erosion shield in snap-down attacks in which rainfall may be encountered. Conversely, at low altitudes, where rainfall is expected, the velocities are lower and the ablation rate becomes lower because of greater drag and the consequent reduction in velocity. Here a substantial portion of the cover is available for use as an erosion shield. The details of the design of such a cover are presented in Reference 21. As shown in Fig. 1-25, the cover extends along the axis of the radome for several inches; the actual length depends on the shape of the radome, the Mach number history, radome material, and the axial stress gradient that is permitted. The cover is



a) PYROCERAM  $1/2 \lambda$  THICK, b) ALUMINA  $1/2 \lambda$  THICK



c) PYROCERAM  $1/12 \lambda$  THICK d) ALUMINA  $1/12 \lambda$  THICK

Figure 1-37. Temperature Gradients at Stagnation Point for Pyrocera and Alumina Radomes with 1.0-in. Tip Radius and Various Wall Thicknesses

thickest at the tip and tapers to zero thickness at the end. Let us consider the conditions used to derive Fig. 1-40 with the added requirements of maximum stresses of 5k psi and 8k psi for Pyroceram and alumina, respectively. The thickness of Teflon required is shown in Fig. 1-41. It can be seen that for each unit increase in launch Mach number, the thickness of the ablative cover must be doubled. Such covers have been used on missiles and have demonstrated their reliability.

#### 1-2.14 STRUCTURAL

A review of the loading imposed on the radome structure shows that the maximum stresses due to aerodynamic pressure occur at the attachment area and that those due to aerodynamic heating occur at the tip of the radome. Investigations show that the loading due to thermal stresses exceeds that due to pressure distributions by at least an order of magnitude. Pressure loading depends primarily on velocity, the shape of the radome, its location, and flight attitude. If the angle of attack is not zero, unsymmetrical pressure loading occurs and causes

a bending moment and a shear load. Such loads, which are greatest at the attachment area, are discussed in Paragraph 1-3. The many works of Timoshenko are excellent references for structural analyses as are the publications of the American Society of Mechanical Engineers (ASME). A designer of thin-wall radomes must consider the effect of acoustic noise that can originate in the boundary layer adjacent to the wall or from a nearby supersonic aircraft. The loadings are then essentially due to pressure and/or vibration and can cause thin sections made of brittle materials to fail. Paragraph 1-5 describes methods of calculating loads induced by acoustic noise. Impact with foreign objects, such as rainfall, and with airborne objects, such as birds or debris from prior attacks, is a serious problem that thin-wall radomes must surmount. As is shown in Chapter 3, rainfall having a mean droplet size of 2 mm can cause a radome to fail at velocities above 2000 ft/sec. Failure due to the last two causes depends on the size of the object. If the radome is mounted on the exterior of an aircraft, small particles of gravel may be thrown against it. Hence, high impact strength is desirable.

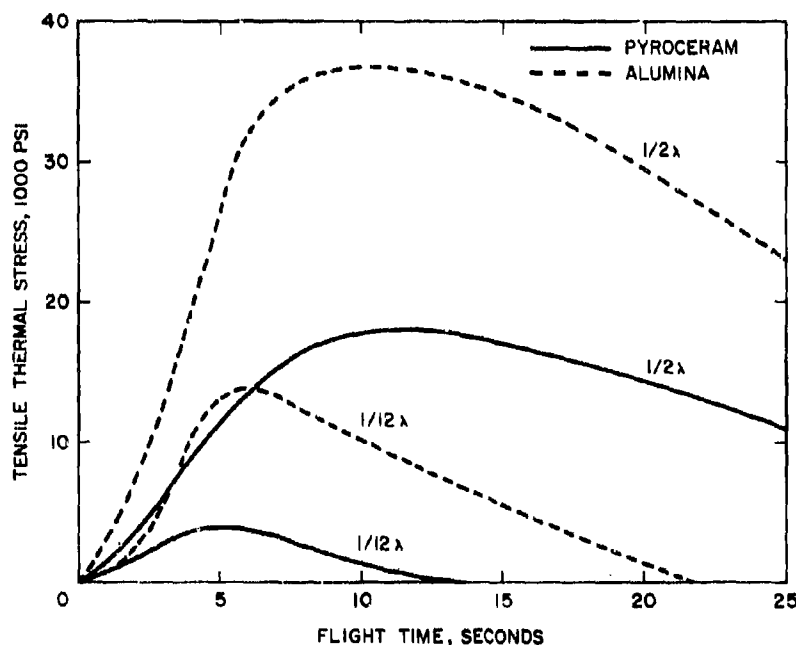


Figure 1-38. Peak Inner Surface Tensile Thermal Stress for Radomes with Wall Thicknesses of One-Half and One-Twelfth Wavelength

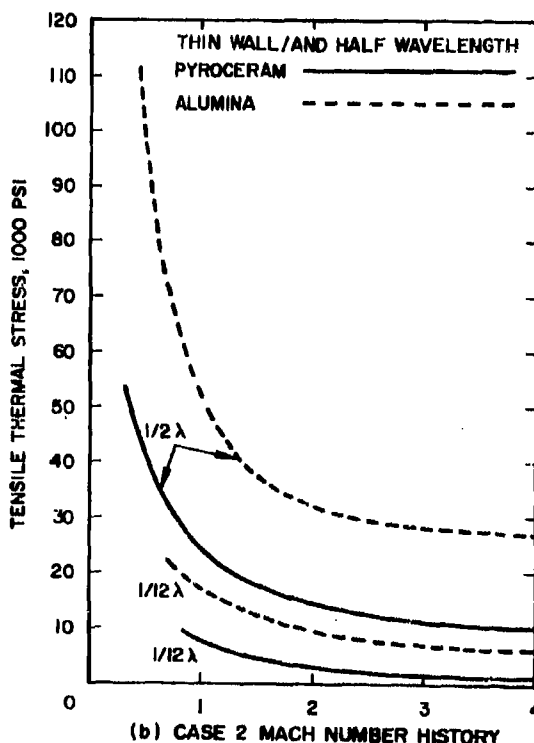
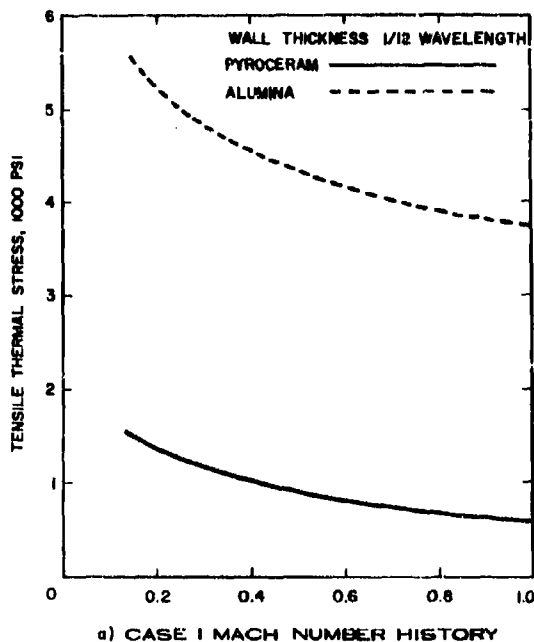


Figure 1-39. Peak Inner Surface Tensile Thermal Stress vs Radome Tip Radius for Two Cases

### 1-2.15 SIZE LIMITATIONS

Thin-wall radomes made of plastic materials have been constructed in various configurations, ranging from hemispherical to power shapes. Base diameters vary from 5 to 12 in. and fineness ratios as high as 2.5:1 are common. The ceramic thin-wall radome has not been investigated extensively. As shown in Chapter 3, small radomes have been fabricated in thin sections. Radomes made of Pyroceram 9606 and alumina have been built in the shape shown in Fig. 1-25. In general, the size of a thin-wall radome can be the same as that of a solid-wall radome, i.e., a maximum length and base diameter of 40 and 20 in., respectively. If the radome is made of a ceramic material, it will be expensive because of the length of time required for grinding and the large amount of material that is wasted in the process.

### 1-2.16 ATTACHMENT

The attachment area must be designed to withstand the thermal and mechanical loads that will be imposed on it and to provide a hermetic seal over wide ranges of external pressure and temperature. The need for internal evacuation or pressurization imposes additional design requirements. A thin-wall radome poses an especially difficult problem since a transition from thin to thick sections takes place over a short length at the aft end of the radome. The problems associated with the methods of radome attachment are discussed in Paragraph 1-3.

### 1-2.17 HANDLING

Ceramic materials, especially those in thin sections, are very fragile if improperly stored or handled. Small radomes usually form an integral part of a radar system and are attached to it. Thus, the means usually employed to protect the assembly also protect the radome. A radome installed on the aircraft or launcher can be protected by a plastic cover in the shape of a paper cup. Such a cover must be removed before the radome is used and reinstalled if the missile is not fired. Large radomes, which do not as a rule form an integral part of the microwave system, must be stored separately and incorporated in the system when required. Since

such units are then subjected to the additional hazards of field assembly, appropriate handling devices, such as jigs, tables, and hoists, should be designed and used to minimize the possibility of failure. Although thin layers of ablative plastic materials, such as Teflon or polyethylene, afford protection from minor loadings, a metallic or dielectric cover gives the best protection.

### 1-3 METHODS OF ATTACHING CERAMIC RADOMES

#### 1-3.1 INTRODUCTION

A radar system usually consists of two basic components: the radome at the forward end

of an aircraft and the bulkhead or aircraft structure at the aft end. The two components must be joined so that the desired atmosphere within the radome is maintained throughout the storage life of the system. Radars containing unsealed free gyroscopes or other rotating devices that require constant pressure loading are usually evacuated. On the other hand, high-power active systems must be pressurized to prevent electrical breakdown. Many systems, however, do not require either evacuation or pressurization but are operational over large pressure ranges. However, all radars need a hermetic seal that not only serves as a barrier to moisture, but also keeps out dust and other contaminants. The attachment area must, there-

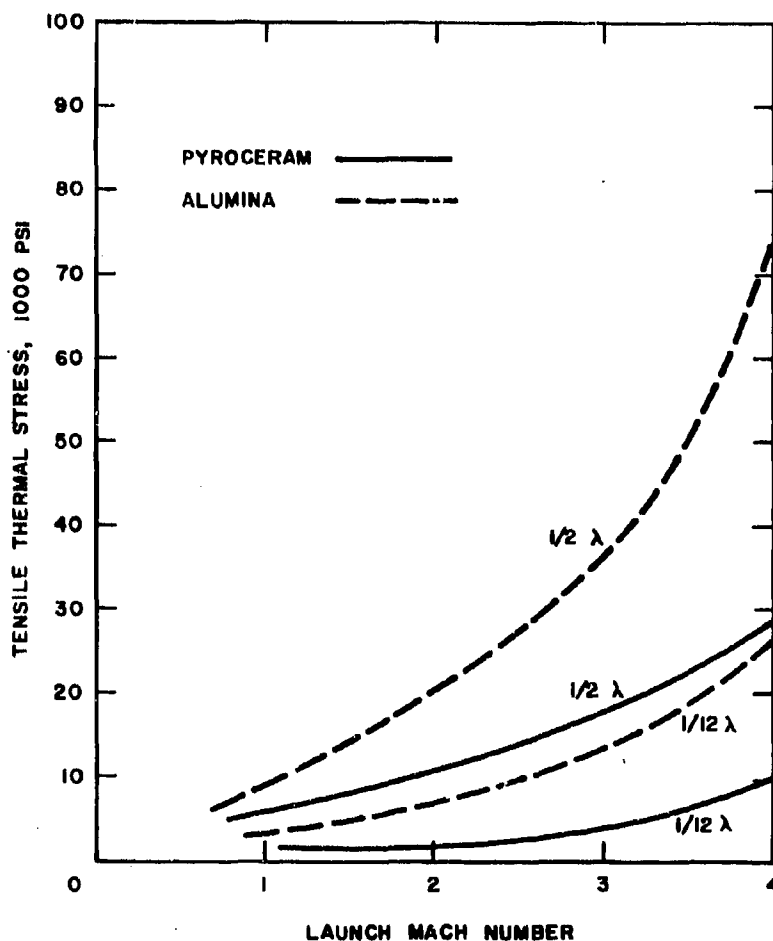


Figure 1-40. Peak Inner Surface Tensile Stress vs Launch Mach Number

fore, be designed to withstand the thermal and mechanical loads that are imposed on it and to provide a reliable seal over wide ranges of external pressure and temperature. Studies of various missiles revealed that the greatest mechanical loads occur at the attachment area because of the large moment about the radome center of pressure. The thermal environment ranges from  $-65^{\circ}\text{F}$  to thousands of degrees Fahrenheit, depending on the trajectory and Mach number history of the missile or airplane. Since the radome usually experiences the most critical aerodynamic loading at maximum temperature, the maintenance of the internal at-

mosphere of the radome is most important at this time.

In designing a radome attachment, it must be remembered that the primary objective is to attach the radome to the base of the antenna assembly while allowing for easy access to components within the radome if they should have to be adjusted or replaced. Other requirements, such as provision for sealing, allowance for differential thermal expansion, and resistance to static and dynamic loads, are secondary considerations and should not be allowed to add excessively to the cost of the design. The attachment must have good fatigue strength and

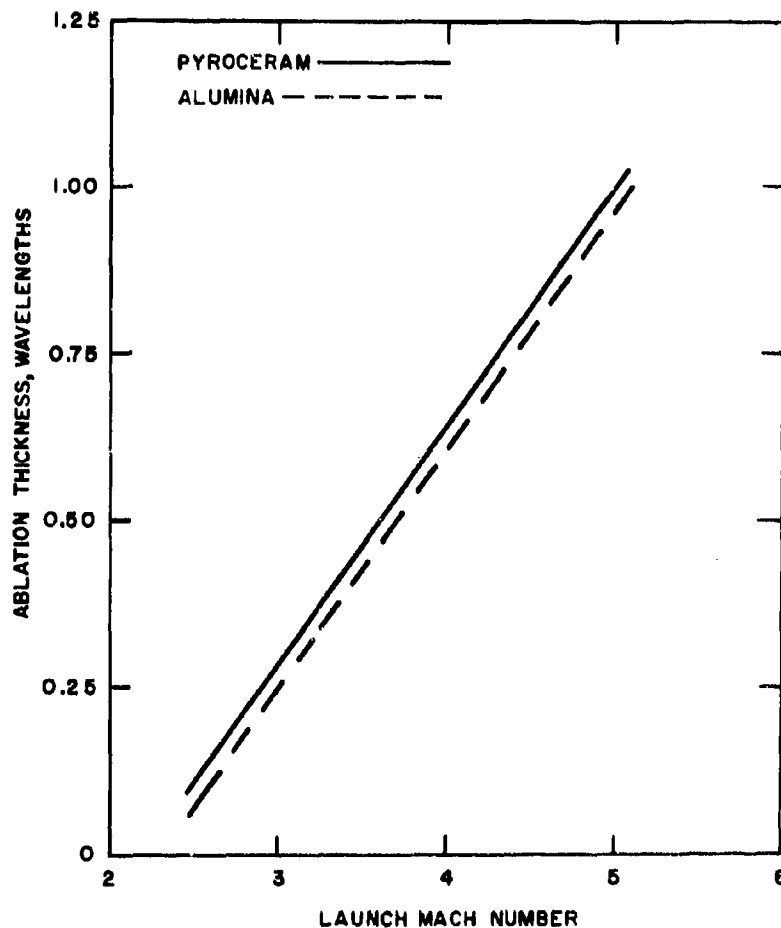


Figure 1-41. Thickness of Teflon Ablative Cover at Tip vs Launch Mach Number for Pyroceram and Alumina Radomes

resiliency to ensure that the radome will have a long operating life and to protect it from vibrational failures.

If metal-to-metal seals are used, galvanic insulation can be provided by means of an appropriate sealant or adhesive. The use of rare or unique materials should be avoided since they not only increase cost but may also be difficult to obtain during times of national emergency. The designer must strive to provide an inexpensive lightweight design that can be easily produced. If field installation is required, dimensional tolerances must permit rapid removal of the radome without undue use of shims or similar adjustment devices.

### 1-3.2 TYPES OF ATTACHMENTS

Attachments are usually classified as chemical or mechanical. Chemical attachments involve such processes as brazing and cementing, whereas with mechanical attachments, such as clamps and bolts, no adhesives are used. Of course, an attachment design can incorporate the best features of both methods.

Plastic adhesives are adequate if bond temperatures less than 400°F to 500°F are encountered for extended periods. Short-term use at temperatures exceeding 800°F is possible if proper adhesives and tolerances are employed. Ceramic adhesives are available that extend the use temperature from 1000°F to 1500°F. Brazing is limited by the melting point of the brazing material, while true mechanical attachments are limited by the differential expansion between the various components. If properly designed, such attachments can be used at temperatures beyond the use range of adhesives and brazes.

### 1-3.3 TYPES OF LOADING

Before considering the various methods of attaching a radome, let us review the various loads imposed on a radome while in operation. Figure 1-42 is a graphic view of the forces acting on a radome. The directions these forces take are determined by many factors. This figure is a free-body diagram for an evacuated radome with an O-ring seal that is subjected to a maneuver while the aircraft is executing a snap-down attack. These forces and their origin are explained in the following paragraphs.

#### 1-3.3.1 Aerodynamic Forces

Aerodynamic forces are due to the buildup of pressure in front of the radome. At zero angle of attack, only the normal drag force is present. However, as the angle of attack increases, the force no longer acts along the radome axis but rather off to the side of this axis; the angular position of the vector depends on the angle of attack. If this force is resolved into a Cartesian coordinate system coincident with the radome axis and the base, the vector can be broken into the components  $F_D$ , the drag force collinear with the radome axis, and  $F_N$ , the force normal to this axis that applies the resolved load at the center of pressure. Note that  $F_D$  compresses the radome, while  $F_N$  causes bending. For the conditions shown in Fig. 1-42, this load produces tensile stress on the upper section of the radome and compressive stress on the lower section. Other aerodynamic forces, such as those caused by turbulence, buffeting, and tumbling, should also be considered in a complete analysis.

#### 1-3.3.2 Inertial Forces

Inertial forces,  $F_I$ , depend on the particular motion executed by the aircraft or missile. If the radome is moving downward, the force due to inertia acts in an upward direction. The force depends on the weight of the radome and the maneuvering load factor.

#### 1-3.3.3 Pressure

As defined in this discussion, pressure loading is the result of a difference in pressure between the interior of the radome and its external environment. If the radome is evacuated, the resultant force,  $F_P$ , acts as a compressive force at the tip of the radome. If the interior of the radome is pressurized, the force tends to cause the radome to become separated from the attachment. In this case, which is illustrated in Fig. 1-42, the designer must consider the effect of temperature on the internal gas. Since this gas expands as the temperature increases, the differential pressure increases. A similar increase in pressure differential occurs as the altitude increases.

O-ring loading occurs in mechanical attachments where an O-ring or a compressed gasket

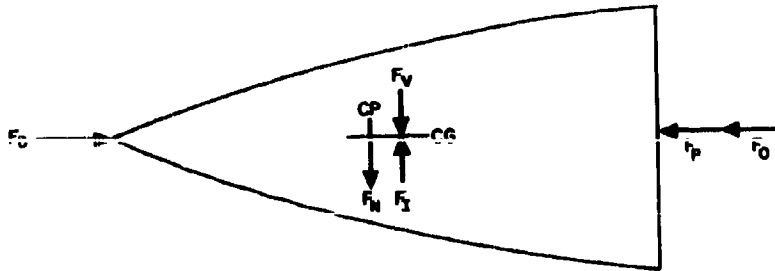


Figure 1-42. Free-Body Diagram of Radome in Flight

is used to effect a vacuum or pressure seal. This force,  $F_0$ , which acts along the radome axis, tends to separate the radome from the attachment ring. The magnitude of  $F_0$  depends on the chamfer angle, the angle at which the radome meets the radome base. If the base is not chamfered,  $F_0$  is equal to the total force exerted by the ring or gasket; if the radome is chamfered,  $F_0$  must be multiplied by the sine of the chamfer angle to obtain the force parallel to the radome axis.

#### 1-3.3.4 Vibrational Forces

The vibration encountered produces another force that is similar to that due to inertia. The magnitude of this force,  $F_v$ , depends on the weight of the radome, the amplification factor, the resonant frequency, and the power spectral density of the vibration. Like the force of inertia, this force acts at the center of gravity.

Differential thermal expansion can induce additional stress. If the radome is attached to a material having a coefficient of thermal expansion that is not the same as that of the radome material, tensile and/or compressive stress can result, depending on the design of the attachment. Therefore, the metal selected for the mounting ring should have a thermal expansion that is compatible with the thermal expansion of the radome over the required temperature range. For high-temperature applications, the oxidation resistance of the metal should be considered. If a free-floating attachment is employed (Fig. 1-46D), differential expansion does not cause stress on the radome.

Thermal stress induced in the radome wall by aerodynamic heating of the outer surface of the radome must also be considered. During accel-

eration, such stress is compressive on the outer surface and tensile on the inner surface. A decelerating missile usually undergoes opposite stresses.

These various forces, acting in different combinations and magnitudes, determine the structural reliability of a radome.

#### 1-3.4 TYPES OF STRESS

Before considering the various methods of attaching a radome, let us review the basic types of stress encountered. Figure 1-43 represents the five basic mechanisms causing stress. If the stress occurs normal to the bond line or along the axis of a clamp, it produces a uniform tensile or compressive load, depending on the direction of the loading. Shear loads are also distributed over the complete bond area; here the stress is parallel to the bond line. In a cleavage load, one side experiences either little or no stress. Thus cleavage joints are not as

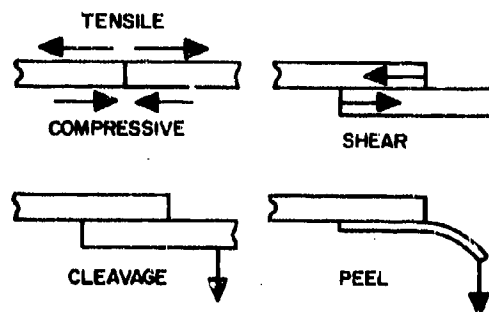


Figure 1-43. Types of Joint Loading



strong as tensile or shear joints. Peel loading, the least favorable type of loading, is rarely encountered in high-temperature attachments since one member must be flexible. It can occur, however, in combination with other loads if one of the materials is a plastic or ductile. In this case, only the edge is stressed and thus a greater percentage of the bond is under no load and does not contribute to the strength of the joint.

The attachment area is rarely subjected to pure tension, compression, shear, peel, or cleavage since the alignment of forces varies with the time that this area is subjected to stress. If thick sections are used, a combination of tensile, compression, shear, and cleavage is encountered. If one section is thin, a peel load can be introduced.

### 1-3.5 ATTACHMENT JOINTS

Configurations that the joint may take can be grouped into six categories: butt, lap, strap, scarf, thread, and clamp. Examples of each of these types are shown in Fig. 1-44. Although

adhesive bonds have been shown for clarity and ease of drawing, all except the butt and thread joint can be made by using rivets or bolts instead of adhesive. However, caution should be exercised in the use of rivets or bolts to prevent undue stress concentration.

When subjected to a bending load, the scarf joint undergoes tensile or compressive and shear stress. As the scarf angle increases, the bond area increases and the shear stress is distributed over a greater area while tensile stress diminishes. The scarf, double scarf, butt scarf, and butt lap types of joint have the advantage of being self-aligning and resist tensile, compressive, torsional, and bending stresses. However, since such joints require machining, they are more expensive than butt joints. The double butt, which is also called the half-lap or inset butt, the butt scarf, and the butt lap joints have sharp corners at which stress is concentrated if ceramic materials are joined.

The mechanical equivalent of these joints is always subject to concentrations of stress. In this case, the corner and edge radii should be large in order to decrease such concentration. If the scarf angle is reduced to zero, a butt joint

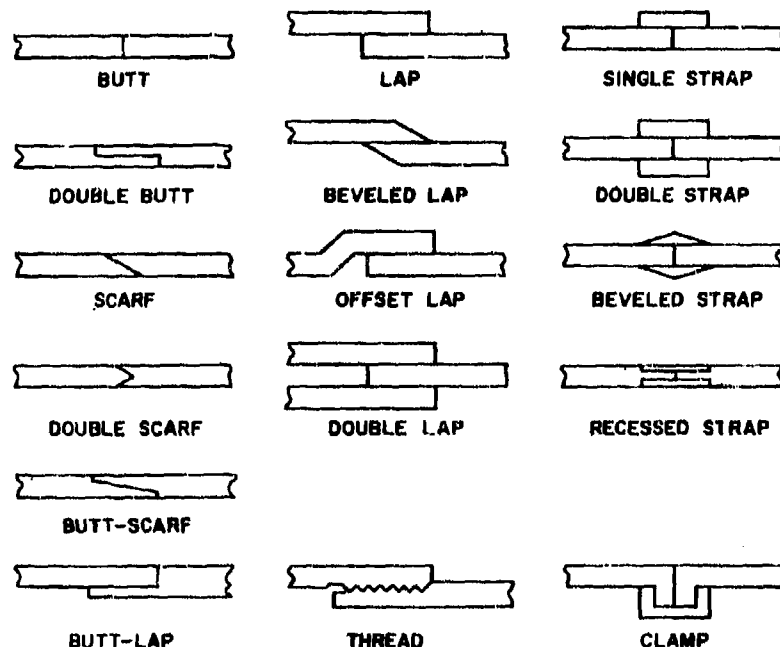


Figure 1-44. Types of Joints

is obtained. As a rule, this type of joint is not satisfactory since it is not self-aligning and involves a small bond area that is primarily under tensile or compressive stress. The butt joint is of little value in attaching thin-wall sections, and even for thick walls it is not recommended if a bending load is expected. If the scarf angle is increased to 180 degrees, the lap joint is obtained. This joint places the adhesive or rivet under shear stress. It has the disadvantage that stress concentrations occur at the edges, and when subjected to a bending load, it puts the adhesive under cleavage. The offset lap, which is also known as the joggle lap, and the beveled lap were developed to eliminate concentrations of stress at the edges of the joint. The double lap, which has been developed to offset local bending at the edge of the joint, has only limited applications since it is difficult to ensure equal loading of the two members. Although this kind of joint is suitable for uniting concentric cylinders of different thicknesses, it requires expensive fixtures to retain the members.

The strap joint, which is an adaptation of the lap joint, is designed to offset bending loads. Since the beveled double strap minimizes edge loading, it is preferred. Since shaping the beveled strap requires expensive machining, this type of joint and the recessed strap joint are both expensive. Although a double strap is shown, a single strap joint has been used in several production attachments. One version of the clamp joint is shown in which a single strap is used. The clamp joints are designed to place the materials under compressive stress. Since ceramic materials have high compressive strength, such joints are preferable. However, they are not desirable if the shear loading and stress concentration at sharp corners are considered. A threaded joint is not usually used for joining a ceramic material to metal since machining a thread in such a material is expensive and entails a great deal of grinding. It is useful if combined with other methods of attachments. As will be shown later, the flight environment and operational requirements rarely permit the use of these simple joints. In practice, elements of each of these various joints are combined to achieve a reliable and inexpensive design.

Mechanical analysis of the various types of joints is encumbered by stress concentration factors and by the combination of the various

stresses previously described. If information on the physical properties of all the materials of interest is available, and if the expected loads and environment are known, this information can be combined with the failure criteria for the materials to determine the stresses that will be encountered. References 67 and 68 present methods for evaluating single and double lap, butt, and scarf joints. Equations defining the stresses in lapped brazed joints and shrink-fit lap joints are given in Reference 69.

### 1-3.6 CHEMICAL ATTACHMENTS

Chemical attachments are those in which plastic or ceramic adhesives or metallic brazes are used to join two similar or dissimilar materials. As a rule, such joints are vacuum tight and resist penetration by moisture. They have the advantage of completely uniting the two parts and minimizing stress concentrations since no holes for bolts or rivets are needed nor reentrant machining, such as is required for grooves and notches for clamping devices. Reference 70 presents a summary of adhesive bonding techniques and an extensive bibliography on this subject.

A ceramic can be bonded to a metallic material by using the active metal or the molybdenum-manganese technique. In the active metal process, metals such as titanium or zirconium bond the ceramic to a metal which, in turn, is mechanically attached to the missile or aircraft fuselage. Although only one firing is needed to obtain the proper bonding, this process has the disadvantage of requiring an inert atmosphere and fixtures for alignment. Also, there are relatively few active metals. Therefore, the number of discrete firings and the maximum use temperatures are limited to the active metals available.

In the molybdenum-manganese process, a mixture of these metals in the form of a fine powder is fired onto the ceramic surface and, if required, the surface is plated with a metal that is compatible with both the braze to be used and the metallic surface. As discussed in Reference 71, any braze material can be used with this method. Thus, the bond may have a use temperature ranging from hundreds to several thousands of degrees Fahrenheit, depending on the braze material employed. This process requires fixtures and, unlike the active metal

process, two or three firings are needed, depending on the procedure used.

Ceramic adhesives can be used not only to cement metal to ceramics, but also to cement metal to metal and ceramic to ceramic. The use of such adhesives must be limited to structural members because of the long periods at high temperature required to form the bond. Thus, these adhesives can be used to seal the radome to a mounting ring, but they are not recommended for sealing the assembly to the bulkhead of a missile guidance system. The feasibility of using cold-setting ceramic adhesives, such as Sauerisin cement, has not been investigated under conditions of high loading and high temperatures. However, such adhesives must be included in a study of bonding agents. For further information on ceramic adhesives, see Final Engineering Report, Parts I and II, on Narmco Contract AF 33(616)-8157 on High-Temperature Radome Attachment Techniques.

Plastic adhesives are either thermosetting or thermoplastic. Thermosetting adhesives, such as epoxy or phenolic, are excellent if used in a joint that is subject to either tensile or shear stress. These materials readily fail if subjected to peel or cleavage. They are recommended for attachments that undergo both static and dynamic loading. Thermoplastic adhesives are also highly resistant to tensile or shear stress, but have little resistance to constant loading over extended periods and are not recommended if an oscillatory load is expected. Rubber-based or elastomeric adhesives are best if used as sealants rather than as adhesives since they offer little resistance to tensile or shear loads but do resist peel and cleavage. As a rule, the addition of metallic oxides increases the high-temperature strength of an adhesive, but also usually decreases its strength at room temperature.

Chemical joints should cover large areas so that stress may be suitably distributed and should be placed in tensile or shear stress or in a combination of both. Care must be exercised to ensure a continuous bond. The selection of a suitable adhesive and the proper cleaning and priming of the adherents will result in a reliable high-temperature bond. Aluminum, for example, is attacked by an alkaline adhesive and the bond fails. If the manufacturer's recommendations are followed regarding temperature cycle and pressures during the curing

process, gas should not become trapped in the bond joint. Such entrapment can cause the bond to fail at high temperatures because of the formation and subsequent explosion of gas bubbles. The adhesive must be insensitive to light or radiation and must be insoluble in ordinary liquids after curing. Reference 72 reviews these factors and presents a detailed list of adhesives and their specifications.

### 1-3.7 MECHANICAL ATTACHMENTS

Mechanical means of attachment include such devices as bolts and rivets that can be used instead of the adhesive joints shown in Fig. 1-44. A shrink-fit attachment is desirable if the section to be joined is short, because such an attachment subjects the ceramic material to high compressive stress if the metal ring is external to the ceramic. This type of attachment cannot be used at temperatures near those employed to shrink the attachment since the two materials expand and separate at these temperatures. If the metal ring does not cover the ceramic for an appreciable distance or if it is not tapered, a large stress concentration occurs at the end of the ring. Thus, this method can be used only at low temperatures. As illustrated in Fig. 1-44, the use of clamp joints presents a complex design problem since stress concentrations result from the notches or undercuts required. Although mechanical attachments are more expensive than chemical attachments, they are preferable in certain designs. Since a mechanical design requires the use of O-rings, gaskets, or elastomeric sealants if a pressure or vacuum seal is needed, such a design is costly. When combined with a chemical lap joint, a clamp attachment is usually employed to join large airborne radomes to the aircraft. It has been also used to seal relatively large evacuated guidance units when evacuation tubes are not desired or when evacuation would require a long pumping time. An example of such an attachment is shown in Fig. 1-46D and is discussed in the next paragraph.

### 1-3.8 DESIGN EXAMPLES

The electrical thickness of the wall of most high-velocity radomes is one-half wavelength. Thus, most experience has been gained in de-

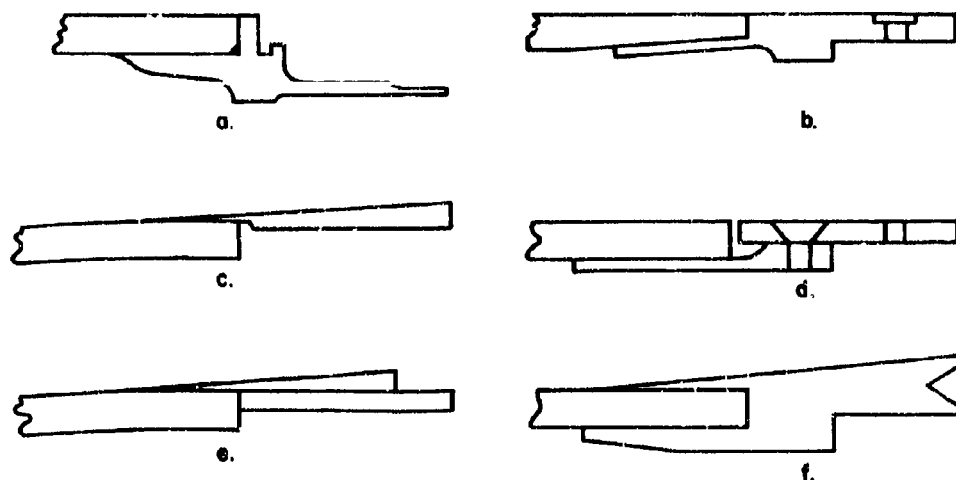


Figure 1-45. Chemical Attachments

signing attachments for radomes with this wall thickness. As stated, these attachments can be either chemical or mechanical. In early methods of radome attachment, the two structures were joined mechanically and the advent of reliable structural adhesives and brazing techniques encouraged the use of these methods. Thus, most radomes in operational use today use chemical attachments. Figure 1-45 illustrates several methods of radome attachment based on these methods. Figure 1-45A shows an adaptation of the butt lap joint. The radome is centered on the mounting ring by filling the adhesive with glass spheres. Although this procedure results in a reliable joint for small radomes, its use with larger structural units is limited by the area available for bonding. The design shown in Fig. 1-45B is a version of the scarf joint; it provides more bonding area and, therefore, greater strength with only a minimum increase in the length of the joint. These two methods of attachment are relatively inexpensive; however, they are not reliable if the radome temperature exceeds 500°F.

The metallic inner ring is usually made of aluminum or magnesium in order to reduce weight. Failure can occur at temperatures in the range of 500° to 1000°F because of differential thermal expansion; however, as reported in Reference 73, this condition can be relieved if the ring is slotted axially. Although the bond

can be achieved by using metallic brazes, the internal ring limits the brazing temperature to values sufficiently low so that differential expansion will not cause fracture during brazing. The design of the external ring shown in Fig. 1-45C minimizes such expansion and, if the fit is proper, this ring can be used to put the ceramic under a compressive load. This ring, which is usually made of Kovar, or of a similar low-expansion metal, is as thin as possible to allow for deflection and differential expansion. If the ring is tapered, the stress concentrations at the end of it that result from a bending load are minimized. This design is not subject to failure during bonding. Thus, the maximum use temperature is limited by the choice of brazing material and the strength of the joint at high temperatures. Figure 1-45D shows the use of a low-expansion ring on the inner surface. This design can be fabricated if the ring is thin enough to permit deflection during brazing. It is not, however, recommended for high-velocity missiles because of its poor structural reliability. Although structurally reliable attachments using a low-expansion material can be designed, they become excessively expensive because of the cost of such a material.

Since hollow cylindrical shapes having the required dimensions are not usually available, both the internal and external rings must be machined from a solid bar or plate and thus

become more expensive. Because the mounting ring must in turn be attached to another metal ring, the unequal expansion of these rings causes additional design problems.

It should be noted that the strength of many low-expansion metals decreases rapidly at high temperatures and that a perfect expansion match is not possible over a wide range of temperatures. A point often overlooked is the hysteresis effect of temperature on the coefficient of thermal expansion. If the temperature increases beyond a specific value, the low-expansion coefficient of the material increases, depending on the number of temperature cycles. This is a consideration of prime importance if the attachment is to be used for a pylon-mounted air-to-air or air-to-ground missile carried by a supersonic aircraft. Another version of the butt lap joint is shown in Fig. 1-45E. It is superior to that in Fig. 1-45C since it provides a reinforced plastic overwrap that is applied under a large tensile load. Thus, when completed, this overwrap not only applies a compressive load to the radome, but also acts as an insulating cover that reduces the temperature and hence the amount of differential thermal expansion. Attachments similar to those shown in Figs. 1-45C and 1-45E have been investigated for use with missiles. (See Reference 74.)

The overwrap is usually made of glass monofilament or roving, but it can be fabricated from fiberglass preforms if no preload is desired. In several systems now in production, alternate layers of preform and wrap are used. Attachments employing such an overwrap can fail through the wrap at the butt joint when subjected to heavy dynamic loads or shocks, and the strength of the overwrap decreases as the temperature increases. An example of the double lap attachment is shown in Fig. 1-45F. The primary advantage of this design is the two-fold increase in bonding area that it provides. Note that if the two outer members are not subjected to equal stresses, this advantage is not realized.

This design can also be used to mount "A" sandwich radomes since it does not depend on the core structure for bonding. It can also be employed for mechanical attachment if bolts are used instead of adhesive. If the holes in the radome are made oversize and if an elastomeric adhesive is used, the bolts subject the radome material to compression but do not decrease its

structural reliability through stress concentrations since they are not in contact with the radome wall. All of these attachment methods offer a means of joining the radome to the aft structure and are suitable for use where a controlled internal atmosphere is desired since they provide a vacuum seal. Appendix 3 in Reference 71 and Reference 75 present detailed analyses of various forms of the double lap attachment shown in Fig. 1-45F. This type of attachment has been analyzed and tested at temperatures exceeding 1000°F and should be considered in designing large, high-velocity ceramic radomes.

Clamps, such as those shown in Figs. 1-46A and B, can be used on very large radomes since they can be segmented and placed at specific points along the circumference of the radome to distribute the load. They permit rapid assembly and disassembly of the attachment and if they are designed to include an O-ring seal, the internal pressure can be controlled. Figure 1-46C shows a type of clamp that requires a groove in the radome wall. The radius of this groove must be large to prevent heavy stress concentrations when a bending load is applied. This attachment, which is designed to be free floating, imposes no stress on the radome because of differential thermal expansion since the metal is not in contact with the radome except at the snap ring, which imposes only a Newtonian drag force as the two materials slide over one another. It also insulates the metallic components within the radome. With the fourth method shown, the radome is simultaneously attached and sealed to the bulkhead. As shown in Fig. 1-46D, this mechanical joint consists of a circumferential groove at the aft end of the radome and another at the forward end of the bulkhead.

Figure 1-46E is an enlarged view of this type of joint. These two portions are joined by a split ring, which is in turn secured to the bulkhead by means of a second inner split ring. Note that the splits in the rings should be on opposite sides of the circumference. The split ring is not fastened to either the radome or to the bulkhead; it is instead a freefloating clamp that applies a minimum load to the radome. An O-ring at the aft end of the radome is used for sealing. Such an attachment does not depend on adhesives or brazing. The attachment area can expand over extended temperature ranges without imposing any direct load on the radome.

If the outer ring is designed to yield, it will not impose a severe structural load on the radome at the groove when a bending load is applied. If the radome and bulkhead are both impermeable to gas and have no evacuation or pressurization ports, the assembly can be made gas tight by designing special evacuating or pressurizing chambers. Consider the case of an evacuated assembly. The radome and bulkhead are inserted in a large chamber and this chamber is evacuated. The radome is then placed over the bulkhead and subjected to a stress that compresses the O-ring. As the chamber returns to atmospheric pressure, the external pressure seals the radome to the bulkhead. The assembly

is removed and the split rings are assembled. A similar procedure can be used to assemble a pressurized unit. A word of caution concerning this attachment is in order. It is obvious that the load should be distributed over as large an area as possible. This occurs if the metal clamping rings have a low spring rate or if the design allows the outer metal ring to yield. In the latter case, care must be exercised to prevent the attachment from reaching the breaking point.

The attachments described previously are based on either chemical or mechanical methods. Combinations of these two methods that have evolved are in certain instances superior to either individual method. The joint shown in

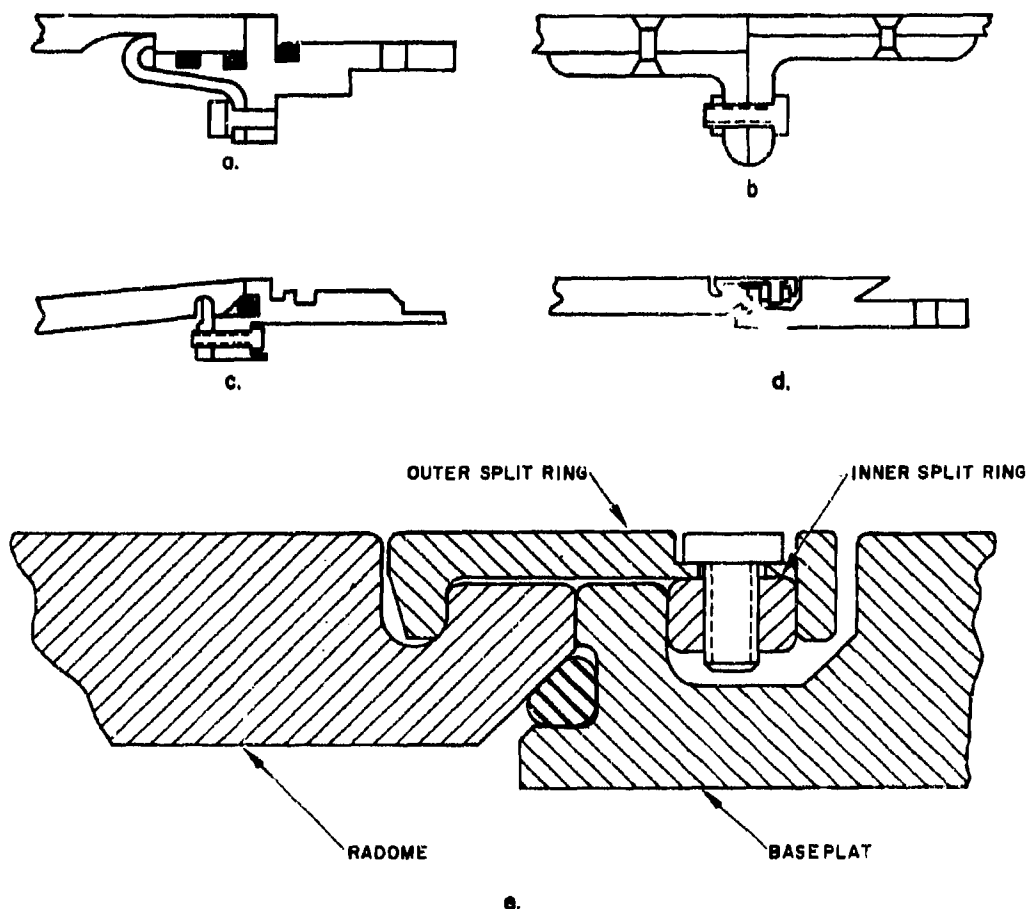


Figure 1-46. Mechanical Attachments

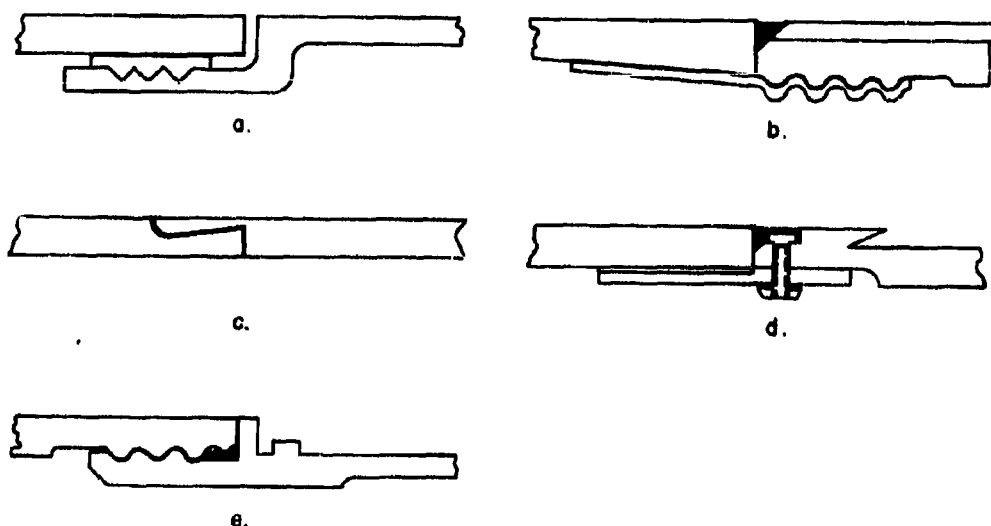


Figure 1-47. Combined Chemical-Mechanical Attachments

Fig. 1-47A uses a threaded plastic insert lap that is bonded to the ceramic structure. This assembly is, in turn, attached by an offset lap joint to the threaded bulkhead. The advantages of this type of assembly are that it can be quickly replaced and sealed with an elastomeric compound. A similar but less expensive attachment is shown in Fig. 1-47B. Figure 1-47C shows perhaps the least expensive construction. It requires a tapered end on the radome that can, however, result in a stress concentration. The bulkhead is machined as a cylinder and is bonded to the radome with an elastomeric adhesive. Before this adhesive is cured, the lip of the bulkhead is depressed by means of a swaging tool; the resulting mechanical attachment does not directly load the radome.

References 76 and 77 discuss a similar method of attachment that is based on the use of a magnetic pulse to form a thin metal ring around an internally notched radome. They also describe in detail a series of tests of the attachment and contain a mechanical analysis of the design. In the method shown in Fig. 1-47D, a chemical lap joint is used in combination with a mechanical lap joint. With this method and that shown in Fig. 1-47B, a Kovar ring welded to the aluminum strap can be used. This ring is cemented to the radome and its coefficient of thermal expansion matches that of the radome

over the temperature range of interest. If this ring is either scalloped or slit at its forward end, it does not impose a load on the radome because of thermal expansion. The method shown in Fig. 1-47E is perhaps the most expensive and is used for ceramic radomes. However, it is inexpensive if a molded insert is used with plastic radomes. The mogul thread is of the same design as that used for the attachment shown in Fig. 1-47B. As can be seen in Fig. 1-47E, this design allows rapid assembly of the parts, as well as internal pressurization or evacuation. If ceramic materials are used, the thread should be large in order to reduce the cost of grinding and the stress concentration the thread causes.

Figure 1-48 presents four methods of attaching the radome mounting ring to a missile. In Figs. 1-48A and B, cone nuts are used for locking to allow for small misalignments and still provide a reliable structural attachment. The use of O-rings makes it possible to control the internal environment. In Figs. 1-48C and D, lap and double lap joints are shown. Although they are less expensive, such joints cannot be readily sealed by O-rings. An elastomeric adhesive can be used to fill the butt joint, but then the radome cannot be quickly removed.

A review of the various attachments shown in Figs. 1-44 through 1-48 reveals that the

chemically bonded lap and double lap can be used for attaching ceramic sandwich radomes. Here the same designs can be employed as those that are available for thick solid walls. Details on the methods of attaching ceramic radomes shown in Fig. 1-49 are discussed in Reference 6. Methods of attaching plastic sandwich radomes are described in Reference 1. When combined with those illustrated in this section, these designs should provide a reliable means of attachment for sandwich radomes. All the designs illustrated are merely combinations of the basic joints shown in Fig. 1-44. Thus, a unique problem can be solved by using these basic joints and the detailed designs presented here as a guide.

The methods of attaching thick-wall radomes are applicable to ceramic and plastic thin-wall radomes if suitable wall sections can be made available at the aft end of the radome. When the desired look angle does not permit a gradual thickening of the wall, variations of the lap and double lap joint can be used. Several such variations that are applicable to thin-wall radomes are discussed in Reference 59.

## 1-4 TEST METHODS FOR DETERMINING THE PHYSICAL PROPERTIES OF RADOMES

### 1-4.1 INTRODUCTION

The physical properties of a radome must be known not only to conduct the various analyses

that are essential for design, but also to evaluate the validity of the resulting design. They can also be used as the basis for a quality control program. Table 1-1, which lists the various properties involved in radome design, should be referred to in the following discussion.

Determining the physical properties of a radome usually involves cutting specimens from the radome wall and then evaluating them by the following procedures. In some instances, the complete radome can be used in these tests; for example, to determine its strength by loading the radome and measuring its resistance to thermal shock. Methods of nondestructive testing have been developed for evaluating such electrical properties as dielectric constant, loss tangent, and transmission and reflection losses. Hence, unless otherwise stated, it is to be assumed that the required test specimens are obtained by removing samples of the material from the radome.

References 78 and 79 contain detailed tabulations of recommended test methods and Reference 80 gives details on test techniques. Additional information on the evaluation of those properties marked in Table 1-1 with a double asterisk is presented in Reference 71 and in Chapters 4 and 5 of this handbook. The following discussion is devoted to methods of determining the physical properties of radome materials.

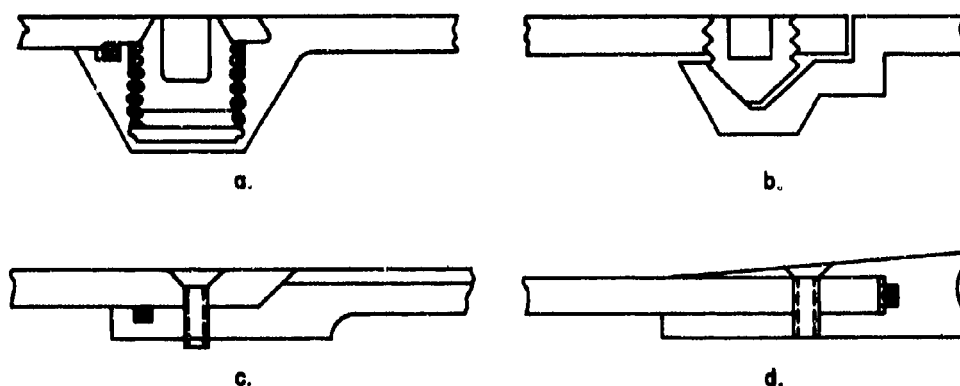


Figure 1-48. Methods of Attaching Radome Mounting Ring to Missile or Aircraft Structure



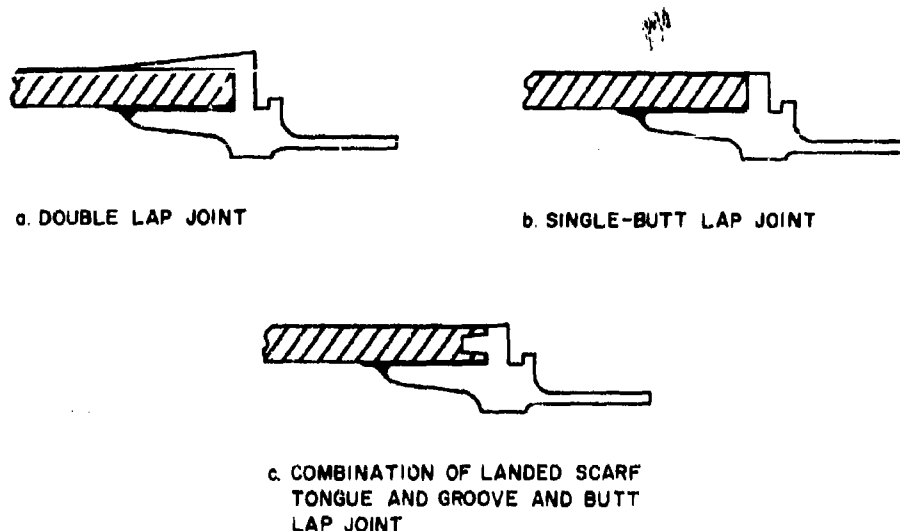


Figure 1-49. Methods of Attaching "A" Sandwich Radomes

#### 1-4.2 GENERAL PROPERTIES

The general properties listed in Table 1-1, such as color, surface texture, and finish, can be determined by visually observing the radome. Surface finish can be assessed by using appropriate fixtures and instruments, such as the Brush Surfindicator, Profilometer, or some other instrument designed for this purpose. The composition of the material can be determined either by chemical analysis of a specimen or, preferably, by a spectrographic analysis of representative sections of the radome. Homogeneity, which is defined as the possession of identical physical properties throughout the radome, can be determined by cutting samples from various portions of the radome and determining the physical properties of specimens ground from these samples. Isotropy, which is defined as the possession of the same physical properties in all directions, is evaluated in a similar manner. In this instance, however, the properties of the same specimen or of one cut from adjacent areas of the sample are usually measured in three orthogonal directions. Homogeneity and isotropy should be determined for each of the physical properties listed in Table 1-1. Note that a radome can be simultaneously both homogeneous and anisotropic; for example, one having a sandwich construc-

tion. The monolithic wall is usually both homogeneous and isotropic.

#### 1-4.3 ENVIRONMENTAL TESTS\*

The environmental tests needed to determine the chemical solubility of a radome material and its resistance to salt spray, fungus, sand, and dust are defined in Reference 78. Since the environmental requirements for a given radome depend on how and where it will be used, the applicable system specification should be consulted to determine the pertinent requirements. Water absorption characteristics can be found by using Procedures C-373-56 or D-116-61T in Reference 80, or the dye penetration method defined in Reference 79 can be used. Gas permeability and outgassing are usually measured by using helium mass spectrometer leak-detection equipment while the test specimen is kept at the appropriate temperature. Tests for chemical solubility, such as those required in Reference 78, are applicable to the usual aircraft fuels and to solutions used in maintenance. Exotic missile fuels and solutions are not, however, covered by this specification. The effects of radiation are determined by sub-

\* See Chapter 3.

jecting a test specimen to the expected source of radiation for the period of time defined in the applicable system specification. Electromagnetic radiation has no adverse effect on the properties of the usual radome materials; however, it has been shown that radiation at higher frequencies, such as that associated with atomic or nuclear environments, weakens many plastic materials. The life expectancy of radomes when in use varies from seconds to hours, while storage requirements of from 2 to 5 years are not uncommon. Procedures such as those defined in Reference 78 are usually used for evaluating life expectancy. Radomes or specimens of radome materials have been subjected to rain-resistance tests that vary from flight through natural rainfall to the simulation of various expected environments by using test apparatus such as cannon shells and machines with rotating arms described in Reference 1 or sleds mounted on dual or monorail tracks. Although it is intended primarily as a handbook covering the principles of rocket sled design, Reference 81 contains a detailed description of sled tracks and rain-erosion test facilities. Specimens of a radome material or samples cut from a radome wall are mounted on the rotating arm or are used as the tip section of the cannon shell. The use of a sled makes it possible to evaluate not only specimens but scaled or full-size radomes. Considerable work has been devoted to determining the rain resistance of radomes and radome materials. Two bibliographies on the subject of rainfall and rain resistance tests (References 82 and 83) together with the data presented in Chapter 3 of this handbook provide a comprehensive review of the work done in this field.

It should be emphasized that the only radome specifications available are MIL-R-7705A (Reference 78), and AIA Reports No. ARTC-3 and ARTC-4. The first two specifications cover the physical properties of radomes and the last specification covers the electrical properties.

#### 1-4.4 THERMAL PROPERTIES\*

The thermal properties of radome materials are evaluated by using specimens cut from the radome. The test methods to be employed de-

pend on the type of material. For example, materials with low conductivity require refinements of the measurement technique that are normally not necessary in evaluating high-conductivity materials. The term *maximum use temperature* is defined as that temperature beyond which a radome can no longer function without impaired performance. Radomes made of plastic materials are limited in electrical performance by the variation in dielectric constant and loss tangent as temperature increases, while the strength of many ceramic radomes decreases appreciably at high temperatures. No method that is acceptable to the various manufacturers of radome materials has yet been devised to determine the melting and softening point. Thus, actual environmental conditions and functional requirements must be considered in determining maximum use temperature and the softening and melting point of the material. The value of specific heat is usually found by using ASTM test method C-351-61. The relationship between thermal conductivity and diffusivity is given by Eq. 1-10. It is, therefore, necessary to measure only density or specific heat; the value of the other property can then be calculated. References 84 and 85 each propose a method of determining thermal conductivity; the method given in Reference 85 has been incorporated in ASTM test C-408-58. The thermal diffusivity of ceramic materials can be found by using the methods described in References 71 and 86. The values of thermal expansion and of the coefficient of linear thermal expansion, sometimes called expansivity, can be found by interferometric methods described in ASTM specification C-328-56 or by applying the dilatometer technique used in ASTM test C-337-57. Data on thermal emittance are primarily of importance at high velocities, where the radome surface reaches high temperatures. In this situation, the effects of radiation play an important role in heat transfer. The various techniques for determining both the spectral and the total normal emittance of transparent, semitransparent, and opaque materials are described in References 87 through 89.

Resistance to thermal shock is primarily of importance in the design of ceramic radomes for high-velocity missiles. It is a measure of the ability of a material to withstand a temperature gradient through its thickness. Speci-

\* See Chapter 5, Paragraph 5-6.

mens cut from the radome wall or prepared in the shape desired are used in these measurements. The use of solid spherical shapes is discussed in Reference 90, and tests of right cylindrical disks are described in Reference 91. A determination of thermal shock resistance and a choice of materials based on these findings do not of themselves guarantee satisfactory radome performance. A full-scale radome must be tested to determine structural reliability. In the most elementary type of such a test, the radome is immersed in heated salt or molten metal (see References 91 and 92). Such tests are limited by the heat transfer coefficient of the fluid because of the peak stress that occurs. In attempts to attain greater temperature gradients, a centrifugal pump is used to move the heated fluid over the outer surface of the radome. As discussed in Reference 74, the radome is supported in the horizontal plane and the heated fluid is sprayed in an axial direction from the tip to the aft portion. A further refinement in technique is to use a heated fluid into which a shroud is submerged. The apex of this shroud is attached to a centrifugal pump, fluid is pumped into the shroud cavity, and the radome is lowered into the shroud at a controlled rate. As the radome descends, the clearance between it and the shroud decreases and the heat transfer rate, therefore, increases. If necessary, the pump velocity can also be varied as the radome descends. Although this technique is most effective when heated fluids are used, it requires the design and fabrication of a shroud matching the size and shape of each radome to be tested. It is, therefore, the most expensive method.

An alternative test technique is based on the principle of radiant heating. The equipment used consists of a cylindrical or conical chamber fitted with infrared lamps. (See References 86, 93, and 94.) The radome is mounted within the chamber and the controlled flow of current to the lamps is increased to produce the desired radome temperature gradients. In the most sophisticated simulation of thermal shock, a metallic contour shroud encloses the radome and heated air is circulated between the shells axially from the radome tip. Reference 95 describes a facility that consists of an arc that heats the air to the desired enthalpy. The air then passes to the shroud through a plenum chamber. Similar facilities in which a blow-

down tunnel is the source of air are discussed in References 74 and 96. Reference 71 contains a complete description and analytic evaluation of a similar facility in which a gas-fired heater is used to warm the air from a large storage vessel. After it is mixed with cool air to achieve the desired heat flux, the heated air passes between the shroud and the outer surface of the radome and produces the desired temperature gradients.

Thus, there are three types of test procedures that produce different thermal conditions. Immersion of a test specimen in a heated fluid can simulate the thermal gradient at only one particular missile station. Since the temperature of the fluid is constant because at a specific bath temperature the temperature gradient through the wall is approximately the same in any axial or circumferential direction, the maximum stress occurs at the tip of the radome. Therefore, this type of test is restricted to simulating thermal stresses only at the stagnation point. The use of a shroud also makes it possible to control the axial temperature gradient, and with infrared heating equipment, rapid variations in surface temperature can be simulated. Because these test methods cannot provide the large heat fluxes that are required for many full-scale tests, the use of heated-gas facilities is mandatory for a three-dimensional simulation of thermal shock caused by severe heat. Although the facilities just described are the best that have been devised for this type of test, because of the high cost of instrumentation and operation, they are usually employed only for final radome tests rather than for the evaluation and screening of materials. Chapter 8 contains additional information on this type of test and a compilation of test data.

#### 1-4.5 ELECTRICAL PROPERTIES\*

The electrical properties of primary importance to a designer of microwave radomes are dielectric constant and loss tangent. They can be measured by using: (1) loaded and shorted waveguide, (2) resonant cavities, and (3) free-space transmission or reflection techniques. The use of loaded and shorted waveguide, which is described in References 97 and 98, requires

\* See Chapter 5, Paragraph 5-6.

that specimens of the material to be tested be either specially fabricated or cut from the radome wall. Although the specimen needed is usually small enough that it can be cut from the wall, this method is limited to measurements at low temperature because of the difference in the thermal expansion characteristics of the waveguide and the specimen. If elaborate corrections for sample fit are made, the use of shorted waveguide can be extended to high temperatures. With the refinements reported in Reference 99, accurate measurements can be made at temperatures beyond 3000°F. The resonant cavity technique that is proposed and analyzed in Reference 100 is not as susceptible to the tolerances and fit of the sample as is the waveguide technique. The use of resonant cavities is discussed in References 101 and 102.

Free-space techniques for measuring the dielectric constant are based on the use of panels of the radome material or the radome itself. Unless large panels are available, this method is not satisfactory for measuring the loss tangent of low-loss materials. References 78 and 97 give details on the construction and use of the reflectometers and interferometers, and Reference 103 presents a mathematical analysis of how the dielectric constant is determined on the basis of measurements of reflection coefficient. These techniques are also employed to determine the transmission and reflection coefficients of radome materials and of full-scale radomes. As discussed in Reference 97, they are useful for quality control because they measure insertion phase difference and, hence, wall thickness and are covered in Chapter 5.

#### 1-4.6 MECHANICAL PROPERTIES\*

The mechanical properties of a radome are determined by removing specimens from it. The methods presented in Reference 104 are generally acceptable to the aircraft industry. Although these methods are intended primarily for plastic materials, in many instances, they are also applicable to the evaluation of ceramic materials. The application of this specification has declined and MIL-STD-401A (Reference

105) is generally used in its place. Note, however, that methods of determining edgewise tensile failure of sandwiches are not covered by the MIL-STD-401A. When combined with those discussed below, these methods provide the reader with a basic set of procedures for evaluating most radome designs. The density or specific gravity of a radome is measured by immersion techniques, such as those outlined in ASTM Specification C329-56. The hardness of dense ceramic materials is measured by using the Rockwell 45 N scale and following the procedures given in ASTM E-18-61. Hardness of the less dense glass-based materials is measured by using the Knoop technique. Although a scratch test enables one to differentiate between many materials, since the more dense ceramic materials all fall in the Moh's scale of 9 or higher, this type of test cannot be used to differentiate between bodies that are 90 or 95 percent alumina, for example. The porosity of a radome material can be determined by comparing the density measured by the technique discussed previously with the theoretical maximum density or by using the methods presented in ASTM specification C-373-56. The Charpy test described in ASTM specification D-256-56 is used for measuring impact strength. Method D appears most suitable for measuring brittle materials. The elastic properties of glass and ceramic materials, Young's modulus of elasticity,  $E$ , the modulus of rigidity,  $G$ , and Poisson's ratio,  $\mu$ , are related by the expression

$$\mu = \left( \frac{E}{2G} \right) - 1 \quad (1-20)$$

Thus, only two of these properties need to be determined. The sonic resonance method, presented in Reference 106, is nondestructive and accurate, and has been applied to ceramic materials, such as alumina, beryllia, and Pyroceram (References 71 and 107). Flexural strength or modulus of rupture (MOR) is measured by either a three- or four-point loading of a rectangular or cylindrical test specimen. The methods defined by ASTM specifications D-116-61T or D-667-44 are representative. A knowledge of flexural strength is important in determining structural and thermodynamic loading. In evaluating MOR data and flexural test methods, consider that three-point loading of cylindrical specimens applies a maximum load to

\* See Chapter 4, Part I, and also Chapter 5, Paragraph 5-6.

only one point, while for rectangular specimens the same type of loading applies a maximum load along a line, and four-point loading applies maximum loads along a line and over an area for cylindrical and rectangular specimens, respectively. Thus, the measured strengths may vary, depending on the type of loading applied. It must also be recognized that in very large specimens there is a greater probability of encountering a flaw; hence they will not be as strong as the microspecimens commonly used. The important point to remember is that measured values of MOR vary inversely with cross-sectional area if the test span is constant and that the edge flaws usually encountered in rectangular specimens can cause a reduction in measured strength. Since the compressive strength of most ceramic materials is exceedingly high, special test methods must be used to evaluate this parameter. If the specimens are cylindrical, they should be supported between a conical anvil made of the same material as the specimens to ensure minimum drag force at the face of the anvil. The methods described in Reference 79 or those in the proposed ASTM specification for compressive tests, C-63T, are recommended.

Measuring tensile strength by using the standard pull type of test is not recommended because it is difficult to align the specimen properly. In this type of test, the specimen may fail at the grip point because of stress concentrations and shear loads. Thus, data obtained by following ASTM methods lead to errors in measurement and interpretation. For these reasons, most manufacturers of ceramics do not use the tensile test, but prefer to measure modulus of rupture instead.

Another method of measuring tensile strength is to use a cylindrical specimen of a ceramic material obtained by cutting rings from the section removed from the skirt of a radome as it is ground to the required length. As an alternative, rings can be cut from the radome itself. Consider a right cylindrical ring subjected to an internal pressure. Using Lamé's method, which assumes that the cylinder consists of a series of thin-walled cylinders one within the other and that a plane transverse section remains plane and parallel to itself, we can show that:

$$\sigma_{\theta} = p \frac{a^2}{b^2 - a^2} \left( \frac{b^2}{r^2} + 1 \right) \quad (1-21)$$

$$\sigma_r = p \frac{a^2}{b^2 - a^2} \left( \frac{b^2}{r^2} - 1 \right) \quad (1-22)$$

where  $b$  = outer radius of ring  
 $a$  = inner radius of ring  
 $r$  = radius at which stress is to be calculated  
 $\sigma_{\theta}$  = hoop stress  
 $\sigma_r$  = radial stress  
 $p$  = internal pressure

The maximum shear stress is

$$\sigma_s = \frac{1}{2} (\sigma_{\theta} + \sigma_r) \quad (1-23)$$

Under these conditions, the hoop stress is tensile and is maximum at the inner surface of the ring. Equations 1-21 and 1-22 then become:

$$\sigma_{\theta} = p \frac{b^2 + a^2}{b^2 - a^2} \quad (1-24)$$

and  $\sigma_r = p \quad (1-25)$

If the ring is very thin,  $b$  is approximately equal to  $a$ , and the stresses through the section can be assumed to be constant and equal to:

$$\sigma_{\theta} = p \frac{r}{\Delta r} \quad (1-26)$$

$$\sigma_r = p \quad (1-27)$$

Thus, if a uniform constant pressure is applied to a thin ring, it experiences tensile stress that increases as the pressure increases. Equation 1-24 has been solved for the various conditions shown in Fig. 1-50, which presents the ratio of tensile stress to pressure as a function of wall thickness for various inner radii. From this figure, it can be seen that the pressure required to break a ring having a constant thickness increases as the radius decreases and that it also increases if the thickness of the ring increases. Figure 1-51 shows the ratio of the outer radius to the inner radius as a function of the ratio of the stress on the inner surface of a thick shell to that on a thin shell. From this figure, it can be seen that the use of a thin-shell approximation is not permissible if the stresses are to be used as a valid means of determining the tensile strength of the ring. An indication of the variation in the calculated values of stress through the wall is given in Fig. 1-52, which shows that the percentage variation in stress

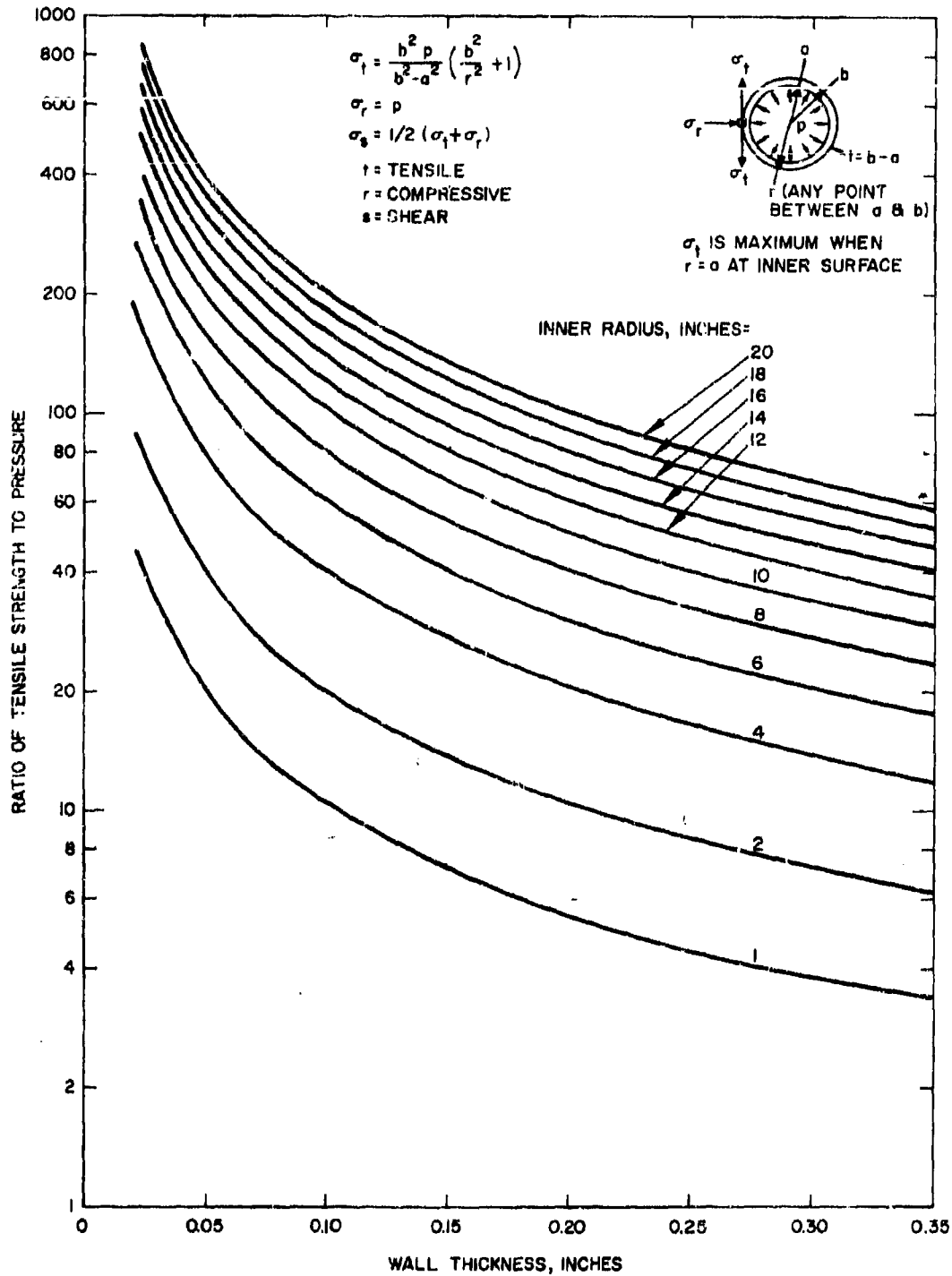


Figure 1-50. Stresses in Cylindrical Ring with Uniform Internal Pressure

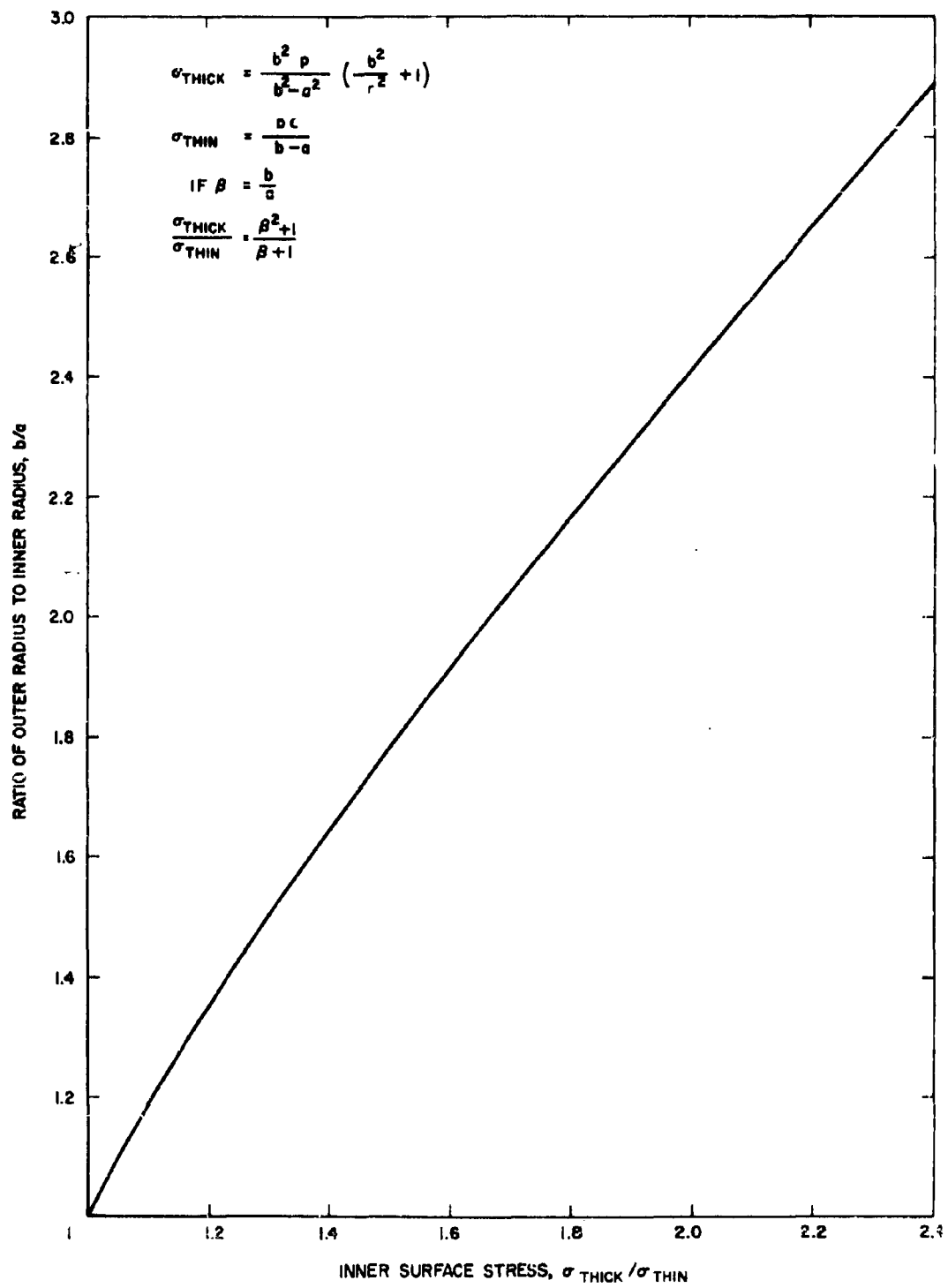


Figure 1-51. Comparison of Stresses on Thick- and Thin-Shell Radomes

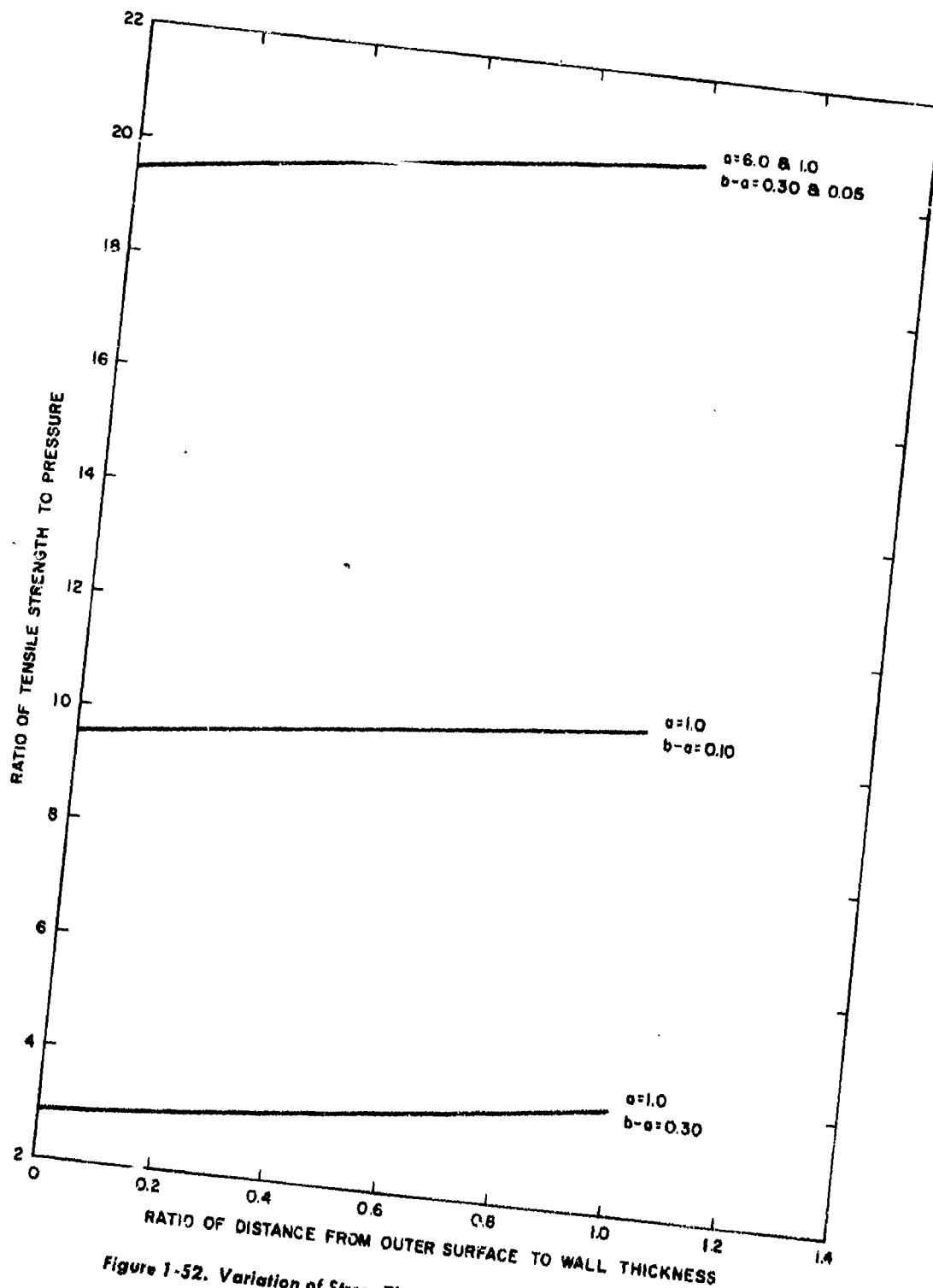


Figure 1-52. Variation of Stress Through Wall Thickness



decreases as the radius increases. This decrease is to be expected since with large radii, the thin-wall approximation approaches the thick-wall approximation.

This analysis suggests a means of determining the tensile strength of sections of the radome or it can serve as a quality control method if the ring removed from the radome skirt is used as a test specimen. The internal pressure required can be obtained by using a bladder made of an elastic material inside the ring or by the method shown in Fig. 1-53. Here the metal loading fixture is lined with an elastic material that applies a uniform load to the ring. The error involved in applying pressure in a direction normal to the load is negligible since the load on a unit area is equal to  $p \cos \gamma$ . Since, in this region, the value of  $\gamma$  approaches 90 degrees and that of  $\cos \gamma$  approaches zero, the force is small compared with the total force. An alternative method of determining tensile strength by using ring specimens is discussed in Reference 108. Here, the specimen is placed under compression across a diameter. The load at failure is a measure of the tensile strength of the specimen. The methods for determining

the strength of a radome by using specimens cut from the wall of the radome are not completely valid since the stress concentrations and other shape factors peculiar to a radome and its attachment are not reproduced in the specimen. The actual radome can be used as a test specimen for determining its strength under tension. The radome is placed in a horizontal or vertical position and attached to a rigid base. A load is applied to the tip area in a direction normal to the radome axis and is increased until failure occurs. Analyses such as those presented in Reference 71 can be used to transform the maximum normal load into a failure stress. As shown in this reference, this method also permits the evaluation of strength at elevated temperatures. In this case, the radome is surrounded by infrared lamps grouped in the form of a cylinder. The radome is loaded as the lamps heat it in a manner that simulates the temperatures expected during flight and its strength is evaluated by using the same analytic techniques as those discussed above.

Dimensional return, the ability of a material to return to its initial dimensions after being subjected to high temperatures, can be deter-

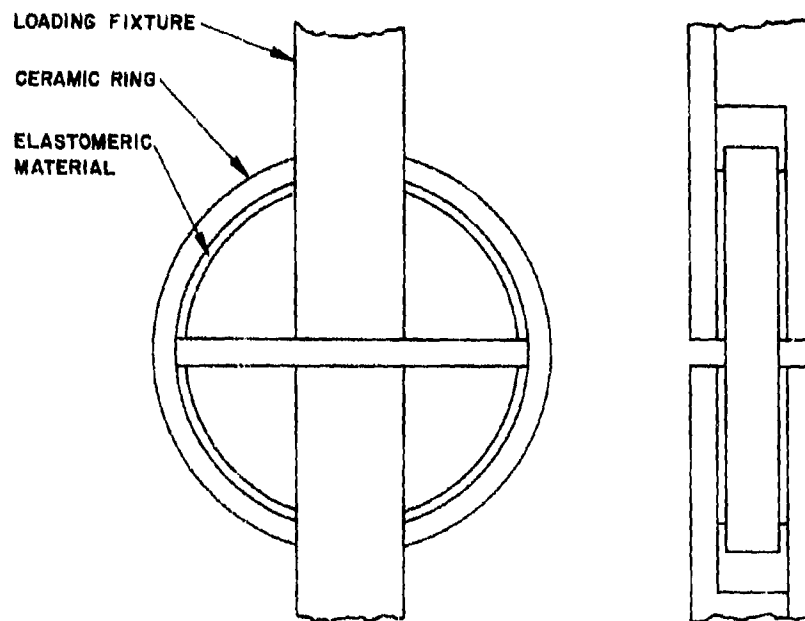


Figure 1-53. Measurement of Tensile Strength by Use of Ceramic Rings

mined by using the actual radome. The radome is dimensionally inspected first and then inspected again after several cycles of heating and cooling. Dimensional stability is measured in a similar manner except that instead of temperature, time is the variable. The effects of fatigue for most ceramic materials are unknown. Since ceramic radomes are now used for missile applications in which the radome is not subjected to cyclic loading for long periods of time, the effect of fatigue is at present of minor importance. For aircraft radomes, on the other hand, fatigue must be considered since they are subjected to repeated loads for long periods of time.

## 1-5 FACTORS AFFECTING THE STRENGTH OF RADOMES

### 1-5.1 SHAPE

The strength of a radome is determined by its aerodynamic contour, wall thickness, fineness ratio, base diameter, and the physical properties of the material of which it is made. The effect of these parameters is illustrated in Fig. 1-42. Aerodynamic drag is a function of the base diameter, the contour, and the fineness ratio. It increases for larger base diameters and decreases with increasing fineness ratio and more pointed contours. The forces due to the difference in pressure within the radome and that outside the radome and the force due to an O-ring, if used, increase as the base diameter increases. The forces due to inertia and vibration are determined by the weight and center of gravity of the radome. Since weight increases with wall thickness, length, and base diameter, low values for these parameters are desirable. The center of gravity is determined by the aerodynamic contour and fineness ratio. The distance from the radome base to the center of gravity increases as the fineness ratio increases; thus, a low value of fineness ratio is desirable. The force due to aerodynamic pressure increases for bulbous shapes. The distance between the radome base and the center of pressure increases as fineness ratio increases and, therefore, the stress at any station becomes greater. Since the strength of the radome increases as the wall thickness and the radius at any section increase, a thick-walled, hemispherical shape with a low fineness ratio is more desirable structurally.

### 1-5.2 THERMAL ENVIRONMENT

When a radome is exposed to sudden increases in surface temperature, a thermal gradient is produced through the wall that results in thermal stress. The various factors that determine the magnitude of this stress are discussed in References 109 through 111.

Approximate equations used to calculate the thermal stress in a hollow spherical shape are presented in Reference 21. The tangential stresses are

$$\sigma_r = \sigma_\phi = \frac{\alpha E}{1 - \mu} \left[ \frac{2r^3 + a^3}{(b^3 - a^3)r^3} \int_a^b Tr^2 dr + \frac{1}{r^3} \int_a^r Tr^2 dr - T \right] \quad (1-28)$$

where  $\alpha$  = coefficient of thermal expansion  
 $E$  = Young's modulus of elasticity  
 $\mu$  = Poisson's ratio  
 $T$  = temperature  
 $b$  = outer radius  
 $a$  = inner radius

Thus, it can be seen that thermal stress increases with an increase in coefficient of thermal expansion, Young's modulus, and Poisson's ratio, and with a decrease in inner and outer radii. The temperature difference between the inner and outer surface increases as thermal emissivity, thermal diffusivity, and thermal conductivity decrease. The radome contour and fineness ratio determine not only the surface temperature experienced by the radome, but also its resistance to thermal stress. Slender shapes with high fineness ratios experience higher temperatures and thermal gradients. Thermal stress decreases with an increase in radius at the section in question; thus, a bulbous shape is desirable if thermal stress is to be reduced. References 109 through 112 list recent studies of the effect of physical properties on thermal stress. References 111 and 112 are studies of the thermal stress resistance of heterogeneous systems and show that the addition of a material having a low modulus of elasticity increases resistance to thermal shock. These references are also applicable to foamed ceramic systems containing spherical pores and show that the thermal-shock resistance of a

foamed ceramic is superior to the same material in monolithic form.

Reference 113 and Chapters 3, 4, and 6 of the handbook discuss the effect of temperature on the physical properties of monolithic structures. These properties usually vary with temperature in such a way that stress increases as strength decreases. The properties of sandwich structures made of ceramic materials are discussed in Reference 114, which shows that thermal shock resistance increases for such structures while their strength generally decreases.

### 1-5.3 MECHANICAL

The strength of a ceramic material is reduced by surface flaws and stress concentration factors, such as notches and surface discontinuities resulting from surface grinding. Internal flaws and residual stresses resulting from improper cooling cycles are also responsible for a decrease in the inherent strength of a ceramic material. The effects of structural size, strain rate, internal stress fields, microstructure, impurities, dislocations, and structural changes, such as twinning and flow, on the strength of ceramics have been the subject of many studies. References 114 through 116 summarize the results of these studies and show that other factors such as prior thermomechanical history and environment also affect strength. References 115 through 117 summarize the various theories on the mechanism of fracture in ceramic materials.

A ceramic radome becomes weaker if its surface is interrupted by sharp discontinuities, notches, or holes. As discussed in Paragraph 1-3, such items are usually required in the attachment area. The structural analysis of attachments must consider the reduction in strength caused by such discontinuities. References 118 through 121 present data on the notch sensitivity of metallic and dielectric materials, which show that the stress concentration factor increases (strength decreases) as the notch radius becomes smaller. Thus, holes and notches having small radii must be avoided if the intrinsic strength of the material is to be retained.

The development of methods to correct for or minimize the electrical degradation produced by the radome has resulted in grinding the wall to a thickness that varies in both the axial and the circumferential directions. In designing such corrections, the resultant stress concentration factors must be considered. Thus, if strength is to be maintained, wall thickness should be made to vary in a gradual taper and not by a discrete series of steps. Other methods of minimizing electrical degradation, such as the use of metallic and dielectric rings and anisotropic devices attached to the inner surface of the wall, can impair the structural reliability of the radome. If the rings used to reduce electrical errors do not have an expansion coefficient identical with that of the radome, a tensile or compressive stress can be established in the bonding material. This stress can cause bond failure or, if the bond does not fail, it can increase the stress in the radome wall.

### REFERENCES

1. *Techniques for Airborne Radome Design*, edited by T. E. Tice, WADC Technical Report 57-67, Wright-Patterson Air Force Base, Ohio (ASTIA Document No. AD 142001), September 1957.
2. Wolin, S. *Theory of Lossy High-Incidence Radomes*, Report NADC EL-5116, U. S. Naval Air Development Center, Johnsville, Pennsylvania (ASTIA Document No. ATI-150525), January 15, 1952.
3. Wolin, S. *Electrical Design of Lossy High-Incidence Radomes*, Report ADC-EL-123-50, U. S. Naval Air Development Center, Johnsville, Pennsylvania (ASTIA Document No. 82721), July 11, 1950.
4. Caldwell, O. G., and Gdula, R. A. *The Development of Microcellular Alumina Ceramics for Broadband Radome Applications*, International Pipe and Ceramic Corporation, Los Angeles, California, July 24, 1962.
5. Caldwell, O. G. "Ceramic Porous-Core Laminates for Broadband Radar Radomes," ASD-TDR-62-676, *Proc. ASD-*

- OSU Symposium on Electromagnetic Windows, Vol 1, July 1962.
6. Loyet, D. L., and Yoshitani, R. "Ceramic Sandwich Radome Design," *Proc. OSU-RTD Symposium on Electromagnetic Windows*, June 1964 (also published as Hughes Aircraft Company document 2785.3/294, May 25, 1964).
  7. Cady, Karelitz, and Turner. *Radar Scanners and Radomes*, Vol. 10, Radiation Laboratory Series, McGraw-Hill Book Co., Inc., New York, 1948.
  8. *Proc. OSU-WADC Radome Symposium—Vol. 2*, WADC TR-56-393, Wright Patterson Air Force Base, Ohio (ASTIA Document No. AD 97150), August 1956.
  9. Blyseth, M. G. "Computer Design and Optimization of Broadband Structures with Arbitrary Dielectric Distributions," ASD-TDR-62-676, *Proc. ASD-OSU Symposium on Electromagnetic Windows*, Vol. 1, July 1962.
  10. Gates, Lent, and Wheeler. *Reentry Materials Research—MACH 10 Radomes and Reentry Decoys*, Report SRS-643, Hughes Aircraft Company, Culver City, California, February 1964.
  11. Bonney, E. A. *Engineering Supersonic Aerodynamics*, McGraw-Hill Book Co., Inc., New York, 1951.
  12. Weinberger, T., and Orabona, J. F. *15th Reference Bibliography—Radomes*, Part I, unclassified reports, Lincoln Laboratory Library, Massachusetts Institute of Technology, January 30, 1963.
  13. Weinberger, T., and Orabona, J. F. *15th Reference Bibliography—Radomes*, Part II, classified reports, Lincoln Laboratory Library, Massachusetts Institute of Technology, February 28, 1963.
  14. Nielsen, J. N. *Missile Aerodynamics*, McGraw-Hill Book Co., Inc., New York, 1960.
  15. Laitone, E. V. "Linearized Subsonic and Supersonic Flow about Inclined Slender Bodies of Revolution," *J. Aeronaut. Sci.*, Vol. 14, No. 11, November 1947.
  16. *Handbook of Supersonic Aerodynamics*, NAVORD Report 1488, Bureau of Ordnance, Navy Department, Washington, D. C., 1950.
  17. Stoney, W. E., Jr. *Collection of Zero-Left Drag Data on Bodies of Revolution from Free-Flight Investigations*, NACA Technical Note 4201, January 1958.
  18. Jorgensen, L. H. *Correlation of the Hypersonic Similarity Rule of Pressure Distributions and Wave Drags for Minimum Drag Nose Shapes at Zero Angle of Attack*, NACA Research Memorandum A53F12, August 31, 1953.
  19. Sommer, S. L., and Stork, J. A. *The Effect of Bluntness on the Drag of Spherical-Tipped Truncated Cones of Finesness Ratio 3 at Mach Numbers 1.2 to 7.4*, NACA Research Memorandum A52B13, April 25, 1952.
  20. Barhydt, H. *Dual-Mode Guidance Techniques*, Ryant SRS 3-335, Hughes Aircraft Company, Culver City, California, December 1, 1959.
  21. Loyet, D. L., and Nolte, L. J. "Hypersonic Radome Design," *Proc. OSU-WADD Symposium on Electromagnetic Windows*, Vol. 3, WADD TR 60-274, June 1960.
  22. Schmidt, H. *A Manual for Determining Aerodynamic Heating of High-Speed Aircraft*, Report 7006-3352-001, Bell Aircraft Corp., Buffalo, New York, June 1959.
  23. "Creep, Ablation and Thermal Stress," Lecture Notes, Course 853AB, University of California at Los Angeles, June 1963.
  24. Fields, A. "The Calculation of Local Hypersonic Environments," ASD-TDR-62-676, *Proc. ASD-OSU Symposium on Electromagnetic Windows*, July 1962.
  25. Bloom, M. H., et al. *Aerodynamic and Structural Analyses of Radome Shells*, Vols. I and II, WADD Technical Report 59-22, Gruen Applied Science Laboratories, West Hempstead, New York, February 1961.
  26. Loyet, D. L., and Leviton, E. S. "Programming Thermal Stress Equations on the IBM 7090 Digital Computer," ASD-TDR-676, *Proc. ASD-OSU Symposium on Electromagnetic Windows*, July 1962.
  27. Eisen, D., and Magnus, D. E. "Structural Investigations of Advanced Electromagnetic Windows," ASD-TDR-62-676, *Proc. ASD-OSU Symposium on Electromagnetic Windows*, July 1962.
  28. *Proc. OSU-WADD Symposium on Electromagnetic Windows*, WADD-TR-60-274, June 1960.

29. Huth, J. H. "Thermal Stresses in Conical Shells," *J. Aeronaut. Sci.*, Vol. 20, No. 9, September 1963, pp. 613 to 616.
30. Gatewood, B. E. *Thermal Stresses*, McGraw-Hill Book Co., Inc., New York, 1957.
31. Boley, B. A., and Weiner, J. H. *Theory of Thermal Stress*, John Wiley and Sons, Inc., New York, 1960.
32. Timoshenko, S., and Goodier, J. N. *Theory of Elasticity*, 2nd Edition, McGraw-Hill Book Co., Inc., New York, 1951.
33. Rubin, Fahrenholtz, and Larah. "Design Criteria for Aerodynamic Windows," *Proc. OSU-WADD Symposium on Electromagnetic Windows*, June 1960, WADD TR 60-274, Vol. II.
34. Stalder, J. R., and Helner, V. N. *Heat Transfer from a Hemisphere-Cylinder Equipped with Flow-Separation Spikes*, NACA TN3287, September 1954.
35. Bogdonoff, S. M., and Vas, I. E. "Preliminary Investigations of Spike Bodies at Hypersonic Speeds," *J. Aerospace Sci.*, Vol. 26, No. 2, pp. 65-74, February 1953.
36. Seaman, C. E. *Shape Study: Boresight Error Vs. Radome Contour*, Hughes Aircraft Company, Culver City, California, Report 4554/154, September 1958.
37. Ferri, A., and Bloom, M. H. *Cooling by Jets Directed Upstream in Hypersonic Flow*, WADC TN-56-382 (ASTIA Document No. AD 97232), September 1957.
38. Gazley, C. *Heat Transfer Aspects of the Atmospheric Reentry of Long-Range Ballistic Missiles*, Report R-273, The Rand Corporation, Santa Monica, California, April 1959.
39. Adams, M. C. "Recent Advances in Ablation," *ARS Journal*, pp. 625-672, September 1959.
40. *Applications of Plastic Materials in Aerospace*, Chemical Engineering Progress Symposium Series, Vol. 59, No. 40, American Institute of Chemical Engineers, May 1963.
41. Kimmel, B. G., and Robertson, G. D. "Dielectric Loading of Radome Fabrication Materials," *Proc. OSU-WADC Radome Symposium*, Vol. 2, WADC TR 58-272, June 1958.
42. *Materials Handbook*, 6th Edition, Corning Glass Works, Corning, New York, April 1963.
43. Walton, J. D., Jr., and Poulos, N. E. *Slip-Cast Fused Silica*, Special Report No. 43, Engineering Experiment Station, Georgia Institute of Technology, Atlanta, Georgia, 1964.
44. Spearman, F. R. J. "A Summary of Research and Development Work Proceeding in Great Britain," *Proc. OSU-WADD Symposium on Electromagnetic Windows*, Vol. 3, WADD TR-60-274, June 1960.
45. Norin, T. L. "The Measured Electrical Characteristics of Several Hypersonic Ablative Materials and Some Nonablative High Temperature Radome Materials," *Proc. OSU-RTD Symposium on Electromagnetic Windows*, June 1964.
46. Basilin, P. J., Litant, I., and Walker, B. M. "Dielectric Materials for Hypersonic Reentry Applications," *Proc. OSU-RTD Symposium on Electromagnetic Windows*, June 1964.
47. *Handbook of Geophysics*, Revised Edition, The MacMillan Book Co., New York, 1960.
48. Strain, R. N. C. "Quantitative Assessment of Rain Erosion," *Proc. OSU-WADC Radome Symposium*, Vol. 1, WADC TR-58-272, June 1958.
49. *Ceram Radome Evaluation Report*, Report TG 249-1, The Johns Hopkins University, Applied Physics Laboratory, Silver Springs, Maryland, June 1955.
50. Beltran, A. A. *Rain Erosion at Subsonic and Supersonic Speeds: An Annotated Bibliography*, Special Bibliography SB-62-6, Lockheed Missiles and Space Division, Sunnyvale, California, March 1962.
51. Allen, J. W. *Supersonic Radome Rain Erosion Testing and Design Criteria*, Report SC/TM 280-62(14), Sandia Corporation, Albuquerque, New Mexico, January 1963.
52. *Tables for the Design of Missiles*, Vol. 17, The Annals of the Computation Laboratory, Harvard University Press, 1948.
53. Berans, Gler, and Dankle. "Comparison of Total Emittances with Values Computed from Spectral Measurements," *Trans. ASME*, pp. 1407-1416, October 1958.
54. Manson, S. S., and Smith, R. W. *Quantitative Evaluation of Thermal Shock Re-*

- sistance, NACA Lewis Flight Laboratory, Cleveland, Ohio, Paper No. 54-A-263 presented at Annual Meeting, ASME, New York, November 28 to December 3, 1954.
55. Campbell, I. E. *High Temperature Technology*, John Wiley and Sons, Inc., New York, 1956.
56. Walker, R. F., and Lief, O. O. *An Evaluation of Ceramic Materials for Applications as Flameholders*, WADC TR-54-234, December 1954.
57. Walton, J. D., Jr., and Poulos, N. E. "Fused Silica for Reentry Radomes," *Proc. OSU-RTD Symposium on Electromagnetic Windows*, June 1964.
58. "Rain Erosion Tests, 15 to 22 November 1961," personal communication from M. J. Madigan (U.S. NADC) to D. L. Loyet (Hughes Aircraft Company), March 9, 1962.
59. *Ceramic Systems for Missile Structural Applications*, Summary Report No. 1, Contract NOW 63-0143-d, Engineering Experiment Station, Georgia Institute of Technology, Atlanta, Georgia, October 31, 1963.
60. Reinell, A. C. *Shrike Radome Rain Erosion Tests*, Technical Note 4021-64-2, Naval Ordnance Test Station, China Lake, California, March 19, 1963.
61. Guarini, J. F. "Rain Erosion Sled Tests," *Proc. OSU-RTD Symposium on Electromagnetic Windows*, June 1964.
62. diToro, J. A. *Graphs of Transmission and Phase Data of Plane Dielectric Sheets for Radome Design*, U.S. Naval Air Development Center Report No. NADC-EL-5313, 1 July 1953 (ASTIA Document No. AD 45316).
63. diToro, J. A. *Supplementary Graphs of Transmission and Phase Delay of Plane Dielectric Sheets and Sandwich Constructions for Radome Design*, U.S. Naval Air Development Center Report No. NADC-EL-5313, (ASTIA Document No. AD 45543), June 16, 1954.
64. Coling, F. L. "The Problems in the Design of a Thin-Wall Ceramic Radome," *Proc. ASD-OSU Symposium on Electromagnetic Windows*, Vol. 1, ASD-TDR-62-676, July 1962.
65. Loyet, D. L., and Stevens, S. "A Comparison of Thin-Wall and Half-Wavelength Ceramic Radomes," *Proc. ASD-OSU Symposium on Electromagnetic Windows*, Vol. 1, ASD-TDR-62-676, July 1962.
66. Kotik, J. *Some Remarks on Thin Dielectric Walls*, Report No. 12283-8M, McMillan Laboratories, Ipswich, Massachusetts, March 15, 1953.
67. Perry, H. A. "Stresses in Adhesive Joints," *Prod. Eng.*, pp. 64-66, July 7, 1958.
68. Perry, H. A. *Adhesive Bonding for Fibrous Glass-Reinforced Plastics*, McGraw-Hill Book Co., Inc., New York, 1958.
69. Pedigo, A. *Radome Handbook*, 2nd Edition, Coors Porcelain Co., Golden, Colorado, 1962.
70. Zisman, W. A. "Influence of Constitution on Adhesion," *Ind. and Eng. Chem.*, Vol. 55, No. 10, pp. 18-38, October 1963.
71. Pedigo, A. *Final Report on Large Ceramic Radomes Manufactured by Dry-Isostatic Pressing Techniques*, Report No. ASD-TDR-62-967, Wright-Patterson Air Force Base, Ohio, 1963.
72. Guttman, W. H. *Concise Guide to Structural Adhesives*, Reinhold Publishing Corp., New York, 1961.
73. Seaman, C. E. "Mounting Ring Design for Ceramic Radomes," *Proc. ASD-OSU Symposium on Electromagnetic Windows*, Vol. 1, ASD-TDR-62-676, July 1962.
74. Sutherland, R. D. "Thermo-Mechanical Testing of a Terrier/Tartar Radome," *Proc. OSU-WADD Symposium on Electromagnetic Windows*, Vol. 2, WADD-TR-60-274, June 1960.
75. Noltimer, R. L., and Oken, S. "Attaching a Ceramic Radome," *Proc. OSU-WADD Symposium on Electromagnetic Windows*, Vol. 1, WADD TR-60-274, June 1960.
76. Wilson, F. M., and Long, R. A. *Alumina Radome Attachment—Part II, Mechanical*, ASD-TDR-62-545, Part 2, February 1963.
77. Long, Wilson, and Gaughey. "Advanced Design of Attachments for Alumina Ceramic Electromagnetic Windows for up to 2500°F Environments," *Proc. ASD-OSU Symposium on Electromagnetic Windows*, Vol. 1, ASD-TDR-62-676, July 1962.

78. *General Specification for Radomes*, Military Specification MIL-R-7705 (ASG), January 12, 1955.
79. *Standards of the Alumina Ceramic Manufacturers Association*, Alumina Manufacturers Association, New York, 1961.
80. *ASTM Standards*, American Society for Testing Materials, Philadelphia, 1963.
81. *Rocket Sled Design Handbook*, Istracon Report No. 60-1, Air Research and Development Command, January 1960.
82. *Rain*, ASTIA Bibliography RB-8838, November 1955.
83. Willey, G. *Rain Erosion of Materials in Spacecraft and Aircraft*, Bibliography, January 1953 through May 1963, Defense Documentation Center Report ARB-16-998 (AD-337181).
84. Franci, J., and Kingery, W. D. "Apparatus for Determining Conductivity by a Comparative Method," *J. Am. Ceramic Soc.*, Vol. 37, p. 80, 1954.
85. Ruh, E. "Improved Method of Measuring Thermal Conductivity of Dense Ceramics," *J. Am. Ceramic Soc.*, Vol. 37, p. 224, 1954.
86. *The Testing of Mycalex and Alumina Radomes*, Hughes Aircraft Company, Culver City, California, November 1958.
87. Wicklein, H. W. *Thermal Emissivity Study of Several Radome Materials*, Hughes Aircraft Company, Culver City, California, Research Study 238, June 238, June 1959.
88. Blau, Miles, and Ashman. *The Thermal Radiation Characteristics of Solid Materials — A Review*, AFCRC-TN-58-132, ASTIA Document No. AD 146833, March 31, 1958.
89. Olson, O. H., and Morris, J. C. *Determination of Emissivity and Reflectivity Data on Aircraft Structural Materials, Part III — Techniques for Measurement*, WADC-TR-56-222, April 1960.
90. Crandall, W. B., and Ging, J. "Thermal Analysis of Spherical Shapes," *J. Am. Ceramic Soc.*, Vol. 38, pp. 44-54, January 1955.
91. Luoma, E. J., and Shand, E. B. "Thermal Shock Resistance," *Aerospace Eng.*, Vol. 18, No. 6, June 1959.
92. Pedigo, A. "Resistance to Impact and Thermal Shock by Solid Alumina Radomes," *Proc. ASD-OSU Symposium on Electromagnetic Windows*, Vol. 1, ASD-TDR-62-676, July 1962.
93. Rayburn, L., and Einarson, M. "Thermal Shock Testing of Ceramic Radomes," *Proc. OSU-WADD Symposium on Electromagnetic Windows*, Vol. 1, WADD-TR-60-274, June 1960.
94. Baer, Gates, and Robertson. *Ceramic Radome Evaluation*, OSU-WADC Radome Symposium, WADC-TR-58-272, Vol. I, ASTIA Document No. AD 155831, June 1958.
95. Gravellese, A. W. *Thermal Stress Tests of Pyroceram Shells*, Technical Memorandum RAD-TM-61-1, AVCO Corporation, Wilmington, Massachusetts, March 6, 1961.
96. *Tests of the HT-8 Terrier Radome in the Blowdown Facility for General Dynamics*, Pomona, Report 663, Ordnance Aerodynamics Laboratory, June 6, 1962.
97. *Electrical Test Procedure for Radomes and Radome Materials*, Report ARTC-4, Aerospace Industries Association of America, Inc., Los Angeles, California, July 30, 1960.
98. Von Hippel, A. *Dielectric Materials and Applications*, John Wiley and Sons, Inc., New York, 1954.
99. Zellner, Pentecost, and Eliason. "Accurate Microwave Measurements of Dielectric Properties to Temperatures of 1600°C," *Proc. ASD-OSU Symposium on Electromagnetic Windows*, Vol. 1, ASD-TDR-62-676, July 1962.
100. Langenberg, D. N., and Lengyel, B. A. *Resonant Cavity Dielectrometers*, Report 4W10-314, Hughes Aircraft Company, Culver City, California, October 1, 1955.
101. Hope, H. R., and Bayless, W. W. "Dielectric Measurements at High Temperatures," *Proc. OSU-WADC Radome Symposium*, Vol. 1, WADC-TR-58-272, June 1958, ASTIA Document No. AD 155831.
102. Sutton, R. W., and Grechny, N. "Design and Development of a High-Temperature Resonant Cavity Dielectrometer," *Proc. OSU-WADD Symposium on Electromagnetic Windows*, Vol. 1, WADD-TR-60-274, June 1960.

103. Moses, H. E., and deRidder, C. M. *Properties of Dielectrics from Reflection Coefficients in One Direction*, Lincoln Laboratory Report 322, Massachusetts Institute of Technology, Lexington, Mass., July 11, 1963.
104. *Mechanical Test Procedures for Radomes and Radome Materials*, Report ARTC-3, Aerospace Industries Association of America, Inc., Los Angeles, California.
105. *Sandwich Construction and Core Materials, General Test Methods*, Military Specification MIL-STD-401, September 20, 1957.
106. Spinner, S. "Elastic Moduli of Glasses by a Dynamic Method," *J. Am. Ceramic Soc.*, Vol. 37, No. 5, pp. 229-234, May 1954.
107. Briggs, P. D. *Elastic Properties of Oxide Ceramics by an Improved Sonic Test Method*, Research Report 63-1, Coors Porcelain Company, Golden, Colorado, May 8, 1963.
108. Bortz, S. A., and Lund, H. H. *Mechanical Properties of Engineering Ceramics*, Interscience Publishers, Inc., New York, 1961.
109. Manson, S. S. *Behavior of Materials Under Conditions of Thermal Stress*, Report 1170, National Advisory Committee for Aeronautics, 1954.
110. "Symposium on Thermal Fracture," *J. Am. Ceramic Soc.*, Vol. 38, January 1955.
111. Shaffer, Hasselman, and Chaberski. *Factors Affecting the Thermal Shock Resistance of Polyphase Ceramic Bodies*, WADD-TR-60-749, Part I, February 1961.
112. Hasselman, D. P. H., and Shaffer, P. T. B. *Factors Affecting the Thermal Shock Resistance of Polyphase Ceramic Bodies*, WADD-TR-60-749, Part II, April 1962.
113. Pearl, et al. *Refractory Inorganic Materials for Structural Applications*, WADC-TR-59-432, February 1960.
114. Smiley, et al. *Mechanical Property Survey of Refractory Nonmetallic Crystalline Materials and Intermetallic Compounds*, WADC-TR-59-448, January 1960.
115. Weil, N. A. *Studies of the Brittle Behaviour of Ceramic Materials*, ASD-TR-61-628, Part I, April 1962.
116. Weil, N. A. *Studies of the Brittle Behaviour of Ceramic Materials*, ASD-TR-61-628, Part II, April 1963.
117. Kinslow, R. *Properties of Spherical Stress Waves Produced by Hypervelocity Impact*, AEDC-TDR-63-197, October 1963.
118. Langer, B. F. "Application of Stress Concentration Factors," *The Bettis Technical Review*.
119. Peterson, R. E. *Stress Concentration Design Factors*, John Wiley and Sons, Inc., New York, 1953.
120. Savin, G. *Stress Concentration Around Holes*, Pergamon Press, New York, 1961.
121. Weiss, et al. *The Effect of Stress Concentration on the Fracture and Deformation Characteristics of Ceramics and Metals*, ASD-TDR-63-380, April 1963.



## **CHAPTER 2**

### **RADOME DESIGN—ELECTRICAL**

*by* **DR. J. H. RICHMOND**  
*Department of Electrical Engineering*  
*The Ohio State University*  
*Columbus 12, Ohio*

## SYMBOLS

A	A constant	k	Phase constant
B	A constant	$k_0$	Phase constant of free space
C	A constant	r	Radial plane
D	Wire diameter; a constant	$r_0$	Interface reflection coefficient, exit surface
E	Electric field intensity; a constant	$r_i$	Interface reflection coefficient, incidence surface
$E_i$	Incident electric field intensity	$r_0$	Radial position on cone measured from the base
$E_r$	Reflected electric field intensity	t	Interface transmission coefficient
H	Magnetic field intensity	$\tan \delta$	Loss tangent
$H_i$	Incident magnetic field intensity	$\alpha$	Full cone angle
$H_r$	Reflected magnetic field intensity	$\epsilon$	Dielectric constant
IPD	Insertion phase delay	$\epsilon_c$	Core dielectric constant, relative
J	A constant	$\epsilon_r$	Dielectric constant, relative
K	A constant	$\epsilon_0$	Dielectric constant of free space
L	A constant	$\epsilon_s$	Skin dielectric constant, relative
L/D	Lift/drag ratio	$\epsilon$	Complex dielectric constant
M	A constant	$\epsilon_c$	Complex dielectric constant, exit surface
N	A constant	$\epsilon_i$	Complex dielectric constant, incidence surface
Q	Figure of merit	$\theta$	Angle of incidence
R	Reflection coefficient of plane sheet or sandwich	$\theta_b$	Brewster angle
T	Transmission coefficient of plane sheet or sandwich	$\theta_r$	Angle of refraction
$T^2$	Power transmission coefficient of plane sheet or sandwich	$\theta_1$	Match angle
a	Wave number	$\lambda$	Wavelength in dielectric material
d	Thickness of radome wall	$\lambda_0$	Wavelength in free space
$d_c$	Core thickness	$\mu$	Permeability
$d_s$	Skin thickness	$\mu_0$	Permeability of free space
$d_x$	Dipole spacing, x direction	$\mu_r$	Permeability, relative
$d_y$	Dipole spacing, y direction	$\omega$	Angular frequency
$e^{j\omega t}$	Time variation factor	$\phi$	$(2\pi d_s/\lambda_0) \sqrt{\epsilon_s - \sin^2 \theta}$
f	Frequency	$\phi_0$	Azimuthal position on a cone
h	Slant cone height		

## CHAPTER 2

### RADOME DESIGN -- ELECTRICAL

In this chapter, the electrical design techniques for aircraft and missile radomes since 1957 are surveyed, thereby providing a supplement to Reference 1, *Techniques for Airborne Radome Design*. Materials gathered from unclassified sources comprise the techniques presented in this chapter to make the chapter of use to the largest group of radome designers. Although this has resulted in the omission of some important data, it has not seriously inhibited the discussion of design techniques. Furthermore, references are given to both classified and unclassified publications to assist the radome designer in additional research.

The scarcity of unclassified reports on (1) combination radome-irdomes, and (2) reduction of boresight error effects by flight control system modification make it impractical to include paragraphs on these important topics. However, references are included.

#### 2-1 ELECTRICAL DESIGN TECHNIQUES

The electrical design studies of electromagnetic windows and radomes are concerned primarily with techniques for minimizing the effects of a radome wall configuration on the electrical performance of an antenna system. The following paragraphs discuss the various types of designs, including the thin wall, half-wave, sandwich, and multilayer radomes.

##### 2-1.1. GENERAL DESIGN CONSIDERATIONS

Chapter 1 defined a radome and described the various types of wall construction. This chapter is concerned with the electrical design for these types (Reference 2).

It is of interest to mention some of the limitations that apply to the use of the radome wall structures. When used at rather high frequencies, the thin-wall radome has poor transmission efficiency for perpendicular polarization at high angles of incidence. The half-wave radome has an inadequate bandwidth for some applications, but this can be improved by using a material, such as fused silica, which has a low dielectric constant. The multilayer sandwiches and the continuously inhomogeneous radomes are rather difficult to manufacture, particularly when high-temperature materials must be employed. In the design of a "B" sandwich, it may be a problem to find a skin material that has a relatively low dielectric constant, high-temperature capabilities, adequate rain-erosion resistance, and resistance to moisture absorption.

##### 2-1.2 THIN-WALL RADOME DESIGN

The design of radomes for hypersonic vehicles involves aerodynamic, structural, and electrical requirements that often result in an ogive shape and a half-wave wall configuration. However, at some frequency bands and for some vehicles, it is possible to employ a thin-wall radome with a considerable savings in weight. A thin-wall radome is defined as one whose thickness is much smaller than one-half wavelength in the dielectric (Reference 3).

A 99.5% alumina ceramic material has been investigated for its characteristics as a thin-wall radome. Figure 2-1 shows the dielectric constant and the loss tangent of the ceramic as a function of temperature, ranging from room temperature to 2500°F. The dielectric constant variation is from 9.5 to 11.1, whereas the loss tangent variation is from 0.0001 to 0.00015.

Figures 2-2 through 2-5 show the characteristics of a thin-wall (0.03-in.) alumina radome at 4500 mc in the C-band, and Figs. 2-3 through 2-9 show the characteristics of a 0.025-in. alumina radome at 9000 mc in the X-band. Room temperature data are shown by the solid line curves and data for 2500°F are shown by the

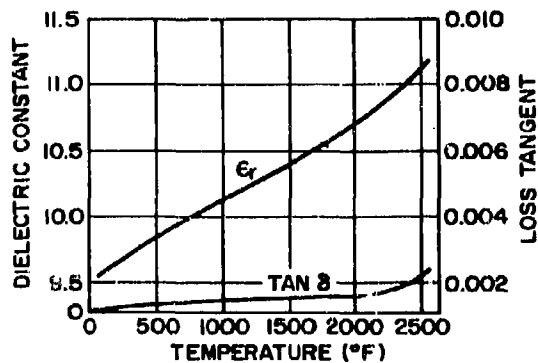


Figure 2-1. Electrical Properties of 99.5% Alumina Ceramic Material

dash line curves. The power transmission and phase data, obtained with the aid of an IBM 7090 digital computer, represent the average for perpendicular and parallel polarization.

The average transmission efficiency of the thin-wall radome decreases steadily as the angle of incidence increases. Satisfactory transmission is obtained for incidence angles of up to 50° to 60°, above which the efficiency drops off rapidly. Transmission efficiency also decreases at the higher temperatures because of increased loss tangent and dielectric constant.

Phase data are important in the design of boresight radomes. Figures 2-4 through 2-9 show that acceptable phase characteristics can be obtained at C- and X-bands for angles of incidence up to 50°. At greater angles, the phase-shift slope increases sharply. The phase-shift slopes are nearly the same at room temperature and at 2500°F.

Wall thickness tolerances at C- and X-bands are shown in Figs. 2-3 through 2-9. At C-band, the phase variation is less than 5 degrees at the highest tolerance considered, which was  $\pm 0.003$  in. About the same variation occurred at X-

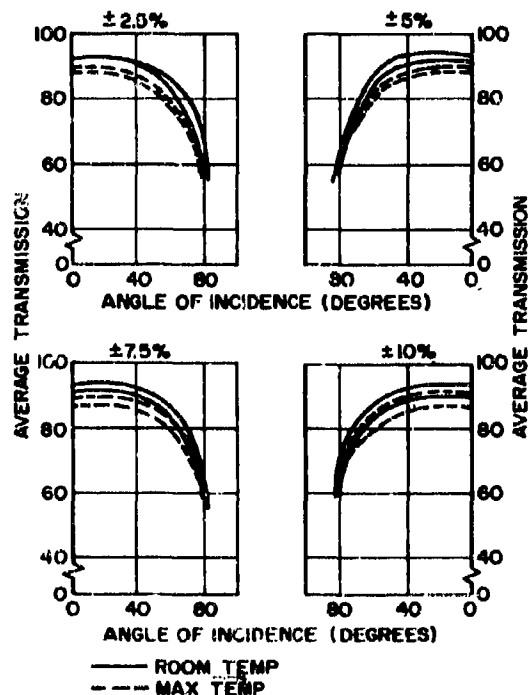


Figure 2-2. Broadband Study of Average Transmission Data of Very Thin Wall at C-Band

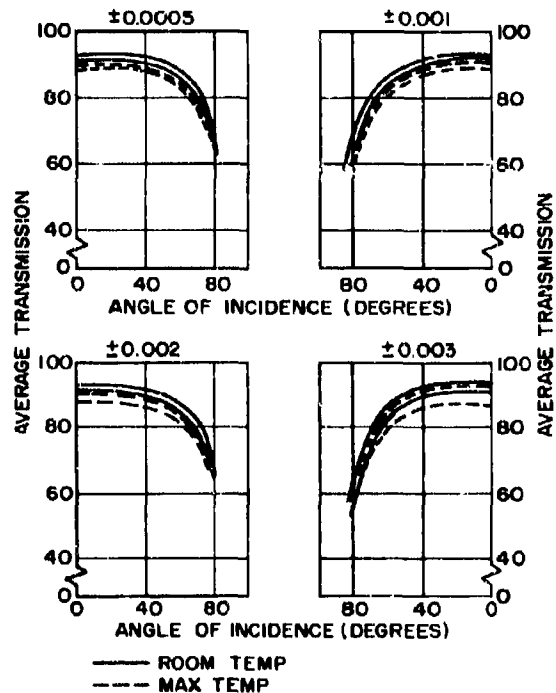


Figure 2-3. Wall Thickness Tolerance of Average Transmission Data of Very Thin Wall at C-Band

band. Since this tolerance can be controlled in manufacturing, it does not seem to be a critical factor for phase variation in thin walls. If temperature is taken into account, the phase deviation is almost doubled. In this case, it is desirable to reduce the allowable tolerance to  $\pm 0.001$  in., to meet the electrical requirements at 2500°F.

The C-band transmission performance does not vary significantly up to a tolerance of  $\pm 0.002$  in. With temperature considered, only a 4% variation exists up to an incidence angle of 50°. A transmission efficiency of at least 84% can be maintained with a tolerance of  $\pm 0.003$  in. At X-band, however, a tolerance of  $\pm 0.001$  in. results in a transmission efficiency of less than 80%. If temperature is considered, the transmission is reduced to approximately 71%.

The effect of frequency tolerances of  $\pm 2$ ,  $\pm 5$ ,  $\pm 7.5$  and  $\pm 10\%$  was studied for the C- and X-band thin-wall radomes. Although the thin-wall radome has a smaller bandwidth at X-band than at C-band, the changes in phase shift and

transmission efficiency do not appear to be excessive with a 10% change in frequency.

Thus, the thin-wall ceramic radome at C- and X-band offers the advantages of weight reduction, greater bandwidth, and increased tolerances in thickness.

The relative merits of large thin-wall and half-wave ogival ceramic radomes with a high fineness ratio have been investigated (Reference 4). The results of this comparison are given in Paragraph 2-2. The design of half-wave radomes is covered in Paragraph 2-1.3.

### 2-1.3 HALF-WAVE RADOME DESIGN

The successful design techniques employed for the half-wave radome of the F-106 airplane with the MA-1 fire control system is discussed because of its usefulness in many other applications (Reference 5). (Reference 6 presents another useful technique for half-wave radome design.)

The initial design considerations permit an

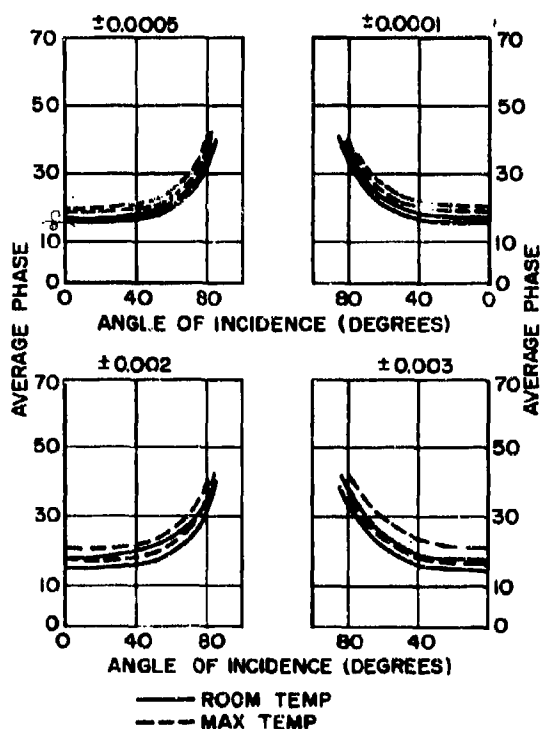


Figure 2-4. Wall Thickness Tolerance Study of Phase Data of Very Thin Wall at C-Band

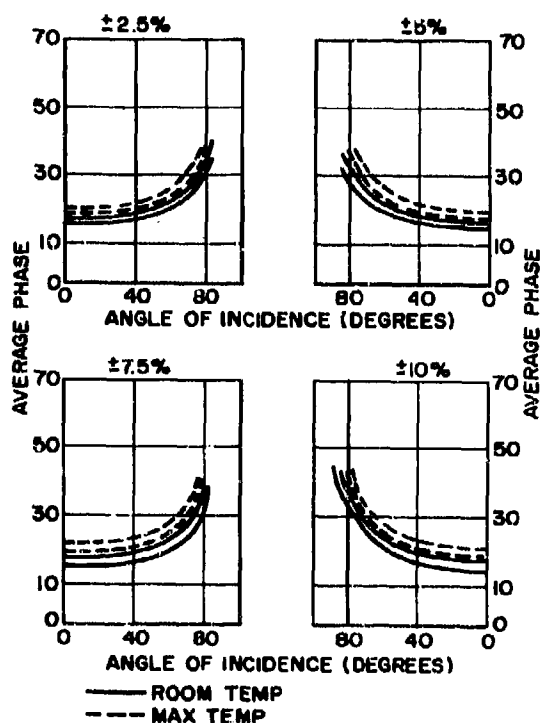


Figure 2-5. Broadband Study of Phase Data of Very Thin Wall at C-Band

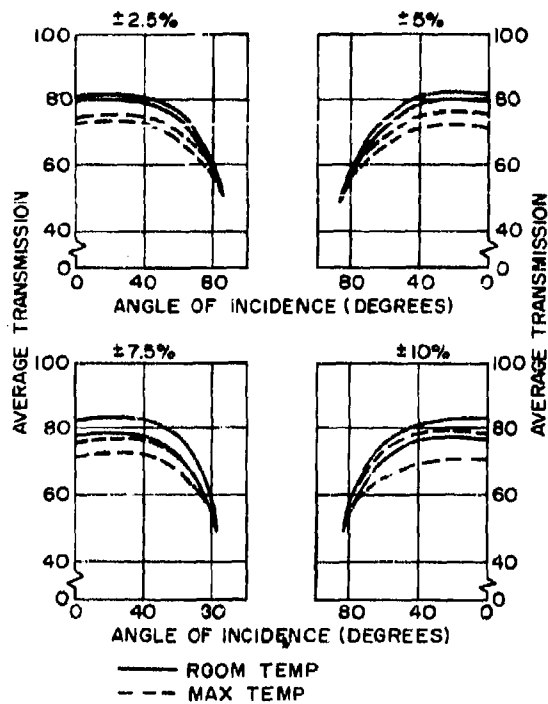


Figure 2-6. Broadband Study of Average Transmission Data of Thin Wall at X-Band

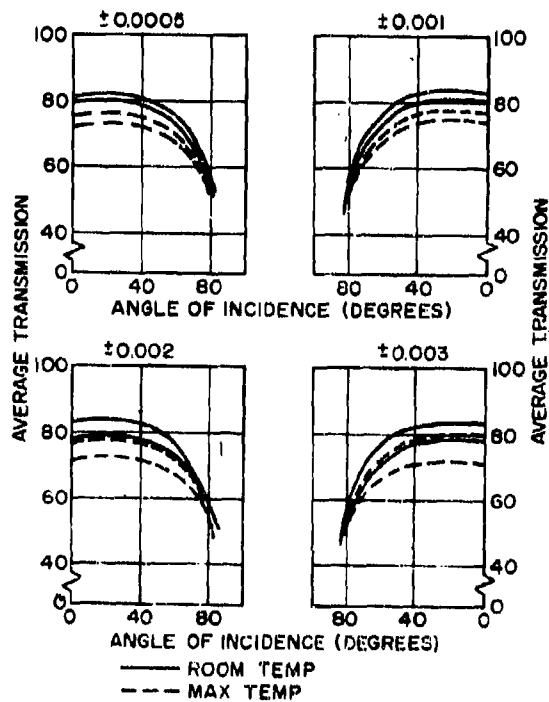


Figure 2-7. Wall Thickness Study of Average Transmission Data of Thin Wall at X-Band

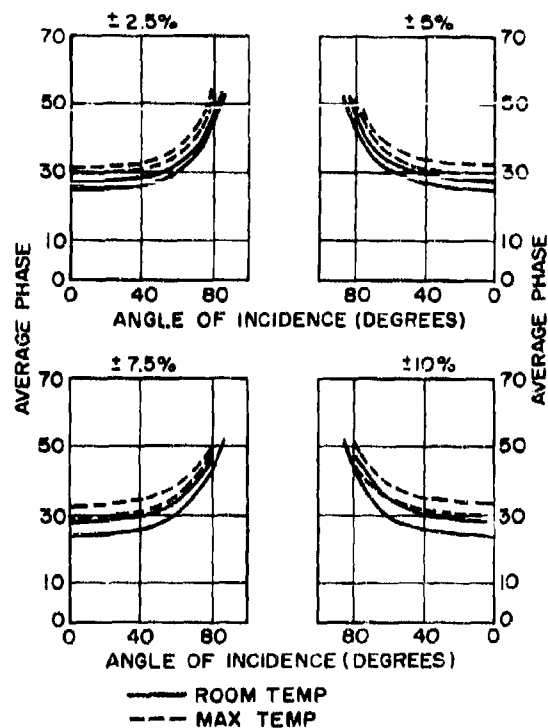


Figure 2-8. Broadband Study of Phase Data of Thin Wall at X-Band

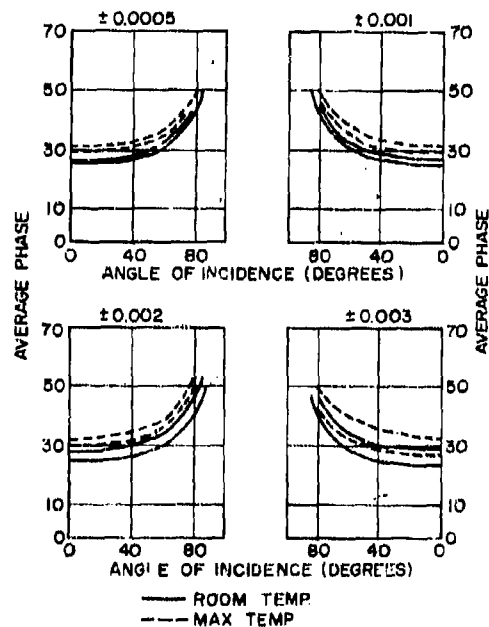


Figure 2-9. Wall Thickness Tolerance Study of Phase Data of Thin Wall at X-Band

evaluation of the effect of shape on boresight error, although radome shape is usually based solely upon aerodynamic considerations. The actual choice of shape is arrived at by considering the basic boresight error characteristics of a group of half-wave radomes having configurations compatible with the overall aerodynamic requirements. They include ogival and exponential power curves, the latter being based on area rule considerations. As a result of this study, an ogival radome is chosen.

With the shape fixed as a specific ogive, the proper nominal wall thickness is obtained by design analysis, utilizing the theory of transmission for plane sheets and an incidence angle study. Calculations are made to optimize the transmission over the required frequency band. No serious attempt is made to calculate the effects of the pitot-static nose boom or the associated hardware in determining the wall thickness of the initial radome.

With the shape fixed and the dielectric constant (5.2), loss tangent (0.012), and nominal wall thickness chosen, error prediction techniques are applied to determine the approximate maximum errors to be expected from the radome. No attempt is made to minimize boresight error by varying the thickness of the radome wall in the first radome. The only control

exercised over boresight error was achieved by the choice of shape. The actual error characteristics for the two principal planes are shown in Fig. 2-10, along with the predicted errors. The maximum errors range from 2 to 4 milliradians for the experimental radome as compared with the predicted range of about 1 to 2 milliradians. Both the theoretical calculations and the experimental data in Fig. 2-10 are obtained for the case of no boom or internal hardware.

Starting with a radome having the approximate nominal wall thickness for optimum transmission and with calculated boresight errors reasonably close to those desired, the next step in the design is to arrive at a method to reduce the total boresight error and error rates to within acceptable limits when the boom and internal hardware are attached. The initial step in the radome correction is determined by a theoretical analysis in preference to an experimental approach. This procedure considers the fact that the antenna platform is fixed with respect to the radome. This allows for a significant improvement in radome performance by essentially avoiding the problem of having to make the radome wall design compatible for any orientation of the polarization vector. The enclosed antenna is horizontally polarized. Thus,

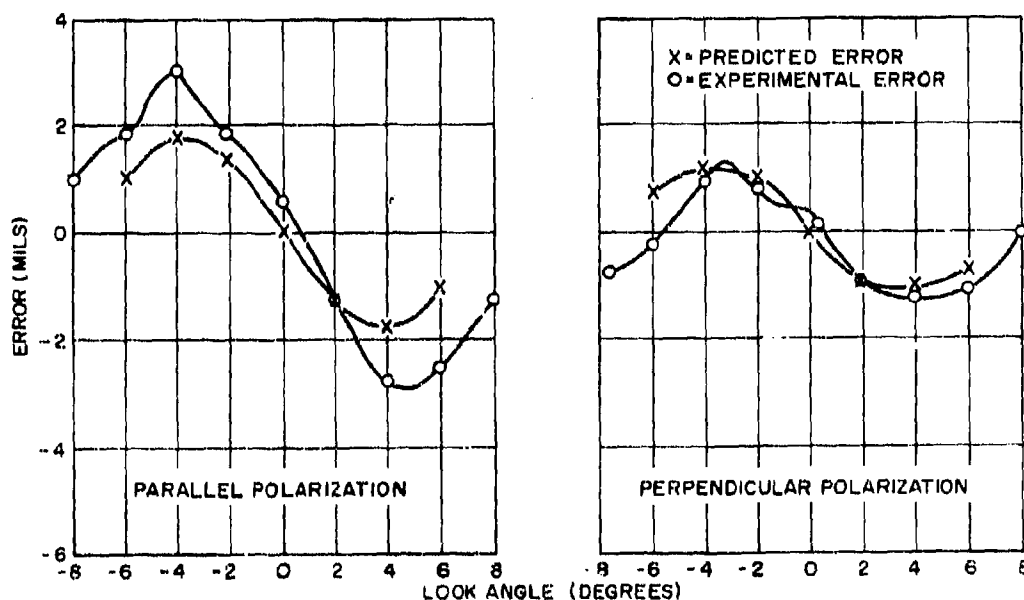


Figure 2-10. F-106A/B Radome, Experimental and Predicted Characteristic Errors

by operating independently on the variations in wall thickness along two principal planes, one horizontal and one vertical, it is possible to make the radome essentially electrically symmetrical. The results of such an approach are twofold: (1) the electrical symmetry of the radome minimizes depolarization effects, and (2) the performance of the radome in terms of error characteristics as a function of frequency can be truly centered within the desired frequency band.

The families of curves in Figs. 2-11 and 2-12 present normalized wall thickness,  $d/\lambda_0$ , plotted as a function of incidence angle,  $\theta$ , for constant values of insertion phase difference, IPD, and transmission,  $T^2$ , with a free-space wavelength of  $\lambda_0$ . The curves are based on the analysis of the transmission of a plane wave through a plane, homogeneous, isotropic sheet of infinite

extent, having a uniform thickness  $d$ , a dielectric constant of 5.2, and a loss tangent of 0.012 for perpendicular and parallel polarization. It should be noted that in the region of high transmission, as shown in Figs. 2-11 and 2-12, the difference between the insertion phase delays (IPD) for the two polarizations is minimized. In addition, the rate of change of IPD as a function of thickness for a constant incidence angle is great for perpendicular than for parallel polarization. This is of particular interest since it permits, for a crosstalk error analysis of a radome, a determination of whether or not the radome wall thickness should be varied in one principal plane with respect to the other. This can best be illustrated with the aid of Fig. 2-13, which shows the associated cutting planes that the antenna traverses as it sweeps horizontally, vertically, or in a com-

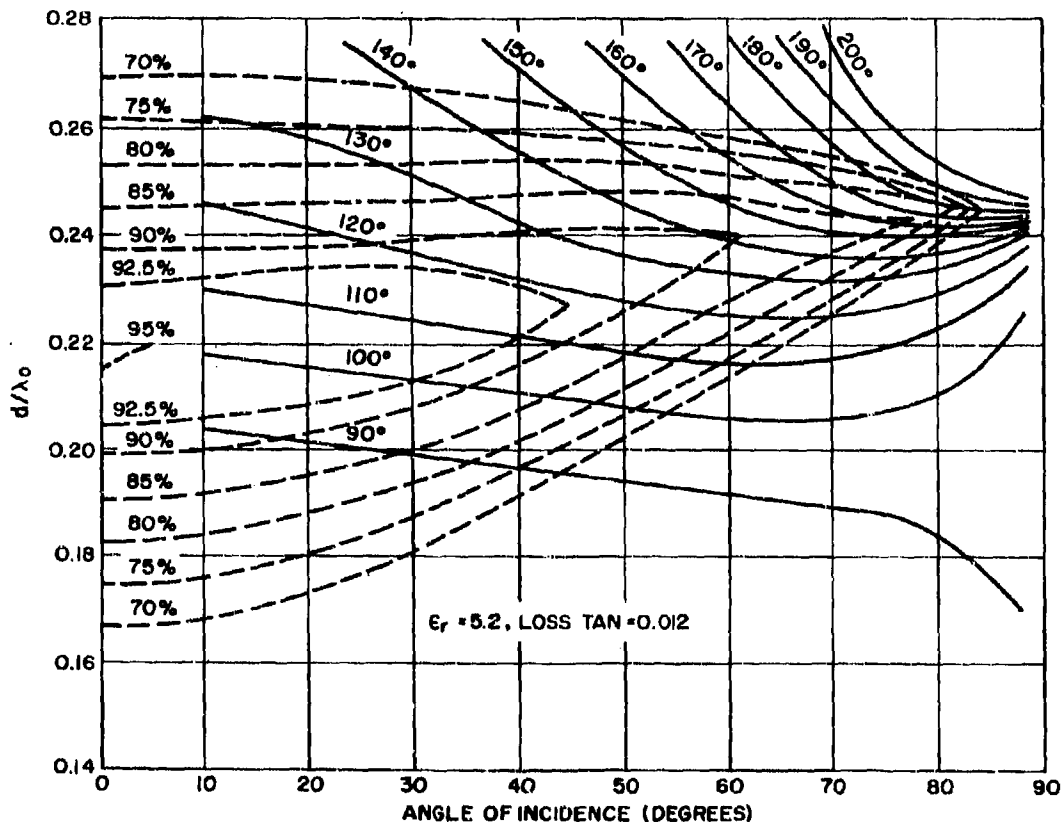


Figure 2-11.  $d/\lambda_0$  vs Incident Angle for Constant Transmission  $|T|^2$  and Constant IPD, Perpendicular Polarization



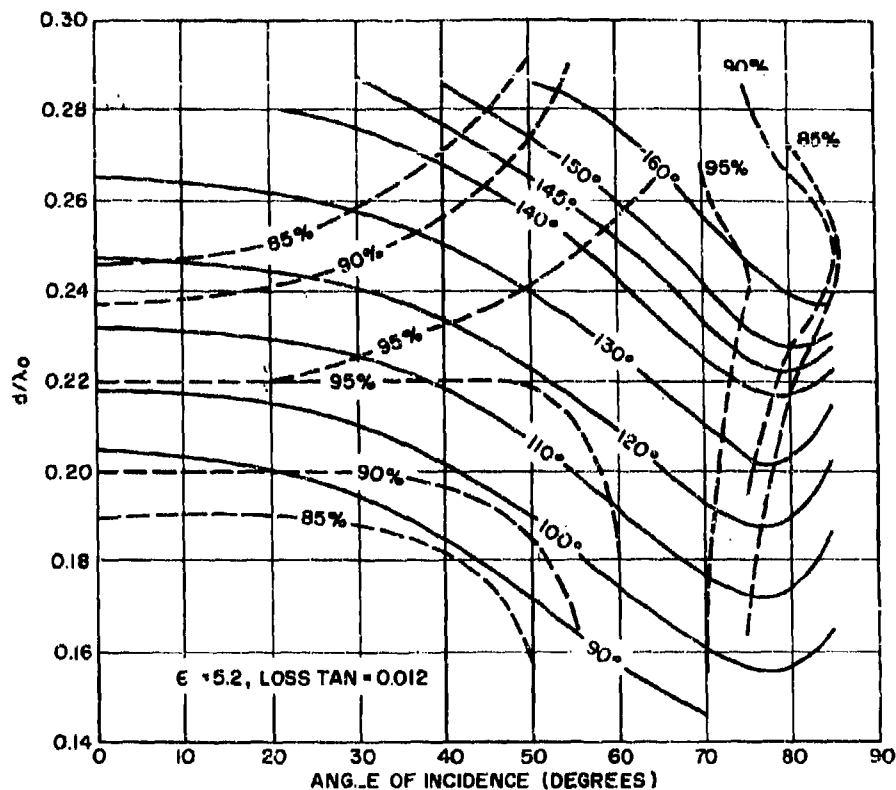


Figure 2-12.  $d/\lambda_0$  vs Incident Angle for Constant Transmission  $|T|^2$  and Constant IPD, Parallel Polarization

bination of horizontal and vertical motion along a  $45^\circ$  plane. It is well known that if the plane of motion of the antenna with respect to the radome is a plane of symmetry for the antenna-radome combination, there will be no deflection of the antenna beam above or below this plane. Thus, for the case shown in Fig. 2-13 with the antenna sweeping either in the horizontal or the vertical plane, the only direction in which beam deflection could theoretically occur would be in the direction of the plane of motion. This assumes that the radome is a true figure of revolution and the antenna's radiated field is symmetrical about the horizontal and vertical planes. This assumption is valid since the radome is a true figure of revolution, except at the extreme aft end, where it fair into the airplane contour.

For the case shown in Fig. 2-13, where the polarization vector is parallel to the horizontal

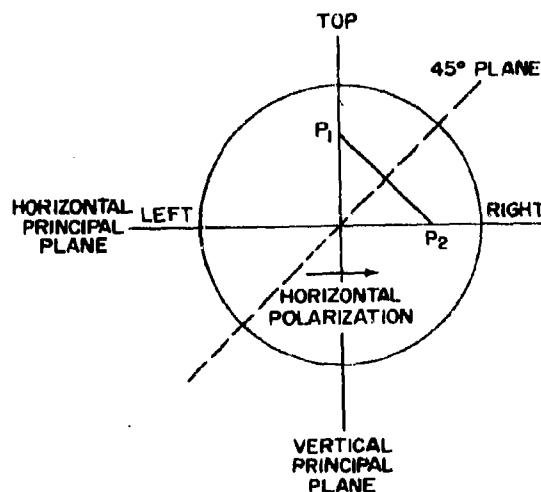


Figure 2-13. End View of Radome and Cutting Planes

plane, an antenna sweep through the radome along the dashed line, noted as the  $45^\circ$  plane, in general, produces crosstalk errors. Although the reason for the existence of crosstalk error for this case is fairly obvious to one familiar with radome design, it sometimes escapes the less familiar observer. Since the absence of crosstalk error implies point-to-point symmetry above and below the antenna cutting plane, it can be seen with the aid of Fig. 2-13 that when the antenna is sweeping in a  $45^\circ$  plane and looking out the upper right side of the radome, points on the radome near the top edge and the right side of the radome are essentially equidistant from the  $45^\circ$  plane. Two such points,  $P_1$  and  $P_2$ , are shown. Although equidistant, what occurs when the antenna is gimbaled to look out the upper right side of the radome is different for  $P_1$  than for  $P_2$ . In the region of  $P_1$ , the incident energy has perpendicular polarization, whereas, in the region of  $P_2$ , it has parallel polarization. Thus, if the insertion phase delays for the two polarizations are not equal at

points  $P_1$  and  $P_2$ , crosstalk errors can exist as the antenna is gimbaled along the  $45^\circ$  cutting plane. For a specific antenna position along the  $45^\circ$  plane, it is possible to choose a common thickness for points  $P_1$  and  $P_2$  that would make the IPD approximately equal for both points. This could be also be done for all other points equidistant above and below the cutting plane so that for this one specific position of the antenna with respect to the radome, the crosstalk error could theoretically be reduced to zero. However, the point-by-point adjustment in thickness would be valid only for one particular position of the antenna. Therefore, in actual design it is necessary to compromise the performance at each point for the whole range of incidence angles that are encountered. This compromise can be achieved in two steps. The step used initially in the design is to maximize the average transmission as a function of antenna position at the center of the frequency band. The results of such an approach are shown in Fig. 2-14, where the crosstalk errors measured

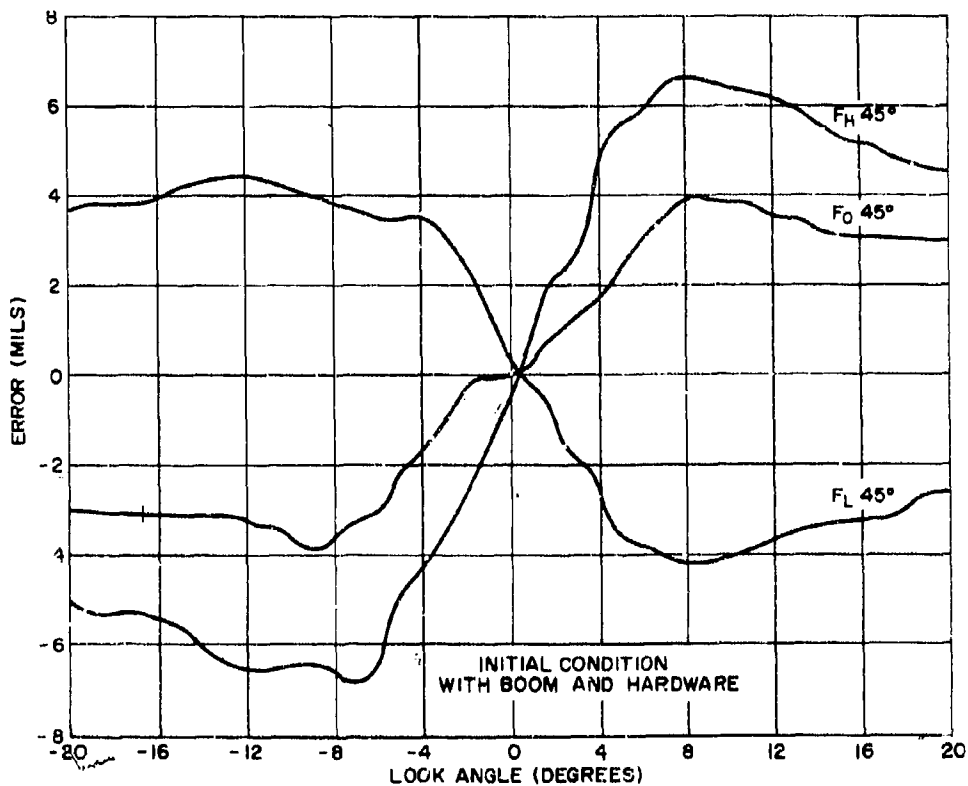


Figure 2-14. F-106A/B Radome,  $45^\circ$  Cut at  $F_L$ ,  $F_O$ ,  $F_H$  — Crosstalk Error vs Look Angle, Before Correction

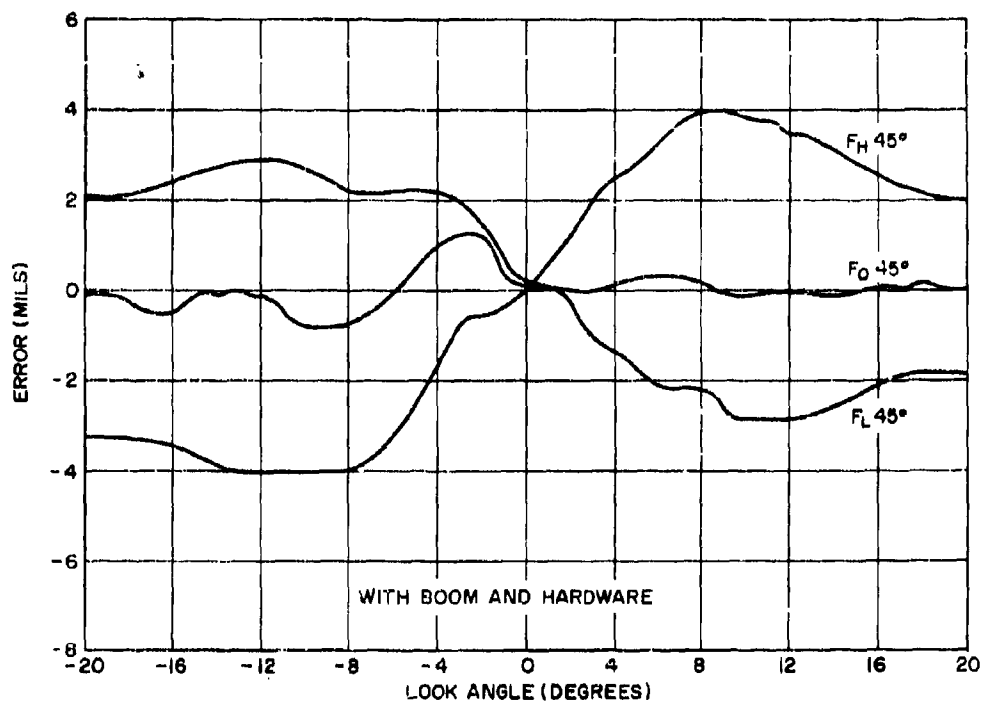


Figure 2-15. F-106A/B Radome, 45° Cut at  $F_L$ ,  $F_0$ ,  $F_H$  — Crosstalk Error vs Look Angle, After Correction

for the 45° plane are plotted against antenna gimbal angle for three frequencies.

The final step requires that the crosstalk be reduced to a minimum for the 45° cut at center frequency by varying the thickness of the top and the bottom of the radome with respect to the sides. Basically, this is an experimental process; however, the curves of Figs. 2-11 and 2-12 are useful in determining the sign of the relative changes in thickness. For example, if one were to observe that for a region of gimbal angles where the antenna is looking out the upper right quadrant of the radome, as shown in Fig. 2-13, and the antenna beam is deflected toward the top of the radome, one could infer that the radome wall is too thick in the region of the radome intercepted by the antenna beam. This conclusion is rather obvious since the IPD is approximately equal for parallel and perpendicular polarization for the optimum wall thickness, and the rate of change of IPD as a function of thickness is greater for perpendicular polarization. Following this reasoning and progressing methodically from small to large

antenna gimbal angles, it is possible to systematically vary the wall thickness circumferentially from the front of the radome to the rear, effectively reducing the crosstalk error at the center frequency for the 45° cut. When the crosstalk at the center frequency is properly reduced for the 45° cut, crosstalk errors for the same cut should diverge as a function of frequency as shown in Fig. 2-15. Upon completion of the crosstalk correction for the 45° cuts, the radome should exhibit minimum crosstalk at the center frequency for all cutting planes containing the radome axis. The wall thickness will vary circumferentially in a continuous manner from thick at the top and the bottom to thinner at the sides if the radome is slightly below optimum thickness, and in the opposite way if the radome is too thick.

All references to circumferential variations in thickness are based on horizontal polarization. If the polarization is vertical, the circumferential variations in wall thickness would, essentially, be reversed. In theory, one might suspect that if the optimum overall thickness

could be arrived at, the circumferential variations in thickness required to minimize crosstalk error might be eliminated. However, the original choice of thickness based on optimum transmission may be shown to be greater or less than the optimum, based on minimum crosstalk error for the 45° cut. Generally, the differences are small and with the proper initial choice of thickness the circumferential variations are of the order 5 to 10%. In the radome considered here, the variation is about 0.02 in.

With the crosstalk error eliminated at center frequency, the problem of reducing the in-plane component may be approached by a combination of experimental methods. As for the case of crosstalk errors, the curves of Figs. 2-11 and 2-12 are also useful in determining the proper method for minimizing the in-plane component of error. Since the crosstalk corrections have the effect of making the radome electrically symmetrical, the in-plane errors represent the total boresight error at center frequency, and, as such, it changes very little between horizontal and vertical antenna cuts. Therefore, the final correction for minimizing in-plane error usually takes the form of longitudinal variations in wall thickness that are usually circumferentially symmetric. In this form, they may be referred to as rings or grooves in the radome wall. Usually, the longitudinal rate of change of wall thickness is small enough so that these changes would be barely perceptible to the eye.

Reference 5 describes the evaluation tests, the radome corrections for the effects of the pitot boom and hardware, the final correction, and the experimental verification of the theoretical techniques. It is concluded that future radomes can be designed with considerably less experimental effort by using the techniques presented here, and that much work is required to refine and develop the present techniques to predict accurately the electrical characteristics of radomes.

Reference 7 gives a method for applying ray tracings to a standard set of radome prints to determine component values of the angles of incidence of radar antenna radiation impinging on a radome wall. Equations are developed that determine the true angles of incidence and polarization as a function of these component angles. A sample ray study is illustrated and a tapered, half-wave, solid-wall design is described in detail.

## 2-1.4 RADOME DESIGN BY INSERTION PHASE DELAY\*

One useful technique employed for the electrical design of low boresight error radomes is based on the insertion phase delay (IPD). The IPD is defined as the phase delay introduced by the presence of a radome wall in the path of a plane wave. For a solid-wall radome, the IPD is given by

$$\text{IPD} = \tan^{-1} \left[ \frac{1+r^2}{1-r^2} \tan \phi \right] - 2\pi (d/\lambda_0) \cos \theta \quad (2-1)$$

where  $d$  = thickness  
 $r$  = interface reflection coefficient  
 $\epsilon_r$  = relative dielectric constant  
 $\lambda_0$  = free-space wavelength  
 $\phi = 2\pi (d/\lambda_0) \sqrt{\epsilon_r - \sin^2 \theta}$   
 $\theta$  = incidence angle

The object is to:

- minimize the difference between the IPD for perpendicular and parallel polarizations over a range of incidence angles, or
- minimize the variation of the IPD for both perpendicular and parallel polarization from point to point on the radome surface or a range of antenna scan angles.

It is generally best to program such a radome design on a digital computer. The computer program includes subprograms for the wall configuration, radome geometry, antenna parameters, and the IPD equations. The output of the computer study is applied directly to the fabrication program, and the grinding operation for the radome wall configuration is geared to the specified IPD distribution. IPD measurements are made at each station on the radome with a one-horn interferometer, and several grinding operations are made until the desired IPD distribution is obtained.

This technique has been utilized in the design of both plastic and ceramic radomes. One outstanding feature of this technique is that each IPD distribution obtained in the design program can be studied on the computer to obtain a range of boresight error data. Then the boresight error is used as the basis for selecting an IPD design for fabrication.

\* Contributed by Forrest L. Coling.

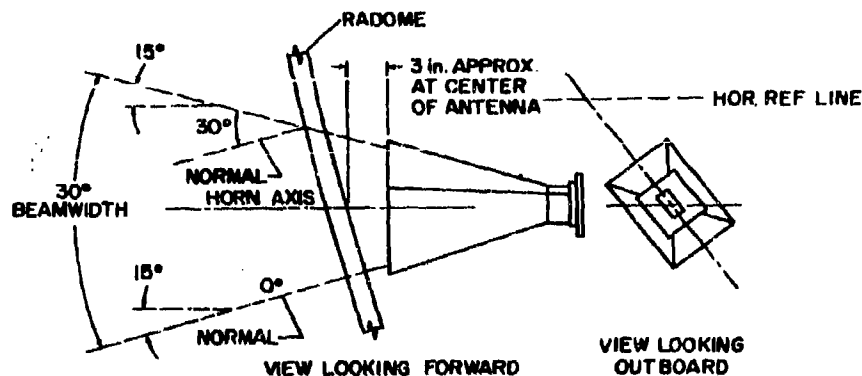


Figure 2-16. Orientation of Horns Behind Radome

### 2-1.5 RADOME SANDWICH DESIGN

Ceramic sandwiches have been given careful consideration, as presented in Reference 2. It was concluded that in view of the complexity and cost of fabricating ceramic sandwiches, a radome designer would naturally choose a one-half-wavelength radome. This has been demonstrated since all ceramic radomes used on production missiles have been of solid-wall (thin or one-half-wavelength) construction. The development of the cored slip-cast technique also makes it possible for the designer to consider the sandwich constructions, such as "A," "B," or air core, and thereby reduce development costs.

Reference 8 describes the design of a sandwich wall for a wedge radome to cover a trihedral corner reflector on a supersonic missile. The wedge angle was chosen to be  $30^\circ$ , which is the maximum angle allowed by aerodynamic considerations. An "A" sandwich was selected for operation in the frequency range from 8650 to 9700 mc at the high angles of incidence that are involved (around  $75^\circ$ ). The skin dielectric constant was chosen as 4.5, with a skin thickness of 0.02 in., the minimum allowed by structural requirements. The core dielectric constant (2.0) and thickness are arrived at with the aid of a set of graphs of the loci of constant power-transmission coefficients. The wedge radome has high transmission over this frequency range with a range of aspect angles (from head-on up to  $\pm 20^\circ$  from head-on) for perpendicular and parallel polarizations.

A sandwich radome for an airborne horn cluster has been designed (Reference 9). This radome is to have a minimum transmission efficiency of 70% for angles of incidence from  $0^\circ$  to  $30^\circ$ , with all linear polarizations for frequencies from 2300 to 10,750 mc. Mechanical strength requirements dictate an 0.04-in. minimum thickness of the outer skin, 0.65-in. minimum total honeycomb core, and 0.10-in. minimum total skin thickness. The cluster of horn antennas is located behind the radome, which also is the skin of a pressurized region of the aircraft. The location of one horn relative to the radome is illustrated in Fig. 2-16. The half-power points of the horn radiation patterns are approximately  $15^\circ$  in all directions from the horn axis. Thus, a maximum angle of incidence of  $30^\circ$  includes almost all of the beam from the peak gain down to 9 db below the maximum.

Good transmission characteristics can be obtained with a three-layer "A" sandwich with 0.03-in. skins of fiberglass laminate and an 0.24-in. honeycomb core. This design does not, however, meet the strength requirements. A double sandwich (i.e., a five-layer "C" sandwich) construction was necessary to meet both the mechanical and electrical requirements. Computations were made of the transmission efficiency of double sandwiches meeting these mechanical strength requirements for frequencies from 0 to 11,000 mc, angles of incidence up to  $30^\circ$ , and parallel and perpendicular polarizations. The final design was obtained by comparing the transmission curves of a large number of sandwiches and selecting that one having the best

transmission characteristics. Figure 2-17 shows the core and skin thicknesses of the final design, and the transmission coefficient for normal incidence and 30° incidence. If the mechanical strength requirements would permit a slight reduction in the total honeycomb thickness, the transmission efficiency could be raised above 80% for all frequencies up to 11,000 mc.

## 2-1.6 DUAL-FREQUENCY AIRBORNE RADOME DESIGN

A dual-frequency "A" sandwich radome has been designed (Reference 10). This radome is mounted on the top centerline of a large, high-speed aircraft and houses a 24-in. parabolic antenna and a 30-in. parabolic antenna (Fig. 2-18). The radome is approximately 17 ft in length, 4 ft wide, and 4 ft high. The forward antenna operates at 16 gc and the aft antenna operates at 6 gc, and each antenna scans through 360° in azimuth. Beamshift must not exceed one milliradian, and the minimum transmission efficiency must be 80%.

A solid-wall construction was considered, but satisfactory transmission efficiency was not obtained at both frequencies. A half-wave "A" sandwich for 16 gc proved to be structurally unsound. Multilayer sandwiches were ruled out

because of fabrication difficulties, cost, and the problems in repairing such a structure. Digital calculations were made with an IBM 7090 computer to study the performance of various full-wave "A" sandwiches. The dimensions, dielectric constants, and transmission curves of the final design are illustrated in Fig. 2-19. This sandwich design provides a transmission efficiency above 80% for angles of incidence up to 30° at 6 gc and 16 gc for both polarizations. The curves in Figs. 2-20 and 2-21 indicate that the IPD is relatively uniform over the important range of incidence angles, making radome bore-sight corrections unnecessary.

An antistatic coating and a rain erosion coating were applied to the outer surfaces of the completed radome, reducing the transmission efficiency by about 5% at 16 gc. The details of the design, fabrication and testing are described in Reference 10.

## 2-2 APPLICATION OF DIGITAL COMPUTERS TO RADOME DESIGN

### 2-2.1 INTRODUCTION

The automatic digital computer has replaced the slide rule, Smith chart and desk calculator in radome analysis and design problems involv-

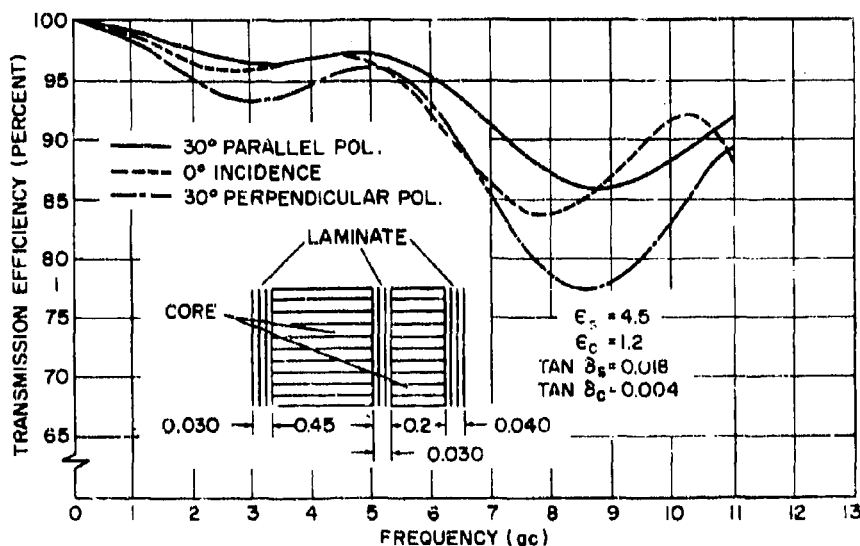


Figure 2-17. Transmission Characteristics of Final Design

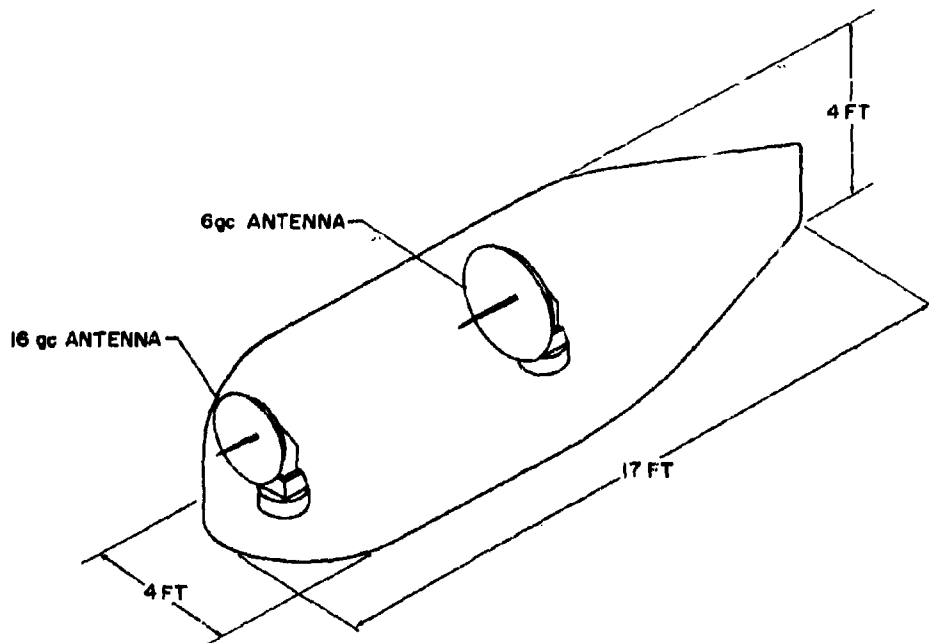


Figure 2-18. Original Concept of Radome Size and Shape

ing large amounts of numerical data. The result has been a tremendous savings in time and cost and an increase in accuracy. Many radome calculations, formerly considered impractical because of computational complexities, are now performed routinely. Numerical errors have been all but eliminated. In some cases, antenna and radome measurements are recorded directly on punched tape, as opposed to a chart recording, to facilitate the digital analysis of the data (References 11 and 12).

Tables of the Fresnel coefficients and the transmission coefficients of plane sheets and sandwiches have been compiled with the aid of digital computers (Reference 13). These tables have found wide use in radome design, although it is sometimes found more efficient to generate these data as needed rather than reading them from a table, punching them on cards, and interpolating.

The matrix-multiplication method for calculating transmission coefficients of multilayer sandwiches has been programmed for digital computations (Reference 14). This matrix method has been found to be rapid and efficient

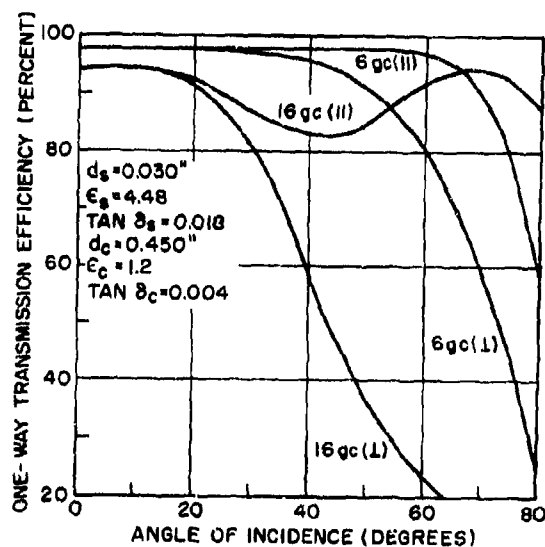


Figure 2-19. Flat Panel Theoretical Data

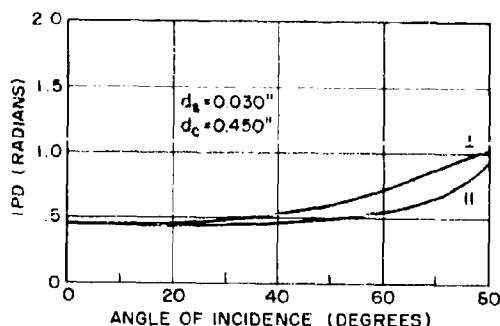


Figure 2-20. IPD vs Angle of Incidence for "A" Sandwich Flat Panel at 6 gc

with respect to computer storage requirements.

Prior to the widespread use of the digital computer, the analysis of inhomogeneous radomes was considered a formidable problem. (A radome may be intentionally inhomogeneous as a result of variable-density loading, or unintentionally inhomogeneous as a consequence of thermal gradients.) Now a plane inhomogeneous layer, in which the permittivity varies continuously as a function of distance into the layer, is analyzed quickly, efficiently and accurately. A computer program which accomplishes this with step-by-step numerical integration is given in Reference 14.

There are innumerable other applications of the digital computer to radome problems, some of which are listed here along with a reference:

- a. Calculating the core thickness of a symmetrical three-layer sandwich for maximum transmission efficiency (Reference 15).
- b. Predicting radome error (References 16 and 17).
- c. Correcting boresight error (Reference 12).
- d. Designing broadband radomes (References 18 and 19).
- e. Designing the overall radome (Reference 20).
- f. Calculating temperature and stress distributions (References 21 and 22).
- g. Determining the electrical effects of radome structural-support members (Reference 23).

The following paragraphs consider the digital optimization of radome walls and complete radome design by digital computations (see Paragraph 6-4.4.2).

## 2-2.2 DIGITAL OPTIMIZATION OF RADOME WALLS

Consider the problem (Reference 18) of designing a radome wall structure consisting of a given number of layers in which the thicknesses and dielectric constants of the layers are to be optimized for the best performance of the final design. The problem is really not well formulated until a specific figure of merit has been defined for assessing a particular wall design or for comparing two different wall designs. Some quantities that generally enter into the definition of the figure of merit are the phase delay and the power transmission coefficient. These are functions of the incidence angle, polarization, and frequency. Hence, the figure of merit is generally a weighted average, with strongest weighting given to those incidence angles, polarizations, and frequencies for which it is most important to have a small phase-delay slope and a large transmission efficiency. The formulas for the phase delay and the power transmission coefficient are too complicated to permit an analytical solution for the optimum wall design. Furthermore, constraints must be introduced to avoid a trivial solution. For example, there may be upper limits on the radome weight and the wall thickness and lower limits on the power transmission coefficient and the flexural strength.

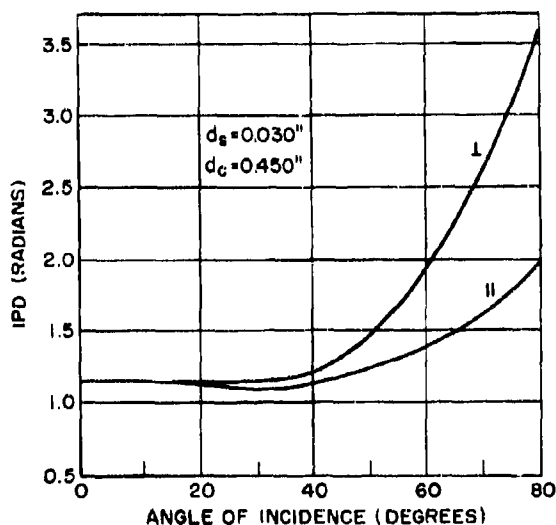


Figure 2-21. IPD vs Angle of Incidence for "A" Sandwich Flat Panel at 16 gc



The most straightforward, but least efficient, method of finding the optimum design is to compute the figure of merit for all allowable combinations of parameters and then to select the optimum by inspection. An appreciable saving in computation cost using this method is provided by digital optimization, as follows. It begins with an initial configuration defined by assigning specific values to each of the independent variables: the dielectric constants and thicknesses of all the layers. For this initial configuration, the figure of merit,  $Q$ , and the gradient of  $Q$  are computed. The gradient is a vector that has one component along each of the independent variables and points in a direction in which the  $Q$  increases most rapidly. A new configuration is then determined by incrementing the independent variables along the gradient vector; that is, a step is taken in the direction of the gradient. The magnitude of the step, however, is a crucial question (Reference 18 for details). At the new configuration, it must be determined whether it satisfies the constraints. If it does not, an auxiliary procedure must be employed. If it does, the  $Q$  of the new configuration must be computed. If the  $Q$  is higher than that of the original configuration, the step is considered to be successful and the process is repeated. If the  $Q$  of the new configuration is smaller, the step was too large, passing a local maximum. It is then necessary to return to the original configuration and take a smaller step.

If the process is continued, a sequence of configurations having increasing values of  $Q$  is generated. To make the process completely automatic, it is necessary to incorporate a considerable decision-making capability into the computer program. For every initial configuration the process climbs to one particular optimum configuration. However, there may be a number of local maxima as well as an absolute maximum. The problem of finding the absolute maximum or all the local maxima has been solved to date only to the extent of applying the process to a large number of initial configurations chosen in a judicious manner.

The overall procedure is divided into the following four steps:

- a. The computer is instructed to optimize the constraining aspect of the wall performance as a figure of merit until it

reaches an acceptable value, and then to proceed to step b. In step a, a fixed step size is employed since only a few steps are normally required. In many investigations, step a can be omitted, since normal wall designs yield configurations that satisfy the constraint employed.

- b. Here an automatic step-size logic is employed. The computer increases the step size until it reaches a workable maximum and proceeds to work toward the local optimum.
- c. In this step, the computer tries to reach the optimum by taking a step into forbidden territory as far as the constraint is concerned. The computer now reduces the step size, as required, and begins to walk around the edge of the forbidden region to find the optimum  $Q$  allowed by this restriction.
- d. The computer reaches the neighborhood of the optimum and then begins repeatedly to halve the step size to locate the optimum to a prescribed degree of precision.

One of the problems investigated in this manner is that of minimizing the average phase delay variation. Half-wave walls are generally acknowledged to have better phase delay characteristics than "A" or "B" sandwiches, but it was found that sandwiches are sometimes superior. This may be of considerable interest in boresight radome design. The starting configuration consisted of three layers of equal thickness and equal dielectric constant, the entire structure being approximately a half-wave wall at an angle and a frequency at the center of the ranges entering into the weighted average phase delay variation. The parameters describing the outside layers were fixed, while the thickness and dielectric constant of the center layer became independent variables. The computer, controlled by the digital optimization program, discovered new sandwich designs having a higher  $Q$  than the half-wave wall.

To illustrate the technique, Fig. 2-22 shows a map of the figure of merit for an "A" sandwich with fixed skins and variable core thickness and dielectric constant. The figure of merit,  $Q$ , is based on the power transmission coefficient with uniform weight for frequencies from 9.8 to 10.2 gc and angles of incidence from 50° to 70°. Perpendicular polarization receives unit

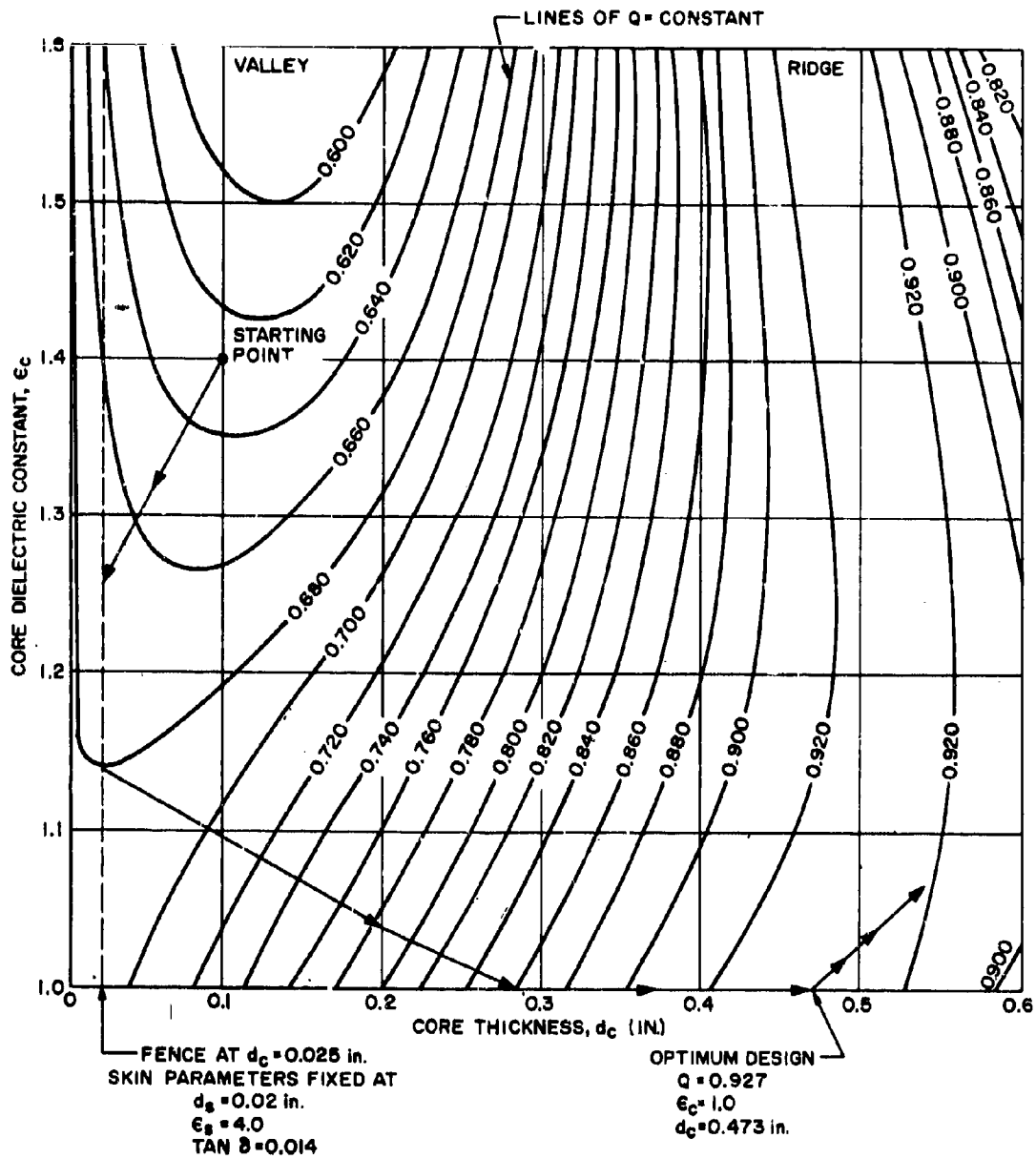


Figure 2-22. Figure of Merit Contour Map for "A" Sandwich and the Path Taken in Arriving at Optimum Design

weight and parallel polarization receives zero weight. A large number of calculations is required to construct this map. If computer optimization is employed, a far smaller number of calculations is involved.

Figure 2-22 also shows the path followed by the computer in optimizing the sandwich core parameters. Each step taken by the computer is shown as an arrow on the contour map, beginning with a starting point of  $\epsilon_c = 1.4$  and  $d_c = 0.1$  in. Although this example involves only two variables, the computer program in its present form will handle up to 22 variables.

### 2-2.3 COMPLETE RADOME DESIGN BY COMPUTER

In order to meet the need for a complete radome design or performance data in a minimum of time, a radome development computer procedure was established (Reference 20). This computer design procedure, which utilizes the IBM 7094 digital computer to supply radome electrical design and performance data, is divided into four program stages: the Gripe Program (General Radome Information Program Effort), the Design Program, the Performance Program, and the Correction Program.

A preliminary design study is made to obtain the various radome, antenna, and geometry parameters. Antenna patterns are taken on a test range, while a ray distribution is determined by a computer study. A radome geometry study is made of the loft lines to determine the equations that describe the radome shape and establish a radome coordinate system. Constraints, which are numerical limits used to judge the acceptability of a particular design, are also determined. These constraints include:

- a. Transmission.
- b. Wall thickness.
- c. Range of dielectric constant.
- d. Reflection.

After the radome shape is known, a material selected, a ray distribution calculated, and design constraints determined, a computer study can be made.

The procedure shown in Fig. 2-23 is used to establish the computer programs geared to allow complete flexibility of input parameters over a wide range of possible radome designs. These variable inputs may include any kind of radome shape, material, or antenna pattern.

The Gripe Program yields the following items of information:

- a. Radome shape definition.
- b. Radome cross section.
- c. Ray distribution.
- d. Ray location.
- e. Ray pattern.
- f. Ray surface area on antenna.
- g. Intensity distribution.
- h. Surface normal.
- i. Incidence angle.
- j. Polarizing angle.
- k. Intersection of ray and radome.

Since the Gripe Program can manipulate any shape, material, or antenna pattern, it can be used with any type of radome or electromagnetic window. Another feature of the program is that the ray distribution is general enough so that rays do not have to be perpendicular to the antenna. A good ray distribution can be set up that fits the entire antenna pattern, including the main beam and the side lobes.

The type of design program used in the computer phase depends on whether a mono-design method or an optimum design method is employed. The mono-design method yields one design configuration for one set of input parameters, while the optimum design method iterates over an interval of input parameters and selects the optimum configuration. The desired radome or electromagnetic window design determines whether the mono-design or the optimum design method will be used. For example, the following are four types of radome or electromagnetic window design:

- a. Maximum transmission.
- b. Low boresight error.
- c. Combination of maximum transmission and low boresight error.
- d. Broadband.

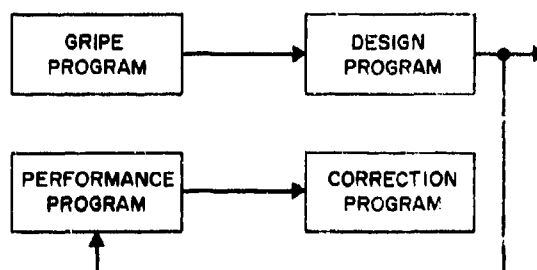


Figure 2-23. Computer Design Procedure

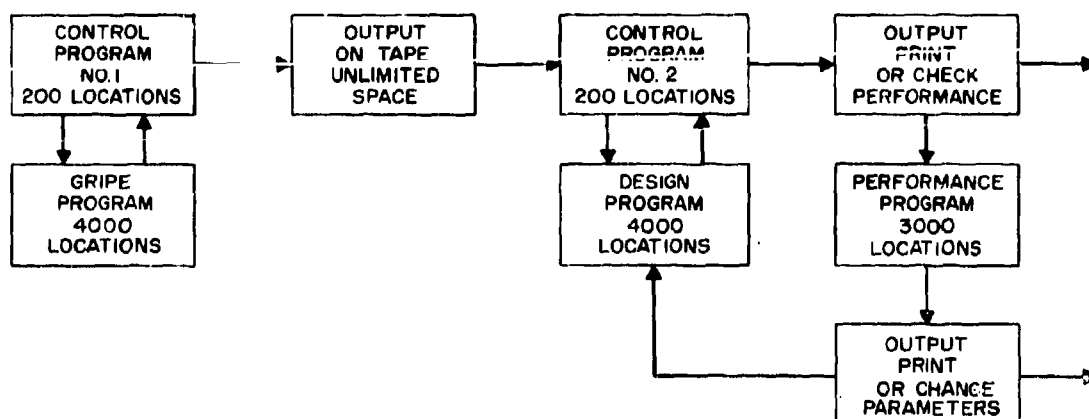


Figure 2-24. Subdivision of Computer Design Program

For the first and second types, the optimum design method would be used in the computer design. For the third, both the mono-design and the optimum design methods would be used, while for the fourth, the mono-design method would be used.

Several types of performance programs have been developed for use with the IBM 7094 computer, including error prediction and transmission programs. These programs are used both as an integral part of the optimum design method and as a means of checking a design obtained by the mono-design method. The correction program is based on an analytical method programmed for the computer. The method may involve phase, error, or the redesign of local areas with weighted antenna look positions, with the selection being determined by the apparent difficulty of the problem and the type of radome or electromagnetic window design. Analytical correction of a design may take place either in the computer design phase or during testing of a prototype.

The IBM 7094 computer has a capability of 32,768 words. Since the monitor system uses approximately 2000 words, there remains about 30,000 words for the radome program. This presents no difficult problems to the programmer, since the various parts of the computer design methods can be manipulated to obtain the final results in one computer run. The computer technique used by the Radome Group at Douglas is shown in Fig. 2-24. The program is divided into several parts, which are in

turn further subdivided. The Gripe Program, for example, is divided into twelve parts, or subprograms. One of two control programs is read into the computer and operation begins. Subprograms are called into core by the control program and instructions are executed. When final answers are obtained, the information is either printed out or stored on a tape for use in the next program, as is the case with the Gripe Program. The computer logic of the program in Fig. 2-24 can be illustrated by the following steps:

- After the Gripe Program is read into the computer, it is followed by Control Program No. 1 and the necessary input parameters for operation of the Gripe Program.
- Operation is started in the Control Program and a transfer is made to the Gripe Program to execute each instruction. The logic of operation of the program remains in the Control Program.
- Final answers are stored on a tape.
- Control is transferred to the next program.
- The next operation sequence is in the Design Program, which has been read into the computer core.
- Execution begins on the first instruction of Control Program No. 2.
- Subprograms of the Design Program, which were also read into the computer, are used when called out and instructions

are executed until final answers are obtained.

- h. Control is then transferred to print out these final answers when doing a mono-design study.
- i. When an optimum design study is being made, control is transferred to store the configuration in core.
- j. The Performance Program is read into the computer and instructions are executed that check the performance of the configuration.
- k. The parameters of the radome are changed and control is transferred back to Control Program No. 2, where the design of the next configuration is calculated.
- l. Steps i through k are repeated until an optimum design is obtained.

## 2-3 TECHNIQUES FOR ELECTRICAL EVALUATION OF ELECTROMAGNETIC WINDOW AND RADOME SHAPES\*

### 2-3.1 INTRODUCTION

The following paragraphs present the electrical evaluation of electromagnetic window and radome shapes, including shape definition, cross-section, and intersection parameters. Computer studies can be made that will determine electrical design and electrical performance data when such techniques are available that can handle general symmetrical and unsymmetrical shapes.

The technique for electrical evaluation of electromagnetic windows and radome shapes used by some radome designers involves the use of radial planes, as shown in Fig. 2-25, for defining three-dimensional general radome shapes. This technique handles all types of symmetrical and unsymmetrical radome shapes. In order to make electrical design and performance studies on the computer, a technique is required that will define the electromagnetic window or radome shape. A variety of shapes has been studied by radome designers. The aerodynamicist prefers a 0.75 power series shape because of minimum pressure drag at high supersonic

\* Contributed by Forrest L. Colling.

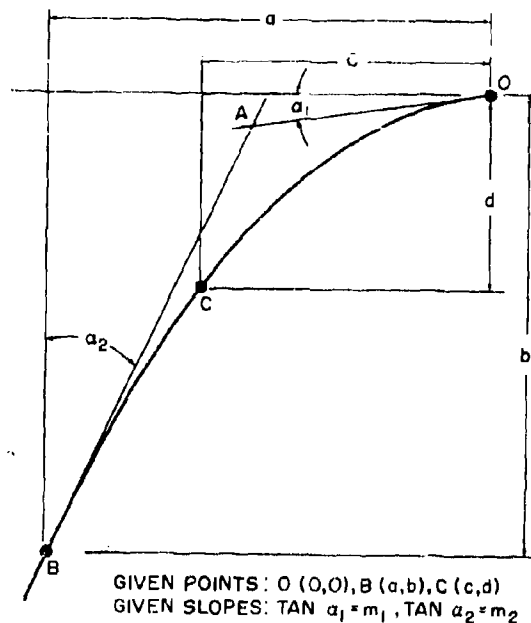


Figure 2-25. Analytic Determination of a Conic by 3 Points and 2 Slopes

speeds. The structural designer prefers a cylindrical shape because of superior mechanical properties. The thermodynamicist prefers a spherical shape because of superior thermal properties. The electrical designer prefers the hemispherical shape because of its superior electrical properties. Compromise must be made in the shape in order to design a radome and performance studies should be made on a variety of shapes to select a shape for a specified vehicle.

### 2-3.2 TYPICAL SHAPES

The following paragraphs describe techniques for use in electrical evaluation of shapes on digital computers. A number of different shapes have been investigated for radome use. See Paragraph 1-1.3 for types of aerodynamic configurations. Some of the classes of shapes studied are: elliptical, hemispherical, logarithmic and equiangular spirals, ogive, power series, parabolic, and others. Some of the shapes

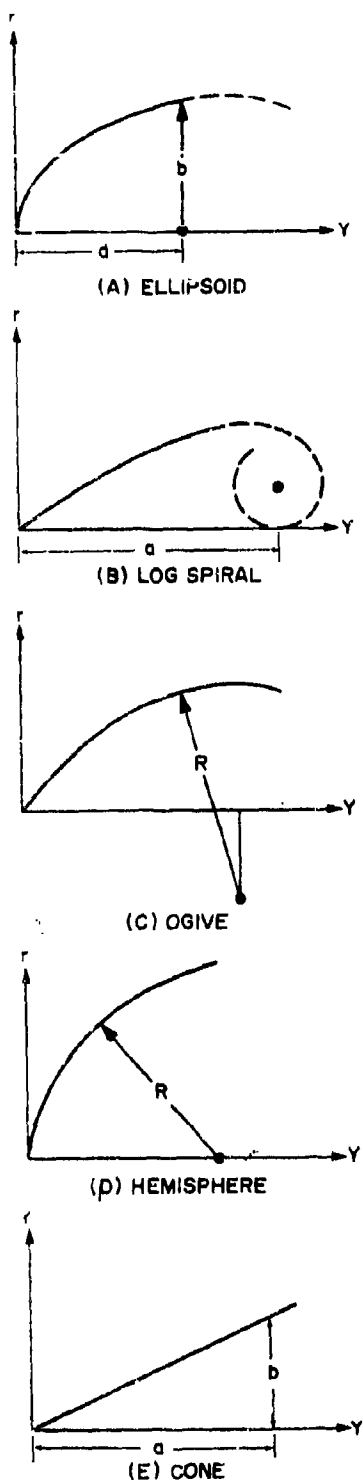


Figure 2-26. Typical Radome Shapes

are shown in Fig. 2-26. A symmetrical, or circle of revolution, radome can be described by one radial plane equation. Some examples of this type of shapes are: hemisphere, ogive, cone, and other power shapes. These specific shapes reduce the time required to prepare a computer study and also reduce the computer time considerably.

### 2-3.3 SHAPE DEFINITION

A technique used to describe a general radome shape for computer studies employs the radial plane definition as shown in Fig. 2-27. This definition uses at least four radial planes per quadrant at any arbitrary cross sectional cut. Each radial plane is equally spaced and emanates from the centerline of the radome. It starts at the point of intersection of the radome centerline and the radome nose and extends aft to a point of shape discontinuity or to the end of the radome. A typical cross-section with nine radial planes is shown in Fig. 2-27C. The figure shows a radome cross-section where upper and lower halves are unsymmetrical, while the right and left halves are symmetrical. Such a radome could be studied on the right side, saving half of the computations. A symmetrical radome would have all radial planes equal and thus could be described by one equation. Each radial plane,  $r$ , will be described by a form of the general shape equation:

$$r = Jy + K \pm \sqrt{Ly^2 + My + N} \quad (2-2)$$

This general shape equation is developed from the general expression for a second-degree curve:

$$Ay^2 + Byr + Cr^2 + Dy + Er = 0 \quad (2-3)$$

Each term of Eq. 2-2 is obtained by solving Eq. 2-3 by the quadratic equation and by substitution of coefficients. It is desirable to employ a method that will handle all types of three-dimensional shapes to minimize design and development time and simplify computer studies.

One technique that is employed by some radome designers when using Eq. 2-2 is to specify the radome shape with three points and two slopes, as shown in Fig. 2-25. This technique requires a detailed drawing of the radome shape, as shown in Fig. 2-26. Points and slopes

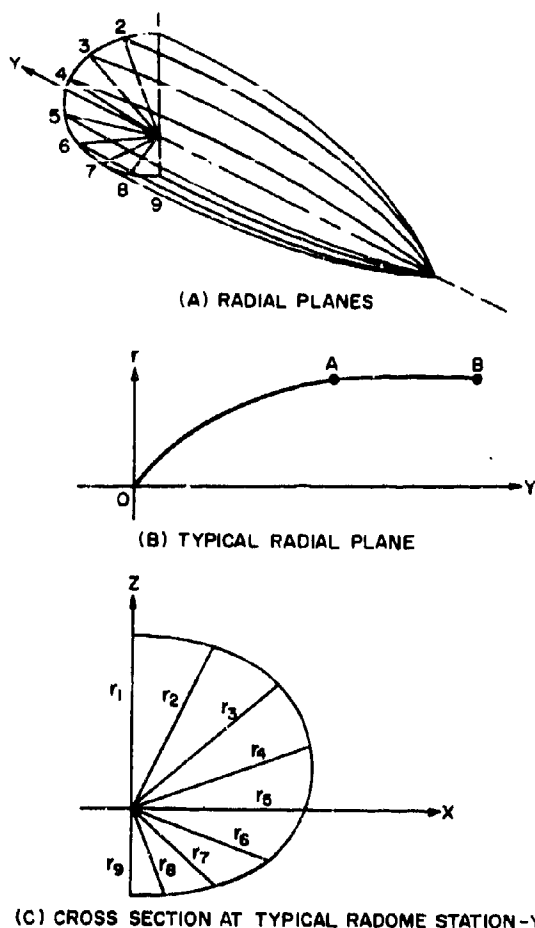


Figure 2-27. Typical Radial Plane Definition

are developed from a drawing of the shape and calculations are made to determine Eq. 2-2, which describes the shape. It would take one equation or radial plane to describe a radome shape that has properties of symmetry, and a continuous contour from nose to base. An unsymmetrical radome with a continuous contour from nose to base would require nine equations to describe the nine radial planes, as shown in Fig. 2-27A. The radome in Fig. 2-27B for an unsymmetrical type, would require eighteen equations to describe each radial plane. An unsymmetrical radome with four sections to each radial plane would require thirty-six equations to describe. Thus a computer program with the capacity for thirty-six equations would seem to

be quite adequate for analyzing most radome shapes.

### 2-3.4 COMPUTER USE

Setting up a computer program to electrically evaluate radome shapes requires other component parts in addition to a shape definition method. Other components of a geometry program include: intersection of ray and radome; calculations of incidence angle, polarizing angle, and surface normal; and an iteration procedure. Data obtained from such a geometry program can be used for a radome design or performance study. A typical computer program is shown in Fig. 2-28. The design or performance program may be for a boresight error or a transmission study.

### 2-3.5 ELECTROMAGNETIC WINDOW SHAPES

It is also desirable to make electrical design and performance studies of electromagnetic window shapes on computers. This requires a shape definition program for electromagnetic windows. It is not easy to develop a technique for defining all possible electromagnetic window shapes. The electromagnetic windows might be located on an ogive, cone, cylinder, frustum, hemisphere, or other shape. An example of an

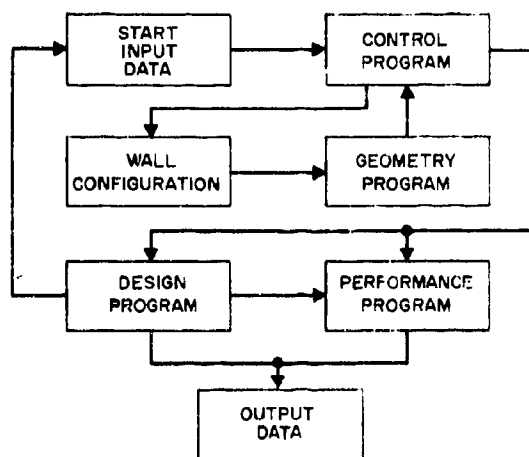


Figure 2-28. Computer Program

electromagnetic window shape would be one as shown in Fig. 2-29, where it is located on an ogive. To illustrate a method for describing electromagnetic windows, consider the two types illustrated in Fig. 2-29. To analytically describe the geometrical shape of these electromagnetic windows, the ogive shape is defined as previously described and the window is defined by means of a set of points  $P(X, Y, Z)$ , such that  $F(X, Y, Z) = 0$ , where

$$\begin{aligned} 0 \leq Z_1 \leq Z \leq Z_2 \leq C \\ \rho = \sqrt{X^2 + Y^2} \\ 0 \leq \rho_1 \leq \rho \leq \rho_2 \\ \theta_1 \leq \theta \leq \theta_2 \\ 0 \leq \theta_1 \\ \theta_2 \leq 2\pi \end{aligned}$$

Window B in Fig. 2-29 can be defined as the set of points  $P(X, Y, Z)$ , such that  $F(X, Y, Z) = 0$ , where

$$\begin{aligned} 0 \leq Z_1 \leq Z \leq Z_2 \leq C \\ B \leq Y_1 \leq Y \leq Y_2 \leq B \end{aligned}$$

$P(X, Y, Z)$  are in quadrant I, Points B and C are in the ogive definition.

Other electromagnetic windows in this general class are defined similar to the one just described. Flat windows can be described in two-dimension as a special case.

### 2-3.6 CONCLUSIONS

Electrical evaluation of radome shapes provides data that can be used to influence preliminary design approaches, provides estimates of design time required to study alternate shapes, provides data for inputs to proposal programs, provides a method for obtaining data on alternate design approaches for a vehicle, provides a means for obtaining design and performance data for many design studies, and saves design time by studying many shapes on the computer, as opposed to empirical (test) approaches on fabricated prototype parts. Comparing data for one radome shape with another primarily shows a change in the magnitude of the incidence angle discontinuity across the radome. Large incidence angles are common to sharp pointed shapes such as cones. However, large incidence angles cause high losses in electrical performance. This results in a decrease in transmission and an increase in reflection and discontinuity in the phase front.

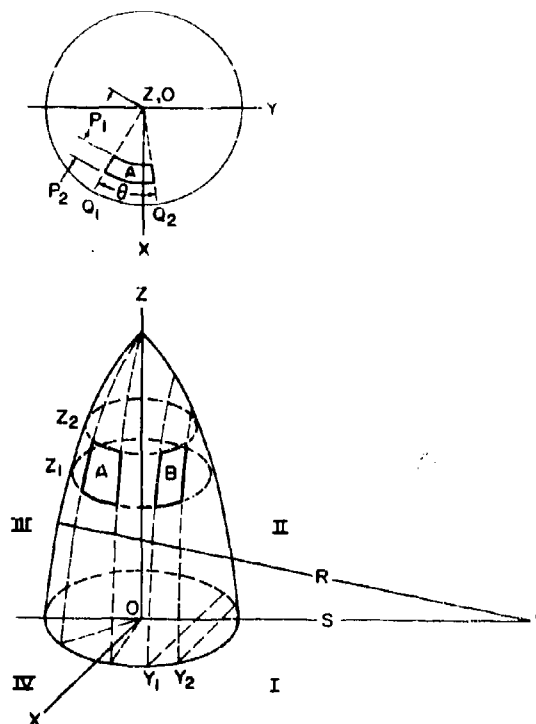


Figure 2-29. Typical Electromagnetic Window Definition

## 2-4 BORESIGHT-ERROR PREDICTION TECHNIQUES

### 2-4.1 INTRODUCTION

The boresight error or beam deflection caused by a radome is defined as the difference between the true angular position of the target and its apparent angular position as indicated by the radar system. For a given radome, the boresight error depends to a considerable extent on the antenna system (conical scan, monopulse, interferometer, etc.), and the antenna polarization (linear, circular, etc.) employed. The antenna size, the aperture distribution of amplitude and phase, and the antenna beamwidth have a considerable effect on the boresight error, with boresight error decreasing as beamwidth decreases.

For a given antenna system, the boresight error depends greatly on the radome shape and its wall construction (solid-wall, sandwich,



etc.). A spherical radome introduces the least boresight error, particularly if the antenna is accurately centered, whereas a highly streamlined radome exhibits an increased boresight error.

It is useful to consider the boresight error to arise from two distinct, though not independent, mechanisms. In the first place, each ray emanating from the antenna aperture undergoes a different phase shift in passing through the radome wall, largely as a result of the different angles of incidence. This phase variation results in a shift in the antenna beam pointing direction. In general, it also introduces a certain amount of pattern distortion. In the second place, scattering from the radome vertex region and variations in the transmission efficiency experienced by each ray in passing through the radome, distort the antenna pattern and thereby contribute to the boresight error.

Optical and ray-tracing solutions are generally quite simple and accurate when applied to a large radome enclosing a narrow-beam antenna, although complications occur when there are structural supporting ribs. On the other hand, the error-prediction calculations for a small streamlined radome are often quite lengthy and the accuracy is poor. Since the optical solutions are not applicable, ray-tracing and scattering techniques are employed for the analysis of small streamlined radomes. Thus, satisfactory techniques are available for large radomes without structural ribs, but new or improved error prediction methods are needed for small streamlined radomes and structural ribs. A considerable portion of the discrepancy between the calculated and measured boresight errors for the small streamlined radomes may arise from tolerances in the radome thickness and dielectric constant, from antenna-radome interaction, and from differences between the true antenna aperture field distribution and the assumed distribution.

In many cases, the goal of a boresight-error prediction effort is simply to determine whether a given radome design meets the specifications. In other cases, it is desired to arrive at an optimum radome design by calculating the boresight-error characteristics of many different radome shapes or wall constructions.

In many missile guidance systems, the angular rate of change of boresight error is much more significant than the boresight error itself.

If the boresight error is rather large but is a slowly varying function of the angular direction of the target, the missile very likely follows a non-optimum trajectory but completes its mission successfully. A rapidly varying boresight error, however, introduces an apparent target motion that may result in sluggish missile control-system response or a tendency toward instability.

Various techniques for predicting the boresight error are described in the following paragraphs.

#### 2-4.2 OPTICAL METHODS TECHNIQUE

The optical methods technique of boresight-error prediction involves the concepts of lenses, magnification, focal lengths, and ray deviations. Useful results can be expected with the optical equations only if the antenna aperture is large (above 10 wavelengths or more in diameter) and the radome wall curvature is small. The optical methods are adequately described in References 24, 25, and 26 and are not described further in this chapter.

#### 2-4.3 RAY-TRACING TECHNIQUE

In the ray-tracing technique, the antenna is generally considered to be in the transmitting condition. Rays are traced from various points on the antenna aperture to points on an equivalent aperture outside the radome. The field intensity associated with each ray is modified in amplitude and phase in accordance with the complex transmission coefficient of the radome. The transmission coefficient is considered to be a function of the angle of incidence, the polarization of each ray, and the wall thickness at the point where the ray strikes the radome. Use is made of the plane-wave, plane-sheet transmission coefficient. When a modified field distribution on the equivalent external aperture is determined, an integration is performed over this aperture to calculate the far-field patterns that determine the boresight error. A summary of the ray-tracing methods is given in Reference 27 and also discussed in Paragraph 2-1.3.

Reference 28 presents an investigation of the ray-tracing solution for the far-field pattern of a line source that is located off-center in a radome consisting of a circular cylindrical shell.

The exact boundary-value solution is also given for shells of various radii and thicknesses with a line source located at various distances from the center. The dielectric constant of the shell is 4.0 in each case. These exact solutions are useful for evaluating the accuracy of various radome boresight error prediction methods. The cylindrical shell is not entirely satisfactory for this purpose, however, since the exact solution is available only for cylinders of rather small radius (1.5 wavelengths). Furthermore, the vertex scattering problem is not simulated in this radome model.

The ray-tracing method has also been employed with the antenna assumed to be in the receiving condition with a plane wave incident on the radome from some distant source (see References 29 to 33). Rays are traced through the radome to the antenna aperture in a direction parallel to the axis of propagation of the incident plane wave. The field intensity associated with each ray is modified in phase and amplitude in accordance with the complex transmission coefficient of the radome wall for the appropriate angle of incidence and polarization of each ray. Again, the plane-wave, plane-sheet transmission coefficients are used. To calculate the voltage received at the antenna terminals, an integration is performed over the antenna aperture of the modified field intensity of the incoming rays, weighted by the complex aperture field intensity of the antenna when it transmits.

Reference 29 shows that accurate results are obtained by this method when the "radome" consists of a plane dielectric sheet that covers part or all of the antenna aperture in which the dielectric sheet is not necessarily parallel with the aperture. Reference 30 reports accurate results with this method at the design frequency (where reflections are minimized) for a streamlined radome, but the method proved inaccurate at frequencies 300 mc above and below the design value. Reference 33 reports some success with this ray-tracing method as applied to boresight-error prediction and correction for a radome enclosing an antenna of 16 wavelengths diameter.

Unfortunately, it appears that no comparison has been made of the relative merits of the two ray-tracing methods, i.e., the receiving problem vs. the transmitting problem. Whenever the

reciprocity theorem is applicable, it is known that any exact or highly accurate solutions produce the same boresight-error data for the receiving and transmitting problems. However, the ray-tracing solutions cannot be considered to be highly accurate when applied to small streamlined radomes, and different results are to be expected from the receiving and transmitting formulations. It has not yet been established which formulation yields the more accurate results.

There appears to be a considerable increase in computation time and expense with the receiving formulation in comparison with the transmitting problem. In either case, it is necessary to calculate several points on the far-field patterns for two or more antenna positions if conical scan is employed to determine the boresight error. If the antenna is considered to transmit, the ray amplitudes and phases are modified by the transmission coefficients only one time to obtain the equivalent external aperture distribution that yields a complete far-field pattern. If the antenna is considered to receive, the incoming plane wave must be carried through the radome (modified by the transmission coefficients) several times (for different angles of arrival) to obtain a useful portion of the far-field pattern. No justification is known at the present time for this added computation in terms of improved accuracy.

#### 2-4.4 SCATTERING TECHNIQUE

The scattering technique for boresight-error prediction is presented in References 24 to 26. Reference 34, however, indicates two errors in the equations presented in References 24 to 26. It also states that, although a method has been worked out for obtaining a numerical solution for the integral equation and attempts have been made to apply it to a specific radome, using a large digital computer in an iterative process, unfortunately, a converging solution has not been obtained.

Two additional errors in the equations of References 24 to 26 are indicated in Reference 33. It also states that preparation of computer programs and codes was about three to four times as expensive for the scattering method as for the ray-tracing method. Actual machine running costs were from 80 to 120 times greater

for the scattering method as for the ray-tracing method. Convergence of iterations in a strict sense was never obtained. Scattering method calculations of patterns agreed more with the general shape of measured patterns than did the ray-tracing calculations. This is true mainly for larger angles. In fact, for some smaller angles, the ray-tracing patterns were in better agreement than were the scattering calculations. (These results occurred in the investigation of a wedge radome with a dielectric constant of 2.6, enclosing a horn antenna with an aperture width of 2 wavelengths.)

#### 2-4.5 INTEGRAL-EQUATION TECHNIQUE

The scattering technique has been employed successfully in some radome problems by avoiding the iteration method presented in References 26 and 35. Reference 35 shows that convergence of the iteration method is not assured unless the dielectric constant and/or thickness is very small. Reference 36 presents the solution of the impedance and the far-field patterns of a dipole located off center in a thin spherical radome. With the approximation of the total field in the dielectric by the incident field, Reference 37 presents the analysis of the scattering patterns of a thin dielectric ring and Reference 38 the scattering patterns of a thin conical radome.

Reference 39 presents the integral-equation technique to calculate the plane-wave scattering pattern of a circular dielectric cylindrical shell, and the results show excellent agreement with the exact classical solution. Similar calculations for the pattern of a horn antenna in a wedge radome and the pattern of a horn with its aperture partially covered with a half-wave dielectric sheet show excellent agreement with experimental measurements. These were treated as two-dimensional scattering problems and were solved with the aid of a relatively small IBM 1620 computer. The technique follows:

- a. The radome is divided into cells sufficiently small so that the electric field intensity is nearly uniform throughout any given cell.
- b. The incident field, i.e., the field set up by the antenna without a radome, is calculated at the center of each cell.
- c. The integral equation for the field is re-

duced to a system of simultaneous linear equations in the unknown field intensity at the center of each cell.

- d. This system of equations is solved to obtain the complex electric field intensity distribution in the radome wall.
- e. The polarization-current concept is employed to calculate the far-field pattern of the antenna with a radome.

Three techniques that are useful in reducing the calculation time are as follows:

- a. Rather than using an iteration procedure that begins with the incident field or with the ray-optics solution, the fields in the radome wall are considered as a set of unknowns in a system of linear equations.
- b. Lagrange interpolation is employed to reduce the number of linear equations by a large factor.
- c. Only the field in the radome vertex region need be considered unknown. The field in the remainder of the radome is given with sufficient accuracy by the ray-optics solution, unless strong reflections or surface-wave excitations occur.

If the approximation in step c is avoided, the solution includes the effects of scattering by the radome vertex region, multiple reflections, and surface-wave excitation in the radome, even though these phenomena need not be considered explicitly in obtaining the solution. The greater part of the calculations involves just the radome geometry. After this is completed, a relatively simple calculation is required to investigate the effects of rotating the antenna or replacing it with a different antenna.

To illustrate the technique, it was applied to the pyramidal horn antenna with a wedge-shaped radome shown in Figs. 2-30 and 2-31. The calculated electric field intensity in the radome wall is illustrated in Fig. 2-32. Figure 2-33 shows the measured and calculated far-field patterns of the horn with the wedge radome. For comparison, the free-space patterns are also shown. It may be noted that excellent agreement occurs between the measured and calculated results. For details of the theory and the calculations, see Reference 39.

The dielectric sheets of the wedge radome in this example are so thin that a ray-tracing solution also provides good results. However, the integral-equation technique just described also

yields accurate far-field patterns for a horn with its aperture partially covered with a half-wave dielectric sheet, a situation in which the ray-tracing technique has been found to be inadequate.

## 2-5 METAL-LOADED RADOME DESIGN

A radome may be loaded with metal particles or metal structures to increase the strength or

the strength-to-weight ratio, the tolerances in the dimensions, and the dielectric constants, or to improve the electrical characteristics, such as the bandwidth and the boresight error. Some types of metal loading offer improvements in some of these parameters, but they generally involve some sacrifice in another parameter.

Loading with tiny straight wires, spheres, helices, etc., has not been entirely successful (Reference 40). It has been shown that the effective dielectric constant can be increased considerably by loading with tiny particles of metal or titanium dioxide, with a slight increase in the loss tangent or a decrease in strength (Reference 41). The dielectric constant may also be adjusted by loading with hollow glass microspheres (Reference 42).

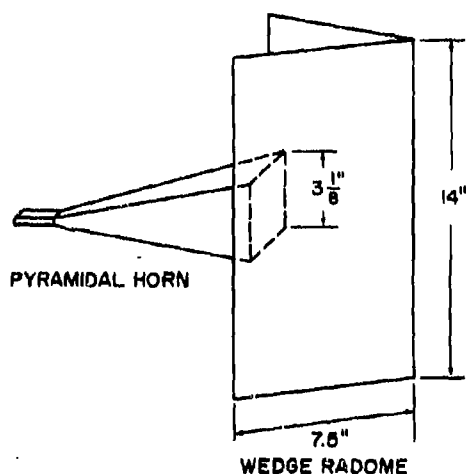


Figure 2-30. Horn Antenna and Wedge Radome Used to Illustrate Integral-Equation Solution

### 2-5.1 METAL GRATING FOR SUPPRESSION OF CROSS-POLARIZATION

The requirement for a polarization grating or filter originated with acquisition problems encountered with vertically polarized, conical-scan, shipboard radars. In these antennas, power modulation is employed to reduce low-angle scatter return. The result is a depressed null axis that does not coincide with the paraboloid axis, and the introduction of a significant amount of cross-polarization on the depressed null axis. When the target is a circularly polar-

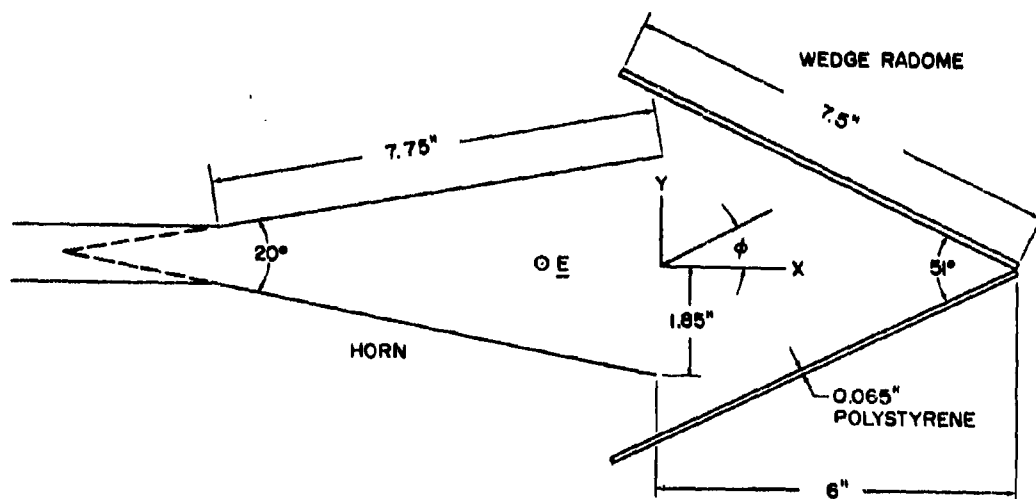


Figure 2-31. Cross-Section View of Horn Antenna and Wedge Radome

ized antenna, the modulation of the cross-polarization component produces a shift of approximately 10 milliradians from the true null or boresight.

To correct this situation, radome polarization gratings were developed to provide environmental protection of the antenna and rejection of the orthogonal polarization (Reference 43). The antenna and radome are shown in Fig. 2-34. A plane grating is employed that is supported by a cylindrical shell. The grating consists of a series of straight parallel aluminum plates spaced approximately one-fourth wavelength apart and supported in a slotted styrofoam structure. The entire structure is covered with a thin epoxy-fiberglass laminate for mechanical protection and strength. The thickness is approximately 2 in. The combination radome-grating is shown in Fig. 2-35. Laboratory tests of the radome-grating were carried out with several different targets, including a horn antenna, a pair of crossed dipoles, and a helical antenna. It was found that the radome-grating virtually eliminated the boresight shift. Shipboard tests of the antenna-grating combinations showed that target acquisition is accomplished much more readily with the modified units.

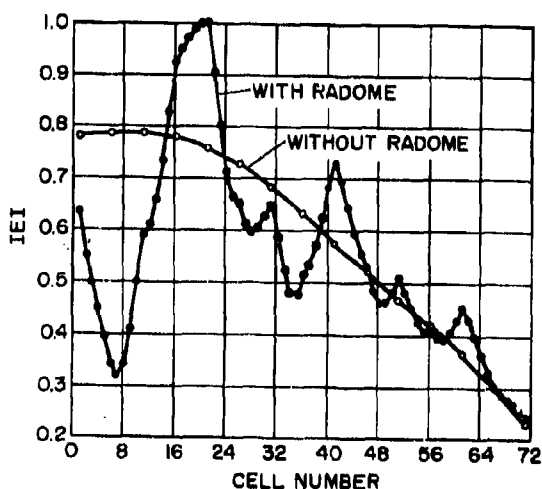


Figure 2-32. Calculated Values of Incident and Total Electric Field Intensity Set Up in Wedge Radome by Horn Antenna at 9400 mc

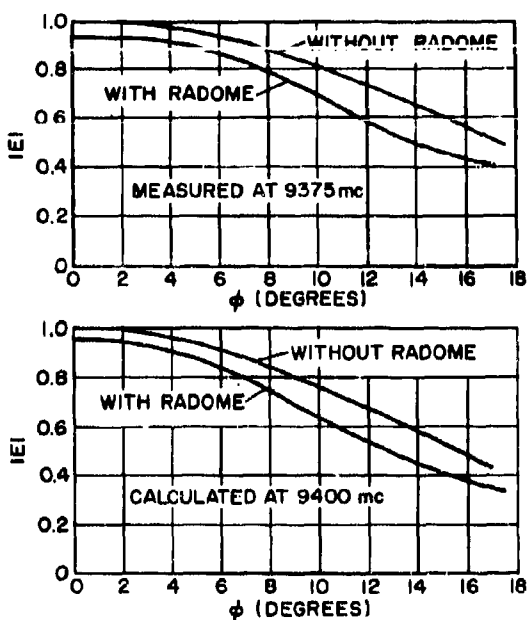


Figure 2-33. Measured and Calculated Far-Field Patterns of Horn Antenna with Wedge Radome Using Integral-Equation Solution (H-Plane Patterns)

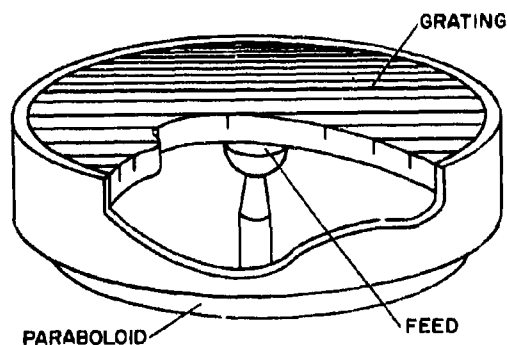


Figure 2-34. Combination Radome-Grating for Paraboloidal Antenna

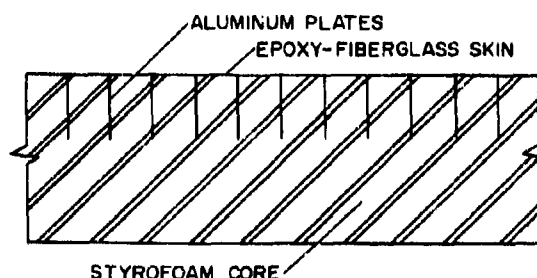


Figure 2-35. Construction Details of Gratings

### 2-5.2 LOADING WITH WIRE GRIDS OR PERFORATED METAL SHEETS

Reference 44 shows that a dielectric sheet can be loaded with wire grids or perforated metal sheets to approach the transparency of a layer of free space at any given frequency for perpendicular polarization. No metal structure is known, however, whose shunt reactance varies in the proper manner to match a thin dielectric sheet over a wide range of incidence angles for parallel polarization.

A thin dielectric sheet with a dielectric constant of 9.3, containing a perforated metal sheet, has the electrical characteristics shown in Fig. 2-36. This figure shows that the effective dielectric constant is indeed very close to unity for perpendicular polarization. This radome, whose design parameters are listed in Table 2-1, is 0.1 free-space wavelengths thick. If the radome were thinner, the transmission would not fall off as rapidly for parallel polarization, but

**TABLE 2-1 DESIGN PARAMETERS FOR RADOME WITH ONE EMBEDDED PERFORATED METAL SHEET**

Match wavelength in free space	$\lambda_0$
Match wavelength in dielectric	$\lambda_d = \lambda_0 / \sqrt{\epsilon_r}$
Match angle	$\theta_1 = 85^\circ$
Match polarization	$\perp$
Relative dielectric constant, $\epsilon_r$	9.3
Radome thickness	$0.305 \lambda_d = 0.100 \lambda_0$ (0.126 in. at 9875 mc)
Position of perforated metal sheet	At radome midplane
Thickness of perforated metal sheet	zero
Shunt reactance of perforated metal sheet normalized to impedance of the dielectric:	
Perpendicular polarization	$(\cos \theta_2) / 2.40$
Parallel polarization	$\frac{1 - 0.3 \sin^2 \theta_2}{2.40 \cos \theta_2}$

the amount of metal in the radome would have to be decreased. The frequency bandwidth of this radome, which is about the same as a one-half-wavelength radome with the same dielectric constant, would also increase if the radome were thinner. Tolerances on the total thickness of this metal-loaded radome are the same as for a one-half-wavelength radome with the same

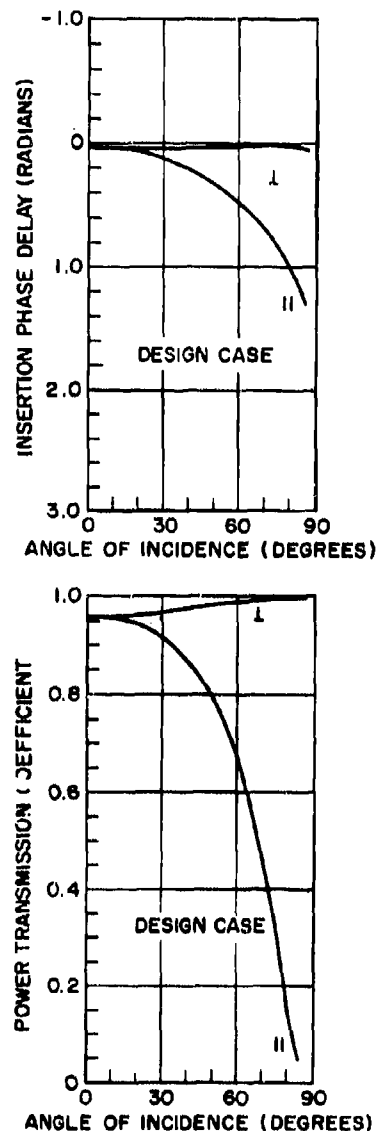


**Figure 2-36. Electrical Characteristics of Thin Dielectric Sheet with Perforated Metal Sheet at Midplane**

dielectric constant, but tolerances on the position of the metal sheet are less stringent. To obtain greater strength without greatly changing the transmission and insertion phase delay characteristics for perpendicular polarization, several of these thin dielectric sheets containing inductive walls can be cascaded. This cannot be done successfully with thin dielectric sheets without the metal structures.

It is practical to obtain fairly good electrical performance for both polarizations by properly spacing two of the thin metal-loaded dielectric layers so that their reflections cancel at some wide incidence angle. If a low-dielectric-constant core is placed between the two high-dielectric-constant skins, a metal loaded "A" sandwich radome results.

The design parameters for two "A" sandwich radomes loaded with wire grids and for two unloaded "A" sandwich radomes are tabulated in Table 2-2. Power transmission coefficient curves are shown in Fig. 2-37A for a radome with wire grids at the skin-to-core interfaces; in Fig. 2-37B for a radome with wire grids embedded within the skins; and in Fig. 2-37C for

an unloaded radome that has skins only one-third as thick as those of the metal-loaded "A" sandwiches. Note that the radome with wire grids between the skins and the core has transmission characteristics as good as the unloaded radome over their usable range of incidence angles, and the radome with wire grids in the skins is usable over a somewhat wider range of incidence angles. Power transmission curves are shown in Fig. 2-37D for an unloaded radome whose skins are of the same thickness as the metal-loaded radomes, and which is also designed to be matched for perpendicular polarization at 85° incidence. It is seen that the transmission of this radome falls off rather sharply near normal incidence. Thus, comparing the three "A" sandwich radomes of equal electrical performance, the metal-loaded radomes would be significantly stronger than the unloaded radomes because of their thicker skins.

Insertion phase delay curves for the four "A" sandwich radomes are given in Fig. 2-38. These curves show that the total variation in insertion phase delay is about the same for the metal-loaded radomes as the unloaded radomes.

TABLE 2-2 DESIGN PARAMETERS FOR "A" SANDWICH RADOMES

Radome type	Metal-loaded "A" sandwich	Metal-loaded "A" sandwich	Unloaded "A" sandwich	Unloaded "A" sandwich
Type of metal inclusions	Wire grids	Wire grids	None	None
Position of metal inclusions	At core-to-skin interfaces	In skins 0.025 in. from core	—	—
Match angle	$\theta_1 = 85^\circ$	$\theta_1 = 85^\circ$	$\theta_1 = 85^\circ$	$\theta_1 = 85^\circ$
Match polarization	$\perp$	$\perp$ and $\parallel$	$\perp$	$\perp$
Relative dielectric constant:				
in skin, $\epsilon_s$	4.5	4.5	4.5	4.5
in core, $\epsilon_c$	1.3	1.3	1.3	1.3
Radome thickness	0.884 in.	0.841 in.	0.601 in.	0.394 in.
Thickness of skin, $d_s$	0.075 in.	0.075 in.	0.025 in.	0.075 in.
Thickness of core, $2d_c$	0.734 in.	0.691 in.	0.641 in.	0.244 in.
Shunt reactance of wire grids (at $\theta_1 = 0$ ) normalized with respect to impedance of skin dielectric	1.56	2.0	—	—
Wire diameter, D	0.010 in.	0.002 in.	—	—
Center-to-center spacing of wires, s	0.357 in.	0.0207 in.	—	—

Note: The physical dimensions are given in inches for a design frequency of 9375 mc. For other design frequencies, multiply the dimensions by the ratio of 9375 mc to the design frequency.

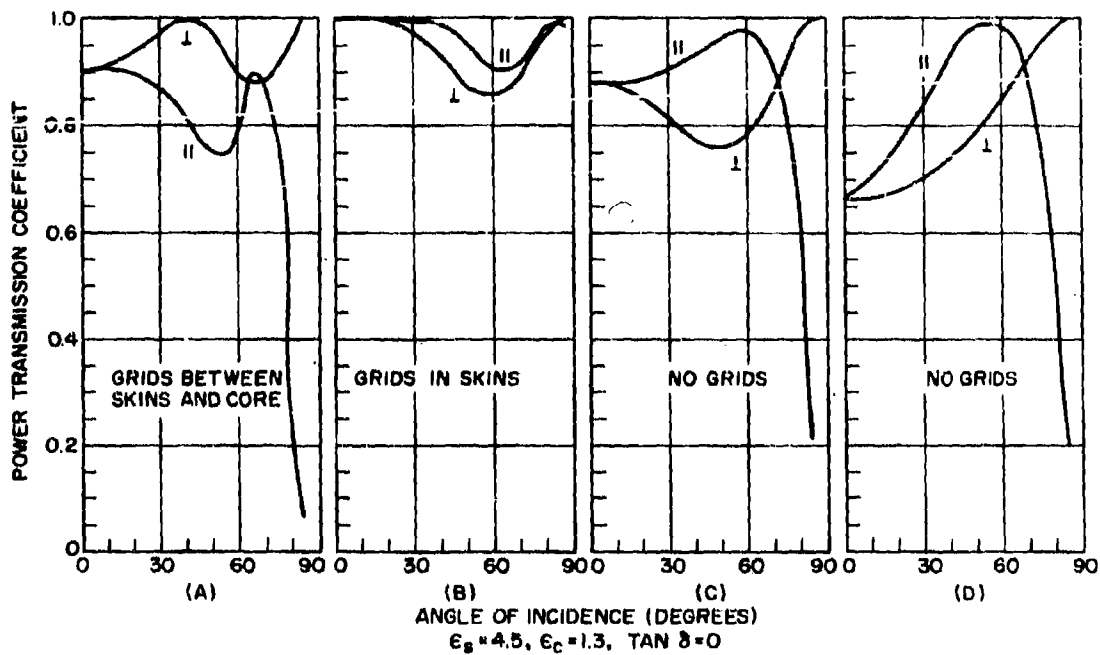


Figure 2-37. Power Transmission of "A" Sandwich Radomes

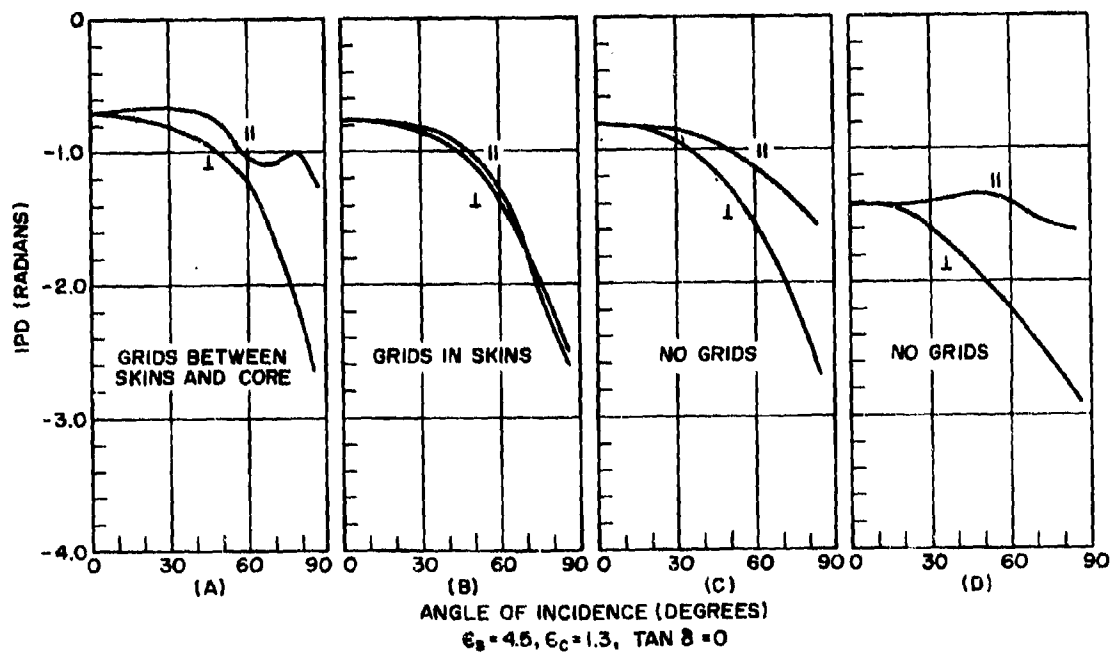


Figure 2-38. Insertion Phase Delay of "A" Sandwich Radomes



Transmission curves are given in Reference 45 for "A" sandwiches loaded with wire grids at the skin-to-core interfaces with a skin dielectric constant of 9.0 and core dielectric constants of 4.0 and 2.0. Reference 45 found that this sandwich construction had two distinct advantages. "A" sandwich radomes loaded with wire grids can be designed to have high transmission for both polarizations over a wide range of incidence angles out to 85°. This is in contrast to conventional unloaded "A" sandwich radomes, for which the transmission for parallel polarization falls off rapidly above the Brewster angle for the skin. The metal-loaded "A" sandwich radomes also require significantly less stringent tolerances on the core thickness than unloaded "A" sandwich radomes using the same dielectric material. Presumably the tolerance on core dielectric constant would also be less stringent for the metal-loaded "A" sandwiches.

The broadband properties of radomes loaded with wire grids are discussed in Paragraph 2-6. Additional information on radomes loaded with wire grids and perforated metal plates is presented in References 46 and 47.

Reference 48 presents a study of the effects of widely-spaced metal grids on the surface of spherical and ogival radomes. The spacing between the elements of the grid exceeded one wavelength, whereas the radomes just described had spacings less than one wavelength. In most of the experiments, strips of metal foil were taped on the outer surface of some production radomes, as shown in Fig. 2-39. The most serious effect of the metal grids was found to be the reduction in antenna gain. In most of the cases considered, the effect of the grid on beam-width, sidelobe level, and boresight error was slight. This was true even though up to 30% of the radome surface area was covered with metal.

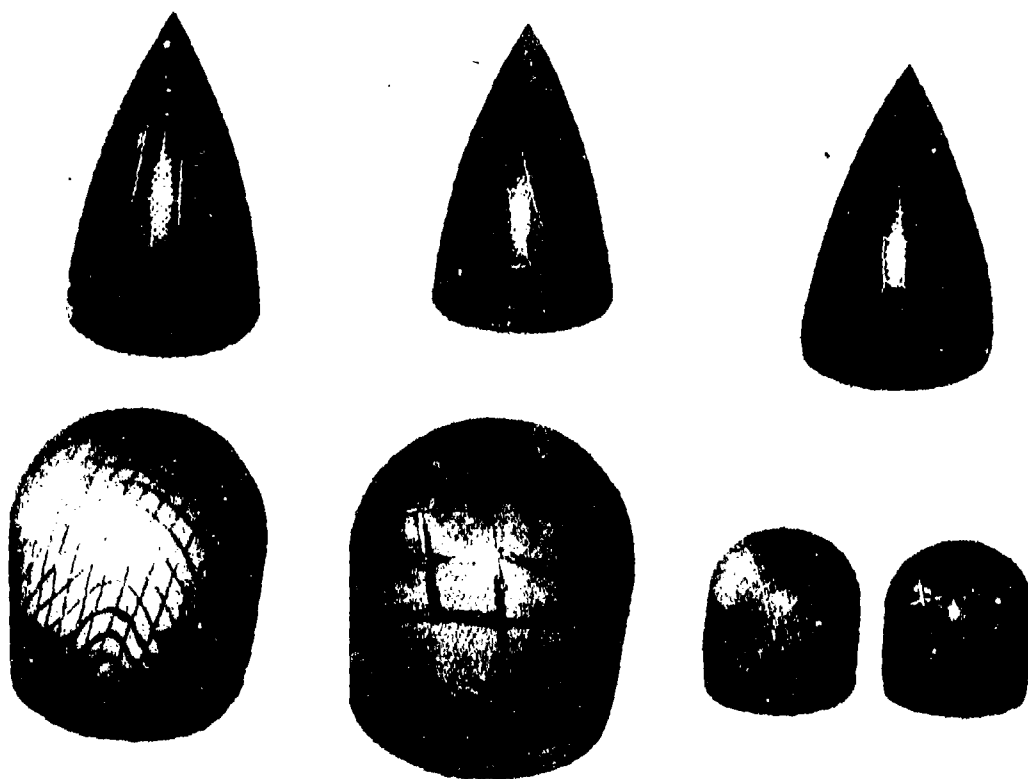


Figure 2-39. Radomes Showing Metal Foil Coverage

### 2-5.3 RESONANT-WALL DESIGNS

The basic resonant-wall radome (Reference 45) consists of a relatively thick metal plate perforated by dielectric-filled resonant cavities all tuned to the same frequency, as shown in Fig. 2-40A. It is also possible to use the perforated metal plate in conjunction with layers of dielectric, as indicated in Figs. 2-40B, C, and D. The resonant-wall radome appears to be the most promising type of metal loading from the mechanical standpoint, since a relatively large percentage of the radome is metal. A nose radome of the resonant-wall type might be similar to that shown in Fig. 2-41. Except for the metal tip and the mounting ring, the outer surface would be covered with solid dielectric to provide protection against rain erosion. No dielectric is shown on the inner surface of the metal plate, since there is no mechanical reason to have it there. The spacing between the perforations is assumed to be sufficiently small that only the

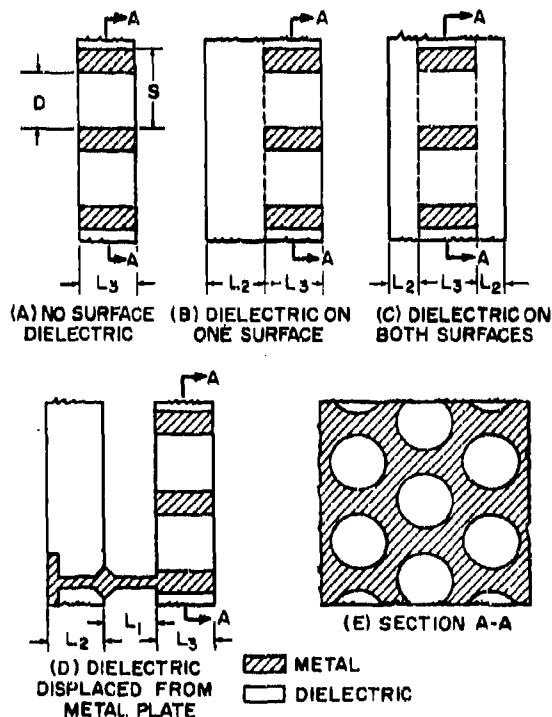


Figure 2-40. Several Resonant-Wall Radome Configurations

principal transmitted and reflected waves need be considered. With greater spacing, it is believed that diffracted waves would decrease the transmission efficiency, contribute to the side-lobe level, and increase the boresight error.

In general, it has been found that resonant-wall radomes can be designed to give high transmission over a wide range of incidence angles, but over a more restricted frequency bandwidth, and with a slightly larger insertion-phase-delay variation as a function of incidence angle than is obtained with conventional half-wave radomes.

Preliminary data have been obtained on the transmission properties of a metal sheet perforated with noncircular holes. Reference 45 found that the resonance frequency of a metal sheet perforated by ridge-loaded apertures depends much less on the incidence angle than does that of a metal sheet perforated by circular apertures.

On the basis of a combined theoretical and experimental study, it is concluded that resonant-wall radomes are intrinsically narrow-bandwidth devices when they are used with perpendicular polarization at wide angles of incidence. Nevertheless, they may be employed in situations where their electrical deficiencies are outweighed by their mechanical strength advantages. Some of the techniques and the problems

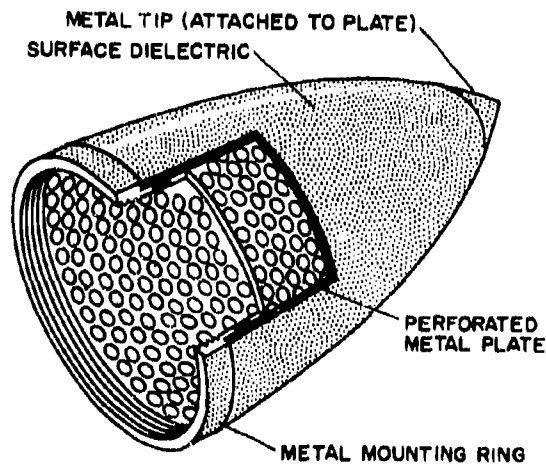


Figure 2-41. Nose Radome of Resonant-Wall Type Covered with Dielectric

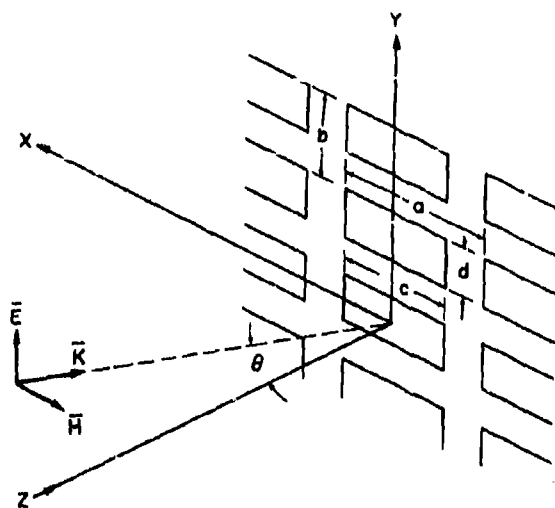


Figure 2-42. Slotted Metal Sheet

of fabricating metal-loaded and resonant-wall radomes are described in References 49 and 50.

#### 2-5.4 SLOTTED METAL RADOMES

References 51 and 52 present a study of a slotted metal radome in an application involving parallel polarization with a rather small range of angles of incidence. Radomes mounted on supersonic vehicles must operate at high temperatures and be able to withstand severe aerodynamic stresses and rain erosion. These requirements have resulted in the use of inorganic materials, such as alumina, ceramics, glass, and glass-bonded mica. In the radome construction, such materials have been used successfully for some missile radomes, but their mechanical strength is apt to be marginal in certain supersonic applications. As a possible alternative, the properties of slotted metal sheets for radome structures have been investigated. One type is the slotted metal plane sheet with air-filled slots, as shown in Fig. 2-42. The thickness of the metal sheet is assumed to be vanishingly small with perfect conductivity. Figure 2-43 shows the theoretical transmission coefficient for normal incidence as a function of normalized frequency,  $k_0 a$ , where  $k_0$  is the wave number. The data in these curves apply to a slotted metal

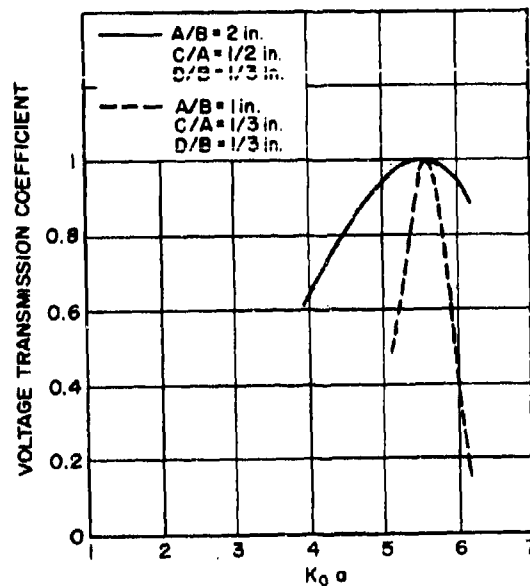


Figure 2-43. Calculated Transmission Coefficient as a Function of  $k_0 a$

sheet without any dielectric layer and clearly indicate the resonance characteristics. Total resonance with complete cancellation of the reflection of the incident wave by the metal part of the sheet is obtained and should be distinguished from the individual slot resonance that may occur at a wavelength approximately equal to the slot circumference.

Theoretical and measured transmission losses of slotted metal sheets are plotted in Fig. 2-44 for normal incidence as a function of the frequency. Discrepancies between the theoretical and measured results may be caused by mechanical imperfection of the slots, the nonplanar incident wave, and the existence of high-order modes. Measured transmission characteristics for oblique incidence are shown in Fig. 2-45. The effect of wave polarization is evident. For perpendicular polarization, attenuation increases with the angle of incidence. For parallel polarization, the attenuation decreases as the angle increases.

The slotted-metal plane-sheet technique was applied to the construction of a full-size nose radome for a Boeing 707 aircraft. The antenna used in the scanning experiments was an AVQ-10 weather radar antenna. Since the AVQ-10

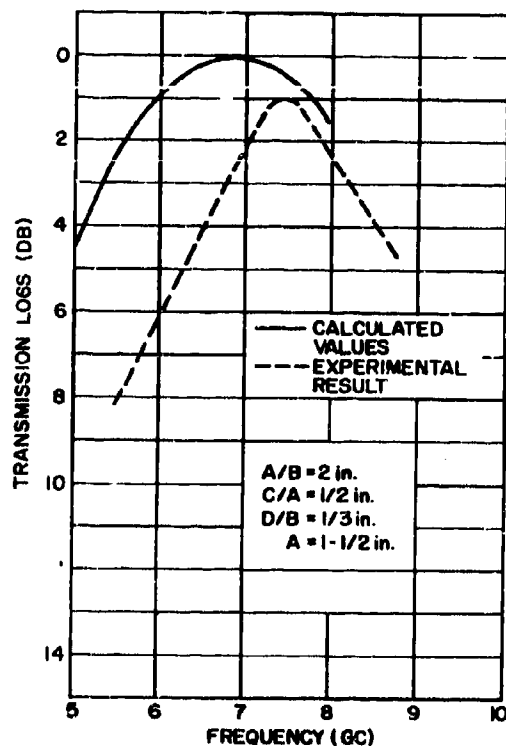


Figure 2-44. Transmission Loss as a Function of Frequency (Normal Incidence)

is an azimuthal-scanning, horizontally polarized antenna, the slots must be arranged in a meridian-line configuration so that the electric field of the signal is parallel to the narrow side of the slot at all usable scan angles. See Fig. 2-46. The AVQ-10 weather radar was mounted inside the metal radome in a position exactly as it would be in the aircraft. The antenna is a 30-in. parabolic dish, operating at a center frequency of 5.4 gc. Radiation pattern measurements were taken with the parabolic antenna rotating on its azimuth axis.

For the construction of a smooth metallic copy of the final radome, a production radome was used as a mandrel. Masking-tape, cut to the size of the desired slots, was placed on the outside surface of the radome in a meridian-line configuration. Conducting silver paint was applied to the radome until microwave transmission through the painted radome became negligible (below 40 db). The tape was then removed, leav-

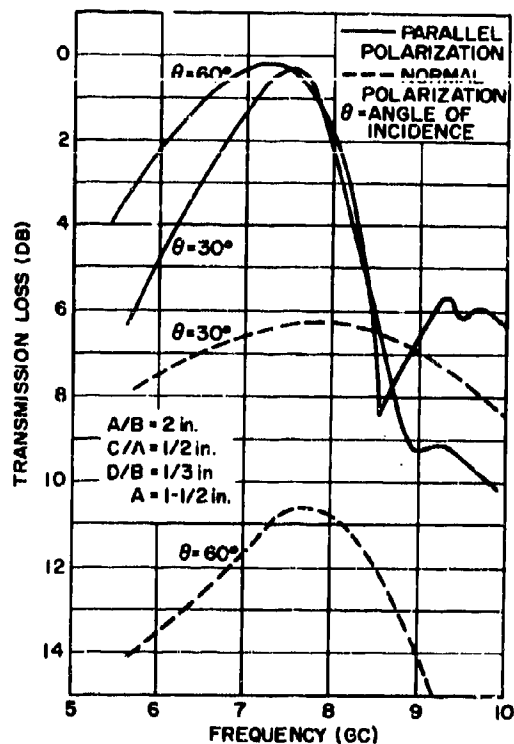


Figure 2-45. Measured Transmission Loss as a Function of Frequency (Oblique Incidence)

ing an array of slots. See Fig 2-47. The dimensions used for the slots were  $a/b = 2$ ,  $c/a = 2/3$ , and  $d/b = 1$ . The calculated free-space resonance was at  $k_0 a = 4.55$ . A value of  $a = 1.5$  in. was chosen to account for the 20% reduction in resonant frequency caused by the dielectric. The radome was expected to operate at 4.6 gc.

Antenna patterns with and without the metal radome are shown in Fig. 2-48 for frequencies from 4 to 6 gc. The frequency of highest transmission efficiency, between 4.5 and 4.875 gc, agreed with the calculated value of 4.6 gc. Figure 2-49 shows the antenna patterns taken at 4.875 gc for scan angles from  $0^\circ$  to  $90^\circ$ . The antenna pattern and the input VSWR were not appreciably modified by the radome; however, the transmission loss was about 1.3 db at 4.875 gc for all scan angles. Some of this loss was caused by attenuation in the dielectric layer. Although the mechanical strength of the slotted metal was not investigated, it is estimated

that such a slotted metal radome will retain 50% of the structural integrity of the solid metal sheet. If a high-strength, high-temperature alloy is used, metal thicknesses of 1/8 to 1/4 in. should be sufficient even at Mach 2 or 3.

### 2-5.5 DIPOLE FEED-THROUGH RADOMES

Reference 53 presents the results of the study of the properties of a metal radome in which the radar energy is intercepted by an array of dipoles, fed through tiny holes in the radome via transmission lines, and reradiated by a similar array of dipoles on the other side. This unusual structure has been called a *scannable ray-fed radome*. An ordinary dish or horn antenna is mounted within the radome to illuminate the inner array of dipoles. Scanning is accomplished in the conventional manner by aiming the enclosed antenna in various directions. One or both of the radome surfaces may be coated with a dielectric layer to achieve a smooth aerodynamic surface, while retaining the mechanical strength of the basic metal radome.

Figure 2-50 illustrates a plane version of the

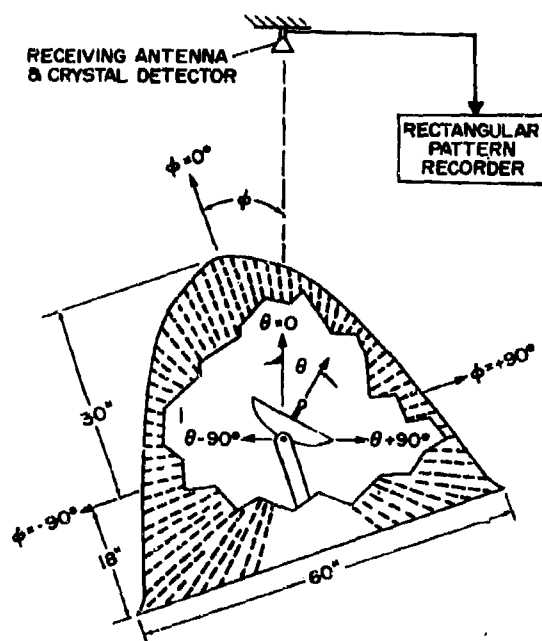


Figure 2-46. Experimental Setup for Radiation Pattern Measurements

dipole feed-through radome constructed for test purposes. This radome contains a pyramidal horn antenna and a large ground plane with an array of dipoles connected through tiny transmission lines to a similar array on the opposite side. Scanning was accomplished successfully with this test model, but the transmission efficiency was rather low as a result of impedance mismatch in the array and the limited area of the dipole array. Studies of the dipole feed-through radome are being continued in an effort to improve the transmission efficiency.

Since impedance matching is a prime consideration, automatic digital calculations were made of the driving-point impedance of the half-wave dipoles in a large plane array over a ground plane. The coordinate system used is shown in Fig. 2-51. Figure 2-52 shows the driving-point resistance for a thin half-wave dipole in a large array as a function of the scan angle in the H-plane from  $\phi = 0^\circ$  (broadside) to  $\phi = 50^\circ$ . The dipole spacing (center-to-center) in the y-direction is  $d_y = 0.6$  wavelength in each case. The dipole spacing in the x-direction is  $d_x$ . The distance of the dipoles above the ground plane is 0.25 wavelengths in each case.

The power transmission efficiency for these arrays, assuming a conjugate impedance match, is shown as a function of scan angle in Fig. 2-53. These results are theoretical and are based

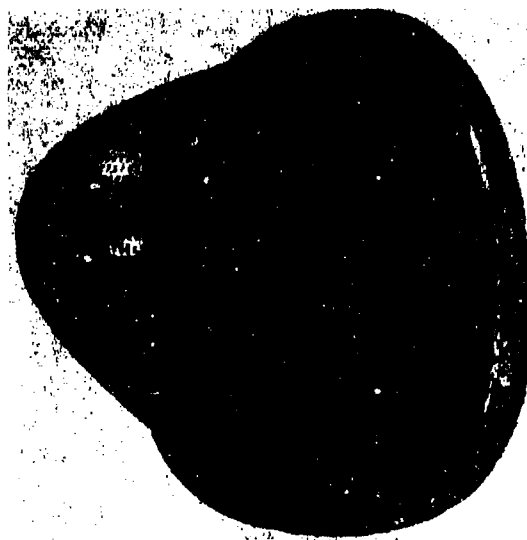


Figure 2-47. Silver Slotted Radome for Boeing 707

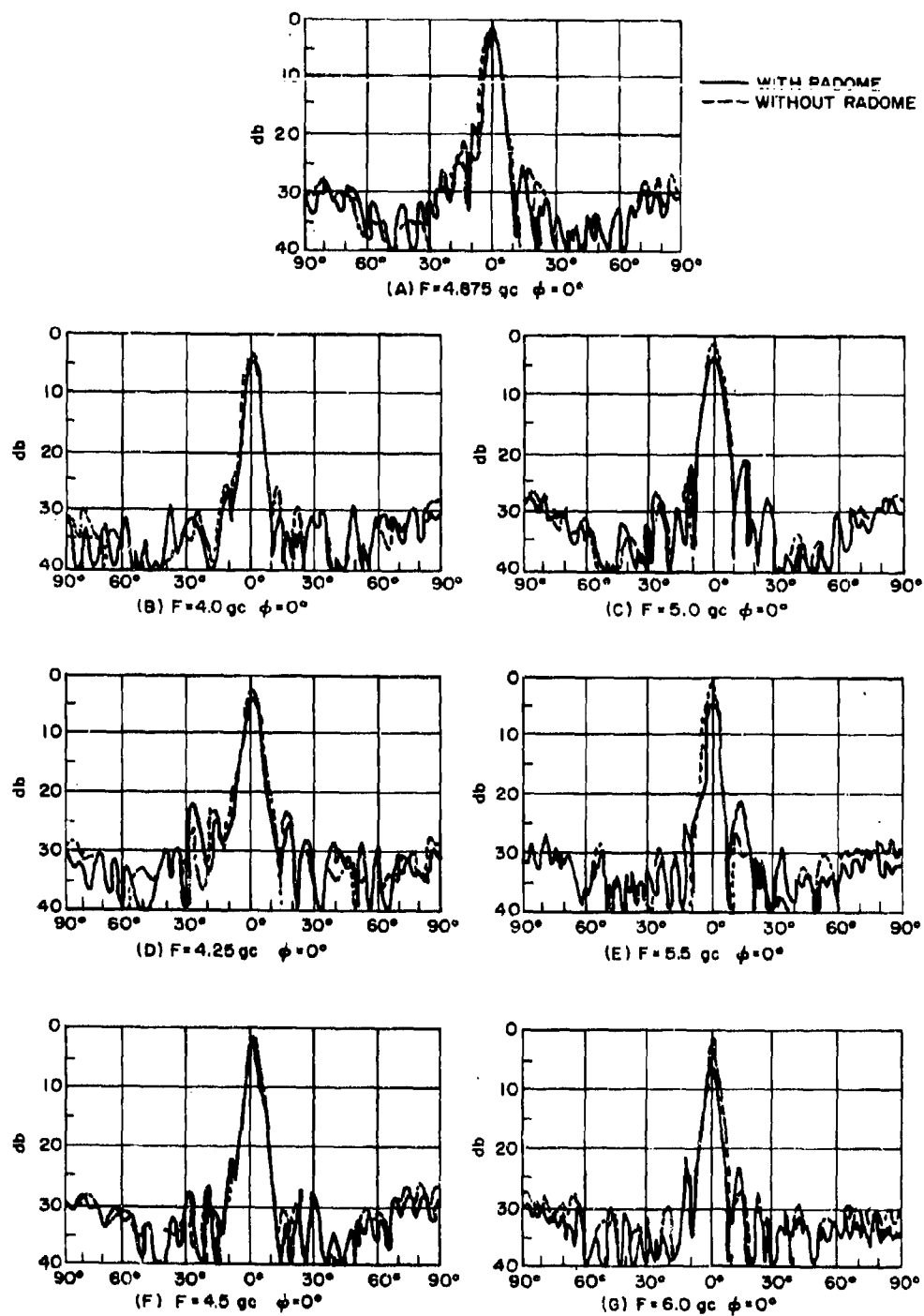


Figure 2-48. Antenna Patterns of Metal Radome Taken at Several Frequencies

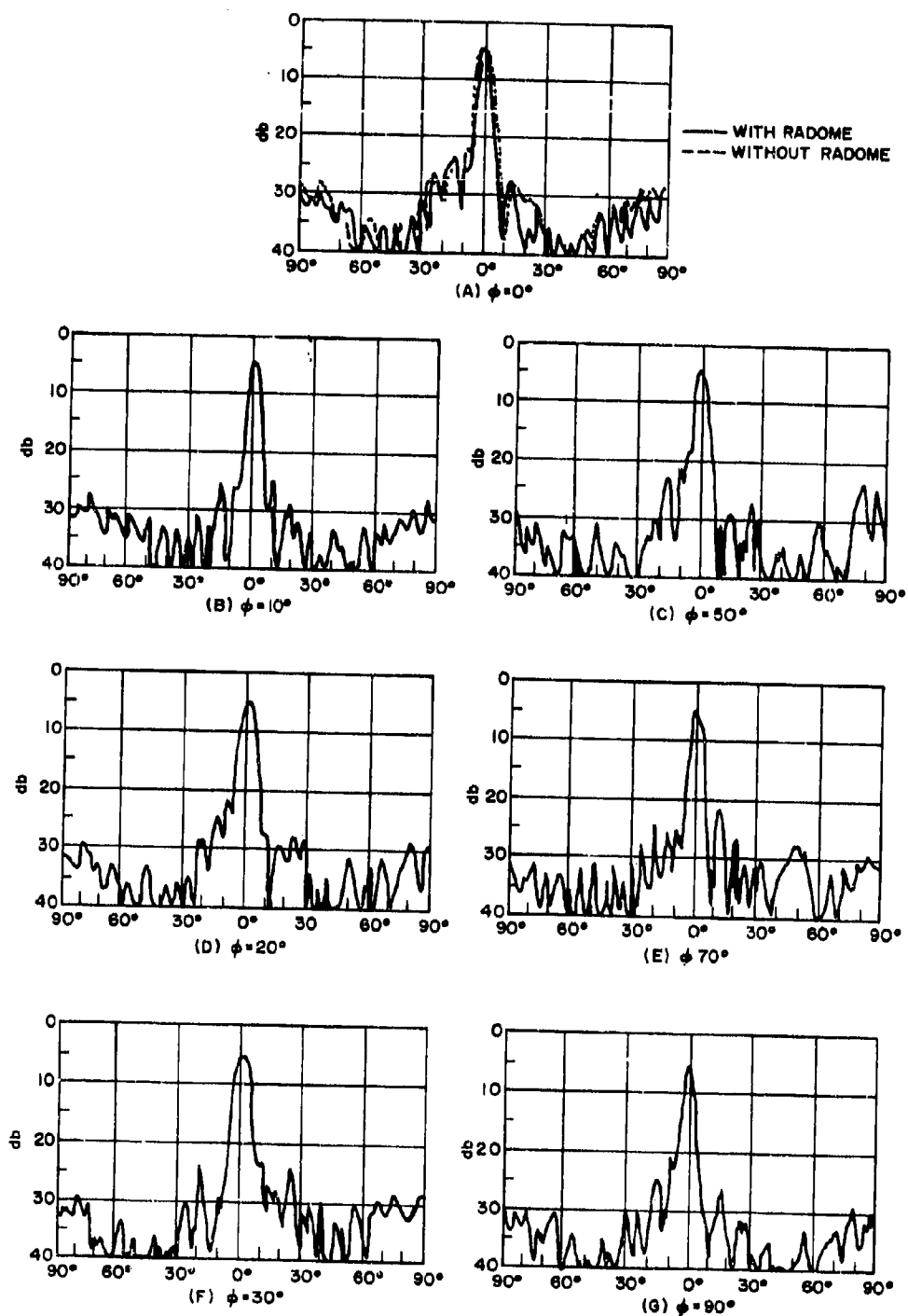


Figure 2-49. Antenna Patterns of Metal Radome at 4.875 gc Taken at Different Scan Angles,  $\phi$

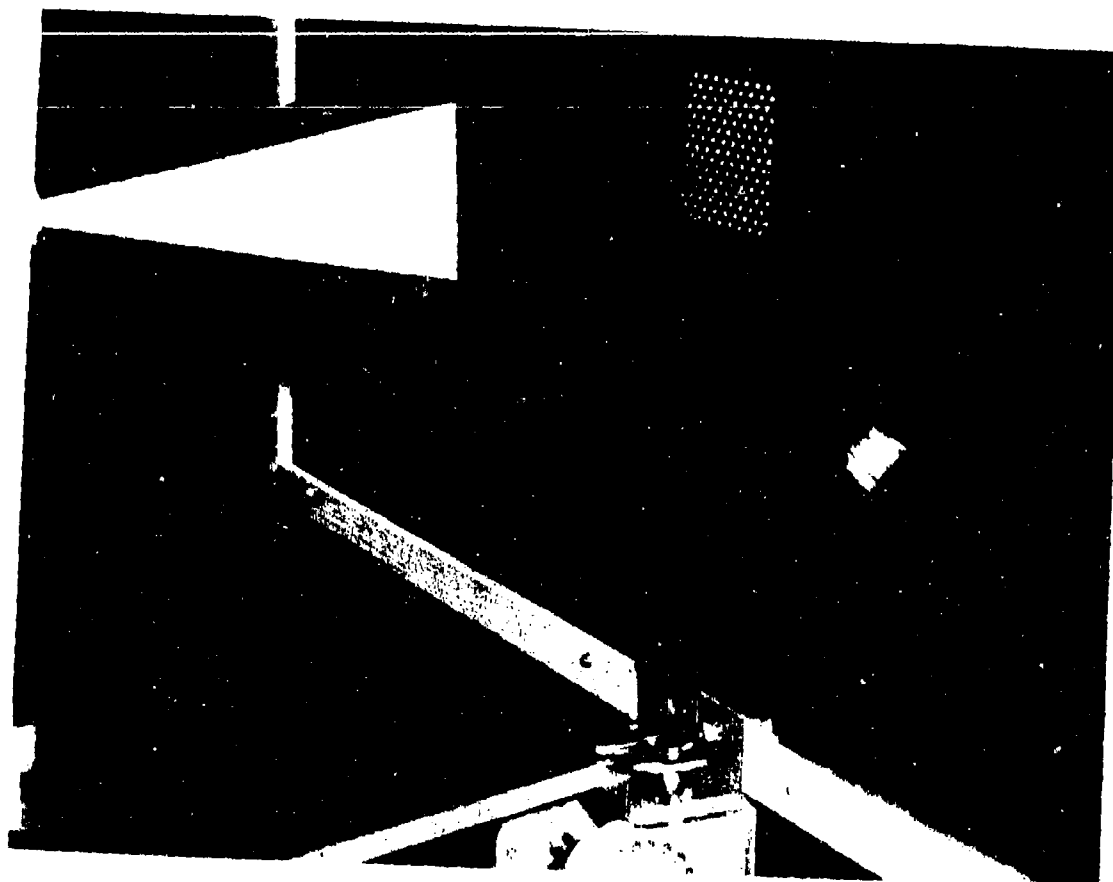


Figure 2-50. Plane Version of Dipole Feed-Through Radome with Pyramidal Horn

on the assumption of perfect conductivity in the dipoles and the ground plane. The data in this figure are not intended to represent a realistic situation because they apply only if the impedances in the array are readjusted to maintain a conjugate match at each new scan angle. In practice, the impedances would no doubt be adjusted for maximum transmission efficiency at one particular angle of incidence. Thus, a mismatch would occur at other scan angles, resulting in an efficiency lower than that shown in the figure.

## 2-6 BROADBAND RADOME DESIGN

A combination of extremely large bandwidth and low boresight error is difficult to obtain in a streamlined radome with high-temperature capabilities, but fortunately, such a combination

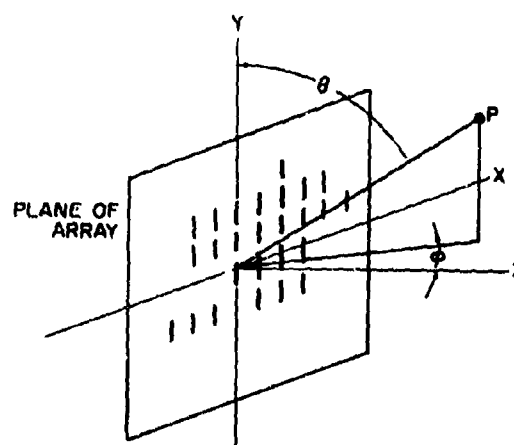


Figure 2-51. Coordinate System for Dipole Array



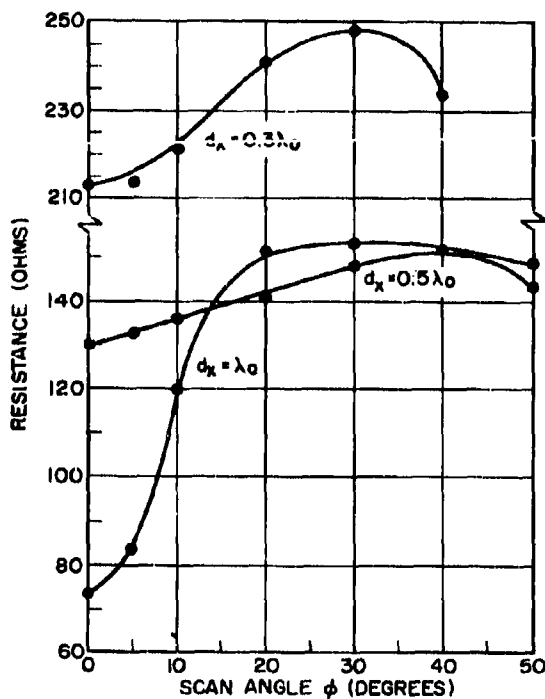


Figure 2-52. Driving-Point Resistance vs Scan Angle for Large Arrays

is seldom required. Streamlined boresight radomes generally operate at a single frequency or over a rather narrow band, but a broadband, streamlined, low-boresight radome will find considerable demand if it can be developed. At the present time, radomes with extreme bandwidths are employed chiefly in electronic countermeasures (ECM) systems, where boresight error is unimportant.

The term *broadband radome* may have different implications in different situations. It may imply a bandwidth of 10 gc or more in an ECM system, or a bandwidth of, say, 500 kc in a streamlined boresight radome operated at 10 gc.

Some of the wall structures proposed for broadband radomes are multilayer sandwiches, inhomogeneous layers, anisotropic media, metal-loaded structures, and tunable radomes. Several of these structures are discussed in the following paragraphs, with emphasis, in most cases, on high transmission over a range of frequencies, angles of incidence, and polarizations.

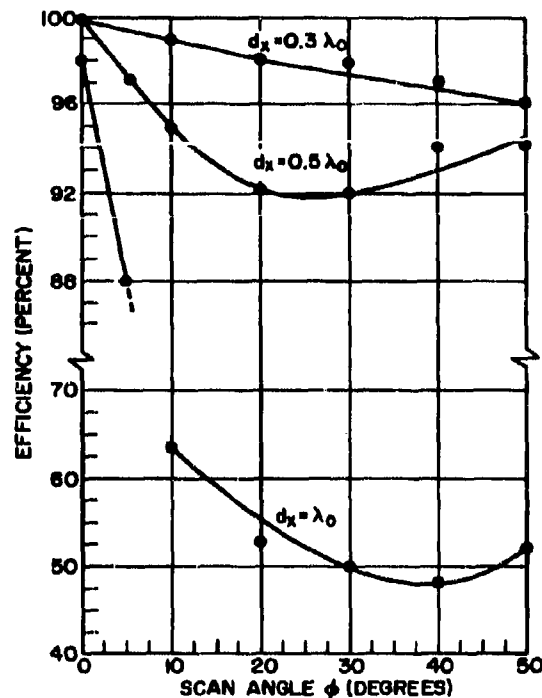


Figure 2-53. Efficiency vs Scan Angle for Impedance-Matched Arrays

## 2-6.1 BANDWIDTH OF SOLID-WALL RADOMES

Reference 54 presents the results of the study of the bandwidth of solid-wall radomes. Figure 2-54 illustrates the transmission coefficient as a function of frequency for a lossless solid-wall radome and shows the bandwidth for a thin wall and a half-wave wall for a given minimum allowable transmission coefficient. The bandwidth of a given lossless wall operated as a half-wave layer is twice the bandwidth it has as a thin wall. Figures 2-55 and 2-56 show the product of the thickness and the bandwidth as a function of angle of incidence for lossless thin walls with perpendicular and parallel polarization, respectively. Reference 54 also gives bandwidth curves for solid walls with dielectric constants from 1.1 to 20.0, and the percent reduction in bandwidth in low-loss solid walls.

In general, the bandwidth for maximum transmission coefficient can be increased by decreasing the dielectric constant, the thickness, the loss tangent, and the angle of incidence. For parallel polarization, the bandwidth can be in-

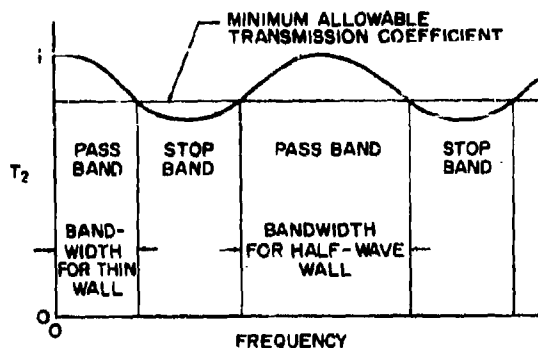


Figure 2-54. Transmission Coefficient vs Frequency for Lossless Solid-Wall Radome, Showing Pass Bands, Stop Bands, and Bandwidth

creased by choosing the dielectric constant such that the Brewster angle falls within the operating range of angles of incidence.

Figures 2-57 and 2-58 are figure-of-merit contour maps for lossless solid walls for perpendicular and parallel polarization, respectively (Reference 55). The figure of merit is taken to be the minimum power transmission coefficient for a given angle of incidence as the frequency is varied over a broad range. These maps are convenient for determining at a glance the useful range of angles of incidence for a solid wall with a given dielectric constant and a prescribed minimum power transmission coefficient. In a system requiring an extremely large bandwidth, the radome operates as a one-quarter-wave radome with minimum transmission at some frequencies in the band. Therefore, the radome

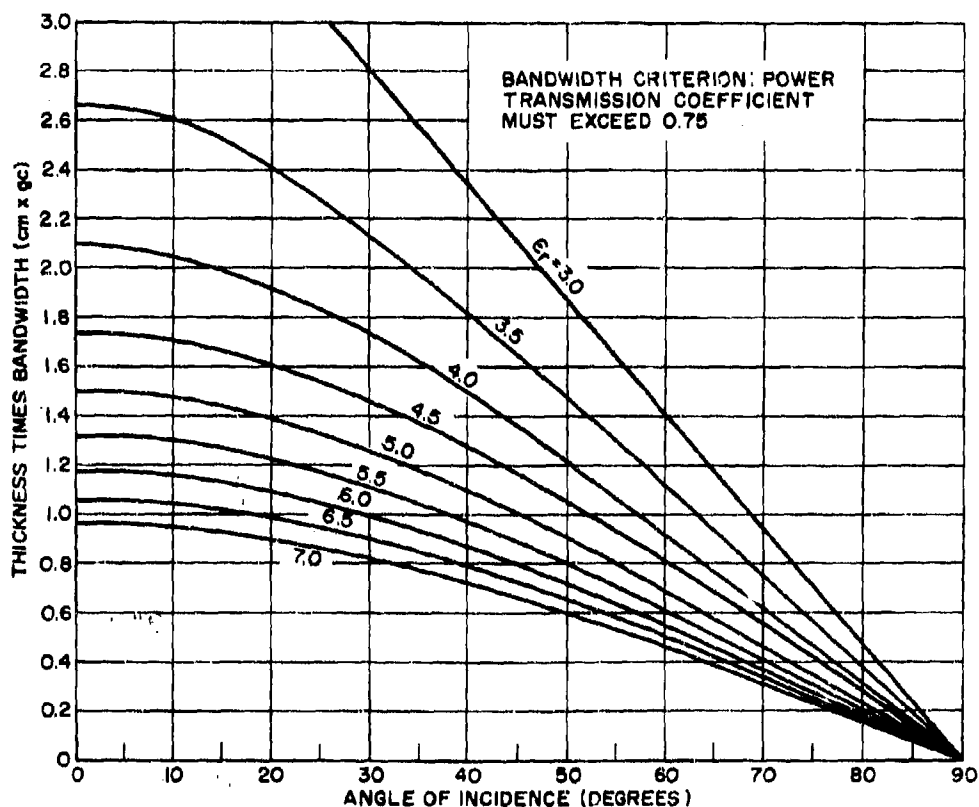


Figure 2-55. Thickness Times Bandwidth for Lossless Thin-Wall Radomes with Perpendicular Polarization

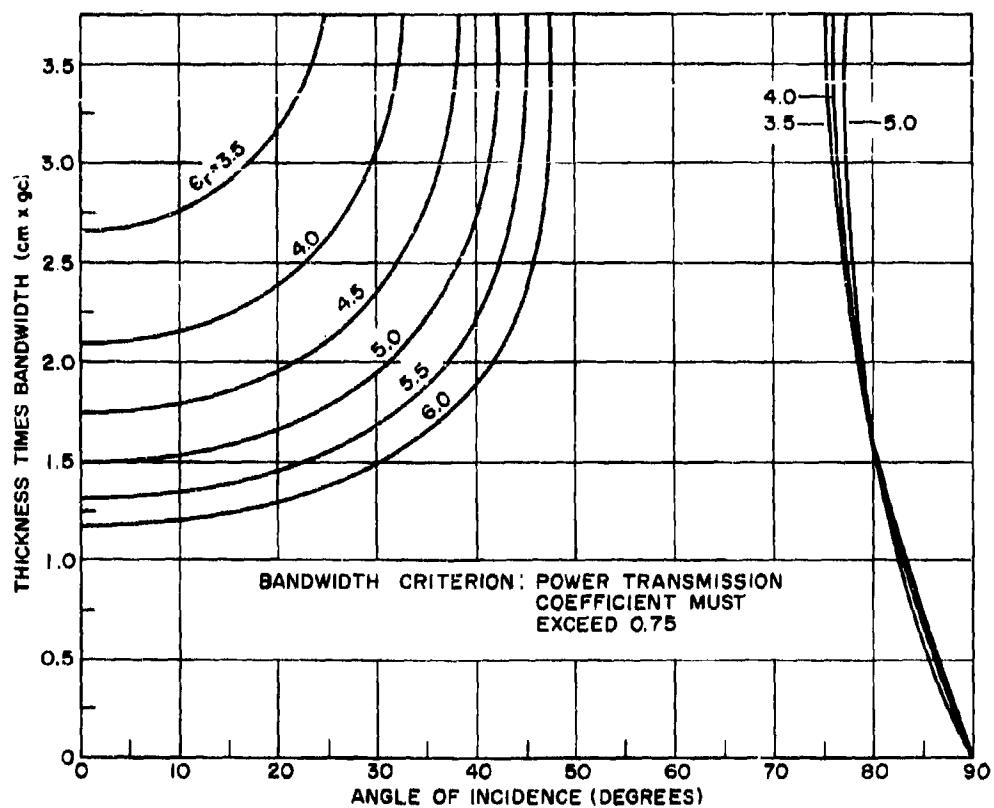


Figure 2-56. Thickness Times Bandwidth for Lossless Thin-Wall Radomes with Parallel Polarization

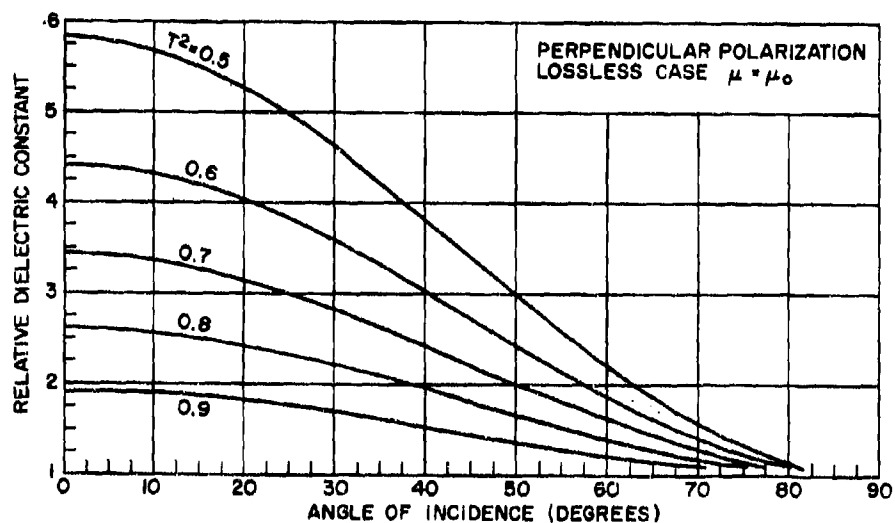


Figure 2-57. Contours of Minimum Power Transmission Coefficient over Broad Frequency Band for Solid-Wall Radomes with Perpendicular Polarization

thickness need not be known in using the contour maps in Figs. 2-57 and 2-58. Figure 2-59 illustrates the transmission properties of a thin-wall radome as a function of frequency for normal and oblique incidence.

A thin-wall radome has high transmission at all frequencies from zero to the upper limiting frequency, where the thickness is no longer a small fraction of the wavelength. Thus, as the radome thickness is decreased, its upper frequency limit increases and the bandwidth is increased. However, mechanical strength requirements put a lower limit on the radome thickness, and this generally prevents the use of thin-wall radomes at frequencies above 15 gc. The upper frequency limit of the thin-wall radome is determined by its low transmission efficiency for perpendicular polarization at high angles of incidence. The upper frequency limit can be extended somewhat by pressurization to improve the mechanical strength and by arrangements that maintain parallel polarization for all scan angles.

It would seem that the upper frequency limit of the thin-wall radome could also be extended by employing a material whose dielectric constant is a function of the frequency, decreasing as the frequency increases. Many materials are

known to have this property, including bakelite, laminated fiberglass, neoprene compound, porcelain, and plexiglass. These are rather high-loss materials, with the exception of laminated fiberglass. Artificial dielectric media, such as those loaded with metallic dielectric particles or constructed of alternate thin layers of high and low dielectric constants, also have effective dielectric constants that vary with the frequency. These materials might provide some increase in the bandwidth of the thin-wall radome while maintaining the required mechanical strength.

## 2-6.2 BROADBAND THREE-LAYER SANDWICHES

A study of unsymmetrical three-layer sandwiches is presented in Reference 56. At a single frequency, the transmission coefficient and insertion phase delay were calculated as a function of angle of incidence for sandwiches having unequal skin thicknesses and dielectric constants. The results of a large number of calculated cases indicate that the unsymmetrical three-layer sandwich has no advantage over the symmetrical sandwich with respect to transmission efficiency or phase delay.

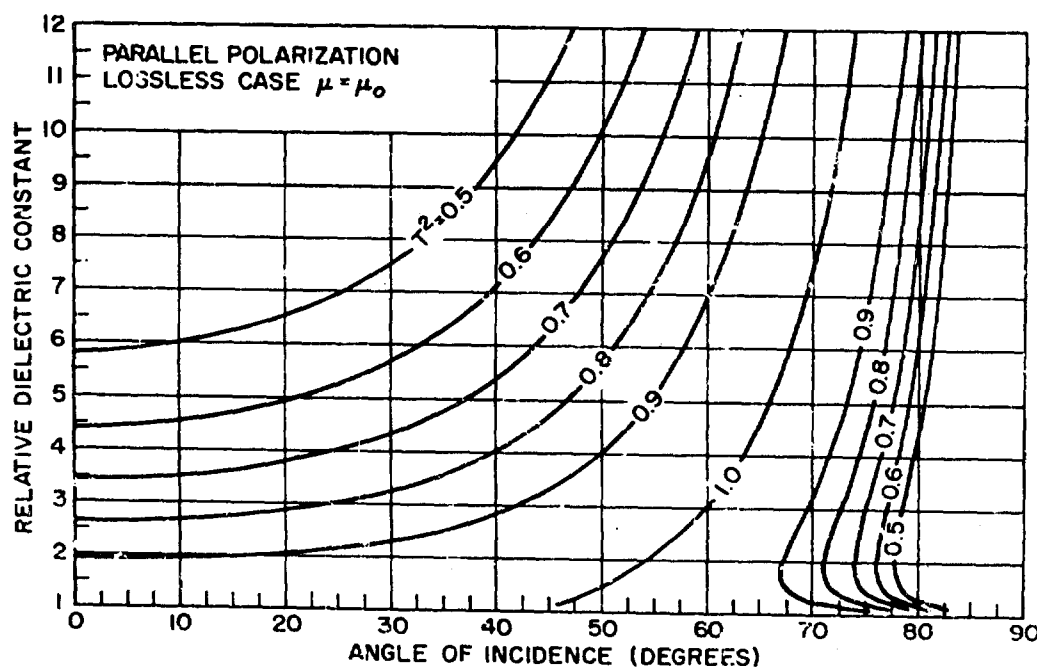


Figure 2-58. Contours of Minimum Power Transmission Coefficient over Broad Frequency Band for Solid-Wall Radomes with Parallel Polarization

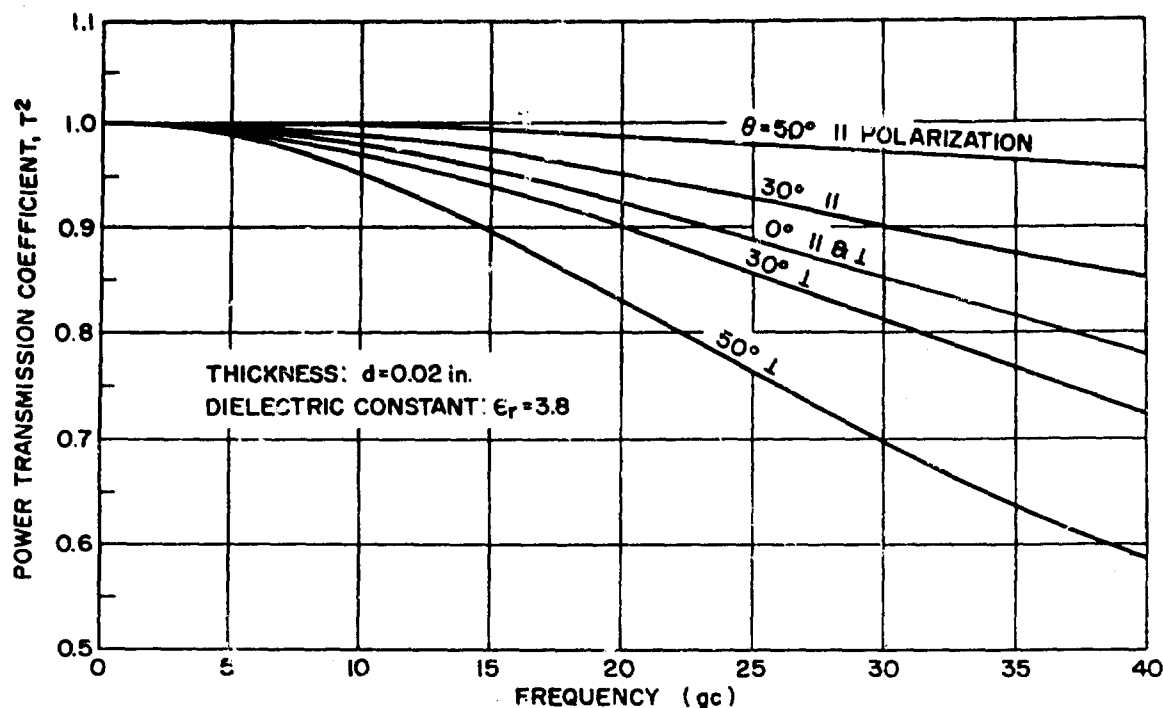


Figure 2-59. Power Transmission Coefficient vs Frequency for Thin-Wall Radomes

Reference 57 presents the results of a study of the broadband properties of "A" sandwiches using a core material having a very low dielectric constant. It was found that an "A" sandwich can be designed to operate efficiently over a frequency band from 0 to 20 gc for rather large angles of incidence, and from 0 to 60 gc for small angles of incidence. As in the thin-wall radome design, the bandwidth of the "A" sandwich increases as the skins are made thinner. Thus, mechanical strength requirements again limit the bandwidth obtainable. To make a valid comparison of the broadband properties of the thin-wall radome and the "A" sandwich, it would be necessary to enforce the same impact strength and flexural strength requirements on both structures.

Figures 2-60, 2-61, and 2-62 show the transmission properties of an "A" sandwich as a function of frequency for normal and oblique incidence (Reference 57). It may be noted that the upper frequency limit occurs when the skin thickness is no longer a small fraction of the wavelength, and the transmission efficiency becomes quite poor for perpendicular polarization at large angles of incidence. From the study,

simplified design equations for "A" sandwiches were derived.

Reference 58 describes the design of an "A" sandwich for a broadband ECM wing-pod radome. The sandwich has a total thickness of 0.7 in., including a 0.01-in. layer of neoprene for rain-erosion protection. An epoxy preimpregnated glass cloth was used for the skins. The core is a preformed nylon phenolic honeycomb material with 3/16-in. cells. No information is given on the bandwidth, layer thicknesses, or dielectric constants.

### 2-6.3 BROADBAND MULTILAYER SANDWICHES

Reference 59 presents the development of two techniques for synthesizing a multilayer sandwich so that it has a specified transmission coefficient over a given frequency range. Reference 58 describes the design of broadband sandwiches having 7 and 11 layers. Reference 60 presents the investigation of computer optimization of broadband multilayers. Case 1 is an attempt to broadband a 12-layer wall from 10 to 26 gc, starting from a highly unacceptable structure. The merit function is simply the

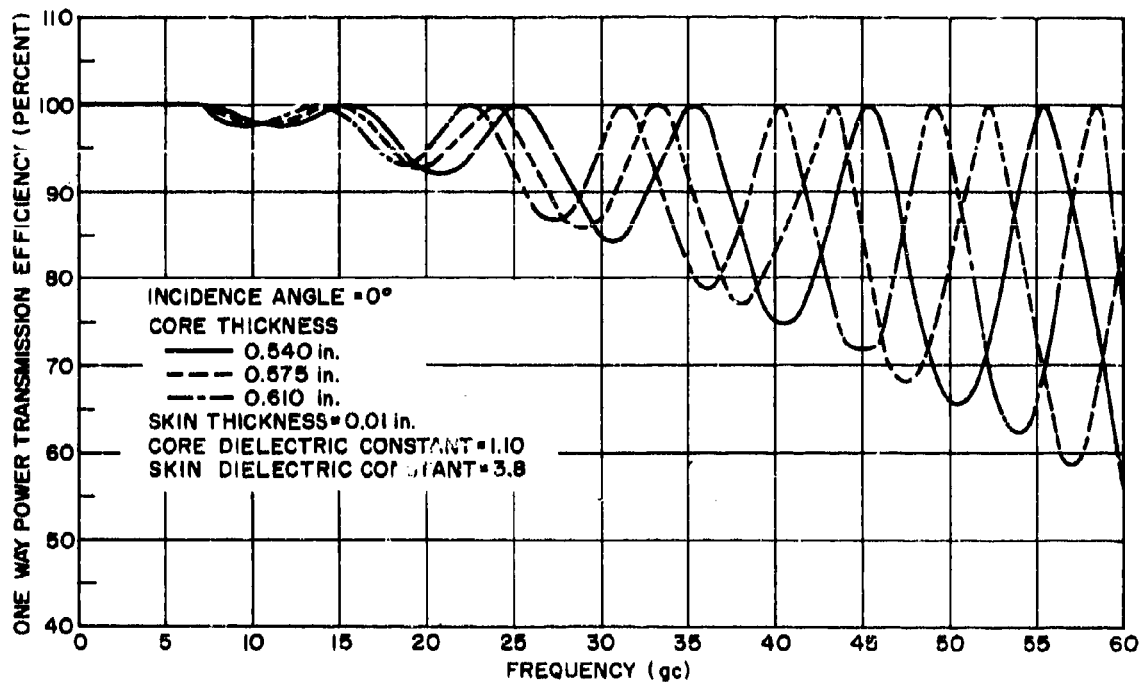


Figure 2-60. Power Transmission Coefficient vs Frequency for Lossless "A" Sandwich with Normal Incidence

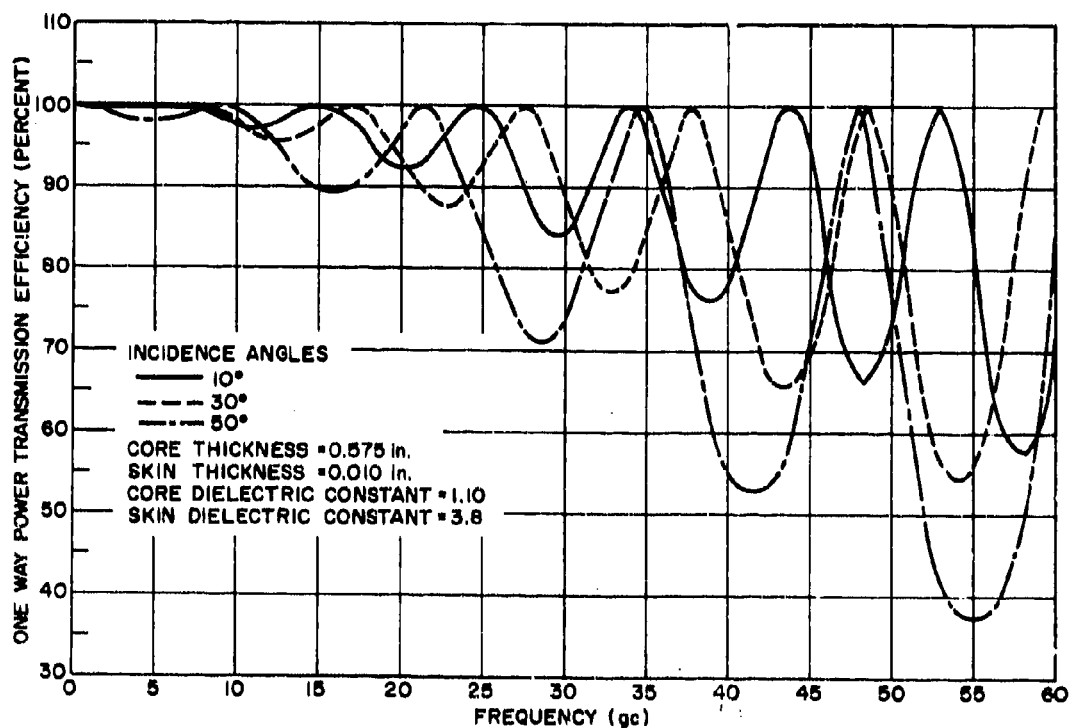


Figure 2-61. Power Transmission Coefficient vs Frequency for Lossless "A" Sandwich with Oblique Incidence and Perpendicular Polarization

total unweighted sum of the perpendicular transmission coefficients with steps of 5 gc in frequency and  $10^\circ$  in incidence angle from  $0^\circ$  to  $70^\circ$ . The initial transmission volume is shown pictorially in Fig. 2-63. The outer layer is a rain-erosion coating with a dielectric constant of 2.99 and a thickness of 0.01 in. The variables are the thicknesses of the 11 remaining layers. Although an optimum design was not achieved because of excessive computer time, the final design is considerably superior to the initial one. The final transmission volume is pictured in Fig. 2-64, and the initial and final parameter values are listed in Table 2-3.

In case 2, the broadband requirements, merit function, and outer rain-erosion coating are identical to case 1. The variables are the dielectric constants of layers 2 through 12. The entire set of parameters is listed in Table 2-4. The minimum and maximum allowed values for the core and skin dielectric constants are 1.1 to 1.4 and 3.8 to 4.4, respectively. The total computer time for the optimization was 0.5 hr with an IBM 7090 computer. Figure 2-65 depicts the rate of improvement with time. As is common

to most problems using the dielectric constants as variables, the program ran smoothly. However, the long slow rate of change near the end, which persisted regardless of efforts to accelerate the process, exemplifies a region of diminishing returns. Peaking-up the final structure can be costly, considering the large amount of computer time necessary to produce a small improvement in the average transmission.

Cases 3 through 6 involve optimizing the average transmission over a discrete set of frequencies. Case 3 is essentially the same as case 2, except that the structure is evaluated at three discrete frequencies (12, 20, and 28 gc). The initial and final parameters are shown in Fig. 2-66. Cases 4 through 6 attempt to maximize the average transmission at 10, 16, 25, and 35 gc. The initial and final configurations and time history for case 4 are shown in Figs. 2-67 and 2-68, respectively. The outer layer was held constant at a thickness of 0.015 in., a dielectric constant of 5.5, and a loss tangent of 0.001. The variables were the remaining dielectric constants, which were constrained between 2.2 and 9.0. Case 6 is identical with case 4 except for

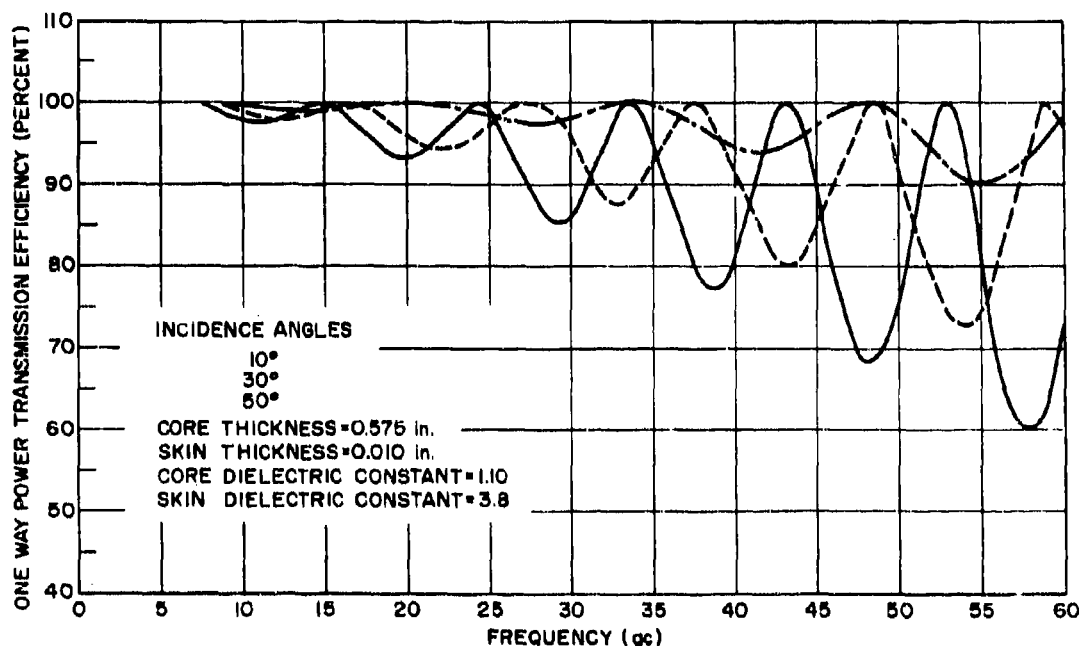


Figure 2-62. Power Transmission Coefficient vs Frequency for Lossless "A" Sandwich with Oblique Incidence and Parallel Polarization

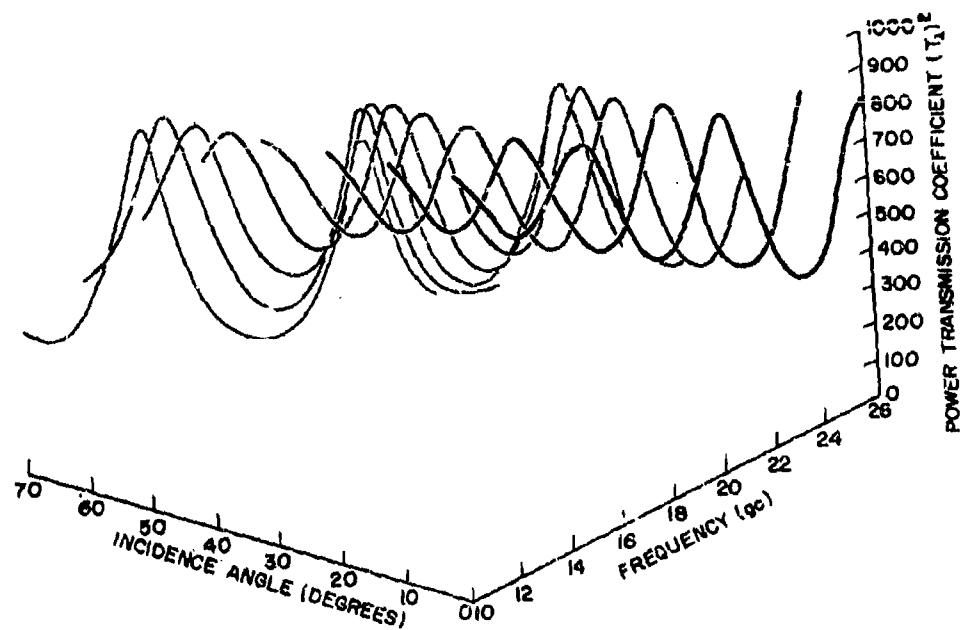


Figure 2-63. Initial Transmission Volume for Case 1

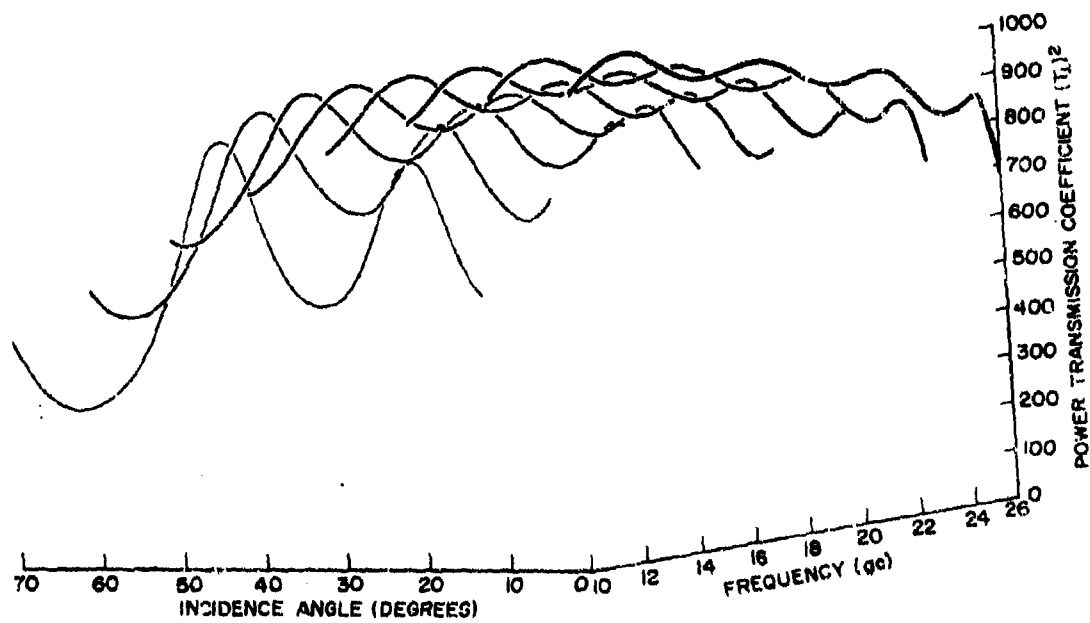


Figure 2-64. Final Transmission Volume for Case 1



the addition of five layers. The initial and final characteristics are shown in Fig. 2-69. The basic structure for case 5 is the same as that for case 4, except the variables are the thicknesses of layers 2 through 5. The thicknesses all have the minimum of 0.01 in. The initial and final characteristics are shown in Fig. 2-70.

Additional information on broadband radome sandwiches is available in References 61, 62, and 63.

#### 2-6.4 SURFACE TREATMENT FOR REDUCED REFLECTION

The broadband properties of a radome may be improved by treating the surfaces to reduce the interface reflection coefficients. One possibility is to cut shallow notches, or grooves, in the surfaces to simulate a surface layer having a low effective dielectric constant (References 65, 66, and 67). To obtain a suitable outer surface, the grooves may be filled with a material having a relatively low dielectric constant.

An array of thin, circular, metal disks has been employed to reduce reflections at the surfaces of dielectric lenses (References 68 and 69). This technique might also prove useful in radome design.

#### 2-6.5 BROADBAND METAL-LOADED RADOMES

Electronic countermeasure equipment in a

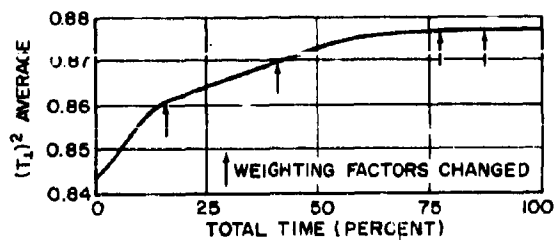


Figure 2-65. Time History for Case 2

supersonic airplane requires a large radome having high strength and high transmission efficiency over a wide band of frequencies (Reference 69). When a solid wall of homogeneous material is used for an ECM radome, the transmission is low at certain frequencies, as shown in Fig. 2-71. If a single sandwich is made with thick skins to obtain the necessary structural integrity, similar poor performance is obtained (Fig. 2-72). The curves for this figure are for an incidence angle of 60°; the situation is increasingly worse as the angle of incidence is increased. In many applications, the angles of incidence are in the range of 40° to 80°.

A strong, broadband sandwich may be realized by employing thick skins in which are embedded wire grids, as shown in Fig. 2-73. For example, Fig. 2-74 shows the performance of such a metal-loaded sandwich for perpendicular polarization with the wires perpendicular to the plane of incidence. The skin thickness

TABLE 2-3 PARAMETER VALUES FOR CASE 1

Layer	$\epsilon_r$	$\tan \delta$	Initial $d$	Final $d$
1	2.99	0.005	0.010	0.010
2	4.10	0.014	0.030	0.020*
3	1.20	0.005	0.150	0.090
4	4.10	0.014	0.010	0.035
5	1.20	0.005	0.150	0.104
6	4.10	0.014	0.010	0.023
7	1.20	0.005	0.150	0.146
8	4.10	0.014	0.010	0.018
9	1.20	0.005	0.150	0.125
10	4.10	0.014	0.010	0.025
11	1.20	0.005	0.150	0.118
12	4.10	0.014	0.030	0.020*
<hr/>				
$ T_{\perp} ^2$	Average		0.8039	0.7911
$ T_{\parallel} ^2$	Average		0.8009	0.8018
$ T_{\perp} ^2$	Minimum		0.0911	0.2793
$ T_{\parallel} ^2$	Minimum		0.4016	0.6345

\* Constrained Value.

TABLE 2-4 PARAMETER VALUES FOR CASE 2

Layer	$d$	$\tan \delta$	Initial $\epsilon_r$	Final $\epsilon_r$
1	0.010	0.005	2.99	2.99
2	0.010	0.014	4.1	3.80*
3	0.138	0.005	1.2	1.10*
4	0.010	0.014	4.1	4.40*
5	0.138	0.005	1.2	1.39
6	0.010	0.014	4.1	4.19
7	0.138	0.005	1.2	1.40*
8	0.010	0.014	4.1	4.18
9	0.138	0.005	1.2	1.32
10	0.010	0.014	4.1	3.80*
11	0.138	0.005	1.2	1.10*
12	0.010	0.014	4.1	3.80*
<hr/>				
$ T_{\perp} ^2$	Average		0.8436	0.8761
$ T_{\parallel} ^2$	Average		0.9138	0.9172
$ T_{\perp} ^2$	Minimum		0.4479	0.6343
$ T_{\parallel} ^2$	Minimum		0.8036	0.7991

\* Constrained Value.

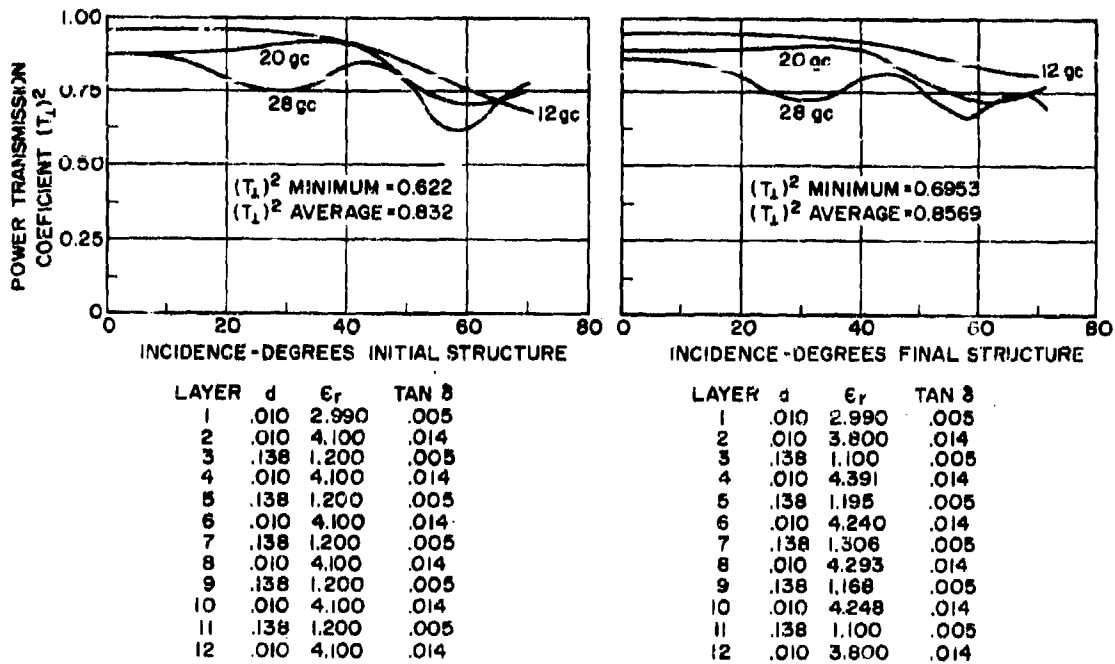


Figure 2-66. Transmission Curves for Case 3

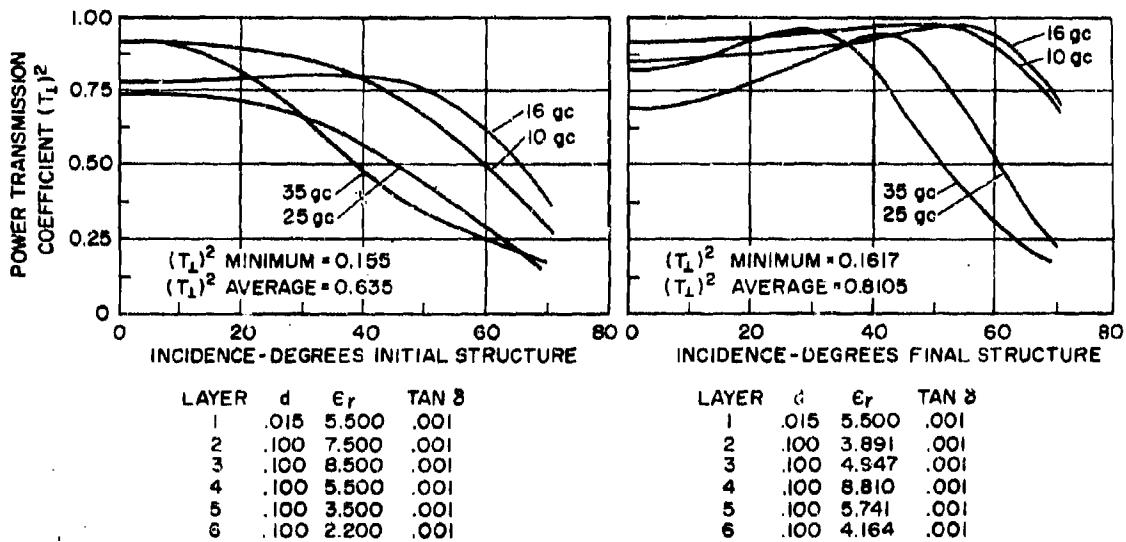


Figure 2-67. Transmission Curves for Case 4

is 0.1 in., the skin dielectric constant is 4, and the wires are copper with a diameter of 0.01 in. Figure 2-74A shows the transmission efficiency for a single skin loaded with a wire grid. The reflection from a single skin is seen to be only about 5% at 12 gc; the maximum reflection from the corresponding sandwich at 12 gc is then about 10%, leaving a power transmission efficiency of about 90%. At 16 gc, the reflection from the single skin will be about 50%.

By separating the identical skins by a low-dielectric-constant core at a distance such as to cancel the reflections from the individual skins at 16 gc, the net reflection from the sandwich can be made very low at this frequency. At frequencies between 12 and 16 gc, the reflection will be greater than at either 12 or 16 gc, but will be small. The performance of this sandwich is expected to be roughly as shown in Fig. 2-74B. It can be further reasoned that if the core is made such a thickness as to affect skin reflection cancellation at a low frequency, such as 8 gc, cancellation will also be obtained at 16 gc. The resulting curve should then be similar to that shown in Fig. 2-74C.

Figure 2-75 shows experimental curves for thick-skin sandwiches with wire grids of this type. These curves do reveal the principal features predicted in the theoretical curves of Fig. 2-74. The power transmission efficiency of the sandwiches approaches 90% at 12 gc. The curves dip on either side of this mid-frequency and peak again at approximately 8 and 16 gc. These experimental sandwiches of  $30 \times 48$  in. polystyrene foam cores were not designed panels, but ones whose construction is based on limited laboratory cut-and-try efforts. It is reasonably certain that a curve such as the dotted-

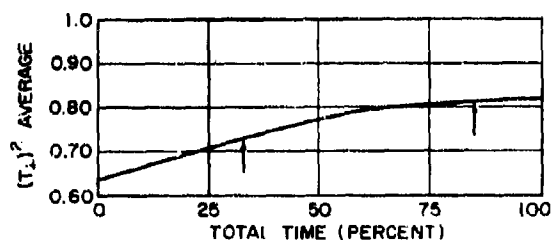


Figure 2-68. Time History for Case 4

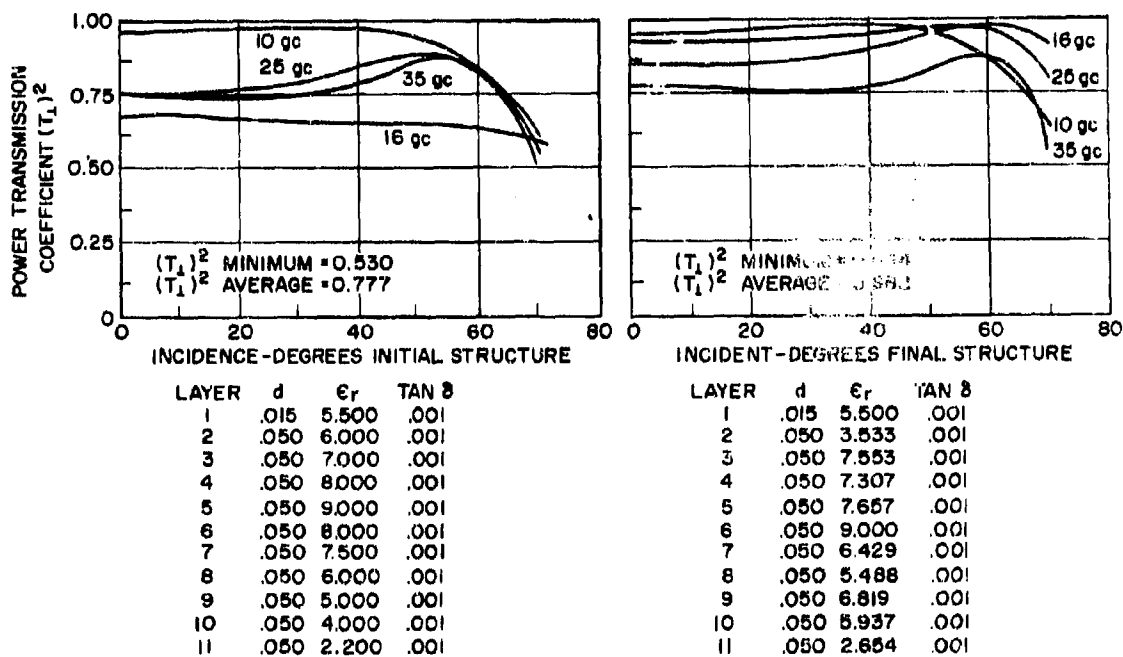


Figure 2-69. Transmission Curves for Case 6

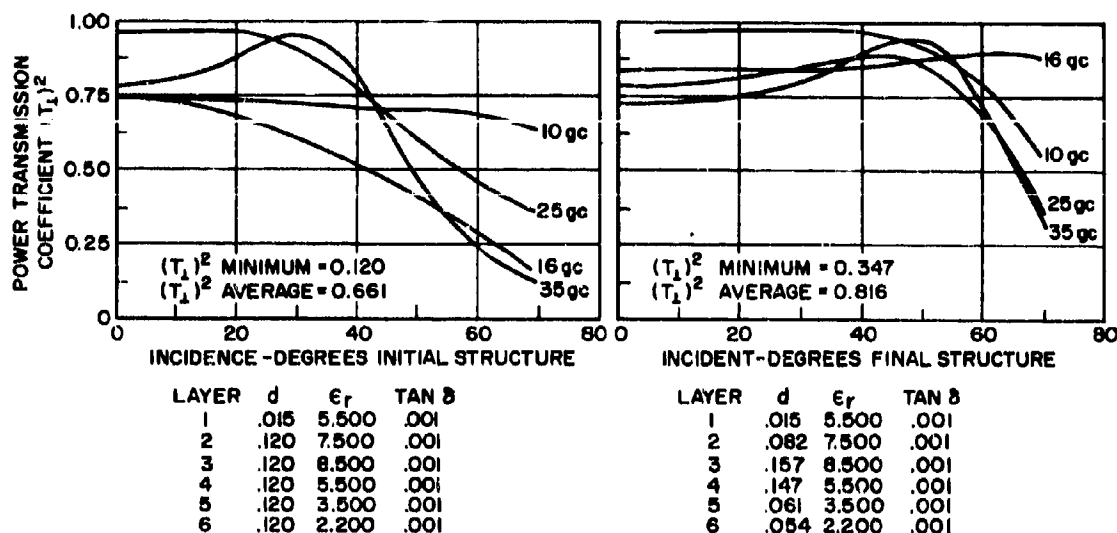


Figure 2-70. Transmission Curves for Case 5

line curve of Fig. 2-75 could be obtained by using a properly designed thick-skin radome with wire grids. If perpendicular polarization is maintained in such a way that the electric vector is parallel with the embedded wires, the performance shown in Fig. 2-75 may be expected. The performance has not yet been adequately investigated for parallel polarization or for perpendicular polarization with the electric vector misaligned with respect to the wires.

The characteristics of solid-wall radomes loaded with wire grids are described in References 70 to 73. Reference 73 shows that a solid-wall radome with a wire grid at the center can

be designed to have good broadband characteristics for both parallel and perpendicular polarization at angles of incidence up to the Brewster angle. Reference 73 discusses the fabrication of such radomes.

#### 2-6.6 INHOMOGENEOUS RADOMES

In theory, a continuously inhomogeneous ra-

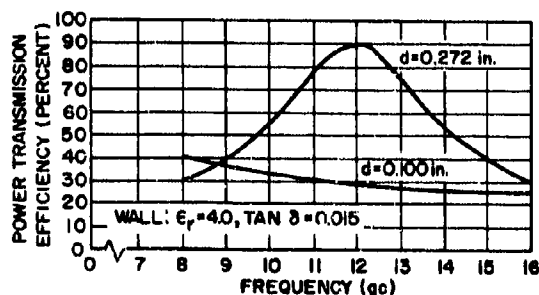


Figure 2-71. Transmission Curves for Solid-Wall Radome with 60° Angle of Incidence and Perpendicular Polarization

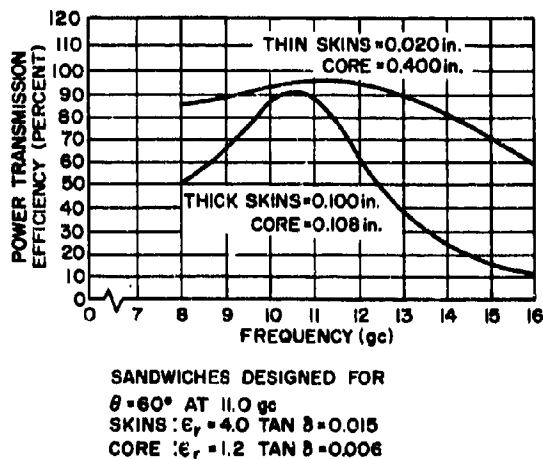


Figure 2-72. Transmission Curves for Single "A" Sandwich Radome with 60° Angle of Incidence and Perpendicular Polarization

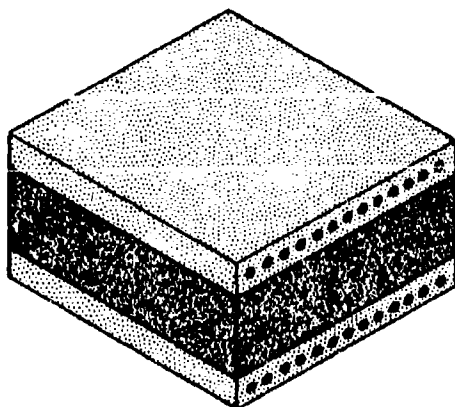


Figure 2-73. Impedance-Matched Thick-Skin Single Sandwich

dome may be achieved by variable loading with tiny metallic or dielectric particles. An adequate approximation can be obtained by constructing the radome of a large number of thin homogeneous laminations, each having a dielectric constant that differs slightly from that of the next layer. It is also possible to employ a variable-density foam to realize the desired effect. At the present time, however, it appears that no satisfactory method has been perfected for manufacturing an inhomogeneous radome with a specified dielectric-constant function to a high degree of accuracy. Nevertheless, a theoretical

study of inhomogeneous radomes is justified by the excellent broadband characteristics that can be obtained and the hope that a suitable manufacturing technique will eventually be developed.

Although exact analytic solutions have been obtained for the linearly inhomogeneous radome and for a few other cases, approximate or numerical solutions must be used to calculate the transmission coefficient of an inhomogeneous layer having an arbitrary dielectric-constant variation as a function of distance through the layer. If the dielectric constant is a slowly varying function, accurate results are provided by the WKB solution with a minimum of computation. The WKB solution for the transmission coefficient of an inhomogeneous layer, for both perpendicular and parallel polarization, is given by Reference 14 as follows:

$$T = \frac{\sqrt{(1-r_a^2)(1-r_i^2)}}{(e^{\alpha} - r_a r_i e^{-\alpha}) \cos \beta + j(e^{\alpha} + r_a r_i e^{-\alpha}) \sin \beta} \quad (2-3)$$

where

$$\alpha = (k_0/2) \int_0^d \frac{\epsilon_r \tan \delta \, dz}{\sqrt{\epsilon_r - \sin^2 \theta}}$$

$$\beta = k_0 \int_0^d \sqrt{\epsilon_r - \sin^2 \theta} \, dz$$

$r_a + r_i$  = interface reflection coefficients at the two surfaces of the inhomogeneous layer (the surface and the incidence surface).

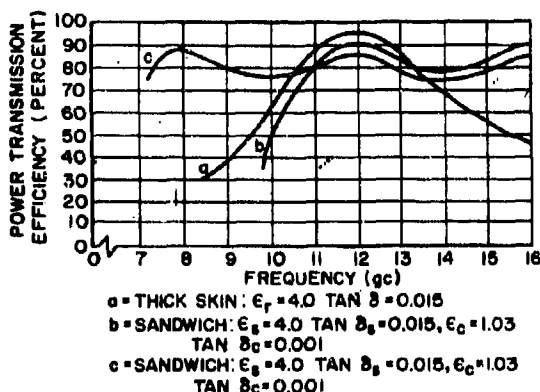


Figure 2-74. Transmission Curves for Impedance-Matched Thick-Skin Sandwich Radoms with 60° Angle of Incidence and Perpendicular Polarization

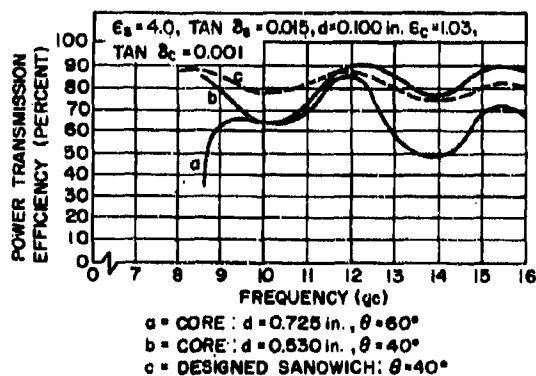


Figure 2-75. Transmission Curves for Impedance-Matched Thick-Skin Sandwich Radome with Wires Parallel to Electric Vector, Perpendicular Polarization

For perpendicular polarization:

$$r_e = \frac{\cos \theta - \sqrt{\epsilon_e - \sin^2 \theta}}{\cos \theta + \sqrt{\epsilon_e - \sin^2 \theta}} \quad (2-4)$$

$$r_i = \frac{\cos \theta - \sqrt{\epsilon_i - \sin^2 \theta}}{\cos \theta + \sqrt{\epsilon_i - \sin^2 \theta}} \quad (2-5)$$

For parallel polarization:

$$r_e = \frac{\epsilon_e \cos \theta - \sqrt{\epsilon_e - \sin^2 \theta}}{\epsilon_e \cos \theta + \sqrt{\epsilon_e - \sin^2 \theta}} \quad (2-6)$$

$$r_i = \frac{\epsilon_i \cos \theta + \sqrt{\epsilon_i - \sin^2 \theta}}{\epsilon_i \cos \theta - \sqrt{\epsilon_i - \sin^2 \theta}} \quad (2-7)$$

where  $d$  = thickness of the layer  
 $z$  = distance into the inhomogeneous layer from one surface  
 $\epsilon_e$  = complex relative dielectric constant, exit surface  
 $\epsilon_i$  = complex relative dielectric constant, incidence surface  
 $\epsilon_r$  = complex relative dielectric constant  
 $= \epsilon_r - j\epsilon_r \tan \delta$   
 $k_0$  = phase constant of free space  
 $= \omega \sqrt{\mu_0 \epsilon_0}$   
 $\theta$  = angle of incidence

The permeability of the layer is assumed to be the same as that of free space and the dielectric constant is assumed to be a continuous function of  $z$  only, except for the discontinuities at both surfaces.

The WKB solution just described may become inaccurate if the dielectric constant is a rapidly varying function. A more general solution, valid even for rapidly varying dielectric constants, is provided by a numerical technique known as *step-by-step numerical integration*. Reference 75 employs this method in the analysis of the lossless and low-loss inhomogeneous radome for both parallel and perpendicular polarization.

As an example, step-by-step numerical integration has been used to calculate the transmission coefficient vs. angle of incidence for an exponentially inhomogeneous layer. The results are shown in Fig. 2-76 and Table 2-5, along with the WKB solution and the exact transmission coefficient of a seven-layer radome that approximates the exponential dielectric constant of the inhomogeneous layer. It may be observed that the three solutions have close agreement for this particular example. In general, it is believed that the step-by-step numerical integration provides the best combination of accuracy and com-

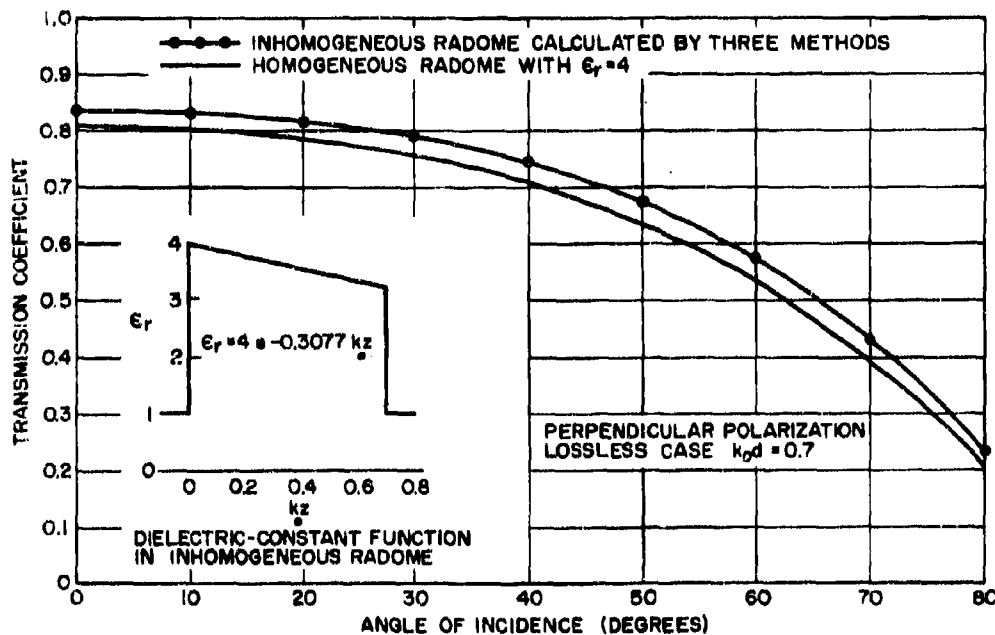


Figure 2-76. Transmission Coefficient vs Angle of Incidence for Homogeneous and Inhomogeneous Radomes

putational economy for the analysis of inhomogeneous layers. Although derived independently and from different approaches, the WKB solution in Reference 74 and the solution in Reference 76 are quite similar.

Reference 77 shows that an inhomogeneous broadband radome, which eliminates the limitation on the bandwidth of solid-wall radomes and sandwiches, is limited by interference among the interface reflections that occur at the surface of the various layers. Thus, an improvement in bandwidth may be achieved by avoiding discontinuous transitions from one medium into another. The use of such inhomogeneous layers for microwave radomes has been investigated theoretically and experimentally and presented in Reference 65. One case shows that the dielectric constant increases linearly from some initial value  $\epsilon_1$  at the front face to a maximum value  $\epsilon_m$  at the center of the layer, and then decreases again linearly to  $\epsilon_1$  at the rear face. For normal incidence, the calculation of the reflection from such a wall of total thickness  $2T$  is a straightforward boundary value problem. The solution for the electric and magnetic fields in the linearly inhomogeneous layer is readily expressed in terms of the Hankel functions of order one-third.

The simplest situation arises when there is no initial discontinuity (i.e.,  $\epsilon_1 = 1$ ). The reflection coefficient is plotted for this case as a function of frequency in Fig. 2-77 by assuming  $\epsilon_m = 2.5$ . For comparison, the reflection from a homogeneous layer with a dielectric constant of 2.5 is also shown. For relatively thin inhomogeneous layers, the gradient in the dielectric constant is large and substantial reflection arises. With increasing  $k_0T$ , maxima and minima occur alternately, which follow, in general, the pattern exhibited by the homogeneous wall, except that the maxima are much lower for the inhomogeneous wall.

To obtain more suitable surfaces from a mechanical or aerodynamical point of view, it may be necessary to have discontinuities in the dielectric constant at the surfaces. Therefore, Fig. 2-77 also shows the results for a linearly inhomogeneous radome with  $\epsilon_1 = 1.2$ . The reflection peaks are somewhat increased in this case. Improved characteristics can be obtained by attaching a thin homogeneous dielectric layer to the outside surface of the inhomogeneous ra-

TABLE 2-5 TRANSMISSION COEFFICIENT OF LOSSLESS INHOMOGENEOUS LAYER WITH PERPENDICULAR POLARIZATION\*

Angle of incidence, $\theta$ (degrees)	WKB Solution (T)	Numerical Integration (T)	Seven Layer (T)
0	0.8332	0.8357	0.8321
10	0.8285	0.8316	0.8277
20	0.8139	0.8161	0.8130
30	0.7869	0.7889	0.7860
40	0.7434	0.7450	0.7423
50	0.6764	0.6774	0.6751
60	0.5757	0.5761	0.5742
70	0.4208	0.4208	0.4284
80	0.2332	0.2331	0.2323

$$\epsilon_r = 4e^{-0.3077k_0T}$$

$$k_0T = 0.7$$

dome. If a fiberglass skin is chosen, with a dielectric constant of 4, a suitable skin thickness is given by  $d_s = 0.011T$ . The reflection curve for this case is shown in Fig. 2-78. It is apparent that the thin skin smooths out the reflection extrema in the frequency range where  $k_0T$  is between 1.6 and 4.0. The power reflection coefficient actually remains below 1% in an even wider frequency range. At very high frequencies, of course, the reflection from the homogeneous skin predominates and results in strong periodic reflection maxima.

Reference 77 states that inhomogeneous walls for radomes provide extremely broadband transmission. It goes on to state that from the earlier investigations by Haddenhorst, it is known that the reflection is also less critically dependent on the angle of incidence than for the homogeneous wall. Particularly for very high microwave frequencies, where thin-wall radomes become impractical due to lack in mechanical stability, inhomogeneous walls appear useful.

## 2-7 TUNABLE RADOME DESIGN

In theory, the tunable radome (References 78 and 79) offers a new approach to the problem of maintaining maximum transmission efficiency or minimum boresight error over a range of frequencies, angles of incidence, temperatures, and ablation-layer thicknesses. Reference 80 suggests the addition of a controlled-parameter layer to a radome to compensate for the reduction in thickness of the ablation layer. The

control layer may contain ferrite, ferroelectric, or photosensitive materials that can be controlled by varying the applied voltage, current, or illumination. Formulas are given for determining the dielectric constant of the control layer as a function of the ablation-layer thickness to maintain constant transmission efficiency in Reference 80.

Although a tunable radome cannot be expected to be broadband in the usual sense, it can in theory provide maximum performance at any given frequency and can be tuned quickly to a new frequency.

A single-layer radome can always be adjusted for maximum transmission if it consists of a ferroelectric material whose dielectric constant is variable through an adequate range. For any given frequency or angle of incidence, the re-

quired dielectric constant is the same for parallel and perpendicular polarization. Figure 2-79 illustrates the manner in which the dielectric constant varies as a function of frequency and angle of incidence for a single-layer tunable radome. The curves are based on the design equation for the single-layer half-wave radome from Reference 79:

$$\epsilon_r = \frac{0.25}{(d/\lambda_0)^2} + \sin^2 \theta \quad (2-8)$$

where  $d$  = thickness  
 $\epsilon_r$  = relative dielectric constant  
 $\lambda_0$  = wavelength in free space  
 $\theta$  = angle of incidence

Another form of the tunable radome is a symmetrical three-layer sandwich with a ferroelectric core. Such a structure can always be

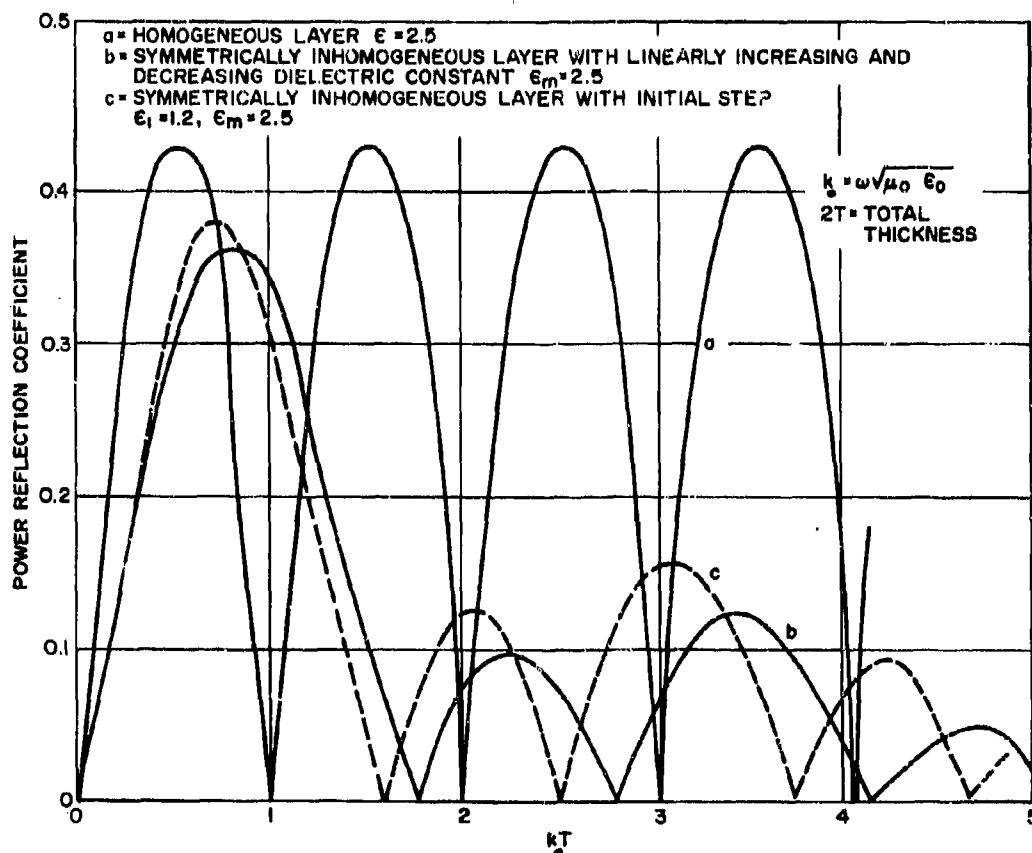


Figure 2-77. Magnitude of Reflection from Plane Lossless Dielectric Walls for Normal Incidence of Plane Wave as a Function of Thickness



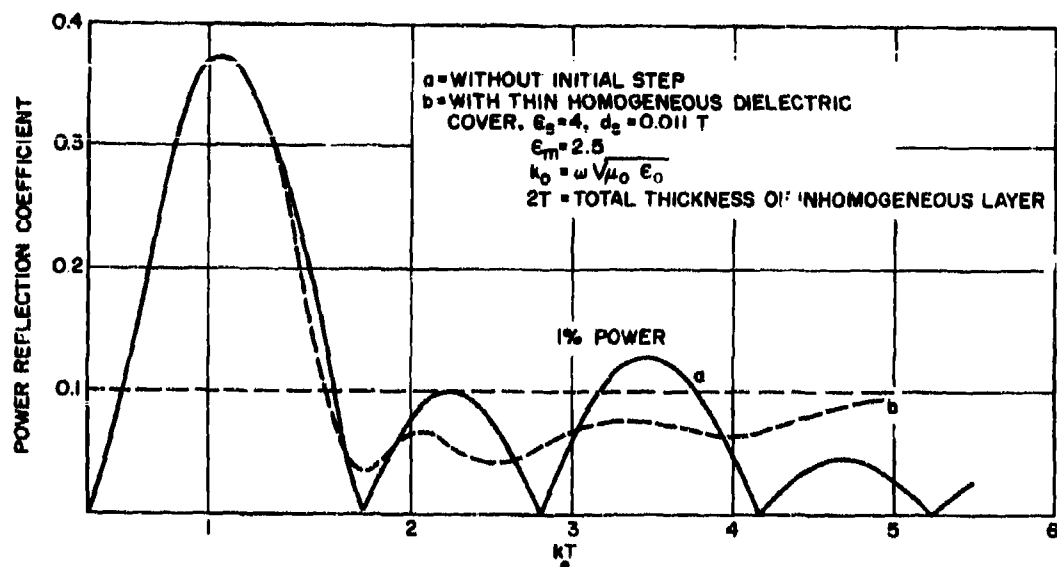


Figure 2-78. Magnitude of Reflection from Symmetrically Inhomogeneous Dielectric Wall

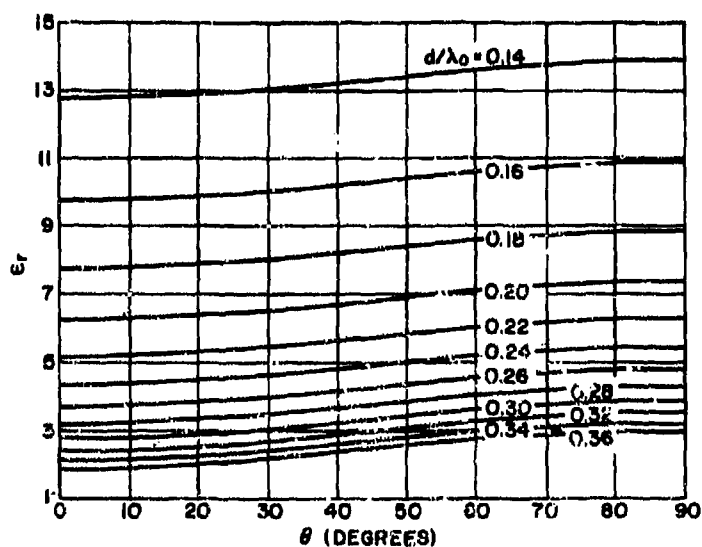


Figure 2-79. Conditions for Maximum Transmission Efficiency for Lossless Solid-Wall Radomes with Parallel and Perpendicular Polarization

tuned for perfect transmission (neglecting dissipation loss) if the core dielectric constant is variable over an adequate range. In some applications, tuning is hardly worthwhile, since the transmission coefficient remains very high without tuning. This is often the case with radomes that are operated at or near normal incidence, although it may occur at high angles of incidence if the dielectric constant is very small or if parallel polarization is maintained. The greatest need for tuning occurs for the following cases:

- a. Broadband radomes, where high transmission efficiency is required over a large range of frequencies but only one frequency is used at a time.
- b. Half-wave radomes at large angles of incidence. If the dielectric constant is 9 and the angle of incidence is 80°, a 10% change in frequency will reduce the power transmission coefficient from 1.0 to 0.08 unless the radome is tunable or parallel polarization is maintained.
- c. Sandwiches at large angles of incidence. A small change in angle of incidence may reduce the transmission coefficient drastically unless the radome is tunable. This is particularly true when the skins are rather thick to provide increased strength.

Techniques for applying the d-c control voltage to a tunable radome are discussed in Reference 78. A thin, poorly-conducting film may be coated on the surfaces of a ferroelectric layer to permit the application of a d-c control voltage. To protect the film, it may be desirable to have dielectric layers or skins on both surfaces of the tunable layer. The resulting structure is a three-layer tunable sandwich. The films must be poorly conducting to avoid excessive power absorption from the radar signal, but they must have sufficient conductivity to achieve a rapid response to changes in the applied control signal. A suitable compromise between these conflicting requirements is possible, unless the radome is very long, a very fast response is required, or the allowable radar power absorption in the films is very small.

If the skins are very thin, the tuning curves of the symmetrical three-layer sandwich are similar to those of the half-wave tunable radomes. If the skins are electrically thick, however, the tuning curves become more dependent

on the polarization. Therefore, thin skins are recommended for the three-layer tunable sandwich.

The transmission efficiency of a low-loss, symmetrical three-layer sandwich is maximized if the following equation from Reference 79 is satisfied:

$$(2\pi d_c/\lambda_0) \sqrt{\epsilon_c - \sin^2 \theta} = n\pi + \tan^{-1} \frac{r_s(r_{sc}^2 - 1) \sin 2\phi}{r_{sc}(1 + r_s^2) + r_s(1 + r_{sc}^2) \cos 2\phi} \quad (2-9)$$

where  $d_c$  = core thickness

$d_s$  = skin thickness

$n$  = any integer

$r_c$  = interface reflection coefficient, wave in the skin incident on the core

$r_s$  = interface reflection coefficient, wave in free space incident on the skin

$\epsilon_c$  = core dielectric constant, relative

$\epsilon_s$  = skin dielectric constant, relative

$\lambda_0$  = wavelength in free space

$\phi = (2\pi d_s/\lambda_0) \sqrt{\epsilon_s - \sin^2 \theta}$

$\pi = 3.1416$

This equation is valid for both parallel and perpendicular polarizations.

Figure 2-80 shows the core dielectric constant vs. angle of incidence for one particular sandwich. As the angle of incidence varies, maximum transmission efficiency will be maintained if the core dielectric constant is tuned in accordance with these curves, which are based on the equation. Tuning curves are given in Reference 79 for sandwiches having other combinations of skin and core thicknesses and skin dielectric constants.

## 2-7.1 SUMMARY

The feasibility of the tunable radome is questionable at the present state of the art. Several problems arise when photosensitive materials are considered. The ambient illumination, such as that from the sun, must be minimized, and a material must be found whose dielectric constant is sensitive to the illumination while its dissipation loss remains low. Ferrite media have problems of excessive dissipation loss and temperature sensitivity. A method would have to be devised for applying a controllable d-c magnetic field to the radome without getting too many wires or magnets in front of the

antenna. Ferroelectric media also pose the problem of temperature sensitivity. Some of these media have a very high dielectric constant, introducing severe tolerances in thickness uniformity.

A tunable radome might be achieved by loading an ordinary radome with hundreds of tiny varactors or voltage-variable capacitors. However, the fabrication and materials costs would be quite large. There is some possibility that a useful tuning range can be realized with an ordinary radome material loaded with powdered ferroelectric material to obtain a practical effective dielectric constant. The advantages offered by the tunable radome warrant an investigation of this possibility and others, but it appears that, in most cases, the tunable radome will require thermal insulation or cooling.

## 2-8 MILLIMETER-WAVELENGTH RADOME DESIGN

Mechanical strength specifications seldom allow the radome thickness to be less than one millimeter. Thus, at millimeter wavelengths, the radome thickness is on the order of one free-space wavelength, or, in some cases, several free-space wavelengths. If a single-layer homogeneous radome is employed, a first-order half-wave wall will provide sufficient strength, in some cases, if the wavelength is 10 mm or 1 cm.

However, at a wavelength of 1 mm, structural specifications usually require a fourth-order, or higher, half-wave wall. It is well known that the bandwidth will decrease and the boresight error and transmission loss will increase considerably in comparison with a first-order half-wave wall. Furthermore, the allowable manufacturing tolerances in thickness and dielectric constant will decrease correspondingly. Thus, there are serious problems opposing the use of a thin-wall or a multiple half-wave wall at millimeter wavelengths. Few, if any, solutions to these problems are known at the present time.

Millimeter-wavelength radome design considerations are basically the same as those for the lower frequency bands with the added restriction that the radome wall must be electrically thick. This, of course, rules out the use of the thin-wall design, and it often rules out even the half-wave wall. The requirement for an electrically thick radome implies that the dissipation losses will be large unless particular attention is given to the choice of low-loss materials. If a homogeneous single-layer wall is employed, the requirement for an electrically thick radome is a distinct disadvantage, as was pointed out before. If, however, a multilayer wall or a continuously inhomogeneous structure is employed, the large electrical thickness may prove to be advantageous in the synthesis of a broadband millimeter-wavelength radome.

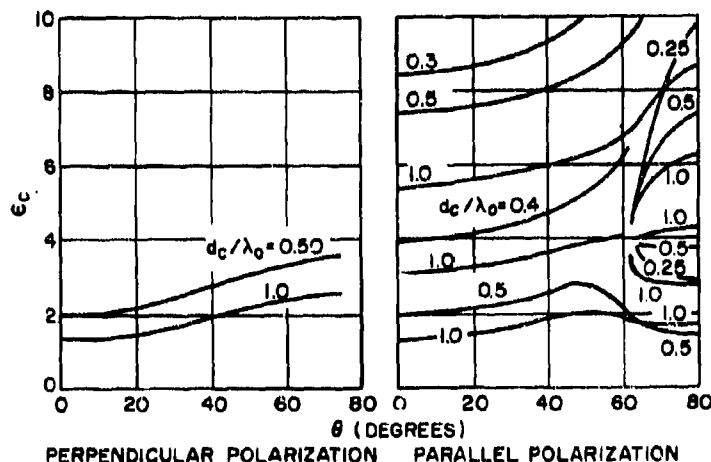


Figure 2-80. Conditions for Maximum Transmission Efficiency for Lossless, Symmetrical Three-Layer Sandwich with  $\epsilon_c = 4$  and  $d_c = 0.05\lambda_0$ .

All of the techniques proposed for high performance radomes at the lower frequencies should also be considered to alleviate the millimeter-wavelength radome design problem. These techniques include: broadband multilayers, computer optimization, inhomogeneous layers, metal-loaded structures, surface impedance matching, synthesis techniques, anisotropic media, materials having a magnetic permeability differing from that of free space, and artificial dielectric media.

It is helpful in millimeter-wave radome design to choose a blunt-nose radome shape to avoid large angles of incidence. Best results are obtained by choosing an antenna system that maintains parallel polarization for all scan angles. The use of polarization diversity and frequency diversity systems, which account in large part for the high transparency of window panes and camera lenses at optical frequencies, should be considered for millimeter-wavelength radar systems.

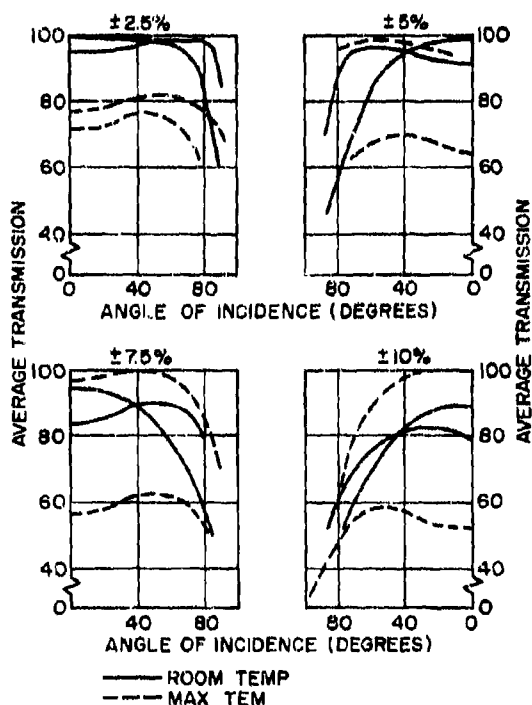


Figure 2-81. Broadband Study of Average Transmission Data of Ceramic Half-Wave Wall at K-Band

Some of the broadband multilayers presented in Reference 81 have good characteristics at millimeter wavelengths. Reference 82 presents the advantages of inhomogeneous radome constructions for these frequencies.

Reference 88 presents the results of the study of the properties of half-wave ceramic radomes at K-band. The electrical properties used in this study are those of a 99.5% alumina-ceramic material. As the temperature varies from room temperature to 2500°F, the dielectric constant varies from 9.5 to 11.1, whereas the loss tangent varies from 0.0001 to 0.0015. Using these temperature data, calculations were made of the power transmission and phase shift for a wall thickness of 0.098 in. at a frequency of 20 gc. An IBM 7090 computer was employed for the calculations and the results are presented in Figs. 2-81 and 2-82. The solid curves are for room temperature, while the broken-line curves are for 2500°F. The power transmission and phase data were averaged for parallel and perpendicular polarization.

At K-band, an electrically thin wall would have a thickness of about 0.012 in. and is not structurally feasible. Figure 2-81 indicates that by optimizing the parameters, a half-wave design would be obtained that would give good transmission performance for an average temperature. A study of flight regimes for a vehicle will determine an average temperature range for which a radome should be designed. The upper broken curve is the minus percent data from the optimum frequency for the maximum temperature. As the average temperature becomes lower, the performance improves from that shown. It may be noted that a half-wave ceramic radome can provide acceptable transmission efficiency at the lower temperatures in the K-band. Phase data will be critical if a boresight radome is being considered. The phase variation appears excessive for the half-wave ceramic radome at K-band (Fig. 2-82), but it could be reduced by modifications such as tapered thickness.

The effect of broadbanding the radome was studied by considering frequency tolerances of  $\pm 2$ ,  $\pm 5$ ,  $\pm 7.5$  and  $\pm 10$ %. A half-wave wall is quite sensitive to frequency changes and considerable variations occur in the performance as the frequency and temperature limits are changed. The curves indicate that a frequency deviation of 2.5% results in a radome with a

transmission efficiency between 70 and 80%. As a result, broadbanding of a solid-wall radome at K-band results in a rather low average transmission efficiency. The phase data indicates that the radome would introduce rather large bore-sight errors, since a  $35^\circ$  phase change is evident. This could be improved by tapering the wall thickness.

Reference 83 states that it may be concluded that the half-wave ceramic radome is feasible at K-band only if the temperature variation and the bandwidth requirements are drastically reduced.

## 2-9 FLUSH-MOUNTED RADIATING SYSTEMS DESIGN

### 2-9.1 INTRODUCTION

As aircraft and missile velocities continuously increase, limitations are encountered in the high-temperature capabilities of nose radomes. While considerable progress has been made in developing radome materials that have the required mechanical strength and electrical properties at high temperatures, no completely satisfactory material is available for the temperature ranges encountered.

Thus, consideration has been given to the use of flush-mounted radiating systems in place of conventional dish-radome configurations (Reference 84). This approach does not eliminate the high-temperature dielectric material problem, but it allows the large conventional radome to be replaced with many small dielectric plugs or inserts, which fill the radiating slots or apertures of the flush-mounted system. This is also accomplished by some of the metal-loaded radome structures. The flush-mounted radiating system cannot be regarded as a solution to the high-temperature radome problem, but only as an alternative approach that is accompanied by its own set of problems.

Some of the flush-mounted systems offer the advantage of high-speed electronic scanning and release of much of the interior space for other equipment. It must be recognized, however, that many of the proposed flush-mounted systems occupy the entire nose-cone volume. Serious problems must be overcome before these advantages can be realized. Among them are the following:

- In the flush-mounted systems, a considerable portion of the nose-cone structure is metallic. A suitable high-temperature metal may be as difficult to find as a high-temperature dielectric material, depending on the maximum temperature encountered and the length of time that it must be endured.
- Flush-mounted systems involve many dielectric-to-metal joints or seals. The different expansion coefficients of the metal and the dielectric, and the weakness for rain erosion at the joints, make this a problem.
- Two-dimensional scanning presents a major problem in flush-mounted systems. To prevent beam deterioration and high sidelobes, the phases and amplitudes in the apertures must be controlled. This

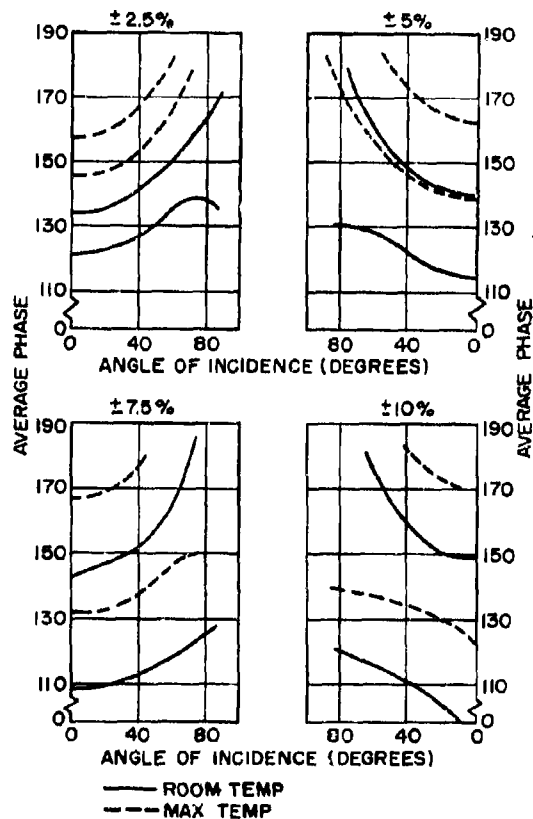


Figure 2-82. Broadband Study of Phase Data of Ceramic Half-Wave Wall at K-Band

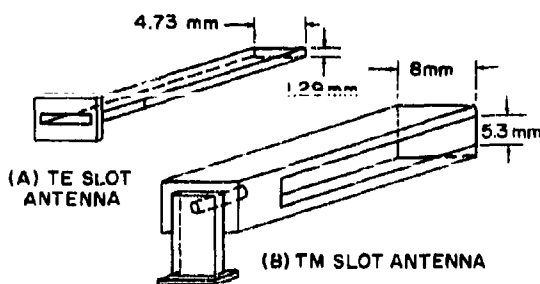


Figure 2-83. TE and TM Slotted Waveguides Used as Radiating Elements in Arrays

may require a large number of variable phase shifters and complex programming equipment. If ferrites or ferroelectrics are employed in electronic-controlled phase shifters, the temperature sensitivity of these materials poses a problem. If scanning is accomplished by frequency variations, this introduces the complication of a frequency-swept transmitter and receiver.

- d. At first, it might appear that the radome boresight-error problem is eliminated in flush-mounted systems. Actually, this problem is merely replaced by an equally severe problem: beam-direction sensing. With electronic scan techniques, beam-direction sensing involves the accurate measurement of the transmitter fre-

quency, if frequency scan is employed, or the control current or voltage applied to the electronic phase shifters. Alternatively, accurate in-flight measurements of the phase or the phase velocity in the radiating apertures are attempted. The measured frequency, control current or voltage, or phase is then compared with the system calibration to determine the beam direction. Any error in the measurement or in the calibration is fully equivalent to the boresight error of a conventional radome.

- e. The problem of excessive weight is serious in some of the proposed flush-mounted radiators. In particular, some of the feed systems require a great deal of waveguide and others involve a weighty collection of parallel-plate transmission lines.

Reference 85 presents the relative merits of the flush-mounted radiators and the conventional dish-radome systems. In spite of these problems, consideration must be given to the flush-mounted radiators in exploring all possible solutions to the high-temperature seeker-system development. A few of the recently proposed flush-mounted radiators are described in the following paragraphs.

## 2-9.2 SLOTTED WAVEGUIDE ARRAYS

Reference 86 investigates the performance of plane arrays of slotted waveguides. Figure 2-83

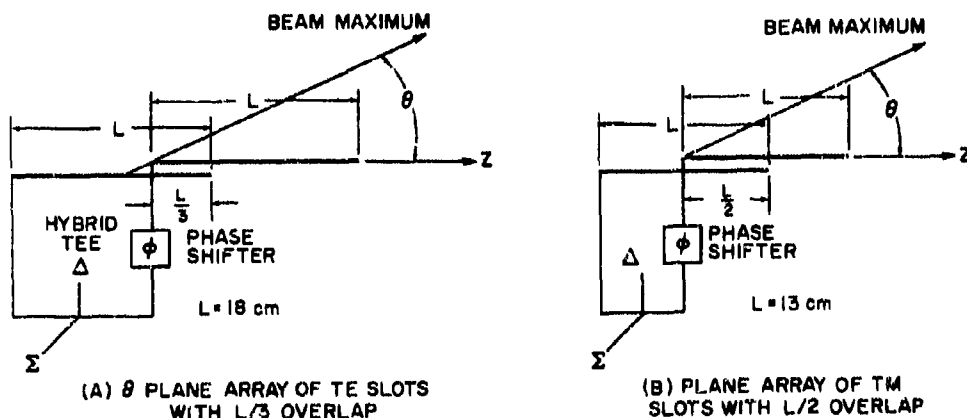


Figure 2-84. TE and TM Slot Arrays in Monopulse System

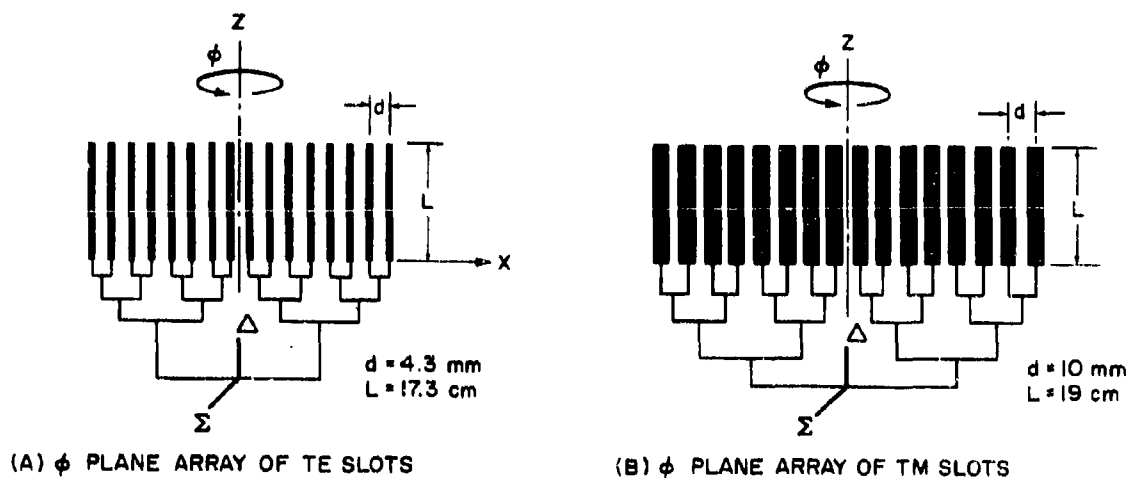


Figure 2-85. TE and TM Slot Arrays in Monopulse System

shows the radiating elements employed to form the TE and TM arrays. Four monopulse antennas were constructed and tested, using these TE and TM slotted waveguides as elements. The details of the arrangement and the dimensions are shown in Figs. 2-84 and 2-85.

These four antennas were tested over a frequency range of 33 to 36.5 gc. Typical patterns are shown in Figs. 2-86 through 2-89. These patterns demonstrate that acceptable monopulse patterns can be obtained with plane arrays of TE and TM slot antennas. Because of the small amplitude taper, one db per wavelength, on the individual slots, the sidelobe levels for the theta plane arrays are quite high. With a better choice of taper, these sidelobe levels can be reduced.

Over the frequency range of the tests, 33 to 36.5 gc, the beam maximum in the theta plane scanned through the range of 20° to 27° for TE arrays, and 41° to 47° for TM arrays. This range of scan angles is rather limited, since the air-filled slots are not highly dispersive. In any final design, the line-source elements would probably be made more dispersive by dielectric loading or other means. Additional information on TE and TM slot arrays on plane and curved surfaces is given in Reference 87.

A flush-mounted nose-cone radiating system has been constructed and tested by the Maxson Electronics Corporation (Reference 88). This antenna utilizes 54 radial nonresonant slot arrays, each 39 in. long. Theta scan is 12° to

52° for a frequency change of 9.1 to 8.55 gc. Base feed is used through an organ-pipe scanner for phi scan. Tapered illumination produces 18-db sidelobes. A constant phase compensation for each linear array was calculated to achieve this sidelobe level.

An investigation of slot arrays on nose cones has been carried out by the Hughes Aircraft Company and the University of Michigan (Reference 89). They found that an obvious method for arranging a distribution of radiating currents on a conical surface is the use of linear arrays lying along cone generators. If this system of arrays can be properly fed, the phase and amplitude of each slot will be just that required to achieve a directive beam at a particular direction in space. The phase distribution on a conical surface necessary to place a circularly polarized beam in a direction ( $\theta', \phi'$ ) is given by:

$$\begin{aligned} \text{Phase} = & \phi_0 - k_0 h [\cos \alpha \cos \theta' - \sin \alpha \sin \theta' \cos (\phi_0 - \phi')] \\ & + k_0 r_0 [\cos \alpha \cos \theta' - \sin \alpha \sin \theta' \cos (\phi_0 - \phi')] \end{aligned} \quad (2-10)$$

where  $h$  = slant cone height  
 $k_0$  = phase constant of free space  
 $r_0$  = radial position on cone measured from the base  
 $\alpha$  = full cone angle  
 $\phi_0$  = azimuthal position on the cone

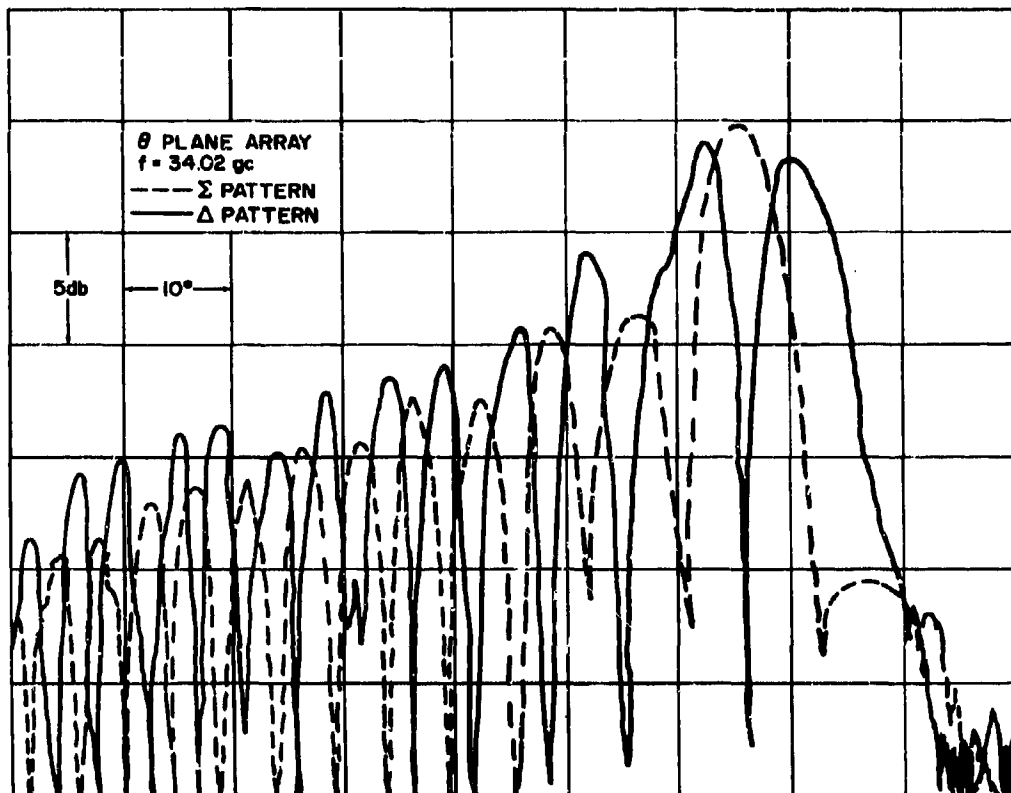


Figure 2-86. Sum and Difference Patterns of Monopulse Antenna Using Plane Array of TE Slots with 1/3 Overlap

This expression is based on a geometrical optics derivation and, accordingly, could not be expected to hold when scanning into the shadow region,  $\theta' > \alpha$ .

The final term in Eq. 2-10 is linear function of slant distance,  $r_0$ , and, therefore, could be readily achieved by changing the phase progression between array elements. The remaining phase terms are independent of slant distance and could be inserted in the feeding network. Both the feeding phase and the linear phase are complicated functions of the scan angle and, thus, must be capable of continuous variation as the beam position is changed.

This equation suggests the possibility of a system of linear arrays driven by feed lines emanating from a small radial waveguide. If the circular waveguide is excited with the rotating  $TE_{11}$  mode, the first term in Eq. 2-10 is

obtained. The second term is achieved by mechanical or ferrite phase shifters in the branch lines, whereas the final term is a function of the propagation constant in the linear arrays.

In the experimental system, the radiating elements are eight traveling-wave waveguide arrays of nonresonant slots. These arrays are equally distributed about the cone circumference. The necessary control of the array propagation constant is obtained by moving a dielectric slab in and out of the waveguide through a narrow nonradiating longitudinal slot cut in the back wall. The insertion depth of the dielectric is controlled by a cam-follower mechanism calibrated so that the desired phase velocity can be preset. Figure 2-90 shows the experimental antenna mounted in pattern-taking position. The eight linear arrays can be seen emanating from the cone tip. An interior view, given in Fig.



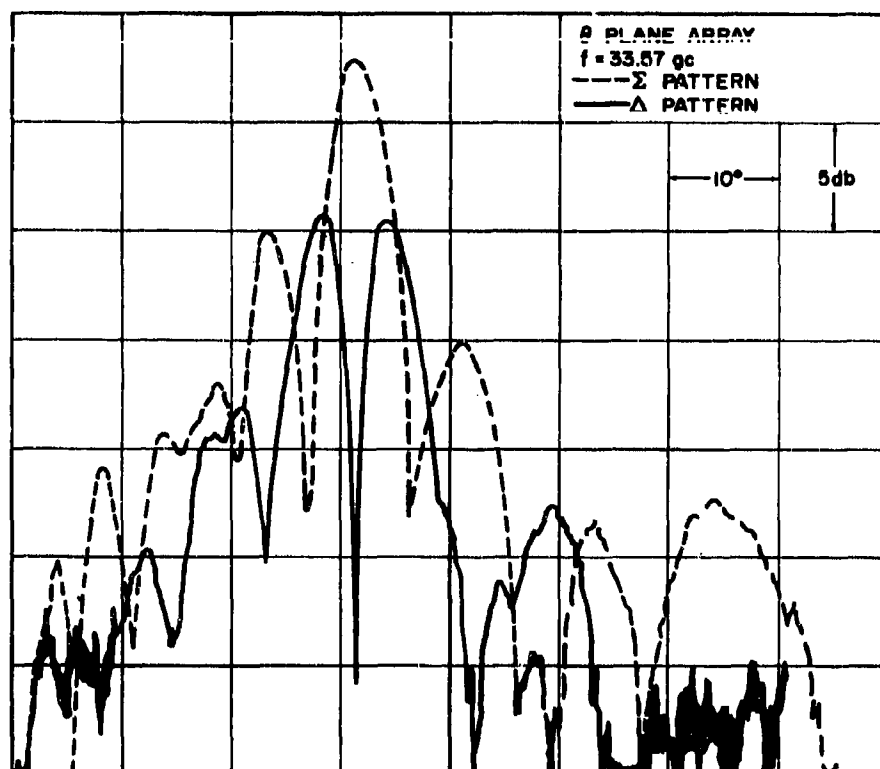


Figure 2-87. Sym and Difference Patterns of Monopulse Antenna Using Plane Array of TM Slots with 1/2 Overlap

2-91, shows the feed network and various phase adjustments. The best experimental patterns for this system are obtained when the phase settings are made by empirical methods. This is accomplished by progressively adjusting the two phase mechanisms (feed phase shifters and array propagation constants) for each array to give maximum radiation in the desired scan direction.

A set of four antenna patterns for beam positions of  $0^\circ$ ,  $10^\circ$ ,  $20^\circ$ , and  $25^\circ$  is shown in Fig. 2-92. For the on-axis beam position, the pattern is circularly polarized, with a slight ellipticity becoming apparent as the beam is scanned. The true pencil-beam character of the radiation is verified by Fig. 2-93, which shows a pattern taken in a plane orthogonal to the plane of scan. The rather high sidelobes indicated by these patterns have two causes: (1) the individual arrays were designed for uni-

form distribution; and (2) the aperture is partially blocked, since the arrays do not extend to the cone tip. Both could be overcome by careful design.

The scanning range of this antenna is restricted to that shown in the patterns for two reasons. First, the scanning sensitivity of the individual arrays is limited to a range of  $40^\circ$  from endfire to the array. Of even greater importance is the shadowing due to the cone surface as the beam moves out of the optical region. (For this cone, the limit of the optical region corresponds to a scan angle of  $20^\circ$ .) The maximum scan of  $25^\circ$  exhibited here results in an antenna capable of scanning a pencil beam throughout a  $50^\circ$  conical volume centered about the forward cone axis. An increased scanning range might be achieved by employing snaked linear arrays with frequency shift or variable path lengths as the scanning mechanism.

### 2-9.3 OTHER FLUSH-MOUNTED RADIATING SYSTEMS

Another conical antenna is based on a system of circular parallel-plate regions stacked coaxially along the cone axis, with radii that decrease as the cone tip is approached. If these parallel-plate regions are fed at their centers, energy will travel outward, resulting in excitation of a current distribution on the cone surface. With proper control of the plate excitation, the conical current distribution can give a linearly polarized pencil beam in an arbitrary

direction. In any final design, the outer surface would be covered with a metallic envelope containing annular rows of sausage link slots that correspond to the positions of the parallel plate apertures.

An artist's conception of a complete multiple-disk cone is shown in Fig. 2-94. Elevation ( $\theta$ ) scanning and pattern formation are obtained by a highly dispersive linear array positioned along the cone axis. This array is formed by cutting slots in the narrow wall of rectangular waveguide wound in the form of a helix. The long path length between slots, by virtue of the heli-

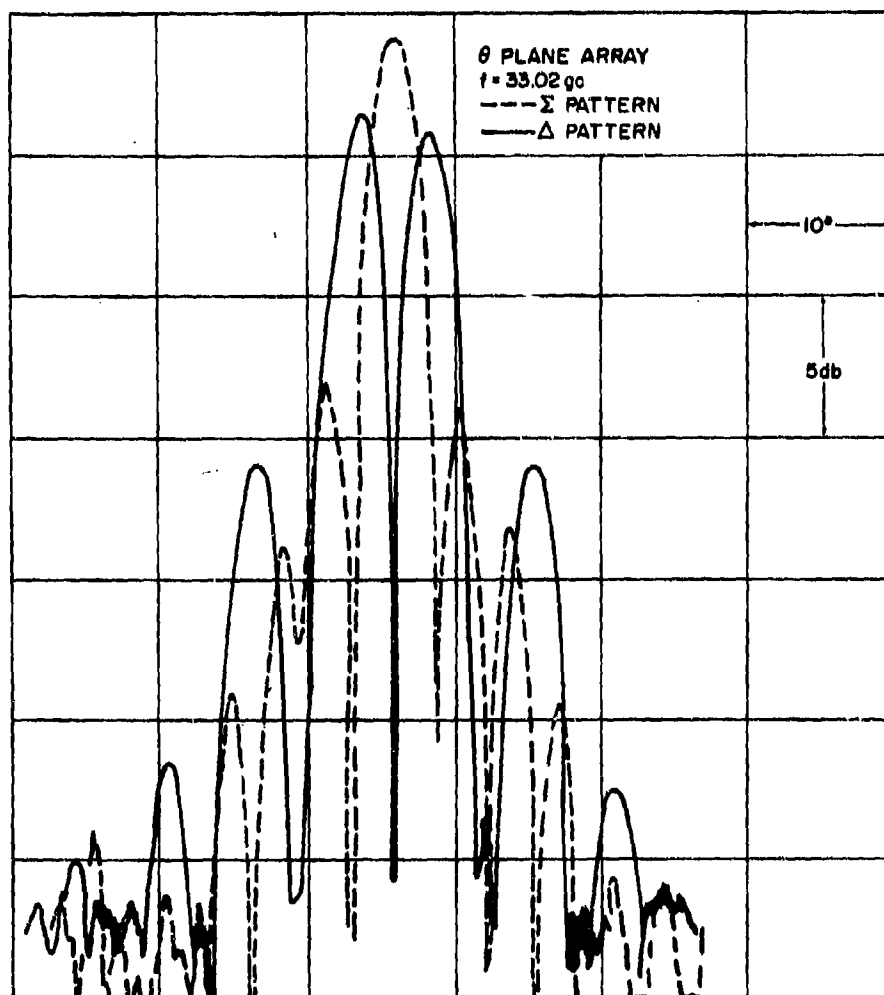
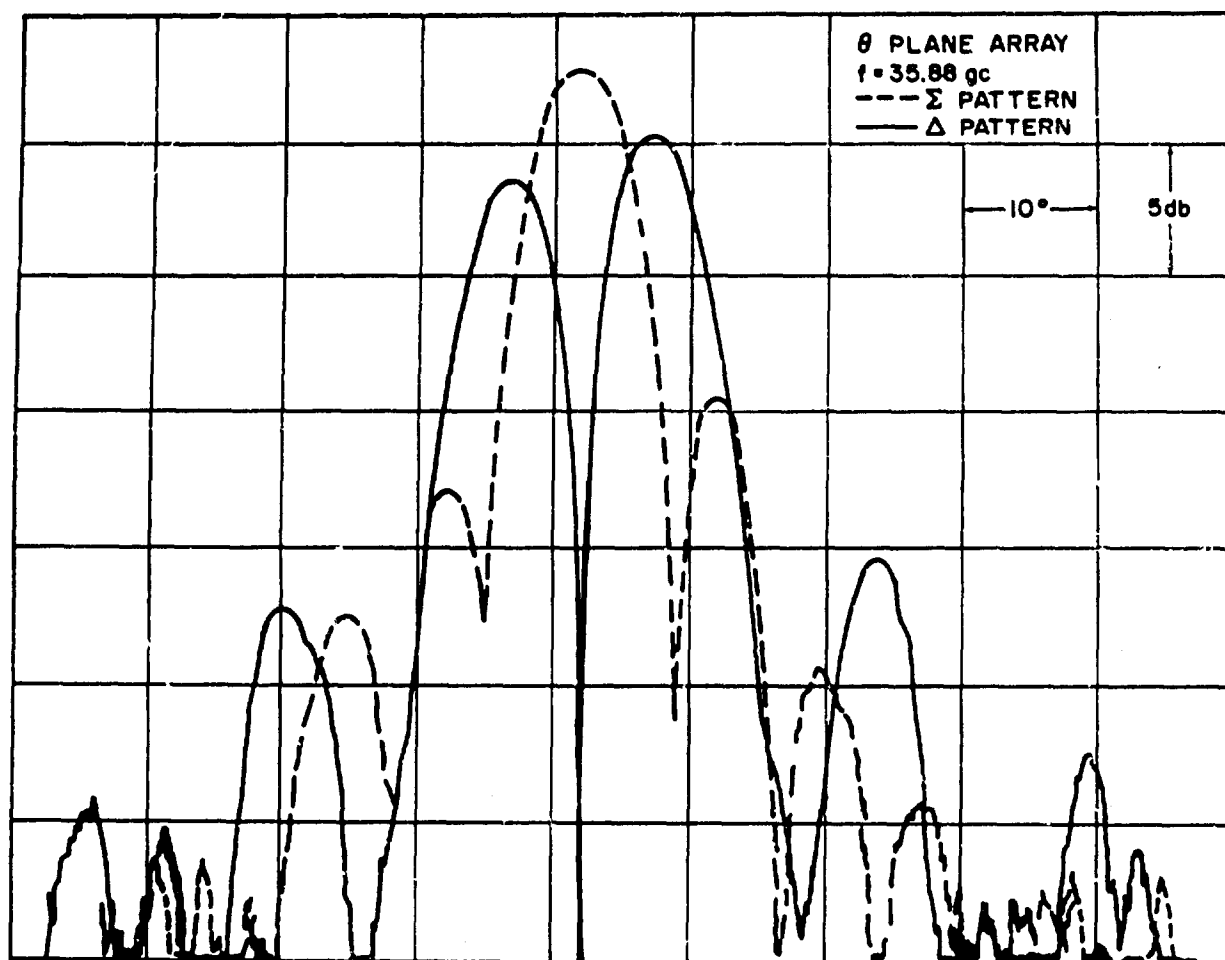


Figure 2-88. Sum and Difference Patterns of Monopulse Antenna Using Plane Array of 16 TM Slots



**Figure 2-89. Sum and Difference Patterns of Monopulse Antenna Using Plane Array of 16 TE Slots**

cal windings, allows large changes in the array phase progression, and hence in the beam position, for small changes in frequency. Each individual slot feeds a sectoral horn, which, in turn, directs the energy into the parallel-plate region. These horns serve the additional purpose of narrowing the beam in the azimuthal direction. The entire central feeding system is rotated to achieve azimuthal scanning. The actual experimental system closely follows this model. Figure 2-95 shows the prototype antenna. Close examination reveals the slotted array and feed horns located along the cone axis. In this prototype, the slotted outer envelope is absent and no means are provided for mechanical rotation of the feed system. These features are not essential to the basic operation of the prototype, but would be included in any terminal design. The results obtained with this

multiple-disk cone antenna are presented in Reference 89.

Another scheme for exciting the cone surface with currents involves consideration of a parallel-plate transmission line whose plates are oriented parallel to the cone axis and fed at the base of the cone by a line source. The leading edges of these plates assume a hyperbolic shape when terminating at the cone surface. When several of these parallel-plate lines are sandwiched one atop the other, a conical system of hyperbolic apertures is formed that can be fed by a two-dimensional array of line sources at the cone base. Figure 2-96 shows an experimental antenna in which the leading edges of the parallel plates form half a cone surface. This configuration is fed at its base by a rectangular plane array designed to provide scanning of the radiated beam in planes essentially perpendicu-

lar to the plates. Another version of this same antenna scheme provided for scan in planes essentially parallel to the plates. Additional information on this hyperbolic aperture antenna is available in Reference 89.

An effort was made to devise compact feeding systems for radiators on the cone surface that would minimize the volume and weight occupying the nose cone interior, thereby preserving this space for auxiliary system components. One result of this effort is the scanning conical transmission line antenna system shown in Fig. 2-97. This antenna consists of an apex-fed conical transmission line in which the outer of two coaxial cones is provided with a system of interrupted annular slots that couple the interior fields to space. The division of these slots into two basic groups provides the phase condition needed for a nominally axial beam.

The cross-section in Fig. 2-98 shows a small air gap centrally located in the dielectric material separating the two coaxial cones. This gap permits the inner cone to be pivoted off the axis of the outer cone, thereby causing the radiated beam to tilt off the cone axis. Experiments showed that a 5:1 scanning scale factor existed with the experimental model in which the beam scanned  $5^\circ$  for each degree of tilt of the inner

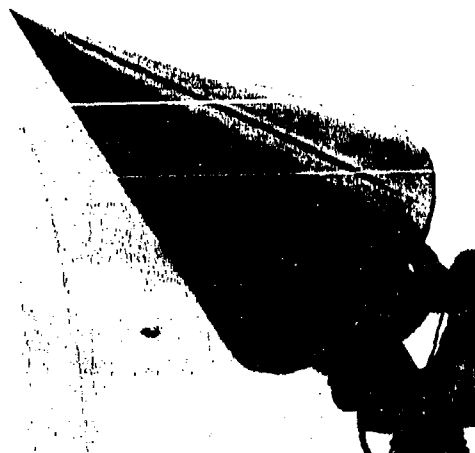


Figure 2-90. Scanning System of Linear Arrays on Cone

cone from the boresight axis. The results obtained with this scanning conical transmission line antenna are included in Reference 89.

Several other flush-mounted antenna systems have been developed by Technical Research Group and are described in Reference 90.

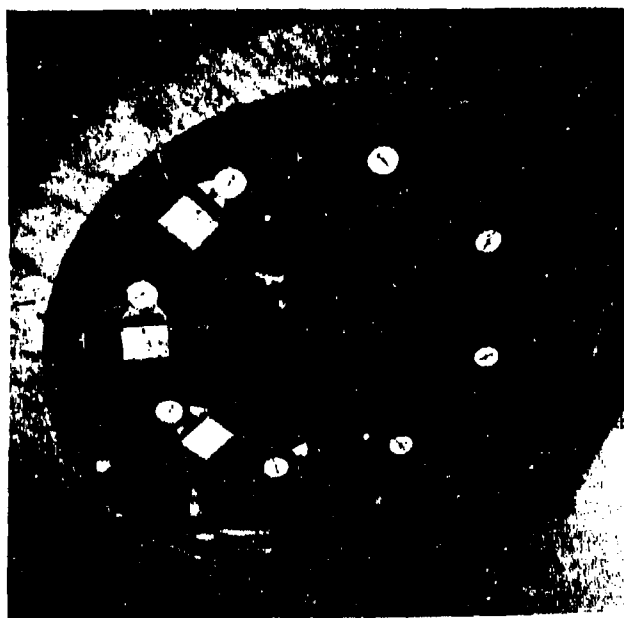


Figure 2-91. Rear View of 8-Array Cone Showing Feed Configuration

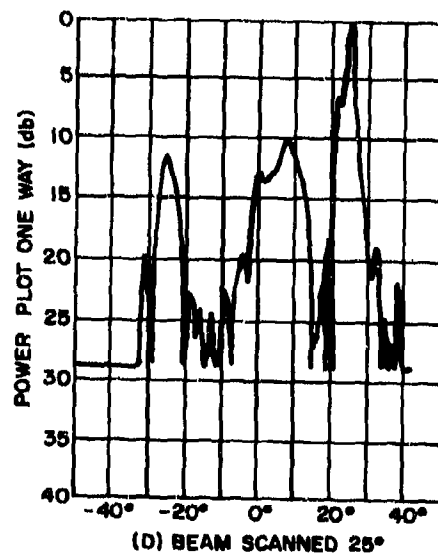
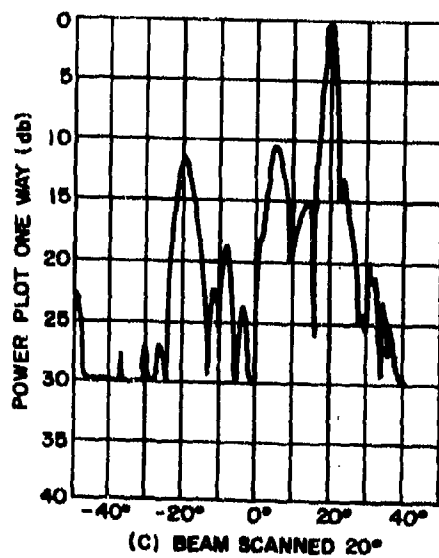
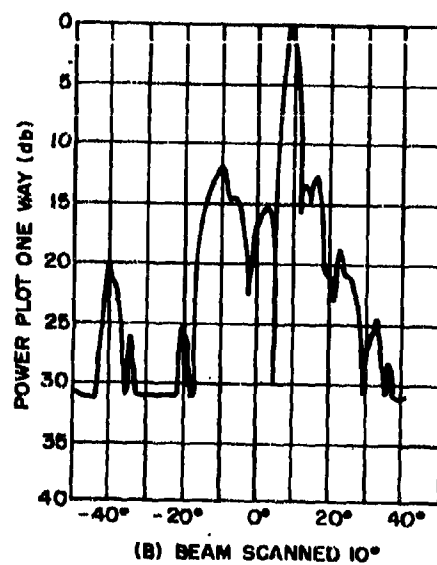
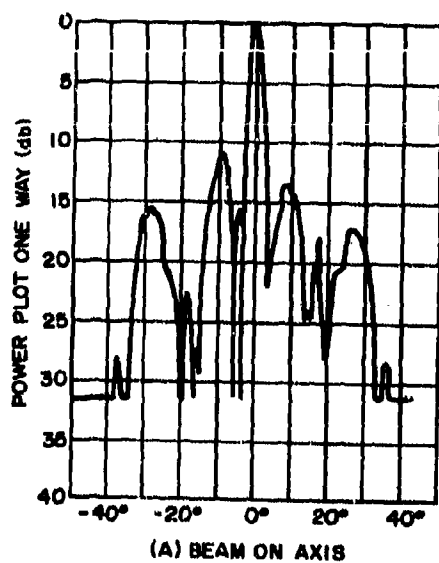


Figure 2-92.  $\theta$ -Patterns in Plane of Scan for 8-Linear Array Cone

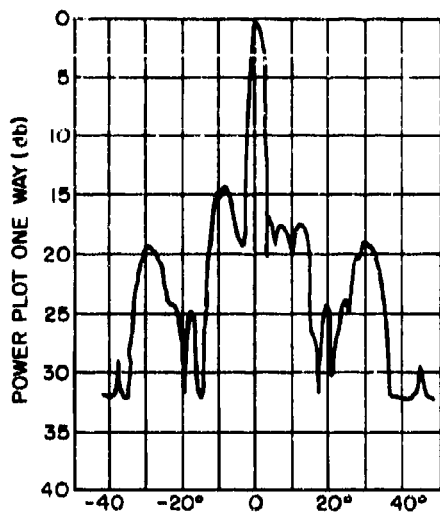


Figure 2-93. Pattern in Plane Perpendicular to Plane of Scan for 8-Linear Array Cone Scanned 10°

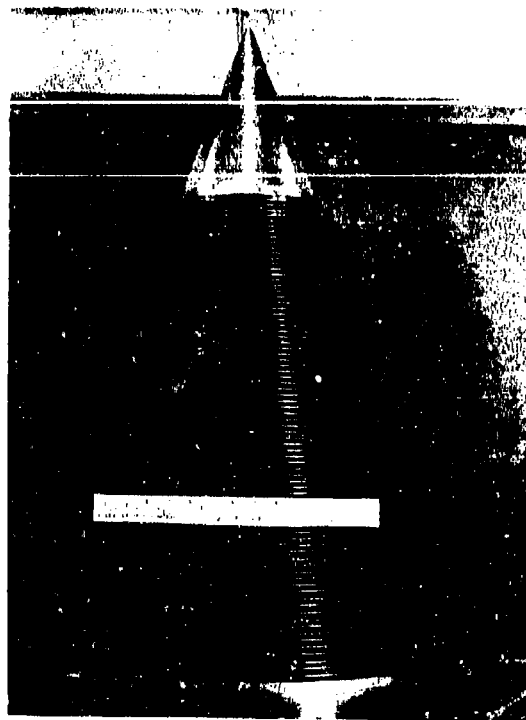


Figure 2-95. Multiple-Disk Cone with Helical Waveguide Scanner

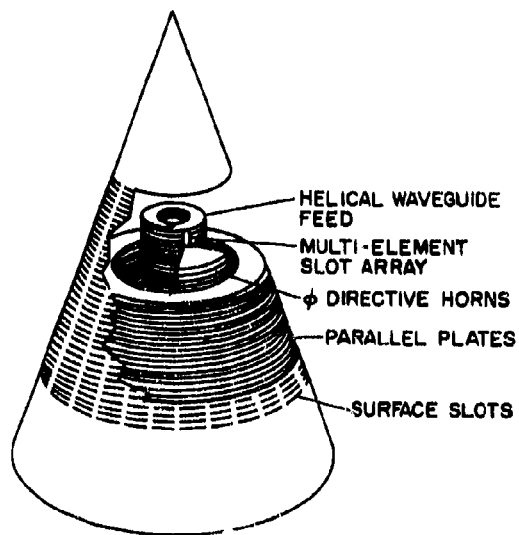


Figure 2-94. Helical Waveguide Frequency Scan Cone

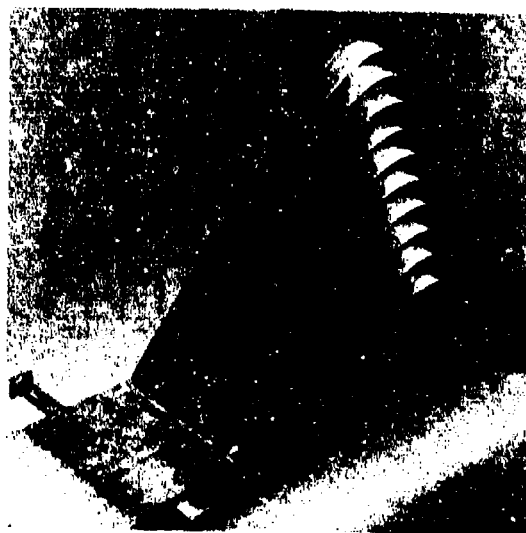


Figure 2-96. Rectangular Array Feeding Hyperbolic Plates

## 2-9.4 GEODESIC LENSES

The properties of a class of geodesic lens antennas that have potential uses in flush-mounted nose cones are described in Reference 91. The promising features of these lens systems include multiple-beam capability, versatility of flush mounting to a wide variety of surfaces, large bandwidth, high power capacity, and ease of scanning. Because of the circular symmetry of these lenses, coverage over  $360^\circ$  about the symmetry axis is possible. The beam position can be controlled in the transverse direction by radial feed position, giving two-dimensional coverage from a fixed lens. The TEM and  $TE_{01}$  waveguide modes can be employed to obtain two modes of orthogonal polarization.

Geodesic lenses are usually constructed from two parallel contoured plates between which energy propagates in the TEM or  $TE_{01}$  waveguide mode, as shown in Fig. 2-99. In general, the index of refraction in the lens may be an arbitrary function of the radius. The lens contour is also a function only of radius and, thus, circular symmetry is maintained. Depending on the index of refraction, the contour of the lens determines its focusing properties. One of the most promising lenses is the unit-index geodesic lens. Since a unit-index lens contains no dielectric material, dielectric losses are eliminated, power handling capability is high, and

weight is reduced.

The type of lens that has been investigated radiates from a circular slot aperture. The contour of the lens is determined so that energy launched from the focal point will have the proper phase distribution over the semicircular portion of the aperture opposite the focus. The phase distribution is that which radiates a beam in a direction diametrically opposite to the focus and at an angle with respect to the plane of the lens rim. The angle of the beam is determined by the lens design. The semicircular aperture produces a fan-shaped beam. The vertical pat-

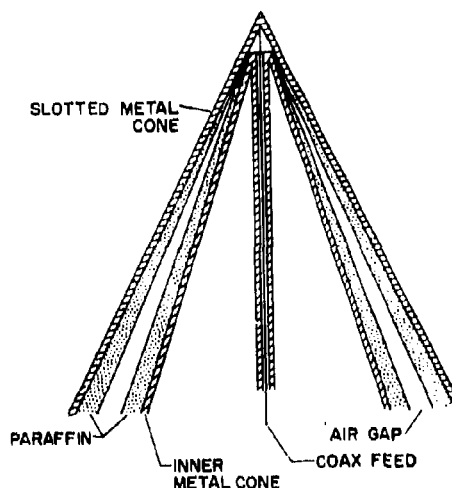


Figure 2-98. Cross-Section View of Transmission Line Antenna

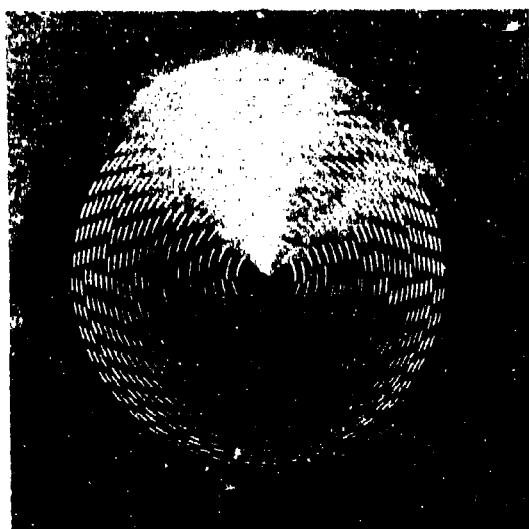


Figure 2-97. End View of Conical Transmission Line Antenna

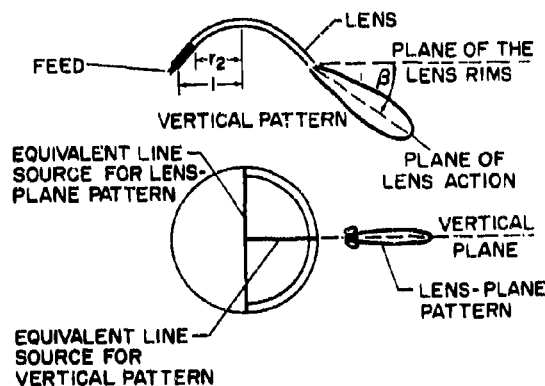


Figure 2-99. Definition of Lens Patterns

tern is broader than the pattern in the plane of lens action because of the relative source lengths, as shown in Fig. 2-99.

A lens design has been determined for which the beam position can be controlled over a conical region of  $70^\circ$  (total cone angle of  $140^\circ$ ) about the symmetry axis of the lens. Beam positioning has been demonstrated in X-band lens

models, and patterns obtained from one model are shown in Fig. 2-100.

Figure 2-101 shows a metallic nose cone with a geodesic lens antenna. In a practical version, the feed would be located internally and two or more such lenses might be arrayed in the nose cone.

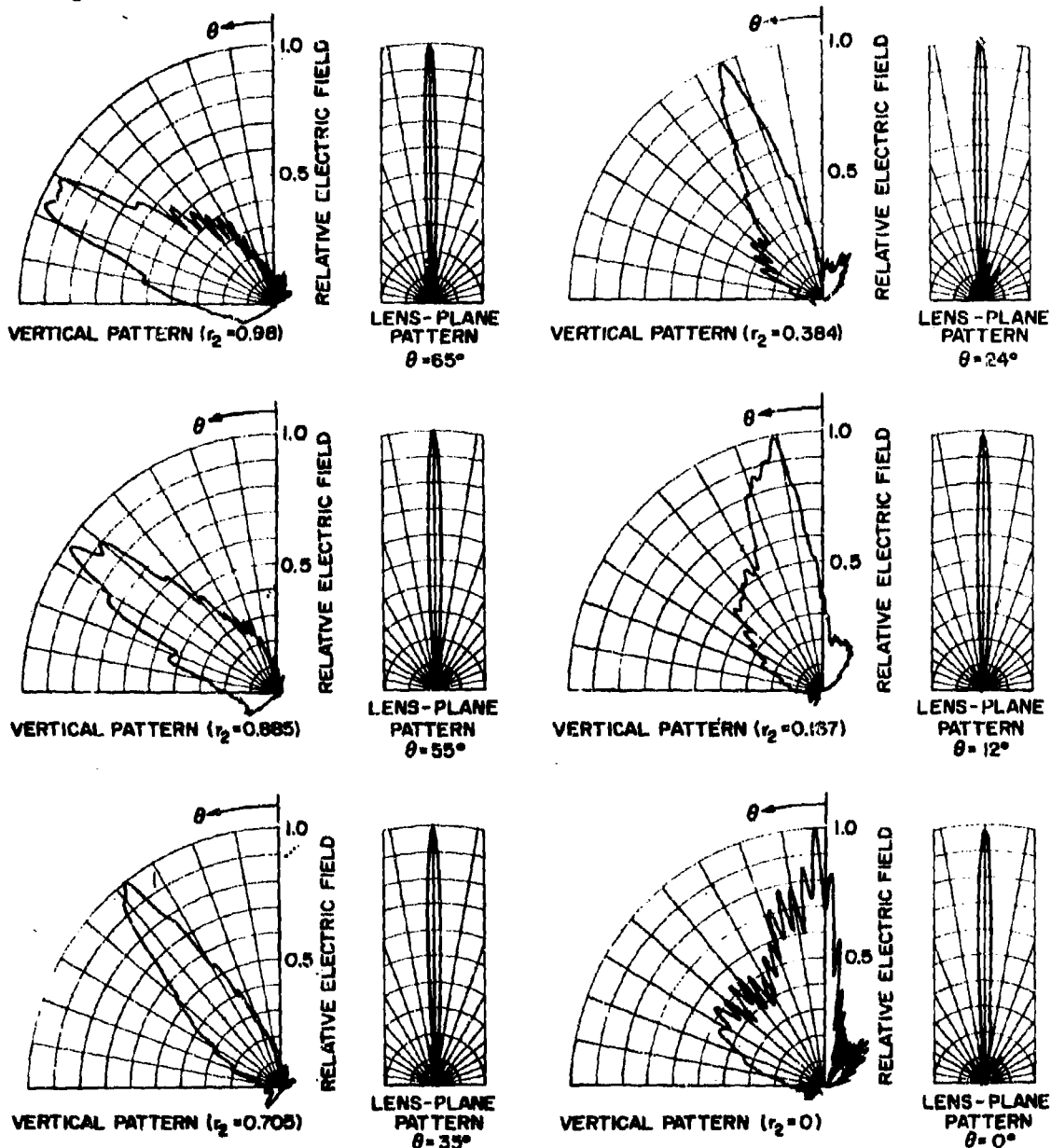


Figure 2-100. Patterns of Beam Elevation Positioning Lens Antenna



## 2-10 SPACE FRAMES FOR RADOME STRUCTURAL SUPPORT

### 2-10.1 INTRODUCTION

Space frames with metal ribs or dielectric ribs have been used for several years in large ground-based radomes. They are now being considered for airborne radomes for the following reasons:

- A space frame is needed to help support the weight of a large, heavy radome, such as a chin radome for a bombing and navigation radar system.
- A space frame may permit a radome to be manufactured in sections that will be held together by the space frame. This would be particularly helpful with large, high-temperature inorganic radomes that are

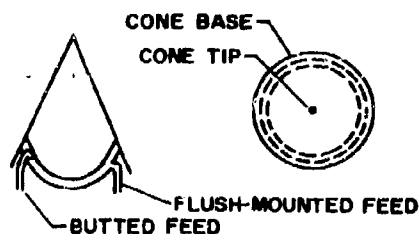


Figure 2-101. Geodesic Lens Mounted in Nose Cone

difficult to manufacture in one piece.

- The use of a space frame simplifies the problem of attaching the radome to the aircraft or missile body.

It should be appreciated that the space-frame approach has most of the same objectives (attaching, supporting, and subdividing the radome) as the metal-loaded radome techniques and the flush-mounted radiating systems. The basic distinction between the metal-loaded radome and the space-frame system is that the former uses at least one metallic member (or one radiating aperture) per wavelength, whereas the latter may have the ribs spaced several wavelengths apart. The metal-loaded radome is fed by radiation from a conventional horn or dish antenna, whereas the apertures in a flush-mounted system are fed by waveguides or transmission lines. Thus, the three alternative approaches differ chiefly in the spacing between the metal ribs or the radiating apertures and the methods of feeding the apertures.

The performance of antennas with one or more radome support members is described in the following paragraphs. Techniques for manufacturing a ceramic radome in sections and supporting it in a metal space frame are described in Reference 92.

### 2-10.2 AXIAL SUPPORTING MEMBER FOR NOSE-CONE RADOME (Reference 93)

Figure 2-102 illustrates a parabolic dish antenna with the feed located at the radome apex. A metal structural member extends from the attachment bulkhead, down through the radome to the radome apex, and beyond. The purpose

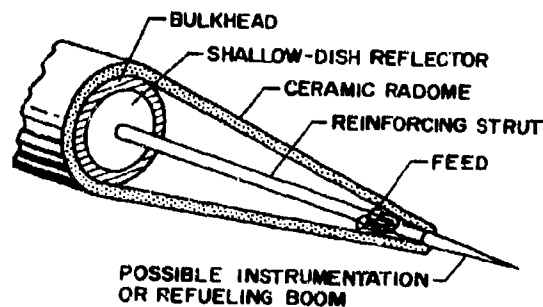


Figure 2-102. Antenna-Radome System Using Long Focal Length Dish and Central Structural Cylinder

of the structural member is to carry any fuel, deicing, or instrumentation lines and to help support the radome. A cross-section view of this configuration is shown in Fig. 2-103. A small hole is provided at the center of the dish for the structural member. For every degree that the dish is rotated off-axis, the beam scans through  $2^\circ$ . Representative field patterns given in Figs. 2-104 through 2-106 indicate that satisfactory electrical performance is possible with this configuration.

### 2-10.3 QUADRIPOD SPACE FRAMES

The quadripod space frame uses four or more structural ribs to support a nose-cone radome,

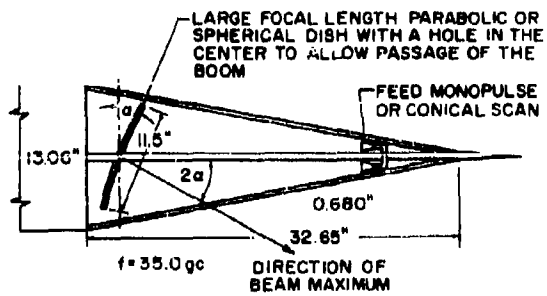


Figure 2-103. Cross-Section View of Dish Antenna, Nose-Cone Radome, and Central Structural Cylinder

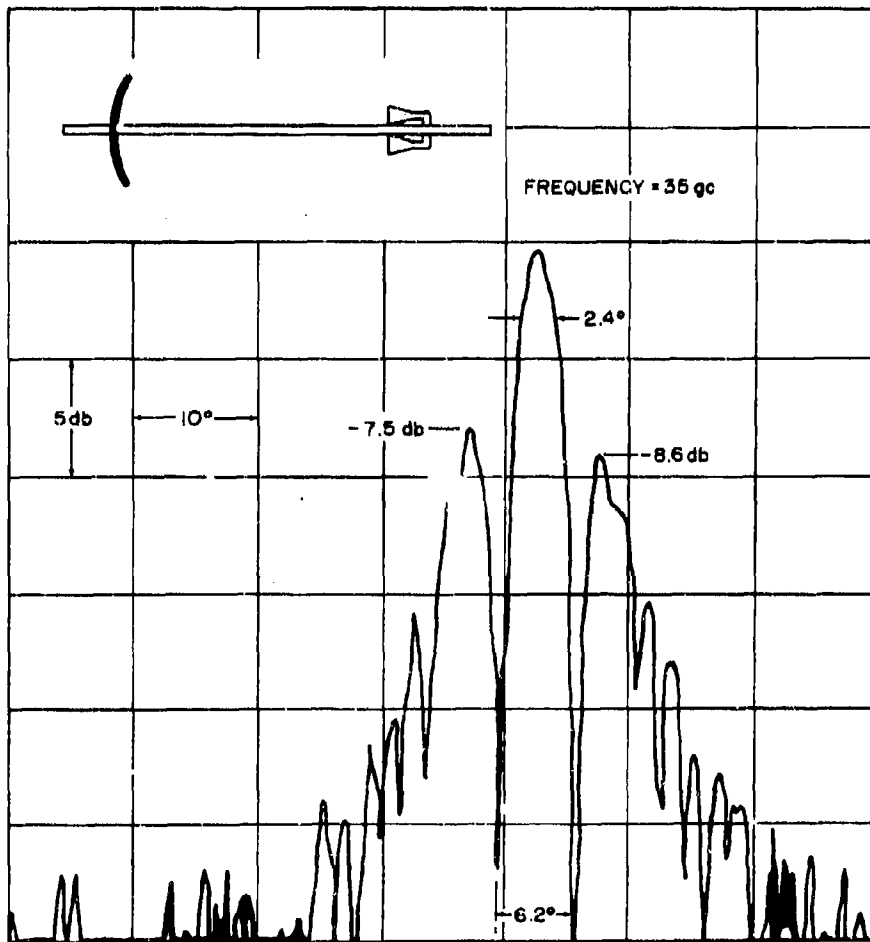


Figure 2-104. Far-Field Pattern of Dish with Two-Horn Feed and  $0^\circ$  Scan Angle

as shown in Fig. 2-107. The waveguides for the antenna can be fed through these structural ribs, as shown in Fig. 2-108. With a small feed mounted at the cone vertex, scanning was accomplished by rotating the paraboloidal reflector to obtain the patterns shown in Figs. 2-109 and 2-110. Reference 94 gives information on the performance of an amplitude monopulse system mounted in the quadripod space frame and the effects of adding circular metal rings to further strengthen the quadripod. Additional data on tripod and quadripod space frames are given in References 95 and 96.

#### 2-10.4 ELECTRICAL EFFECTS OF METAL RIBS IN LARGE CHIN RADOMES (Reference 97)

One or more metal ribs may prove helpful in supporting a large chin radome on an aircraft. Reference 97 presents the study of the pattern distortion that results when such a rib is placed in front of a shaped-beam antenna of the type often used in bombing and navigation radars. The antenna feed and reflector are shown in Fig. 2-111. Figure 2-112 shows the antenna with a structural cylinder for radome support. This antenna has essentially a  $(\sin x)/x$  field

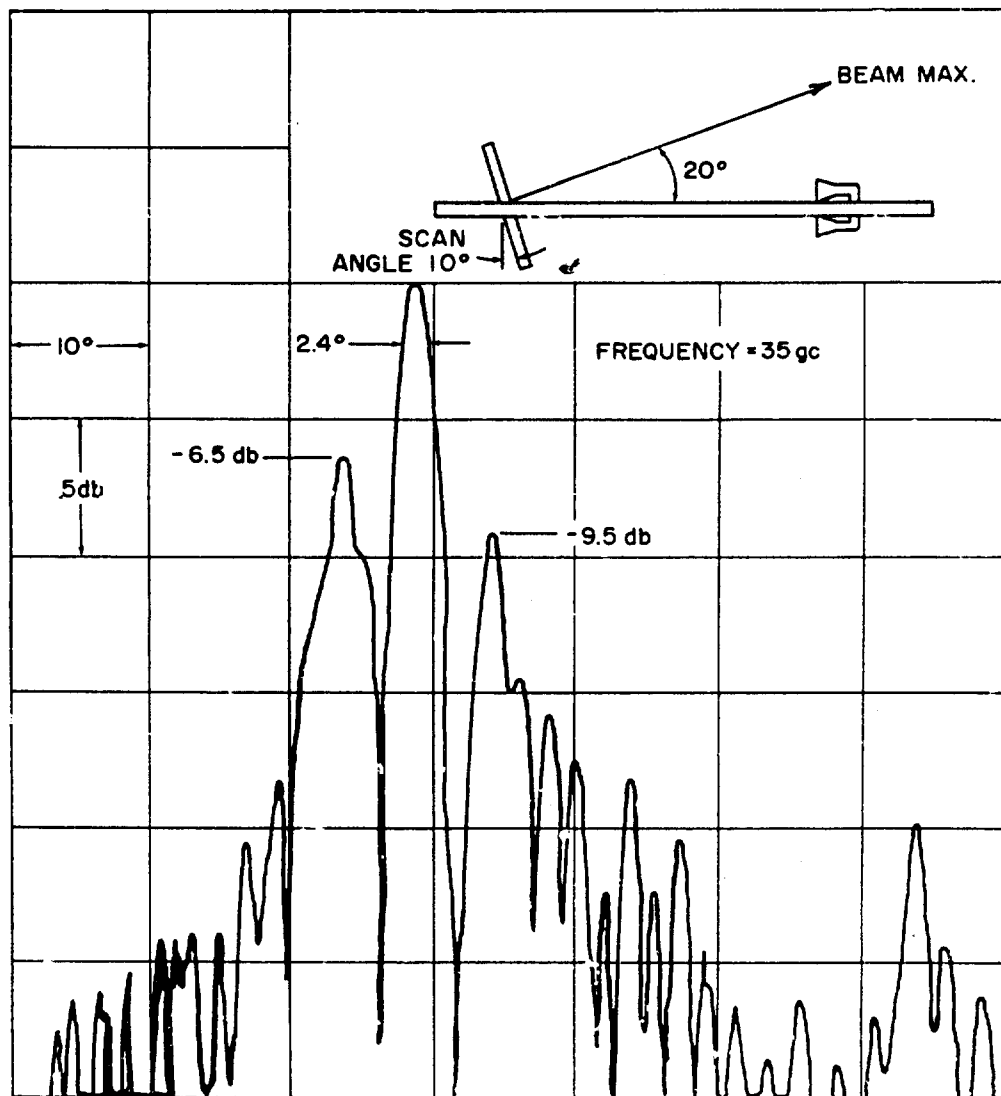


Figure 2-105. Far-Field Pattern of Dish with Two-Horn Feed and 10° Scan Angle

pattern vs. azimuth and a cosecant field pattern vs. elevation. It was found that the narrow-beam  $(\sin x)/x$  pattern suffered very little distortion when a cylinder was placed in front of the antenna. Pattern measurements were taken with the cylinder located at positions 1, 2, 3, and 4, as defined in Fig. 2-113. Figure 2-114 shows this pattern without a cylinder and the pattern with a cylinder of 1-wavelength diameter located at position 1. Although the cylinder raised the sidelobes slightly, this effect was reduced when the cylinder was moved to another location or replaced with a cylinder of smaller diameter.

The pattern distortion was more noticeable in the cosecant pattern. Typical results are shown in Figs. 2-115 through 2-118 with a

cylinder of 0.5-wavelength diameter at positions 1, 2, 3, or 4. If position 1 is avoided, it appears that a metal rib of 0.5-wavelength diameter or less can be tolerated unless the exact pattern shape is critical.

In these examples, the cylinder axis was parallel with the generating element of the reflector. Therefore, the field incident on the cylinder when the antenna transmits had essentially a uniform phase along the length of the cylinder. The scattering pattern of the cylinder was then a  $(\sin x)/x$  pattern in the plane of the cylinder and nearly a circular pattern in the plane orthogonal to the cylinder axis. On the other hand, it was found that a cylinder produces far less distortion in the antenna patterns in both planes if the cylinder axis is per-

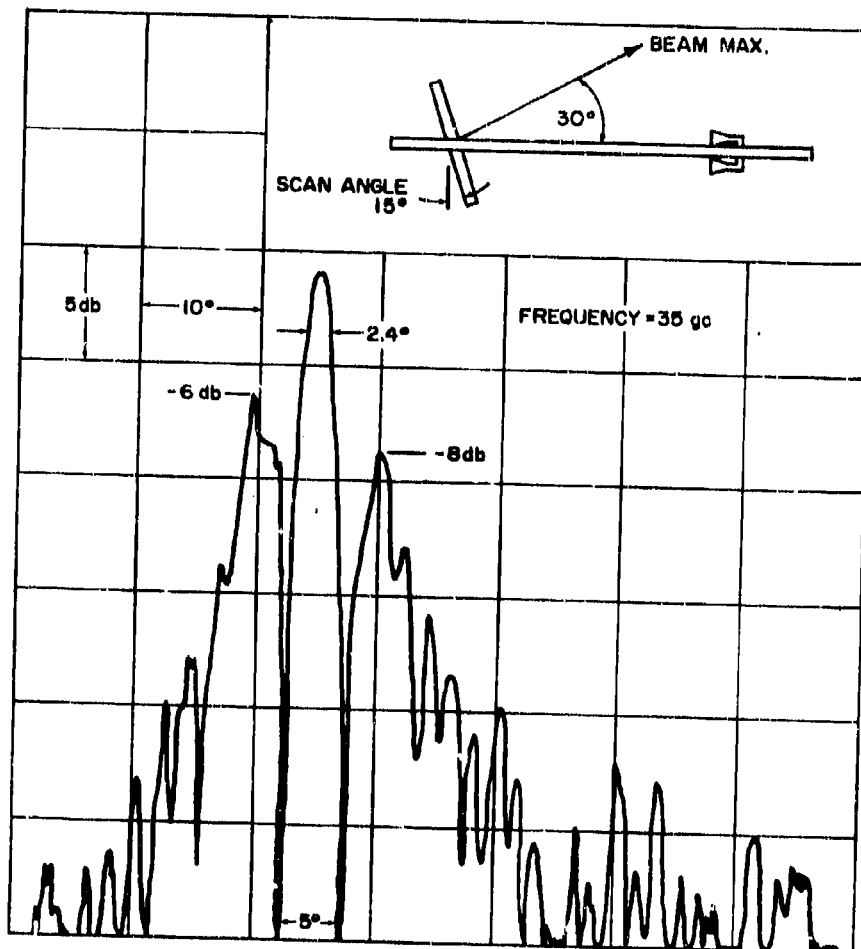


Figure 2-106. Far-Field Pattern of Dish with Two-Horn Feed and 15° Scan Angle

pendicular to the generating element of the reflector. There are two reasons for this:

- A metal cylinder has stronger scattering effects if the incident electric field intensity vector is parallel with the cylinder axis.
- If the cylinder axis is perpendicular to

the generating element of the reflector, the phase of the wave incident on the cylinder has a considerable variation along the length of the cylinder. The cylinder scattering pattern is then less directive.

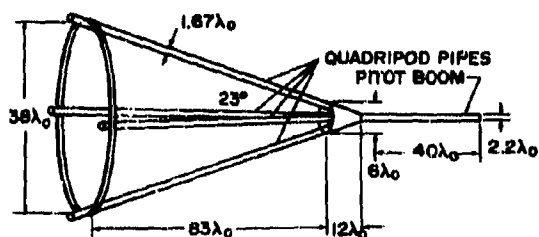


Figure 2-107. Quadripod Space Frame

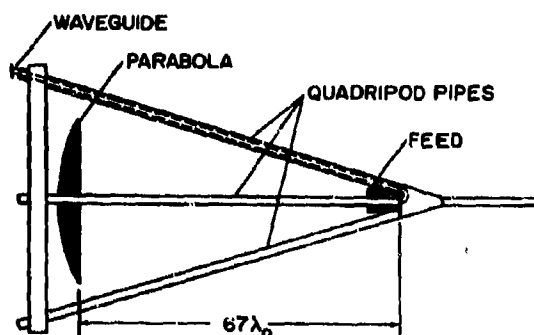


Figure 2-108. Quadripod and Long Focal Length Fixed-Feed Antenna

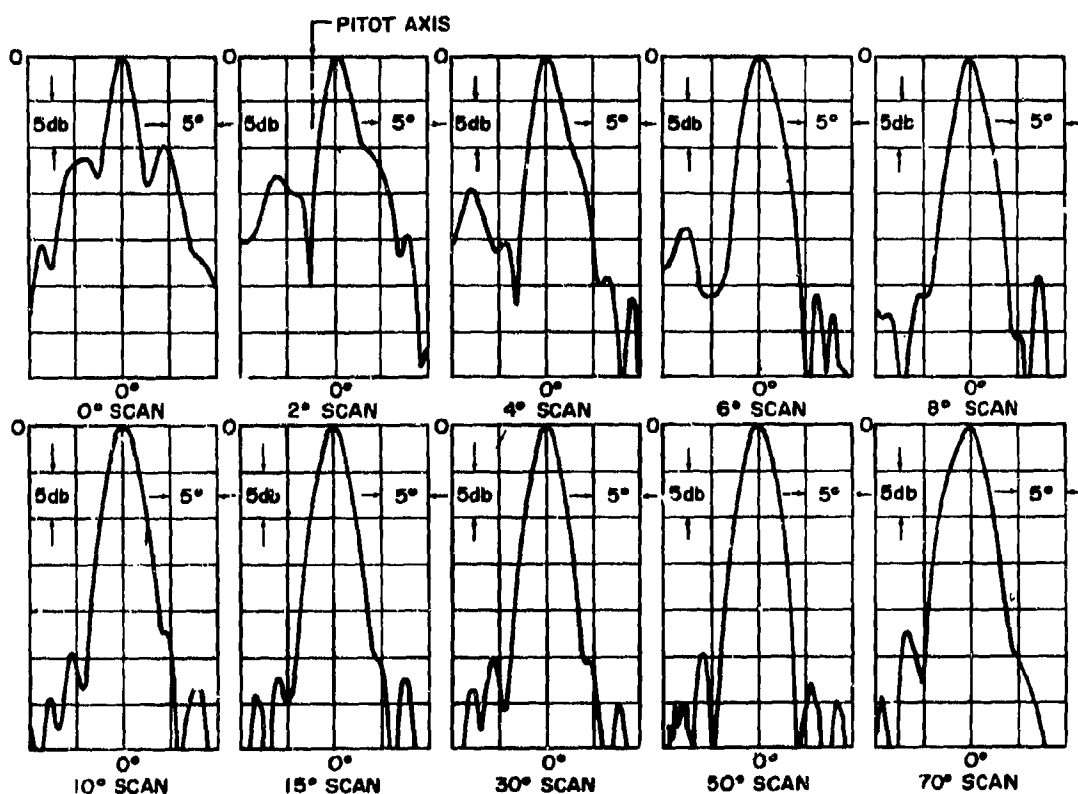


Figure 2-109. H-Plane Patterns of Long Focal Length Antenna in Space Frame

Additional information on metal ribs and simplified techniques for predicting their effects are given in Reference 97. An excellent account of an extensive theoretical and experimental investigation of space frames for large radomes is given in Reference 98.

## 2-10.5 DIFFRACTION BY OBSTACLES IN THE NEAR ZONE OF AN ANTENNA

Reference 99 shows that a useful reduction

in sidelobe level can be obtained by choosing the proper spacing between the antenna and the radome. It also shows that the boresight error introduced by a metal boom can be compensated for by correcting the radome thickness in two opposite quadrants. Reference 100 gives a summary of several techniques for calculating the pattern of an antenna in the presence of one or more conducting obstacles. As examples, the calculated patterns of horn antennas with

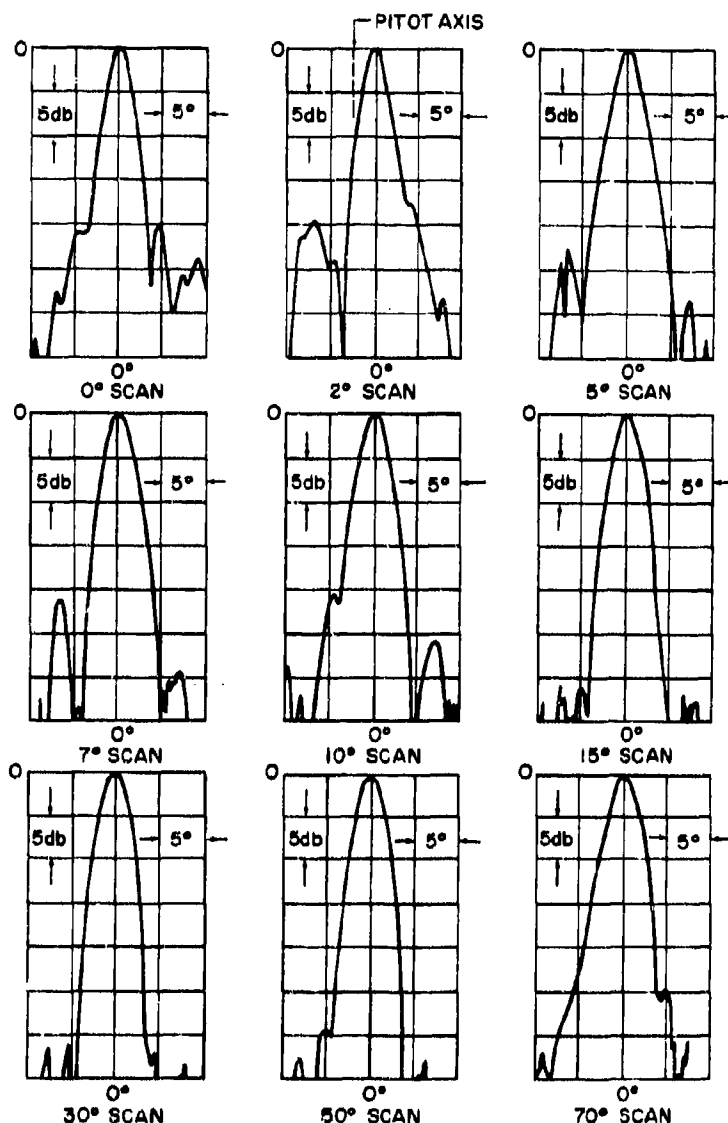


Figure 2-110. E-Plane Patterns of Long Focal Length Antenna in Quadripod

one or two metal cylinders in the near zone are given. The calculations show excellent agreement with measured results. References 101 and 102 present a computer program for the far-field patterns of an antenna in the presence of a conducting obstacle. Computed and measured data are included for an antenna whose aperture is partially blocked by a metal sphere, circular metal disk, or rectangular metal plate in the near zone. These results are useful in predicting the effects of installing an infrared or millimeter-wavelength radar system in front of the main radar antenna.

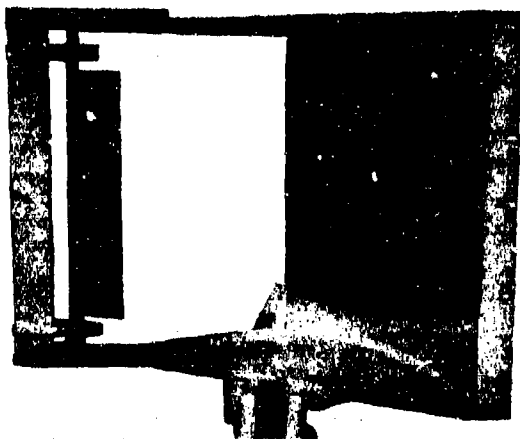


Figure 2-111. Shaped-Beam Antenna

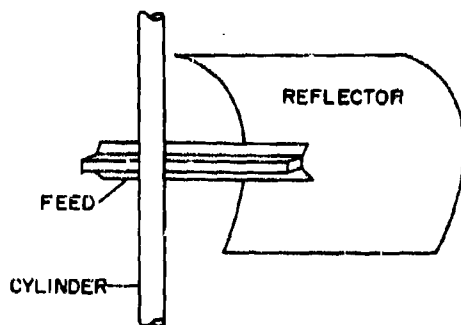


Figure 2-112. Cylinder Perpendicular to Generating Element of Reflector

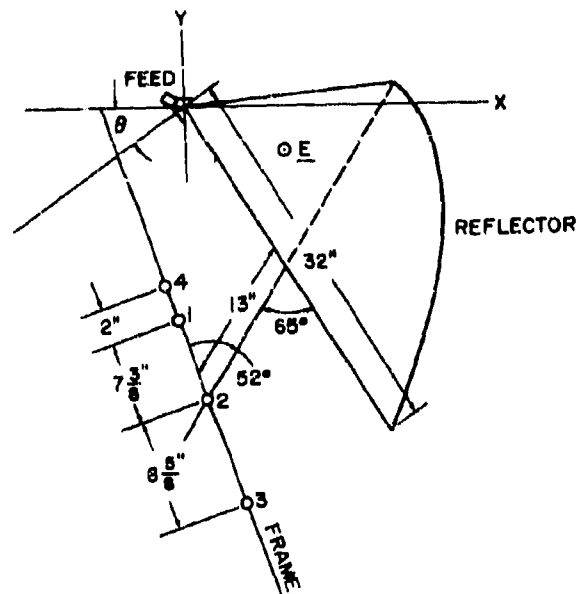


Figure 2-113. Cross Section of Antenna in Transverse Plane Showing Location of Cylinders and Dimensions of Cylinder Spacing

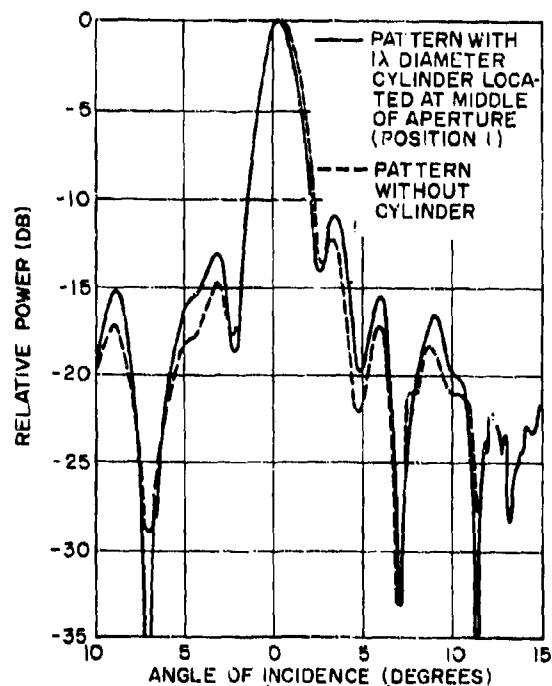


Figure 2-114. Comparison of Principal Longitudinal Plane Pattern with and without Cylinder

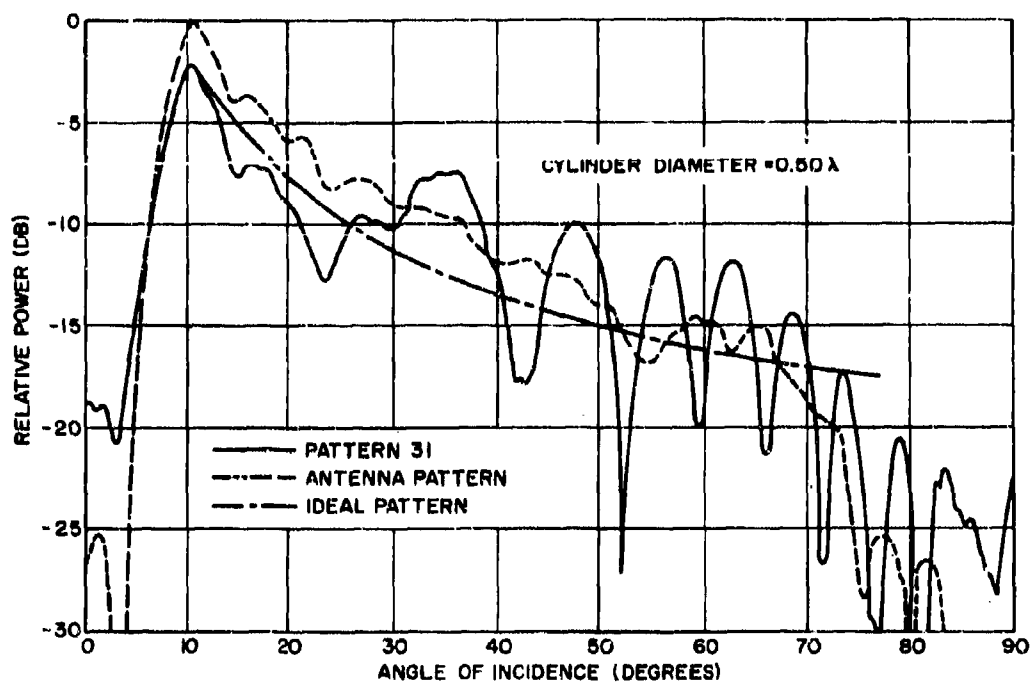


Figure 2-115. Measured Principal Transverse Plane Pattern of Antenna with and without Cylinders, Position 1

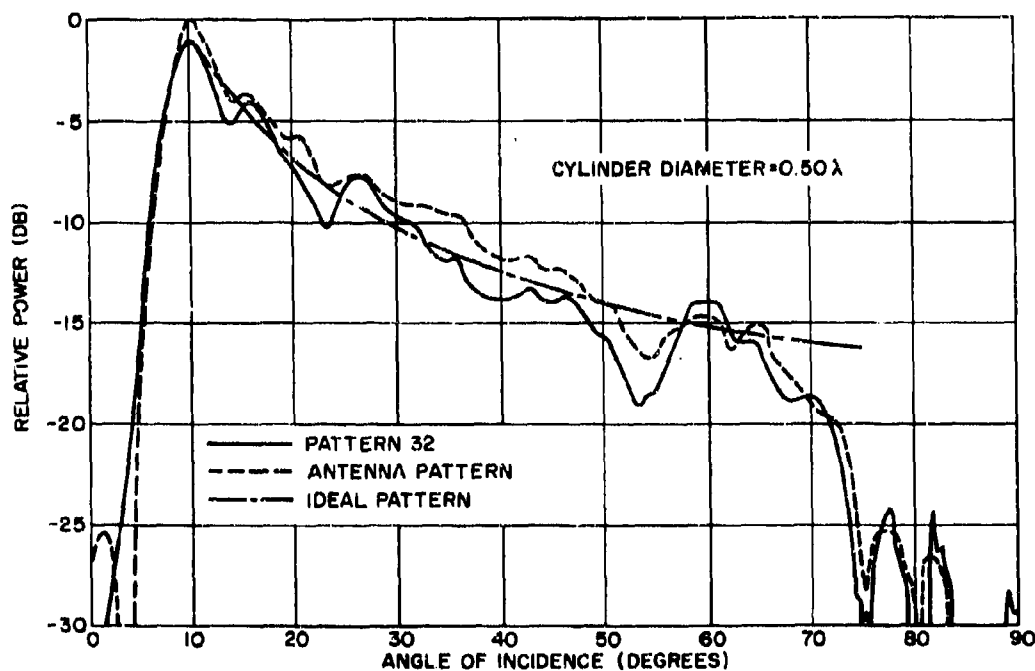


Figure 2-116. Measured Principal Transverse Plane Pattern of Antenna with and without Cylinders, Position 2



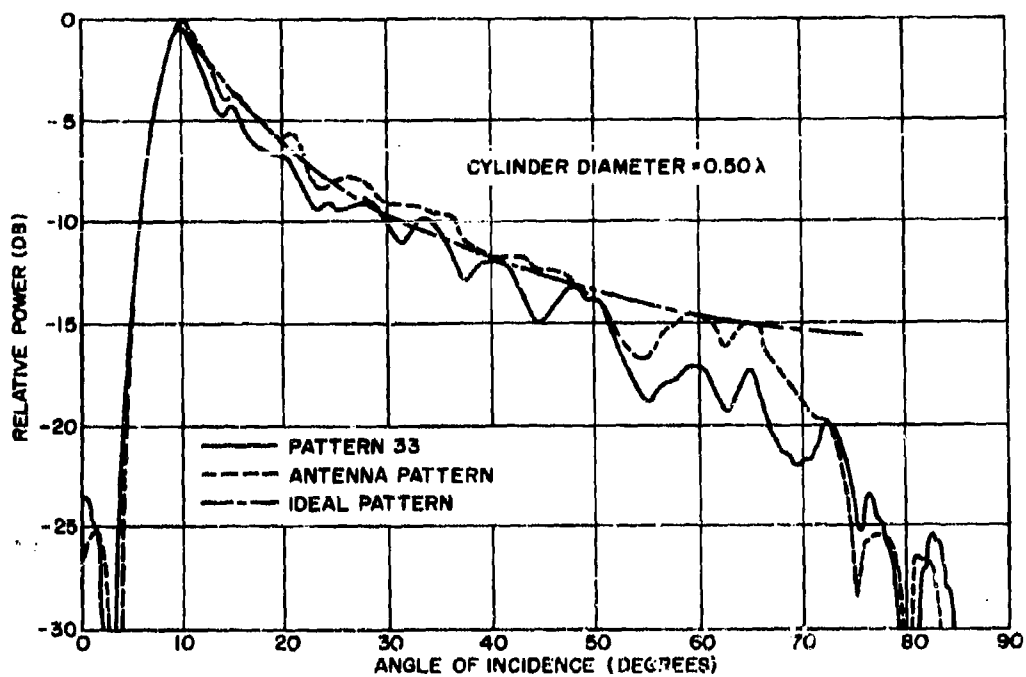


Figure 2-117. Measured Principal Transverse Plane Pattern of Antenna with and without Cylinders, Position 3

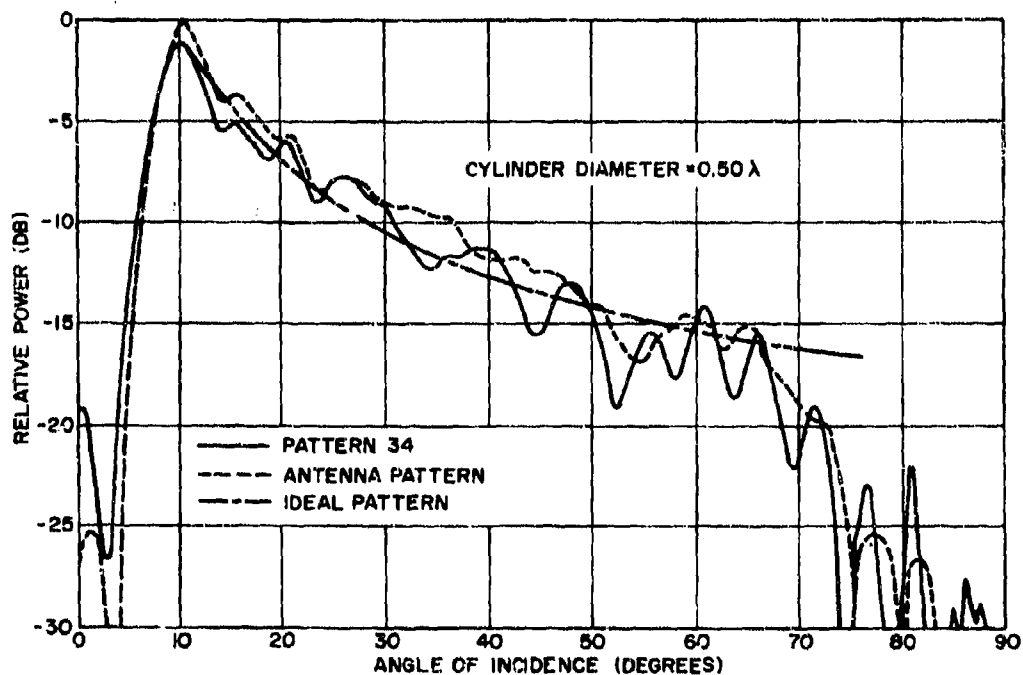


Figure 2-118. Measured Principal Transverse Plane Pattern of Antenna with and without Cylinders, Position 4

## 2-10.6 PLANE-WAVE SCATTERING BY METAL RIBS OF ARBITRARY CROSS-SECTION SHAPE

The plane-wave scattering patterns of conducting cylinders of rectangular cross-section are given in Reference 104. The integral-equation technique for calculating the scattering patterns of conducting cylinders of arbitrary cross-section is also given.

Reference 103 presents the calculations for the scattering patterns of conducting I-beams. The I-beam seems attractive for space-frame construction because of its mechanical strength

and because the edges of a radome section will fit securely into its channels. Figure 2-119 shows the scattering patterns of conducting cylinders of circular, square, and I-beam cross-section shapes with comparable dimensions. The incident electronic field intensity vector is assumed to be parallel with the cylinder axis in each case.

Reference 105 investigates the electrical and mechanical characteristics of ceramic radomes supported by metal I-beams. Figure 2-120 illustrates the cross-section of a radome wall with I-beams. In the theoretical studies, the electromagnetic field is expanded in a series of waveguide modes with unknown coefficients, includ-

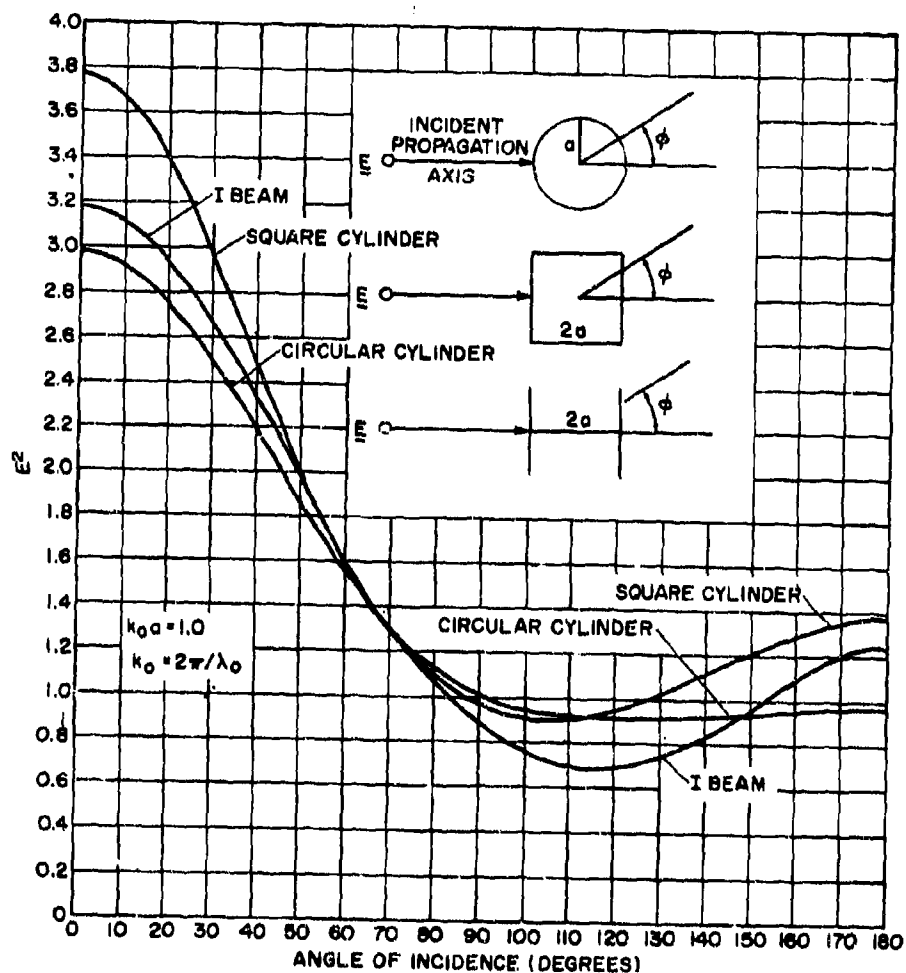


Figure 2-119. Scattering Patterns of Perfectly Conducting Cylinders of Circular, Square, and I-Beam Cross-Section Shapes

ing the higher-order modes that are beyond cut-off. The unknown coefficients are then calculated by matching the tangential field components at a discrete set of points along the surface of the dielectric wall. Figure 2-121 shows measurements of insertion phase delay as a function of the spacing between the I-beams.

#### 2-10.7 DIFFRACTION BY METAL AND DIELECTRIC RINGS

Reference 106 presents the analysis of the scattered fields of thin dielectric rings. The results are useful in the design of dielectric rings for boresight-error correction. Reference 107

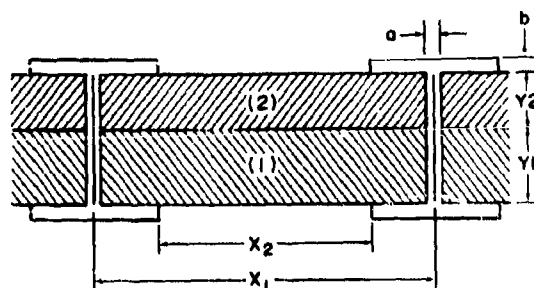


Figure 2-120. Dielectric Wall, Fenestrated by I-Beam Members

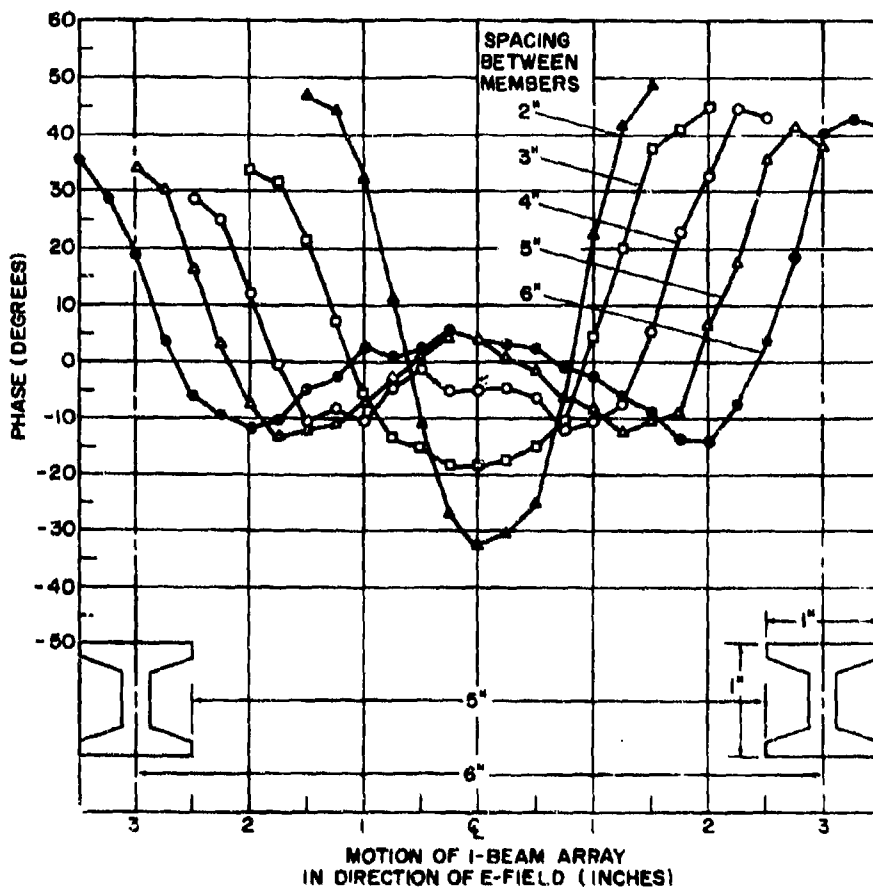


Figure 2-121. Insertion Phase Delay: Perpendicular Polarization at 45° Incidence; I-Beams Perpendicular to E-Field

presents the calculations of the scattering patterns of thin dielectric and metal rings and coaxial arrays of such rings. Figure 2-122 shows the patterns of a magnetic line source on the axis of a thin metal ring. The phase velocity of the line source is adjusted to obtain scan angles of  $40^\circ$ ,  $60^\circ$ , and  $80^\circ$  as measured from the axis. The wire has a radius of 0.00796 wavelengths (i.e.,  $k_0 b = 0.05$ ) and the radius of the ring is 2.4 wavelengths. The length of the line source is 4 wavelengths and the plane of the wire ring passes through one end of the line

source. This particular wire ring is undoubtedly too thin to serve as a structural support, but the calculation technique is also applicable to metal rings of large cross-section and with arbitrary cross-section shape. Figure 2-123 shows the results for a magnetic dipole at the center of a dielectric ring. The calculations were carried out by means of an integral-equation technique. Although the field within the dielectric is usually approximated by the incident field, this approximation is avoided in this method to obtain more accurate results.

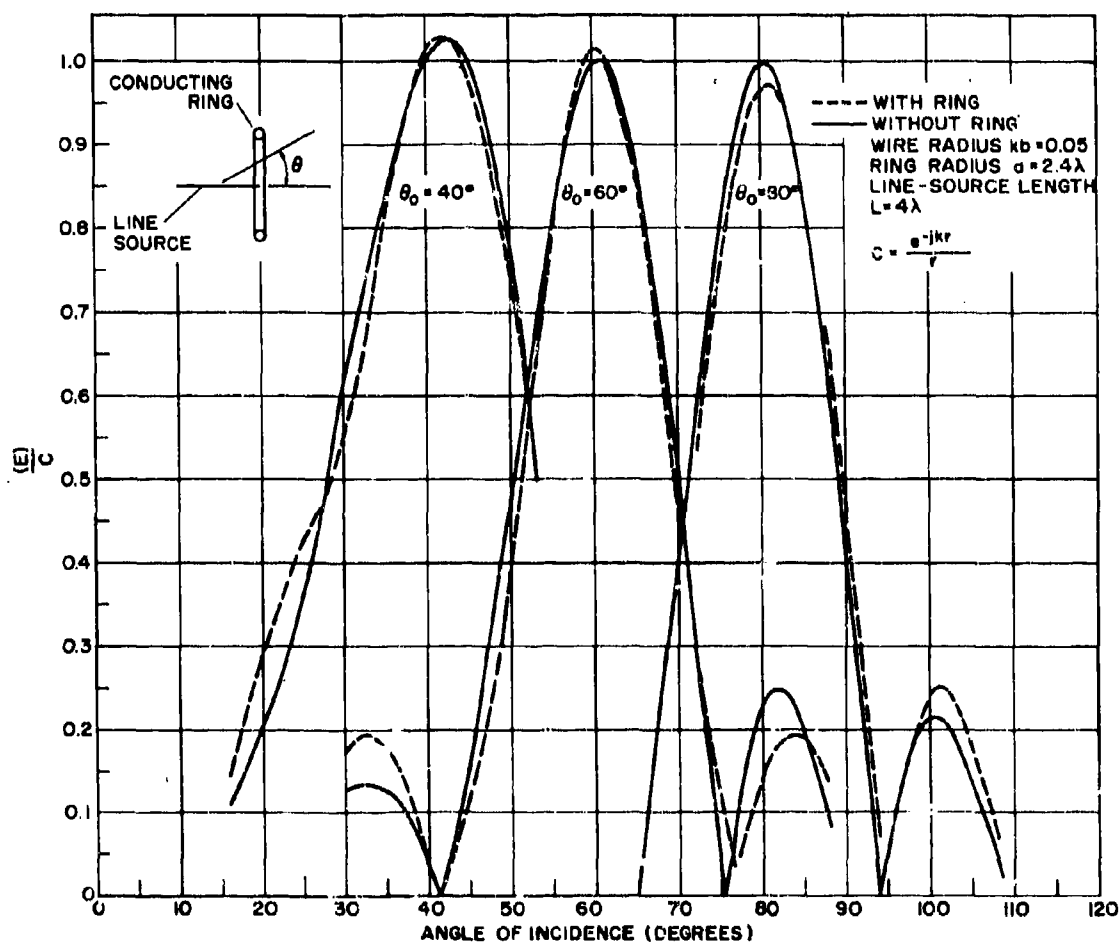


Figure 2-122. Patterns of Magnetic Line Source on Axis of Metal Toroid

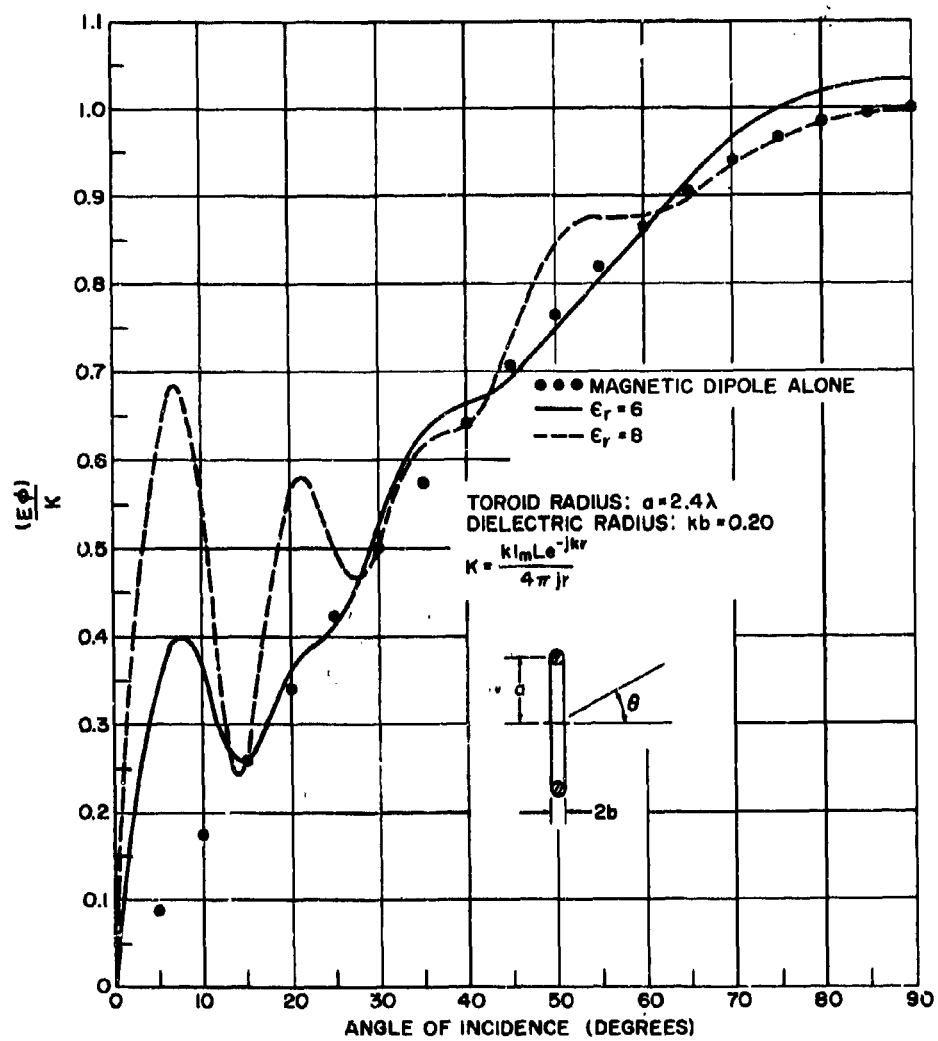


Figure 2-123. Patterns of Magnetic Dipole at Center of Dielectric Toroid

## REFERENCES

1. *Techniques for Airborne Radome Design*, edited by T. E. Tice, WADC Technical Report 57-67, Wright-Patterson Air Force Base, Ohio (ASTIA Document No. AD 142001), September 1957.
2. Loyet, D. L., and Yoshitani, R. "Ceramic Sandwich Radome Design," *Proc. OSU-RTD Symposium on Electromagnetic Windows*, June 1964 (also published as Hughes Aircraft Company document 2785.3/294).
3. Coling, F. L. "The Problems in the Design of a Thin-Wall Ceramic Radome," Douglas Aircraft Company, *Proc. ASD-OSU Symposium on Electromagnetic Windows*, Vol. 1, ASD-TDR-62-676, July 1962.
4. Loyet, D. L., and Stevens S. "A Comparison of the Thin Wall and Half-Wavelength Ceramic Radomes," Hughes Aircraft Company, *Proc. ASD-OSU Symposium on Electromagnetic Windows*, Vol. 1, ASD-TDR-62-676, July 1962.
5. Boyce, W. E. L., Dobyne, J. C., and MacAllister, W. G. "Electrical Design of Filament-Wound Nose Radomes for the F-106 Airplane," Convair, *Proc. OSU-WADC Radome Symposium*, Vol. 2, pp. 132-160 (ASTIA Document No. AD 155832), June 1958.
6. Barthez, J. "A Simplified Method for Calculating Single Wall Radomes," *Annales de Radioelectricité*, Vol. 18, pp. 49-57 and 78-79, January 1963.
7. Carroll, P. J. *A Graphic Technique for Radome Ray Analysis*, U. S. Naval Air Development Center, Aeronautical Electronic and Electrical Laboratory, Report NADC-EL-6368 (ASTIA Document No. AD 429185), January 27, 1964.
8. Taylor, W. C. "The Design of a Sandwich Wall for a 30° Wedge Radome," Lockheed Missile Systems Div., *Proc. OSU-WADC Radome Symposium*, Vol. 1, pp. 267-272 (ASTIA Document No. 155831), June 1958.
9. Harman, D. G. *Radome for Airborne Horn Cluster*, General Dynamics, Fort Worth, FZM-2529 (ASTIA Document No. AD 278408), March 1, 1962.
10. Price, C. L., Jr., and Tricoles, G. P. "The Design and Testing of a Large, Streamlined Dual Frequency Airborne Radome," General Dynamics, *Proc. OSU-RTD Symposium on Electromagnetic Windows*, June 1964.
11. Damon, E. K. *Digital Instrumentation for Antenna Near-Field Measurements*, The Ohio State University, Dept. of Electrical Eng., Report No. 662-22 (ASTIA Document No. AD 216414), February 1, 1959.
12. Hansen, R. C., and Behnke, M. C. "Bore-sight Correction by Computer Synthesis," Hughes Aircraft Co., *Proc. OSU-WADC Radome Symposium*, Vol. 2, pp. 161-173 (ASTIA Document No. AD 155832), June 1958.
13. U. S. Naval Air Development Center, Johnsville, Pennsylvania, Report Nos. NADC-EL-5104, NADC-52188, NADC-EL-52195, Vols. 1 and 2, and NADC-EL-53189.
14. Richmond, J. H. *Calculation of Transmission and Surface-Wave Data for Plane Multilayers and Inhomogeneous Plane Layers*, The Ohio State University, Dept. of Electrical Eng., Report No. 1751-2, October 31, 1963.
15. Richmond, J. H. *On the Design of One-Layer and Three-Layer Tunable Radomes*, The Ohio State University, Dept. of Electrical Eng., Report No. 1751-4 (ASTIA Document No. AD 433839), January 15, 1964.
16. Powis, S. "Radome Investigations at English Electric Co., Ltd., England," *Proc. OSU-WADC Radome Symposium*, Vol. 2, pp. 199-218 (ASTIA Document No. AD 155832), June 1958.
17. Richmond, J. H. *The Calculation of Radome Diffraction Patterns*, The Ohio State University, Dept. of Electrical Engineering, Antenna Lab., Report No. 1180-13, September 15, 1963.
18. Kotik, J., and Cope, D. "Digital Optimization of Radome Walls," Technical Research Group, *Proc. OSU-WADD Symposium on Electromagnetic Windows*, Vol. 1, pp. 220-234, June 1960.

19. Blyseth, M. C. "Computer Design and Optimization of Broadband Techniques with Arbitrary Dielectric Distributions," Grumman Aircraft Eng. Corp., ASD-TDR-62-676, *Proc. ASD-OSU Symposium on Electromagnetic Windows*, Vol. 1, July 1962.
20. Coling, F. "Radome Design by Computer," Raytheon Co., *Proc. OSU-WADD Symposium on Electromagnetic Windows*, Vol. 1, pp. 261-266, June 1960.
21. Magnus, D. E., and Eisen, D. *Research on Advanced Physical Approaches to Electromagnetic Window Design*, General Applied Science Lab., ASD-TDR-62-40, Part 1, October 1962.
22. Loyet, D. L., and Levitan, E. S. "Programming Thermal Stress Equations on the IBM 7090 Digital Computer," ASD-TDR-62-676, Hughes Aircraft Co., *Proc. ASD-OSU Symposium on Electromagnetic Windows*, Vol. 1, July 1962.
23. Luoma, E. J., Stetson, R., and Mason, S. J. "Design Techniques for Sectionalized, Structurally Supported Airborne Ceramic Radomes—A Progress Report," Emerson and Cuming, Inc., *Proc. OSU-RTD Symposium on Electromagnetic Windows*, June 1964.
24. Gunther, R. C., and Hahn, G. M. *Radar Error Prediction Study*, Fifth Scientific Report, Dalmo Victor Co., February 17, 1955.
25. *Techniques for Airborne Radome Design*, edited by T. E. Tice, WADC Technical Report 57-67, Wright-Patterson Air Force Base, Ohio (ASTIA Document No. 142001), pp. 192-193, September 1957.
26. Hahn, G. M. *Optical and Electromagnetic Techniques for Prediction of Radome Boresight Errors*, Dalmo Victor Co., WADC Technical Note 59-257, August 1959.
27. *Techniques for Airborne Radome Design*, edited by T. E. Tice, WADC Technical Report 57-67, Wright-Patterson Air Force Base, Ohio (ASTIA Document No. 142001), pp. 187-205 and 521-522, September 1957.
28. Jacobson, A. D. *Two-Dimensional Model for the Evaluation of Radome Analysis Approximations*, Hughes Aircraft Co., Technical Memorandum 580, June 1958.
29. Richmond, J. H. "Antenna Pattern Distortion by Dielectric Sheets," *IRE Trans.* Vol. AP-4, No. 2, pp. 139-142, April 1956.
30. Powis, S. "Radome Investigations at English Electric Co., Ltd., England," *Proc. OSU-WADC Radome Symposium*, Vol. 2, pp. 199-212 (ASTIA Document No. AD 155832), June 1958.
31. Tricoles, G. "A Radome Error Prediction Method Based on Aperture Fields and Rays: Formulation and Application," Smyth Research Assoc., *Proc. OSU-WADD Symposium on Electromagnetic Windows*, Vol. 1, pp. 267-286, June 1960.
32. Tricoles, G. "Measurement, Computation, and Special Frequency Analysis of Microwaves Propagated Through Radomes," Smyth Research Assoc., *Proc. OSU-WADD Symposium on Electromagnetic Windows*, Vol. 1, pp. 544-564, June 1960.
33. Tricoles, G., and Turley, D. G. *Radome Error Prediction*, Smyth Research Assoc., ASD TR 61-612 (ASTIA Document No. AD 274348), January 1962.
34. Milnor, D. P. *A Critical Examination of the Hahn Scattering Technique for Predicting Radome Boresight Error*, Thesis, Institute of Technology, Air University, Wright-Patterson Air Force Base, Ohio, Report No. GE-59-B-12, August 1959.
35. Rhodes, D. R. *On the Theory of Scattering by Dielectric Bodies*, The Ohio State University, Dept. of Electrical Eng., Antenna Lab., Report No. 475-1, July 1, 1953.
36. Andressen, M. G. "Radiation From a Radial Dipole Through a Thin Dielectric Spherical Shell," *IRE Trans.*, Vol. AP-5, No. 4, pp. 337-342, October 1957.
37. Philipson, L. L. *An Analytical Study of Scattering by a Thin Dielectric Ring*, Hughes Aircraft Co., Technical Memorandum 416, January 3, 1956.
38. Philipson, L. L. *Transmission Through a Thin Conical Radome*, Hughes Aircraft Co., Technical Memorandum 480, February 1957.
39. Richmond, J. H. *The Calculation of Radome Diffraction Patterns*, The Ohio State University, Dept. of Electrical Eng., Antenna Lab., Report No. 1180-13, September 15, 1963.
40. Klotzbaugh, G. A., Flaherty, J. M., and

- Hughes, R. H. *A Study of Artificial Dielectrics With Unity Dielectric Constants*, Westinghouse Research Lab., Report No. GR-177, April 2, 1954.
41. Grosjean, B. G. "Preparation of Artificial Dielectric Materials With Low Loss," North American Aviation, *Proc. OSU-WADD Symposium on Electromagnetic Windows*, Vol. 1, pp. 119-129, June 1960.
  42. Cuming W. R. "Dielectrics for Radomes Based on Hollow Glass Microspheres," Emerson and Cuming, Inc., *Proc. OSU-WADC Radome Symposium*, Vol. 1, pp. 428-434, June 1958.
  43. Schaufelberger, A. H. "Antenna Radome Gratings for Conical Scan Systems," Sperry Rand Corp., *Proc. OSU-RTD Symposium on Electromagnetic Windows*, June 1964.
  44. Robinson, L. A. "Composite Dielectric-Metal Radomes," Stanford Research Inst., *Proc. OSU-WADC Radome Symposium*, Vol. 2, pp. 112-131, June 1958.
  45. Robinson, L. A. *Electrical Properties of Metal-Loaded Radomes*, Stanford Research Inst., WADD Technical Report 60-84 (ASTIA Document No. AD 249410), February 1960.
  46. Worthington, H. R., Jr. *Design of Metal Screens to Improve Radome Wall Performance*, Bjorksten Research Lab., U. S. Naval Air Development Center, Report NADC-EL-5874, September 3, 1958 (Confidential).
  47. Robinson, L. A. "Perforated-Metal-Plate Radomes," Stanford Research Inst., *Proc. OSU-WADD Symposium on Electromagnetic Windows*, Vol. 2, pp. 75-96, June 1960 (Confidential).
  48. Kay, A. F. "Metal Inclusions in Radomes," Technical Research Group, *Proc. OSU-WADC Radome Symposium*, Vol. 1, pp. 273-290, June 1958.
  49. Atlas, L. M., Jahn, P. F., and Sumida, W. K. "Reinforced Alumina Ceramics for Radomes," Armour Research Foundation, *Proc. OSU-WADC Radome Symposium*, Vol. 1, pp. 406-422, June 1958.
  50. MacDonald, J. B., Jr., and Adams, R. M. *Fabrication of Reinforced Ceramic Radome*, Raytheon Co., WADC Technical Report 59-419, December 1959.
  51. Chiou, C. H., Oh, L. L., and Lunden, C. D. "Slotted Metal Radome for High-Speed Flight," The Boeing Co., *Proc. OSU-RTD Symposium on Electromagnetic Windows*, June 1964.
  52. Oh, L. L., Lunden, C. D., and Chiou, C. "Fenestrated Metal Radomes," *Microwave J.*, Vol. 7, pp. 62-66, April 1964.
  53. Gotkis, S. J. "The Scannable Ray-Fed Radome," The Ohio State University, *Proc. OSU-RTD Symposium on Electromagnetic Windows*, June 1964.
  54. Kaiser, R. L. *On Bandwidth of Radome Panels*, The Ohio State University, Dept. of Electrical Eng., Antenna Lab., Report No. 786-24 (ASTIA Document No. AD 229166), September 15, 1959.
  55. Heffner, W. H. (Technical report in preparation) The Ohio State University, Dept. of Electrical Eng., Antenna Lab.
  56. Smith, W. C. *An Investigation of the Transmission Properties of the Asymmetric "A" Sandwich Radome Wall*, Thesis, Institute of Technology, Air University, Wright-Patterson Air Force Base, Ohio (ASTIA Document No. AD 161838), March 1958.
  57. Zuzolo, P., Horn, C., and Jurczak, S. "An Application of Radome Broadbanding," Republic Aviation Corp., *Proc. OSU-RTD Symposium on Electromagnetic Windows*, June 1964.
  58. Harder, J. F., and Guarino, W. P. "Wide Band ECM Radomes on High Performance Aircraft," Grumman Aircraft Eng. Corp., *Proc. OSU-RTD Symposium on Electromagnetic Windows*, June 1964.
  59. Tricoles, G. "Two Synthetic Approaches to Transmission Through Dielectric Sheets", Convair, *Proc. OSU-WADC Radome Symposium*, Vol. 1, June 1958, pp. 291-323.
  60. Blyseth, M. C. "Computer Design and Optimization of Broadband Structures With Arbitrary Dielectric Distributions," Grumman Aircraft Eng. Corp., ASD-TDR-62-676, *Proc. ASD-OSU Symposium on Electromagnetic Windows*, Vol. 1, July 1962.
  61. McClure, D. H. "A Study of Radome Frequency Broadbanding," Zenith Plastics Co., WADC Technical Report 58-151



- (ASTIA Document No. AD 302791), April 1959 (Confidential).
62. Kotik, J. *A Study of Broadband Radome Design Techniques for ECM Radar Systems*, Technical Research Group, WADD Technical Report 60-29 (ASTIA Document No. AD 321806) (Secret).
  63. Munoz, D., and Van Doren, L. *Research and Investigation of Broadband Inorganic Electromagnetic Window Techniques*, Smyth Research Assoc., Technical Documentary Report RTD-TDR-63-4160, December 1963.
  64. Garnham, R. H. *Some Methods of Preventing the Reflection on Electromagnetic Waves at the Boundary Between Two Dielectrics*, Telecommunications Research Establishment, England, ATI 116 059, August 1951.
  65. Haddenhorst, H. G. *Z. angew. Physik*, Vol. VII, p. 487, 1955.
  66. Collin, R. E. "Properties of Slotted Dielectric Interfaces," *IRE Trans.*, Vol. AP-7, No. 1, p. 62, January 1959.
  67. Jones, E. M. T., Morit, T., and Cohn, S. B. "Measured Performance of Matched Dielectric Lenses," *IRE Trans.*, Vol. AP-4, No. 1, p. 31, January 1956.
  68. Morita, T., and Cohn, S. B. "Microwave Lens Matching by Simulated Quarter-Wave Transformers," *IRE Trans.*, Vol. AP-4, No. 1, p. 33, January 1956.
  69. Kofoid, M. J., and Truttman, P. M. "A Practical High-Strength Broad-Band Radome Wall," The Boeing Co., *Proc. OSU-WADC Radome Symposium*, Vol. 1, pp. 257-266, June 1958.
  70. Jones, E. M. T., Cohn, S. B., and Robinson, L. A. "Wide-Band Radomes Matched by Reactive Walls," Stanford Research Inst., *Proc. OSU-WADC Radome Symposium*, Vol. 1, pp. 52-67, June 1955.
  71. Worthington, H. R., Jr. *Design of Metal Screens to Improve Radome Wall Performance*, U. S. Naval Air Development Center, Report NADC-EL-5874, September 3, 1958 (Confidential).
  72. Miller, B. M., and Brown, D. L. "Grids for Radomes," Goodyear Aircraft Corp., *Proc. OSU-WADC Radome Symposium*, Vol. 1, pp. 138-149, June 1957.
  73. Telew, W., and Bailey, R. "Application of Reactive Wall Matching Techniques to Electromagnetic Window Design," North American Aviation, *Proc. ASD-OSU Symposium on Electromagnetic Windows*, Vol. 1, July 1962.
  74. Richmond, J. H. "The WKB Solution for Transmission Through Inhomogeneous Plane Layers," *IRE Trans.*, Vol. AP-10, No. 4, pp. 472-473, July 1962.
  75. Richmond, J. H. "Transmission Through Inhomogeneous Plane Layers," *IRE Trans.*, Vol. AP-10, No. 3, pp. 300-305, May 1962.
  76. Taylor, W. C. "Transmission and Reflection by a Dielectric Sheet With Complex Permittivity Variable in the Transverse Direction," Lockheed Missile Systems Div., *Proc. of the OSU-WADC Radome Symposium*, Vol. 1, pp. 75-80, June 1957.
  77. Schmitt, H. J. "Radomes With Inhomogeneous Walls," McMillan Lab., *Proc. OSU-WADC Symposium on Electromagnetic Windows*, Vol. 1, pp. 249-260, June 1960.
  78. Chung, C., Mathis, H. F., Richmond, J. H., and Russo, P. M. "Electrically-Tunable Radome Sandwiches," The Ohio State University, *Proc. ASD-OSU Symposium on Electromagnetic Windows*, Vol. 1, July 1962.
  79. Richmond, J. H. *On the Design of One-layer and Three-layer Tunable Radomes*, The Ohio State University, Dept. of Electrical Eng., Antenna Lab., Report 1751-4 (ASTIA Document No. AD 433839), January 15, 1964.
  80. Moulemans, J. I. *Controlled-Parameter Compensation for a Radome With an Ablation Layer*, Thesis, Institute of Technology, Air University, Wright-Patterson Air Force Base, Ohio, Report GE/EE/60-10, August 1960.
  81. McClure, D. H. *A Study of Radome Frequency Broadbanding*, Zenith Plastics Co., WADC Technical Report 58-151, (ASTIA Document No. AD 302791), April 1959 (Confidential).
  82. Schmitt, H. J. "Radomes With Inhomogeneous Walls," McMillan Lab., *Proc. OSU-WADC Symposium on Electromagnetic Windows*, Vol. 1, pp. 249-260, June 1960.
  83. Coling, F. L. "The Problems in the Design of a Thin-Wall Ceramic Radome," Doug-

- las Aircraft Co., *Proc. ASD-OSU Symposium on Electromagnetic Windows*, Vol. 1, ASD-TDR-62-676, July 1962.
84. Richmond, J. H., and Tice, T. E. *Proposed Unified Scanner-Radome Approach to Radiating System Research and Development Planning*, The Ohio State University, Dept. of Electrical Eng., Antenna Lab., Report No. 786-16 (ASTIA Document No. AD 319467), December 15, 1958.
  85. Portune, W. J. "Flush Scanning Antenna Radome Systems," Wright Air Development Center, *Proc. OSU-WADC Radome Symposium*, Vol. 2, pp. 52-63 (ASTIA Document No. AD 155832), June 1958.
  86. Crosswell, W. F., Moore, D. P., and Richmond, J. H. "Unified Antenna-Radome Seeker Systems," The Ohio State University, *Proc. OSU-WADC Radome Symposium*, Vol. 2, pp. 64-88 (ASTIA Document No. AD 155832), June 1958.
  87. Crosswell, W. F. *Arrays of Frequency-Scanned Antennas*, The Ohio State University, Dept. of Electrical Eng., Antenna Lab., Report No. 677-44 (ASTIA Document No. 221640), July 31, 1958.
  88. King, D. D., and Moore, E. J., *Flush-Mounted Seeker Antenna Program of the Air Force*, Stanford Research Inst., Memorandum Report SRI Project 1197, June 1957 (Secret).
  89. Chernin, M. G., et al. "Integral Nose Cone Antenna," Hughes Aircraft Co. and University of Michigan, *Proc. OSU-WADC Radome Symposium*, Vol. 2, pp. 174-198, (ASTIA Document No. AD 155832), June 1958.
  90. *Flush Scanning Missile Seeker Antenna*, Final Report, Technical Research Group, Contract AF33(616)-8936, February 28, 1958.
  91. Rudduck, R. C., Ryan, C. E., and Walter, C. H. "Geodesic Lenses for Aerospace Applications," *IEEE Trans. on Aerospace*, Vol. 2, No. 2, pp. 289-293, April 1964.
  92. MacDonald, J. B., Jr., and Adams, R. M. *Fabrication of Reinforced Ceramic Radome*, Raytheon Co., WADC Technical Report 59-419, December 1959.
  93. Crosswell, W. F., Moore, D. P., and Richmond, J. H. *Unified Antenna-Radome Seeker Systems*, The Ohio State University, *Proc. OSU-WADC Radome Symposium*, Vol. 2, pp. 64-88 (ASTIA Document No. AD 155832), June 1958.
  94. Charlton, T. E. *The Quadripod Space Frame and Antenna System Performance*, The Ohio State University, Dept. of Electrical Eng., Antenna Lab., Report No. 1180-2 (ASTIA Document No. AD 324248), March 15, 1961.
  95. Collier, J. R. *The Effect of Various Space Frame Configurations on the Directivity and Sidelobe Level of an Antenna*, The Ohio State University, Dept. of Electrical Eng., Antenna Lab., Report No. 1180-11 (ASTIA Document No. AD 289340), October 25, 1962.
  96. Richmond J. H., and Charlton T. E. "Potentialities of Radome Scanner Integration," The Ohio State University, *Proc. OSU-WADC Symposium on Electromagnetic Windows*, Vol. 2, pp. 58-74, June 1960.
  97. Lawrie, R. E. *Beam Distortion by a Conducting Cylinder in the Aperture of a Ground-Search Antenna*, The Ohio State University, Dept. of Electrical Eng., Antenna Lab., Report No. 1751-1, November 1, 1963.
  98. Kay, A. F. "Electrical Design of Metal Space Frame Radomes," Technical Research Group, August 20, 1963.
  99. Tricoles, G. "The Effects of Various Obstacles on the Performance of Radomes and Antennas," Smyth Research Assoc., *Proc. OSU-WADC Symposium on Electromagnetic Windows*, Vol. 1, pp. 287-290, June 1960.
  100. Charlton, T. E. *An Analysis of Antennas Confronted by Obstacles*, The Ohio State University, Dept. of Electrical Eng., Antenna Lab., Report No. 1180-8 (ASTIA Document No. AD 268389), November 30, 1961.
  101. Collier, J. R. "Effects of Antenna Aperture Blocking," The Ohio State University, *Proc. ASD-OSU Symposium on Electromagnetic Windows*, Vol. 1, July 1962.
  102. Collier, J. R. *Digital Calculation of E. M. Diffraction from Aperture Blocking*, The Ohio State University, Dept. of Electrical Eng., Antenna Lab., Report No. 1180-5

- (ASTIA Document No. AD 266310), September 15, 1961.
103. Richmond, J. H. *Scattering by an Arbitrary Array of Parallel Wires*, The Ohio State University, Dept. of Electrical Eng., Antenna Lab., Report No. 1522-7, April 30, 1964.
  104. Mei, K. K. and Van Bladel, J. G. "Scattering by Perfectly-Conducting Rectangular Cylinders," University of California, *IRE Trans.*, Vol. AP-11, No. 2, pp. 185-192, March 1963.
  105. Luoma, E. J., Stetson, R., and Mason, S. J. "Design Techniques for Sectionalized, Structurally Supported Airborne Ceramic Radomes—A Progress Report," Emerson and Cuming, Inc., *Proc. OSU-RTD Symposium on Electromagnetic Windows*, June 1964.
  106. Philipson, L. L. "An Analytical Study of Scattering by Thin Dielectric Rings," Hughes Aircraft Co., *IRE Trans.*, Vol. AP-6, No. 1, pp. 3-8, January 1958.
  107. Richmond, J. H. *Diffraction by a Coaxial Array of Metal or Dielectric Toroids*, The Ohio State University, Dept. of Electrical Eng., Antenna Lab., Report No. 1751-5, July 9, 1964.

## BIBLIOGRAPHY

### A ALLEVIATION OF BORESIGHT-ERROR PROBLEM BY CONTROL-SYSTEM MODIFICATION

Cosgriff, R. L. "Alleviation of Radome Tolerances by System Modification," The Ohio State University, *Proc. of the OSU-WADC Radome Symposium*, Vol. 2, pp. 25-31 (ASTIA Document No. AD 155832), June 1958.

Frye, H. E., and O'Brien, R. M. "Effect of Boresight Error Rate on Terminal Guidance and Control," The Boeing Co., *Proc. OSU-WADD Symposium on Electromagnetic Windows*, Vol. 1, WADD Technical Report 60-274, pp. 471-496, June 1960.

Smith, G. L. *A Homing Missile Control System to Reduce the Effects of Radome Diffraction*, National Aeronautics and Space Administration, Technical Memo X-395 (ASTIA Document No. AD 319677), October 1960 (Confidential).

### B COMBINATION RADOME-IRDOME DESIGN TECHNIQUES

*Integrated Infrared-Radar Airborne Detection Study*, California Technical Industries, Interim Report 467-12 (ASTIA Document No. AD 338978), October 24, 1957 (Confidential).

Wolfe, W. L. "A Comparison and Contrast of Nomenclature and Techniques in the Microwave and Infrared Regions," University of Michigan, *Proc. OSU-WADD Symposium on Electromagnetic Windows*, Vol. 1, June 1960, WADD Technical Report 60-274, pp. 1-14.

McKusick, W., et al., "New Dome Materials for Dual-Mode Applications," Eastman Kodak Co., *Proc. OSU-WADD Symposium on Electromagnetic Windows*, Vol. 1, June 1960, WADD Technical Report 60-274, pp. 30-38.

Wolfe, W. L., and Ballard, S. S. "Window Materials for the Infrared Region of the Electromagnetic Spectrum," University of Michigan and University of Florida, *Proc. OSU-WADD Symposium on Electromagnetic Windows*, Vol. 1, June 1960, WADD Technical Report 60-274, pp. 39-52.

Runyan, W. R. "Silicon for Infrared Optical Use," Texas Instruments, Inc., *Proc. OSU-WADD Symposium on Electromagnetic Windows*, Vol. 1, June 1960, WADD Technical Report 60-274, pp. 53-73.

Kallmann, H., Rennert, J., and Sidran, M. "Infrared Photography Using Persistent Internal Polarization in Phosphor Plates," New York University, *Proc. OSU-WADD Symposium on Electromagnetic Windows*, Vol. 1, June 1960, WADD Technical Report 60-274, pp. 106-118.

Rosett, B., and Jerger, J., Jr. "Infrared Achromatization," Servo Corp. of America, *Proc. OSU-WADD Symposium on Electromagnetic Windows*, Vol. 1, June 1960, WADD Technical Report 60-274, pp. 130-146.

Stierwalt, D. L. "Spectral Emissivity of Germanium and Silicon," U. S. Naval Ordnance Laboratory, *Proc. OSU-WADD Symposium on Electromagnetic Windows*, Vol. 1, June 1960, WADD Technical Report 60-274, pp. 162-174.

Rubin, E. S., Fahrenholz, F. E., and Lorah, L. D. "Design Criteria for Aerodynamic Windows," Massachusetts Institute of Technology, *Proc. OSU-WADD Symposium on Electromagnetic Windows*, Vol. 2, June 1960, WADD Technical Report 60-274, pp. 14-42 (Confidential).

Bray, B. C., and Turner, W. L. "Dual Mode Dome Design Problems," Convair, *Proc. OSU-WADD Symposium on Electromagnetic Windows*, Vol. 2, June 1960, WADD Technical Report 60-274, pp. 43-56 (Confidential).

*A Study to Investigate Compatible Aerodynamic and Optical Configurations for an Advanced-Type Missile Environment*, RCA Defense Electronic Products, Final Report, (ASTIA Document No. AD 332127), September 1962 (Confidential).

Li, P. C., Capriulo, A. J., and Lepie, M. P. "Chemically Vapor Deposited Boron Nitride," Raytheon Co., *Proc. OSU-RTD Symposium on Electromagnetic Windows*, June 1964.

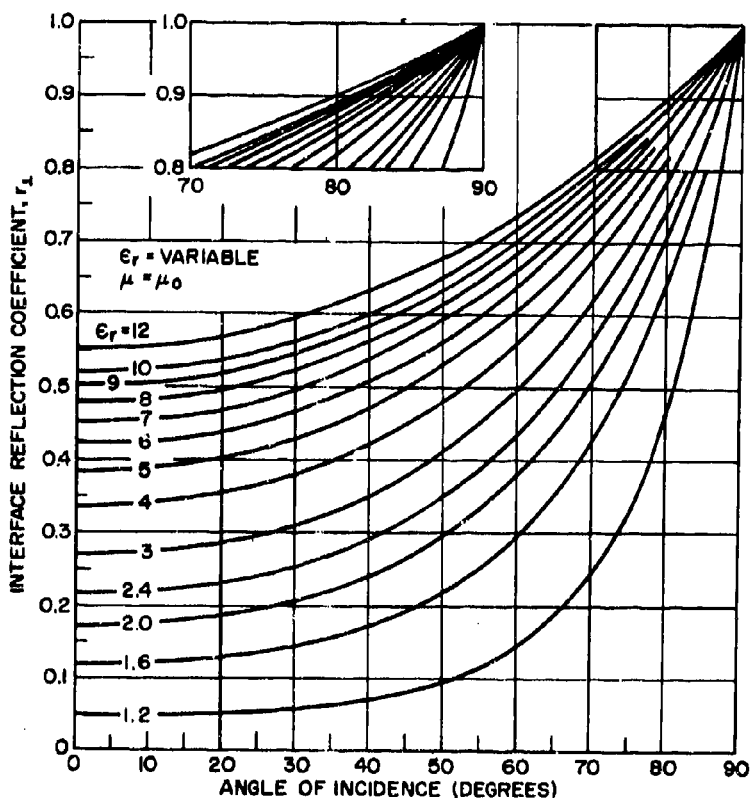


Figure 2-A1. Interface Reflection Coefficient for Lossless Dielectric with Perpendicular Polarization

## APPENDIX

### 2-A1 RADOME DESIGN CURVES

This appendix presents some of the sets of curves that are useful in radome design. Since it is not feasible to include a great number of curves, an attempt has been made to select representative data for solid-wall radomes and sandwiches.

#### 2-A1.1 THE INTERFACE REFLECTION COEFFICIENTS

When a plane wave in free space is incident on the plane surface of a homogeneous dielectric medium of infinite thickness, the reflection coefficients are given by (assuming  $\mu = \mu_0$ ):

$$r = \frac{\cos \theta - \sqrt{\epsilon_r - \sin^2 \theta}}{\cos \theta + \sqrt{\epsilon_r - \sin^2 \theta}} = E_r/E_i \quad (\text{perpendicular polarization}) \quad (2-A1)$$

and

$$r = \frac{\epsilon_r \cos \theta - \sqrt{\epsilon_r - \sin^2 \theta}}{\epsilon_r \cos \theta + \sqrt{\epsilon_r - \sin^2 \theta}} = H_r/H_i \quad (\text{parallel polarization}) \quad (2-A2)$$

where  $r$  = interface reflection coefficient

$\theta$  = angle of incidence measured

$\epsilon_r$  = complex relative dielectric constant, which is given by:

$$\epsilon_r = \epsilon/\epsilon_0 = \epsilon_r(1 - j \tan \delta) \quad (2-A3)$$

The loss tangent of the medium is represented by  $\tan \delta$ . Figures 2-A1 and 2-A2 (Reference 1) show the interface reflection coefficient vs. angle

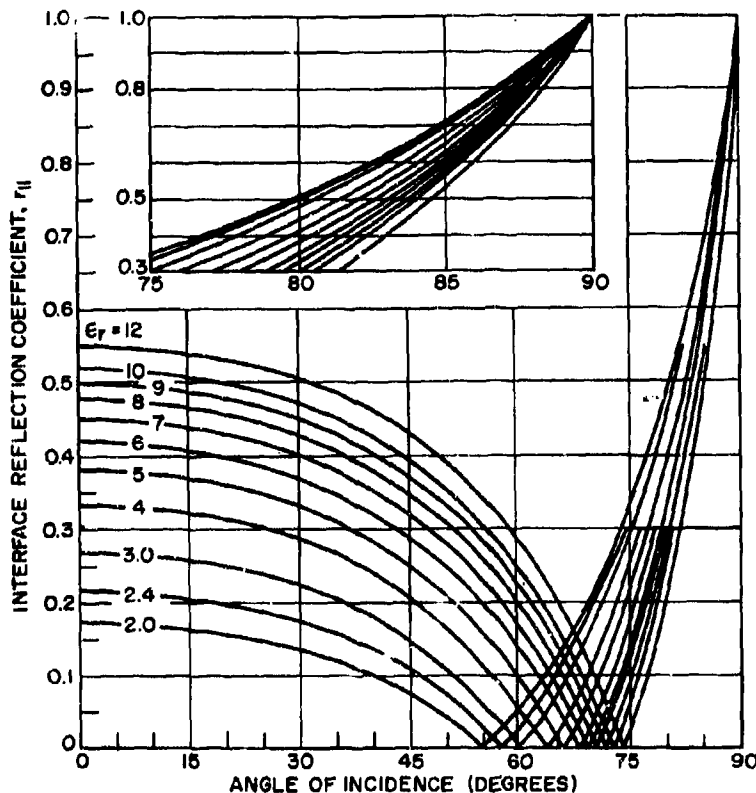
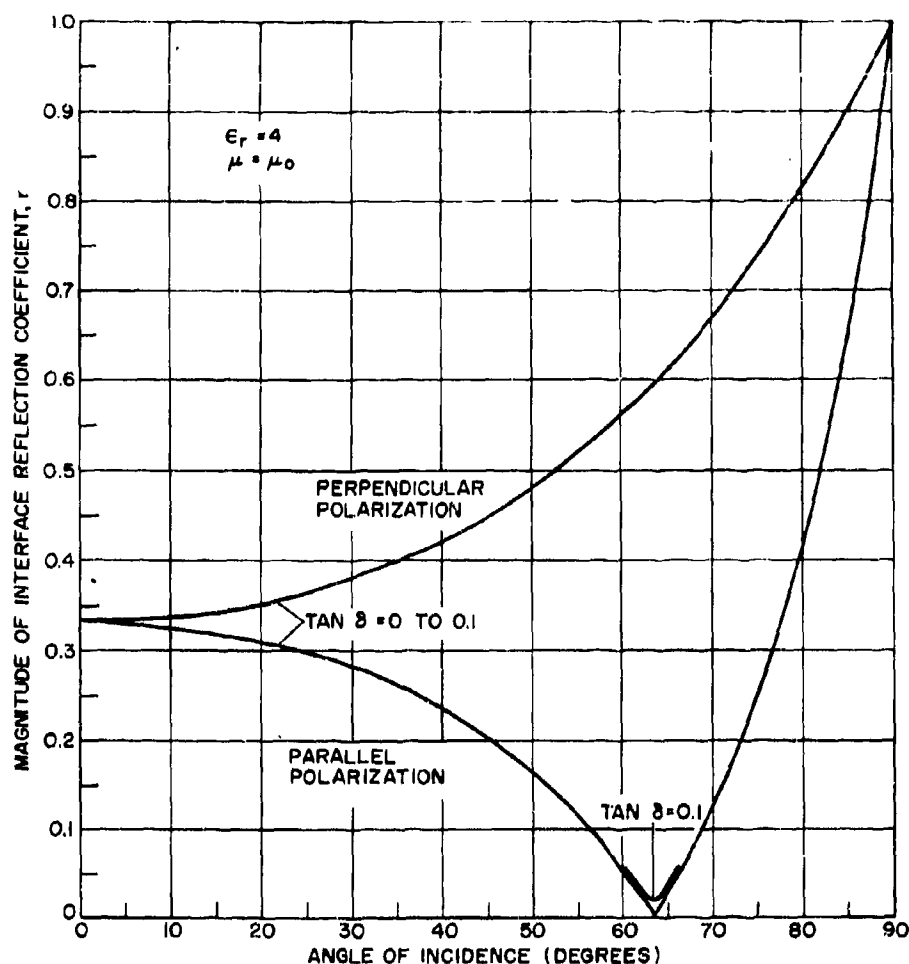


Figure 2-A2. Interface Reflection Coefficient for Lossless Dielectric with Parallel Polarization



**Figure 2-A3. Magnitude of Interface Reflection Coefficient vs Angle of Incidence for Lossless and Lossy Dielectric Materials**

of incidence for lossless media having relative dielectric constants up to 12. Figures 2-A3 and 2-A4 illustrate the magnitude and phase of the interface reflection coefficients vs. angle of incidence for a medium with a relative dielectric constant of 4.0 and loss tangents of 0, 0.01, and 0.1. Figure 2-A3 shows that loss tangents in this range have no noticeable effect on the reflection magnitude except in the immediate vicinity of the Brewster angle. While the reflection coefficients of a lossless medium are real, they are complex if the loss tangent exceeds

zero (Fig. 2-A4). Except in the vicinity of the Brewster angle, however, the phase angle of the reflection coefficient is very small when the loss tangent is less than 0.01. These results suggest that the loss tangent may be neglected when calculating the interface reflection coefficients of low-loss radome media, with little loss of accuracy in the transmission coefficient for solid walls or sandwiches.

Figure 2-A2 shows that the interface reflection coefficient goes to zero for parallel polarization at an angle of incidence known as the

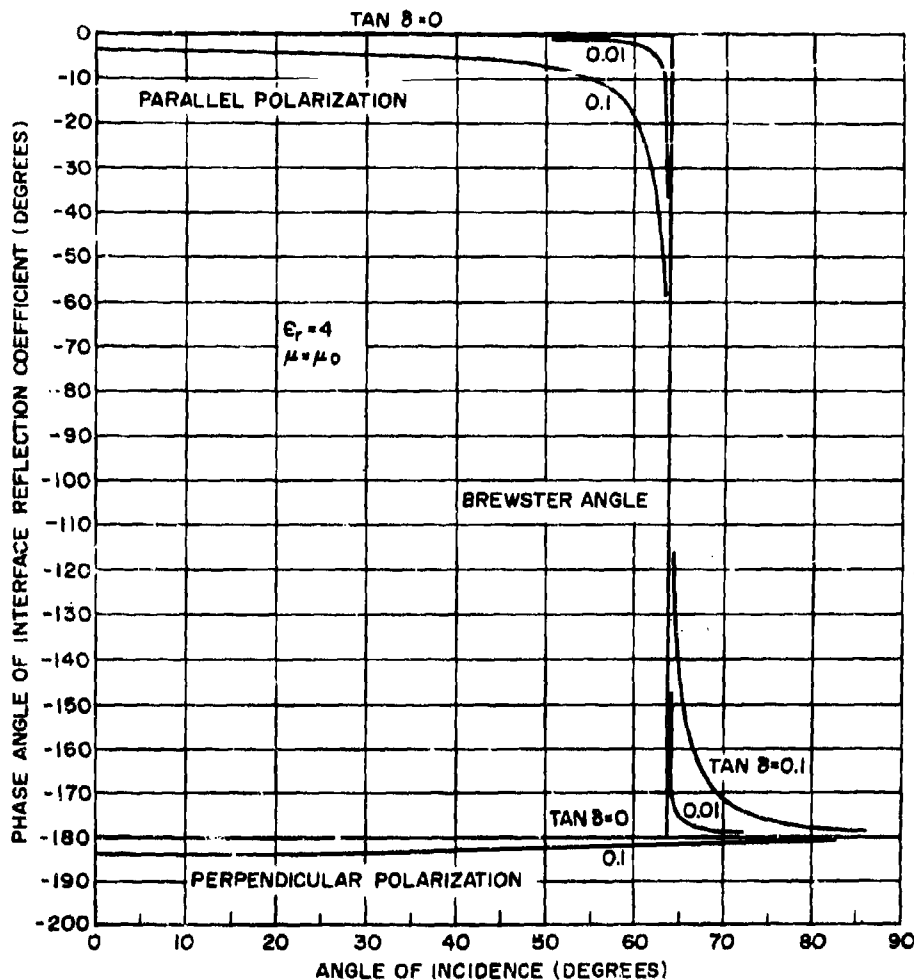


Figure 2-A4. Phase Angle of Interface Reflection Coefficient vs Angle of Incidence for Lossless and Lossy Dielectric Materials

Brewster angle. The Brewster angle,  $\theta_b$ , is given by:

$$\theta_b = \tan^{-1} \sqrt{\epsilon_r} \quad (2-A4)$$

if  $\mu = \mu_0$ . A graph of the Brewster angle vs. dielectric constant is given in Fig. 2-A5.

When a plane wave in free space is incident at an angle  $\theta$  on the surface of a dielectric layer, it is found that the wave in the dielectric layer travels at a new angle, known as the angle of refraction,  $\theta_r$ . The relation between the two angles of propagation is expressed by Snell's

law. If  $\mu = \mu_0$  and the media are lossless, Snell's law is given by

$$\sin \theta_r = \frac{\sin \theta}{\sqrt{\epsilon_r}} \quad (2-A5)$$

The angle of refraction vs. the angle of incidence for relative dielectric constants from 1 to 15 is shown in Fig. 2-A6. From the figure, note that the axis of propagation is bent toward the normal when a wave travels from free space into a dielectric region.

## 2-A2 SOLID-WALL RADOME CURVES

Consider a plane, homogeneous dielectric slab in free space. Let it have thickness  $d$ , permeability  $\mu = \mu_0$ , complex relative dielectric constant  $\epsilon_r$ , and loss tangent  $\tan \delta$ . When a plane wave is incident on such a slab, with an angle  $\theta$ , the transmission coefficient is given by

$$T = \frac{(1 - r^2) \exp [j (2\pi d / \lambda_0) (\cos \theta - \sqrt{\epsilon_r - \sin^2 \theta})]}{1 - r^2 \exp [-2j (2\pi d / \lambda_0) \sqrt{\epsilon_r - \sin^2 \theta}]} \quad (2-A6)$$

where  $\exp [x] = e^x$

$\lambda_0$  = wavelength in free space

$r$  = interface reflection coefficient for perpendicular or parallel polarization, as the case may be

If the incident wave has elliptical polarization, or if it has linear polarization with the electric vector neither parallel nor perpendicular with the plane of incidence, it may be resolved into components having parallel and perpendicular polarizations. The transmission coefficient for each of these component waves is given by Eq. 2-A6.

The complex relative dielectric constant is given by  $\epsilon_r = \epsilon_r (1 - j \tan \delta)$ . For low-loss media, the following approximation is useful in calculating the transmission coefficient:

$$\sqrt{\epsilon_r - \sin^2 \theta} \cong \sqrt{\epsilon_r - \sin^2 \theta} - j \frac{\epsilon_r \tan \delta}{2\sqrt{\epsilon_r - \sin^2 \theta}} \quad (2-A7)$$

The power transmission coefficient of a lossless solid wall is given by:

$$T^2 = \frac{1}{1 + (2r \sin \phi)^2 / (1 - r^2)^2} \quad (2-A8)$$

where  $r$  is the interface reflection coefficient for perpendicular or parallel polarization and

$$\phi = (2\pi d / \lambda_0) \sqrt{\epsilon_r - \sin^2 \theta} \quad (2-A9)$$

The insertion phase delay of a solid wall is equal to the phase angle of the complex transmission coefficient given above, but of opposite sign. For a lossless solid wall, the insertion phase delay is given by:

$$\text{IPD} = \tan^{-1} \left[ \frac{1 + r^2}{1 - r^2} \tan \phi \right] - 2\pi (d / \lambda_0) \cos \theta \quad (2-A10)$$

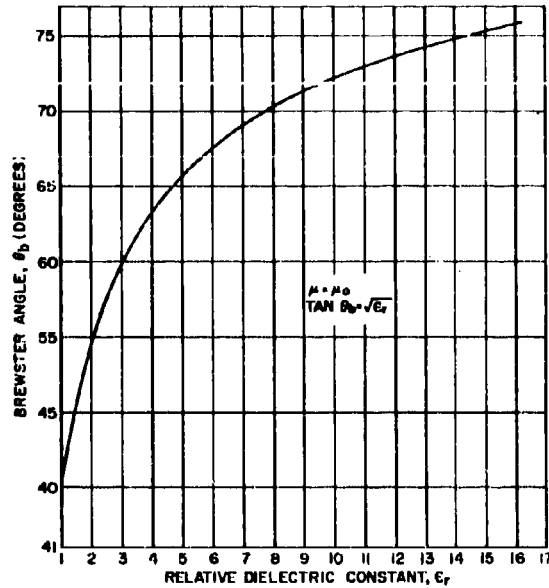


Figure 2-A5. Brewster Angle vs Relative Dielectric Constant

Perfect transmission is obtained through a lossless solid wall at angle of incidence  $\theta$  if the thickness is given by:

$$d = \frac{n\lambda_0}{2\sqrt{\epsilon_r - \sin^2 \theta}} \quad (2-A11)$$

where  $n$  is any positive integer. Figure 2-A7 shows the frequency-times-thickness vs. angle of incidence for perfect transmission through solid walls having dielectric constants up to 12 (Reference 1).

Figures 2-A8 and 2-A9 show the contours of constant power transmission for lossless solid walls with a dielectric constant of 3.5. Movement along a vertical line on these graphs can be used to determine how the transmission coefficient varies with frequency for a fixed angle of incidence. Movement along a horizontal line can be used to determine how the transmission varies with angles of incidence at a given frequency. Similar graphs can be constructed for other dielectric constants. Graphs of this type are particularly useful in designing a solid-wall radome that must operate over a given range of frequencies and angles of incidence with a specified minimum transmission efficiency.

Contours of 80% power transmission effi-



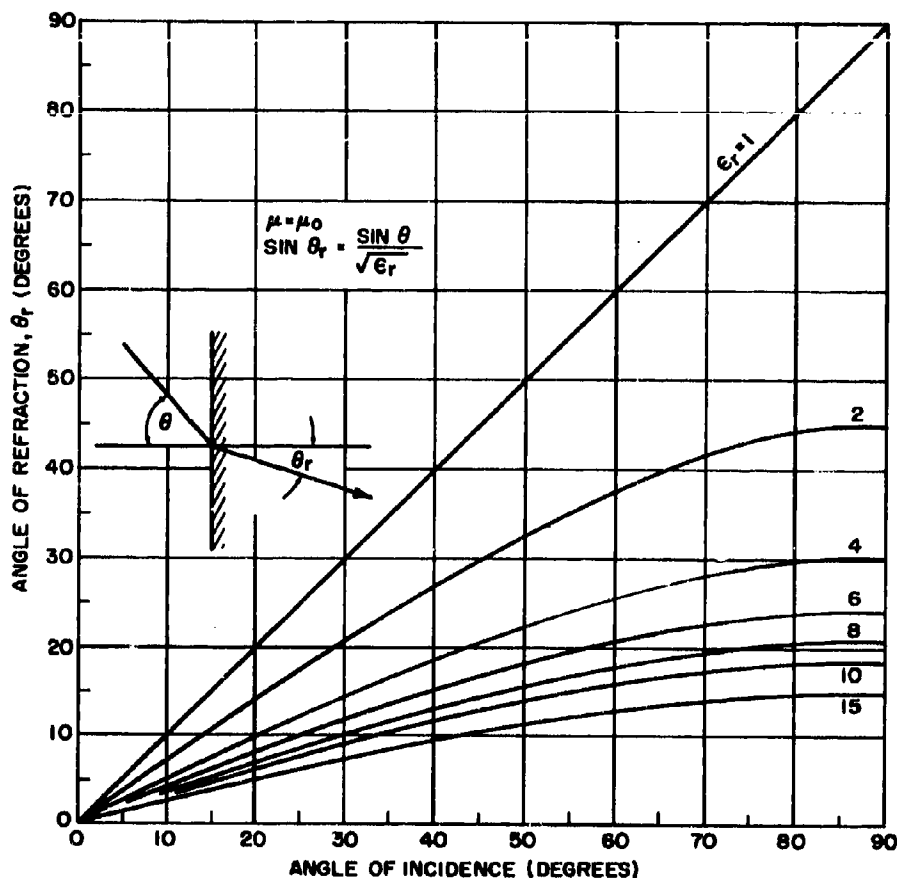


Figure 2-A6. Angle of Refraction vs Angle of Incidence (Snell's Law) for Lossless Dielectric Media

efficiency are shown in Fig. 2-A10 for lossless solid walls with perpendicular polarization. Dielectric constants from 2 to 10 are represented in this figure. As the dielectric constant increases, the decrease in bandwidth and incidence-angle range is clearly evident.

Figures 2-A11 through 2-A16 are curves of the power transmission coefficient and insertion phase delay vs. thickness in free-space wavelengths for lossless solid walls with dielectric constants of 2, 4, and 6. Data are given for perpendicular and parallel polarization with incidence angles of 0°, 20°, 40°, 60°, and 80°. Figures 2-A17 through 2-A20 are curves of the power transmission coefficient and insertion phase delay vs. thickness in free-space wavelengths for lossless solid walls with a dielectric

constant of 9. Data are given for perpendicular polarization for incidence angles of 0°, 30°, 50°, 60°, 70°, and 80°.

Figures 2-A21 through 2-A24 are nomographs prepared by the Naval Air Development Center for the purpose of determining the weight of a tangent ogive nose in terms of base diameter, L/D ratio, wall thickness, and material specific weight.

### 2-A3 RADOME SANDWICH CURVES

Reference 2 presents a novel method for graphing the transmission efficiency of symmetrical three-layer sandwiches. This technique makes it possible to determine, at a glance, the performance of a given sandwich over a range

of frequencies and angles of incidence. Examples are shown in Figs. 2-A25 through 2-A28, which are based on data from the NADC tables (Reference 3). These figures present families of curves of constant power-transmission efficiency for perpendicular polarization at four angles of incidence, for an "A" sandwich comprising two skins with a dielectric constant of 4 and loss tangent of 0.014, and a core with a dielectric constant of 1.2 and loss tangent of 0.004. Values of  $T^2$  range from 80% to 95% in 5% increments. Skin thickness in wavelengths ( $d_s/\lambda_0$ ) and core thickness in wavelengths ( $d_c/\lambda_0$ ) are represented as continuous variables over ranges suitable for most radome applications.

Since both thickness values are normalized to the free-space wavelength and are plotted as coordinates on equal logarithmic scales, the effect of an increase in frequency for a fixed combination of thickness values in in. is found simply by translating a point along a diagonal line in the  $+45^\circ$  direction. In this way, the curves

on a single graph yield values of theoretical bandwidth over a specified range of incidence angles with a specified value of the transmission efficiency at the frequency limits. Portions of curves from two graphs of this type can be used to obtain theoretical values of bandwidth for various combinations of limiting values of  $T^2$  (90% at the upper frequency limit and 80% at the lower frequency limit).

Reference 4 develops the graphs shown in Figs. 2-A29 through 2-A31 for "A" sandwiches. These graphs show the skin and core thicknesses required for maximum transmission efficiency at various angles of incidence for perpendicular polarization.

## 2-A4 FREQUENCY BANDS AND WAVELENGTH

Figure 2-A32 is a graph of the free-space wavelength (cm and in.) vs. frequency. This is convenient for general reference to determine either wavelength or frequency when one of

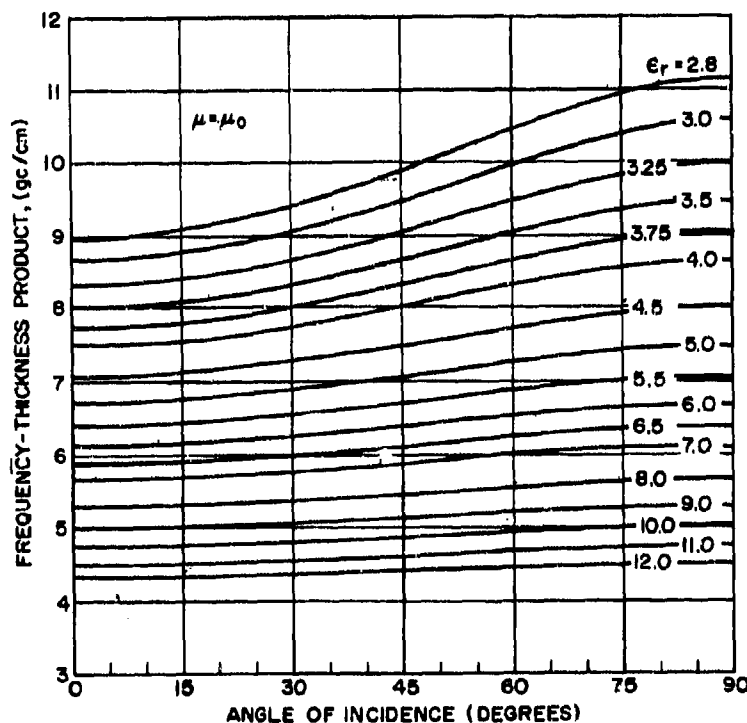


Figure 2-A7. Conditions for Perfect Transmission Through Lossless Half-Wave Radomes

these is known. Table 2-A1 shows the frequency limits of the various bands. In radar and radome work, the operating frequency range is frequently given in terms of the band designation, for example, S-band, X-band, or K-band.

#### APPENDIX REFERENCES

1. Munoz, D. R., and Van Doren, L. *Research and Investigation of Broadband Inorganic Electromagnetic Window Techniques*, Smyth Research Assoc., Technical Documentary
2. Bowie, D. M. *Radome Design Curves*, Aero Geo Astro Corp., Technical Paper ANT-5, February 27, 1959.
3. *Tables of Transmission and Reflection Coefficients of Lossy, Symmetrical Dielectric Radome Sandwiches*, Report NADC-EL-52188, October 22, 1958.
4. Loyet, D. L., and Yoshitani, R. "Ceramic Sandwich Radome Design," Hughes Aircraft Co., *Proc. OSU-RTD Symposium on Electromagnetic Windows*, June 1964.

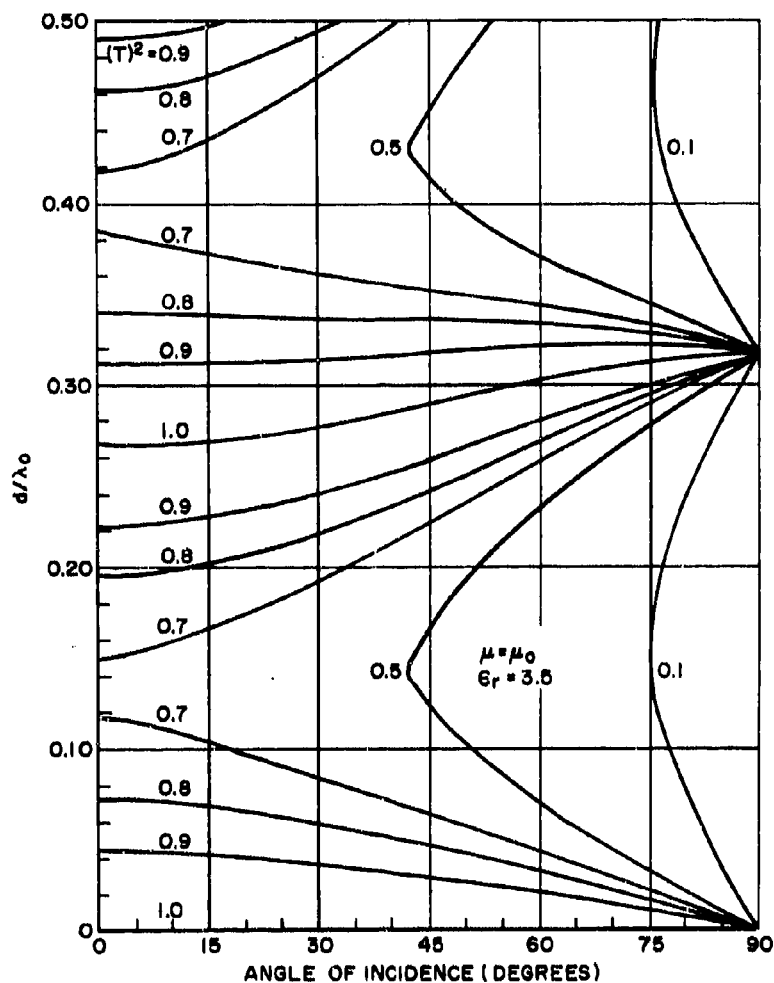
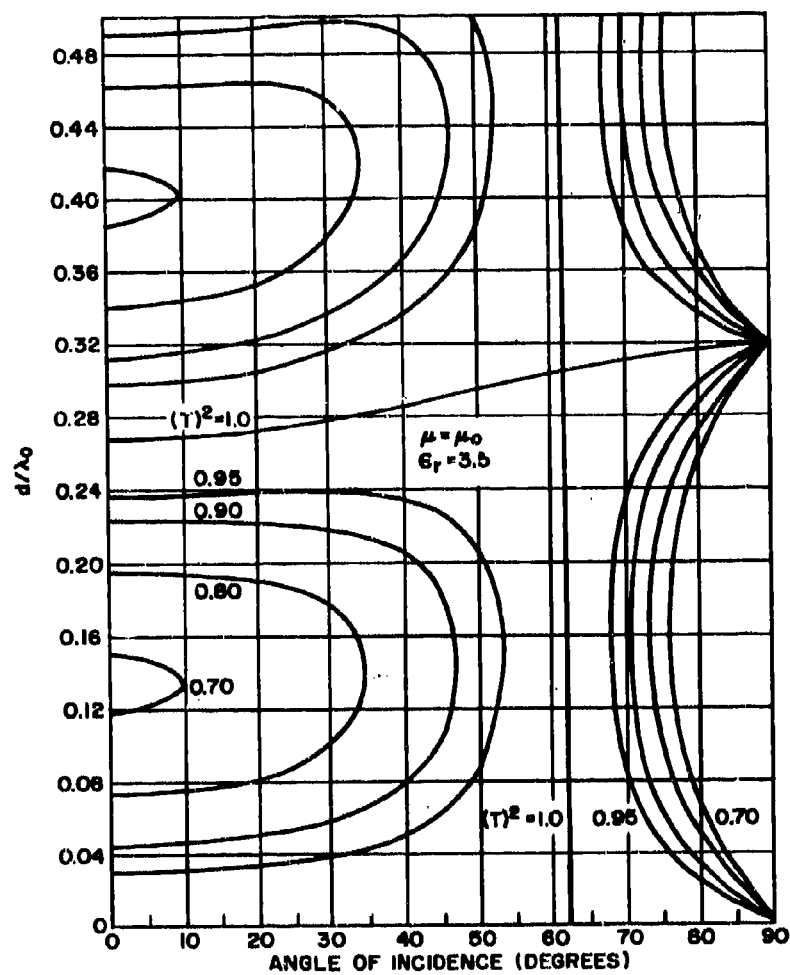


Figure 2-A8. Contours of Constant Power Transmission for Lossless Solid Walls with Perpendicular Polarization

TABLE 2-A1 REFERENCE TABLE OF BAND CODE LETTERS VS FREQUENCY\*

P BAND			S BAND			C BAND Designation includes Sz thru Xv from 3.9-6.2 kmc/s	K BAND			Q BAND		
FREQ.	λ		SUB	FREQ.	λ		SUB	FREQ.	λ	SUB	FREQ.	λ
0.225	133.3		E	1.55	19.3		P	10.90	2.75	A	36.00	0.834
0.390	76.9			1.65	18.2	12.25		2.45	38.00		0.790	
UHF TELEVISION BAND Channels 14 thru 83 0.470 to 0.890 kmc/s			F	1.65	18.2	S	12.25	2.45	B	38.00	0.790	
				1.85	16.2		13.25	2.26		40.00	0.750	
L BAND			T	1.85	16.2	E	13.25	2.26	C	40.00	0.750	
SUB	FREQ.	λ		2.00	15.0		14.25	2.10		42.00	0.715	
P	0.390	76.9	C	2.00	15.0	C	14.25	2.10	D	42.00	0.715	
	0.465	64.5		2.40	12.5		15.35	1.95		44.00	0.682	
C	0.465	64.5	Q	2.40	12.5	U	15.35	1.95	E	44.00	0.682	
	0.510	58.8		2.60	11.5		17.25	1.74		46.00	0.652	
L	0.510	58.8	Y	2.60	11.5	B	17.25	1.74	V BAND			
	0.725	41.4		2.70	11.1		20.50	1.46				SUB
Y	0.725	41.4	G	2.70	11.1	R	20.50	1.46	A	46.00	0.652	
	0.780	38.4		2.90	10.8		24.50	1.22		48.00	0.625	
T	0.780	38.4	S	2.90	10.8	C	24.50	1.22	B	48.00	0.625	
	0.900	33.3		3.10	9.68		26.50	1.13		50.00	0.600	
S	0.900	33.3	A	3.10	9.68	L	26.50	1.13	C	50.00	0.600	
	0.950	31.6		3.40	8.83		28.50	1.05		52.00	0.577	
X	0.950	31.6	W	3.40	8.83	S	28.50	1.05	D	52.00	0.577	
	1.150	26.1		3.70	8.11		30.70	0.977		54.00	0.556	
K	1.150	26.1	H	3.70	8.11	X	30.70	0.977	E	54.00	0.556	
	1.350	22.2		3.90	7.69		33.00	0.909		56.00	0.536	
F	1.350	22.2	Z	3.90	7.69	F	33.00	0.909	K1 BAND Designation includes Ku thru Kv 15.35 to 24.5 kmc/s			
	1.450	20.7		4.20	7.15		36.00	0.834				
Z	1.450	20.7	D	4.20	7.15	K	LEGEND: SUB = Identifying subletter. FREQ. = Band limits in kilomegacycles/sec. λ = Equivalent wavelength in centimeters.					
	1.550	19.3		5.20	5.77							

\* By permission of Vectron, Inc. This chart has been compiled from various sources and, although believed accurate, is for general information only. This data is not necessarily official.



**Figure 2-A9. Contours of Constant Power Transmission for Lossless Solid Walls with Parallel Polarization**

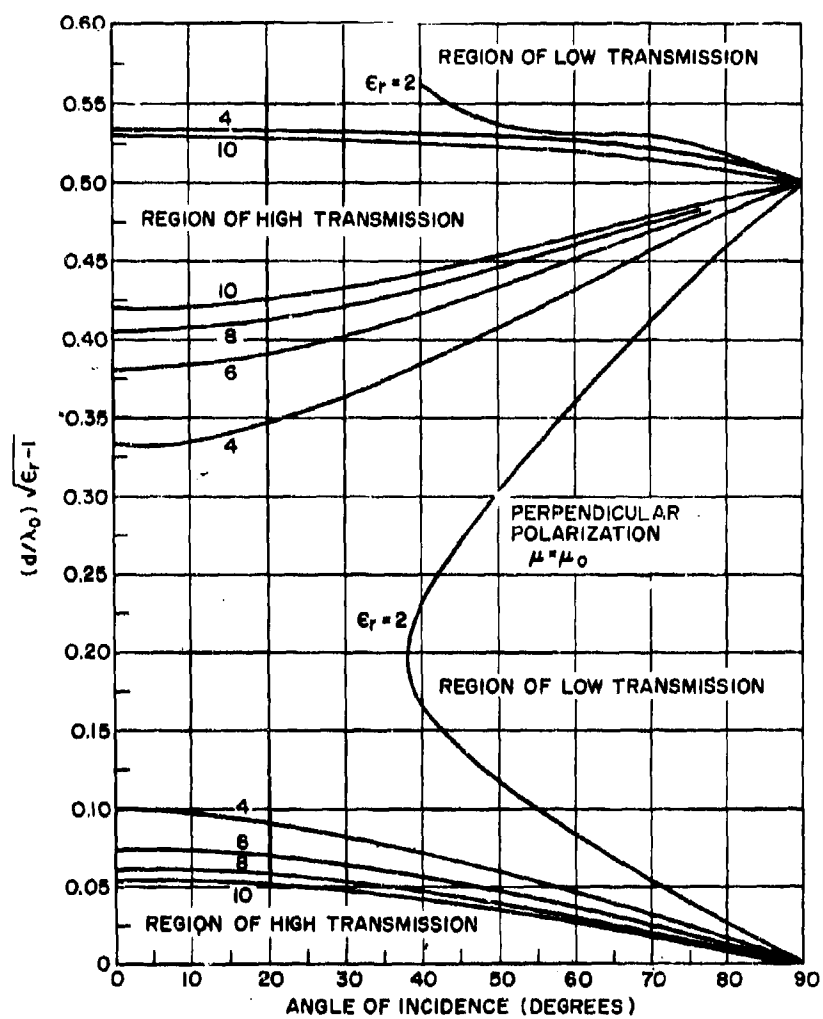


Figure 2-A10. Contours for 80 Percent Power Transmission Efficiency for Lossless Solu Walls with Perpendicular Polarization

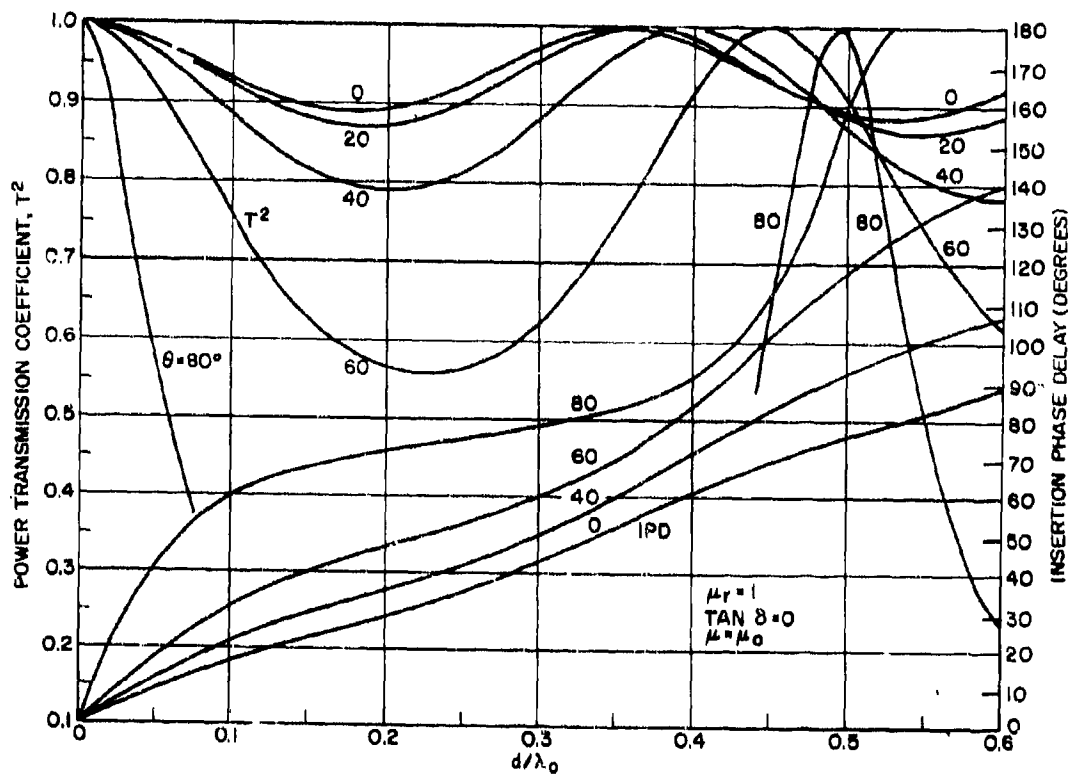


Figure 2-A11. Power Transmission and Insertion Phase Delay vs Thickness for Lossless Solid Walls with  $\epsilon_r = 2$  and Perpendicular Polarization

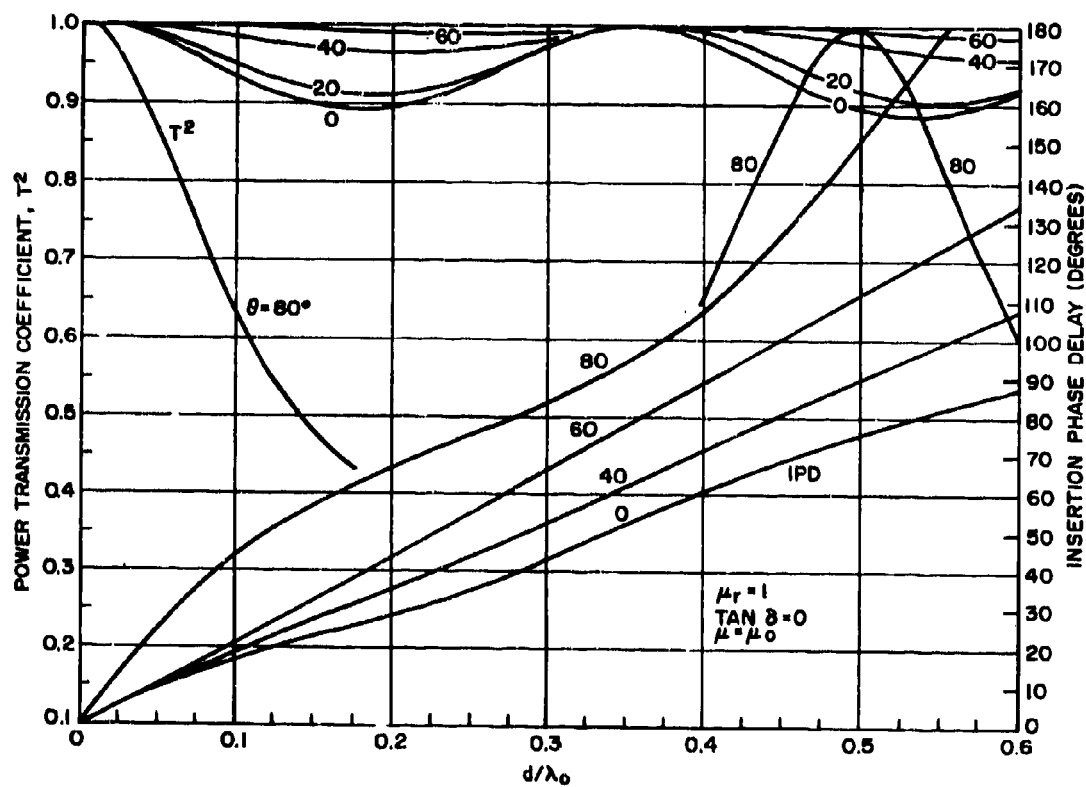
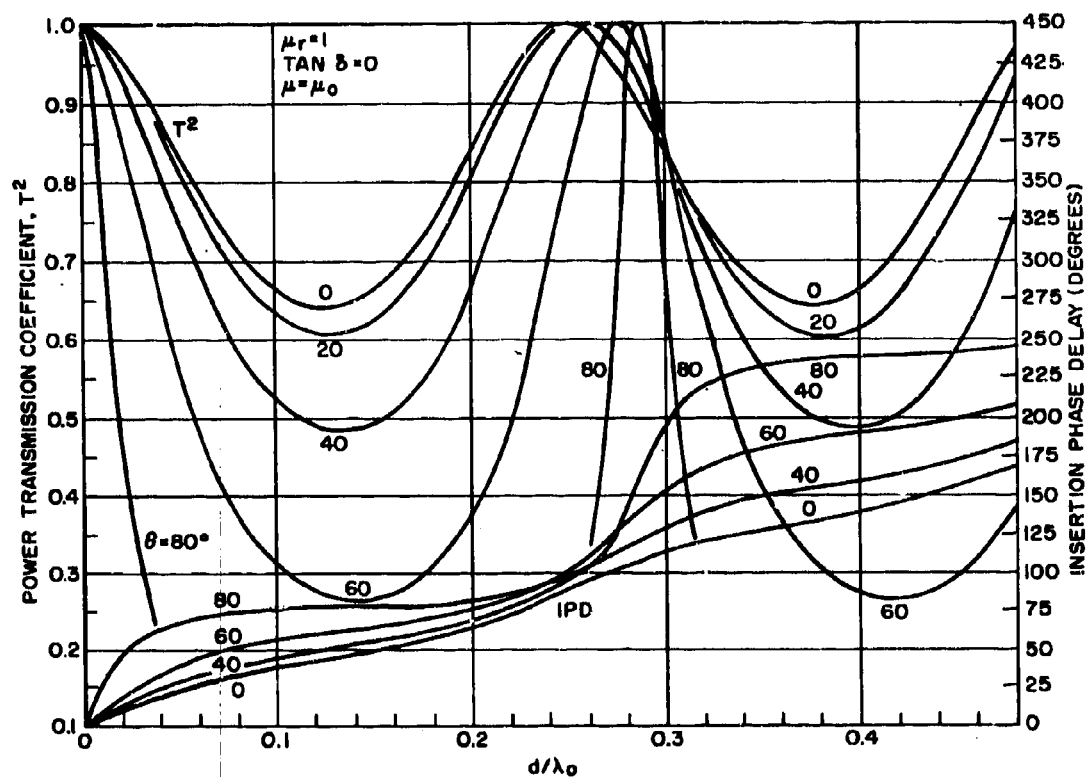


Figure 2-A12. Power Transmission and Insertion Phase Delay vs Thickness for Lossless Solid Walls with  $\epsilon_r = 2$  and Parallel Polarization





**Figure 2-A13. Power Transmission and Insertion Phase Delay vs Thickness for Lossless Solid Walls with  $\epsilon_r = 4$  and Perpendicular Polarization**

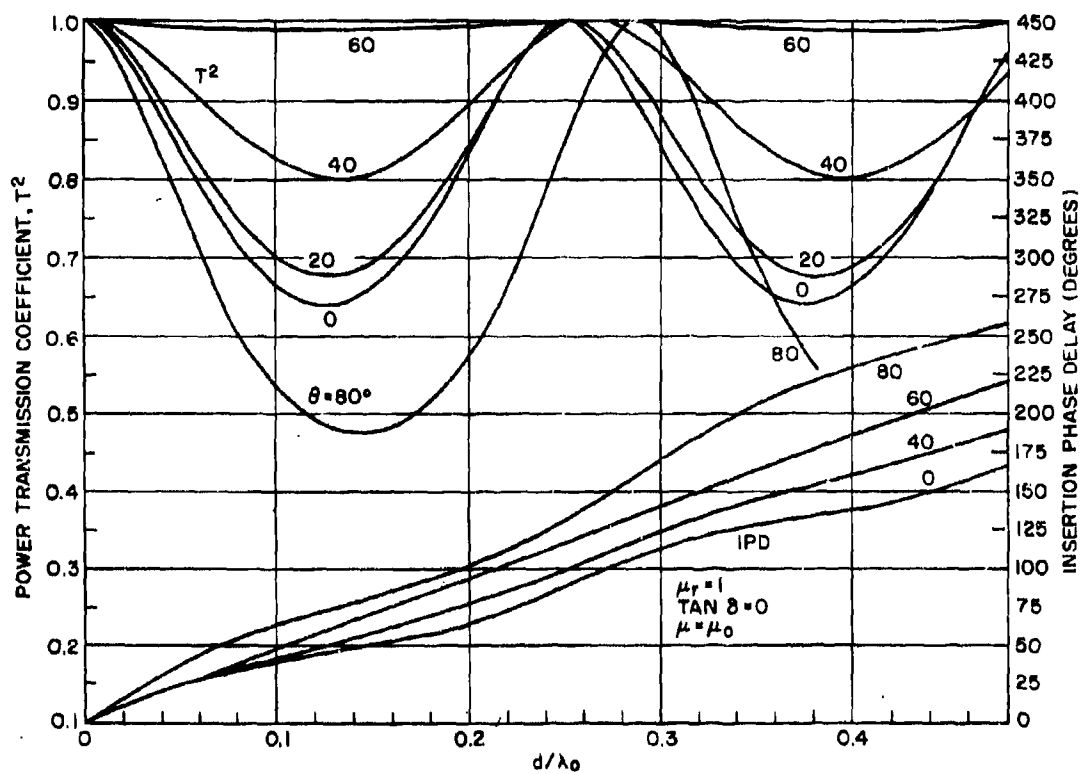


Figure 2-A14. Power Transmission and Insertion Phase Delay vs Thickness for Lossless Solid Walls with  $\epsilon_r = 4$  and Parallel Polarization

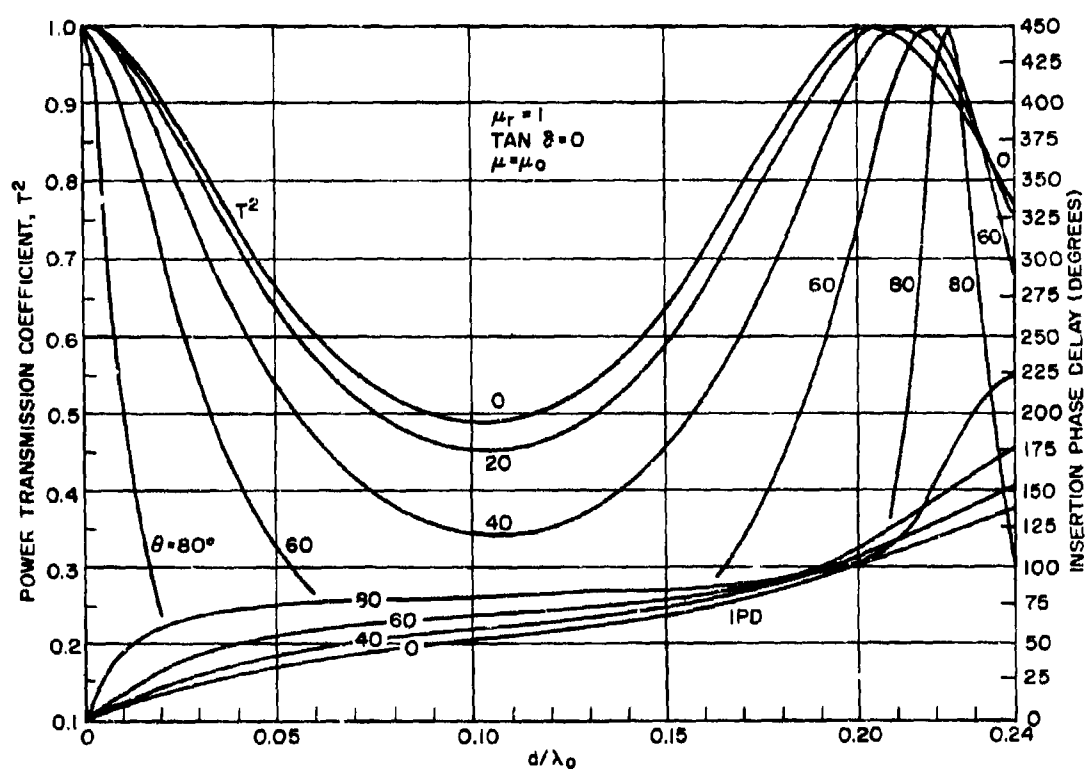


Figure 2-A15. Power Transmission and Insertion Phase Delay vs Thickness for Lossless Solid Walls with  $\epsilon_r = 6$  and Perpendicular Polarization

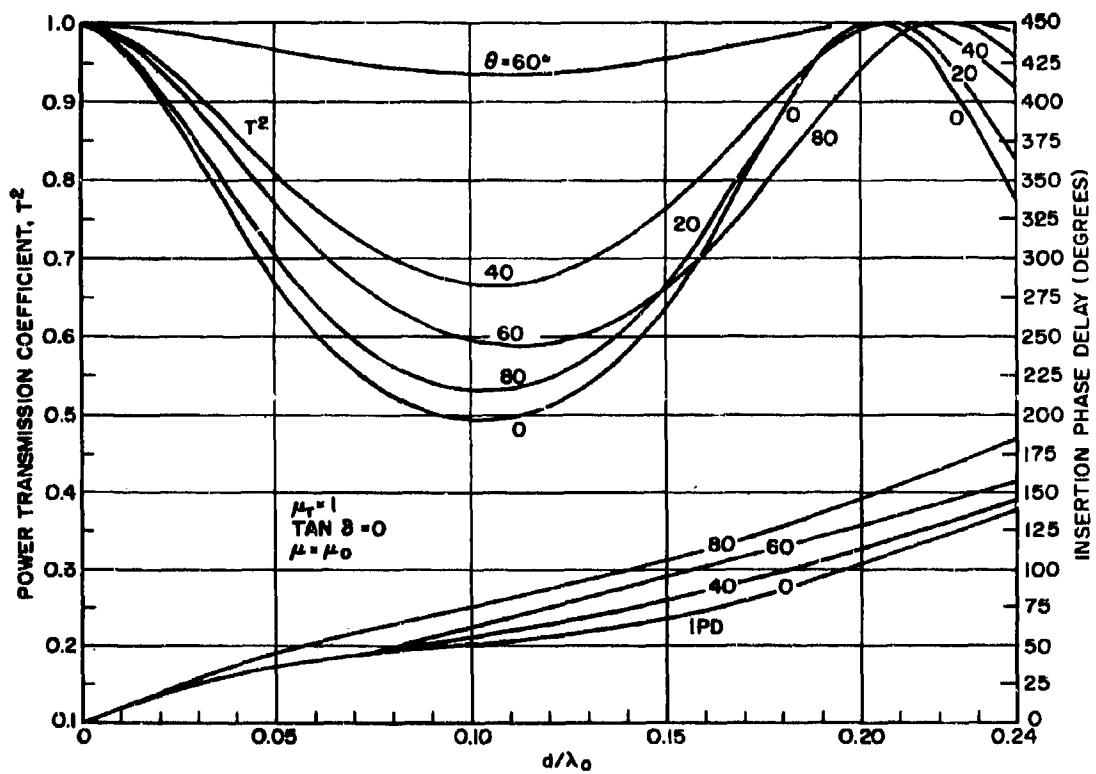


Figure 2-A16. Power Transmission and Insertion Phase Delay vs Thickness for Lossless Solid Walls with  $\epsilon_r = 6$  and Parallel Polarization

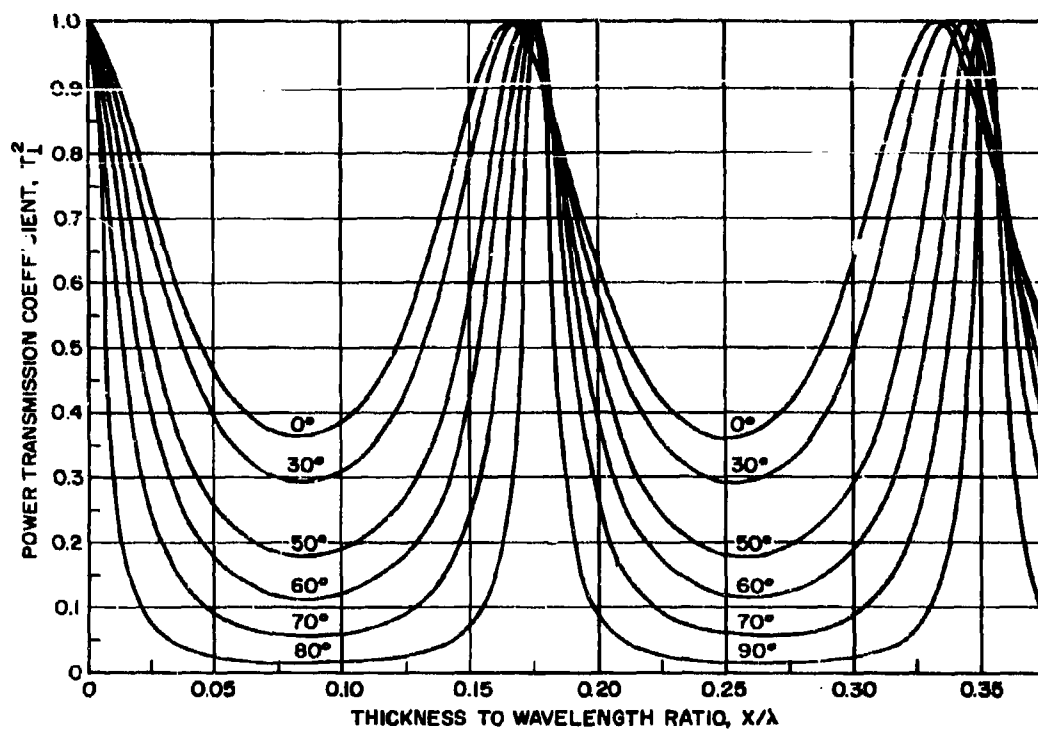


Figure 2-A17. Power Transmission vs Thickness for Lossless Solid Walls with  $\epsilon_r = 9$  and Perpendicular Polarization

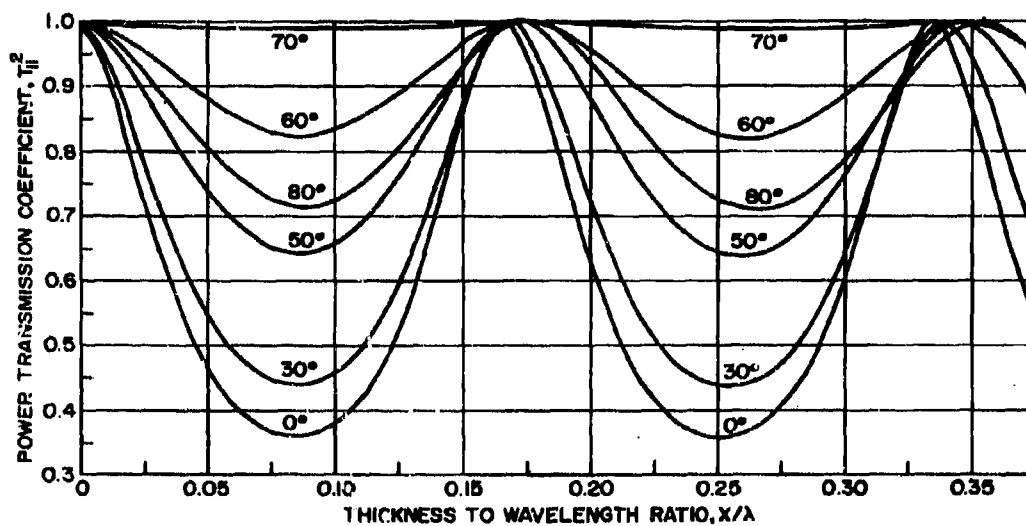


Figure 2-A18. Power Transmission vs Thickness for Lossless Solid Walls with  $\epsilon_r = 9$  and Parallel Polarization

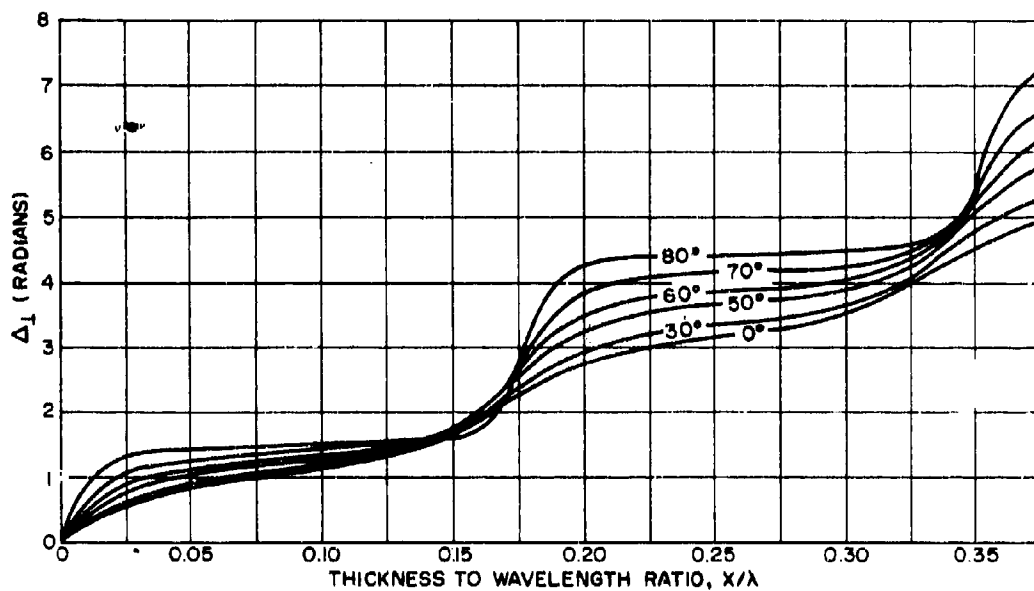


Figure 2-A19. Insertion Phase Delay vs Thickness for Lossless Solid Walls with  $\epsilon_r = 9$  and Perpendicular Polarization

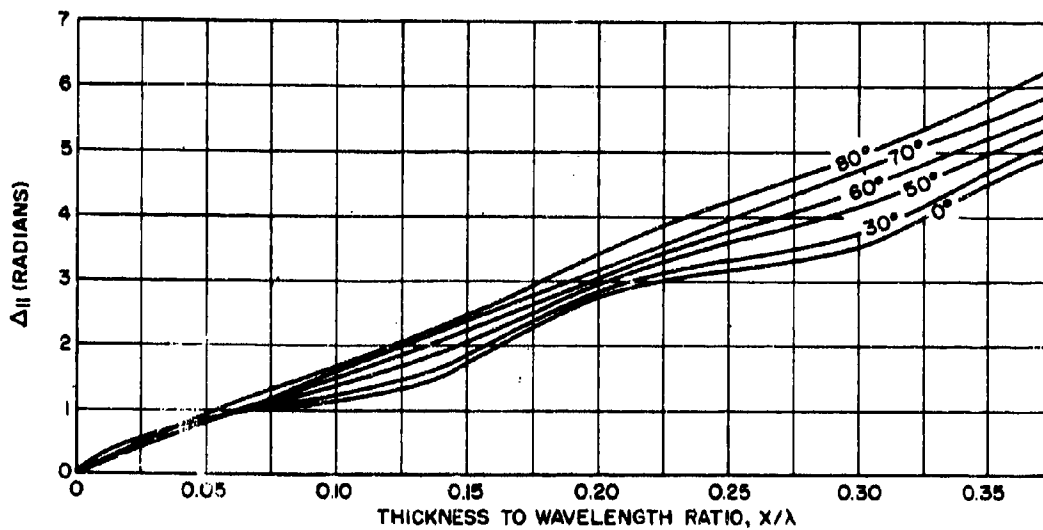


Figure 2-A20. Insertion Phase Delay vs Thickness for Lossless Solid Walls with  $\epsilon_r = 9$  and Parallel Polarization

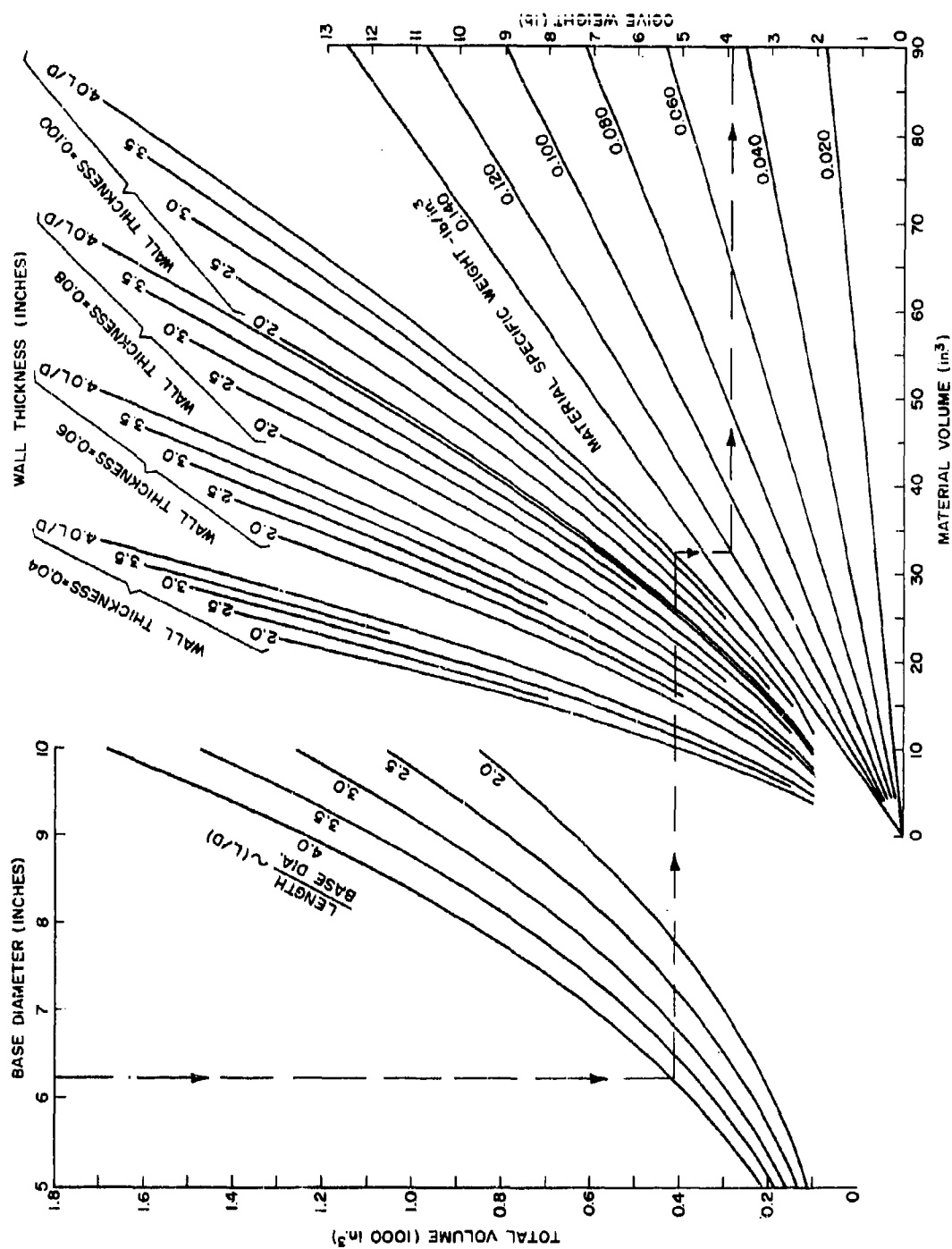


Figure 2-A21. Nomograph Giving Weight of Tangent Ogive Nose in Terms of Base Diameter, L/D Ratio, Wall Thickness, Material Specific Weight, and Very Low Material Volume

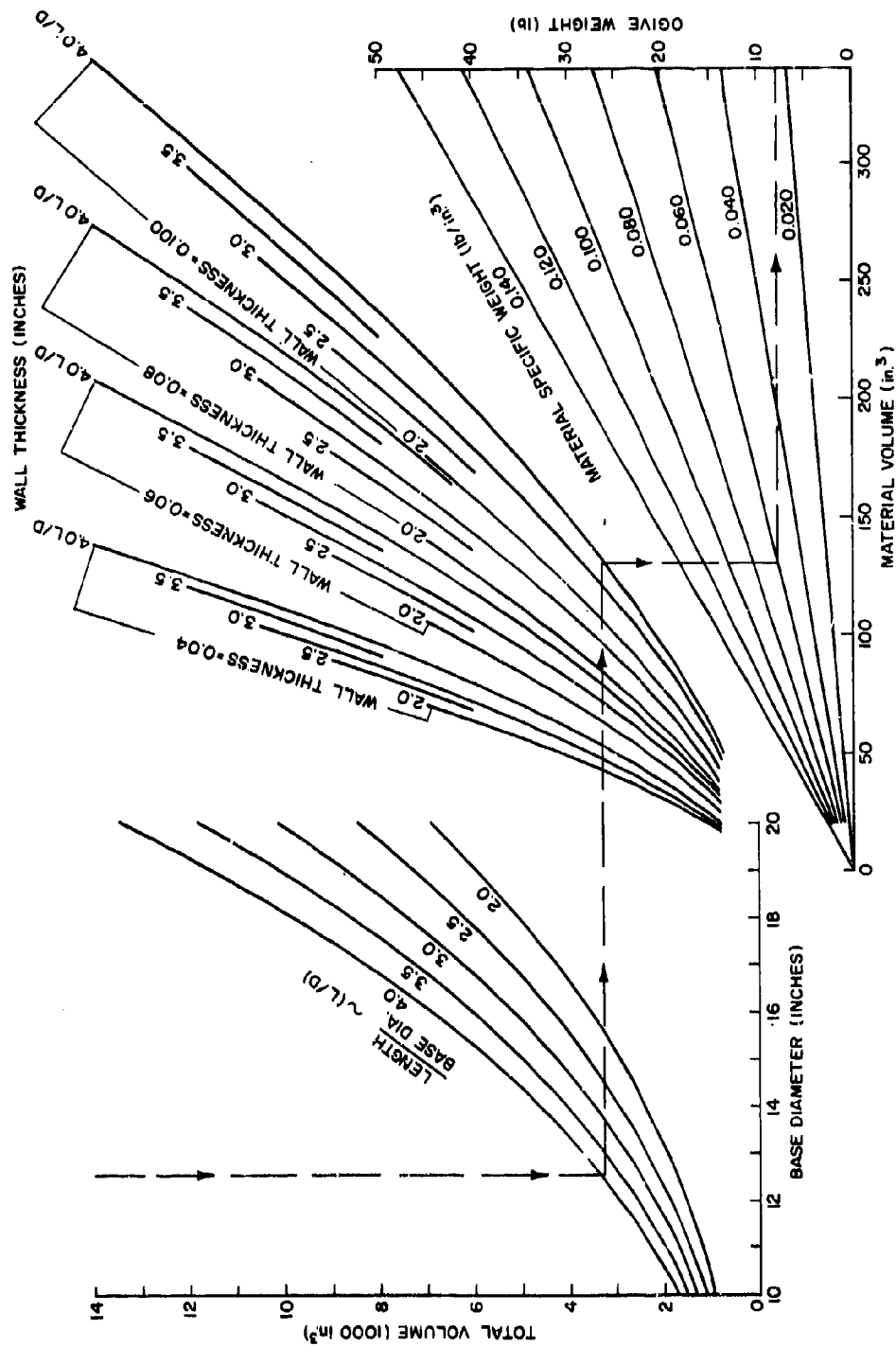


Figure 2-A22. Nomograph Giving Weight of Tangent Ogive Nose in Terms of Base Diameter, L/D Ratio, Wall Thickness, Material Specific Weight, and Low Material Volume



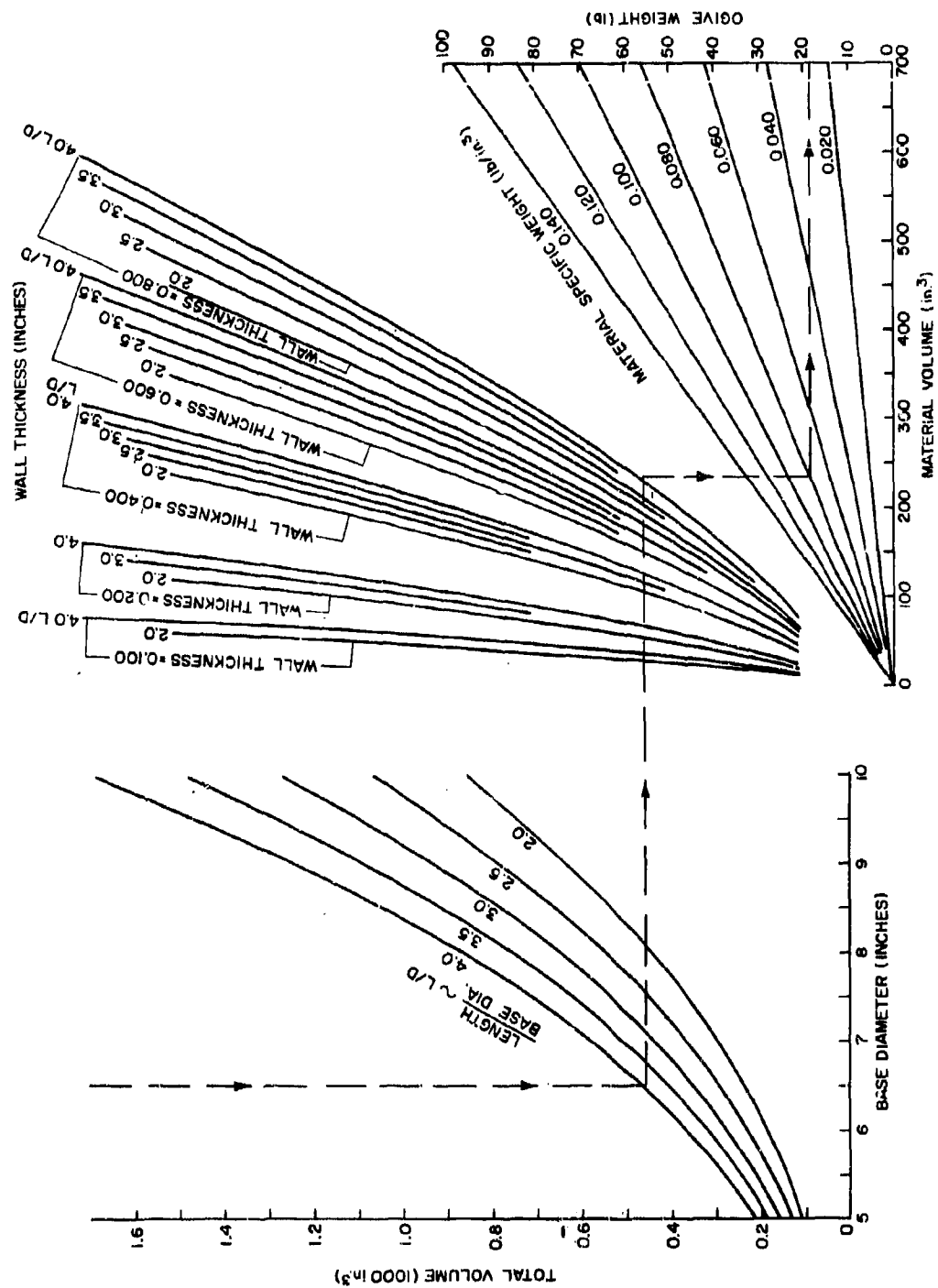


Figure 2-A23. Nomograph Giving Weight of Tangent Ogive Nose in Terms of Base Diameter, L/D Ratio, Wall Thickness, Material Specific Weight, and Moderate Material Volume

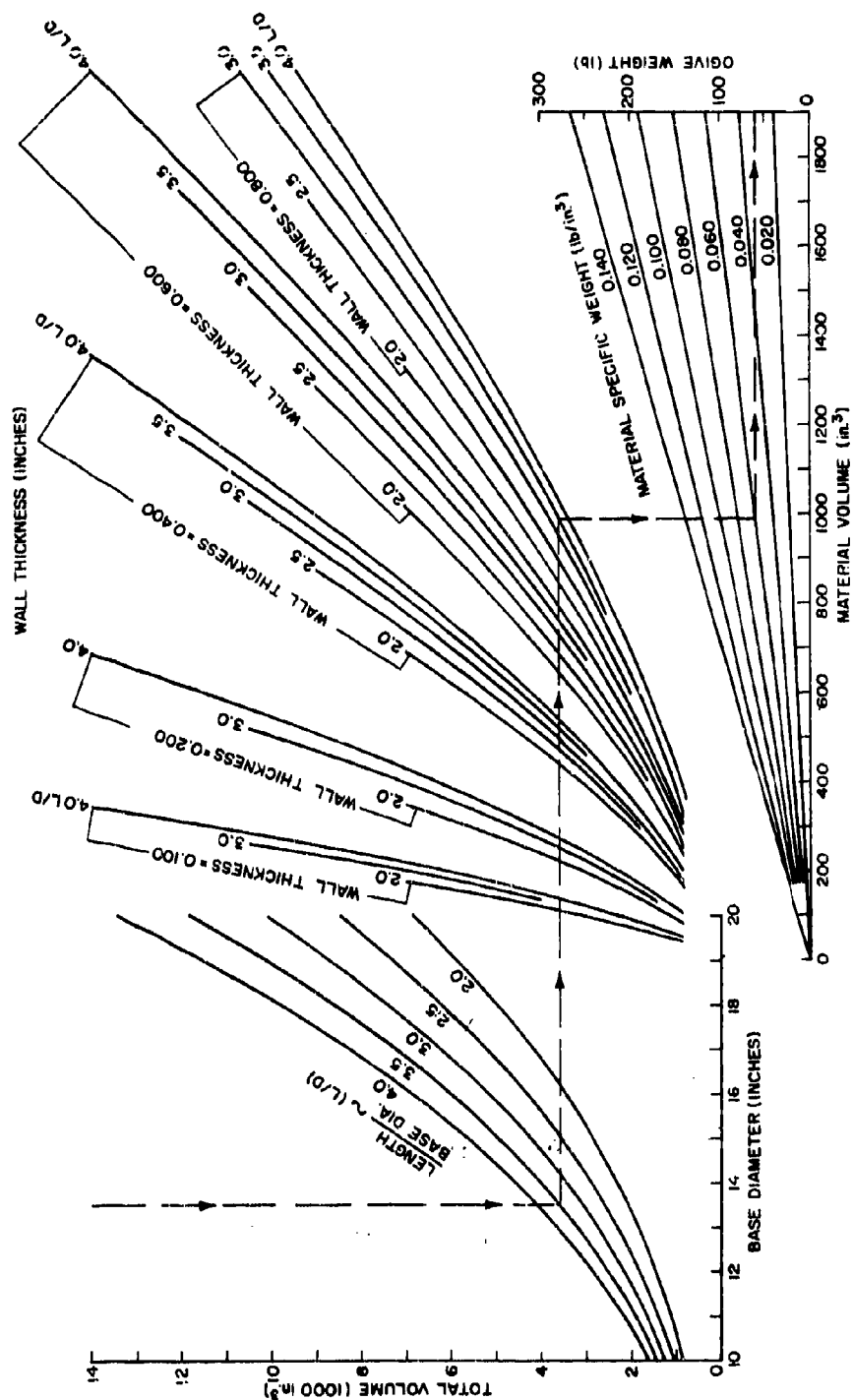


Figure 2-A24. Nomograph Giving Weight of Tangent Ogive Nose in Terms of Base Diameter, L/D Ratio, Wall Thickness, Material Specific Weight, and High Material Volume

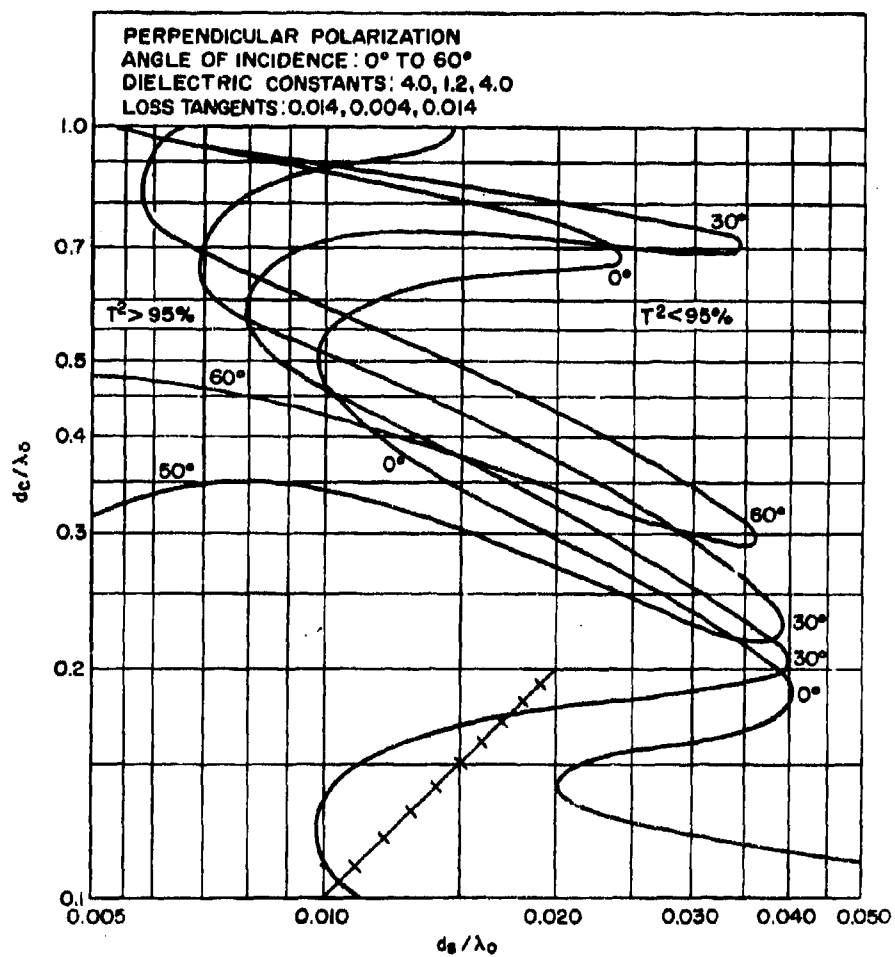


Figure 2-A25. Contours of Constant Power Transmission Efficiency for "A" Sandwich with 95 Percent Power Transmission Coefficient

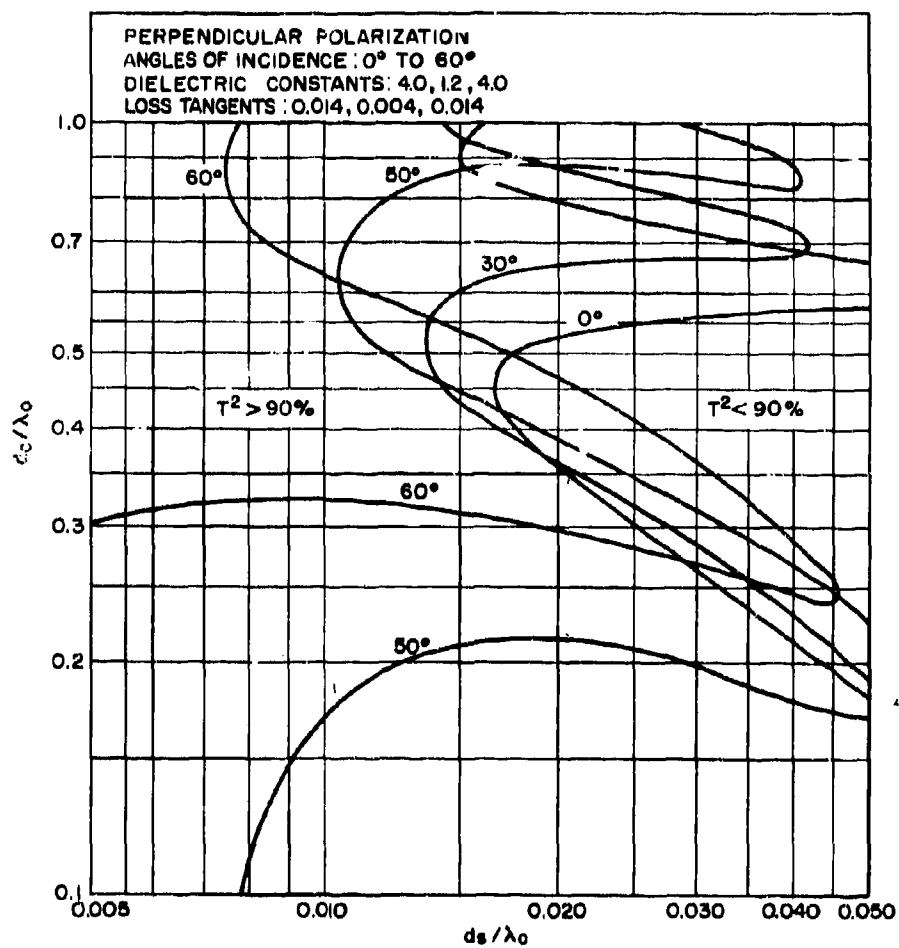


Figure 2-A26. Contours of Constant Power Transmission Efficiency for "A" Sandwich with 90 Percent Power Transmission Coefficient

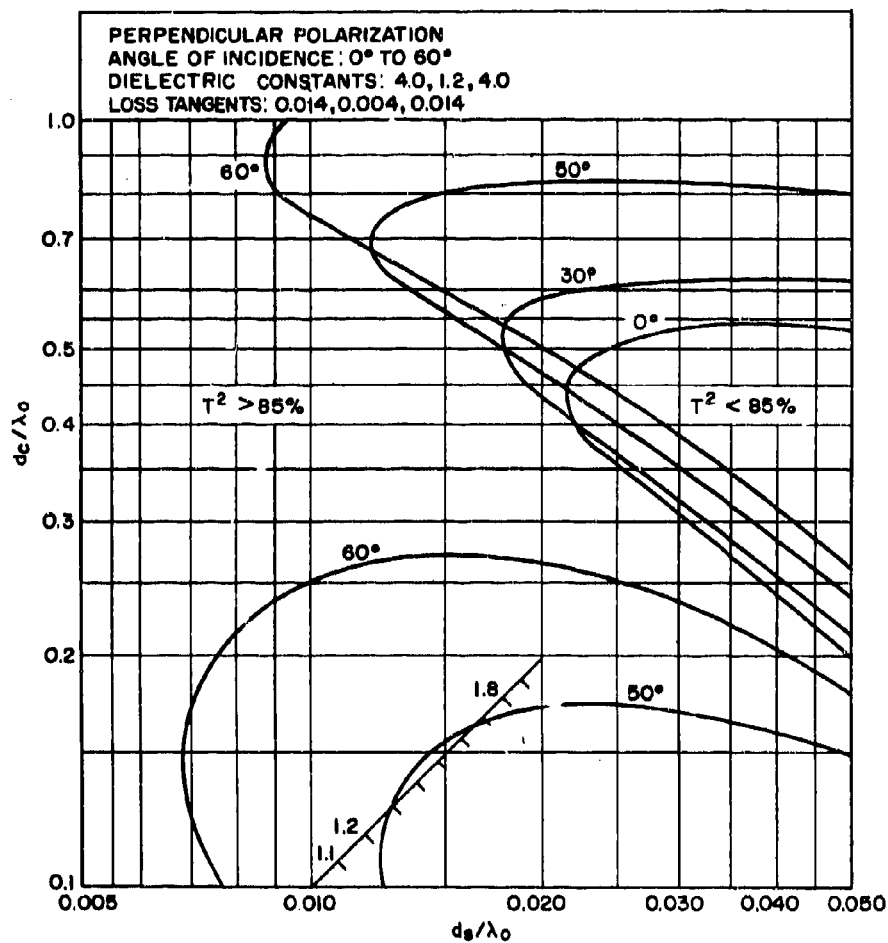


Figure 2-A27. Contours of Constant Power Transmission Efficiency for "A"  
 Sandwich with 85 Percent Power Transmission Coefficient

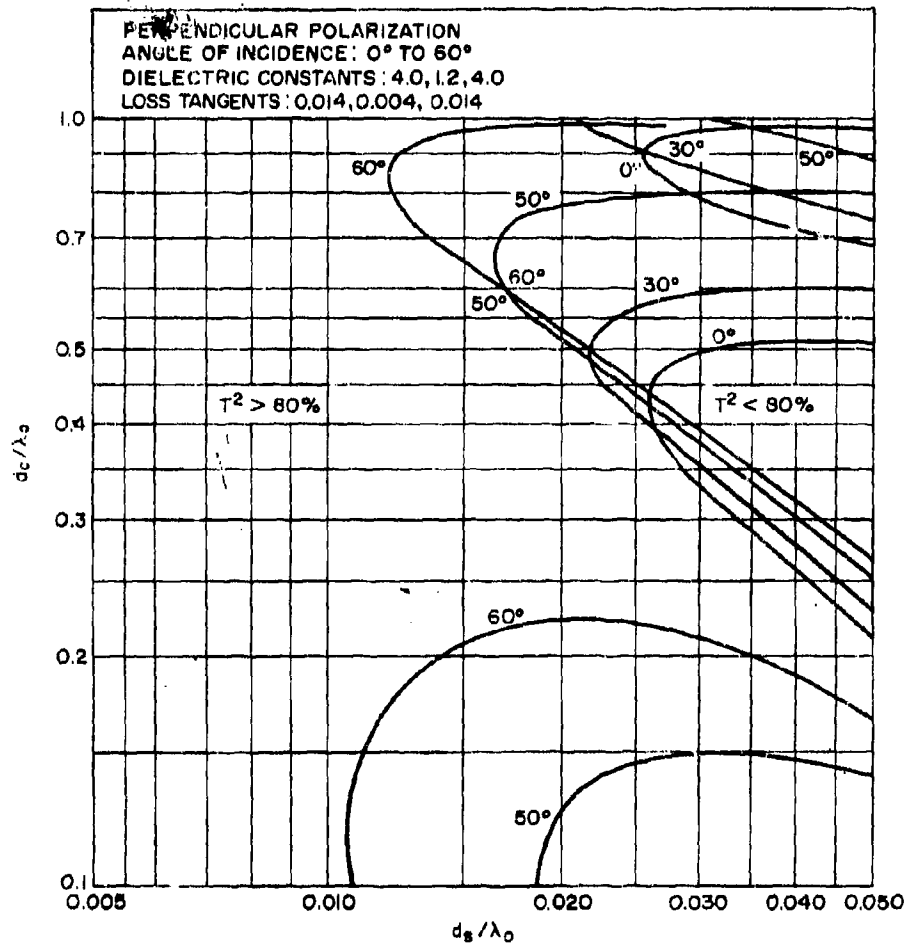


Figure 2-A28. Contours of Constant Power Transmission Efficiency for "A" Sandwich with 80 Percent Power Transmission Coefficient

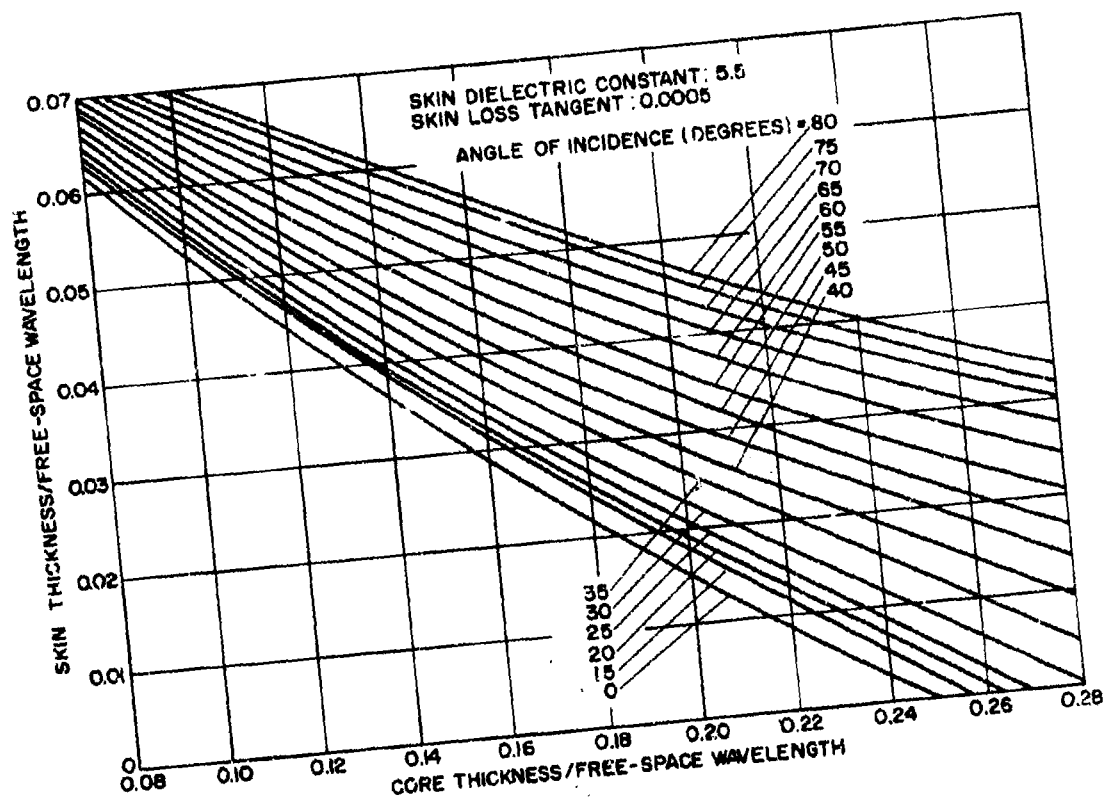
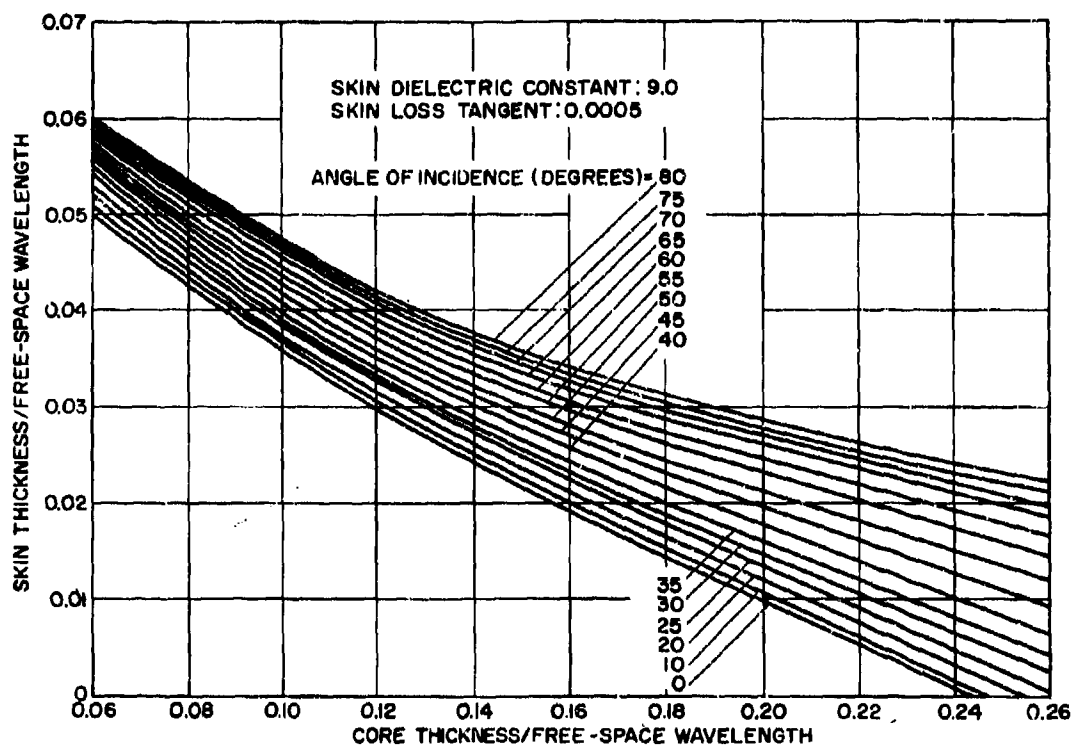


Figure 2-A29. Conditions for Maximum Transmission Efficiency for Pyroceram Air-Core Sandwiches with Perpendicular Polarization and Various Angles of Incidence



**Figure 2-A30. Conditions for Maximum Transmission Efficiency for Alumina Air-Core Sandwiches with Perpendicular Polarization and Various Angles of Incidence**



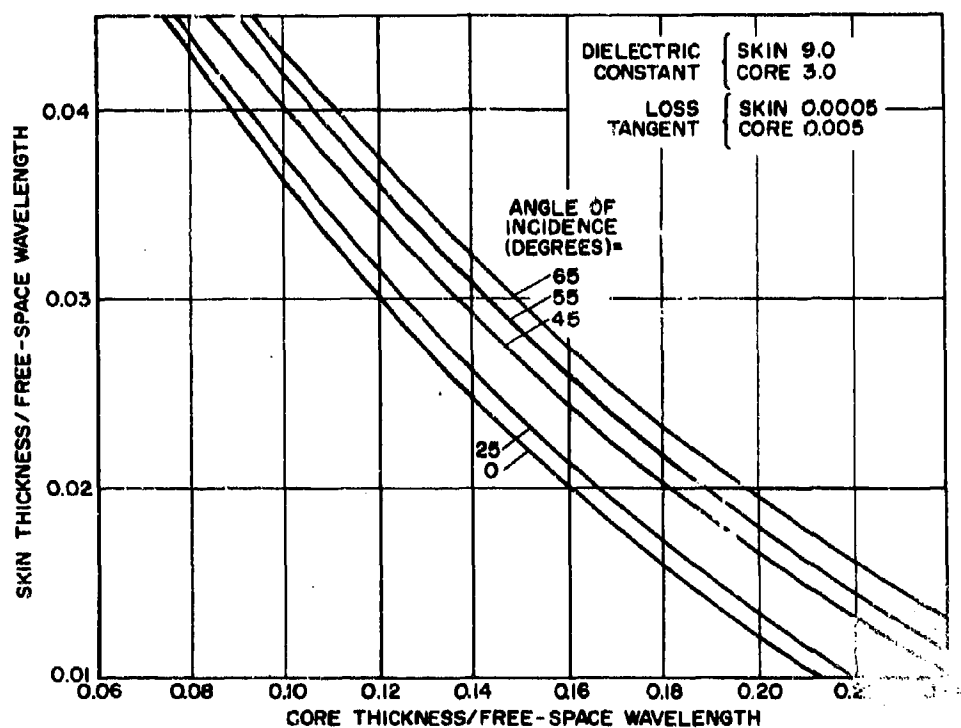
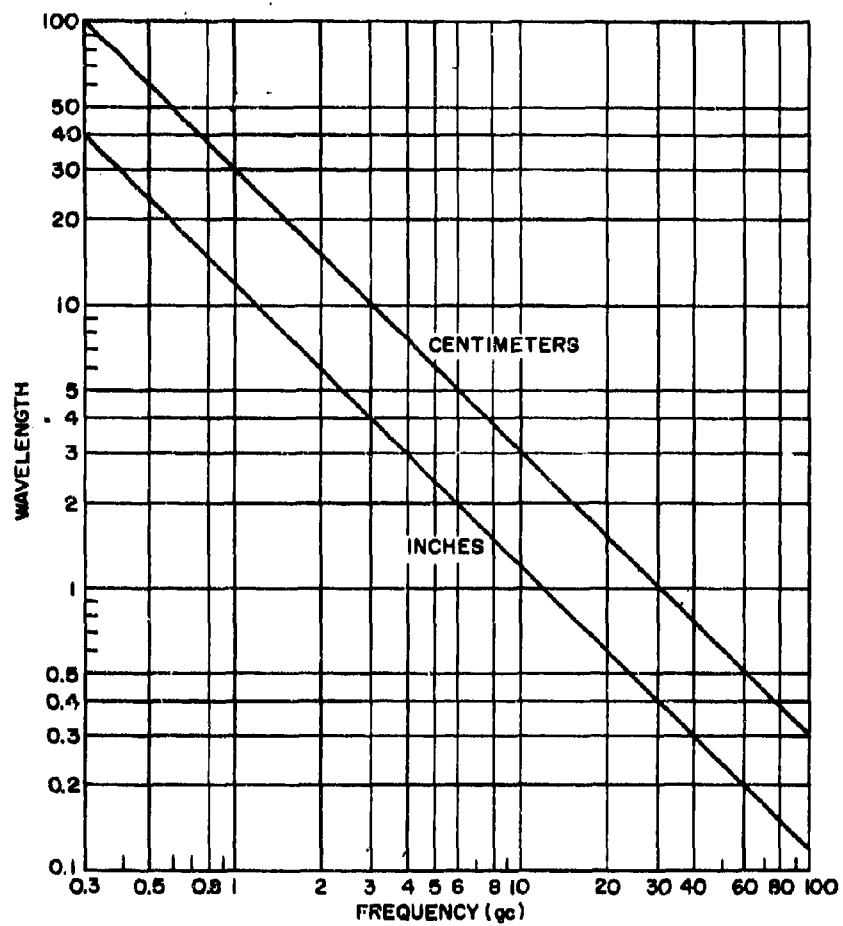


Figure 2-A31. Conditions for Maximum Transmission Efficiency for "A" Sandwiches with Perpendicular Polarization and Various Angles of Incidence



**Figure 2-A32. Free-Space Wavelength vs Frequency**

## CHAPTER 3

### ENVIRONMENTAL SIMULATION AND TEST DATA

*by* JERRY GUARINI  
*CDB Enterprises, Inc.*  
*Warminster, Pa.*

GEORGE TATNALL  
*U.S. Naval Air Development Center*  
*Johnsville, Pennsylvania*

JESSE D. WALTON, JR.  
*High Temperature Materials Branch*  
*Georgia Institute of Technology*  
*Atlanta, Georgia*

## SYMBOLS

A	Rain accumulation, in.
C	Speed of sound in water
D	Median rain drop diameter, mm
I	Rain intensity, in./hr
K	Materials constant
N	Number collisions/in. <sup>2</sup>
R	Erosion weight loss, mg
R <sub>N</sub>	Total normal radiation
T <sub>b</sub>	Brightness temperature
T <sub>r</sub>	Radiation temperature
T <sub>t</sub>	True temperature
V	Free stream velocity, ft/sec
V <sub>a</sub>	Threshold velocity below which erosion does not occur
t	Time, hr
x	Materials constant; coating thickness, mils
α	Flow factor, which is slightly less than unity
ε	Effective emittance
ΔT	Maximum temperature differential
ρ	Density of water
σ	Stefan-Boltzmann factor
θ	Time to reach erosion

## CHAPTER 3

### ENVIRONMENTAL SIMULATION AND TEST DATA

Each generation of high-velocity vehicles further complicates the electrical and structural design of the radome required by its corresponding weapons system. The selection of refractory materials, while enabling the designer to satisfy the stringent temperature requirements encountered with these new profiles, presents an entirely new family of difficulties.

As can be seen from the discussions presented in Paragraphs 1-1.5 and 6-3.4, the thermal environment, with its associated thermal shock, is of paramount importance in the selection of the appropriate design parameters. Another problem that arises, because of the intrinsically brittle nature of most refractory materials, is the impingement of rain droplets at these high velocities. This chapter discusses recent findings in the field of simulation of both the rain and thermal shock environments.

In addition to these environments, the radome designer has to overcome the effects of nuclear radiation. Of late, most radome specifications, whether for ground-based, shipboard, or airborne applications, have been required to meet some radiation specification. This chapter concludes with a brief discussion of the effects of nuclear radiation on some of the more prominent radome materials.

#### 3-1 THE RAIN ENVIRONMENT

Any discussion of the rain erosion problem must begin with an explanation of the natural rain environment, so that the radome designer can properly select realistic test methods and rain rates, and properly conduct trade-off studies involving reliability, system performance, and the rain environment.

#### 3-1.1 RAIN INTENSITY AND FREQUENCY

Maximum rain rates occur in thunderstorms, generally when the ground air temperature is near 70°F. Except for a few select and relatively small isolated localities, the maximum rain rates in the United States are representative.

The maximum rainfall accumulation for the entire western half of the United States is given in Table 3-1 (Reference 1). Rain accumulation is given for time intervals ranging from 5 minutes (1/12 hour) to 24 hours. The data shows that only once in a 2-year period was there recorded 0.35 in. of rain over a 5-minute interval. This is equivalent to an average rainfall rate of 4.2 in./hr. Once in a 10-year period, 0.5 in. was measured in 5 minutes for an average rate of 6 in./hr. Maximum rainfall expectancy for a given time interval usually increases with the number of years over which the records are observed.

Table 3-1 shows that the rainfall rate and accumulation both decrease as the time duration increases. The maximum accumulation is related to the time duration,  $t$ , as follows:

$$A = 14.3 \sqrt{t} \quad (3-1)$$

where  $A$  = accumulation, in.  
 $t$  = time, hr

The rainfall expectancy along the Gulf Coast is the most severe in the United States and is about twice the values given in Table 3-1. Instantaneous rain rate expectancy for New Orleans is given in Fig. 3-1. The figure shows that this area can expect a rainfall rate of 1 in./hr 0.8% of the time. The probability of encountering 1 in./hr is 1 in 750. A very intense rainfall of 5 in./hr would be expected to occur only

**TABLE 3-1 MAXIMUM RAINFALL ACCUMULATION AND AVERAGE  
RAINFALL RATE FOR WESTERN USA\***

Frequency	Duration (hrs)									
	1/12	1/6	1/4	1/2	1	2	4	8	16	24
Once in 2 yr	0.35 (4.2)	0.60 (3.6)	0.75 (3.0)	1.00 (2.00)	1.25 (1.25)	1.50 (0.75)				
Once in 5 yr	0.45 (5.4)	0.75 (4.5)	0.90 (3.6)	1.30 (2.6)	1.50 (1.0)	1.90 (0.85)	2.25 (0.66)	2.75	2.85	2.95
Once in 10 yr	0.50 (6.00)	0.80 (4.8)	1.10 (4.4)	1.60 (3.2)	1.75 (1.75)	2.25 (1.12)	2.65 (0.66)	3.00	3.25	3.50
Once in 25 yr	0.55 (6.60)	0.90 (5.4)	1.25 (5.0)	1.80 (3.4)	2.20 (2.20)	2.50 (1.25)	3.00 (0.75)	3.50	3.85	4.00
Once in 50 yr	0.60 (7.20)	1.00 (6.0)	1.40 (5.6)	2.00 (4.0)	2.50 (2.50)	3.00 (1.50)	3.50 (0.875)	4.00 (0.5)	4.15	4.50
Once in 100 yr	0.65 (7.8)	1.10 (6.6)	1.55 (6.2)	2.20 (4.4)	2.80 (2.80)	3.50 (1.75)	4.00 (1.0)	4.50 (0.66)	4.75	5.00

\* Top number is the accumulation in in. Number in parentheses is average rate in in./hr.

0.05% of the time, with a probability of occurring of 1 in 35,000.

### 3-1.2 CLASSIFICATION OF RAIN

Rainfall is produced by two different weather conditions and may be classified as either thunderstorm rain or normal rain. Normal rain generally covers a very large area, lasts for several hours or even days, and usually has a moderate rainfall rate between 0.01 and 1.0 in./hr. In contrast, thunderstorm rain is generally localized over a relatively small area and may last from only a few minutes to several hours. Its instantaneous rate may approach 40 in./hr, but rarely exceeds 5 to 10 in./hr even for very short durations.

A characteristic distribution of rainfall rate at different altitudes for both normal and thunderstorm rain is shown in Fig. 3-2. The curves indicate a typical decrease of the rate with increased altitude for normal rain having a given rate at ground level. Thunderstorm rain rate distribution vs. altitude is quite erratic by comparison and usually has an instantaneous rate at relatively low altitudes considerably greater than at ground level. A typical thunderstorm

diameter distribution vs. altitude is given in Fig. 3-2.

Normal rain rate diminishes to very low values above 25,000 to 30,000 feet. Thunderstorm rain is rare above 40,000 feet, but has been observed at altitudes as high as 60,000 feet. Terminal velocity of raindrops varies with altitude and drop size, with larger drops having higher velocities. Values may range between 16 and 30 ft/sec.

Normal rainfall particle size distribution is shown in Fig. 3-3 for rain rates between 0.01 and 6.0 in./hr. At the 1.0-in./hr rate, 23% (i.e., 62%-39%) of the volume would have drop diameters from 2.0 to 2.25 mm. The curves demonstrate a definite nonlinear increase in drop size with increased rainfall rate. The median diameter,  $D$ , increases more slowly than the intensity,  $I$ , and generally satisfies the equation:

$$D = 2.23 I^{0.1288} \quad (3-2)$$

where  $D$  = median diameter, mm  
 $I$  = intensity, in./hr

For  $I$  of 2 in./hr, the median diameter is 2.53 mm. The median diameter divides the drops of larger and smaller diameter into groups of equal total volume.

### 3-2 THE MECHANISM OF RAIN EROSION

#### 3-2.1 CONDITIONS FOR RAIN DAMAGE IN MATERIALS

Radome rain damage is caused by the collision of a material traveling at high velocity with free falling water drops of random size falling at low velocity. Such damage may occur from either of two conditions, or as a result of a combination of both conditions.

The first condition, known as *rain erosion damage*, assumes the material body to be infinitely rigid, with little or no deflection resulting from the material's absorption of the kinetic energy of the water particles. The erosion, or wearing away of the material, is a surface condition only and may be either quite slow or very rapid, depending on its properties, finish, velocity of the material, and the rain rate.

The second condition, known as *rain impact damage*, may result from inadequate structural rigidity and may be more of a design problem than a materials problem. Rain impact damage may occur in plastic radomes, either of the solid laminate or sandwich type, when the skin is quite thin. The laminate may suffer extreme deflection, delamination of the layers, and complete deterioration of the resin. Such has been experienced in conventional plastic "A" sandwich radomes having skins approximately 0.020 in. thick when used for high-speed subsonic aircraft. In solid thin-wall ceramic radomes, because of their intrinsic brittleness, catastrophic failure can result from the impact of several or even a single drop when the instantaneous high pressure resulting from the impact causes excessive tensile stresses on the back side of the material.

Failures of these types can be corrected in design and are classified primarily as structural problems. For this discussion, the radome body is assumed to be capable of absorbing the energy without serious deflection or excessive stress levels. The main concern is the problem of surface erosion.

#### 3-2.2 MATERIALS THAT RESIST RAIN DAMAGE

Rain erosion testing of radome materials over the past decade indicates that the two types of materials least affected by rain are soft re-

silient materials, such as neoprene, and very hard materials, such as glass and ceramics. Materials with properties between these two extremes have consistently demonstrated low resistance to erosion. This has led to the widespread use of resilient coatings to protect the surface of plastic materials in the subsonic velocity range and to the acceptance of ceramics for supersonic velocities.

#### 3-2.3 EXPERIMENTAL CONSIDERATIONS OF RAIN EROSION

Reference 4 demonstrates that plastic and metal erosion, for a given material-sample geometry and rain rate, may be fitted to an expo-

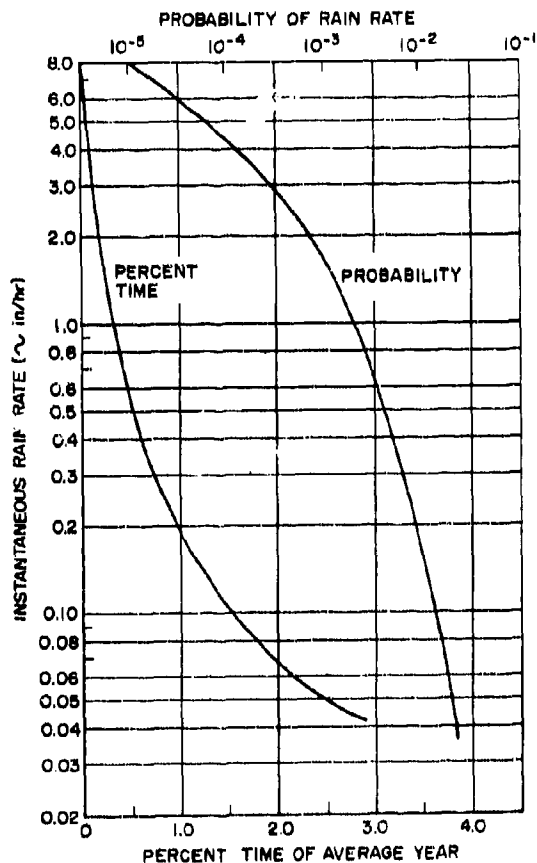


Figure 3-1. Instantaneous Rain Rate Expectancy for New Orleans (Ref. 2)

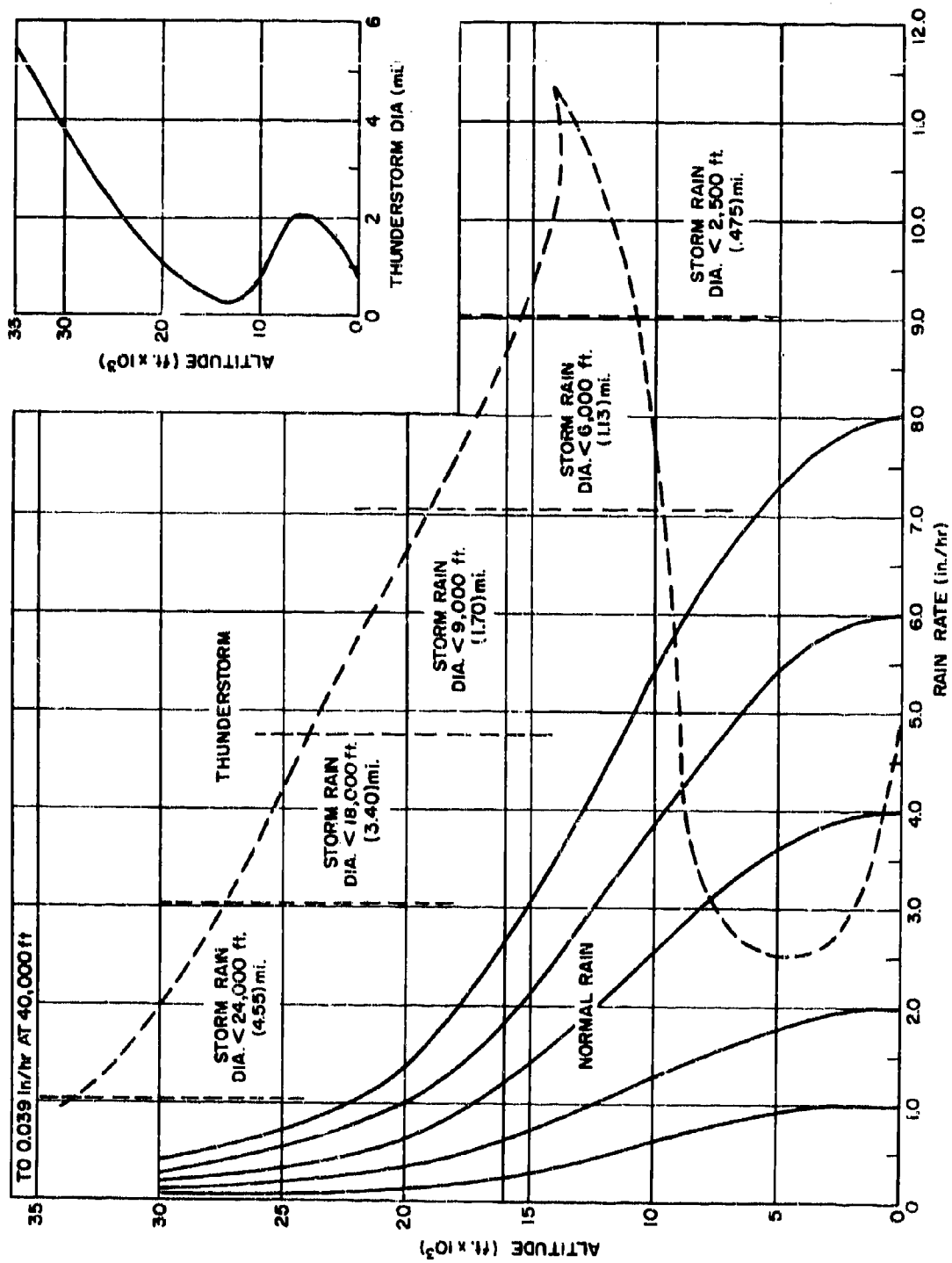


Figure 3-2. Rain Rate vs Altitude for Normal Rain and Mature Thunderstorm (Ref. 2)



nential expression, such as:

$$R = KV^x \quad (3-3)$$

where  $R$  = erosion weight loss, mg  
 $V$  = test velocity, ft/sec  
 $K$  = materials constant  
 $x$  = materials constant

This equation may be rewritten as:

$$R = K (V - V_a)^x \quad (3-4)$$

where  $V_a$  = threshold velocity below which erosion does not occur for the particular material.

From these experiments, it was found that a smooth surface was the longest wearing. This was due to the time before the surface finish was sufficiently roughened to erode. After the surface was roughened, erosion caused a measurable weight with time. The time,  $\theta$ , to reach this state was dependent upon the material, surface finish, and test velocity.

Although no specific work was performed to develop a better understanding of constants  $K$  and  $x$ , they are dependent upon the surface finish, hardness, water drop incidence angle, and other specific materials properties. Further description of the constants requires a detailed investigation of all the variables. Results for selected materials are shown under Test Results.

Reference 5 shows the deformation of a spherical water drop in collision with a hard surface at normal and oblique incidence angles and at velocities up to 1750 ft/sec. The sphere deforms into a flattened teardrop, then to a mushroom top, and finally to a thin disk as impact velocity increases. Along with these results, radial flow velocities parallel with the material surface have been determined. This radial flow velocity was found to be greater than twice the free stream velocity,  $V$ .

References 5, 6, and 7 present the studies and photographs of water drops striking materials at impact velocities up to 3200 ft/sec. The

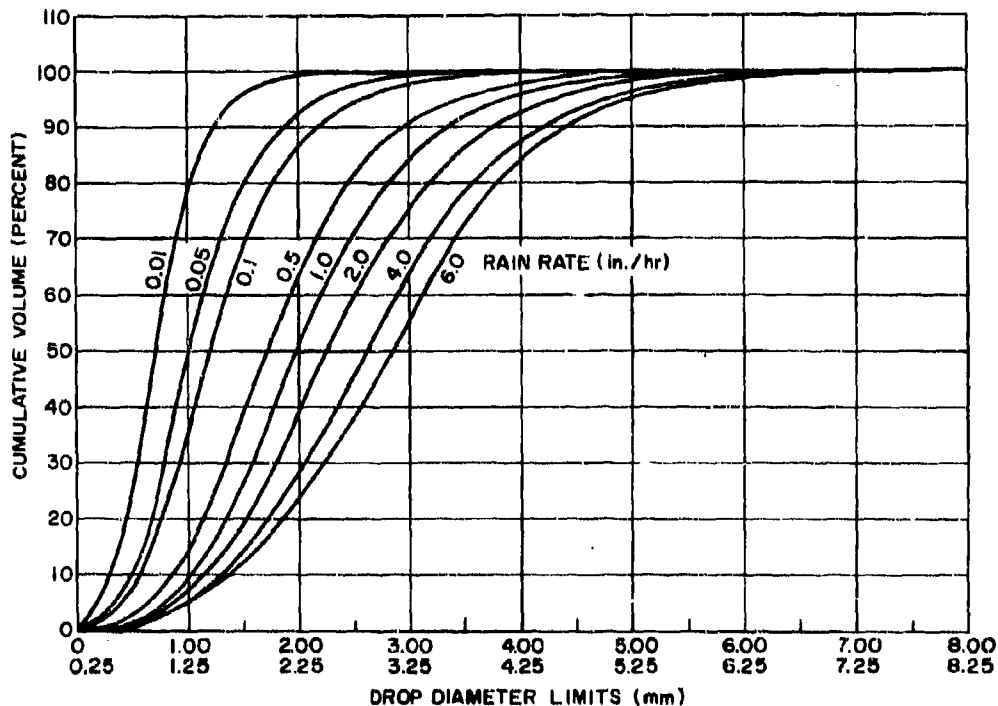


Figure 3-3. Particle Size Distribution of Natural Rainfall (Ref. 3)

resulting radial force acts upon the peaks within the surface finish of the material with an impact pressure equal to:

$$\alpha/2\rho CV$$

where  $C$  = speed of sound in water

$\alpha$  = flow factor, which is slightly less than unity

$\rho$  = density of water

The material must resist this high pressure scrubbing action or erode. Elastic coatings may deform and spring back as long as the ultimate tensile stresses are not exceeded for the elastic material and the bond is not broken between the coating and the subsurface. Uncoated rigid materials must resist shearing stresses across the base of the jagged surface peaks. Therefore, the smoother the finish and higher the maximum shear stress, the more resistant the material is to rain erosion. It follows that erosion first occurs at weak spots or areas of poor surface finish. Likewise, a porous surface is less resistant than a nonporous surface.

As the impact incidence angle of the rain is decreased, the radial velocity component, the resulting radial pressure, and the erosion damage rate are decreased proportionately. Qualitative test data substantiate this impact angle effect.

Fragmentation of water drops as a result of passing through the separation region behind a shock wave has been investigated over a limited range of conditions by the National Bureau of Standards. Reference 9 shows that rain drops are reduced to a mist in the Mach 1.3 to 1.7 range, resulting in a detached shock wave, such as would be generated by a sphere. Fragmentation results when there is a sufficient velocity differential between the water drop and the separated region behind the shock front and when the transit time from the shock wave to the body surface is sufficiently long.

The same phenomenon occurs with shapes other than spheres, at higher supersonic velocities, and with bodies of other sizes. Where the nose shape and Mach number are such that the shock wave is oblique, attached fragmentation may still occur if the transit time is of sufficient duration. For a given nose configuration and Mach number, this reaction time increases directly as the size of the body is increased. Where the body is small and there is insufficient time

to fragment the drops, the addition of a spike extends the wave front and permits sufficient time for water-drop breakup.

### 3-3 TEST METHODS FOR SIMULATING RAIN EROSION

#### 3-3.1 THE CENTRIFUGE

The centrifuge, or whirling arm, has proven to be a very effective instrument for the measurement of rain erosion resistance of materials. Two facilities employing such instruments have been in operation for many years: one at the Cornell Aeronautical Laboratory and one at the University of Cincinnati (Reference 11). Both facilities use two-blade zero-lift propellers. These arms are designed to test leading edge samples, as shown by Fig. 3-4. The CAL facility places the center of the test sample  $23\frac{1}{2}$  in. from the axis of rotation; the UC facility places an identical specimen 21 in. from the axis.

In their present form, both centrifuges are limited to subsonic velocities. The propeller profiles are such that compressibility is encountered in the region of 600 mph (880 ft/sec). Above this speed, the power required to drive the unit rises sharply and the wave front from the tip tends to fragment the free-falling simulated rain. The specimen is thus exposed to the turbulent wake of the previous revolution, which is a very poor simulation of the natural environment.

The Cornell whirling arm produces a rain-drop collision rate, at 1-in./hr rainfall rate and 1.9-mm average drop size, given by:

$$N = 5.09Vt \quad (3-5)$$

where  $N$  = number collisions/in.<sup>2</sup>

$V$  = velocity, mph

$t$  = exposure time, min

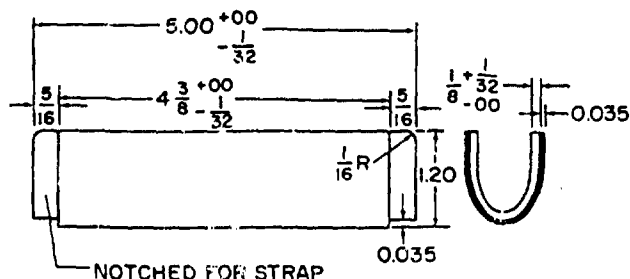


Figure 3-4. Test Specimen for "Whirling Arm" Rain Erosion Simulator

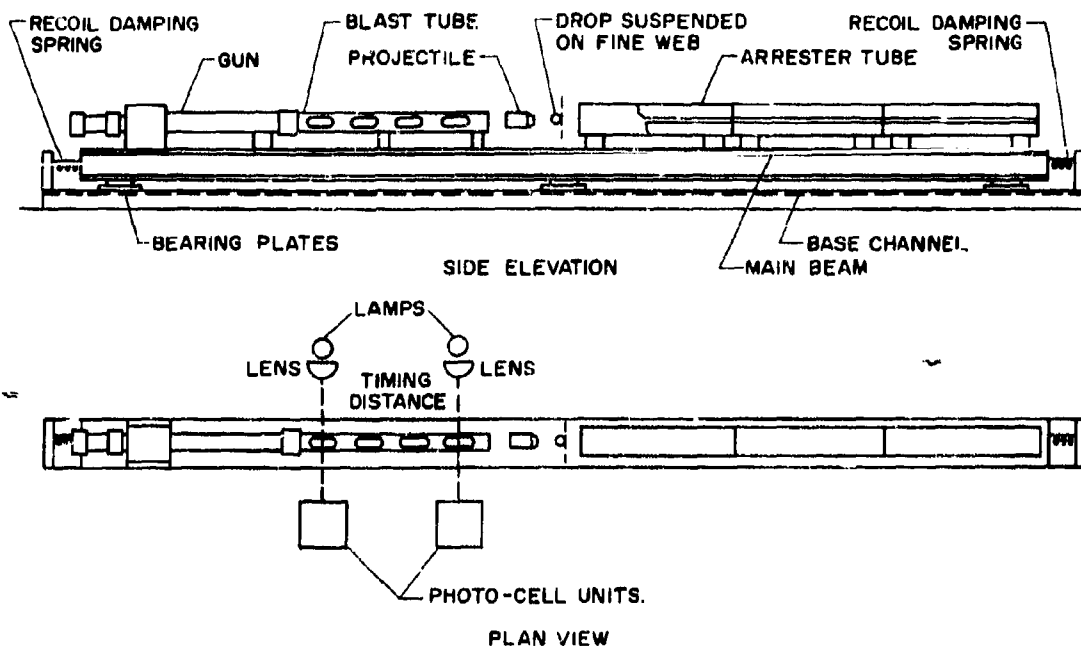


Figure 3-5. Diagrammatic Arrangement of Supersonic Liquid Drop Impact Apparatus

These facilities have produced extremely useful data in the evaluation of many possible rain erosion coatings. For example, the Goodyear 23-56 neoprene coating, at standard test conditions of 560 mph and 1 in./hr rainfall, relates coating thickness with time to erode by:

$$t = 0.53x^2 \quad (3-6)$$

where  $t$  = time for coating to erode, min  
 $x$  = coating thickness, mils

At this speed and rain rate, a 10-mil coating of the Goodyear material lasts approximately 53 minutes in the rain and a 20-mil coating lasts about 212 minutes (Reference 9).

This type of data has enabled designers to select adequate laminates and coatings for aircraft in the high subsonic speed range. Although these coatings may be damaged or stripped off in flight through heavy rainstorms, they prevent damage to the radome. The radome can be recoated to renew the protection.

### 3-3.2 THE RAIN GUN

An apparatus for the study of the impact of liquid drops on a surface moving at supersonic

speeds has been designed and operated by the Royal Aircraft Establishment (Reference 6). The device consists of a gun, a blast tube, and a projectile arresting mechanism, as shown in Fig. 3-5. The gun has a 1.25-in. diameter smooth-bore barrel screwed to a breech block that receives a 1.0-in. engine-starter cartridge with electric igniter. The blast tube prevents the gases from the gun barrel from reaching the water drops before the projectile. The blast tube is 6 ft long with the same diameter as the gun barrel.

The arrester tube consists of a series of washers and spacers. The washers have an inside diameter smaller than the projectile diameter and are deformed in absorbing the kinetic energy of the projectile while capturing it intact. The washers have a 0.9-in. bore and are graded in three sections from 0.018-in. thickness at the entry section to 0.048 in. in the third section. The top half of the tube is hinged for installation of new disks after each firing.

Single drops up to 2.5 mm in diameter can be suspended on the projectile flight line on a drop holder ring. The drops are held in place by a very fine web. With careful positioning of

the drops, repeated impacts on the same area of a test specimen can be obtained. The detached normal shock wave of the projectile deflects the low mass web instantaneously, leaving the spherical drop to impact with the test specimen, as shown in Figs. 3-6 and 3-7.

Disk-shaped test specimens may be tested in either a supported or unsupported condition. Typical projectiles, as shown in Figs. 3-8 and 3-9, are made of plastic and have a steel nose. The steel nose, in contact with the aluminum stopping disks, provides good resistance. The plastic keeps the projectile mass low and helps to keep the body center of gravity forward to assist in projectile stability.

The velocity is measured by two photo cells looking through holes in the blast tube. According to the projectile charge used, the apparatus is capable of velocities between 500 and 3200 ft/sec. Velocities are limited only by the maximum allowable breech pressure of 10,000 psi.

Progressive deformation by the water drop on the material surface is recorded by photographs from successive firings. This device is simple to operate and permits precisely controlled experiments at a reasonable cost.

### 3-3.3 MITHRAS EROSION SIMULATOR

Under a Navy BuWeps contract, a wind-tunnel test device was constructed by Mithras, Inc. (Reference 12). The test setup, mounted in the David Taylor Model Basin supersonic blow-down tunnel, is shown in Fig. 3-10. This erosion simulator consists of a pylon on which is mounted a high-pressure line and water-injection nozzle. A slug or cylinder of water is accelerated from the nozzle using a high-pressure source and is controlled by a quick-opening valve. The slug of water, when ejected, is disrupted into a form, shown typically by Fig. 3-11, in which the water distribution is dependent upon discharge pressure and the relative velocity between the water particles and the local air stream.



**Figure 3-6. Projectile About to Strike 2-mm Diameter Water Drop at 1200 ft/sec**

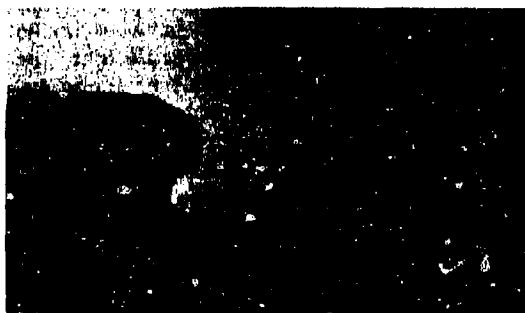


**Figure 3-7. Projectile About to Strike 2-mm Diameter Water Drop at 3000 ft/sec**

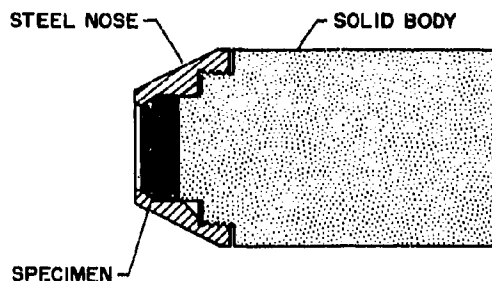


**Figure 3-8. Projectile with Molded Polyethylene Body for Carrying Solid Specimen**

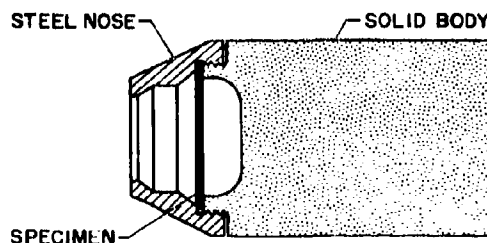


**Figure 3-9. Projectile with Molded Polyethylene Body for Carrying Sheet Specimen**

Unfortunately, the distribution of particle size has not been determined. The test method at this time must be considered qualitative, but it may prove useful in comparing two different materials and their resistances. Experiments have been conducted in the velocity range between 1000 and 2000 ft/sec.

### 3-3.4 THE BALLISTIC RANGE

A 1500-ft rainfall system, known as the Supersonic Rain Erosion Ballistic Range, was constructed at Camp Elliot, California. An overhead spray nozzle system, capable of producing rain rates of up to 11.9 in./hr with a drop size distribution similar to 1.0 in./hr of natural rainfall, is used as a source of rain. Special 57-mm shells were designed for testing cones and

flat samples with 2-in. base diameter. The cone half angles tested were  $15^\circ$ ,  $22\frac{1}{2}^\circ$ , and  $30^\circ$ . Mach 2.0 data are available for laminates of phenolic, Epon 828, silicone, polyester, and other materials (References 13 and 14). The test program included metal-tipped cones, alumina ceramics, and elastomeric erosion coatings.

The extreme axial acceleration forces make this system much more desirable for plastic materials than for ceramics. Similarly, the recovery system, a time-delay parachute device, necessitates ground impact of the test piece at velocities sufficiently high to cause recovery damage to brittle materials. Extension of this technique to higher velocities would result in



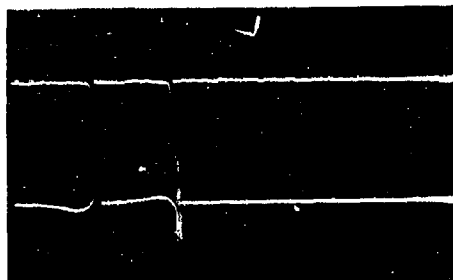
Figure 3-10. View of Model, without Sleeve, in Extreme Downstream Position and Water Nozzle in Extreme Upstream Position



INITIAL SHAPE



SUBSEQUENT SHAPE



TIMING SCALE (100 ALS LARGE DIVISOR)

Figure 3-11. Test Photos of Water Slug with Sleeved Model

even higher acceleration forces and recovery damage and is not used. The 57-mm test program is one of the most comprehensive erosion programs and is recommended for review by the radome designer when selecting materials for use at Mach 2 or lower.

### 3-3.5 THE ROCKET SLED

For velocities of Mach 2.0 and higher, the supersonic rocket sled is the most realistic rain erosion test method. Many tests have been made in the Mach 1.5 to 3.0 range, using many different materials for radomes of various sizes and configurations. Artificial rain fields have been installed at Holloman Air Force Base, Edwards Air Force Base, and the Naval Ordnance Test Station. Much has been learned about the use and limitations of radome materials in supersonic rocket design from this rocket sled testing in controlled artificial rain. However, it should be recognized that this test method is extremely expensive for the limited information obtained and produces little in the way of quantitative engineering data. Its greatest value is probably as a means of qualification testing a radome for a given aircraft or missile system early in the program without jeopardizing a costly developmental missile.

The cost of a sled test program is dependent upon many factors, including the number of runs, sled complexity, degree of instrumentation, propulsion system selected, and amount of design and analysis required. Monorail sleds are less expensive to build and require lower thrust levels to attain a required velocity; therefore, they have been used extensively for testing small missile radomes. The testing of large radomes requires a dual-rail sled with higher weight, greater thrust, more complex stopping mechanisms, and, therefore, are higher in cost.

Both single-stage and dual-stage propulsion systems have been used. To achieve constant velocity within the rain field, a second-stage rocket is generally selected, since most single-stage thrust programs only permit the designer to achieve maximum velocity somewhere within the rain field. Thrust program selection is influenced by the available track length between the starting point and the rain field, by the run-out distance after the rain, and by the stopping mechanisms available.

Overall testing costs are affected by struc-

tural failures, weather delays, instrumentation malfunctions, and extensive setup times between runs. Careful planning, including a second sled, backup instrumentation, preliminary testing, and scheduling when the weather conditions are least likely to interfere, will likely reduce the overall cost and yield more information for a given expenditure.

In full-scale radome qualification testing, at least one dummy run should be made using a metal dome to verify predicted sled performance. Three-axis vibration levels can be measured for preliminary laboratory vibration simulation. Shock and vibration levels experienced on the track may be much more severe than in flight. Many radome failures have resulted from this environmental condition rather than rain damage. When failure occurs, it is sometimes very difficult to determine or separate rain failures from sled vibration failures.

The sled designer should select low-cost, readily available rocket motors with well-established performance. Instrumentation should be selected that is capable of recording velocity and track station at time of failure. Proven track methods should be employed where possible.

All United States supersonic track facilities have published reports disclosing detailed track and rain field information. An existing sled may be available that would require minor rework and save the cost of a new sled design. All tracks, facilities, and available sleds should be considered before selecting a track facility for radome testing.

Small light-weight sleds for the Mach 4 to 5 range are presently under development. Designing in this range presents many problems and may result in numerous failures before success is achieved. However, when this is accomplished, materials can be tested at and above the sonic velocity in water, 4800 ft/sec. Beyond this speed, the water drop behaves like a rigid particle rather than a fluid. This presents an unexplored area of study on rain erosion.

### 3-4 SLED TESTS

As can be seen by the foregoing discussions of various simulation techniques, considerable time, effort, and money have been spent in an attempt to obtain rain erosion data. Each of these techniques has intrinsic limitations and disadvantages, since each one is an attempt to

TABLE 3-2 COMPARISON OF THREE SLED-TEST FACILITIES

Activity	R. A. E.	Sandia Corp.	USNADC & USNOTS SNORT
Track	Pendine, Eng.	Holloman Air Force Base	China Lake
Track Length (ft)	3000	34,000	21,000
Rain Field (ft)	500	6000	2500
Rain Rate (in./hr)	1-6	5	2
Drop Size (mm)	1.6-2.8	1.5	1.8
Max Velocity (ft/sec)	1760	2800	3030
Sample Type	Flat	Ogival	Ogival
Length (in.)		6½-14	13
Diameter (in.)		7½-8	5
Materials	Plastic Ceramic	Plastic Ceramic	Plastic Ceramic

simulate the actual environmental conditions encountered by a radome in flight. Other than the use of actual missile firings through a rain environment, the costly technique of firing test materials carried aboard a supersonic sled through a calibrated rain field comes closest to simulating actual conditions. This is not to say that sled testing affords conclusive information. As will be shown in the following paragraphs, this technique can also provide dubious results. The major contributions to this field of sled test information in recent years have been made by Royal Aircraft Establishment, Ministry of Aviation, England, at the Pendine Track Facility; Sandia Corporation, Albuquerque, New Mexico, at Holloman Air Force Base; and Naval Ordnance Test Station, Shrike Project and the Naval Air Development Center, Johnsville, Pennsylvania; Supersonic Naval Ordnance Research Tract (SNORT) at China Lake, California. Table 3-2 lists a comparison of the various facilities used by these groups. Each of the facilities uses a monorail sled for its rain erosion testing. Both the Radome Section, NADC, and the Shrike Project personnel, NOTS, use the same sled at the SNORT facility.

### 3-4.1 NADC TESTS

Considerable controversy existed within the Eagle Missile program in 1960 because of the

lack of rain erosion information. Because of the combination of size, C-band operation, and weight limitations, the selection of a thin-wall design was necessary. However, the usual question arose concerning the ability of ceramic and plastic materials to withstand a rain environment, especially in this instance, since a maximum velocity of Mach 4.5 would be encountered. Provisions were made by the Bendix Research Laboratories to obtain the necessary information in a sled test program at Edwards Air Force Base, California. Unfortunately, cancellation of the Eagle Missile Program in early 1961 curtailed the planning of sled testing. Having seen the controversy that arose because of the lack of the erosion data at supersonic velocities, the Radome Section at NADC immediately set upon a sled test program to obtain some data. Funds were provided by the Bureau of Naval Weapons to undertake a modest program of testing at the Supersonic Naval Ordnance Tract (SNORT), China Lake, California.

One of the first steps taken under this program was an extension of the original 500-ft rain field to a more realistic value of 2500 ft. To give an idea of the tremendous costs encountered, \$21,000 of the \$48,000 allocated for the overall project was consumed in the materials and labor for this extension. Figure 3-12 is an uptrack view of the completed 2½00-ft trackside rain field. Design and fabrication of the Mach

2.5 monorail sled was assigned to the personnel at the SNORT facility. In an attempt to obtain as much data as possible, it was requested by NADC that the sled also have provision to carry small ( $1\frac{1}{2}$  in.  $\times$  3 in.) flat samples of test materials in addition to two test domes. Figure 3-18 clearly shows a triangular wedge section protruding from the forward midsection of the monorail sled. This bulkhead is designed so that three separate wedges of  $20^\circ$ ,  $30^\circ$ , and  $40^\circ$  half angles can be interchanged throughout the ten firings. Since the radomes to be tested were all of the same geometrical configuration, the wedge would provide highly desirable erosion-vs.-angle-of-incidence information. Each wedge exposes six samples ( $1\frac{1}{2}$  in.  $\times$  8 in.), three on

each side, to the rain environment. A whip antenna is seen extended from the top of the main housing. This telemeters both accelerometer and thermocouple information back to a remote location. The primary sources of braking are inertia-actuated air scoops that open out into the air stream upon burn-out of the sled motors. On November 15, 1961, a dummy firing, using two stainless steel radomes, was conducted to determine sled performance. Excessive aerodynamic drag and sled weight resulted in a maximum velocity of 1900 ft/sec, considerably lower than the expected 2800 ft/sec. In addition, the single axis accelerometers showed that lateral accelerations in excess of 150 g's and vertical accelerations in excess of 200 g's were obtained.

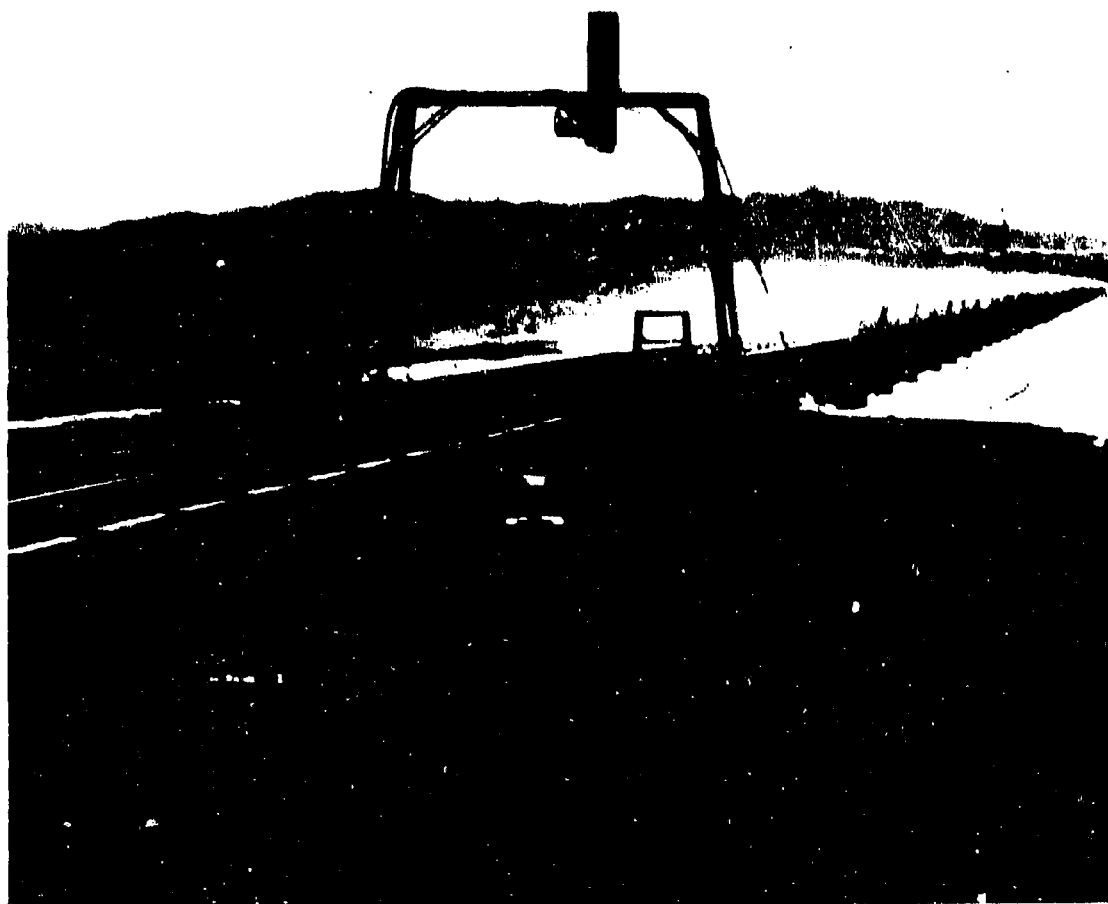


Figure 3-12. Uptrack View of NADC SNORT Track





**Figure 3-13. SNORT Sled Showing Methods of Attaching Test Specimens. Coors Porcelain 99% Alumina Radome on Right (Head-On View) and Corning Glass Ware Pyroceram Radome on Left**

At this point in the program, there was considerable uncertainty. Because of the relatively low velocity, it was obvious that the flat sample holder would not be in the free stream but at some point aft of the intersection of the shock waves from the adjacent radomes. Thus, because the shock waves from adjacent radomes interacted before the sample wedge, a true test of erosion could not be made. More importantly, there was no assurance that the domes could withstand the vibrational loads. Despite these shortcomings, it must be remembered that this was only the second time that a sled with radomes had been fired and recovered at velocities in excess of 1900 ft/sec. The Sandia Corporation was conducting a similar program at Holloman Air Force Base and had successfully retrieved a vehicle only one month previously. A maximum velocity of 2000 ft/sec was reached during these tests. The primary reason for this series of tests was to find the thickness of the refractory dome needed to withstand catastrophic failure caused by rain impact and erosion.

A meeting was held at NADC with prospective radome suppliers to determine the size, shape, and thickness of the test radomes. Since the test items were being donated to the test program by the various manufacturers, it was highly desirable that costs be minimized. Because of sled weight and aerodynamic drag, it was also desirable to test a relatively small object. It was agreed that each test item would be of the same configuration so that geometry would not be a variable. A survey showed that all of the contributing manufacturers had fabricated Mauler ogival radomes, which were 18 in.  $\times$  5 in. Because of varying grinding and machining preferences of the manufacturers, it was agreed that the first 2 in. of the radome would be finished at the manufacturers' discretion.

However, no one could guarantee which thickness would survive the test environment. After giving much consideration to the structural and electrical properties of the materials of interest, as well as the most prominent frequencies of operation, it was decided to use a 0.050-in. wall



**Figure 3-14. Coors Porcelain 99% Alumina (AD-99) Radome with  $t = 0.050$  in. on Right (Head-On View) Survived the Environment. Corning Pyroceram with  $t = 0.050$  in. and Nylon Tip on Left Survived the Environment. (Maximum Run Velocity = 1960 ft/sec)**

thickness. In addition to a 0.050-in. radome from each of the test materials, radomes of equivalent electrical thickness would also be submitted for evaluation. The rain field was set up for 2-in./hr rain rate centered about a 2-mm median drop size (Reference 16).

Figures 3-18 through 3-22 present the conditions and results for this series of tests.

Depletion of funds cancelled some of the planned runs, but the assessment of the data obtained was encouraging. The most important determination was that the 0.050-in. walls of Pyroceram, aluminum oxide, and fiberglass had survived not only the rain environment but also the tremendous accelerations that were experienced. Photographs reaffirmed that the angle of impingement of the droplets on the radome surface is a major design factor. They illustrated that maximum erosion occurred at normal incidence and fell off rapidly as the angle of incidence increased. The ever-appearing value of

15°, specified in the design of erosion protection for manned aircraft radomes, persisted throughout the examination of the test specimens. However, the information was not complete in that there still remained a need for data at higher velocities. During the project, it became obvious that erosion information at velocities in excess of Mach 3.0 was necessary. New materials and fabrication techniques were being developed that also would have to be subject to the question of erosion resistance. One of these, slip-cast fused silica, was becoming popular because of its favorable dielectric properties, thermal properties, and relatively inexpensive fabrication.

As a result, NADC initiated a second program with BuWeps for testing at higher velocities. However, increasingly severe problems were encountered. Sled velocity was increasing; therefore, stopping the sled within the same track length would be even more difficult. The

costs of higher impulse rocket motors, as well as a new sled design, were rising rapidly. The NADC designed and fabricated the monorail vehicle to be used for this second test series. In order to facilitate braking, a small parachute was housed atop the vertical stabilizer, which also contained a slot antenna for telemetering purposes. The new sled was fired on January 31, 1963, but suffered a premature chute deployment that resulted in violent sled vibrations and subsequent sled breakup. Rather than delay the entire program until a complete structural analysis could be performed and the second sled completed, the NOTS immediately modified the sled used for the earlier runs. Cajun rocket mo-

tors replaced the original HPAG motors and the wedge assembly was removed to lessen the likelihood of structural failure. On March 5, 1963, this vehicle attained a peak velocity of 3030 ft/sec at the midpoint in the rain field after a 0.85-second hold back of the sled. Auxiliary stopping of the sled was accomplished by placing water-filled plastic tubes atop the track head between the 20,000- and 21,500-ft stations. Stainless steel domes were used during this checkout firing. The first live firing in this new series commenced on March 22, 1963.

Figures 3-23 through 3-46 present the conditions and results of these ten firings.



**Figure 3-15. Brunswick Corp. Filament Wound Radome with Vibrin 135 and  $t = 0.100$  in. (Left). Zenith Plastics Compression Model Diallyl 128 with  $t = 0.100$  in. (Right)**



**Figure 3-16. Brunswick Radome (Left) Is Heavily Eroded Over First Inch of Tip Area, with Secondary Erosion Over Next Two Inches. Zenith Radome (Right) Has Minor Erosion on Tip, with Negligible Pitting as Far Back as 5 1/2 in. (Maximum Run Velocity = 1985 ft/sec)**

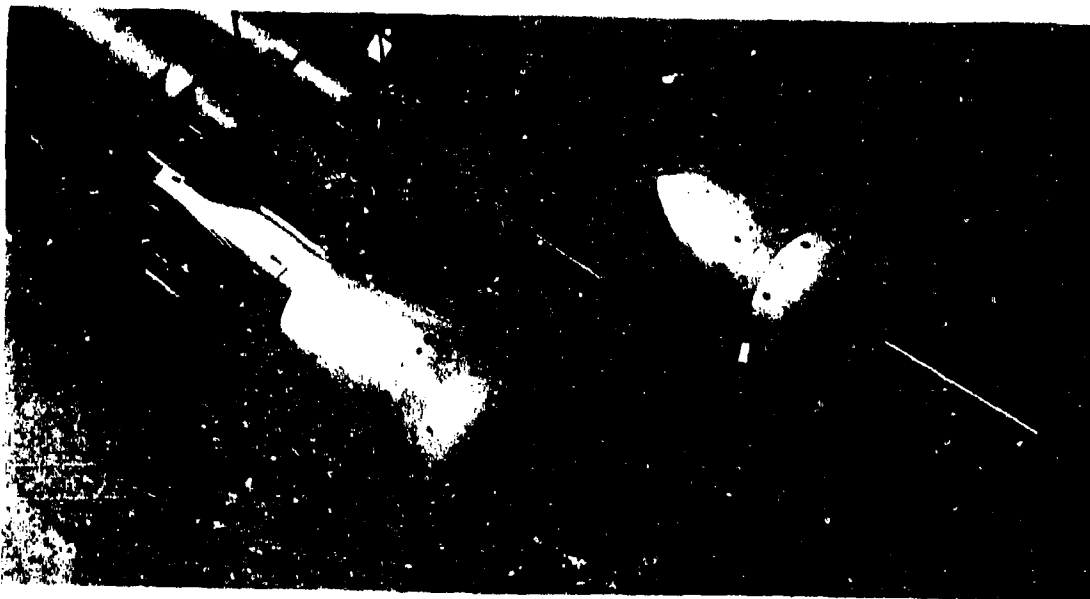


**Figure 3-17. USNADC Fiberglass Laminated Radome with  $t = 0.250$  in. (Left). USNADC Fiberglass Laminated Radome with  $t = 0.250$  in. and Spike ( $l/r = 3.4$ ) (Right)**



**Figure 3-18. USNADC Radome without Spike Is Heavily Eroded Across Face of Dome. USNADC Radome with Spike Is Heavily Eroded Across Face of Dome Except for Small 2-in. Diameter Area at Base of Spike**

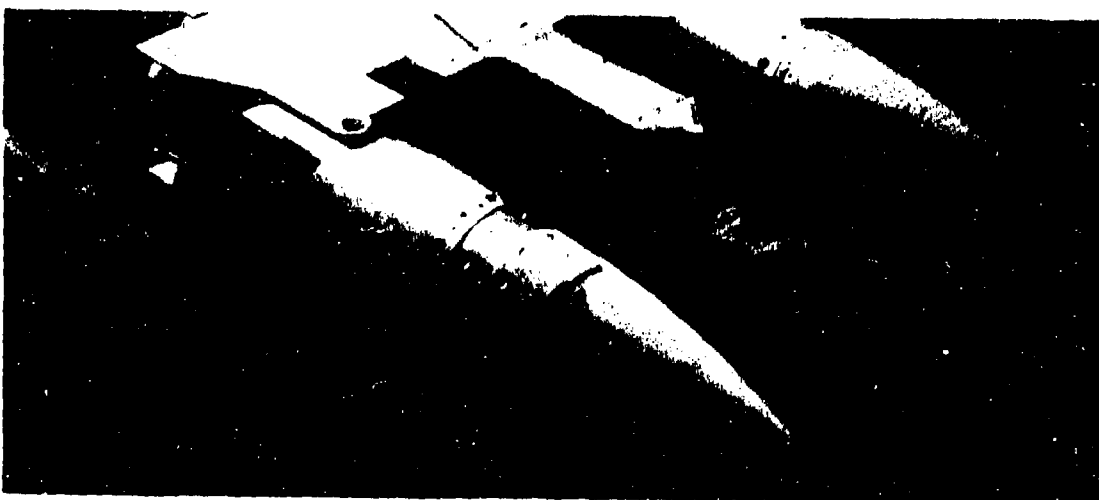


**Figure 3-19. Douglas Aircraft Ribbon Wound Radome with DC-7141 Silicone and  $t = 0.100$  in. (Left). Brunswick Corp. Filament Wound Radome with Vibrin 135 and  $t = 0.050$  in. (Right)**



*Figure 3-20. Douglas Radome (Left) Is Lightly Eroded Over First 0.5 in.  
Brunswick Radome (Right) Is Heavily Eroded in Tip Area*



*Figure 3-21. Douglas Aircraft Ribbon Wound Radome with DC-7141 Silicone  
and 1.5 in. Stainless Steel Tip (Left). Zenith Plastics Compression Molded  
Diallyl 128 with  $t = 0.100$  in. (Right)*

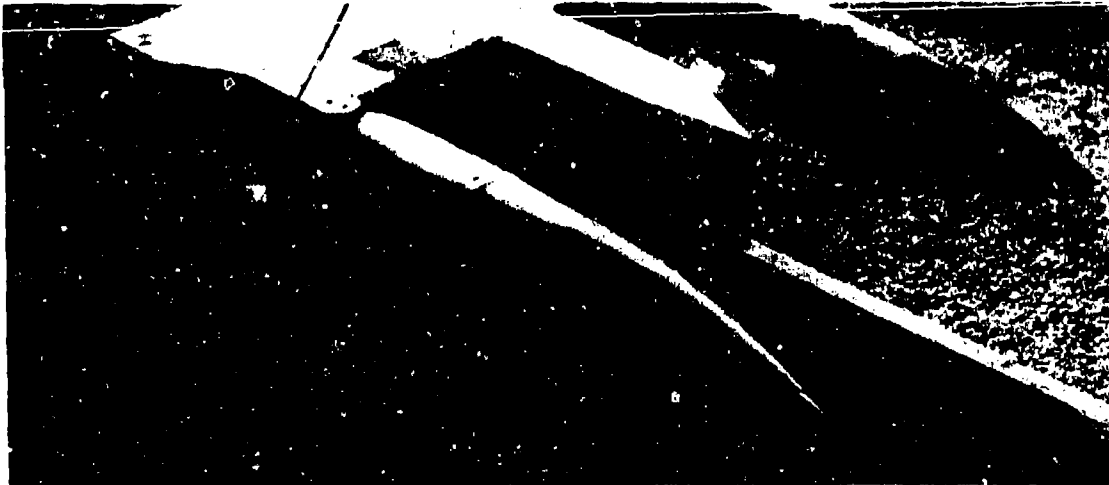


**Figure 3-22. Douglas Radome (Left) Is Very Lightly Eroded Aft of Tip, and Tip Is Loosened. Zenith Radome (Right) Has Minor Erosion on Tip, with Negligible Pitting as Far Back as 5 1/2 in.**

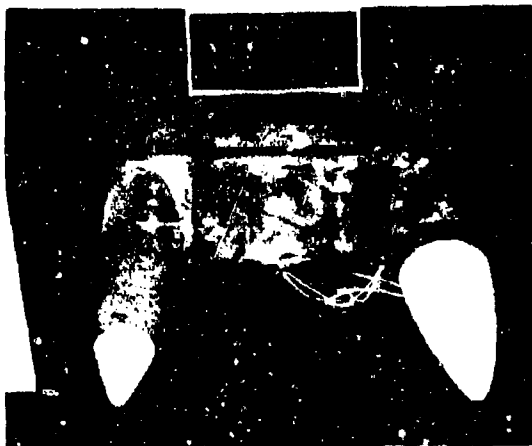


**Figure 3-23. Brunswick Corp. Chopped Fibers with DC-2106 Silicone Resin Binder Radome, with  $t = 0.375$  in., and Sprayed Ceramic Cap 0.015 in. Thick Deposited Over First 3 in. of Dome (Left). Corning Multifomed Fused Silica (CGW#7941) Radome with  $t = 0.375$  in. (Right)**



**Figure 3-24. Brunswick Radome (Left); Synchro-Ballistic Photos Showed Ceramic Cap Completely Eroded During First Half of Rain Field and Plastic Body Heavily Eroded During Second Half of Rain Field. Corning Radome (Right); Synchro-Ballistic Photos Showed Dome Broke Before Rainfield Entrance Due to Poor Attachment Bonding. (Maximum Sled Velocity = 2775 ft/sec)**

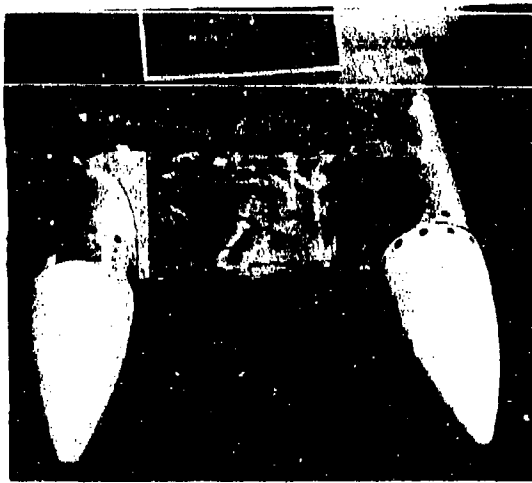


Figure 3-25. Coors 99% Alumina (AD-99) Radome with  $t = 0.050$  in. (Left). Corning Pyroceram Radome with  $t = 0.050$  (Right)

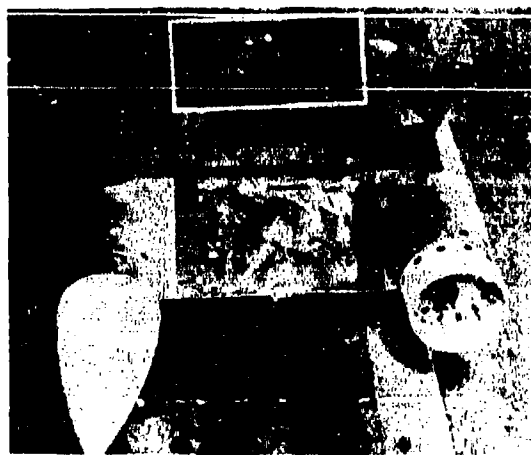


Figure 3-26. Coors Radome (Left) Survived Environment But Showed Evidence of Hairline Fracture Pattern. Corning Radome (Right) Failed During First Half of Rain Field (Maximum Sled Velocity = 2839 ft/sec)

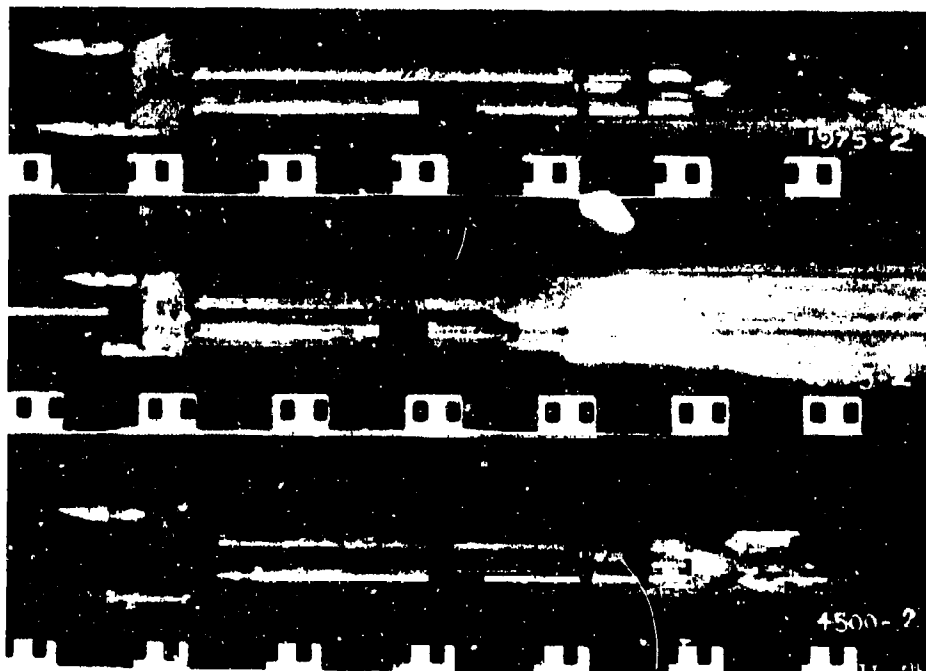


Figure 3-27. Corning Radome (Bottom) Lost During First Rain Field



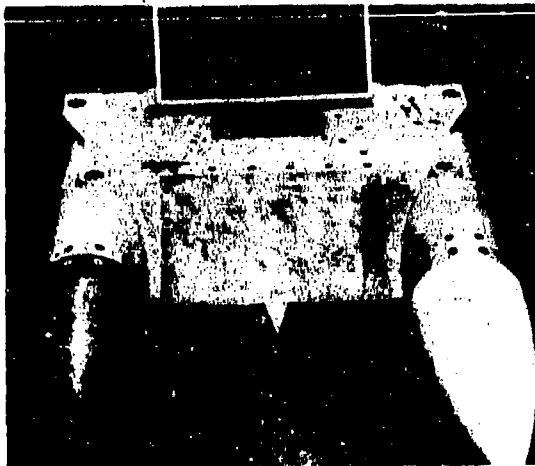


Figure 3-28. RDI Woven Fiberglass Sock Radome with Epoxy Resin and  $t = 0.050$  in. (Left). Raytheon 97% Alumina Radome with  $t = 0.050$  in. (Right)

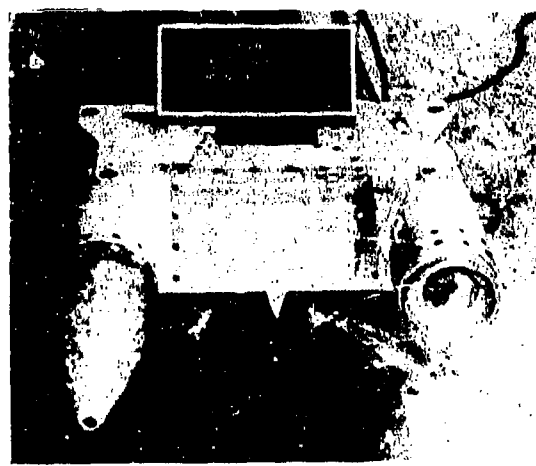


Figure 3-30. Corning Pyroceram (960X) Radome with  $t = 0.090$  in. (Left). Coors 99% Alumina (AD-99) Radome with  $t = 0.090$  in. (Right)

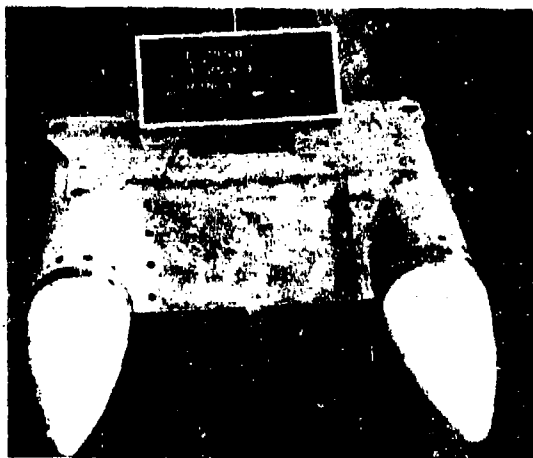


Figure 3-29. RDI Radome (Left) Survived Environment But Received 1-in. Diameter Hole in Nose. Raytheon Radome (Right); Synchro-Ballistic Photos Showed Dome Broke Before Midpoint in Rain Field (Maximum Sled Velocity = 2908 ft/sec)

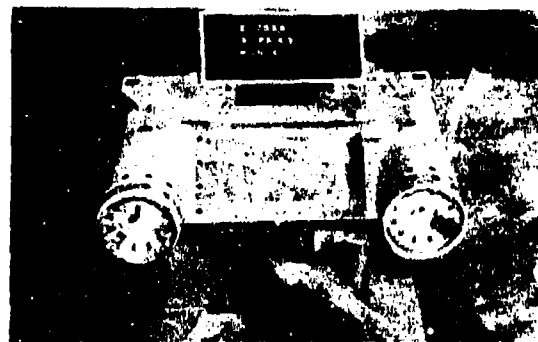
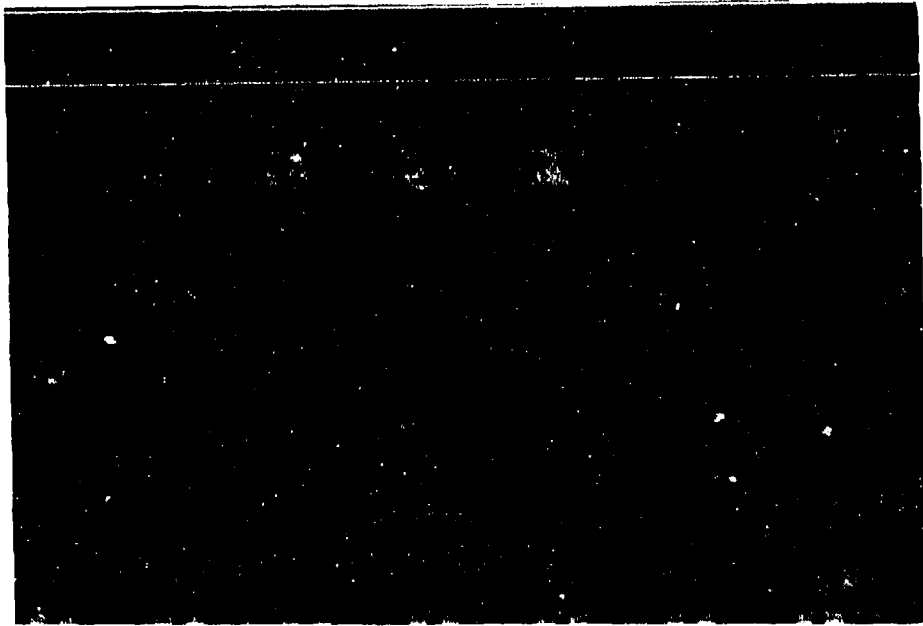


Figure 3-31. Corning Radome (Left); Synchro-Ballistic Photos Showed Dome Broke Before Rain Field. Coors Radome on Right Survived Rain Field But Broke After Middle of Rain Field (Maximum Sled Velocity = 2852 ft/sec)



**Figure 3-32. Coors Radome (Bottom) Survived Rain Impact Well Beyond Peak Velocity But Broke in Second Half of Rain Field**



**Figure 3-33. Convair Slip-Cast Fused Silica Radome with 1 0.350 in. and Unglazed Round Tip on Left. Same Radome with Glazed Tip (Right)**

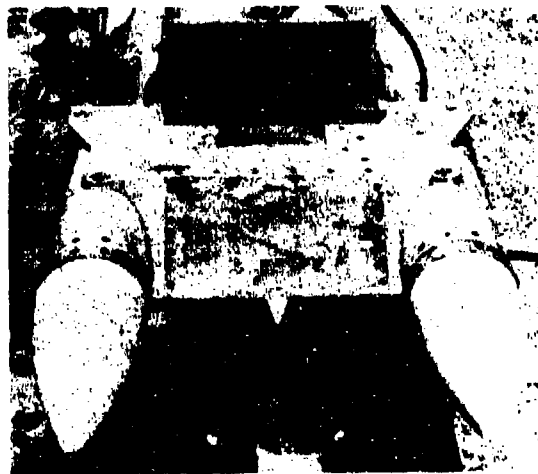


**Figure 3-34. Both Radomes Survived Environment But Showed Heavy Tip Erosion (Maximum Sled Velocity -- 2950 ft/sec)**

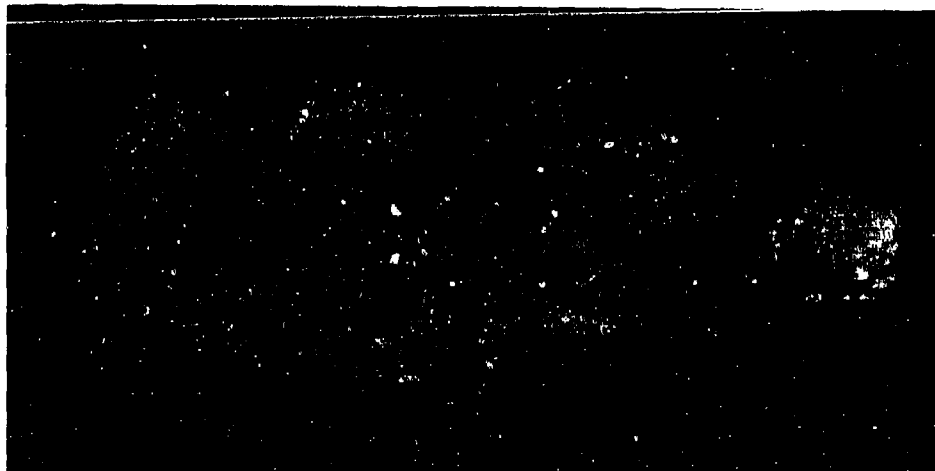


**Figure 3-35. Convair Fused Silica Radome with Unglazed Tip After Test Shows Heavy Tip Erosion**



**Figure 3-36. Convair Slip-Cast Fused Silica Radome with  $t = 0.350$  in. and Unglazed Pointed Tip (Left). Same Radome with Glazed Tip (Right)**

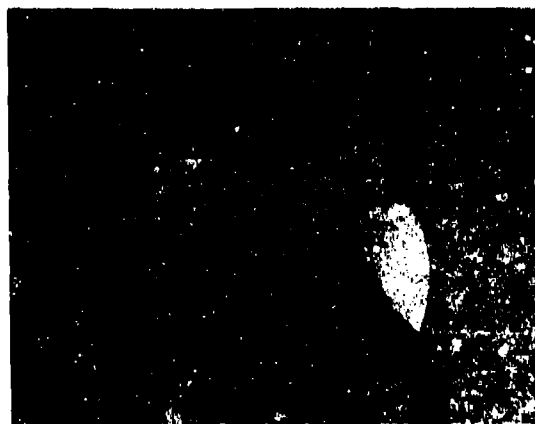


**Figure 3-37. Convair Radome (Left) Broke Between 1975 and 3175 Feet of Run. Convair Radome (Right) Survived Environment But Showed Heavy Tip Erosion (Maximum Sled Velocity = 2930 ft/sec)**



**Figure 3-38. Coors 99% Alumina (AD-99) Radome with  $t = 0.100$  in. (Left Rear), Douglas Ribbon Wound Radome with Silicone Resin and  $t = 0.100$  in. (Right Front). Special 1 1/2-in. Long Stainless Steel Tip Is Bonded to Front of Douglas Radome**



**Figure 3-39. Coors Radome (Left) Survived Environment with No Signs of Erosion. Douglas Radome (Right) Showed Heavy Erosion for 5 in. Behind Steel Tip (Maximum Sled Velocity  $= 2852$  ft/sec)**

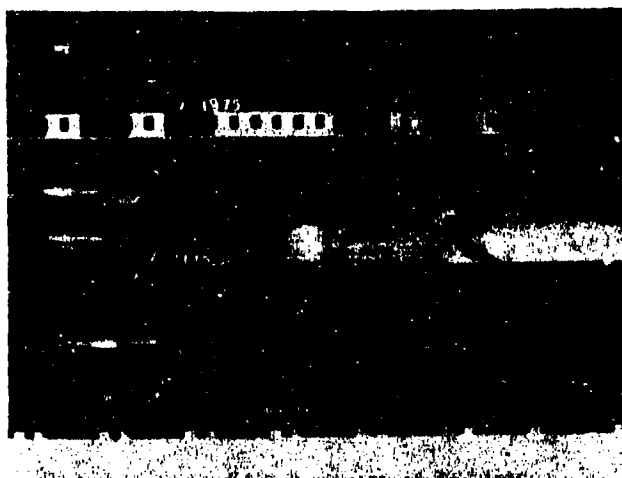


**Figure 3-40. Synchro-Ballistic Photos Showed Rocket Motor Breaking Loose From Vehicle**

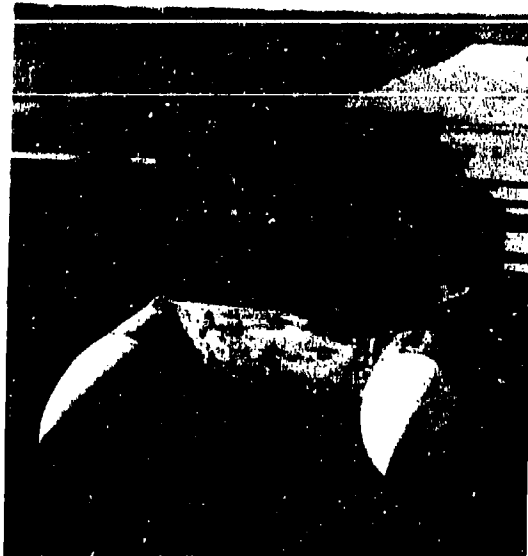


Figure 3-41. Convair Slip-Cast Fused Silica Radome with  $t = 0.350$  in. (Left) Is Rerun of Radome Shown in Figure 3-33 (Left) with Metal Tip Added. Convair Slip-Cast Fused Silica Radome with  $t = 0.350$  in. and Pointed Shape Glazed Tip (Right)

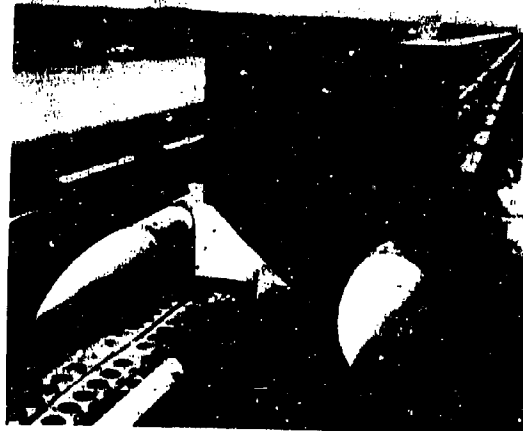


Figure 3-42. Convair Radome (Left) Survived Environment But Showed Minor Erosion Aft of Tip. Convair Radome (Right) Survived Environment But Showed Slight Erosion On Tip



Figure 3-43. Corning Multifomed Fused Silica Radome with  $t = 0.350$  in. (Left). Attachment Area of This Radome Is Strengthened with Fiberglass Warp. Convair Slip-Cast Fused Silica Radome with  $t = 0.350$  in. (Right) Is Rerun of Radome Shown in Figure 3-41 (Right)



Figure 3-44. Corning Radome (Left) Broke During First Half of Rain Field. Convair Radome (Right) Showed Additional Erosion in Tip Area



**Figure 3-45. USNADC Fiberglass Hemisphere Radome with  $t = 0.250$  in. (Left). Same Radome with Metallic Spike ( $1/r = 3.4$ ) (Right)**



**Figure 3-46. Both Radomes Survived Environment but Showed Heavy Erosion Except for Small Annular Ring at Base of Spike**

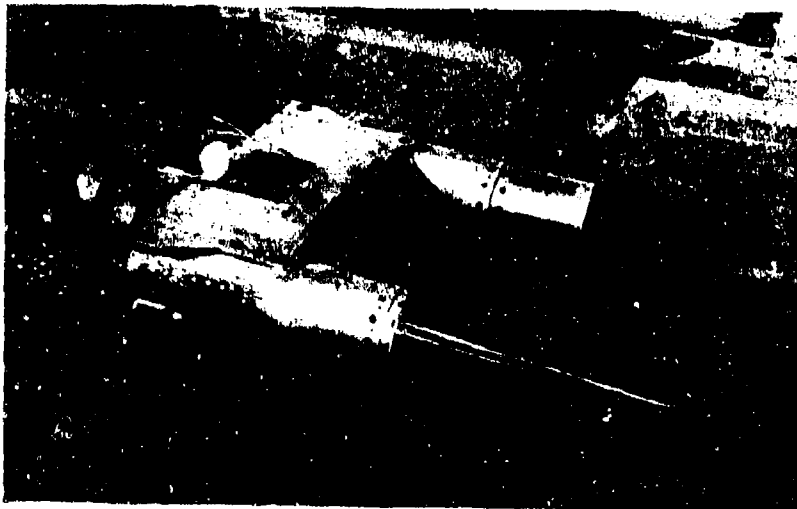


**Figure 3-47. Silicone-Impregnated Radome in Shrike Configuration (Left). Same Radome with Thicker Skin and Different Radius of Curvature (Right)**

### 3-4.2 U.S. NAVAL ORDNANCE TEST STATION RUNS

During the conduct of the 1961 and 1963 NADC rain erosion tests, it became apparent to the Shrike personnel at NOTS that erosion testing would be necessary for their thin-wall radome. Increased temperature requirements were necessitating the selection of refractory materials in lieu of the plastics originally considered for this missile.

In mid-December 1962, a test was conducted by Alan Remell (NOTS) on two silicone-impregnated radomes (Reference 17). The left radome of Fig. 3-47 is the Shrike configuration. The right radome was fabricated from the same material but was 0.060-in. thick, as compared to 0.080 in. on the Shrike radome, and had a 16.00-in. radius of curvature. Figure 3-48 illustrates the damage encountered by these radomes while passing through the SNORT rain field with a peak velocity of 2565 ft/sec. Examination of the synchro-ballistic photos revealed that the right radome failed in the second half of the rain field. It was concluded that failure was caused by insufficient strength of this design and not erosion. The left radome experienced most of its erosion over the first 3 in. of the tip area. It should be noted that this particular radome had a solid phenolic tip.

The following five runs were conducted by this same group between September and November 1963 on radomes of the Shrike configuration (see Reference 18). The characteristics of the radomes and the results of these tests are given in Table 3-3.

### 3-4.3 SANDIA TESTS

Concurrent with the NADC series of tests, the Sandia Corporation was also conducting a program to study the effects of rain impingement at supersonic velocities (Reference 19). The purpose of these tests was to provide quantitative data that could correlate erosion, velocity, and time for three radome materials.

As mentioned earlier, the 35,000-ft track at Holloman Air Force Base, with its associated 6000-ft artificial rain field, was used to conduct these runs. A two-stage monorail sled was used to sustain a desired velocity within the rain field. These tests were performed at nominal velocities of 1100, 1600, 2000 and 2400 ft/sec.



**Figure 3-48. Shrike Configuration Radome (Left) Survived Environment but Showed Heavy Tip Erosion. Radome on Right Failed in Second Half of Rain Field**

It should be noted that the standard shape referred to throughout this series of tests is a radome with a 6.5-in. length, a 7.5-in. base diameter, and a 2.35-in. radius spherical nose.

Figure 3-49 is a composite photo taken at 1000-ft intervals during run No. 10. The display illustrates the erosion experienced by an epoxy fiberglass material contoured to a standard shape, and subjected to a rain environment at velocities of 1860 and 2400 ft/sec (see Reference 20).

Table 3-4 is a compilation of the data obtained during the period of October 1961 through March 1963.

Figures 3-50 and 3-51 were taken after completion of the runs at the indicated velocities. Both the initial erosion time and penetration time are taken from the high-speed photographs made during the experiments. These data are then plotted for a given material and presented in the form illustrated in Fig. 3-52.

### 3-4.4 SUMMARY OF SLED TESTS

The information presented in the previous paragraphs indicates that plastic and thin-walled ceramic radomes do not meet the typical rain specification at velocities of 2500 ft/sec and greater. Where the weight requirement permits, half-wave ceramic radomes (through the Ku band) will survive the maximum available sled velocities. The failure point for such radomes has not yet been reached because of test velocity limitations.

Silica, which because of its lower density is usable in thicker configurations, has proven interesting because of its tendency to erode rather than fail because of catastrophic impact (Reference 21). High-purity alumina has demonstrated the greatest resistance to impact failure.

As expected, all data have verified that a pointed shape minimizes the effects of rain impingement. When electrically tolerable and economically feasible, a pointed radome should be selected if rain erosion is a design consideration.

Obviously, the rain requirement for a high-altitude operational vehicle is considerably less than that of an air-to-ground missile. For the most part, water droplets are non-existent at altitudes greater than 3500 ft. A study made at NADC early in the Eagle Missile Program (air-to-air; Mach 4.5; typical flight profile in the 60,000- to 80,000-ft altitude) showed that the

probability of encountering the specified rain environment in many of the fleet theatres of operation was typically one in a thousand. Why then should the entire radome design be penalized in view of such a low probability? Thus, it is of the utmost importance that the systems designers state realistically the rain environment that is to be encountered by their particular radome.

It would be ideal to provide a correlation between erosion, velocity, time, and material properties. Accumulation of rain erosion data is extremely expensive and somewhat haphazard. To date, there has been no attempt to correlate available information. Such a correlation would greatly enhance the possibility of replacing sled tests with a less expensive and more reliable simulation technique.

TABLE 3-3 SUMMARY OF RADOME RAIN EROSION EXPERIMENTS AT NAVAL ORDNANCE TEST STATION

Run No.	Radome Material and Remarks	Entrance Velocity (ft/sec)	Exit Velocity (ft/sec)
1	Silicone-impregnated fiberglass (0.090 in.) with a 6 in. long cap of alumina (0.010 in.). This radome survived the run but received a hole through the tip. Silicone-impregnated fiberglass (0.090 in.) with a phenolic plug in the nose (already flown for 5 min. through natural rain by an A4C aircraft). The radome broke prior to the midpoint in the rain field.	2100	2950
2	9-in. long Pyrocera radome tapered from 0.060 in. in the frontal area to 0.100 in. at the base. (The tip was 0.218 in.) The radome broke during the run. Two-layer alumina radome. Dense outer skin of 0.025 in. and lightweight inner layer of 0.070 in. (7 in. long). The radome broke during the run.	2200	3000
3	Silicone-impregnated fiberglass (0.090 in.) with an 0.010-in. alumina cap. This radome failed in the second half of the rain field. An epoxy-impregnated fiberglass with a 6-in. cap of alumina, which tapers from 0.040 in. in the tip to 0.010 in. The radome survived with the ceramic tip removed, and some erosion of substrate.	2175	3030
4	Identical to first radome of run No. 2 except that the taper is 0.082 in. to 0.100 in. This radome broke 700 ft after the rain field. Epoxy-impregnated fiberglass with a 6-in. cap of alumina, which tapers from 0.020 in. in the tip to 0.010 in. The radome survived with the coating removed, and some erosion of substrate. (It is believed that failure was caused by a mounting ring that broke loose and wedged itself forward in the dome area.)	2230	2970
5	Two-layer dome of alumina with a dense outer skin of 0.040 in. and a lightweight inner layer of 0.040 in. The radome was undamaged and there was no evidence of erosion. Two-layer dome of alumina with a dense outer skin of 0.020 in. and a lightweight inner layer of 0.110 in. This radome broke just prior to the rain field exit.	2230	3000



### 3-5 THERMAL SHOCK TESTING

#### 3-5.1 INTRODUCTION

The discussion of environmental testing of radomes should include at least a summary of

some of the techniques and limitations of the many methods of thermal shock simulation.

Because of the different methods used for thermal shock testing, the following paragraphs will consider them according to their primary method of heat transfer and will classify them



Figure 3-49. Synchro-Ballistic Photos of AEC-Sandia Epoxy Fiberglass Radome During Run No. 10

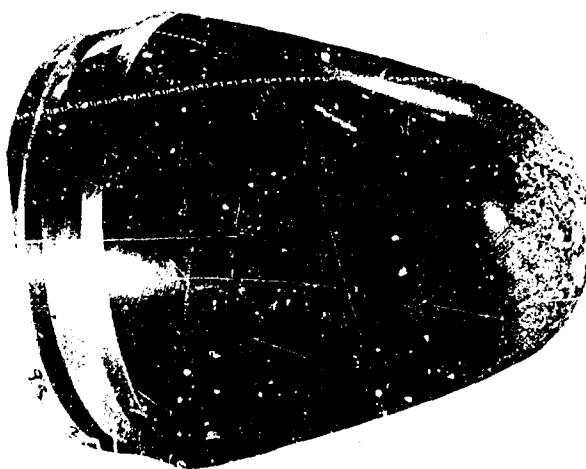


Figure 3-50. Standard Epoxy Fiberglass Radome After One Exposure to Rain Facility at 1100 ft/sec, Sandia Run No. 4



Figure 3-51. Standard Epoxy Fiberglass Radome After One Exposure to Rain Facility at 1600 ft/sec, Sandia Run No. 5

TABLE 3-4 SUMMARY OF RADOME RAIN EROSION EXPERIMENTS BY SANDIA CORP.

Run No.	Test No.	Date	Nominal Speed (ft/sec)	Radome Material and Remarks
1	RM85E	Oct. 3, 1961	2000	Epoxy fiberglass, standard shape, checkout run.
2	RM86E	Oct. 26, 1961	2000	Sled checkout run.
3	RM63E	Nov. 15, 1961	1100	Neoprene-covered epoxy fiberglass, standard shape.
4	RM64E	Nov. 16, 1961	1100	Epoxy fiberglass, standard shape.
5	RM66E	Nov. 16, 1961	1600	Epoxy fiberglass, standard shape.
6	RM67E	Nov. 16, 1961	1600	Epoxy fiberglass, standard shape.
7	RM68E	Nov. 17, 1961	2000	Neoprene-covered epoxy fiberglass, standard shape.
8	RM69E	Nov. 17, 1961	2000	Epoxy fiberglass, standard shape.
9	RM77E	Nov. 29, 1961	2800	Classified antenna experiment.
10	RM78E	Nov. 29, 1961	2400	Epoxy fiberglass, standard shape.
11	RM89E	Apr. 27, 1962	2800	Sled-vibration damper checkout.
12	RM90E	May 11, 1962	2000	Phenolic chopped fiberglass, defective rocket.
13	RM87E	May 18, 1962	2400	Phenolic chopped fiberglass, sample lost.
14	RM88E	June 18, 1962	2000	Phenolic chopped fiberglass, repeat of RM90E.
15	RM70E	June 29, 1962	2000	Ceramic, standard shape.
16	RM71E	July 6, 1962	2000	Ceramic, same cone as RM70E.
17	PM72E	July 20, 1962	2000	Ceramic, same cone as RM70E and RM71E.
18	RM79E	July 27, 1962	2400	Ceramic, standard shape, broken in 1500 to 2000 ft.
19	RM91E	Aug. 31, 1962	2400	Phenolic chopped fiberglass, ceramic-tipped ogive
20	RM92E	Sept. 14, 1962	2400	Ceramic, standard shape, dry run, no breakage.
21	RM93E	Sept. 28, 1962	2400	Ceramic, standard shape, broke at 1360 ft.
22	RM94E	Oct. 26, 1962	2000	Phenolic, ceramic capped, standard shape.
23	RM95E	Dec. 14, 1962	2000	Phenolic chopped fiberglass with 0.030-in. neoprene coating, standard shape.
24	RM96E	Jan. 18, 1963	2400	Ceramic, ogive shape, no breakage.
25	RM97E	Feb. 1, 1963	2400	Ceramic, ogive shape, broke after leaving rain field.
26	RM98E	Feb. 1, 1963	2000	Ceramic, standard shape, broke at 400 ft.
27	RM99E	Mar. 1, 1963	2200	Ceramic, ogive shape, defective rocket motor.
28	RM100E	Mar. 29, 1963	2200	Ceramic, ogive shape, no breakage.
29	RM101E	Mar. 29, 1963	2200	Cone-sample experiment.

as hot gas, hot liquid bath, and electrical heating, which represent convective, conductive, and radiative heat transfer, respectively. Each method has its own advantages and disadvantages in providing a realistic single-side thermal simulation of the true environment.

These methods encompass a wide range of facility and item tested costs, and available heat flux. Certain methods may provide a good prototype proof test, but be too expensive as a quality control acceptance test. Other methods can be programmed to give a true simulation of thermal stress distribution, but possibly at material temperatures somewhat different from that of the true flight environment. Selection of a test method must, therefore, be made only after considering the reliability required, availability of test facilities, and the time and money available for testing. The radome material should also be considered to determine whether a single proof testing or a production acceptance testing of every radome is required.

Paragraph 1-1.5 considers the analysis of the thermal shock environment and the ideal behavior of the radome in this environment. It would be highly desirable for this paragraph to relate thermal shock testing directly to the analytical work. It is regrettable, however, that thermal shock testing has been carried out almost universally on an empirical basis. Therefore, the following paragraphs will briefly describe the various methods in current use, leaving the designer to choose the method that best satisfies his thermal, mechanical, size, and economic requirements.

At present, the Air Force is sponsoring a project at the Georgia Institute of Technology to compile a Designer's Manual of Ceramic Materials. It will correlate existing thermal shock case histories with predicted behavior according to current thermal shock theory. The project was carried out under Contract No. AF 38 (615)-1308.

### 3-5.2 CONVECTIVE HEAT TRANSFER

Convection is the primary mechanism of heat transfer provided by hot-gas generators. As a class, hot-gas generators are the most widely used thermal shock test devices. The following types of hot-gas generators are discussed in the order of increasing heat transfer rates that are normally provided by the device.

#### 3-5.2.1 The Hot Flue

The hot flue presents the least severe thermal shock environment. Although the temperatures available may easily reach 3000°F, the relatively low velocity provides for low heat transfer rates. This method, described in Reference 22, was one of the first techniques used for radomes because of its simplicity and availability in the glass, ceramic, and other industries. The test item is exposed to the exhaust gases of a flue or chimney at a point in the system where temperatures can be measured and the exposure time generally is determined by a total heat flux or by the peak temperature and time experienced by the nose of the body. It is difficult to achieve an approximate distribution of heat rise with time or flux distribution along the body surface. The method must be considered as crude when compared with more sophisticated but expensive methods.

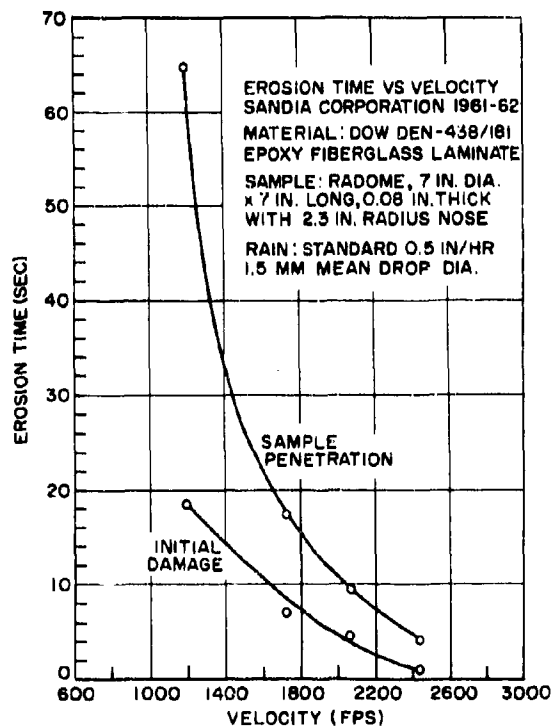


Figure 3-52. Supersonic Radome Rain Erosion  
Graph of Erosion Time vs Velocity

### 3-5.2.2 The Supersonic Wind Tunnel

Many radomes have been tested in large test section supersonic tunnels when no better methods were available. Tunnels suitable for this type of testing usually require large test sections to test full-scale, continuous-operation, and fairly high test section pressures. Unlike most other methods, it produces true boundary layer conditions and dynamic pressures, along with heating.

In simulating a given flight temperature profile, certain factors should be recognized about wind tunnel testing. The model usually starts from room temperature in a closed test section. When the bypass valve to the test section is opened, a normal shock front passes rapidly through the throat, past the model, and downstream into the diffuser section. This induces, essentially, a step rise from zero velocity to the design Mach number of the nozzle blocks being used. This results in an attendant step rise to a high heat flux. If the back face or inside surface of the test radome is at room temperature at starting time, the wall temperature difference and, therefore, thermal stress may exceed flight conditions. For some simulations, this condition may be partly alleviated with programmed internal heating. For certain types of trajectories, the radome wall will experience a brief period during which the true thermal stress will be experienced before reaching equilibrium.

There is a very limited number of tunnel facilities where this type of testing would be permitted for brittle material radomes. Unless the facility has special provisions for capturing broken particles, severe damage may result in the diffuser section, turning vanes, or in the low-velocity return section.

### 3-5.2.3 The Hot-Gas Wind Tunnel

Several facilities incorporate hot gases in wind tunnels. These hot gases may be the products of combustion from a burner, air heated through some type of heat exchanger, or a combination of both. One such wind tunnel using combustion products was used to simulate aerodynamic heating on alumina radomes (Reference 23). Several such tunnels are available at OAL, Daingerfield, Texas (Reference 24).

### 3-5.2.4 Jet Engine Exhaust

Many manufacturers and government agencies have ready access to aircraft turbojet engines mounted on static test stands. Exhaust gas distribution characteristics are usually well established. These include velocity, temperature, and pressure surveys at incremental distances from the nozzle centerline for a series of stations behind the nozzle base and for a fixed engine speed. Afterburners are used to increase the range of temperatures and velocities obtainable with such engines.

In studying such a distribution, the radome tester may find an engine power setting and distance from the jet that approaches the missile flight environment needed. If the test model is on a movable mount, such that the station is varied with time, this method is quite flexible. Engine speed variation with time, combined with location change with time, will extend the potential even further. Ramjet engines are also used for testing when higher temperatures and heat fluxes are required.

Jet engine exhausts typically attain temperatures in the 1000°F to 3000°F range over a wide range of distances from the axis and aft of the nozzle. One difficulty with turbojet engines is the swirling action produced by the turbine. This should be considered when designing the test fixture for holding the radome.

### 3-5.2.5 Oxypropane Burners

With one or a number of propane burners, it is possible to provide a wide range of heat fluxes from low values (10 Btu/ft<sup>2</sup>-sec) up to those expected for orbital reentry (100-200 Btu/ft<sup>2</sup>-sec). Thus, it is possible to test small specimens or large models using this system. The X-20 nose cap model was reported as successfully tested using multiple propane burners (Reference 25). The reentry trajectory was simulated by programming the distance from the model to the burners to provide the desired heat flux-time relationship. This facility used 30 oxypropane torches to provide the desired heat flux.

### 3-5.2.6 Oxyacetylene Burners

One of the most commonly used test setups

uses single or multiple arrangements of a conventional welding torch. This equipment is generally available, is well understood, and can always be used when the more elaborate techniques are not available.

This method can produce a heat flux from 100 to 1000 Btu/ft<sup>2</sup>-sec, depending upon nozzle spacing, distance to the specimen, and gas pressures used in the burners. As done with the propane burner, the test specimen may be moved in and out of the flame or gas pressures may be programmed to extend simulation versatility. These burners are particularly useful when temperatures from 4000°F to 5000°F are required (Reference 26).

### 3-5.2.7 Oxyhydrogen Burners

The oxyhydrogen burner, as the oxyacetylene burner, has recently become a very useful tool for nose cone testing. Heat fluxes in excess of 800 Btu/ft<sup>2</sup>-sec are easily achieved. This stagnation heating rate is comparable to approximately 6000 ft/sec at sea level or about 10,000 ft/sec at a 100,000-ft altitude. The respective equilibrium stagnation temperatures would be 2600°F and 4000°F. This type of facility has proven adequate for meeting the requirements of most current reentry testing. Reentry simulation for the Apollo radome was carried out

with such a system, as noted in Reference 27.

Water-cooled, multiple-flame burner units are available and may be arranged to surround any body shape. The simplest arrangement uses one, four, or possibly nine units surrounding the stagnation region of the test body. A water-cooled shroud can be built around the body and shaped to control the flame or longitudinal flux distribution. The test radome may also be mounted off the shroud, cam driven into the shroud at a planned rate, and withdrawn to closely simulate a trajectory profile. Very-thin-wall shells of the same configuration and made from a high-temperature, high-thermal-conductivity material may be used as calibration models. The calibration model requires the installation of high-response high-temperature thermocouples on the inner surface of the thin shell model. With control of the shroud shape, model insertion rate, and burner pressure, a close approximation to the true thermal distribution is effected.

An elaborate oxyhydrogen furnace comprising some 600 burner units has been constructed by the Lockheed Missiles and Space Company for the Navy. This furnace, shown in Fig. 3-53, can test models up to 2 ft in diameter and 3 ft in length. It represents a very large initial cost, high operating costs, and could be hazardous in its operation. In operation, a remote control

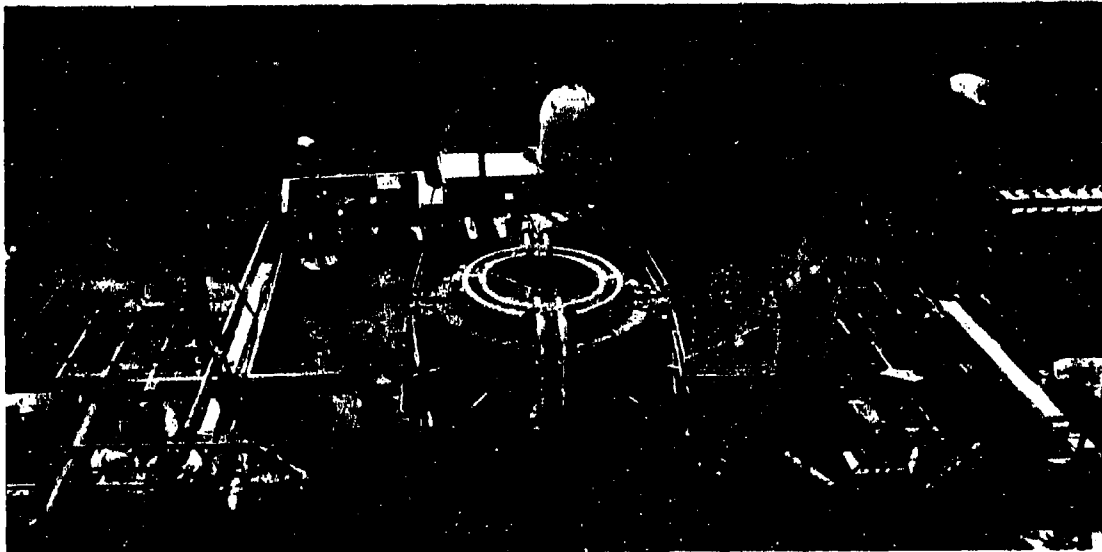
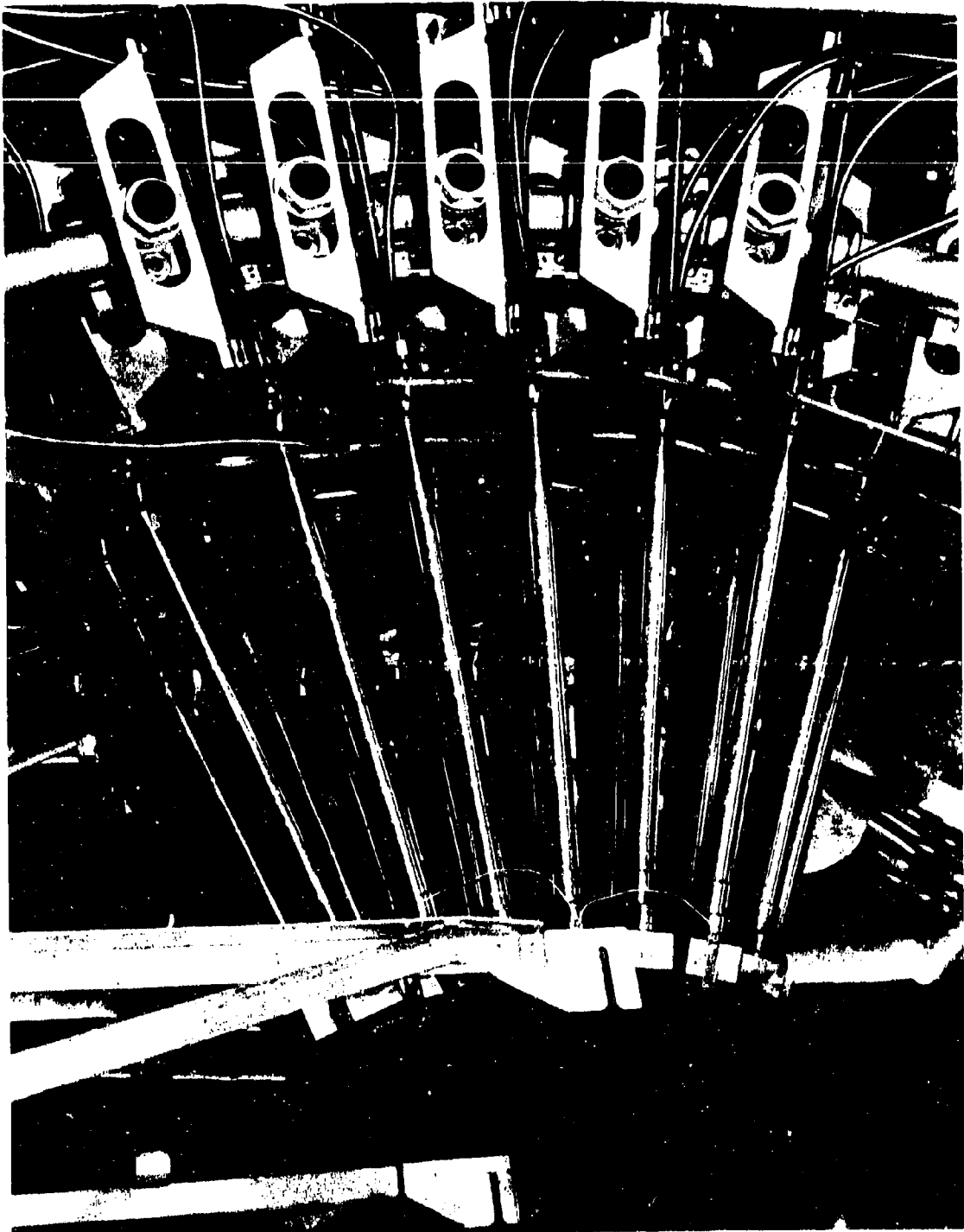


Figure 3-53. 600-Burner Oxyhydrogen Thermal Test Facility



*Figure 3-54. Water-Cooled Oxyhydrogen Burners in Thermal Test Facility*

television monitoring system is used. Figure 3-51 shows a group of the water-cooled burner units with provision for adjustment of spacing between the test body surface and the burner faces. Figure 3-55 shows the furnace in operation.

#### 3-5.2.8 Rocket Motor Exhausts

Rocket motor exhausts do not necessarily provide higher heat transfer rates than the three chemical burners just discussed, but they do provide the highest degree of mechanical shear and vibration of any burner system in use. Also, because of their availability from missile and space propulsion systems, they may be used to simulate reentry thermal shock on large shapes. An 18,000-lb thrust rocket motor was used in such a program at Huntsville, Alabama (Reference 28). A small oxyhydrogen rocket motor has been used for several years at Georgia Tech for

measuring ablation rates of ceramic materials (Reference 29). A similar motor is used at NOL, Silver Spring, Maryland, for studying the ablation of organic materials.

#### 3-5.2.9 Plasma Jets

During the past few years, plasma jets have come into wide use for screening reentry materials. Heat fluxes of the order of 1000 to 2000 Btu/ft<sup>2</sup>-sec are easily obtainable. However, the high costs associated with these devices have limited the average laboratory to small units. The average unit usually ranges from 50 to a few hundred kilowatts. This limits the general use of plasma jets to the evaluation of test specimens of the order of 0.5 to 1 in. in diameter.

The plasma jet offers several advantages over the other systems discussed in the previous paragraphs. The hot-gas products may be tailored to simulate the composition as well as the

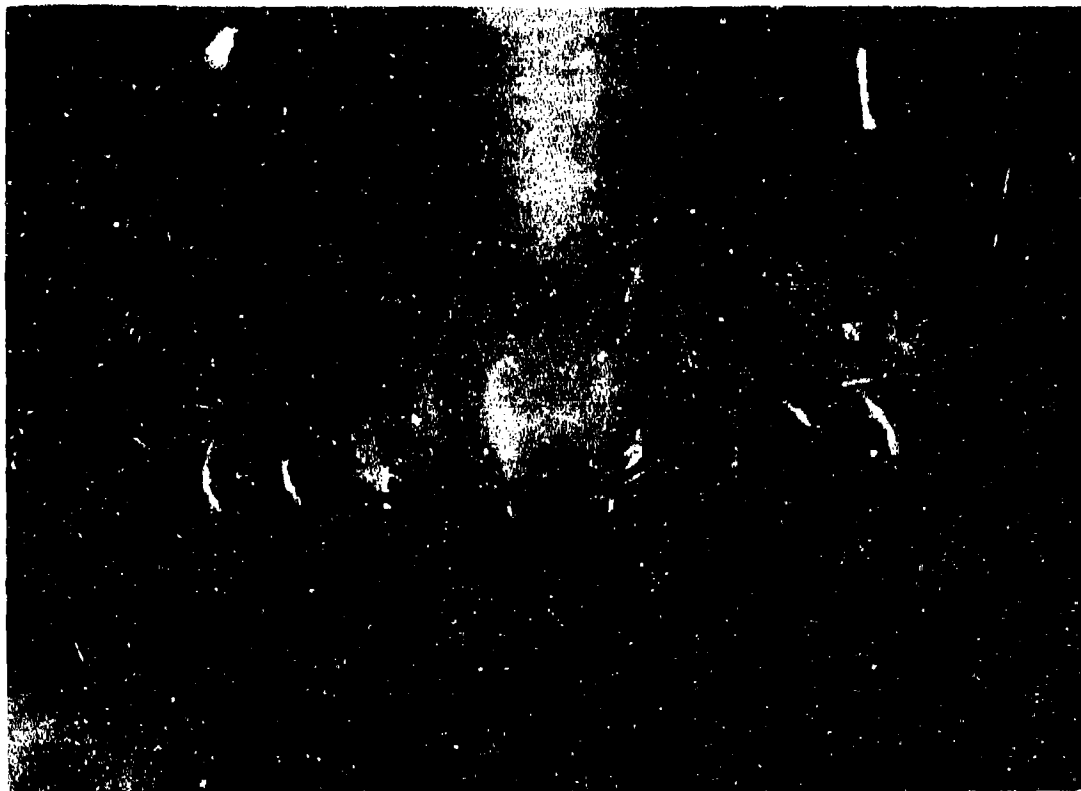


Figure 3-55. Oxyhydrogen Thermal Test Facility in Operation

temperature of the environment anticipated from aerodynamic heating over a rather wide range of altitudes and velocities. Plasma jets may also be incorporated into low-pressure tunnels to obtain supersonic flow. These attractive features have encouraged a few companies to build relatively large plasma jet wind tunnel facilities. These facilities range from one to several megawatts in power consumption. Avco, CTL Division of Studebaker, Plasmadyne Division of Gianini Scientific Corporation, and Thermal Dynamics are some of the companies that have large-scale plasma jet facilities for use and/or sale.

### 3-5.3 CONDUCTIVE HEAT TRANSFER

Hot molten baths are used when very high heat transfer rates are desired at relatively low temperatures. The primary method of heat transfer provided by such baths is conduction. Two general types of baths are used for ceramic radomes: the hot salt bath and the hot metal bath.

#### 3-5.3.1 The Hot Salt Bath\*

This method has been used extensively for production acceptance testing of ceramic radomes. Both the initial cost and unit testing price are relatively low. Any high boiling point salt solution may be used that is not injurious to the bath hardware or the material being tested. For example, fused silica should not be tested in a hot salt bath, since the molten salt will react with silica and promote devitrification. Hot salt baths may be operated with the fluid at 1000°F or higher.

A typical salt bath consists of a large tank, generally of stainless steel, immersion heaters, a circulator pump, and some mechanical or hydraulic external system that holds the test body and plunges it into the bath at a given velocity. A more realistic simulation of heat distribution over the body is accomplished if the radome is plunged into an open-ended shroud ring having a pump impeller mounted at the entrance. The shroud expansion can be adjusted to suit the

radome shape and the pump speed can be varied to control the heat transfer to the body.

Thin wall stainless steel models are generally thermocoupled on the inner surface and immersed with varying entry speeds, pump mass flow, bath temperature, and shroud shape until the proper operating conditions are determined for the best simulation of thermal stress with time and body station.

#### 3-5.3.2 The Molten Metal Bath

Liquid metals can be used and operated like the hot salt bath. Babbitt has been most commonly used. Molten iron has been used to thermal-shock fused silica. Other metals may be used, but the complexity of the system increases with the melting point of the metal, particularly above 2000°F.

### 3-5.4 RADIATIVE HEAT TRANSFER

Since the development of quartz lamps, particularly those with filaments capable of power as high as 500 watts/in., quartz lamp heating has become a very useful test method. It can produce precision heating rates for programmed heating cycles with its rapid energy output and high radiant efficiency. Figure 3-56 shows a radome covered with poster paint black in place and ready for thermal shock testing with a quartz lamp clamshell heater at General Dynamics, Pomona. (See Paragraph 3-5.7.3.)

Tungsten filaments in an argon atmosphere are enclosed by small-diameter quartz tubing. At rated voltage, the 4000°F tungsten filaments act as infrared emitters, which reach 90% of their operating temperature within 3 or 4 sec. Their radiant efficiency is rated at 88% and they can operate in any type of atmosphere.

These lamps are available in standard straight lengths ranging from 5 to 25 in. or may be purchased in other shapes on special order. Standard ratings are 100, 200 and 360 watts/in. at 240 volts. They may be operated at 480 volts with reduced life and almost double the radiated power.

Reflectors are generally used and are commercially available, although special reflectors are often designed to best suit a given test shape. Good reflectors reradiate some 70% of the incident energy, but require either air or

\* See Paragraph 1-4.3.



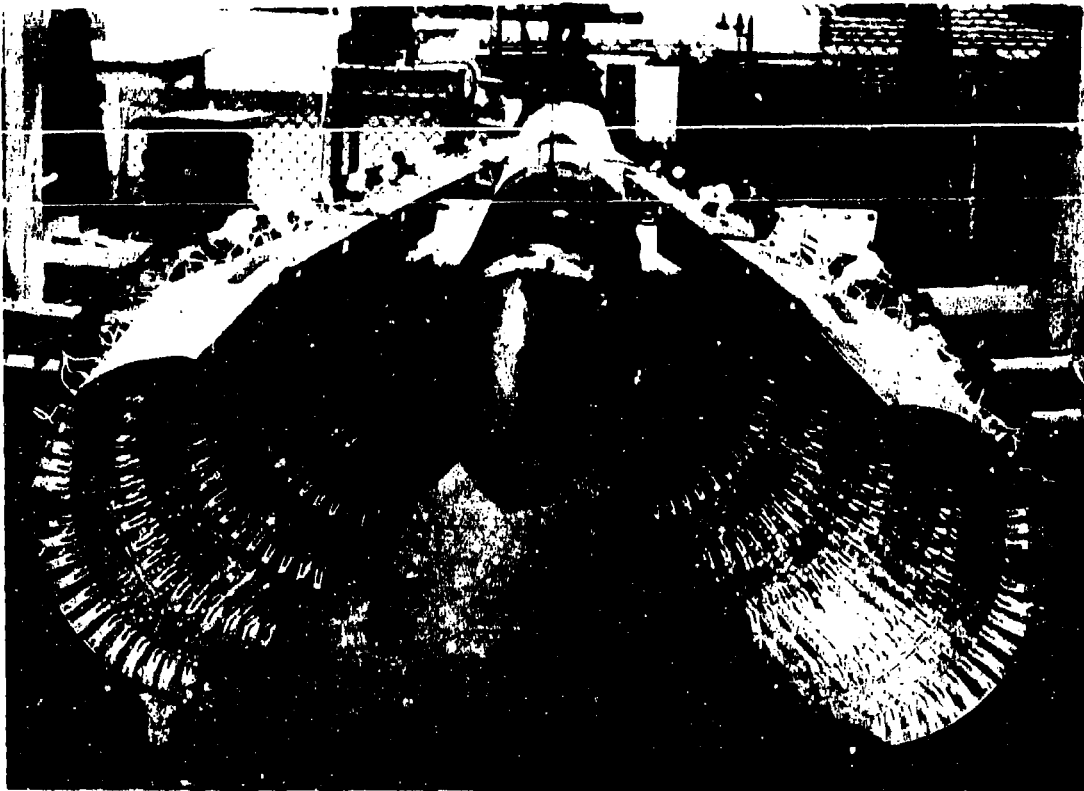


**Figure 3-56 General Dynamics/Pomona Infrared High-Temperature Test Facility**

water cooling when operated longer than a few seconds.

When the lamps are operated at overload voltage with an efficient reflector system, a heat flux of 200 Btu/ft<sup>2</sup>-sec is attainable. This is sufficient for most interceptor missile types, all sustained flight vehicles, and some reentry cases.

To test large radomes, the required electrical power becomes a significant factor. At overload rating, the 360-watts/in. lamp requires 0.75 kw/in.<sup>2</sup> if the tubes are spaced 1 in. apart, or about 1.0 kw/in.<sup>2</sup> for the same spacing and 70% reflector efficiency. An available 1000 kva continuous power should be capable of heating 6 ft<sup>2</sup> of surface area at 200 Btu/ft<sup>2</sup>-sec.

Automatic control of power to the lamps for temperature-time-station simulation requires a host of transformers, reactors, switch gears, programmers, and controllers. When combined with the necessary data-recording equipment,

the cost of a 1000-kva installation might exceed \$100,000.

One of the attractive features of radiant heating with quartz lamps is the absence of hot gases. Therefore, they provide the cleanest form of heat, both chemically and electrically. Also, as pointed out, they can be operated in almost any environment. Raytheon and General Dynamics/Pomona are among the radome users who have carried out boresight measurements on radomes heated in this manner. Figure 3-57 shows a test setup at the General Dynamics/Pomona boresight range, using the quartz lamp clamshell heater to determine boresight shift as a function of radome heating. Since it was not possible to get measurements with the heater in place, the Pyroceram radome was boresighted cold; the heaters were then swung in place to heat the radome to a given temperature. After heating the radome, the clamshell was swung

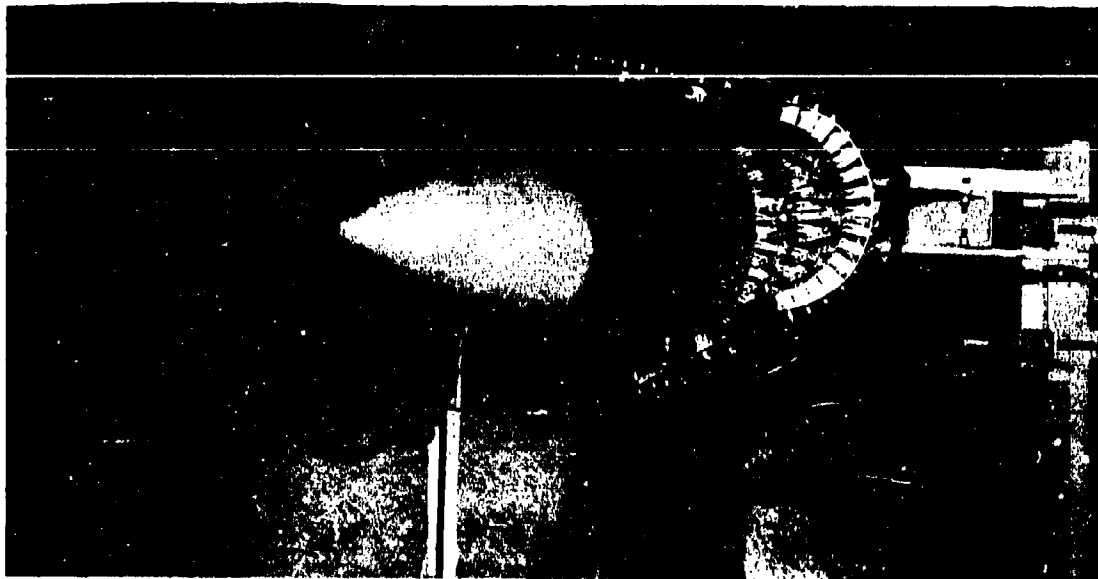


**Figure 3-57. High Temperature Boresight Test Setup at General Dynamics/Pomona**

away and boresight was recorded as a function of time and change in temperature. The boresight shift was very small. Reference 30 reports the use of quartz lamps to heat dielectric panels while their electrical characteristics were being measured (Paragraph 5-5.1).

Quartz lamps have also been used to evaluate the combined structural-thermal performance of radomes. Figure 3-58 shows such a test setup at General Dynamics/Pomona. This setup can be used to simulate flight temperature gradients while the radome is mechanically stressed to simulate aerodynamic and maneuvering loads. In this test, considerable preparation was necessary to program the power as a function of time to produce the desired gradients in temperature in both the radome and mounting ring.

### **3-5.5 EVALUATING THERMAL SHOCK TEST DATA**

The value of any thermal shock test data is dependent on the degree with which numerous environmental, material, and test conditions are known and controlled. The more important ones are

1. Environmental test conditions
  - a. Gas velocity

- b. Gas enthalpy
  - c. Gas composition
  - d. Gas temperature
  - e. Mass flow rate
2. Test specimen conditions
  - a. Configuration
  - b. Size
  - c. Thickness
  - d. Homogeneity
  - e. Surface condition (scratches, flaws, etc.)
  - f. Stress condition (residual stresses, stresses in attachment area, etc.)
  - g. Physical and mechanical properties
  - h. Thermal properties (thermal diffusivity, emittance, etc.)
3. Reproducibility of test conditions from run to run
4. Reproducibility between test specimens supplied by one manufacturer and between specimens supplied by different manufacturers
5. Method of attaching test specimen to holding device
6. Instrumentation

There are no thermal shock test data available

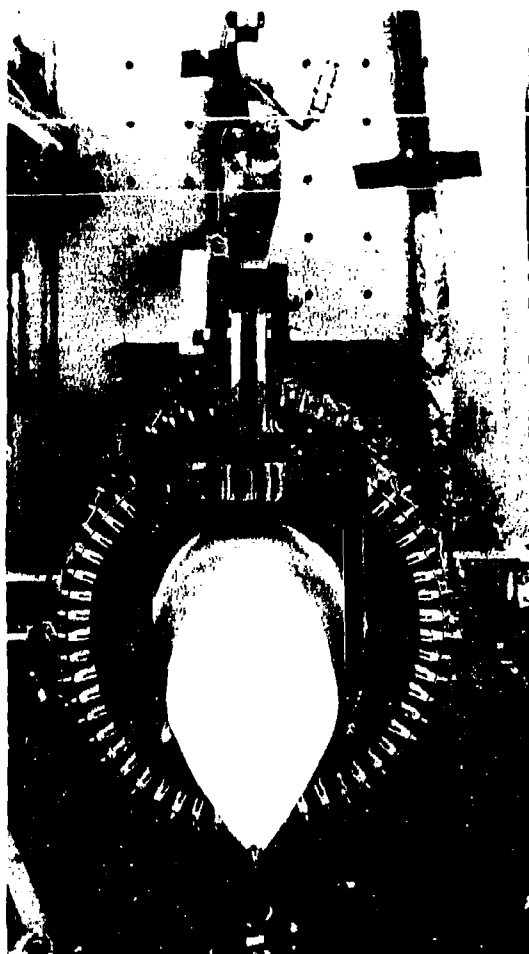


**Figure 3-58. High Temperature Structural Test Setup at General Dynamics/Pomona**

for which all of the above conditions are adequately known, controlled, and reported. However, even if all the conditions were met, there is the overriding fact that data describing the actual flight environment under hypersonic conditions are not known precisely. Also, the interactions between the hypersonic flight environment and ceramic materials of interest to the radome designer are not rigorously defined.

Flight data for ceramic materials under these conditions are essentially nonexistent. This is due in part to the lack of telemetered data during reentry or other hypersonic flight trajectories and to the lack of electromagnetic window materials to allow obtaining these data. Thus,

the development of radomes capable of performing under these conditions will not only satisfy the requirement for future hypersonic missile systems, but will also allow the attainment of critically needed flight environment data so necessary to the optimum development of such missiles.

As pointed out, the methods for thermal shock testing are many and varied; not only in the primary methods of heat transfer, but also varied in the degree of thermal shock provided. Therefore, before thermal shock test results are presented, the designer should be cautioned as to the interpretation and use of such data.

It is not always appreciated that the thermal shock resistance of a material is dependent not only upon the physical and mechanical properties of the material, but also upon the severity of the thermal shock environment. The severity of the environment is not a function of the temperature, but rather the heat transfer rate to the material. This relationship can be illustrated by considering air and water at 200°F. Obviously, the heat transfer rate is much higher in the water than in the air. This difference would be evident by placing an ice cube into each environment. Although each environment is at the same temperature, the heat transfer rate is different.

In Paragraphs 1-1.5.5 and 6-3.4, it is pointed out that the thermal shock resistance of a material depends as much upon the properties of the particular thermal shock environment as upon the properties of the material. In Fig. 1-22, the predicted thermal shock resistance of nine possible radome materials are plotted as a function of the thermal shock environment. All nine materials change in their order of merit as the environment changes. For example, beryllia should be the best material under low heat transfer rates, but it is rated as eighth at the high heat transfer rates predicted to be associated with hypersonic flight. According to these data, alumina should be more thermal shock resistant than Pyroceram at low heat transfer rates. The reverse should be true at high heat transfer rates. At the highest heat transfer rates shown, slip-cast fused silica should be an order of magnitude better than the next best material, Pyroceram.

### 3-5.6 CHOICE OF THERMAL SHOCK TEST FACILITIES

Since the exact thermal shock environment cannot be simulated with any of the facilities described, the value of thermal shock testing might be questioned. However, there are useful purposes for which such testing is usually carried out, such as:

1. Screening new materials and new fabrication techniques
2. Evaluating a particular radome shape or system in simulated hypersonic environment
3. Obtaining data on thermal response for production radomes
4. Quality control or proof testing

The following presentation of typical thermal shock test data, obtained for each of the purposes described, will help in assessing the value of such data.

### 3-5.7 RESULTS OF SELECTED THERMAL SHOCK TESTS

#### 3-5.7.1 Screening Tests

Small, laboratory-size gaseous and plasma jet torches are the most frequently used test devices for screening possible radome materials for thermal shock resistance.

The value of screening tests to the materials engineer has been the subject of discussion and study by the Refractory Composites Working Group (Reference 31). The Working Group was set up to recommend standard test conditions using an arc plasma jet that might be reproduced between various facilities using standard reference materials for calibration purposes. Three heat flux levels were set up to represent mild, moderate, and severe thermal shock environments. Nominal cold-wall heat flux levels were 100, 300, and 500 Btu/ft<sup>2</sup>-sec. A standard specimen dimension of 2 in. × 2 in. × 0.5 in. was selected. However, the only ceramic radome material evaluated in this facility was slip-cast fused silica, which was selected as one of the standard materials to represent a monolithic, insulating, high-temperature, oxidation-resistant material. Figure 3-59 shows the type of data obtained from this facility at the University of

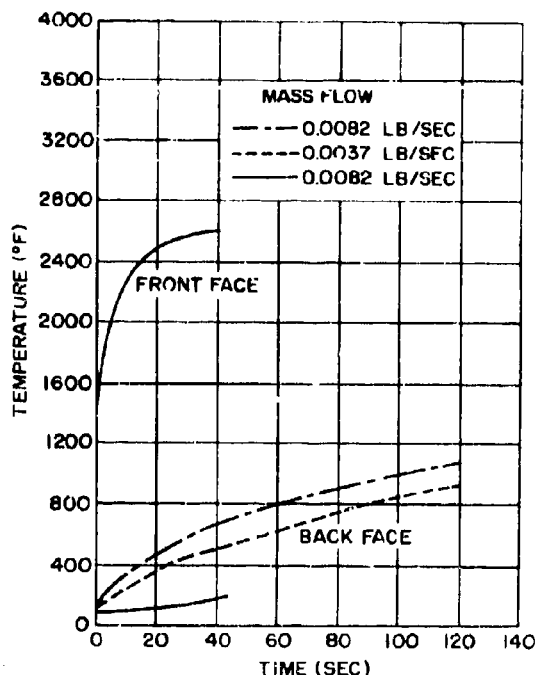


Figure 3-59. Temperature-Time History of Fused Silica Exposed to 300 Btu/sq ft-sec Heat Flux Environment

Dayton (Reference 32). It should be noted that the cold-wall heat flux for all three data curves was the same (300 Btu/ft<sup>2</sup>-sec). The difference in backside temperature is due to different frontside temperatures, as shown in Table 3-5. Similar data for 109- and 504-Btu/ft<sup>2</sup>-sec cold-wall heat flux are presented in Table 3-6.

A small oxyhydrogen rocket motor has been used at Georgia Tech for screening materials for radome, nose cone, and rocket nozzle applications. A typical setup for evaluating materials in the exhaust of this motor is shown in Fig. 3-60. The impingement angle of the exhaust on the sample can be varied from 45° to 90°. The sample-to-motor distance can be varied from 6 to 20 in. The cold-wall heat flux is shown as a function of distance from the nozzle for impingement angles of 45° and 90° in Fig. 3-61. The operational parameters for this motor are shown in Table 3-7.

To compare the thermal response of slip-cast fused silica, Pyroceram, and alumina, 0.25-in.

**TABLE 3-5 TEST CONDITIONS AND RESULTS FOR FUSED-SILICA SPECIMENS  
EXPOSED TO AN ARC PLASMA JET EFFLUENT**

Heat flux, Btu/ft <sup>2</sup> -sec	300	300	300
Gas enthalpy, Btu/lb	2340	2080	4000
Gas velocity, ft/sec	1030	750	730
Stagnation pressure, in. H <sub>2</sub> O	18.5	0.488	6.0
Gas temperature, °F	5670	5400	7800
Test duration, sec	120	40	120
Depth of erosion, in.	Nil	0.0100	Nil
Final Back Face Temperature, °F	1050	160	920
Final Front Face Temperature, °F	3120	2790	3600
Remarks	Mass Flow = 0.0082 lb/sec.	Mass Flow = 0.0082 lb/sec.	Mass Flow = 0.0037 lb/sec.

**TABLE 3-6 TEST CONDITIONS AND RESULTS FOR FUSED-SILICA SPECIMENS  
EXPOSED TO AN ARC PLASMA JET EFFLUENT**

Heat flux, Btu/ft <sup>2</sup> -sec	109	504
Gas enthalpy, Btu/lb	980	3750
Gas velocity, ft/sec	600	1870
Stagnation pressure, in. H <sub>2</sub> O	...	24.1
Gas temperature, °F	3150	7200
Test duration, sec	360	72
Depth of erosion, in.	0.003	0.029
Final Back Face Temperature, °F	330	310
Final Front Face Temperature, °F	...	...
Remarks	Very little effects were observed, except discol- oration of the surface.	Volume of specimen increased slightly after test. Evidence of a clear glassy phase on sur- face. Max. surface temp. > 3200°F (optical pyro.).

thick plates of all three materials were exposed to the exhaust of the oxyhydrogen rocket motor at a distance of 14 in. from the exit plane (Reference 33). This distance was selected because it was the closest distance at which Pyroceram and alumina could survive the thermal shock. The frontside temperature, backside temperature, and temperature difference between these two surfaces for all three materials are shown in Figs. 3-62 to 3-64.

The alumina specimen cracked after approximately 45 sec. Pyroceram failed in a similar manner when exposed to the rocket exhaust at a distance of 12 in. from the exit plane. Slip-cast fused silica has not been observed to thermal-shock at any distance. However, at a distance of 6 in., ablation occurs. The ablation rate at this point is approximately 0.001 in./sec.

Oxyacetylene and oxypropane torches provide similar data at similar cold-wall heat flux

conditions. However, because of the very low gas velocities of these facilities as compared with the rocket motor exhaust, the shear stresses on the surface of the test specimen are much less. Therefore, ablation rates are less for equivalent heat fluxes.

In addition to being more economical to operate, these facilities offer the advantages of being much safer and quieter and may be operated in the laboratory. Therefore, the oxyacetylene and oxypropane torches are very useful high-temperature heat sources for thermal property measurements of radome materials.

The oxyacetylene facility shown in Fig. 3-65 has been used at Georgia Tech to heat specimens for the purpose of obtaining emittance data. From optical pyrometer and radiation pyrometer data, effective emittance may be calculated using the method shown in Appendix 3A. The emittance data presented in Fig. 4-32 were obtained using this method. The Marquardt Corporation has used this method with oxyacety-

lene and oxypropane facilities to obtain emittance data (Reference 34).

### 3-5.7.2 Aerodynamic Heat Simulation

Reference 35 reports the results of a program that uses an ablative coating to reduce the thermal shock to an alumina radome. The aerodynamic heating conditions that were anticipated for the bare radome are shown in Fig. 3-66. The maximum temperature anticipated was of the order of 2800°F, which would be reached in approximately 120 sec. The maximum temperature differential ( $\Delta T$ ) of 174°F was considered sufficient to produce failure at a temperature of 1800°F and for a wall thickness of 0.25 in. Through the use of ablative coatings,  $\Delta T$  was determined to be 73°F during ablation and 131°F after ablation. These temperature gradients produced stresses of 12,200 psi and 24,360 psi, respectively, which represented  $\frac{1}{4}$  to  $\frac{2}{3}$  of the ultimate strength of the alumina used.



**Figure 3-60. Setup for Evaluating Ceramic Materials in Exhaust of Oxyhydrogen Rocket Motor**

**TABLE 3-7 OPERATIONAL DATA FOR  
OXYHYDROGEN ROCKET MOTOR**

<i>Motor</i>	
Fuel mixture ratio, $V_{H_2}:V_{O_2}$	4:1
Hydrogen flow rate, S.C.F.M.	36
Oxygen flow rate, S.C.F.M.	9
Chamber pressure, psia	275
<i>Exhaust gas at exit plane</i>	
Pressure, psia	15.1
Velocity, ft/sec	7966
Temperature, °R	3214
Stagnation temperature, °R	5400
Mach number	2.5

A model of the radome under consideration was coated with the ablative material for simulated environmental testing. The radome was approximately of 12-in. diameter and 40-in. length. The test facility used ramjet engine exhaust. The test conditions are shown in Table 3-8. The results were stated in Reference 36 as follows: "Upon ignition of the ram jet, the radome began to vibrate in the exhaust stream. Ablation of the coating began within 5 sec. The coating ablated, evenly exposing a small portion of the radome at the stagnation point. After approximately 15 sec of run time, a crack developed at the base of the radome. The radome then broke away from the mounting ring and fell intact, shattering immediately upon striking the bottom of the chamber. Ablation had proceeded to the shoulder of the radome nose. The test terminated at this point."

It should be emphasized that alumina would be expected to survive thermal shock only under

**TABLE 3-8 RAMJET TEST CONDITIONS FOR  
ALUMINA RADOME FLIGHT SIMULATION**

Total pressure, psia	30
Total exhaust temperature, °F	3000
Exhaust Mach number	2.24
Approximate exhaust velocity, ft/sec	5700
Run time, sec	27

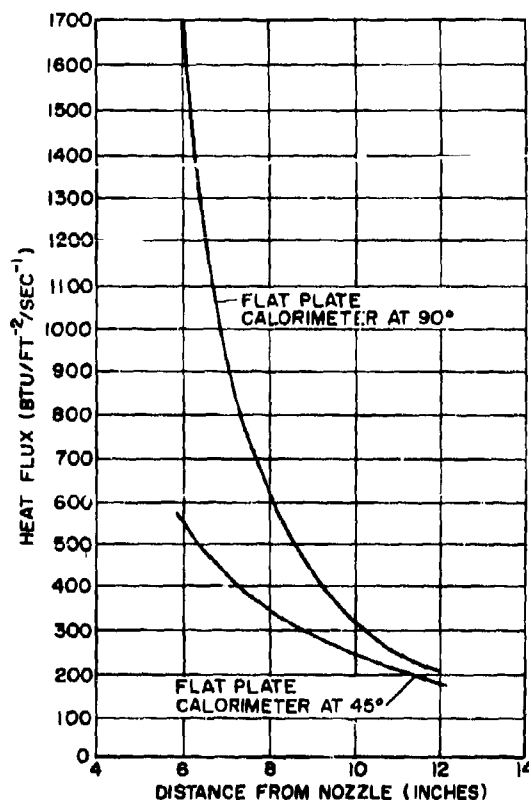


**Figure 3-61. Heat Flux of Exhaust of Oxyhydrogen Rocket Motor**

conditions that allow a very minimum temperature differential between the frontside and backside of the radome. It would be safe to say that this temperature should be less than 300°F for the 0.25-in. wall. One way of reducing this gradient would be to make the wall thickness as thin as possible.

During one phase of a project to evaluate slip-cast fused silica for nose cone applications, a slip-cast nose cone model 25 in. high, 19 in. in diameter at the base, and 0.75 in. thick was exposed to the exhaust of an 18,000-lb thrust rocket motor (see Reference 36). This nose cone model was mounted like a radome, as shown in Fig. 3-67, at a distance of 30 in. from the exit plane, as shown in Fig. 3-68. The conditions provided by this rocket motor were:

Exit velocity, ft/sec	6790
Exhaust gas temp., °F	3920
Exposure time, sec	17.16

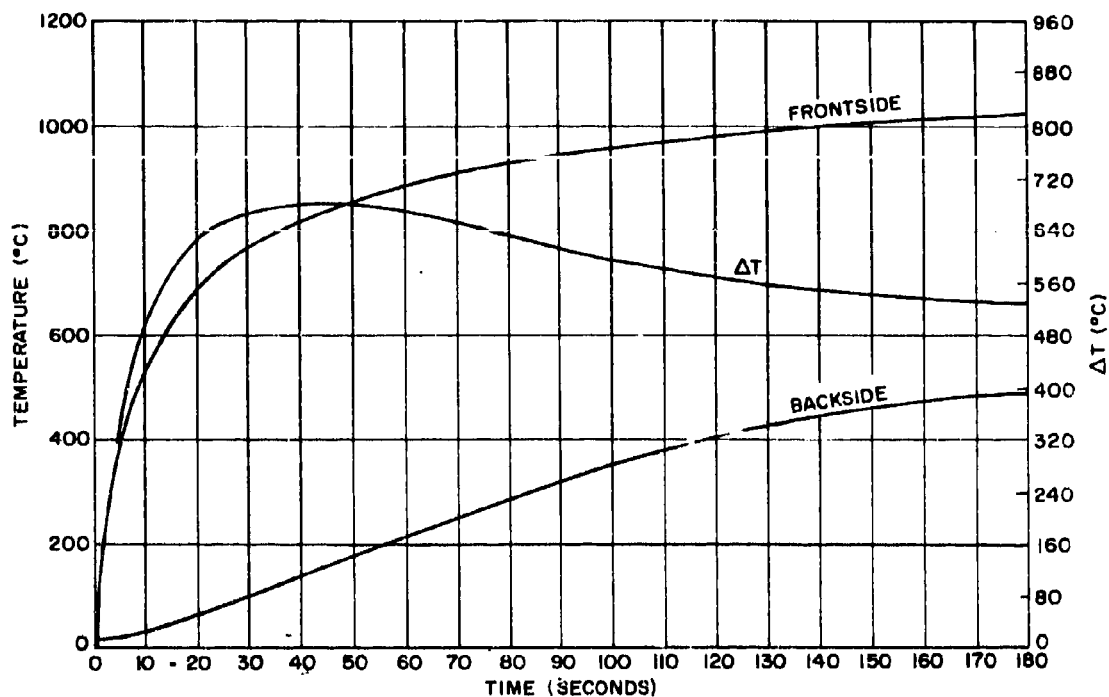


Figure 3-62. Temperature Measurements of 1/4-in. Thick Slip-Cast Fused Silica Plate Located 14 in. from Exit Plane of Oxyhydrogen Rocket Motor

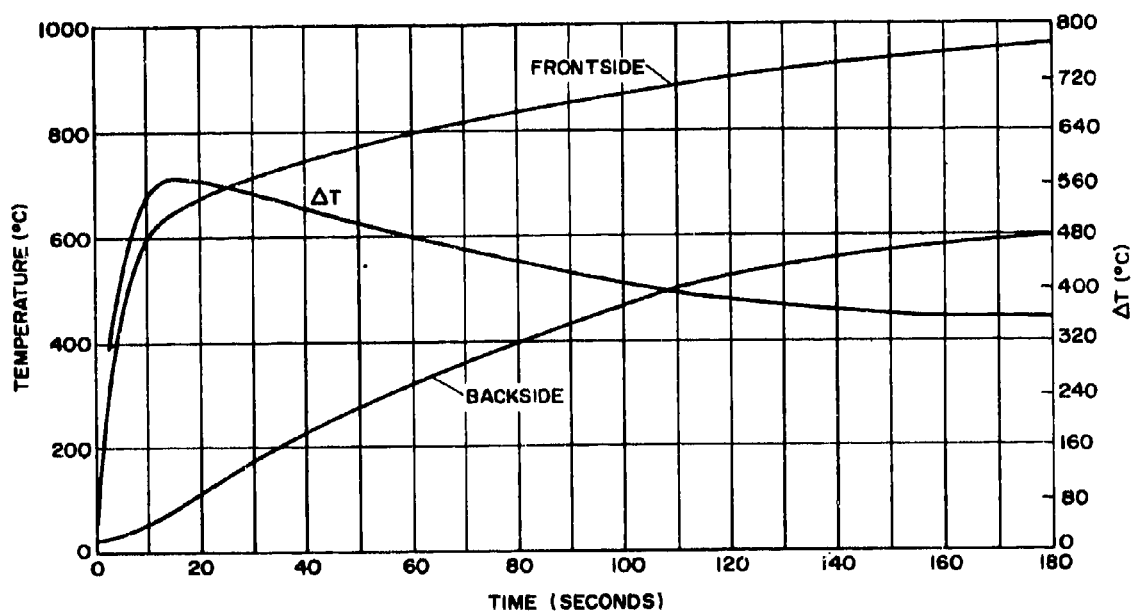


Figure 3-63. Temperature Measurements of 1/4-in. Thick Pyroceram Plate Located 14 in. from Exit Plane of Oxyhydrogen Rocket Motor



The slip-cast fused-silica nose cone survived this test with only localized melting at the tip. Figure 3-69 shows two views of the nose core after exposure to the rocket exhaust. The ablation rate was difficult to determine precisely, but ranged between 0.0003 and 0.0017 in./sec maximum. The use of this test motor to evaluate nose cone materials is described in Reference 28.

### 3-5.7.3 Obtaining Thermal Data on Production Radomes

Reference 38 reports the use of hot gases from a kiln to thermal-shock an alumina radome. The radome was an ogive of 5.5-in. diameter and 13-in. length. Thermal shock was accomplished by swinging the radome into the center of the gas stream in 1 sec. The temperature of the flue inlet wall measured 2510°F and combustion conditions assured gas temperatures over 3100°F. The same radome was thermal-shocked three successive times, each time returning substantially to room temperature before the next insertion. During the first thermal shock run, the radome was kept in the flue 27 sec. On the second run, it remained 20 sec, and on the third run 52 sec.

The calculated inside and outside wall temperatures are presented in Fig. 3-70 (Reference 40). From these data, it can be seen that the maximum thermal gradient in the wall was of the order of 100°F. The fact that there was no failure agrees with the general observations (presented in Reference 35) that alumina should survive a thermal shock environment that produces no thermal gradient greater than 100°F.

The heat transfer rate provided by the hot flue gas, however, was probably of a lower order than would be associated with the usual hypersonic flight trajectory. Also, it is probable that the thermal shock provided by the hot flue gas was approaching the maximum that the alumina could survive.

Reference 41 describes the use of quartz lamps to thermal-shock alumina radomes of approximately 6-in. diameter and 14-in. length. These radomes were also ogival and had half-wave X-band wall thickness.

The radomes were thermal-shock tested by exposure to the radiant heat generated by banks of quartz tube lamps. The lamps were assembled into a cylindrical oven, in the center of which the radome was mounted. The oven consisted of six lamp banks, each containing nine

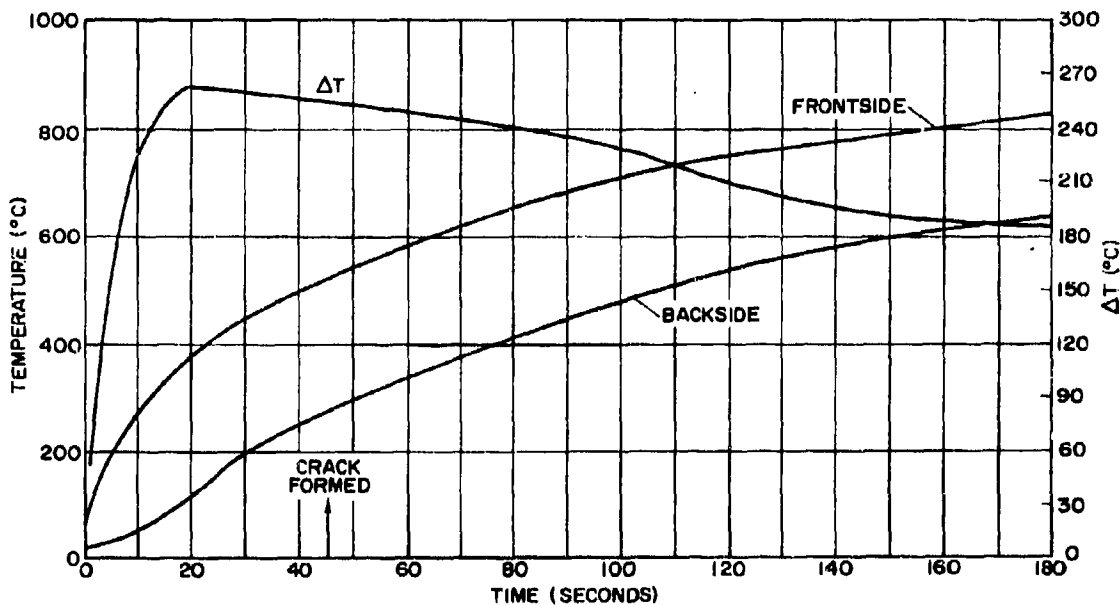


Figure 3-64. Temperature Measurements on 1/4-in. Thick Alumina Plate Located 14 in. from Exit Plane of Oxyhydrogen Rocket Motor

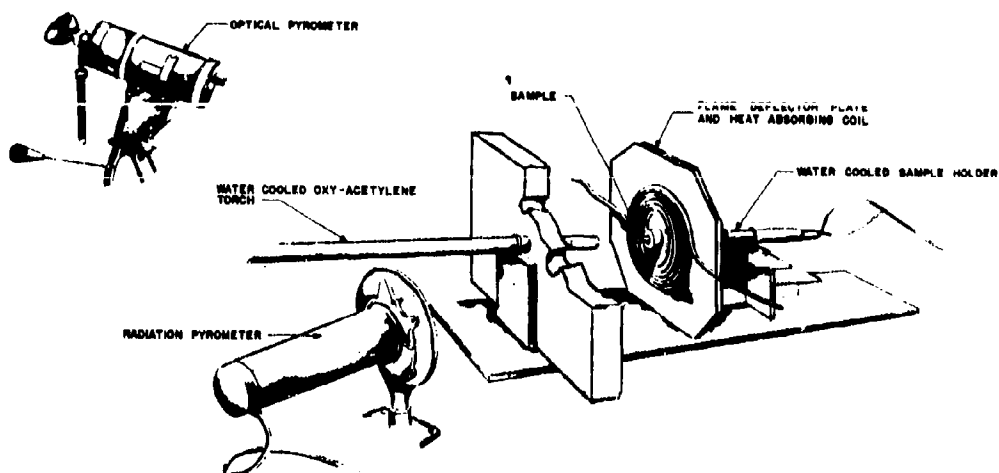


Figure 3-65. Oxyacetylene Test Facility

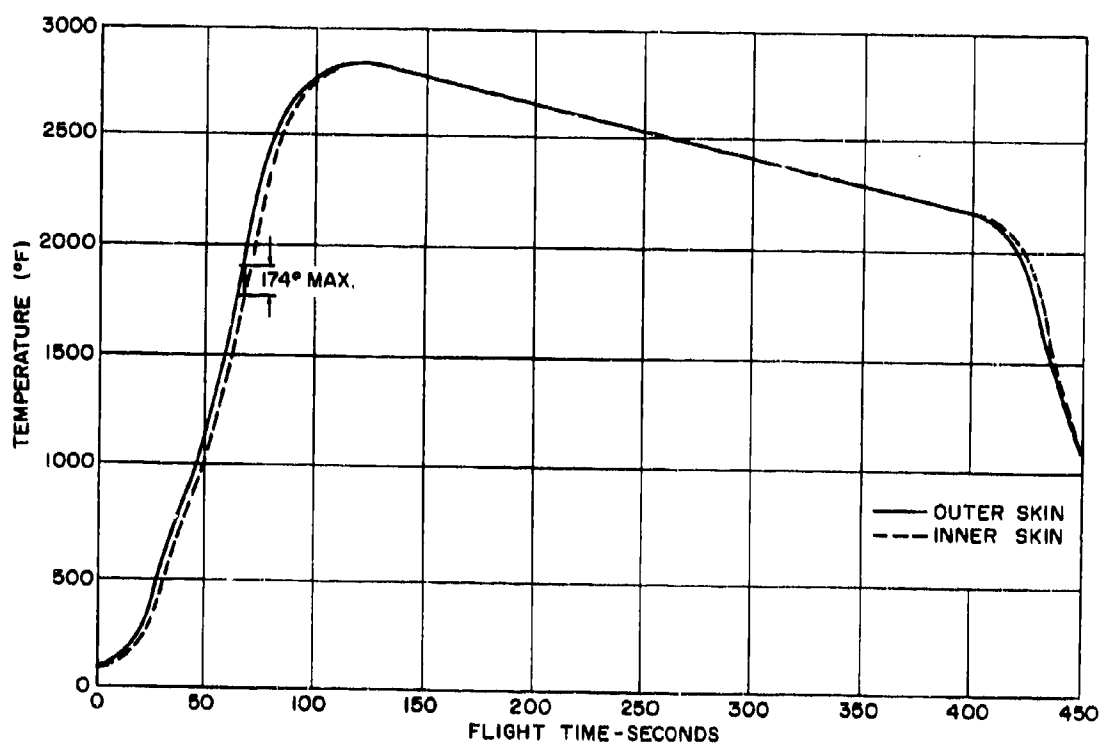


Figure 3-66. Outer Skin-Inner Skin Temperature vs Flight Time for Alumina Radome

lamps mounted in front of water-cooled aluminum reflectors. The radomes were equipped with thermocouples on both the inner and outer surfaces at three locations on the circumference, at a distance of 10 in. from the nose.

In a given test, heat was applied to the radome as rapidly as possible until the preselected wall temperature difference was attained, after which the heat input was adjusted to maintain this difference. The heating was continued until failure occurred or the surface temperature reached about 1900°F. The test results are given in Table 3-9.

**TABLE 3-9 THERMAL SHOCK CONDITIONS FOR ALUMINA RADOMES**

Radome Number	Wall Temperature Difference, °F	Maximum Outer Surface Temperature, °F	Rate of Rise of Surface Temperature, °F/min.	Radome Failure
4	50	1920	80	No
4	100	1800	160	No
1	150	1420	180	Yes
2	220	880	1000	Yes
8	240	1250	1000	Yes
4	300	1720	400	Yes

The alumina radomes usually broke into several pieces when failure occurred; the time period over which the fractures occurred was only a fraction of a second.

The fact that thermal gradients of 150°F and higher all produced failure is further evidence that for an alumina wall of approximately 0.22 in., the maximum thermal gradient for which the radome should be designed should be of the order of 100°F.

Reference 37 reports the use of the quartz lamp clamshell heater (shown in Fig. 3-56) to thermal-shock Pyroceram radomes at General Dynamics/Pomona. These radomes were covered with poster paint black to improve the heat transfer rate to the surface. Some ten or more of these radomes were tested to the capacity of the facility. Some of the radomes were reported to have failed explosively, breaking a number

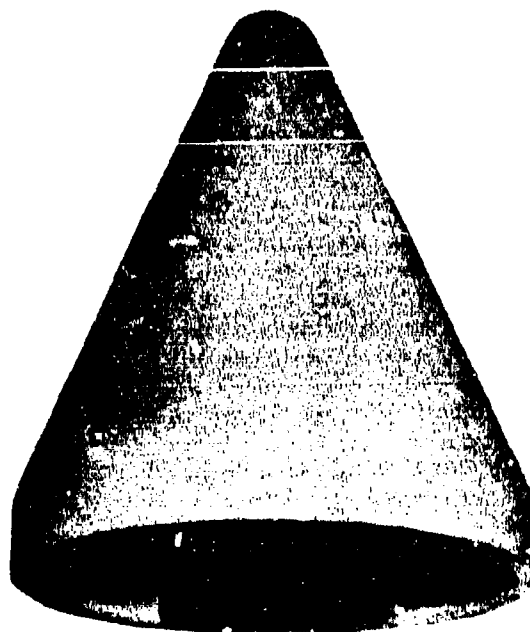


**Figure 3-67. Fused Silica Nose Cone Showing Mounting Brackets Cemented in Place with Adhesive Resin**

of the quartz lamps in the process.

The maximum heat input with this clamshell was approximately 70 Btu/ft<sup>2</sup>-sec. The efficiency of the operation was about 50%. 100 Btu/ft<sup>2</sup>-sec is possible by using these lamps in staggered rows, gold reflector surfaces, and higher voltages. The lamps shown in Figs. 3-56 to 3-58 are G.E. Infrared Heaters, Type T-3.

#### 3-5.7.4 Quality Control on Proof Testing

Reference 38 reports thermal shock data obtained from alumina radomes immersed in molten babbitt. Figure 3-71 shows the two radomes that were used in these tests, with the location of thermocouples to measure backside temperature. The graph of Fig. 3-72 presents the backside temperature plotted as a function of time after the radome was immersed in the molten babbitt. Only the outside of the radome was exposed to the babbitt.

Reference 39 computes the temperature distribution for the case above with the results shown in Fig. 3-73. These data emphasize that,

although the radome heats up rapidly, most of the temperature gradient occurs in the boundary layer and not in the radome wall. The maximum stress was found to be about 4300 psi or less than 10% of the flexural strength at 800°F. From these results, it is pointed out that such a test would be satisfactory only if larger temperature gradients could be obtained in the radome wall.

Radomes for the Mauler missile have been evaluated using a similar test. In this test, however, the molten metal was circulated around the radome to vary the heat transfer over the radome surface. This provided the highest heat transfer rate at the nose, which more nearly simulates the heat transfer profile anticipated in flight.

### **3-6 RADIATION EFFECTS ON RADOME MATERIALS**

#### **3-6.1 INTRODUCTION**

More recently, the design of radomes has been

complicated by the added requirement that the dielectric materials remain stable when subjected to high levels of radiation. Ground-based and shipboard radomes now include, as part of their specifications, structural and electrical performance that must be maintained when that particular radome is in the vicinity of a nuclear detonation. The use of antimissile missiles with nuclear warheads poses similar problems for the airborne radome design. Dielectric materials on orbiting vehicles had the added problem of extraterrestrial bombardment presented by cosmic rays, Van Allen radiation, etc.

For some time, many facilities have been subjecting materials to controlled radiation sources in an attempt to determine the structural and electrical degradation after exposure. Only a small percentage of these data is applicable to electromagnetic window design, because the major portion of this testing has dealt with structural metals, reactor materials, and electrical components. The following paragraphs will evaluate the performance that can be expected from the more common radome mate-



**Figure 3-68. Nose Cone Engulfed in Flame from Oxyacetylene Test Nozzle**

rials, plastic and ceramic, after they are subjected to radiation.

To adequately cover the entire field of radiation effects on materials would, in itself, require a text. The following paragraphs will present the radiation problem, with the hope that the references will provide a starting point for further research.

### 3-6.2 PLASTICS

Considerable use is still being made of various fiberglass-resin combinations for electromagnetic window applications. If we now impose on these designs a radiation environment, the two obvious considerations are the electrical and structural degradation that is to be expected upon exposure.

When exposed to high-intensity radiation, organic materials are altered because of molecular excitation and ionization. The resultant changes demonstrate themselves in either a physical or chemical manner, or a combination of both. Cross linking, bond cleavage and degradation, unsaturation, gas formation, and polymerization are a few of the changes encountered. Whether or not any one of these phenomena occurs depends upon the material in question and the nature of the radiation.

Exact comparison of data is often difficult because of the many parameters varied during the exposure of the material in question. For example, considerable data have been reported wherein the test material is simultaneously exposed to a source of radiation and a thermal environment that can range from ambient temperature to 1000°C. In addition, evaluations are also reported wherein the test material is subjected to a vacuum. The induced changes are a function of the combination of these three environments that is utilized.

Reference 42 states that gamma and fast neutron radiation produce physical and electrical changes in structural plastics that are quite similar when compared on an energy absorbed basis. Reference 42 also states that a radiation effects program, performed in a gamma field, reflects the behavior of a material after exposure to a mixed radiation environment. This is an important factor because it allows use of the more readily available gamma sources. In addition, gamma source facilities can handle larger sam-

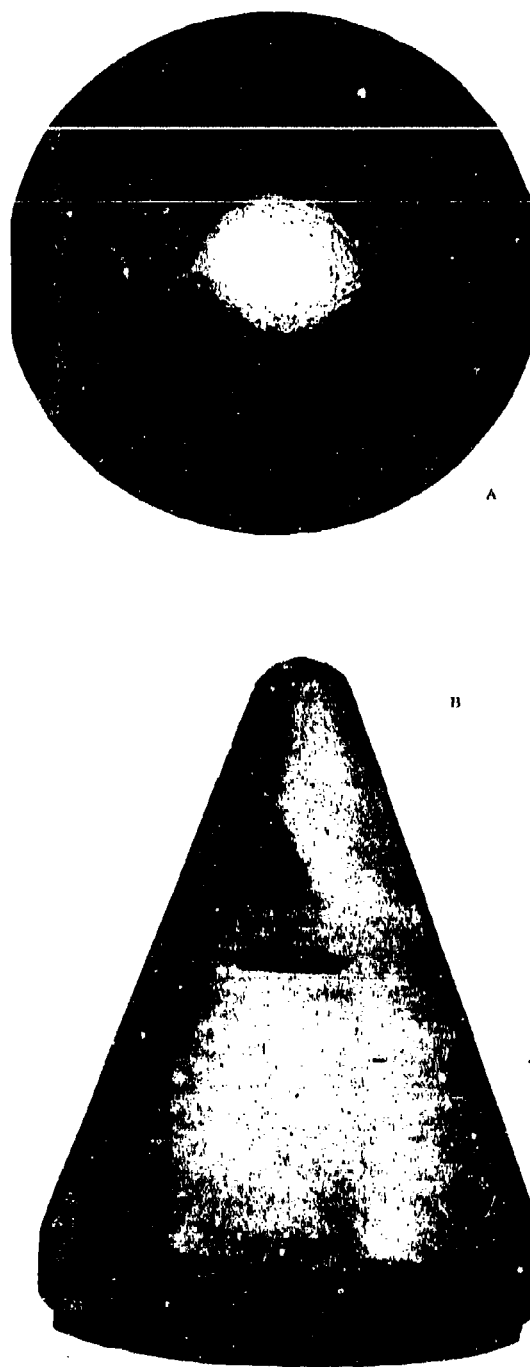


Figure 3-69. Slip-Cast Fused Silica Nose Cone After Test

pies, are far more accurate because of advanced gamma dosimetry, and present fewer handling problems because such sources do not induce radioactivity.

Table 3-10 lists some of the physical and electrical changes after exposure of various laminates to a gamma radiation source. The structural values in this table are the average of five specimens. The electrical values are the average of three readings taken at 8.5 kmc.

The structural and electrical test samples were irradiated in the spent-fuel gamma facility at the Materials Testing Reactor (MTR), National Reactor Testing Station, Idaho Falls, Idaho. Dynamic electrical studies were performed in a 1500-curie  $\text{Co}^{60}$  source located at WADC. The latter measurements were performed to determine if ion buildup during irradiation is significant. This proved to be negative. A Red Wing dielectrometer was used to determine the dielectric constant and loss tangent values.

Reference 43 gives a comparison of various reactor facilities. References 44 through 47 provide additional performance data on various plastic laminates after they were subjected to severe radiation levels. Reference 48 is men-

tioned individually because it is one of the best sources for the effects of radiation on plastics and elastomers.

### 3-6.3 CERAMICS

Considerable information exists describing the effects of radiation on all types of ceramics. The data reported are not directly pertinent to the design of radomes because most investigations concerned components, insulators, tube elements, reactor fuel elements, etc. Nonetheless, a consensus of reported data (Reference 49) indicates that these inorganic materials can withstand levels up to at least  $10^{20}$  nvt with no adverse effects.

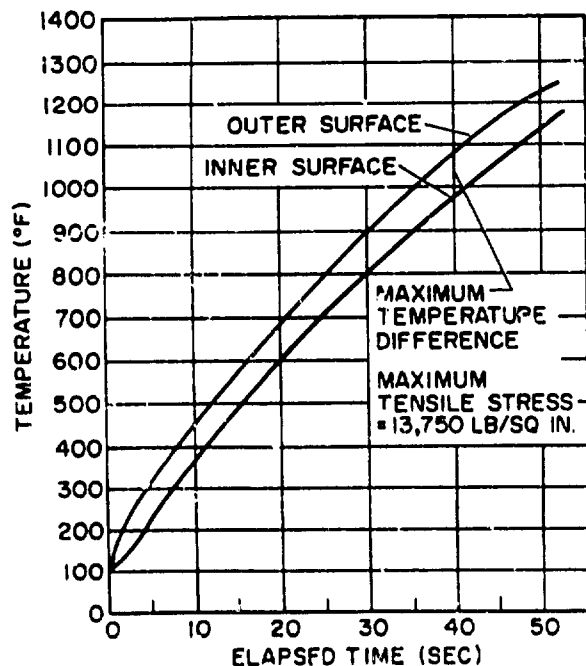
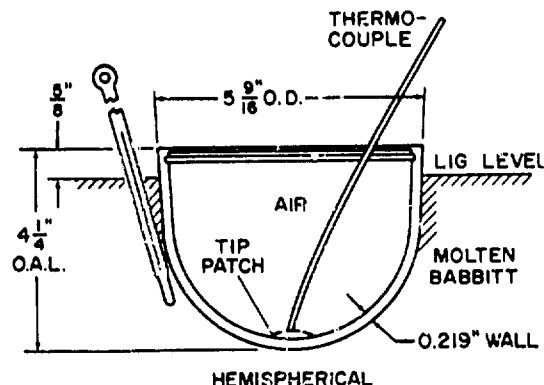


Figure 3-70. Calculated Inner Surface and Outer Surface Temperatures for Aluminum (AD-99) Radome Exposed to Hot Flue Gas Test



HEMISPHERICAL  
THIS RADOME WAS SUBJECTED TO  
THREE SUCCESSIVE SHOCKS OF RUNS  
NO. 1, 2 & 3 WITHOUT DAMAGE

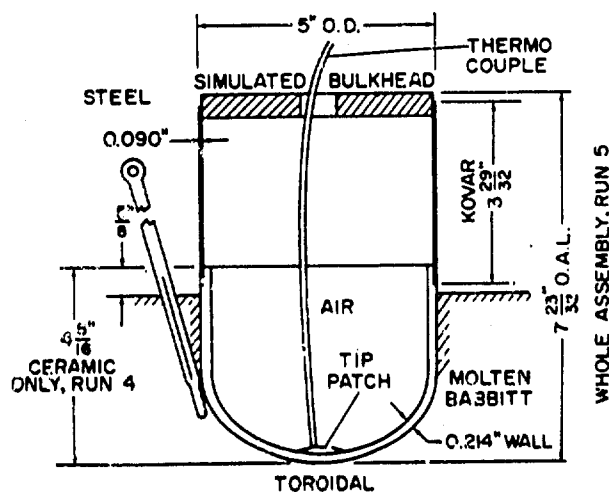


Figure 3-71. Hemispherical and Toroidal Radomes Used to Obtain Thermal Shock Data

It is interesting to compare the quoted radiation resistance of these ceramic materials with the exposure to be encountered in the inner Van Allen belts. Reference 50 evaluates several IR window materials at levels to  $10^8$  roentgens and indicates that it would require 110 years within the inner Van Allen belt to experience an equivalent exposure.

In summary, considering the radiation sources that are available for material evaluation, it is obvious that radome materials are relatively unaffected in the radiation environments as specified by the present generation of weapons systems.

In an attempt to centralize the collection of radiation data, the Air Force has established the Radiation Effects Information Center (REIC) at Battelle Memorial Institute. Reference 51 is the most recent compilation by REIC on Radiation-Effects State of the Art, 1962-63, and is the best starting point to pursue this area of interest.

### 3-7 VIBRATION TESTING

Vibration requirements for radomes are a part of the overall design parameters of a particular missile. However, since these requirements vary from missile to missile, there are no standard vibration tests for radomes.

Experience has shown that the mechanical requirements for advanced hypersonic missile

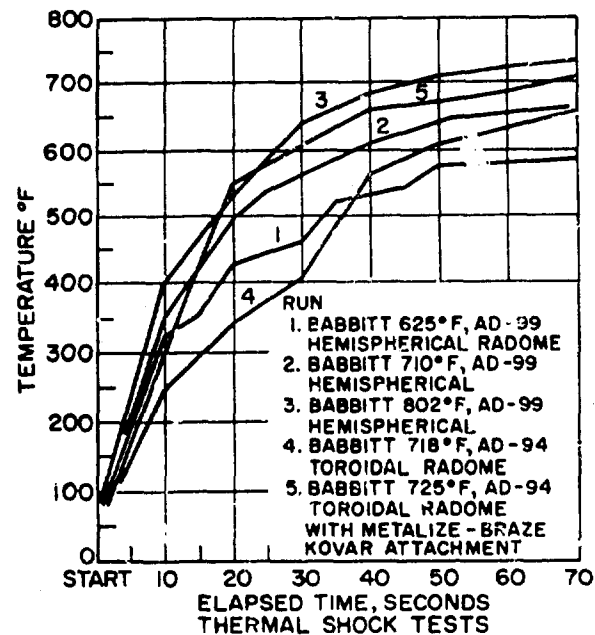


Figure 3-72. Graph of Temperature of Inside Surface of Radome Nose After Instant Immersion of Radome into Superheated, Molten Babbitt

radomes are minor when compared with the thermal shock requirements. For the case of alumina and Pyroceram radomes, the strength required to withstand thermal shock is so much higher than that required to withstand mechanical loads that the primary emphasis has been on thermal shock testing. In the case of slip-cast

TABLE 3-10 CHARACTERISTICS OF VIBRIN AND SELECTRON POLYESTERS AFTER EXPOSURE TO RADIATION

Material	Exposure, roentgens	Flexural Strength, psi	Tensile Strength, psi	Compressive Strength, psi	Dielectric Constant	Loss Tangent
Vibrin 135 Heat-Resistant Polyester	None	56.3	33.3	40.2	4.348	0.0139
	$6.2 \times 10^7$	47.2	26.9	38.0	.....	.....
	$2.9 \times 10^8$	47.8	27.6	43.2	4.453	0.0163
	$9.5 \times 10^8$	53.0	29.5	46.0	4.149	0.0117
Selectron-5003 Polyester	None	34.8	40.2	26.4	4.099	0.0114
	$6.2 \times 10^7$	39.4	38.8	33.8	.....	.....
	$2.9 \times 10^8$	39.5	34.0	29.9	4.123	0.0121
	$9.5 \times 10^8$	40.1	37.8	31.6	4.347	0.0129

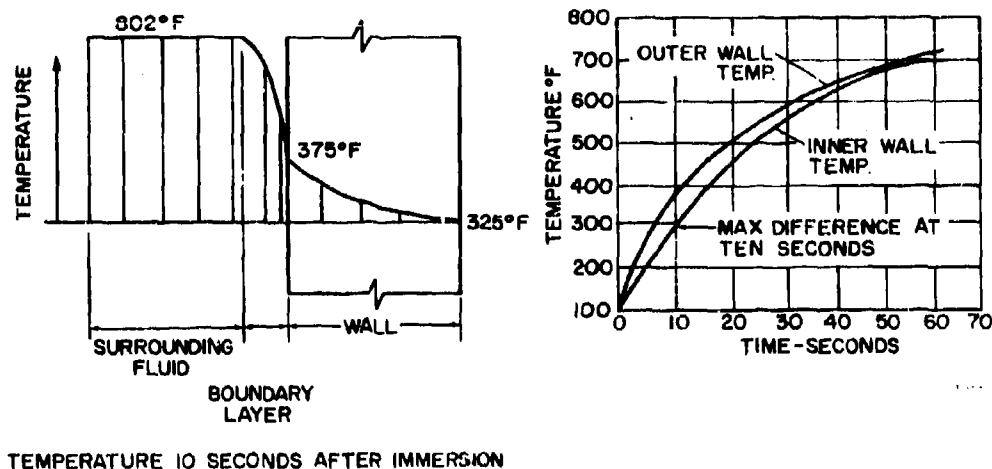


Figure 3-73. Inner to Outer Wall Temperature Distribution vs Time

fused silica, however, this is not necessarily true. For example, the strength required for this material to withstand even the most severe thermal shock environment would be very low. It may be even lower than that required to withstand mechanical loads. This would be particularly true in the case of radomes over 30 in. long.

In preparation for the sled tests reported in Paragraph 3-4.1, General Dynamics subjected the slip-cast fused-silica radomes to vibrational tests (Reference 52). Three radomes were vibrated in the three major planes at 60 g's from 90 to 2000 cycles. There was no visual degradation. After the sled tests, the first radome from run No. 8 (sled tested twice) was cut into test specimens. The transverse strength of this radome was only 2500 psi. Many radome designers had previously stated that strength of the order of 20,000 psi was the minimum required for

such a radome. The point should be made that the attachment plays a major role in the performance of a radome under mechanical loads. A good attachment system that minimizes stress concentration and distributes the load over as wide an area as practical, can result in the successful performance of a rather weak material. On the other hand, a poor attachment can result in the failure of the strongest radome materials.

It should be mentioned that most radome designers require 20,000 psi for alumina and Pyroceram, since this order of strength is required for thermal loading because of the high thermal expansion of these materials. Slip-cast fused silica has little thermal expansion and requires little strength for thermal loading. Therefore, strength requirements for slip-cast fused silica should be considered almost entirely for mechanical and aerodynamic loading.



## REFERENCES

1. Sissenivine, N., and Court, A. *Climatic Extremes for Military Equipment*, Office of the Quartermaster General, Environmental Protection Branch, Report No. 146, November 1951.
2. *Handbook of Geophysics for Air Force Designers*, AFCRC, Air Force Cambridge Research Laboratories, Office of Aerospace Research, U.S. Air Force, 1957.
3. *Trans. 24th Annual Meeting*, American Geophysical Union, Part II, April 1943.
4. Tyall, A. A., King, R. B., and Strain, R. A. *Gravimetric Assessment of the Erosion Resistance of Various Materials*, Royal Aircraft Establishment, Report Chem 518, September 1957.
5. Jenkins, D. C., and Booker, J. D. A *Photographic Study of the Impact Between Water Drops and a Surface Moving at High Speed*, Aeronautical Research Council, C.P. No. 501, 1960.
6. Jenkins, D. C., Booker, J. D., and Sweed, J. W. *An Experimental Method for the Study of the Impact Between a Liquid Drop and a Surface Moving at High Speed*, Aeronautical Research Council, R&M No. 3203, 1961.
7. Jenkins, D. C. *Note on the Possibility of Raindrops Being Shattered by the Air Disturbances Caused by a Moving Body*, RAE-TN-ME 239, October 1957.
8. Jenkins, D. C. *Interim Note on the Design and Development of a Laboratory Apparatus to Study the High-Speed Impact Between a Liquid Drop and a Surface*, RAE Technical Note No. Mech. Eng. 193, December 1954.
9. Engel, Olive G. "Fragmentation of Water Drops in the Zone Behind an Air Shock," *J. Res. UBS*, Vol. 60, No. 3, March 1958.
10. *Techniques for Airborne Radome Design*, edited by T. E. Tice, WADC Technical Report 57-67, Wright-Patterson Air Force Base, Ohio (ASTIA Document No. AD 142001), September 1957.
11. "Construction of the U. C. Rain Erosion Testing Equipment," University of Cincinnati, Applied Science Research Laboratory, BuAer Contract NOas 52-306c, May 9, 1955.
12. Figler, B. D., Parkan, W. J., and Wilson, J. C. *Rain Erosion Suppression at Supersonic Speeds*, Mithras, Inc., Report MC-61-6-R1, October 1962.
13. *A Study of Rain Erosion Testing Methods for Supersonic Speeds*, WADC Technical Report 53-173, August 1958.
14. King, R. B. *An Assessment of Various Materials*, Royal Aircraft Establishment, Part V, September 1960.
15. *Summary Compilation of Supersonic Rain Erosion Results*, WADC Technical Report 58-427, July 1959.
16. *The Design of the Rain Erosion Test Facility at the SNORT*, NOTS TP3232, July 1963.
17. Remell, A. C. *Radome Rain Erosion Test*, USNOTS, China Lake, California, Test Data Memo 4021-4-1963, March 15, 1963.
18. Remell, A. C. *Shrike Radome Rain Erosion Tests*, USNOTS, China Lake, California, Technical Note 4021-64-2, March 1964.
19. Allen, John W. *Supersonic Rain Erosion Testing and Design Criteria*, Sandia Laboratory, Albuquerque, New Mexico, Report No. SC-TM253-63(14), March 1963.
20. Reynolds, Marcel C. *Rain Measurement and Simulation for Supersonic Erosion Studies*, Sandia Corp., Report No. SRC-474, February 1962.
21. Fountain, R. A. *Results of Testing Slip-Cast Fused-Silica Radomes Under Rain Environment*, General Dynamics, Pomona, California, Technical Memo No. 6-223-571, July 18, 1963.
22. Pedigo, Alan. "Resistance to Impact and Thermal Shock by Solid Alumina Radomes," *Proc. ASD-OSU Symposium on Electromagnetic Windows*, Vol. 1, ASD-TDR-62-676, July 1962.
23. Pergament, H. S. "Thermal Shock Testing of Scaled Alumina Radomes," Appendix II in *Final Report for Large Ceramic Radome Manufacture by Dry-Isostatic Pressing Techniques*, Alan Pedigo, AST-TDR-62-967.
24. *Facility Handbook*, Ordnance Aerophysics Laboratory, Daingerfield, Texas, OAL, Report 655, February 27, 1963.

25. Seegee, J. W., Lowrance, D. T., and Rogers, D. C. *X-20 Nose Cap Materials Summary Report*, Report No. 311.29, LTV Astronautics Division, June 15, 1964.
26. Walton, J. D., Jr., and Poulos N. E. "Fused Silica for Reentry Radomes," *Proc. OSU-RTD Symposium on Electromagnetic Windows*, Vol. III, June 1964.
27. Bessley, R. M., and Izu, Y. Douglas. "Design and Construction Techniques for Radomes for Superorbital Missions," *Proc. OSU-RTD Symposium on Electromagnetic Windows*, Vol. III, June 1964.
28. Lucas, W. R., and Houston, M. E. "Planning a Reentry and Recovery Test Program," *Astronautics*, pp. 30-31, 88, March 1959.
29. Walton, J. D., and Bowen, M. D. "The Evaluation of Ceramic Materials Under Thermal Shock Conditions," *Mechanical Properties of Engineering Ceramics*, pp. 149-171, Interscience Publishers, New York, 1963.
30. Norin, T. Larry. "The Measured Electrical Characteristics of Several Ablative and Some Nonablative High-Temperature Radome Materials," *Proc. OSU-RTD Symposium on Electromagnetic Windows*, Vol. I, June 1964.
31. *Refractory Composites Working Group*, Monitored by RTD-NASA, Chairman L. N. Hjelm, RTD, MAAE, Wright-Patterson Air Force Base, Ohio.
32. Rosenbery, J. W., Smith, H. E., and Wurst, J. C. *Evaluation of Materials Systems for Use in Extreme Thermal Environments Utilizing an Arc-Plasma Jet*, WADD Technical Report 60-926, March 1961.
33. Mason, C. R., Walton, J. D., Bowen, M. D., and Teague, W. T. *Investigation of High-Temperature Resistant Materials*, Summary Report No. 3, Georgia Tech Project No. A-212, BuOrd Contract No. NOrd-15701, October 31, 1959.
34. Sklarew, S. "The Problem of Accurately Measuring Changing Temperatures of Nonmetallic Surfaces," Presented at the Eighth Refractory Composites Working Group Meeting, January 14-16, 1964.
35. Cavanaugh, J. F., and Sterry, J. P. *Heat Protective Ablative Coatings for Radomes*, WADD Technical Report 60-507, August 1960.
36. Poulos, N. E., Walton, J. D., Teague, W. T., and Bower, M. D. *Development of Monolithic Ceramics and Heterogeneous Ceramic-Metal Bodies of Aerodynamic Applications at High Velocities and Temperatures*, Final Report, Georgia Tech Project No. A-330, U.S. Army Ordnance ABMA Contract No. DA-01-009-ORD-548, March 31, 1959.
37. Private communication from Mr. C. E. Dunn to Mr. J. D. Walton, September 17, 1964.
38. Pedigo, Alan. *Radome Handbook*, Second Edition, Coors Porcelain Co., Golden, Colorado, April 1962.
39. Fitzgerald, E. A. *Thermal Stresses in Thin Shells of Revolution for Axisymmetric Temperature Distributions*, Missile & Space Systems Division, Douglas Aircraft Company, Inc., Santa Monica, California, Report No. SM-42009, June 1962.
40. Pedigo, Alan. "Resistance to Impact and Thermal Shock by Solid Alumina Radomes," *Proc. ASD-OSU Symposium on Electromagnetic Windows*, Vol. I, ASD-TDR-62-676, July 1962.
41. Baer, D. H., Gates, L. E., and Robertson, G. D. "Evaluation of Ceramic Radomes," *Proc. OSU-WADC Radome Symposium*, WADC-Technical Report 58-272, Vol. I, June 1958.
42. Tomashot, Robert C., and Harvey, D. G. *Nuclear Radiation of Reinforced Plastic Radome Materials*, USAF, WADC Technical Report 56-296 (ASTIA Document No. AD-97254), September 1956.
43. Stephenson, Richard. *Introduction to Nuclear Engineering*, Chemical Engineering Series, McGraw-Hill Book Co., New York, 1958.
44. Weller, Richard L. *Nuclear Radiation of Reinforced Plastics*, WADC Technical Report 56-296, Supp. I (ASTIA Document No. AD232888), December 1958.
45. "Nuclear Thermal and Radiation Effects on Radome Materials," *Proc. Symposium on Rigid Radomes*, Vol. I, Lincoln Labs., MIT (ASTIA Document No. AD232582), October 15, 1958.

46. *Material and Component Utilization for Nuclear-Powered Vehicles; Radiation Effects Design Data*, Convair, Fort Worth, Texas, FZA-54-026, AF 33(600)-38946, September 30, 1959.
47. Gray, P. D. *Rockets in Space Environment, Phase II: Individual Component Investigation (Reinforced Plastics)*, Aerojet, General Corp., AGC-2263, AF 04(611)-7441, March 30, 1962.
48. King, R. W. *The Effect of Nuclear Radiation on Elastomeric and Plastic Components and Materials*, Battelle Memorial Institute, REIC No. 21, September 1, 1961.
49. Johnson, E. R. *Literature Survey on Effects of Nuclear Radiation to Electron Tube Materials*, Stevens Institute of Technology, Hoboken, New Jersey, Final Report DA-36-039-SC-73146, October 31, 1960.
50. Lusk, T. E. *The Effects of Gamma-Ray Irradiation on the IR Transmission of 16 Materials*, General Electric Co., Ithaca, New York, R60ELC10(DA-99-459-57), February 1960.
51. *Radiation-Effects State of the Art, 1962-63*, Report No. 28, Radiation Effects Information Center, Battelle Memorial Institute, Columbus, Ohio, June 30, 1963.
52. *Results of Testing Slip-Cast Fused Silica Under Rain Environment*, General Dynamics/Pomona, Technical Memorandum No. 6-223-571.

### APPENDIX 3A

#### EFFECTIVE EMITTANCE CALCULATION

The effective emittance of a material can be determined from two temperature measurements, total radiation temperature, and optical temperature. For the preliminary data presented, the assumption is made that the spectral emittance at 6500 Å is equal to the effective emittance. This assumption simplifies the analysis and provides for rapid numerical solutions.

Consider a surface at some true temperature,  $T_r$ , with a radiation temperature,  $T_r$ , and an optical temperature,  $T_o$ . The measured radiation temperature,  $T_r$ , suggests that the surface is "black" in nature and has a unit area radiant flux of:

$$R_N = \sigma T_r^4 \quad (3-A1)$$

However, if the surface is not "black," the radiant flux will be:

$$R_N = \epsilon \sigma T_r^4 \quad (3-A2)$$

From Eqs. 3-A1 and 3-A2,

$$\sigma T_r^4 = \epsilon \sigma T_o^4$$

$$\text{or} \quad \epsilon = T_r^4 / T_o^4 \quad (3-A3)$$

The true temperature,  $T_r$ , is tabulated as a function of optical temperature,  $T_o$ , for 49 effective spectral emissivities in a National Bureau of Standards Monograph (Reference 1).

Thus, Eq. 3-A3 can be written as:

$$\epsilon = \left[ \frac{T_r}{T_o(T_o, \epsilon)} \right]^4 \quad (3-A4)$$

Solutions are obtained by trial and error, and are accomplished by assuming an effective emittance, determining the true temperature,  $T_r$ , associated with this particular emittance and optical temperature,  $T_o$ , and evaluating the expression until equality is reached between the right- and left-hand portions of Eq. 3-A4.

### APPENDIX REFERENCES

1. Poland, D. E., Green, J. W., and Margrave, J. L. *Corrected Optical Pyrometer*, U.S. Department of Commerce, National Bureau of Standards, NBS Monograph 30, April 21, 1961.

**CHAPTER 4**

**RADOME MATERIALS AND CONSTRUCTION**

**PART I**

*by* **DR. G. M. BUTLER**

*Interpace*

*Los Angeles 38, California*

*and*

**PART II**

*by* **S. A. MILLER**

*Technical Plastics*

*San Francisco, California*

## SYMBOLS

B.W.	Bandwidth, in.
D	Density
$D_m$	Diameter of mandrel
F	Frictional force
NQ	Number of helical layers
P	Normal force or pressure, psi, between the mandrel and the first layer of glass
R	Tangential force
$R'$	Reflected phase, degrees
S	Interferometer horn to radome wall spacing, in.
TPI	Threads per in.
T	Tension, lb/thread
$V_1$	Volume of part at the base with radius $r_m$
$V_m$	Volume of the mandrel
$V_n$	Volume at any given station; for a cone $V_n = \pi r_p^2 h/3 - \pi r_m^2 h/3$
$V_p$	Volume of part
d	Physical thickness, in.
h	Height of cone, in.
r	Radius of curvature, in.
$r_m$	Radius of mandrel, in.
$\alpha$	Winding angle, degrees
$\epsilon$	Emittance; dielectric constant
$\epsilon'$	Relative dielectric constant
$\lambda_0$	Wavelength, in., at the interferometer frequency
$\phi$	Electrical thickness
$\theta$	Included angle, degrees, between the tangential force and the y-axis in cartesian coordinate system.

## CHAPTER 4

### RADOME MATERIALS AND CONSTRUCTION

#### PART I—CERAMIC RADOMES

##### 4-1 INTRODUCTION

*Techniques for Airborne Radome Design* (Reference 1) lists and discusses many ceramic materials worth considering in the construction of radomes. Alumina and glass-ceramics are applied in numerous missiles. Beryllia and sintered fused silica are undergoing considerable development and testing, but have not yet been accepted for a specific missile. This chapter considers only these four ceramic radome materials.

When service conditions become too severe for glass-reinforced plastic radomes, ceramic materials offer the only practical combination of high hardness and heat resistance to withstand rapid aerodynamic heating and erosion by rain and other particles. Ceramics for this application may be considered as inorganic, nonmetallic, electrically insulating materials that have been subjected to temperatures above a red heat ( $\sim 1000^{\circ}\text{F}$ ) during their fabrication. This processing temperature may vary from  $1000^{\circ}\text{F}$  below the melting temperature of the material, as with slip-cast fused silica, to a temperature above the melting point, as with glass-ceramics. Such ceramics consist of the oxides of several metals and metalloids. Oxide ceramics are inert to oxidation at high temperatures and have useful physical properties at temperatures high enough to destroy plastics and to melt most metals and glasses. Many of them also have electrical properties very desirable for radome use.

Alumina and glass-ceramic radomes have been used on at least five operational missiles and on others in developmental stages. High-volume fabrication processes for ceramic radomes have been perfected by several com-

panies, and much has been learned about the behavior of ceramic radomes. Designers now turn with comparative confidence to ceramics when conditions are too severe for plastics. Enough has been learned about the mechanical and electrical properties of the leading ceramics to permit quite accurate computer programming and calculation of their performance in both dense and laminated forms.

The principal properties of ceramics that have led to their use in radomes are

1. Ability to sustain temperatures into the white heat range without chemical change or destructive deterioration, while retaining a useful degree of strength
2. High hardness, providing resistance to rain erosion
3. Excellent dielectric properties, even at high temperatures
4. Complete resistance to corrosion, fungus, bacteria, and similar destructive agents

Offsetting these favorable properties are some less favorable characteristics:

1. Greater weight than resin-glass radomes of similar size
2. Greater sensitivity to severe thermal shock conditions
3. Brittleness (lack of any elongation before fracture, hence inability to distribute localized stresses)
4. High cost of fabrication compared to glassplastics, especially in large sizes and when finished by diamond grinding to final dimensions
5. High rate of change in dielectric constant with temperature

---

\* See Paragraph 4-16.

Cooperation between ceramic manufacturers and radome designers has stimulated notable progress in minimizing or adjusting for these shortcomings. This, in turn, has made possible the hypersonic, accurately-guided missiles on which so much military strategy is based. Advanced missile development imposes severe thermal requirements on ceramic materials. These requirements may not even be satisfied by the properties of alumina, beryllia, glass-ceramics, or silica (when in the dense, monolithic form). Use of composite or laminated structures seems to offer the only hope for success in withstanding the extreme heat shock caused by the tremendous velocity of these missiles.

This chapter outlines the properties of the four leading materials considered for ceramic radomes (in monolithic and other forms), and explains the processes by which they are manufactured. It also covers a new inorganic-bonded glass fiber material. Mixtures of glass fibers and organic materials\* are excluded, since techniques for bonding glass fibers or oxide "whiskers" with inorganic binders have not advanced to the point of becoming active candidates for radome use.

## **4-2 PROPERTIES OF CERAMIC RADOME MATERIALS\***

### **4-2.1 GENERAL COMPARISON OF CANDIDATE MATERIALS**

Each of the types of ceramic materials discussed in this chapter has advantages and limitations. For a general comparison to be made of these characteristics, Table 4-1 has been compiled from data on the individual materials presented in more detail later in this chapter. Values in the table are only illustrative. Some have been obtained by extrapolation—most have been rounded off for easy comparison.

---

\* For a more extensive compilation of physical and electrical property data for ceramic radome materials, see ML-TDR 64-296 *A Survey of High-Temperature Ceramic Materials for Radomes*, September 1964, under Contract No. AF 33 (657)-10519.

#### **4-2.1.1 Alumina**

Alumina in dense, monolithic form (the first commercial ceramic radome material) has certain important characteristics. It is the hardest and strongest of the radome ceramics. Dense alumina cannot be scratched by any common materials and is immune to rain erosion up to very high speeds, although it can be broken by rain drop impingement if it is too thin. Dense alumina is easily produced to zero permeability and absorption. Its raw materials are abundant and inexpensive.

On the other hand, of the four materials, alumina is the most vulnerable to thermal shock damage at temperatures below red heat because of its combination of moderately high expansion, moderate thermal conductivity, and high elastic modulus. Its dielectric constant is high and it has the highest specific gravity of the four. It requires complete grinding after sintering to correct for shrinkage. Because of its hardness, costly diamond grinding wheels must be used.

#### **4-2.1.2 Glass-Ceramics**

*Glass-ceramics* is a generic term for the family of crystallized glasses represented by Corning Code 9606 material, the composition most generally used for radomes, trademarked Pyroceram. These glass-ceramics are shaped by glass-working techniques such as spinning, which is faster and less costly than forming ceramics from powders. Glass-ceramics are fine-grained, fully dense, and offer a wide range of properties, such as thermal expansion and dielectric constant, whose values may be changed with variations in composition. Compared to alumina, Pyroceram has a substantially lower dielectric constant, lower heat conductivity, lower thermal expansion, and better thermal shock resistance. Its major shortcoming is its relatively low service temperature range. It is also vulnerable to scratching and surface damage. It is currently available from only one manufacturer.

#### **4-2.1.3 Sintered Fused Silica**

Sintered fused silica is unique in its out-

**TABLE 4-1 COMPARISON OF PROPERTIES OF THE FOUR PRINCIPAL  
CERAMIC MONOLITHIC RADOME MATERIALS**

	99% Alumina	Pyroceram	99% Beryllia	Sintered Fused Silica
Density, gm/cm <sup>3</sup>	3.75 to 3.9	2.59 to 2.62	2.85 to 2.95	1.9 to 2.0
Melting point, °F	3700	≈2600	4050	≈3000
Coefficient of linear thermal expansion, per °F to 1500°F, micro-in./in.	4.5	3	4.8	0.3
Specific heat, Btu/lb/°F	0.27	0.18	0.24	0.16
Thermal conductivity, Btu/ft <sup>2</sup> /hr/ft/°F				
At room temperature	10	2.1	150	0.35
At 1500°F		1.9	15	0.4
Bend strength, psi				
At room temperature	45,000	35,000	35,000	5000
At 1500°F	35,000	17,000	30,000	6000
Modulus of elasticity, psi × 10 <sup>6</sup>	52	17	52	4
Dielectric constant at 10 gc				
At room temperature	9.2	5.6	6.5	3.3
At 1500°F	10.1	5.8	7.6	3.3
Loss tangent at 10 gc				
At room temperature	0.0003	0.0003	0.0003	0.0008
At 1500°F	0.0005	0.01	0.0004	0.0006
Hardness, Knoop, kg/mm <sup>2</sup>	2000	619	1220*	560**
Permeability	Nil	Nil	Nil	High†
Normal total emittance	0.75	0.85	0.85	....
<p>* See Reference 1.  ** For dense silica; indeterminate for porous fused silica.  † Requires fused surface layer or impervious glaze.</p>				

standing resistance to thermal shock. The thermal expansion of silica is so low that fracture due to heating and cooling rates encountered in missile service is almost impossible. Other advantages are its low dielectric constant that changes very little with temperature, its low density, its ready machinability, and its availability at moderate cost from several manufacturers. Large shapes are readily fabricated and the fabrication technology is public knowledge (see Reference 2).

Sintered fused silica is relatively weak at low temperatures. However, its strength increases with temperature, so that it becomes as strong as some of the other materials at high temperatures. Since it is also very porous and permeable, its surface must be sealed for radome use. This has been accomplished both

by fusing a thin surface layer with intense local heat and by applying a low-expansion glaze.

#### 4-2.1.4 Beryllia

Beryllia has received less study for radomes than the other three materials because of its high cost and possible toxicity. Its high cost is due principally to the high cost of raw materials and precautions taken to prevent ingestion during manufacture. Its principal advantage is its high thermal conductivity at low temperatures, which excels all other candidates for radome use and provides high resistance to thermal shock under moderately rapid heating conditions. It has a very high melting point and a high maximum service temperature, and its



moderate dielectric constant and low loss tangent give it especially good electromagnetic transmission at high temperatures. The density of beryllia is lower than that of alumina, and it is sufficiently hard to resist scratching and surface damage. Its strength is comparable to glass-ceramics and only moderately less than alumina, and, except for the necessity for dust control, its fabrication process is very similar.

The cost of beryllia raw materials has dropped substantially and shows possibilities of dropping further. Since it should be feasible to fabricate beryllia in sandwich form with porous cores, it may yet become a major radome ceramic.

#### 4-2.1.5 Other Ceramics

Other monolithic oxide ceramics that have been considered for radome use have many shortcomings, such as excessive weight, unstable properties, and inadequate electrical properties, that have discouraged further testing. An inorganic-bonded glass fiber material (described in Paragraph 4-7) may become an important composite radome ceramic. Two non-oxide ceramics silicon nitride and boron nitride, were the subjects of papers at the 1964 Radome Symposium (References 3 and 4). They have excellent electrical and refractory properties. Silicon nitride is normally permeable, requiring techniques to make it dense or to seal its pores, and boron nitride is very expensive. However, their desirable features may outweigh their disadvantages and lead to further consideration.

#### 4-2.1.6 Summary

While all four of the ceramics have properties that qualify them for use on some missiles, it is evident that flight profiles of the missiles now being planned and tested will impose heat fluxes and rates of heating higher than those experienced by any radome material. These operational conditions will generate higher internal stresses in monolithic alumina, glass-ceramic, and even beryllia than previously encountered. Sintered fused silica can resist the thermal shock; likewise, it appears that laminated or sandwich constructions of the other materials

may have the requisite heat shock resistance, plus favorable weight and dielectric properties. Accordingly, such composite formulations are discussed in Paragraphs 4-3.1, 4-8.1.5., and 4-8.1.6.

#### 4-2.2 EVALUATING PHYSICAL PROPERTY DATA\*

Certain mechanical property data of importance to the radome designer cannot be stated with the precision desirable for stress analysis and thermal shock calculations because of the inherent characteristics of ceramics. These must be understood and borne in mind when comparing and applying strength data given for ceramic materials.

Ceramics have no yield point. At moderate temperatures, they break without measurable elongation. Notches, scratches, and abrupt changes of section induce stress concentrations that can lead to fracture at abnormally low applied stresses. Conventional tensile testing, so simple and economical for metals and plastics, is extremely difficult and costly for ceramics. Specimens must be shaped by grinding with diamond wheels; threaded ends are not possible because of premature thread fracture; avoidance of nonaxial loading is very difficult; and surface finish has a marked influence on results. For these reasons, reliable tensile data on ceramics are extremely scarce.

Measurement of bending strength, or transverse modulus of rupture, is much simpler and is the usual manner in which the strength of ceramics is expressed. The test's simplicity is misleading; many variables affect the results: Thin samples give higher values than thick ones; cylindrical samples give higher values than square or rectangular ones; and the distance between supporting points must be long with respect to the sample thickness if errors due to compression are to be minimized. Span-to-thickness ratios in excess of 10:1 are usually favored.

Ultimate tensile strengths from carefully-run true tensile tests usually give results ranging between one-half and two-thirds of those from transverse bending tests. The scatter of results is apt to be considerable in both tests; the prin-

\* See Paragraphs 1-1.5.5, 5-9, 5-10, and 6-3.4.

cial problem is establishing the minimum confidence level. For a given radome material and geometry the preferred procedure utilizes samples of thickness comparable to the radome wall, or even samples cut from the radome itself.

In addition to the test technique, two inherent ceramic characteristics affect their strength levels. Porosity, found to varying but significant degree in all ceramics except those that are melted into glass, must be carefully controlled to achieve consistent results. Figure 4-1 shows the effect of porosity on the bend strength of an alumina body. Note that even 5% porosity can cause as much as 20% drop in strength. Also, grain size has a considerable effect: the finer the grain size, the stronger the ceramic. Figure 4-2 is a three-dimensional representation of the relation between grain size, strength, and temperature. The strength of an oxide ceramic with a 1- to 2-micron average grain size may be twice that of a chemically identical material with a grain size in excess of 10 microns. Alumina and beryllia radomes are apt to have grain sizes ranging from 10 to 80 microns, since they are rather large pieces of pure oxide ceramic and require slow heating and cooling, which is conducive to grain growth. Fully dense, nonporous, very fine-grained pure alumina has a bend strength approaching 100,000 psi when tested in small, thin samples; beryllia can be made nearly as strong. Such strengths cannot yet be achieved in sizable radomes.

Toughness is another property significant for metals and plastics but with little meaning for ceramics. Although conventional swinging-hammer impact test results are occasionally presented for ceramics, their interpretation is even more difficult than tensile test data. No attempt has been made to present impact test data because of the problems involving surface quality, porosity, geometry, structure, and mechanics of the test. In qualitative terms, the ability of a ceramic to withstand blows is proportional to its strength. A truly dense, very fine-grained pure oxide such as alumina is tough in that it is hard to break, makes a fine cutting tool, and has been made into springs.

Moduli of elasticity can be determined with less ambiguity, but are strongly influenced by porosity. Dynamic methods, such as sonic techniques, are usually preferred over static methods, such as bending. Hardness measured by

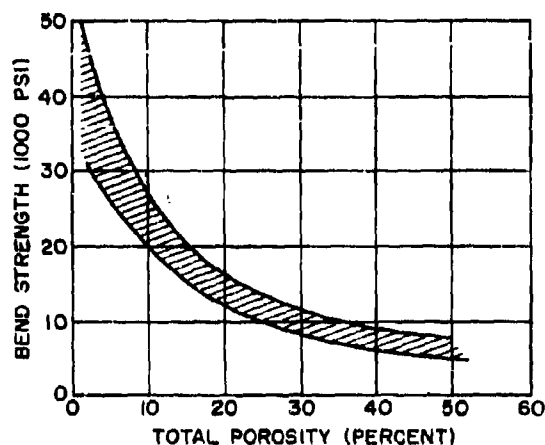


Figure 4-1: Effect of Porosity on Room-Temperature Bend Strength of Aluminas (Ref. 5)

the Knoop indentation method discloses substantial differences among the four ceramics, but the results of various investigators are inconsistent.

Close agreement and little uncertainty are found in measurements of specific heat, thermal expansion, dielectric properties, and resistivity. Compositional and structural variations have minor effects on these properties. Thermal conductivity is more difficult to measure and agreement is poorer between reported results, but results are affected mainly by porosity differences between samples.

In summary, most of the property data reported herein can be used with confidence in calculations, but the designer will do well to demand strength data determined on specimens cut from shapes similar in size and thickness to his radome and tested by methods that he selects.

#### 4-3 PROPERTIES OF ALUMINA RADOME MATERIALS

Two different types of alumina currently used for radomes are differentiated by their alumina content as 97 to 98% alumina and 99% (or more) alumina. Although this classification by composition is convenient, within each of these ranges the alumina from one manufacturer may vary significantly from that of

another. The differences at room temperature will be mainly caused by structural factors, such as variations in grain size and porosity. At temperatures in the red heat range and beyond, differences in content of minor impurities will cause significant variations in electrical properties and in load-carrying ability.

Several manufacturers offer high quality monolithic alumina radomes. Their raw materials are supplied from several established sources of refined aluminas, so that raw materials are ample, produced in large volume, and quite closely controlled for purity and particle size. Each manufacturer, however, adds small quantities of other oxides to control sintering and grain growth, so that aluminas of the same nominal alumina content can differ somewhat in behavior.

Table 4-2 shows some properties of the two

principal alumina compositions used for monolithic radomes, as distinguished from sandwich, segmented, and other multicomponent alumina radome structures. Those properties for which elevated-temperature data are available are shown in Figs. 4-3 to 4-10.

Considering these data, it is evident that the 97% alumina composition differs appreciably from the higher-purity material. This formulation was selected for the spray-isostatic forming process because it had minimum shrinkage, about 10%, during firing. This was accomplished by using a high percentage of fused or highly calcined alumina particles in the mix. This accomplished the desired low shrinkage, but resulted in substantial porosity, lower dielectric constant, and lower strength.

The high-purity formulations, 99% (or more) alumina, shrink more in sintering, thereby de-

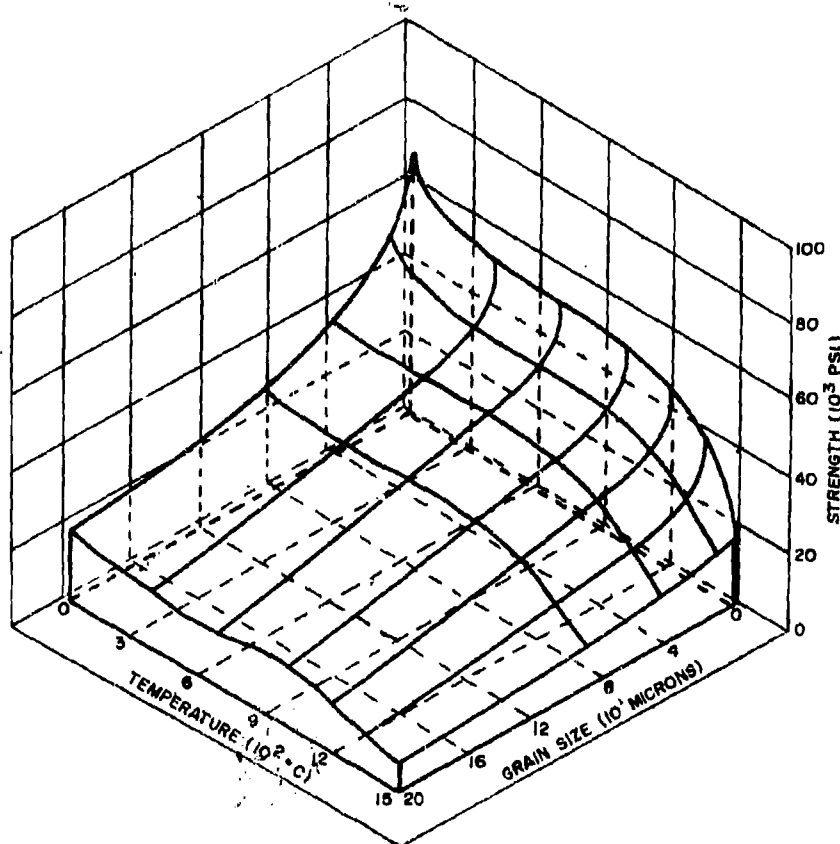


Figure 4-2. Strength-Temperature-Grain Size Surface for Dense Pure Hot-Pressed Alumina (Ref. 6)

TABLE 4-2 PROPERTIES OF MONOLITHIC RADOME ALUMINAS

Property	97% Alumina	99% Alumina
Nominal alumina content, %	97 to 98	99 to 99.5
Additions, optional	SiO <sub>2</sub> , MgO, CaO	MgO, Cr <sub>2</sub> O <sub>3</sub>
Apparent density, gm/cm <sup>3</sup>	3.55 to 3.6	3.75 to 3.9
Porosity, %	8 to 12	2 to 6
Water absorption, %	0.0	0.0
Permeability	Nil	Nil
Hardness, Knoop, 100-gm load, kg/mm <sup>2</sup>	≈1800	≈2000
Compressive strength, × 10 <sup>3</sup> psi	200 to 300	250 to over 400
Poisson's ratio	0.24	0.28
Resistivity, ohm-cm	Over 10 <sup>14</sup>	Over 10 <sup>14</sup>

veloping low porosity, higher dielectric constant, and improved strength. Their loss tangent remains low to higher temperatures than the 97% material because of lower impurity content.

Alumina radomes may be expected to be serviceable up to equilibrium temperatures of over 2000°F, provided that heating rates are moderate. The thermal shock resistance of alumina bodies is limited by their relatively low thermal conductivity, moderately high thermal expansion, and high modulus of elasticity.

The pronounced effect of variations in composition upon loss tangent is evident from Fig.

4-8. Very pure alumina changes little up to 2500°F. The 99% bodies change little up to 2000°F, whereas the 97% formulation undergoes rapid increase in loss at 1600°F to 1800°F. The divergent results are mainly attributable to differences in kind and amount of impurities.

Alumina undergoes no transformation or other change up to the onset of rapid grain growth in excess of 2500°F, so that the property curves are smooth, without sudden changes. Under sustained loads above 2000°F, alumina undergoes measurable creep or plastic deformation; but the brief exposures to high temperatures, characteristic of radome service, are unlikely to cause any measurable plastic flow.

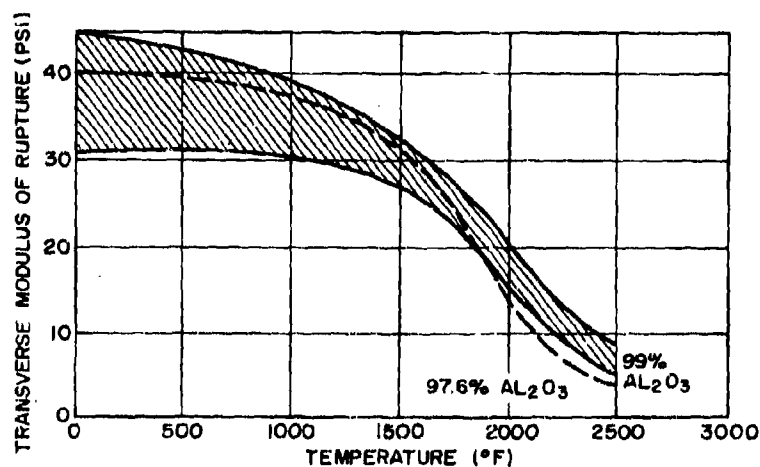


Figure 4-3. Bend Strengths of Radome Alumina.

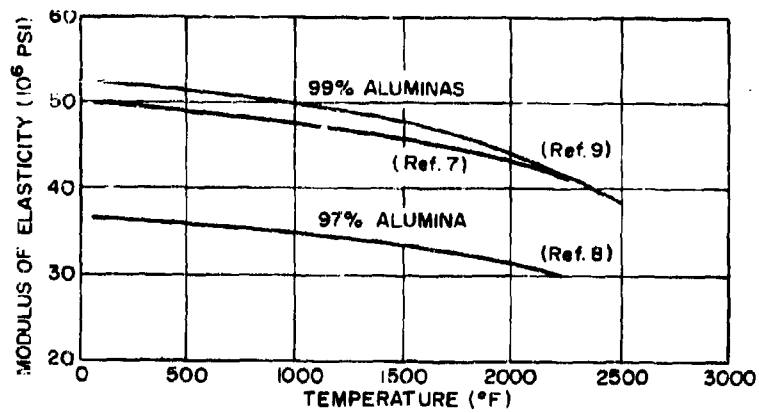


Figure 4-4. Modulus of Elasticity of Radome Aluminas

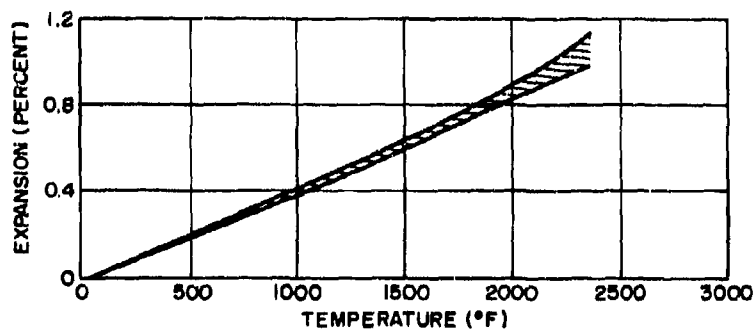


Figure 4-5. Linear Thermal Expansion of Radome Aluminas

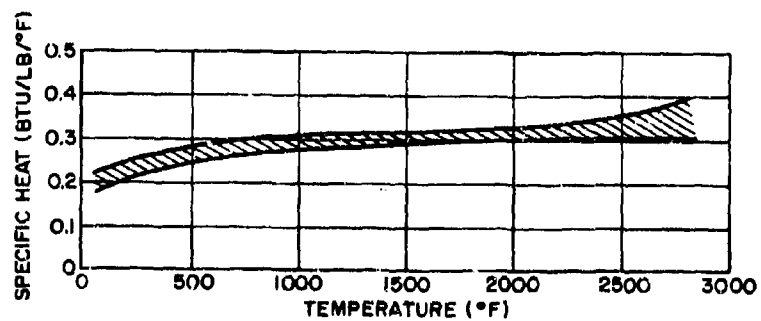


Figure 4-6. Specific Heat of Aluminas (Ref. 5)

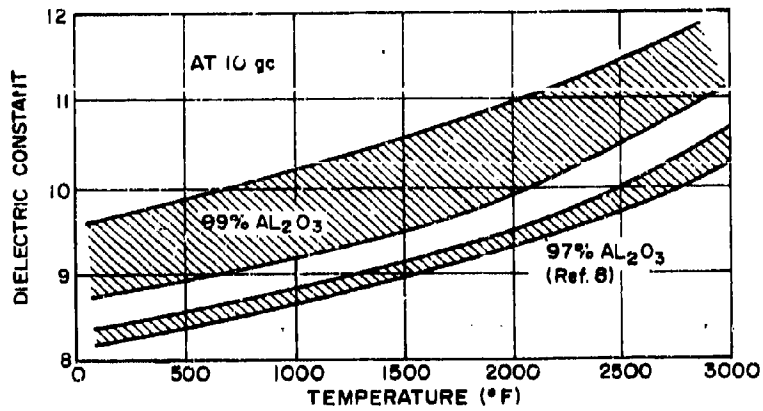


Figure 4-7. Dielectric Constant of Aluminas as a Function of Temperature

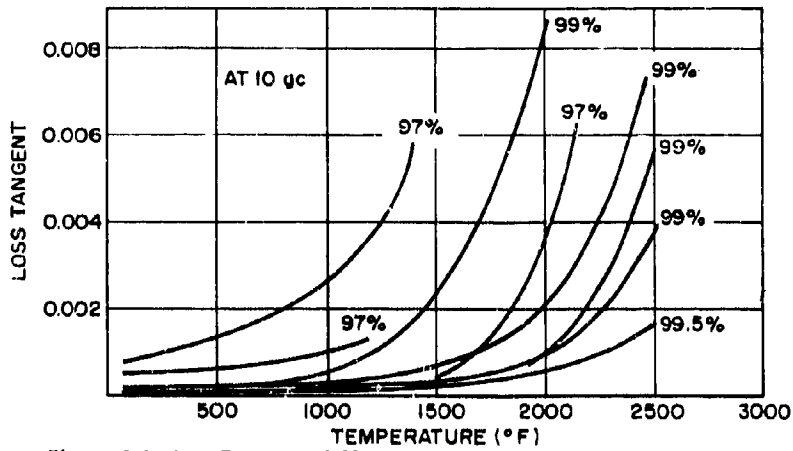


Figure 4-8. Loss Tangent of Aluminas as a Function of Temperature

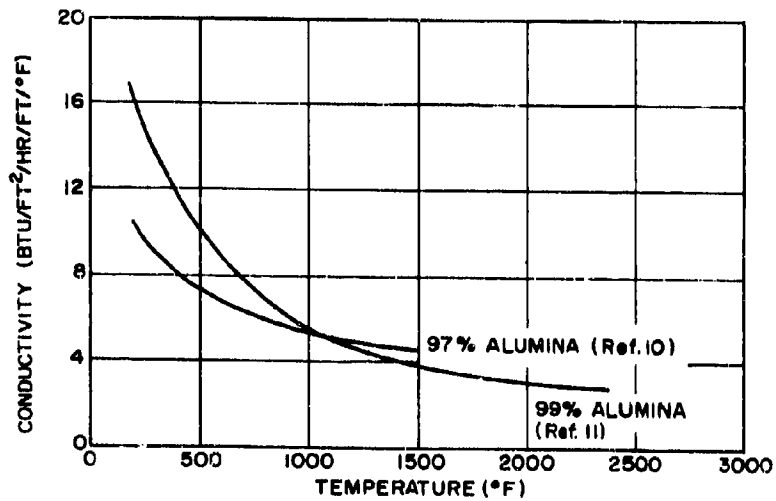


Figure 4-9. Thermal Conductivities of Radome Aluminas

#### 4-3.1 POROUS ALUMINA AND SANDWICH ALUMINA MATERIALS

Like plastics, ceramics can be made in a highly porous form. The potential advantages of porous ceramics for radome use include weight savings, lower dielectric constant than the dense material, reduced heat conduction, and greater resistance to thermal shock. Both the Air Force and the Navy have sponsored programs (References 13 to 17) to develop porous or foamed ceramics for radomes and to make sandwich constructions with dense, impervious skins and lightweight, porous cores. The Navy has supported "A" sandwich alumina radome development work at Interpace. The Air Force has undertaken similar work on corrugated and honeycomb ceramic structures. Further, work on foamed core "A" sandwich ceramics has also been accomplished (see Paragraph 1-1.2).

Porous alumina shapes are produced commercially by several manufacturers, but the application of an integrally bonded skin or skins of matching alumina has been a recent development. By the slip-casting technique described in Paragraph 4-8.1.2.2, radomes can be made of considerable size, with skins of dense 95% alumina enclosing a core of porous 95% alumina whose density can be closely controlled within limits of less than one-quarter to more than one-third of theoretical density. Pores are extremely small and uniform, and the core and

skins are formed as a unit. Figure 4-11 is an enlarged cross-section view of this material as an "A" sandwich and Fig. 4-12 shows the interface between the dense skin and the porous core at higher magnification. Table 4-3 presents the properties of the material in the form of an "A" sandwich. Preliminary dielectric properties of skin and core as a function of temperature are shown in Figs. 4-13 and 4-14. The effect of temperature on the modulus of elasticity of three different 95% alumina "A" sandwich structures is shown in Fig. 4-15 (Reference 8). Rough qualitative burner tests indicate that the ceramic "A" sandwich has substantially greater thermal shock resistance than dense monolithic alumina. Rain erosion tests on the rocket sled at Naval Ordnance Test Station (Reference 18) have shown that a radome shape consisting of dense outer skin 0.04 in. thick, backed by 0.04 in. of porous alumina impregnated with epoxy resin, can withstand travel at 3000 ft./sec. in a rain field equivalent to 2 in./hr. Several programs are evaluating this alumina sandwich material for new missiles because of its availability at effective dielectric constant of about 3 and its success in forming small experimental radomes, such as those produced in the Glendale Research Center of International Pipe and Ceramics Corp. Some design considerations for this ceramic sandwich have been published (Reference 19).

Other attempts to apply dense surface layers to porous ceramics have involved electrophoretic

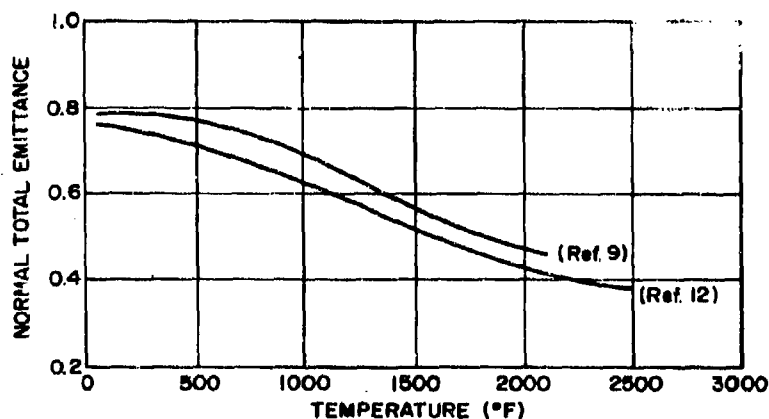
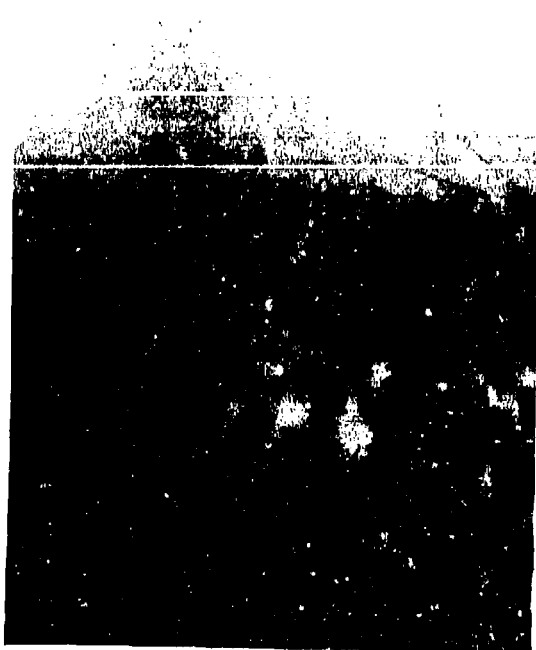


Figure 4-10. Normal Total Emittance of Aluminas



**Figure 4-11. Interface Between Dense Alumina Skin and Porous Alumina Core: Magnification 100X**

deposition and spraying. Results were unpromising; the skins were rough and tended to penetrate into the porous core.

#### **4-3.2 PROPERTIES OF MOSAIC ALUMINA CONSTRUCTION**

The Air Force has sponsored a project to assemble alumina segments or mosaics into a large radome structure by joining the individual pieces with ceramic cement (Reference 20). The objective is to fabricate very large radomes that would be impracticable by the conventional techniques for manufacturing monolithic radomes. Cementing formulations have been developed that form strong bonds between 97.6% alumina pieces accurately ground to fit together into ogive shapes, assembled, and then sintered to mature the cement bond. Several adhesives were evaluated, with a magnesium-aluminosilicate selected as best. Tooling to support the alumina tiles and cement during sintering was made of high-silica refractory castable. Properties of the selected adhesive and of alumina samples bonded with it are shown in Table 4-4.



**Figure 4-12. Enlarged View of Cross-section of 95% Alumina "A" Sandwich Skins 0.023-in. Thick; Core 0.207-in. Thick (Density 1.3 gm-cm<sup>-3</sup>); Magnification 10X**

Another approach to the problem of large ceramic radomes, that of sectionalized, structurally supported radomes, is being explored as part of the Air Force program to develop lightweight ceramic radomes (Reference 21).

#### **4-3.3 COMPOSITE PLASTIC-ALUMINA RADOMES**

Rain erosion rapidly destroys glass fiber-reinforced plastic radomes at velocities exceeding Mach 1 (see Paragraph 3-2). The erosion damage is most severe at the extreme tip. An erosion-proof protective cap on the tip extends the useful life of glass-resin radomes to higher speeds. Since alumina has been demonstrated to be the material that is most resistant to rain erosion while having good electromagnetic transmission properties, the problem of protecting the tips of glass-plastic radomes with thin alumina caps is under study.



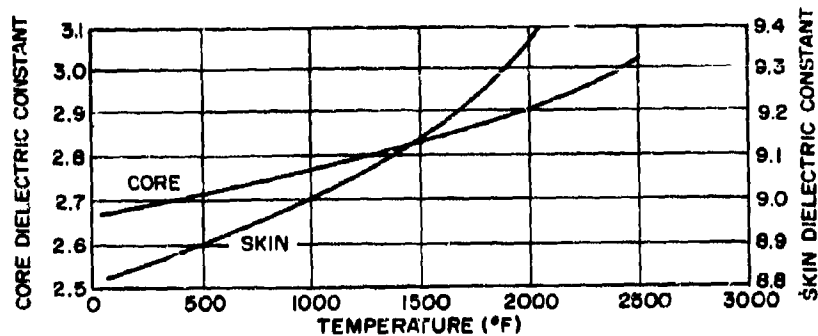


Figure 4-13. Approximate Dielectric Constants of 95% Alumina Sandwich Skin and Core Materials: Core Density 1.29 gm/cm<sup>3</sup> at 10 gc

TABLE 4-3 PROPERTIES OF 95% ALUMINA "A" SANDWICH MATERIALS

Property	Skin	Core	"A" Sandwich Core 1.3 gm/cm <sup>3</sup>
Density, gm/cm <sup>3</sup>	3.7 ± 0.15	1.3 ± 0.15	*
Porosity, %	± 1	66 ± 3	.....
Water absorption, %	0.0	35 ± 5	0.0 as radome
Modulus of rupture, psi × 10 <sup>3</sup>	30 to 45	2 to 4	10 to 20*
Linear thermal expansion, (75°F to 1300°F) × 10 <sup>-6</sup> /°F	4.3 ± 0.3	4.3 ± 0.3	4.3 ± 0.3
Hardness, Knoop, kg/mm <sup>2</sup>	≈1800	.....	.....

\* Depends upon relative thicknesses of skin and core.

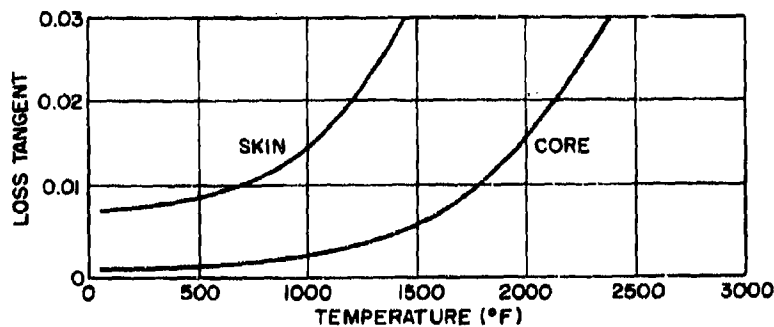


Figure 4-14. Approximate Loss Tangents of 95% Alumina Sandwich Skin and Core Materials: Core Density 1.29 gm/cm<sup>3</sup> at 10 gc

One Navy project is directed toward fabrication of a ceramic-coated plastic radome by electrophoretic deposition (Reference 22). This program is aimed at the fabrication of a ceramic shell 0.01 to 0.02 in. thick by depositing an alumina ceramic electrophoretically upon a refractory metal radome mandrel, sintering this while on the mandrel, removing after supporting with a temporary outer layer of plastic, then preparing the plastic lay-up inside the ceramic shell and removing the outer supporting layer. Flat and small samples have been successfully made.

Another approach being studied is flame or arc plasma spraying of an alumina layer upon a plastic radome. Rain erosion sled tests on such coated radomes have not yet shown the desired degree of resistance to damage, but continued improvements in technique may make flame-sprayed coatings adequately rain resistant.

A modification of the sandwich technique described in Paragraph 4-3.1 permits the formation of thin-walled, dense, fully sintered alumina shells up to about 6 in. high by 5 in. in base diameter, with wall thickness of 0.02 to 0.025 in. These are being experimentally applied to plastic- and inorganic-bonded glass radomes for erosion testing.

**TABLE 4-4 TYPICAL PROPERTIES OF ADHESIVES AND JOINTS BETWEEN 97.6% ALUMINA TILES**

Property	Room Temperature	1000 °F
Joint lap shear strength, psi	11,200	10,000
Solid compressive strength, psi	49,000	.....
Joint tensile strength, psi	10,400	.....
Joint flexural strength, psi	21,500	.....
Dielectric constant (9.375 gc)		
Solid adhesive	5.86	6.79
Composite joint	8.26	8.70
Loss tangent (9.375 gc)		
Solid adhesive	0.0154	0.0815
Composite joint	0.0009	0.0032
Thermal expansion, micro-in./in./°F		
Room temperature to 1000°F	.....	3.6

#### 4-4 PROPERTIES OF GLASS-CERAMIC RADOME MATERIALS

Only Corning produces glass-ceramic radomes, sold under the trademark Pyroceram. While there are many compositions of glass-ceramics, the formulation used to date, Corning Code 9606, is the only one that has been extensively used and evaluated.

As discussed in Paragraph 4-9, glass-ceramics are unique in that they are melted and shaped as a true glass, then heat treated to cause many tiny crystals to grow from nuclei, until most of the volume consists of this crystalline phase, within which is a small amount of residual glass. The amount of this glass and its composition have an important effect on high-temperature strength and electrical properties.

Unlike other radome ceramics, glass-ceramics are very fine-grained and are free from porosity. Therefore, the effects of these factors need not be considered when appraising data on this product. On the other hand, the mechanical property data, especially strength, are closely

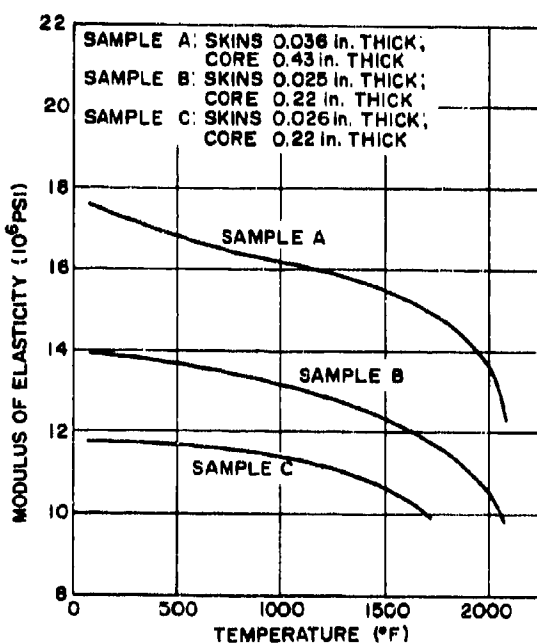


**Figure 4-15. Modulus of Elasticity of 95% Alumina "A" Sandwich Material (Ref. 8)**

dependent upon the manner in which the surface has been prepared and the depth and size of grinding scratches. Tests are generally performed on samples ground and lapped inside and out in the same manner as a radome.

Table 4-1 contains typical physical properties of Pyroceram. Figures 4-16 to 4-24 show the effects of temperature upon some properties of Pyroceram (Reference 23).

The data on this glass-ceramic shows that it embodies a number of very important characteristics. The dielectric constant increases very little with temperature up to at least 2100°F, and the loss tangent begins to increase rapidly at about 1500°F. The linear thermal expansion and thermal conductivity of Pyroceram are relatively low. The curves showing the effects of temperature upon modulus of elasticity and Poisson's ratio show a pronounced abnormality at about 300°F.

The satisfactory thermal shock resistance of Pyroceram has been confirmed by service experience on numerous production missiles and

by a production control test, utilized by Corning, in which each radome is plunged into a molten, circulating salt bath. Weak or defective radomes will crack and be rejected.

One quality of glass-ceramics that facilitates inspection and discovery of defects is the transparency of the material after it has been formed and before the final heat treatment that causes crystallization and converts it into an opaque substance. Examination by transmitted light will disclose inclusions, voids, and other defects.

The relatively low hardness of Pyroceram necessitates protection of finished radomes against scratching and other mechanical damage due to contact with other objects, especially on the inside surface, where stress concentrations are at a maximum during aerodynamic heating.

As with the other ceramics used for radomes, glass-ceramic is not affected by fungus, bacteria, or weathering agents during prolonged storage under extreme conditions. The mounting area is vulnerable to long term static loading failure,

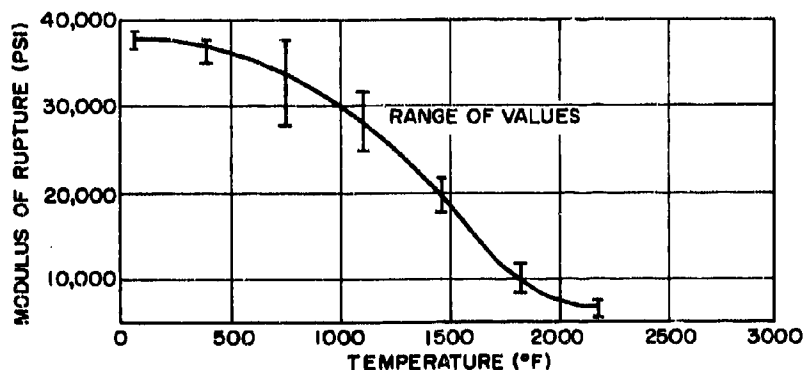


Figure 4-16. Modulus of Rupture of Pyroceram

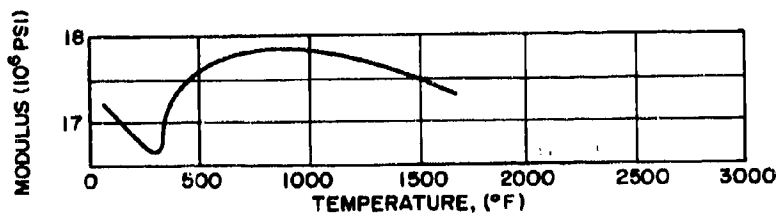


Figure 4-17. Modulus of Elasticity of Pyroceram by Sonic Method

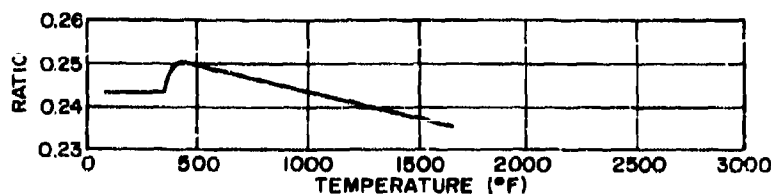


Figure 4-18. Poisson's Ratio of Pyroceram

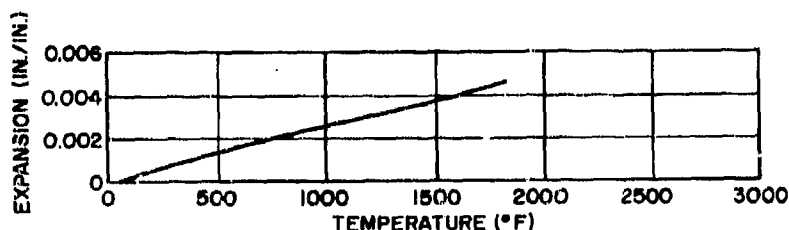


Figure 4-19. Linear Thermal Expansion of Pyroceram

and care must be taken in design to place the ceramic in compression and avoid inducing tensile stresses.

As with glass, the strength of glass-ceramics is very sensitive to surface finish. Ground surfaces give values lower than those shown, which are for chemically treated surfaces.

Corning has indicated that a new glass-ceramic under development has improved thermal shock resistance because of its reduced thermal expansion — approximately one-half that of Pyroceram. This, plus higher strength at elevated temperatures, provides three times the thermal shock resistance of Pyroceram. No claims are made for serviceability at higher temperatures. The new material has been made only in laboratory quantities.

## 4-5 PROPERTIES OF FUSED SILICA

### 4-5.1 VITREOUS SILICA

Fused silica is commercially available in two forms. The older and better-known form is vitreous silica, which is a clear or milky glass, completely noncrystalline, formed by melting and shaping quartz or other quite pure silica materials. Vitreous silica has been used for small electromagnetic windows, especially for those undergoing conditions of extreme thermal shock, as in reentry. Of all ceramics and glasses, vitreous silica has by far the greatest resistance to thermal shock because it undergoes almost no expansion or contraction during heating and cooling.

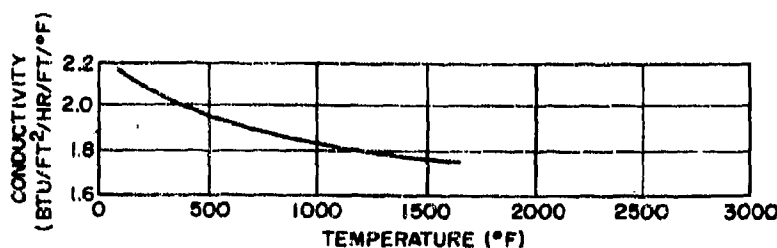


Figure 4-20. Thermal Conductivity of Pyroceram

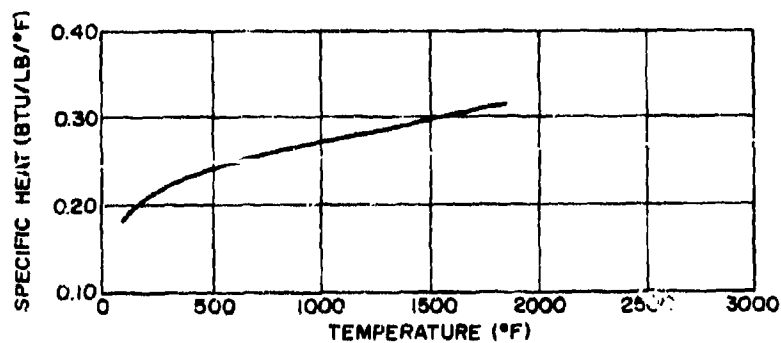


Figure 4-21. Specific Heat of Pyroceram

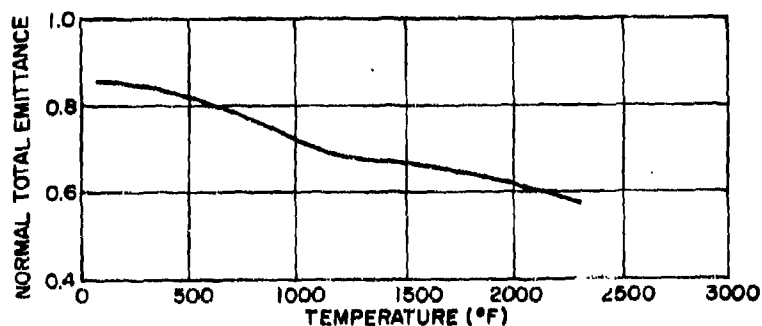


Figure 4-22. Normal Total Emittance of Pyroceram (Ref. 12)

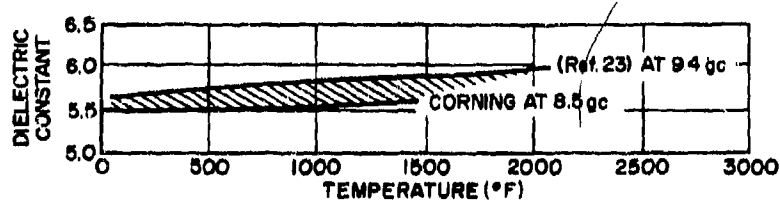


Figure 4-23. Dielectric Constant of Pyroceram

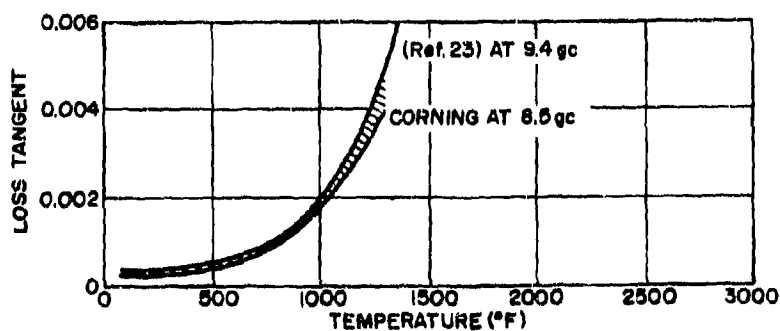


Figure 4-24. Loss Tangent of Pyroceram

TABLE 4-5 PHYSICAL PROPERTIES OF VITREOUS SILICA

Apparent density, gm/cm <sup>3</sup>	2.2
Porosity, %	0.00
Water absorption, %	0.00
Gas permeability	Nil
Hardness, Knoop, 100-gm load, kg/mm <sup>2</sup>	560
Bend strength, psi (abraded specimen), at 77°F	7160
Modulus of elasticity (Young's modulus), psi $\times 10^6$	10.5 at 77°F
Poisson's ratio, at 77°F	0.16
Dielectric constant, 10 <sup>6</sup> and 10 <sup>10</sup> cps, From room temperature to 900°F	3.85
Loss tangent, cps $\times 10^6$	0.00002 to 560°F 0.0001 at 730°F 0.001 at 915°F
Specific heat, Btu/lb/°F	0.17 at 77°F
Coefficient of linear thermal expansion, to 500°F, (in./in./°F) $\times 10^{-6}$	0.31
Thermal conductivity, Btu/ft <sup>2</sup> /hr/ft/°F at 77°F	0.77

Important properties of clear, vitreous, wholly dense fused silica are given in Table 4-5 (Reference 23).

While telescope lens blanks larger than any ceramic radome have been made of vitreous silica, it is improbable that missile radomes will be fabricated from vitreous silica. Its low strength and especially its glassy brittleness make it vulnerable to rain erosion and handling damage, and its fabrication cost would be excessive. Also, its high thermal conductivity would require internal insulation for protection of electronic equipment.

#### 4-5.2 SINTERED FUSED SILICA

Another form of silica is produced by wet-grinding fused vitreous silica to a powder, shaping it to a desired form by slip-casting in a plaster mold, then sintering it to bond the particles into a strong, coherent, porous solid. The resulting material, termed *sintered fused silica* to distinguish it from vitreous silica, is inexpensively shaped into large or complex forms and has most of the advantages of vitreous silica.

Sintered fused silica must be regarded as a candidate for radome use, rather than as an established radome ceramic. At this time, it has not been accepted for use on any missile.

Very substantial research and development effort has been applied to its processing and property evaluation, mainly at the Engineering Experiment Station of Georgia Tech. Numerous publications (summarized in Reference 2) have emanated from the studies and the results have given impetus to detailed consideration of sintered fused silica for missiles. Its outstanding resistance to severe thermal shock, such as developed under reentry conditions, has been demonstrated and large radome shapes have been successfully made and subjected to various tests. The raw material, fused silica, as powder or slip, is available from several sources and several ceramic manufacturing companies have applied the results from Georgia Tech to produce radomes and other shapes. Its ready availability, together with its ease of fabrication and probable low cost, have stimulated several missile contractors to work with this material.

The physical properties of sintered fused silica have been determined in as a great detail as have those of the other ceramics discussed. One reason is that the material is quite sensitive to variations in time and temperature of sintering, so that a "standard" material has been fully defined. The explanation for this sensitivity lies in the mechanism postulated for the process of sintering the silica particles. It

TABLE 4-6 PHYSICAL PROPERTIES OF SLIP-CAST SINTERED FUSED SILICA

	Georgia Tech	Corning Code 7941
Apparent density, gm/cm <sup>3</sup>	1.9 to 1.95	1.9 to 2.1
Porosity, void volume, %	14 to 15	2.5 to 12
Water absorption, %	7 to 8	1 to 6
Permeability	Permeable	....
Bend strength (modulus of rupture), psi	4500	6300
Compressive strength, psi	17,000	....
Modulus of elasticity (Young's modulus), psi $\times 10^6$	3.8	5 to 8.5
Poisson's ratio	....	0.15
Tensile strength, psi	3500	....
Dielectric constant		
Frequency, gc	10	8.6
Constant	3.17*, 3.38**	3.32
Loss tangent		
Frequency, gc	10	8.6
Tangent	0.0002*, 0.0008**	0.0007 to 0.0016
Specific heat, Btu/lb/°F	0.16	0.18
Coefficient of linear thermal expansion, in./in./°F	0.3	0.3
Thermal conductivity, Btu/ft <sup>2</sup> /hr/ft/°F	0.35	0.5
Thermal diffusivity, ft <sup>2</sup> /hr	0.018	0.025

\* See Reference 2.

\*\* See Reference 24.

is believed that the development of a strong bond between the individual particles of silica requires the generation of at least a small amount of a crystalline form of silica known as cristobalite. Cristobalite forms when vitreous silica is heated to temperatures in the vicinity of 2000°F and greater. Its formation is a time-temperature function; the hotter it becomes, the faster it forms, up to perhaps 2600°F. When the slip-cast article is heated to its sintering temperature of 2100°F to 2200°F, cristobalite forms first at the exterior of each tiny fused silica grain. If the sintering time is carefully limited, only enough forms to make a good bond between the grains.

Cristobalite is, however, very undesirable in larger quantities. Its thermal expansion is far greater than that of fused silica, so that its

presence in appreciable amounts is ruinous to thermal shock resistance. The art of sintering consists of balancing conditions to develop adequate strength without seriously degrading thermal shock resistance. The parameters are now quite well defined and reproducible properties are readily developed.

Published data on sintered fused silica are issued mainly from the work at Georgia Tech. Data on a similar material have been published by Corning (Reference 23). The data from Georgia Tech represent bodies sintered 3-1/3 hr at 2200°F; processing details of the Corning body are not given. Table 4-6 compares the data from the two sources, at room temperature, unless otherwise indicated. Figures 4-25 to 4-31 present available elevated-temperature property data.

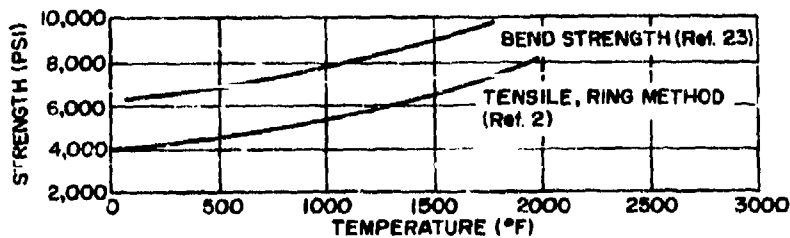


Figure 4-25. Strength Data on Slip-Cast Sintered Fused Silica

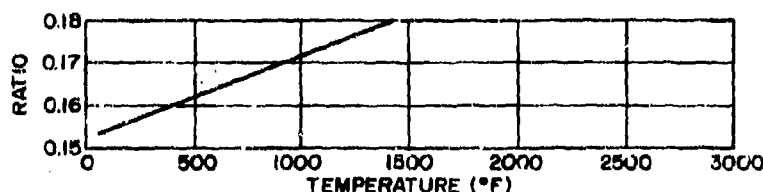


Figure 4-26. Poisson's Ratio of Slip-Cast Sintered Fused Silica (Ref. 23)

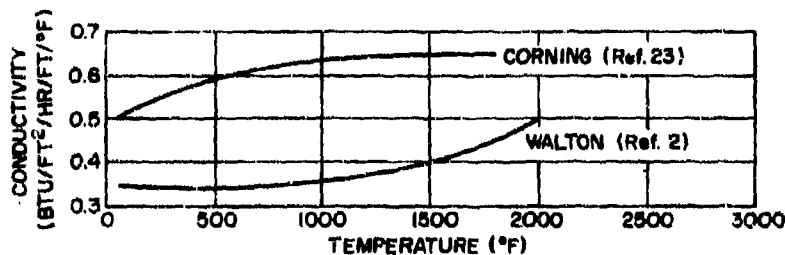


Figure 4-27. Thermal Conductivity of Slip-Cast Sintered Fused Silica

Certain characteristics of sintered fused silica are immediately evident:

1. Very low thermal expansion, conferring extremely high resistance to thermal shock
2. Low strength, from 400 to 7000 psi
3. Low thermal conductivity
4. Low specific gravity
5. Good dielectric properties up to fairly high temperatures
6. Porosity and permeability

Without some form of impervious surface layer, sintered fused silica would be vulnerable to moisture penetration and, therefore, not suitable for radome use. Fortunately, the low thermal expansion of silica makes possible a special technique for coating its surface, simply by rapidly fusing the surface by high-intensity

heat sources, such as oxyacetylene flames or arc plasma torches. If the surface fusion operation is carefully conducted, a thin layer of fused vitreous silica is formed that is impervious and seals the porous structure against moisture penetration. The fused skin is chemically identical to the rest of the radome, so that there is no problem of matching thermal expansion of skin and core. Techniques have been developed for rotating a radome beneath a high-intensity heat source to melt and solidify progressively an overlapping spiral, and thus eventually coat the whole structure with a layer of rapidly melted and chilled vitreous silica (Reference 2).

Another approach is to seal the surface with a glaze-like material whose coefficient of thermal expansion is low enough to match the



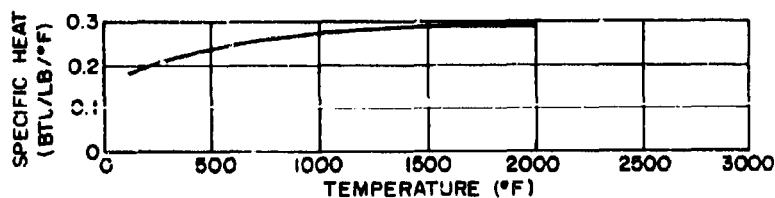


Figure 4-28. True Specific Heat of Slip-Cast Sintered Fused Silica (Ref. 23)

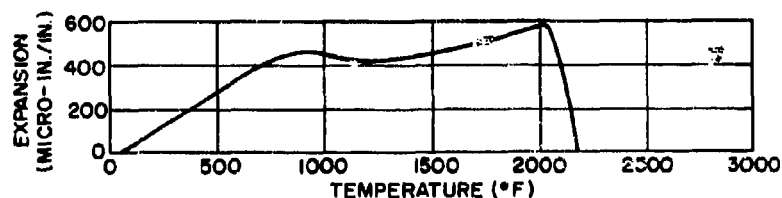


Figure 4-29. Thermal Expansion of Slip-Cast Sintered Fused Silica (Ref. 23)

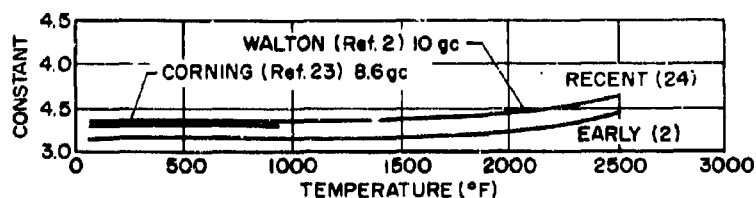


Figure 4-30. Dielectric Constant of Slip-Cast Sintered Fused Silica

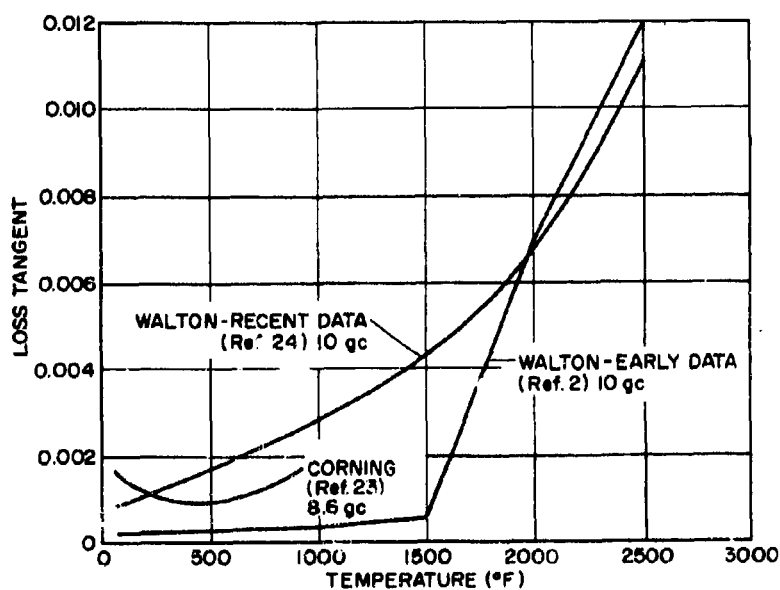


Figure 4-31. Loss Tangent of Slip-Cast Sintered Fused Silica

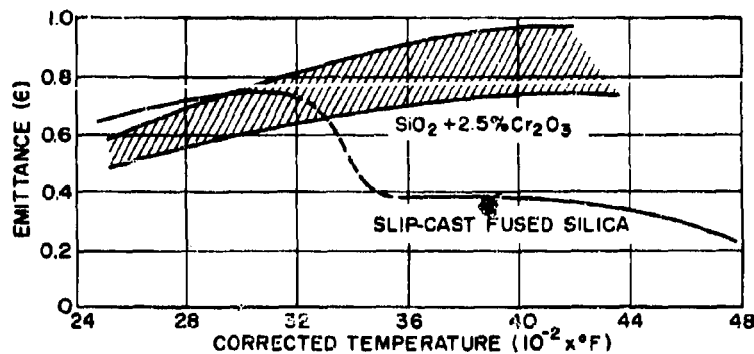


Figure 4-32. Comparison of Effective Emittance vs Corrected Surface Temperature of Slip-Cast Fused Silica with and without Chromium Oxide

sintered fused silica. International Pipe and Ceramics Corporation has made such a coating available for testing.

Much effort at Georgia Tech has been devoted to modifying sintered fused silica by additives that will improve its ablation resistance and increase its thermal emittance, and that will make it suitable for short-time resistance to temperatures of 3500°F to 4000°F that develop under reentry conditions. This work has been carried out under Air Force sponsorship.\* It has been demonstrated that  $\text{Cr}_2\text{O}_3$  in quantities of about 2-1/2%, is the one additive that confers significantly improved emittance and ablation resistance. The effective emittance of slip-cast fused silica and slip-cast silica plus 2-1/2%  $\text{Cr}_2\text{O}_3$  was reported in Reference 2 and is shown in Fig. 4-32.

The low strength of sintered fused silica has discouraged many potential users, who fear it would not stand ordinary handling. Corning states that it has developed a chemical treatment for sintered fused silica that increases its bend strength to 17,000 psi; it appears that this development has not yet been evaluated on actual radomes. In contrast to alumina, which may require all of its strength for thermal loading, slip-cast fused silica requires very little strength for thermal loading. Practically all of its strength is available for structural and aerodynamic loading. Also, the strength of

slip-cast fused silica increases with temperature, and above 2000°F, its strength is comparable to alumina.

The low thermal conductivity of sintered fused silica permits the surface to be intensely heated, up to incipient or actual fusion, while the bulk of the radome stays at a temperature at which strength is sufficient to maintain structural integrity. Although long-term exposure to temperatures above 2000°F to 2200°F will cause crystallization (devitrification), loss of toughness and heat shock resistance, rapid heating for short periods can be carried to much higher temperatures.

Rain erosion tests on a sled at speeds approaching Mach 3 revealed that this material erodes considerably in a rain field at such speeds, but that radomes will survive if the nose thickness is made substantial enough to tolerate such erosion. The mechanical strength of the radomes was entirely adequate to withstand the severe vibrations encountered during the sled runs, estimated to generate vertical accelerations up to 100 g's. The presence of a fused, impervious surface skin did not seem to have a major effect upon rain erosion resistance.

The extreme thermal shock resistance of sintered fused silica has been abundantly demonstrated. When tremendous heat fluxes must be withstood for relatively short times, as in reentry, there is little doubt that this material warrants thorough service testing.

\* AF 33(657)-11504, Air Force Avionics Laboratory, RTD, Wright-Patterson Air Force Base, Ohio.

#### 4-6 PROPERTIES OF BERYLLIA RADOME MATERIALS

The general mechanical properties of beryllia are those of a sintered oxide ceramic. It is brittle, with no measurable ductility except at very high temperatures. It is hard, capable of a high surface finish by diamond grinding, dimensionally and physically stable to very high temperatures, and very acceptable from a dielectric standpoint. Its unique property is its high thermal conductivity, especially at moderate temperatures. In this ability to conduct heat, it exceeds all ceramics and most metals at temperatures up to the red heat range. Its conductivity decreases very quickly with increasing temperature, so that its outstanding superiority disappears at high temperatures.

Beryllia's mechanical strength is only slightly less than that of alumina. However, great progress has been made toward obtaining higher strengths. Part of this improvement has been achieved by going to a high purity; this has offsetting disadvantages, however, such as higher sintering temperature and more distortion. As with alumina, it is difficult to state a representative value for modulus of rupture. Beryllia manufacturers now claim values of 35,000 to 40,000 psi on small specimens fired with larger objects. This compares with values of 45,000 to 60,000 psi claimed for similar small

samples of alumina with 99% (or higher) purity. It seems probable that the longer sintering cycles needed for large radomes would lead to grain growth that would, in turn, result in lower transverse rupture strengths, perhaps 25,000 to 30,000 psi for beryllia and 35,000 to 45,000 psi for alumina.

Beryllia has a relatively high coefficient of thermal expansion as compared to the other ceramic radome materials. This offsets to some degree the beneficial effect upon thermal shock resistance conferred by its extraordinary thermal conductivity.

Table 4-1 contains the properties of beryllia of importance from a radome standpoint, and Figs. 4-33 to 4-40 show the effect of temperature on some of these properties. There is good agreement among the cited sources of most of the data; the principal uncertainty remains that of bend strength or modulus of rupture, as mentioned earlier. No recent data were found on the effect of elevated temperatures upon strength properties of beryllia with high density and purity. The summary of refractory ceramics prepared by Battelle under Air Force sponsorship (Reference 5) graphically suggests that strength in tension is only slightly lower at about 2000°F than at room temperature, but much lower at 2500°F, whereas compressive strength may decrease by nearly 50% at only 1000°F.

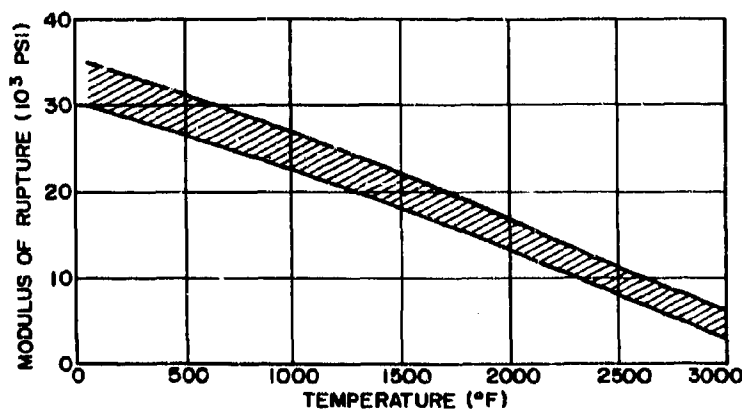


Figure 4-33. Approximate Modulus of Rupture of Radome Beryllia, 99% Pure, 95% Dense (Ref. 25)

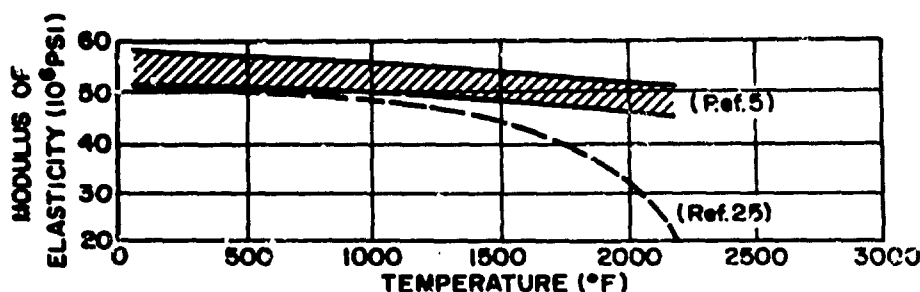


Figure 4-34. Modulus of Elasticity of Beryllia

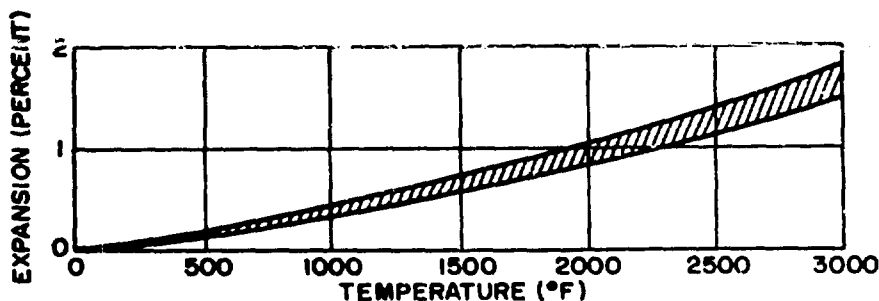


Figure 4-35. Linear Thermal Expansion of Beryllia (Ref. 5)

The dielectric constant of beryllia increases gradually with temperature, increasing by only about 30% up to at least 3000°F, with a rate of change similar to alumina. See Fig. 4-39. The loss tangent is sensitive to minor impurities. High-purity beryllias do not undergo rapid increase in loss below 2400°F to 2500°F, but other beryllia samples only slightly less pure may undergo an excessive increase in loss tangent below 2000°F. At lower frequencies, the loss tangent starts to increase rapidly at slightly lower temperatures. Note that such measurements are made under isothermal conditions, whereas in a radome there is generally a thermal gradient, so that most of the ceramic is substantially cooler than the tip and outer surface. Such gradients will be appreciable even in a good thermal conductor such as beryllia; Fig. 4-36 shows that thermal conductivity in the red heat range is only a small fraction, 10% to 15% of the room temperature conductivity.

Beryllia ceramic producers, striving for higher purity and density, have made significant improvements in strength and dielectric loss properties. Even more significant has been the progress in reducing the lack of reproducibility of properties that was a problem in

earlier efforts to promote beryllia. Improved controls over raw materials processing and ceramic fabricating have been effective in minimizing variations from lot to lot and from piece to piece.

There is, then, no doubt that beryllia can be fabricated into radomes with excellent properties. Cost will be the major problem, not only because the raw materials are expensive, but because beryllia is a health hazard and requires an unusually high sintering temperature. Also, for large radomes, the high firing temperature and high shrinkage would further increase the cost of such radomes.

#### 4-7 PROPERTIES OF INORGANIC-BONDED GLASS FIBER LAMINATES

A project to develop a glass fiber laminate using an inorganic binder to provide resistance to high temperatures has been sponsored by the Air Force at the Brunswick Corporation, Defense Products Division (Reference 23). The objective is to produce a radome capable of prolonged service at temperatures up to 1200°F.

Techniques have been developed to bond refractory glass fibers by aluminum phosphate

formed by the reaction, in situ, of aluminum hydroxide and phosphoric acid. Radomes of considerable size have been made, as shown in Fig. 4-41, and physical properties have been determined, as shown in Table 4-7.

The problem of low flexural strength values at temperatures around 600°F is causing concern and is being studied. Strength loss during aging at elevated temperatures is also receiving further study through the use of low-expansion fillers.

Techniques for protecting radome shapes of this material against rain erosion, such as the use of nose caps of thin alumina or metal, are being studied, and the material is being proposed for use in new missiles.

Work on a similar formulation, using vitre-

ous silica fibers instead of refractory glass, was carried out by General Electric under Navy sponsorship (Reference 29). Phosphate-bonded silica fibers had good short-time properties at 1000°F, but weakened severely upon prolonged heating at that temperature.

Another approach, using vitreous silica fibers filament-wound, bonded with silica, then cured and impregnated with acrylic resin, was studied at Lockheed Missiles and Space Company (Reference 30). The resin was to provide transpiration cooling in the outer layer, which was backed by a low-density insulating inner shell of randomly oriented silica fibers bonded with a silica binder.

The availability of small quantities of alumina whiskers or monocrystalline fibers a few

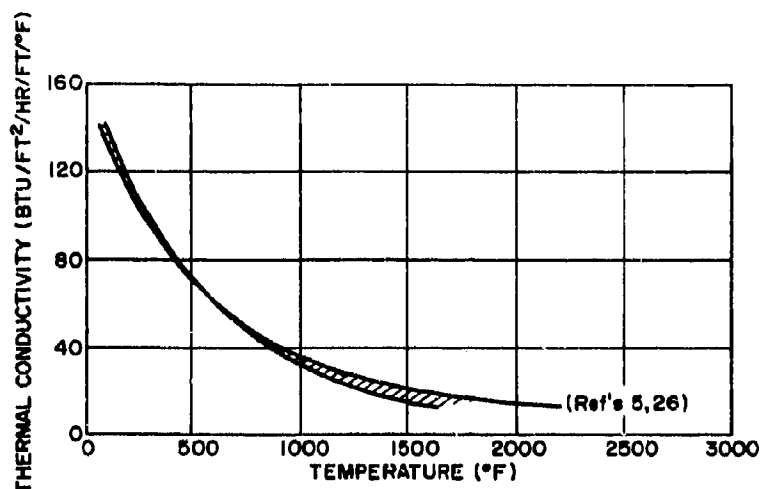


Figure 4-36. Thermal Conductivity of Beryllia as a Function of Temperature

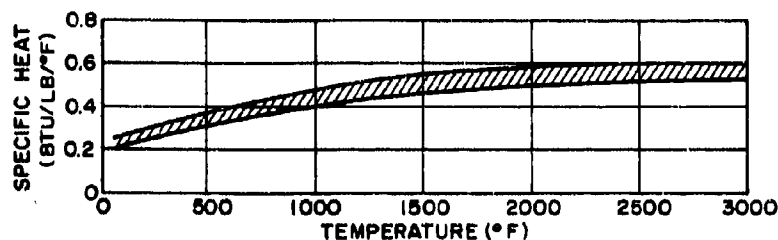


Figure 4-37. Specific Heat of Beryllia as a Function of Temperature (Ref. 5)

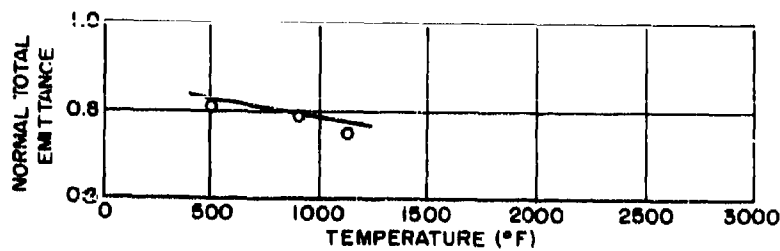


Figure 4-38. Normal Total Emittance of Beryllia (Ref. 12)

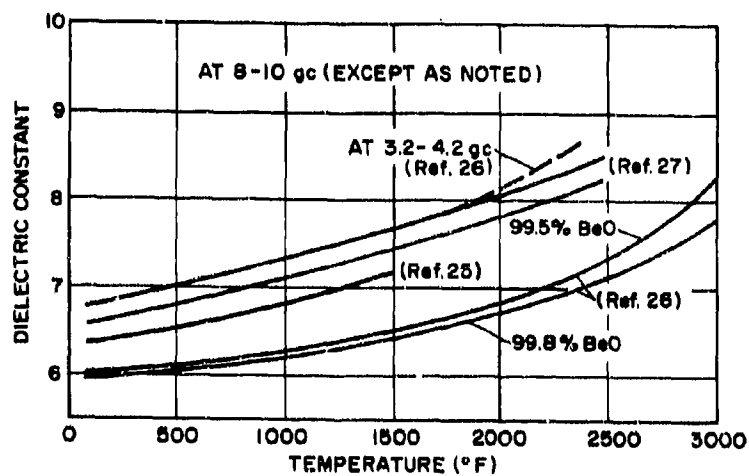


Figure 4-39. Dielectric Constant of Radome Beryllias

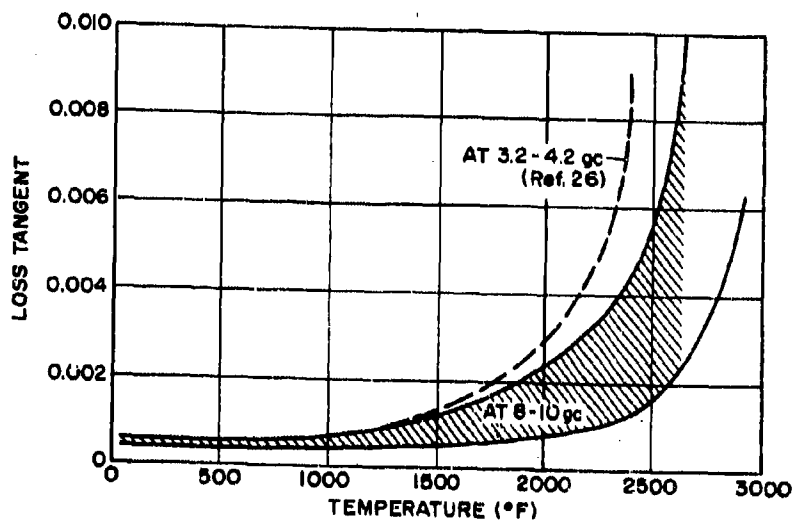


Figure 4-40. Loss Tangent of Beryllia as a Function of Temperature

**TABLE 4-7 INTERIM PROPERTIES OF GLASS REINFORCED ALUMINUM  
PHOSPHATE MATERIAL\***

Temperature	Room	500°F	1000°F	1100°F	1200°F
Flexural strength, psi $\times 10^3$	30	15	.....	25	.....
Tensile strength, psi $\times 10^3$	30	24	6	.....	.....
Compressive strength, psi $\times 10^3$	5	.....	.....	.....	7
Flexural modulus, psi $\times 10^5$	4	2	.....	.....	4
Thermal expansion					
Dielectric constant, gc $\times 10$	3.4	3.6	3.6	.....	3.6
Loss tangent, gc $\times 10$	0.008	0.01	0.015	.....	0.02
Average thermal expansion to 1200°F					
Parallel to ply, $\times 10^{-6}/^\circ\text{F}$				2.2	
Perpendicular to ply, $\times 10^{-6}/^\circ\text{F}$				6.0	
Thermal conductivity to 1200°F, Btu-in./hr/ft <sup>2</sup> /°F				4.3	
Specific heat (500°F), Btu/lb/°F				≈0.2	
Specific gravity				1.8	
Moisture absorption, % (24 hours, after 200 hours at 1000°F)				0.63	

\* Made with Owens Corning S-994 glass fibers coated with Dow Corning 805 silicone resin, woven as style 143 fabric.

microns in diameter has stimulated efforts to use them as reinforcing agents in ceramic or inorganic polymer structures. An Air Force project has been carried out with Horizons, Inc. to incorporate alumina filaments into a radome structure (Reference 31). Such filaments have tensile strengths in excess of 200,000 psi; the problem is to utilize such strength. Ceramic materials and cements tend to react destructively with the filaments when heated into the red heat range. No inorganic polymers have been developed with sufficiently good properties to warrant intensive efforts to reinforce them with whiskers. However, the art of using these enormously strong little fibers may eventually advance to a degree that will make possible a new type of radome, with appreciable toughness coupled with the high-temperature resistance of ceramic materials.

#### **4-8 PROCESSES FOR FABRICATING CERAMIC RADOMES**

##### **4-8.1 PRODUCTION OF ALUMINA RADOME BLANKS**

The technology of fabricating high-alumina materials into radome shapes has now been developed by several manufacturers. Each process follows the same general steps:

1. Blend powdered alumina with minor additions of other powdered ceramic oxides and organic binders to form either a fluid suspension or a dried, free-flowing granular powder.
2. Form the blended ingredients into desired shape, with allowance for shrinkage and grinding.
3. Heat the shape to a high temperature to

sinter and consolidate the individual powder particles into a strong, impervious solid structure.

Within each of these process steps, there are variations that distinguish the practice of one manufacturer from that of another. These variations are described in the following paragraphs, together with the reasons for their use.

#### 4-8.1.1 Raw Materials and Their Processing and Blending

Commercial alumina powders are available in a wide range of particle size, purity, and reactivity. The ceramic behavior of aluminas is profoundly affected by both purity and particle size and surface area. Shrinkage of an alumina article during sintering can range from less than 10% if it is made from relatively coarse, dense particles, to over 20% if very fine, high-surface-area powders are used. Serious departures from desired dimensions in a radome can result if the particle distribution of the alumina powder departs appreciably from the normal pattern.

Although the use of coarse, dense alumina powders leads to less shrinkage and better dimensional control, such powders are relatively inert and require very high sintering temperatures to achieve impermeability. Finer powders sinter at lower temperatures. Their greater shrinkage may be offset by fuel savings because of lower firing temperatures, and by less distortion of the sintered radome because the supporting refractories undergo less warpage and movement.

One solution to this problem of particle sizing vs. sintering temperature is to presinter the alumina powders, after the addition of minor amounts of fluxing oxides, such as magnesia, silica, and calcia, into dense fragments that are then ground to a fineness suitable for forming by slip-casting. This approach, pioneered at Rutgers (References 32, 33), permits substantial lowering of the sintering temperature while still achieving impermeability and required density. The cost of this additional processing must be balanced against the benefits of the reduced sintering temperature.

When commercial alumina powders are used without this presintering, careful control on



Figure 4-41. Radome Finish of Glass-Reinforced Aluminum Phosphate

particle size distribution of incoming powders ensures the needed degree of reproducibility of sintering shrinkage. A batch of alumina powder that shows particle sizing outside of specified limits may be rejected or blended with acceptable material in small quantities until consumed. While the primary standard for particle size determination is usually the time-consuming Andreason pipette method, the routine plant inspection of incoming batches and blends may be quickly performed by checking the rate of change of specific gravity, by using a hydrometer, or by other quick tests.

When proper powder size distribution has been verified, the alumina may be mixed with the minor flux additions and with organic "temporary binders." These binders are needed to hold the powders together after forming; they would cohere only weakly or not at all if such binders were not mixed with the powders before forming. Many diverse kinds of organic binders are used, including waxes, resins, gums, and other compounds. Their selection is part of the art of making oxide ceramics. They must disperse readily throughout the powders, bind the powder mass during the forming process strongly enough to permit handling the formed object, and burn off without leaving any residue



during the early stages of the sintering process.

Blending may be either dry or wet. Dry blending is carried out by tumbling or by mixing in bread-mixer or muller-type mills. The mix may be further processed by screening or pulverizing to give a dry, free-flowing powder. Wet blending is usually done in rubber-lined ball mills, in which the balls perform a mixing, rather than a grinding, function. The proper quantity of water or nonaqueous liquid is added to give a slurry of the desired consistency for subsequent processing.

One common practice is to spray-dry the wet mix, to give dry, spherical powder particles. Advocates of this technique believe that wet milling followed by spray drying gives a more uniform dry mix than dry milling. The spray-drying step is an added cost, but the powdered mix so produced has excellent flowing and forming characteristics. Such mixes are used in dry-fill radome forming, described later.

When the radome is to be formed by slip-casting, the blend of oxide powders and binders is ground to extreme fineness with water in a ball mill. The mill is usually lined with alumina and alumina balls are used to prevent contamination of the mix by material abraded from the mill or balls. Milling time is determined by experience and is the major control over particle size distribution, after the ratio of charge to ball weight in the mill has been determined by experiments.

Whatever the sequence of blending steps, the end result is either a dry powder or a fluid suspension, carefully compounded to ensure proper forming properties and uniformity of sintered physical characteristics in the finished radomes.

#### 4-8.1.2 Forming and Shaping the Radome Blank

Alumina radomes are now generally formed either by isostatic pressing or by slip-casting. Since slip-casting is presently of only minor commercial importance, it warrants only brief discussion. Commercially produced alumina radomes are being manufactured by several firms today by variations of the isostatic pressing method (otherwise known as hydrostatic pressing).

**4-8.1.2.1 Forming by Isostatic Pressing.** When powder or a compacted shape of low density is sealed within a rubber envelope and subjected to hydrostatic pressure by immersion in a fluid under pressure in a heavy pressure vessel, it is compressed uniformly from all directions. No other pressing method for compacting powders is capable of increasing density in such a uniform manner, nor can such high pressures be readily attained by other methods. Compacting at very high pressure reduces the amount of shrinkage that takes place during subsequent sintering.

Two alternate practices are used to prepare an alumina radome shape for isostatic pressing. Both practices use a heavy steel mandrel shaped to the inside contours of the radome, plus an allowance for shrinkage. In one method, the layer of mix is applied to the mandrel by spraying; in the other, it is applied by filling a cavity between the mandrel and the enclosing rubber bag by flowing a free-flowing dry mix into the cavity and vibrating it to ensure absence of pockets. In both cases, the rubber bag is then evacuated, the evacuating tube clamped tight, and the mandrel and surrounding bag and contents lowered into the massive steel pressure vessel. Here, it is subjected to pressures that may range between 5000 and 35,000 psi, by means of water or hydraulic fluid pumped into the vessel.

The radome shape is uniformly compacted to high density and freedom from voids or soft spots by this pressure. When the pressure is released and the bag removed, the radome blank expands slightly and slips readily off the mandrel. A description of one manufacturer's process is given in Reference 34.

Other manufacturers of alumina radomes modify this process by machining the blank just as it is isostatically pressed, in the so-called *green* condition, rather than after a preliminary sintering step.

**4-8.1.2.2 Forming by Slip-Casting.** *Slip* is a potter's term for a fluid suspension or slurry of finely-ground particles of ceramic ingredients in water or other liquid. Slip-casting is a long-established method for forming relatively intricate shapes by pouring slip into a porous mold, generally made of gypsum plaster, which sucks liquid out of the slip at a rate that causes a skin of the ceramic ingredients to build up

gradually against the mold surfaces. When this skin has grown to the desired thickness, the excess slip can then be decanted. The resulting shaped article within the mold cavity is rubbery and tenacious. As it dries, it shrinks away from the plaster mold wall and can be readily removed for further drying.

Alumina formulations can be slip-cast without much trouble, after the optimum particle sizing, deflocculent and binder additions, pH, and other factors to make the slip behave properly have been worked out. The slip can simply be poured into a plaster mold, base end up, and allowed to stand until the skin has become sufficiently thick. Pioneering work on radome manufacture by slip-casting was carried out at Rutgers University under Navy sponsorship (References 32 and 33).

The Rutgers process, which has formed the basis for considerable work by others, embodies two steps:

1. A unique body preparation technique particularly suitable for high-alumina bodies, wherein the ceramic raw materials are blended and formed into some convenient shape and presintered or given a preliminary fire. This effects all phase changes and the shrinkage due to them and volatilization of raw materials components. The fired body is then wet ground to a slip of carefully controlled particle size distribution.
2. Pressure slip-casting, which entails forcing slip into the annular space defined by two sections of a hard plaster mold, one a female cavity to define the external configuration and the other a mandrel to define the internal configuration of the radome. The high pressure (50 to 200 psi) literally forces the water out of the casting into the mold sections so effectively that, in a matter of minutes, a piece forms that is capable of supporting itself and has almost no drying shrinkage.

The effect of precalcining is to reduce the temperature at which the radome must be sintered to achieve impermeability and strength, and to eliminate shrinkage due to phase changes. Casting under pressure reduces the time needed to build up the desired wall thickness by driving the liquid out into the plaster mold instead of waiting for it to migrate of

its own accord. Shortening the casting time is helpful, because the particles in the slip tend to settle out and a nonpressure casting of considerable size tends to be thicker at the bottom than at the top. Pressure also eliminates the tendency of the skin to pull away from the mold wall and thereby further retard liquid migration into the mold. High pressure also eliminates drying shrinkage by effectively forcing the layer of water surrounding each particle out of the piece.

Pressure slip-casting has also been investigated by Shenango China Company under Navy sponsorship (Contract NO262073d), as a means for forming radomes so accurately to desired wall thickness and contour that little or no grinding would be required after sintering. The results on Sparrow III radome blanks of 97% alumina have shown encouraging results. Shenango holds a patent on pressure slip casting.

#### 4-8.1.3 Shaping, Sintering, Grinding, and Inspecting

The cast or pressed radome blank may be machined to desired shape in the soft or green state if the organic binders used give sufficient strength to permit handling the green piece. Whether or not this step is carried out, the blanks are next heated to a low temperature to burn out the organic binders. Next, they are sintered at a high temperature in the vicinity of 3000°F; sometimes they are sintered first at a lower temperature of about 2400°F. In the latter case, they emerge in a firm but rather chalky state, soft enough to permit accurate machining to desired contour and wall thickness. After this so-called *bisque* machining, they are reheated, this time to the high sintering temperature.

As with all pure oxide ceramics, control of time and temperature in sintering is critical. Excessive grain growth and shrinkage result from overheating or holding too long, while insufficient exposure to heat will leave the blank in a weak, porous condition.

The fully sintered blanks are then ground inside and out to precise wall thickness and contour; the external contour may be altered by grinding to form *lens* contours adapted to requirements of the guidance system. This

grinding requires diamond wheels and special precision grinders.

At various stages, blanks are inspected for cracks, surface defects, excessive warpage, and other defects. After grinding, electrical bore-sight testing reveals areas in which corrective removal of alumina or addition of patches is necessary to achieve desired electrical transmission patterns.

#### 4-8.1.4 Limitations on Size of Alumina Radomes

Monolithic alumina radomes have been made up to 42 in. high by 14 in. in base diameter. The cost increases rapidly as sizes exceed this presently achievable limit. Diamond grinding costs are probably the most significant factor in this rapid increase. Small radomes can be made close enough to final size and wall thickness to require only a modest extra thickness to compensate for warpage and variable shrinkage, but much greater excess wall thickness is required as size increases. The high shrinkage of alumina, like other sintered oxide wares, is the factor causing this provision for grinding allowance. The linear shrinkage of current radome alumina formulations is from 10% to nearly 20% during sintering to desired density. The larger the shape, the greater its weight, and the higher the load imposed on the bottom portion of the radome during sintering. Although very large shapes can be successfully fabricated, their walls must be quite thick to support their weight during sintering. Numerous expedients have been considered for supporting large shapes during sintering, but none gives complete control over distortion.

In 1958, the Air Force, through Wright Air Development Command, and later the AMC Manufacturing and Materials Technology Division, sponsored a project to investigate the feasibility of monolithic 99% alumina radomes 9 ft. high. Three companies competed in preliminary contracts to develop techniques on scale models 40% of the final size. Radomes 39 in. high by 13 in. in base diameter, with wall thicknesses of 0.100 in., were successfully produced and submitted for thermal shock testing. While several companies submitted proposals to produce the desired 9 ft. shape, the costs of tooling and of fabricating prototypes were considered prohibitive.

In addition to the costs imposed in diamond grinding the excessively heavy wall to final thickness, the costs of production equipment increase rapidly as the size of the blank increases beyond present capability. Principal items are isostatic presses, grinding lathes, and kilns. While sufficiently large equipment can be made in each of these categories, no ceramics manufacturer now has any of these three essential items in extra-large sizes. Accordingly, each quotation for very large alumina radomes must include large capital costs in addition to manufacturing costs.

#### 4-8.1.5 Composite Alumina Radome Fabrication Project\*

The extremely high cost estimates submitted for fabricating monolithic radomes 9 ft. high by 3 ft. in base diameter led the Air Force to seek alternate methods of achieving the desired large radome. In 1962, Contract AF 33(657)-1011 was awarded to Narmco Research and Development, a Division of Whittaker Corporation, under ASD Project NR 7-984, to carry out a research program directed toward the fabrication of large ceramic radomes by bonding small segments together into a large structure capable of operation to 1000°F (Reference 20).

Initial work was carried out not only on alumina, but also on beryllia and zirconia, with which a number of possible refractory cement formulations were tried. Zirconia was eliminated from further testing because of poor electromagnetic properties and beryllia was eliminated later because it was found to offer no advantage over alumina sufficient to justify its much higher cost.

Cements were found that matured to quite strong bonds when sintered at temperatures well below the softening temperature of alumina. Good electromagnetic properties were obtained in the assembled composite samples because the cement layers were very thin. The cements themselves had rather high loss tangents. Progress was made toward supporting tooling materials and design to hold the assembly during sintering of the cement.

\* See also Paragraph 4-3.2.

This contract is still active, with procurement of large numbers of accurately shaped segments underway preparatory to trials on a larger scale.

#### **4-3.1.6 Fabrication of Multilayer Alumina Sandwich Radomes**

Dense, monolithic alumina radomes become very thick and heavy when designed for the lower range of frequencies. They also lack adaptability to broadband requirements. What is more serious is that calculations of thermal shock on radomes of the new generation of very fast missiles show that neither alumina nor glass-ceramics can withstand the higher thermal stresses.

It has long been recognized that highly porous ceramics, often called foamed ceramics, offer lower dielectric constants and lighter weight. Under Navy sponsorship, Contract NOas 59-6222C, highly porous alumina formulations have been studied for radome use. For broadband requirements, sandwiches consisting of alternating layers of dense and porous alumina were found to have promising transmission characteristics. Further development led to a technique for fabricating radome shapes having a dense skin, all of approximately 95% alumina, under Navy Contract N62269-1370.

Such composite structures in the general category of "A" sandwiches are formed by slip-casting. A plaster mold with the exterior contours of the radome, with allowance added for shrinkage, is filled with slip suitable for dense alumina. When a skin of desired thickness has formed against the porous mold, the excess slip is removed. Then a slip of similar composition but containing tiny organic particles is poured and allowed to sit until a second layer has formed to desired core thickness and containing a uniform dispersion of the tiny organic pore formers. Lastly, a slip for dense alumina is poured to form the inner skin. After drying and sintering at about 3000°F, the structure is firmly and coherently bonded into a composite, the core of which has many tiny pores left by the organic burnout addition.

At present, the dense skins can be made to thickness between 0.025 and 0.050 in., and the porous core can vary between thicknesses of

about 0.1 and 0.5 in. Shapes up to 9 in. high by 7 in. in diameter have been made, and much larger sizes are in preparation at Interpace.

Such a composite radome cannot be finished by grinding because the dense exterior skin is too thin. Since it is the equivalent of a thin-wall radome from an electromagnetic transmission viewpoint, however, achievement of precise contours and wall thickness is not by any means as important as would be the case for a half-wave wall thickness.

#### **4-9 FABRICATION OF GLASS-CERAMIC RADOMES**

Information covering the manufacture of glass-ceramic radomes is limited to that released by Corning Glass Works. The information supplied by Corning is as follows:

The raw materials, or batch, used in making Pyroceram are processed in an optical glass melting unit to ensure absolute temperature control and to eliminate contamination factors. Treatment of the molten batch includes stirring for homogenization prior to delivery through an orifice. The flow rate through the orifice is precisely metered on a continuous basis 24 hr a day. The material flowing through the orifice is periodically loaded into steel molds having a configuration that produces the external radome shape required, including excess stock to allow for finish grinding.

The configuration of the glassy blank required indicates the kind of steel mold equipment and forming process that will be employed. Large blanks are centrifugally cast in a female mold maintained within a critical temperature range. Small blanks are usually pressed between a plunger and female mold cavity. The material has the same composition and is subjected to the same thermal treatment for either blank forming operation.

The hot, formed blank is placed in a glass annealing kiln, called a lehr in the glass industry, to undergo controlled cooling and remove stresses. The cooled blanks can then be inspected. When cooled, the radome blanks are transparent, glassy bodies, thereby permitting 100% visual inspection by transmitted light for possible imperfections in the material, such as blisters and inclusions of foreign matter.

Marginal defects are evaluated under a bright light with the aid of a microscope. Rejected radome blanks are physically broken. Those blanks having acceptable glass quality are inspected dimensionally.

After this inspection, the blanks are placed in the ceramming kiln to undergo the thermal treatment that converts the glassy blank into a glass-ceramic material having prescribed properties.

#### 4-9.1 RADOME FINISHING

The internal surface of the radome configuration is established during the initial phase of the finishing process by a combination of diamond wheel grinding and abrasive grit lapping. The internal surface is by necessity generated as a figure of revolution and is virtually identical from piece to piece.

The external surface is generated as a figure of revolution using diamond wheel grinders. Each radome fits on a common mandrel having a conjugate surface that supports the glass-ceramic part uniformly. Pyroceram radomes with a wall thickness of 0.050 in. and an area of 5 sq. ft. have been successfully ground.

A prescription is ground on the external surface of a radome having excess wall thickness, following the preliminary external grinding operation on a less complex grinding machine having a plane template. A prescription grinder must be equipped with a three-dimensional template, such as a patched radome developed during a prototype program. Wall thickness and other critical dimensions are held to  $\pm 0.002$  in. Reproducibility of the complex radome shape and the prescription has been demonstrated on thousands of radomes by comparison with a common dimensional master and uniformity of electrical data.

#### 4-9.2 PRODUCTION CAPABILITY

Glass-ceramic radomes have been made in sizes up to 16 in. in diameter and lengths to 42 in. Finished wall thickness has varied between 0.050 and 0.600 in. Nose geometry has varied from pointed to 5 in. in diameter. Constant wall, tapered wall, and prescription wall domes are produced using basic machinery of the metal

trades adapted to ceramic work. In all sizes and shapes the conventional wall tolerance is  $\pm 0.002$  in.

The present equipment in use at Corning is capable of producing a radome 2 ft in diameter by 5 ft in height. Even larger radomes can be finished on the massive grinding lathes. The measuring unit and blank forming equipment would have to be enlarged to fulfill requirements in Pyroceram, utilizing the size capability available for contour grinding.

The inherent process techniques are claimed to be adaptable, with the addition of new and larger equipment, to producing radomes 4 to 5 ft in diameter and 12 to 15 ft in length, should the need arise.

#### 4-10 FABRICATION OF SINTERED FUSED SILICA RADOMES

The term *sintered fused silica* is used to differentiate the product made by consolidating particles of fused silica by ceramic sintering techniques from the glassy or vitreous product made by shaping molten silica into desired form. The sintered product is fabricated by slip-casting or by pressing fluid or plastic masses of finely powdered fused silica, whereas the vitreous product is made by glass-working techniques. The vitreous form of silica is being used for small electromagnetic windows, whereas the sintered fused form is proposed for radomes. Since the latter material is of much greater interest, it alone is considered.

Information on the manufacturing process was derived from Reference 2, which contains many details. Others have adopted these techniques with only minor modifications.

The raw material for the sintered product is a granular powder made by grinding fused silica. The latter is generally made by fusing silica sand or crushed quartz in an electric resistance furnace in which carbon or graphite resistance elements are surrounded by the sand and heated to the fusion temperature range. After the fused mass has cooled and is removed from the furnace, the fully fused, glassy material is separated from any incompletely melted outer portions. The glassy portions are then crushed and wet-ground in ball mills to form a finely divided powder suspended in water or slip.

This slip must be adjusted to the proper hydrogen ion concentration and particle size distribution so that it will be reasonably stable and not quickly settle. A satisfactory slip will have a pH between 2 and 6, and particles that range in size from 50 microns to about 20% less than 2 microns. Solids concentration may be about 80% to 85%, or have a density of about 1.8 gm/cm<sup>3</sup>.

#### 4-10.1 SLIP-CASTING

The technique for casting fused silica differs very little from that used for alumina, as described in Paragraph 4-8.1. The porous plaster mold is filled with slip and a coherent, leathery skin builds up gradually against the mold surfaces. Moderate pressure on the slip, on the order of 25 to 50 psi, has been found desirable to speed deposition of the skin and to minimize settling of the particles. A patent on pressure slip-casting is held by Shenango China Company (Reference 34). Normally, the plaster mold cavity is shaped to the contours of the exterior of the radome and the skin grown inwardly until the desired thickness is achieved. The mold may be oriented with the radome tip either up or down; the lower part will tend to be thicker than the upper. The slip is drained when the wall is sufficiently thick and the radome blank is gently removed after it has dried somewhat. Air may be forced inwardly through the porous plaster to assist in freeing the casting from the mold.

Wall thicknesses up to 1 in. are readily achievable, although thinner walls are usually specified for radomes. The time for casting increases quite rapidly as wall thickness is increased, especially above about 0.75 in. There are no major problems involved in casting very large shapes, other than the limitation that wall thickness must be adequate to permit subsequent sintering without distortion.

Slip-cast fused silica shrinks very little during drying and sintering. Representative linear drying shrinkage is about 0.5%, and linear shrinkage during sintering will average about 1%. Molds can, therefore, be made very nearly to final size, with little shrinkage allowance.

#### 4-10.2 SINTERING

The thoroughly dried radome blank is heated in a kiln to about 2100°F to 2200°F. The rates of heating and cooling are not critical, but the maximum temperature must be carefully controlled and the time at this temperature should be no longer than needed to develop adequate sintering. The particles of fused silica, which are wholly vitreous or amorphous before sintering, undergo a slow crystallization at temperatures above about 2000°F. During this crystal-forming process, termed *devitrification*, tiny crystals of a form of silica known as cristobalite develop, starting from the outsides of the particles and working inward. Cristobalite has higher thermal expansion than the vitreous form of silica and is, therefore, undesirable in substantial quantities. Formation of a little cristobalite is desirable and necessary to give adequate strength in the sintered article. The art of sintering is to permit only this small amount, in the order of a few percent, to form, but to avoid heating longer or hotter and thus forming too much.

#### 4-10.3 FINISHING THE SINTERED RADOME

Because silica is softer than alumina, it can be ground quite easily. In addition, turning is feasible with tungsten carbide or alumina tools. On the Mohs scale of scratch hardness, silica is seventh, alumina is ninth, and diamond is tenth. The Knoop indentation hardness value for vitreous, nonporous silica is 560; for sintered silica, with considerable porosity, it is somewhat less. Alumina has a Knoop value of about 2000 and glass-ceramics about 620. Therefore, silica is softer and easier to grind than the other ceramic radome materials. Its low thermal expansion also makes it quite insensitive to grinding damage caused by local heating under the grinding wheel.

At this time, no applications of ground sintered silica radomes have been reported.

#### 4-10.4 SURFACE TREATMENTS FOR SINTERED SILICA RADOMES

Sintered silica radomes made to date have been quite porous. Their densities do not usually

exceed  $1.85 \text{ gm/cm}^3$ , compared with  $2.2 \text{ gm/cm}^3$  for wholly dense fused silica. This corresponds to porosity of about 16%, much of which is interconnected.

Such porous structures would absorb water during storage and handling, which would seriously affect the dielectric properties. For this reason, an impervious coating becomes a necessity for sintered silica radomes. Development of such coatings has proceeded along three lines: glaze-like applied films; glassy skins formed by fusing the silica itself under intense local heat; and Teflon coatings.

The major problem in glazing silica is its very low thermal expansion. Conventional glazes used for chinaware, tile, and other ceramics expand and contract under heating and cooling far more than does silica. If attempts were made to apply them to sintered silica, they would crack and spall during cooling from the glaze firing operation, or through aerodynamic heating during service. Certain ceramic materials, notably the lithium aluminosilicates, have expansion properties comparable to silica and coatings have been successfully applied to formulations of this class. These coatings are less refractory than silica, with melting points in the vicinity of  $2200^\circ\text{F}$ , so they are protective only for moderately severe service.

Surface fusion, a second technique for sealing the radome surface, has been successfully applied to radomes as large as 31 in. high by 13 in. in diameter. The radome is supported upon a rotating turntable in a furnace heated to slightly over  $2000^\circ\text{F}$ . An arc plasma torch or oxyacetylene torch is directed against the outside of the hot radome and is systematically made to traverse the entire surface at a rate and heat intensity that result in melting a thin surface layer. This molten film solidifies into a glassy layer that is integrally bonded to the underlying porous material and that is chemically the same. It behaves, therefore, like the material itself and its thermal expansion characteristics match so closely the underlying silica that it forms an impervious, adherent coating throughout the service temperature range of the sintered silica itself.

Teflon, regarded as a low-temperature, non-charring ablator, is not expected to interfere with electromagnetic transmission when applied as a thin sprayed coat to seal the pores.

#### 4-11 PRODUCTION OF BERYLLIA RADOMES

Beryllia radomes are formed by the same processes as described for alumina. Both oxides are produced as refined powders derived from natural minerals by chemical processes, with purities of 99% or higher. Ceramic-grade beryllia powder may contain less than 0.01% impurity. Beryllia, a more recent possibility for radome use, has not yet benefited from extensive radome production experience; only a few relatively small radomes have been made of beryllia, although the Bureau of Naval Weapons sponsored several programs to develop beryllia foams, pressure casting techniques for forming beryllia radomes, and pyrolytic deposition techniques for beryllia (References 35 to 38).

Like alumina, beryllia is fabricated into radomes by slip-casting, either by gravity or under pressure, or by isostatic pressing. In slip-casting, a suspension of the pure oxide with organic additives and dispersing agents, at solids contents of 25% to 50%, is cast into conventional plaster molds under gravity or pressure, drained, and removed and dried as described for alumina. The toxicity of finely divided beryllia dictates that all of this work must be conducted in hoods with efficient ventilation and filter systems to prevent release of dust into the atmosphere. In isostatic pressing, the rubber envelope, when filled with powder and sealed, may be handled without ventilation, but the pressed blank must be removed under hooded conditions until sintered. The unfired blanks have a density of about  $1.5$  to  $1.7 \text{ gm/cm}^3$ ; the organic additives confer sufficient strength to permit handling.

Sintering to high density and freedom from porosity requires somewhat higher temperatures than used for alumina. Optimum thermal conductivity and dielectric loss properties are achieved in beryllia with purity in excess of 99%, which limits the fluxing oxide additions to very small amounts.

Because of this high degree of purity, beryllia for radome use has to be sintered at temperatures as high as  $3300^\circ\text{F}$ , in either gas or electric kilns. This high sintering temperature is a factor in the cost of beryllia and leads to more difficulty with distortion during sintering than is encountered with alumina.

When a beryllia radome has been properly sintered, it is entirely safe to handle without precautions, since no loose dust can escape from it. Subsequent grinding operations must, however, be conducted under stringent control of dust and splashing of grinding fluids because the finely divided oxide powder must be considered as highly toxic. Grinders and lathes are hooded or totally enclosed and suction ducts carry all dust to an efficient collection system. This complicates the grinding process and adds to costs. The grinding equipment and operation are otherwise identical with the practice for other ceramic radomes.

Following grinding, the beryllia radome is thoroughly cleaned, using detergents and ultrasonic cleaners. A final clean firing may be necessary to remove waxing agents or lubricants used in grinding. These precautions leave the radome in a dust-free condition and its hardness is more than sufficient to prevent generation of any dust during subsequent handling and use.

As with other ceramic radomes, detailed physical inspection for dimensions, freedom from cracks, and achievement of density precedes shipment.

## REFERENCES

1. *Techniques for Airborne Radome Design*, edited by T. E. Tice, WADC Technical Report 57-67, Wright-Patterson Air Force Base, Ohio (ASTIA Document No. AD 142001), September 1957.
2. Walton, J. D., Jr., and Poulos, N. E. "Fused Silica for Reentry Radomes," and Poulos, N. E., and Walton, J. D., Jr. "Slip-Casting Large Fused Silica Radomes," both in *Proc. OSU-RTD Symposium on Electromagnetic Windows*, June 1964.
  - a. Walton, J. D., Jr., and Hallse, R. L. "Slip-Cast Fused Silica Radomes," *ASD-OSU Symposium on Electromagnetic Windows*, Technical Documentary Report No. ASD-TDR-62-676, Vol. 1, July 1962.
  - b. Walton, J. D., and Poulos, N. E. *Slip-Cast Fused Silica*, ML-TDR-64-195, October 1964
3. Wells, W. "Silicon Nitride as a High-Temperature Radome Material," *Proc. OSU-RTD Symposium on Electromagnetic Windows*, June 1964.
4. Li, P. C., Capriulo, A. J., and Lepie, M. P. "Chemically Vapor Deposited Boron Nitride," *Proc. OSU-RTD Symposium on Electromagnetic Windows*, June 1964.
5. *Refractory Ceramics of Interest in Aerospace Structural Applications—A Materials Selection Handbook*, Technical Documentary Report No. ASD-TDR-63-4102, available from Defense Documentation Center, October 1963.
6. Mitchell, J. B., Spriggs, R. M., and Vasilos, T. *Microstructure Studies of Polycrystalline Refractory Oxides*, Research and Advanced Development Division, Avco Corp., Summary Technical Report, p. 21, Contract NO 62-0648-c, June 12, 1963.
7. Pedigo, A. *Radome Handbook*, Second Edition, Coors Porcelain Co., Golden, Colorado, 1962.
8. Unpublished data obtained by Melpar, Inc., on samples from International Pipe and Ceramics Corp., Los Angeles.
9. Seiler, M. R., and Ritt, P. E. *Radome Specimen Testing*, Interim Technical Engineering Report NR. 1, Melpar, Inc., under Contract AF33(600)-37908, ASC Project 7-632d, July 1959.
10. Baer, D. H., Gates, L. E., and Robertson, G. D. "Ceramic Radome Evaluation," *Proc. OSU-WADC Radome Symposium*, WADC Technical Report 58-272, Vol. 1, pp. 382-405 (ASTIA Document No. AD 155831), June 1958.
11. "Thermal Conductivity," Parts III, IV, VI, *J. Am. Ceramic Soc.*, Vol. 37, No. 2, February 1954.
12. "The Emittance of Ceramics and Graphite," Defense Metals Information Center, Battelle Memorial Institute, DMIC Memo 148 (ASTIA Document No. AD 274148), March 28, 1962.
13. Metzger, A. J. Final Report, Navy Contract N388s-95917, Virginia Engineering Experiment Station, VPI, February 1955.
14. Giles, T. M., and Hessler, P. S. "Low Dielectric Constant Ceramic Foams," *Proc.*



- Radome Symposium*, p. 179, Ohio State University, June 1955.
15. Lefforge, J. W. "Ceramic Foams for Microwave Windows," *Proc. ASD-OSU Symposium on Electromagnetic Windows*, Technical Documentary Report No. ASD-TDR-62-676, Vol. 1, July 1962.
  16. Caldwell, O. G. "Ceramic Porous Core Laminates for Broadband Radar Radomes," *Proc. ASD-OSU Symposium on Electromagnetic Windows*, Technical Documentary Report No. ASD-TDR-62-676, Vol. 1, July 1962.
  17. Kalounek, G. L. and Dence, R. B. *Development and Fabrication of Inorganic Sandwich Radomes*, WADC Technical Report 54-197, April 1954.
  18. Guarini, J. F. "Rain Erosion Sled Test," *Proc. OSU-RTD Symposium on Electromagnetic Windows*, June 1964.
  19. Loyet, D. L., and Yoshitani, R. "Ceramic Sandwich Radome Design," *Proc. OSU-RTD Symposium on Electromagnetic Windows*, June 1964 (also published as Hughes Aircraft Company document 2785.3/294, May 25, 1964).
  20. Filippi, F. J., and Barr, F. A. "Materials for Ceramic Radomes Utilizing Mosaic Techniques," Narmco Research and Development Div., Whittaker Corp., AF 38 (657)-1011, *Proc. OSU-RTD Symposium on Electromagnetic Windows*, June 1964.
  21. Luoma, E. J., Stetson, R., and Mason, S. J. "Design Techniques for Sectionalized, Structurally Supported Airborne Ceramic Radomes—A Progress Report," Emerson and Cuming, Inc., *Proc. OSU-RTD Symposium on Electromagnetic Windows*, June 1964.
  22. *Fabrication of a Ceramic-Coated Plastic Radome by Electrophoretic Deposition*, Vitro Corp. of America, W. Orange, N. J., under current Navy Bureau of Naval Weapons Contract N600 (19)59628.
  23. *Materials Handbook*, Sixth Edition, Corning Glass Works, Corning, New York, April 1963.
  24. Walton, J. D., Jr., Georgia Institute of Technology, private communication.
  25. Hessinger, P. S. Beryllium Oxide Radomes, National Beryllia Corp., Haskell, N. J., unpublished communication, February 1964.
  - a. "Berlox" Technical Data Sheet, National Beryllia Corp.
  26. Brown, R. J., Brush Beryllium Corp., private communication.
  27. Sutton, R. W., and Bowlby, C. W., The Boeing Company, private communication.
  28. Miller, S. A., Chase, V. A., and Copeland, R. L. "Development of a 1200°F Radome," *Proc. OSU-RTD Symposium on Electromagnetic Windows*, June 1964.
  29. Plant, H. T. "Inorganic Laminates for 1000°F Radomes," *Proc. ASD-OSU Symposium on Electromagnetic Windows*, Technical Documentary Report No. ASD-TDR-62-676, Vol. 1, July 1962.
  30. Beasley, R. M., and Izu, Y. D. "Design and Construction Techniques for Radomes for Suborbital Missions," *Proc. OSU-RTD Symposium on Electromagnetic Windows*, June 1964.
  31. Kelsey, R. H., and Raynes, B. C. "Filamentized Ceramic Radome Techniques," *Proc. ASD-OSU Symposium on Electromagnetic Windows*, Technical Documentary Report No. ASD-TDR-62-721, August 1962.
  32. Smyth, H. T. "Development of Dense Ceramic Radomes at Rutgers University," *Proc. Radome Symposium*, Vol. 1, p. 174, Ohio State University, June 1955.
  33. Smoke, E. J. "Alumina Ceramics Made by the Slip-Casting Process," *Proc. OSU-WADC Radome Symposium*, WADC Technical Report 57-314, Vol. 1, pp. 194-210 (ASTIA Document No. AD 130929), June 1957.
  34. Anderson, W. D. "Hydrostatic Pressing of Alumina Radomes," *Proc. OSU-WADC Radome Symposium*, Vol. E, WADC Technical Report 57-314 (ASTIA Document No. AD 130929), June 1957.
  35. U.S. Patent 2,964,822, issued 1960 to Shenango Ceramics, Inc.
  36. *Development of Fabrication Techniques for Beryllium Oxide Radome Materials*, National Beryllia Corp., Bureau of Naval Weapons Contract NOW-60-0057.
  37. *Beryllium Oxide Radome Development*, National Beryllia Corp., Bureau of Naval Weapons Contract NOW-62-0592c.
  38. *Fabrication of Beryllium Oxide Radomes by Pyrolytic Deposition*, National Beryllia Corp., Bureau of Naval Weapons Contract NOW-63-0412-C.

## PART II—REINFORCED PLASTIC RADOMES

### 4-12 RADOME MATERIAL DESIGN

Compared to the present state of the art, the manufacture of radomes using concrete molds and plywood materials appears crude. Today's radome is a result of a vast complex of economics, aerodynamics, electronics, and materials selection. In the past, radomes were designed from available materials; today, materials are being specifically designed, modified, and manufactured for electromagnetic windows.

Materials are being designed to provide the electronics engineer with a broader spectrum from which to select a dielectric constant. Researchers are seeking ways to reduce loss tangent characteristics. Materials engineers are screening materials of reduced weight, reduced sensitivity to frequency changes, and increased resistance to temperature exposure for both transient and steady-state environments. To further complicate the picture, radome structures are increasing in size, thereby requiring internal space frames.

The requirement of control in the dielectric constant is a stimulus to materials design for selection of a dielectric constant in the range of 3.0 to 9.0, allowing for more efficient radome design and less compromise between aerodynamics and electronics. It also allows the consideration of "B" sandwich solid-wall composites.

The thermal environments now require radomes to survive thousands of hours at temperatures of 500°F to 700°F and 500 to 1000 hours in the temperature range of 1000°F to 1200°F.

Frequency requirements have increased so that 16.5-gc operation is frequently the rule rather than the exception. Engineers are now

considering 35-gc structures. Millimeter radome techniques for the 50- to 150-gc range investigated by the Air Force in fiscal year 1965, extended the frequency range to 250 to 300 gc in fiscal year 1966. This will require additional improvement in structural materials. Therefore, materials design will continue to contribute to the complex field of radome design for many years to come.

### 4-13 THE ANISOTROPIC NATURE OF FIBER-REINFORCED PLASTIC RADOMES

Before discussing fiber-reinforced plastics, the following terms should be defined:

*End*: Each strand in a roving or yarn.

*Fiber*: A slender filament. (Used interchangeably with fiber.) The smallest component of a strand.

*Filament*: A very fine thread or threadlike structure (of glass); a fiber or fibril.

*Roving*: Glass fiber roving consists of a number of continuous, untwisted glass strands that have been plied together. Continuous strand roving may contain a number of ends, the most common being 20 and 60.

*Strand*: A number of fibers or filaments, usually 204, collected as a unit. Continuous glass strand is usually supplied in the form of yarn or roving.

*Yarn*: A collection of continuous glass strands that have been twisted together and plied to prevent individual filaments from separating when tension on the strands is relaxed.

Reinforced plastic radomes are anisotropic; that is, they respond unequally when external forces are applied normal to different planes in

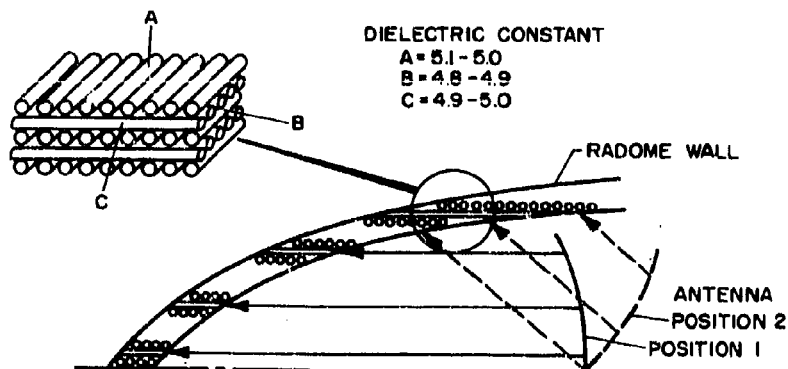


Figure 4-42. Sketch Showing Anisotropic Nature of Reinforced Plastic Radomes

the structure, as shown in Fig. 4-42. In a similar manner, the composite wall presents a different structure to the electromagnetic radiation from the antenna in the two positions shown.

Materials used in composites that have high dielectric constants are also more anisotropic when a distinct fiber orientation or directionality is introduced. For the radome designer, this presents the problem of compensating for this anisotropy when designing the radome wall.

#### 4-14 MATRIX MATERIALS

The matrix is defined as the material that holds or binds the reinforcement in place. This material is usually organic in composition, but may also be completely inorganic\*. The matrix represents less than half of the weight or volume of the total composition. Organic resins are the matrix materials most often used for radomes. Only organic matrix materials and primarily those new materials that extend the state of the art are covered.

The organic materials may be classed according to their method of polymerization or their major molecular structure. They may also be classified as those that give off no byproducts and those that give off byproducts; or those that are 100% reactive and by condensation methods. However, we are only concerned with those systems most commonly used or those that offer unique characteristics.

\* Inorganic matrix materials are covered in Paragraph 4-7.

Table 4-8 provides a partial list of available materials and a comparison of their shear properties. Appendix 4A presents additional data for candidate resins for use in fiberglass-reinforced plastic radomes.

The organic matrix most widely used for high-performance filament-wound radomes is Vibrin 135, qualified under Mil R 25042. This resin system contains trially cyanurate (TAC) as a major component and is qualified up to 500°F operation. Properties of this resin and a composite made with this resin are given in Tables 4-9 and 4-10, and Fig. 4-43.

This resin system is ideally suited for filament-wound structures. Its viscosity range is low, 2000 to 3000 centipoises, and change in viscosity vs. temperature is fairly low. The shelf life may extend to 30 days in impregnated form at 40°F. It requires low initial cure for short times (2 to 4 hr) at 200°F to 250°F. Cure is complete enough at this time to permit grinding. After grinding, it is again cured to 480°F. There is one difficulty with Vibrin 135, however. It is sensitive to post-curing conditions when the temperature is increased over 480°F. As a consequence, caution must be exercised to avoid blistering.

#### 4-15 TYPES OF GLASS FIBERS USED IN RADOME PRODUCTION

Glass is defined as an amorphous substance, usually transparent, consisting ordinarily of a mixture of silicates, but in some cases of bo-

**TABLE 4-8 AVERAGE INTERLAMINAR SHEAR VALUES  
OF SELECTED RESIN SYSTEMS**

Type of Resin System	Shear Strength Based on Cross Sectional Area, psi			Shear Strength Based on Resin Content,* psi		
	Room	500° F	750° F	Room	500° F	750° F
<i>Commercial, 100% Reactive</i>						
DEN 438/MNA/DMP-30	7706	3427	681	26,730	11,940	2350
Epon 828/CL	7446	.....	.....	27,800	.....	.....
Epon 820/MNA	6120	2293	366	30,140	7620	1750
Epon 1031/MNA	9138	3658	885	23,400	9450	3170
Epon 1031/BF <sub>3</sub> MEA	7794	2979	421	26,800	9000	1280
DEN 438/BF <sub>3</sub> MEA	9685	4378	627	33,100	14,900	2140
DEN 438/PMDA Adduct A	9882	2306	718	27,200	6675	2100
DEN 438/TAC	5500	1270	529	30,600	6920	2940
NRC 1174/3	5288	2525	373	31,530	15,240	2250
EP 207/MA/Glycerol	7440	3830	546	26,800	14,400	2420
AG-13E/MA/TME	6220	2510	350	27,700	11,290	1540
Oxiron 2000/MA	7505	2475	648	34,300	11,250	2950
RDGE/MNA	6640	1470	603	35,200	7570	3350
Laminac 4232	4566	3169	890	23,400	14,700	4040
Vibrin 136A (135)	6021	2978	770	30,200	14,800	3890
Polyite AZ-1695	4880	2760	887	23,200	13,100	4210
<i>Commercial, Condensation</i>						
DC R-7141	2060	679	382	8813	2913	1640
Plaskon V-204	7920	3042	1902	23,200	11,100	6220
Resinox SC-1013	2598	1421	587	12,450	6750	2820
Resinox SC-1008	7972	2371	1129	36,025	8540	5260
CTL 37-9X	7010	4330	1368	23,680	14,840	4678
V4-38	10,970	1840	604	33,800	540	1860
<i>Experimental</i>						
Diallyl Epoxy No. 2/MNA	6630	734	358	29,700	3420	1610
TGC/MNA	4376	2306	.....	23,850	12,495	.....
ADC/MNA/PMDA	5403	2622	825	19,850	9680	3040
ADC/DEN 438/MNA	6043	3012	568	27,183	13,650	2563
VRDGE/MNA	7740	2830	607	31,400	11,880	2540

\* The resin content of the composites reported in this table ranges between 18% and 24%.

rates, phosphates, etc. Most glass is made by fusing silica, as sand, and alkali, as potash or soda, and some other base, as lime or lead oxide. This definition emphasizes that glass is non-crystalline and, although essentially rigid, is similar in structure to liquids. It is this structure that gives glass its unusual characteristics and differentiates it from crystalline solids.

Glass is sometimes defined as a "supercooled liquid" because it can go from the molten state to the solid state without undergoing an abrupt molecular rearrangement and resultant physical changes. However, a very indistinct crystal lattice, called a "random network," does form in this transition. As a result, the room temperature properties of glass are dependent upon its thermal history (annealing).

Although the above characteristics apply to all glass, all glass is not alike. The types of glass that are of interest in radome production are only those that can be drawn into very fine diameter continuous filaments. They provide the fiberglass yarns that are used to reinforce plastics.

TABLE 4-9 PROPERTIES OF VIBRIN 135

Viscosity, centipoise at room temperature	1800 to 3000
Shrinkage, %	3 to 5
Specific gravity	1.32
Cure temperature, °F	200 to 500

The brittleness of window and bottle glass is usually associated with low strength. Thus, if glass fibers display very high strength, an apparent anomaly exists. However, examination of the mechanism of glass failure reveals the actual nature of this material. Glass always fails abruptly without previous yield from a tensile component of stress, even when a load is applied in compression (Reference 2). The fractures originate as small imperfections or flaws, usually on the glass surface. In fibers, the size and distribution of these flaws are physically limited. The result is that the relative strength of glass fibers increases as the diameter decreases.

TABLE 4-10 COMPOSITE PROPERTIES  
E-GLASS AND VIBRIN 135

Flexural strength, psi	
Room temperature	60,000 to 80,000
500°F	30,000 to 50,000
Compression strength, psi	
Room temperature	40,000
500°F	20,000
Specific gravity	1.75 to 1.85
Dielectric constant, $mc \times 10^4$	4.0 to 4.2
Loss tangent, $mc \times 10^4$	0.008 to 0.015
Hoop tensile, psi	220,000 to 300,000
	fiber stress
Interlaminar shear, psi	4000 to 6000

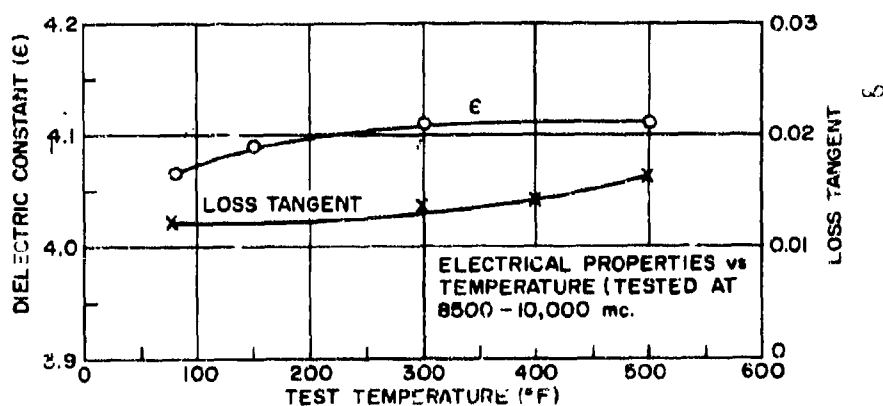


Figure 4-43. Vibrin 135 and Glass Composite.—Dielectric Constant and Loss Tangent, Electrical Properties vs Temperature

#### 4-15.1 DRAWING CONTINUOUS FILAMENTS

The process of manufacturing fiberglass yarn consists of melting the glass in bushings fitted with 204 orifices. The filaments from each orifice are drawn together to form a single strand. The filament diameter results from three factors: (1) the initial viscosity of the melted glass, (2) the size of the orifice, and (3) the speed at which the filament is drawn. The last factor, speed, is controlled by an electrically driven rotating winding tube, whose surface speed may reach 12,000 ft/min. The nominal diameter of the individual filaments used for plastic reinforcement is 0.00038 in. As the yarn is drawn, sizing is applied to lubricate the filaments and to hold them together as yarn.

#### 4-15.2 GLASS FIBER COMPOSITION AND PROPERTIES

Examination of the manufacturing process reveals that the working properties of the glass are the only requisites for forming filaments. However, end uses of the glass also determine its composition. The primary requirements of fiberglass for radome manufacturing are electrical, physical, and chemical. The chemical requirement is primarily resistance to weathering. The large surface area of the filaments and their natural hygroscopic nature clearly illustrate the problem faced by the fiberglass formulator. Atmospheric moisture is the most significant attacking agent. All glass used in radome production today has good durability, but is dependent upon sizing or binders for maximum protection against moisture.

Mechanical properties of glass used in filament winding are greatly dependent upon chemical composition. The standard glass, called "E-Glass," has been used extensively. The composition of E-Glass is approximately 54.5%  $\text{SiO}_2$ , 14.5%  $\text{Al}_2\text{O}_3$ , 22.0%  $\text{CaO}$ , 8.5%  $\text{B}_2\text{O}_3$ , and 0.5%  $\text{Na}_2\text{O}$  (Reference 2). Its specific gravity is approximately 2.54. The tensile strengths of single filaments of E-Glass removed from production yarns vary between 250,000 and 300,000 psi. This glass is the most widely used reinforcement for radome manufacturing today.

The effectiveness of a fiberglass reinforcement is proportional to the volume concentration of the reinforcement and to the ratio of

the modulus of elasticity of the reinforcement to the modulus of elasticity of the matrix. Therefore, it is desirable to have a fiber with as high a modulus of elasticity as possible.

In order to provide radome structures for advanced missile systems, the Air Force undertook a program to develop a fibrous glass reinforcement with a higher modulus of elasticity or stiffness than E-Glass. This program resulted in the development of a glass designated as YM-31A, which had a modulus of elasticity about 50% higher than E-Glass. Its approximate composition is 53.75%  $\text{SiO}_2$ , 12.94%  $\text{CaO}$ , 8.96%  $\text{MgO}$ , 7.96%  $\text{BeO}$ , 1.99%  $\text{ZrO}_2$ , 7.96%  $\text{TiO}_2$ , 2.99%  $\text{Li}_2\text{O}$ , 2.99%  $\text{CeO}$ , and 0.50%  $\text{Fe}_2\text{O}_3$  (Reference 3). The BeO component, which is extremely toxic, has limited the use of YM-31A.

A further Air Force development has been AF-994 glass (commercially designated S-994 by Owens-Corning Fiberglas Corporation). This glass was a development of a program whose objective was to develop a fiber with high tensile strength at high temperatures. Its composition is 64%  $\text{SiO}_2$ , 26%  $\text{Al}_2\text{O}_3$ , and 10%  $\text{MgO}$ . Room temperature tensile strength of S-994 is approximately 650,000 psi. Its specific gravity is 2.48 (Reference 4). S-994 roving has been used extensively in rocket motor case production and offers excellent potential for radomes where attachment problems or other high tensile strength applications are present.

In addition to the mechanical property requirements, the electrical property requirements of glass for radome fabrication are important. E-Glass has a dielectric constant of 6.26 at room temperature (8.5 gc), whereas S-994 under the same conditions has a dielectric constant of 5.28. The loss tangents of the two glasses are 0.001 and 0.0072, respectively.

The dielectric constant of the composite radome wall is a function of the dielectric constant of the fiberglass and the resin. For a half-wave wall, a lower dielectric constant fiber requires a thicker radome wall. Therefore, if the physical properties of a low dielectric constant glass are comparable to those of a higher dielectric constant glass, the lower dielectric constant glass will provide a stronger and more rigid structure because of the greater wall thickness of the composite. Two recently developed glasses are of interest here. D-556 was developed to have a low dielectric constant: 4.0 at room tem-

perature (9375 gc). While its physical properties are not as good as E-Glass, its low dielectric allows the design of a half-wave radome wall with greater strength than the E-Glass composite because of the greater physical thickness.

A radome wall with high strength plus a reduction in weight results from the use of hollow E-Glass fibers. These fibers, developed by the Fiber Glass Division of Pittsburgh Plate Glass Company, have inside-to-outside diameter ratios of approximately 0.6. With so much emphasis placed on aircraft weight reduction, hollow glass fibers offer a new approach to strong lightweight electrical radomes. The dielectric constant of the hollow glass is lowered by the approximately 15% void volume in the composite. The strengths of the fibers are, how-

ever, comparable.

As mentioned, the dielectric constant of the fiberglass reinforced plastic is a function of the dielectric constant of the resin and glass. This relationship may be expressed as:

$$\text{Log } \epsilon = (\text{log } \epsilon \text{ resin}) (\text{vol } \% \text{ resin}) + (\text{log } \epsilon \text{ glass}) (\text{vol } \% \text{ glass})$$

The dielectric constants for E-Glass, hollow glass, and S-994 glass, all with Vibrin 135, are shown as a function of resin content in Figs. 4-44 to 4-46, respectively. Also, the effect of void content of up to 2% on the dielectric constant of the composite is presented in these figures (Reference 5).

The consideration of reinforcement must include the sizing or coupling agents applied to the yarn at the time it is collected on the

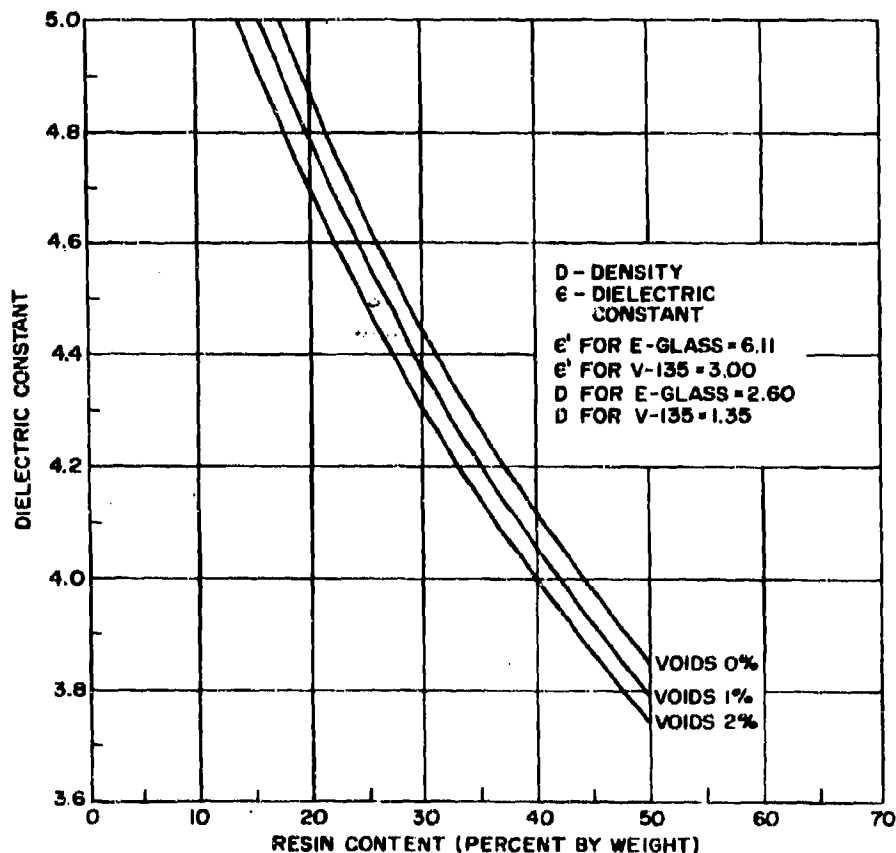


Figure 4-44. E-Glass and Vibrin 135—Dielectric Constant vs Resin Content

winding tube. As previously pointed out, the size performed two functions in the drawing operation: lubrication and binding. Lubrication is necessary to protect the glass filaments from interacting. If the filaments are allowed to come in contact, flaws and scratches will result and seriously deteriorate the strength of the glass reinforcement.

The lubricant is usually a starch-oil combination. The starch also acts as a binder to hold the filaments together to form a strand of yarn. To develop the optimum strength of a fiberglass-resin laminate, it is necessary for the resin to bond firmly to the glass. Few, if any, resins bond to the bare glass because of differences in molecular "fit" at the surfaces. The best bonds have been developed through the use of coupling agents. The coupling agents are complex molecules that bond with the silano groups on the glass surface and react with the organic reactive sites of the resins during the curing process. Two general types are in use today:

chrome methacrylates and silanes. The chrome complex salts are generally used with polyester resins, the silanes with epoxy resins.

Briefly, the sizing performs three functions: lubrication, binding, and coupling. However, a substance that acts as a good lubricant may have an adverse effect on bonding. For textile yarns, the size, usually starch oil, may be burned off by slowly oxidizing the woven fabric at 650°F for 24 hr or more with an optimum coupling agent added in a bath. In the case of roving, however, the glass is not handled as much during processing and the lubricant is less critical than in the case of filaments. Therefore, combination lubricant-coupling agents have been developed that do not have to be removed by heat-cleaning and subsequent re-coating.

Coupling agents are most advantageous when the laminate is subject to the presence of moisture. If the chemical bond between the glass (through the coupling agent) and the resin is

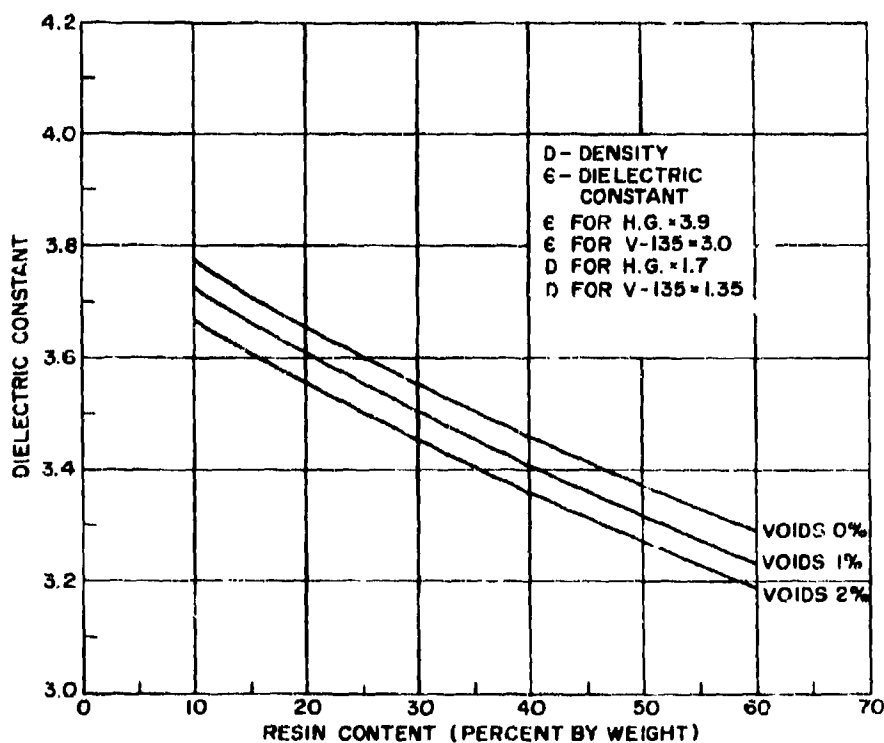


Figure 4-45. Hollow Glass and Vibrin 135—Dielectric Constant vs Resin Content



very strong, water is prevented from entering the laminate by "wicking" along the shaft of glass. If the water is kept out, the adhesion and the laminate will be kept strong and the properties of the radome will be optimum.

best be illustrated by Fig. 4-47. This illustration provides the basis for discussing the techniques for filament winding of electromagnetic windows in the following paragraphs. For a detailed presentation of filament winding processes and application, see Reference 6.

## 4-16 FABRICATION

### 4-16.1 INTRODUCTION

In its simplest form, filament fabrication may

### 4-16.2 FILAMENT CONTROL

One of the major factors governing the

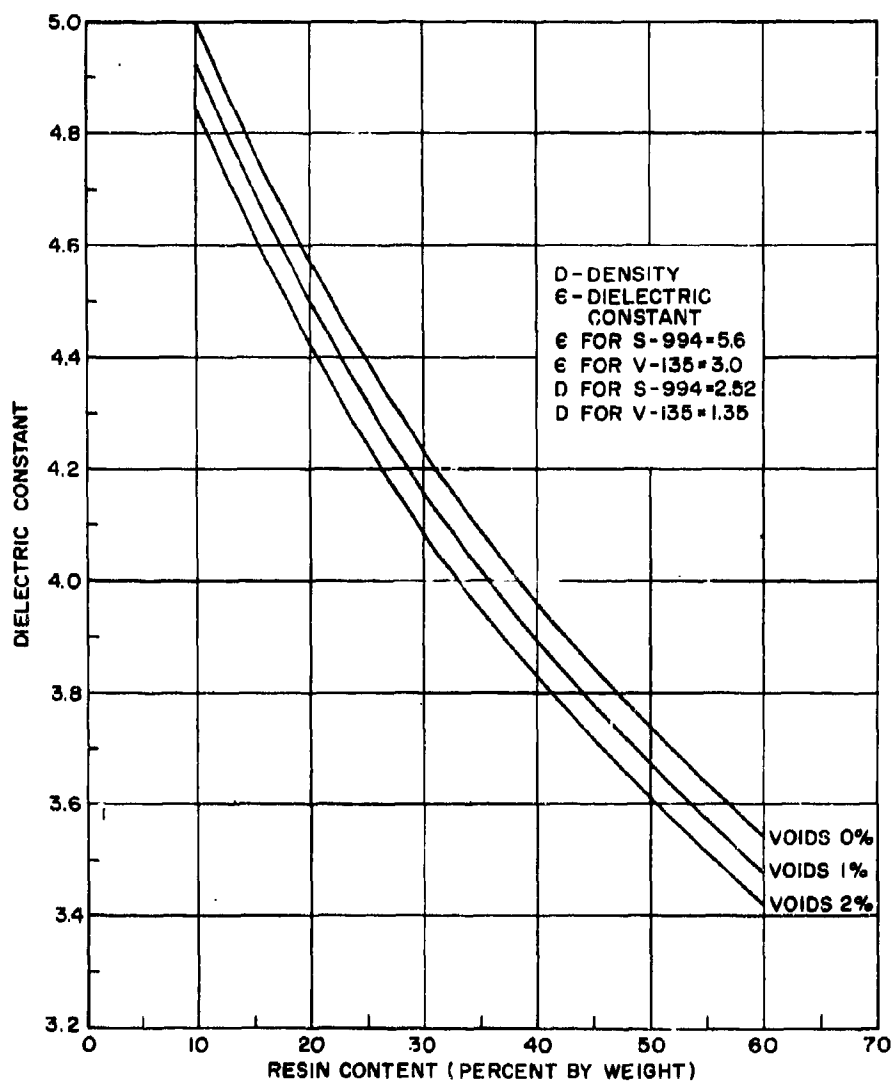
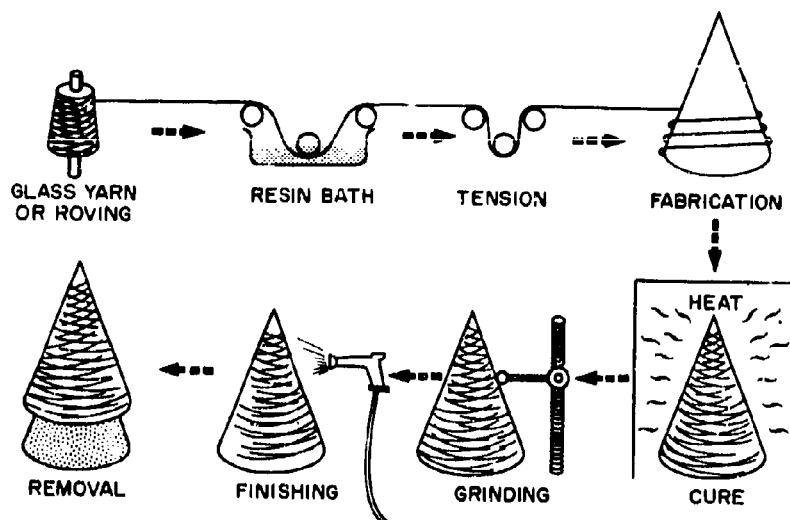


Figure 4-46. S994 Glass and Vibrin 135—Dielectric Constant vs Resin Content



**Figure 4-47. Schematic Diagram of Radome Filament Fabrication**

quality of the end product is control of the tension applied to the filaments of a filament-wound part during the winding operation. Composite properties that are influenced by tension are resin content, void content, and specific gravity. These properties, in turn, affect the mechanical and electrical properties of the system. The tension applied is sometimes influenced by part configuration, especially in the nose area of radomes. Therefore, close control of the tension is important in the control of the quality of the composite.

Tensioning of the filaments is generally accomplished at one of two places. It may be applied through a braking action on the spool or package, or it may be applied to the yarn or roving itself. Application of tension at the spool is usually undesirable, especially when a pre-impregnated roving is used. This can result in excessive resin squeeze-out, deformation of the roving package, fuzzing, and degradation of the roving. Better control is usually obtained by applying tension to the yarn or roving.

The three types of tensioning devices most commonly used are classified as electromagnetic, magnetic, and friction tensioners.

#### 4-16.2.1 The Electromagnetic Tensioner

The electromagnetic system provides greater

flexibility and better control of the tension. This system acts through a retarding torque applied to a guide pulley, around which several turns of roving are passed alternately with an idler pulley. Adjustment is made by varying the voltage (usually dc) to the power unit. When the desired tension is obtained, the operator notes the voltage indicated on the control panel, so that later adjustments may be made and still be returned to the original setting for the desired tension. Since this tension is applied to the roving, a back-up tensioner is required at the serving pool to prevent backlash. This is usually a magnetic tensioner, set with sufficient tension to prevent the spool from rotating freely.

#### 4-16.2.2 The Magnetic Tensioner

The magnetic tensioner, sometimes called a hysteresis tensioner, operates by the mutual attraction of two magnets. Control is obtained by adjusting the distance between the magnets to increase or decrease the braking action on the mechanism. Very good results may be obtained with this type of tensioning device.

#### 4-16.2.3 The Friction Tensioner

The friction type of tensioning device uses disks, bands, and other devices specially de-

signed to mechanically apply a braking action by increasing or decreasing the friction between two moving parts. Tension may be applied either at the spool or to the glass roving or strand. This type of mechanism generally is not as accurate because of wear on the friction surfaces, the introduction of foreign matter on the friction surfaces, and the adjustment mechanisms of the tensioning device. Where close tension control is not so necessary, however, this type of tensioner will perform satisfactorily.

One other type of friction tensioner sometimes used for yarn filament winding should be mentioned. This device consists of two ceramic coated posts placed approximately perpendicular to the path of travel of the yarn. The yarn is passed under the bottom of one post and over the top of the other. Adjustment is made by moving these posts in a circular motion to increase or decrease the angle of travel of the yarn. This brings to bear a greater friction surface, thereby increasing tension on the yarn. There is some possibility of degradation of the filament yarn by this method of tensioning.

In conjunction with the tensioners noted above, there is sometimes a need for sensing or damping devices. This is especially true for filament strands traveling at a high speed during the winding operation. These devices are usually spring-loading mechanisms designed to reduce the tension differential due to sudden acceleration or deceleration.

In summary, the tensioning device is a machine designed to provide the desired filament tension at the desired location during the filament winding operation.

#### 4-16.3 THE RESIN BATH

The specific resin characteristics are discussed in Appendix 4A. Development of the art of impregnation during the past 15 years has resulted in four or five methods available to the fabricator.

##### 4-16.3.1 The Wet-Dip Method

In the wet-dip method, the roving is removed from the glass ball and passed through a dip tank. This may be a one-end roving or a one-

hundred every-end roving. The resin pickup or resin content is controlled by the speed at which the roving is fed into the tank, the tension placed upon the roving, and the viscosity of the resin. Control is also affected by sliding the impregnated stock over two or three rollers or blades immediately after removal from the tank. The roving end count and roving glass finish also affect resin pickup. A typical tank diagram is shown in Fig. 4-48. This method is rapid and allows a direct tie to the mandrel without intermediate steps. It is more applicable for circumferential and helix windings, but not particularly satisfactory for longitudinal winding.

The resin content control range of 3% to 5% is not considered accurate when compared to other methods of impregnation. The choice of resins is limited to given ranges of viscosity and pot life. High-viscosity resin systems must be heated or have reactive diluents added to bring the viscosity to about 1000 to 2000 centipoises. Pot life of the resin limits the choice of materials, since radomes may require as long as 4 to 12 hr winding time for a given stage prior to cure. This allows the resin cure reaction to proceed in the dip tank and requires a constant correction for resin pickup.

Included in this method is the hot-dip or hot-melt system, which is quite similar to the wet-dip method. However, in this case, the resin used is solid at room temperature. Therefore, it must be heated to its melting point or slightly higher before the glass filament can be passed through. The roving is then passed through a double roller or blades to remove the excess resin and achieve resin content control. It is difficult to obtain thorough wet-out of the strand with this method and the resin content range is high.



Figure 4-48. Diagram of Resin Bath Setup for Wet-Dip Method

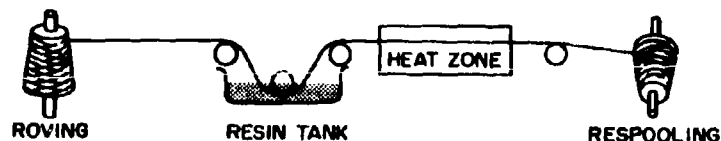


Figure 4-49. Schematic Diagram of Pre-impregnation Operation

#### 4-16.3.2 The Pre-impregnation Method

As the name of the method implies, the glass yarn or roving is impregnated prior to application in production. This allows packaging, storing, and/or shipping of the stock. This system is widely used for radome fabrication. It is used primarily for resins other than polyesters, which do not readily lend themselves to this type of handling. To be handled efficiently as a pre-preg material, the resin must be capable of undergoing partial polymerization or be soluble in a common solvent. A pre-preg may be prepared by running the glass roving through a cut resin solution and then through a drying or B-staging tower. This reduces both the tack of the roving and the softness of the package when it is respooled from the tower. A schematic diagram is shown in Fig. 4-49. It is necessary to make sure that the roving is nearly dry, or nontacky, before it can be respooled. The heating zone is designed to remove excess solvent and promote polymerization to a given point. If the solvent content is too high or the resin has not reached the desired degree of B-stage, it will, when respooled, produce a soft and sticky package. With additional age on the package, it becomes nearly impossible to unspool on a winding machine. The soft package allows the roving to pull into the build and to break easily. This makes it impossible to find the broken strand in the build, and results in scrapping the entire spool. If the resin is not advanced to the right degree of B-stage, the roving does not separate readily when unwound. This causes hang-up, fraying, and eventually loss of the strand. When the strand is lost in a tacky spool, it is nearly impossible to start the spool again.

Phenolics, silicones, epoxy amides, etc., may be delivered to the respooling fixture in the state of controlled tack, nearly dry. Polyesters, on the other hand, are a "go-no go" type of

system that cannot be delivered to the respooling fixture in a partially polymerized state. Drying additives must be used to compensate for this characteristic. Pre-preg materials may be obtained in roving, yarn, cordage and unidirectional tapes. Resin content tolerance is in the range of 0.75% by weight. Pre-preg suppliers can produce almost any type of wind pattern in the spool with almost any degree of tack required by the various types of winding machines. Its main disadvantages are resin content control, additional handling of the glass, and, with some systems, poor shelf life.

#### 4-16.3.3 The Hybrid Impregnation Method

This system is an offspring of the wet-dip and preimpregnation methods. The hybrid uses the resin undiluted and catalyzed as in the wet-dip method, then respools the stock without any forced polymerization or B-staging, as in the usual pre-preg materials. This is illustrated in Fig. 4-50. The roving strand, A, is pulled from the inside of the package or ball and delivered to B. Item B is a grooved wheel, with the width of the groove governing the spread of the fiber or band width. From point C, resin is forced from the nozzle by the pump. The amount of resin delivered is governed by the weight of the glass strand being impregnated. The resin is injected into the groove of the spool and, as

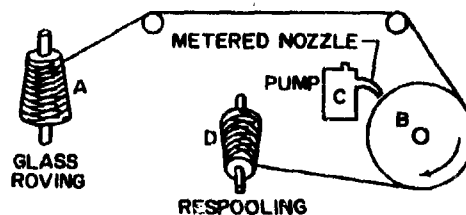


Figure 4-50. Schematic Diagram of Hybrid Impregnation Operation

the wheel turns, forces the resin through the fibers down into the groove. The rate of delivery, the glass weight, and the pump must be synchronized to deliver the quantity of resin to provide the desired resin content. After the roving is respooled at D, it is packaged and placed in a storage box at 72°F to 80°F for 24 to 48 hr. This permits a more thorough wetting of the fibers. When the strand of glass is pulled from the ball, a certain amount of twist is introduced, which tends to slow down the complete wetting of the fiber. This type of system allows extremely close control over resin content to within  $\pm 1\%$  by weight. The primary disadvantage of this system is one of economics, since a separate machine is required for each roving strand. The method is also limited to those resin systems possessing a relatively long pot life. If B-staging takes place, as would be the case using an amine epoxy system, it becomes nearly impossible to remove the roving from the spool during the winding operation. The viscosity change causes the tack to increase. This, in turn, causes fraying and loss of the roving end during winding. When this occurs, the glass must be scrapped and cut from the spool. The method is quite efficient for polyesters using peroxide catalysts, epoxies using latent or anhydride catalysts, or a solid polymer suspended in a solvent vehicle.

#### 4-16.4 FILAMENT WINDING

Since 1957, several new techniques have been developed for filament winding radome structures, which are basically variations of two methods: helix and polar fabrication. The discussion of fabrication will cover the steps involved as the impregnated stock is delivered to the mandrel.

##### 4-16.4.1 Helical Winding

A helix is defined as the curve formed on any cylinder by a straight line in a plane that is wrapped around the cylinder, as the ordinary screw thread. Herein lies one of the problems in radome manufacture by this method. As shown by Fig. 4-51 the fiber must cross over, not the end of the structure, such as the cylinder in one case, but over part of the ogive of a given value. This produces two problems: (1) roving slippage; (2) as roving strands are

added, it eventually leads to a crosshatch or crossover pattern. At each point of crossover, a space is formed. This produces a void if the resin content of the impregnated roving is 15% to 20% by weight. This space will be filled by resin if the resin content is greater than 30% by weight in the roving.

With a cylinder, the crossover pattern is quite uniform and provides a unit with a resin content similar to a laminated fabric (30% to 35%). In the case of a radome, however, the curvature produces a nonuniform spacing of the roving. This produces a variation in the electrical thickness of the wall, since the dielectric constant is dependent upon what medium, air or resin, fills the crossover space. For a conical shape, the electrical taper will be relatively uniform, but for an ogive or hemisphere, the change in electrical thickness will be variable. Measurements have shown that for a 36-in. unit (an ogive 36 in. in length with a base diameter of 13 in.), the resin content from base to tip may vary as much as 10% by weight. This will cause an electrical thickness change of about 5 to 7 degrees.

##### 4-16.4.2 The Circ-Longo Drop-Stitch Method

The circumferential, longitudinal-fiber drop-out method of winding is by far the most complicated technique for radome manufacture employing filament winding. But, in return for complexity, the greatest uniformity in electrical and mechanical properties is obtained. This method is more accurately described as circumferential and polar orientation, as shown in Fig. 4-52. The radome is fabricated in distinct layers or plies. Each ply is either longitudinally (polar) oriented or circumferentially oriented.

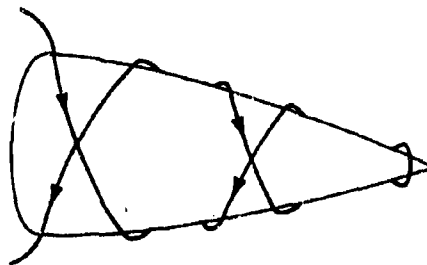


Figure 4-51. Helical Pattern on Radome Mandrel

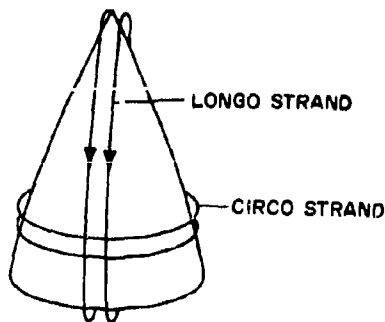


Figure 4-52. Circo and Longo Fiber Pattern on Radome Mandrel

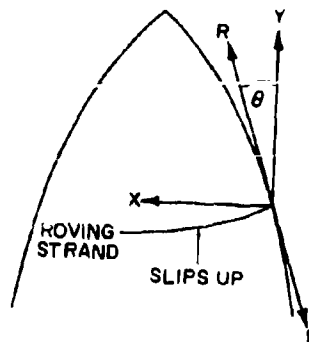


Figure 4-54. Diagram of Circo Fibers on High Curvature Portion of Mandrel

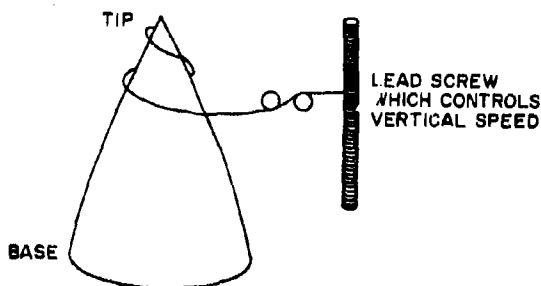


Figure 4-53. Diagram for Calculating Circo and Longo Fibers for Desired Wall Thicknesses

For the application of the circumferential strands, the band width, number of roving strands, total distance traveled, and rotational speed of the machine are known, so that the pattern may be calculated, as shown in Fig. 4-53.

The basis for figuring part thickness is TPI (threads per inch)  $\approx$  0.001 in. thickness/layer or ply (using 30 end roving).

Example:

30 end roving, 15 TPI = 0.015 in./layer

30 end roving, 20 TPI = 0.020 in./layer

1. Circo: To obtain circo thickness, the correct gear ratio must be determined to obtain the necessary TPI. The circo thickness is the thickness provided by the circumferentially wound roving.
2. Longo: To determine how many longos are needed for the desired thickness, multiply TPI by the circumference of the mandrel and divide by 2. If the mandrel is

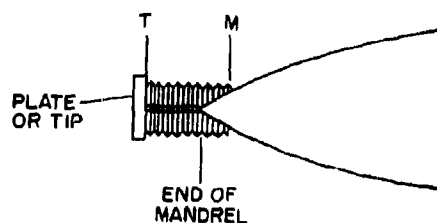


Figure 4-55. Diagram of Plate of Tip Method for Controlling Slippage of Circo Fibers on High Curvature Portion of Mandrel

tapered, the circumference of the base is used.

The normal sequence of operation is to apply the roving at the tip and move toward the base. Many of the high-performance radomes are not cones but ogives. When the roving is applied at the point of high curvature, it slips, as shown in Fig. 4-54.

Consequently, if the frictional force,  $F$ , is less than  $R$ , the strand will move forward. This generally limits the included angle,  $\theta$ , made by the tangent of the surface to a maximum of 15 degrees. If this is exceeded, auxiliary means must be used to hold the strand in place. Such methods include roughing the mandrel surface, applying abrasive strips, reducing the tension applied to roving, or using a dummy tip, plate, or back wind as shown in Fig. 4-55. This is accomplished by filling space T-M so that when the roving is applied to the mandrel proper, the vertical force is against the buildup; this

simply prevents the strands from being displaced. Once the critical point of curvature is passed, the winding proceeds as if winding on a cylinder.

Application of circumferential strands also has a limit to the bandwidth of the roving that may be used. This is shown in an exaggerated form in Fig. 4-56. From this, it can be seen that the greater the bandwidth, the smaller the value for  $y$ . This has the effect of stretching the roving. If the bandwidth becomes sufficiently large the roving must be distorted to conform to the mandrel, which allows the void content of the composite to increase.

The application of longitudinal fibers, as shown in Fig. 4-57, is somewhat more complicated. This figure shows that in polar winding, the fibers have only two apparent points of origin, one at the base and one extended beyond the end of the mandrel. Consequently, the same number of fibers is carried to the tip or reduced diameter of the mandrel. For a given pattern or thickness of longitudinal fibers at the nose, the thickness of the ply at any given station on the mandrel may be found as follows:

$V_1$  = volume of the part at the base with radius  $r_m$

Since the mass of material applied has not changed,  $V_1$  is constant and is equal to  $V_n$ , the volume at any given station, then

$$V_1 = V_n = V_p - V_m$$

where  $V_p$  = volume of the part

$V_m$  = volume of the mandrel

$$V_n = \pi r_p^2 h / 3 - \pi r_m^2 h / 3 \quad \text{for a cone} \quad (4-2)$$

$$V_n = \frac{\pi h}{3} (r_p^2 - r_m^2) \quad (4-3)$$

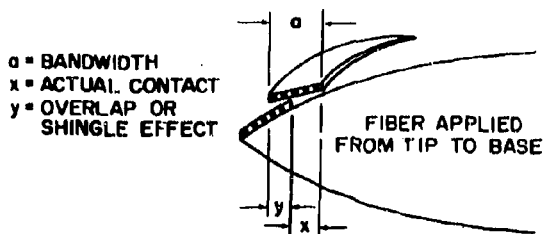


Figure 4-56. Diagram Showing Effect of Bandwidth of Fiber on Overlap Pattern

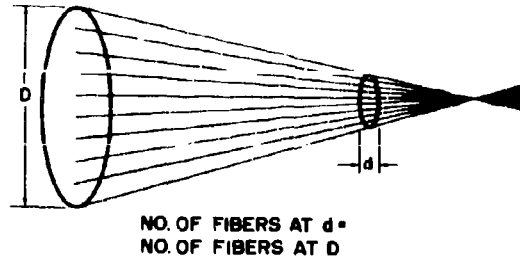


Figure 4-57. Diagram of Longitudinal Fiber Pattern

The problem then arises of reducing the unit to a constant thickness. This is accomplished by drop-stitching. By knowing the geometry of the mandrel and rate change of curvature for any given station, and what  $r_p$  should be in Eq. 4-4 for that station, it is possible, using specialized equipment, to tag a sequence of fibers as they are applied.

These strands are mechanically tagged or located. When the desired thickness is obtained at the base of the mandrel, the turntable is reversed. Then certain strands are thrown out of the pattern according to the sequence in which they were tagged. By means of a template set to the outside contour of the part, the fibers are located according to station line and cut to give  $r_p$  of Eq. 4-4. When this is completed, the longo pattern is a constant thickness from tip to base and contains continuous fibers from tip to base.

$$\begin{aligned} \frac{3V_n}{\pi h} &= r_p^2 - r_m^2 \\ r_p^2 &= \frac{3V_n}{\pi h} + r_m^2 \\ r_p &= \sqrt{\frac{3V_n}{\pi h} + r_m^2} \end{aligned} \quad (4-4)$$

#### 4-16.4.3 The Circ-Gore Method

The circ-gore method differs from the previous one only with respect to the application of the longitudinal fibers. A *gore* may be defined as a triangular or wedge-shape insert or section of a whole. In this method, the circumferential fibers are applied as previously mentioned (Paragraph 4-16.4.2). The gore simply replaces the longitudinal winding. The surface to be cov-

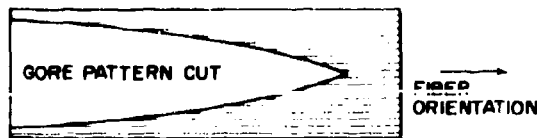


Figure 4-58. Sketch of Gore Pattern on Fiberglass Tape

ered is marked in equal sections, so that the gores appear as shown in Fig. 4-58. The gore is cut from a unidirectional tape or sometimes from a glass fabric. The tape, depending upon the width of the gore, may be commercially available. If the width is greater than commercial stock, the tape may be manufactured conveniently by winding circumferential fibers on a drum to the desired width of the gore. The fibers may be overlaid with polyvinyl alcohol (PVA) or paper that serves as a backing to facilitate handling. Then the circles are cut and the whole winding laid out flat. Next, the gore is cut, using a template, and applied to the unit very much like a standard hand lay-up, using either a butt joint or an overlap joint.

From this description, it can be seen that the fabrication of high-performance radomes requires considerable hand tailoring to obtain an unbroken pattern. Therefore, for radomes that must withstand very high stress levels, this method does not obtain efficient use of the structural characteristics of the longitudinal fibers.

#### 4-16.4.4 The Circ-Longo Grind and Circ-Longo Sock Method

This method is the same as that covered in Paragraph 4-16.4.2, except that a grinding operation replaces that of drop-stitching. Thus, a cure stage is required after every application of a longo layer. This method allows the build-up of fibers due to change in diameter and simply grinds the surface to the desired physical thickness. This method lends itself more to conical shapes. In some ogive shapes, the fiber pattern might be such that the longo may be ground through, thus leaving an extreme discontinuity of fiber from base to tip.

The primary advantage of this method is that it facilitates rapid production by the use of a "longo sock" in place of winding directly on the

mandrel. Two rings are employed: One fits the base of the mandrel and the other has a diameter of 4 to 6 in. The rings are mounted on a spike or wind axis. The longo fibers are wound from one ring to the other to produce the longo sock. The rings, in turn, rotate to present a new surface to the filament after each loop is completed.

The machine winds a longo pattern just as it would if it were winding directly on the mandrel or part. The required number of revolutions is made to provide the desired thickness at the base of the mandrel; then the two rings are disengaged. The sock may then be stored by folding or by simply hanging it by one of the rings. When the sock is to be used, it is dropped over the top of the mandrel and the base and top rings are locked. Circs are wound to hold it in place and provide pressure, and the entire system is cured until sufficiently hard for grinding. With the proper choice of resin systems, the socks may be stored for long periods of time and be ready for immediate use. Control of fiber orientation is poor and electrical uniformity of the unit is much poorer than with other methods. Also, as pointed out, this method is generally limited to the production of conical shapes.

#### 4-16.5 METHODS OF CURE

The curing of filament-wound radomes is carried out under conditions normally used for the manufacture of reinforced plastic. There are limitations, however, imposed by the maximum temperature and the rate of heating that may be used. If it is necessary to cure the unit above 350°F to 425°F, the part usually separates from the mandrel. This causes a loss of reference and accurate wall thickness cannot be obtained. Therefore, when conditions require such a cure, the part is ground to the required physical and/or electrical thickness after the part has had an initial cure below 350°F. The change in physical thickness caused by post-cure and any change in dielectric constant of the composite may then be determined. With these data, the radome wall may be ground, after an initial cure, to reach the target thickness upon post-curing. The final configuration will then be on target after post-cure, which, for some systems, may be quite long (150 hr) and at relatively high temperatures (550°F to 700°F).



The rate of heating must not be too high. However, this is usually not a problem unless the part is small. For certain radomes, it is desirable to provide curing heat from the inside of the mandrel as well as from the outside. This technique reduces the chances of forming hot spots, which may result in separation of the radome from the mandrel.

In summary, the properties, behavior, and general nature of the various resin systems should be carefully considered before they are incorporated in a filament-wound radome structure.

#### 4-16.6 DIMENSIONAL CONTROL\*

Control of the physical thickness of the radome wall is of prime importance not only to the radome designer, but also to the fabricator. The degree of control depends upon the time required for range correction and whether the radome will meet the electrical requirements. Dimensional control is not limited to the tolerance on wall thickness, but must also be considered in the pattern of each individual layer or ply. The control is necessary for electrical uniformity and is often used to obtain the maximum structural efficiency from the unit. The bunching of fibers, as well as crossover and voids, produces dielectric holes that, in turn, affect boresight error and rate, which are quite difficult to correct by range testing. The final grinding of the wall thickness to a given target may be accomplished in several ways. These are discussed in the following paragraphs.

##### 4-16.6.1 Physical Grinding Control: Ultrasonics

Ultrasonics may be defined as pertaining to vibrations and waves that have frequencies greater than those that affect the human ear; that is, greater than 20,000 cps. The ultrasonic gauge has been widely used to measure radome wall thickness. It employs a continuously varying frequency that may range from  $0.5 \times 10^{-6}$  to  $25 \times 10^{-6}$  cps. This signal is changed to a mechanical vibration via transducers. As in

electromagnetics, when the waves or vibrations strike a different medium, reflection occurs. This reflection is picked up by the same transducer and is amplified. When the reflected wave is in resonance with an outgoing signal, a change in load on the circuit results. The resultant signal is fed to a cathode-ray tube and shows up as a fundamental or harmonic resonant frequency. The resonant frequency of sound varies inversely with the thickness of the medium. Thus, the resonant frequency of a given material may be correlated to thickness. Therefore, calibration of a scale with the material being measured allows a direct reading of the thickness with the ultrasonic gauge.

Use of this type of measurement has many economic advantages. The instrument may be relatively small and portable. Measurements may be made with the radome on the mandrel or on the radar range. If the radome has a high degree of homogeneity, measurements of thickness to 0.001 in. are possible. One difficulty may be encountered; a reflected wave may be distinct enough to cause a standing wave that exceeds the range of the calibration scale, preventing distinct readings from being made.

##### 4-16.6.2 Electrical Grinding Control

The reflection interferometer (one-horn interferometer) is a convenient instrument used by Brunswick Corporation to control the manufacture of filament-wound radomes. The device provides readings of the electrical thickness of a radome, because it is sensitive to changes in both physical thickness and dielectric constant.

The reflection interferometer consists of a microwave bridge, a suitable graphic recording device, and the mechanical devices necessary to position the interferometer and survey the radome in known portions. The microwave bridge compares the phase of a stable reference signal to the phase of signal reflected from the metal mold, or mandrel, on which the radome is built. The reflected signal travels twice through the radome wall; thus, its phase is dependent on the electrical wall thickness. The manner in which reflected phase depends on electrical wall thickness is described by the following equation:

\* See paragraph 5-4.

$$R' = 180^\circ - 2 \tan^{-1} \left( \frac{\tan \phi}{\sqrt{\epsilon'}} \right) - 720^\circ S / \lambda_0 \quad (4-5)$$

where:

$R'$  = reflected phase, degrees

$S$  = interferometer horn to radome wall spacing, in.

$d$  = physical thickness, in.

$\epsilon'$  = relative dielectric constant

$\lambda_0$  = wavelength, in., at the interferometer frequency

$\phi$  = electrical thickness (degrees) =  $360^\circ d / \lambda_0 \sqrt{\epsilon'}$

$-2 \tan^{-1} \left( \frac{\tan \phi}{\sqrt{\epsilon'}} \right)$  = term dependent on the electrical wall thickness

$180^\circ$  = phase reversal caused by reflection at metal surface

$-720^\circ S / \lambda_0$  = term dependent on the spacing of the interferometer horn and the radome wall

The third term of Eq. 4-5 is known because the spacing is measured for the desired scan paths.

Reference dielectric panels are usually constructed for the range of electrical thickness values specified in a particular radome design. The reflection interferometer is then calibrated by utilizing the known panels. This procedure is necessary because the microwave bridge reads relative phase only; it does not have an absolute starting point. This calibration procedure also verifies that the interferometer is operating properly, i.e., that deviations from Eq. 4-5 are small.

In the manufacturing process, the reflection interferometer is used to obtain continuous plots of electrical thickness as a function of position on the radome. Compensation is made for deviations from the design value by appropriately changing the physical thickness of the radome wall (by grinding). The tolerance within which this target value may be reached

is a function of many variables (including the capability of the grinder to make small changes), but is usually  $\pm 1$  electrical degree at X-band frequencies.

#### 4-16.6.3 Physical Thickness Measurement: The Feeler Gauge Method

Measurement of the physical thickness of a radome wall during the grinding operation by the feeler gauge method is based primarily on the relationship of two objects: the grinding head or wheel and the mandrel. This relationship is established or determined by means of a reference point or position, thereby giving a starting point from which other measurements may be taken.

There are three common methods for determining this reference point:

1. Measurements and positions of the grinding wheel and mandrel are taken at the time of grinding the mandrel. It is then known that if all of these measurements and positions are duplicated, the same relationship will be reestablished.
2. On a surface of revolution part, the diameter of the part can be measured, and if the mandrel diameter is known at this position, the part thickness is calculated and the grinding mechanism adjusted and positioned at a predetermined distance from the part.
3. Measurement of part thickness may be determined by means of a depth gauge through a small hole drilled in the part. The grinding mechanism is then adjusted as in 2.

After the relationship is established, physical thickness may be measured throughout the length of the part by letting the grinding head traverse the part, taking measurements of the distance between the part and the grinding wheel by means of a feeler gauge. The difference in the "feel" at these positions will give the part thickness at the reference points.

The traverse of the grinding mechanism is controlled by two methods: a production cam or a profile template. Both of these devices are contoured to the Outer Mandrel Line (OML), or the configuration of the outer surface of the finished part. When the production cam is used, the grinding mechanism is moved through a

following or duplicating system activated from a follower wheel rotating on the surface of the production cam. At any position of the follower wheel on the production cam, the grinding wheel is moved to a corresponding position on the part. From this position, a feeler gauge measurement can be taken between the part and the grinding wheel and the part thickness calculated. The profile template is similar except that the grinding mechanism traverses the part at a constant distance from the part as controlled by rollers and guides working on the edge of the template. Measurements are taken much in the same manner as with the production cam measurements. Adjustments are then made, if required, and the part is ground to the desired physical thickness.

There are many variables inherent in this measuring system that must be considered. They are grinding wheel diameter, grinding wheel edge radius, follower wheel diameter and radius, grinding wheel wear, machine inaccuracies, operator proficiency, and preliminary machine setup. However, with sufficient knowledge of the machine's history and ordinary precautions taken in the machine setup, consistently good results can be obtained with this method of physical thickness control.

#### 4-16.7 ADDITIONAL METHODS OF COMPOSITE RADOME FABRICATION

With the use of any of the methods described in Paragraph 4-16.1, several variations may be used, as in conventional laminating. Honeycomb structures may be incorporated for "A" sandwich construction. The inner skin is fabricated as a thin-wall composite. The honeycomb of a given density is then applied to the composite if uncured, or to an adhesive film over the composite if cured. The honeycomb is bonded under the pressure of a vacuum bag or an autoclave. Then the outer skin is applied as a thin-wall composite. This allows the fabrication of very thin skins to close dimensional control and high mechanical characteristics. To prevent resin drain into the honeycomb, a controlled B-stage roving or a film adhesive is used for the outer skin. This will find more application for doppler and side-looking radomes than nose radomes.

As an extension of the honeycomb approach,

foam may be used to replace the honeycomb. Since the honeycomb causes serious problems because of the look angle in nose radomes, a dielectric filled syntactic foam may be used. Again, each skin is treated as a thin-wall composite. The syntactic foam, with a dielectric to match the skin, is applied to the inner skin and cured. The foam is sealed with a very thin coating to prevent resin absorption from the filament. The outer skin is then applied. This method has the advantage that each section may be monitored for electrical thickness control, so that final grinding of the outer skin to compensate for electrical thickness may be minimized. The primary use is to reduce weight; for example:

Filament Composite	
Specific Gravity	2.1
Density	131 lb/ft <sup>3</sup>
Dielectric Foam	
Density	15 to 30 lb/ft <sup>3</sup>

It is not efficient to use this approach with a combination of roving and glass fabric where attachment areas require high bearing or pin pull-out loads. This requires a higher than normal pressure, particularly if a resin system is used that produces byproducts such as water of condensation. It is possible to exert high pressure by using filament over-wrap, as indicated by the following equations:

$$P = \frac{T \times TPI}{r} \quad \text{for winding at } 90^\circ \text{ to the axis} \quad (4-6)$$

$$P = \frac{4T \alpha \times TPI \times NQ}{D_m \times B.W.} \quad \text{for helical winding} \quad (4-7)$$

where B.W. = bandwidth, in.

$D_m$  = diameter of mandrel, in.

NQ = number of helical layers

P = normal force or pressure, psi,  
between the mandrel and the  
first layer of glass

T = tension, lb/thread

TPI = threads/in.

r = radius of curvature, in.

$\alpha$  = winding angle, degrees

With this technique it is possible to develop the high pressures required for molding condensation polymers.

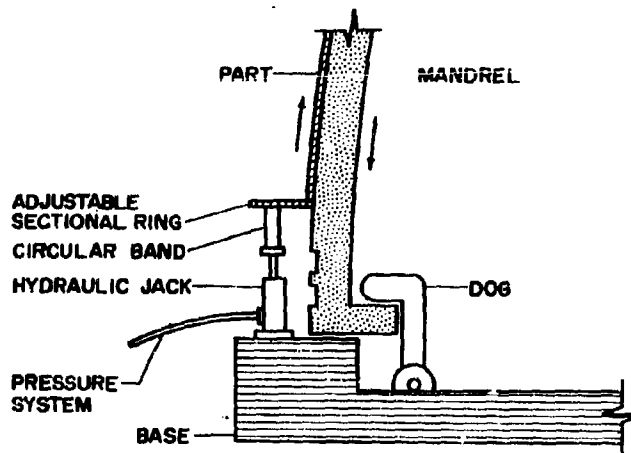


Figure 4-59. Drawing of Setup Used to Remove Filament-Wound Radome from Mandrel

#### 4-17 FINISHING METHODS

As the filament-wound radome leaves the grinding operation, it has a surface finish of approximately 140 micro-in. This finish may be improved by a seal-coat operation.

The first step in the seal-coat operation consists of hand sanding very lightly with a 200-grit paper. This cleans, as well as smooths, the surface. Next, a coating formulation is squeegeed onto the part in a very thin layer, taking care to avoid ridges and uneven areas. This formulation consists of Epon-828 epoxy resin with Cab-o-sil as a filler. Curing agent DTA is used and the coating is cured for 1 hr. at 180°F. The surface is again sanded, usually immediately before the final coating is applied. This type of coating will give a surface finish of approximately 100 micro-in. on the filament-wound part.

The final finish will, of course, depend on the type of coating required on the radome. In some cases, epoxy paint is used for a coating, but on most radomes, the finish consists of a rain-erosion resistant coating, which is discussed in Chapter 3.

#### 4-18 PART REMOVAL METHODS

After completion of the final grind and meas-

urement of physical thickness, the radome is ready for removal from the mandrel. A diamond cutoff blade is used to cut through the part to the mandrel surface and the lock ring portion of the part is removed. Location of this cut is usually 2 or 3 in. lower or aft of the final trim line. In some cases, especially with a thin-wall radome, a second cut is made 1 or 2 in. below the first cut to provide a buffer or protection ring. This prevents damage to the radome during the removal operation. The radome and mandrel are then removed from the grinder and placed in the part removal jig. (See Fig. 4-59.)

The mandrel is securely fastened to the removal jig by means of dogs that are located to catch inside the mandrel. Spaced evenly around the perimeter of the part are six or eight (or as required) hydraulic jacks, positioned vertically. These jacks rest upon the base structure of the jig and, when extended, bear against the bottom of a heavy steel band that encircles the mandrel. Clearance between this band and the mandrel is sufficient to prevent the two pieces from coming into contact, thereby avoiding damage to the mandrel. On the top edge of this band is a sectional ring, the inner edge of which is contoured to correspond to the mandrel surface. This ring is bolted to the band through slotted holes so that it can be adjusted to the mandrel surface.

To remove the part, pressure is applied to the jacks through a distribution system, allowing equal pressure to be exerted by all jacks. The sectional ring is moved up to contact the edge of the radome. Sufficient pressure is applied to break the radome loose from the mandrel. The amount of pressure required varies according to radome size, configuration, parting agent, and condition of mandrel surface. As a general rule, a radome such as the F4B requires hydraulic pressure in the range of 40,000 lb. On more difficult parts, this pressure could be considerably higher. After the radome is loosened from the mandrel, it is lifted by means of a harness. The inside is inspected for damage at this time.

Some of the difficulties encountered during part removal could be caused by the surface finish of the mandrel. Most steel mandrels need a surface finish of 32 micro-in. or better to provide an efficient removal operation. The surface is treated with a silicone compound and baked on at 450°F to 500°F. This finish is good for approximately 10 radomes before the surface must be retreated. In addition to the silicone, a release agent is applied for every part fabricated. This release agent must be compatible with the resin system used. It also must be able to withstand the cure temperatures encountered without breaking down or dispersing into the resin system.

#### REFERENCES

1. *High-Temperature Resins, Analysis of Process Parameters and Evaluation Procedures for Filament-Wound Composites*, WADD Technical Report 60-791, May 1962.
2. Shand, E. B. *Glass Engineering Handbook*, McGraw-Hill Book Company, New York, 1960.
3. *High - Modulus, High - Temperature Glass Fibers for Reinforced Plastics*, WADD Technical Report 60-24, November 1960.
4. *A Superior Glass Fiber Reinforcement for Structural Composites*, ASD-TDR 63-81, AF-994, March 1963.
5. Edwards, B. L. *Calculated Dielectric Constant of Various Glass Resin Composites at Different Resin Contents*, Brunswick Defense Report, BR-122-057, December 1963.
6. Rosato, D. V., and Grove, C. S. *Filament Winding*, John Wiley and Sons, Inc., New York, 1964.

# **APPENDIX 4A** **PROPERTIES OF SELECTED RESINS\***

## **A. Vibrin 135-136A: Naugatuck Chemical Co.**

1. Casting: Vibrin 135  
 Specific gravity: 1.34  
 Dielectric constant:  
     9.375 gc (100% RC) : 2.896  
     16.5 gc (100% RC) : 2.874  
 Loss tangent:  
     9.375 gc : 0.0124  
     16.5 gc : 0.0118
2. Laminate: Vibrin 135 (Bomarc panel)  
 Specific gravity: — — —  
 Dielectric constant:  
     9.375 gc (18% RC) : 4.93  
     9.375 gc (17% RC) : 4.99  
     9.375 gc (19% RC) : 4.71  
 Loss tangent:  
     9.375 gc (18% RC) : 0.0119  
 Reinforcement: Corning E-Glass 181  
 Note: See Fig. 4-A1 for dielectric constant  
 and resin content vs. temperature.
3. Casting: Vibrin 136-A  
 Specific gravity: 1.35  
 Dielectric constant:  
     9.375gc (100% RC) : 2.88  
 Loss tangent:  
     9.375 gc : 0.0110
4. Laminate: Vibrin 136-A  
 Specific gravity: 1.68  
 Dielectric constant:  
     9.375 gc—R.T.     4.07  
                   100°F: 4.08  
                   240°F: 4.16  
                   300°F: 4.16  
                   390°F: 4.17  
                   520°F: 4.15  
                   585°F: 4.17  
                   690°F: 4.21  
                   700°F: 4.15  
 Loss tangent:  
     9.375 gc: 0.0065  
 Reinforcement: Corning E-Glass 181  
 Resin content: 35.5%

## **B. VC-8359 epoxy resin: Brunswick Corp.**

1. Casting: VC-8359 epoxy  
 Specific gravity: 1.34  
 Dielectric constant:  
     9.375 gc (100% RC) : 2.99  
 Loss tangent:  
     9.375 gc : 0.0220
2. Laminate: VC-8359 epoxy  
 Specific gravity: 1.85  
 Dielectric constant:  
     9.375 gc (33.0% RC) : 4.41  
     16.5 gc (33.0% RC) : 3.92  
 Loss tangent:  
     9.375 gc (33.0% RC) : 0.0170  
     16.5 gc (33.0% RC) : 0.0314  
 Reinforcement: E-Glass 181  
 Resin content: 33.0%

Note: See Fig. 4-A2 for both measured and calculated values of VC-8359 epoxy in dielectric constant vs. percent resin by volume.

## **C. JC-1571: Brunswick Corp.**

1. Hydrocarbon resin:  
 Casting: JC-1571 hydrocarbon  
 Specific gravity: 1.03  
 Dielectric constant:  
     9.375 gc (100% RC) : 2.46  
 Loss tangent:  
     9.375 gc : 0.007  
 Laminate: JC-5171 hydrocarbon  
 Specific gravity: — — —  
 Dielectric constant:  
     9.375 gc : 4.083  
 Loss tangent:  
     9.375 gc : 0.002  
 Reinforcement: E-Glass 181  
 Resin content: 28%  
 Laminate: JC-1571 hydrocarbon  
 Specific gravity: — — —  
 Dielectric constant:  
     10 cps : 3.62  
 Loss tangent:  
     10 cps : — — —  
 Reinforcement: E-Glass 181  
 Resin content: 28%

\* From D. P. Parks, Brunswick Defense Division  
 Internal Report No. BR-122-040, May 1963.

2. Polybutadiene—Butarez 15: Phillips Petroleum Co.

Casting

Specific gravity: 0.992

Dielectric constant:

1 mc: 2.42

Loss tangent:

1 mc: <0.0005

#### D. Polyesters

1. Laminac 4110 general polyester:

Cyanamid Co.

Benzoyl peroxide

Specific gravity: 1.12

Dielectric constant:

9.375 gc: 2.85

Loss tangent:

9.375 gc: 0.014

State: Casting

2. Paraplex P-43 general polyester: Rohm and Haas Co.

Specific gravity: 1.23

Dielectric constant:

9.375 gc: 2.89

Loss tangent:

9.375 gc: 0.019

State: Casting

3. Selectron 5016: Pittsburgh Plate Glass Co.

Specific gravity: 1.18

Dielectric constant:

1 mc: 3.15

Loss tangent:

1 mc: 0.05

State: Casting

4. Hetron 92: Hooker Chemical and Plastic Corp.

Specific gravity: 1.28

Dielectric constant:

1 mc (100% RC): 4.52

Loss tangent:

1 mc: 0.034

Reinforcement: Kraft paper base

5. Stypols: Freeman Chemical Corp.  
*Stypol 25*

Specific gravity: 1.288

Dielectric constant:

1 mc (100% RC): 3.19

Loss tangent:

1 mc: 0.024

State: Casting

*Stypol 6B*

Specific gravity: 1.268

Dielectric constant:

9.375 gc: 2.92

Loss tangent:

9.375 gc: 0.0108

State: Casting

*Stypol 705*

Specific gravity: 1.182

Dielectric constant:

9.375 gc: 2.85

Loss tangent:

9.375 gc: 0.020

State: Casting

*Stypol 705*

Specific gravity: 1.745

Dielectric constant:

9.375 gc: 4.37

Loss tangent:

9.375 gc: 0.015

Resin content: 34.7%

State: Laminate

Reinforcement: Fiberglass-181-136 fabric

*Stypol 40-2025*

Specific gravity: 1.288

Dielectric constant:

1 mc: 3.19

Loss tangent:

1 mc: 0.024

State: Casting

6. Polylite ED-386—rigid polyester:

Reichhold Chemical Co.

Specific gravity: 1.22

Dielectric constant:

1 mc: 3.24

Loss tangent:

1 mc: 0.068

State: Casting

7. AR-1075—HT polyester: General Electric Co.

Specific gravity: 1.27

Dielectric constant:

8500 to 10,000 mc: 3.0

Loss tangent:

8500 to 10,000 mc: 0.020

#### E. Epoxies

1. Casting: Epon 826 and 828: Shell Chemical Co.

*Epon 826*

Specific gravity: 1.164

Dielectric constant:

16.5 gc: 2.844

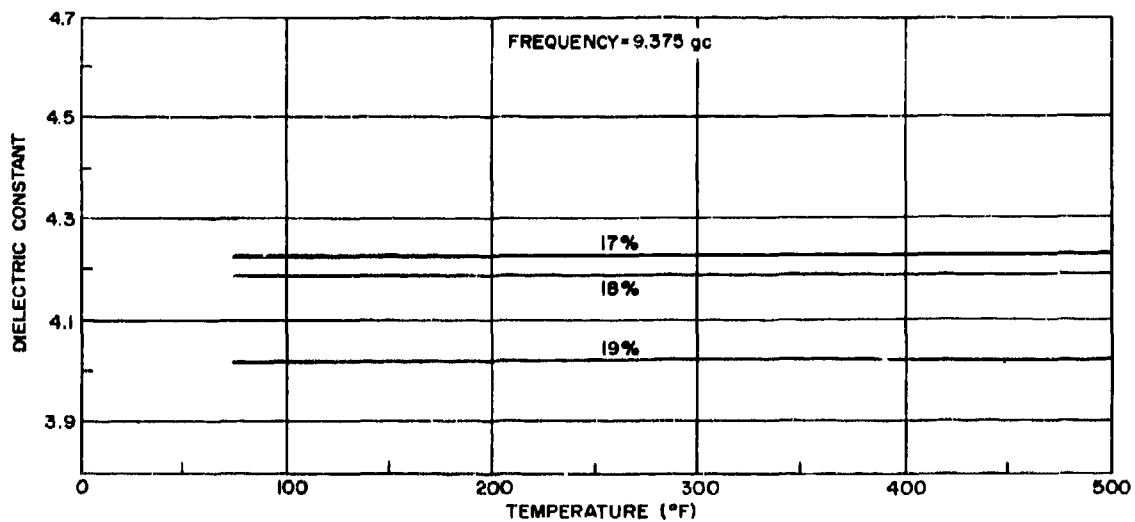


**Figure 4-A1. Vibrin 135 and S994 Glass—Dielectric Constant vs Temperature and Resin Content**

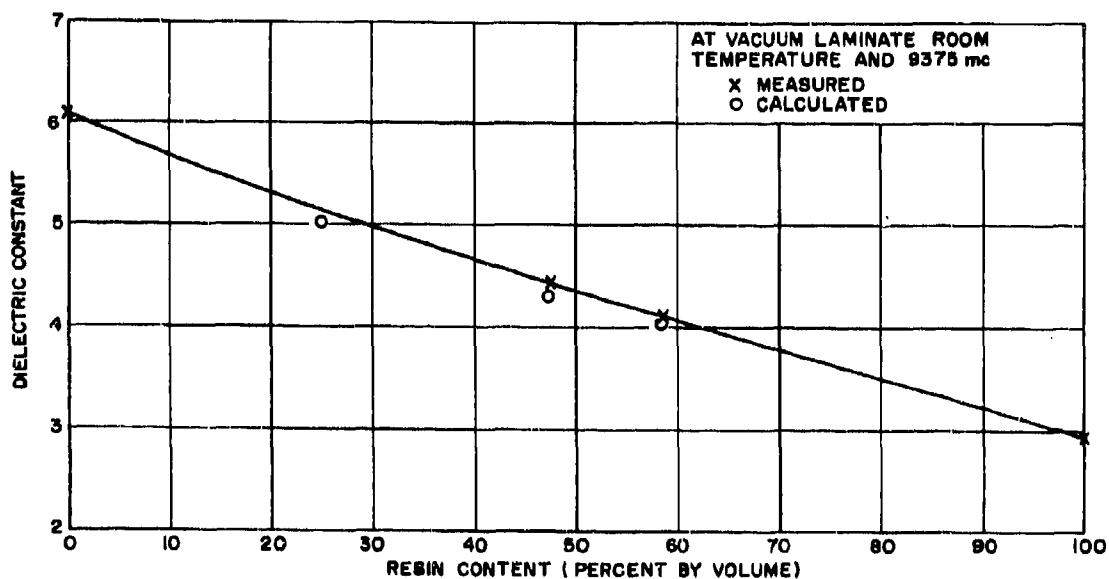


**Figure 4-A2. Measured and Calculated Values at Vacuum Laminar Room Temperature and 9375 mc for VC-8359 Epoxy—Dielectric Constant vs Resin**



- Loss tangent:  
16.5 gc: 0.0188  
State: Casting  
Curing agent: 6 PHR BF<sub>3</sub>400  
*Epon 828*  
Specific gravity: 1.168  
Dielectric constant:  
9.0 gc: 3.0  
Loss tangent:  
9.0 gc 0.015  
State: Casting  
Curing agent: 10.5 PHR "D"  
*Epon 828*  
Specific gravity: 1.22  
Dielectric constant:  
9.375 gc: 2.81  
Loss tangent:  
9.375 gc: 0.029  
State: Casting  
Curing agent: 90 PHR MNA  
1 PHR BMDA  
*Epon 828*  
Specific gravity: 1.18  
Dielectric constant:  
9.375 gc: 2.83  
Loss tangent:  
9.375 gc: 0.041  
State: Casting  
Curing agent: USB-91 (17 PHR)  
*Epon 828*  
Specific gravity: 1.23  
Dielectric constant:  
9.375 gc: 2.97  
Loss tangent:  
9.375 gc: 0.040  
State: Casting  
Curing agent: USB-5 (15 PHR)
2. Epon 828 laminates: Filament-Wound and Fabric: Shell Chemical Co.  
*Epon 828*  
Specific gravity: — — —  
Dielectric constant:  
1 mc: 5.22  
Loss tangent:  
1 mc: 0.0202  
Resin content: 30%  
State: Wet lay-up panel  
Reinforcement: Corning E-Glass-181  
*Epon 828*  
Specific gravity: — — —
- Dielectric constant:  
9.375 gc: 3.55  
Loss tangent:  
9.375 gc: 0.013  
Resin content: 32%  
State: Laminate (wet lay-up)  
Reinforcement: Corning E-Glass-181
3. Araldites: Ciba Products Corp.  
*Araldite DP-419*  
Specific gravity: — — —  
Dielectric constant:  
10<sup>5</sup> cps: 3.60  
Loss tangent:  
10<sup>5</sup> cps: 0.0250  
State: Casting  
Curing agent: "Hardener 951"  
*Araldite DP-412*  
Specific gravity: — — —  
Dielectric constant:  
10<sup>5</sup> cps: 3.32  
Loss tangent:  
10<sup>5</sup> cps: 0.0135  
State: Casting  
Curing agent: MDA methylene
4. DER-DEN epoxy resins: Dow Chemical Co.  
*DER-331*  
Specific gravity: 1.17  
Dielectric constant:  
1 mc: 3.35  
Loss tangent:  
1 mc: 0.032  
State: Casting  
Curing agent: MDA (methylene dianiline)  
*DEN-438*  
Specific gravity: 1.22  
Dielectric constant:  
1 mc: 3.39  
Loss tangent:  
1 mc: 0.024  
State: Casting  
Curing agent: MDA (methylene dianiline)
5. Bakelite: Union Carbide Co.  
*ERL-2795*  
Specific gravity: 1.14  
Dielectric constant:  
10 mc at R.T.: 3.68  
10 mc at 176°F: 4.60  
10 mc at 212°F: 5.22

Loss tangent:  
10 mc at R.T.: 0.0373  
10 mc at 176°F: 0.0670  
10 mc at 212°F: 0.0830

*ERL-2774*

Specific gravity: 1.17  
Dielectric constant:  
10 mc at R.T.: 3.42  
10 mc at 176°F: 3.37  
10 mc at 212°F: 3.41

Loss tangent:  
10 mc at R.T.: 0.0212  
10 mc at 176°F: 0.0185  
10 mc at 212°F: 0.0180

*ERL-3794*

Specific gravity: 1.21  
Dielectric constant:  
10 mc at R.T.: 3.70  
10 mc at 176°F: 3.85  
10 mc at 212°F: 4.49

Loss tangent:  
10 mc at R.T.: 0.088  
10 mc at 176°F: 0.045  
10 mc at 212°F: 0.044

F. Phenolic resins

1. 91-LD: American Reinforced Plastics

Specific gravity: 1.9  
Dielectric constant:  
X-Band at 77°F: 4.14  
X-Band at 392°F: 4.40  
X-Band at 437°F: 4.54

Loss tangent:  
X-Band at 77°F: 0.026  
X-Band at 392°F: 0.042  
X-Band at 437°F: 0.042

State: Laminate

Resin content: 25 to 35%

Reinforcement: E-Glass-181 Fabric

2. Plyonol 23-017: Reichhold Chemical Co.

Specific gravity: 1.06 to 1.07  
Dielectric constant:

10 mc: 5.00

Loss tangent:

10 mc: — — —

State: Laminate

Resin content: 25 to 35%

Reinforcement: 181 style glass

G. Polyamide Resins (Nylon)

1. Zytol 101: DuPont Co.

Specific gravity: 1.14

Dielectric constant:

1 mc: 3.6

Loss tangent:

1 mc: 0.04

State: Casting (thermoplastic)

2. BC1 No. 6601-F: Belding Corticelli Ind.

Specific gravity: 1.32

Dielectric constant:

1 mc: 3.4

Loss tangent: — — —

State: Casting (thermoplastic)

H. Fluorocarbon Resin

1. KEL-F81: 3M Co.

Specific gravity: 2.124

Dielectric constant:

10<sup>5</sup> cps at 77°F: 2.40

10<sup>5</sup> cps at 392°F: 2.62

Loss tangent:

10<sup>5</sup> cps at 77°F: 0.0143

10<sup>5</sup> cps at 392°F: 0.0036

2. "Teflon" FEP fluorocarbon: DuPont Co.

Specific gravity: 2.15

Dielectric constant:

10<sup>5</sup> cps: 2.10

Loss tangent:

10<sup>5</sup> cps: 0.0004

State: Molded specimen

3. "Teflon" TFE fluorocarbon: DuPont Co.

Specific gravity: 2.1 to 2.3

Dielectric constant:

10<sup>5</sup> cps: 2.0

Loss tangent:

10<sup>5</sup> cps: <0.0005

State: Molded specimen

I. Acrylic Resins

1. Nypol 46-4001

Specific gravity: 1.226

Dielectric constant:

1 mc: 3.61

Loss tangent:

1 mc: 0.024

State: Casting

2. Nypol 46-4020

Specific gravity: 1.190

Dielectric constant:

1 mc: 2.83

Loss tangent:

1 mc: 0.023

State: Casting

J. Silicones

1. DC-2106 resin: Dow Corning. The following was supplied by North American

- on pure DC-2106 casting supplied by Dow Corning.
- Specific gravity : 1.26
- Dielectric constant :
- 9.375 gc at 80°F : 2.85
- 9.375 gc at 200°F : 2.77
- 9.375 gc at 320°F : 2.71
- 9.375 gc at 440°F : 2.62
- 9.375 gc at 560°F : 2.56
- Loss tangent :
- 9.375 gc at 80°F to 560°F : 0.006
2. R-7145 resin : Dow Corning
- Specific gravity : 1.13
- Dielectric constant :
- 1 mc : 2.90
- Loss tangent :
- 1 mc : 0.001
- State : Casting
3. DC-2106 resin : X-556 F. W. with 15% R-7145
- Specific gravity : 1.75
- Dielectric constant :
- 9.375 gc : 3.42
- State : Laminate
- Resin content : 25.9%
4. DC-2106 resin : X-556 fabric with 15% R-7145
- Specific gravity : 1.78
- Dielectric constant :
- 9.375 gc : 3.58
- Resin content : 23.8%
- State : Laminate
5. DC-2106 resin : E-Glass fabric with 15% R-7145
- Specific gravity : 1.78
- Dielectric constant :
- 9.375 gc : 4.20
- Resin content : 36.7%
- State : Laminate
6. DC-2106 resin : quartz fabric with 15% R-7145
- Specific gravity : 1.5 to 1.6
- Dielectric constant :
- 9.375 gc at 77°F : 3.16
- 9.375 gc at 500°F : 3.35
- 9.375 gc at 700°F : 3.25
- 9.375 gc at 900°F : 3.10
- Loss tangent :
- 9.375 gc at 77°F to 900°F : 0.0032 to 0.0033
- Resin content : 32.38%
- State : Laminate
- K. Phenyl silane resins
1. 37-9X : Cincinnati Testing Lab.
- Specific gravity : — — —
- Dielectric constant :
- 9.375 gc : 2.37
- Loss tangent :
- 9.375 gc : 0.008
- State : Casting
2. 37-9X : 181-Volan A glass fabric
- Specific gravity : 1.80 to 1.95
- Dielectric constant :
- 10<sup>10</sup> cps at 77°F : 5.20
- 10<sup>10</sup> cps at 300°F : 5.20
- 10<sup>10</sup> cps at 500°F : 5.10
- Loss tangent :
- 10<sup>10</sup> cps at 77°F : 0.023
- 10<sup>10</sup> cps at 300°F : 0.033
- 10<sup>10</sup> cps at 500°F : 0.031
- State : Laminate
3. SC-1013 : Monsanto Chemical Corp.
- Specific gravity : 1.654
- Dielectric constant :
- 9.375 gc : 3.225
- Loss tangent :
- 9.375 gc : 0.022
- State : Laminate (fabric)
- Reinforcement : Sil-temp fabric
- Resin content : 24.48%
4. SC-1013
- Specific gravity : — — —
- Dielectric constant :
- 9.375 gc : 3.251
- Loss tangent :
- 9.375 gc : 0.046
- State : Casting (100% solids)

**APPENDIX 4B**  
**DIELECTRIC PROPERTIES OF SELECTED RESINS,  
GLASSES, AND LAMINATES**

The data shown in Figs. 4-B1 through 4-B17 were obtained from A. B. Raney, *An Introduction to Radome Electrical Design*, 1964 Edition, Brunswick Defense Report No. BK-124-001, Revision A, March 9, 1964.

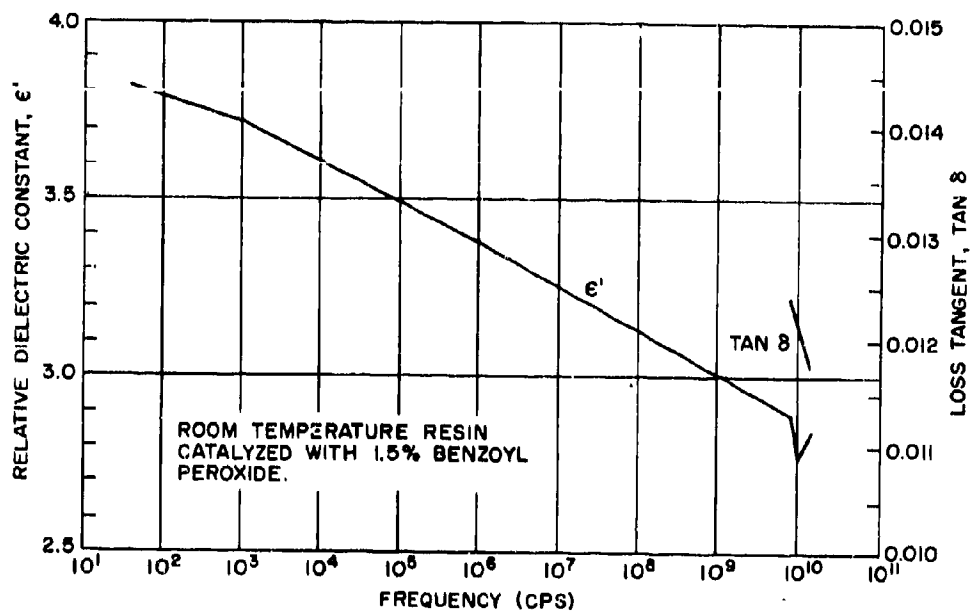


Figure 4-B1. Vibrin 135 Resin—Dielectric Constant and Loss Tangent vs Frequency

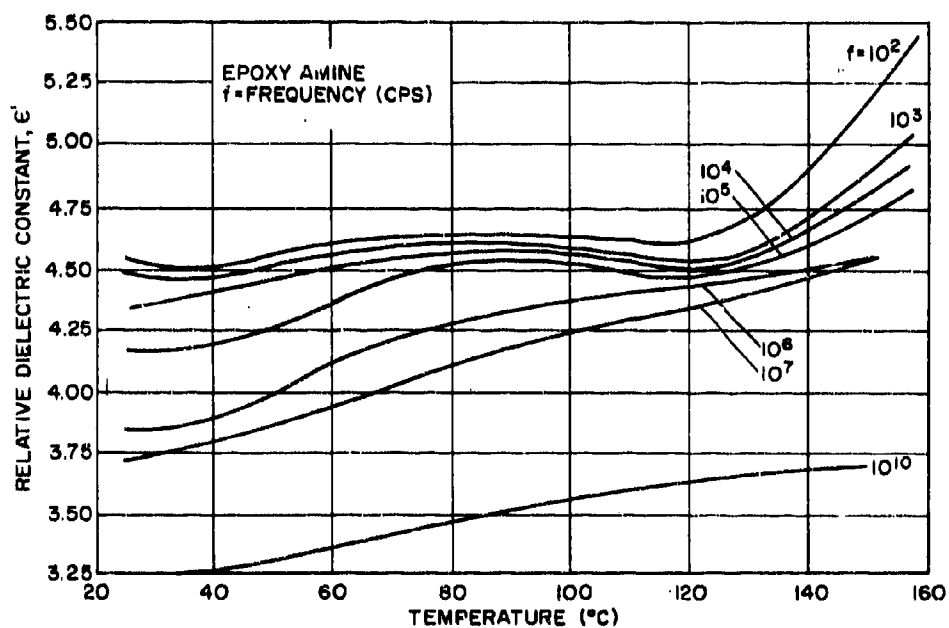


Figure 4-B2. Epon 828-Cl Resin—Dielectric Constant vs Temperature for Various Frequencies

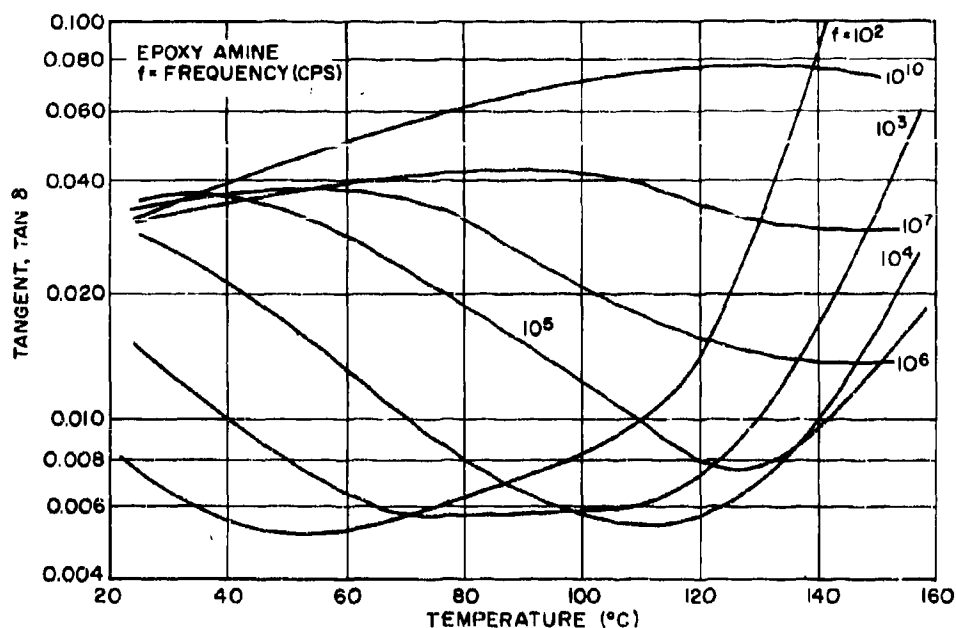


Figure 4-B3. Epon 828-CL Resin—Loss Tangent vs Temperature for Various Frequencies

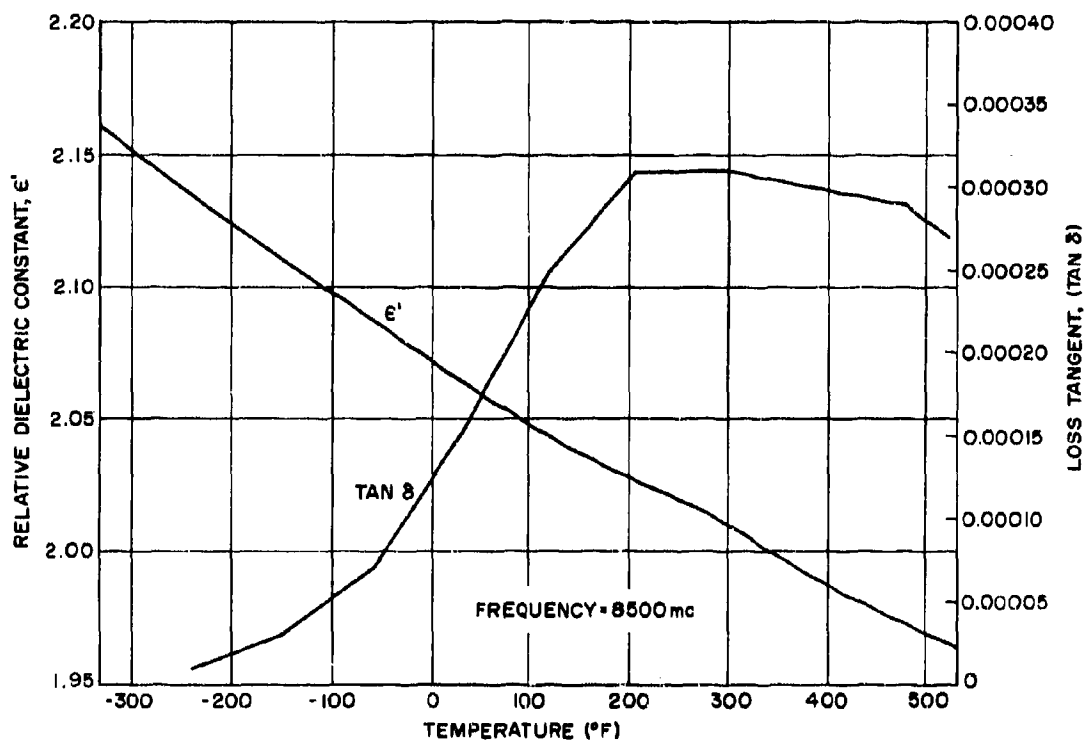


Figure 4-B4. Teflon—Dielectric Constant and Loss Tangent vs Temperature

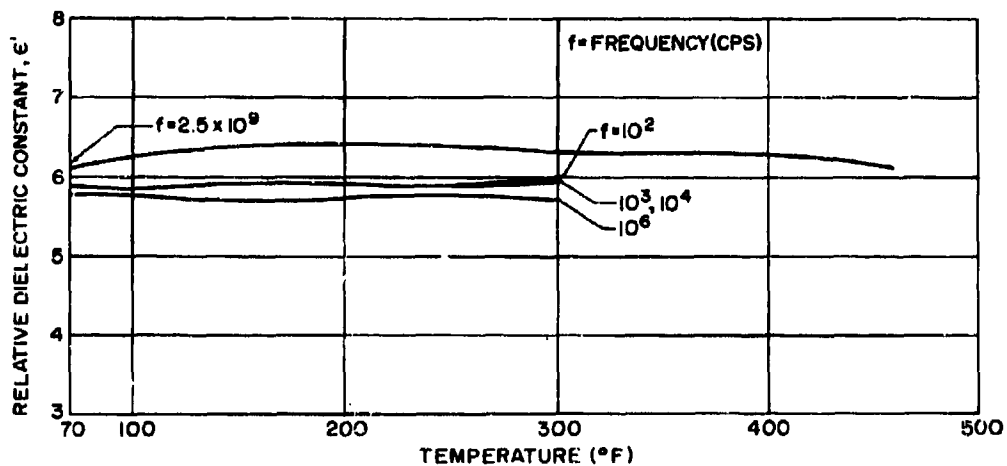


Figure 4-B5. E-Glass—Dielectric Constant vs Temperature for Various Frequencies

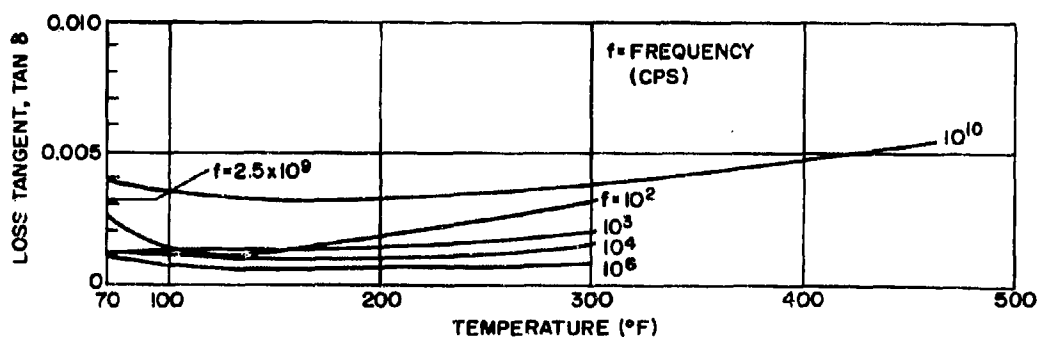


Figure 4-B6. E-Glass—Loss Tangent vs Temperature for Various Frequencies

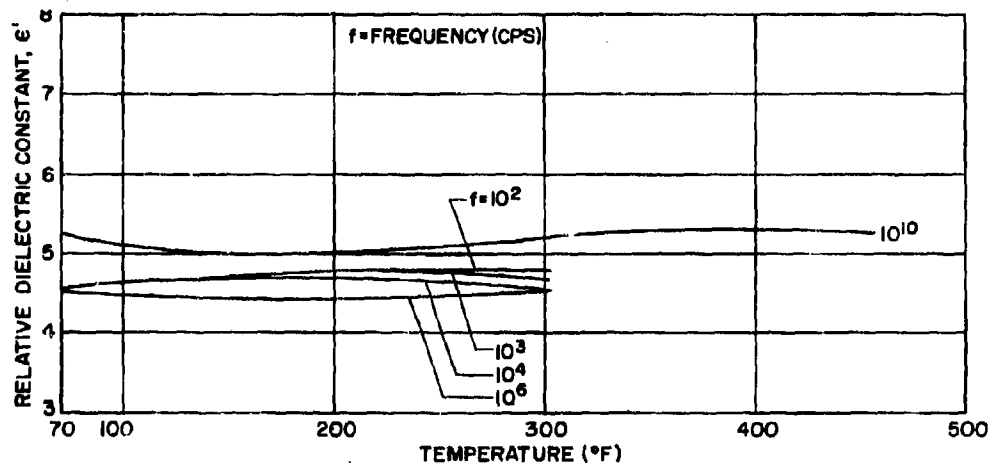


Figure 4-B7. S994 Glass—Dielectric Constant vs Temperature for Various Frequencies

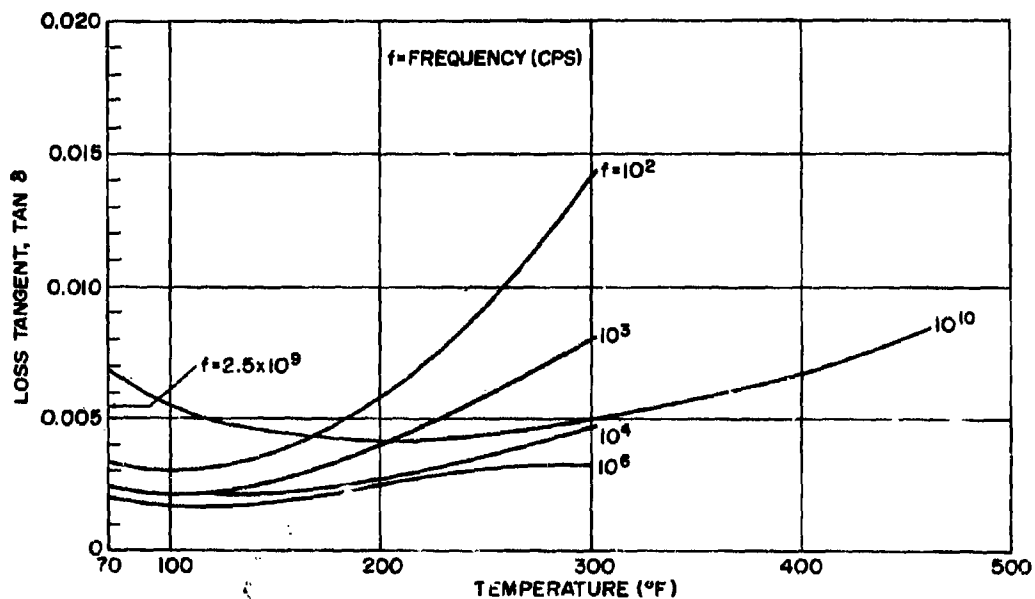


Figure 4-B8. S994 Glass—Loss Tangent vs Temperature for Various Frequencies



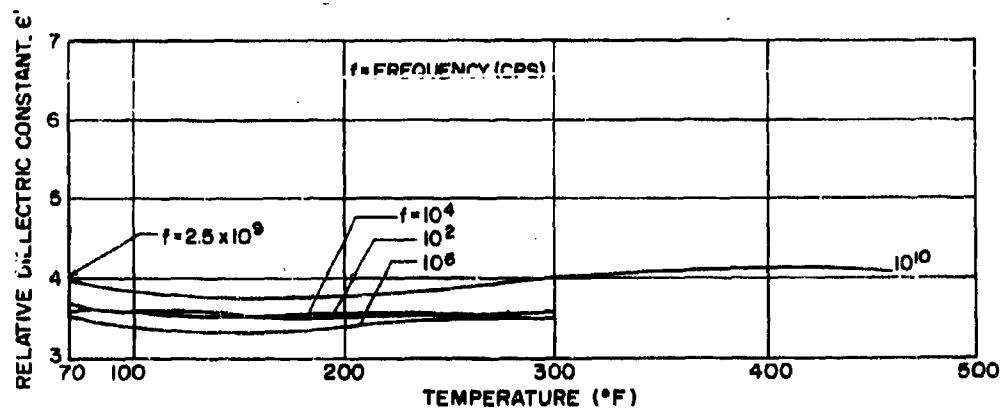


Figure 4-B9. D556 Glass—Dielectric Constant vs Temperature for Various Frequencies

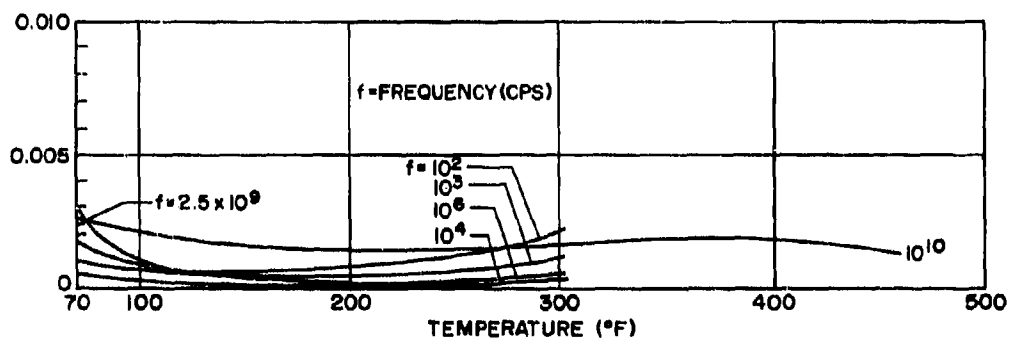


Figure 4-B10. D556 Glass—Loss Tangent vs Temperature for Various Frequencies

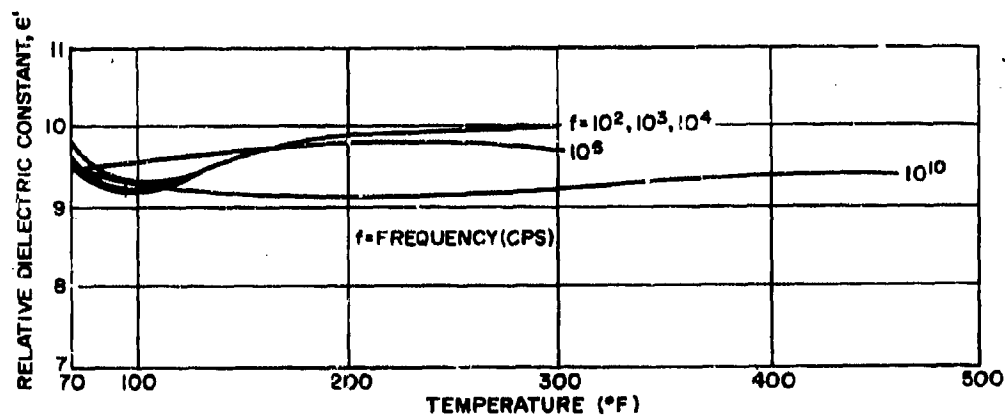


Figure 4-B11. L498 Glass—Dielectric Constant vs Temperature for Various Frequencies

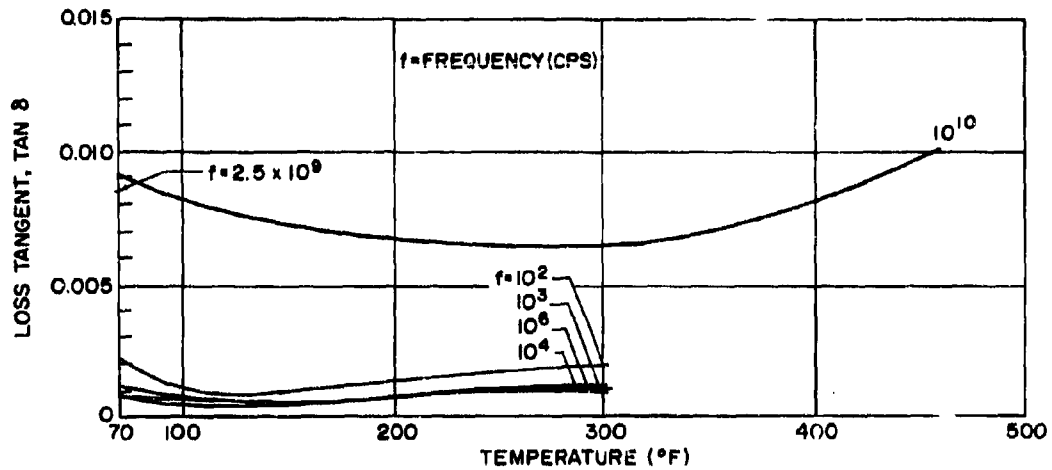


Figure 4-B12. L498 Glass—Loss Tangent vs Temperature for Various Frequencies

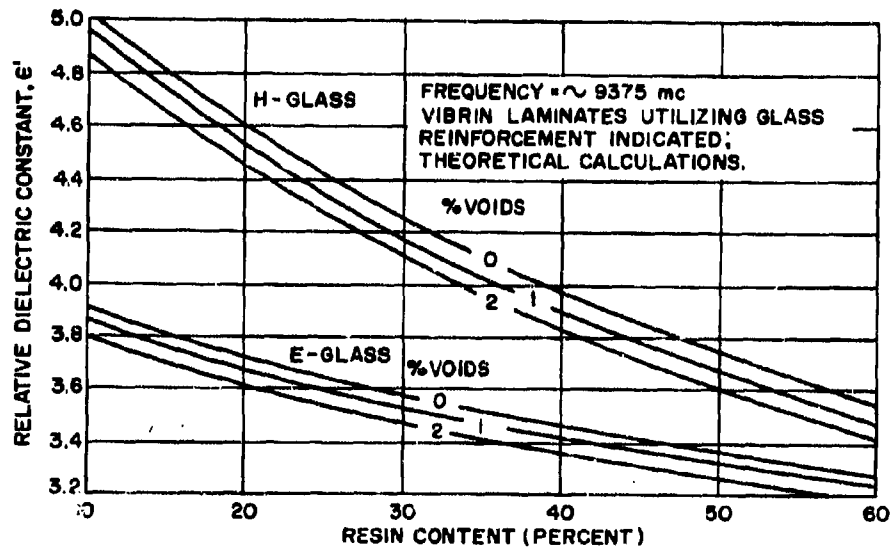


Figure 4-B13. Vibrin Laminates of E-Glass and H-Glass—Dielectric Constant vs Resin Content for Various Void Percentages

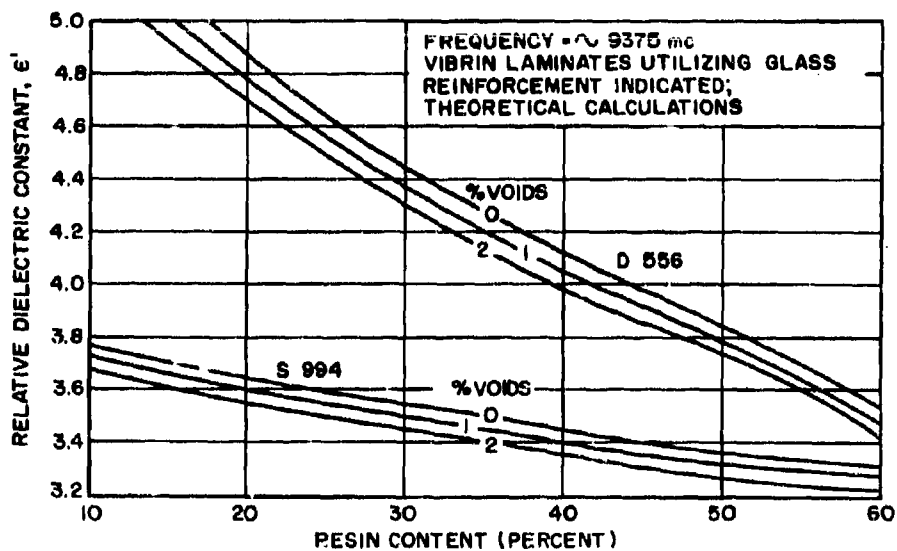


Figure 4-B14. Vibrin Laminates of D556 Glass and S994 Glass—Dielectric Constant vs. Resin Content for Various Void Percentages

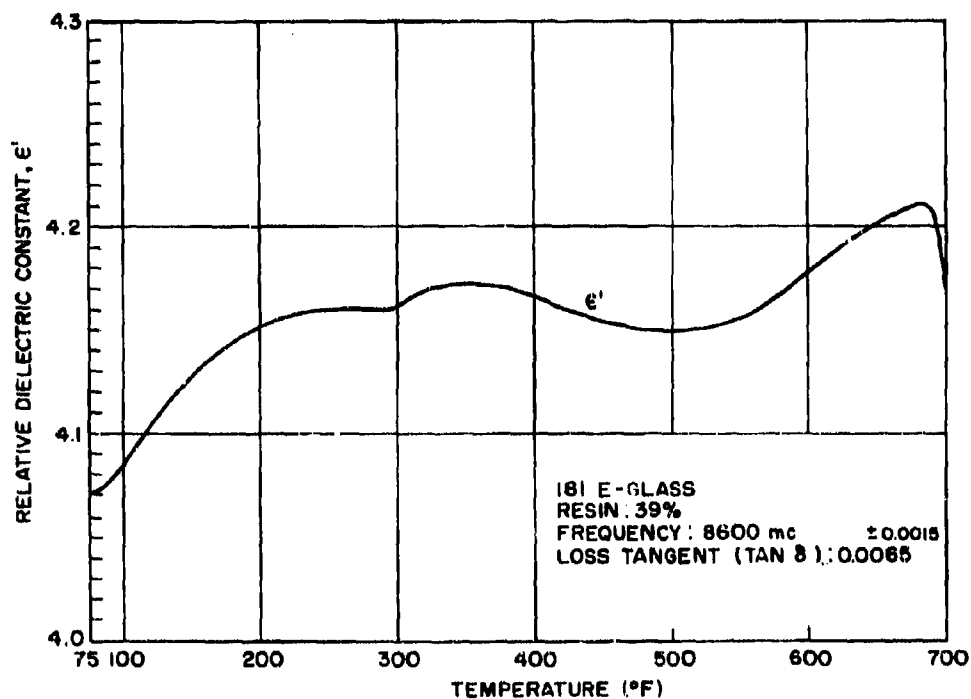


Figure 4-B15. Vibrin 135 (Polyester) Laminate—Dielectric Constant vs Temperature

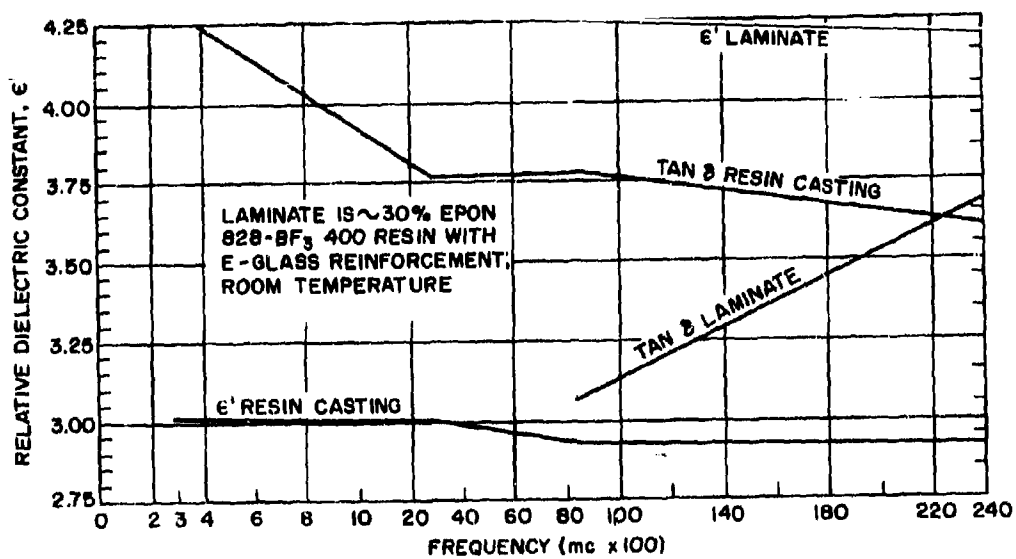


Figure 4-B16. Epon 828-BF<sub>3</sub> 400 Resin Casting and Laminate—Dielectric Constant and Loss Tangent vs Frequency

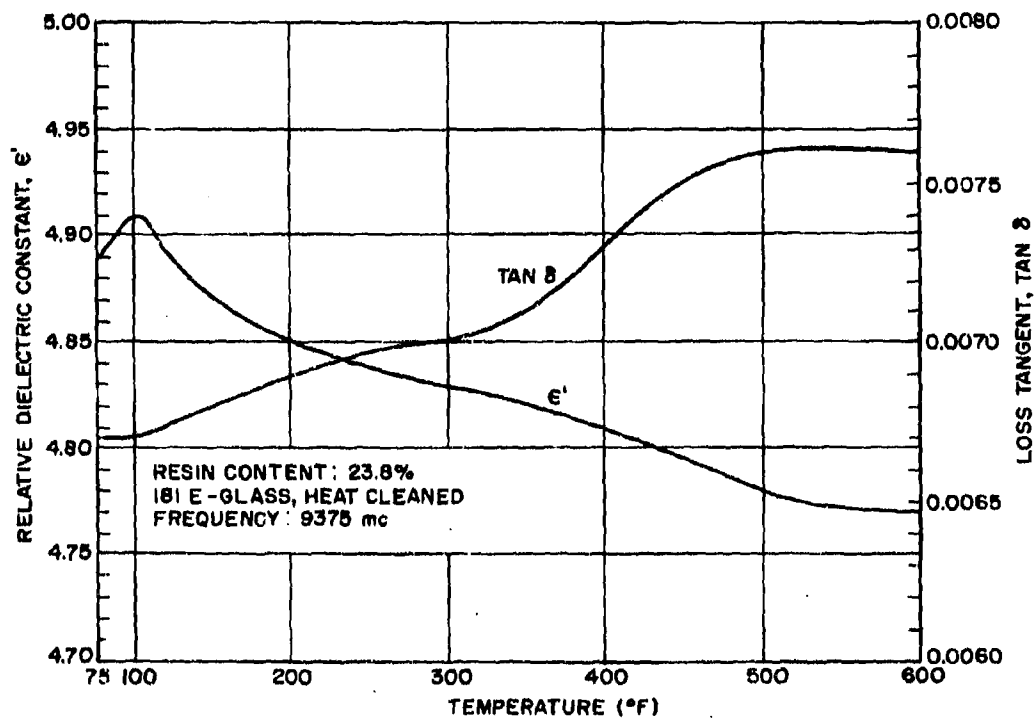


Figure 4-B17. Polybenzimidazole Laminate (PBI)—Dielectric Constant and Loss Tangent vs Temperature

**CHAPTER 5**  
**RADOME EVALUATION AND CORRECTION TECHNIQUES**

**PART I**

*by* **EINO J. LUOMA**  
*Emerson and Cuming, Inc.*  
*Dielectric Materials Division*  
*Canton, Massachusetts*

*and*

**PART II**

*by* **J. L. PENTECOST**  
*Melpar, Inc.*  
*Falls Church, Virginia*

*and*

**PART III**

*by* **DR. E. F. BUCKLEY**  
*Emerson and Cuming, Inc.*  
*Dielectric Materials Division*  
*Canton, Massachusetts*

# SYMBOLS

$B^2$	A function defined for convenience in expressing the equations for the $\tan \delta$ measured in a resonant cavity	$X_0$	Distance of first minimum from sample face
$C_p$	Specific heat	$X^1$	Magnitude of off-peak direct-ray vector
$D$	Cavity diameter, cm	$Y^1$	Magnitude of reflected-ray vector
$E_1$	Direct signal voltage	$a$	Effective cavity radius
$E_2$	Reflected signal voltage	$b^*$	A function defined for convenience in expressing the equations for the $\tan \delta$ measured in a resonant cavity
$I$	Current	$b'/b$	Ratio of sample height to waveguide inside dimension (narrow dimension)
$K$	Thermal conductivity	$c$	A function defined for convenience in expressing the equations for the $\tan \delta$ measured in a resonant cavity
$M_1$	Micrometer reading for $TE_{014}$ resonant cavity, empty	$d$	Length or physical thickness of dielectric sample
$M_2$	Micrometer reading for $TE_{015}$ resonant cavity, empty	$f$	Frequency
$M_3$	Micrometer reading for $TE_{015}$ resonant cavity with sample	$h$	Height of $TM_{010}$ cavity
$N$	An integer	$k$	A function of the effective cavity radius, $a$ ; the calculated dielectric constant, uncorrected for sample fit
$Q_w$	A function of wall losses in $TM_{010}$ cavity	$k^*$	Complex dielectric constant, relative
$R$	Voltage reflection coefficient; numerical ratio of maximum to minimum field strengths	$k'$	Relative dielectric constant
$R'$	Reflection phase	$k''$	Relative dielectric loss factor
$R_M$	Voltage reflection coefficient with metal-backed sample	$l$	Distance from node to the open end of coaxial line; effective sample length or thickness
$R_M'$	Reflection phase with metal-backed sample	$l'$	A function defined for convenience in expressing the equations for the $\tan \delta$ measured in a resonant cavity
$R_\infty$	Voltage reflection coefficient for infinitely thick sample	$l_e$	Length of empty cavity at resonance
$R_\infty'$	Reflection phase for infinitely backed sample	$n$	Index of refraction $= \sqrt{k}$
$S_{1/2}$	A constant that is dependent on experimental conditions and sample characteristics	$p$	Parameter used in shorted waveguide calculations
$T$	Voltage transmission coefficient	$q$	Heat input; parameter used in shorted waveguide calculations
$T'$	Transmission phase	$r$	Interface voltage reflection coefficient; radius of sample to measuring point in sample
$T_1$	Inner temperature of dielectric structure, $^{\circ}C$		$\frac{\cos \theta - \sqrt{\epsilon^* - \sin^2 \theta}}{\cos \theta + \sqrt{\epsilon^* - \sin^2 \theta}}$
$T_2$	Outer temperature of dielectric structure, $^{\circ}C$		
$V$	Voltage	$r_{\perp}$	

# SYMBOLS (Cont'd.)

$r_1$	$\frac{\epsilon^* \cos \theta - \sqrt{\epsilon^* - \sin^2 \theta}}{\epsilon^* \cos \theta + \sqrt{\epsilon^* - \sin^2 \theta}}$	$\Delta M$	Width of resonance curve at the 3-db point
$s$	Resistivity of cavity metal relative to copper	$\Delta X$	Node width at the 10-db point without sample
$\tan d$	Loss tangent	$\Delta X'$	Node width at the 10-db point with sample
$\tan \delta$	Dielectric loss factor = $k''/k'$	$\Delta X_1$	Node width at the 3-db point without sample
$t_{1/2}$	Time for back sample surface to cool from one-half the maximum temperature excursion	$\Delta X_2$	Node width at the 3-db point with sample
$\alpha$	Thermal diffusivity	$\epsilon$	Real part of complex dielectric constant
$\alpha_a$	Atomic polarizability	$\epsilon^*$	Complex relative dielectric constant = $\epsilon - j\epsilon \tan d$
$\alpha_d$	Dipole orientation polarizability	$\epsilon'$	Dielectric constant
$\alpha_e$	Electronic polarizability	$\epsilon''$	Dielectric loss factor
$\alpha_p$	Polarizability	$\theta$	Angle of incidence
$\alpha_i$	Interfacial or space charge polarizability	$\lambda$	Wavelength
$\beta_e$	Phase constant of empty cavity	$\lambda_c$	Cutoff wavelength of waveguide
$\beta_s$	Phase constant in the sample in the cavity	$\lambda_g$	Wavelength in waveguide
$\beta_2$	Phase constant in the sample in the waveguide	$\lambda_0$	Wavelength in air or free space
$\Delta$	Distance the interferometer horn is moved from a minimum without sample to a minimum with sample	$\rho$	Voltage standing wave ratio; density
$\Delta f$	Change of frequency	$\phi$	Electric thickness in radians = $(2\pi d/\lambda)$
			$\sqrt{\epsilon^* - \sin^2 \theta}$ ; aspect angle
		$\phi_A$	$(2\pi d/\lambda) \cos \theta$
		$\psi$	Phase shift due to sample

## CHAPTER 5

### RADOME EVALUATION AND CORRECTION TECHNIQUES

#### PART I—MICROWAVE DIELECTRIC INSTRUMENTATION

##### 5-1 INTRODUCTION

A radome is a shaped wall of dielectric material that is designed to transmit electromagnetic radiation with minimum disturbance of the radiated pattern. To date, all the dielectric materials used in radomes are nonmagnetic; that is, their magnetic permeability is unity and their magnetic loss tangent is zero. Thus, the electrical properties of concern are the dielectric constant and the dielectric loss tangent.

If the dielectric constant and the loss tangent of the radome material are known and if the physical dimensions of a proposed radome design are fixed, modern computation techniques permit accurate prediction of the electrical performance of the radome, including insertion loss, effect on antenna pattern, and directional error.

Often, in either the development of a new radome design or quality control in production of radomes with established design, the measured performance of the radome does not agree with theoretical predictions. In the development of new radome designs, it is possible that the discrepancy is caused by a theoretical model that is not a sufficiently accurate approximation of the physical system. On the other hand, as modeling and computing techniques improve, this will be less likely. Latest prediction techniques, discussed in Chapter 2, are probably as accurate as is consistent with the state of the art of experimental verification techniques, which are covered in this chapter.

In the manufacture of production radomes, it is common practice to simply make copies of successful prototypes. If one of these production units fails to meet electrical performance requirements, the failure must be caused by

failure to copy correctly, which, in turn, is often caused by failure to measure completely and correctly.

Table 5-1 is a check list of possible reasons for unsatisfactory electrical performance of a production radome. It is intended for use in an electrical performance failure analysis problem of a radome production line, for example. With this check list and a complete radome electrical measurement facility, diagnosis becomes fairly straightforward. The check list also forms a basis for later discussion of measurement techniques. Table 5-1 contains the possible questions to ask when analyzing electrical differences between radome prototype and copy. These questions can also be asked when analyzing electrical differences between actual performance of a radome and the theoretically predicted performance.

##### 5-2 DIELECTRIC INSTRUMENTATION TERMINOLOGY

By way of introduction, the following paragraphs on the terminology of microwave dielectric instrumentation are in order. It is interesting to note that the low-frequency instrument for dielectric property determination has never been referred to as a dielectrometer. These instruments, referred to as bridges, do not measure dielectric constant; instead, they measure capacitance and are often very properly referred to as capacitance bridges.

###### 5-2.1 THE DIELECTROMETER

Unfortunately, a short-circuited waveguide with a slotted section and provisions for sample insertion is known in the microwave field



TABLE 5-1 RADOME DIELECTRIC CHECK LIST

Question	Applicable To			
	Dielec- trometer	Interfer- ometer	Reflec- tometer	Resonant Frequency
1. Does the sample fit well into the waveguide or cavity?	X			X
2. Was the sample fit in the waveguide or cavity corrected?	X			X
3. If measurements were made over a temperature range, was the differential expansion between the sample and waveguide or cavity accounted for in the sample fit correction?	X			X
4. If measurements were made over a temperature range, was the change in thickness of the sample with temperature taken into account?	X	X	X	X
5. At extreme temperatures, did any metal or other contaminants from the waveguide or surroundings migrate into the sample?	X	X	X	X
6. Is the radome material homogeneous?	X	X	X	X
7. If the radome material is not homogeneous, are the measured values good, average, representative numbers?	X	X	X	X
8. Is the radome material isotropic?	X	X	X	X
9. If the radome material is not isotropic, was the direction of the electric field during the measurement of the prototype and copy taken into account?	X	X	X	X
10. Does the sample have skins, glaze, or is it a sandwich in any sense?	X	X	X	X
11. If it does have skins or resembles a sandwich, has this been taken into account?	X	X	X	X
12. Have the variations due to the electrical effects of obstacles in the radome been accounted for, including metal tips, cables, attachments, metal supporting frame-works, etc.?	X	X	X	X
13. Is the radome material impervious to moisture absorption?	X	X	X	X
14. If the material is not impervious to moisture absorption, is the moisture content in the radome copy as measured the same as in the prototype?	X	X	X	X
15. Is the dielectric measuring instrument sufficiently accurate to produce the desired copy accuracy?	X	X	X	X
16. Has the copy of the radome been compared as to its dielectric properties with the prototype over its entire surface?	X	X	X	X
17. Was the copy of the radome compared as to its dielectric properties with the prototype at the operating frequency of the radome, thus eliminating dielectric dispersion as a variable?	X	X	X	X

as a *dielectrometer*. The term is misleading because this so-called dielectrometer does not measure dielectric constant and loss tangent; rather, it measures null shift and null width on a standing wave as produced by the sample insertion. From these measured values, the dielectric constant and loss tangent are computed. Other, more appropriate names for this device are *shorted slotted line*, *impedance meter*, and *reflectometer*. A resonant cavity is also referred to as a dielectrometer.

### 5-2.2 THE INTERFEROMETER

*Interferometer* is the common term for microwave bridges that are designed to read insertion loss and insertion phase delay for a sample through which the microwave energy is made to pass. The sample itself can be either in a waveguide or in free space between two horns. Again, the term is misleading because interferometer implies phase interference between two waves, and all microwave instruments used for dielectric constant and loss tangent measurement use phase interference.

### 5-2.3 THE REFLECTOMETER

*Reflectometer* is the common term for a device that measures reflection loss and/or reflection phase from a flat sample. The flat sample could be enclosed in a waveguide or it could be a flat sheet in free space. Of the three expressions, its interpretation is subject to the least confusion.

In the following paragraphs, a new term, *inspection zone*, is introduced. With reference to various techniques of measuring dielectric constant and loss tangent, the inspection zone is the volume of material that is exposed to the major portion (at least two-thirds) of the microwave energy taken into account in the measurement.

The resonant frequency techniques in this discussion include both the closed-cavity technique and free-space resonant-wall technique.

## 5-3 INTERFEROMETER, REFLECTOMETER, AND ULTRASONIC TECHNIQUES FOR QUALITY CONTROL OF RADOMES

Microwave interferometers and reflectom-

eters can be used in radome and dielectric sheet measurements to measure the following dependent parameters:

1. Insertion loss
2. Insertion phase
3. Reflection loss
4. Reflection phase
5. Reflection loss with metal-backed sample
6. Reflection phase with metal-backed sample
7. Frequency at which reflection loss peaks
8. Frequency at which transmission loss is at a minimum

In addition, it is possible to set the operating frequency of a reflectometer or interferometer at the broad minimum of the reflection loss vs. frequency curve or at the correspondingly broad maximum of the transmission loss vs. frequency curve (the antiresonance case or quarter-wave case), respectively. At this frequency, measurements of insertion loss, insertion phase, reflection loss, and reflection phase can be made with some resulting simplification in data reduction.

Considering that these measurements can be made with a choice of incidence angle and polarization, the versatility and potential of free-space interferometer and reflectometer techniques is tremendous and is deserving of further exploration. It is possible, with correct interpretation, to use microwave energy to diagnose a radome wall not only as to its electrical thickness but also as to the electrical thickness of its components (if it is a sandwich) and presence of voids, moisture, or other contaminants. This is best illustrated by considering a typical application. For the sake of simplicity and aptness, the simple solid wall is chosen. Corresponding theory can be developed for sandwiches and other structures, but would be more complex.

The three basic physical properties of a solid radome wall on which the parameters listed above depend are dielectric constant, loss tangent, and thickness. Usually, thickness can be best measured directly. Assuming that this is the case, it can be argued mathematically that it should be sufficient to measure any combination of two of the dependent parameters listed above to determine the dielectric constant and the loss tangent.

The formulas that characterize transmission through, and reflection from, a flat dielectric

sheet illuminated by a plane electromagnetic wave are

$$T e^{jT'} = \frac{(1 - r^2) e^{-j(\phi - \phi_A)}}{1 - r^2 e^{-j2\phi}} \quad (5-1)$$

and 
$$R e^{jR'} = \frac{r(1 - e^{-j2\phi})}{1 - r^2 e^{-j2\phi}} \quad (5-2)$$

where  $R$  = voltage reflection coefficient

$R'$  = reflection phase

$T$  = voltage transmission coefficient

$T'$  = transmission phase

$r$  = interface voltage reflection coefficient

$$\phi = (2\pi d/\lambda) \sqrt{\epsilon^* - \sin^2 \theta}$$

$$\phi_A = (2\pi d/\lambda) \cos \theta$$

In addition, a third formula can be written for the reflection case with a metal-backed sample:

$$R_M e^{jR_M'} = \frac{r - e^{-j2\phi}}{1 - r e^{-j2\phi}} \quad (5-3)$$

where  $R_M$  = reflection coefficient for metal-backed sample

$R_M'$  = reflection phase for metal-backed sample

There is another case for reflection for which an additional formula can be expressed. In this case, the sample is made to have an effectively infinite thickness by sample geometry or by a special design of a reflectometer horn. The measurement of reflection at normal incidence is expressed by:

$$R_x e^{jR_x'} = \frac{1 - \sqrt{\epsilon^*}}{1 + \sqrt{\epsilon^*}} \quad (5-4)$$

where  $R_x$  = voltage reflection coefficient for an infinitely thick sample

$R_x'$  = reflection phase for an infinitely thick sample

Most of the past equations on radomes assume that the radome wall is lossless. With this assumption and with some loss in accuracy, the separation of Eqs. 5-1 through 5-4 into their real and imaginary parts or into the power and phase expressions is relatively simple. Of course, this procedure prevents their use in the determination of loss tangent.

If loss tangent is not ignored, the three power and three phase expressions from Eqs. 5-1 through 5-4 can still be written, but will appear quite formidable. Hereinafter, these eight

parameters will be referred to as insertion loss, insertion phase, reflection loss, reflection phase, reflection loss with metal-backed sample, reflection phase with metal-backed sample, reflection loss for infinite sample, and reflection phase for infinite sample. The analytic approach to the determination of dielectric constant and loss tangent from these eight functions, assuming that all other variables are known, is to select any two and solve them simultaneously for dielectric constant and loss tangent. Present mathematical techniques are incapable of this and if they were capable, the resulting expressions would undoubtedly be too lengthy for practical use.

Fortunately, there are other alternatives: use of graphs or of tables. Present-day digital computer capabilities make this approach very practical. The approach is as follows:

1. Any two of the eight transcendental functions above are selected.
2. The incidence angle in the functions is fixed at a convenient or desired value for the measurement.
3. The polarization in the functions is fixed to orient the electric field in the direction of interest for the measurement.
4. The thickness is fixed at the desired value; if this is not a firm value, two thicknesses, one at and one near the desired nominal thickness, are chosen to permit thickness interpolation later.
5. A digital computer is programmed to compute explicitly any pair of the following as a function of dielectric constant and loss tangent: insertion loss, insertion phase, reflection loss, reflection phase, reflection loss with metal-backed sample, and reflection phase with metal-backed sample.
6. When the digital computer is used, the dielectric constant values and loss tangent values are chosen at sufficiently close increments to permit good interpolation and over a range that will cover the measurements of interest.
7. The digital computer is programmed to print the output in a convenient table or graph. Tables 5-2 and 5-3 are sample tables computed in this fashion and can be used as examples of format.

If these steps are properly taken, the result

TABLE 5-2 SAMPLE COMPUTER PRINTOUT OF INTERFEROMETER TABLES\*

Dist. K = 45,000		45,500		46,000		46,500		45,000		45,500		46,000		46,500 = Dist. K	
Tem D	DS	Deg	DS	Deg	DS	Deg	DS	Deg	DS	Deg	DS	Deg	DS	Deg	Tem D
.0000	9.76	232.2	10.01	232.8	10.25	233.5	10.48	234.1	4.81	220.2	5.00	221.3	5.18	222.3	.0000
.0005	9.77	232.1	10.02	232.8	10.26	233.4	10.49	234.0	4.82	220.1	5.00	221.2	5.19	222.3	.0005
.0010	9.77	232.0	10.02	232.7	10.26	233.3	10.49	233.9	4.82	220.0	5.01	221.1	5.20	222.2	.0010
.0015	9.78	231.9	10.03	232.6	10.27	233.3	10.50	233.9	4.83	220.0	5.02	221.1	5.20	222.1	.0015
.0020	9.78	231.9	10.03	232.5	10.27	233.2	10.50	233.8	4.84	219.9	5.03	221.0	5.21	222.1	.0020
.0040	9.80	231.6	10.05	232.2	10.29	232.9	10.52	233.5	4.87	219.7	5.06	220.8	5.24	221.9	.0040
.0060	9.82	231.3	10.07	232.0	10.31	232.6	10.53	233.2	4.90	219.5	5.09	220.6	5.27	221.7	.0060
.0080	9.84	231.0	10.09	231.7	10.32	232.3	10.55	233.0	4.93	219.3	5.12	220.4	5.30	221.4	.0080
.0100	9.86	230.7	10.11	231.4	10.34	232.1	10.57	232.7	4.96	219.0	5.15	220.2	5.33	221.2	.0100
.0120	9.88	230.4	10.13	231.1	10.36	231.8	10.59	232.4	4.99	218.8	5.18	219.9	5.36	221.0	.0120
.0140	9.90	230.1	10.15	230.8	10.38	231.5	10.61	232.2	5.03	218.6	5.21	219.7	5.39	220.8	.0140
.0160	9.92	229.8	10.17	230.5	10.40	231.2	10.63	231.9	5.06	218.4	5.24	219.5	5.42	220.6	.0160
.0180	9.95	229.5	10.19	230.2	10.42	230.9	10.64	231.6	5.09	218.2	5.27	219.3	5.45	220.4	.0180
.0200	9.97	229.2	10.21	230.0	10.44	230.7	10.66	231.3	5.12	218.0	5.30	219.1	5.48	220.2	.0200
.0250	10.02	228.5	10.26	229.3	10.49	230.0	10.71	230.7	5.20	217.4	5.38	218.6	5.55	219.7	.0250
.0300	10.08	227.8	10.32	228.6	10.54	229.3	10.76	230.0	5.28	216.9	5.46	218.1	5.63	219.2	.0300
.0350	10.14	227.1	10.37	227.9	10.60	228.6	10.82	229.4	5.36	216.4	5.54	217.6	5.71	218.7	.0350
.0400	10.20	226.4	10.43	227.2	10.65	228.0	10.87	228.7	5.45	215.9	5.62	217.1	5.78	218.2	.0400
.0500	10.32	225.1	10.55	225.9	10.77	226.7	10.98	227.5	5.61	215.0	5.78	216.1	5.94	217.2	.0500
.0600	10.45	223.8	10.67	224.6	10.89	225.5	11.10	226.2	5.78	214.0	5.94	215.2	6.10	216.3	.0600
.0700	10.59	222.5	10.80	223.4	11.01	224.2	11.22	225.0	5.95	213.2	6.11	214.3	6.26	215.4	.0700
.0800	10.72	221.3	10.94	222.2	11.14	223.0	11.35	223.9	6.12	212.3	6.27	213.5	6.42	214.6	.0800
.0900	10.87	220.1	11.08	221.0	11.28	221.9	11.48	222.8	6.29	211.5	6.44	212.6	6.59	213.8	.0900
.1000	11.01	218.9	11.22	219.9	11.42	220.8	11.61	221.7	6.46	210.7	6.61	211.9	6.75	213.0	.1000
.1200	11.32	216.8	11.51	217.7	11.71	218.7	11.89	219.6	6.81	209.2	6.95	210.4	7.09	211.5	.1200
.1400	11.63	214.7	11.82	215.7	12.01	216.7	12.18	217.6	7.16	207.9	7.30	209.0	7.43	210.2	.1400
.1600	11.96	212.8	12.14	213.9	12.32	214.8	12.49	215.8	7.51	206.6	7.64	207.8	7.77	208.9	.1600
.1800	12.29	211.1	12.47	212.1	12.63	213.1	12.80	214.1	7.86	205.5	7.99	206.6	8.11	207.8	.1800
.2000	12.63	209.5	12.80	210.5	12.96	211.5	13.12	212.5	8.22	204.4	8.34	205.6	8.46	206.7	.2000

**TABLE 5-2 SAMPLE COMPUTER PRINTOUT OF INTERFEROMETER TABLE\* (cont)**

Dist. K = 45.000			45.500			46.000			46.500			45.000			45.500			46.000			46.500 = Dist. K		
Tem D	DB	Deg	DB	Deg	DB	DB	Deg	DB	Deg	DB	Deg	DB	Deg	DB	Deg	DB	Deg	DB	Deg	DB	Deg	Tem D	
0.250	13.49	205.9	13.65	207.0	13.80	208.1	13.94	209.1	9.10	202.2	9.21	203.3	9.32	204.5	9.44	205.6	0.250						
0.300	14.37	203.1	14.51	204.2	14.65	205.3	14.79	206.4	9.97	200.4	10.08	201.6	10.19	202.7	10.29	203.9	0.300						
0.350	15.25	200.9	15.38	202.0	15.51	203.1	15.64	204.2	10.84	199.1	10.94	200.3	11.04	201.4	11.15	202.5	0.350						
0.400	16.12	199.1	16.25	200.2	16.37	201.3	16.50	202.4	11.69	198.1	11.79	199.3	11.89	200.4	11.99	201.6	0.400						
0.450	16.98	197.8	17.11	198.9	17.23	200.0	17.35	201.1	12.53	197.4	12.63	198.6	12.73	199.8	12.83	200.9	0.450						
0.500	17.84	196.8	17.96	198.0	18.08	199.1	18.19	200.2	13.36	197.0	13.46	198.2	13.56	199.4	13.66	200.5	0.500						
0.600	19.51	195.8	19.63	196.9	19.74	198.1	19.86	199.3	14.98	196.9	15.09	198.1	15.19	199.3	15.28	200.4	0.600						
0.700	21.13	195.7	21.25	196.9	21.37	198.1	21.48	199.3	16.56	197.5	16.66	198.7	16.77	199.9	16.87	201.1	0.700						
0.800	22.71	196.4	22.83	197.6	22.95	198.8	23.06	200.0	18.08	198.7	18.19	199.9	18.30	201.1	18.41	202.3	0.800						
0.900	24.23	197.6	24.36	198.9	24.48	200.1	24.60	201.3	19.56	200.3	19.68	201.5	19.79	202.8	19.90	204.0	0.900						
1.000	25.71	198.8	25.84	200.6	25.96	201.9	26.09	203.1	21.00	202.3	21.12	203.6	21.24	204.8	21.35	206.1	1.000						
1.100	27.14	201.4	27.27	202.7	27.41	204.0	27.54	205.3	22.39	204.6	22.52	205.9	22.64	207.2	22.77	208.5	1.100						
1.200	28.53	203.8	28.67	205.1	28.81	206.4	28.94	207.7	23.74	207.1	23.87	208.4	24.00	209.8	24.13	211.1	1.200						
1.300	29.87	206.4	30.02	207.7	30.16	209.1	30.31	210.4	25.05	209.8	25.19	211.2	25.33	212.5	25.46	213.9	1.300						
1.400	31.18	209.1	31.33	210.5	31.48	211.9	31.63	213.3	26.32	212.7	26.47	214.1	26.61	215.4	26.76	216.8	1.400						
1.500	32.45	212.0	32.61	213.5	32.76	214.9	32.92	216.3	27.56	215.7	27.71	217.1	27.86	218.5	28.01	219.9	1.500						
1.600	33.68	215.1	33.85	216.5	34.01	217.9	34.17	219.4	28.76	218.8	28.92	220.2	29.08	221.6	29.24	223.0	1.600						
1.800	36.05	221.4	36.22	222.9	36.40	224.3	36.57	225.8	31.07	225.1	31.24	226.5	31.41	228.1	31.58	229.5	1.800						
2.000	38.29	227.9	38.48	229.4	38.66	231.0	38.84	232.5	33.27	231.7	33.45	233.2	33.63	234.7	33.81	236.2	2.000						
2.200	40.42	234.6	40.62	236.1	40.81	237.7	41.01	239.3	35.55	238.3	35.75	239.9	35.94	241.4	36.13	242.9	2.200						
2.400	42.45	241.3	42.66	242.9	42.86	244.5	43.07	246.1	37.84	245.0	38.04	246.6	38.23	248.2	38.42	249.8	2.400						
2.600	44.39	248.0	44.61	249.6	44.82	251.3	45.03	252.9	39.25	251.7	39.46	253.3	39.67	254.9	39.88	256.6	2.600						
2.800	46.25	254.7	46.48	256.4	46.70	258.1	46.92	259.7	41.07	258.3	41.30	260.0	41.52	261.7	41.73	263.3	2.800						
3.000	48.03	261.3	48.27	263.1	48.50	264.8	48.73	266.5	42.53	264.9	42.86	266.7	43.29	268.4	43.52	270.1	3.000						
3.200	49.75	267.9	49.99	269.7	50.24	271.5	50.48	273.2	44.52	271.5	44.76	273.2	45.00	275.0	45.23	276.7	3.200						
PERPENDIC. POL., THK/LAMBDA = 0.0910, 45 DEG. INCIDENCE																							
PARALLEL POL., THK/LAMBDA = 0.0910, 45 DEG. INCIDENCE																							

\* Courtesy of Emerson and Cuming, Inc.

TABLE 5-3 SAMPLE COMPUTER PRINTOUT OF DIELECTRIC SLAB TABLES\*

Tem D	Dist. K = 3.900		3.950		4.000		4.050		3.950		3.900		4.000		4.050 = Dist. K	
	DB	Deg	DB	Deg	DB	Deg	DB	Deg	DB	Deg	DB	Deg	DB	Deg	DB	Deg
.0000	0.01	203.8	0.01	203.8	0.01	203.9	0.01	203.9	0.34	15.9	0.35	16.2	0.36	16.4	0.37	16.7
.0005	0.01	203.8	0.01	203.8	0.01	203.9	0.01	203.9	0.34	15.9	0.35	16.2	0.36	16.4	0.37	16.7
.0010	0.01	203.8	0.01	203.8	0.01	203.9	0.01	203.9	0.34	15.9	0.35	16.2	0.36	16.4	0.37	16.7
.0015	0.01	203.8	0.01	203.8	0.01	203.9	0.01	203.9	0.34	15.9	0.35	16.1	0.36	16.4	0.37	16.7
.0020	0.01	203.8	0.01	203.8	0.01	203.9	0.01	203.9	0.34	15.9	0.35	16.1	0.37	16.4	0.38	16.5
.0040	0.01	203.8	0.01	203.8	0.01	203.9	0.01	203.9	0.35	15.9	0.36	16.1	0.37	16.4	0.38	16.6
.0060	0.01	203.8	0.01	203.8	0.01	203.9	0.01	203.9	0.36	15.9	0.37	16.1	0.38	16.4	0.39	16.6
.0080	0.01	203.8	0.01	203.8	0.01	203.9	0.01	203.9	0.36	15.9	0.37	16.1	0.38	16.4	0.39	16.6
.0100	0.01	203.8	0.01	203.8	0.01	203.9	0.01	203.9	0.37	15.8	0.38	16.1	0.39	16.4	0.40	16.6
.0120	0.01	203.8	0.01	203.8	0.01	203.9	0.01	203.9	0.37	15.8	0.38	16.1	0.40	16.3	0.41	16.6
.0140	0.01	203.8	0.01	203.8	0.01	203.9	0.01	203.9	0.38	15.8	0.39	16.1	0.40	16.3	0.41	16.6
.0160	0.01	203.8	0.01	203.8	0.01	203.9	0.01	203.9	0.39	15.8	0.40	16.1	0.41	16.3	0.42	16.6
.0180	0.01	203.8	0.01	203.8	0.01	203.9	0.01	203.9	0.39	15.8	0.40	16.1	0.41	16.3	0.43	16.6
.0200	0.01	203.8	0.01	203.8	0.01	203.9	0.01	203.9	0.40	15.8	0.41	16.0	0.42	16.3	0.43	16.5
.0250	0.01	203.8	0.01	203.8	0.01	203.9	0.01	203.9	0.41	15.8	0.42	16.0	0.44	16.3	0.45	16.5
.0300	0.01	203.8	0.01	203.8	0.01	203.9	0.01	203.9	0.43	15.7	0.44	16.0	0.45	16.2	0.46	16.5
.0350	0.01	203.8	0.01	203.8	0.01	203.9	0.01	203.9	0.44	15.7	0.45	16.0	0.47	16.2	0.48	16.5
.0400	0.01	203.8	0.01	203.8	0.01	203.9	0.01	203.9	0.46	15.7	0.47	15.9	0.48	16.2	0.49	16.4
.0500	0.01	203.8	0.01	203.8	0.02	203.9	0.02	203.9	0.49	15.6	0.50	15.9	0.51	16.1	0.52	16.4
.0600	0.02	203.8	0.02	203.8	0.02	203.9	0.02	203.9	0.52	15.6	0.53	15.8	0.54	16.1	0.55	16.3
.0700	0.02	203.8	0.02	203.8	0.02	203.9	0.02	203.9	0.55	15.5	0.56	15.8	0.57	16.0	0.58	16.3
.0800	0.02	203.8	0.02	203.8	0.02	203.9	0.02	203.9	0.58	15.5	0.59	15.7	0.60	16.0	0.62	16.2
.0900	0.02	203.8	0.02	203.8	0.02	203.9	0.02	203.9	0.60	15.4	0.62	15.7	0.63	15.9	0.65	16.1
.1000	0.02	203.8	0.02	203.8	0.03	203.9	0.03	203.9	0.63	15.4	0.65	15.6	0.64	15.8	0.68	16.1
.1120	0.03	203.8	0.03	203.8	0.03	203.9	0.03	203.9	0.69	15.3	0.71	15.5	0.72	15.7	0.74	16.0
.1140	0.03	203.8	0.03	203.8	0.03	203.9	0.03	203.9	0.75	15.2	0.77	15.4	0.78	15.6	0.79	15.9
.1160	0.04	203.8	0.04	203.8	0.04	203.9	0.04	203.9	0.81	15.1	0.82	15.3	0.84	15.5	0.85	15.8
.1180	0.04	203.8	0.04	203.8	0.04	203.9	0.04	203.9	0.87	15.0	0.88	15.2	0.90	15.4	0.91	15.7

TABLE 5-3 SAMPLE COMPUTER PRINTOUT OF DIELECTRIC SLAB TABLE\* (cont)

Die L K = 3.900			3.950			4.000			4.050			3.900			3.950			4.000			4.050 = Die L K		
Tem D	DB	Deg	DB	Deg	DB	Deg	DB	Deg	DB	Deg	DB	Deg	DB	Deg	DB	Deg	DB	Deg	DB	Deg	Tem D		
0.200	0.04	203.8	0.04	203.8	0.05	203.9	0.05	203.9	0.92	14.9	0.94	15.1	0.96	15.3	0.97	15.6	0.97	15.6	0.97	15.6	0.200		
0.250	0.05	203.8	0.05	203.8	0.06	203.9	0.06	203.9	1.06	14.7	1.08	14.9	1.10	15.1	1.12	15.3	1.12	15.3	1.12	15.3	0.250		
0.300	0.06	203.8	0.06	203.8	0.07	203.8	0.07	203.8	1.20	14.4	1.22	14.6	1.24	14.9	1.26	15.1	1.26	15.1	1.26	15.1	0.300		
0.350	0.07	203.8	0.07	203.8	0.08	203.8	0.08	203.9	1.34	14.2	1.36	14.4	1.38	14.6	1.40	14.9	1.38	14.6	1.40	14.9	0.350		
0.400	0.08	203.8	0.08	203.8	0.09	203.8	0.09	203.9	1.47	14.0	1.50	14.2	1.52	14.4	1.54	14.6	1.52	14.4	1.54	14.6	0.400		
0.450	0.09	203.8	0.09	203.8	0.10	203.8	0.10	203.9	1.61	13.8	1.63	14.0	1.65	14.2	1.68	14.4	1.65	14.2	1.68	14.4	0.450		
0.500	0.10	203.8	0.10	203.8	0.11	203.8	0.11	203.9	1.74	13.6	1.76	13.8	1.79	14.0	1.81	14.2	1.79	14.0	1.81	14.2	0.500		
0.600	0.12	203.8	0.12	203.8	0.13	203.8	0.13	203.8	2.00	13.3	2.02	13.5	2.05	13.7	2.08	13.9	2.05	13.7	2.08	13.9	0.600		
0.700	0.14	203.8	0.14	203.8	0.15	203.8	0.15	203.8	2.25	13.0	2.28	13.2	2.30	13.3	2.33	13.5	2.30	13.3	2.33	13.5	0.700		
0.800	0.16	203.8	0.16	203.8	0.17	203.8	0.17	203.8	2.49	12.7	2.52	12.9	2.55	13.0	2.58	13.2	2.55	13.0	2.58	13.2	0.800		
0.900	0.18	203.8	0.18	203.8	0.19	203.8	0.19	203.8	2.73	12.4	2.76	12.6	2.80	12.7	2.83	12.9	2.80	12.7	2.83	12.9	0.900		
1.000	0.20	203.7	0.20	203.8	0.20	203.8	0.21	203.8	2.96	12.2	3.00	12.3	3.03	12.5	3.07	12.7	3.03	12.5	3.07	12.7	1.000		
1.100	0.22	203.7	0.22	203.7	0.22	203.8	0.23	203.8	3.19	11.9	3.23	12.1	3.26	12.3	3.30	12.4	3.26	12.3	3.30	12.4	1.100		
1.200	0.24	203.7	0.24	203.7	0.24	203.7	0.25	203.7	3.41	11.7	3.45	11.9	3.49	12.0	3.53	12.2	3.49	12.0	3.53	12.2	1.200		
1.300	0.26	203.7	0.26	203.7	0.26	203.7	0.27	203.7	3.63	11.5	3.67	11.7	3.71	11.8	3.75	12.0	3.71	11.8	3.75	12.0	1.300		
1.400	0.28	203.7	0.28	203.7	0.28	203.7	0.29	203.7	3.84	11.4	3.88	11.5	3.92	11.7	3.96	11.8	3.92	11.7	3.96	11.8	1.400		
1.500	0.30	203.6	0.30	203.7	0.30	203.7	0.31	203.7	4.05	11.2	4.09	11.3	4.13	11.5	4.17	11.6	4.13	11.5	4.17	11.6	1.500		
1.600	0.31	203.6	0.32	203.6	0.32	203.6	0.33	203.6	4.25	11.1	4.30	11.2	4.34	11.3	4.38	11.5	4.34	11.3	4.38	11.5	1.600		
1.800	0.35	203.5	0.36	203.6	0.36	203.6	0.37	203.6	4.64	10.8	4.69	10.9	4.74	11.1	4.78	11.2	4.74	11.1	4.78	11.2	1.800		
2.000	0.39	203.5	0.39	203.5	0.40	203.5	0.41	203.5	5.02	10.6	5.07	10.7	5.12	10.9	5.17	11.0	5.12	10.9	5.17	11.0	2.000		
2.200	0.43	203.4	0.43	203.4	0.44	203.4	0.44	203.4	5.38	10.4	5.43	10.6	5.48	10.7	5.54	10.8	5.48	10.7	5.54	10.8	2.200		
2.400	0.46	203.4	0.47	203.4	0.48	203.4	0.48	203.4	5.73	10.3	5.78	10.4	5.84	10.6	5.89	10.7	5.84	10.6	5.89	10.7	2.400		
2.600	0.50	203.3	0.51	203.3	0.51	203.3	0.52	203.3	6.07	10.2	6.12	10.3	6.18	10.4	6.23	10.6	6.18	10.4	6.23	10.6	2.600		
2.800	0.53	203.2	0.54	203.2	0.55	203.2	0.56	203.2	6.39	10.1	6.45	10.3	6.50	10.4	6.56	10.5	6.50	10.4	6.56	10.5	2.800		
3.000	0.57	203.1	0.58	203.1	0.58	203.1	0.59	203.1	6.70	10.1	6.76	10.2	6.82	10.3	6.88	10.5	6.82	10.3	6.88	10.5	3.000		
3.200	0.60	203.0	0.61	203.0	0.62	203.0	0.63	203.0	7.01	10.1	7.07	10.2	7.13	10.3	7.19	10.4	7.13	10.3	7.19	10.4	3.200		
BACKED REFL. THK/LAMBDA = 0.0317 NORMAL INCIDENCE																TRANSMISSION THK/LAMBDA = 0.0317 NORMAL INCIDENCE							

\* Courtesy of Emerson and Cuming, Inc.

will be a convenient two-by-two table that can be used to convert any two of eight measured functions listed above into the dielectric constant and loss tangent. This type of tabulation is referred to as a two-by-two conversion table. It differs from the one-by-one table (for example, a log table) in that a pair of known functions instead of a single function can be converted into another pair of dependent functions. It can be used directly or inversely, just as a log table can be used to look up either the log or the antilog. It very neatly overcomes the mathematical obstacle of obtaining the implicit solution to two simultaneous transcendental equations. The computer accomplishes this by computing the explicit function for a great number of cases. The implicit solution for a particular case is then obtained by looking in the resulting two-by-two conversion table. Interpolation in this table is possible just as in a one-by-one table. The interpolation is known as double interpolation and is only slightly slower and only slightly more complex than single interpolation. If the thickness of the sample does not coincide exactly with the thickness for which the conversion table was computed, it will be necessary to do one of the following:

1. Since tables of this type are normally computed for a given thickness-to-wavelength ratio, a slight change in the measurement frequency may often be sufficient to obtain the thickness-to-wavelength ratio for which the conversion table was computed.
2. If there is interest in a specific frequency, and thickness is fixed, and if a conversion table is not available for exactly this thickness-to-wavelength ratio, another double interpolation can be made between two tables whose thickness-to-wavelength ratio is near that of the measurement.

For a given application, the question of which pair of the measurable parameters listed above should be measured to obtain the dielectric constant and loss tangent should be considered very carefully. In this determination, such considerations as the relative ease and accuracy with which the various parameters can be measured should be included. To assist in this determination, the measurable quantities in

descending order of their accuracy are frequency, thickness, phase, and loss.

Other factors should also be considered. For example, reflection loss with a metal-backed sample will be so small for a low-loss material as to be difficult to measure. Therefore it should be used only with lossy dielectrics, such as microwave absorber materials. As another example, since loss is lowest in accuracy, it would not be wise to use a pair of loss measurements; at least one measurement should be phase or frequency.

For making the required measurements, the following guidelines are useful:

1. All of these measurements are substitution measurements. Loss and phase, for example, are measured with and without the sample dielectric in place, the differences being, respectively, insertion loss and insertion phase delay. In this case, the loss and phase measurements are with reference to an air dielectric; the dielectric constant of air as unity and loss tangent of air as zero are used as standards. Air is almost an ideal standard because of its availability and because of the constancy of its dielectric constant and loss tangent. However, if the dielectric constant of the sample is high, for example, above 5, air may not be the best standard because its dielectric properties are so much different from those of the sample. If a standard can be obtained that has a dielectric constant in the neighborhood of the unknown, the accuracy of the measurement will be improved. With conversion tables, it is no more difficult to use a known dielectric material as a standard than it is to use air. The thickness of this standard should also be in the neighborhood of the unknown.
2. As an example of how a suitable standard will improve measurement accuracy, consider the geometry of a typical interferometer horn, as shown in Fig. 5-1. Assuming that microwave energy emanates from the transmitting horn as though from a point source from the phase center of the horn at point A,  $\angle BAC$  is the angular sector of the energy pattern received by the receiving horn without the sample in place. When the sample is introduced,



because of refraction effects as shown by the dashed lines,  $\angle DAF$  is the angular sector of the transmitting horn energy pattern received by the receiving horn. Since  $\angle DAF$  is larger than  $\angle BAC$ , there is a gain due to refraction that might be referred to as a sample focusing effect. This sample focusing effect would, of course, disappear if the horns could be placed far enough apart to have a perfect plane wave incident on the sample. If this were done, the sample would have to be impractically large to avoid edge effects. Therefore, this focusing effect must be accounted for by a suitable correction factor. Figure 5-2 is a graph of this effect computed for a 18-in. horn spacing. This graph gives the required correction. A more accurate way to eliminate this problem is to use a standard that has a dielectric constant and thickness close to that of the unknown sample. The focusing effect for the standard will then be approximately the same as that for the unknown sample. It should be noted that this focusing effect due to sample insertion is present to a greater or lesser extent in all free-space interferometers; omission of this effect may be one reason why interferometers are not accurate in loss measurement. Free-space reflectometers may be subject to a similar source of error, depending on the distance of the

sample from the horn and the type of horn used.

3. With the large number of measurable parameters available—and for self calibration, consideration should be given to measuring more than just the two that were chosen for the dielectric constant and loss tangent. For example, if three parameters are measured, two different conversion tables are possible, each with its own pair of measured parameters convertible into dielectric constant and loss tangent. For example, if insertion loss, insertion phase, and reflection phase were measured, the two conversion tables could be insertion loss and insertion phase to dielectric constant and loss tangent, and insertion phase and reflection phase to dielectric constant and loss tangent. Thus, from three measurements there result two independent determinations of dielectric constant and loss tangent. The agreement between the two sets of determinations is a good check on the accuracy of the method.
4. Another source of error is the trapped or surface wave effect. This is caused by a sample whose surface dimensions, in the practical case, are never infinite. If the transmitting horn excites in the sample, a trapped or surface wave that follows the surface of the sample to its edges, from where it is reflected back into the

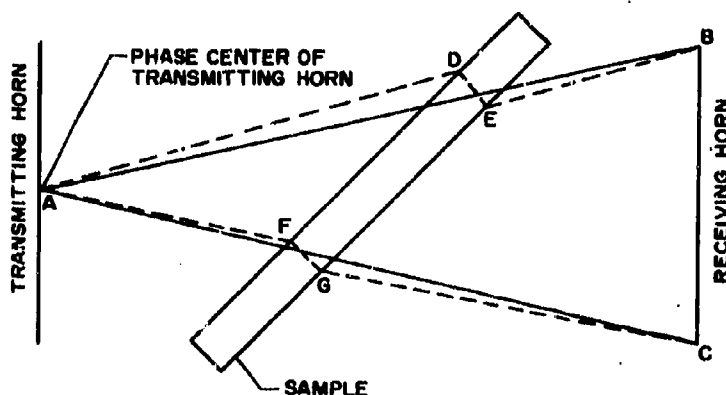


Figure 5-1. Geometry of Typical Interferometer Horn Showing Sample

inspection zone, an error will be introduced into the measurement. The presence of this effect can be detected by probing the sample surface exterior to the inspection zone with a small pickup horn. Another way of detecting this effect is with a known homogeneous sample. If on the

homogeneous sample, different dielectric constant and loss readings are obtained for small movements of the inspection zone on the sample, this is good evidence of the presence of a trapped or surface wave. The employment of a dielectric standard is not effective in reducing error

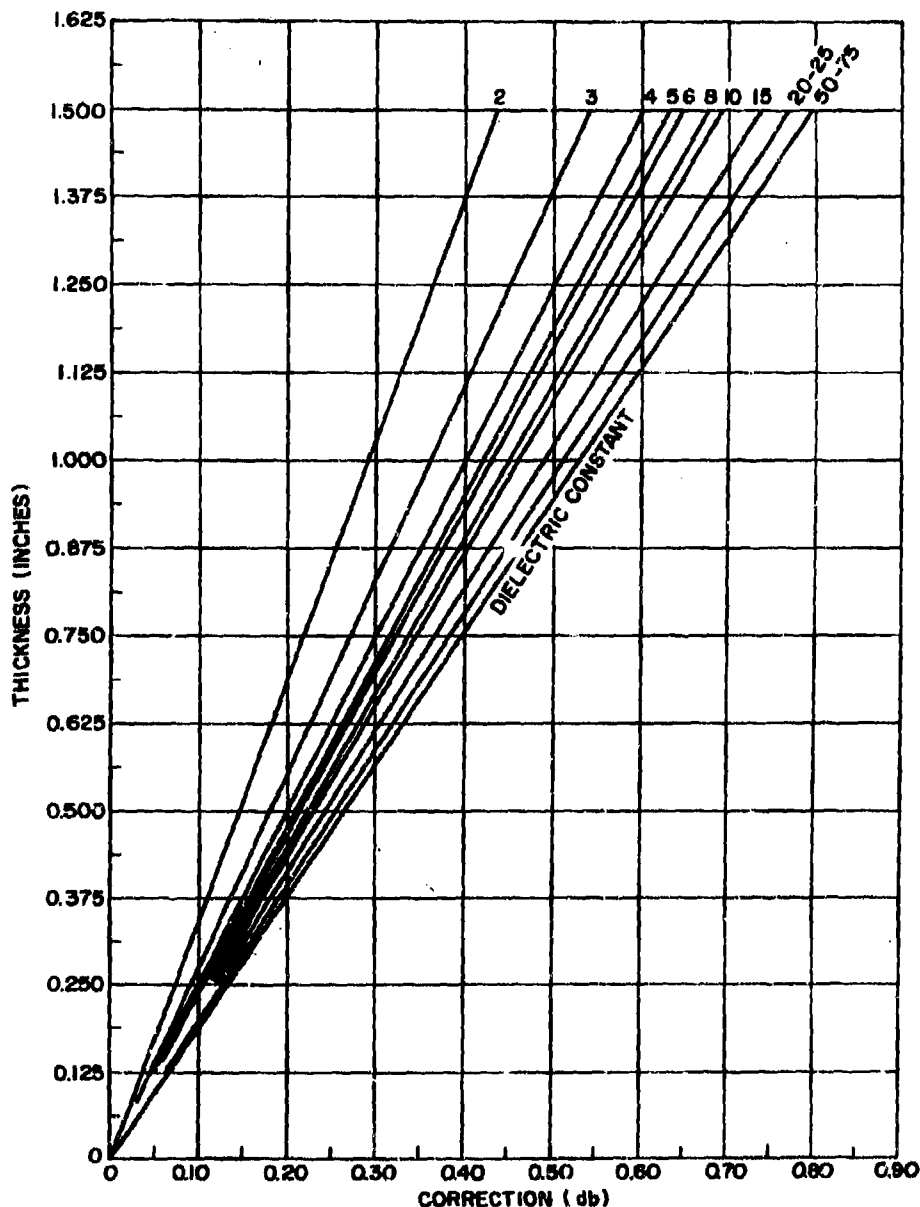


Figure 5-2. Graph for Focusing Correction

caused by this effect because the standard will be subject to the presence of the same type of trapped wave, with an unpredictable effect. Possibly the best way to minimize this effect is to surround the inspection zone with a microwave absorber in intimate contact with the surface of the sample. Another way might be to taper all edges of the sample to prevent reflection of the trapped wave back into the inspection zone.

5. Another problem that plagues both interferometers and reflectometers is the so-called free-space standing wave effect. This is caused by multiple reflections between the antenna or antennas and the sample. It is encountered only at incidence angles below about 30°. Thus, it is always present in a one-horn reflectometer. On the other hand, if an interferometer is operated at incidence angles above 30°, this effect is not a problem.

#### **5-4 APPLICATIONS OF INTERFEROMETERS, REFLECTOMETERS, AND PHYSICAL THICKNESS GAGES IN QUALITY CONTROL OF RADOMES\***

To complete the preceding general discussion of free-space measurement techniques, it is useful to consider detailed descriptions of application experiences that have taken place in the radome industry with each of several specific instruments. The following paragraphs contain extracts from papers by engineers in the radome industry. Instruments discussed include those used for physical thickness measurements as well as those used for measurements of electrical properties of a radome wall. Since many of these instrument types were covered adequately in *Techniques for Airborne Radome Design*, the instruments discussed are those that are new or have undergone new developments since 1957.

##### **5-4.1 SHEFFIELD RADOME THICKNESS GAGE**

With the growing use of ceramics instead of fiberglass-plastic laminates in radomes, there

\* See Paragraph 4-16.6.

has been a change in the significance of the measurement of physical thickness of a radome because the dielectric constant of the ceramic radome is generally very well controlled. Thus, it is possible to make good copies of radome prototypes that are satisfactorily equivalent electrically simply by making a point-by-point comparison of physical thickness between copy and prototype and correcting thickness of the copy where it falls outside the specification. The Sheffield Radome Thickness Gage is the first step towards automatizing this measurement.

##### **5-4.1.1 Typical Applications**

**5.4.1.1.1 Wall Thickness Gage During Final Inspection.** In this application, the radome is placed vertically on the special gaging fixture (see Fig. 5-3). The part rests on a spherical ball bearing that locates itself in the tip of the radome. The part is held steady by four fixed buttons located at four quadrants radially approximately halfway up the four arms of the fixture.

A graduated ring on the base of the fixture allows the operator to position the part radially during the checking procedure. The inside diameters of the radome are contacted by 25 Sheffield Plunjet gaging cartridges. These Plunjets are located on one arm of the gaging fixture. Matched sets of Plunjets, to contact the outside diameters of the radome, are mounted on a ball slide fixture, which is moved into contact with the part by means of an air cylinder.

The readings of wall thickness are indicated directly on the multiple-column Precisionaire instrument and represent the wall thickness at 25 points on the radome.

The time required for complete inspection of a part depends on the operator's ability to load and unload the part from the fixture, as well as the number of checks that are required radially. The readings on the Precisionaire instrument are obtained instantaneously.

##### **5.4.1.1.2 Inside Diameter and In-Process Gage.**

This particular application is designed to check the inside diameter of the radome during the lapping operation (see Fig. 5-4). The part is located over the special fixtures and rests on two sets of ball contacts. With the base of the part against an adjustable rest, the part is oriented until a fiducial indicating contact

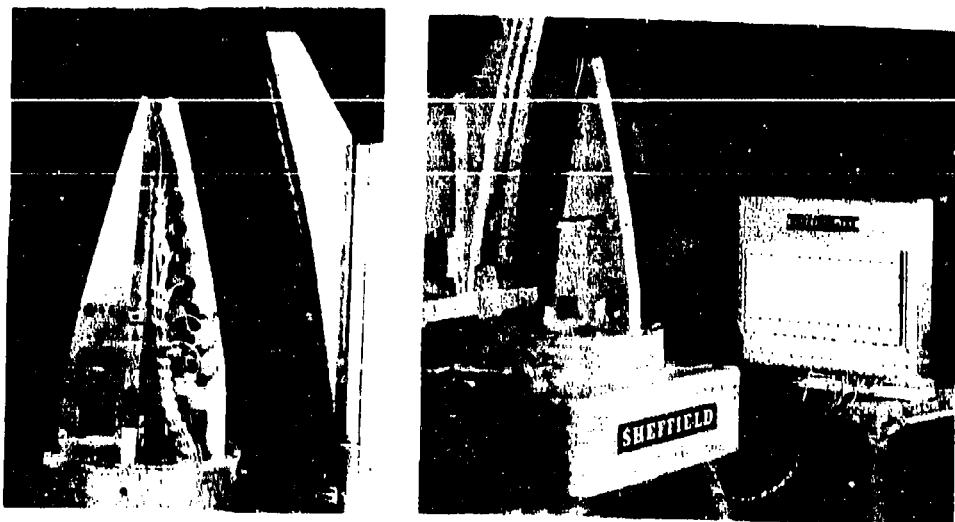


**Figure 5-3. Sheffield Radome Thickness Gage; Used as Wall Thickness Gage During Final Inspection**

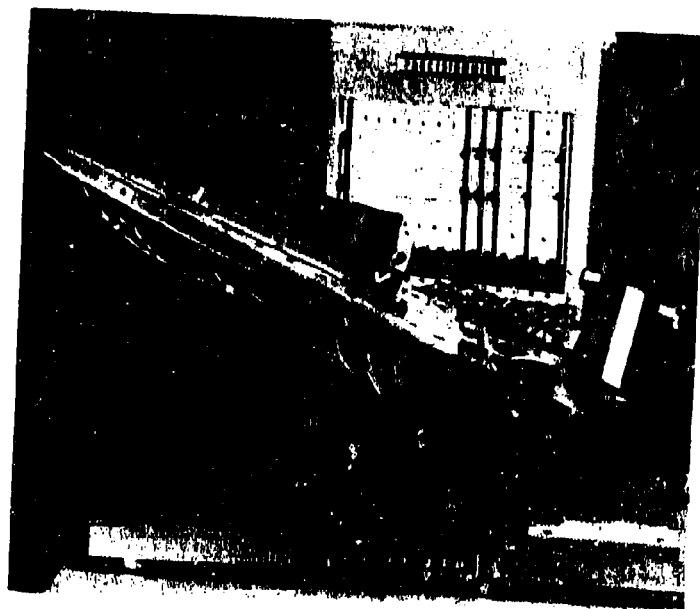


**Figure 5-4. Sheffield Radome Thickness Gage; Used as In-Process Gage to Check Inside Diameter**



reaches a specific reading. When this point is reached, the two sets of ball rests are located at their respective datum positions on the inside diameters.

The diameters are contacted by Pluniet gaging cartridges and indicate the diameter directly by the position of the indicating floats on the Precisionaire column instrument. Three sets of adjustable measuring contacts at the base of the gaging fixture check a straight inside diameter at the base of the radome.

A total of 17 internal diameters are checked simultaneously on this fixture. A special Leafjet air spindle is located at the tip of the fixture to check the inside diameter of the tip of the radome. Inspection time per part, as in the previous illustration, depends on the time to load and unload the part and the amount of exploration desired. The readings by the Precisionaire instrument appear instantaneously.

According to Reference 2 the instrument with its associated tooling is accurate to within 5% of the total measuring range (e.g., for a 0.002-in. measuring range, the accuracy would be 0.0001 in.).

#### **5-4.2 BRANSON VIDIGAGE—AN ULTRASONIC PHYSICAL THICKNESS GAGE**

For measurement of the physical thickness of a radome wall at a single point, the Branson Vidigage is quite popular. Its principal advantage over a micrometer caliper is that it permits wall thickness measurements where access is available to only one side of the radome wall. The wall thickness indication that the instrument displays is a function of the actual physical thickness of the wall and the acoustic propagation constants which include elastic modulus and density, of the wall material. Thus, care must be taken in the interpretation of measurement data that variations in the apparent wall thickness as measured by the instrument are not due to variations in the elastic modulus or density. Thus, with proper care and with homogeneous materials, measurements to an accuracy of  $\pm 0.001$  in. can be made. Voids and delaminations would also affect the readings taken with the instrument. It is natural, therefore, that the efficiency of the instrument is better with ceramic radome materials than with fiberglass-plastic laminates because of the

greater homogeneity of the ceramic materials. On the other hand, the sensitivity of instruments of this type to discontinuities in walls has led to their use in the detection of defects. One version, the Branson Sonoray Flaw Detector is adaptable to the through-transmission of acoustic energy.

##### **5.4.2.1 Principle of Operation**

The Vidigage employs a sweep oscillator to generate a range of frequencies that are displayed on the cathode-ray tube as a horizontal base line (Reference 3). The frequencies produced by the oscillator are converted into ultrasonic energy by a transducer. When the transducer is placed on a test piece, the ultrasonic energy is transmitted into the part as a continuous wave train.

Each thickness of a given material has its own natural resonance frequency. At this frequency (or multiples of it), when the transmitted and reflected waves are in phase, there will be a relatively large increase in the amplitude of the waves in the material. These are resonance conditions occurring at the fundamental frequency, which is inversely proportional to twice the thickness and directly proportional to the velocity of sound in the material, and also occurring at harmonics (multiples of the fundamental frequency). Since the velocity is a known constant, the fundamental frequency required to produce resonance is an accurate and reliable measure of the unknown thickness.

As the oscillator sweeps through the resonant frequency of the part, or any of the harmonics of that frequency, a vertical resonance indication appears on the cathode-ray tube. This indication is used to determine approximate thickness. Actual thickness measurements are made by placing a thickness scale in front of the cathode-ray tube.

Reference 4 presents ultrasonic techniques in the quality control of radomes. The following paragraphs are extracted from this source and Figs. 5-5 and 5-6 illustrate the use of the equipment.

##### **5-4.2.2 Typical Applications**

The usefulness of ultrasonics for inspection

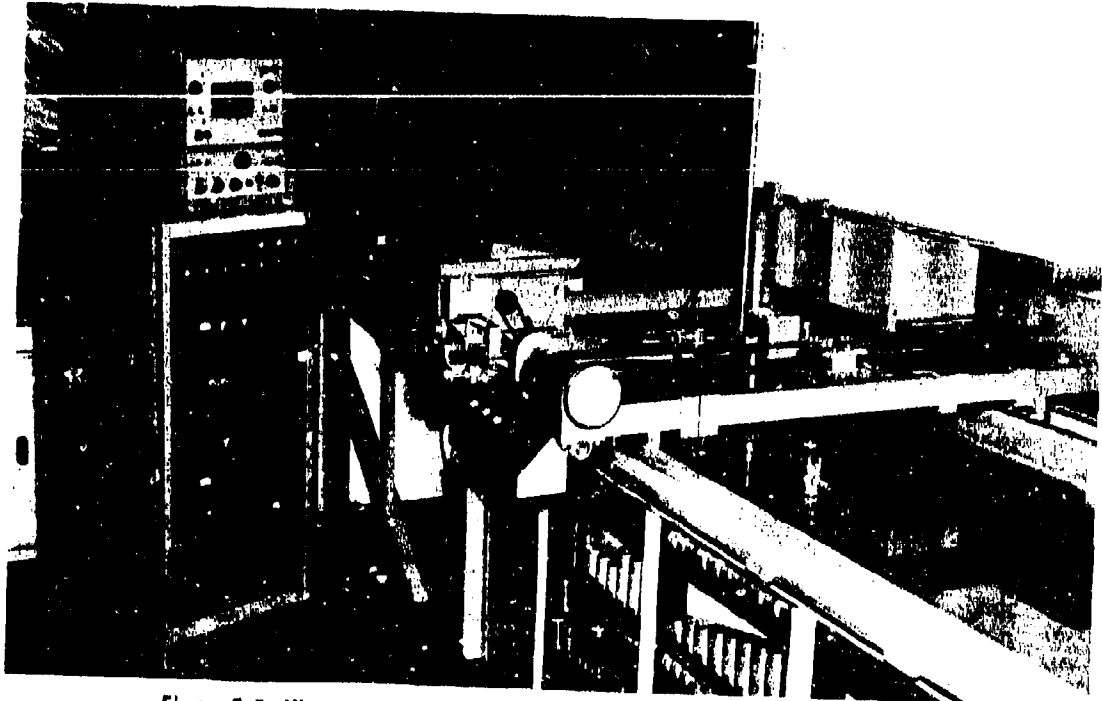


*Figure 5-5. Ultrasonic Equipment Setup at Douglas Aircraft Company*

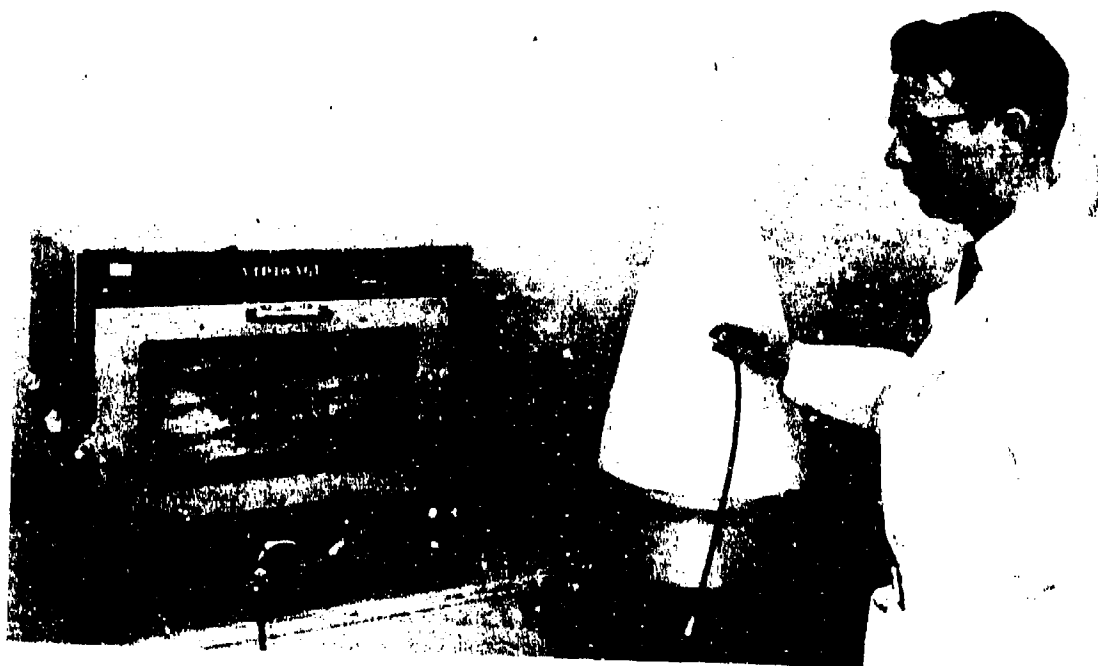


*Figure 5-6. Vidigage Being Used to Measure Radome Wall Thickness*

purposes is dependent upon the change in behavior of these waves as they propagate in a material. The acoustical properties of a material can result in the occurrence of reflection, refraction, mode conversion, attenuation, and diffraction, or any combination of these effects. To generate an ultrasonic wave, it is necessary to use an electromechanical transducer that is capable of transforming electrical energy into mechanical energy and vice versa. At frequencies above 200 kc, piezoelectric materials such as quartz, barium titanate, and lithium sulfate are used. Quartz has been used most extensively, primarily because of its electrical and mechanical stability, resistance to aging, high-temperature capability, and high degree of insolubility. Its major disadvantages are inefficiency and a mode conversion susceptibility. For ceramic and fiberglass materials, test frequencies from 1 to 25 mc are used. It is usually desirable to use the lowest frequency that will give satisfactory results.

**5-4.2.2.1 Methods Available.** Both reflection and through-transmission methods have been successfully applied to radome materials. The reflection method can be extensively utilized with homogeneous materials such as Pyroceram, fused silica, and alumina. This method can provide rapid evaluation of the physical wall thickness of a radome and will locate defects, such as cracks and porous areas. The reflection method has had limited success with nonhomogeneous materials, such as fiberglass laminates. A more practical approach has been the through-transmission method. This method is useful for locating voids, resin content variations, delaminations, and other fabrication defects in fiberglass laminates.

**5-4.2.2.2 The Reflection Test.** For the reflection test, a quartz transducer can be made to oscillate by applying a pulsed, oscillating voltage. An ultrasonic beam generated in the crystal can be made to pass through the test material, provided there is an adequate coupling medium between the crystal and the test sample. The coupling medium can be of any of several liquids that are capable of wetting the surfaces and staying between the crystal and the test sample during the test. Water or oil is used extensively as a coupling material. Oil provides better coupling in some cases, but water is

preferable if the material being tested has a tendency to absorb liquids. A resonance condition is established in the test sample by varying the ultrasonic frequency. When this condition is obtained, reflections from the first surface will be in phase with reflections from the opposite surface. Resonance will occur only when the test sample thickness is one-half the ultrasonic wave length. To calculate the sample thickness, it is necessary to know the fundamental operating frequency and the velocity of sound propagating through the material. The formula for this calculation is

$$d = \frac{1}{2} \lambda = \frac{1}{2} v/f \quad (5-5)$$

where  $d$  = wall thickness

$f$  = fundamental frequency

$v$  = velocity of sound propagating through the test material

$\lambda$  = wavelength of the fundamental frequency

Accuracy of the measurement will normally be within 3% of the actual thickness.

**5-4.2.2.3 The Through-Transmission Test.** The through-transmission test is dependent upon the principle that variations in the test sample will produce significant changes in the ultrasonic energy level. The basic equipment for this test consists of an ultrasonic generator, a receiving apparatus, the test sample, and a suitable coupling liquid. A practical system also includes a scanning system and recording equipment to reduce test time to a minimum. The through-transmission test can be most readily applied to the qualification testing of low-frequency radomes that, because of excessive range reflections, cannot be satisfactorily range tested. Any degree of uniformity desired can be established in the test by determining a minimum acceptable attenuation level. It is necessary to establish this level with radomes of known electrical and structural characteristics, but once this is accomplished, the ultrasonic test will provide an efficient screening of parts that are defective structurally or that vary electrically as a result of resin content variations, improper wall thickness, or contaminants in the material.

**5-4.2.2.4 Summary of Tests.** The ultrasonic test method can be used to advantage for both the electrical and structural quality control of ra-

domes. It has the advantage of instantaneous indication; it gives the ability to inspect a wide range of samples for size, geometry, and area of flaw; there are no safety hazards involved; it is a sensitive and highly directive test; it is easy to operate; and in the case of the reflection equipment, it can be made portable. Flaws that can be detected are voids, cracks, inclusions, lamination separations and resin content variations. The method has application wherever range tests are not feasible and also as a supplement to range tests to reduce test time and costs. An investment in ultrasonic equipment has an additional advantage over microwave equipment in that ultrasonic equipment can be used for applications other than radomes where structural quality must be determined.

#### 5-4.3 NORTH AMERICAN AVIATION MICROWAVE THICKNESS GAGE

The North American Microwave Thickness Gage is a type of reflectometer designed to portray, on an oscilloscope, the standing wave produced in a waveguide by reflection from a radome wall. Thus the instrument responds to reflection phase.

Reference 5 presents the use of this gage in quality control and non-destructive testing of dielectric components. The following paragraphs are extracted from this source.

##### 5-4.3.1 Typical Application

The instrument is designed so that nontechnical personnel can satisfactorily perform the desired grinding operation of a radome with a minimum of instruction; this is due to the unique go-no-go presentation on the oscilloscope.

Figure 5-7 shows typical presentation for various radome wall thicknesses as seen by an operator. The presentation on the oscilloscope is the resultant standing wave pattern generated in the microwave pickup probe, since the microwave thickness gage is an R-F resonance device whose effectiveness depends upon reflected electromagnetic energy. It is essential that enough power be returned to assure accurate detection of electrical thickness variations or voids in the dielectric material. In the microwave spectrum, metallic surfaces reflect

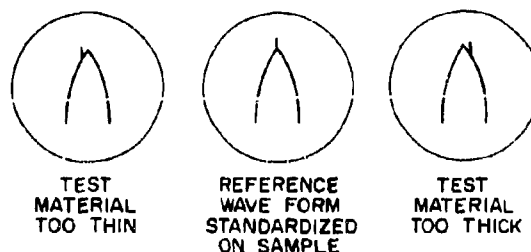


Figure 5-7. Oscilloscope Presentation for Wall Thickness Measurement Using North American Aviation Microwave Thickness Gage

all incident electromagnetic energy; thus, by placing a metallic surface behind the dielectric material to be tested, the necessary level of energy is reflected. Variations of thickness from a predetermined value caused by such factors as nonuniformity of materials, voids, and discontinuity will either advance or retard the standing wave pattern, therefore displaying the resultant null pattern to the right or left of a fixed pip or marker. A calibrated grid placed on the oscilloscope face can determine the displacement.

Radomes fabricated with the use of the microwave thickness gage have excellent electrical properties and can be duplicated with minimum effort during production fabrication. Figure 5-8 shows the close match of electrical curves of several radomes manufactured consecutively.

The problems in the nondestructive testing of dielectric materials are similar to the problems in fabricating high-quality radomes. Therefore, preliminary investigations were made to determine the feasibility of utilizing the microwave thickness gage for other nondestructive testing.

**5-4.3.1.1 Instrument Sensitivity.** To determine the sensitivity of the microwave thickness gage in detecting discontinuities, voids, and delamination of dielectric material, the following test were performed on a typical sample, as shown in Fig. 5-9.

The sample was divided into four areas: A, B, C, and D. The instrument was calibrated and referenced in each area before modifications. In area A, the thickness gage indicated that



the material was 0.002 in. thinner after a 0.027-in. diameter hole was drilled in the sample. A 0.039-in. diameter hole gave an indication of it being 0.003 in. thinner and a 0.056-in. diameter hole, 0.008 in. thinner.

In area B, 0.027- and 0.056-in. diameter holes caused an indication of 0.001 and 0.003 in. less than before, respectively. The decrease in sensitivity in area B is due to the polarization of the electromagnetic wave. In area C, the results were the same as those for area B.

Delamination tests were performed in area D. The instrument indicated the thickness to be 0.002 in. thicker after delamination of the top plies.

Tests performed on printed circuit material indicated results similar to those achieved in area D.

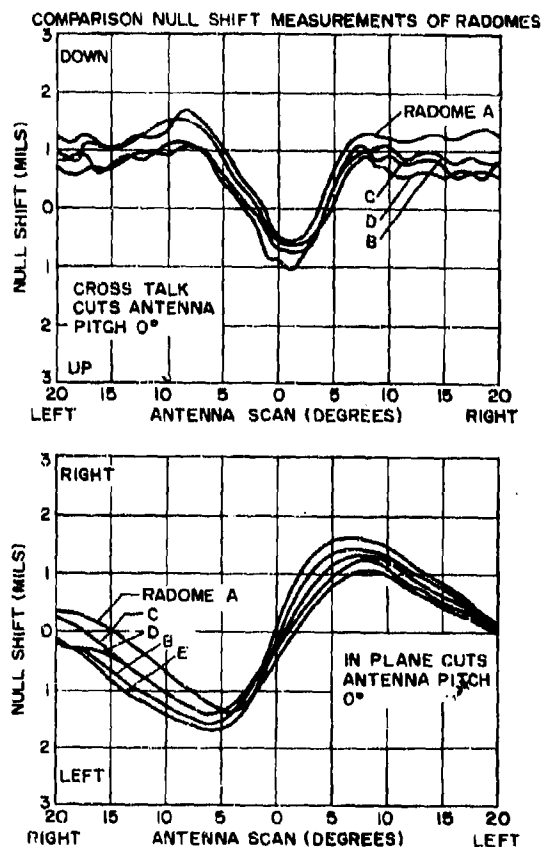


Figure 5-8. Comparison Null Shift Measurements of Radomes Using Microwave Thickness Gage

**5-4.3.1.2 Summary of Tests.** The use of the microwave thickness gage at North American Aviation has resulted in vastly improved manufacturing methods in A3J radome production; radome testing procedures also have been greatly simplified.

Results obtained using the gage in nondestructive testing to measure the equivalent discontinuities in metallic materials are comparable to those obtained with the ultrasonic test equipment. The gage gives improved performance with tests made on nonmetallic materials.

#### 5-4.4 MICROWAVE INSTRUMENTS CO.— MICROWAVE THICKNESS GAGES FOR NONMETALS

A series of thickness gages is available from the Microwave Instruments Company (see Reference 6). According to the manufacturer, the operating principle of the reflection gage, Model 622A, is different from that of the North American Aviation radome thickness gage. For information on the general performance of this gage, refer to the manufacturer's Bulletin No. 122, October 1963.

#### 5-4.5 MICROWAVE INSTRUMENTS CO.— DIELECTROMETER MODEL 611A

The Microwave Instruments Company also manufactures a dielectrometer, model 611A, that operates as a reflectometer. Its outstanding feature is that it reads the dielectric constant and loss tangent directly. The electric

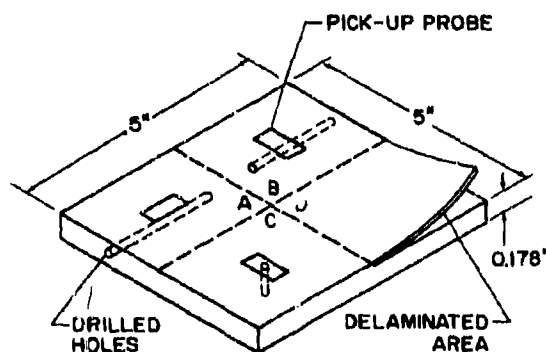


Figure 5-9. Fiberglass Laminate Test Sample

field is in the plane of the sample. Both circularly and linearly polarized heads are available. An inspection zone as small as 1/8-in. diameter hemisphere at 8.6 gc is claimed. Measurement is independent of the sample thickness, provided that the sample thickness is greater than 1/4 in. Therefore, it seems that the instrument is a reflectometer that gains its information from the first interface reflection coefficient. For further information, refer to manufacturer's Bulletin No. 121, October 1963.

#### 5-4.6 A MICROWAVE REFLECTOMETER THAT READS DIELECTRIC CONSTANT DIRECTLY

For additional background in the problem of designing microwave reflectometers to read dielectric constant and loss tangent directly, the following paragraphs are presented (Reference 7). Success was achieved in reading directly the dielectric constant of small disks.

The dielectric constant, or its square root, the index of refraction, can be determined by measuring either capacitance, velocity of propagation, Brewster angle, refraction angle, or reflected power. Reflected power measurements eliminate the computation required by other techniques. The following describes a method of using reflected power for direct reading of the dielectric constant.

The power reflection coefficient from a flat sheet of dielectric material for the lossless case is

$$|R|^2 = \frac{4r^2 \sin^2 \phi}{(1-r^2)^2 + 4r^2 \sin^2 \phi} \quad (5-5)$$

where  $R$  = the voltage reflection coefficient

$r$  = the interface voltage reflection coefficient

$\phi$  = electrical thickness in radians at normal incidence

$$r = (1 - \sqrt{\epsilon}) / (1 + \sqrt{\epsilon}) \quad (5-6)$$

where  $\epsilon$  = the dielectric constant

When the sheet is an odd multiple of quarter waves in thickness, the  $\sin^2 \phi$  term in Eq. 5-5 reduces to unity and by substituting Eq. 5-6, Eq. 5-5 becomes:

$$R = (\epsilon - 1) / (\epsilon + 1) \quad (5-7)$$

$$\text{But } R = (\rho - 1) / (\rho + 1) \quad (5-8)$$

where  $\rho$  = voltage standing wave ratio

Therefore, from Eqs. 5-7 and 5-8,

$$\epsilon = \rho$$

Since  $\rho$  can be read directly using a microwave ratiometer technique, it is possible to read the dielectric constant directly. To do this, it should be sufficient to read the voltage standing wave ratio,  $\rho$ , at the frequency at which the thickness is any odd multiple of quarter waves. However, in applying this principle, several complications arise.

One such complication is frequency ambiguity. For a sample of a given thickness, the quarter-wave thickness occur at discrete frequencies that are themselves dependent on the dielectric constant to be determined. This is shown in Fig. 5-10 for 1/8-, 1/4-, 3/8-, and 1/2-in.-wall thicknesses. Power reflection coefficient curves are shown for dielectric constants of 5 and 6. This difficulty is overcome by using a microwave ratiometer technique that uses a sweep generator, as shown in Fig. 5-11. The X-Y recorder at the output of the ratiometer records the curves of Fig. 5-10 directly. Since the dielectric constant can be determined by measuring the height of one of the peaks, frequency ambiguity is eliminated, provided that the dielectric constant itself does not vary with frequency. Generally, for the dielectrics used in radomes, the dielectric constant does not change throughout the microwave region.

The output of the ratiometer varies with the power reflection coefficient, not with  $\rho$ , which was shown to be equal to the dielectric constant at quarter-wave frequencies. On the other hand, over narrow ranges of  $\rho$ , say 5 to 6, the relationship between  $\rho$  and power reflection coefficient is nearly linear. Therefore, if two standards with different dielectric constant values are used, both close to the unknown dielectric constants, a scale can be recorded with the X-Y recorder and subsequently the unknown can be read directly from this linear scale. For routine quality control in producing the same dielectric materials, two standards are sufficient. If the instrument is used to measure a series of samples with widely varying dielectric constants, a correspondingly larger number of standards is required.

The ideal sample is small and inexpensive. For correlation, it is also desirable to measure the same samples as are used in a shorted waveguide type of dielectrometer. However,

# EFFECT OF DIELECTRIC THICKNESS ON CURVES

Dielectric Thickness (in.)	$\epsilon$	Frequency in gc													
		f1	f2	f3	f4	f5	f6	f7	f8	f9	f10	f11	f12	f13	f14
0.125	6	9.64		19.28		29.88		38.57		48.21		57.86		67.50	
	5		10.56		21.28		31.69		42.25		52.82		63.38		73.94
0.250	6	4.82		9.64		14.46		19.28		24.10		28.93		33.75	
	5		5.82		10.56		15.84		21.12		26.41		31.69		36.97
0.375	6	3.21		6.42		9.64		12.85		16.07		19.28		22.50	
	5		3.52		7.04		10.56		14.08		17.60		21.12		24.65
0.500	6	2.41		4.82		7.23		9.64		12.05		14.46		16.87	
	5		2.64		5.28		7.92		10.56		13.20		15.84		18.47

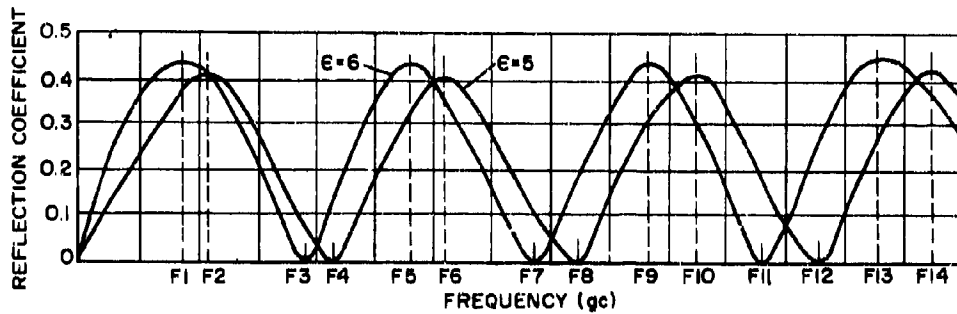


Figure 5-10. Power Reflection Coefficient for Plane Sheet at Normal Incidence

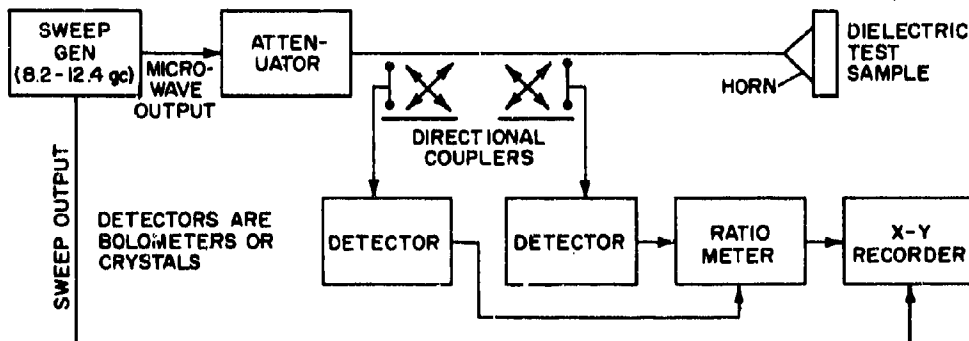


Figure 5-11. Microwave Instrumentation for Dielectric Constant Measurement

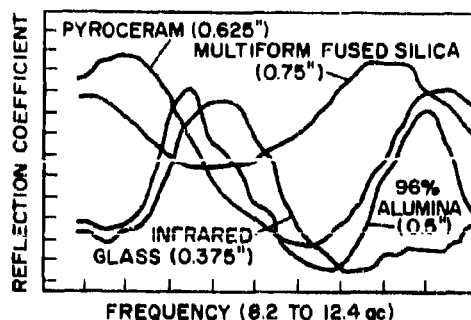


Figure 5-12. Reflection Coefficient Curves for Four Different Materials

the measurement is based on the assumption that the sample is an infinite-plane flat sheet. Therefore, a compromise is made. This compromise is determined experimentally. These experiments show that the 1 in. circular disks in the shorted waveguide dielectrometer, when placed over the open end of a  $1 \times 1/2$  in. rectangular waveguide, give good reproducibility and correlation with the shorted waveguide instrument. Samples should either be very small or very large (6 in. or more), with intermediate sizes the worst choice. Samples should also have smooth surfaces and constant thickness.

When the sample is placed directly over the open end of the waveguide, the open end becomes an antenna, the sample being in the near field. Measurement was insensitive to reflecting objects placed as close as 6 in. from the antenna. The reason is that with samples of a dielectric constant of 5 or higher, a large percentage of the energy is reflected back into the waveguide, especially at the quarter-wave frequency and its odd multiples. Also, any undesired reflection from surrounding objects is reflected away at this frequency.

Figure 5-12 shows curves recorded with the direct-reading dielectrometer for four materials.

The peaks of the power reflection coefficient curves follow a scale (similar to a logarithmic scale) that is the relationship between power reflection coefficient and  $p$ . It would be impossible to read this scale to more than two significant figures. For quality control of the dielectric constant, at least three significant figures are required; therefore, instrument sensitivity must be increased. When this is done, the

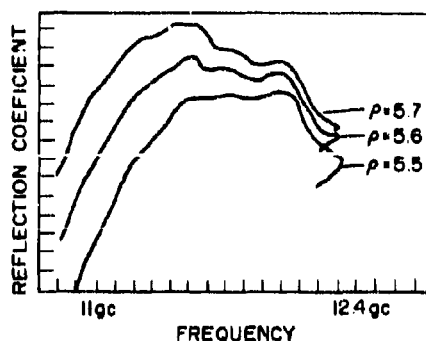


Figure 5-13. Increased Sensitivity Measurement for Pyroceram

complete curve no longer fits the recorder. Therefore, the frequency scale is reduced to consider only the peak area. Figure 5-13 shows the result of this on three  $1/2$ -in. specimens of Pyroceram with dielectric constants of 5.5, 5.6, and 5.7. This scale is now suitable for reading directly the dielectric constants of  $1/2$ -in. specimens of Pyroceram. The experimental curves are not as smooth as the theoretical curves. When the sensitivity is increased, the curves become even rougher. These imperfections are due to variations of antenna characteristics, directional-coupler characteristics, and/or detector characteristics with frequency.

There are several remedies. One is, if a multiplicity of minor peaks occurs in the quarter-wave region as a modulation of the major peak, to use the highest peak as the reading. Since the dielectric constant changes slightly, the highest peak changes the most.

Another remedy is to design a better antenna. For 1-in. disks, best results were achieved by sharpening the ends of the open waveguide, as shown in Fig. 5-14. This minimizes the ground-plane effect.

A third remedy is to increase the sweep speed and filter out the modulating peaks with a large capacitance across the ratiometer output. This results in a smoother curve, but accuracy is not as good.

A fourth remedy is to use well-matched directional couplers and detectors.

In applying reflectometer measurements directly to radomes, other complications arise. The spot covered by the waveguide horn excites a trapped wave in the radome wall that

moves parallel to the electric field at the spot. This wave circulates around the radome wall and returns to the spot to affect the measurement; therefore, the thickness of the entire radome wall and variations of this thickness enter into the measurements. Thus, measurements must be made at that stage in radome production when the thickness is constant or nearly so. Unfortunately, at this stage the radome wall is likely to be a half-wave instead of an odd multiple of quarter waves in the frequency band at which the radome is to be used. Consequently, it is necessary to make the measurement at frequency bands immediately below or above the band at which the radome is to be a half-wave. Due to lack of instrumentation, this is yet to be tried.

In radome measurements, the antenna horn can be placed into intimate contact with the radome wall or at a fixed distance from it. If placed in contact with the wall, it is important to have good coupling with the curved surface. This was obtained by using a horn with spring fingers, as shown in Fig. 5-15.

Loss tangent will affect the power reflection

coefficient at the quarter-wave frequency. However, if it is low and relatively constant, as with ceramics, its effect can be neglected in the quality control dielectric constant measurements on the same material.

The microwave reflectometer can be adapted to read the loss tangent directly. This is done by working with the power transmission coefficient instead of the power reflection coefficient. As seen in Fig. 5-16, the peak of the power transmission curve at the half-wave frequency departs linearly from unity as a function of loss tangent. If loss tangent standards are provided with two different loss tangents near the unknowns and with approximately the same dielectric constant, the loss tangent can be read directly. For manufacture of microwave absorbers, it is expected this feature would be attractive. The adapting horns permitting this measurement with the reflectometer instrumentation are shown in Fig. 5-17.

The correlation of dielectric constant readings with the shorted waveguide dielectrometer readings is, at the worst, about  $\pm 0.05$ . This can be improved upon by providing samples

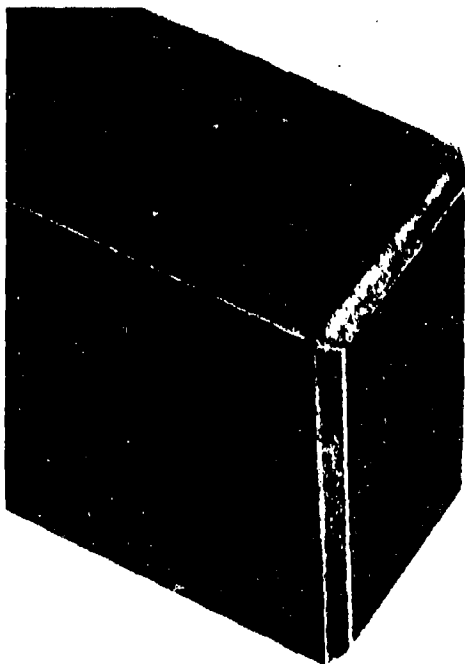


Figure 5-14. Modified Ends of Waveguide



Figure 5-15. Horn with Spring Fingers

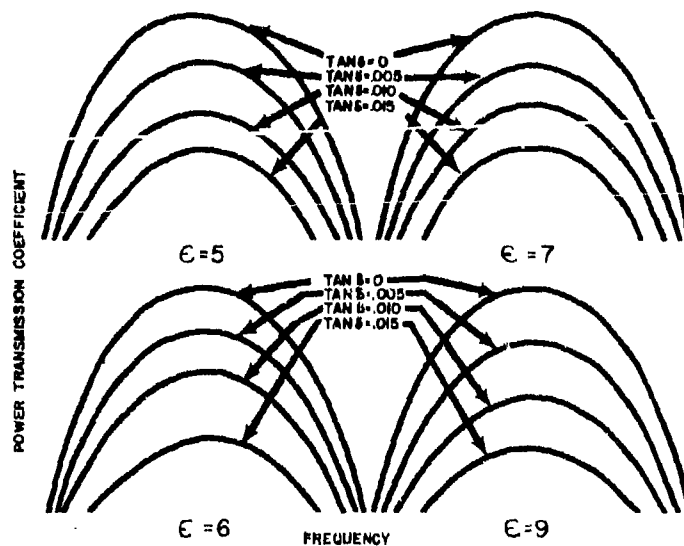


Figure 5-16. Quarter-Wave Peaks of Power Transmission Coefficient

that are mechanically perfect. Mechanical imperfections in the samples appear to have considerably more effect on the shorted waveguide dielectrometer readings than on the reflectometer readings.

There is no difficulty in reading dielectric constant values to three significant figures for dielectric constants about 6.

Measurement is rapid, since the sample need not be inserted into a waveguide or cavity, and the reading is direct, requiring no computation. There are improvements that would still further improve the usefulness of the instrument. A better antenna or means of coupling to a small sample could be designated to eliminate multiplicity of peaks. By cooling the end of the waveguide with a water jacket, the method has already been applied successfully to read dielectric constants at up to 1000°C.

#### 5-4.7 EMERSON AND CUMING, INC.—THE ECCO INTERFEROMETER

The Ecco Interferometer circuitry is similar to that of microwave interferometers that have been used to check radomes in the past. The principal innovation in the Ecco Interferometer is the Ecco Interferometer Tables used in conjunction with it. These tables permit the rigor-



Figure 5-17. Adapter Used for Loss Tangent Measurements

ous conversion of the insertion and insertion phase into the dielectric constant and loss tangent, without resorting to the approximations of Brewster angle measurements, as has been past practice. Thus, the measurements can be made at perpendicular polarization with the electric field in the plane of the sample, which is more desirable. To date, Brewster angle measurements using parallel polarization have not been checked on curved radomes. However, they have been used successfully on flat sheets.

For a detailed description of the operation of the interferometer and use of the Interferometer Tables and Dielectric Standards, refer to technical bulletins published by Emerson and Cuming (References 8, 9, and 10).

### **5-5 TECHNIQUES FOR ELECTRICAL TESTING OF RADOMES AND PANELS AT ELEVATED TEMPERATURES**

The principal difficulty in the testing of radomes and panels at elevated temperatures is the attainment of the high temperature throughout the thickness of the panel.

There are two types of tests that are appropriate to consider:

1. The first is testing at elevated temperatures in the attempt to simulate the heating of the radome or panel in a manner that would typify a given flight contour. In this type of testing, a thermal gradient is intentionally established in the radome or panel through its thickness. If the complex dielectric constant of the radome or panel varies with temperature, the dielectric wall will no longer be homogeneous. Thus, any attempt to convert the insertion loss and insertion phase into the dielectric constant and loss tangent would be subject to error. The only meaningful application of this type of testing is the measure of the effect on transmitted or reflected power or the effect on bore-sight error due to the heating.
2. The second type of testing is done at elevated temperatures to measure the temperature coefficients of dielectric constant and loss tangent. Most of this type of testing is now done with cavity or waveguide type dielectrometers, as discussed in Paragraph 5-6; it can also be done using radomes and panels. Measur-

ing the temperature coefficients in this manner has the advantage of eliminating the complications of sample clearance variation due to differential expansion between metal and sample as experienced in waveguide and cavity measurements. In addition, this approach makes it possible to make measurements all the way to the decomposition or melting temperatures of the dielectric material, which would not be possible in waveguides or cavities without damaging the equipment. On the other hand, since this is a free-space measurement, i.e., an interferometer or reflectometer measurement, considerable care must be taken to avoid other sources of error. For example, with the large panel, it is more difficult to ensure uniform temperature throughout a given inspection zone. As another example, care must be taken so that undesired microwave energy reflections from heating elements or furnace walls do not affect the accuracy of measurement.

#### **5-5.1 THE BOEING CO.—X-BAND HIGH-TEMPERATURE TRANSMISSION GAGE**

Reference 11 describes how heating a panel affects the electrical power transmission coefficient that is measured. The behavior of dielectric materials at high temperatures using a high-temperature transmission gage was studied, and the following paragraphs are from this reference.

##### **5-5.1.1 X-Band High-Temperature Transmission Gage**

A high-temperature transmission gage was used to measure the power transmission characteristics of the test materials (see Figs. 5-18 and 5-19). Temperature and attenuation measurements were made as heat was applied and the surface temperature was increased; these measurements were continued as the material underwent ablation.

Basically, the transmission gage consists of a large water-cooled steel chamber with the inside lined by a silicon carbide refractory microwave absorber. A 12 × 12 in. test panel of the material under investigation is heated by a radiant heat source consisting of thirty-seven 1500-watt quartz glass lamps in a con-

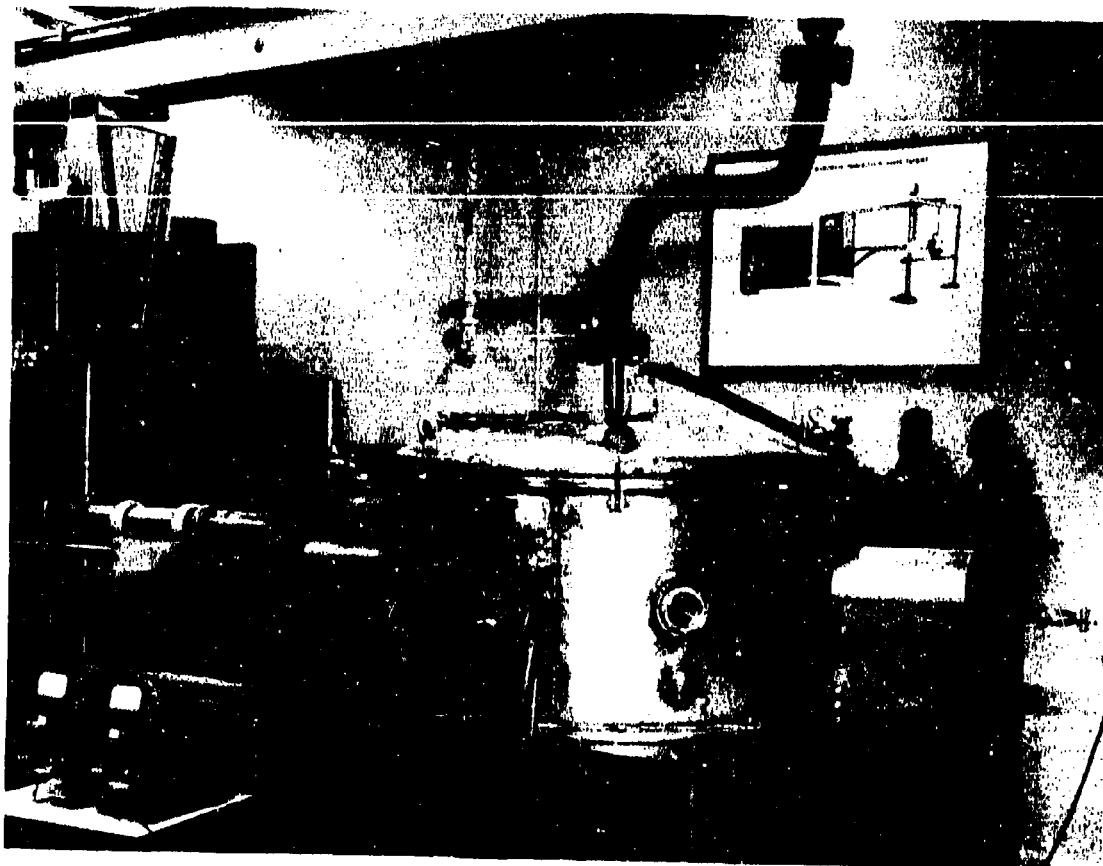


**Figure 5-18. High-Temperature Transmission Gage**

figuration 16 in. wide and 18.5 in. high. Maximum heat flux radiated from this source is approximately 20 to 25 Btu/ft<sup>2</sup>-sec. The test panel is located 9 in. from the lamp reflector. The test panel surface temperature is monitored by thermocouples located at various points on the heated side of the panel, from which a mean surface temperature is obtained. The power transmission through the test panel is monitored by a pair of platinum coated ceramic, conical horn antennas. The horn antennas are parallel-polarized and the angle of incidence at the material surface is 60°, approximately Brewster angle for the materials tested. With this configuration, reflections are minimized and the losses encountered are due primarily to the absorption properties of the test material.

By comparative measurements with and without the test panel in place, the power attenuation as a function of sample surface tem-

perature and exposure time was measured. (See Paragraph 6-5.5.)

#### **5-5.1.2 Emerson and Cuming, Inc.—High-Temperature Reflectometer**

Measurements of the effect of high temperatures, up to 2000°F, on lossy dielectrics used in high-temperature microwave absorbers have been made at Emerson and Cuming, Inc. Figure 5-20 shows the test instrument, which measures the power reflection coefficient at normal incidence. Energy is introduced into the furnace by means of a water-cooled, standard gain horn, which serves both as the transmitter and receiver of the reflected energy. The measurement is of the substitution type; that is, the power reflected from the sample is compared with the power reflected from a standard metal plate.



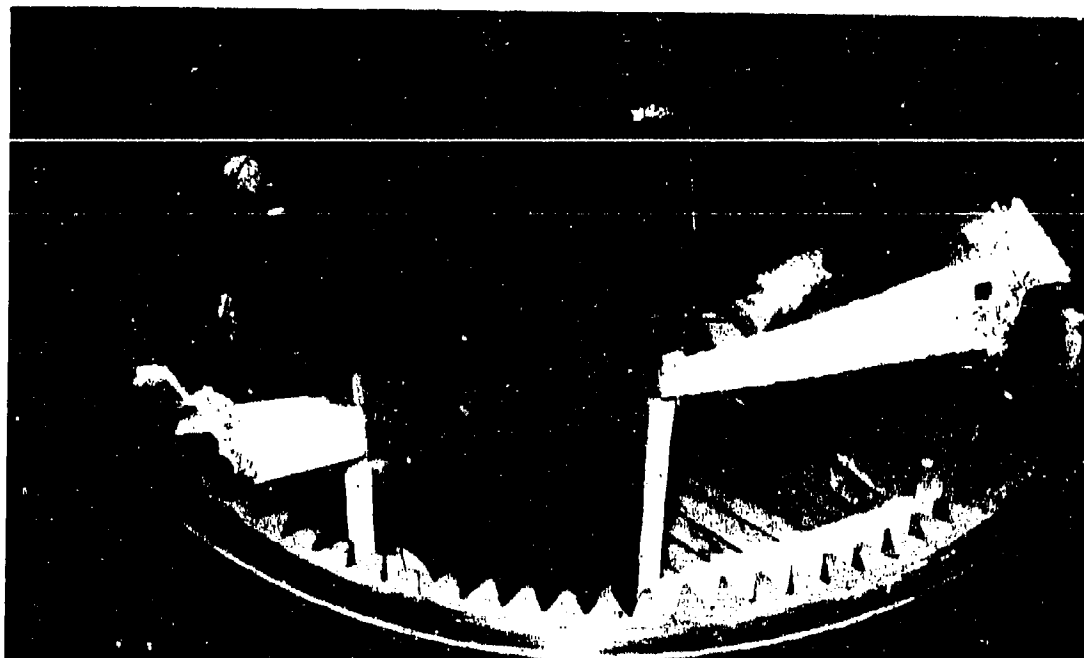


*Figure 5-19. Inside High-Temperature Transmission Gage*



*Figure 5-20. Instrument to Measure Power Reflection Coefficient at Normal Incidence*

## **PART II—MATERIAL TESTING AT VERY HIGH TEMPERATURES (2000°F TO 4000°F)**

### **5-6 INTRODUCTION**

#### **5-6.1 NEED FOR HIGH-TEMPERATURE DATA**

The dielectric properties of many materials have been measured at temperatures of 1800°F to 2000°F. As the speeds of aircraft and missiles have increased, the temperatures experienced by the radome have frequently exceeded 2000°F and the need for accurate dielectric property information has required improved measurement techniques. In many current vehicle flight profiles, the transient heating of radomes is sufficiently serious to require calculation of the radome wall characteristics during heating. This requires knowledge of the temperature profile and the electrical characteristics vs. temperature of the radome material.

Thermal shock and mechanical stresses during transient heating must also be considered in the aerothermoelastic study and comprehensive mechanical and thermal property data are required. While measurement of these properties for dielectric materials presents a broad spectrum of measurement problems, only the electrical measurements are considered.

Hypervelocity, low-level vehicles, boost glide vehicles, and all types of ballistic or reentry vehicles experience severe aerodynamic heating in traversing the dense atmosphere at high velocity. In all of these vehicles, the leading edge, nose, or front surface area experiences the most severe heating. In many designs, radar antennas must have an unobstructed view in the direction of travel and this inevitably requires placement of the radome in an area of the greatest heating and hence the most severe thermal problem area. The use of reinforced organic plastic radomes for these applications has given way to inorganic materials

of the ceramic, recrystallized glass, and glass types because of improved high-temperature electrical properties.

#### **5-6.2 TYPES OF MATERIALS USEFUL IN THE 2000°F TO 4000°F RANGE\***

The materials most useful in high-temperature radome applications may be classified as follows:

1. Oxide ceramics
2. Refractory glasses
3. Recrystallized glasses
4. Nonoxide ceramics (such as BN and  $\text{Si}_3\text{N}_4$ )

##### **5-6.2.1 Oxide Ceramics**

Of the polycrystalline oxide ceramics that have been used for radome applications, the greatest emphasis has been placed on aluminum oxide base materials. Satisfactory performance to 3000°F has been demonstrated, but thermal shock remains a problem. The use of alumina at temperatures above 3200° is questionable based on recent electrical data, but the wide variation in electrical properties with composition requires consideration of specific compositions. Beryllia has the advantage of lower density and higher thermal conductivity than alumina, but has the problems of cost, toxicity, and limited availability. Magnesite deserves further consideration on the basis of published information. Magnesium aluminate spinel ( $\text{MgAl}_2\text{O}_4$ ) also has electrical properties that deserve further consideration for high-temperature applications.

\* See Paragraph 4-2.

### 5-6.2.2 Refractory Glass

High-purity silica has excellent electrical performance up to 2550°F and deserves consideration as a thermal shock resistant radome material. Small concentrations of impurities, however, markedly change the high-temperature properties.

### 5-6.2.3 Recrystallized Glass (Pyroceram)

Of the commercially available materials, Pyroceram is a sole representative. The useful temperature range of Pyroceram bridges the gap between reinforced plastics and the oxide ceramics.

### 5-6.2.4 Nonoxide Ceramics (BN, Si<sub>3</sub>N<sub>4</sub>)

Several nonoxide ceramics exhibit dielectric characteristics. While not yet applied to radomes, these materials deserve consideration for future vehicles.

## 5-6.3 GENERAL DIELECTRIC BEHAVIOR OF MATERIALS AT HIGH TEMPERATURES

Extensive treatments on the behavior of dielectric materials are presented in References 12 through 14, and the behavior of radome materials is covered in Chapter 4. Only a brief discussion of microwave dielectrics at high temperatures is possible, since there remain broad gaps in the data on their behavior.

For most materials, the sources of loss are given a general description by using the complex permittivity  $\epsilon^*$ , where

$$\epsilon^* = \epsilon' - j\epsilon'' \quad (5-9)$$

and a corresponding dielectric constant

$$k^* = k' - jk'' \quad (5-10)$$

In describing the material thus,  $k''$  is the dielectric loss factor and

$$\tan \delta = k''/k' \quad (5-11)$$

It can be seen that the power factor,  $\cos \theta = \sin \delta$ , and hence for low-loss materials the power factor,  $\cos \theta$  or  $\sin \delta$ , is equivalent to the loss tangent,  $\tan \delta$ , since  $\tan \delta = \sin \delta$  for small values of  $\delta$ . Some confusion in loss factor ( $k''$ ), loss tangent ( $k''/k'$ ), and power factor

$[k''/\sqrt{(k')^2 + (k'')^2}]$  exists because of notation differences and the approximations often used.

The polarizability,  $\alpha_p$ , of a dielectric material is thus related to its dielectric constant,  $k'$ , by the classical Clausius-Mossotti equation. Structural interpretation of dielectric data attempts to relate the  $k'$  of a material to the polarizability,  $\alpha_p$ , of its molecules. Four mechanisms can contribute to molecular polarizability,  $\alpha$ .

$$\alpha_p = \alpha_e + \alpha_a + \alpha_d + \alpha_s \quad (5-12)$$

where  $\alpha_a$  = atomic polarizability (requires about  $10^{-12}$  to  $10^{-14}$  sec)

$\alpha_d$  = dipole orientation polarizability (requires about  $10^{-6}$  sec or longer)

$\alpha_e$  = electronic polarizability (requires about  $10^{-16}$  sec)

$\alpha_s$  = interfacial or space charge polarizability (may require  $10^2$  sec)

Dielectric relaxation is the exponential decay of polarization after removal of the applied field. This relaxation causes dispersion in which the dielectric constant decreases with increasing frequency, as shown in Fig. 5-21. As dispersion in  $k'$  occurs, loss  $k''$ , due to relaxation, reaches a maximum. Reference 15 presents the theory of this phenomenon to explain internal molecular structure. Extensive treatments of structural interpretation techniques are presented in References 12 to 14.

In ionic solids, which represent the major dielectric materials of interest at high temperatures, the contribution of  $\alpha_s$ , atomic polariza-

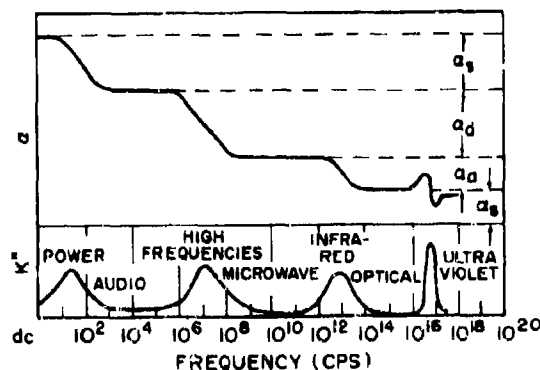


Figure 5-21. Dielectric Dispersion and Absorption

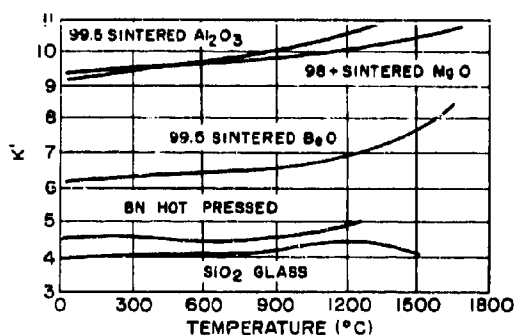


Figure 5-22. Dielectric Constant vs Temperature for Selected Dielectric Materials

bility, are usually more important than  $\alpha_e$ , electronic polarizability.

Increasing temperatures tend to decrease  $k'$ , since the number of molecules per unit volume is decreasing. However, since the ions are separated more, their atomic polarizability,  $\alpha_a$ , increases and this effect is usually several times that due to reduction of the density.

Since the measurement frequencies customarily used are far below the resonant frequencies for electronic motion or ionic motion, the losses of ionic crystals vary little with frequency. However, the presence of appreciable d-c conductance or the increased electronic conductance at high temperatures will increase the loss of most materials.

Researchers disagree on the effect of lattice defects on loss behavior of single crystals. Small loss maxima attributed to the jumping of the positive ion in alkali halides has been reported in Reference 16 and differences in loss behavior of polycrystalline alumina and sapphire single crystal reveal grain boundary effects. In examining high-temperature dielectric loss data, Reference 17 concludes that low-frequency transconductance accounts for only 1/10 to 1/5 of the microwave loss, but that impurities (and their associated dislocations and lattice imperfections) that cause charge transfer at low frequencies also extend the infrared vibrational losses to lower frequencies.

The performance of typical dielectric materials at high temperatures is shown in Figs. 5-22 and 5-23. The purity of the samples, surface contamination, and stoichiometry largely

determine the exact shape of the curves. Small conductive inclusions isolated in a dielectric matrix may be much less evident in high-temperature dielectric measurements at microwave frequencies than impurities that slightly increase the electronic conductivity. Pure boron nitride, BN, probably has better properties than shown in Fig. 5-23, but the small  $B_2O_3$  impurity rapidly increases the loss above  $1100^\circ\text{C}$ . Most samples exhibit a decrease in loss above  $100^\circ\text{C}$  and this may be interpreted as the contribution of adsorbed moisture on the surface.

Samples of high-purity alumina, beryllia, and magnesia have shown useful dielectric properties at  $1650^\circ\text{C}$ . The loss is sufficiently low ( $<0.05$ ) to justify their use at these temperatures; however, the loss is increasing at such a rate as to make higher operating temperatures questionable, unless extreme care is taken in reducing impurity levels even further.

Single crystal samples have not been carefully studied at high temperatures. For anisotropic crystals, such as alumina, there is often difficulty in obtaining measurements with the electric field in any direction other than the "easy" direction of polarization. Other than the desired field configuration may be excited within the sample and the energy absorbed by these fields appears as extraneous loss peaks at some temperature at which the geometry is favorable. For isotropic materials, measurements are more reliable. In addition, optical-quality silica glass is a good standard sample material for comparative measurements, since its optical index of refraction may readily be rechecked and stria, or inclusions, observed.

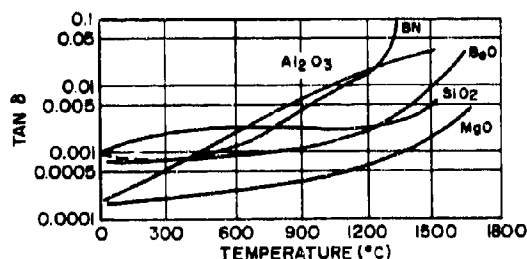


Figure 5-23. Loss Tangent vs Temperature for Selected Dielectric Materials

#### 5-6.4 PROBLEMS ASSOCIATED WITH HIGH-TEMPERATURE DIELECTRIC MEASUREMENTS

Most of the discussion in this chapter is related to electrical measurement techniques. However, the generation, control, and measurement of high temperatures is a serious consideration. Electrical resistance furnaces are useful up to 3000°F (in air) and represent simple, clean, and controllable heat sources. Above 3000°F, the use of an inert atmosphere or a vacuum is almost essential if resistance heating is used. Also, the pyrometry is considerably more difficult.

With the increased temperature range of the measurements, the physical stability of the sample and the measurement apparatus is an important consideration. The measurement of electrical characteristics at microwave frequencies ultimately depends on determining certain physical dimensions in a resonant system, and the mechanical stability of the system limits the precision or reproducibility of the electrical measurements. The stability of the construction materials in high-temperature systems is of particular concern, since most of the materials with which designers are familiar are not applicable above 2000°F. Diffusion, oxidation, recrystallization, and interactions in materials used in apparatus construction limit their ultimate temperature and useful life.

The effect of atmosphere on the sample during heating and measurement, and the effects of atmosphere on the measurements at high temperatures have received only minor attention.

### 5-7 DIELECTRIC MEASUREMENT TECHNIQUES

#### 5-7.1 GENERAL

Considerably different problems are encountered in measurements made at 1 gc compared to those made at 40 gc. The requirements for each frequency must be considered separately. For convenience, the frequencies are in three regions: 1 to 5 gc, 5 to 15 gc, and above 15 gc.

##### 5-7.1.1 The 1- to 5-Gc Region

In the 1- to 5-gc region, the sample size re-

quirements and cavity dimensions for high-temperature measurements are inconveniently large. For example, the use of  $TE_{011}$  at 1 gc requires a cavity 25 cm in diameter and 3 cm high. However, the physical dimensions of the sample and the cavity can be readily determined to sufficient accuracy in the frequency region. Coaxial line techniques are also popular in the frequency range, despite certain inherent mechanical problems.

##### 5-7.1.2 The 5- to 15-Gc Region

In the 5- to 15-gc region, both sample and cavity are of a convenient size. While waveguide and cavity techniques are easily applied, free-space techniques are useful for plates that are several inches in diameter. In addition, the availability of many commercial components allows rapid assembly of measurement equipment.

##### 5-7.1.3 The Region Above 15 Gc

Above 15 gc, the sample size requirements for cavity or waveguide techniques become inconveniently small, but usable to perhaps 50 gc. Free-space techniques, using interferometry or direct phase delay and attenuation measurements, become more convenient and the required plate sample is only several inches in diameter.

##### 5-7.1.4 Construction Materials for Specialized Equipment

The greatest difficulty in assembling microwave equipment for measurement of electrical characteristics above 2000°F is the choice of materials for constructing cavity, waveguide, and horn equipment that must be subjected to the high temperatures. All base metal (nickel, chromium, cobalt, or iron) alloys capable of withstanding temperatures above 2000°F for extended periods have high electrical resistivity and form undesirable oxide films. Operation of base metals above 2400°F is impractical and attempts to clad or plate these metals with platinum or other noble metals have been generally unsatisfactory.

Three other approaches to waveguide or cavity materials have been used: (1) refractory

metals, such as molybdenum or tungsten, have been used in an inert atmosphere (Reference 18); (2) platinum metal alloys (Reference 19), and (3) metal coated ceramics (Reference 20). In general, the latter two are limited to 3000°F. Platinum-10% rhodium alloy waveguide has been produced in a number of standard sizes for 8- to 40-gc operation and is easily welded, joined, and maintained in normal heating (Reference 21).

Refractory metal technology has advanced rapidly as improved welding techniques and improved alloys have become available. These metals are a good choice for large, low-frequency assemblies, or for cylindrical cavity designs.

While platinum-coated aluminum oxide has been used for waveguide and cavity construction, its fabrication cost is difficult to justify.

Specialized equipment required for dielectric measurements often includes a precise slotted-line assembly. Most commercial slotted-line carriages do not provide adequate stability, reproducibility of setting, and readability of probe position to make adequate vswr measurements. Careful modification of a carriage is often required to ensure mechanical rigidity and to add a dial gage or micrometer traverse measurement.

## 5-7.2 LABORATORY EQUIPMENT

High-temperature dielectric measurements have been made in the microwave region using many techniques. For convenience, these techniques are grouped into: (1) coaxial techniques, (2) cavity measurement techniques,

(3) waveguide techniques, and (4) free-space (interferometer) techniques. A discussion of each technique, including basic procedure, is found in the following paragraphs.

### 5-7.2.1 Coaxial Techniques

A common technique for dielectric measurements below 5000 mc is the coaxial line technique (Reference 22). By fitting a measuring line with a suitable extension of platinum-10% rhodium alloy, or other high-temperature alloy, the specimen may be heated and measured simultaneously. The greatest disadvantage of this technique is that small gaps between the sample and the conductors may cause large errors. Other errors include: (1) the changing gap between the inner and outer conductors and the sample's inside and outside dimensions with temperature and (2) the concentricity of the central conductor in the line, since central conductor supports are minimized to reduce errors in the measured parameters. Accuracy is largely limited by sample fit, and the sample fabrication for many ceramic specimens is difficult and expensive.

A commercial measuring line made by General Radio Corp. and fitted with a 36-cm extension of platinum-10% rhodium tubing with dimensions comparable to those of the measuring line is shown in Fig. 5-24. A stable variable-frequency source, frequency meter, and vswr meter complete the required electrical measuring equipment, as shown in Fig. 5-25. A short water-cooling sleeve between the furnace and the slotted section is generally required to prevent overheating. A simplified calculation is

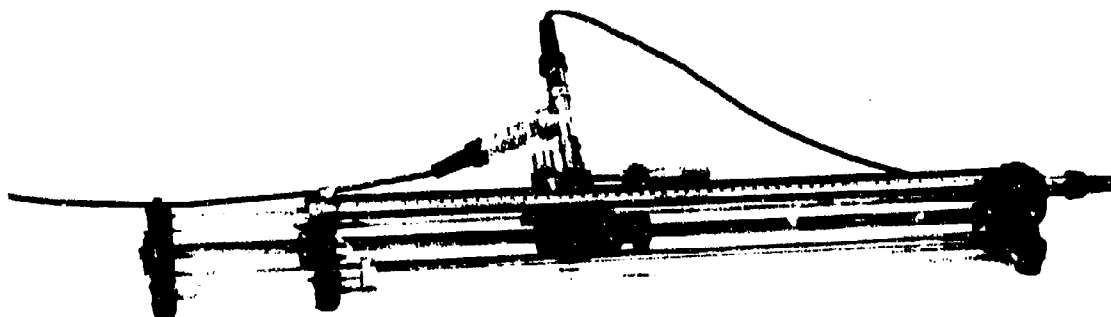


**Figure 5-24. Coaxial Dielectric Measuring Line Modified for High Temperature Measurements by Adding Length of Platinum Alloy Tubing**

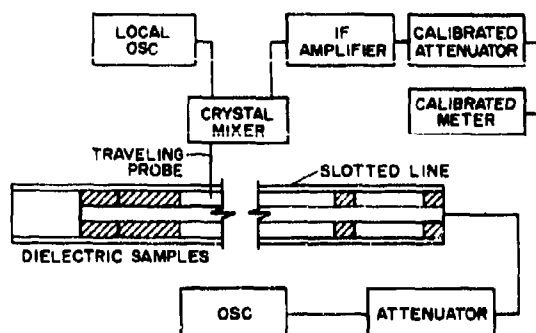


Figure 5-25. Block Diagram of Equipment Used with Coaxial Line Dielectric Measurements

possible (Reference 22) if the measurement frequency is adjusted so that the first voltage minimum falls just at the face of the sample. The probe actually measures the position of the minimum  $\lambda/2$  from the face of the specimen, so that the position of the sample face must be calculated for each temperature. Since the frequency at which the sample length is  $\lambda/4$  changes with temperature (resonant frequency generally decreases with temperature) and the sample face position changes slightly with the thermal expansion, several trials at each temperature are usually required before the exact frequency is determined. Loss is determined by measurement of the width of the vswr minima at points 10 db from the minimum.

The calculation of  $k'$  and  $\tan \delta$  is as follows (Reference 22):

$$k' = \frac{N\lambda_0}{4(d + X_0)} - \frac{0.46}{l} \quad (5-13)$$

where  $N$  = odd integer

$X_0$  = distance of first minimum from sample face >1.0 mm; <2.0 mm

$d$  = length of sample

$\lambda_0$  = wavelength in free space

$$\tan \delta = \frac{\Delta X}{3(d + X)} - \frac{\Delta X'}{8l} \quad (5-14)$$

where  $\Delta X$  = node width at the 10-db point with sample

$\Delta X'$  = node width at the 10-db point without sample

$l$  = distance from node to open end of line

Sample fit corrections are important in this measuring technique since a 25-micron gap around a sample of  $k' = 10$  can cause more than a 6% error in  $k'$ . Charts for correction of  $k'$  for sample fit up to  $k' = 7.5$  have been published by von Hippel. For high-temperature measurements, thermal expansion corrections for sample length and sample clearance must be made. An accuracy better than  $\pm 2\%$  in dielectric constant and  $\pm 5\% + 0.0001$  in loss is difficult to achieve, but good indications of relative changes in dielectric properties are possible by this method in the 1000- to 5000-mc range.

The exact solution of the equations for coaxial line measurements with  $\lambda/4$  samples and for other length samples is presented in References 23 and 24.

Other dielectrometers, such as the Central Research Laboratory model (Fig. 5-26), use a coaxial sample holder, and provide for the required vswr and node measurement with and without the specimen, not limiting the measurement to specimen lengths that are electrically  $\lambda/4$ .

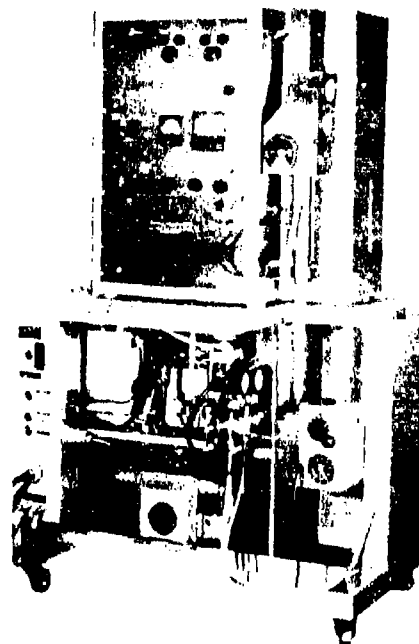


Figure 5-26. Commercial Dielectrometer for Use to 500°C at 1, 3, and 8.5 gc. Coaxial Sample Holder Used at Two Lower Frequencies Is Used without Center Conductor at Higher Frequencies

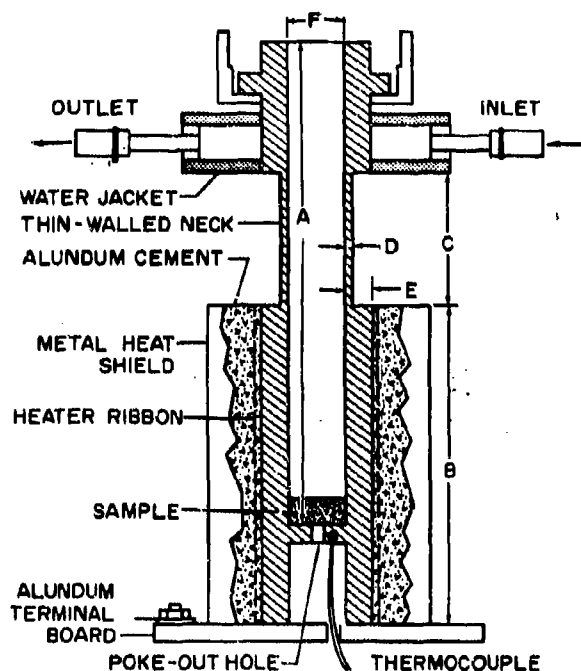
Several variations of these basic methods are used, including a short-circuited line, the sample at the line end and displaced  $\lambda/4$  from the line end, and the attenuation and phase shift through a sample of known length. Generally, these variations offer little advantage over the techniques described.

### 5-7.2.2 Waveguide Techniques

Both the circular waveguide operating in the  $TE_{11}$  mode and the rectangular waveguide operating in the  $TE_{11}$  mode are used for high-temperature measurements of  $k'$  and  $\tan \delta$ . Reference 25 presents measurements based on a short-circuited circular waveguide with a disk sample, whereas References 26 and 29 present

measurements based on a shorted rectangular waveguide and a rectangular bar sample. Reference 25 describes circular waveguides useful up to 3000°F for 8.6 to 50 gc (see Fig. 5-27). The Central Research Laboratory dielectrometer (Fig. 5-26) uses a silver plated stainless steel circular guide for measurements up to 930°F, but can be used with some of the waveguides in Fig. 5-27. Commercial components and a platinum alloy waveguide extension are capable of measuring up to 2910°F when equipped with suitable furnace equipment, such as shown in Fig. 5-28.

The precautions in sample length selection and the effects of sample fit on measurement accuracy are discussed in Reference 26. Samples that are electrically one-half wavelength simplify calculation, but  $\lambda/4$  or  $3\lambda/4$  samples



NOMINAL FREQUENCY	$8.6 \times 10^9$	$1.4 \times 10^{10}$	$2.4 \times 10^{10}$	$5 \times 10^{10}$
A. INSIDE LENGTH	15.0 CM	7 CM	5.3 CM	3.1 CM
B. LENGTH HEATED	10.0 CM	4.2 CM	3.6 CM	2.4 CM
C. LENGTH OF NECK	3.6 CM	2.1 CM	1.0 CM	0.8 CM
D. NECK THICKNESS	0.030 IN.	0.012 IN.	0.010 IN.	0.008 IN.
E. WALL THICKNESS	1/8 IN.	1/8 IN.	1/16 IN.	1/16 IN.
F. INSIDE DIAMETER	1.0 IN.	5/8 IN.	3/8 IN.	11/64 IN.

Figure 5-27. Sample Holder for 1-in. Disks to 2550°F with Pt Foil, or >1400°C with Pt-Rh Foil (Longitudinal Cross Section)



improve the accuracy of the measurement. Experience has shown that for materials with losses greater than 0.002, satisfactory measurements can be made on almost any convenient sample length. The advantages of a circular waveguide are the sample symmetry and ease in sample insertion and removal. The rectangular waveguide provides a precisely known field in the sample and for measurement of homogeneity, samples can often be rotated 90° and measured in mutually perpendicular directions.

Sample fit is important in all waveguide techniques, since the clearance at the waveguide wall results in a low value of measured  $k'$ . References 26 and 27 present expressions for correction of this fit error. Empirical techniques based on systematically removing material from a sample with extrapolation of the

resulting curve back to zero clearance appear best (Reference 18), since derived expressions are accurate for only limited ranges of  $k'$ .

The basic equations for both circular and rectangular waveguides are equivalent, differing only in the propagation constants for the different waveguide dimensions or geometry. (The derivation of the equations is discussed in Volume I of TR 57-67.) Only the rectangular case will be illustrated, since rectangular waveguide and components are more commonly available.

It is customary to solve for  $\beta_d d$  in Eq. 5-15 by using  $\tan X/X$  tables and to substitute for  $\beta_d d$  in Eq. 5-16.

$$-\lambda_g \frac{\tan 2\pi X_0/\lambda_g}{2\pi d} = \frac{\tan \beta_d d}{\beta_d d} \quad (5-15)$$

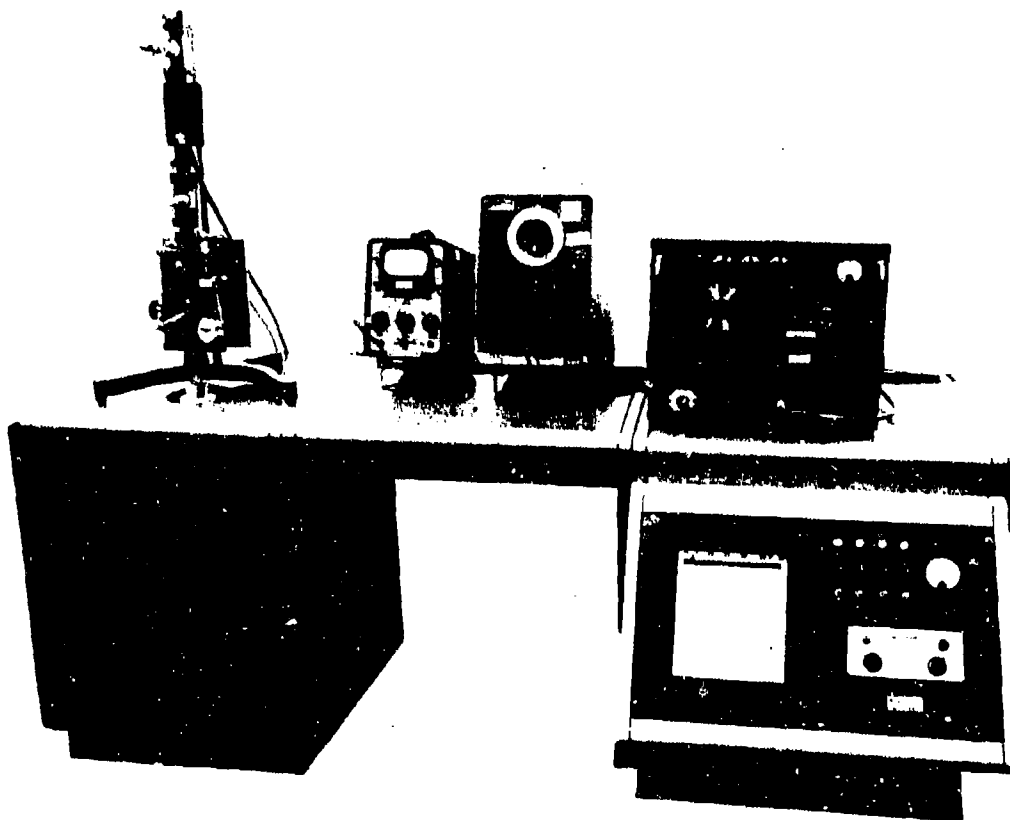


Figure 5-28. High-Temperature (1650°C) Shorted Waveguide Dielectric for Operation Near 10 gc

where  $X_0$  = distance from sample face to minimum (see Fig. 5-29)

$\lambda_c$  = wavelength in waveguide

$$k_1' = \frac{(1/\lambda_c)^2 + (\beta_2 d / 2\pi d)^2}{(1/\lambda_c)^2 + (1/\lambda_g)^2} \quad (5-16)$$

where  $\lambda_c$  = cutoff wavelength for waveguide

$k_1'$  is the uncorrected value for  $k'$  and must later be corrected for sample fit.

$X_0$  is obtained from the measured data:

$$X_0/\lambda_g = N/2 - d/\lambda_g - (X_2 - X_1)/\lambda_g \quad (5-17)$$

where  $N$  = minimum positive integer chosen so that  $X_0/\lambda_g$  is positive

$X_1$  and  $X_2$  = as shown in Fig. 5-29

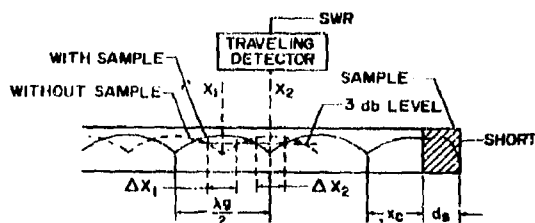


Figure 5-29. Notation Used in Shorted Waveguide Calculations

Several values for  $k_1'$  are possible, since the  $\tan X/X$  function is periodic. Hence, it is necessary to have some knowledge of the approximate dielectric constant, or to measure two different length samples to overcome this ambiguity.

For correcting  $k_1'$  for sample fit, the expressions suggested in Reference 18 are shown in Fig. 5-30. The most critical experimental parameters in making accurate measurements of  $k'$  are (1) filling the narrow dimension of the waveguide completely, (2) assuring that the sample faces are perpendicular, and (3) maintaining the sample against the short.

For high-temperature measurements, the dimensions of the waveguide, the sample dimensions, and the values calculated from these quantities must be corrected for changes in dimensions with temperature. The thermal expansion of the waveguide and of the sample, and the ambient temperature dimensions of

these quantities are used to calculate the high-temperature dimensions.

The calculation of loss tangent from the shorted waveguide data is somewhat simpler than that for the cavity, though it, too, is time consuming. This calculation is as follows:

$$\tan \delta = \frac{(\Delta X_2 - \Delta X_1)}{d} (F_p) (F_q) \quad (5-18)$$

where  $\Delta X_2$  and  $\Delta X_1$  represent the values for the width of the minima at the 3-db point with and without the sample, respectively.

$$F_p = \frac{(1/\lambda_c)^2 + (1/\lambda_g)^2 - (1/\lambda_c)^2/k'}{(1/\lambda_c)^2 + (1/\lambda_g)^2} \quad (5-19)$$

$$F_q = \frac{1 + \tan^2 2\pi X_0/\lambda_g}{1 + \tan^2 \beta_2 d - \tan \beta_2 d / \beta_2 d} \quad (5-20)$$

In systematic calculations,  $F_p$  and  $F_q$  are easily obtained from values derived during the calculation of  $k'$ . In cases where the sample length is electrically a multiple of one-half wavelength,  $F_q$  becomes unity.

For high-temperature measurements, 80% platinum-20% rhodium alloy waveguides can be obtained in 30- to 40-cm lengths for the sample cavity. A platinum alloy short may be welded to one end and a conventional flange brazed to the other. The short may also be removable, but in service to 2910°F or above, removable shorts often diffusion-bond to the waveguide. Sample insertion and removal with a welded short are often tedious if clearances are small, and a small electric vibrating tool often aids removal. A satisfactory design for the welded short on a standard 8- to 12-gc guide consists of a weld along only the wide dimension of the guide, with a 0.5-mm gap left at each edge (narrow dimension), through which a steel shim can be passed to aid in removal of the sample.

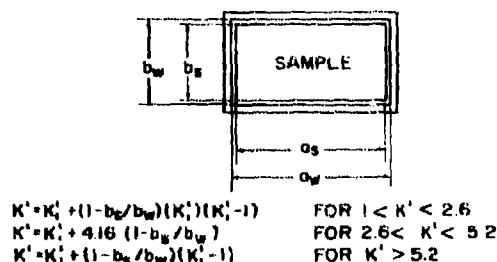


Figure 5-30. Sample Fit Corrections

For accurate measurement of vswr and node position, conventional slotted sections are inadequate and must be supplemented with a micrometer drive or dial gage capable of reading to 2 microns. This usually involves only simple modification of existing slotted-line carriers and probe assemblies, if the original design is mechanically stable and precisely machined. Operation of the slotted section in the vertical plane over the shorted section is desirable. This arrangement allows the use of a vertical-tube furnace to heat the sample and assures that the sample will remain in place against the short. Only minor supplementary air cooling of the waveguide outside the furnace is usually required to maintain temperatures of 100-120°F at the slotted section. For measurements above 12 gc, particular care is needed to maintain adequate signal stability so that accurate measurements of node shift can be made. Extreme care also must be used in disassembly and reassembly of the waveguide components during sample insertion, or errors may be introduced in the node position measurements.

### 5-7.2.3 Resonant Cavities for Use Above 5 Gc

Several cavity designs for high-temperature service have been reported. The features that

should be incorporated in a high-temperature cavity design are discussed briefly and a typical calculation procedure is presented.

Most cavity designs are based on work reported in References 28 and 29. These original designs provide the required equations and experimental verification of the theory. Cylindrical cavity designs are operated almost exclusively in the  $TE_{01n}$  mode for dielectric measurements. This mode has an absence of radial currents; hence, a movable noncontacting plunger may be used as one end of the cavity cylinder without reducing cavity  $Q$  or introducing serious deviations from theoretical behavior.

To excite the  $TE_{01n}$  mode, a balanced-input coupling to one cylinder end is preferred. An Adcock balanced-Tee input (Reference 30) and a Bleaney input coupling (waveguide) (Reference 29) have been used satisfactorily with the cavity fed through slots or circular irises located radially on the cylinder diameter at the point of maximum field. See Fig. 5-31. Reference 20 presents dielectric-filled waveguides for coupling to the cavity to reduce the size of the waveguide and for other mechanical advantages.

The output coupling to a  $TE_{01n}$  cavity should be located approximately  $\lambda/4$  from the top end

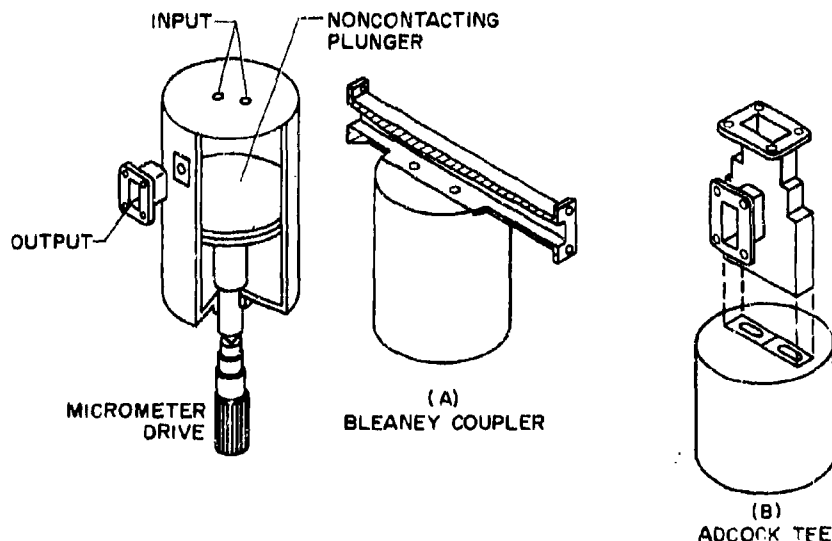


Figure 5-31. General Features of Resonant Cavity Showing Methods of Input Coupling; (A) Bleaney Coupler, (B) Adcock Tee

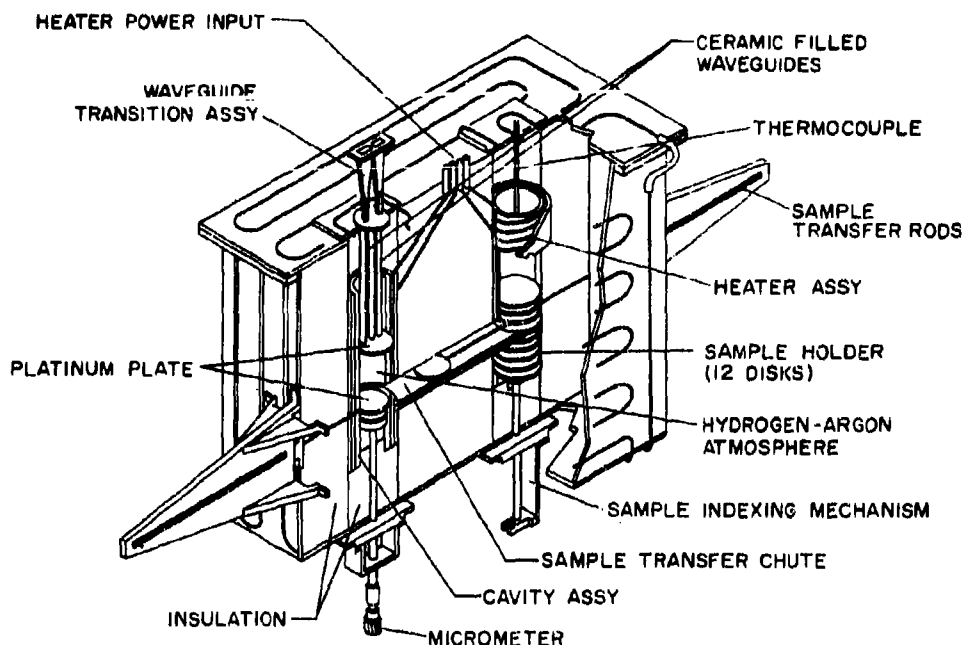


Figure 5-32. High-Temperature (1500°C) Resonant Cavity Dielectrometer for Operation near 10 gc

of the cylinder and if it is placed at either 45° or 90° from the diameter plane containing the input coupling holes, either unwanted  $TE_{21n}$  or  $TE_{11n}$  modes, respectively, can be suppressed. With careful balancing of the inputs and with proper cavity design, responses to modes other than the  $TE_{01n}$  mode can be suppressed more than 100 db at room temperature, and for high-temperature cavity systems, 20- to 50-db suppression of unwanted modes is common. Mode suppression is important in cavity design, since excitation of unwanted modes removes power from the desired modes and this appears as a reduction in cavity  $Q$ , hence producing questionable loss data.

Suppression of unwanted modes is also possible by carefully selecting cavity dimensions. Most investigators have used the  $TE_{014}$  and  $TE_{015}$  modes, requiring a rather long cavity. Operation in the  $TE_{012}$  and  $TE_{013}$  modes is also satisfactory, and although this shorter cavity can eliminate the troublesome  $TE_{21n}$  modes, several other unwanted modes can occur.

Cavity tuning is accomplished by micrometer drives precise to 0.005 cm or better. The plunger face is moved by an expansion, a suit-

able high-temperature material, such as silica glass or alumina ceramic, connected to the micrometer drive. For high-temperature operation, the arrangement in Reference 20 for sample changing (see Fig. 5-32) is of particular interest, since the cavity does not require disassembly to change samples. In this design, the cavity is constructed with a slot at the bottom end through which a sample can be inserted over the plunger. The sample is then raised into the measuring position inside the cavity with the micrometer drive. Samples are preheated before insertion and are returned to the sample rack after measurement.

Cavity construction for high-temperature service requires the use of dimensionally stable materials. Silver plated Invar has been used (Reference 31) to 500°F; platinum coated alumina ceramic was used in the design of Reference 20, but this was later replaced with a thin platinum cylinder liner for a ceramic tube. Molybdenum is an electrically ideal material, but requires the use of a neutral or reducing atmosphere during service and is difficult to fabricate. Stainless steels plated with silver and gold have been used (Reference 31)

for cavities designed to operate to 930°F, but are limited by the diffusion of the gold and silver at higher temperatures. Feed hardware and output coupling fittings require similar consideration.

The experimental procedure for cavity measurements is rather straightforward; the wavelength in the cavity,  $\lambda_g/2$ , is measured by noting the cavity length for two successive modes, such as TE<sub>014</sub> and TE<sub>015</sub>. The resonant length of the cavity for one of these modes is then measured with the sample in place. This provides data sufficient for calculating the dielectric constant. Loss tangent measurements require measurement of the Q of the cavity with and without the sample.

For cavity designs where the sample is inserted into the cavity by disassembly of the cavity at ambient temperatures, the measurement of empty cavity and cavity-with-sample conditions as a function of temperature introduces an obvious source of error in reproducibility. The exact temperature conditions under which calibration data were obtained must be reproduced during the actual sample measurement. For the high-temperature dielectrometer design (Reference 20), this source of error is minimized, since calibration and sample measurements can be made only a few minutes apart in time and the sample is easily removed for a check on the original calibration without seriously disturbing the temperature equilibrium.

Calculations are performed (Reference 31) by solving the following expression for  $\beta_s$ :

$$\frac{\tan \beta_s d}{\beta_s d} = - \frac{\tan \beta_e (M_3 - M_1 - d)}{\beta_e d} \quad (5-21)$$

where  $M_1$  = micrometer reading for the TE<sub>014</sub> resonance cavity, empty

$M_2$  = micrometer reading for the TE<sub>015</sub> resonance cavity, empty

$M_3$  = micrometer reading for the TE<sub>015</sub> resonance cavity with the sample

$d$  = sample thickness

$\beta_e$  = phase constant of the empty cavity

$\beta_s$  = phase constant in the sample

and where

$$\beta_e = \frac{\pi}{M_2 - M_1} \quad (5-22)$$

For low-loss samples,  $\tan \delta < 0.1$ , the dielectric constant,  $k'$ , is

$$k' = \frac{\beta_e^2 + k^2}{\beta_e^2 + k^2} \quad (5-23)$$

where  $k = 3.823/a$  for the TE<sub>01n</sub> mode and  $a$  is the effective cavity radius. This effective cavity radius must be computed from

$$a = \sqrt{\frac{\lambda_0^2 / \lambda_g}{2.6896 (\lambda_g^2 - \lambda_0^2)}} \quad (5-24)$$

where  $\lambda_g = 2(M_2 - M_1)$

It can be seen that all quantities except  $\lambda_0$ , the free-space wavelength, may be expressed in terms of the micrometer readings,  $M_1$ ,  $M_2$ , and  $M_3$ . Solution for  $\beta_s$  requires that  $\tan \beta_s d / \beta_s d$  be derived from a table of  $\tan X/X$ . Machine computation of the data is discussed in Paragraph 5-8.2.

For high-temperature measurements, the recorded micrometer readings have the inherent corrections for temperature changes in the measuring system and  $d$ , the sample thickness, is the only quantity requiring further correction for thermal expansion. The sample diameter must, of course, be selected so that a small gap ( $< 0.25$  mm) is maintained throughout the temperature range of the measurement. Any differences in thermal expansion of the sample and cavity result in changes in this gap, but no corrections in the calculations are required for small gaps (Reference 31).

Loss tangent is calculated from the Q of the cavity by either measurement of the width of the resonance curve at the 3-db points,  $\Delta M$ , with the micrometer, or by measuring the change in frequency,  $\Delta f$ , 3 db from resonance. The latter can be done somewhat more accurately, since  $\Delta M$  for a well-designed cavity may be 0.02 mm or less. A Boeckeler micrometer head (manufactured by the Arizona Tool and Die Manufacturing Company) precise to  $\pm 0.3$  microns is useful for measuring  $\Delta M$ . The system for measuring  $\Delta f$  reported in Reference 32 is rapid and accurate to  $\pm 5$  kc.

The calculation of  $\tan \delta$  requires the evaluation of a complicated expression. Although Reference 28 gave an exact expression for  $\tan \delta$ , the equivalent expression in the form given in Reference 33 is used most frequently.

$$\tan \delta = \frac{\beta_s^2}{(\beta_s^2 + k^2) k' B^2 b^*} \left\{ \Delta M_s - \frac{c}{a} \left[ a \left( 1 + B^2 \frac{\beta_s^2}{\beta_s'^2} \right) + \frac{l^2}{\beta_s'^2} (B^2 b^* + l') \right] \right\} \quad (5-25)$$

$$\text{where } B^2 = \left\{ 1 + \left[ \left( \frac{\beta_s}{\beta_s'} \right)^2 - 1 \right] \cos^2 \beta_s d \right\}^{-1}$$

$$b^* = d \left( 1 - \frac{\sin 2\beta_s d}{2\beta_s d} \right)$$

$$l' = (M_3 - M_1 - d) \left( 1 - \frac{\sin 2\beta_s (M_3 - M_1 - d)}{2\beta_s (M_3 - M_1 - d)} \right)$$

$$\frac{c}{a} = \frac{\beta_s^2}{k^2 + 2\beta_s'^2 (a/l_e)} \frac{\Delta M_0}{l_e}$$

$l_e$  = length of empty cavity at resonance

It can be seen that tables of  $\sin 2X/2X$  are useful in this calculation and that machine computing is desirable. The further simplification or approximation of this expression for  $\tan \delta$  has not been attempted; however, it should be possible. For temperature corrections, all values for lengths should represent those under the temperature conditions, including sample size.

#### 5-7.2.4 Low-Frequency Cavity Designs (1 to 5 Gc)

The cavity design shown in Fig. 5-33 for a  $TE_{010}$  cavity has been used for dielectric measurements and an analysis for the effect of a center sample insertion hole has been published (Reference 34). While this cavity has not been used at high temperatures, its advantages in terms of sample requirements (13-mm diameter  $\times$  8-cm height), the ease of changing samples at temperature, and its simplicity offer promise for 1- to 5-gc measurements in the  $TE_{010}$  or  $TE_{020}$  modes. The major limitation is its size, about 25 cm in diameter for 1 gc which requires a rather large heating furnace.

Another cavity design, by Westphal, has been used in the 3- to 5-gc region. The cavity consists of a metal foil pressed into intimate contact with a solid cylindrical sample that is somewhat shorter axially than in diameter. The resulting configuration is one of a dielectric-filled cavity. Excitation is achieved through two iris openings on the cylinder faces, as shown in Fig. 5-34. By the use of a 25- to 250-micron thick platinum

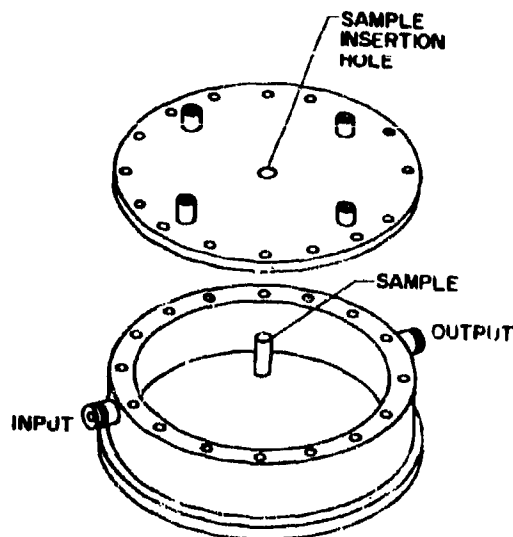


Figure 5-33. Typical TE Cavity Configuration. Small Cylindrical Sample Is Inserted into Center of Cavity

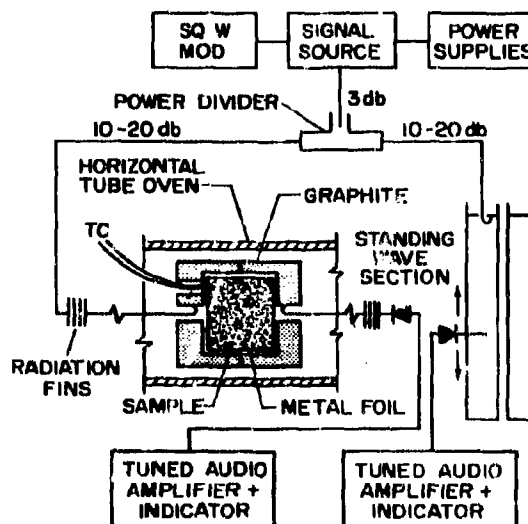


Figure 5-34. Equipment for Resonant Cavity Measurements

foil carefully rolled onto a 1-in. diameter  $\times$  7/8-in. high sample and hot pressed in a graphite die, a wrinkle-free cavity can be formed around the dielectric sample. For high-temperature measurements, the graphite cups placed

over the sample, as shown in Fig. 5-34, may be induction heated, or heated to the desired temperature in a resistance furnace.

The equations used for a cylinder resonant in the lowest-frequency  $TM_{010}$  mode are

$$\lambda = 1.30637 D \sqrt{k'} \quad (5-26)$$

where  $D$  = cavity diameter, cm

$k'$  = dielectric constant of the filling material

$\lambda$  = resonant - frequency free - space wavelength

The cavity  $Q$  with a lossless dielectric is

$$Q_w = \frac{10^4 \sqrt{\lambda/s}}{1 + 0.38\lambda/h} \quad (5-27)$$

where  $h$  = cavity height, cm

$s$  = resistivity of metal walls relative to copper

the loss tangent,  $\tan \delta$ , of the dielectric is simply:

$$\tan \delta = \Delta\lambda/\lambda - 1/Q_w \quad (5-28)$$

where  $\Delta\lambda$  = width of the resonant curve (for the cavity filled with dielectric) at its half-maximum power points (3 db)

The face foils require careful attention to achieve high  $Q$  and must be smooth, without warping or separation. The  $TE_{111}$  mode, the next higher-frequency mode (about 40% higher), is also useful and the equations for this mode are

$$\lambda = \frac{\sqrt{k'}}{\left(\frac{0.3434725}{D^2} + \frac{0.25}{h^2}\right)^{1/2}} \quad (5-29)$$

$$Q_w = \frac{1.31 \times 10^4 h}{\sqrt{\lambda/s} \left(\frac{2.39 h^2 + 1.73 D^2}{3.39 h^2/D + 0.73 Dh + 1.73 D^2}\right)} \quad (5-30)$$

Values for  $\tan \delta_w (= 1/Q_w)$  have been tabulated by Westphal for various length samples vs. frequency and cavity foil material.

This technique, with minor modification, is also useful at higher frequencies, but is most useful in the region below 5 gc, where larger samples are required by most measurement

techniques. Its advantages are a simple sample configuration and a simple calculation procedure. A variable-frequency signal source with a rather broad frequency range is required, however, and the  $\Delta f$  measurement for  $\tan \delta$  measurements requires careful attention for very low-loss materials. For low-loss samples, the loss measured with the filled resonant cavity at room temperature agreed with values determined at 8.5 gc, within limits of error. Some of the higher-loss materials showed appreciably lower loss in the 4-gc region of resonance measurements. There is some question as to the validity of the calculations used in this technique, since it is never possible to confirm the characteristics of the empty cavity.

### 5-7.2.5 Free-Space Techniques

At high temperatures, free-space techniques become somewhat cumbersome, since a sample several wavelengths on a side is usually required. The entire sample must also be heated without the furnace parts introducing extraneous reflections. Two basic techniques have been used at high temperatures. The one-horn and two-horn interferometers have received most attention, and the Michelson type interferometer reported in Reference 35 has been used to 1100°F.

For radomes, a relatively large section of dielectric is illuminated so that free-space techniques closely approximate the actual service conditions. The limitation of two-horn interferometers is largely in their inability to measure losses below 0.1 with any degree of accuracy. For the Michelson interferometer, however, losses as low as 0.001 have been evaluated. Where local inhomogeneities in a sample or anisotropic materials would require measurement of a large number of small samples to obtain statistically significant values for  $k'$  and  $\tan \delta$  by a waveguide technique, the interferometer methods provide the averaging over a large sample area that is desired. As frequencies above 25 gc are required, cavities and waveguides become small, and progressively more difficult to handle. At the same time, free-space techniques become more attractive because the required sample is reasonably small and sample tolerances are less critical. Above 50 gc, interferometer techniques are probably the most de-

sirable, since the horn, waveguide, and other hardware become sufficiently small to make platinum alloys economically practical for use inside a moderate size furnace.

The high-temperature Michelson interferometer designed by the English Electric Company (Reference 35) used a focused horn system to reduce the size of the sample illuminated. A simplified diagram of its operation is shown in Fig. 5-35. The sample, slightly more than 10 cm in diameter, is placed in the AC leg of the interferometer in the dash line position and heated in a furnace whose door consists of two thin mica sheets spaced  $\lambda/4$  apart. The beam splitter, comparable to a partial mirror in optics, is a grid of equally spaced copper wires, rotated to allow just 50% transmission. The difference between the null position of B, with and without a sample, is determined, and the width of the null is measured at the 3-db point. Calculations of  $k'$  for the interferometer are simply

$$\frac{\tan(2\pi/\lambda_0)(X_0 + d)}{2\pi nd/\lambda_0} + \frac{\tan(2\pi nd/\lambda_0)}{2\pi nd/\lambda_0} \quad (5-31)$$

where  $X_0$  = shift in reflector position to null with a sample

$d$  = thickness of sample

$n$  = index of refraction =  $\sqrt{k'}$

$\lambda_0$  = wavelength in air

With the Michelson interferometer arrangement, loss measurement is also practical and this is calculated by:

$$\tan \delta = \frac{\Delta X}{\lambda_0} \frac{4\pi \csc 4\pi (X_0 + d)/X_0}{4\pi \csc \frac{4\pi nd}{\lambda_0} - 1} \quad (5-32)$$

where  $\Delta X$  = node width at the 3-db point

Some errors exist in the focusing interferometer because of the difference between the wavelength of the focused beam and the actual free-space wavelength. This error must be calculated and measured where accuracy greater than  $\pm 1\%$  is required in  $k'$ .

Adequate measurements of dielectric constant have been made by conventional two-horn interferometers (Reference 36) and calculation of  $k'$  is relatively simple from the formula:

$$k' = 1 + 2(\Delta/d) \cos \theta + (\Delta/d)^2 \quad (5-33)$$

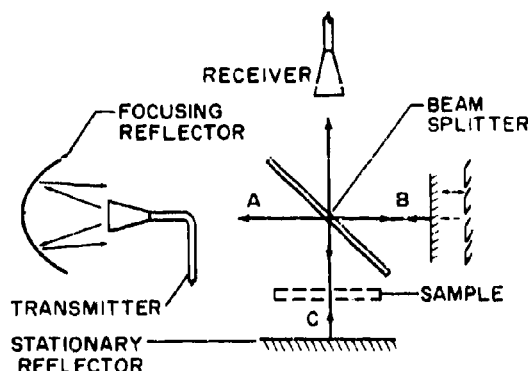


Figure 5-35. Schematic Diagram of 10 gc Analogue of Michelson Interferometer

where  $d$  = sample thickness

$\Delta$  = distance the interferometer horn is moved from minima without a sample to minima with a sample

$\theta$  = angle of incidence

Instead of a change in the horn separation, the measurement of the phase shift and attenuation required to rebalance the interferometer also provides the information required for measurement of  $k'$ . The following expression can therefore also be used:

$$k' = [1 + \cos \theta (\psi \lambda_0 / 360d)]^2 \quad (5-34)$$

where  $d$  = physical thickness of sample, cm

$k'$  = relative dielectric constant

$\lambda_0$  = free-space wavelength, cm

$\theta$  = angle of incidence with the normal, degrees

$\psi$  = phase shift, degrees

Although this technique is not readily used at high temperatures, it has the advantage of simplicity.

Measurements above 50 gc at high temperatures have not been reported; however, several approaches are available for extending presently used techniques to higher frequencies. Operation of a shorted waveguide or cavity in a higher mode would allow the use of larger, more convenient samples. Interferometric measurements using microwave analogues of the Michelson or Fabry-Perot type interferometers (Reference 37) offer the greatest promise for this frequency range and should be applicable



Quantity To Be Determined	Code Number	Coded Derivation (operation)	VALUE	Quantity To Be Determined	Code Number	Coded Derivation (operation)	VALUE	Quantity To Be Determined	Code Number	Coded Derivation (operation)	VALUE
$T^{\circ}C$	(0)	Input		$1 - p$	(21)	1-(20)		$1$	(42)	$\gamma \kappa'$	(41)(39)
$B_w$	(1)	Input		$\sqrt{1-p}$	(22)	(21)½		$1 \leq \kappa_1 \leq 2.6$	(43)	$\kappa_1$	(39)÷(42)
$B_g$	(2)	Input		$\lambda_g = \lambda/\sqrt{1-p}$	(23)	(18)÷(22)		$\xi$	(44)	$\xi$	4.16 (28)
$B^*_{\theta}$	(3)	Input		$d^*_{\theta}/\lambda_g$	(24)	(16)÷(23)		$2.6 \leq \kappa_2 \leq 5.2$	(45)	$\kappa_2$	(39)÷(44)
$f$	(4)	Input		$2 \pi d^*_{\theta}/\lambda_g$	(25)	2 π(24)		$III \mid \kappa_3 \geq 5.2$	(46)	$\kappa_3$	(39)÷(41)
$a_w$	(5)	Input		$\lambda_g/2 \pi d^*_{\theta}$	(26)	(25) <sup>-1</sup>		$\Delta X = \Delta X_2 - \Delta X_1 > 0$	(47)		(12)-(11)
$b_w$	(6)	Input		$b^*/\lambda^*_w$	(27)	(15)÷(14)		$\Delta X/d^*_{\theta}$	(48)		(47)÷(16)
$b_g$	(7)	Input		$1 - b^*/\lambda^*_w$	(28)	1-(27)		$P/\kappa_1 = 1, 2, 3$	(49)		(20)÷ (48) (48)
$d_g$	(8)	Input		$X_2 - X_1 \geq 0$	(29)	(10)-(9)		$1 - P/\kappa_1$	(50)		1-(49)
$X_1$	(9)	Input		$X_2 - X_1/\lambda_g$	(30)	(29)÷(23)		$\tan^2 2 \pi X_g/\lambda_g$	(51)		(33) <sup>2</sup>
$X_2$	(10)	Input		$0 < X_g/\lambda_g \leq \frac{1}{2}$	(31)	N/2(24)-(30)		$X \tan^2 2 \pi X_g/\lambda_g$	(52)		(35)(51)
$\Delta X_1$	(11)	Input		$2 \pi X_g/\lambda_g$	(32)	2 π(31)		$X + 2 \pi X_g/\lambda_g$	(53)		(35) + (52)
$\Delta X_2$	(12)	Input		$\tan (2 \pi X_g/\lambda_g)$	(33)	tangent look up		$\tan X$	(54)		-(54)(35)
$a^*_{\theta w}$	(13)	Formula: $e^* = \pi c/(1 + B T)$		$\tan X/X$	(34)	-(33)(26)		$\tan^2 X$	(55)		(54) <sup>2</sup>
$b^*_{\theta w}$	(14)			$X$	(35)	table look up		$X \tan^2 X$	(56)		(35)(55)
$b^*_{\theta g}$	(15)			$q$	(36)	(26)(35)		$X + X \tan^2 X$	(57)		(35) + (56)
$d^*_{\theta g}$	(16)			$q^2$	(37)	(36) <sup>2</sup>		$X + X \tan^2 X - \tan X$	(58)		(57)-(54)
$\lambda_c = 2a^*_{\theta w}$	(17)	2(13)		$q^2 - 1$	(38)	(37)-1		$F q$	(59)		(53)÷(58)
$\lambda$	(18)	$\frac{2.998 \times 10^{10}}{f}$		$\kappa'$	(39)	(21)(38) + 1		$(1 - P/\kappa_1) F q$	(60)		(50)(59)
$\lambda/\lambda_c$	(19)	(18)÷(17)		$\kappa' - 1$	(40)	(39)-1		$\text{loss } \tan \delta$	(61)		(48)/(60)
$P = (\lambda/\lambda_c)^2$	(20)	(19) <sup>2</sup>		$Y$	(41)	(28)(40)					

Figure 5-36. Computation Sheet for Shorted Waveguide Technique

to frequencies greater than 200 gc. Stable signal sources with adequate power and detector technology for the frequency range above 50 gc offer some limitations at present, but measurements to 120 gc and at temperatures up to 2910°F or 3270°F are currently feasible.

## 5-8 DIELECTRIC DATA PROCESSING

For accurate dielectric measurements at high temperatures, careful calculation of all thermal expansion contributions to critical dimensions is required. While the solution of the complex transcendental function present in most cavity or waveguide type equations is time consuming, systematic calculation sheets for these equations have been published. Graphical solution to the equations has also been used. When the added complication of making thermal expansion corrections to the complex equations is necessary, automated computing becomes a natural choice. The computational methods often used are briefly discussed in the following paragraphs.

### 5-8.1 MANUAL METHODS

The system presented in Reference 19 using Bowie's equations for the waveguide technique is shown in Fig. 5-36. In this calculation sheet, the values marked with an asterisk (\*) are temperature-corrected dimensions. To perform the entire calculation requires a table of trigonometric functions and a table of  $\tan X/X$  functions. The latter is not common, but an abbreviated table has been published by von Hippel. A more extensive table prepared by Dakin is available. An experienced operator with a desk calculator can perform the entire calculation of the dielectric constant and loss tangent in about 30 minutes using this technique.

The graphical calculation technique used by Bowie is simple, but does not provide adequate readability for the most accurate work. The required graphs are shown in Figs. 5-37 through 5-39. These graphs essentially reduce the calculations to a minimum and eliminate the need for  $\tan X/X$  tables.

Use is made of the existing relationship between  $X_0$ , the calculated distance from the sample face to the first minimum, and the uncor-

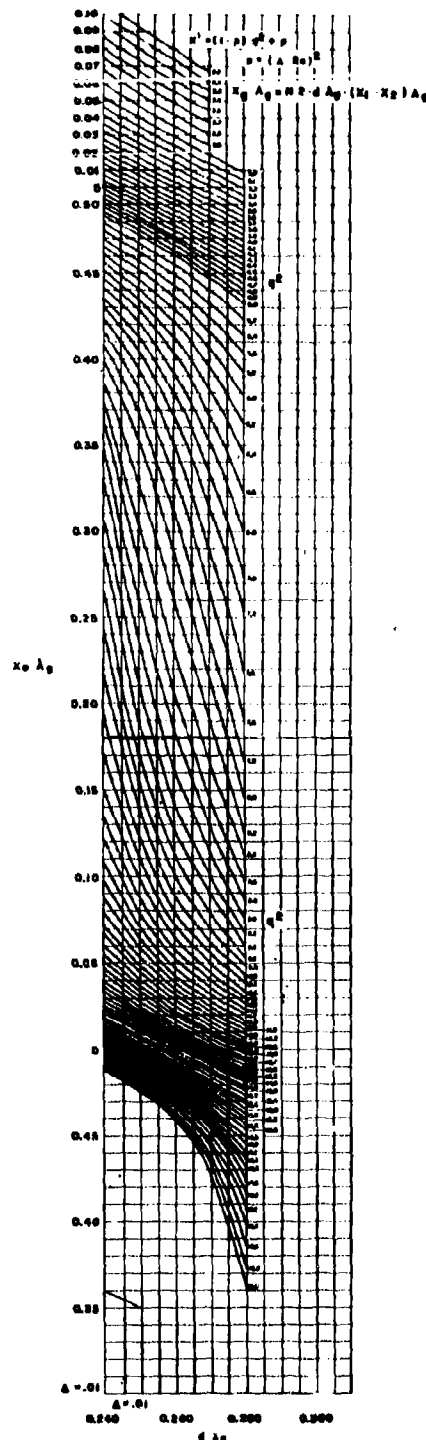


Figure 5-37. Graphical Solution of Waveguide Equation for Calculating Dielectric Constant

rected dielectric constant, expressed parametrically by the equation:

$$k = (1 - p) q^2 + p$$

where  $p = (\lambda_0/\lambda_c)^2$

The parameter  $q$  represents the ratio of the guide wavelength in air to that in the sample. Evaluation of  $q$  is accomplished graphically by plotting lines of a constant  $q^2$  value on a grid of  $X_0/\lambda_g$  vs.  $d/\lambda_g$ . See Fig. 5-37.

Similarly, a simplified expression for the dielectric loss tangent is obtained by the equation:

$$\tan \delta = \frac{\Delta X}{d} (Fp) (Fq) \quad (5-35)$$

where  $Fp = 1 - p/K$

$Fq =$  See Fig. 5-38

$\Delta X =$  shift in node width at double power or 3 db points

The correction for sample fit is also accom-

plished using Fig. 5-39, where the ratio of  $b'/b$  is the sample height, waveguide inside dimension (narrow).

Von Hippel's calculation technique using the exact solution of the equations and hyperbolic function is seldom required except for materials with high losses, which would be unsuitable for radomes. The simplified equations presented for low-loss materials are usually employed, or in an equivalent but slightly modified form.

## 5-8.2 AUTOMATED COMPUTATIONS

Initial investigation of the necessary calculations indicates that automated computation is an excellent prospect. However, many investigators had difficulty in achieving high accuracy and reliability in a computer program, and found that rather sophisticated techniques were necessary to solve the  $\tan X/X$  function and other logic steps in the program. These difficulties are presented in Reference 38 with an

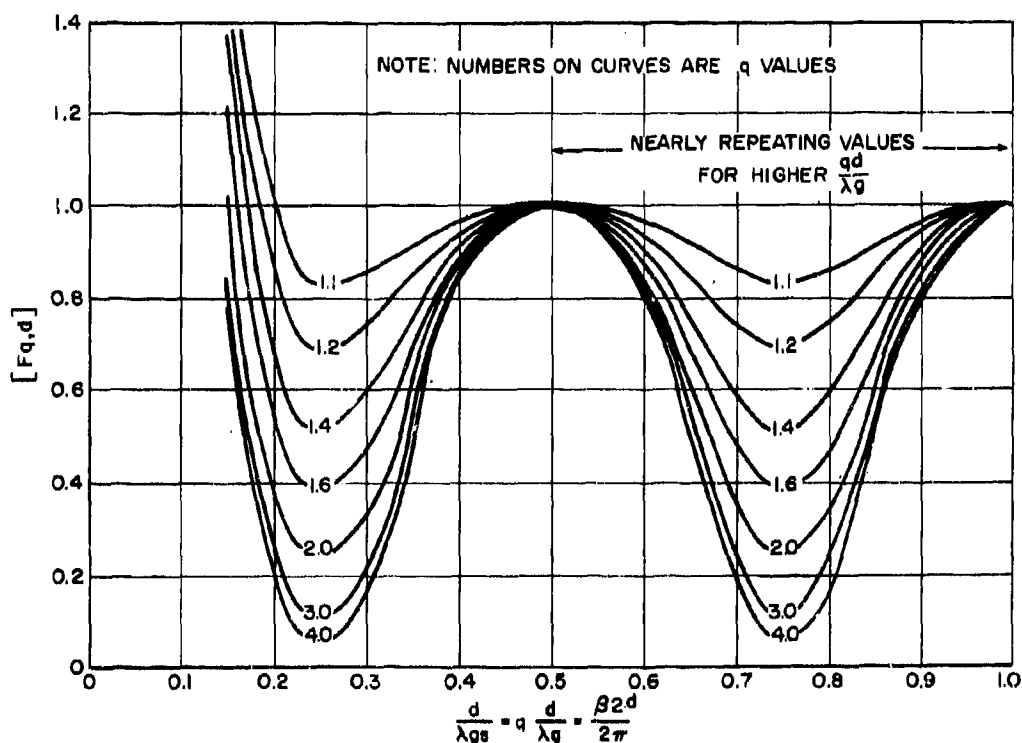


Figure 5-38. Graphical Solution of  $F_q$  for Use in Calculating Loss Tangent

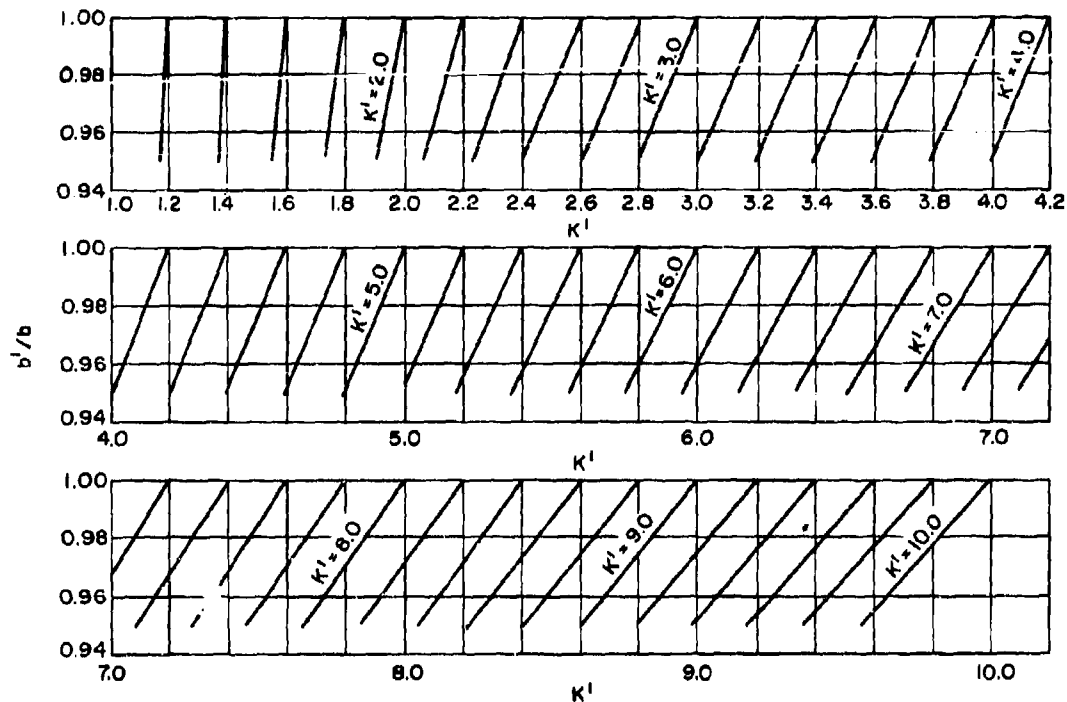


Figure 5-39. Graphical Correction for Sample Fit

elegant solution to the computer programming of this problem that has made it a routine computation. With this technique, typical computation times with an IBM 7090 or CDC 1604 computer are less than 2 seconds for each dielectric constant and loss value.

The same type of programming is required for both cavity and shorted waveguide type techniques. However, the loss calculation in the former is somewhat more lengthy. Where any significant number of data points are to be reduced, the use of automated computing rapidly becomes the most economical method. One additional advantage of automated reduction of raw data is that more individual points can be reduced rapidly and cheaply. This encourages more comprehensive raw data to be taken and the shape of the temperature-dielectric property curves to be defined more carefully. The use of a greater number of data points and the reduction of human error in computation also improve the reliability of the final property data.

## 5-9 THERMAL MEASUREMENTS

For dielectric materials used above 2000°F, the thermal properties become important for two reasons: (1) the heat transfer into the structure and the temperature reached during aerodynamic heating depend on thermal properties, and (2) the mechanical performance of dielectric materials is highly dependent upon the magnitude of the thermal stresses developed during transient heating. Calculation of these mechanical stresses requires precise knowledge of thermal properties.

Thermal conductivity, thermal diffusivity, specific heat, and radiation properties are briefly discussed in the following paragraphs. Thermal expansion measurements are discussed in Paragraph 5-10.5.

The relationship between thermal conductivity, thermal diffusivity, and specific heat is shown by:

$$K = \alpha \rho C_p \quad (5-36)$$

where  $C_p$  = specific heat  
 $K$  = thermal conductivity  
 $\alpha$  = thermal diffusivity  
 $\rho$  = density

Generally, thermal conductivity measurements are made from steady-state heat transfer in a well defined geometry. Thermal diffusivity measurements are usually performed during transient or cyclic heating or cooling with well defined boundary conditions. Specific heat values are usually derived from measured enthalpy values. Since the latter can be derived with reasonable ease and accuracy, compared to other thermal property measurements, little difficulty is experienced in converting from thermal conductivity to diffusivity, or vice versa. Since the useful radome materials are dielectrics and hence electrical insulators, low thermal conductivity values might be expected. However, the range of values normally encountered may be from very low (such as silica) to values comparable to those for highly conductive materials (such as beryllia). The use of a single technique or a single sample configuration over such a range of conductivity values is not generally possible or, if possible, is rarely optimum for either extreme. The techniques selected for discussion are representative of current experimental procedures in the temperature range above 2000°F and are applicable to a wide range of materials.

#### 5-9.1 THERMAL CONDUCTIVITY MEASUREMENTS

Measuring techniques may be divided into two general classifications: (1) envelope techniques and (2) longitudinal heat-flow or comparative techniques. Many investigators prefer the envelope techniques at high temperatures because of the difficulty in establishing true longitudinal heat flow with planar isotherms at high temperatures. (See References 39 through 43.)

The basic requirements for a radial heat-flow thermal-conductivity measurements are shown in Fig. 5-40. The measurement of thermal conductivity using this technique can be calculated by:

$$K = \frac{(V \times I) \ln r_2/r_1}{2\pi l(T_1 - T_2)} \quad (5-37)$$

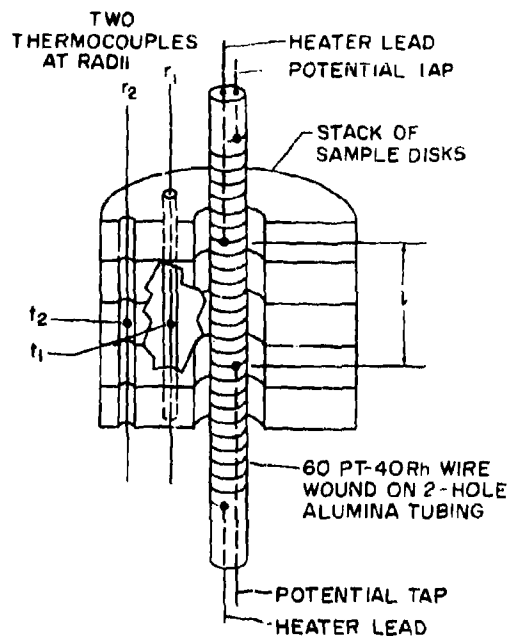


Figure 5-40. Details of a Typical Radial Heat-Flow Thermal Conductivity Technique

where  $K$  = thermal conductivity, watts-cm<sup>-1</sup> °C<sup>-1</sup>  
 $T_1$  = inner temperature, °C  
 $T_2$  = outer temperature, °C  
 $V$  = voltage across the potential taps, volts  
 $I$  = current through heater, amperes  
 $V \times I = q$  = heat input, watts  
 $r_2$  = outer radius, cm  
 $r_1$  = inner radius, cm  
 $l$  = distance between the potential taps, cm

From Eq. 5-37, it can be seen that it is necessary to record two temperatures and three length dimensions ( $r_1$ ,  $r_2$ ,  $l$ ) accurately in addition to the heat input,  $q$ , which is  $V \times I$ . Generally, the greatest errors in this technique arise from the uncertainty in the length measurements. With care, the uncertainty in thermocouple position can be reduced to  $\pm 2\%$  or less. This requires the use of fine thermocouple wire and small holes in the sample if

the diameter of the holes is not to be an appreciable fraction of the distance between the holes. The accuracy in locating the spacing of the potential taps requires the same consideration. The errors in measuring temperature and heat input can generally be reduced below the level of those errors in dimension measurements. However, large thermocouple holes also introduce errors in temperature measurements, since each side of the hole is a different temperature and the thermocouple seldom reads the average temperature, but reads the approximate wall temperature of the hole at a point of contact.

In spite of the above difficulties, using holes as large as 0.040 in., reproducibility of typical conductivity measurements may be better than 5% if reasonable care is exercised. The use of sample disks, rather than a solid monolithic block for the specimens, introduces little error, since the individual disks can be ground flat to stack with negligible gap and any film coefficients at this interface actually discourage the undesirable longitudinal heat flow.

Longitudinal heat-flow techniques have been used at temperatures up to 2800°F to obtain accurate data (Reference 44). However, the data obtained by many previous investigators using these techniques have been questioned where inadequate "guarding" techniques were

used. A careful guard-heater technique, establishing a gradient along the guard tube similar to the gradient along the sample standard rod, and the use of insulating powder filler between the sample and guard are generally necessary to achieve accurate results (Reference 45). For absolute, rather than comparative, measurements, some calorimetric method must also be included. In general practice, this is seldom done and the thermal conductivity of the sample is compared to that of a known material, such as Armco Iron (References 39, 41, 46, and 47). A range of samples of known thermal conductivity is required, however, if high accuracies are to be achieved, since the conductivity of the standard should approximate that of the sample (Reference 44). The essential features of a longitudinal heat-flow method are shown in Fig. 5-41.

A planar heat-flow technique or "guarded hot-plate" technique that has been used at high temperatures is shown in Fig. 5-42. Accurate measurements are possible if care is given to (1) the fabrication of an accurate, symmetrical flat-plate heater with guard winding, (2) the use of two sample plates of similar density and the same thickness, and (3) the careful measurement of surface temperatures of the two plates, or the temperature at two points within the sample plates (Reference

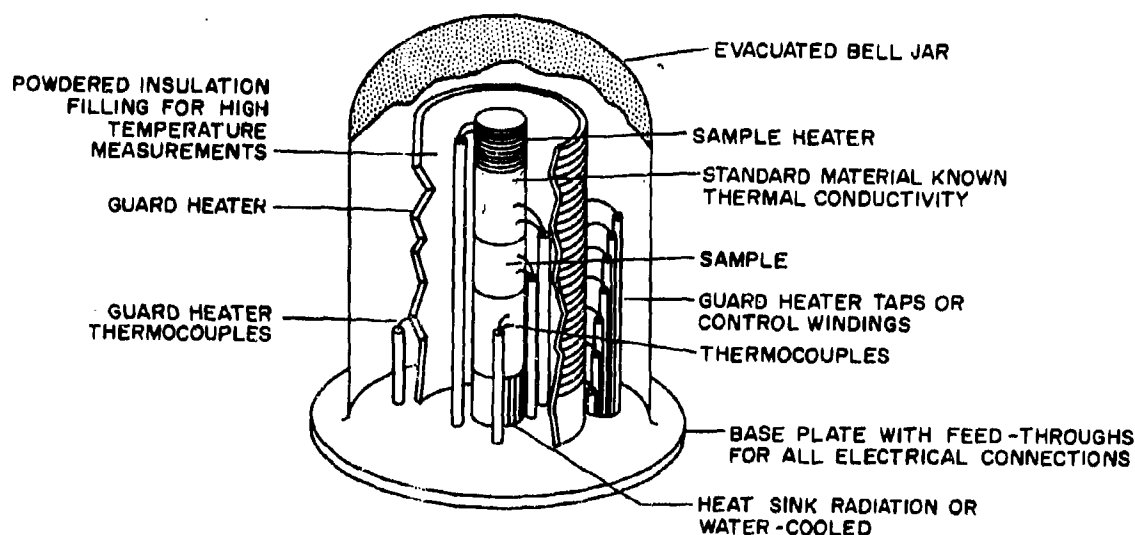


Figure 5-41. Essential Features of a Cut-Bar or Longitudinal Heat-Flow Technique for Thermal Conductivity Measurements

48). The advantage of this method is that simple plate samples can be used. Experimentally, the larger sources of error result from achieving symmetry in heat flow and from the measurement of temperatures at or near the sample-heater interface.

A calorimeter version of this device has often been used (Reference 49). The symmetrical heater-sample arrangement is replaced with a single heater, a single sample, and a flat-plate calorimeter of some type. The difficulties with such an arrangement are that the calorimeter usually operates at or near the boiling point of water and, for high-temperature measurements, the large temperature gradient and the difficulty of achieving a high *average* sample temperature make this technique less desirable.

### 5-9.2 THERMAL DIFFUSIVITY MEASUREMENTS

The advantage of thermal diffusivity measurements lies largely in their speed, compared to the time required for steady-state conductivity measurements. Often, the diffusivity data from 500°F to 2500°F or higher can be obtained in the time required for only one or two accurate thermal conductivity measurements. The time advantage also means that more data, or more closely spaced points, can be obtained at a reasonable cost. The major difficulty with diffusivity measurements is either the complex math required for calculations or the attainment of well defined boundary conditions for the transient heat flow.

A recent approach to diffusivity measurements uses an intense radiant heating pulse to

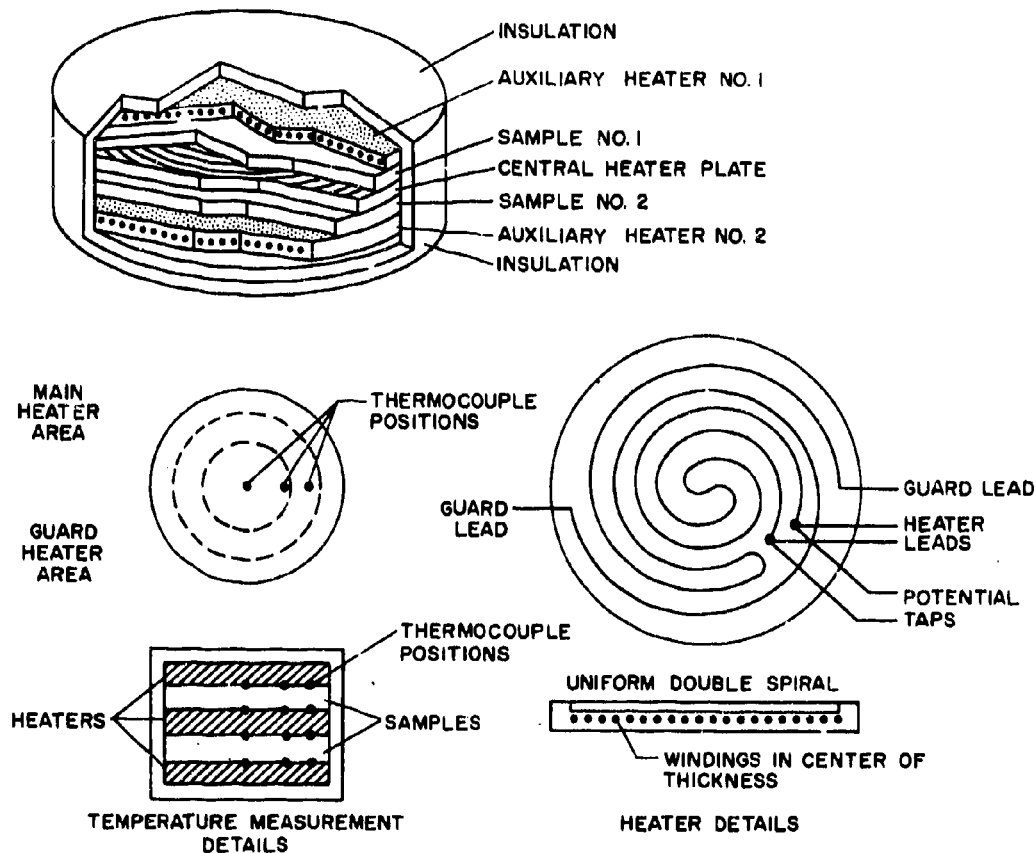


Figure 5-42. Essential Features of a Guarded-Hot-Plate Method for Measuring Thermal Conductivity

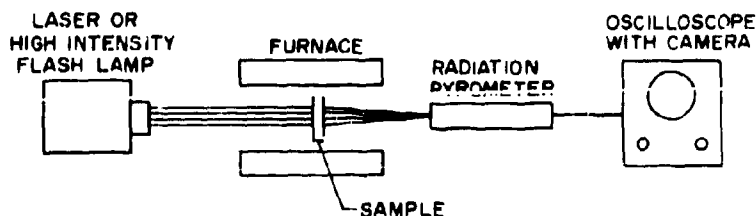


Figure 5-43. Schematic Diagram of Flash Technique for Thermal Diffusivity Measurement

heat one face of a disk and measures the temperature perturbation on the reverse side (References 50, 51, and 52). This method has developed rapidly and the data from this measurement technique have shown excellent agreement with steady-state data where comparisons are possible. The assumptions in this technique, which make it more difficult to apply to some dielectric materials, are that the sample is opaque and that the heating pulse of radiant energy is absorbed completely at the front face. For materials that are partially transparent, a thin opaque coating of evaporated metals has been used (Reference 53). For application of this technique at high temperatures, some corrections for radiation losses are also necessary (References 51 and 53). A schematic representation of the measurement technique is shown in Fig. 5-43.

The calculation procedure for this technique is described in Reference 50. For opaque samples, the thermal diffusivity,  $\alpha$ , for the sample is simply:

$$\alpha = \frac{S_{1/2} l^2}{\pi^2 t_{1/2}} \quad (5-38)$$

where  $S_{1/2} = 1.37$ , if there are no radiation losses

$t_{1/2}$  = time required for back surface to decrease from one-half maximum temperature, sec

$\alpha$  = thermal diffusivity

$l$  = sample thickness, cm

This expression is applicable for materials of high diffusivity, such as metals, up to their melting point. Radiation losses for these materials can generally be neglected. However, for dielectric materials of lower diffusivity, the value for  $S_{1/2}$  is less than 1.37 because of radia-

tion losses, and can be determined experimentally by examining the back surface temperature-time profile for longer times after the initial perturbation. References 51 and 54 describe methods for approximating the value of  $S_{1/2}$  directly and for an iterative solution for  $\alpha$  with successive approximations for the radiation loss.

The duration of the initial flash pulse has been shown in Reference 54 to be negligible for typical flash lamp or laser sources and samples of reasonable thickness. Longer duration pulses are feasible with thick samples or materials of low diffusivity.

A longitudinal diffusivity technique, using a rod and concentric cylinder joined and heated at one end, has been used at high temperatures with good results (Reference 55). The sample requirements and the instrumentation are reasonable; however, calculation of the diffusivity is usually a computerized operation. The basic sample is shown in Fig. 5-44 with a schematic of the data recording apparatus. The sample is held at a uniform ambient temperature with no input to the sample-heater. The sample-heater assembly is then heated by the internal sample-heater and the temperature change at each thermocouple position is recorded. The change in sample temperature is only a few degrees and the duration of the measurement only a few minutes. The basic technique consists of using the outer thermocouples to record a temperature-vs.-time profile at two points along the uniform rod specimen. These temperature-time functions are used to define the heat transfer conditions. The temperature-time curve at the center thermocouple (experimental) is then approximated by an iterative solution that yields the thermal diffusivity when a matching occurs. The calculation tech-



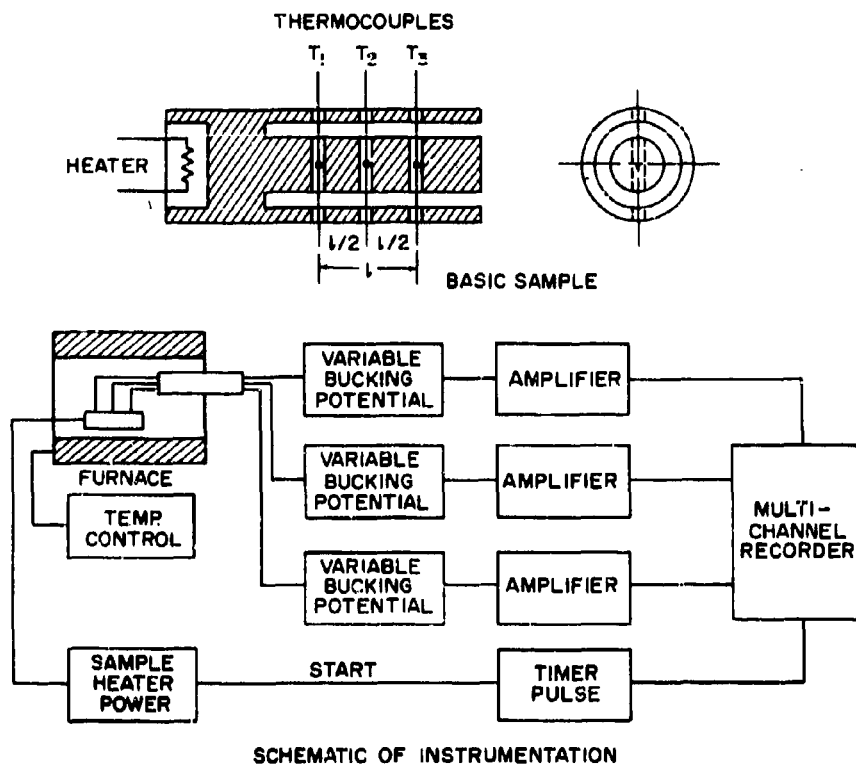


Figure 5-44. Sample and Instrumentation for Longitudinal Thermal Diffusivity Technique

nique for this measurement has been described in References 56 and 64.

The advantages of this technique are the relatively simple sample; the simplification of the heat-flow conditions by using a "guard" heater of similar material; and the relative ease of measurement, since only arbitrary temperature units are used for each thermocouple position. This means that radiation thermometry or refractory metal thermocouples can be used for temperature measurements as long as the temperature-output calibration curves of each sensor have the same slope. The ambient temperature output is normally balanced for each sensor so that only the disturbance caused by additional heating is recorded.

### 5-9.3 SPECIFIC HEAT MEASUREMENTS

The accuracy normally achieved in specific heat measurements is usually better than 1%

below 2000°F and hence most specific heat values are more reliable than the corresponding conductivity or diffusivity values. The techniques for making specific heat measurements may be divided into two classes: (1) adiabatic calorimetry, and (2) "dropping" type calorimetry. In both cases, the enthalpy of the sample material is determined accurately and the slope of the enthalpy-temperature curve is calculated to yield specific heat values. Enthalpy measurements are generally highly accurate by either method and accuracies better than  $\pm 0.2\%$  may be achieved.

#### 5-9.3.1 Adiabatic Calorimetry

In adiabatic calorimetry, a sample is carefully heated for a known temperature interval while losses to the surroundings are prevented by maintaining an adiabatic shield around the sample. (For measurements above 1470°F, the

difficulty of maintaining adiabatic conditions increases.) The heat input to the sample is then a direct measurement of the enthalpy change for the selected temperature interval. Several accurate adiabatic calorimeter designs are described in References 57 and 58; these calorimeters are most useful for materials that have abrupt discontinuities in the specific heat curves because of transitions in structure. For most dielectric materials, the full advantages of adiabatic calorimetry are seldom realized, since the specific heat curves are usually smooth functions.

#### 5-9.3.2 "Dropping" Calorimetry

For "dropping" calorimetry, the sample is heated uniformly in an accurately controlled furnace and dropped into a suitable calorimeter. While the furnace requirements are stringent, they are straightforward; therefore, attention will be given to the calorimetry only. Two types of calorimeters are in current use: (1) Bunsen ice calorimeters, and (2) copper block calorimeters. The ice calorimeter is described in References 59 and 60, and the precautions to be observed in obtaining accurate enthalpy measurements are given in Reference 61. Basically, the ice calorimeter consists of a container system in which an ice-water-mercury arrangement allows the conversion of the heat input to the calorimeter to melting (or freezing) of the ice. This change of volume is then sensed by an accurate mercury column. The calibration constant, the ratio of mercury mass to heat input, is accurately known (Reference 60). A typical design is shown in Fig. 5-45. The calorimeter assembly is submerged in an ice-water bath and provides, essentially, isothermal calorimetry at the ice point. The heat losses from the ice calorimeter can be minimized, made very reproducible, and seldom exceed 1 calorie per hour. Even this heat leak is readily measured (Reference 61).

Copper block calorimeters (References 62 and 63) are somewhat simpler than ice calorimeters; however, they require careful design to minimize heat leak. (See Fig. 5-46.) By placing the copper block in an isothermal enclosure controlled to  $\pm 0.003^\circ\text{F}$  and by using polished gold plated surfaces outside the calorimeter and inside the isothermal enclosure to reduce radiation transfer, the heat exchange

between the calorimeter block and surroundings can be reduced to about  $0.001^\circ\text{F}$  per minute per degree. Since a  $5^\circ\text{F}$  or  $10^\circ\text{F}$  change in temperature of the block occurs during enthalpy measurements and a resistance thermometer in the block can be made sensitive to  $0.00005^\circ\text{F}$ , the accuracy of the measurements can be comparable to those of an ice calorimeter. Even with all precautions, however, about 1% of the total heat may be transmitted to the surroundings during a measurement and a suitable correction is required.

For "dropping" type measurements, it is customary to place the sample in a capsule and measure the enthalpy of the capsule with and without the sample. This minimizes the error due to radiation losses during transfer from the furnace to the calorimeter (Reference 61). Reference 63 calculates the losses by either varying the mass-to-surface ratio and extrapolating to zero surface, or by varying the duration of the transfer operation and extrapolating to zero time. The capsule technique has generally been preferred where a container material that does not react with the specimen is available.

### 5-10 MECHANICAL PROPERTY MEASUREMENTS

Mechanical property measurements on brittle dielectric materials have always led to controversy in terms of proper loading rate, sample size, and sample configuration. The philosophy that has been adopted in this discussion is that of (1) obtaining useful, reliable design data, (2) using the best practical sample-loading design (no better utilization of the material should be expected in real designs), (3) assuming that the ductility is still extremely limited even about  $2000^\circ\text{F}$ , but that slight inelastic deformations could occur, and (4) assuming that creep, though possibly important in some applications, is not generally the limitation of dielectric materials.

#### 5-10.1 TENSILE STRENGTH MEASUREMENTS

For materials with as much as 2% elongation at fracture, the grip and sample design are not highly critical if adequate care is taken in alignment. For most dielectric materials, the gripping is a significant problem and must re-

ceive careful consideration. Generally, it is desirable to utilize a loading system where the top grip is allowed to pivot about an E-W axis and the bottom grip is allowed to pivot about a N-S axis, with both grips free to rotate. The sample and its grips form a single load train, which is allowed to orient itself as the actual load is applied. Figure 5-47 shows a system for both specimen and grip at temperatures to 3100°F, when only ultimate strength is desired. This system provides two degrees of free-

dom when the sample is suspended from the top pivot point. The grips are cooled and the specimen is surrounded by an oven providing the desired test temperature at the center of the gage length; a very sharp gradient exists outside of this area. The break is well defined in the gage length, which is typical of the results achieved when testing materials that decrease in strength with increasing temperature. The specimen configuration shown is adequate for *all* temperatures (for materials hav-

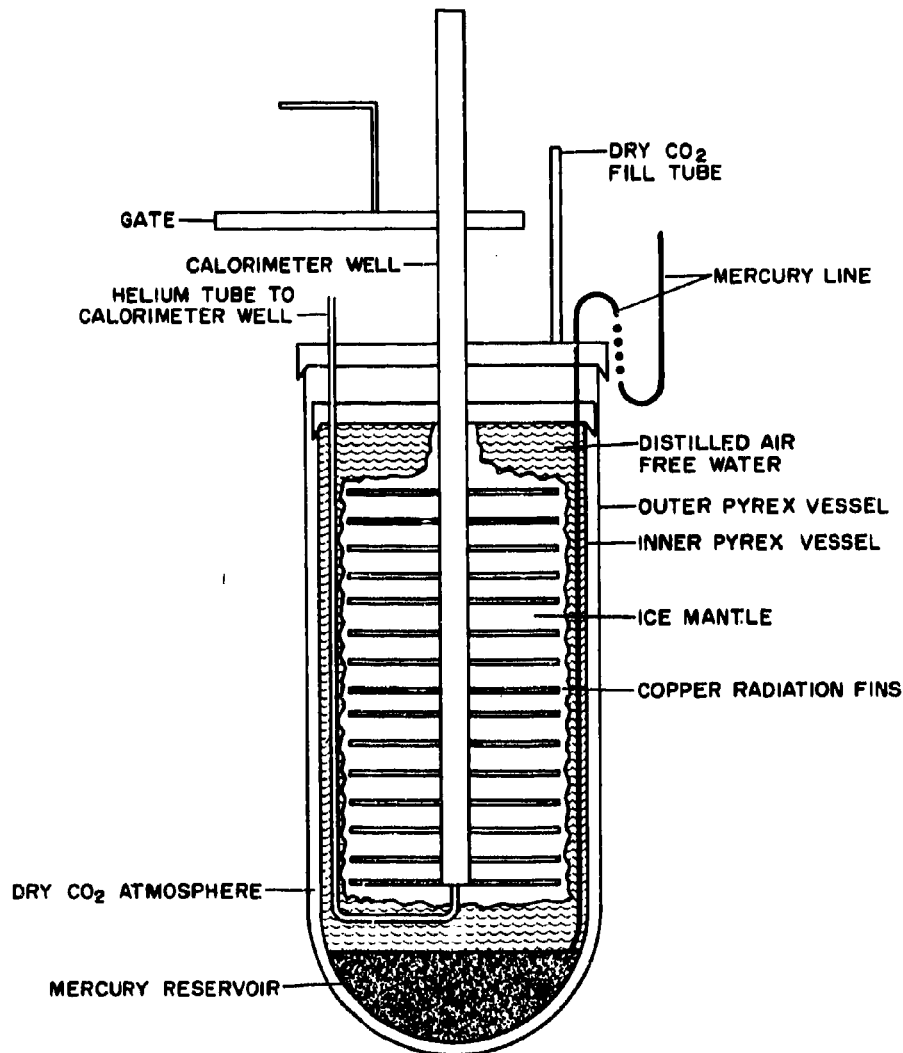


Figure 5-45. Ice Calorimeter

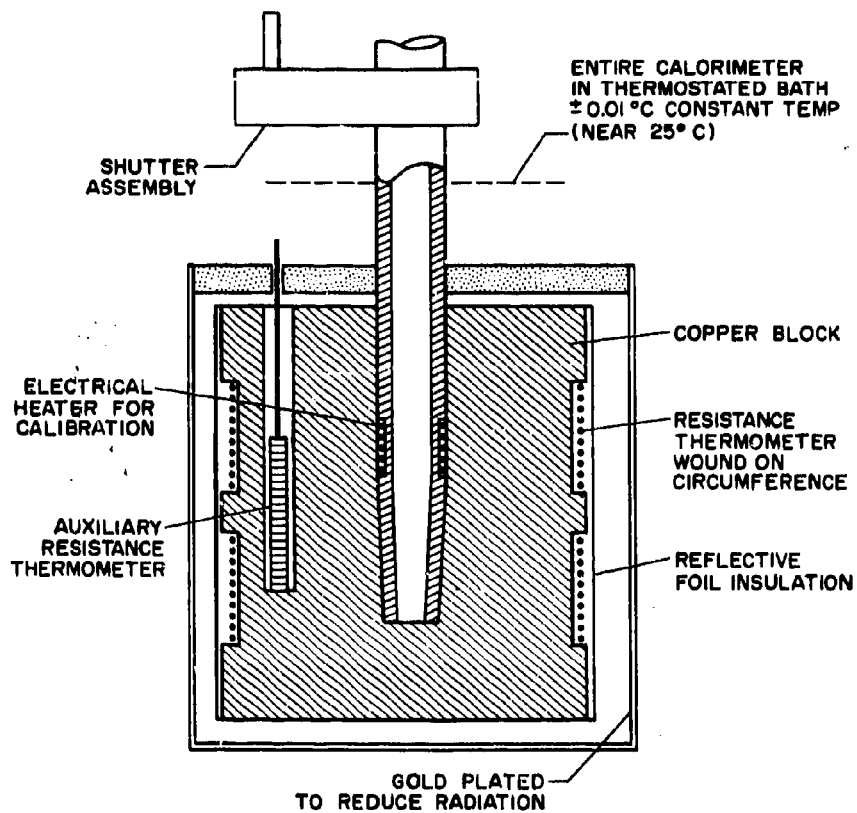


Figure 5-46. Copper Block Calorimeter Design Features

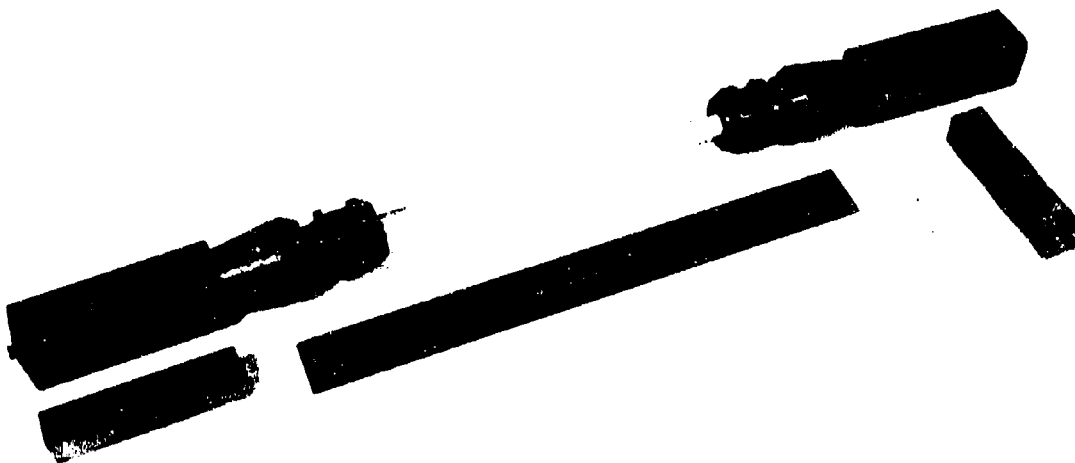


Figure 5-47. Grip and Loading System for Use to  $3000^\circ\text{F}$  with Brittle Materials

ing strength that decreases with temperature). However, at high temperatures, it may be unnecessary to use a necked specimen. A uniform, straight rod about 1/4 in. in diameter and 12 in. long, gripped in accurately machined collet-type chucks, can be loaded to about 80% of its ultimate strength before failure will occur at the grip junction. Thus, a constant cross-section specimen can be heated in the center, and will fail in the uniformly heated region if the strength at that temperature is 80%, or less, of its low-temperature value.

For the few materials having strength that increases with temperature, such as silica, a much shorter length gage having a massive end section (also maintained near the test temperature) may be required to define the break in the gage section. Flexural strength measurements are generally more reliable for these materials.

Various investigators have used many techniques to ensure accurate axial loading of the tensile specimen during test. One of the more elaborate pieces of equipment is shown in Fig. 5-48. This system, developed by Southern Research Institute (Reference 65) uses a self-aligning hemispherical air bearing to apply the load axially.

The problems associated with the measurement of sample elongation at temperatures above 1800°F warrant discussion. Normal strain gage instrumentation can be used at temperatures to 1000°F with little difficulty and has recently been extended to 1800°F with reasonable reliability. Above 1800°F, many attempts have been made to monitor the sample elongation by placing small clamps on either end of the gage length and running extension rods from these points to the outside of the hot zone, where either variable differential transformers or dial indicators are used to indicate the motion of these points. This method has many inherent problems: if the clamps are placed on the actual gage section of the specimen, they often contribute to the specimen failure as a consequence of notch sensitivity or chemical reaction with the specimen. Further errors are introduced because, during loading, the cross-section is reduced and the clamps tend to loosen and slip, so that the original gage length is not preserved. In several studies this effect has been overcome by marking the gage length and following its movement with a

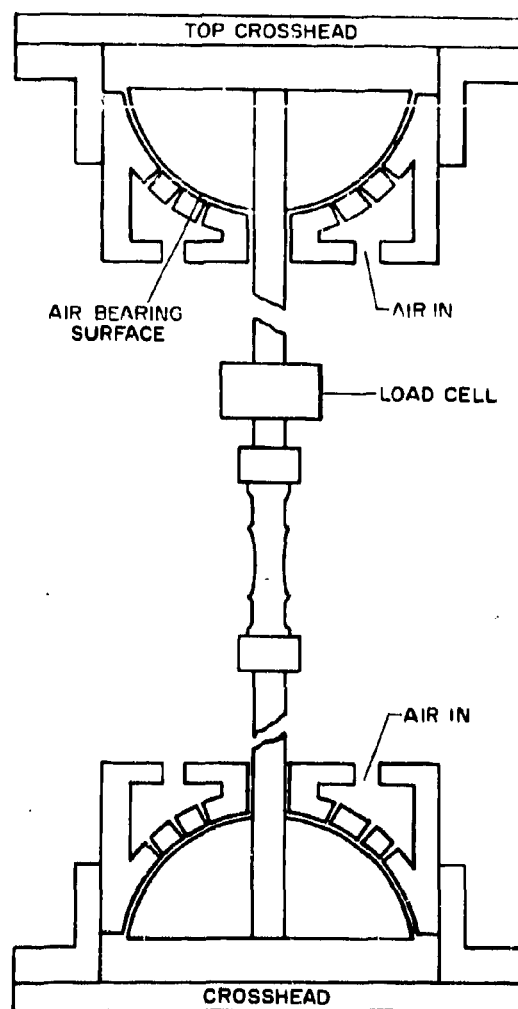


Figure 5-48. Schematic Diagram of Self-Aligning Air Bearing for Axial Loading of Tensile Specimen

cathatometer. While this is suitable for studies of long-term extension, such as creep, the rapid extension rate realized in short-term tensile determinations does not lend itself to manual measurement.

Several test facilities have added the capability of measuring sample elongation at temperatures as high as 5000°F (Reference 66). In all cases, the sample deformation is monitored automatically by an optical tracking system. The specimen must be prepared so that a distinct reference area protrudes from it. One

technique uses a sample with a sharp shoulder protruding at that point where the radius of the gage length begins. In all cases, the furnace is provided with sight tubes so that the material marking the gage length is easily visible. These reference points are back-lighted and the optical system monitors their movement as the specimen is loaded. The motion is converted to an electrical signal and is plotted directly on a recorder. The optical tracking may be provided by a servo system that balances the output of a photocell, moving it so that it always sees the same edge of the reference point; or this result may be accomplished by a more complicated system using an image tube in conjunction with an aperture and a sensitive photocathode providing a usable signal that may be recorded directly (Reference 67). This latter system has extremely rapid response characteristics.

#### 5-10.2 COMPRESSIVE STRENGTH MEASUREMENTS

Compressive strength measurements present many of the same problems when measuring deformation as occur in the elongation measurements discussed previously. The problem is even more acute in that the sample length is usually smaller for compressive testing. The most satisfactory compressive strength sample configuration (Reference 68) has been a right circular cylinder with a height-to-diameter ratio of about two, and a diameter of from 1/4 to 1/2 in. The specimen ends should be ground flat and parallel to within 0.001 in. or better. Bearing "blocks" of the same material should be larger cylinders (or truncated cones) about two or three times the diameter of the specimen and of equal height. Equal care should be given to grinding the faces of the bearing blocks so that they are flat and parallel. A short cylindrical-necked specimen, similar to a tensile specimen but with a gage section only about two diameters long, combining both specimen and bearing "blocks," may also be used effectively. These configurations have been found to be satisfactory for specimens of extremely high compressive strength at low temperatures and are equally useful at high temperatures.

Uniform heating and axial loading are constant problems, but the same considerations hold as for tensile measurements. One consid-

eration in compressive measurements is the mass of the loading rams and the resulting heat leak, causing gradients in the sample. Use of ceramic oxide rods (such as alumina) for this purpose provides both mechanical and thermal advantages.

#### 5-10.3 FLEXURAL STRENGTH MEASUREMENTS

For brittle materials (or those with very limited deformation before fracture), flexural strength measurements are common. The general preference for flexural strength measurements is a 4-point loading using rectangular bars. This arrangement generally reduces the scatter of individual specimens, but yields slightly lower average strength values than round bars or bars having a 3-point loading. The averaging effects of this loading arrangement are caused by the entire bottom area of the specimen being under maximum tension between the center loading points. Serious errors can develop in this loading arrangement if each load point is not parallel and the loading causes torsion in addition to bending. The linkage that divides the load for the two equal center loading points must also be reliable, since it is usually subjected to the temperatures of measurement.

A loading rate of 500 psi per minute on a 1/2 in. or 1/4 in.  $\times$  8 in. bar supported 6 in. apart and loaded symmetrically at two points 2 in. apart is a reasonable experimental condition. Three-point loading, small samples, round bar specimens, and higher loading rates can also be used, but the data for any set of conditions can be compared to those taken under different conditions only with some reservations. Often the change in loading conditions results in only simple, or approximately linear differences, if only average strength values are of interest.

#### 5-10.4 ELASTIC MODULI

Elastic moduli may be determined by either static or dynamic techniques. Where elongation is measured in mechanical testing, static modulus values are readily calculated and are usually slightly lower than the dynamic values. Dynamic techniques described in Reference 69 are useful above 2000°F and require relatively

simple instrumentation. A method of supporting the sample must be provided so as not to dampen the vibrations at resonance. Excitation is normally achieved by suspension techniques, by an air column, or by mechanical coupling. (See Fig. 5-49.) A preferred suspension technique has a rectangular bar ( $0.2 \text{ cm} \times 2 \text{ cm} \times 15 \text{ cm}$ ) suspended near each end ( $0.24 \times \text{total sample length}$ ) by two quartz fiber threads or platinum wires. By allowing the suspension threads (or wires) to be wound in opposite directions around the sample, terminating vertically from opposite sides of the sample, torsional modes as well as flexural modes can be excited. This allows calculation of Poisson's ratio from the shear and flexural moduli values. For temperatures or specimens where the suspension technique is inadequate, several other methods are useful for exciting the specimen from outside the furnace: (1) by acoustic energy directed on the specimen through an air or gas column, or (2) by direct mechanical coupling to the specimen with a lightweight rod (Reference 70). The pickup is usually directly coupled to the specimen

through a lightweight rod. For excitation, magnetic cutting heads are frequently used; however, several reliable vibration transducers are available that can be driven with up to 10 watts of power. At temperatures above  $2500^\circ\text{F}$ , major emphasis is normally placed upon the modulus of elasticity measurements with little attention given to the modulus of rigidity. This is a consequence of the increased difficulty in exciting torsional modes at the higher temperatures.

#### 5-10.5 THERMAL EXPANSION MEASUREMENTS

Thermal expansion measurements may be made at very high temperatures by direct measurement or by comparison with a known standard. Most investigators have used the direct measurement technique above  $2300^\circ\text{F}$ . One investigator (Reference 71) has used a 5-mc induction-heated furnace, oxide susceptor rings, and air atmosphere for measurements up to  $4000^\circ\text{F}$ . Direct optical measurements of extension were made. Accurate comparative values are possible to  $3100^\circ\text{F}$ , using oriented sapphire as a standard. A sapphire rod dilatometer, using

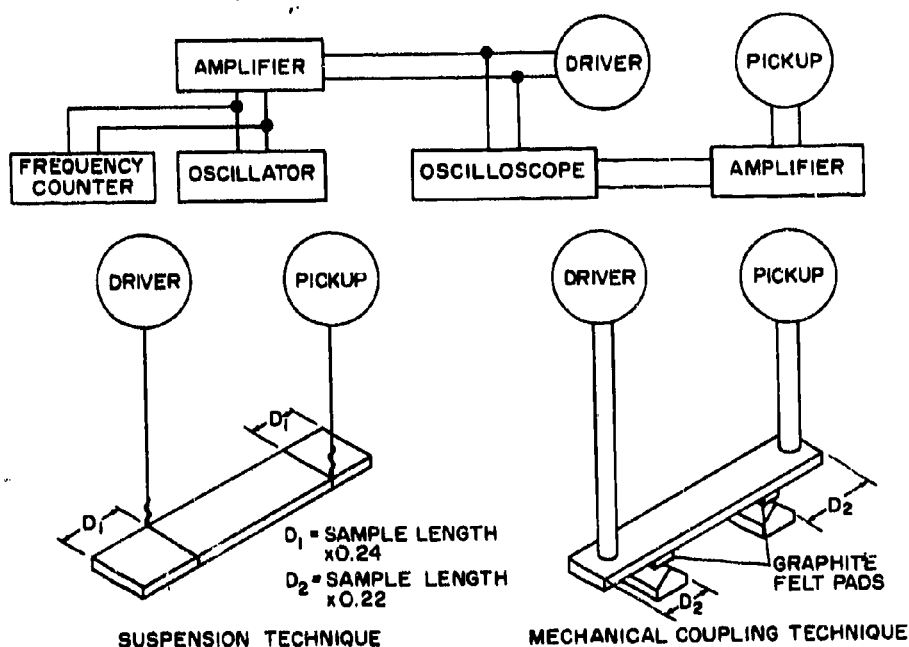


Figure 5-49. Schematic Diagram of Dynamic Modulus Measurement Showing Excitation Techniques

three long sapphire rods joined at the ends for the cage and a center "push-rod" that actuates the measuring transducers is shown in Fig. 5-50. It is similar to the standard fused silica model, except that the push-rod is in two equal lengths, with the sample at the center of the dilatometer. The sample is heated uniformly in

a short-tube furnace that allows the dilatometer ends to remain cool. Such an arrangement is readily constructed and is reliable. X-ray techniques that have been used (References 72 and 73) on powder or polycrystalline plates in the region above 2800°F, agree closely with data obtained from other measurement techniques.

## **PART III—DESIGN, EVALUATION AND PERFORMANCE OF MODERN MICROWAVE ANECHOIC CHAMBERS**

### **5-11 INTRODUCTION**

As pointed out in Chapter 1, the radome must not only protect the system, but it must also have a minimum effect on antenna characteristics. In particular, its effect on the boresight error angle and the rate of change of this angle with antenna beam position must be kept to a minimum. To determine the performance of a radome, it is important that precise boresight measurements be made. To assure that such measurements are valid, unwanted reflections must be eliminated. Boresight measurements on small radomes are best carried out in a microwave absorbing room known as an anechoic chamber. Microwave anechoic chambers are currently in use for a great variety of indoor measurements on antennas, antenna systems, associated radomes, and other components. There are three types of measurements performed routinely. As discussed in some detail in Reference 74, they are

1. Antenna pattern measurements.
2. Radar cross-section measurements of passive or active targets.
3. Antenna impedance, antenna coupling, or antenna-RFI-compatibility measurements.

Antenna pattern, boresight, and radome work in the operation of the chamber with one-way energy propagation only. The prime requirement is that an appropriate transmitting antenna at one location within the chamber set up an essentially plane-wave field in dimensions sufficient to encompass the antenna or array whose characteristics are to be measured. The volume of this field is frequently referred to as the quiet zone and its "quietness" or reflectivity level is evaluated by one of several

methods discussed in the following paragraphs. All of these methods involve determination of the ratio of the reflected field intensity to the direct transmitted field intensity at points of interest with the specific antennas and antenna orientations.

Major emphasis in this part is placed upon the functioning of anechoic chambers having one-way energy propagation as is appropriate to most radome boresight testing. Radar cross-section and antenna impedance measurements require energy propagation both from and to the vicinity of the transmitting antenna. Some differences in chamber design may be involved and evaluation procedures are quite different for two-way energy propagation. No discussion of these procedures is included here but the reader is referred to References 75 and 76 for information on radar cross-section performance and evaluation of anechoic chambers.

### **5-12 DESIGN OF MICROWAVE ANECHOIC CHAMBERS**

The achievement of the lowest possible level of reflected energy in an anechoic chamber depends upon the proper manipulation of two variables:

1. The characteristics of the absorbing materials used to cover the internal chamber surfaces.
2. The shaping of the chamber to direct residual reflected energy away from the quiet zone or working volume.

Reference 77 presents many of the important aspects of chamber design and of absorber and chamber evaluation. The reference should be used as a general reference and bibliography to supplement the information given here.



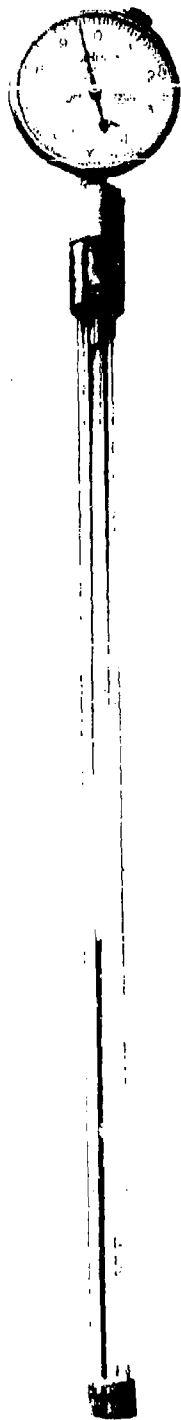


Figure 5-50. Saphire Rod Dilatometer

Since experimentation with a large anechoic chamber is prohibitively expensive and since several proven chamber configurations and absorber arrangements are available, the design of anechoic chambers is usually best left to experienced designers. The following paragraphs summarize various factors that should be considered in any design effort.

#### 5-12.1 CHARACTERISTICS OF ABSORBING MATERIALS

Currently available premium quality absorbing materials exhibit reflectivities of  $-40$  to  $-50$  db at normal incidence and under conditions of specular reflection at equal incidence and reflection angles up to as much as  $60^\circ$ . This means that the energy reflected in the direction of the receiving test antenna is 40 to 50 db below that reflected in the same direction by a highly conducting flat plate, but does not mean that the remaining major portion of the incident energy is *totally absorbed* by the material. Particularly when absorbing materials are shaped in the form of pyramids, or cones, that are relatively large with respect to incident wavelength, there is a somewhat diffuse scattering of unabsorbed incident energy in essentially all directions.

For argument's sake, we might assume that true absorption occurs for 99% of incident energy and that zero through-transmission results because of a metallic mounting surface. Therefore, the remaining 1% of the energy is reflected, corresponding to a "total" power reflection coefficient of  $-20$  db. Conceivably, scattering may be such that, in any small solid angular increment subtended by a distant test antenna (including that increment in the specular direction), the energy reflected is 50 db below that which would be specularly reflected by a flat conducting surface. For any given application, therefore, the best "absorber" is the one that *reflects least* in those directions of maximum interest. In a flat-wall antenna pattern or boresight range, the forward specular direction, at areas midway between transmitter and receiver, is most critical. In the cross-section range, however, straight back-scatter into the region of the transmitting antenna may be equally important for the absorbing material located in heavily illuminated areas.

In flat-wall chambers suitable for pattern and boresight tests, it is usual practice to employ scattering absorber materials of long pyramidal or conical configurations over large areas midway between the transmitter and receiver as well as behind the receiver, and frequently to use less expensive materials in other regions where the usually stronger specular reflection from these materials will not be directed into the vicinity of the receiver.

Even with physically tapering absorbing materials that are characterized by a strong tendency to scatter incident energy in many directions at the higher frequencies, there is usually a relatively strong specular component that becomes more and more predominant as frequency decreases, because the taper dimensions decrease in terms of wavelength and the material appears as a "smoother" reflecting surface. Shaping of the internal surfaces of the chamber then offers advantages in directing the more predominant specular reflection component away from the working volume.

#### 5-12.2 SHAPING OF THE ANECHOIC CHAMBER

The simplest configuration of an anechoic chamber is, of course, a rectangular room with flat internal surfaces covered with absorbing material. The obvious and experimentally well established limitation of such a structure is first-bounce specular reflection of energy from areas on side walls, floor, and ceiling, midway between the transmitting and receiving antennas. This assumes, of course, that the line of sight of the transmitting antenna is essentially parallel to these surfaces. While it may be possible for short-range work to transmit more or less diagonally in a horizontal plane to minimize side-wall effects, one is economically obliged for long-range operations to transmit approximately along the axis of an enclosure whose length is substantially greater than its width and its height.

Several alternative steps can be taken to minimize the limiting first-bounce reflections of a rectangular flat-wall chamber. Operationally, antennas of minimum side-lobe level and minimum possible beamwidth (consistent with far-field and other experimental requirements) will reduce the illumination level of offending areas near the transmitter and the sensitivity of the

receiver to reflections from the offending areas. Similar improvement is possible by making the chamber width and height as large as possible with respect to transmission length, but economic limitations usually will not permit sufficient increase in these dimensions when transmission length exceeds approximately 50 ft.

As mentioned above, a strongly scattering absorber may be used on flat chamber surfaces to minimize specularly-reflected energy in the frequency range where the absorber is an effectively "rough" reflecting surface. Nevertheless, the specular component continues to predominate at lower frequencies and there appears to be a trend toward the use of very thick absorbers to keep this low-frequency region well below the range when maximum performance is required; 18-in. pyramidal absorbers have been used for S- and X-band operation. This approach is expensive and subject to rapidly diminishing returns.

After maximum advantage has been gained by the use of directive antennas and by scattering absorbing materials, further reduction of chamber reflectivity (or equivalent reflectivity at reduced cost) is frequently possible by the addition of one of several varieties of baffles or by modifications of chamber shape.

There is considerable controversy concerning the effectiveness of baffles in improving the performance of anechoic chambers, much of which arises from proprietary or patent-enforced positions of commercial manufacturers. Independent studies (References 77 and 78) have concluded that appropriate baffles can improve chamber performance when dimensions are large in terms of wavelength.

There is ample evidence of the necessity for greatly reducing the magnitude of half-way reflections from the flat surfaces of anechoic chambers as well as from outdoor antenna test ranges. These reflections, in chambers, were particularly severe in the days when the best absorbers exhibited reflectivity of only about -20 db and were characterized by maximum reflection in the specular direction. Most of the common baffle configurations were developed during that period.

Outdoor test ranges were equipped with transverse "fences" to prevent illumination of the areas half way between transmitter and receiver and the diffraction effects from the top edge of the fence were much more easily toler-

able than the ground reflections that they replaced. The idea of the transverse fence was applied to anechoic chambers in the form of a shallow, transverse absorber-covered baffle projecting normally from side walls, floor, and ceiling, approximately midway between the transmitting and receiving stations. The idea was soon extended to a series of transverse baffles to accommodate different transmission lengths in the same chamber. Rather elaborate shaping of transverse baffles was used in an effort to entrap reflected energy and/or to ensure that all but direct-ray energy to the quiet zone suffered two, three, or even more reflections (References 79 and 80).

The performance limitation in a chamber having many transverse baffles is imposed by edge-

diffracted energy from the peaks of the baffles. Such energy has a sizable forward-scattered component over which very little control can be exercised by choice of absorbing material. These considerations prompted the "aperture-type" chamber, in which the basic element is a *single* transverse baffle (preferably placed close to the transmitting end of the chamber) having an opening sufficiently small so that direct illumination of side, floor, and ceiling surfaces on the receiving side of the aperture is not possible (Reference 81).

Figure 5-51 is a view through the aperture toward the transmitter in Eccosorb Anechoic Chamber No. 225 at Warner-Robins Air Force Base, Georgia. This chamber was designed specifically for boresighting operations on cer-

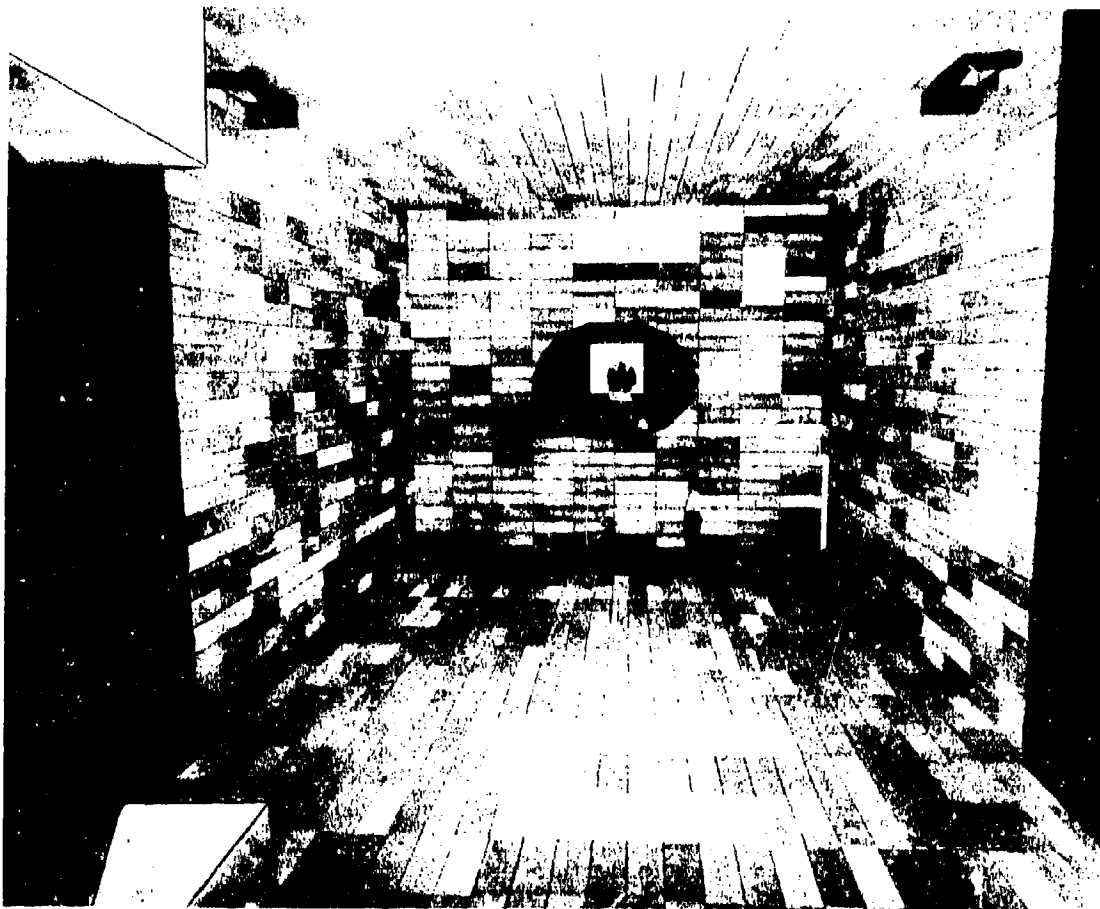


Figure 5-51. Aperture-Type Anechoic Chamber. View Toward Transmitter in Eccosorb Anechoic Chamber No. 225 at Warner-Robins Air Force Base, Georgia

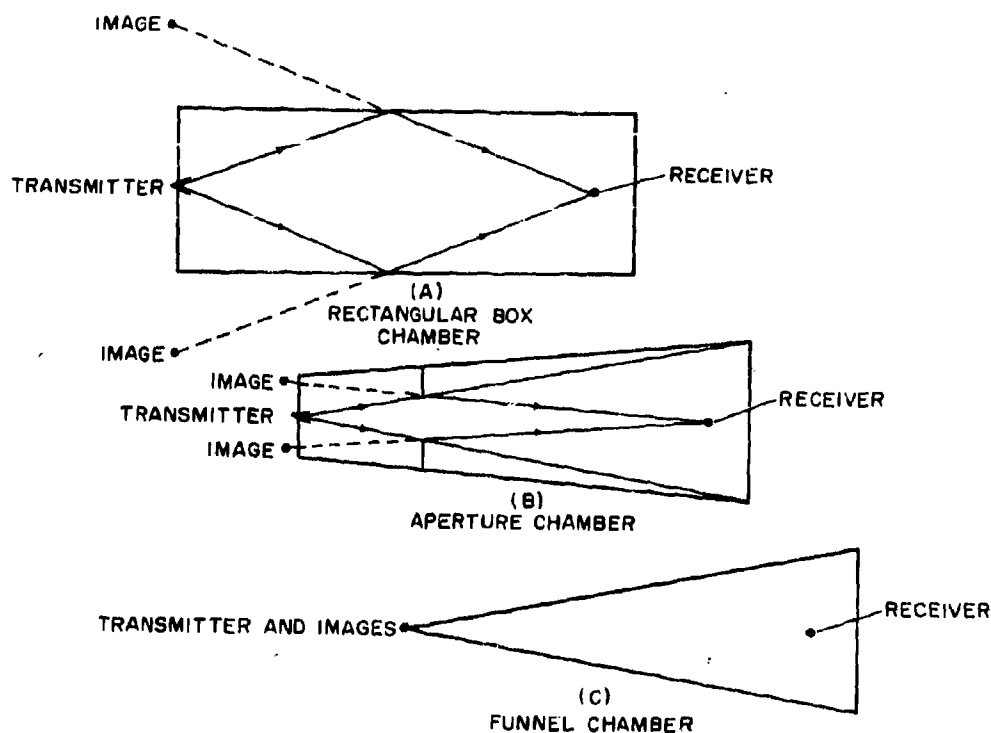


Figure 5-52. Evolution of Aperture and Funnel Anechoic Chambers

tain B-58 antennas and the transmission length is approximately 1000 in. Performance of this and similar chambers is discussed in the following paragraph.

Figure 5-52 illustrates the evolution (from a rectangular box) of the aperture-type chamber and, more recently, the funnel or horn type. In Fig. 5-52A, energy reflected from regions midway between transmitter and receiver appears to proceed toward the receiver from the image points shown. In addition to phase shifts occurring at the reflection points, the considerable difference in path length to the receiver along the direct-ray path from the transmitter and along the reflected-ray paths from the images, generates a pronounced interference pattern between the direct and reflected rays as a function of receiver position. The path length difference also permits substantial changes in the interference pattern with changes in frequency.

In Fig. 5-52B, the aperture edges constitute the major reflection points and, since these

points are closer to the direct-ray path than those in Fig. 5-52A, the transmitter images approach the transmitter. The differences between direct-ray and reflected-ray path lengths are much less in the aperture chamber and the cycles of the interference pattern are physically much longer. This effect, coupled with the reduced magnitude of reflected energy at the aperture edges, results in much more nearly uniform illumination of the chamber in the vicinity of the receiver and, therefore, much lower chamber reflectivity.

The aperture-type chamber, in addition to exhibiting lower reflectivity than the rectangular box type, can have much reduced width and height at the transmitting end, as shown in Fig. 5-52B, and is therefore more economical. Aperture-type chambers have recently been reported as very successful pulsed back-scatter ranges (Reference 82).

As the aperture is moved closer and closer to the transmitter, the dimensions of the transmitting end of the chamber can be correspond-

ingly reduced. The funnel of Fig. 5-52C appears as the limiting case in which the aperture edges coincide with the physical extremities of the transmitting antenna and the longitudinal chamber surfaces are defined by lines joining the transmitting antenna extremities to a suitable limiting contour on the receiver-end wall. Under these conditions, the transmitter and its images essentially coincide and the troublesome path length differences noted above essentially disappear. The validity of this argument becomes nebulous, of course, in the frequency range where a scattering-type absorber on the funnel generates diffuse reflection components comparable in magnitude with specular components.

There are two clear disadvantages to the limiting funnel chamber configuration of Fig. 5-52C. First, the quiet zone must be within the flaring portion of the funnel for minimum reflectivity, rather than within a rectangular extension of the large end of the flared section, for example, as might be desirable for a long quiet zone. Secondly, bistatic reflectivity measurements of a target in the quiet zone are not feasible, since separate transmitting and receiving antennas cannot be spaced apart as required in the throat of the funnel. Additionally, at microwave frequencies, physical alignment and fitting of the transmitting antenna in the throat of the funnel may be critical. A few funnel-type chambers have been proposed or constructed by The B. F. Goodrich Company. Performance data and test procedures are not available to date.

The most widely used type of shaped anechoic chamber is the longitudinal baffle that is designed to avoid the multiple edge-diffraction effects of many transverse baffles in a chamber where the transmission length must be variable. Ray tracing is used to determine a configuration that directs specularly reflected energy away from a central cylindrical quiet zone that extends essentially the full length of the chamber (Reference 82). Figure 5-53 illustrates a typical configuration. Baffles of this type are undoubtedly effective in controlling the specular component of energy reflected from side walls, floor, and ceiling of a chamber throughout the frequency range where the slant surfaces of the baffles extend at least several wavelengths in the dimension normal to the line of the peak.

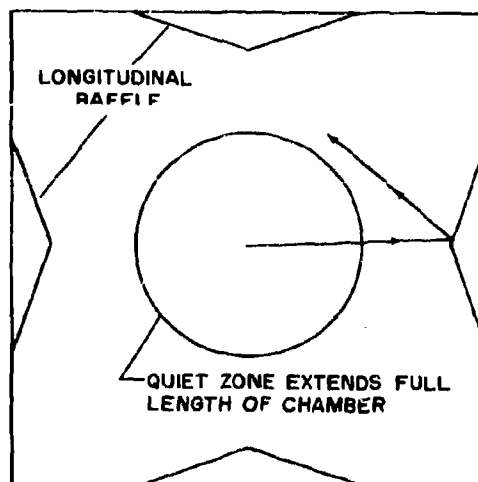
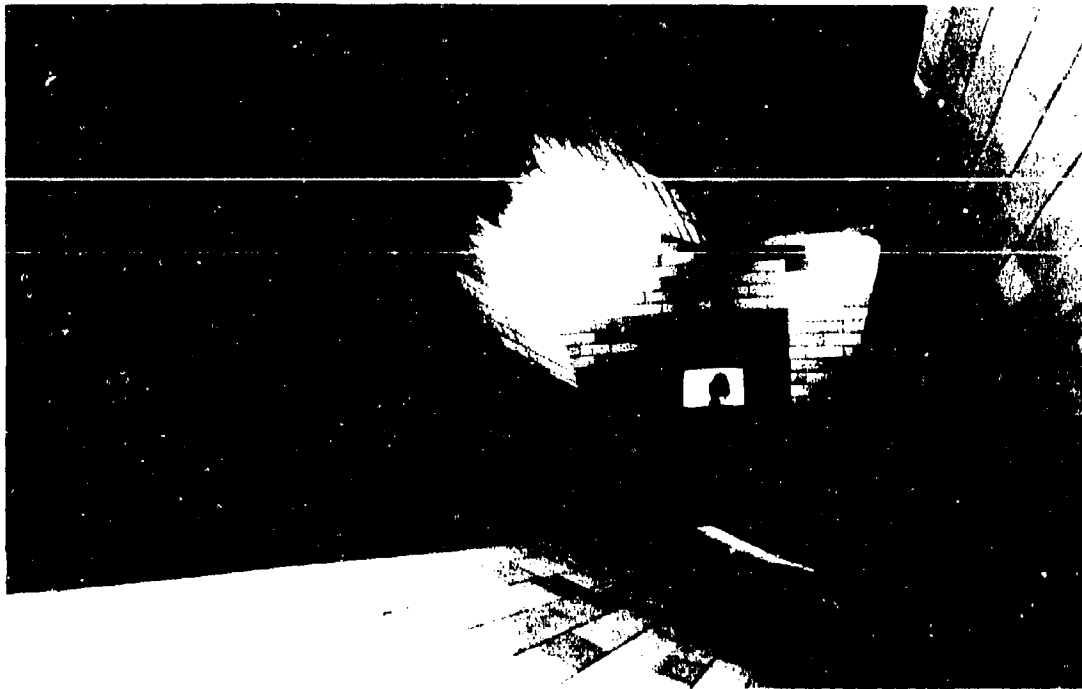


Figure 5-53. Vertical Transverse Section Through Typical Longitudinal Baffle Chamber Configuration

Figure 5-54 shows the longitudinal baffle construction of Eccosorb Anechoic Chamber No. 250, installed at Canadian Westinghouse Company, Ltd., Hamilton, Ontario. The chamber was designed for boresight testing of NATO aircraft antennas. The transmission length is approximately 1000 in. Figure 5-55 illustrates a smaller chamber of similar design at Motorola, Scottsdale, Arizona. This chamber is used for boresight testing of small-missile antennas. Performance of these chambers is discussed briefly in Paragraph 5-14.

The end wall of an anechoic chamber behind the receiving antenna is usually in the form of a vertical wedge or cylinder, or at least a slanted flat surface, so that specular reflections are directed away from the receiver. A flat wall behind the transmitting antenna is adequate, in general, unless high-level backlobes or dipole-type patterns, for example, must be tolerated in the transmitting antenna. In the latter instances, baffling or shaping of the transmitting-end wall should be employed to avoid specular reflections directly downrange.

Reference 84 describes and illustrates several flat-wall and baffled anechoic chambers, as well as outdoor test ranges. The emphasis in this reference is on use of these facilities as radar cross-section ranges, but many of them are obviously suitable for antenna pattern and boresighting work.



*Figure 5-54. Longitudinal-Baffle Eccosorb Anechoic Chamber No. 250 at Canadian Westinghouse Co., Ltd., Hamilton, Ontario*

### **5-13 EVALUATION OF MICROWAVE ANECHOIC CHAMBERS AS ANTENNA PATTERN AND BORESIGHT RANGES**

Many procedures for evaluating the reflectivity of anechoic chambers have been employed. These range from simple comparison of antenna patterns recorded in a chamber with those obtained for the same antenna on a proven outdoor range, to much more elaborate techniques, such as described in the following paragraphs. Most of these procedures are referenced and summarized in Reference 77. For modern low-reflectivity chambers, only a few techniques appear to be satisfactorily comprehensive: (1) the "antenna pattern comparison" procedures introduced and widely used by Emerson and Cuming, Inc., (2) the "free space vswr" technique, championed by The B. F. Goodrich Company, and (3) a thorough field probe found valuable by several laboratories, particularly at VHF and lower UHF frequencies where methods (1) and (2) may be difficult to use. Each of the above methods has certain

features that make it attractive for specific purposes.

All the procedures to be described attempt to relate the level of reflected field intensity to direct transmitted field intensity, under the conditions of interest. In all cases, the measured level of reflected energy is dependent upon the directivity of the antennas used in measuring the quantities. The purist would undoubtedly be happier with defined characteristics that apply strictly to the chamber or test range itself under illumination by a truly isotropic radiator. While such quantities can certainly be defined, their adequate measurement would likely be difficult, if not impossible, and their practical utility in predicting chamber performance with typically directive antennas would be limited. Therefore, it seems preferable to recognize at the outset that the errors in a recorded antenna pattern, for example, due to reflected energy, depend not only upon the distribution of illuminating energy (i.e., the directivity of the transmitting antenna), but also upon the reflected energy accepted by the re-

ceiver (i.e., the directivity of the receiving antenna).

#### **5-13.1 THE PATTERN COMPARISON EVALUATION METHOD**

The method described here is equally applicable to evaluation of the performance of any antenna pattern range, whether it be an open

range, outdoors, or a fully enclosed microwave anechoic chamber (Reference 85).

Evaluation of the performance of a microwave anechoic chamber where the magnitude of the reflected field within the design quiet zone is required to be below that of the direct field by a specific number of decibels (frequently 50 db or more in today's designs) requires precise measurement of extremely minute variations in total received signal strength, corre-

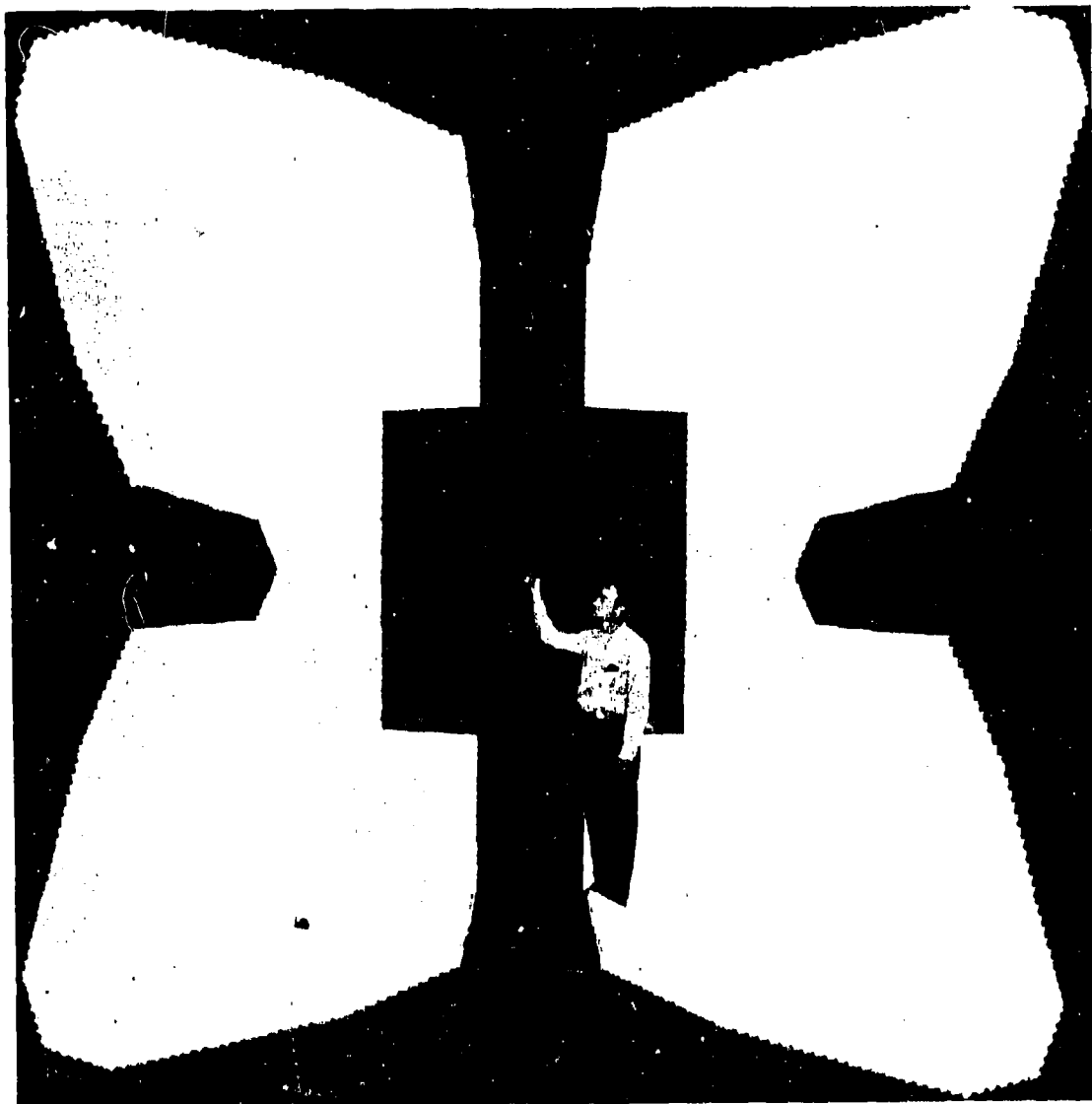


**Figure 5-55. Longitudinal-Baffle Eccosorb Anechoic Chamber No. 423 at Motorola, Scottsdale, Arizona**

sponding to in-phase and out-of-phase addition of direct-ray and reflected-field components. For example, a 0.055-db total excursion in the peak value of the main lobe of a probe antenna pattern indicates -50 db quiet zone reflectivity.

The accurate detection and read-out of such a small change in peak response cannot be accomplished without relatively elaborate precision circuitry. Therefore, most chamber evaluation procedures depend on various "off-peak" detection methods in which the probe antenna is oriented so that its response to "direct-ray" is greatly reduced and the minute effects of reflected energy are observed as now relatively much larger variations. For example, if the main lobe of the probe antenna is aimed so that the direct ray causes a response 20 db below the peak value, the maximum excursion corresponding to quiet zone reflectivity of -50 db is now 0.55 db and is clearly observable with standard pattern recording instruments. This is the basis for the method to be described.

#### 5-13.1.1 Data Accumulation

**5-13.1.1.1 Test Equipment.** The following test techniques should be adhered to:

**Test Frequencies.** To make a realistic initial evaluation with minimum effort, tests may be made at a single frequency that is in the lower portion of the microwave range where the reflectivity of the absorbing material is rated at about -40 db, since chamber performance almost invariably improves at higher frequencies and adequate evaluation at very low frequencies poses special problems.

**Antennas.** The transmitting antenna is located and oriented in the manner for which the chamber was designed, usually near one end of the quiet zone with its major lobe directed along the chamber axis.

The receiving antenna is mounted on an azimuth and/or elevation positioner within the design quiet zone and in a transverse plane at a typical, preferably a maximum, distance from the transmitting antenna, thus to reveal the minimum performance of the chamber.

Directivity of both antennas has a very important bearing on test results. Tests are made usually with 15- to 20-db antennas, both transmitting and receiving, and are frequently limited to one polarization.

**Transmitting Equipment.** For the majority of tests, transmitting equipment is similar to that generally used in an antenna pattern range, with output power levels between 100 and 500 milliwatts.

When tests are in progress, all equipment and personnel must be excluded from the part of the chamber between the transmitting and receiving antennas and should be kept within the area back of the transmitting antenna.

**Recording Equipment.** The received signal is preferably recorded on a standard rectangular pattern recorder where the pen continuously records relative signal strength in decibels and the chart movement is synchronized with azimuth or elevation movement of the receiving antenna positioner.

**5-13.1.1.2 Pattern Recording.** Sets of 360° patterns (usually azimuth patterns) are recorded with the receiving antenna located successively at closely adjacent test points along the radii of the quiet zone, usually making one horizontal and one vertical traverse at one polarization. A very substantial collection of data shows that this amount of testing is sufficient to evaluate the performance of an anechoic chamber at most frequencies of interest.

For each pattern, the location of the receiving antenna relative to the chamber axis should be known fairly accurately (e.g., scale measurement to within one or two inches), and increments of linear movement between test stations should be uniform (e.g., 2 in.). For horizontal traverses, this is commonly done by laying out on the chamber floor a series of marks to which a convenient reference point on the antenna positioner can be matched successively. For vertical traverses, a telescoping column for vertical adjustment of the antenna can be provided with an appropriate scale.

To facilitate subsequent comparison of patterns, the peak of the main lobe of each pattern is preferably set precisely at a convenient level, such as -2 db on the chart, and it may be helpful to center the pattern about chart angle zero. It is usually convenient, for example, to operate the chart recorder so that the left-hand side of a recorded azimuth pattern corresponds to the aiming of the receiving antenna toward the left-hand side of the range as viewed from the transmitting antenna.



The patterns thus recorded provide all the data needed to derive a measure of the reflective performance of the chamber.

The distance between points at which patterns must be recorded along any traverse depends primarily upon the test frequency, but is influenced also by chamber geometry. Patterns must be taken sufficiently close together so that the individual cycles of the interference pattern between direct-ray and reflected energy are reasonably well defined. This discussion may be better appreciated after examination of the deviation plots in Fig. 5-57. As a general rule, the following increments are satisfactory: 4 in. at 1 gc, 2 in. at 3 gc, 1 in. at 10 gc, and 1/2 in. to 3/4 in. at 25 gc.

#### 5-13.1.2 Data Reduction

Data reduction is discussed by means of a specific example, with the necessary mathematical derivations and other comments inserted where applicable.

The following example is the actual S-band evaluation of Eccosorb Anechoic Chamber No. 385, built for the U. S. Army Electronic Research and Development Laboratory at Fort Monmouth, New Jersey. The outer dimensions of this chamber are: length, 80 ft; width, 33 ft; and height, 17 ft. The evaluation described below was performed at 2.6 gc using 20-db pyramidal horn antennas separated by approximately 65 ft. Azimuth patterns with vertical polarization were recorded at 2-in. increments along two traverse lines, the lower vertical radius and the left horizontal radius of the quiet zone, out to a distance of 48 in. from the chamber axis. The patterns are analyzed and the chamber reflectivity is computed as follows.

The pattern of each set that was recorded on the axis of the chamber is usually chosen as a reference for that set, but any single pattern of the set will serve equally well. The remaining patterns of that set are superimposed upon this reference one by one, with the peaks of the main lobes coinciding. This is done most conveniently on a translucent tracing table lighted from below.

Working typically at those angles where the reference pattern levels are -10, -15, -20, -25, -30db (and -35 db, if workable) from the peak value, called "reference levels," the

level of the superimposed pattern at each of the same angles is read off, not directly but as its deviation, positive or negative as the case may be, from the associated level in the reference pattern. Other reference levels and angles may be used if desired.

Figure 5-56 shows a typical pattern superimposed on its reference pattern and the method of reading out the deviation. For each "reference level" on each side of the reference pattern, the deviation from that level of each of the other patterns is plotted vs. the radial distance from the chamber axis to the test point at which that pattern was recorded. Figure 5-57 contains the deviation plots obtained from the left sides of the set of patterns taken along the lower vertical traverse. A similar set of plots results from the right sides of this set of patterns and two additional sets are obtained from the horizontal traverse.

#### 5-13.1.3 Computation of Chamber Reflectivity

The following steps indicate an orderly procedure for detailing the chamber reflectivity and illustrate one simple method for obtaining an "average" performance number. (After all of the "local reflectivity" values have been determined in step 5, some users may wish to compute standard deviation or mean deviation as well as average reflectivity. Other statistical treatment of the data may also be appropriate.) Refer to Fig. 5-57, which illustrates the usual computational steps.

1. For each reference level, establish the envelope of the deviation plot by drawing a series of straight lines that connect separately the extreme high values and the extreme low values. The height of this envelope is the only characteristic of these curves that is used to extract data. This will define the several "local cycles" (both positive and negative loops of the curve are included) within each of which we will determine "local reflectivity."
2. Since there may frequently be some doubt as to whether a short or shallow ripple in a deviation curve actually constitutes a significant cycle, the entire set of deviation curves for all reference levels should be surveyed as a whole at

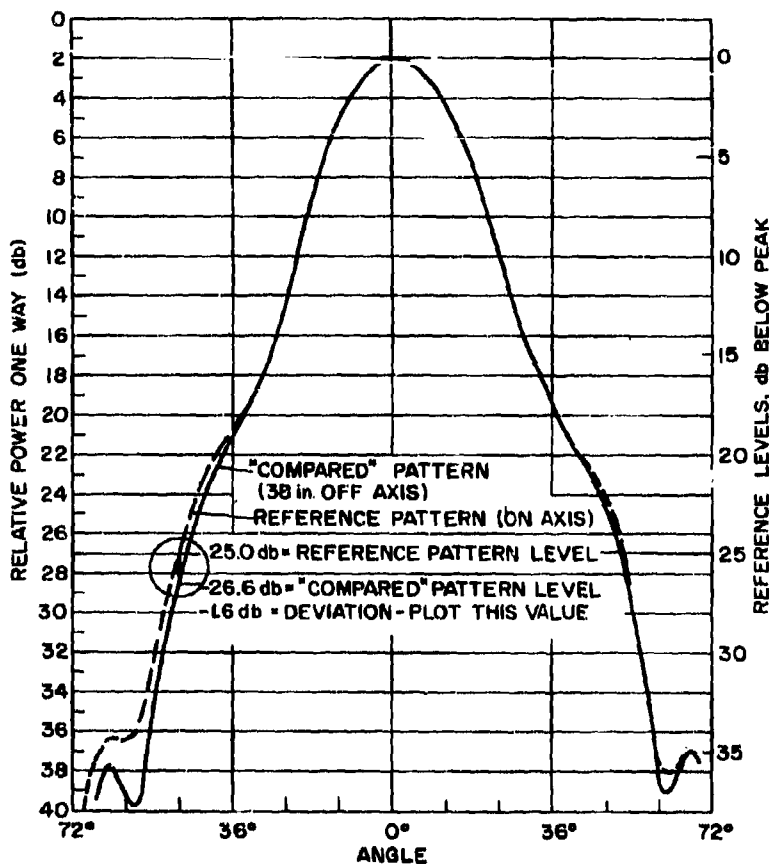


Figure 5-56. Comparing Patterns by Pattern Comparison Evaluation Method

this point. Since approximately the same number of cycles usually exists at all levels and they are in roughly the same positions, such a survey will usually assist in deciding whether small ripples should be included as cycles or disregarded as due to instrumentation or procedural inaccuracies in recording or in deviation readout.

In some instances, cycles of length typical of the entire set may be superimposed upon atypically long cycles of greater amplitude and the longer cycles may be significant if they are not clearly caused by an effect such as the beam shape of the illuminating transmitter. Such atypically long cycles have been taken as additional significant devia-

tions in Fig. 5-57 in the region of 24 to 42 in. off axis (primarily in the region outside the main quiet zone). Thirteen data producing cycles are identified at all levels in Fig. 5-57, except at  $-15$  db. At this level, only eleven cycles are reasonably clear and these have been accepted as the complete set, although it would be justified to assume two additional cycles of negligible amplitude.

To further illustrate this latter point, it sometimes happens that the deviation curve for the  $-10$  db reference level, for example, is essentially a straight line except for two obvious loops, one positive and one negative, while the curves for the other levels show perhaps 5 loops. It is axiomatic that a region of very

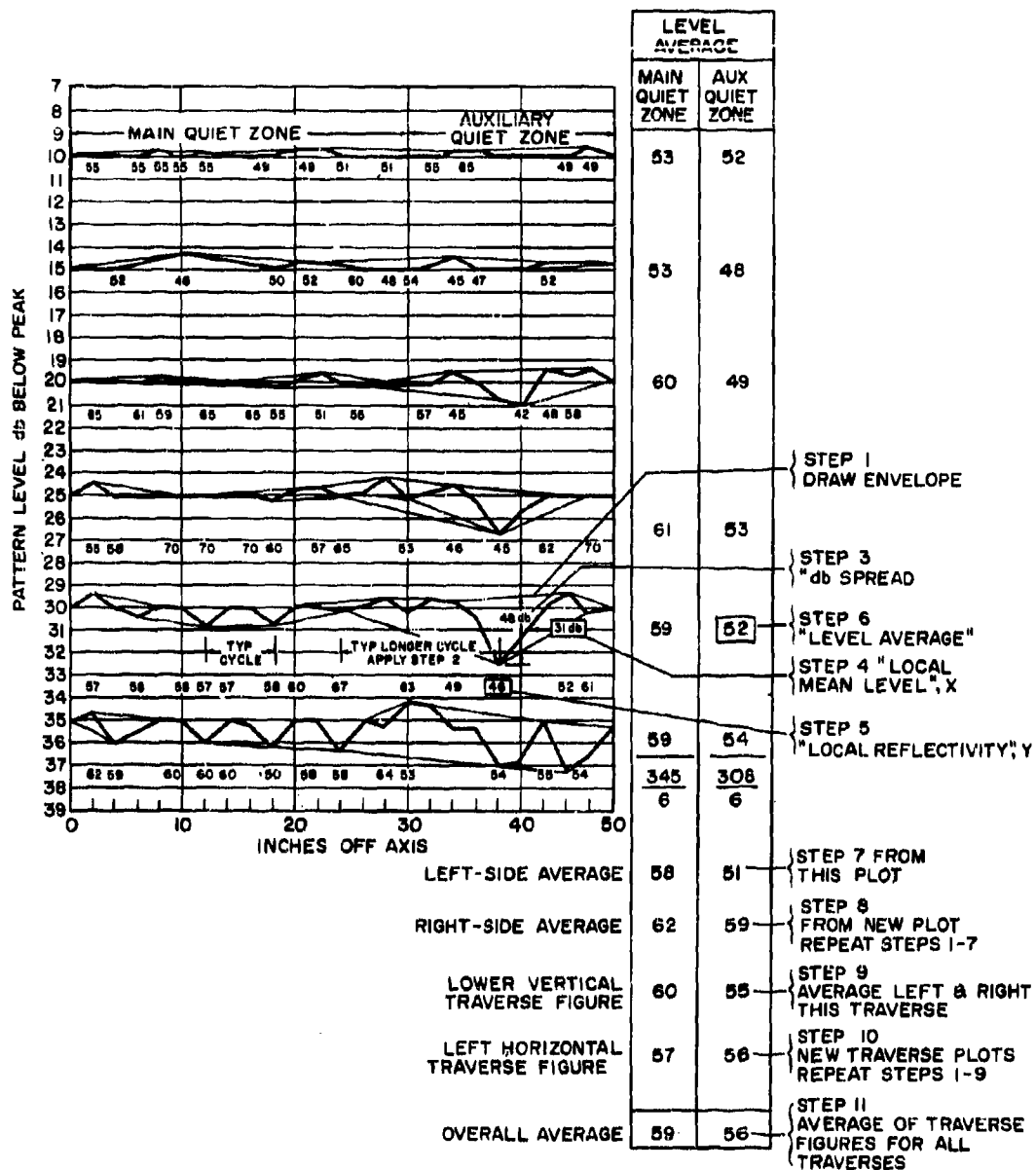


Figure 5-57. Deviation Plot and Computation of Results by Pattern Comparison Evaluation Method

small amplitude in a deviation plot can be indicative only of superior performance and, therefore, should be included in the evaluation. Therefore, three loops of negligible amplitude, in addition to the two measurable loops, should be assumed to exist in this -10 db curve. Consistent engineering judgment is essential in this step and experience in analyzing deviation plots will quickly establish confidence in the exercise of such judgment.

3. At each reference level, determine the "db spread" for each cycle as the arithmetic difference in decibel numbers between each high or low peak of the deviation plot and the point on the opposite straight line of the envelope directly above or below that peak.
4. Determine the local "mean level" of the deviation plot (corresponding closely to zero perturbation due to reflected energy) as the arithmetic mean of the same db numbers that define "db spread."
5. Using these values of the "db spread" and the "mean level" (X), refer to the chart, Fig. 5-58, and read the "local reflectivity" (Y) from the family of oblique curves. Record this value on the deviation plot in clear relation to the local cycle to which it applies. (The derivation and applicability of Fig. 5-58 follow immediately below.)

Figure 5-58 is, in essence, a graphical means of evaluating the ratio of the magnitudes of two vector quantities in terms of the ratio of the sum of these magnitudes to the difference. In the following derivation, let 1.00 represent the magnitude of the *peak-of-pattern direct-ray* vector, let  $X^1$  represent the magnitude of the *off-peak direct-ray* vector, and let  $Y^1$  represent the magnitude of the *reflected-ray* vector; each is expressed as a fraction of the peak-of-pattern or on-peak value. Then the maxima along each cyclical deviation plot correspond to the in-phase addition of the local direct-ray and reflected vectors (magnitude of sum =  $X^1 + Y^1$ ) and the minima correspond to out-of-phase addition (magnitude of sum =  $X^1 - Y^1$ ).

Hence, for each cycle of the deviation curve,

$$\text{db spread} = 20 \log \left( \frac{X^1 + Y^1}{X^1 - Y^1} \right) \quad (5-39)$$

$$\left( \frac{X^1 + Y^1}{X^1 - Y^1} \right) = \log^{-1} \left( \frac{\text{db spread}}{20} \right) \quad (5-40)$$

and

$$Y^1 = \frac{\left[ \log^{-1} \frac{\text{db spread}}{20} \right] - 1}{\left[ \log^{-1} \frac{\text{db spread}}{20} \right] + 1} X^1 \quad (5-41)$$

Unless the "db spread" values are very large, only negligible error results in assuming that the mean level = X calculated in step (4) is identical with  $X^1$  and hence to a very good approximation, the local reflectivity

$$Y = \frac{\left[ \log^{-1} \frac{\text{db spread}}{20} \right] - 1}{\left[ \log^{-1} \frac{\text{db spread}}{20} \right] + 1} X \quad (5-42)$$

Figure 5-58 is a plot of this functional relationship and Y can be read out directly or interpolated as necessary.

Although the curves of Fig. 5-58 are plotted as straight lines, they are actually very slightly concave upward. They may be extrapolated as straight lines to the left and downward as far as may be desired, but should not be extended upward and to the right without additional calculations. For example, the curve for -20 db reflectivity should intersect the -15-db abscissa at 11.05 db, and all other curves should be parallel to this one. All lines are correct as plotted at the 5.7-db ordinate value.

6. Compute the "level average" as the average of all "local reflectivities" for each reference level. In this example, separate averages are obtained for the main quiet zone and for the auxiliary (lower-performance) zone. Record these values at the side of the deviation plot and adjacent to the associated reference level as shown.

7. Compute the "left-side average" reflectivity for each zone as the arithmetic average of all the corresponding "level averages." Record these below the columns of "level averages."
8. Repeat steps 1 through 7 for the deviation plots derived from the right-hand sides of the patterns for this same traverse and thereby obtain the "right-side average" reflectivities.
9. Average the left-side and right-side averages of steps 7 and 8 to obtain the "traverse figure" applicable to the set of patterns analyzed.
10. Repeat steps 1 through 9 for all other traverses, if any, performed at the same frequency and range, but with other polarizations or other directions of traverse.
11. Average all the "traverse figures" from steps 9 and 10 to obtain the "overall average" reflectivity of the chamber for each zone at the given test frequency and range for the antennas and antenna configuration used.

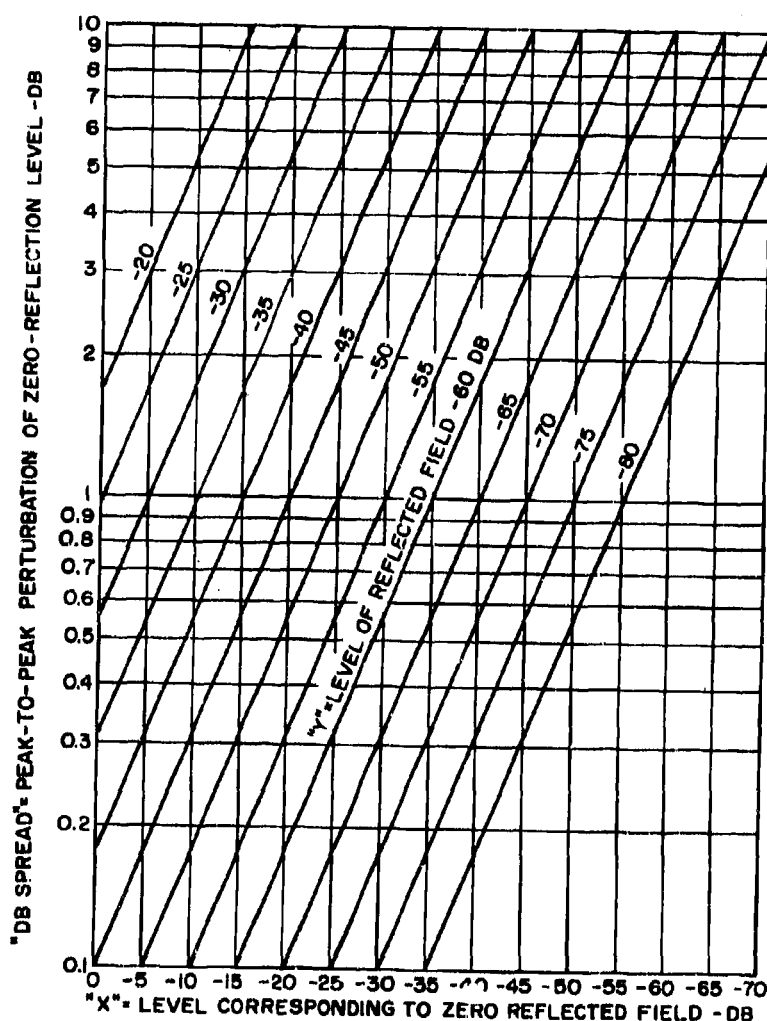


Figure 5-58. Perturbation of Antenna Pattern by Reflected Energy

### 5-13.2 THE FREE-SPACE VSWR EVALUATION METHOD

Since there does not appear to be any readily available reference that describes this technique in detail, the following excerpts from Reference 77 serve as a summary.

Transmitting and receiving horns are set up as they would be for an antenna pattern test. Room reflectivity data are obtained as a function of the aspect angle,  $\phi$ , of the receiving horn, with  $\phi$  varied in discrete steps (for example,  $10^\circ$ ) from  $\phi = 0^\circ$  (looking at the transmitter) to  $\phi = 180^\circ$ . At each aspect, the horn is moved back and forth along its axis to produce a change in the received signal from a maximum to a minimum. It is assumed that this results from the in- and out-of-phase addition of the direct signal  $E_1$  and the reflected signal  $E_2$ , the ratio of which can be obtained from the maximum to minimum ratio  $R$  using Eq. 5-43.

$$E_2 = E_1 \frac{R - 1}{R + 1} \quad (5-43)$$

The value used for  $E_1$  depends on the orientation of the horn and is found from the average signal received as the horn is moved along its axis by normalizing this relative to the peak value observed when  $\phi = 0^\circ$ .

This B. F. Goodrich method provides the ratio for one antenna location as a function of the receiver orientation. The measurement would be repeated for the desired number of locations within the quiet zone to give a complete picture of the room performance.

### 5-13.3 THE FIELD-PROBE EVALUATION METHOD

Neither the pattern comparison procedure nor the free-space vswr technique, as described above, extracts detailed information about the uniformity of the total illuminating field over wide areas. For strictly pattern work, when the shape of an antenna pattern is the characteristic under study, relatively large variations in illumination level within the quiet zone are tolerable if the antenna aperture is small with respect to the dimensions of the quiet zone. Under such circumstances, the pattern comparison procedure is highly instructive, since it gives range performance in terms of small changes in pattern shape.

Where accurate measurements of antenna gain must be made and when the aperture of the gain standard antenna is significantly different in shape or size from the aperture of the antenna under test, uniformity of illuminating field is of greater importance than in the above application. If it can be assumed that transmitter power and receiver sensitivity remain constant, then the variations of the on-peak or zero-aspect response of the test antenna observed as a function of antenna position in either the pattern comparison or free-space vswr technique constitute a partial map of the illuminating field magnitude. A survey more nearly complete than provided by the above techniques may be required when field-intensity variations throughout a sizable volume must be known. Point-by-point measurements are tedious and time consuming, and long-time equipment stability may seriously limit accuracy.

Probing and mapping of illuminating field intensity have been automated to some extent by driving a probe receiving antenna along a straight-line path by means of a lead screw while a strip-chart recorder plots antenna response vs. antenna position. Care must be taken to prevent interfering reflections from moving parts and different orientations of the lead screw require a fairly elaborate supporting mechanism. Off-peak orientation of the probe antenna can be used both to relax the required precision of recording and to obtain additional information about chamber performance.

When variations of field intensity of less than about 0.1 db are to be measured accurately, ordinarily available equipment stability is insufficient and instrumentation becomes more elaborate. From Fig. 5-58, a 0.1-db peak-to-peak perturbation of the on-peak ( $X = 0$ ) level corresponds to a reflectivity of  $-45$  db. Reference 86 describes a null-balance technique for point-to-point measurement of field intensity variations down to 0.01 db. A two-channel comparison system uses the following:

1. A moving receiving antenna, oriented for maximum output, to probe the field as required.
2. A stationary pickup antenna, or other means of sampling transmitter output, to provide a reference energy level.
3. An accurate amplitude-sensitive null detector capable of measuring minute differ-

ences between the response of the moving antenna and the reference signal (e.g., Weinschel Dual-Channel Insertion Loss Test Set).

Curves of the response of the receiving antenna vs. its transverse off-center position show cyclic variations very similar to the deviation curves of Fig. 5-49, and chamber reflectivity may be derived as in the pattern comparison procedure by entering Fig. 5-58 at the  $X = 0$  or peak-of-pattern level with the values of the db spread measured from the curves. Curve plotting is not necessary if it is known that the pattern of the *transmitting* antenna has resulted in field intensity variations very much smaller than those observed by the moving probe. It is then sufficient to note the decibel differences between the maximum and minimum probe outputs and enter Fig. 5-58 with these differences at  $X = 0$ . Alternatively, the following equation may be used:

$$E_2 = E_1 \frac{R - 1}{R + 1} \quad (5-44)$$

where  $E_1 =$  unity, since the on-peak probe output has been recorded

$R =$  numerical ratio of maximum to minimum field strengths

$E_2 =$  effected reflected field strength expressed as a fraction (e.g., 0.01, corresponding to -40 db)

If the volume explored by the probe antenna is very large or three-dimensional, inverse-square corrections for the varying distance between the transmitter and the probe must be included unless they are very much smaller than the observed variations of the probe output.

#### 5-13.4 COMPARISON OF EVALUATION METHODS AND THEIR APPLICABILITY TO BORESIGHT RANGES

The field-probe evaluation technique is by far the most rigorous of the test procedures described. It is required for a typical pattern range only when detailed information about field uniformity is needed to ensure the accuracy of absolute gain measurements. One of the other procedures is entirely adequate in most cases where accuracy of pattern shape is the antenna characteristic of major interest. Never-

theless, when the field-probe method is automated to the extent that curves similar to those of Fig. 5-57 can be recorded directly without the necessity of recording and comparing patterns, this is a relatively rapid test procedure.

The reflectivity levels measured by the methods described can be related to the accuracy of the boresight measurements when detailed knowledge of the antenna patterns to be tested is at hand. Figure 5-58 permits readout of the peak-to-peak variation at any pattern level caused by measured reflectivity and the corresponding angular variations are immediately evident from the known pattern. When using the pattern comparison procedure for evaluation of a boresight range, it may be sufficient to compare patterns, for example, near the level corresponding to pattern crossover in a monopulse system to obtain a direct indication of the angular resolution permitted by range reflections.

The vswr evaluation method should also indicate the boresight resolution directly when the antenna to be boresighted is used as the probe and is oriented at the crossover angle, for example. Motion of the antenna in a direction at right angles to the transmitter line of sight may be equally as important as motion along the probe axis.

When a beam seeker or null seeker, such as the Carco Electronics or California Technical Industries boresight-error measuring system is employed, a field probe in the transverse plane by an antenna oriented for peak response on axis should yield data that are easily interpreted in terms of angular resolution.

#### 5-14 PERFORMANCE OF MICROWAVE ANECHOIC CHAMBERS AS ANTENNA PATTERN AND BORESIGHT RANGES

This paragraph summarizes the measured performance of several anechoic chambers that were designed for boresighting tests.

Eccosorb Anechoic Chamber No. 225, of the aperture type, as shown in Fig. 5-52, is located at Warner-Robins Air Force Base, Georgia. Chamber dimensions are approximately 31 ft wide, 25 ft high, and 102 ft long. The chamber was evaluated at 13.5 gc by the null-balance technique of probing the field in the vicinity of the receiving antennas. In this case, the probe antenna was one of the 22-db

pyramidal horns that are used in the California Technical Industries Beam Seeker installed as part of the boresight test facility. The probe was traversed  $\pm 25$  in. horizontally with respect to chamber axis and  $\pm 21$  in. vertically in a plane normal to the chamber axis at a distance of 1160 in. from the location of the transmitting antennas being boresighted. Average reflectivity varied from  $-52$  db to  $-55$  db, depending upon the beamwidth of the parabolic orange-peel antennas under test. These reflectivity levels correspond to peak-to-peak variations of 0.03 to 0.045 db in the illuminating field strength.

The longitudinally baffled Eccosorb Anechoic Chamber No. 250, Fig. 5-54, was installed at Canadian Westinghouse Co., Ltd., Hamilton, Ontario, Canada for boresight testing of X-band monopulse antenna systems. This chamber, whose dimensions are approximately 30 ft  $\times$  30 ft  $\times$  98 ft, was evaluated by both the null-balance and pattern comparison methods at 9.375 gc with a separation of 900 to 1000 in. between the transmitting and receiving antennas. A 20-db-gain transmitting antenna was used in both tests. In the field-probe test, 6-ft long traverses of a 15-db probe antenna were executed along horizontal, vertical, and 45-degree diameters of the quiet zone at the receiving end, and the measured average reflectivity was  $-41$  db, corresponding to an average peak-to-peak variation of approximately 0.16 db in illuminating field strength. In the pattern comparison tests, patterns of a 20-db receiving-horn antenna were recorded at 1-in. increments along vertical and horizontal radii of the 6-ft diameter quiet zone and an average reflectivity of  $-54$  db was computed. The difference between this value of  $-54$  db and the value of

$-41$  db indicated by the field-probe technique is caused by two factors:

1. Directivity of the receiving antenna was 6 db greater in the pattern comparison test.
2. Normalization of pattern peaks were used in the pattern comparison data reduction, so that computed reflectivity is based only upon the shape of the recorded patterns rather than upon small variations in peak-of-pattern level.

A chamber installed at N. V. Hollandse Signaalapparaten in the Netherlands is essentially identical with the Canadian Westinghouse facility and was evaluated by a slightly modified pattern comparison procedure. The measured reflectivity of  $-53$  db compares very favorably with  $-54$  db in the Canadian chamber.

Eccosorb Anechoic Chamber No. 423, Fig. 5-55, is a smaller, longitudinally baffled anechoic chamber (16 ft  $\times$  16 ft  $\times$  28 ft) in use at Motorola Inc., Scottsdale, Arizona for production boresight testing of small-missile seeker antennas. Evaluation of this chamber was by the pattern comparison procedure at 9 gc using vertically polarized 20-db horn transmitter and receiver at a separation of approximately 20 ft. The patterns recorded at 1-in. increments along 36-in. horizontal and 18-in. vertical traverses showed no deviation within  $\pm 72^\circ$  that was sufficient to indicate a reflectivity greater than  $-65$  db. Similar tests, using as a receiver the circularly polarized Motorola antenna to be boresighted, showed no detectable deviation at any pattern level down to 30 db below peak. At the critical  $-3$ -db pattern points on this antenna, a reflectivity of  $-65$  db corresponds to a peak-to-peak perturbation of 0.013 db and to an angular resolution of  $\pm 0.01^\circ$ .

## REFERENCES

1. Private communication from J. M. Price, April 30, 1964.
2. Private communication from J. M. Price, May 11, 1964.
3. Bulletin V-200 5M 963, Branson Instruments, Inc., Brown House Road, Stamford, Connecticut.
4. McManus, Leslie J. *Radome Wall Measurements and Evaluation*, Missiles and Space Systems Engineering, Douglas Aircraft Co., Inc., Santa Monica, California.
5. Leonard, J. D., and Stropki, G. T. *Utilization of Microwave Frequencies for Quality Control and Non-Destructive Testing of Dielectric Components*, North American Aviation, Inc., Columbus, Ohio.



6. Microwave Instruments Company, 3111 Second Avenue, Corona del Mar, California, 92625.
7. Luoma, E. J. *Microwave Instrument Measures Dielectric Constants*, Electronics Engineering Manual, Volume IX, pp. 155-157. McGraw-Hill Book Co., Inc., New York.
8. *Ecco Interferometer*, Preliminary Technical Bulletin 30-2-1, Emerson and Cuming, Inc., Microwave Products Division, Canton, Massachusetts.
9. *Ecco Interferometer Tables*, Preliminary Technical Bulletin 30-2-2, Emerson and Cuming, Inc., Microwave Products Division, Canton, Massachusetts.
10. *Ecco Interferometer Dielectric Standards*, Preliminary Technical Bulletin 30-2-3, Emerson and Cuming, Inc., Microwave Products Division, Canton, Massachusetts.
11. Norin, T. L. "The Measured Characteristics of Several Ablative and Some Non-Ablative High Temperature Radome Materials," *Proc. OSU-RTD Symposium on Electromagnetic Windows*, Vol. 1, June 1964.
12. Smyth, C. P. *Dielectric Behavior and Structure*, McGraw-Hill Book Co., Inc., New York, 1955.
13. von Hippel, A. R. *Dielectrics and Waves*, John Wiley and Sons, Inc., New York, 1954.
14. Frohlich, H. *Theory of Dielectrics*, Oxford, London, 1949.
15. Debye, P. *Polar Molecules*, Chemical Catalog Publishing Co., New York, 1929.
16. Breckenridge, R. G. *J. Chem. Phys.*, Vol. 16, No. 959, 1948. See also Reference 12, p. 138.
17. Westphal, W. B. *Dielectric Constant and Loss Measurements on High-Temperature Materials*, TR 182, Laboratory for Insulation Research, Massachusetts Institute of Technology, October 1963.
18. Bowie, D. M. "Microwave Dielectric Properties of Solids for Applications at Temperatures to 3000°F," *1957 IRE National Convention Record*, Part I, pp. 270-281, IEEE, N.Y., March 1957; *Elec. Manufacturing*, Vol. 61, No. 2, pp. 144-147, 316, February 1958.
19. Zellner, G. C., Pentecost, J. L., and Eliason, L. K. *Proc. ASD-OSU Symposium on Electromagnetic Windows*, ASD Technical Report ASD-TDR-62676, July 1962.
20. Sutton, R. W., and Grechny, N., Jr. "Design and Development of a High-Temperature Resonant Cavity Dielectrometer," *Proc. OSU-WADD Symposium on Electromagnetic Windows*, WADD Technical Report 60-274, Vol. 1, June 1960.
21. Englehard Industries, Baker Platinum Division, Newark, New Jersey.
22. *General Radio Experimenter*, Vol. 32, No. 12, May 1958.
23. Roberts, S., and von Hippel, A. R. *J. Appl. Phys.*, Vol. 17, p. 610, 1946.
24. Dakin, T. W., and Works, C. N. *J. Appl. Phys.*, Vol. 18, p. 798, 1947.
25. Westphal, W. B. "Dielectric Measurement Technique in the Very High-Frequency Region," Technical Report No. XVII, Laboratory for Insulation Research, Massachusetts Institute of Technology, (ASTIA Document No. ATI 54, 534), February 1949.
26. Redheffer, R. M. *Technique of Microwave Measurements*, Edited by C. G. Montgomery, Chapter 10, p. 576, McGraw-Hill Book Co., Inc., New York, 1947.
27. Gervers, M., and duPre, F. K. *Trans. Faraday Soc.*, Vol. 42A, p. 47-55, 1946. Gervers, M. "Measurement of Dielectric and Magnetic Properties of Solids at Microwave Frequencies," Paper No. 3, *Precision Electrical Measurements Symposium*, Philosophical Library, New York, 1956.
28. Horner, F. *et al.*, *Proc. IEE*, Vol. 93, No. III, pp. 53-68, 1946.
29. Bleaney, B. *et al.*, *Proc. Phys. Soc. (London)* Vol. 49, pp. 185-199, 1947.
30. Adcock, M. D. High-Frequency Measurements Conference, Washington, D.C., January 1953.
31. Hope, H. R., and Bayless, W. W. *Microwave Dielectric Measurements at High Temperatures*, Hughes Aircraft Company Technical Memorandum No. 577, June 1958.
32. Young, L. B. *Technique of Microwave Measurements*, Edited by C. G. Montgomery, Chapter 6, p. 396, McGraw-Hill Book Co., Inc., New York, 1947.
33. Langenberg, D. N., and Lengyel, B. A. Appendix B, Ref. 31.

34. Estlin, A. J., and Bussey, H. E. *IRE Trans. on Microwave Theory and Techniques*, Vol. MIT-8, pp. 650-653, November 1960.
35. Kaeburn, A. M. et al., English Electric Co., Ltd., Guided Weapons Division, (ASTIA Document No. AD 205-161), 1958.
36. Luoma, E. J. et al., *Measurements of Dielectric Constants and Loss Tangent by Transmission Measurement with a Free-Space Microwave Interferometer with Sample at 45° Incidence Angle*, Section II, Report No. 9, Contract AF 33(616) 7047, (ASTIA Document No. AD 275-425), March 1962.
37. Culshaw, W. *IRE Trans. on Microwave Theory and Techniques*, Vol. MIT-8, p. 182, 1960.
38. Gum, P. H., and Schoomer, B. A. *Elec. Ind.*, Vol. 22, No. 9, pp. 90-94, 1963.
39. Powell, R. W. "Further Measurements of the Thermal and Electrical Conductivity of Iron at High Temperatures," *Proc. Phys. Soc. (London)*, Vol. 51, No. 407, 1939.
40. Moeller, C. E. and Wilson, D. R. "Thermal Conductivities of Several Metals and Non-metals from 200° to 1300°C by the Radial Heat-Flow Technique," *Proc. Phys. Soc. (London)*, Vol. 51, No. 407, p. 224, 1939.
41. Godfrey, T. G., Fulkerson, W., McElroy, D. L., and Moore, J. P. "Thermal Conductivity of  $UO_2$  and Armco Iron by a Radial Heat-Flow Apparatus," *Proc. 3rd Annual Thermal Conductivity Conference*, Vol. 1, p. 113, Oak Ridge, Tennessee, October 1963.
42. Feith, A. D. "Thermal Conductivity of  $UO_2$  by a Radial Heat-Flow Method," *Proc. 3rd Annual Thermal Conductivity Conference*, Vol. 1, p. 162, Oak Ridge, Tennessee, October 1963.
43. Styhr, K. H. "Thermal Conductivity Measurements Between 1000°C and 2500°C," *Proc. 3rd Annual Thermal Conductivity Conference*, Vol. 1, p. 428, Oak Ridge, Tennessee, October 1963.
44. Flynn, D. R., and Robinson, H. E. "The National Bureau of Standards High-Temperature Absolute Cut-Bar Apparatus," *Proc. 3rd Annual Thermal Conductivity Conference*, Vol. 1, p. 353, Oak Ridge, Tennessee, October 1963.
45. Flynn, D. R. "Thermal Guarding of Cut-Bar Apparatus." Unpublished Proceedings of the Conference on Thermal Conductivity Methods held at Battelle Memorial Institute, Columbus, Ohio, October 1961.
46. Laubitz, M. J. "Thermal and Electrical Properties of Armco Iron at High Temperatures," *Can. J. Phys.*, Vol. 38, No. 7, pp. 887-907, 1960.
47. Powell, R. W., Hickman, M. J., Tye, R. P., and Woodman, M. J. "Armco Iron as a Thermal Conductivity Standard." Part I, "Review of Published Data." Part II, "New Determinations at the National Physical Laboratory," *Progress in International Research on Thermodynamic and Transport Properties*, Edited by J. F. Masi and D. H. Tsai, p. 454, The American Soc. of Mech. Eng. and Academic Press, New York, 1962.
48. Bowen, M. D. "The Measurement of Thermal Conductivity at High Temperatures." Masters Thesis in Mechanical Engineering, Georgia Institute of Technology, 1959.
49. *Thermal Conductivity of Fireclay Refractories*, ASTM Standard C202-47.
50. Parker, W. J., Jenkins, R. J., Butler, C. P., and Abbot, G. L. "Flash Method of Determining Thermal Diffusivity, Heat Capacity and Thermal Conductivity," *J. Appl. Phys.*, Vol. 32, pp. 1679-1684, 1961.
51. Cowan, R. D. "Pulse Method of Measuring Thermal Diffusivity at High Temperatures," *J. Appl. Phys.* Vol. 34, pp. 926, 927, 1963.
52. Deem, H. W., and Wood, W. D. "Thermal Diffusivity Measurements Using a Laser," *Proc. 3rd Annual Thermal Conductivity Conference*, Vol. 2, p. 794, Oak Ridge, Tennessee, October 1963.
53. Rudkin, R. L. "Thermal Diffusivity Measurements on Ceramics at High Temperatures," *Proc. 3rd Annual Thermal Conductivity Conference*, Vol. 2, p. 794, Oak Ridge, Tennessee, October 1963.
54. Cape, J. A., and Lehman, G. W. "Temperatures and Finite Pulse-Time Effects in the Flash Method for Measuring Thermal Diffusivity," *J. Appl. Phys.*, Vol. 34, pp. 1909-1913, 1963.
55. Kennedy, W. L., Sidles, P. H., and Davidson, G. C. "Thermal Diffusivity Measure-

- ments on Finite Samples," *Advan. Energy Conversion*, Vol. 2, pp. 53-58.
56. Kennedy, W. L. U.S. Atomic Energy Commission Report, IS-137, Iowa State University, Ames, Iowa.
  57. Stansbury, E. E. "The Adiabatic Calorimeter," *Proc. 3rd Annual Thermal Conductivity Conference*, Vol. 2, p. 639, Oak Ridge, Tennessee, October 1963.
  58. West, E. D., and Ginnings, D. C. "An Adiabatic Calorimeter for the Range 30° to 500°C," *NBS J. Res.*, Vol. 60, pp. 309-316, 1958.
  59. Ginnings, D. C., and Corruccini, R. J. "An Improved Ice Calorimeter—The Determination of Its Calibration Factor and the Density of Ice at 0°C," *NBS J. Res.*, Vol. 38, p. 583, 1947.
  60. Furukawa, G. T., Douglas, T. B., McCoskey, R. E., and Ginnings, D. C. "Thermal Properties of Aluminum Oxide from 0°C to 1200°K," *NBS J. Res.*, Vol. 57, pp. 67-82, 1956.
  61. Douglas, T. B. "The Dropping-Type Calorimeters," *Proc. 3rd Annual Thermal Conductivity Conference*, Vol. 2, p. 661, Oak Ridge, Tennessee, October 1963.
  62. Southard, J. C. "A Modified Calorimeter for High Temperatures. The Heat Content of Silica, Wollastonite and Thorium Dioxide above 25°C," *J. ACS*, Vol. 63 pp. 3142-3146, 1941.
  63. Kirillian, V. A., Sheindlin, A. E., and Chekhovskoy, V. Y. "Enthalpy and Heat Capacity of Some Solid Materials at Extremely High Temperatures." International Symposium on High Temperature Technology. Proceedings to be published by Butterworths Publications, Ltd.
  64. Klein, Arthur H. *Fortran Programs for Thermal Diffusivity Calculations*, U.S. Atomic Energy Commission Report IS-883, Iowa State University, Ames, Iowa.
  65. *True Stress-Strain Properties of Brittle Materials to Very High Temperatures*, U.S. Atomic Energy Commission Report ORO 461, 1962.
  66. Some of these laboratories are Jet Propulsion Labs, Pasadena, Calif.; Argon Labs, Chicago, Ill.; Douglas Aircraft, Santa Monica, Calif.; General Electric, Evandale, Ohio; North American Aviation, Inglewood, Calif.; Southern Research Institute, Birmingham, Ala.
  67. Optical Extensometer, manufactured by Optron Corp., Santa Barbara, Calif.
  68. *Tentative Method for Compressive Strength of High-Strength Ceramic Materials*, ASTM C 528-63T, ASTM Standards Part 13, 1964.
  69. Spinner, S., and Tefft, W. E. "A Method for Determining Mechanical Resonance Frequencies and for Calculating Elastic Moduli from These Frequencies," *Proc. ASTM*, Vol. 61, 1961.
  70. Johnson, S. O., and Dull, R. B. *A Method For Determining Young's Modulus of Graphite at Elevated Temperatures*, WADD-TR 61-72, Vol. XXIII, Air Force Materials Laboratory, Wright-Patterson Air Force Base, Ohio, February 1964.
  71. Nielsen, T. H., and Leipold, M. H. *Thermal Expansion in Air of Ceramic Oxides to 2200°C*, JPL Technical Report 32-297, California Institute of Technology, Pasadena, California, October 1962.
  72. Grain, C. F., and Campbell, W. J. *Thermal Expansion and Phase Inversions of Six Refractory Oxides*, U.S. Bureau of Mines Report 5982, 1962.
  73. Smith, D. K. *Norelco Reporter*, Vol. 10, No. 1, 1963.
  74. Buckley, E. F. "Outline of Evaluation Procedures for Microwave Anechoic Chambers," *Microwave J.*, pp. 63-75, August 1963.
  75. *Evaluation of Radar Cross-Section Ranges for Continuous-Wave Operation*, Emerson and Cuming, Inc., March 1964.
  76. Emerson, W. H., and Brownell, F. P. *State-of-the-Art Anechoic Backscatter Ranges*, M.I.T. Lincoln Laboratory Radar Reflectivity Measurements Symposium, June 1964, Advance Record published as Rome Air Development Center Technical Documentary Report No. RADC-TDR-64-25, Vol. 1, pp. 50-65, April 1964.
  77. Hiatt, R. E., Knott, E. F., and Senior, T. B. A. *A Study of VHF Absorbers and Anechoic Rooms*, The University of Michigan Report No. 5391-1-F, p. 60, February 1963.
  78. Ferris, J. E., Hiatt, R. E., Senior, T. B. A., and Shamp, D. J. *On the Design of a*

NASA-MSA Antenna Facility, The University of Michigan Report No. 05921-1-F, pp. 52-53, August 1963.

79. Iby, Frank J. *Anechoic Chamber Design, Construction and Test of Model, Using Light Beams to Simulate Microwave Energy*, Lockheed Aircraft Corp., Missile Systems Div., Palo Alto, California, Report MSD 2112, March 15, 1957.
80. Smith, Chester L., and Gargaro, Dolores T. "Design of Two Anechoic Chambers." Raytheon Manufacturing Co., Missile Systems Div., Bedford, Massachusetts, *Proc. OSU-WADC Radome Symposium*, Vol. 1, WADC-TR-58-272, June 1958.
81. U.S. Patent No. 3,113,271. E. F. Buckley, Emerson and Cuming, Inc., Canton, Massachusetts.
82. Wohlers, R. J. *Indoor Range Design*, Rome Air Development Center Technical Documentary Report No. RADC-TDR-64-25, Vol. 1, pp. 257-288, April 1964.
83. U.S. Patent No. 3,120,641. E. F. Buckley, Emerson and Cuming, Inc., Canton, Massachusetts.
84. Radar Reflectivity Measurements Symposium, Rome Air Development Center Technical Documentary Report No. RADC-TDR-64-25, Vol. 2, Section VII, Range Descriptions, pp. 197-372.
85. *Antenna Pattern Range Evaluation by Pattern Comparison Method*, Booklet published by Emerson and Cuming, Inc., August 1963.
86. Buckley, E. F. "The Design and Evaluation of Microwave Anechoic Chambers," Paper presented at Joint Meeting of IRE-PGME, PGMTT and PGAP, Chicago, Illinois, April 8, 1960, pp. 14-16 (available from Emerson and Cuming, Inc., Canton, Massachusetts).

## **CHAPTER 6**

### **HYPERSONIC RADOME APPLICATIONS**

*by R. W. SUTTON  
The Boeing Company  
Seattle, Washington*

# SYMBOLS

A	Area	$\dot{q}$	Heating rate, Btu/ft <sup>2</sup> -sec
C	Concentration (moles/cc); ratio = $\frac{\rho_w \mu_w}{\rho_0 \mu_0}$	$\dot{q}_{LFP}$	Laminar flow, flat-plate heating rate, Btu/ft <sup>2</sup> -sec
$C_p$	Specific heat at constant pressure	$\dot{q}_{Ls}$	Laminar flow, stagnation heating rate, Btu/ft <sup>2</sup> -sec
$C_L$	Laminar concentration	$\dot{q}_{TRF}$	Turbulent flow, flat-plate heating rate, Btu/ft <sup>2</sup> -sec
D	Drag = $\frac{1}{2} \rho_\infty V^2 C_D A$ ; diameter	$\dot{q}_{TS}$	Turbulent flow, stagnation heating rate, Btu/ft <sup>2</sup> -sec
E	Modulus of elasticity	$\dot{q}_{Tmax}$	Maximum turbulent heating rate near the sonic point, Btu/ft <sup>2</sup> -sec
IPD	Insertion phase difference	r	Radius
K	Thermal conductivity	$r_e$	Radius of earth, naut. mi
M	Thermal shock merit index	$r_i$	Radius of segment i (to centroid) from center of cylinder
$N_e$	Number of electrons/meter <sup>3</sup>	t	Time, sec
R	Radius; range	$\tan \delta$	Loss tangent
$R_0$	Nose tip radius	x	Distance, ft
T	Temperature	$x_i$	Thickness of segment i
$T_{max}$	Equilibrium temperature	$\alpha$	Angle of attack, degrees; coefficient of thermal expansion; attenuation constant
$T_w$	Wall temperature	$\beta$	Phase constant
V	Flight velocity, ft/sec	$\gamma$	Ratio of specific heats; reentry angle
$V_i$	Initial velocity prior to reentry, ft/sec	$\delta$	Tensile strength, psi
$V_\infty$	Free-stream velocity, ft/sec	$\epsilon$	Density ratio across the shock = $\rho_x/\rho_0$ ; emittance; dielectric constant
W	Weight, lb	$\epsilon_0$	Dielectric constant of free space
$W/C_D A$	Ballistic parameter	$\epsilon_r$	Dielectric constant, relative
$W/C_L A$	Glide parameter	$\eta$	A constant relating atmospheric density to altitude = $4.15 \times 10^{-6}/ft^{-1}$
X	Distance from tip, ft	$\lambda$	Wavelength of incident radiation
Z	Polarization	$\mu$	Poisson's ratio
a	Inside radius of cylinder; half thickness of plate	$\nu$	Electron collision frequency
b	Outside radius of cylinder	$\rho$	Density, lb/ft <sup>3</sup>
$b_{min}$	Minimum acceptable thickness of ablative window, ft	$\rho_{sl}$	Density at sea level
c	Velocity of light	$\rho_\infty$	Free-space density
e	Charge of electron, coulombs	$\sigma$	Altitude density ratio = $\rho_x/\rho_{sl}$ ; stress, psi
g	Gravitational acceleration	$\sigma_r$	Radial stress, psi
h	Altitude, ft; enthalpy, ft/sec; heat transfer coefficient	$\sigma_t$	Tangential stress, psi
$h_{eff}$	Heat of ablation, Btu/lb	$\sigma_\theta$	Angular stress, psi
$h_s$	Stagnation enthalpy, ft <sup>2</sup> /sec <sup>2</sup>	$\sigma_z$	Longitudinal stress, psi
$h_w$	Wall enthalpy, ft <sup>2</sup> /sec <sup>2</sup>	$\omega$	Signal angular frequency
i	Number of each segment; $\sqrt{-1}$	$\omega_p$	Plasma frequency
j	Segment being investigated		
k	Dielectric constant		
m	Mass of an electron, kilograms; an integer		
p	An integer		
q	Heat per unit area, Btu/ft <sup>2</sup> ; total number of segments		
$q_T$	Total heat input, Btu/ft <sup>2</sup>		

## CHAPTER 6

### HYPERSONIC RADOME APPLICATIONS

#### 6-1 INTRODUCTION

The design of a radome for a World War II aircraft was initially a challenging problem. However, by the end of the war, analytical and empirical techniques had been developed that permitted the engineer to approach the design of an aircraft radome as a routine problem. This situation changed with the development of aircraft and missiles capable of supersonic flight in the early 1950's. Their aerodynamic requirements dictated radomes with high fineness ratios. The range of incident angles seen by energy from the radar antenna striking the inner surface of the radome often ranged from  $0^\circ$  to  $75^\circ$ , making the electrical design of the radome difficult. To further complicate the problem, the aerodynamic heating associated with supersonic flight produced changes in both the physical and electrical properties of the radome material.

New materials were required that would ensure the physical integrity of the radome at the elevated temperature and that were also suitable electrically. The challenge was met by the development of polyester and epoxy laminated fiberglass radomes capable of short-term use to  $500^\circ\text{F}$  and extended use to  $400^\circ\text{F}$  (see Chapter 4, Part II). Electrical design procedures were developed to account for the changes in electrical thickness produced by temperature changes occurring during flight. The design of a radome became a compromise involving the flight profile of the vehicle, the temperature dependence of the physical and electrical properties of the radome material, and its desired (or required) boresight error, error rate, and r-f transmission characteristics. Rain erosion of the radome surface, which had been a bothersome but tolerable problem for subsonic vehi-

cles, became a subject of great concern. Resilient rain erosion boots and paint-on coatings, which had proved successful at subsonic velocities, offered little protection above Mach 2. To date, the rain erosion problem for velocities greater than Mach 2 has not been solved, except for the use of ceramic radomes (see Chapter 3).

When interceptor missile velocities began to exceed Mach 3, ceramic and glass-ceramic radomes came into use (see Chapter 4, Part I). Although their use eased the temperature problem, ceramic radomes brought with them an entirely new set of design problems. The organic resin-fiberglass laminates were relatively flexible, whereas ceramic radomes were quite brittle. The design of an attachment was a formidable problem, one that had not been encountered in fiberglass radomes. The problem of thermal shock became one of great concern, since a thermal shock failure was generally catastrophic and meant loss of the vehicle (see Paragraphs 1-1.5 and 3-5).

In spite of the problems, ceramic radomes began to appear on operational missiles in the latter 1950's and are quite widely used now.

In the mid-1950's, requirements were being generated for vehicles with earth orbital and atmospheric reentry capabilities. Such vehicles were to be of both the manned and unmanned variety, but, in either case, were to require communication systems that operated before, during, and after reentry. Again, an entirely new set of requirements and problems was generated for the radome engineer. Because of the extremely high heating rates encountered during reentry, the typical forward-mounted ogival shaped radome appeared to be ruled out. Radomes for hypersonic orbital and reentry vehicles have, with few exceptions, taken the form

of flush-mounted windows generally located well aft of the bow shock region. Because of the high heating rates, electromagnetic windows for hypersonic reentry vehicles have often been of the ablative type, wherein cooling is accomplished by allowing certain physical, chemical, and mass transfer processes to take place at the surface.

An electromagnetic design problem unique to the hypersonic vehicle is that of transmission through the plasma sheath. While not specifically a part of the electromagnetic window design, the effect of the plasma sheath is of great concern. Briefly, the plasma sheath is a layer of ionized air that covers a reentering hypersonic vehicle or, for that matter, any vehicle in the atmosphere that exceeds a velocity of about Mach 10. The thickness and density of the plasma is a function of altitude, velocity, location on the vehicle, and shape factor of the vehicle. As a simplification, the plasma sheath can be thought of as an electromagnetic window and can take on the properties of a dielectric, or even a conductor, under certain combinations of the above conditions and operating frequency.

We have discussed how radome design has progressed from the relatively simple requirements of a subsonic aircraft to the complexities of an electromagnetic window for a hypersonic vehicle. At this point, a closer look at the specific steps that should be taken in determining the requirements and approaching the solution to the design of an electromagnetic window for a hypersonic vehicle is in order.

#### **6-1.1 DETERMINATION OF THE THERMAL ENVIRONMENT**

Before any specific approach can be considered, the thermal environment in which the window will operate must be determined. This will be dependent to a great extent on the mission profile of the vehicle. If it is to be a ballistic reentry vehicle, the heating rate will be intense for a relatively short period of time. Ceramics, with the possible exception of slip-cast fused silica, cannot withstand the thermal shock caused by the high heating rate. An ablative window is, therefore, generally indicated for this type of trajectory.

If the heating rate and surface temperature

are relatively low, such as in the glide reentry and in certain orbital decay reentry profiles, a radiation cooled, nonablative window may be considered, bearing in mind the attachment and thermal shock problems associated with this type of electromagnetic window (see Paragraph 1-1.4.2).

#### **6-1.2 THE STRUCTURAL DESIGN**

Once the heating rate, total heat input, and maximum surface temperature have been established, the structural design of the window can begin. For an ablative window, the structural design consists primarily of determining the minimum acceptable physical thickness that will be sufficient to protect the antenna and other equipment behind the window when considering the heating rate, total heat input, and surface temperature. This implies that material requirements be established and materials be specified during this stage. The edge attachment design must also be considered at this time, although for typical organic resin-fiberglass ablators, the modulus of elasticity is low enough to make this a noncritical part of the design. For a nonablative window or for an ogival radome, the structural design becomes more difficult. In order to determine the ability of the window (or ogival radome) to withstand the thermal environment, the surface temperature profile, the heating rate, the thermal constants of the window material, the thermal gradient through the wall, and the edge fixity must be known. As will be shown in Paragraph 6-3.2, using certain simplifying assumptions, one can calculate the stresses imposed by the environment to determine if they are within the allowable stress limits of the material (also see Paragraph 1-2.13).

#### **6-1.3 THE ELECTRICAL DESIGN**

Assuming that at this point a structural configuration has been established that can survive the environment, the electrical design can begin. For the ablative window, a minimum acceptable thickness will have been established and may not be optimum electrically. The electrical design must consider the variable nature of an ablative window. The outside surface, which is undergoing ablation, will have con-



siderably different electrical properties than the virgin inner surface. In fact, the window can best be described electrically as a multi-layered dielectric sandwich, with each layer having a slightly different dielectric constant and loss tangent than adjacent ones by virtue of its different temperature. By using a mathematical model consisting of a finite number of layers, propagation through the sandwich can be calculated using the techniques described in Reference 8. Within the limitations imposed by the minimum thickness established by the thermal analysis, the wall thickness can be optimized to provide best performance during the most critical phase of the mission. If the window is a nonablative type, the minimum acceptable thickness will generally be a compromise between structural and electrical requirements. For best thermal shock resistance, a thin wall is desired. However, if the most desirable thickness, structurally, is not compatible with electrical requirements, a thicker wall may be specified. This is particularly true if the optimum structural thickness is near one-quarter wavelength. In this case, the thickness would be increased to approximately one-half wavelength and the structural problem calculated again. The optimum thickness can thus be established after one or two such iterations. In the case of a radome in which boresight as well as transmission characteristics are of concern, the optimization between structural and electrical thickness must of necessity be weighed in favor of the electrical requirements, bearing in mind, of course, that the primary requirement is one of survival.

Keeping in mind these introductory remarks concerning the design of radomes for hypersonic vehicles, we may now proceed to the more detailed descriptions of the various design processes (see Paragraph 2-1).

## **6-2 THE THERMAL ENVIRONMENT**

### **6-2.1 INTRODUCTION**

The design of an electromagnetic window for a hypersonic vehicle poses problems that differ considerably from those of slower vehicles. Intense surface heating rates are produced by the viscous and compressive effects of the fluid (air) in which the vehicle moves. The excessive

surface temperatures associated with these high heating rates complicate both the structural and electrical design of surface located electromagnetic windows.

Dielectric materials, such as ceramics, which are capable of withstanding high temperatures, often have high elastic moduli and expansion coefficients and cannot survive the thermal shock associated with the more severe hypersonic environments. The interface between the dielectric window and its supporting structure also presents a formidable design problem. When the expansion coefficient of the dielectric differs from that of the supporting metallic structure, careful design is required to prevent the buildup of stresses at the interface that could cause catastrophic failure of the joint.

The electrical design of an electromagnetic window for a hypersonic vehicle is complicated by the temperature dependent characteristics of most refractory dielectric materials. The performance of the window, whether a flush-mounted antenna cover or a high-finesse-ratio ogival shape, can be determined by knowledge of the dielectric constant ( $\epsilon_r$ ), loss tangent ( $\tan \delta$ ), physical thickness of the wall, and the angle of incidence at which the energy strikes the wall. All of these characteristics vary with temperature. A window designed for optimum performance at ground ambient temperature might be very much less than optimum when its temperature is 3000°F. It becomes apparent that the design of an electromagnetic window for a hypersonic vehicle requires, first, a knowledge of the range of thermal inputs and surface temperatures expected and, secondly, knowledge of the variation of the electrical and structural properties of the materials involved.

### **6-2.2 AERODYNAMIC HEATING AT HYPERSONIC VELOCITIES**

The precise determination of aerodynamic heating of a hypersonic vehicle is a task for an aerothermodynamicist. The electromagnetic window designer is, however, often called upon to make estimates of expected thermal inputs and surface temperatures. Fortunately, several excellent references (References 1 through 4) are available, giving the results of approximate aerothermodynamic analyses of various types of hypersonic vehicles subjected to a variety

of flight regimes. Much of the following information and data has been abstracted from Reference 1, *Design Procedures for Computing Aerodynamic Heating at Hypersonic Speeds*. Some of the graphical data is reproduced herein to illustrate the results.

Hypersonic vehicles fall into four general categories. These are the radiation cooled glide reentry, ballistic reentry, orbital decay reentry, and high-acceleration boost vehicles. The vehicles differ considerably in the heating rates experienced, the maximum surface temperatures encountered, and the span of time over which the heating takes place. The reentry characteristics of these vehicles as described in the above reference are quoted in the following paragraphs.

#### 6-2.2.1 Ballistic Reentry

In the ballistic reentry, the heating rate is intense (thousands of Btu/ft<sup>2</sup>-sec) for a short period of time (tens of seconds) and the reentry path angle is relatively large. In this type of vehicle, the heat is either absorbed by the heat capacity of a thick shielding material, such as copper or beryllium, or is dissipated by ablation of a surface coating. In the latter case, the kinetic energy of the vehicle is absorbed by the latent heat during the change of phase that occurs when the surface material is vaporized and carried away by the air stream.

#### 6-2.2.2 Glide Reentry

The reentry of the lifting or glide type of vehicle involves much less severe heating rates than for the ballistic type (tens of Btu/ft<sup>2</sup>-sec), but the total heat transfer quantity is actually greater because of the extremely long periods of time of flight (tens of minutes). In this case, the reentry path angle is relatively small compared with the ballistic mode angle and the heat sink or ablation techniques have not proven to be practical; therefore, a radiation cooled structure is used. Since the vehicle is exposed to high heating for such long periods, a steady state is reached in which the incoming aerodynamic convective heating equals the outgoing radiation, resulting in an equilibrium temperature of the surface. This temperature

is maintained below the limit of the surface material (approximately 3000°F) by carefully designing the vehicle shape and designating flight paths that will avoid the critical heating region.

#### 6-2.2.3 Orbital Decay Reentry

The orbital decay or low-path-angle nonlifting trajectory involves heating rates and times that fall between those of ballistic and lifting reentries. In the orbital decay mode of reentry, the vehicle in circular orbit loses energy as a result of drag and spirals to the earth. The time to reenter (~10 min.) is greater than that of the ballistic (tens of seconds) and considerably less than that of the glide (tens of minutes). For survival, the peak heating rate must be maintained near that of the glide and the total heat comparable to that of the ballistic. Analysis of the orbital decay reentry is more complicated than either of the other two modes in that neither external radiation nor transient effects may be neglected in a refined design. However, it appears that radiation cooling, heat sink, or ablation techniques may be used successfully to accomplish the mission.

#### 6-2.2.4 High-Acceleration Boost

The high-acceleration boost trajectory, like the ballistic reentry, involves intense heating for relatively short periods of time. However, the heat input is such that ablation cooling appears to be the most satisfactory way of dissipating the heat.

Four types of hypersonic flight conditions have been described. Examples of vehicles in these four categories are

1. Ballistic: Minuteman, Atlas, Titan, and Polaris warheads
2. Glide: Dyna-Soar and Asset
3. Orbital Decay: Mercury and Gemini
4. High-Acceleration: Nike Zeus, Sprint, and Hibex Boost

Figure 6-1 shows the relationship between the heating rate and reentry time for ballistic, glide, and orbital decay reentries. The high-acceleration boost condition would be similar to the ballistic curve.

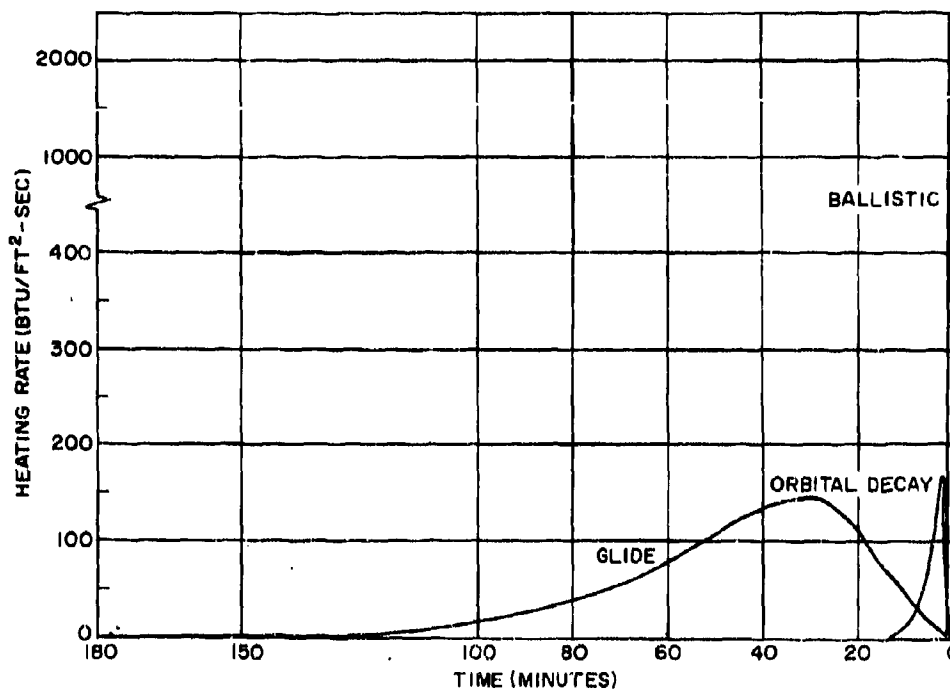


Figure 6-1. Heating Rate vs Reentry Time for Ballistic, Glide, and Orbital Decay Vehicles

### 6-2.3 HEATING RATE AND SURFACE TEMPERATURE CALCULATIONS

The calculations of heating rates and surface temperatures for any hypersonic vehicle require that certain assumptions be made concerning the nature of the air surrounding the vehicle. The equations used here are those of Reference 1 and are subject to the following conditions:

1. The shock layer is thin and sharply discontinuous. Although some "slip" flow may exist in the cases considered here, the slip-flow corrections tend to amount to small reductions in the heat transfer coefficients and can be neglected without causing appreciable errors.
2. Flow within the boundary layer may be either laminar or turbulent. Whichever gives the higher value of heating rates will be used.
3. Real gas properties are used, although the use of an ideal gas assumption gives

values approaching those obtained with the real properties.

4. Reaction at the boundary is in chemical equilibrium.

#### 6-2.3.1 Heating Rates and Surface Temperatures of Glide Reentry Vehicles

The glide reentry vehicle trajectory is characterized by a shallow reentry angle producing moderate heating rates over a relatively long period of time. Vehicles such as Dyna-Soar and Asset had swept wings with blunt leading edges and relatively blunt noses. Areas of interest for locating electromagnetic windows are the nose, the bottom surface, and the upper surface of the vehicle. Of these locations, the upper surface is the most desirable from the heating standpoint, with the nose the least desirable. Mission requirements generally dictate an antenna system with coverage below, as well as above, the vehicle; so, from this standpoint, locating the electromagnetic window on the

upper surface does not meet the requirements. The solution generally lies in providing combinations of antennas and their windows, some located on the upper surface and some on the lower. The use of the nose for an antenna location, while desirable, does not appear feasible considering the present state-of-the-art in materials. Although the above may be the case, calculation of the heat input and equilibrium temperature of the stagnation point is required before these quantities can be obtained for a flat-plate region aft of the nose.

**6-2.3.1.1 Stagnation Point Heating, Laminar Flow.** The approximate laminar-flow stagnation-point heating equation as used in Reference 1 is

$$\dot{q} = 1.068 \frac{\sigma^{0.5}}{R_0^{0.5}} \left( \frac{V_\infty}{1000} \right)^3 \left( 1 - \frac{h_w}{h_s} \right) \quad (6-1)$$

where  $R_0$  = nose tip radius, ft

$V_\infty$  = free-stream velocity, ft/sec

$h_s$  = stagnation enthalpy, ft<sup>2</sup>/sec<sup>2</sup>

$h_w$  = wall enthalpy, ft<sup>2</sup>/sec<sup>2</sup>

$\dot{q} = dq/dt$  = heating rate, Btu/ft<sup>2</sup>-sec

$\sigma$  = altitude density ratio =  $\rho_z/\rho_{sl}$

(For hypersonic flight, the approximation  $h_w/h_s \ll 1$  can be used without gross error.)

Figure 6-2 is a plot of the parameter

$$\dot{q} \frac{R_0^{0.5}}{1 - \frac{h_w}{h_s}}$$

as a function of altitude and velocity. Figure 6-3 shows typical glide vehicle trajectories for glide parameters ( $W/C_{DA}$ ) of 10, 100, and 1000. Figures 6-2 and 6-3 can be used to estimate the heating rate at the stagnation point for various combinations of glide parameter, tip radius, velocity, and altitude. As an example, assume an estimate of the stagnation heating rate is desired for a glide reentry vehicle under the following conditions:

$R_0 = 0.5$  ft     $W/C_{DA} = 100$   
velocity = 21,000 ft/sec

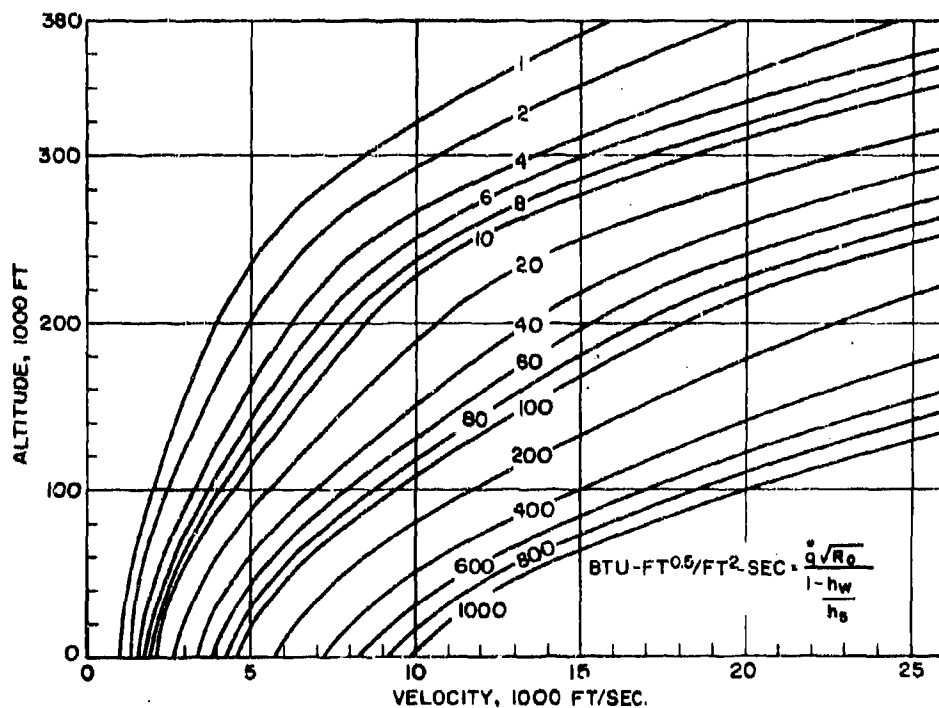


Figure 6-2. Nose Laminar Heating Rate at Stagnation Point

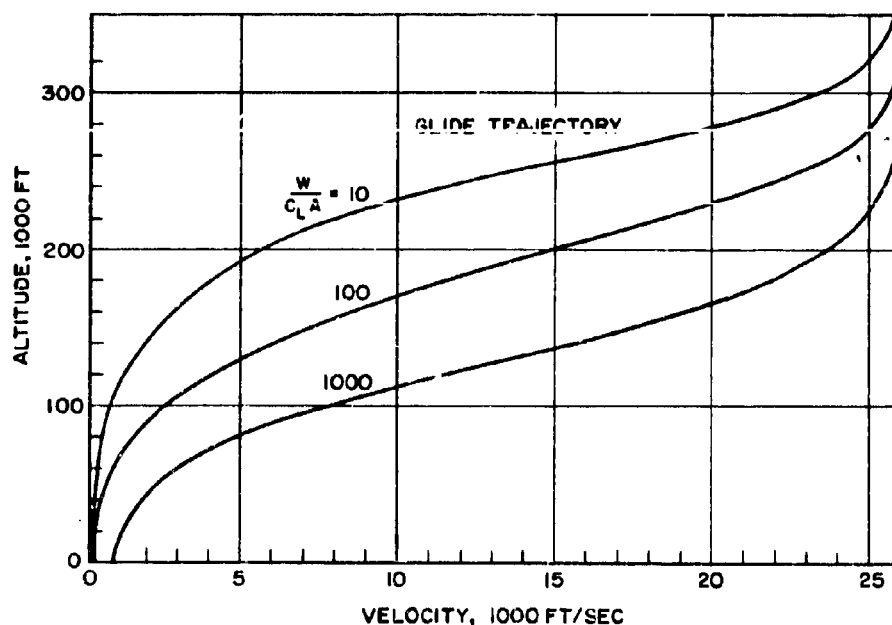


Figure 6-3. Glide Reentry Flight Spectrum

From Fig. 6-3, the altitude associated with a velocity of 21,000 ft/sec and  $W/C_L A$  of 100 is 235,000 ft. From Fig. 6-2, the value for  $\dot{q} \frac{R_0^{0.5}}{1 - \frac{h_w}{h_s}}$  associated with this altitude and velocity is approximately 80. Therefore,

$$\dot{q} = 80 / 0.5^{0.5} = 113 \text{ Btu/ft}^2\text{-sec}$$

The altitude of 235,000 ft and velocity of 21,000 ft/sec were chosen because they represent the conditions under which maximum laminar heating occurs for a typical glide reentry.

**6-2.3.1.2 Stagnation Point Temperature.** The wall temperature at the stagnation point can be calculated from

$$T_w = 1000 (\dot{q} / 0.481\epsilon)^{0.25} \quad (6-2)$$

where  $T_w$  = wall temperature, °R

$\epsilon$  = emittance of the nose material

Figure 6-4 is a plot of  $T_w$  (in °F) as a function of  $\dot{q}$  for various emittances. For the case considered in (a),  $T_w = 3700^\circ\text{F}$  for an assumed  $\epsilon$  of 0.8.

**6-2.3.1.3 Turbulent Heating Near the Sonic Point.** The equation for turbulent heating near the sonic point is

$$\dot{q} = 5.0 \frac{\sigma^{0.8}}{R_0^{0.2}} \left( \frac{V_\infty}{1000} \right)^3 \left( 1 - \frac{h_w}{h_s} \right) \quad (6-3)$$

Figure 6-5 is a plot of the parameter

$$\frac{\dot{q} R_0^{0.2}}{1 - \frac{h_w}{h_s}}$$

as a function of altitude and velocity. Figs. 6-3 and 6-5 can be used to estimate the heating rate for turbulent flow near the sonic point for various combinations of glide parameter, tip radius, velocity, and altitude. As an example, the heating rate due to turbulent flow near the sonic point is desired for the following conditions:

$$R_0 = 0.5 \text{ ft} \quad W/C_L A = 100 \\ \text{velocity} = 18,000 \text{ ft/sec}$$

From Fig. 6-3, the altitude associated with a velocity of 18,000 ft/sec and  $W/C_L A$  of 100

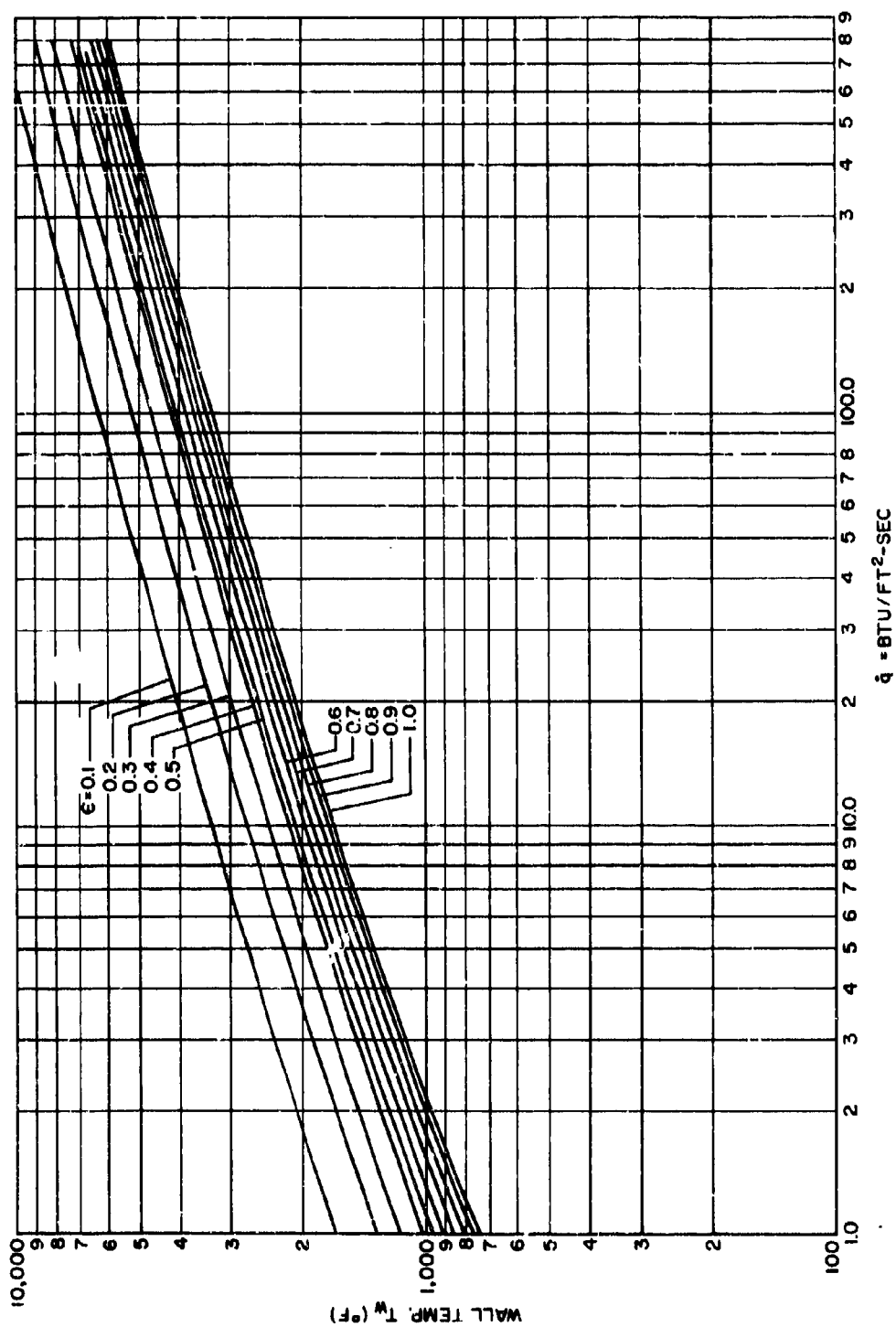


Figure 6-4.  $T_w$  as a Function of  $\dot{q}$

is 217,000 ft. From Fig. 6-5, the value for

$$\frac{\dot{q} R_0^{0.2}}{1 - \frac{h_w}{h_s}}$$

associated with this altitude is 25. Therefore,

$$\dot{q} = \frac{25}{0.5^{0.2}} = 29 \text{ Btu/ft}^2\text{-sec}$$

The velocity of 18,000 ft/sec and altitude of 217,000 ft were chosen because they represent the conditions under which maximum turbulent heating occurs for a typical glide re-entry.

It is obvious that for this particular set of conditions, the laminar heating rate exceeds the turbulent and should be used as a worst-case estimate.

A nose-mounted electromagnetic window for a vehicle of the above configuration and reentry trajectory would be required to withstand maximum surface temperatures of 3700°F at its tip (emittance of 0.8 assumed). Since the time of exposure is relatively long, backside temperatures would tend to be high. Materials are not presently available that have the combination of electrical, structural and thermal

properties required for use in such an electromagnetic window.

**6-2.3.1.4 Flat-Plate Heating. Laminar Flow.** The simplified heating rate equation for laminar flow over a flat plate aft of the stagnation point is

$$\dot{q}_{LFP} = \dot{q}_{LS} (0.0292) (R_0/X)^{0.5} \alpha^{0.667} \quad (6-4)$$

where  $\dot{q}_{LFP}$  = laminar flow, flat-plate heating rate, Btu/ft<sup>2</sup>-sec

$\dot{q}_{LS}$  = laminar flow, stagnation heating rate, Btu/ft<sup>2</sup>-sec

$X$  = distance from tip, ft

$\alpha$  = angle of attack, degrees

Consider the case of section (a) where the stagnation heating rate for laminar flow was 118 Btu/ft<sup>2</sup>-sec. The tip radius,  $R_0$ , is 0.5 ft. The heating rate into a flat plate located 5 ft aft of the stagnation and at an angle of attack of 45° is

$$\begin{aligned} LFP &= (118) (0.0292) (0.5/5)^{0.5} (45)^{2/3} \\ &= 13.2 \text{ Btu/ft}^2\text{-sec.} \end{aligned}$$

From Eq. 6-2 or Fig. 6-4, the equilibrium sur-

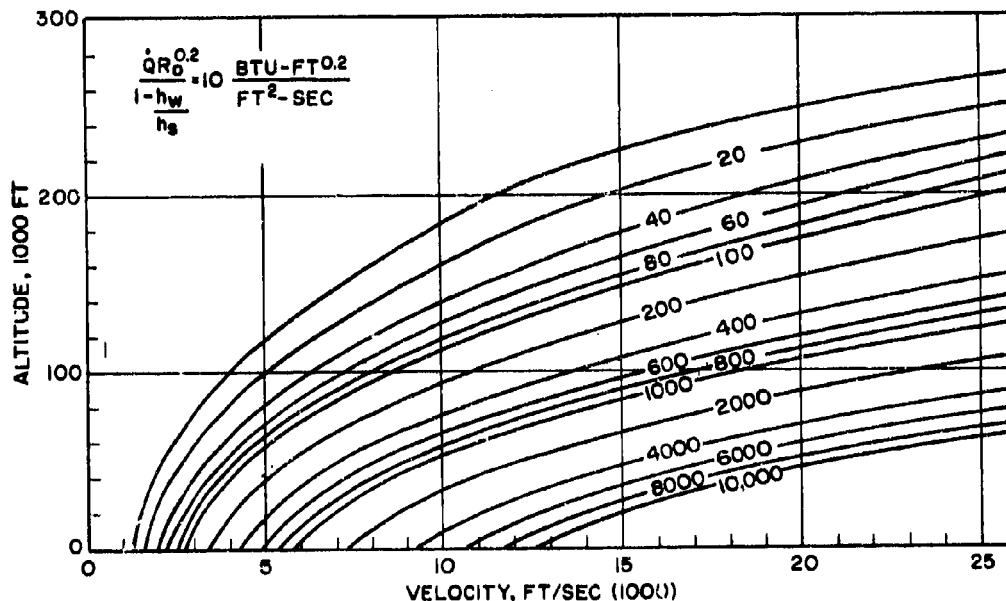


Figure 6-5. Nose Turbulent Heating Rate at Sonic Point

face temperature at the flat-plate region is 1965°F (assumed emittance of 0.8).

**6-2.3.1.5 Flat-Plate Heating, Turbulent Flow.** For turbulent flow,

$$\dot{q}_{TFP} = \dot{q}_{TS} (0.0666) \left( \frac{R_0}{X} \right)^{0.2} \frac{\alpha}{\left( 1 + \frac{11}{3} \frac{h_w}{h_s} \right)} \quad (6-5)$$

where  $X$  = distance from tip, ft

$\dot{q}_{TFP}$  = turbulent flow, flat-plate heating rate, Btu/ft<sup>2</sup>-sec

$\dot{q}_{TS}$  = turbulent flow, stagnation heating rate, Btu/ft<sup>2</sup>-sec

$\alpha$  = angle of attack, degrees

Using the case of section (c) as an example, where  $\dot{q}_{TS} = 29$  Btu/ft<sup>2</sup>-sec, and  $R_0 = 0.5$  feet,  $\dot{q}_{TFP}$  for a location 5 ft aft of the sonic point at  $\alpha = 45^\circ$  is

$$\begin{aligned} \dot{q}_{TFP} &= (29) (0.0666) (0.5/5)^{0.2} \frac{45}{\left( 1 + \frac{11}{3} \right)} \\ &= 11.8 \text{ Btu/ft}^2\text{-sec} \end{aligned}$$

The equilibrium temperature from Fig. 6-4 is 1900°F for an assumed emittance of 0.8.

The procedures and methods described in Paragraphs 6-2.3.1.1 through 6.2.3.1.5 allow an approximate value for the thermal input and surface equilibrium temperatures associated with glide reentry vehicles to be obtained. It should be recognized that these techniques are valid for estimating thermal inputs for preliminary design of electromagnetic windows and should not be considered as sufficient for determining final thermal design.

#### 6-2.3.2 Heating Rates and Surface Temperatures of Ballistic Reentry Vehicles

Although electromagnetic windows are not common on current ballistic reentry vehicles, there is no doubt that future requirements will dictate vehicle-borne radiating systems. As with the glide reentry vehicle, the preliminary design of an electromagnetic window for a ballistic reentry vehicle requires a knowledge of the thermal input to the window and its surface temperature.

**6-2.3.2.1 Turbulent Heating Near the Sonic Point.** A simplified expression for maximum turbulent heating near the sonic point for a ballistic reentry vehicle is

$$\dot{q}_{T_{max}} = 3.359 \left( \frac{V_1}{10,000} \right)^3 \left( \frac{W \sin \gamma}{C_D A} \right)^{0.8} \frac{1}{R_0^{0.2}} \quad (6-6)$$

where  $R_0$  = nose tip radius, ft

$V_1$  = initial velocity prior to reentry, ft/sec

$\frac{W}{C_D A}$  = ballistic parameter

$\dot{q}_{T_{max}}$  = maximum turbulent heating near the sonic point, Btu/ft<sup>2</sup>-sec

$\gamma$  = reentry angle

For a minimum energy trajectory,

$$\gamma = \pi/4 - R/4r_0 \quad (\text{radians}) \quad (6-7)$$

where  $R$  = range, naut. mi

$r_0$  = 3438, radius of earth in naut. mi

As an example, consider a ballistic reentry from a 1500-naut. mi range.  $\gamma$  is calculated at 39.75° and  $V_1$  is determined from:

$$\begin{aligned} V_1 &= [q\gamma_0 (1 - \tan^2 \gamma)]^{0.5} \\ &\quad (g = 32.2 \text{ ft/sec}^2) \\ &\approx 15,500 \text{ ft/sec} \end{aligned} \quad (6-8)$$

For  $R_0 = 0.25$  ft and  $W/C_D A = 100$ ,

$$\begin{aligned} \dot{T}_{max} &= 3.359 (15500/10000)^3 \\ &\quad \times (100 \sin 39.75^\circ)^{0.8} (1/0.25^{0.2}) \\ &= 456 \text{ Btu/ft}^2\text{-sec} \end{aligned}$$

Figure 6-6 shows the heating rate as a function of  $(\eta V_1 \sin \gamma)t$ , where  $V_1$  and  $\gamma$  are as before,  $\eta = 4.15 \times 10^{-5}$ /ft (a constant relating atmospheric density to altitude), and  $t$  = time from the time when maximum heating rate occurs. The approximate heating rates for any ballistic reentry can be obtained from Fig. 6-6 if the maximum rate is known.

The total thermal input based on sonic point turbulent flow can be obtained by integration of the area under the curve in Fig. 6-6, and is

$$q_T = 34.1 \left( \frac{V_1}{10000} \right)^3 \left( \frac{W}{C_D A} \right)^{0.8} \frac{1}{(R_0 \sin \gamma)^{0.2}} \quad (6-9)$$

For the case just considered,  $q_T = 4710$  Btu/ft<sup>2</sup>.



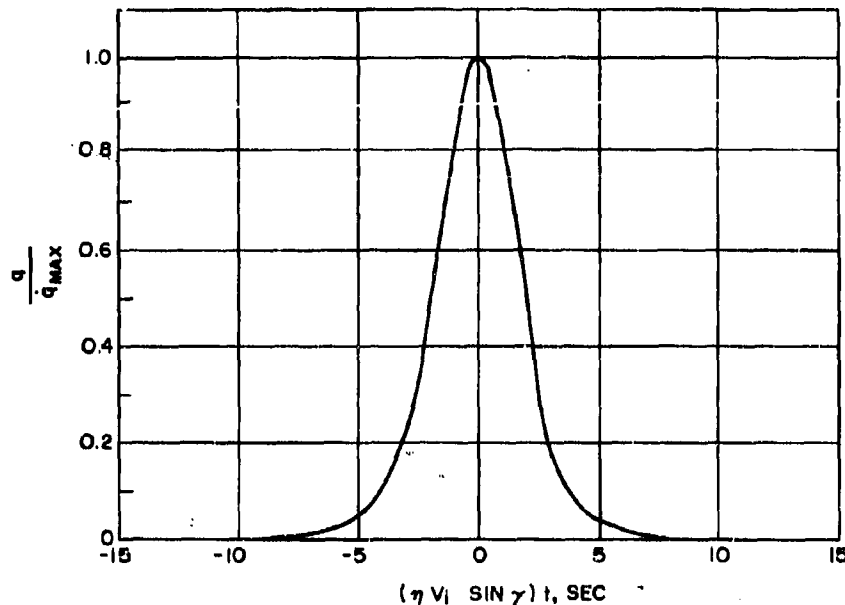


Figure 6-6. Generalized Ballistic Reentry Heating Rate for Laminar and Turbulent Flow

**6-2.3.2.2 Surface Temperatures of Ballistic Reentry Vehicles.** Ballistic reentry vehicles may be protected by either a heat sink or by ablation. Heat sinks usually consist of covering the forward portion of the vehicle with a high-heat-capacity metal, such as copper or beryllium. The thickness of the sink is designed so that the mission is completed prior to the time the surface reaches its melting point. The heat sink approach generally rules out the possibility of an electromagnetic window because of the electrical conductive nature of most suitable sink materials.

An ablative covering is the more common method of thermally protecting a ballistic reentry vehicle. The material is often a combination of organic resin and inorganic fillers. The kinetic energy of the vehicle is absorbed by the latent heat during the change of phase occurring when the surface material is vaporized and carried away by the air stream. Once ablation has initiated, the surface temperature stabilizes at a value characteristic of the material. Organic base materials, such as filled Teflon and phenolic-nylon, have surface temperatures during ablation of 1000°F to 2500°F, while inorganics such as slip-cast fused silica

ablate in the 3500°F to 5000°F range.

The problem in the thermal design of an ablative electromagnetic window is primarily that of determining the thickness required to provide protection for the substratum. This requires the establishment of an acceptable back-wall temperature. The minimum thickness required if no restrictions are put on the back-wall temperature is

$$b_{min} = q_T / \rho h_{eff} \quad (6-10)$$

where  $b_{min}$  = minimum acceptable thickness of ablative window, ft

$h_{eff}$  = heat of ablation, Btu/lb

$q_T$  = total heat input, Btu/ft<sup>2</sup>

$\rho$  = material density, lb/ft<sup>3</sup>

For a typical inorganic-filled organic resin,  $\rho h_{eff} = 2 \times 10^5$  and from Eq. 6-9,  $q_T = 4710$ ; therefore,

$$b_{min} = \frac{4710}{2 \times 10^5} = 0.0235 \text{ ft} = 0.282 \text{ in.}$$

Actual thickness is obtained by establishing an acceptable back-wall temperature and then solving the transient one-dimensional heat-flow equation for the required thickness.

### 6-2.3.3 Heating Rates and Surface Temperatures of Orbital Decay Reentry Vehicles

The orbital decay reentry mode is similar in some respects to both the glide and ballistic reentries. The peak heating rates are maintained near that of the glide whereas the total heat input is near that of the ballistic mode.

A conservative estimate of the total heat input (laminar flow assumed) to an orbital decay reentry vehicle following a typical reentry trajectory is given by:

$$q_T = 4672 (W/C_D A R_n)^{0.5} \quad (6-11)$$

This equation is valid where  $W/C_D A R_n$  does not exceed a value of about 25.0. The method generally used to achieve this to make  $R_n$  large, i.e., make the vehicle very blunt. Consider a typical case where  $W/C_D A = 100$ ,  $R_n = 10$  ft; then

$$q_T = (4672) (100/10)^{1/2} = 13,750 \text{ Btu/ft}^2$$

The minimum thickness required of a typical, filled organic resin ablative shield to protect the vehicle is, using Eq. 6-10,

$$b_{\min} = \frac{13750}{2 \times 10^5} = 0.06875 \text{ ft} = 0.825 \text{ in.}$$

As before,  $b_{\min}$  represents the minimum thickness of the ablative covering with no restrictions placed on back-wall temperature. When back-wall temperature requirements and safety factors are considered, the thickness can be several times  $b_{\min}$ . If an ablator is used, the surface temperature will be determined by the properties of the material. If radiation cooling is used, the maximum temperature can be calculated from:

$$T_{\max} = 2680 (W/C_D A R_n)^{1/4} \epsilon^{-1/4}$$

where  $T_{\max}$  = equilibrium temperature, °R  
 $\epsilon$  = emittance (assumed 0.8 here)

For the orbital decay vehicle previously considered,

$$\begin{aligned} T_{\max} &= 2680 (100/10)^{1/4} 0.8^{-1/4} \\ &= 3770^\circ\text{R} = 3310^\circ\text{F} \end{aligned}$$

The limitation on the electrical design of electromagnetic windows for orbital decay vehicles is that of radio-frequency attenuation through the ablating heat shield. This applies only to those antennas that look through the shield,

since it should be recognized that there are other, more favorable locations downstream from the shield where antennas can be located.

### 6-2.3.4 High-Acceleration Boost Vehicles

The trajectories and, hence, the heating rates and temperatures of most current vehicles of this nature are classified. About all that can be said is that the thermal input is such that ablative techniques are required and that the maximum heat inputs can exceed those of ballistic reentry vehicles.

In this paragraph, techniques have been described that allow the electromagnetic window designer to estimate surface temperatures and thermal inputs to aid in the preliminary design of windows. It cannot be stressed too often that these techniques provide only estimates, and that actual temperatures and thermal inputs must be provided by a detailed aerothermodynamic analysis of each particular case.

## 6-3 THE STRUCTURAL DESIGN OF RADOMES FOR HYPERSONIC VEHICLES

### 6-3.1 GENERAL STRUCTURAL DESIGN CONSIDERATIONS

As discussed in Paragraph 6-1, an electromagnetic window for a hypersonic vehicle can take one of several forms, depending on the type of vehicle, its mission profile, and the r-f system requirements associated with the mission. To date, most electromagnetic windows for hypersonic vehicles have been of the flush-mounted type, cooled either by ablation or radiation. Recently, it has been demonstrated that forward-mounted, aerodynamically shaped radomes are feasible for some hypersonic vehicle applications (see Reference 5). The major limitations of this configuration appear to be the severe thermal shock requirements placed on the material and the presence, generally, of a dense plasma sheath surrounding the radome.

The structural design of an ablative window, on the other hand, is relatively simple. The minimum thickness for thermal protection of the antenna located behind the window is established during the thermal environment analysis. Since most ablative materials have relatively low elastic moduli, thermal shock is not gen-

erally a problem. The main structural design problem for an ablative electromagnetic window is the design of an attachment that will maintain the window in a mechanically stable position throughout the ablation process.

The structural design of a radiation cooled, flush-mounted electromagnetic window located aft of the low shock region falls somewhere between the two other types of windows mentioned above in complexity. Ceramics are usually required because of the high surface temperatures encountered. Attachment design is particularly critical because of the danger of catastrophic thermal shock failure caused by stress concentration at the attachment points. If the emittance of the window material is less than that of the surrounding structure, the window will reach thermal equilibrium at a temperature greater than that of the surrounding structure. While not, strictly speaking, part of the structural design, surface coatings are usually required to match the emittance of the window to that of the support structure.

### 6-3.2 CALCULATION OF STRESSES IN AN ELECTROMAGNETIC WINDOW

If the thermal input and surface temperature of an electromagnetic window are known and if the physical constants of the wall material and its mounting constraints are known, the maximum stress can be calculated. This can then be compared with the allowable design values for stress in the material to determine whether it is suitable for the application (see Paragraph 1-2.13).

Consider the case of a flat, rectangular window with fixed edges subjected to a total uniform temperature change of  $\Delta T$ . The resulting stress would be compressive in nature and is calculated (Reference 6) from:

$$\sigma = \frac{\Delta T \alpha E}{(1 - 2\mu)} \quad (6-12)$$

where  $E$  = modulus of elasticity

$T$  = temperature,  $^{\circ}F$

$\alpha$  = coefficient of thermal expansion

$\mu$  = Poisson's ratio

$\sigma$  = stress, psi

For the same window with a temperature gra-

dient of  $\Delta T$  between faces, the resulting stress would be a bending stress and is calculated from

$$\sigma = \frac{\Delta T}{2} \frac{\alpha E}{(1 - \mu)} \quad (6-13)$$

The plate would be in compression on the hot side and tension on the cold side.

Each shape of flat plate (rectangular, square, circular, triangular, etc.), each mounting condition (fixed, free, partially constrained, etc.), and each temperature distribution (uniform throughout, gradient between faces, symmetrical, asymmetrical, etc.) is a variable that will influence the nature and magnitude of the stress induced. It becomes obvious, therefore that each application that one might consider is unique and must be treated as such, and that simplified general approaches using unreal assumptions must be used only as a guide in the approach to the problem's solution. This also points up the need for adequate proof testing of the design prior to its use on a flight test vehicle.

If the case of the flush-mounted flat-plate window appears to be a complex design problem, that of a forward-mounted ogival shaped radome is even more complex. As a first approximation, one can consider the radome to be made up of two sections, one cylindrical and the other a hemispherical cap.

To determine the thermal stresses in the ogival portion of the radome, consider a section perpendicular to the longitudinal axis in the form of a long circular cylinder with a concentric circular hole. Assuming that the cylinder is free to expand radially and circumferentially but is restrained longitudinally and the temperature only varies radially, the following equations can be used to evaluate the stresses in the wall:

$$\sigma_r = \frac{\alpha E}{1 - \mu} \frac{1}{r^2} \left( \frac{r^2 - a^2}{b^2 - a^2} \int_a^b T r dr - \int_a^r T r dr \right) \quad (6-14)$$

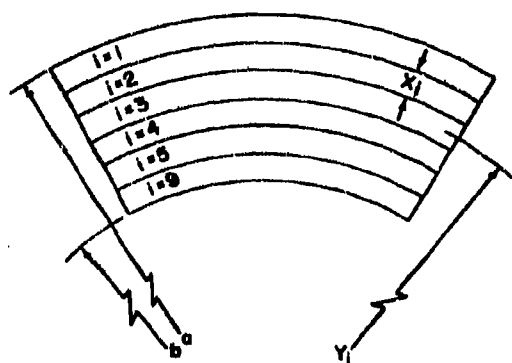
$$\sigma_\theta = \frac{\alpha E}{1 - \mu} \frac{1}{r^2} \left( \frac{r^2 + a^2}{b^2 - a^2} \int_a^b T r dr + \int_a^r T r dr - T r^2 \right) \quad (6-15)$$

$$\sigma_z = \frac{\alpha E}{1 - \mu} \left( \frac{2}{b^2 - a^2} \int_a^b T r dr - T \right) \quad (6-16)$$

where  $E$  = modulus of elasticity

$T$  = temperature  
 $a$  = inside radius of cylinder  
 $b$  = outside radius of cylinder  
 $r$  = radius of element under investigation  
 $\alpha$  = coefficient of thermal expansion  
 $\mu$  = Poisson's ratio

To make Eqs. 6-14 to 6-16 easier to use, they can be rewritten in summation form. The number of segments is varied by using the following designations:



where  $T_i$  = temperature change of segment  $i$   
 ( $T - T_0$ )  
 $q$  = total number of segments - last segment  
 $j$  = segment being investigated  
 $i$  = number of each segment ( $i = 1$  to  $9$ )  
 $r_i$  = radius of segment  $i$  (to centroid)  
 from center of cylinder  
 $x_i$  = thickness of segment  $i$

In summation form, the equations are as follows:

$$\sigma_{ij} = \frac{\alpha E}{1 - \mu} \left( \frac{r_i^2 - a^2}{r_j^2(b^2 - a^2)} \sum_{i=1}^q \Delta T_i r_i x_i - \frac{1}{r_j^2} \sum_{i=q}^j \Delta T_i r_i x_i \right) \quad (6-17)$$

$$\sigma_{ii} = \frac{\alpha E}{1 - \mu} \left( \frac{r_i^2 + a^2}{r_i^2(b^2 - a^2)} \sum_{i=1}^q \Delta T_i r_i x_i - \frac{1}{r_i^2} \sum_{i=q}^j \Delta T_i r_i x_i - \Delta T_i \right) \quad (6-18)$$

$$\sigma_{\theta i} = \frac{\alpha E}{1 - \mu} \left( \frac{2}{b^2 - a^2} \sum_{i=1}^q \Delta T_i r_i x_i - \Delta T_i \right) \quad (6-19)$$

For the hemispherical portion of the nose (at the stagnation point), an element is considered to be cut from a sphere with a hole at the center (Reference 7). The temperature was assumed to have a symmetrical distribution with respect to the spherical center and to be a function of radius only. Because of symmetry, the three stress components are the radial component,  $\sigma_r$ , and two tangential components,  $\sigma_t$ . The equations used are

$$\sigma_r = \frac{2\alpha E}{1 - \mu} \left( \frac{r^3 - a^3}{r^2(b^3 - a^3)} \int_a^b T r^2 dr - \frac{1}{r^3} \int_a^r T r^2 dr \right) \quad (6-20)$$

$$\sigma_t = \frac{2\alpha E}{1 - \mu} \left( \frac{2r^3 + a^3}{2(b^3 - a^3)r^3} \int_a^b T r^2 dr + \frac{1}{2r^3} \int_r^a T r^2 dr - \frac{1}{2} T \right) \quad (6-21)$$

where all terms are the same as previously described. These equations can also be put in the summation form as follows:

$$\sigma_{ij} = \frac{2\alpha E}{1 - \mu} \left( \frac{(r_i^3 - a^3)}{r_i^3(b^3 - a^3)} \sum_{j=q}^{i-1} \Delta T_j r_j^3 x_j - \frac{1}{r_i^3} \sum_{j=q}^{i-1} \Delta T_j r_j^3 x_j \right) \quad (6-22)$$

$$\sigma_{ii} = \frac{2\alpha E}{1 - \mu} \left( \frac{2r_i^3 - a^3}{a(b^3 - a^3)r_i^3} \sum_{j=q}^{i-1} \Delta T_j r_j^3 x_j + \frac{1}{2r_i^3} \sum_{j=q}^{i-1} \Delta T_j r_j^3 x_j - \frac{1}{2} \Delta T_i \right) \quad (6-23)$$

The stress equations as used in the summation form lend themselves to semiautomatic operation on a small computer. Temperature gradients are calculated from knowledge of the thermal input to the outer surface of the wall, the thermal properties of wall material, and its thickness. The assumption of a one-dimensional heat flow (radial) is valid for the configuration described above.

As with the flush-mounted window, approximate theoretical calculations should be used only as a guide. The final proof is whether the radome can survive a thermal shock test that approximates the time-temperature profile of the worst-case mission it will be called upon to survive.

### 6-3.3 THE ABLATIVE WINDOW

In Paragraph 6-5.5, it is mentioned that the structural design of an ablative window for a hypersonic vehicle is somewhat simpler than the design of a radiation cooled window or ogival reentry radome. The major problem consists of determining the minimum physical thickness that will provide adequate protection for the antenna. This thickness is generally arrived at during the thermal analysis and since thermal shock is not a problem for most organic ablators, the major structural design problems involve mechanical stabilization of the window. Teflon, a material that is very desirable electrically and adequate thermally for some of the less severe environments, presents some unusual problems in this respect. The high expansion coefficient of Teflon makes it very difficult to attach without some buckling occurring at the ablation temperature. Ceramic fiber reinforcement can be added to Teflon to minimize the effect of its high expansion coefficient and improve its overall performance as an ablator.

For more severe environments, the charring ablators, such as phenolic-refrasil, phenolic-nylon or phenolic-fiberglass, are often used. In addition to being easier to attach and stabilize (because of their lower expansion coefficients), they generally perform better as ablators than their thermoplastic counterparts. Their major disadvantage is, however, their relatively high electrical loss. In the process of ablation, these materials form a carbonaceous char layer at the outer surface. During flight, most of this is carried away by the slip-stream. However, that which remains appears as a lossy dielectric layer to any electromagnetic energy being propagated through it. The nature and effect of this layer has been the subject of much study, but to date there is still controversy over its effect on transmission.

Although inorganics do not generally come

under the heading of ablatives, recent work done at Georgia Tech indicates the suitability of modified slip-cast fused silica for use as a material for an ablative, nose-mounted reentry radome (Reference 5). Indications are that for certain reentry applications, a radome fabricated of slip-cast fused silica modified by the addition of  $\text{Cr}_2\text{O}_3$  can survive. This appears to be one of the few cases where a nose-mounted radome has been considered and shown to be feasible for a reentry vehicle.

### 6-3.4 THE THERMAL SHOCK PROBLEM

For a material to function as a radome under reentry conditions, it has to possess an almost unobtainable combination of physical properties. For a monolithic structure merely to survive the thermal shock associated with such an environment demands the ultimate in material performance. Therefore, thermal shock characteristics are considered of primary importance in selecting a material for a reentry radome (see Paragraphs 1-1.4.2, 1-2.13, and 3-5).

It is not always appreciated that the thermal shock resistance of a material is not only dependent upon the physical and mechanical properties of the material, but also upon the severity of the thermal shock environment. Further, the severity of the environment is not necessarily associated with temperature, but rather with the heat transfer rate to the material. This relationship can be illustrated by considering air and water at  $200^\circ\text{F}$ . Obviously, the heat transfer rate is much higher in the water than in the air. This difference would be evident by placing an ice cube into each environment. It is often desirable to compare two or three materials as to their relative thermal shock resistance. To do this, it is not uncommon to use the expression:

$$M = K\delta/E\alpha \quad (6-24)$$

where  $E$  = modulus of elasticity

$K$  = thermal conductivity

$M$  = merit index

$\alpha$  = coefficient of thermal expansion

$\delta$  = tensile strength, psi

What is overlooked in using this expression is that this relationship holds only for low heat transfer rates, or a very mild thermal shock

environment. Expressions have been developed that take into account the thermal shock environment (References 8 and 9). These expressions relate the maximum temperature from which a material can be quenched (to room temperature) to the severity of the quench. The term  $ah$  has been used to denote this severity, where  $a$  = half thickness of plate, and  $h$  = heat transfer coefficient.

If the term  $T_{0 \max}$  is the maximum temperature from which the material can be quenched, then for a mild condition (low values of  $ah$ ):

$$T_{0 \max} \propto K\delta/E\alpha \quad (6-25)$$

but for severe conditions (high values of  $ah$ ):

$$T_{0 \max} \propto \delta/E\alpha \quad (6-26)$$

These expressions emphasize the fact that a material may have satisfactory thermal shock resistance under mild thermal shock conditions by possessing a high thermal conductivity. However, it will receive essentially no benefit from this property under very severe conditions.

The thermal shock resistance of radome materials is stressed here because of the importance, from the standpoint of material selection, of specifying the thermal environment in which the material is to be used. It has often been the practice to give a single number, or merit index, to indicate the thermal shock resistance of materials using Eq. 6-24. However, as pointed out above, such a number is of value only under conditions of rather mild thermal shock, such as reentry, these numbers may not only provide meaningless data, but may be seriously misleading.

### 6-3.5 NEW TECHNIQUES

With few exceptions, the extreme environment in the nose region of a hypersonic vehicle makes the use of a conventional antenna-radome system impractical. It is necessary to replace this lost capability by devising other techniques for providing r-f sensing capability in the region of the nose. Although it is recognized that the plasma sheath is the more fundamental of the problems responsible for this lack of capability, the development of survivable dielectric on metallic-dielectric nose structures

must be pursued if the compound problem is ever to be solved.

Chapter 2 discusses techniques that show promise for use in cases where monolithic wall radomes cannot survive. The various alternatives discussed range from arrays of dielectric filled slots on a cone to geodesic lens structures integrated into the nose of a vehicle. The alternatives all suffer when compared to conventional seeker-radome configurations, particularly in scanning flexibility, and gain and side-lobe level deterioration as a function of scan angle.

While there appears to be no miracle refractory dielectric material on the horizon, the extension of r-f system capability equivalent to that of current high-speed aircraft and missiles to hypersonic vehicles (not necessarily reentry vehicles) appears to depend on the development of just such a material.

## 6-4 ELECTRICAL DESIGN OF RADOMES FOR HYPERSONIC VEHICLES

### 6-4.1 GENERAL CONSIDERATIONS

The design procedure used in the electrical design of a radome for a hypersonic vehicle varies considerably, depending upon the specific application being considered. For a flush-mounted, relatively flat window, the major requirement is usually to optimize the design for maximum transmission during the most critical phase of the mission. Boresight error is generally not a consideration in such designs. In the case of a radiation-cooled, nonablative window, the electrical thickness changes as a function of the temperature dependence of the material's dielectric properties and expansion coefficient. If these properties are known and if the wall thickness and temperature profile are known, an electrical design can be achieved that will provide maximum transmission at any desired look angle and temperature.

If the window is cooled by ablation, the electrical design becomes more complicated. The electrical thickness of the wall is still dependent upon the dielectric properties of the material and their variation with temperature. However, the temperature profile is greatly different from that of the radiation cooled window. The surface is undergoing ablation while the region

(0)	(1)	(2)	...	(m-2)	(m-1)	(m)
$k_{\epsilon_0}$	$k_{\epsilon_1}$	$k_{\epsilon_2}$	...	$k_{\epsilon_{m-2}}$	$k_{\epsilon_{m-1}}$	$k_{\epsilon_m}$
$\tan \delta_0$	$\tan \delta_1$	$\tan \delta_2$	...	$\tan \delta_{m-2}$	$\tan \delta_{m-1}$	$\tan \delta_m$
	$\leftarrow a_1 \rightarrow$	$\leftarrow a_2 \rightarrow$	...	$\leftarrow a_{m-2} \rightarrow$	$\leftarrow a_{m-1} \rightarrow$	

Figure 6-7. Electrical Design of a Flat Window

just behind the ablating layer has very steep temperature gradients. The dielectric properties of the ablating layer are very difficult to determine and generally must be estimated. In addition, the physical thickness of an ablative window can and generally does decrease appreciably during a mission whereas the physical thickness of the radiation cooled window varies only as a function of its expansion coefficient. The result is that the electrical design of an ablative window is generally based on estimates of what the window thickness will be and what the dielectric properties of the ablation layer are at the most critical part of the mission. Fortunately, the problem is somewhat mitigated by the fact that most ablative window materials have dielectric constants below 5.0 and, as such, do not cause excessive mismatch losses even though the wall thickness may be very much less than optimum. The greatest unknown by far in the design of ablative windows is the effect of the ablative layer. This is particularly true of the char forming ablators, such as the phenolics and cork compositions, where the char layer can become very lossy.

Although nose-mounted radomes are not used in current reentry vehicle design because of materials limitations and the plasma problem, some mention should be made of the problems involved in their electrical design. In this type of radome, boresight error and error rate as well as transmission are critical performance parameters. As with the flat window, all three of these parameters are functions of the electrical thickness of the wall. Therefore, an optimum design requires that the insertion phase difference (IPD) exhibited by the radome during the most critical phase of the mission be that which produces the best compromise between boresight error, error rate, and transmission. This requires an experimental pro-

gram to determine the relationship between IPD, boresight error, error rate, and transmission. This fortunately, can be done at room temperature by utilizing several radomes of differing IPD values.

#### 6-4.2 ELECTRICAL DESIGN OF A FLAT WINDOW

The transmission and reflection coefficients of a flat window can be calculated using the method presented in Reference 10. This method assumes that transmission is plane wave. The window is divided into  $m$  arbitrary layers, each being assigned a dielectric constant, loss tangent, and thickness. The following computational method (Reference 10) has proved to be highly useful when programmed on a digital computer.

It will be assumed that all of the parameters (i.e., all the dielectric constants, loss tangents, and thicknesses) are given. If the incident medium is designated by (0), and if the wave enters into the media designated by (1), (2), ..., (m) in that order, the situation is described in Fig. 6-7.

The quantities that will be given are

$$\begin{aligned} &k_{\epsilon_0}, k_{\epsilon_1}, k_{\epsilon_2}, \dots, k_{\epsilon_m} \\ &\tan \delta_0, \tan \delta_1, \dots, \tan \delta_m \\ &a_1, a_2, \dots, a_{m-1} \\ &\lambda \end{aligned}$$

where  $\lambda$  = wavelength of incident radiation.

It is now possible to determine the transmission and reflection ratios for each angle of incidence in the following manner.

1. Find  $k_0, k_1, \dots, k_m$

$$\begin{aligned} \text{where } k_p &= (2\pi/\lambda) [k_{\epsilon_p} (1 + i \tan \delta_p)]^{1/2} \\ p &= 0, 1, \dots, m \\ i^2 &= -1 \end{aligned}$$

2. Find  $Z_{01\perp}, Z_{12\perp}, \dots, Z_{m-1,m\perp}$

$$\text{where } Z_{pq\perp} = \frac{k_p \cos \theta_{2p}}{k_p \cos \theta_{2p}} = \frac{\sqrt{k_p^2 - k_0^2 \sin^2 \theta_0}}{\sqrt{k_p^2 - k_0^2 \sin^2 \theta_0}}$$

$$p = 0, 1, \dots, m-1$$

$$q = p + 1$$

3. Find  $Z_{01\parallel}, Z_{12\parallel}, \dots, Z_{m-1,m\parallel}$

$$\text{where } Z_{pq\parallel} = (k_p^2/k_0^2) Z_{pq\perp}$$

$$p = 0, 1, \dots, m-1$$

$$q = p + 1$$

In all subsequent calculations,  $Z_{pq\perp}$  should be used for perpendicular polarization and  $Z_{pq\parallel}$  should be used for parallel polarization. With this in mind,  $\parallel$  and  $\perp$  subscripts will be omitted.

4. Find  $r_{01}, r_{12}, \dots, r_{m-1,m}$   
 $r_{10}, r_{21}, \dots, r_{m,m-1}$

$$\text{where } r_{pq} = \frac{1 - Z_{pq}}{1 + Z_{pq}} = -r_{qp}$$

$$p = 0, 1, \dots, m-1$$

$$q = p + 1$$

5. Find  $t_{01}, t_{12}, \dots, t_{m-1,m}$   
 $t_{10}, t_{21}, \dots, t_{m,m-1}$

$$\text{where } t_{pq} = 1 + r_{pq}$$

$$t_{qp} = 1 - r_{pq}$$

$$p = 0, 1, \dots, m-1$$

$$q = p + 1$$

6. Find  $a_{11}, a_{22}, \dots, a_{m-1,m-1}$

$$\text{where } a_{pp} = e^{i k_p k_p \cos \theta_{2p}}$$

$$k_p \cos \theta_{2p} = \sqrt{k_p^2 - k_0^2 \sin^2 \theta_0}$$

$$p = 1, 2, \dots, m-1$$

7. Find  $r_{012}, r_{210}, t_{012}$ , and  $t_{210}$

$$\text{where } r_{012} = \frac{r_{01} + r_{12} s_{01} a_{11}^2}{1 - r_{10} r_{12} a_{11}^2}$$

$$t_{012} = \frac{t_{01} t_{12} a_{11}}{1 - r_{10} r_{12} a_{11}^2}$$

$$r_{210} = \frac{r_{21} + r_{10} s_{21} a_{11}^2}{1 - r_{10} r_{12} a_{11}^2}$$

$$t_{210} = \frac{t_{10} t_{21} a_{11}}{1 - r_{10} r_{12} a_{11}^2}$$

$$s_{01} = t_{01} t_{10} - r_{01} r_{10} = 1$$

$$s_{21} = t_{21} t_{12} - r_{21} r_{12} = 1$$

8. Find  $r_{0123}, r_{3210}, t_{0123}$ , and  $t_{3210}$

$$\text{where } r_{0123} = \frac{r_{012} + r_{23} s_{012} a_{22}^2}{1 - r_{210} r_{23} a_{22}^2}$$

$$t_{0123} = \frac{t_{012} t_{23} a_{22}}{1 - r_{210} r_{23} a_{22}^2}$$

$$r_{3210} = \frac{r_{32} + r_{210} s_{32} a_{22}^2}{1 - r_{210} r_{23} a_{22}^2}$$

$$t_{3210} = \frac{t_{210} t_{32} a_{22}}{1 - r_{210} r_{23} a_{22}^2}$$

$$s_{32} = t_{32} t_{23} - r_{32} r_{23} = 1$$

$$s_{012} = t_{012} t_{210} - r_{012} r_{210}$$

9. Find  $r_{01234}, r_{43210}, t_{01234}$ , and  $t_{43210}$

$$\text{where } r_{01234} = \frac{r_{0123} + r_{34} s_{0123} a_{33}^2}{1 - r_{3210} r_{34} a_{33}^2}$$

$$t_{01234} = \frac{t_{0123} t_{34} a_{33}}{1 - r_{3210} r_{34} a_{33}^2}$$

$$r_{43210} = \frac{r_{43} + r_{3210} s_{43} a_{33}^2}{1 - r_{3210} r_{34} a_{33}^2}$$

$$t_{43210} = \frac{t_{3210} t_{43} a_{33}}{1 - r_{3210} r_{34} a_{33}^2}$$

$$s_{43} = t_{43} t_{34} - r_{43} r_{34} = 1$$

$$s_{0123} = t_{0123} t_{3210} - r_{0123} r_{3210}$$

10. This process is continued until one finds

$$r_{012 \dots m-1}, r_{m-1,m-2}, \dots, 0,$$

$$t_{012 \dots m-1}, t_{m-1,m-2}, \dots, 0$$

where  $r_{012 \dots m-1} =$

$$\frac{r_{012 \dots m-2} + r_{m-2,m-1} s_{012 \dots m-2} a_{m-2,m-2}^2}{1 - r_{m-2,m-3}, \dots, 0 r_{m-2,m-1} a_{m-2,m-2}^2}$$

$$r_{m-1,m-2}, \dots, 0 =$$

$$\frac{r_{m-1,m-2} + r_{m-2,m-3}, \dots, 0 s_{m-1,m-2} a_{m-2,m-2}^2}{1 - r_{m-2,m-3}, \dots, 0 r_{m-2,m-1} a_{m-2,m-2}^2}$$

$$t_{012 \dots m-1} =$$

$$\frac{t_{012 \dots m-2} t_{m-2,m-1} a_{m-2,m-2}}{1 - r_{m-2,m-3}, \dots, 0 r_{m-2,m-1} a_{m-2,m-2}^2}$$

$$t_{m-1,m-2}, \dots, 0 =$$

$$\frac{t_{m-2,m-3}, \dots, 0 t_{m-1,m-2} a_{m-2,m-2}}{1 - r_{m-2,m-3}, \dots, 0 r_{m-2,m-1} a_{m-2,m-2}^2}$$

$$s_{m-1,m-2} = t_{m-1,m-2} t_{m-2,m-1} - r_{m-1,m-2} r_{m-2,m-1} = 1$$

$$s_{012 \dots m-2} = t_{012 \dots m-2} t_{m-2,m-3}, \dots, 0 - r_{012 \dots m-2} r_{m-2,m-3}, \dots, 0$$



11. The reflection and transmission ratios for the  $(m - 1)$ -ply sandwich can now be calculated using the following formulas

$$r_{012 \dots m} = \frac{r_{012 \dots m-1} + r_{m-1,m} s_{012 \dots m-1} a_{m-1,m-1}^2}{1 - r_{m-1,m-2} \dots 0 r_{m-1,m} a_{m-1,m-1}^2}$$

$$t_{012 \dots m} = \frac{t_{012 \dots m-1} t_{m-1,m} a_{m-1,m-1}^2}{1 - r_{m-1,m-2} \dots 0 r_{m-1,m} a_{m-1,m-1}^2}$$

$$\text{where } s_{012 \dots m-1} = t_{012 \dots m-1} t_{m-1,m-1} \dots 0 \\ - r_{012 \dots m-1} r_{m-1,m-1} \dots 0$$

If the media designated by (0) and (m) are such that  $k_{00} = k_{em} = 1$  and  $\tan \delta_0 = \tan \delta_m = 0$ , the squares of the magnitudes of  $r_{012 \dots m}$  and  $t_{012 \dots m}$  are equal to the reflection and the transmission coefficients, respectively. Under this assumption, the reflection and transmission coefficients and their associated phases can be found by determining

$$\begin{aligned} |r_{012 \dots m}|^2 \\ |t_{012 \dots m}|^2 \\ \gamma_{012 \dots m} \\ \delta_{012 \dots m} \end{aligned}$$

$$\text{where } r_{012 \dots m} = |r_{012 \dots m}| e^{i\gamma_{012 \dots m}} \\ t_{012 \dots m} = |t_{012 \dots m}| e^{i\delta_{012 \dots m}}$$

The insertion phase difference, IPD, is then

$$\text{IPD} = \delta_{012 \dots m} - \frac{360}{\lambda} \cos \theta_0 \sum_{i=1}^{m-1} a_i$$

The method of Reference 10 can be extended to allow optimization of transmission as a function of layer thickness. This optimization scheme has also been programmed for digital computation and has been found to be very useful (see Paragraph 2-2). The thermal profile determined in the thermal analysis and structural design can be used as a basis for dividing the wall into layers. The number of layers is a function of the slope of the temperature profile; the steeper the gradient, the more layers are required to get a good approximation of the continuously varying gradient through the wall.

The values of dielectric constant and loss tangent assigned to each layer must be predetermined by the use of a high-temperature dielectrometer (Reference 11).

#### 6-4.3 ELECTRICAL DESIGN OF NOSE-MOUNTED OGIVAL SHAPED RADOMES

As previously mentioned, the use of this type of radome for hypersonic vehicles is severely restricted because of the thermal shock and plasma problems. However, because of the probability that these problems will eventually be solved or at least reduced, some consideration must be given to the design techniques used for such radomes. One of the most successful design approaches to nose radomes that must operate over a wide temperature range is presented in Reference 12. The basic design philosophy is that once the basic radome and antenna configuration have been specified, the radome IPD is the fundamental parameter controlling the far zone fields and, consequently, the radome boresight error and transmission. By determining the optimum frequency of the radome and antenna combination in terms of IPD, the design can then be based on IPD values rather than actual boresight error transmission values. This results in considerable simplification of the design problem in that the relationship of the radome parameters (dielectric constant, physical thickness, and loss tangent) to IPD is much simpler than their relationship to the far zone field patterns or boresight error. An additional advantage of this design procedure is that the variation of IPD with temperature, which can be calculated from the material characteristics, can be used to design a radome to operate at any given temperature. For a detailed discussion of the design approach, refer to the reference.

#### 6-4.4 EFFECT OF PLASMA ON RADIO-FREQUENCY PROPAGATION

While this chapter is concerned primarily with radomes and antenna covers for hypersonic vehicles, it would be incomplete without a brief discussion of plasma effects. Reentry into the earth's atmosphere at velocities in excess of Mach 10 and below 400,000 ft is generally accompanied by the presence of ionized air covering the vehicle and extending aft into the wake region. The level, thickness, and uniformity of the ionized air about the vehicle vary considerably over its surface. The air at the stagnation region on the nose is normally

more intensely ionized, although relatively thin, whereas the regions further aft are less dense but normally much thicker. The presence of free electrons in the ionized air behind the shock wave is responsible for attenuation of radio-frequency signals, antenna pattern distortion, voltage breakdown, and coupling between antennas in close proximity in the plasma sheath. These effects result from the very substantial change in the conductivity of the air in the presence of these charged particles.

Ballistic reentry vehicles generate relatively strong shock waves with accompanying high levels of ionization. These shocks, however, are generally thinner than those for a glide reentry vehicle. Reentry time is but a few minutes with surface ranges of a few hundred miles.

Glide reentry vehicles generate relatively weaker shock waves and therefore lower levels of ionization. Shock layers are relatively thick compared to the ballistic types. Reentry intervals range from 15 minutes to beyond an hour's time, depending upon glider design parameters and the angle of attack to the free stream. These vehicles exhibit much greater changes in the ionization level over their surfaces than do ballistic vehicles, particularly for the region aft of the nose cap. This results because of the lift and control surfaces, such as the wings and rudders, which generate oblique shock patterns over surface regions that are free from the strong bow shock.

The occurrence of radio-frequency "black-out" at 220 mc and 5.0 gc is commonly experienced with ballistic missiles. Theoretical calculations for glide reentry vehicles, such as Dyna-Soar and Asset, indicate probable satisfactory performance in the general frequency range of X-band and higher frequencies. The theory has been borne out by an Asset flight in which X-band communication was maintained all the way from liftoff to splash-down, including a full 10 min. of glide reentry. Injection of Asset into the glide reentry took place at 203,000 ft with the vehicle traveling at 16,000 fps.

#### 6-4.4.1 Prediction of R-F Performance in a Plasma Environment

As a rather useful oversimplification of the situation, the plasma sheath can be thought of

as an electromagnetic window through which r-f signals, passing to and from the vehicle, must propagate.

The striking difference between the plasma sheath and an ordinary electromagnetic window is the wide range of values that the attenuation and phase constants of a plasma may assume. The attenuation and phase constants of a plasma may be expressed by:

$$\alpha = \frac{\omega}{\sqrt{2}c} \sqrt{\left\{ -\epsilon_r + \sqrt{\left[ \epsilon_r^2 + \frac{\nu^2}{\omega^2} (1 - \epsilon_r)^2 \right]} \right\}} \quad (6-27)$$

$$\beta = \frac{\omega}{\sqrt{2}c} \sqrt{\left\{ \epsilon_r + \sqrt{\left[ \epsilon_r^2 + \frac{\nu^2}{\omega^2} (1 - \epsilon_r)^2 \right]} \right\}} \quad (6-28)$$

$$\text{where} \quad \epsilon_r = 1 - \frac{\omega_p^2}{\nu^2 + \omega^2} \quad (6-29)$$

and  $c$  = velocity of light

$\alpha$  = attenuation constant

$\beta$  = phase constant

$\nu$  = electron collision frequency

$\omega$  = signal angular frequency

$\omega_p$  = plasma frequency

Reference 13 presents the graphs of the normalized attenuation and phase constants of a plasma as functions of collision frequency and signal angular frequency. These are shown in Figs. 6-8 and 6-9. Figure 6-8 is divided into four regions of interest, all of which can occur in reentry plasmas. Region I is characterized by an attenuation that decreases with increasing  $\omega$  and increases with increasing  $\nu$ . In Region II, attenuation is relatively constant with  $\omega$  and  $\nu$ , and is several orders of magnitude greater than that of Region I. In Region III, attenuation increases slowly with increasing  $\omega$  and decreases with increasing  $\nu$ . In Region IV, attenuation is essentially independent of  $\omega$  but decreases with increasing  $\nu$ . Figure 6-9 is the companion graph illustrating the dependence of phase constant,  $\beta$ , on collision frequency and signal angular frequency. Again, the graph is divided into regions. Region I is characterized by  $\beta/\omega_p$ , which varies linearly with increasing  $\omega/\omega_p$ , but is independent of  $\nu$ . This corresponds to the free-space value. In region II,  $\beta/\omega_p$  varies rapidly with both  $\nu/\omega_p$  and  $\omega/\omega_p$ . Region II is

characterized by high values of reflection coefficient and, hence, poor transmission. Region III shows a  $\beta/\omega$ , decreasing with increasing  $\nu/\omega$ , and increasing with increasing  $\omega/\omega_p$ . The characteristics of Region III can vary all the way from those of free space, such as Region I, to those of a highly reflective medium, such as Region II.

As seen in Figs. 6-8 and 6-9, the propagation properties of a plasma can take on the characteristics of a lossy dielectric, a conductor, or free space, depending upon the plasma critical frequency,  $\omega_p$ , and the mean electron collision frequency. The plasma frequency is related to the electron density by:

$$\omega_p = (N_e e^2 / \epsilon_0 m)^{1/2} \quad (6-30)$$

where  $N_e$  = number of electrons/meter<sup>3</sup>  
 $e$  = charge of electron, coulombs  
 $m$  = mass of an electron, kilograms  
 $\epsilon_0$  = dielectric constant of free space

The collision frequency and electron density are both temperature-dependent variables. In order to obtain  $\alpha$  and  $\beta$  directly from Figs. 6-8

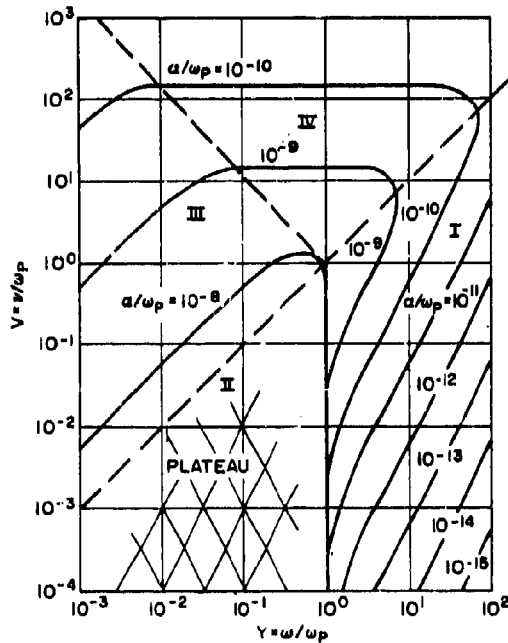


Figure 6-8. Normalized Attenuation Constant as a Function of Normalized Collision Frequency and Wave Frequency

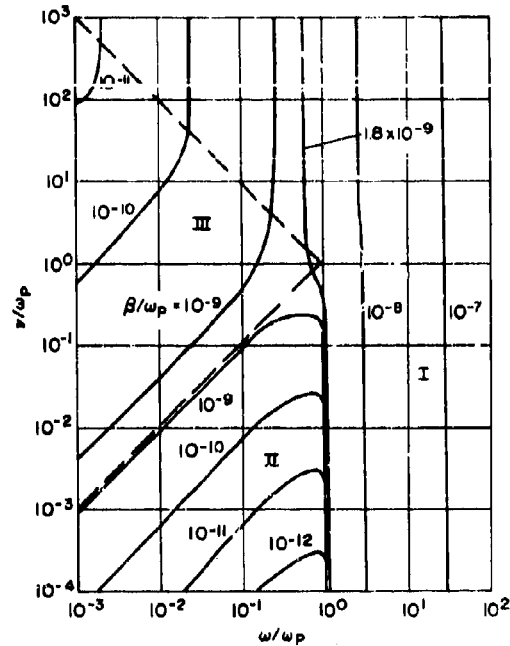


Figure 6-9. Normalized Phase Constant as a Function of Normalized Collision Frequency and Wave Frequency

and 6-9, it is necessary to know the collision frequency and plasma frequency (or electron density) for the aerothermodynamic situation being considered. Reference 14 presents a series of graphs to obtain values for the electron density and collision frequency of shocked air as functions of temperature and air density ratio. The data are divided into two categories: (1) that in which the aerothermodynamic parameters are known and (2) that in which only altitude and velocity are known. With Figs. 6-8 and 6-9 and the appropriate graphs from Reference 14, values for  $\alpha$  and  $\beta$  can be calculated. The problem is then resolved into the one familiar to the radome designer, i.e., propagation through a material with a complex propagation constant.

#### 6-4.4.2 Inhomogeneous Plasmas

As with a radome wall, the plasma layer is often inhomogeneous. The case of a plasma layer with gradients in the direction of propagation can be analyzed in much the same man-

ner as a multilayer radome. Consider the case of an aerothermodynamic profile in which the temperature and the density ratio of a plasma are functions of distance from the surface of the vehicle in the direction of wave propagation. The plasma can be described as being made up of many discrete layers, all normal to the direction of propagation. The mean temperature and air density ratio for each layer are determined from the aerothermodynamic profile. The  $\alpha$  and  $\beta$  associated with each layer can be determined as previously described. The problem is then resolved into one of calculating the transmission and reflection coefficients of a multilayered medium for which  $\alpha$  and  $\beta$  are known for each layer. This is a formidable problem without the aid of a digital computer. There are, however, numerous computer programs in existence to handle such problems, one of the better known ones is described in Reference 10 (also, see Paragraph 2.2).

#### 6-4.4.3 Plasma-Induced Antenna Pattern Distortion

The plasma sheath, like a radome, can distort the pattern of an antenna located behind it. Because of the generally inhomogeneous nature of a plasma, the complex propagation constant can vary not only in the direction of propagation, but also in the plane normal to the direction of propagation. Since the thickness of the plasma may also vary over the surface of the vehicle, serious phase errors, and hence, pattern distortion can occur. One can think of the plasma as causing random variations in the amplitude and phase distribution of the antenna. The far-field pattern of the antenna when observed from beyond the plasma appears as the far-field pattern of a source whose amplitude and phase distribution is a combination of that of the original source and the modification caused by the presence of the plasma.

The problem of the effect of a plasma on the radiating characteristics of antennas has been investigated both experimentally and theoretically (References 15 to 17). Figure 6-10 (Reference 16) shows the effect of a helium plasma on the far-field radiation pattern of a horn antenna at 9.7 gc. The most significant feature is a pronounced minimum observed at normal incidence, which becomes more predominant with increasing plasma density.

Figure 6-11 shows patterns of a slot antenna covered with a simulated isotropic plasma (Reference 17). The simulation technique utilizes a tank filled with low-loss oil as the propagation medium. A plasma is simulated by covering the slot antenna with a dielectric material (in this case, styrofoam) whose dielectric constant is less than that of the oil in which it is immersed. This, then, is analogous to the slot antenna in free space covered with a plasma

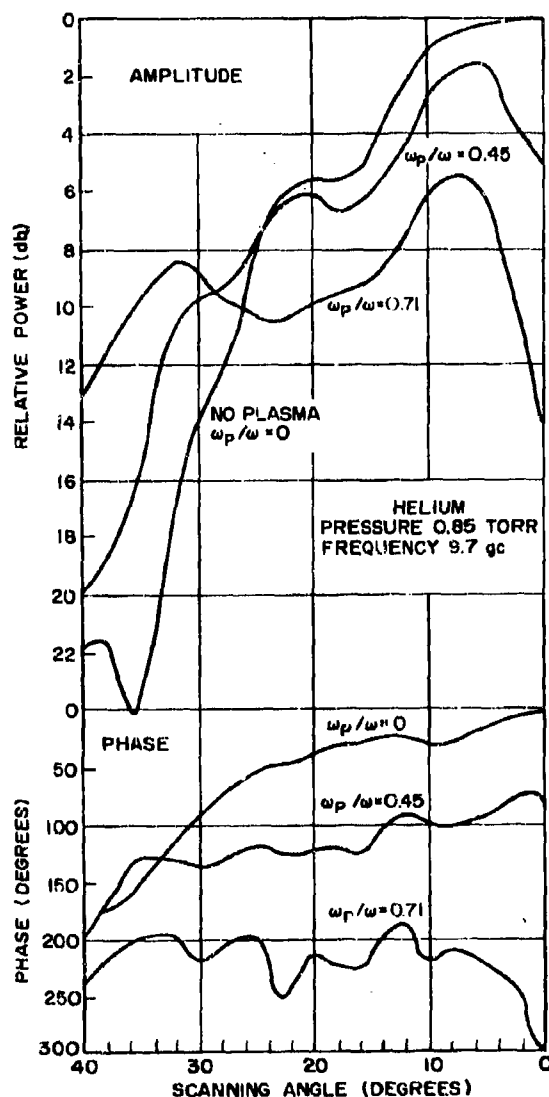
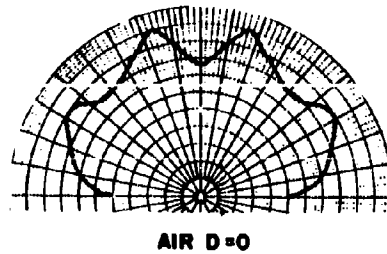


Figure 6-10. Effect of Helium Plasma at X-Band on Far-Field Radiation Pattern of Horn Antenna

FREQ. 4.0gc  
 SLOT ANTENNA  
 VERTICAL POLARIZATION  
 $\theta = 90^\circ$   
 $\phi$  = VARIABLE  
 D = PLASMA THICKNESS



OIL

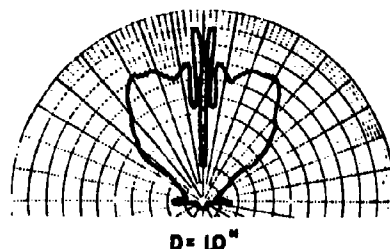
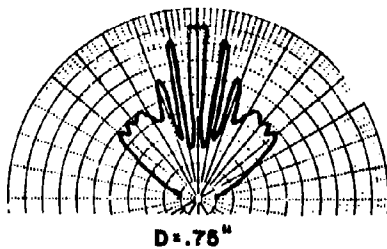
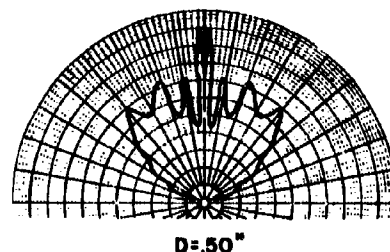
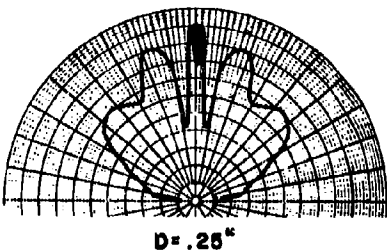
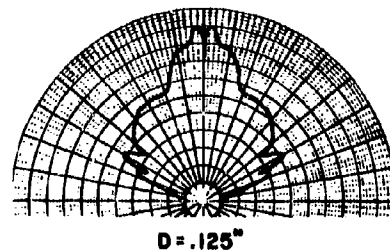
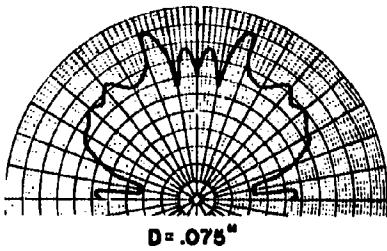
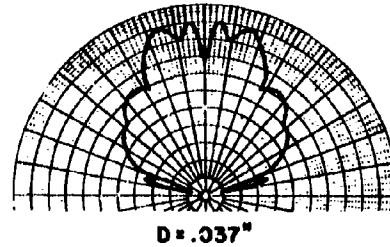
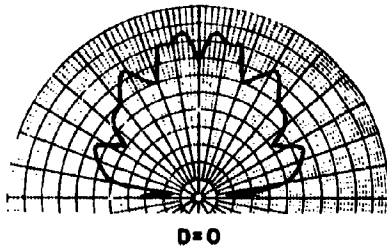


Figure 6-11. Patterns of Slot Antenna Covered with Simulated Isotropic Plasma

slab with a dielectric constant less than unity. The antenna pattern is obtained by measuring the field about the antenna in the oil-filled tank. The inside of the tank is lined with absorber material to prevent reflections from the tank walls. This simulation technique permits a wide range of plasma conditions to be studied. The major limitations are that materials for simulating very lossy plasmas or plasmas with negative dielectric constants are not available.

#### 6-4.4.4 Alleviation of Plasma Effects on R-F Propagation

Techniques for alleviating or eliminating signal attenuation in the presence of a plasma have been the subject of concern and study since the late 1950's. Among the techniques that have been considered are:

1. The use of radio frequencies higher than the plasma resonance frequency to decrease plasma attenuation to satisfactory system levels.
2. The use of sharply pointed reentry bodies to generate a thin shock layer with low overall attenuation.
3. The injection of fluids that decrease the electron density by attacking electrons and/or forcing their recombination with positive ions.
4. The use of aerodynamic spikes on the nose of a reentry vehicle to produce a thin shock layer, which is also cooled by gas injection.
5. The use of a steady magnetic field in the direction of propagation to obtain an efficient propagation mode at operating frequencies below plasma resonance.

**6-4.4.4.1 Operating Frequency Above Plasma Resonance.** The use of an operating frequency above plasma resonance is generally the simplest way of solving the plasma attenuation problem, if the plasma density is such that reasonable radio frequencies can be used. During the X-20 (Dyna-Soar) program, detailed studies were conducted for determining regions of low electron densities that might also be suitable for antenna locations. Consideration was given to structural requirements, weight, volume, and probability of good pattern coverage. Antenna locations on the lower surface were chosen, outboard from the vehicle's cen-

terline and near the wing's leading edge. To meet the requirement of omnidirectional coverage, top-mounted antennas were used in conjunction with the bottom surface antennas.

Signal attenuation studies indicated that attenuation levels of 40 to 70 db would be encountered in penetrating the vehicle's plasma sheath, requiring an impractically large airborne transmitter.

The SHF band (10.4 gc to 13.5 gc) was considered and, after a thorough study, was selected for the X-20 communications system. Radio blackout for the X-20, using the SHF communications system would be expected only for high angles of attack ( $40^\circ$  to  $50^\circ$ ) and would not normally be encountered at normal angles of attack ( $30^\circ$ ).

The results of the plasma sheath study for the X-20 program are included in Reference 18.

**6-4.4.4.2 Sharply Pointed Reentry Bodies.** This concept employs a low cone-angle, equiaxial, symmetrical, cone-shaped body incorporated into the forward tip of the vehicle's nose cap. It functions by reducing the bow shock at the tip to a thin ionized cover, with the antenna incorporated within the cone so that it propagates through the electrically thin shock wave. This method has been used successfully in providing telemetry transmission at 200 mc from a reentering target vehicle nose cone (Reference 19).

**6-4.4.4.3 Injection of Fluids Into the Boundary Layer.** This approach reduces the plasma density on the vehicle's surface by one or both of the following mechanisms: (1) cooling the gas, thereby causing electrons to recombine with positive ions, and (2) attaching electrons to molecules, thereby reducing their influence on the electrical conductivity and, thus, on electromagnetic propagation.

The injection of electron acceptor additives, such as fluorine, has been considered as a method of reducing the electron density in the plasma layer. In general, the improvement provided by this technique has been insufficient to justify the cost and complexity of the system. Cooling, however, has an important effect in decreasing the electron density, and any fluid with a high heat capacity and high ionization potential would be useful. Liquid water, for example, if it could be injected behind the

shock front so as to cool the plasma about an antenna, would require feasible rates of water injection. Results of recent test flights on a vehicle using water injection into the plasma layer indicate complete alleviation of plasma attenuation at 200 mc.

**6-4.4.4.4 Aerodynamic Spikes.** The injection of a gas along the axis of a hollow nose-mounted probe into the free stream produces a thin shock layer of cooled gas about the probe resulting in low, ionized gas density in the vicinity of the probe. Utilization of this concept has been suggested, with the probe designed for use as a telemetry antenna. This approach combines the techniques of cooling by injection of a gas or liquid into the boundary layer and providing a thin shock layer by use of a sharply pointed protrusion, in this case, the gas jet.

**6-4.4.4.5 Steady Magnetic Field.** The principle of propagation in magneto-ionic media has been understood since at least 1927, when Appleton published his magneto-ionic theory. The application then was propagation in the ionosphere in the presence of the earth's magnetic field. The longitudinal magnetic field approach for the penetration of a plasma has recently gained attention in connection with propagation in the "whistler" mode. This approach functions by establishing particular propagation modes that can efficiently transmit signal energy in magneto-ionic media at communication frequencies below the plasma resonance of the ionized gas.

The first definitive laboratory verification of propagation in the whistler mode demonstrated, under carefully controlled conditions, the propagation of a right-hand circularly polarized wave in a plasma along a d-c magnetic field (Reference 20). As much as a 25-db difference in transmission was noted for a right-hand, circularly polarized X-band signal propagating through a strong plasma first with and then without a 4-kilogauss, parallel magnetic field. Propagation in the whistler mode has been demonstrated by numerous other sources in recent years. The only drawback to implementing the system seems to be that bulky magnets are needed to provide the strong magnetic fields required. Various techniques have been proposed using permanent magnets, electromagnets, and superconducting magnets. They all

suffer from size, weight, and, in the case of the cryogenic superconducting device, relative complexity.

It appears that, although propagation through a plasma by means of the whistler mode requires bulky magnets, this is the only available approach for transmitting through a plasma whose critical frequency is higher than the signal frequency.

## **6-5 MATERIALS FOR USE IN HYPERSONIC VEHICLE ELECTROMAGNETIC WINDOWS\***

### **6-5.1 INTRODUCTION**

The spectacular advances in aerospace technology in the last decade have been made possible, in part, by the development of new materials and the use of existing materials in new and different applications. In the field of metals, the continuing development of the superalloys and the refractory group has allowed the development of types of reentry vehicles not previously feasible. Vehicles such as Dyna-Soar and Asset are examples of structures whose survival depends upon the performance of superalloys and their oxidation resistant coatings. In ballistic missiles, the development of high-performance ablative coatings has led to missiles that are much lighter for a given range-payload product than their predecessors.

In the field of dielectric materials, materials are available that can withstand all but the most severe thermal environments associated with hypersonic vehicles. Inorganic laminates, the counterpart of the well known organic resin-fiberglass composites, offer promise as high-temperature materials without the usual drawback of an excessively high modulus of elasticity. Even organics are being developed for use at temperatures well beyond those deemed possible only several years ago. The Polybenzimidazole family and the polyamides show promise of continuous use at 100°F to 200°F above present organic resin-fiberglass laminates. Oxide ceramics with low loss tangents even at their maximum temperature limit have been developed for use beyond 3000°F. Nitrides have been developed that have operating tem-

\* See Chapter 4.

peratures beyond 3000°F and yet can be machined with ordinary carbide cutting tools.

The following paragraphs are concerned primarily with the use of dielectric materials in the design of high-temperature electromagnetic windows for hypersonic vehicles. In Paragraph 6-2, the range of temperatures to which electromagnetic windows for hypersonic vehicles are exposed was calculated. In Chapter 1 and in Paragraph 6-3, the physical properties required to withstand the stresses imposed by aerothermodynamic inputs are examined. Paragraph 6-4 indicates the necessity for materials that have low electrical loss characteristics and minimum change in dielectric constant as temperature varies.

The purpose, then, is to present the characteristics of currently available dielectric materials and to determine their suitability for electromagnetic window applications within the framework of the thermal, structural, and electrical requirements developed in the previous paragraphs.

#### 6-5.2 CERAMICS

Ceramics find application in electromagnetic windows where long-term continuous operation is required and where the thermal input is such that catastrophic thermal shock does not occur (Reference 21). Ceramic radomes are also often used for short time-of-flight missiles where the surface temperature exceeds the decomposition point of organic resin-fiberglass laminates, and

in which the critical electrical performance requirements do not permit the change in wall electrical thickness associated with an ablative radome.

Examples of current vehicles that use ceramic radomes are: Asset, which uses flush-mounted alumina radomes, and the Mauler ground-to-air missile, which uses a Pyroceram radome. Some of the specific ceramic materials and their characteristics are listed in Table 6-1.

##### 6-5.2.1 Alumina

Alumina ( $\text{Al}_2\text{O}_3$ ) is one of the most widely used of the oxide ceramic group. It is available in a range of purities from 85% to 99.9%  $\text{Al}_2\text{O}_3$ . The available range of densities varies from a low of less than 1 gm/cm<sup>3</sup> for foams to a maximum theoretical density of 3.97 gm/cm<sup>3</sup>. Alumina finds application in flush-mounted electromagnetic windows for glide re-entry vehicles and as radomes for interceptor missiles where the thermal shock environment is not too severe. Successful attachment techniques have been developed using both ceramic-to-metal brazing and mechanical clamping schemes. The electrical properties of alumina are excellent even at temperatures near its maximum short-term working limit of 3100°F. However, it should be mentioned that the change in dielectric constant from room temperature to 2500°F is sufficient to detune the signal for some applications. Alumina components are readily available on a custom fabri-

TABLE 6-1 PHYSICAL AND THERMAL PROPERTIES OF CERAMICS

Material	Flexural Strength, 10 <sup>3</sup> psi		Modulus of Elasticity, 10 <sup>6</sup> psi	Expansion Coefficient, °F 10 <sup>-6</sup>	Density, gm/cm <sup>3</sup>	Melting Temperature °F
	@ 75°F	@ 2200°F				
Alumina	40	10	50	4.35	3.97	3720
Beryllia	35	12	46	5.1	3.0	4660
Pyroceram 9606	(25 to 30)	<5	17.3	2.7	2.6	2462 (Softens)
Slip-Cast Fused Silica	(4 to 5)	10	3.8	0.3	1.9	3038
Boron Nitride	15		12	4.2	2.1	4950
Magnesia	23		40	7.7	3.57	5072
Magnesium Aluminate Spinel	20		30	3.6	3.57	3860
Fused-Silica Glass	10		10	0.3	2.2	3038



cated basis from several technical ceramic manufacturers (see Paragraph 4-3).

#### 6-5.2.2 Beryllia

Beryllia ( $\text{BeO}$ ) finds application in situations where the combination of high temperature capability, low loss tangent, and high thermal conductivity is required. The most striking characteristic of  $\text{BeO}$  is its high thermal conductivity (125 Btu/hr-ft- $^{\circ}\text{F}$  at room temperature), which is almost that of copper. Under certain conditions, this property gives  $\text{BeO}$  outstanding resistance to thermal shock. However, for very high heating rates, a high thermal conductivity does not ensure superior thermal shock resistance. This is shown graphically in Fig. 1-22, which compares the thermal shock resistance of various ceramics. The high cost and toxicity of the beryllia raw material have limited its use in radome applications (see Paragraph 4-6).

#### 6-5.2.3 Pyroceram

Pyroceram is the trade name for a family of glass-ceramics developed by the Corning Glass Works. The type of greatest interest for electromagnetic window applications is Pyroceram, code 9606. This material has found use in numerous surface-to-air and air-to-air interceptor missile radomes. Its primary advantages are a relatively low expansion coefficient and modulus of elasticity, and its high flexural strength. This combination of properties makes Pyroceram 9606 one of the most widely used ceramic materials for electromagnetic windows where resistance to thermal shock is a requirement. However, the use of this material is limited to about 1800 $^{\circ}\text{F}$  because of decreased strength and increased loss tangent.

A summary of the physical and thermal properties of Pyroceram 9606 is given in Paragraph 4-4.

#### 6-5.2.4 Slip-Cast Fused Silica

Slip-cast fused silica offers a solution to the electromagnetic window problem when structural requirements due to aerodynamic loading are relatively low, but the thermal shock envi-

ronment severe (Reference 22). Recent experimental data (Reference 22) indicate that it is not possible for a slip-cast fused silica window to fail in thermal shock under any conceivable condition of thermal input. In addition to this remarkable property, slip-cast silica has a low dielectric constant and loss tangent with only slight temperature dependence. The major disadvantages of the material are its relatively low flexural strength and the fact that it is somewhat porous and absorbs moisture if the surface is not properly sealed.

The physical and thermal characteristics of typical slip-cast fused silica are given in Paragraph 4-5.

#### 6-5.2.5 Other Ceramics

The following is a list of some lesser-used ceramics, with a summary of comments on their use as electromagnetic windows: (1) *Magnesia*: Good strength and dielectric properties, but very poor thermal shock resistance. (2) *Magnesium aluminate spinel*: Good strength and dielectric properties. Not readily available. Shows no particular advantages over cheaper and more readily available alumina. (3) *Boron nitride*: Fair strength, good dielectric properties, readily machinable. Oxidizes above 1800 $^{\circ}\text{F}$ . Pyrolytic boron nitride appears to be very superior to the ordinary hot-pressed product. (4) *Barium aluminum silicate*: Good strength. Relatively low dielectric constant. Low loss tangent, even at 1800 $^{\circ}\text{F}$ . Relatively low expansion coefficient.

The physical and thermal properties of these materials are summarized in Table 6-1. Their dielectric constants and loss tangents are shown in Figs. 6-12 through 6-18.

#### 6-5.3 ORGANIC RESIN-FIBERGLASS LAMINATES

Organic resin-fiberglass laminate materials have little use in electromagnetic window applications for hypersonic vehicles, except as ablators. However, several recently developed organic resins show promise of continuous use at temperatures up to 900 $^{\circ}\text{F}$  and short-term (minutes) use well above that without appreciable surface degradation. Materials in this category are the polybenzimidazole and polyamide resins. Although little data on their physical properties

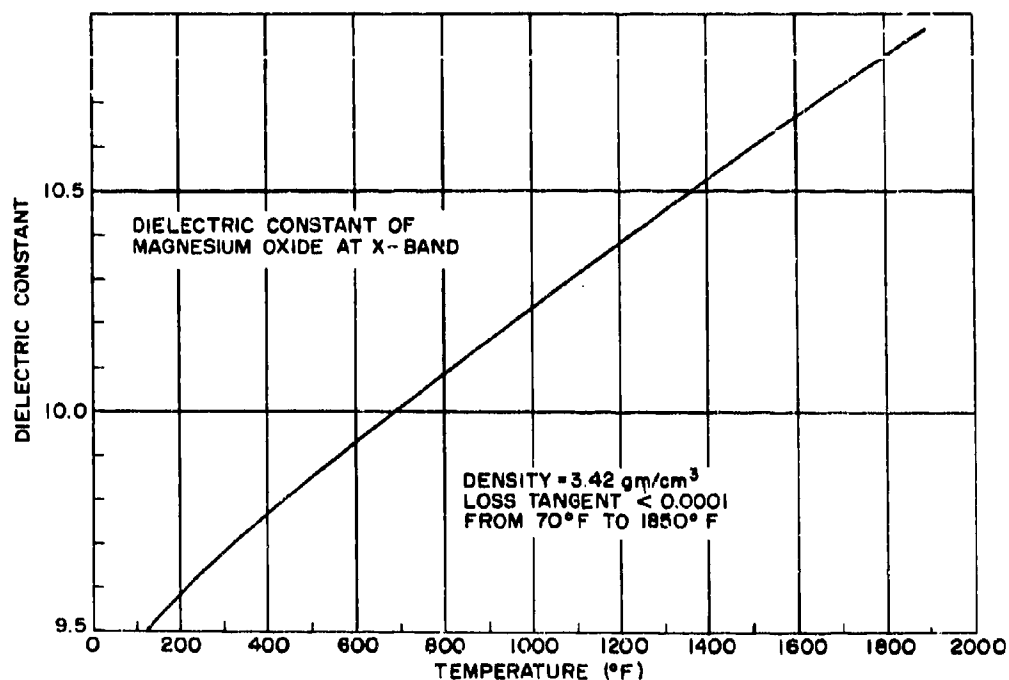


Figure 6-12. Dielectric Constant of Magnesia at X-Band

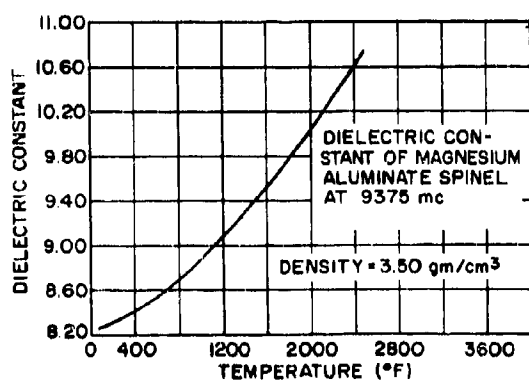


Figure 6-13. Dielectric Constant of Magnesium Aluminate Spinel at 9375 mc

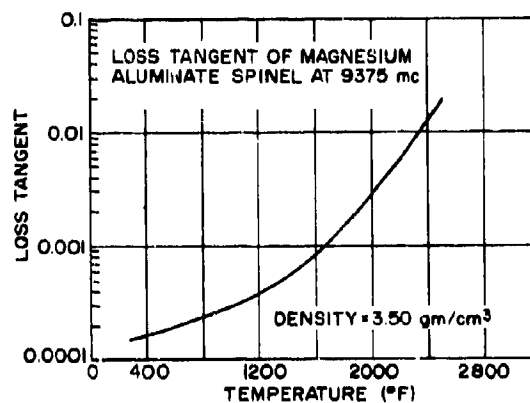


Figure 6-14. Loss Tangent of Magnesium Aluminate Spinel at 9375 mc

are available, indications are that flexural strengths are equal to, and in some cases greater than, those of epoxy, polyester, and silicone resin laminates. In addition, the electrical properties are excellent and do not appreciably degrade with temperature. The dielectric constant and loss tangent of a typical polyamide resin-fiberglass laminate are shown in Figs. 6-19 and 6-20.

#### 6-5.4 INORGANIC LAMINATES

One of the major advantages of organic resin-fiberglass laminates over monolithic ceramic materials is their resiliency coupled with high strength. This is achieved by reinforcing a matrix having a relatively low modulus of elas-

ticity with a high-strength fiber. Most monolithic ceramics are brittle. That is, they tend to fracture without appreciable deformation and under low stress. It has long been recognized that an all-inorganic laminate, having the refractoriness of a ceramic but the resiliency and strength characteristics of an organic resin-fiberglass laminate, would be a near-ideal structure. Research aimed at developing an inorganic laminate was relatively unsuccessful prior to 1958. The major problems were those of the fibers being attacked and weakened by the matrix material (the equivalent of the resin in organic laminates) and the development of a suitable matrix and fiber system that would allow a significant portion of the load to be carried by the fibers.

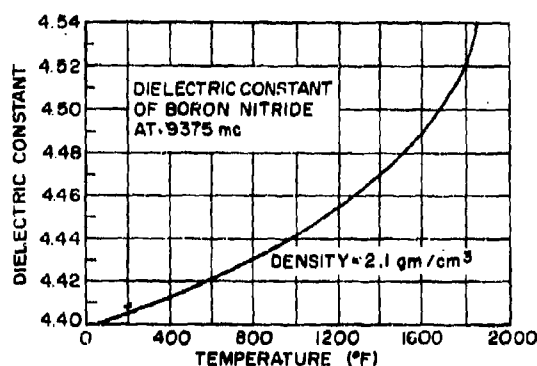


Figure 6-15. Dielectric Constant of Boron Nitride at 9375 mc

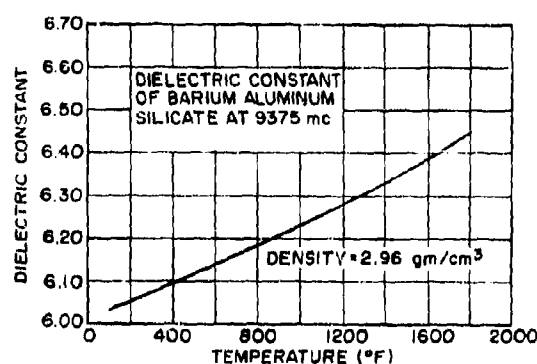


Figure 6-17. Dielectric Constant of Barium Aluminum Silicate at 9375 mc

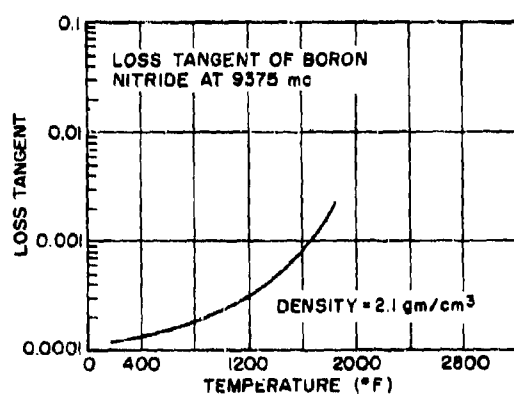


Figure 6-16. Loss Tangent of Boron Nitride at 9375 mc

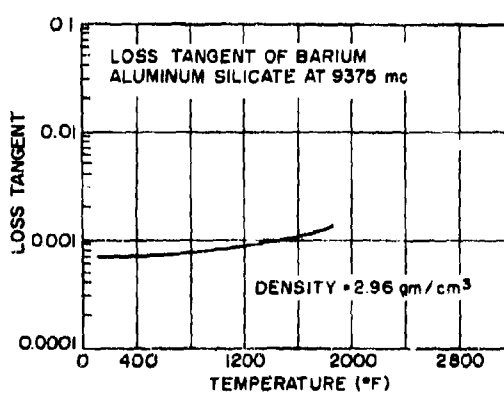


Figure 6-18. Loss Tangent of Barium Aluminum Silicate at 9375 mc

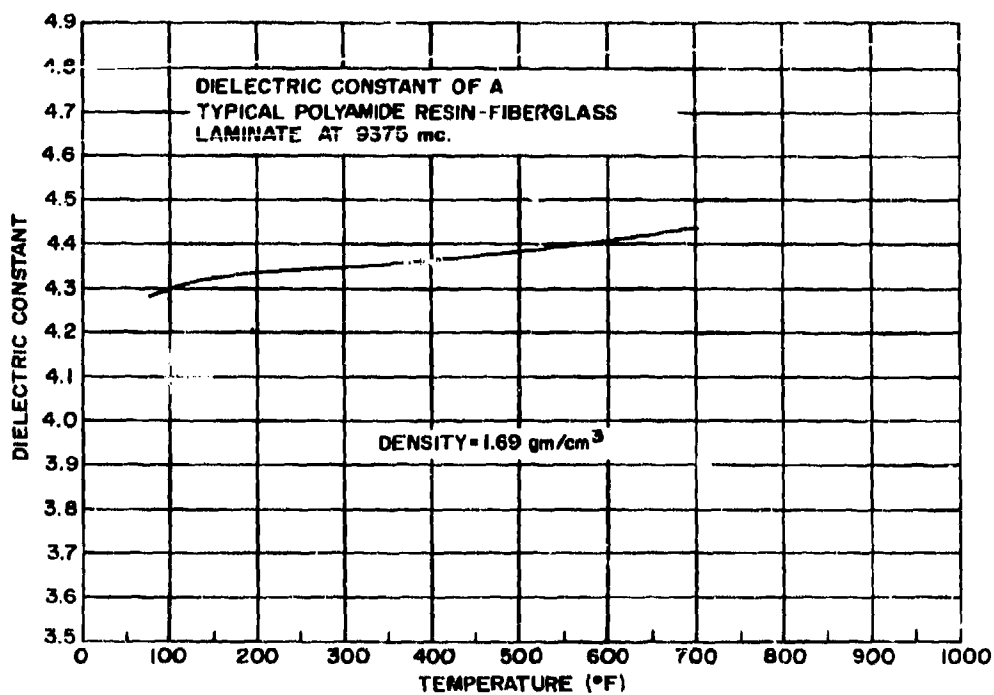


Figure 6-19. Dielectric Constant of Typical Polyamide Resin-Fiberglass Laminate at 9375 mc

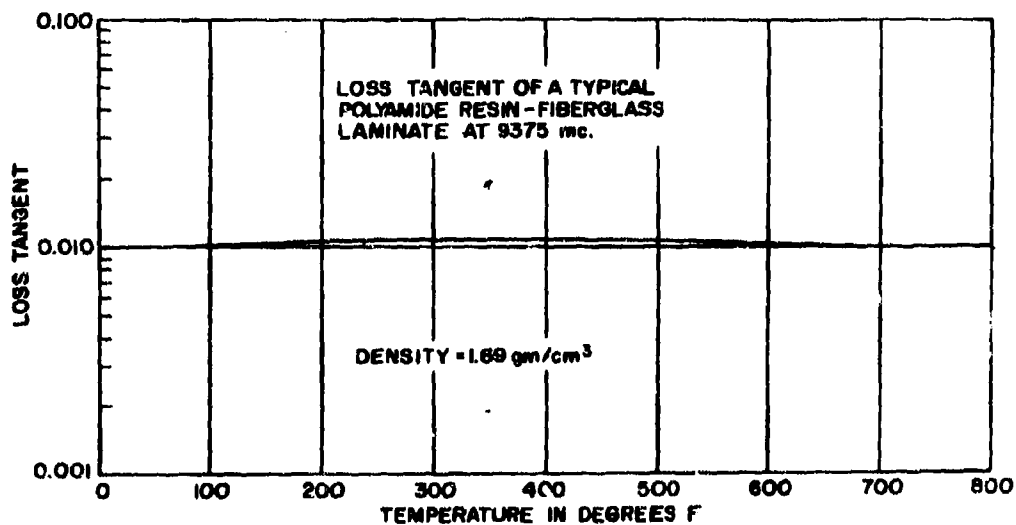


Figure 6-20. Loss Tangent of Typical Polyamide Resin-Fiberglass Laminate at 9375 mc

Reference 24 demonstrates the feasibility of inorganic laminates. A laminate was developed that had good dielectric properties, was stable at 1000°F, was relatively resilient, and had a flexural strength of almost 24,000 psi at room temperature. The matrix material was colloidal silica and Owens Corning E-Glass was used as the reinforcing fiber.

Recent developments in inorganic laminates (Reference 25) indicate the feasibility of con-

structing large radomes from inorganic laminate materials. A 65-in. ogive nose radome has been constructed having an aluminum phosphate binder and S994, style 143 glass fabric. The working temperature of the material is in excess of 1200°F. The dielectric constant and loss tangent of a typical sample of the material are shown in Figs. 6-21 and 6-22. The flexural strength and flexural modulus typical of the material are shown in Figs. 6-23 and 6-24 (see Paragraph 4-7).

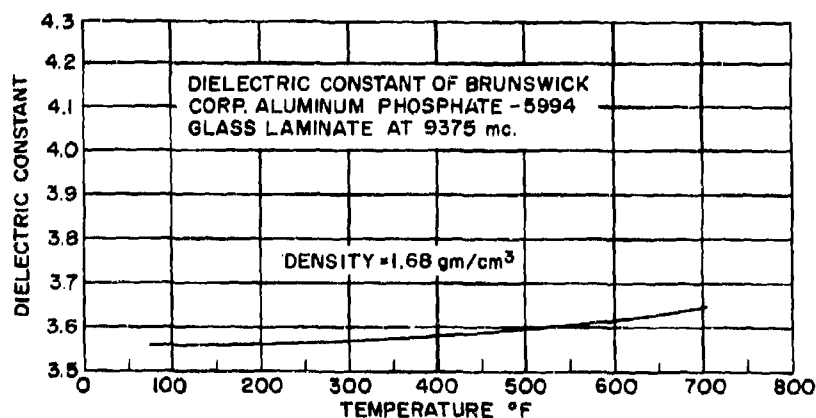


Figure 6-21. Dielectric Constant of Brunswick Corp. Aluminum Phosphate-5994 Glass Laminate at 9375 mc

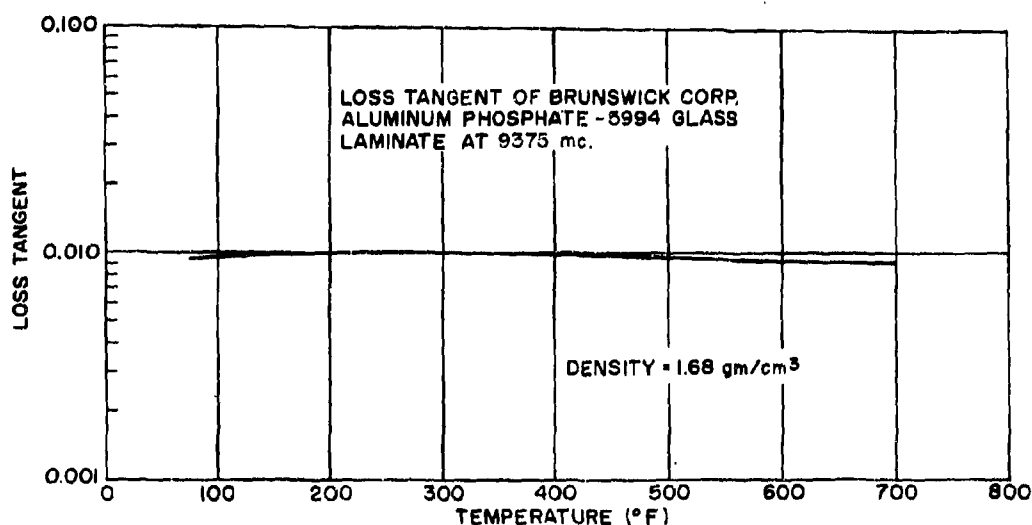


Figure 6-22. Loss Tangent of Brunswick Corp. Aluminum Phosphate-5994 Glass Laminate at 9375 mc

### 6-5.5 ABLATIVE MATERIALS

The problem of aerodynamic heating of ballistic missiles and other reentry vehicles is one of extreme importance and must be given considerable attention in the design of radomes for hypersonic vehicles. Depending on the specific mission of a given hypersonic vehicle, it may encounter peak heating rates as high as 6000 Btu/ft<sup>2</sup>-sec. A typical ballistic missile may encounter stagnation point heat fluxes as high as 2500 Btu/ft<sup>2</sup>-sec with a total exposure time of tens of seconds. For such vehicles as reentry satellites, the peak heating rate may be only 100 Btu/ft<sup>2</sup>-sec, but a typical exposure time may be as much as 5 to 10 minutes. Needless to say, these high heat fluxes produced by the atmosphere retarding the speed of the reentry vehicles are quite detrimental if allowed to transfer their thermal energy to an antenna or associated electrical systems. The ablation radome, then, is a solution to the problem of thermal protection in addition to electrical transparency, structural, and aerodynamic requirements.

A method of actual mass transfer of a heated material away from the vehicle to be protected is known as ablation cooling. The ablation process is a self-cooling process in which a great deal of heat may be absorbed by the surface of a material, causing the material surface to melt. Then through a subliming process (vaporization from the solid state to a gas or condensation to a solid without passing through the liquid state) and depolymerization (forming of two or more molecules of a compound from a

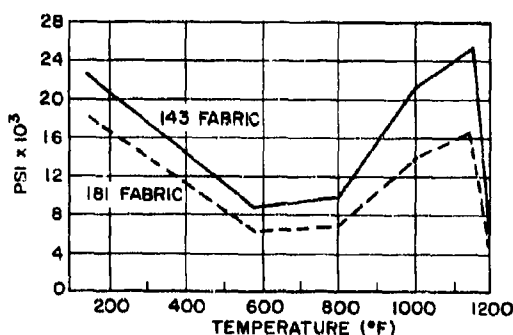


Figure 6-23. Flexural Strength of Glass Reinforced Aluminum Phosphate

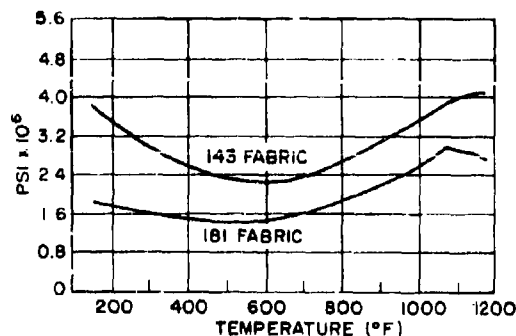


Figure 6-24. Flexural Modulus for Glass Reinforced Aluminum Phosphate

higher molecular weight compound), a residue is formed that may be injected into the hypersonic boundary layer, as in the case of a reentry vehicle.

One of the advantages of the ablation process as a cooling method is its "self-contained" features. Other cooling methods require extra weight and volume. Such methods as heat sinks, heat shields, insulation, and circulation of coolants are considerably more complex. Another outstanding feature of the ablation cooling method is that, as the heating rate of the radome material increases, the rate of ablation increases automatically to give additional thermal protection.

Ablation cooling is very effective for extremely high heating rates of relatively short duration. Therefore, an ablation material radome provides a relatively simple, but very reliable, means of protecting a ballistic reentry vehicle antenna from extremely high heating rates.

For the general case, a radome material undergoing ablation will consist of a layer of material that is in the molten state nearest the heat source. This layer is followed by a region that is undergoing heating and will decompose and eventually become molten if the heating process continues. An unheated, or virgin, region of the radome material is the final region of the "thermal model" before reaching the antenna or other structure being protected.

Eventually, of course, all the protective material would ablate and be injected into the boundary layer if a sufficient amount of heat were applied. As the radome electrical thick-

ness changes, of course, the electrical performance changes.

When considering the use of an ablative radome material, such factors as the maximum allowable degradation in electrical performance and the amount of thermal protection needed must be evaluated. These fundamental requirements must be considered before, during, and after the ablation process occurs, since the radome configuration is continually changing.

If a change in an ablative radome's electrical thickness is detrimental to the performance of a system, the only alternative is to use a thermally stable nonablative radome material and provide some other means of meeting the thermal protection requirement.

An ablation material is used in electromagnetic window applications when there is a need for the window to act as a thermal shield as well as an electromagnetic window. When selecting a material for use as an ablative window, the electrical transparency must be weighed against the thermal protection and the structural integrity provided by the material for the particular application. In addition to having a high heat of ablation, good ablators should have a low thermal conductivity, which aids in maintaining the substructure at a relatively low temperature level.

Because of the mechanism of ablation, ablative materials generally fall into one of the following general categories:

1. Reinforced plastics, such as various plastic resins reinforced with either organic or inorganic fibers to form a composite material. A carbonaceous char layer forms during ablation.
2. Pure thermoplastics, differing from most reinforced plastics by a lack of a carbonaceous char formation after the material sublimates.
3. Graphites, characterized by combustion only at the material surface and a relatively low ablation rate. The combustion of a graphite or carbon causes a net reduction of the heat transfer through the material. Graphites generally do not lend themselves to easily fabricated large parts. They are not generally of interest for electromagnetic window applications because of poor electrical properties.
4. Oxides. Oxide ceramics, such as  $\text{Al}_2\text{O}_3$ ,

$\text{BeO}$ ,  $\text{MgO}$ , and others, which have excellent electrical properties, are very poor ablators because of their inability to gasify when subjected to a hypersonic reentry environment. This characteristic is brought about by a major retardation in the ability of the material to vaporize with increased surface pressures. As a result, most oxides become poorer as a thermal protecting medium if used on a hypersonic vehicle proceeding to re-enter the earth's atmosphere. One exception to this rule is slip-cast fused silica, which is a relatively efficient inorganic ablator, having an apparent heat of ablation on the order of 18,000 Btu/lb. By increasing the emittance with  $\text{Cr}_2\text{O}_3$ , this value has been increased to an apparent value of 60,000 Btu/lb.

Most ablation materials with radome applications fall into the reinforced plastics group.

Ideally, the behavior of a material as it undergoes ablation may be analyzed by considering it as a multilayer configuration with discrete actions and reactions occurring in each layer. This approach is not straightforward, however, since the thermal, chemical, structural, and electrical properties are not accurately known in the general case. If one can reasonably estimate or measure the dielectric constant and loss tangent properties, and the thickness of the various layers, it is relatively straightforward to compute the electrical performance of such a configuration using multilayer dielectric theory. However, from a practical standpoint, it is difficult, if not impossible, to accurately determine the dielectric properties of the ablative char layer. Often, the only approach is to choose some worst-case estimate of the dielectric properties of the char layer.

A method of determining the worst-case effects of the ablation process on the electrical performance is to subject test samples to high thermal inputs and measure the corresponding degradation in transmission efficiency as the material ablates. The power transmission losses of a number of ablative materials have been measured using such a technique (Reference 26). Some of these results are shown to demonstrate the relative merit of typical materials. The data are based upon measurements made using 12 in.  $\times$  12 in. test panels uniformly

TABLE 6-2 ABLATION MATERIALS TESTED

Material	Density	Description	Manufacturer
Armstrong-2755 Cork	23.78 lb/ft <sup>3</sup> 0.525 gm/cm <sup>3</sup>	Natural cork granules with resorcinol binder	Armstrong Cork Company Lancaster, Pennsylvania
Tayloron-P/N Phenolic-Nylon	73.54 lb/ft <sup>3</sup> 1.178 gm/cm <sup>3</sup>	Phenol formaldehyde resin reinforced with Nylon (6-6 polyamide) fabric	The Taylor Fibre Company San Carlos, California
Teflon-TFE	128.61 lb/ft <sup>3</sup> 2.06 gm/cm <sup>3</sup>	Polytetrafluoroethylene	E. I. duPont de Nemours and Co. Wilmington, Delaware
Duroid-5650	138.97 lb/ft <sup>3</sup> 2.226 gm/cm <sup>3</sup>	Teflon reinforced with ceramic fibers	Rogers Corporation Rogers, Connecticut
Thermolag-500	79.72 lb/ft <sup>3</sup> 1.277 gm/cm <sup>3</sup>	Proprietary item with the manufacturer	The Emerson Electric Manufacturing Co. St. Louis, Missouri
Avcoat-II	65.61 lb/ft <sup>3</sup> 1.051 gm/cm <sup>3</sup>	Epoxy-polyamide resin modified with phenol, glycine, precipitated silica, and color toner	Avco Corporation Cincinnati, Ohio

heated on one surface. The power transmission through the test panels was monitored by a pair of X-band, platinum-coated conical-horn antennas. The horn antennas were parallel-polarized and the angle of incidence with respect to the material surface was 60 degrees.

Table 6-2 describes six ablation materials (cork, phenolic-nylon, Teflon, Duroid, Thermolag, and Avcoat) that were evaluated. All of these materials except Teflon are in the reinforced plastics category. Teflon is a pure thermoplastic. The electrical performance data presented in Figs. 6-25 through 6-28 are based upon actual tests that used a high-temperature transmission test facility. These curves show power attenuation vs. time and temperature. Although the heating rates during these tests were somewhat less than those that might be encountered during hypersonic reentry, the total heat pulse was close to simulation of some worst-case reentry conditions.

Figures 6-29 through 6-32 show the relative dielectric constant and loss tangent properties at stabilized material temperatures from ambient to several hundred degrees Fahrenheit as measured with an X-band resonant-cavity dielectrometer. This information gives an insight as to the basic electrical properties of the subject materials before the ablation process begins.

From an electrical performance standpoint, the noncharring Teflon is considerably superior to the char-forming materials. However, Teflon without reinforcement is dimensionally unstable when heated. The reinforced plastics are more desirable from both the structural and thermal protection standpoints. Therefore, a compromise must be made in choosing an ablation material to meet the thermal, structural, and electrical requirements of a given system. Detailed consideration must be given to all performance requirements of the radome in the selection of satisfactory material.

## 6-6 EXAMPLES OF ELECTROMAGNETIC WINDOWS

### 6-6.1 GENERAL CONSIDERATIONS

It is unfortunate that many of the most interesting and timely examples of electromagnetic windows for hypersonic vehicles fall under military security classifications. However, there is enough unclassified information available to get a reasonably clear picture of the techniques that are actually being employed for particular types of hypersonic reentry vehicles. The following paragraphs briefly describe several electromagnetic window configurations that have recently been developed.



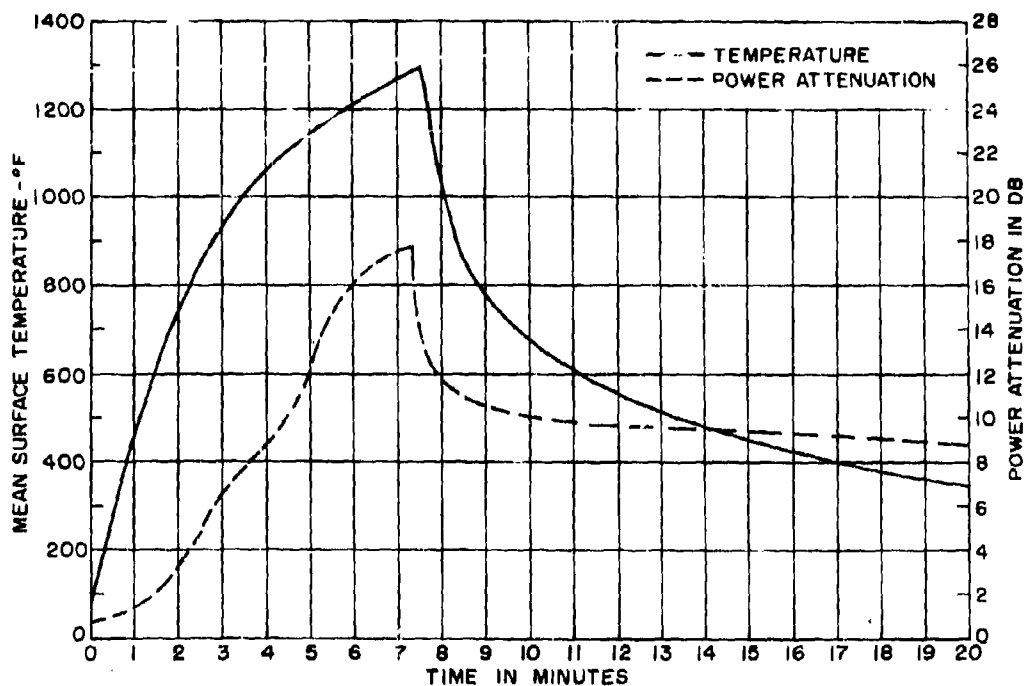


Figure 6-25. Electrical Performance Data on Armstrong 2755 Cork

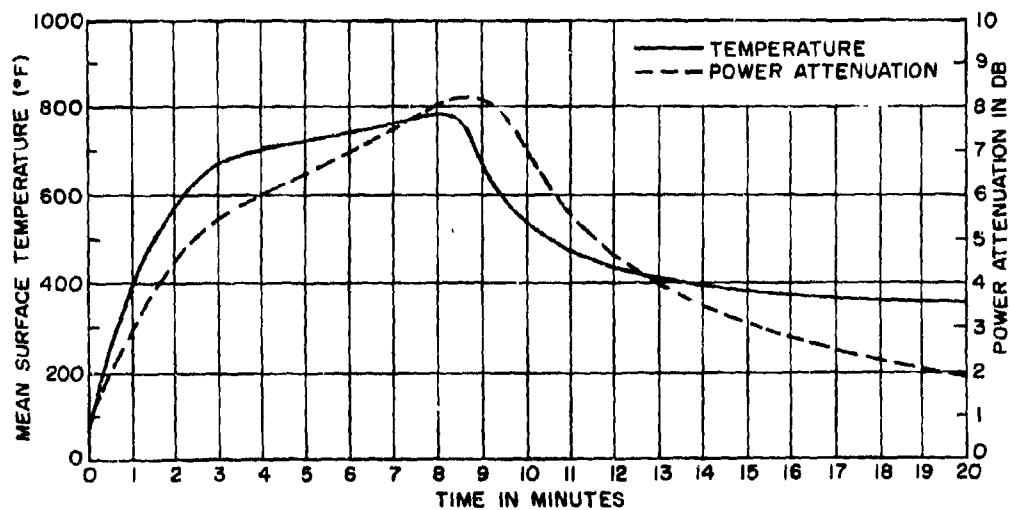


Figure 6-26. Electrical Performance Data on Tylaren Phenolic-Nylon

## 6-6.2 EXAMPLES OF GLIDE REENTRY ELECTROMAGNETIC VEHICLES

### 6-6.2.1 Asset

The acronym Asset stands for Aerothermodynamic/elastic Structural Systems Environmental Tests. The primary objective of the Asset program is to obtain basic aerodynamic, thermodynamic, structural, and flutter data from a hypersonic glide reentry vehicle (Reference 27). To fulfill this mission, information concerning vehicle performance during reentry is telemetered to tracking sites by means of an X-band link and, when plasma conditions permit, a VHF link. The vehicle-borne antennas for these two links were an X-band, flush-mounted waveguide with an integral alumina window and an alumina loaded, flush-mounted, U-slot VHF antenna. Surface temperatures in excess of 2000°F were predicted for the VHF antenna (Reference 28).

The VHF antenna was constructed by metalizing a solid block of alumina, leaving only the slot area exposed. Nickel plating over a moly-

manganese base was the technique used to form the conductive portions of the antenna.

The mechanical installation of the antenna flush with the vehicle surface presented a problem because of the difference in expansion coefficient between the alumina and the structure to which it attached. The problem was solved by mounting the metallized ceramic antenna between two clamping surfaces. A high-emittance (0.8) coating was applied to the exposed ceramic surface to reduce surface temperature during a flight.

A second version of this antenna, using an 0.125-in. quartz cover, reduced the alumina temperature to 700°F, thereby providing better impedance-matching characteristics between the antenna and transmitter.

The X-band antenna-window combination also used alumina for the window. The optimum window thickness was 0.215 in. at 9320 mc.

### 6-6.2.2 Dyna-Soar

Although this program was cancelled before it reached the flight-test phase, a significant

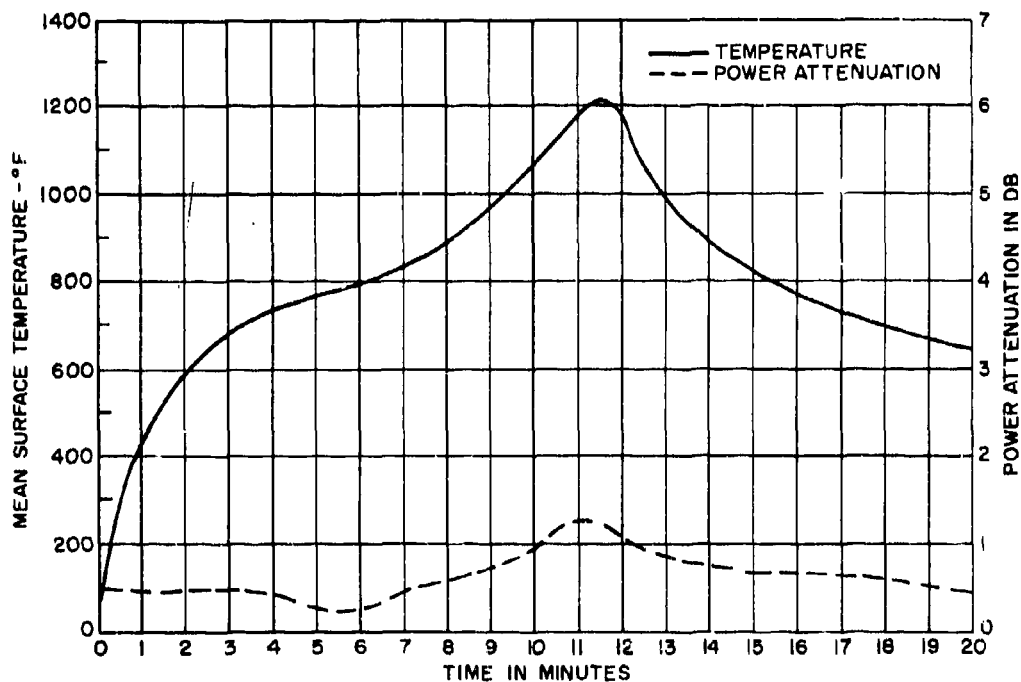


Figure 6-27. Electrical Performance Data on Teflon TFE

amount of work was done in the development of flush-mounted antenna-window structures. The antennas developed for Dyna-Soar were cylindrical structures fed by slotted waveguides. The patterns were similar to those produced by an annular slot with the null partially filled. This was due to the excitation of the cylindrical section in both the  $TE_{11}$  and  $TM_{01}$  modes simultaneously. The cylindrical section was mounted flush to the skin of the vehicle and had an alumina window, also flush with the skin surface. The outer surface of the alumina was coated with a high-emittance metallic oxide to provide an emittance equal to that of the surrounding metal.

The thickness of the window was optimized to provide best performance during the most critical phase of the flight. The antenna-window structures were designed for use from C-band through K<sub>a</sub>-band, being scaled to fit the particular frequency requirement.

Considerable proof testing was done to demonstrate the capability of the antenna-window assembly to operate beyond 2000°F.

### 6-6.3 BALLISTIC REENTRY VEHICLES

The Trailblazer program is designed to study the physical phenomena that occur during the reentry of high-speed objects into the earth's atmosphere (Reference 29). It utilizes a four-stage vehicle. The first two put the vehicle into place in the desired trajectory. After coasting through the highest point in the trajectory, the payload is fired by the third and fourth stages back towards earth at a velocity of 18,000 feet per second. One of the objectives of the program is to obtain in-flight data on the extent of the microwave-plasma interaction problem. It is thus desirable to have a thermal protection system that has a minimum effect on the flow field surrounding the vehicle during reentry. The use of charring ablators was ruled out because of the contamination problem. Final selection was a modified, slip-cast fused-silica, ogival radome 48 in. in height. The material is modified by the addition of chrome oxide to provide a very low ablation rate. This is the first and only known program where a forward-

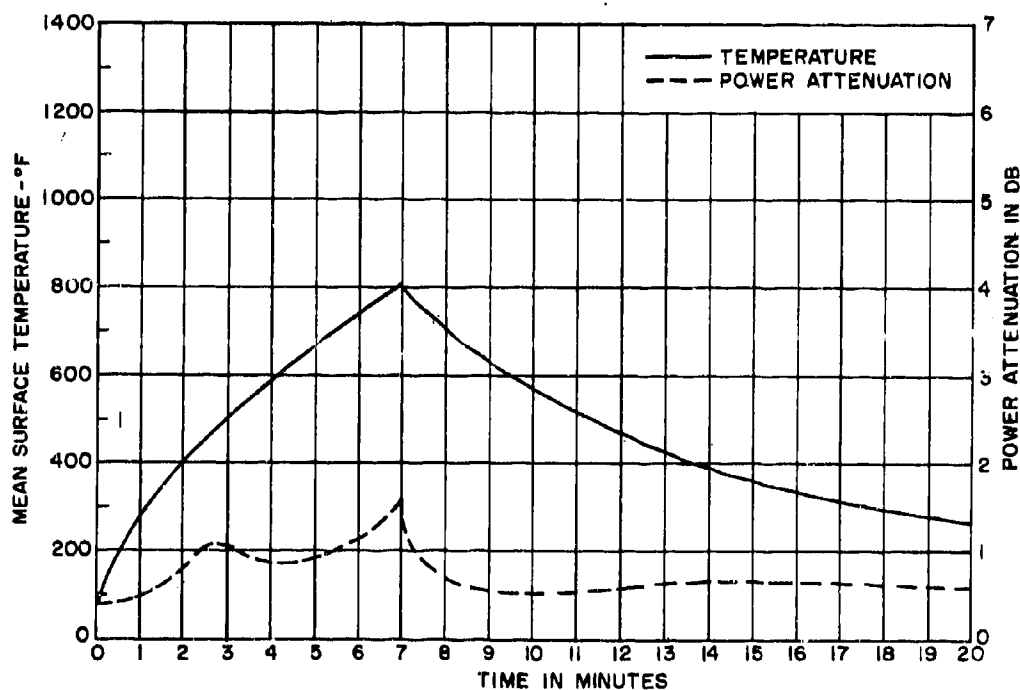


Figure 6-28. Electrical Performance Data on Duroid 5650

mounted ogival radome has been considered and developed for a ballistic reentry vehicle.

## 6-7 FUTURE RADOME REQUIREMENTS

### 6-7.1 CURRENT STATE-OF-THE-ART

A discussion of future radome requirements must be prefaced by a few summarizing remarks concerning the present state-of-the art in the design and development of radomes and windows for a wide variety of vehicles. Current requirements can be divided into the categories of radomes for supersonic aircraft, radomes for supersonic ground-to-air and air-to-air missiles, and radomes and electromagnetic windows for hypersonic reentry vehicles. Although this chapter is concerned primarily with vehicles that fall in the latter category and some of those in the second category, comments concerning supersonic aircraft radomes are included for the sake of continuity.

#### 6-7.1.1 Supersonic Aircraft

Nose radomes of up to 12 ft in length and 4 ft in base diameter have been developed for

Mach 2.2+ aircraft. Environmental requirements are such that surface temperatures of over 500°F are reached. Organic resin-fiber-glass laminates are usually specified, with filament winding the most commonly used fabrication technique. Silicone resins are favored because of the vast amount of data available on their long-term properties. Considerable effort is being expended to develop new, higher-temperature organic resins. The most promising of these to date are of the polyamide and polybenzimidazole families. The development of an all-inorganic laminate shows promise of extending the working temperature of large, aircraft radomes to beyond 1000°F (References 25 and 30). The problems of damage caused by rain erosion and the very long lifetime required for commercial supersonic radome applications remain.

#### 6-7.1.2 Ground-to-Air and Air-to-Air Supersonic Missiles

Missiles of these types currently operational or in development achieve terminal velocities in excess of Mach 2.5. Since these velocities often occur at relatively low altitudes, the heat-

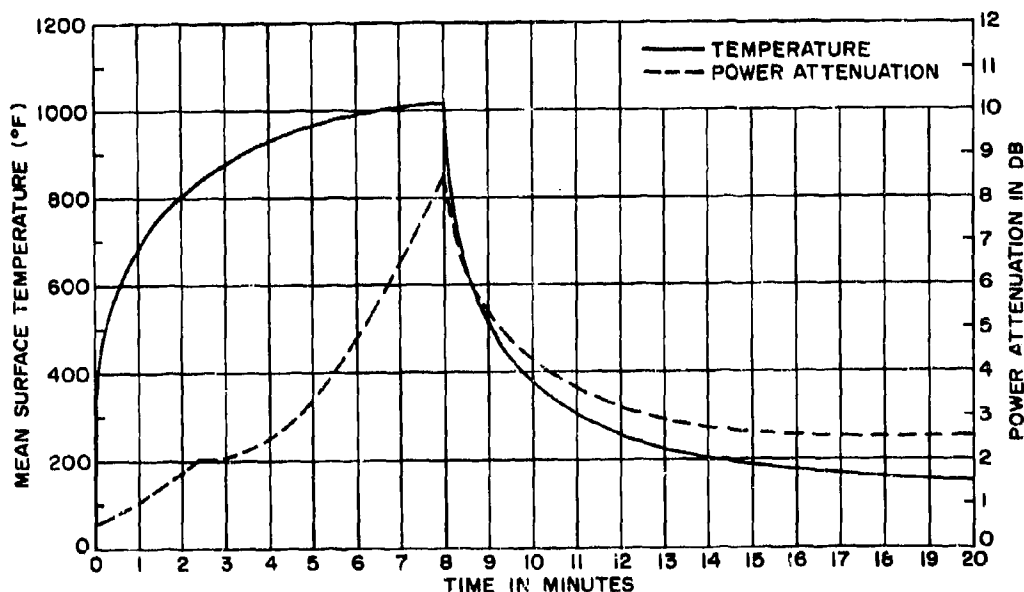


Figure 6-29. Electrical Performance Data on Thermolag 500

ing rates are high and thermal shock presents a serious design problem. Small ceramic radomes (less than 2 ft in length) have been designed to operate successfully where the terminal surface temperature reaches 1600°F after a time-of-flight of less than 30 seconds. A significant part of such a design is the ability to provide ceramic-to-metal attachments capable of surviving the thermal stresses developed during the flight.

Current technology in this area favors the use of low-expansion ceramics, which have generally superior thermal shock resistance. Considerable effort is currently being expended to develop refractory fiber-matrix composites composed entirely of inorganic materials. The present goal is to develop such a material with a working temperature of 2500°F (References 31 and 32; also see Paragraph 6-5.4).

New techniques are being investigated in the fabrication of large solid-wall ceramic radomes. Present capability in industry limits ceramic radomes to about 4 ft in length. The fabrication of a large (9 ft or greater in length) ceramic radome by bonding small ceramic tiles with high-strength refractory adhesives is being studied (Reference 33) as a method of overcoming the present size limit.

### 6-7.1.3 Electromagnetic Windows for Hypersonic Vehicles

As discussed in Paragraph 6-2.2, vehicles in this category fall into general classifications of glide, ballistic and orbital decay reentry, and high-acceleration boost. Electromagnetic windows have been successfully developed and, in most cases, flight proven for each of these types of vehicles.

In the case of the glide reentry vehicle, the Asset (Reference 34) and Dyna-Soar vehicles both utilized flush-mounted ceramic radomes. Considerable effort was expended in developing integrated antenna-radome structures that could successfully survive the high surface temperatures and relatively large total thermal input associated with a glide reentry vehicle. An intensive laboratory test program, conducted during the Dyna-Soar development, demonstrated the ability of this type of antenna to survive and operate at surface temperatures beyond 2000°F. The Asset flight test program demonstrated the successful operation of flush-mounted, integrated ceramic radome-antenna assemblies under actual operating conditions.

The development of flush-mounted radomes for orbital decay vehicles was accomplished in

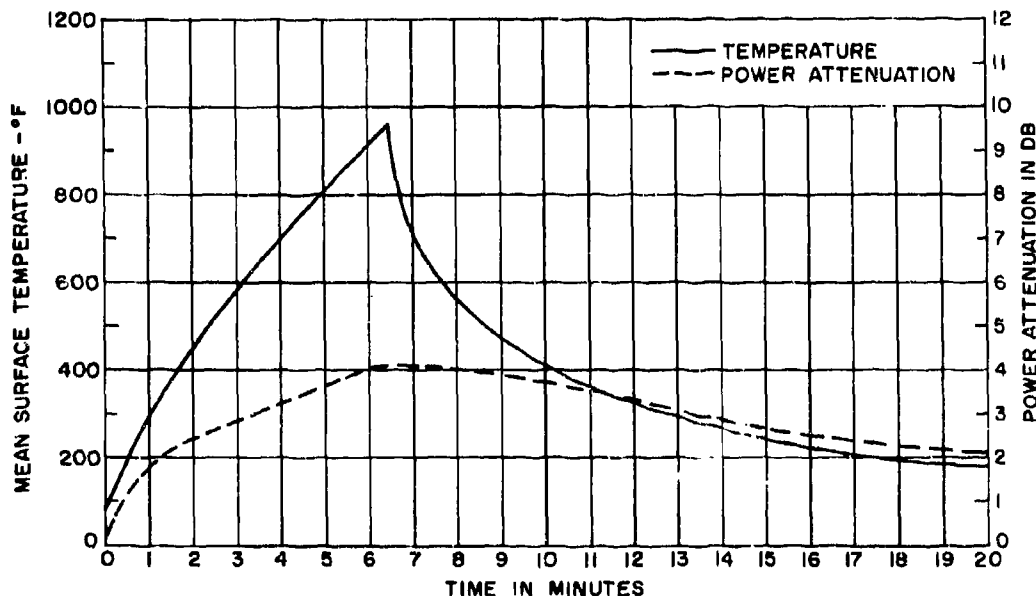


Figure 6-30. Electrical Performance Data on Avcoat II

the Mercury and Gemini programs. Flush-mounted radomes for orbital decay vehicles are generally located well aft of the heat shield and do not experience the high temperatures of glide reentry antennas.

With the previous comments on the current state-of-the-art, let us consider what the future may hold in the way of radome requirements.

## 6-7.2 FUTURE ELECTROMAGNETIC WINDOW REQUIREMENTS

### 6-7.2.1 Aircraft

There is little doubt that future manned military aircraft will operate at speeds well beyond those of currently operational types. As speeds increase, r-f sensor requirements will become more stringent. Concurrently, the ability to provide radomes with performance characteris-

ties even equivalent to those of their current counterparts will become difficult. This will be a direct result of the aerodynamic requirement for radomes of higher fineness ratios and radomes that must operate over much wider ranges of temperature. Additionally, the rain erosion problem, which to date has been more bothersome than significant, will become a critical technical problem.

The partial solution to these problems lies in the development of materials and fabrication techniques that will yield an aircraft radome capable of intermittent operation at temperatures in the 1000°F to 1200°F region and that will not fail catastrophically during exposure to rainfall at velocities in excess of Mach 2. Such materials and techniques are currently in development (References 25, 31, to 33) and show promise of approaching this goal. However, because of the wide temperature range over

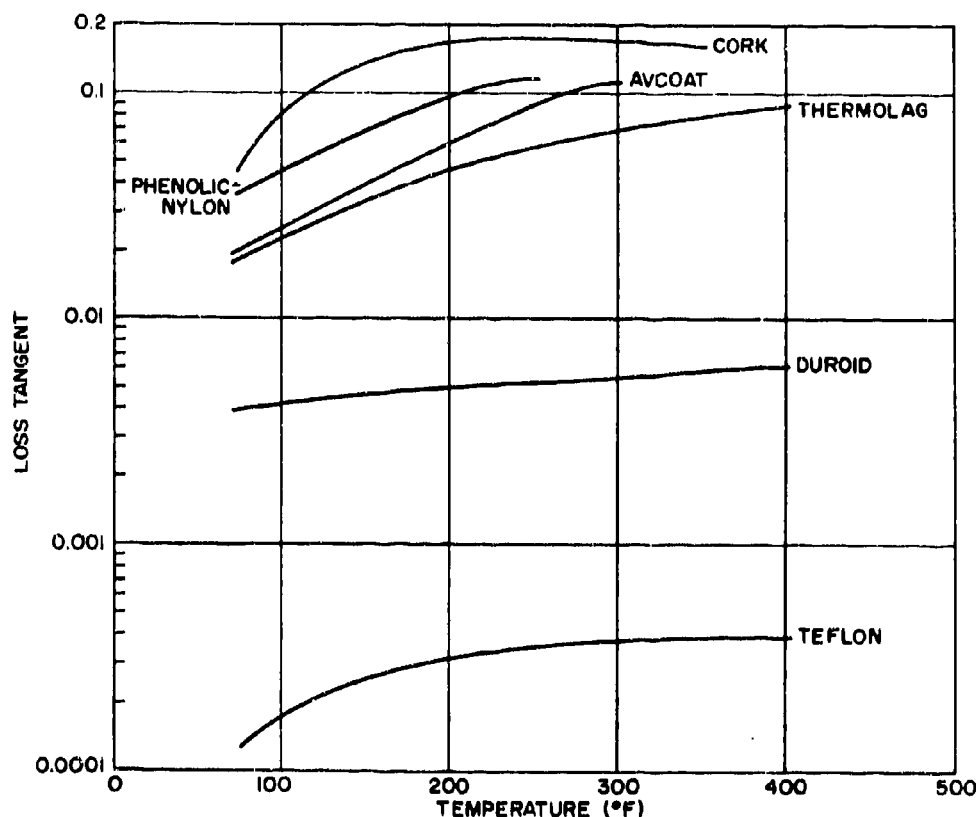


Figure 6-31. Loss Tangent Properties of Ablation Materials

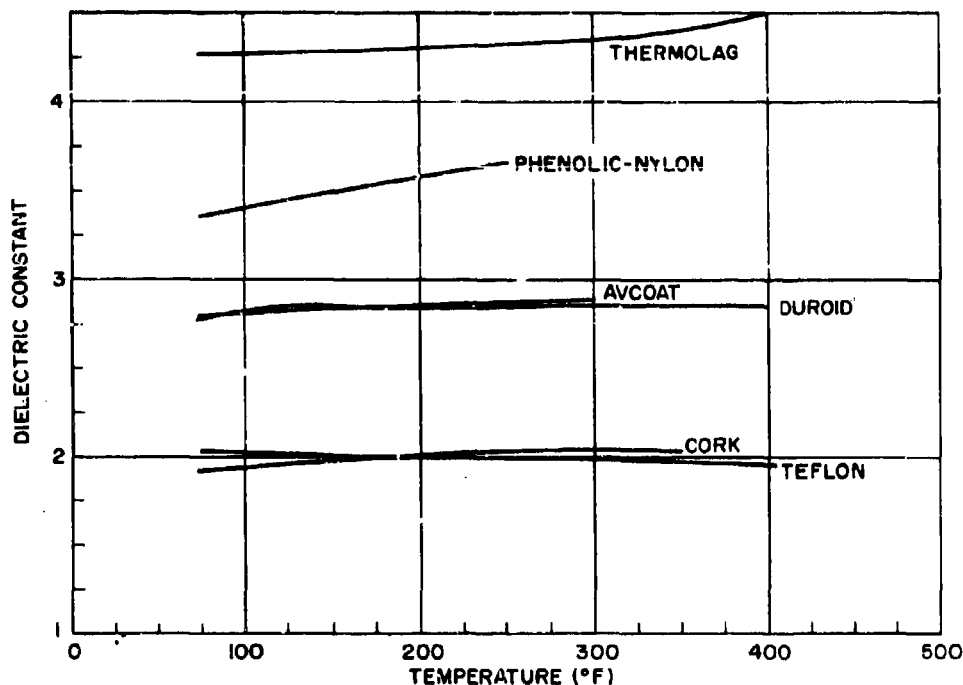


Figure 6-32. Dielectric Constants of Ablation Materials

which these radomes must operate and because of the inherently poor performance achievable with very high-fineness-ratio radomes, the point will be reached vertically where the nose-mounted radome-radar system can no longer provide the performance required to achieve a given mission objective. In anticipation of this situation, a number of schemes have been proposed and investigated that eliminate the need for a large, solid-wall, self-supported radome. Several of these techniques are described in Chapter 2. They all involve, basically, an integration of the radiating structure with the basic nose structure of the aircraft. Although some of these integrated antenna-radome techniques can provide performance that approaches that of a radome-radar antenna system, they have, in general, significant limitations. These are: decreased polarization purity; increased boresight error and error rate; scan angle limitations; nonconstant effective aperture and sidelobe level variation with scan angle; and greatly increased mechanical complexity. Metal-loaded and space-frame radomes,

while having application for relatively low-fineness-ratio situations, suffer in performance when fineness ratios (and hence incidence angles), such as those required in high-speed aircraft, are involved.

In summary, the immediate radome needs for military aircraft are being met by high-temperature organic resin-inorganic fiber laminate structures. The needs for the next generation of military aircraft will be met by inorganic laminates presently under development, but eventually, the entire concept of the nose-mounted radome-radar configuration may have to be discarded in favor of integrated antenna-radome techniques with their attendant decrease in performance. This latter situation may well lead to the extensive use of sidelooking radar, where the entire length of the aircraft's fuselage can be used as an antenna aperture. This provides an order of magnitude increase in target resolution and permits mounting the antenna in a location that is thermally non-critical. A combination of a side-looking radar and a limited-scan forward-looking attack radar

using an integrated antenna-radome appears attractive.

#### 6-7.2.2 Offensive Missiles

Future operational offensive missiles may employ reentry vehicles that are terminally guided to their targets. Such systems will require radomes that can survive ballistic reentry and, when plasma conditions permit, allow transmission and reception of energy from the on-board terminal guidance radar. An electromagnetic window for this application may take the form of a nose-mounted ogival radome protecting a forward-looking radar, a side-mounted conformable window protecting a slot array, or numerous dielectric slot closures mounted flush with the surface of the vehicle. Since boresight error rate could be critical in such a system, a constant insertion phase difference is desirable, making the use of ablative materials undesirable.

#### 6-7.2.3 Defensive Missiles

Current requirements for ground-to-air and air-to-air defensive missiles approach the limit of thermal shock capability for solid-wall ceramic radomes. The exception is slip-cast fused silica, but this material has a relatively low modulus of rupture. Future missile radome requirements will necessitate a material with a modulus of elasticity much lower than that of an oxide ceramic, but with the refractoriness and strength of the ceramic. The most fruitful approach to this problem appears to be the development of an all-inorganic laminate, using a highly refractory fiber-matrix system (References 31 and 32).

**6-7.2.3.1 Missiles: Electronic Countermeasures.** Systems have been considered whereby a small vehicle with the function of homing on and destroying local enemy radar is carried aboard and released from a reentry vehicle. Such a device requires a radome to protect its homing antenna. The radome requirement would be for either a highly thermal-shock-resistant ceramic radome or an organic resin-fiber composite type, depending on the altitude from which the vehicle is ejected from its carrier.

#### 6-7.2.4 Aerospace Plane

The concept of a vehicle that can be launched as an airplane, boost itself into earth orbit, then reenter and land as an airplane will undoubtedly be implemented at some future time. The radome requirements for such a vehicle appear to be a composite of those of a reentry vehicle and of an aircraft. While the development of such a vehicle is undoubtedly well in the future, the successful culmination of some of the current materials and integrated antenna-radome studies could well lead to a solution to the aerospace plane radome problem well before the need arises.

#### 6-7.2.5 Mars Exploration Vehicles

The design of electromagnetic windows for a Mars entry capsule presents a different and unique problem. The composition of the atmosphere is not well known. Plasma attenuation is expected during entry, but because of the lack of appreciable amounts of oxygen, the nature of the ablation mechanism will be different from that of an earth entry. The testing of an electromagnetic window for a Mars capsule may well have to be done under simulated Mars thermal and atmospheric entry conditions.

## REFERENCES

1. Hankey, Wilbur L., Jr., Neumann, Richard D., USAF, and Flinn, Evard. *Design Procedures for Computing Aerodynamic Heating at Hypersonic Speeds*, WADC TR 59-610.
2. Bloom, Martin H., et al. *Aerodynamic and Structural Analysis of Radome Shells*, WADC TR 59-22, Vol. 1.
3. Bloom, Martin H. *Thermal Conditions Associated with Aircraft in Flight*, WADC TR 55-169.
4. *Temperature Profile for Hyperenvironmental Radomes*, TDR-AFAL-64-342, prepared under Contract No. 33(615)-1277 by North American Aviation, Inc.
5. Poulos, N. E., et al. *Design and Development*



- ment of an EM Window for Air Lift Reentry Vehicles, Interim Engineering Report 1-5, 1963-1964, Project No. 4161, Air Force Avionics Laboratory, RTD Wright-Patterson Air Force Base, Ohio.
6. Roark, Raymond J. *Formulas for Stress and Strain*, Third Edition, McGraw-Hill Book Co., New York, 1954.
7. Timoshenko, S., and Goodier, J. N. *Theory of Elasticity*, Second Edition, McGraw-Hill Book Co., New York, 1951.
8. Mason, S. S. *Behavior of Materials Under Conditions of Thermal Stress*, NACA Report 1170, Lewis Flight Propulsion Laboratory, Cleveland, Ohio, 1954; "Thermal Stress in Design," Part 1, *Machine Design*, Vol. 30, No. 12, pp. 114-120, June 12, 1958; and "Thermal Stress in Design," Part 2, *Machine Design*, Vol. 30, No. 13, pp. 19-103, June 26, 1958.
9. Kingery, W. D. "Factors Affecting Thermal Stress Resistance of Ceramic Materials," *J. Amer. Ceramic Soc.*, Vol. 38, No. 1, pp. 3-15, 1955.
10. Carpenter, James F. *Reflection and Transmission of Plane Electromagnetic Waves by a Lossy Multi-Ply Sandwich*, WADC TR 51-314, Vol. 1, p. 81.
11. Sutton, R. W., and Grechny, N., Jr. "Design and Development of a High-Temperature Resonant Cavity Dielectrometer," *Proc. OSU-WADD Symposium on Electromagnetic Windows*, Vol. 1, June 1960.
12. Holman, Frank S., and Paisley, Milvyn R. "Radome Design Through Correlation of Radome Optimum Frequency and Insertion Loss Difference," *Proc. OSU-WADC Radome Symposium*, Vol. 1, June 1957.
13. Taylor W. C. "Thermodynamic and Electrical Properties of Shock Ionized Flow Fields," *Planetary and Space Science*, Vol. 6, June 1961.
14. Sisco, W. B., and Fiskin, J. M. "Basic Hypersonic Plasma Data of Equilibrium Air for Electromagnetic and Other Requirements," *Planetary and Space Science*, Vol. 6, June 1961.
15. Hassserjian, G., and Higgins, T. P. *Fields of a Curved Plasma Layer Excited by a Slot*, Boeing Scientific Research Laboratories Mathematical Note No. 321, September 1963.
16. Bachynski, M. P. *Analytical and Experimental Investigation of the Presence of Ionized Media on Antenna Properties*, AFCRL Report 63-541.
17. Johnson, T. L. *Radiation Pattern Measurements Using Simulated Thin Plasmas*, Boeing Company Document D2-35112.
18. *Ion Sheath Studies for the X-20 Vehicle*, Dyna-Soar Symposium, Wright Field, Dayton, Ohio, 1962.
19. *Applicability of the Nike Zeus Communication Experimental Results to the Dyna-Soar Communications*, AF Technical Memorandum ASNR-TM-62-3, July 24, 1962 (Secret).
20. "Microwave Propagation Through a Plasma in a Magnetic Field," *Phys. Rev.*, Vol. 129, No. 4, pp. 1481-1489, February 14, 1963.
21. Eliason, L. K., and Zellner, G. C. *A Survey of High-Temperature Ceramic Materials for Radomes*, ML-TDR-64-296, AF Materials Laboratory, Research and Technology Div., Air Force Systems Command, Wright-Patterson Air Force Base, Ohio, September 1964.
22. Walton, J. D., and Poulos, N. E. *Slip-Cast Fused Silica*, ML-TDR-64-195, AF Materials Laboratory, Research and Technology Div., Air Force Systems Command, Wright-Patterson Air Force Base, Ohio, October 1964.
23. Walton, J. D., and Poulos, N. E. "Fused Silica for Reentry Radomes," *Proc. OSU-RTD Symposium on Electromagnetic Windows*, June 1964.
24. Harmon, Cameron, and Beasley, Robert M. *Inorganic Laminate Radome for 1000°F*, WADC TR 58-434.
25. Chase, Vance A., and Copeland, R. L. "Development of a 1200°F Radome," *Proc. OSU-RTD Symposium on Electromagnetic Windows*, 1964.
26. Norin, T. L. "The Measured Electrical Characteristics of Several Ablative and Some Nonablative High-Temperature Radome Materials," *Proc. OSU-RTD Symposium on Electromagnetic Windows*, 1964.
27. *Analysis of Asset Communication Links*, ASD-TDR-62-778, Directorate of Aeromechanics, ASD, AFSC, Wright-Patterson Air Force Base, Ohio, August 1962.

28. Krah, John W. "High-Temperature Telemetry Antennas for Asset," McDonnell Aircraft Corp., *Proc. OSU-RTD Symposium on Electromagnetic Windows*, Volume III, June 1964.
29. Walton, J. D., et al. *Design and Development of an EM Window for Air Lift Re-entry Vehicles*, Interim Engineering Report No. 2, Georgia Institute of Technology, October 31, 1963.
30. *Large Sectionalized High-Temperature Radome Structures*, Emerson and Cuming, Inc., Air Force Contract No. AF 33(615)-1376.
31. *Experimental Research on Filamentized Ceramic Radome Materials*, Interim Engineering Progress Reports to September 30, 1964, Project 6799-4161, Task 416103, Contract No. AF 33(615)-1167, Horizons, Inc., Cleveland, Ohio.
32. *Filamentized Ceramic Radome Techniques*, Technical Documentary Report ASD-TDR-62-721, August 1962, prepared under Contract No. AF 33(616)7872, Horizons, Inc., Cleveland, Ohio.
33. *Composite Ceramic Radome Manufacture by Mosaic Techniques*, Interim Engineering Reports 1-5, November 1962-April 1964, IR-7-984 (1-5). Contract No. AF 33(657)-10111, Whittaker Corp., Narmco Research and Development Div., San Diego, California.
34. Krah, John W. "High-Temperature Telemetry Antennas for Asset," McDonnell Aircraft Corp., St. Louis, Mo., *Proc. OSU-RTD Symposium on Electromagnetic Windows*, Vol. IV, June 2-4, 1964.

## INDEX

For convenience in finding the subject topics in TR 57-67, a combined index is included in both volumes. The volume number, in boldface, precedes the page number of each index entry.

### A

- "A" sandwich, 1-238, 1-271, 1-544, 1-569, 2-92, 2-94
  - alumina, 2-269, 2-270
  - construction, 2-5
  - foamed-in-place radomes, 1-13
  - radome, 2-107
    - attachment, 2-61
    - power transmission, 2-108
    - three-layer, 1-8
  - transmission and phase delay, contours, 1-43
  - transmission curves, 2-128
- Ablative cover, 2-19, 2-49
- Ablative materials, 2-446, 2-448
  - dielectric constant, 2-455
  - loss tangent properties, 2-454
- Ablative window, 2-429
- Absorption, dielectric, 2-362
  - energy, 2-392
- Acceleration boost, 2-418, 2-426
- Acrylic resins, 2-319
- Adiabatic calorimetry, 2-384
- Aerodynamic, configuration, 2-6, 2-31
  - design factors, 2-9
  - forces, 2-51
  - heat, 2-44, 2-417
  - heat simulation, 2-242
  - loads, 1-281
- Air loading, unsymmetrical, 1-282
- Air pressure, 1-322
- Air prism, 1-456
- Air, thermal conductivity, 1-289
- Airborne radar, 1-439, 2-86
  - dual-frequency, 2-90
  - installation, 1-439
  - pressurization, 1-439
- Aircraft, attitude axis correction, 1-444
  - early-warning radomes, 1-19
  - environment, 1-455
  - supersonic, 2-452
- Alumina, 1-422, 2-36, 2-46, 2-50, 2-260, 2-440
  - "A" sandwich, properties 2-270
    - skins, 2-269
  - bend strength, 2-263, 2-265
  - dielectric constant vs. temperature, 2-267
  - electrical properties, 2-80
  - emittance, 2-268
  - loss tangent vs. temperature, 2-267
  - machining, 1-422
  - modulus & elasticity, 2-266
  - mosaic, 2-269
  - properties, 2-265
  - porous, 2-268
  - radome, blanks, 2-284
    - fabrication, 2-288
    - flight simulation, 2-243
    - sizes, 2-288
    - skin temperature, 2-246, 2-250
  - sandwich, core, 2-270
    - materials, 2-268
    - multilayer, 2-289
    - skin, 2-270
  - specific heat, 2-266
  - thermal conductivity, 2-267
  - thermal expansion, 2-266
  - tiles, 2-271
    - joints and adhesives, 2-271
- Aluminum die, pressure-cast, 1-404
- Aluminum phosphate, 2-445
  - glass reinforced, 2-284, 2-446
- Amplitudes, near-field, 1-68, 1-70, 1-507
  - comparison, 1-136
  - monopulse system, 1-203
- Ambient loads, 1-283
- AN/APS-20E radome, 1-397
- Anechoic chamber, aperture-type, 2-394
  - Eccosorb, 2-397
  - funnel, 2-395
  - microwave, 2-391
  - shapes, 2-393
- Angle, offset, 2-39

Angle of incidence, 1-55, 1-63, 2-38, 2-84, 2-92  
 Anisotropic capacitor, 1-53  
 Anisotropic constructions, 1-55  
 Anisotropic materials, 1-55  
 Anisotropy, 1-58  
 Antenna, clearance, 1-443  
     conical scan, 1-209, 1-503  
     conical transmission line, 2-147  
     cosecant-squared, 1-98  
     depolarization, 1-153  
     deviation, 1-153  
     elevation planes, 1-114  
     half-wave dipole, 1-220  
     horn, 1-69, 2-104  
     lens, 2-147  
     mount, 1-501  
     oblique planes, 1-114  
     obstacles, 2-154  
     paraboloidal, 1-576  
     pattern, 2-114, 2-397, 2-406  
         cosecant-squared, 1-98  
         E-plane, 2-42  
         distortion, 1-101, 2-152, 2-155  
         H-plane, 1-75, 2-48  
         parameters, 2-41  
         perturbation, 2-404  
     performance degradation, 1-101  
     planes, oblique, 1-114  
     polarization, parallel, 1-153  
     radome, 1-126  
     -radome design, 1-10  
     -radome interaction, 1-77, 1-221  
     -radome radiating system, 1-576  
     -radome systems, 1-188, 1-521  
     search radar, 1-97  
     stabilization, 1-443  
     systems, monopulse, 2-138  
 Anti-icing, 1-317  
 Antistatic rain erosion coatings, 1-344  
 Aperture-type anechoic chamber, 2-394  
 Araldites, 2-318  
 Armstrong 2755 Cork, 2-449  
 AR-1075—HT polyester, 2-316  
 Artificial dielectrics, 1-19  
 Asymmetry, 1-215  
 Attachments, 1-407  
     "A" sandwich radome, 2-61  
     ceramic radomes, 2-49  
     chemical, 2-51, 2-54, 2-56  
     joints, 2-53  
     mechanical, 2-51, 2-55, 2-58  
     radome, 2-48

Altitude axis correction, aircraft, 1-444  
 Avcoat II, 2-453  
 Axial load, 1-302  
 Axial support, radome, 2-149  
 Axially symmetric sector scanner, 1-441  
 Azimuth run, 1-207

## B

"B" sandwich, 1-238, 1-271  
     construction, 2-5  
     radomes, 1-11, 1-47  
 Baffle chamber, 2-396  
 Bag molding, 1-392  
 Bakelite, 2-318  
 Ballistic range, 2-209  
 Ballistic reentry, 2-418  
     surface temperatures, 2-425  
     vehicles, 2-451  
 Bandwidth, 1-237, 2-42, 2-117  
 Barium aluminum silicate, 2-443  
 Batch preparation, steatite radome, 1-420  
 BC1 No. 6601-F polyamide resin, 2-319  
 Beam depression, 1-452  
 Beam deviation, 1-190  
 Beam tilt, 1-444  
 Beamrider missiles, 1-145  
     applications, 1-146  
 Bearing blocks, preparation, 1-392  
 Bend strength, alumina, 2-263, 2-265  
 Beryllia, 1-423, 2-261, 2-280, 2-441  
     dielectric constant, 2-283  
     emittance, 2-283  
     loss tangent, 2-283  
     modulus of elasticity, 2-281  
     modulus of rupture, 2-280  
     thermal conductivity, 2-282  
     thermal expansion, 2-281  
     radomes, production, 2-292  
 Bisque firing, steatite radome, 1-422  
 Bisque machining, 2-287  
 Blast pressure, 1-283  
 Blister radome, semistreamlined, 1-9  
 Bomarc radome, 1-16  
 Bond strength and flexibility, 1-298  
 Bonding adhesives, 1-376  
 Boresight error, 1-502, 2-43, 2-100  
     monopulse system, 1-199  
     prediction, 1-17  
         integral equation technique, 2-103  
         optical technique, 2-101  
         scattering technique, 2-102  
 Boresight ranges, 2-397, 2-406

Boresight test setup, 2-238  
 Boron nitride, 2-443  
 Branson Vidigage, 2-348  
 Brewster angle, 2-172  
 Boundary layer, 1-456  
   temperature, 1-291  
 Broadband radomes, 1-237, 2-116, 2-125  
   multilayer, 2-120  
   surface treatment, 2-125  
 Buckling, 1-316  
   coefficients, 1-306  
   sandwich wall, 1-301  
   solid wall, 1-302  
   thermal, 1-295

## C

"C" sandwich, 1-238, 1-572  
   construction, 2-5  
   radomes, 1-47  
 Calorimeter, copper block, 2-387  
   "dropping," 2-385  
 Calorimetry, adiabatic, 2-384  
 Capacitor, anisotropic, 1-58  
   isotropic, 1-58  
 Casting, steatite radome, 1-421  
 Catalysts, 1-373  
 Cavitation effect, 1-346  
 Cavity effect, 1-149  
 Centrifuge, 2-206  
 Ceramic materials, 1-419, 2-29  
   elastic constants, 1-430  
   electrical properties, 1-431  
   Knoop hardness, 1-431  
   physical properties, 1-427  
   refractoriness, 1-431  
   temperature effects, 1-432  
   thermal conductivity, 1-429  
   thermal expansion coefficients, 1-430  
 Ceramic radomes, 1-18, 2-259  
   attachment, 2-49  
   fabrication, 2-284  
   properties, 2-260  
 Ceramics, 2-440  
   dense fired, 1-419  
   density, 1-431  
   nonoxide, 2-362  
   oxide, 2-262, 2-361  
   porous, 1-424  
   radiation effects, 2-250  
   subsonic rain erosion properties, 1-340  
 Ceramoplastics, 1-427  
 Chemical attachments, 2-51, 2-54, 2-56

Chemical-mechanical attachments, 2-59  
 Chin radome, 1-11, 2-151  
   fluted core, 1-394  
 Chopped fiber preform, 1-400  
 Circ-gore filament winding, 2-308  
 Circ-longo drop-stitch filament winding, 2-306  
 Circ-longo grind process, 2-309  
 Circ-longo sock process, 2-309  
 Circo fibers, 2-307  
 Circularly polarized incident waves, 1-567  
 Coatings, erosion, 1-397  
   neoprene, 1-12  
   polyurethane, 1-339  
   rain erosion, 1-344  
   properties, 1-335  
 Coaxial line dielectric measurements, 2-365  
 Coaxial waveguide, 1-485  
 Coherent phase discriminator, 1-512  
 Command guidance, 1-145  
 Compressive strength, 1-400, 2-389  
 Computer design of radomes, 2-90  
 Conductive heat transfer, 2-236  
 Conductivity, thermal, 1-284, 2-380  
 Cone angles, 1-290  
   effect, 1-354  
 Conical fairing, 1-61  
   ogive radome, 1-63  
 Conical radome, 1-105, 1-282  
 Conical scan antenna, 1-503  
   axis, 1-209  
 Conical scan radar system, 1-132  
 Conical transmission line antenna, 2-147  
 Construction, half sandwich, 2-6  
   sandwich radomes, 1-378  
   sandwich wall, 1-301  
   solid-wall radomes, 1-378  
 Convective heat transfer, 2-231  
 Copper block calorimeter, 2-387  
 Cordierite, 1-424  
 Core, construction, 1-394  
   fluted, 1-380  
   foam, 1-380  
   honeycomb, 1-378, 1-396  
   joint gaps, 1-299  
   materials, 1-378  
   shear strength, 1-298  
   thickness, 1-259, 1-275, 1-298  
   tolerance, 1-573  
 Cork, Armstrong 2755, 2-449  
 Cornu spiral, 1-448  
 Coscant-squared antenna, 1-98  
 Creep, 1-316

Cristobalite, 2-276  
 Cross-polarization suppression, 2-104  
 Crosstalk error, 2-86  
 Curing, filament-wound radomes, 2-309  
 Cut-bar thermal conductivity measurements, 2-381  
 Cutting planes, 2-85  
 Cylinders, isotropic, 1-307  
 Cylindrical radome, 1-189  
 Cylindrical ring stresses, 2-66  
 Cylindrical sandwich, 1-303

## D

DC-2106 silicone resin, 2-319  
 Deflection, 1-325  
 Dense fired ceramics, 1-419  
 Density, ceramics, 1-431  
 Depolarization, 1-151  
   antenna, 1-153  
   target, 1-154  
 DER-DEN resins, 2-318  
 Deviation, antenna, 1-153  
 Diamond wheel grinding, 1-404  
 Dielectric constant, 1-48, 1-68, 1-474, 1-478, 1-526, 2-31, 2-38  
   ablation materials, 2-455  
   alumina sandwich skin and core, 2-270  
   beryllia, 2-283  
   calculations, 2-377  
   interferometer, 1-405  
   measurements, 2-354  
   Pyroceram, 2-274  
   slip-cast sintered fused silica, 2-278  
   vs. resin content, E-Glass and Vibrin 135, 2-300  
   vs. resin content, hollow glass and Vibrin 135, 2-301  
   vs. resin content, S-Glass and Vibrin 135, 2-302  
   vs. temperature, 2-303  
   alumina, 2-267  
 Dielectric diffraction, 1-74  
 Dielectric dispersion and absorption, 2-362  
 Dielectric homogeneity, 1-495  
 Dielectric instrumentation, microwave, 2-335  
 Dielectric loadings, 1-59  
 Dielectric loss, 1-431, 1-478, 1-495  
 Dielectric materials, electrical characteristics, 1-483  
   high temperature, 2-362  
   thermal properties, 2-379

Dielectric measurements, 2-364  
   coaxial line, 2-365  
   free-space, 2-374  
   interferometer, 2-374  
   open-circuit method, 1-490  
   resonant cavity, 1-494, 2-370  
   slotted-line method, 1-494  
   waveguide, 2-367  
 Dielectric patches, 1-209  
 Dielectric properties, porous ceramics, 1-426  
   resins, glasses, and laminates, 2-321  
 Dielectric rings, 1-208, 1-214  
   scattering, 1-218  
 Dielectric sheets, 2-106  
 Dielectric thickness, 2-354  
 Dielectrics, artificial, 1-19  
   inhomogeneous, 1-58  
   lossy, 1-519  
   medium-loss, 1-490  
   plane, 1-519  
 Dielectrometer, 2-325, 2-352, 2-366  
   microwave, 1-494  
   surface-wave, 1-494  
 Diffraction, dielectric, 1-74  
   edge, 1-447  
 Diffusivity, thermal, 2-382  
 Dilatometer, sapphire rod, 2-392  
 Dipole antenna, half-wave, 1-220  
 Dipole feed through radomes, 2-113  
 Dispersion, dielectric, 2-362  
 Dissipation factor, solid wall, 1-475  
 Distortion, antenna pattern, 2-152, 2-155  
 Double sandwich, 1-563  
 Double-wall radomes, 1-7, 2-6  
 Drag coefficient, 2-11  
 Driving point resistance, 2-117  
 "Dropping" calorimetry, 2-385  
 Duroid 5650, 2-451  
 Dynamic modulus measurement, 2-390

## E

ECCO interferometer, 2-357  
 Eccosorb anechoic chamber, longitudinal baffle, 2-397  
 Edge compression, 1-308  
 Edge diffraction, 1-447  
 E-Glass, 2-298, 2-300  
 Elastic constants, ceramic materials, 1-430  
 Elastic moduli, 2-389

Electrical design considerations, 2-79  
     flat window, 2-431  
     hypersonic, 2-430  
     window, 2-416  
 Electrical factors, 2-26  
 Electrical gage, 1-473  
 Electrical grinding control, 2-310  
 Electrical index, 2-21  
 Electrical non-uniformity, radome walls, 1-207  
 Electrical properties, alumina, 2-80  
     ceramic materials, 1-431  
     joints, 1-387  
 Electrical requirements, 1-105, 2-19  
     search radomes, 1-99  
 Electrical tests, 2-32, 2-63  
 Electrical thickness, radome wall, 1-468  
     effect of moisture, 1-473  
 Electromagnetic field theory, 1-27  
 Electromagnetic tensioner, 2-303  
 Electromagnetic windows, 2-448  
     shape, 2-97, 2-99  
     stresses, 2-426  
 Electromechanical gage, 1-473  
 Electronic guidance, current missiles, 1-140  
 Elevation planes, antenna, 1-114  
 Ellipsoidal shape, 2-7  
 Ellipsoidal missile radome, 1-170  
 Elliptical polarization, 1-50, 1-169  
     transmission coefficients, 1-51  
 Emissivity, 1-284  
 Emission, beryllia, 2-283  
     Pyroceram, 2-274  
     slip-cast sintered fused silica, 2-279  
 Environment, aircraft, 1-455  
     rain, 2-201  
     thermal, 2-416  
     thermal shock, 2-28  
 Environmental considerations, precipitation  
     static, 1-319  
 Environmental design, 1-316  
     radome, 1-281  
 Environmental factors, 2-26  
 Environmental requirements, 2-22  
 Environmental testing, 1-326, 2-61  
 E-plane antenna pattern, 2-42  
 E-plane transmission loss, 2-39  
 Epon 828 laminates, 2-313  
 Epoxy resins, 1-339, 1-372, 1-403  
     VC-3359, 2-315  
 Equiangular shape, 2-7

Erosion, coating, 1-397  
     rain, 2-203  
     simulator, Mithras, 2-208  
 Error, boresight, 1-502  
     crosstalk, 2-86  
     in-plane, 1-201, 1-217  
 Exhausts, rocket motor, 2-235  
 Expanded hardboard radomes, 1-7  
 Expansion, thermal, 2-390  
 Exposure time, thermal shock, 1-284  
 External pressure, 1-305

## F

Fabric, lay-up, 1-393  
     glass, 1-403  
     preparation, 1-392  
 Fabrication, alumina radome, 2-288  
     ceramic radomes, 2-284  
     composite radome, 2-312  
     glass-ceramic radome, 2-289  
     glass fiber filament, 2-302  
     multilayer alumina sandwich radome, 2-289  
     plastic radomes, 1-391  
 Fabry-Perot interferometers, 2-375  
 Face thickness, 1-298  
 Fairing, ogive, 1-65  
 Far-field antenna patterns, 1-75, 1-521  
     horn antenna, 2-105  
     interference, 1-102  
 Far-field zones, 1-222  
 Fatigue, 1-315  
 Feed-through radomes, dipole, 2-113  
 Feeler gauge thickness measurement, 2-311  
 Fiber, polystyrene, 1-7  
 Fiber reinforced plastic radomes, 2-295  
 Fiberglass yarn filaments, 2-299  
 Fibers, glass, 1-367, 2-296  
 Field-probe evaluation, 2-405  
 Filament winding, 2-306  
     circ-gore, 2-308  
     circ-longo drop-stitch, 2-306  
     helical, 2-306  
 Filament-wound radomes, curing, 2-309  
     finishing process, 2-313  
 Filaments, fiberglass yarn, 2-299  
 Fineness ratio, 1-61, 2-11, 2-21  
 Finishing process, 1-395  
     filament-wound radome, 2-313  
     radome, 2-290  
     sintered radome, 2-291  
 Fire control radar systems, 1-131, 1-178  
 Fire control radomes, 1-14, 1-129

Firing ceramics, 1-425  
 Flat panel (see "Panel" and "Wall" entries)  
 Flat-plate heating, 2-423  
 Flat sandwich, 1-38, 1-301  
 Flat sheet, homogeneous, 1-27  
     lossless, 1-34  
 Flat window, electrical design, 2-431  
 Flexural strength, 1-390, 2-389  
 Flight simulation, alumina radome, 2-243  
 Fluorocarbon resin, 2-319  
 Flush-faired radomes, 1-11  
 Flush-mounted radiating systems, 2-137, 2-142  
 Fluted core, 1-380  
     chin radome, 1-394  
     wall construction, 1-299  
 Foam, core, 1-380  
 Foam, polyurethane, 1-380, 1-400  
 Foaming, 1-424  
 Foamed-in-place core wall construction, 1-299  
 Foamed-in-place radomes, 1-13  
 Focusing effect, streamlined radomes, 1-66  
 Forming, 1-425  
 Forming and shaping radome blanks, 2-286  
 Forsterite, 1-424  
 Four-horn phase comparison system, 1-506  
 Free-space, dielectric measurements, 2-374  
     vswr evaluation, 2-405  
     wavelength, 2-38  
 Frequency, 1-241  
     rain, 2-201  
     vs. wavelength conversions, 2-198  
 Friction tensioner, 2-303  
 Funnel anechoic chambers, 2-395  
 Fused silica, 2-273  
     nose cone, 2-247  
     slip-casting process, 2-291  
 Fusion cast materials, 1-427

## G

Gage, electrical, 1-473  
     in-process, 2-346  
     inside diameter, 2-346  
 Generator, r-f, 1-495  
 Geodesic lenses, 2-147  
 Geometrical optics, 1-189  
 Glass, 1-426  
     -bonded mica, 1-427  
     -ceramics, 2-260  
     properties, 2-271  
     radome fabrication, 2-289

Glass (cont)  
     cloth, 1-390  
     dielectric properties, 2-321  
     fabric, 1-403  
         filament fabrication, 2-302  
         sizing, 1-375  
     fibers, 1-367, 2-296  
         composition and properties, 2-299  
         laminates, 2-281  
         tension, 2-303  
     laminate, aluminum phosphate-5994, 2-445  
     recrystallized, 2-362  
     refractory, 2-362  
     reinforced aluminum phosphate, 2-284, 2-446  
     reinforced plastics, longitudinal, 1-388  
         low-pressure, 1-388  
         mechanical properties, 1-388  
     parallel laminated, 1-388  
     reinforced sandwich radome, 1-408  
     subsonic rain erosion properties, 1-340  
 Glazing, 1-425  
 Glide reentry, 2-418  
     vehicles, 2-450  
 Gore filament pattern, 2-309  
 Gratings, 2-104  
 Grinding, circ-longo process, 2-309  
     electrical control, 2-310  
     ultrasonic control, 2-310  
     radome blanks, 2-287  
 Ground illumination, 1-97  
 Guarded hot-plate, 2-382  
 Guidance radomes, 1-16  
 Guidance systems, 1-140  
     effect of radome errors, 1-178  
     radomes, 1-129  
     proportional navigation, 1-144  
     remote, 1-145  
     self-contained, 1-141  
 Guided missiles, 1-141  
 Gunfire control radomes, 1-16

## H

Haack-Von Karman shape, 2-8  
 Half-sandwich construction, 2-6  
 Half-wave dipole antenna, 1-220  
 Half-wave homogeneous flat sheet, 1-35  
     first-order, 1-36  
 Half-wave radome, 2-81  
 Half-wave wall, 1-121, 1-191, 2-117  
     higher-order, 1-81  
 Handling precautions, 2-48



- Hardboard, expanded, 1-7
- Heat flow, planar, 2-381
- Heat resistant rain erosion coatings, 1-344
- Heat simulation, aerodynamic, 2-242
- Heat transfer, coefficient, 1-234
  - conductive, 2-236
  - convective, 2-231
  - radiative, 2-236
- Heating, aerodynamic, 2-44, 2-417
  - flat-plate, 2-432
  - laminar, 2-420
  - sonic point, 2-421, 2-424
  - turbulent, 2-421, 2-424
  - rates, 2-419, 2-424, 2-426
- Helical filament winding, 2-306
- Helium plasma effects, 2-436
- Hemispherical radome, 1-60, 1-104, 1-217, 2-250
- Hetron 92, 2-316
- Hollow glass, 2-301
- Homing missiles, 1-142
- Homogeneity, dielectric, 1-495
- Homogeneous flat sheet, 1-27
  - half-wave, 1-35
  - thin, 1-33
- Homogeneous panels, 1-567
- Homogeneous radomes, transmission coefficient, 2-130
- Honeycombs, 2-312
  - core, 1-378, 1-396
  - lay-up, 1-396
  - thickness, 1-403
  - sandwich radomes, 1-10
  - wall construction, 1-298
- Horns, 2-89
  - antenna, 1-69, 2-104
  - far-field pattern, 2-105
  - interferometer, 2-344
- Hot-air deicing, 1-318
- Hot flue, 2-231
- Hot-gas wind tunnel, 2-232
- Hot-plate, guarded, 2-382
- Hot salt bath, 2-236
- H-plane, 1-229
  - antenna patterns, 1-75, 2-43
  - near-field amplitudes, 1-70
  - near-field, phase, 1-70
  - transmission loss, 2-40
- Hybrid impregnation resin bath, 2-305
- Hydraulic jacks, 1-322
- Hydrocarbon resin, 2-315
- Hypersonic, electrical design, 2-430
  - materials, 2-439
  - radomes, 2-413
  - structural design, 2-426
  - vehicles, 2-453
  - velocities, 2-417
- I
- Ice calorimeter, 2-386
- Icing control, 1-316
  - anti-icing fluid, 1-317
  - hot-air system, 1-318
  - internal heating, 1-318
  - rubber boot, 1-317
- Illumination, ground, 1-97
- Impact, 1-314
  - resistance, 1-296, 1-429
  - testing, 1-327
- Incidence angle, 1-55, 1-110, 1-114, 1-275, 1-519, 2-38, 2-84, 2-92
  - components, 1-117
- Incident polarization, 1-153
  - elliptical, 1-169
  - linear, 1-168
  - parallel, 1-153
- Incident waves, linearly polarized, 1-174
  - polarized, 1-153
  - right-circularly polarized, 1-567
- Inertia loads, 1-282, 2-51
- Infrared systems, 1-83, 2-237
- Inhomogeneities, radome surface, 1-210
- Inhomogeneous, dielectrics, 1-58
  - plasmas, 2-435
  - radome reflection, 2-132
  - radomes, 2-128
  - transmission coefficient, 2-130
- Inorganic laminates, 2-443
- Inorganic materials, 1-366, 1-419
- Inorganic matrix materials, 2-296
- In-plane error, 1-201, 1-217
- In-process gage, 2-346
- Insertion phase, 1-34, 1-528, 1-560, 2-88, 2-159
  - contours, single sheet, 1-106
  - delay, 1-124
    - "A" sandwich radome, 2-108
    - lossless plane dielectric sheet, 1-83
  - difference, 1-465, 2-84, 2-92
  - constant, 2-34
  - effects, 1-122
  - variation vs. angle of incidence, 1-55
  - vs. incidence angle, 1-120

- Inserts, 1-392
- Inside diameter gage, 2-346
- Inspection methods, 1-406
- Instability buckling, 1-301
- Installation, airborne radar, 1-439
- Instrumentation, 1-325
- Integral equation, 1-195, 2-103
- Interceptor radome, 1-168, 1-218
- Interface reflection coefficients, 1-27, 1-56, 2-169
  - phase angle, 2-171
- Interference, 1-101
  - effects, 1-445
- Interferometer, 2-337
  - dielectric constant, 1-405
  - dielectric measurements, 2-374
  - ECCO, 2-357
  - horn, 2-344
  - magic T, 1-467
  - Michelson, 2-375
  - micrometer, 1-466
  - reflection, 2-310
  - two-horn, 1-465
  - tables, 2-339
  - Fabry-Perot, 2-375
- Interlaminar shear values, 2-297
- Internal heating, 1-318
- Internal pressure, 1-283
- Isotropic capacitor, 1-58
  - cylinders, 1-307
  - plasma, simulated, 2-437
  - sandwich, 1-306

## J

- JC-1571 hydrocarbon resin, 2-315
- Jet engine exhaust, 2-232
- Jets, plasma, 2-235
- Joint gaps, core, 1-299
- Joint loading, 2-52
- Joints, attachment, 2-53
  - electrical properties, 1-387

## K

- K-band radomes, 1-9
- KEL-F81 fluorocarbon resin, 2-319
- Knitted-sock laminated radomes, 1-10
- Knoop hardness, ceramic materials, 1-431

## L

- Laminac 4110, 2-316
- Laminated radomes, 1-10
  - knitted-sock, 1-10

- Laminated wall construction, 2-5
- Laminates, 1-367
  - dielectric properties, 2-321
  - Epon 828, 2-318
  - glass fiber, 2-281
  - inorganic, 2-443
  - organic resin-fiberglass, 2-441
  - polyamide resin-fiberglass, 2-444
  - slotted, 1-338
  - resins, 1-13
  - void elimination, 1-393
  - walls, 1-478
- Lathe grinding, 1-402
- Lathe turning, 1-400
- Lens, 1-206
  - antennas, 2-147
  - feeding, 1-80
  - geodesic, 2-147
  - Luneberg, 1-78
  - manufacture, 1-79
  - radome transmission loss, 1-80
- Lightning, 1-319
- Line-of-sight stabilization, 1-440
- Linear polarization, 1-51, 1-168
- Lithium aluminum silicates, 1-424
- Lloyd's mirror effect, 1-76
- Load application, 1-322
- Load, axial, 1-302
- Loaded core sandwiches, 1-18
- Loads, 1-297
  - ambient, 1-288
  - aerodynamic, 1-281
  - dielectric, 1-59
  - inertia, 1-282
  - joint, 2-52
  - operational, 2-51
  - pickup probe, 1-495
- Lobe comparison, sequential, 1-147
- Lobing, sequential, 1-133
- Leg spiral, 1-64
- Logarithmic shape, 2-7
- Longitudinal-baffle Eccosorb anechoic chamber, 2-397
- Longitudinal heat-flow measurements, 2-381
- Longitudinal plastics, glass, reinforced, 1-388
- Longo fibers, 2-307
- Look angle, 2-86
- Loss, correction, 1-490
  - dielectric, 1-431, 1-478, 1-495
  - reflection, 2-38

Loss tangent, alumina sandwich skin and core, 2-270  
 beryllia, 2-283  
 calculations, 2-378  
 measurements, 2-357  
 properties, ablation materials, 2-454  
 Pyroceram, 2-274  
 slip-c. st sintered fused silica, 2-278  
 vs. temperature, 2-363  
 alumina, 2-267  
 Lossless dielectric, Snell's law, 2-178  
 Lossless homogeneous plane sheets, 1-49  
 Lossless plane dielectric sheet, 1-82  
 Lossless plane sheet, 1-85  
 Lossless thin flat sheets, 1-84  
 Lossy dielectrics, 1-519  
 Low density materials, 1-381  
 Low-frequency resonant cavities, 2-373  
 Lumped fields, 1-196  
 Luneberg lens, 1-78

## M

Mach number factors, 2-11  
 Machining, alumina, 1-422  
 Magic T, interferometer, 1-467  
 Magnesia, 1-423, 2-442  
 Magnetic materials, 1-54  
 measurements, 1-492  
 Magnetic tensioner, 2-303  
 Magnetron, frequency pulling, 1-100  
 performance, 1-100  
 Marco vacuum injection, 1-399  
 Matched-die mold, 1-401  
 Matched-tool molding, 1-396  
 Materials, 2-32  
 ablative, 2-446, 2-448  
 alumina sandwich, 2-268  
 anisotropic, 1-55  
 ceramic, 1-419, 2-29  
 construction, 2-257  
 core, 1-378  
 dielectric, 1-483<sup>1</sup>  
 full density, 1-383  
 fusion cast, 1-427  
 hypersonic, 2-439  
 inorganic, 1-366  
 low density, 1-381  
 magnetic, 1-492  
 organic, 1-365  
 plastic, 1-335  
 rain-resistant, 2-203  
 testing, high temperatures, 2-361

Matrix formulation, 1-40  
 Matrix materials, inorganic, 2-296  
 Measurements, dielectric, 2-364  
 near-field, 1-221, 1-230, 1-507  
 no-dome, 1-224  
 radar cross section, 1-154  
 radome wall, 1-463  
 specific heat, 2-384  
 tensile strength, 2-69  
 transmission impedance, 1-486  
 Mechanical, attachment, 2-51, 2-55, 2-58  
 -chemical attachments, 2-59  
 factors, 2-27  
 micrometer, 1-472  
 properties, glass reinforced plastic, 1-388  
 properties, testing, 2-64  
 physical properties, 2-385  
 strength, 2-71  
 Mechanism, rain erosion, 1-345  
 Medium-loss dielectrics, 1-490  
 Melamine resins, 1-368  
 Metal ribs, 2-151  
 Metal-loaded radomes, 2-104, 2-125  
 perforated, 2-106  
 Metal sheets, 1-59  
 Metal slats, 1-59  
 Mica, glass-bonded, 1-427  
 Michelson interferometers, 2-375  
 Micrometer, 1-472  
 Microwave, anechoic chambers, 2-391  
 dielectric instrumentation, 2-335  
 dielectrometer, 1-494  
 interferometer, 1-466  
 radar, 1-5  
 reflectometer, 2-353  
 thickness gage, 1-406, 2-351  
 nonmetals, 2-352  
 Millimeter-wavelength radomes, 1-80, 2-135  
 phase data, 2-137  
 wall construction, 1-84  
 Missiles, beamrider, 1-145, 1-146  
 guidance radomes, 1-16  
 homing, 1-142  
 radome, 1-401  
 ellipsoidal, 1-170  
 fabric lay-up, 1-401  
 supersonic, 2-452  
 Mithras erosion simulator, 2-203  
 Modulated scatterer, 1-514  
 Modulus of elasticity, 1-390, 2-389  
 alumina, 2-266  
 "A" sandwich, 2-271

Modulus of elasticity (cont)  
   beryllia, 2-281  
   Pyroceram, 2-272  
 Modulus of rupture, beryllia, 2-280  
   Pyroceram, 2-272  
 Moisture, 1-320  
   effects, 1-478  
 Mold, matched-die, 1-401  
 Molten metal bath, 2-286  
 Molding, matched tool, 1-396  
 Monopulse system, 1-505, 2-138  
   amplitude comparison, 1-203  
   boresight errors, 1-199  
   errors, 1-136  
   radiation pattern difference, 1-135  
   sum radiation pattern, 1-134  
   time sequential systems, 1-136  
 Mosaic alumina construction, 2-269  
 Movable piston phase shifters, 1-509  
 Multilayer sandwiches, 1-239, 2-121  
   "A" sandwich radome, 1-8  
   alumina radome, fabrication, 2-289  
   construction, 2-6  
   panels, 1-38  
   wall radome, 1-273  
 Multiple thickness gage, 1-406

## N

Nacelle, clearance, 1-454  
   lining absorbers, 1-10  
   placement, 1-445  
 Navigation, proportional, 1-144  
 Near-field, amplitude, 1-68  
   measurements, 1-507  
   distribution, 1-230  
   H-plane amplitude, 1-70  
   H-plane phase, 1-70  
   measurements, 1-221  
   phase measurements, 1-507  
   reflection, 1-102  
 Neoprene protective coating, 1-12  
 91-LD Phenolic resin, 2-319  
 No-dome measurements, 1-224  
 Nondimensional time, 1-310  
 Nonoxide ceramics, 2-362  
 Nose blunting, ogival shape, 2-11  
 Nose cone, fused silica, 2-247  
   slotted arrays, 2-144  
 Nose laminar heating, 2-420  
 Nose mounted ogival shaped radomes, 2-438  
 Nose radomes, 1-14, 1-238

Nuclear radiation, 1-321  
 Null shift measurements, 2-352  
 Nypol 46-4001 and 46-4020 acrylic resins, 2-319

## O

Oblique planes, antenna, 1-114  
 Obstacles, antenna, 2-154  
 Offset angle, 2-39  
 Offset run, 1-207  
 Ogive, 1-162  
   fairing, 1-65  
   plastic, 1-358  
   radome, 1-172, 2-433  
     conical fairing, 1-63  
   shape, 2-8  
     nose blunting, 2-11  
 181 glass cloth, 1-390  
 One-half wave wall, 2-117  
 One-half wavelength, multiple, 2-4  
   radome, 2-31  
     thickness, 2-31  
 Open-circuit method, 1-490  
 Operational loads, 2-51  
 Optics, 1-447  
   boresight error prediction, 2-101  
   geometrical, 1-189  
   theory, 1-27  
 Orbital decay reentry, 2-418, 2-426  
 Organic materials, 1-365  
   properties, 1-381  
   resin-fiberglass laminates, 2-441  
 Oxide ceramics, 2-262, 2-361  
 Oxyacetylene burners, 2-252  
 Oxyacetylene test facility, 2-246  
 Oxyhydrogen burners, 2-233  
 Oxyhydrogen rocket motor, 2-243  
 Oxypropane burners, 2-232

## P

Panels, flat (see also "Walls" entries), 2-91  
   homogeneous, 1-567  
   multilayer, 1-38  
 Parabolic shape, 2-8, 2-10  
   antenna, 1-576  
 Parachute, 1-353  
 Parallel laminated glass reinforced plastics,  
   1-388  
 Parallel polarization, 1-32, 1-153, 1-527, 1-573,  
   2-34  
   antenna, 1-153  
 Parallel-ray theory, 1-75

- Parallel-ray transmission, 1-75
- Parameters, antenna pattern, 2-41
- Paraplex P-43, 2-316
- Pass bands, 2-118
- Patches, dielectric, 1-209
- Pattern, antenna, 1-97, 2-114, 2-297, 2-406
  - gore filament, 2-309
  - distortion, 1-101, 2-39
    - plasma antenna, 2-436
    - radar, 1-445, 1-455
    - radome, 1-499
  - scattering, 2-158
- Perforated metal-loaded radome, 2-106
- Permittivity, complex, 1-483
- Perpendicular polarization, 1-28, 1-241, 1-526, 1-573, 2-35, 2-34
- Phantom feed, 1-150
- Phase-amplitude system, 1-136
- Phase comparison, 1-136
  - monopulse system, 1-200
  - four-horn system, 1-506
- Phase data, 2-81, 2-137
- Phase delay, 1-11
- Phase shift, 1-478, 1-509
  - reflection, 1-530
- Phase variation, 2-39
- Phenolic-nylon, Tayloron, 2-449
- Phenolic resin, 1-367, 2-319
  - plyophens 23-017, 2-319
- Phenylsilane resins, 2-320
- Physical design considerations, 2-1
- Physical properties, ceramic materials, 1-427
- Pickup probe, 1-509
  - loading, 1-495
- Pitch stabilization, 1-441
- Placement, radome, 1-445
- Planar heat flow, 2-381
- Plane dielectric sheet, 1-32, 1-526
- Plane dielectric, 1-519
- Plane sheet refraction, 1-66
- Plane-wave, reflection, 1-28
  - refraction, 1-31
  - transmission, 1-28
- Plasma, antenna pattern distortion, 2-436
  - effects, 2-433
  - helium, 2-436
  - inhomogeneous, 2-435
  - jets, 2-235
  - resonance, 2-438
- Plastic-alumina radomes, 2-269
- Plastics, classification, 1-366
  - fiber reinforced, 2-295
- Plastics (cont)
  - glass reinforced, 1-388
  - low-pressure, 1-388
    - reinforcements, 1-374
  - materials, 1-335
    - rain erosion properties, 1-335
  - ogive, 1-358
  - radiation effects, 2-249
  - radomes, fabrication methods, 1-391
    - reinforced, 1-366
- Platform stabilization, 1-440
- Plyophens 23-017 phenolic resin, 2-319
- Plywood radomes, 1-5
- Pointing errors, 1-147, 1-150
- Poisson's ratio, Pyroceram, 2-273
  - slip-cast sintered fused silica, 2-277
- Polarization, 1-50
  - efficiency, 1-177
  - elliptical, 1-50
  - linear, 1-51, 1-168
  - gratings, 2-104
  - incident, 1-153
  - parallel, 1-32, 1-153, 1-527, 1-573, 2-34
  - phenomena, 1-152
  - relative, 1-117
- Polarized incident wave, 1-153
- Polyamide resin, BC1 No. 6601-F, 2-319
  - fiberglass laminate, 2-444
- Polyester, AR-1075-HT, 2-316
  - resins, 1-370, 2-316
  - Selectron, 2-251
  - Vibron, 2-251
- Polyfiber radomes, 1-365
- Polylite ED-386, 2-316
- Polystyrene fiber, 1-7
  - K-band radomes, 1-9
- Polyurethane, 1-339
  - foams, 1-380, 1-400
- Porous alumina, 2-268
- Porous ceramics, 1-424
  - dielectric properties, 1-426
- Post-curing, 1-395
- Power reflection, 1-271
  - coefficient, 2-354
- Power shape, 2-8, 2-10
- Power transmission, "A" sandwich radome, 2-108
  - coefficient, 1-526, 1-532, 2-34, 2-122, 2-357
  - solid-wall radome, 2-119
  - lossless homogeneous plane sheets, 1-49
  - lossless plane dielectric sheet, 1-82

- Power transmission (cont)
  - constant, 1-124, 1-554
  - contours, 2-172
  - minimum, 2-120
    - coefficient, 2-119
  - solid wall radome, 2-120
  - vs. core thickness, 1-544
- Precipitation static, 1-319
- Prefabricated foam wall construction, 1-299
- Preform molding, 1-399
- Pre-impregnation resin bath, 2-305
- Preserved incident component, 1-567
- Pressure, 1-325
  - cast aluminum die, 1-404
  - injection, 1-400
  - load, 2-51
  - slip-casting, 2-287
- Pressurization, 1-439
- Production, beryllia radomes, 2-292
- Protective cover, 2-18
- Pyroceram, 2-34, 2-46, 2-50, 2-260, 2-362, 2-441
  - dielectric constants, 2-274
  - emittance, 2-274
  - loss tangent, 2-274
  - modulus of elasticity, 2-272
  - Poisson's ratio, 2-273
  - sensitivity measurement, 2-355
  - specific heat, 2-274
  - thermal conductivity, 2-273
  - thermal expansion, 2-273

## Q

- Quadripod space frame, 2-150
- Quality control, 2-346

## R

- Radar, airborne, 1-439
  - antenna configuration, 1-166
  - conical scan, 1-132
  - fire control, 1-131, 1-178
  - cross section measurement, 1-154
  - cross section vs. target scattering, 1-156
  - microwave, 1-5
  - pattern distortion, 1-445, 1-455
  - range reduction, 1-99
  - VHF, 1-3
- Radial plane definition, 2-99
- Radiated field, 1-221
- Radiating system, antenna-radome, 1-576
  - flush-mounted, 2-137, 2-142

- Radiation effects, 2-248
  - ceramics, 2-250
  - plastics, 2-249
  - Selectron polyesters, 2-251
  - Vibrin polyesters, 2-251
- Radiation, nuclear, 1-321
- Radiation pattern, far-field, 1-521
- Radiation pattern difference, monopulse
  - antenna, 1-135
- Radiative heat transfer, 2-236
- Radome, airborne, 2-86
  - antenna systems, 1-188
  - anti-icing, 1-15
  - applications, 1-6
  - blanks, alumina, 2-284
    - forming and shaping, 2-286
  - grinding, 2-287
  - blister, 1-9
  - bonding adhesives, 1-376
  - boresight errors, monopulse system, 1-199
    - prediction, 1-17
  - broadband, 2-120, 2-125
  - ceramic, 1-18, 2-259
  - chemical attachment, 2-51, 2-54, 2-56
  - composite, 2-312
  - conical, 1-105, 1-282
  - construction, 1-365, 1-419
  - cylindrical, 1-189
  - de-icing, 1-18
  - depolarization, 1-167
  - diffraction, 1-70
  - dipole feed-through, 2-113
  - double-wall, 1-7, 2-6
  - electrical design problem, 1-6
  - errors, 1-148, 1-502
    - correction, 1-205
    - correction, vector method, 1-214
    - measurement, 1-207
    - monopulse, 1-136, 1-199
    - prediction, 1-187
  - fabrication, 1-391
  - finishes, 1-408
  - geometry, 1-111
  - guidance, 1-16
  - high-temperature, 2-327, 2-358
  - homogeneous, 2-130
  - inhomogeneous, 2-130
  - loft lines, 1-115
  - materials, 1-297, 2-24
    - anisotropic, 1-55
    - inorganic, 1-419
    - magnetic, 1-54

- Radome (cont)
  - materials (cont)
    - organic, 1-381
    - metal-loaded, 2-104, 2-125
    - millimeter-wavelength, 1-80, 2-135
    - missile, 1-401
    - ogival shaped, 1-172, 2-433
    - one-half wavelength, 2-31
    - pattern distorted, 1-499
    - placement, 1-445
    - plastic, 1-391
    - plastic-alumina, 2-269
    - plywood, 1-5
    - polyfiber, 1-365
    - resonant-wall, 2-110
    - sandwich, 1-9, 1-396
      - design curves, 2-173
    - search, 1-97, 1-99
    - semistreamlined, 1-9
    - shape, 1-60, 1-104, 1-297, 2-91, 2-97
      - weight factor, 1-106
    - size, 1-441
      - limitations, 2-48
    - skin temperature, 1-292
    - slotted metal, 2-111
    - solid-wall, 2-117
    - spheroidal, 1-61, 1-63
    - strength factors, 1-297
    - supersonic, 1-16
    - surface inhomogeneities, 1-210
    - transmission efficiency, 1-496
    - reflection, 1-498
    - scattering technique, 1-194
    - structural support, 2-149
    - structural design, 1-281
    - subsonic, 1-282
    - testing, 2-60
    - thick-shell, 2-67
    - thin-shell, 2-31
    - toroidal, 2-250
    - tunable, 2-131, 2-133, 2-135
    - types, 2-3
    - wall, measurements, 1-463
    - wall thickness, electrical, 1-468
    - wedge, 2-104
    - wire grid loaded, 2-106
- Rain, classifications, 2-202
  - environment, 2-201
  - erosion, 1-11, 2-203
    - coatings, 1-335, 1-344
    - mechanism, 1-345
    - plastic materials, 1-335
- Rain (cont)
  - erosion (cont)
    - rain gun, 2-207
    - rocket sled, 2-210
    - simulation, 2-206
    - subsonic, 1-331
    - supersonic, 1-17, 1-331, 1-360
    - test, 1-332
    - test results, 2-228, 2-230
    - time vs. missile velocity, 2-231
    - frequency, 2-201
    - gun, 2-207
    - intensity, 1-355, 2-201
    - particle size distribution, 2-205
    - rate vs. altitude, 2-204
    - resistant materials, 2-203
  - Rainfall, accumulation, 2-202
    - intensity, 1-355
    - rate, 2-202
  - Range, ballistic, 2-209
    - boresight, 2-397, 2-406
  - Ray tracing, 1-189
    - techniques, 1-521
      - boresight error prediction, 2-101
  - Recrystallized glass, 2-362
  - Rectangular waveguide, 1-485
  - Reentry, ballistic, 2-418
    - glide, 2-418
      - vehicles, 2-450
    - orbital decay, 2-418, 2-426
  - Reflection, 1-447, 2-182
    - coefficient, 1-520
      - complex, 1-470
    - interferometer, 2-310
    - loss, 2-38
    - measurement, slotted line method, 1-499
    - near-field, 1-102
    - phase shift, 1-530
    - plane-wave, 1-28
    - radome, 1-498
    - test, 2-350
  - Reflectometer, 1-500, 2-337
    - high-temperature, 2-359
    - microwave, 2-353
  - Refraction, 1-148
    - magnitude, 1-148
    - plane sheet, 1-66
    - plane-wave, 1-31
    - theory, 1-76
  - Refractive shift, 1-54, 1-67
  - Refractoriness, 1-431

Refractory glass, 2-362  
 Reinforced plastic radomes, 1-366, 2-295  
 Reinforcements, plastics, 1-374  
 Resin bath, 2-304  
     hybrid impregnation, 2-305  
     pre-impregnation, 2-305  
     wet-dip, 2-304  
 Resin-fiberglass laminate, polyamide, 2-444  
     organic, 2-441  
 Resins, DER-DEN, 2-318  
     dielectric properties, 2-321  
     epoxy, 1-339, 1-372, 1-403  
     laminating, 1-13  
     melamine, 1-368  
     phenolic, 2-319  
     phenylsilane, 2-320  
     polyester, 2-316  
     preparation, 1-392  
     properties, 2-315  
     silicone, 2-319  
     systems, interlaminar shear values, 2-297  
 Resistance, driving-point, 2-117  
     impact, 1-296, 1-429  
     thermal shock, 2-28  
 Resonance, 1-487  
     plasma, 2-438  
 Resonant cavities, low frequency, 2-378  
     dielectric measurements, 1-494, 2-370  
 Resonant-wall radomes, 2-110  
 R-F generator, 1-495  
 Ribs, metal, 2-151  
 Ring, geometry, 1-219  
     dielectric, 1-208, 1-214  
 Rocket motor exhausts, 2-235  
 Rocket sled, 1-355  
     rain erosion simulator, 2-211  
     test facilities, 2-211  
     test results, 2-213  
     track, SNORT, 2-211  
 Roll run, 1-207  
     fixed polarization, 1-209  
 Roll stabilization, 1-441  
 R-7145 silicone resin, 2-320  
 Rubber boot, 1-317

## S

Sandwich, "A", 1-238, 1-271, 1-544, 1-569, 2-92,  
     2-94  
     construction, 2-5  
     alumina materials, 2-268

Sandwich (cont)  
     "B", 1-238, 1-271  
         construction, 2-5  
         radomes, 1-11, 1-47  
     "C", 1-238, 1-572  
         radomes, 1-47  
     cylindrical, 1-303  
     design, 2-89  
     design curves, 2-173  
     double, 1-563  
     flat, 1-38, 1-301  
     honeycomb, 1-10  
     isotropic, 1-306  
     loaded core, 1-18  
     multilayer, 1-239, 2-121  
     radome, 1-9, 1-396  
         alumina, 2-289  
         construction, 1-378  
         glass reinforced, 1-408  
         multilayer, 1-8  
     single, 2-129  
     symmetrical, 1-41  
     thick-skin, 2-129  
     wall, 1-123, 1-301  
         buckling, 1-301  
         lightweight cores, 1-464  
 Sapphire rod dilatometer, 2-392  
 Scattering, 1-218  
     patterns, 2-158  
     radome error prediction, 1-194, 2-102  
     target, 1-156  
 Screening tests, 2-240  
 Search radomes, 1-97  
     electrical requirements, 1-99  
 Sector scanner, 1-441  
 Selectron 5016, 2-316  
 Selectron polyesters, 2-251  
 Sensitivity measurement, Pyroceram, 2-355  
 Sequential lobing, 1-133  
     comparison, 1-147  
 Shaped-beam antenna, 1-450, 2-155  
 Shapes, anechoic chamber, 2-393  
 Shapes, electromagnetic window, 2-97  
 Shapes, radome, 1-60, 1-104, 1-297, 2-91, 2-97,  
     2-99  
     ellipsoidal, 2-7  
     ogival, 2-8  
     parabolic, 2-8, 2-10  
     power, 2-8  
     requirements, 1-104  
     strength factor, 2-70  
     typical, 2-98



Shear loads, 1-303  
 Shear strength, core, 1-298  
 Shear stress coefficients, 1-303  
 Sheets, dielectric, 1-55  
 Sheffield thickness gage, 2-346  
 Shift, refractive, 1-54  
 Shock front, 1-455  
 Shock testing, 1-327  
 Shock wave, effect, 1-348  
     refraction, 1-458  
 Silica, fused, 2-273  
     vitreous, 2-273  
 Silicate, barium aluminum, 2-443  
     lithium aluminum, 1-424  
 Silicone resin, DC-2106, 1-390, 2-319  
     R-7145, 2-320  
 Silicones, 1-369  
 Simulated isotropic plasma, 2-437  
 Simulation, rain erosion, 2-206  
 Simultaneous lobe comparison, 1-133  
     errors, 1-137, 1-147  
 Single-horn interferometer, 1-465  
 Single-horn reflectometer, 1-470  
 Single-layer walls, 1-464  
 Single sandwich radome, 1-259  
 Single sheet, 1-106  
 Sintered fused silica, 2-260, 2-275  
     finishing process, 2-291  
     radome fabrication, 2-290  
     surface treatments, 2-291  
 Sintering, 2-287  
 Sintering process, fused silica, 2-291  
 Size, radome, 1-441, 2-48, 2-91  
     alumina, 2-288  
 Sizing, glass fabric, 1-375  
 Skin layers, curing, 1-394  
 Skin temperature, alumina radome, 2-246, 2-250  
     transient, 1-287  
 Skin thickness, 1-259  
 Skin tolerance, 1-573  
 Sled, rocket, 1-355  
 Slip-cast, forming, 2-286  
     fused silica, 2-441  
     sintered fused silica, 2-276, 2-278  
         emittance, 2-279  
         Poisson's ratio, 2-277  
         specific heat, 2-278  
         strength, 2-277  
         thermal conductivity, 2-277  
         thermal expansion, 2-278  
 Slip casting, 1-420  
     fused silica process, 2-291  
     pressure, 2-287  
 Slip control, 1-420  
 Slotted arrays, nose cone, 2-144  
 Slotted laminates, 1-338  
 Slotted line, 1-494  
     phase shifters, 1-509  
     radome reflection measurement, 1-499  
 Slotted metal radomes, 2-111  
     transmission coefficient, 2-111  
     transmission loss, 2-112  
 Slotted waveguide, 2-138  
     arrays, TE mode, 2-138  
     arrays, TM mode, 2-138  
 Snell's law, lossless dielectric, 2-173  
 S-994 glass, 2-302  
 SNORT rocket sled track, 2-211  
 Sock process, circ-longo, 2-309  
 Solid sheet, 1-464  
     dielectric, 1-120  
 Solid wall, 1-301  
     buckling, 1-302  
     construction, 2-4  
     dissipation factor, 1-475  
     radome, 1-238, 1-241, 2-117  
         bandwidth, 2-117  
         construction, 1-378  
         design curves, 2-172  
         one-half wave, 2-117  
         transmission coefficient, 2-118  
         transmission curves, 2-128  
 Sonic point heating, 2-421, 2-424  
 Space frames, 2-149  
     quadripod, 2-150  
 Specific heat, air, 1-288  
     alumina, 2-266  
     measurements, 2-384  
 Pyroceram, 2-274  
     slip-cast sintered fused silica, 2-278  
     vs. temperature, beryllia, 2-282  
 Spherical mode transformation, 1-197  
 Spheroid, 1-61  
 Spheroidal lens-radome, 1-79  
 Spheroidal radomes, 1-63  
 Spinel, magnesia-alumina, 1-424  
 Stabilization, 1-439  
     antenna, 1-443  
 Stagnation point, electrical effects, 2-20  
     heating, 2-420  
 Stagnation temperature, 1-285, 2-15, 2-17, 2-46

- Static testing, 1-321
  - elevated temperatures, 1-323
  - instrumentation, pressure, 1-325
- Steatite, 1-420
  - bisque firing, 1-422
  - final firing, 1-422
  - radome batch preparation, 1-420
  - radome casting, 1-421
- Stop bands, 2-118
- Streamlined lens-radomes, 1-77
- Streamlined radomes, 1-66
  - focusing effect, 1-66
- Strength, radome, 1-297, 2-70
  - shape, 2-70
  - slip-cast sintered fused silica, 2-277
  - tensile, 2-385
  - thermal environment, 2-70
  - vs. temperature, alumina, 2-264
- Stress, cylindrical ring, 2-66
  - electromagnetic window, 2-426
  - methods, 1-300
  - rupture, 1-316
  - thermal, 2-44
    - shock, 1-309
  - thick-shell radomes, 2-67
  - thin-shell radome, 2-67
  - variation, 2-68
- Structural design, hypersonic, 2-426
  - radome, 1-281
  - window, 2-416
- Structural factors, 2-47
- Structural requirements, 2-22
- Structural support, 2-149
- Structural testing, high-temperature, 2-239
- Stypols, 2-316
- Subsonic radome, 1-282
- Subsonic rain erosion, 1-334
  - ceramics, 1-340
  - glass, 1-340
- Supersonic aircraft, 2-452
- Supersonic missiles, 2-452
- Supersonic radomes, 1-16
- Supersonic rain erosion, 1-17, 1-360
  - parachute testing, 1-353
  - test methods, 1-351
- Supersonic wind tunnel, 2-232
- Support, axial, 2-149
- Support, effect on rain erosion, 1-338
- Surface-reflection interference, 1-449
- Surface temperature, 2-14, 2-29, 2-419, 2-424, 2-426
  - ballistic reentry, 2-425

- Surface treatment, 2-125
- Surface-wave dielectrometer, 1-494
- Symmetrical sandwiches, 1-41

## T

- Taper, 1-206
- Target depolarization, 1-154
- Target scattering, 1-156
- Tayloron phenolic-nylon, 2-449
- TE mode slotted waveguide arrays, 2-138
- Teflon, 2-319
- Teflon TFE, 2-450
- Temperature, 1-325
  - boundary layer, 1-291
  - distribution, 1-284
  - effects, 1-337, 1-432
  - equilibrium, 1-287
  - high, dielectric materials, 2-362
    - radomes, 1-378, 1-477
    - reflectometer, 2-359
    - structural test setup, 2-239
    - structural testing, 2-239
    - test facility, 2-237
    - testing, 2-358
    - transmission gage, 2-358
  - recovery factor, 1-290
  - skin, 2-287, 2-292
  - surface, 2-14, 2-29, 2-419, 2-424, 2-426
- Tensile strength, 2-385
  - measurement, 2-69
- Tensile thermal stress, 2-17, 2-30, 2-47
- Tension, glass fiber, 2-303
- Tensioner, electromagnetic, 2-303
  - friction, 2-303
  - magnetic, 2-303
- Terminal guidance, 1-143
- Tests, 2-60
  - electrical, 2-32, 2-63
  - elevated temperatures, 1-327
  - environmental, 1-326
  - low temperature, 1-327
  - rain erosion, 1-332
    - results, 2-213, 2-228, 2-230
  - reflection, 2-350
  - rocket sled, 2-211
  - screening, 2-240
  - supersonic rain erosion, 1-351
  - thermal, 2-62
  - thermal shock, 1-326, 2-229
  - through-transmission, 2-350
- Thermal buckling, 1-295

Thermal conductivity, 1-284, 1-429, 2-380  
     air, 1-289  
     alumina, 2-267  
     beryllia, 2-282  
     cut-bar, 2-381  
     Pyroceram, 2-273  
     slip-cast sintered fused silica, 2-277  
 Thermal diffusivity, 2-382  
 Thermal environment, 2-70, 2-416  
 Thermal expansion, 2-390  
     alumina, 2-266  
     beryllia, 2-281  
     ceramic materials, 1-430  
     Pyroceram, 2-273  
     slip-cast sintered fused silica, 2-278  
 Thermal factors, 2-26  
 Thermal properties, 2-62  
     dielectric materials, 2-379  
 Thermal shock, 1-284, 2-429  
     environment, 2-28  
     resistance, 2-28  
     stress, 1-309  
     tests, 1-326, 2-229, 2-240  
         oxyacetylene burners, 2-252  
         oxyhydrogen burners, 2-233  
         oxypropane burners, 2-282  
 Thermal stress, 1-295, 1-313, 2-16, 2-44  
     tensile, 2-17, 2-30, 2-47  
 Thermally reflective rain erosion coatings, 1-344  
 Thermocouple, 1-326  
 Thermolag 500, 2-452  
 Theta patterns, 2-145  
 Thick-shell radomes, stresses, 2-67  
 Thick-skin single sandwich, 2-129  
 Thickness, 2-38  
     core, 1-275, 1-298  
     dielectric, 2-354  
     electrical, 1-478  
     face, 1-298  
     gage, 1-406  
         microwave, 1-406, 2-351  
         null shift measurements, 2-352  
         ultrasonic, 2-348  
     honeycomb core, 1-378, 1-396  
     measurement, 2-311  
     one-half wavelength radome, 2-31  
     sandwich wall, 1-123  
     solid-wall, 1-238  
     thin-wall radome, 2-31  
     tolerance, 1-48, 1-521  
 Thin flat sheets, 1-56  
 Thin homogeneous flat sheet, 1-33  
 Thin-shell radomes, stresses, 2-67  
 Thin wall, 1-120, 2-117  
     construction, 2-4, 2-30  
     radome, 2-31  
 Three-layer "A" sandwich radome, 1-8  
 Three-layer sandwiches, 2-120  
 Through-transmission test, 2-350  
 Tiles, alumina, 2-271  
 Time sequential antenna systems, 1-136  
 Time sequential lobe comparison systems, 1-132  
 Tip radii, 2-29, 2-48  
 TM mode slotted waveguide arrays, 2-138  
 Tolerances, 1-404  
     core, 1-573  
     thickness, 1-48  
 Tooling, 1-401  
 Toroidal radomes, 2-250  
 Transfer molding, 1-400  
 Transformation spherical mode, 1-197  
 Transmission, 1-113, 1-273  
     characteristics, 2-90  
     coefficients, 1-37, 1-520  
         axial ratios, 1-51  
         elliptical polarization, 1-51  
         homogeneous radomes, 2-130  
         inhomogeneous radomes, 2-130  
         lossless plane sheet, 1-85  
         slotted metal radomes, 2-111  
         solid dielectric sheet, 1-119  
         solid-wall radome, 2-118  
         variation, 1-149  
     constant, 2-84  
     contours, 1-106  
         "A" sandwich, 1-43, 2-128  
         solid-wall radome, 2-128  
     efficiency, 1-241  
         radome, 1-496  
         tunable radome, 2-133, 2-135  
     gage, high-temperature, 2-358  
     impedance measurement, 1-486  
         resonance method, 1-487  
     loss, 2-33  
         E-plane, 2-39  
         H-plane, 2-40  
         lens-radome, 1-30  
         slotted metal radome, 2-112  
     millimeter-wavelength radome, 2-136  
     parallel-ray, 1-75  
     plane-wave, 1-28  
     thin wall radome, 2-80

Trapped waves, 1-77, 1-151  
 Tunable radome, 2-131, 2-133, 2-135  
 Turbulence, 1-455, 1-458  
 Turbulent heating, 2-421, 2-424  
 Two-horn interferometer, 1-465

## U

Ultrasonic grinding control, 2-310  
 Ultrasonic thickness gage, 2-348  
 Uniform ground illumination geometry, 1-98  
 Unsymmetrical air loading, 1-282

## V

Vacuum injection, 1-399  
 VC-8359 epoxy resin, 2-315  
 Vehicles, ballistic reentry, 2-451  
   hypersonic, 2-458  
 Velocities, hypersonic, 2-417  
   effect, 1-354  
 VHF radar, 1-3  
 Vibration testing, 1-327, 2-251  
 Vibrational forces, 2-52  
 Vibrin, 2-298  
 Vibrin 185, 2-300  
 Vibrin 135-136A, 2-315  
 Vibrin polyesters, radiation effects, 2-251  
 Vidigage, Branson, 2-848  
 Viscosity, air, 1-290  
 Vitreous silica, 2-273  
   properties, 2-275  
 VSWR evaluation, free-space, 2-405

## W

Waffle core, 1-300  
 Walls (see also "Panels" entries)  
   construction, 1-297, 2-3, 2-23  
     fluted core, 1-299  
     framed-in-place core, 1-299  
     honeycomb, 1-298  
     laminated, 2-5  
     lost wax core, 1-300  
     millimeter-wavelength radome, 1-84  
     prefabricated foam, 1-299  
     solid, 2-4  
     waffle core, 1-300

## Walls (cont)

  dimension tolerances, 1-521  
   gage, electromechanical, 1-478  
   half-wave, 1-121, 1-191, 2-117  
   laminate, 1-478  
   measurements, 1-463  
   sandwich, 1-123, 1-301  
   solid, 1-301  
   thin, 1-120  
   thickness, 1-118, 2-46  
     gage, 2-346  
   tolerances, 1-471, 2-44, 2-80  
 Waveguide, circular, 1-485  
   coaxial, 1-485  
   dielectric measurements, 2-367  
   principles, 1-483  
   rectangular, 1-485  
   slotted, 2-138  
   wall, loss correction, 1-490  
 Wavelength, free-space, 2-38  
 Wedge radome, 1-69, 2-104  
 Weight factor, 1-106  
 Wet-dip resin bath, 2-304  
 Wind tunnel, supersonic, 2-232  
 Window, ablative, 2-429  
   electrical design, 2-416  
   electromagnetic, 2-448  
   flat, 2-431  
   structural design, 2-416  
 Wire grids, 1-59, 2-106  
 Wollastonite, 1-425

## X

X-band, 1-509  
 Xenonlite, conversion, 1-425

## Y

Yaw, stabilization, 1-441

## Z

Zircon, 1-424  
 Zirconia, 2-288  
 Zytol 101 polyamide resin, 2-319

UNCLASSIFIED

Security Classification

DOCUMENT CONTROL DATA - R&D		
<i>(Security classification of title, body of abstract and indexing annotation must be entered when the overall report is classified)</i>		
1. ORIGINATING ACTIVITY (Corporate author)		2a. REPORT SECURITY CLASSIFICATION
Georgia Institute of Technology Atlanta, Georgia		UNCLASSIFIED
		2b. GROUP
3. REPORT TITLE		
TECHNIQUES FOR AIRBORNE RADOME DESIGN		
4. DESCRIPTIVE NOTES (Type of report and inclusive dates)		
Final		
5. AUTHOR(S) (Last name, first name, initial)		
Walton, Jesse D. Jr.,		
6. REPORT DATE	7a. TOTAL NO. OF PAGES	7b. NO. OF REFS
December 1966	520	
8a. CONTRACT OR GRANT NO.	9a. ORIGINATOR'S REPORT NUMBER(S)	
AF33(616)-3279		
a. PROJECT NO.		
4161		
c. Task No.	9b. OTHER REPORT NO(S) (Any other numbers that may be assigned this report)	
416102	AFAL-TR-66-391, Volume II	
10. AVAILABILITY/LIMITATION NOTICES		
This document is subject to special export controls and each transmittal to foreign governments or foreign nationals may be made only with prior approval of AFAL (AVPT), Wright-Patterson AFB, Ohio 45433.		
11. SUPPLEMENTARY NOTES		12. SPONSORING MILITARY ACTIVITY
		Air Force Avionics Laboratory Research and Technology Division Wright-Patterson AFB, Ohio
13. ABSTRACT		
<p>This is the second report on radome design. It was written to provide information on the technological gains made since the first volume was released. Both volumes are intended to provide scientists and engineers working on radomes with a concise reference containing most of the information they will need. Topics covered in this volume are: physical design; electrical design; environmental simulation and testing; materials and construction; evaluation and correction; and hypersonic applications. Comprehensive bibliographies are included. (This abstract is subject to special export controls and each transmittal to foreign governments or foreign nationals may be made only with prior approval of AFAL (AVPT), Wright-Patterson AFB, Ohio.)</p>		

DD FORM 1473

1 JAN 64

UNCLASSIFIED

Security Classification

UNCLASSIFIED

## Security Classification

14 KEY WORDS	LINK A		LINK B		LINK C	
	ROLE	WT	ROLE	WT	ROLE	WT
Reentry Radome Design Techniques Ceramic Radome Techniques Hyperenvironmental Radome Design						

## INSTRUCTIONS

1. **ORIGINATING ACTIVITY:** Enter the name and address of the contractor, subcontractor, grantee, Department of Defense activity or other organization (*corporate author*) issuing the report.

2a. **REPORT SECURITY CLASSIFICATION:** Enter the overall security classification of the report. Indicate whether "Restricted Data" is included. Marking is to be in accordance with appropriate security regulations.

2b. **GROUP:** Automatic downgrading is specified in DoD Directive 5200.10 and Armed Forces Industrial Manual. Enter the group number. Also, when applicable, show that optional markings have been used for Group 3 and Group 4 as authorized.

3. **REPORT TITLE:** Enter the complete report title in all capital letters. Titles in all cases should be unclassified. If a meaningful title cannot be selected without classification, show title classification in all capitals in parentheses immediately following the title.

4. **DESCRIPTIVE NOTES:** If appropriate, enter the type of report, e.g., interim, progress, summary, annual, or final. Give the inclusive dates when a specific reporting period is covered.

5. **AUTHOR(S):** Enter the name(s) of author(s) as shown on or in the report. Enter last name, first name, middle initial. If military, show rank and branch of service. The name of the principal author is an absolute minimum requirement.

6. **REPORT DATE:** Enter the date of the report as day, month, year, or month, year. If more than one date appears on the report, use date of publication.

7a. **TOTAL NUMBER OF PAGES:** The total page count should follow normal pagination procedures, i.e., enter the number of pages containing information.

7b. **NUMBER OF REFERENCES:** Enter the total number of references cited in the report.

8a. **CONTRACT OR GRANT NUMBER:** If appropriate, enter the applicable number of the contract or grant under which the report was written.

8b, 8c, & 8d. **PROJECT NUMBER:** Enter the appropriate military department identification, such as project number, subproject number, system numbers, task number, etc.

9a. **ORIGINATOR'S REPORT NUMBER(S):** Enter the official report number by which the document will be identified and controlled by the originating activity. This number must be unique to this report.

9b. **OTHER REPORT NUMBER(S):** If the report has been assigned any other report numbers (either by the originator or by the sponsor), also enter this number(s).

10. **AVAILABILITY/LIMITATION NOTICES:** Enter any limitations on further dissemination of the report, other than those

imposed by security classification, using standard statements such as:

- (1) "Qualified requesters may obtain copies of this report from DDC."
- (2) "Foreign announcement and dissemination of this report by DDC is not authorized."
- (3) "U. S. Government agencies may obtain copies of this report directly from DDC. Other qualified DDC users shall request through \_\_\_\_\_."
- (4) "U. S. military agencies may obtain copies of this report directly from DDC. Other qualified users shall request through \_\_\_\_\_."
- (5) "All distribution of this report is controlled. Qualified DDC users shall request through \_\_\_\_\_."

If the report has been furnished to the Office of Technical Services, Department of Commerce, for sale to the public, indicate this fact and enter the price, if known.

11. **SUPPLEMENTARY NOTES:** Use for additional explanatory notes.

12. **SPONSORING MILITARY ACTIVITY:** Enter the name of the departmental project office or laboratory sponsoring (paying for) the research and development. Include address.

13. **ABSTRACT:** Enter an abstract giving a brief and factual summary of the document indicative of the report, even though it may also appear elsewhere in the body of the technical report. If additional space is required, a continuation sheet shall be attached.

It is highly desirable that the abstract of classified reports be unclassified. Each paragraph of the abstract shall end with an indication of the military security classification of the information in the paragraph, represented as (TS), (S), (C), or (U).

There is no limitation on the length of the abstract. However, the suggested length is from 150 to 225 words.

14. **KEY WORDS:** Key words are technically meaningful terms or short phrases that characterize a report and may be used as index entries for cataloging the report. Key words must be selected so that no security classification is required. Identifiers, such as equipment model designation, trade name, military project code name, geographic location, may be used as key words but will be followed by an indication of technical context. The assignment of links, rules, and weights is optional.

UNCLASSIFIED

Security Classification